FOSSIL ENERGY

DOE/BC/14942-15
(OSTI ID: 797639)

ADVANCED RESERVOIR CHARACTERIZATION AND EVALUATION OF CO_2 GRAVITY DRAINAGE IN THE NATURALLY FRACTURED SPRABERRY TREND AREA

Final Report
September 1, 1995-July 23, 2002

By:
Bill Knight
David S. Schechter

Date Published: July 2002

Work Performed Under Contract No. DE-FC22-95BC14942

Pioneer Natural Resources
Irving, Texas

National Energy Technology Laboratory
National Petroleum Technology Office
U.S. DEPARTMENT OF ENERGY
Tulsa, Oklahoma

DISCLAIMER

This report was prepared as an account of work sponsored by an agency of the United States Government. Neither the United States Government nor any agency thereof, nor any of their employees, makes any warranty, expressed or implied, or assumes any legal liability or responsibility for the accuracy, completeness, or usefulness of any information, apparatus, product, or process disclosed, or represents that its use would not infringe privately owned rights. Reference herein to any specific commercial product, process, or service by trade name, trademark, manufacturer, or otherwise does not necessarily constitute or imply its endorsement, recommendation, or favoring by the United States Government or any agency thereof. The views and opinions of authors expressed herein do not necessarily state or reflect those of the United States Government.

This report has been reproduced directly from the best available copy.

DOE/BC/14942-15
Distribution Category UC-122

Advanced Reservoir Characterization and Evaluation of CO_2 Gravity Drainage in the Naturally Fractured Spraberry Trend Area

By
Bill Knight
David S. Schechter

July 2002

Work Performed Under DE-FC22-95BC14942

Prepared for
U.S. Department of Energy
Assistant Secretary for Fossil Energy

Dan Ferguson, Project Manager
U.S. Department of Energy
National Energy Technology Laboratory
National Petroleum Technology Office
One West Third Street, Suite 1400
Tulsa, OK 74103

Prepared by
Pioneer Natural Resources
Suite 1400
5205 N. O'Connor Blvd.
Irving, TX 75039-3746

TABLE OF CONTENTS

TABLE OF CONTENTS iii

LIST OF TABLES vii

LIST OF FIGURES x

ABSRACT xix

ACKNOWLEDGEMENTS xxxiii

FINAL TECHNICAL REPORT 1

1. RESERVOIR CHARACTERIZATION 1

1.1 Geological Characterization of the Spraberry Formation 1

1.2 Core-Log Integration for Characterization of the Spraberry Trend Shaly Sands 12

1.3 Acquisition of Horizontal Cores from the Dual Lateral E.T. O'Daniel #28 29

1.4 Fracture Analysis of the E.T. O'Daniel #28 Horizontal Core 37

1.5 Investigation of Fracture Diagenesis from Spraberry Natural Fractures 45

1.6 Application of Rock-Log Model to the Horizontal Core Well 53

1.7 Pay Zone Identification Using "Old" Cased-Hole Logs 61

1.8 Core Interpretation and Sedimentological Analysis 66

1.9 Petrography and Diagenesis 70

1.10 Petrophysics: Combined Rock and Fluid Character 87

1.11 The effects of Mechanical Stratigraphy on Fracture Variability and Reservoir Behavior 106

1.12 Transcending Conventional Log Interpretation – A More Effective Approach for the Spraberry Trend Area 135

2. INVESTIGATION OF CRUDE OIL/BRINE/ROCK INTERACTION 149

2.1 Determination of Initial Water Saturation 149

2.2 Rock Wettability as Determined by Imbibition Experiments 149

2.3 Water-Oil Interfacial Tension Measurements 151

2.4 Water-Oil Capillary Pressure Determination 152

2.5 Comparison of Up-Scaled Imbibition Results to Field Data 161
2.6 Crude Oil/Brine/Rock Interaction at High-Temperature and Pressure Conditions.....182
2.7 Experimental Study of Crude/Brine/Rock Interaction at Reservoir Conditions.....191
2.8 Spontaneous Imbibition Modeling of Sparberry Cores using a Finite Difference Scheme.....212
2.9 Imbibition Flooding Modeling of Artificially Fractured Core.....224

3. RESERVOIR PERFORMANCE ANALYSES.....243
3.1 Scaling Analysis of Water Imbibition Results.....243
3.2 Analysis of Imbibition Mechanism in The Naturally Fractured Reservoirs.....250
3.3 Analysis of Inflow Performance of Spraberry Trend Wells.....271
3.4 Well Productivity During Primary Production.....297
3.5 Well testing Analysis of the E.T. O'Daniel Wells.....315
3.6 Analysis of Step Rate Injection Tests.....325
3.7 Numerical Modeling of Solid Deformation and Stress-Dependent Permeability in Naturally Fractured Reservoirs.....332
3.8 Interference Test Analysis in E.T. O'Daniel Pilot.....349
3.9 Characterization of the Dynamic Fracture Transport Properties in a Naturally Fractured Reservoir.....366
3.10 Review of Water Injection Performance in the Naturally Fractured Spraberry Trend Area, West Texas.....383
3.11 Development of a Fracture Model for Spraberry Field, Texas USA.....398
3.12 Spraberry Reservoir Simulation Model.....418
3.13 Simulation of Tracer Response in E.T O'Daniel Pilot Area.....430
3.14 Hypothetical Two Wells and Multiwell Simulation of E.T O'Daniel Pilot Area.....439
3.15 Full Field Simulation of E.T. O'Daniel Pilot Area.....458
3.16 Analysis of Logging Observation Wells (LOW) in E.T O'Daniel Pilot.....472
3.17 A 10-Acre Field Demonstration Pilot Area.....487

4. INVESTIGATION OF CO2/CRUDE OIL PHASE BEHAVIOR AND RECOVERY MECHANISM BY CO_2 INJECTION IN FRACTURED SYSTEMS 511

4.1 Minimum Miscibility Pressure (MMP) 511

4.2 Interfacial Tension Measurements 512

4.3 Experimental Investigations of CO_2 Gravity Drainage in Fracture Systems 515

4.4 Investigation of CO_2 Gravity Drainage after Water Injection in Fracture Systems 533

4.5 Mathematical Modeling of CO_2 Gravity Drainage 548

LIST OF TABLES

Chapter 1

Table 1.1-1 XRD analysis, parts in 10 6

Table 1.2-1 Log-based rock model 21

Table 1.4-1 Fracture Orientation 41

Table 1.4-2 Fracture Spacing 41

Table 1.5-1 Summary of Naturally Fractured Cores 50

Table 1.6-1 Comparison of Horizontal Cores from the 1U Zone in the E.T. O'Daniel #28 56

Table 1.9-1 Mineralogical averages for point curves of thin sections for six categories of smal scale lithofacies 83

Table 1.9-2 X-Ray diffraction data for clay mineralogy covering all lithologic types in the Spraberry formation 84

Table 1.9-3 A summary of the pore types encountered in SEM samples from the Spraberry formation 84

Table 1.10-1 Summary of grain density data correlated with the major rock types 103

Table 1.10-2 Summary of helium, nitrogen and mercury injection data for plugs of different rock types that form the Spraberry formation 103

Table 1.11-1 Fracture Data Summary 125

Chapter 2

Table 2.4-1 Estimated macroscopic displacement efficiency (E_{dm}) in cores from Spraberry Trend Area Reservoirs 152

Table 2.4-2 Properties of rock and fluids used in 8 completed tests 153

Table 2.4-3 Rock properties and results of water imbibition experiments 153

Table 2.5-1 Rock Properties and Conditions for Imbibition Experiments 174

Table 2.5-2 Reservoir Properties of the E.T. O'Daniel Unit, Spraberry Trend Area, West Texas 174

Table 2.5-3 Alternative Matching Parameters 175
Table 2.6-1 Summary of Results of Imbibition Experiments with Berea Cores and Spraberry Fluids 185
Table 2.6-2 Properties of Fluids Used in the Experiments 185
Table 2.6-3 Contact Angles Measured Using Standard Adsorption Method 186
Table 2.7-1 Physical Properties of the Reservoir Core Samples 198
Table 2.7-2 Composition of Synthetic Spraberry Reservoir Brine 198
Table 2.7-3 Properties of Spraberry Crude Oil 199
Table 2.7-4 Spraberry Crude Oil Composition 199
Table 2.8-1 Core and Fluid Properties 219
Table 2.9-1 Core and Fluid Properties for Berea Core 233
Table 2.9-2 Core and Fluid Properties for Spraberry Core 233
Table 2.9-3 Rock Properties of Spraberry and Berea Cores 234
Table 2.9-4 Critical Injection Rates for Wells in O'Daniel Pilot Area 234
Table 3.2-1 The Average Permeability and Porosity for both Sand Units (1U and 5U) in Spraberry Trend Area Reservoir 262
Table 3.2-2 Evaluation of Water Saturation and Current Oil Saturation 262
Table 3.2-3 Evaluation of Displacement Efficiency (Ed) and Volumetric 262
Table 3.2-4 Reservoir parameters as input data 263
Table 3.2-5 Fracture Spacing 263
Table 3.3-1 Well Productivity Before and After Hydraulic Fracturing Treatment for Primary Production 284
Table 3.3-2 Data Used for Matching Productivity Decline of X. B. Cox A-4 284
Table 3.3-3 Productivity of Depleted Wells in Driver Unit Before and After Large Scale Hydraulic Treatment 285
Table 3.4-1 Parameters Used for Analyzing Performance of Spraberry Trend Area Reservoir Wells in the Driver Unit 307
Table 3.4-2 Production Data of Six Shut-In Test Wells in the Driver Area, Spraberry Trend Area Field, Texas 308
Table 3.4-3 Production Data of Six Regularly Producing Wells in the Driver Area,

Spraberry Trend Area Field, Texas 309
Table 3.51.1 Fracture Propagation 319
Table 3.6-1 Reservoir Parameters 328
Table 3.7-1 Model Parameter Employed 343
Table 3.8-1 Well Coordinates 359
Table 3.8-2 Time and Pressure Matches from Exponential-Integral Curve and Observed Data 359
Table 3.8-3 Well Reservoir Data from E.T. O'Daniel Pilot 359
Table 3.8-4 Interference Test Results 359
Table 3.9-1 Summary of Recent Spraberry Permeability Analyses 374
Table 3.9-2 Spraberry Interference Tests Results 375
Table 3.11-1 Fracture characteristics and permeability contrast, Spraberry Trend area Field 417
Table 3.11-2 Results of Sensitivity Runs; Effect of Different Fracture Aperture and Fracture Height (Using Fracture Orientations from 5U) 418
Table 3.13-1 Schedule of Tracer Injection 433
Table 3.13-2 Summary of Result for the Four High Interwell Responses 433
Table3.13-3 Tracer Breakthrough Velocity for Injector Producer pairs 434
Table 3.16-1 Well Inventory 476
Table 3.16-2 Logging Runs Conducted 476

Chapter 4

Table 4.3-1 Physical Properties of the Core Samples Used in Previous Experiments and Partial Results Obtained 521
Table 4.3-2 Physical Properties of the Core Sample Used in This Experiment. 521
Table 4.3-3 GC Results of the Spraberry Dead Oil Used in The Experiment 522
Table 4.3-4 Experimental Results During Different Stages. 523
Table 4.3-5 GC Results of Different Group Components of Oil Samples Obtained from CO_2 Gravity Drainage/Injection 523
Table 4.3-6 Properties of Oil Samples Obtained from CO_2 Gravity Drainage/Injection 523

Table 4.3-7 Mole Fraction of Oil Samples Obtained from CO_2 Gravity Drainage/Injection....524
Table 4.3-8 Weight Percent of Oil Samples Obtained from CO_2 Gravity Drainage/ Injection....525
Table 4.4-1 Physical Properties of the Core Samples Used in Previous Experiments and Partial Results Obtained....540
Table 4.4-2 Properties of the artificially fractured and non-fractured Berea core samples....541
Table 4.4-3 Comparison of the results from the artificially fractured and non-fractured Berea core samples....541

LIST OF FIGURES

CHAPTER 1

Fig. 1.1-1 Gamma-ray log, porosity and permeability 7

Fig. 1.1-2 Gamma-ray response, porosity and clay content 8

Fig. 1.1-3 Gamma-ray response, porosity and percentage of carbonate 9

Fig. 1.1-4 Porosity and clays plus carbonate percentage 10

Fig. 1.1-5 Relative contributions of percent clay and carbonate 11

Fig. 1.2-1 Log-derived water saturation 22

Fig. 1.2-2 Open-hole log for the DOE pilot well E.T.O'Daniel #37 23

Fig. 1.2-3 Open-hole logs from the E.T.O'Daniel #26 24

Fig. 1.2-4 Open-hole logs from the E.T. O'Daniel # 28 25

Fig. 1.2-5 Cased-hole logs from the E.T. O'Daniel "G" #1 26

Fig. 1.2-6 Effective porosity vs. volume of shale 27

Fig. 1.2-7 Fractured zone identification from logs for E.T. O'Daniel #37 28

Fig. 1.3-1 Division of Spraberry Formation in the central trend area, TXL Fee "B" No. 1 Well) 34

Fig. 1.3-2 Bottom hole coring and orientation assembly 35

Fig. 1.3-3 A schematic diagram showing coring intervals in the E.T. O'Daniel #28 36

Fig. 1.4-1 Orientation of fractures in the 5U reservoir 42

Fig. 1.4-2 Orientation of fractures in the 1U reservoir 42

Fig. 1.4-3 Distribution of fracture spacing 43

Fig. 1.4-4 Correlation between core fracture and wellbore image log fracture 44

Fig. 1.5-1 Type log of Spraberry in the O'Daniel lease 51

Fig. 1.5-2 Schematic diagram of the horizontal cores from the E.T. O'Daniel #28 well 52

Fig. 1.5-3 Summary of fracture characteristics noted in the two horizontal cores from the E.T. O'Daniel #28 well 52

Fig. 1.6-1 Open-hole logs from the horizontal well E.T. O'Daniel #28 57

Fig. 1.6-2 Gamma ray log from the E.T. O'Daniel #28 well, vertical and horizontal logs 58

Fig. 1.6-3 Lithodensity/Neutron crossover log 59
Fig. 1.6-4 Crossplot of volume of shale vs. effective porosity 60
Fig. 1.7-1 Cased-hole logs from the E.T. O'Daniel "G" #1 (Upper Spraberry) 64
Fig. 1.7-2 Effective porosity (NIP) calculated from the old neutron log (API unit) vs. volume of shale 65
Fig. 1.8-1 Depth profiles showing the correlation of gamma ray log with core description for E.T. O'Daniel 37 well 69
Fig 1.9-1 SEM photomicrographs showing different types of illite clay accumulation, dolomite cement, and pyrite occurrence in the Spraberry Formations 85
Fig 1.9-2 Two X-Ray diffractograms showing clay mineralogical composition (C1, I, and K) 86
Fig 1.10-1 Core E.T O'Daniel 37 – Integration of Petrographic and Petrophysics Data 96
Fig 1.10-2 Cross plots illustrate the differences in porosity-permeability correlation for samples above and below 7195 ft depth for E.T. O'Daniel 37 core 97
Fig 1.10-3 Set of porosity-permeability cross plots shows the lithological control upon and k. Shackelford 138-A core(*Data compoiled from Reservoirs Inc. internal report*) 98
Fig 1.10-4 Set of cross-plots showing the lithological control upon porosity and permeability for six large scale lithofacies. Core E.T. O'Daniel 37 99
Fig 1.10-5 Comparison of florescing pay zone and non-pay zones richer in clay content (Shackelford 1-38A) 100
Fig 1.10-6 Non fluorescent zones are commonly lower quality reservoirs and non-reservoir rocks strongly affected by pore lining and pore bridging clays 100
Fig 1.10-7 Porosity vs water saturation from the E.T. O'Daniel 37 and Shackelford 1-38A. 101
Fig 1.10-8 Grain density vs porosity cross-plot suggests strong lithological controls on reservoir quality 102
Fig 1.10-9 Graph showing several curves for Sw and capillary pressure from imbibition experiments done with core plugs from various depths 104
Fig 1.10-10 Three cross-plots presenting mercury injection data correlated with porosity-

permeability and pore throat radius. 105
Fig 1.11-1 Location map, showing the Spraberry trend of West Texas 126
Fig 1.11-2 Stratigraphic column/Gamma-Ray profile through the Spraberry formation in the O'Daniel unit, Midland basin, West Texas. IU and 5U intervals are the main producing reservoir units of the Spraberry trend. The horizontal cores were taken from the thinner sandstones near the tops of the 1U and 5U intervals. 127
Fig 1.11-3 Rose diagrams of fracture strikes in horizontal cores from the O'Daniel #28 well. a) Fractures from the lower cored unit associated with the 5U interval; b) Fractures from the upper cored unit associated with the 1U interval, c) Superimposed rose diagrams of fracture strikes from the upper and lower units. 128
Fig. 1.11-4 Schematic planview of the locations of natural fractures in horizontal core from the upper Spraberry unit, O'Daniel #28 well. (Note: the bedding planes that define lithologic changes are portrayed in side view.) 129
Fig. 1.11-5 Schematic planview of the locations of natural fractures in horizontal core from the lower Spraberry unit, O'Daniel #28 well. (Note: the bedding planes that define lithologic changes are portrayed in side view.) 130
Fig. 1.11-6 Spacing histograms of the three cored Spraberry natural fracture sets. (Shading patterns are keyed to the shading of the rose diagrams in Fig. 3) 131
Fig. 1.11-7 Ideal geometry of a conjugate fracture pair with an extension fracture set that bisects the acute conjugate angle. 132
Fig. 1.11-8 Comparison of the yield strengths for different confining stresses for samples of the upper (1U) and lower (5U) Spraberry siltstone-sandstone units. The lower unit is significantly weaker, causing conjugate fractures to form in this interval whereas extension fractures formed concurrently in the stronger, upper unit. 133
Fig. 1.11-9 Structure contour map on top of the Spraberry formation in the O'Daniel unit area, Midland basin, West Texas. Dashed line is the azimuth of the two horizontal side tracks of the O'Daniel #28 well. 134

Fig 1.12-1 Methodology of analysis 142
Fig 1.12-2 Upper Spraberry model from core studies 143
Fig 1.12-3 Lithology analysis from density neutron cross plot in O'Daniel 37 143
Fig 1.12-4 Determination of matrix density from core 144
Fig 1.12-5 q(x) vs total porosity crossplot 144
Fig 1.12-6 Correlation of porosities to core porosity 145
Fig 1.12-7 Hingle Pickett Interplay 145
Fig 1.12-8 $P^{1/2}$ vs Cumulative frequency (all zones) 146
Fig 1.12-9 Cumulative frequency (water zones) vs $P^{1/2}$ 146
Fig. 1.12-10 Log Interpretation for well #37 147
Fig 1.12-11 Correlation of core porosity with density, sonic and effective porosities from logs 147
Fig 1.12-12 Log Interpretation for 1U zone of well#39 148
Fig 1.12-13 Log Interpretation of 5U zone of well #39 148

CHAPTER 2

Fig 2.4-1 Initial water saturation in Spraberry sandstone 154
Fig.2.4-2 Oil recovery from untreated cores during water imbibition 154
Fig.2.4-3 Oil recovery from cleaned cores during water imbibition 155
Fig.2.4-4 Effect of permeability on final oil recovery 155
Fig.2.4-5 Brine recovery from a cleaned core during oil imbibition. 156
Fig.2.4-6 Final recovery versus corresponding aging time in oil 156
Fig.2.4-7 Effect of aging of core in oil on wettability to water 157
Fig.2.4-8 Diagram of experimental set-up for IFT measurements 157
Fig.2.4-9 J-function calculated from mercury injection capillary pressure data, cores from Shackelford #1-38A 158
Fig.2.4-10 J-function calculated from mercury injection capillary pressure data, cores from Judkins A#5 158
Fig.2.4-11 J-function calculated from mercury injection capillary pressure data, cores from Judkins A#5 and Shackelford #1-38A 159

Fig.2.4-12 Estimated water-oil capillary pressure in Spraberry sand 159
Fig.2.4-13 Measured and estimated (from mercury injection pressure data) drainage water-oil pressure in Spraberry 1U and 5U pay sand 160
Fig.2.5-1 An analogue model for imbibition waterflooding in naturally fractured reservoirs with spontaneous imbibition acting as the rate-limiting step 175
Fig.2.5-2 Oil recovery curves obtained from water imbibition under ambient conditions 176
Fig.2.5-3 Brine recovery curve obtained during oil imbibition on core sample from the Spraberry Trend Area 176
Fig.2.5-4 Oil recovery curves obtained from water imbibition under reservoir temperature and pressures 177
Fig.2.5-5 Comparison of drainage capillary pressure curves obtained using various methods for core samples from the Spraberry Trend Area 177
Fig.2.5-6 Comparison of imbibition capillary pressure curves obtained using various methods for core samples from the Spraberry Trend Area 178
Fig.2.5-7 Oil recovery curves from Fig. 2.5-2 plotted using dimensionless variables 178
Fig.2.5-8 Comparison between composite imbibition oil recovery curves obtained from Berea sandstone and Spraberry Trend Area reservoir sandstone 179
Fig.2.5-9 Match between imbibition scaling model and production decline data from the E.T. O'Daniel Unit, Spraberry Trend Area 179
Fig.2.5-10 A typical image of oil drop attachment in contact angle measurement 180
Fig.2.5-11 Comparison between imbibition model calculated oil recovery and observed oil recovery from the E.T. O'Daniel Unit, Spraberry Trend Area 180
Fig.2.5-12 Match between imbibition model calculated oil recovery and observed oil recovery from the Humble pilot, Spraberry Trend Area. 181
Fig.2.5-13 Comparison between imbibition scaling model and production decline data from the Humble pilot, Spraberry Trend Area 181
Fig.2.6-1 Density and viscosity of Spraberry crude oil versus temperature 186
Fig.2.6-2 IFT of Spraberry brine/cruide oil at elevated pressures 187
Fig.2.6-3 Thermal expansion of Spraberry crude oil 187

Fig.2.6-4 Imbibition oil recovery at different temperatures. 188
Fig.2.6-5 Imbibition oil recovery at different pressures 188
Fig.2.6-6 Imbibition oil recovery under different aging conditions 189
Fig.2.6-7 Imbibition oil recovery from cores with different initial water saturations 189
Fig.2.6-8 Normalized imbibition oil recovery curves from cores with different initial water saturations 190
Fig.2.7-1 Schematic experimental program....200
Fig.2.7-2 Variation in viscosity of synthetic Spraberry brine with temperature increase....201
Fig 2.7-3 Variation in density of synthetic Spraberry brine with temperature increase 201
Fig 2.7-4 Variation in viscosity of Spraberry oil with temperature increase....202
Fig 2.7-5 Variation in density of Spraberry oil with temperature increase....202
Fig 2.7-6 Interfacial tension of Spraberry oil-brine at elevated pressure....203
Fig 2.7-7 Interfacial tension of Spraberry oil-brine at elevated temperature....203
Fig 2.7-8 Thermal expansion of Spraberry oil....204
Fig 2.7-9 Spontaneous imbibition apparatus 204
Fig 2.7-10 Effect of elevated pressure on rate of imbibition and recovery using Berea sandstone....205
Fig 2.7-11 Effect of changing temperature on rate of imbibition and recovery using Berea sandstone....205
Fig 2.7-12 Effect of temperature in imbibition tests 206
Fig 2.7-13 Effect of temperature changes on oil recovery by imbibition 206
Fig 2.7-14 Oil recovery curve obtained from imbibition experiment performed at reservoir temperature 207
Fig 2.7-15 Effect of aging time on the recovery of oil by imbibition....207
Fig 2.7-16 Total recoery versus aging time to exclude the effects of aging time on the recovery mechanism....208
Fig 2.7-17 Effect of aging time on total recovery at elevated temperatures....208
Fig 2.7-18 Wettability Index to water versus aging time for the different experiment temperatures....209
Fig 2.7-19 Effect of initial water saturation on oil recovery by imbibition....209

Fig 2.7-20 Effect of initial water saturation on total recovery....210
Fig 2.7-21 Effect of permeability on recovery by imbibition....210
Fig 2.7-22 Effect of permeability on total oil recovery....211
Fig 2.8-1 Imbibition capillary pressure obtained from matching spontaneous imbibition data....219
Fig 2.8-2 Matching between spontaneous imbibition experiments with numerical solution using 0.2 S_{or}....220
Fig 2.8-3 Non linear diffusion co-efficient....220
Fig 2.8-4 Effect of different capillary pressures on oil volume recovered....221
Fig 2.8-5 Effect of different oil relative permeabilities on oil volume recovered....221
Fig 2.8-6 Effect of different water relative permeabilities on oil volume recovered....222
Fig 2.8-7 Effect of different oil viscosities on oil volume recovered....222
Fig 2.8-8 Effect of different water viscosities on oil volume recovered....223
Fig 2.8-9 Effect of different initial water saturations on oil volume recovered....223
Fig 2.9-1 Concept of dynamic imbibition process....235
Fig 2.9-2 Experimental setup of dynamic imbibition....235
Fig 2.9-3 Relative permeability curves....236
Fig 2.9-4 Schematic representation of matrix and fracture where the viscous and capillary forces are effective....237
Fig 2.9-5 Matching between experimental data and the numerical solution (Berea core - cumulative water production, injection rate = 4.0 cc/hr)....237
Fig 2.9-6 Matching between experimental data and the numerical solution (Berea core - cumulative oil production, injection rate = 4.0 cc/hr)....237
Fig 2.9-7 Matching between experimental data and the numerical solution (Spraberry core - cumulative water production, injection rate = 1.0 cc/hr)....238
Fig 2.9-8 Matching between experimental data and the numerical solution (Spraberry core - cumulative oil production, injection rate = 1.0 cc/hr)....238
Fig 2.9-9 Capillary pressure obtained as a result of matching experimental data (Berea and Spraberry cores)....239
Fig 2.9-10 Reproducibility of the dynamic imbibition flooding results in Berea

sandstones 239
Fig 2.9-11 Oil recovery from fractured Berea cores during water injection using different injection rates 240
Fig 2.9-12 Watercut during the dynamic imbibition experiments for fractured Berea cores 240
Fig 2.9-13 Oil recovery from fractured and unfractured Spraberry cores during water injection, using different injection rates 241
Fig 2.9-14 Watercut during the dynamic imbibition experiments for fractured and unfractured Spraberry cores 241
Fig 2.9-15 Injection rate vs. oil cut (TOP/TFP) 242
Fig 2.9-16 E.T. O' Daniel pilot area 242

CHAPTER 3

Fig.3.1-1 Imbibition oil recovery from cleaned Spraberry cores 247
Fig.3.1-2 Dimensionless imbibition oil recovery curves 247
Fig.3.1-3 Calculated imbibition oil recovery for Spraberry reservoirs 248
Fig. 3.1-4 Calculated imbibition oil recovery for 5U Unit, Upper Spraberry 248
Fig. 3.1-5 Oil-water relative permeability curves for Spraberry sands 249
Fig. 3.1-6 Calculated imbibition oil recovery for 5U Unit, Upper Spraberry 249
Fig. 3.2-1 Oil recovery curves obtained under reservoir condition 264
Fig.3.2-2 Averaging of imbibition using the Aranofsky equation 264
Fig. 3.2-3 Porosity and absolute permeability of upper Spraberry 1 U unit versus depth 265
Fig. 3.2-4 Porosity and absolute permeability of upper Spraberry 5 U unit versus depth 265
Fig. 3.2-5 Calculated imbibition oil recovery for five years of waterflooding from Upper Spraberry 1 U formation 266
Fig. 3.2-6 Calculated imbibition oil recovery for five years of waterflooding from Upper Spraberry 5 U formation 266
Fig. 3.2-7 History of waterflooding recovery profiles from upper Spraberry 1 U formation 267
Fig. 3.2-8 History of waterflooding recovery profiles from upper Spraberry 5 U

formation 267
Fig. 3.2-9 Calculated imbibition oil recovery for 40 years of waterflooding from spraberry 1 U and 5 U formation 268
Fig. 3.2-10 Initial water saturation in the spraberry reservoir 268
Fig. 3.2-11 Effect of matrix permeability on oil recovery mechanism 269
Fig. 3.2-12 Effect of matrix permeability on calculation of production rates 269
Fig. 3.2-13 Effect of fracture spacing on recovery mechanism 270
Fig. 3.2-14 Effect of matrix permeability and fracture spacing on decline rate constant 270
Fig. 3.3-1 Matching between calculated and actual productivity for Cox A-4 285
Fig. 3.3-2 Calculated and actual productivity for Davenport B-5 286
Fig. 3.3-3 Calculated and actual productivity for Davenport B-7 286
Fig. 3.3-4 Calculated and actual productivity for Davenport C-6 287
Fig. 3.3-5 Calculated and actual productivity for Davenport C-8 287
Fig. 3.3-6 Calculated and actual productivity for Bryans A-2 288
Fig. 3.3-7 Calculated and actual production rates in Driver Unit waterflood 288
Fig. 3.3-8 Calculated and actual productivity indices 288
Fig. 3.3-9 Calculated pressure distribution along a stress-insensitive fracture 288
Fig. 3.3-10 Calculated pressure distribution along a stress-sensitive fracture 288
Fig. 3.3-11 A model to interpret cyclic waterflooding performance 290
Fig. 3.3-12 Geometry of a reservoir drained by a wing of a fracture 291
Fig. 3.4-1 Initial water saturation in the Spraberry Trend Area as a function of rock permeability 310
Fig. 3.4-2 Water-oil relative permeability curves for the spraberry trend area 310
Fig. 3.4-3 Oil-gas relative permeability curves for the spraberry trend area 310
Fig. 3.4-4 Calculated and actual oil production rates for Davenport C-6 Driver unit 311
Fig. 3.4-5 Calculated and actual oil production rates for Davenport C-8 Driver unit 311
Fig. 3.4-6 Calculated and actual oil production rates for Davenport B-5 Driver unit 311
Fig. 3.4-7 Calculated and actual oil production rates for Davenport B-7 Driver unit 312
Fig. 3.4-8 Calculated and actual oil production rates for X.B. Cox A-4 Driver unit 312
Fig. 3.4-9 Calculated and actual oil production rates for J.C. Bryans A-2 Driver unit 312

Fig. 3.4-10 Calculated and actual oil production rates for Davenport C-5 Driver unit.....313
Fig. 3.4-11 Calculated and actual oil production rates for Davenport C-10 Driver unit.....313
Fig. 3.4-12 Calculated and actual oil production rates for Davenport B-8 Driver unit.....313
Fig. 3.4-13 Calculated and actual oil production rates for Davenport B-14 Driver unit.....314
Fig. 3.4-14 Calculated and actual oil production rates for X.B. Cox A-5 Driver unit.....314
Fig. 3.4-15 Calculated and actual oil production rates for J.C. Bryans A-1 Driver unit.....314
Fig. 3.5-1 Step rate test (SRT) design for O'Daniel injection well 46.....319
Fig. 3.5-2 Plot of injection pressure versus cumulative time for O'Daniel well 46.....320
Fig. 3.5-3 Radial Odeh & Jones plot for well 46.....320
Fig. 3.5-4 Pressure versus cumulative injection during SRT O'Daniel well 46.....321
Fig. 3.5-5 Odeh & Jones linear time plot for O'Daniel well 46.....321
Fig. 3.5-6 Step rate test history of O'Daniel well 47.....322
Fig. 3.5-7 Pressure/time history plot for O'Daniel well 47.....322
Fig. 3.5-8 Cumulative injection plot during SRT on O'Daniel injection well 47.....323
Fig. 3.5-9 Odeh & Jones multirate radial plot for O'Daniel well 47.....323
Fig. 3.5-10 Odeh & Jones multirate linear time plot for O'Daniel well 47.....324
Fig. 3.6-1 Well configuration in E.T. O'Daniel Pilot.....328
Fig. 3.6-2 Step rate injection test for O'Daniel well 46.....329
Fig. 3.6-3 Step rate injection test for O'Daniel well 47.....329
Fig. 3.6-4 Multi-rate analysis of SRIT O'Daniel well 46.....330
Fig. 3.6-5 Multi-rate analysis of SRIT O'Daniel well 47.....330
Fig. 3.6-6 Match between simulation result and observation data for SRIT O'Daniel well 46.....331
Fig. 3.6-7 Effect of injection rate on fracture propagation and stress sensitivity.....331
Fig. 3.7-1 Two-dimensional fracture-matrix idealization.....343
Fig. 3.7-2 Permeability reduction curve as function of pore pressure from humble pilot simulation.....344
Fig. 3.7-3 Solid displacement distribution in x-direction at 20 days.....344
Fig. 3.7-4 Fracture pressure distribution at 20 days.....345
Fig. 3.7-5 Effective stress distribution in x-direction at 20 days.....345

Fig. 3.7-6 Reduction of effective fracture permeability in the x-direction 346
Fig. 3.7-7 Reduction of effective fracture permeability in the y-direction 346
Fig. 3.7-8 Flow rate as a function of bottomhole pressure from the conventional simulator 347
Fig. 3.7-9 Flow rate as a function of bottomhole pressure from the stress dual-porosity simulator 347
Fig. 3.7-10 Comparison of performance of conventional and stress dual porosity simulators 348
Fig. 3.8-1 Well configuration in E.T. O'Daniel pilot 360
Fig. 3.8-2 E.T. O'Daniel pilot producers BHPBU overlay during pulse and interference tests 361
Fig. 3.8-3 Pressure responses against normalized distance from observation wells 362
Fig. 3.8-4 Dimensionless pressure for a single well in an infinite system 363
Fig. 3.8-5 Type curve matches of data from observed wells (injection in well 47) and the line source solution 364
Fig. 3.8-6 Type curve matches of data from observed wells(injection in well 45) and the line source solution 364
Fig. 3.8-7 Anisotropic trend estimated from active well 47 is N65W 365
Fig. 3.8-8 Anisotropic trend estimated from active well 45 is N65W 365
Fig. 3.9-1 Maps of units Local to Midkiff and E.T. O'Daniel pilot 376
Fig. 3.9-2 Petrophysical analysis 377
Fig. 3.9-3 Section 4 of the E.T. O'Daniel Lease 378
Fig. 3.9-4 Well 47 SRT profiles showing breakdown pressure, fracture propagation pressure and fracture closure 378
Fig. 3.9-5 Well 46 Earlougher SRT Analysis 379
Fig. 3.9-6 Well 47 Earlougher SRT Analysis 380
Fig. 3.9-7 Bottomhole pressure at each of the observation wells 380
Fig. 3.9-8 Map of communication path 381
Fig. 3.9-9 Well 40 square-root plot for Earlougher, direct fracture analysis 381
Fig. 3.9-10 Well 47 Post-interference Falloff test 382

Fig. 3.9-11 Direct fracture causes pressure response at well 40 382
Fig. 3.10-1 Line drive pattern configuration in anisotropic reservoirs 390
Fig. 3.10-2 Units and reservoir extent in the Spraberry trend area 390
Fig. 3.10-3 Atlantic Richfield waterflood pilot 1952 391
Fig. 3.10-4 Humble water injection pilot in the Spraberry Midkiff unit 1955 392
Fig. 3.10-5 Production and injection data for the Humble pilot 393
Fig. 3.10-6 Waterflood Map, O'Daniel Unit Co-Op Flood 1959 394
Fig. 3.10-7 Performance of O'Daniel Unit Co-Op waterflood 395
Fig. 3.10-8 Areas developed for waterflood expansion in Spraberry Driver unit, 1960 395
Fig. 3.10-9 Map of O'Daniel pilot area and pilot well configuration 396
Fig. 3.10-10 Response to water injection for 7 on-trend and 23 off-trend wells 397
Fig. 3.11-1 Map of Spraberry trend illustrating location of the E.T. O'Daniel lease 407
Fig. 3.11-2 Division of Spraberry formation in the central trend area 408
Fig. 3.11-3 Schematic diagram of Spraberry fracture system 409
Fig. 3.11-4 Azimuth of FMS Anomalies from Judkins A#5 and Perston #37 well 409
Fig. 3.11-5 Humble deviated well showing fracture behaviour and pattern 410
Fig. 3.11-6 Fracture length frequency of Delaware outcrop data 410
Fig. 3.11-7 Fracture map of Delaware outcrop data 411
Fig. 3.11-8 O'Daniel interference test 411
Fig. 3.11-9 O'Daniel interference test with arrows noting the strength of the response and horizontal well fracture 412
Fig. 3.11-10 Humble interference test 412
Fig. 3.11-11 Injection profile log on well 45 413
Fig. 3.11-12 Fracture pathways inferred from Tracer tests 414
Fig. 3.11-13 Brunson D1 tracer produced vs time 415
Fig. 3.11-14 Fraction of injected stream influencing production wells on sulfate sampled 415
Fig. 3.11-15 Steps involved in development of a DFN model 416
Fig. 3.11-16 Calculation of Directional permeability 416
Fig. 3.12-1 Map of Spraberry showing location of the Humble waterflood pilot 423
Fig. 3.12-2 Comparison between observed water injection rate and simulation result 424

Fig. 3.12-3 Comparison between observed water production rate and simulation result.....424
Fig. 3.12-4 Comparison between observed BHP and simulation result.....425
Fig. 3.12-5 Match between observed water cut and simulation result.....425
Fig. 3.12-6 Effect of reservoir size on simulating two wells in Humble waterflood pilot.....426
Fig. 3.12-7 Effect of reservoir size on well performance during high water injection rate.....427
Fig. 3.12-8 Effect of fracture permeability on well performance during high water inj rate.....428
Fig. 3.12-9 Effect of different well orientation on oil recovery during high water injection rate.....429
Fig. 3.13-1 Response of surrounding wells on Tracer Injection at E.T. O'Daniel pilot area.....434
Fig. 3.13-2 Typical and actual tracer responses.....435
Fig. 3.13-3 Schematic of Fracture orientation as a Result of tracer injection.....435
Fig. 3.13-4 Effect of grid size in 35degree orientation with Kx/Ky = 100/15000.....436
Fig. 3.13-5 Effect of on-trend permeability on Breakthrough time.....436
Fig. 3.13-6 Effect of on-trend permeability on Peak concentration.....437
Fig. 3.13-7 Effect of off-trend permeability on Breakthrough time for 43 degree orientation.....437
Fig. 3.13-8 Effect of off-trend permeability on Peak concentration for 43 degree orientation.....438
Fig. 3.13-9 History match result.....438
Fig. 3.14-1 Location of Brunson C-2 amd Brunson E-1 in the O'Daniel Lease.....442
Fig. 3.14-2 Production performance of Brunson C-2.....443
Fig. 3.14-3 Production performance of Brunson E-1.....443
Fig. 3.14-4 1/8" area pattern grid block used in the simulation.....444
Fig. 3.14-5 Oil rate and injection rate constraints of Brunson C-2.....444
Fig. 3.14-6 Water rate match between actual and simulation result of Brunson C-2.....445
Fig. 3.14-7 Gas Production rate match between actual and simulation result of Brunson C-2.....445
Fig. 3.14-8 Oil rate and injection rate constraints of Brunson E-1.....446

Fig. 3.14-9 Water rate match between actual and simulation result of Brunson E-1 446
Fig. 3.14-10 Top structure and well location.....447
Fig. 3.14-11 Fracture permeability enhancements to match the performance of the individual wells.....448
Fig. 3.14-12 Water saturation distribution at the end of the simulation.....449
Fig. 3.14-13 Oil rate constraints of Boone A-1 450
Fig. 3.14-14 Water rate match between actual and simulation result of Boone A-1.....450
Fig. 3.14-15 Oil rate constraint of Brunson C-2.....451
Fig. 3.14-16 Water rate match between actual and simulation result of Brunson C-2.....451
Fig. 3.14-17 Oil rate constraint of Brunson E-1 452
Fig. 3.14-18 Water rate match between actual and simulation result of Brunson E-1 452
Fig. 3.14-19 Oil rate constraint of McClintic E-1 453
Fig. 3.14-20 Water rate match between actual and simulation result of McClintic E-1 453
Fig. 3.14-21 Oil rate constraint of McClintic E-32 454
Fig. 3.14-22 Water rate match between actual and simulation result of McClintic E-32 454
Fig. 3.14-23 Oil rate constraint of ET O Daniel-13.....455
Fig. 3.14-24 Water rate match between actual and simulation result of ET O Daniel-13.....455
Fig. 3.14-25 Oil rate constraint of ET O Daniel-30.....456
Fig. 3.14-26 Water rate match between actual and simulation result of ET O Daniel-30.....456
Fig. 3.14-27 Water injection rate constraint of ET O Daniel-10W 457
Fig. 3.15-1 Units and Reservoir Extent in the Spraberry trend area.....463
Fig. 3.15-2 Map of O'Daniel pilot area and pilot well configuration.....464
Fig. 3.15-3 Response to water injection for On-trend and Off-trend wells outside the O'Daniel pilot area.....465
Fig. 3.15-4 Simulation result from the hypothetical model.....465
Fig. 3.15-5 Structural map for the simulation model 466
Fig. 3.15-6 3D simulation model for the O'Daniel pilot area 467
Fig. 3.15-7 Wells matched in and around the pilot area after introducing the fractures 468
Fig. 3.15-8 Injectivity improved for the injector O'Daniel 37W.....468
Fig. 3.15-9 Injectivity improved for the injector O'Daniel 48W.....469

Fig. 3.15-10 Improved water cut response for the producer O'Daniel 38 469
Fig. 3.15-11 Wells matched after introducing existing fractures 470
Fig. 3.15-12 Simulation model after introducing existing fractures 471
Fig. 3.15-13 Map of fracture saturation at the end of the 471
Fig. 3.16-1 Neutron porosity and resistivity profile of well 49(jan-mar) 477
Fig. 3.16-2 Neutron porosity and resistivity profile of well 49(jan-aug) 478
Fig. 3.16-3 Neutron porosity and resistivity profile of well 50(mar-jun) 479
Fig. 3.16-4 Neutron porosity and resistivity profile of well 50(mar-aug) 480
Fig. 3.16-5 Relative and cumulative frequency of well 49 in 1U layer 481
Fig. 3.16-6 Relative and cumulative frequency of well 49 in 5U layer 482
Fig. 3.16-7 Relative and cumulative frequency of well 50 in 1U layer 483
Fig. 3.16-8 Relative and cumulative frequency of well 50 in 5U layer 484
Fig. 3.16-9 Cumulative frequency distribution of NPHI from well 49 in all zones 485
Fig. 3.16-10 Cumulative frequency distribution of NPHI from well 50 in all zones 485
Fig. 3.16-11 Cumulative frequency distribution of NPHI from well 49 in clean zones only 486
Fig. 3.16-12 Cumulative frequency distribution of NPHI from well 50 in clean zones only 486
Fig. 3.17-1 E.T. O'Daniel pilot map area 493
Fig. 3.17-2 Comparison between on-trend and off-trend production rate of upper Spraberry in the ET O'Daniel pilot 494
Fig. 3.17-3 On-trend incremental oil recovery of upper Spraberry in the ET O'Daniel pilot 494
Fig. 3.17-4 Percentage of CO_2 produced in the interior well and ET O'Daniel A-1 495
Fig. 3.17-5 Total water injection maintained during water and CO_2 injection 495
Fig. 3.17-6 Gas production rate in the interior well and ET O'Daniel A-1 496
Fig. 3.17-7 Total production rate in the interior well and ET O'Daniel A-1 496
Fig. 3.17-8 Comparison between amount of CO_2 injection and CO_2 production 497
Fig. 3.17-9 Comparison between amount of water injection and water production 497
Fig. 3.17-10 Volume of water injection until on-trend production wells start responding 498
Fig. 3.17-11 Comparison between oil produced from interior wells to ET O'Daniel 498
Fig. 3.17-12 Oil rate and gas rate performances of ET O'Daniel 499

Fig. 3.17-13 Water rate performances produced from interior wells to ET O'Daniel 499
Fig. 3.17-14 Hydrocarbon mol fractions of the OD A-1 at different sampling data 500
Fig. 3.17-15 Hydrocarbon mol fractions of the ET O'Daniel #38 at different sampling data.....500
Fig. 3.17-16 Hydrocarbon mol fractions of the ET O'Daniel #39 at different sampling data.....501
Fig. 3.17-17 Hydrocarbon mol fractions of the ET O'Daniel #40 at different sampling data.....501
Fig. 3.17-18 Relative enrichment of the C-1 component in interior wells to O'Daniel A-1.....502
Fig. 3.17-19 Relative enrichment of the gas component in interior wells to O'Daniel A-1.....502
Fig. 3.17-20 Amount of CO_2 fraction in off-trend wells during CO_2 injectioo.....503
Fig. 3.17-21 Amount of CO_2 fraction in on-trend wells during CO_2 injection 503
Fig. 3.17-22 Relative enrichment of the C-1 component in on-trend wells 504
Fig. 3.17-23 Relative enrichment of the gas component in on-trend wells.....504
Fig. 3.17-24 Oil rate history in ET O'Daniel A-1 before and after CO_2 injection 505
Fig. 3.17-25 Decline curve analysis 505
Fig. 3.17-26 Cumulative oil production after the base line with different decline rate.....506
Fig. 3.17-27 Decline curve analysis taken after waterflooding started in the pilot area..... 506
Fig. 3.17-28 Cumulative oil production after the base line with different decline rate taken after waterflooding conducted in the pilot area.....507
Fig. 3.17-29 Logging observation well response.....508
Fig. 3.17-30 Temperature Log response indicating the regions at which CO_2 is entering the formation.....509

CHAPTER 4

Fig 4.2-1 Measured densities of CO_2/oil systems at reservoir temperature of 138°F.....513
Fig 4.2-2 Effect of pressure on IFT of two CO_2/oil systems at 138°F.....513
Fig 4.2-3 Relationship between density difference and IFT for two CO_2/oil systems at 138°F.....514
Fig 4.3-1 Oil recovery curves obtained from the five experiments with different

permeabilities and initial water saturations....526
Fig 4.3-2 Effect of permeability on oil recovery of CO_2 injection....526
Fig 4.3-3 Effect of initial water saturation on oil recovery of CO_2 injection....527
Fig 4.3-4 Set-up for water and CO_2 gravity drainage experiment....527
Fig 4.3-5 Oil and water producing history during the experiment....528
Fig 4.3-6 Oil recovery curve for the whole experiment....528
Fig 4.3-7 Oil and water saturation history and oil recovery curve....529
Fig 4.3-8 Oil recovery and volume of CO_2 used during CO_2 drainage....529
Fig 4.3-9 Mole fraction of oil samples from CO_2 gravity drainage....530
Fig 4.3-10 Weight percent of components of oil samples from CO_2 drainage....530
Fig 4.3-11 Mole fraction of component groups of oil samples during CO_2 drainage....531
Fig 4.3-12 Weight percent of component group of oil samples during CO_2 drainage....531
Fig 4.3.13 Average molecular weight and density of oil samples from CO_2 drainage....532
Fig 4.3-14 Oil recovery curves vs. rock permeability of the six experiments....532
Fig 4.4-1 Oil recovery curves obtained from the previous six experiments with different permeabilities and initial water saturations....542
Fig 4.4-2 Sketch of the fractures split on Core #7....542
Fig 4.4-3 Sketch of the fractures split on Core #8....543
Fig 4.4-4 Water and oil produced during CO_2 gravity drainage for Core #7....543
Fig 4.4-5 Oil recovery by CO_2 gravity drainage for Core #7....544
Fig 4.4-6 Water and oil produced during CO_2 gravity drainage for core #8....544
Fig 4.4.7 Oil recovery by CO_2 gravity drainage for Core #8....545
Fig 4.4-8 Oil recovery with correction of Cores #7 and #8....545
Fig 4.4-9 Comparison of oil recoveries obtained during CO_2 gravity drainage from the artificially fractured cores and non-fractured core....546
Fig 4.4-10 Weight composition of oil samples produced during CO_2 drainage....546
Fig 4.4-11 Changes of C_{11+} component distribution in weight % versus CO_2 injection time....547
Fig 4.4-12 Changes of average molecular weights of C_{11+} components with time....547
Fig 4.5-1 Solution to demarcator and recovery for Fs = 1....559

Fig 4.5-2 A typical solution for demarcator (zd) movement and recovery (R) 559
Fig 4.5-3 Model calculated dimensionless gas concentration diffusing into rock matrix from fracture faces 560
Fig 4.5-4 Comparison of calculated recoveries with experimental data 560
Fig 4.5-5 Comparison of calculated recovery with experimental data, CO_2/oil gravity drainage in a 500md Berea Core.....561
Fig 4.5-6 Comparison of calculated recovery with experimental data, CO_2/oil gravity drainage in a 50md Berea Core.....561
Fig 4.5-7 Comparison of calculated recovery with experimental data, CO_2/oil gravity drainage in a 0.01md Berea Core.....562

ABSTRACT

The goal of this project is to assess the economic feasibility of CO_2 flooding the naturally fractured Spraberry Trend Area in west Texas. This objective is being accomplished through research in four areas: 1) extensive characterization of the reservoirs, 2) experimental studies of crude oil/brine/rock (COBR) interactions in the reservoirs, 3) reservoir performance analysis, and 4) experimental investigations on CO_2 gravity drainage in Spraberry whole cores. This provides results of the final year of the six-year project for each of the four areas.

In the first area, reservoir characterization has been established based on petrophysical and geological analysis combined with core-log integration. A shaly sand rock model for describing the Spraberry Trend Area Reservoir has been established, and as a result, a better log interpretation algorithm for identifying Spraberry pay zones has been developed.

We have completed the reservoir characterization, which includes matrix description, and pay zone detection (from core-log integration), and fracture characterization. The first horizontal core ever taken from the Spraberry as part of this project proved beyond a doubt that Spraberry pay sands are densely fractured with not one, but three sets of natural fractures with varying orientations. The coring operation, description of the horizontal core, diagenesis investigation of fracture faces, along with application of our rock-log model to open-hole logs from the horizontal well. We have also included our analysis, which allows application of the rock-log model to old cased hole logs.

We have completed the reservoir characterization, which includes matrix description, and pay zone detection (from core-log integration), and fracture characterization. We have provided a detailed analysis of petrography and diagenesis of the varying rock types. We have extended the classification of rock types and finally we have developed relationships between depositional features, petrophysical parameters and reservoir quality.

We have extended the fracture characterization, which provides a detailed analysis of the effect of mechanical stratigraphy on fracture variability and reservoir behavior.

Finally in this area, we have improved water saturation calculations for the Spraberry reservoirs by integrating extensive geological, physical and petrophysical data into a modern shaly-sand log interpretation model. The results provide recommendations for logging suites that will allow a better description of the water saturation in pay zones.

In the second area, COBR interaction in the Spraberry matrix has been analyzed based on results of laboratory experiments. Initial water saturation and historical water saturation in the Spraberry sands has been determined to be between 0.20 and 0.40 depending on permeability of the sand. Macroscopic displacement efficiency during water imbibition has been estimated to be about 50%. Wettability of the Spraberry sands has been determined. The Amott wettability index to water was estimated to be about 0.55 indicating that the Spraberry sands are weakly water wet. Water-oil capillary pressure has been established. The experimental capillary pressure curve confirms the rock wettability

determined based imbibition test. Interfacial tension (IFT) between Spraberry oil and brine has been measured to be 32 mN/m. Experimental results have been used in analytical and numerical reservoir simulations.

We have completed extensive imbibition experiments at room and reservoir conditions. The experimental results clearly indicate that the weakly water-wet behavior of the reservoir rock may have been responsible for poor waterflood response observed in many Spraberry fields. We have also explored the effect of reservoir conditions on wettability determination in the Spraberry. It was found that brine imbibition rate was accelerated by elevated temperature and delayed by elevated pressure. Aging condition in oil decelerated brine imbibition while the wettability index to water was essentially unchanged. Comparison has been made between the up-scaled imbibition data and production decline in areas of E.T O'Daniel lease and Humble pilot. Consistency between the up-scaled imbibition data and production decline in the two areas was observed indicating that low permeability weakly-water-wet reservoirs is the major mechanism for the waterflood recovery.

We have conducted a detailed investigation of both static and dynamic imbibition at reservoir temperature. We have demonstrated that there is a significant difference between modeling static imbibition and dynamic imbibition experiments. Our results suggest that static imbibition tests do no reproduce the behavior characteristic of dynamic conditions that prevail in the reservoir. We have used a numerical, commercial simulator (ECLIPSE) in order to demonstrate the difference in the two experimental procedures. We have completed static and dynamic imbibitions, both experiments and modeling. The results were used to determine the critical injection rate during waterflooding in naturally fractured reservoirs. An equation to determine the critical injection rate was developed to scale up laboratory results to field dimensions. We found that optimization of the injection rate is important prior to conducting waterflooding in naturally fractured reservoirs. As the flow rate increases, contact time between matrix and fluid in fracture decreases, thereby reducing the effectiveness of capillary imbibition. The imbibition transfer is more effective for low injection rates due to lower viscous forces and longer contact time with the matrix. Increasing injection rate beyond the critical injection rate causes high water cut, which results in significantly faster water breakthrough.

In the third area, performance of the Spraberry reservoirs has been explored based on reservoir characterization and laboratory investigations. Scaling of imbibition oil recovery results to reservoir geometry indicates that higher oil recovery should have been achieved during water flooding, although the Spraberry sands are weakly water wet. Reasons for the poor performance of water flood were analyzed. Inflow performance of Spraberry Trend wells has been analyzed using a new mathematical model developed for wells intersecting long fractures. Computer simulation of a Spraberry waterflood pilot has been conducted using laboratory measured parameters to understand Spraberry waterflood performance.

We have made significant progress in analytical and numerical simulation of performance in Spraberry reservoirs. Reservoir performance has been analyzed through skin analysis in the Driver Unit wells, anisotropic fracture permeability response as indicated by pressure test data, and numerical reservoir simulation. Application of a

newly developed steady-flow-model to wells in the Driver Unit indicated that fluid damage to the rock matrix is unlikely a crucial issue, while fracture permeability may have altered due to pressure decline during oil production.

Buildup and step-rate tests have been analyzed to further characterize the reservoir and define the proper reservoir management strategy. The buildup tests were taken at E.T. O'Daniel Wells 38, 39, and 40. The analysis shows that the calculated permeability is in the range of 0.01-0.04 md. The pressures determined from these tests are low and below the MMP necessary for CO_2 flood. The step rate injection test to obtain formation parting pressures were conducted in the new well injection wells E.T O'Daniel 46 and 47. The parting pressure is conservatively estimated to be 2215 psia. The Analysis also indicates that the fracture may propagate during the test.

The step rate injection tests were conducted in the new injection wells E.T O'Daniel 46 and 47. The SRITs were conducted prior to the multi-well interference test to determine the formation parting pressure. The analysis clearly demonstrates that the fractures are stress-sensitive, one of the phenomena that influence the performance of waterflooding in Spraberry Trend Area. The fracture parting pressure (FPP) was also calculated using equation derived by Salazar and Kumar. The calculated FPP values were then compared to the values obtained from the Step Rate Test analysis. The interference tests were performed to determine the location of well candidates for CO_2 injectors. The schematic procedures to analyze the interference tests by diagnostic plots and by using interference analysis with two observation wells are given in this report. The result from this study reveals that the E.T. O'Daniel pilot exhibits both isotropic and anisotropic behaviors, depending on the degree of permeability ratio calculated at a particular position within the pilot area.

We have described that the fracture length and fracture connectivity (permeability) change due to pressure and stress effects based on a number of field tests done on Spraberry wells. The field tests included constant pressure decline rate tests, build up tests, step-rate tests, falloff tests and a multi-well interference tests. The tests were carried out to minimize the risk of induced fractures, which can cause reduced sweep efficiency and fluid losses to other non-pay zones. Results indicate that the fracture systems are very stress-sensitive in the Spraberry formation, with fractures opening and the effective permeability increasing at high injection rates.

We conducted Humble pilot simulation in order to derive necessary parameters used for simulating waterflood and CO_2 injections in the E.T O'Daniel pilot. We have determined the on trend and off trend fracture permeability and recommended where to place the production wells relative to the fracture trend to have a fast and good waterflood response. We performed another simulation study to analyze the response of surrounding wells on tracer injection in the E.T O'Daniel pilot. The objective of this study is to determine the fracture orientation and fracture permeability by matching the tracer response (breakthrough time and peak concentration) collected from producing wells. The analysis shows only four tracer concentrations near or exceeding 100,000 ppt in producing wells due to tracer injection. The remaining wells have only shown weak tracer response or the tracer wave is just beginning to arrive at the well. In the three wells with high peak tracer concentration, tracer shows up in a few days after tracer injection. Tracer breakthrough in this short time is usually indicative of fast communication in the

reservoir via isolated natural fractures or extremely high permeability and thin intervals. The results of the tracer simulation confirm fracture permeability is extremely high and highly anisotropy. In addition, the fracture orientation obtained from the tracer study is similar with the average orientation obtained from natural fracture counts in horizontal core acquired in a near-by well.

Information from our previous study has been included into our full-field ET O'Daniel Pilot Area simulation. The methods described here can be used to investigate areas of Spraberry where little or no water injection has occurred. The results of this work will provide a method to assess the economic feasibility of large-scale water injection in the remainder of the field. It is possible to match most of the wells in the O'Daniel field simulation by using the permeability anisotropy (K_x/K_y), permeability enhancement and fracture orientation obtained from the tracer simulation in the O'Daniel field model. It was also observed that the fracture trend obtained from this study show similar direction as obtained from the interference test and horizontal core analysis.

In the last part of this section, we discuss the progress of the CO_2 pilot project through the interpretation of logs from the observation wells in the E.T O'Daniel CO_2 flood pilot. The purpose is to monitor the movement of CO_2 and saturation changes of oil, water and gas in the upper Spraberry interval of E.T O'Daniel wells. Finally, the field activity during CO_2 injection in the E.T. O'Daniel Pilot is reported in this section.

In the fourth area, efficiency of CO_2 gravity drainage has been investigated based on laboratory experiments. Minimum Miscibility Pressure (MMP) was measured to be 1,550 pisg. IFT of the CO_2/Spraberry oil under reservoir conditions was determined. The IFT at the MMP is about 1.5 mN/m. We have completed several suites of CO_2 gravity drainage experiments in Spraberry and Berea whole cores at reservoir conditions. The results of these experiments have been useful in developing a mathematical model for free-fall gravity drainage and have validated our premise that CO_2 will recover oil from tight, unconfined Spraberry matrix. Carbon dioxide gravity drainage experiments have been performed using two more reservoir cores. One of the experiments was conduced with a simulated fracture around the whole core under high water saturation in the core. The other experiment was conducted using a whole core with natural fractures under gravity-stable displacement conditions. The result indicates that free water in the core reduced the efficiency of CO_2 gravity drainage. The efficiency of CO_2 injection decreases as permeability decreases and initial water saturation increases. Cyclic CO_2 injection could enhance oil recovery during CO_2 gravity drainage process. Temperature does not have a significant effect on oil recovery during the CO_2 gravity drainage process.

ACKNOWLEDGMENTS

This work has been financially supported by the United States Department of Energy's National Petroleum Technology Office and the following consortium of companies; Chevron, Marathon Oil Co., Mobil Research and Development Corp., Mobil E&P USA, Pioneer Natural Resources (formerly Parker and Parsley Petroleum Co.), Petroglyph Operating Co., Texaco E&P Technology Dept., The Wiser Oil Co. and Union Pacific Resources. This support is gratefully acknowledged. Geographix Inc. donated software used in reservoir characterization. GeoQuest donated ECLIPSE software used in reservoir simulation. I greatly appreciate diligent efforts from the following individuals who contributed to this project: Erwinsyah Putra, Tanvir Chowdhury, Dickman Alfred, Vivek Muralidharan and Gokul Lakshman of Texas A&M University, R.O. Baker and Rupam Bora of Epic Consulting Ltd., Paul McDonald, William H. Knight, Paul Leonard and Carl Rounding of Pioneer Natural Resources (USA) Inc.

The authors would like to show our appreciation to the Spraberry CO_2 pilot team for their enthusiasm and lively discussions. Richard Baker, President of Epic Consulting Ltd., Paul M^{c}Donald, William H. Knight and Tracy Heckman of Pioneer Natural Resources and Steve Melzer continue to lead the team. Other acknowledgments go to Eric Denbina of Epic Consulting, Paul Leonard of Pioneer and Loren Stiles. In addition we recognize the contributions and spirit of Lincoln Elkins in pioneering many of the practical techniques used today in naturally fractured reservoirs.

David S. Schechter
Texas A&M University
June 2002

FINAL TECHNICAL REPORT

1. RESERVOIR CHARACTERIZATION

1.1. Geological Characterization of the Spraberry Formation

Introduction

Spraberry reservoirs are typically low porosity, low permeability fine sandstones and siltstones that are interbedded with shaly non-reservoir rocks. Large scale geological characterization of Spraberry reservoirs has in general been limited to definition of reservoir targets based primarily on the shape and strength of the gamma ray response (GR).[1] Some information has been published on lithology and reservoir heterogeneity,[2] but there has been very limited work performed concerning detailed description and understanding of individual reservoirs and units within the Spraberry. Basing reservoir models primarily on gamma response has several drawbacks: different amounts and types of clays emit different levels of radioactivity, distortion in GR response can be caused by the presence of potassium feldspar, micas, and accessory minerals like rutile and zircon, and, GR curves provide little information on the presence of porosity-occluding authigenic minerals like calcite and quartz. Therefore, one can either erroneously assume that all high gamma response units are poor quality reservoirs, or that all low gamma responses correspond to clean sandstone, when neither may be true. To accurately define relationships between lithology, reservoir quality, and log response, various techniques were used to examine the Spraberry Trend Area reservoir and non-reservoir rocks.

During the first year, most work has been directed at understanding the vertical heterogeneity of lithofacies. Cores from three Upper Spraberry wells were evaluated by various techniques including X-ray diffraction (XRD) analysis, Scanning Electron Microscopy (SEM), petrographic analysis, detailed minipermeameter analysis, and log evaluation. The three main wells that have been used as a sources of information for geological characterization are the Arthur Judkins A#5, the Shackelford 1-38A, and the E.T. O'Daniel #37.

Core Analysis

Detailed lithologic studies of cores were performed using a variety of techniques. Petrographic thin sections were cut from cores from three wells. An attempt was made to obtain representative material from all the various lithologies, however most of the thin sections were made from the reservoir portions of the Spraberry 1U unit. Point counts were made from most thin sections to assess framework and cement mineralogy. Diagenetic features were described. Additional detailed analysis of certain portions of the core were made by XRD and SEM analysis. XRD was done to determine clay mineralogy and the relative proportions of clay minerals within the various rock types, also to identify fracture-filling minerals. Scanning electron microscopy was used to examine pore structure and also to perform qualitative identification of various mineral

phases. Minipermeameter measurements were performed using a close spacing of half to one inch separation between measurements. This close spacing of measurements allowed for observation of permeability variability at small scales, as well as creating relatively long sequences of measurements in a log profile type showing larger scale behavior that is easily correlated with wireline logs. An analysis of the relationship between log behavior and reservoir quality is presented, using supporting evidence from the core analysis.

Results

Figures 1.1-1 through **1.1-5** present a series of log profiles for the petrographic data, minipermeameter measurements, and gamma ray logs from the Shackelford 1-38A core that cover the 1U unit (7083-7093 ft) of the Upper Spraberry. Also included are cross-plots for some petrographic data showing the principal quality controls on porosity. Figure 1.1-1 shows log tracks of permeability, porosity, and the gamma ray log. It can be seen that there is a reasonably close relationship between the porosity and the gamma ray curve, however not everywhere does the high gamma ray (usually corresponding to high clay content) correspond to a low porosity. The same can be seen from a permeability/gamma ray plot. The two arrows in the porosity plot point to depths that, by gamma ray curve interpretation alone, would be probably considered to be an oil saturated sand unit. A look at porosity logs shows that these zones are also low porosity and should not be included in net pay calculations.

By examination of log profiles of various components, it is possible to determine lithologic variations that correlate to the gamma ray response. Figure 1.1-2 shows a log of porosity, gamma ray response, and percent clay (determined by point count). High gamma ray values, in general, correspond to high percentages of clay. Especially in tracking the sandy ten feet of the 1U unit (7083-7093 ft) along each log, it is noticeable that the sections with lowest amounts of clay have the highest overall porosities of the 1U. The two sand peaks and the high GR of the shale layer in between are easily correlated to the clay content derived from petrographic data and the minipermeameter measurements. However, at 7076 feet, there is a GR low that corresponds to a region of lower porosity. In Figure 1.1-3, it can be seen that a high percentage of carbonate cement is completely occluding the porosity of this layer. Figure 1.1-4 combines both the carbonate and clay matrix. As can be seen, the log track of the combined totals of percent clay and carbonate very closely parallel the track of porosity with depth.

Figure 1.1-5 shows a comparison of the relative contributions of percent clay matrix and percent carbonate cement to the overall reservoir porosity degradation. It can be seen that there is a reasonably well defined trend of increasing clay and decreasing porosity. The contribution of carbonate cement is less obvious, but it is clear that rocks with a high proportion of carbonate cement usually have low porosities and indeed there are a few layers within the 1U that are almost entirely carbonate. Gamma logs alone will not provide enough information to define these zones, and additional logs are necessary in order to delineate the best reservoir rocks within the Spraberry. Data from core analysis agree well with the log analysis presented in the following section. If effective porosity is

plotted against shale volume, it is found that there are three basic groups of rock in the Upper Spraberry: one with porosity <7% and shale volume >15% (mostly mudstones and siltstones), one with porosity <7% and shale volume <15% (dolostones and dolomitic siltstones), and the reservoir pay zones that have shale volume of <15% and porosity >7%. Additionally, log and core analysis demonstrates that the best pay zone targets are most probably those that show considerable thickness, good porosities and a low GR response. Thin layers showing very low GR values are very common within the stratigraphic column but these are not considered to be significant contributors to overall reservoir quality because of their relatively insignificant volume and the fact that many of the low gamma ray zones are also low porosity carbonate-rich layers.

Diagenesis

Detailed petrographic analysis of diagenetic events has not yet been completed. Preliminary results showing results of XRD investigations on clay mineralogy are presented here.

Clay Diagenesis

Hoffman and Hower[3] proposed a time-temperature model for illitization of smectite with increase of depth. Such models have been found applicable to other geologic and petroleum studies of sedimentary rocks and basins of Miocene age or older,[4,5] thus should apply to the Permian-aged Spraberry. In a previous study of the Spraberry Formation, Houde[6] mentioned that XRD analysis of rocks contained primarily illite and kaolinite. Part of Houde's investigation is a very complete study on source bed geochemistry of the shales in the Spraberry Formation. In this work, Houde calculated temperatures from the present geothermal gradient of the area, which indicate that the minimum temperature at which the Spraberry was exposed is at least 63°C and could be as much as approximately 77°C near the base of the core studied. His kerogen coloration data agrees well with the previous geothermal gradient calculated temperatures, which showed that the Spraberry was exposed to temperature ranges at which initial generation of oil should begin. The temperature information suggests that the potassic clays in the Spraberry Formation should have compositions smectite to randomly-ordered mixed illite/smectite (R=0 (I/S)) region, assuming that clay behavior is similar to Gulf Coast models of smectite diagenesis.[7]

In the present study, however, clay assemblages (Table 1.1-1) show very small amounts of smectite and illite/smectite mixed layer (typical of the ordering range mentioned above) clays. Instead illite and chlorite are more abundant. These results are supported by additional XRD data from Reservoirs Inc. for the E.T. O'Daniel # 37 and Shackelford # 1-38A wells, and suggest that perhaps Spraberry clays may have been exposed to higher burial temperatures than previously believed. There are several alternate explanations. Smectite may have been relatively insignificant in abundance in the original detrital sediments. Additionally, brine chemistry and pressure are also important controls on clay diagenesis and can accelerate or slow various reactions. Without a more complete study of polytypes assemblages and clay mineralogy data from younger and older rocks

within the stratigraphic sequence as well as age equivalent rocks of different burial depths, it is difficult to interpret properly clay mineralogy data.

Some lines of evidence do relate the clay mineralogy of this formation to diagenetic alteration of smectitic detrital clays with increase with burial depth and temperature. First, the geological setting of a basin fill rich in argillaceous material and organic matter is a common setting for highly smectitic clays.[8] Second, there is a significant amount of partially dissolved or altered K-feldspar to provide a source of potassium necessary to drive the reaction of smectite to illite. This reaction in turn liberates a number of cations such as Si, Mg, Ca, and Fe. The assemblage of diagenetic minerals within the Spraberry rocks examined (to be discussed in more detail in future reports) includes quartz, dolomite, and ferroan dolomite. These cements could easily be byproducts of the smectite/illite conversion. Also, organic matter present might be associated with the production of acidic fluids and CO_2 that in turn are responsible for widespread dissolution of grains and cements (secondary porosity enhancement). Although the temperatures found[9] are considered good enough for a first stage of ordering polytypes (smectite-to-R=0 I/S) (based on Hoffman and Hower model[3]), the assemblages of clays found in our study with dominant amounts of illite and chlorites and absence of good amounts of expandable layers, resembles better the higher temperature polytypes. This ambiguity could be solved by pursuing XRD analysis of unoriented samples, and sample examination of younger and older strata.

Fracture Diagenesis

Study of the diagenesis of natural fractures can provide useful information about the timing of natural fractures, as well as something of the nature of the fluids and relationships to cements in the matrix rock. Fractures within the Spraberry Formation are both mineralized and unmineralized; to date, two samples of mineralized fractures have been examined petrographically, as well as two unmineralized fractures.

Paragenesis of a large (>1 mm wide) mineralized fracture, recovered from a depth of 7088 feet in Shackelford # 1-38A consists of the following sequence:

After fracturing, a thin layer of minerals was precipitated on fracture walls. This layer consisted of quartz and dolomite in subequal proportions, with dolomite being more abundant. The minerals were precipitated into void space, as evidenced by the presence of many euhedral crystal faces and terminations, only possible where minerals are growing into unoccupied (or fluid-filled) space. This early generation of mineralization utilized the grains of the matrix as nucleation sites, quartz growing on detrital quartz grains and dolomite growing on detrital and authigenic dolomite within the matrix. When examined by UV fluorescent light microscopy, it is clear that there are at least two generations of dolomite cement within the sample aside from the original detrital carbonate grains; one generation (the first) has a brownish fluorescence while the second generation does not fluoresce. It is nonfluorescing dolomite that forms one of the early fracture cements, whereas fluorescing dolomite comprises a significant proportion of the dolomite in some thin sections. The early fracture mineralization only comprises a layer

about one crystal thick within this fracture.

The bulk of the mineralized fracture is comprised of the mineral barite ($Ba(SO)_4$), a common fracture-filling mineral. The barite may possibly have replaced precursor quartz and dolomite, there are inclusions of both minerals within the fracture. As well as inclusions of these minerals, the barite contains numerous 2-phase fluid inclusions (liquid and vapor phase). In one area of the thin section, a fourth mineral phase is present as a surface lining on the barite crystals. This is a very fine-grained, highly birefringent material. It may be very finely crystalline dolomite, anhydrite, clay (unlikely), or possibly even some kind of drilling mud; it is too fine-grained to be identified with certainty through standard petrographic microscopy. The smooth, draping quality of this coating indicates possible deposition from a liquid (as opposed to growth as a crystal), and it could possibly be some component of the drilling mud.

A second thin section from Sun Oil Co. Hutchinson #7 contained several hairline fractures that were both mineralized and unmineralized. The mineralization in the fractures appears to be exclusively nonfluorescing carbonate, possibly dolomite, and no barite was seen. This thin section contained numerous fossil echinoderm fragments which may have been a source of Ca for fracture mineralization. The unmineralized fracture terminated against the mineralized one, suggesting formation at a later period. More fractures will need to be examined before any significant conclusions can be drawn concerning fracture timing, sources of cementation, and relationships between mineralized and unmineralized fractures and lithology.

Fracture Model

Reasons for fracturing may be varied, but one possible model is that fracturing was caused by overpressuring. The gradual increase in burial depth produced an increase in compaction, pressure, and temperature. The Spraberry Formation is dominantly fine clay material with minor amounts of fine sands and siltstones, a typical lithologic environment for production of significant overpressuring. Clay sediments mixed with organic matter are characterized by having the highest initial porosity. Burial compaction and diagenesis of this material usually results in almost total destruction of porosity within the clay sediments accompanied by a remendous loss of fluids. At the same time the principal vertical stresses are being increased by burial, the pore pressure mainly within the sandy, less porous and more competent layers of the formation are increasing because of migration of a large volume fluid derived from shale dewatering and possible diagenesis. These conditions probably caused the necessary reduction of principal effective stresses to a level where enough unconfinement[7] is created to give way to fracturing. Pressure solution features, typical of overpressured sands, have been found during petrographic analysis. Also, matrix free sandy siltstones and very fine sandstones show the effect of compaction and grains show both flat and concave-convex contacts.

References

1. Tyler, N., and Gholston, J.C.: " Heterogeneous Deep-Sea Fan Reservoir, Shackelford and Preston Waterflood Units, Spraberry Trend, West Texas," Report of Investigation No. 171, Bureau of Economic Geology, The University of Texas, Austin, 1988.
2. Guevara, E.H.: "Geological Characterization of Permian Submarine Fan Reservoirs of the Driver Waterflood Unit, Spraberry Trend, West Texas," Report of Investigation No. 172, Bureau of Economic Geology, The University of Texas, Austin, 1988.
3. Hoffman, J. and Hower, J., 1979. Clay mineral assemblages as low grade metamorphic geothermometers: application to the thrust faulted disturbed belt of Montana, U.S.A., in: Scholle, P. A. and Schluger, P.R. (eds.) Aspects of Diagenesis. SEPM Special Publication No. 26, p. 55-79.
4. Pollastro, R. M., 1989, Clay Minerals as Geothermometers and Indicators of Thermal Maturity--Application to Basin History and Hydrocarbon Generation, AAPG Bull., v. 73, No. 9, p. 1171.
5. Lanson, B., Champion, D, 1997, The I/S-To-Illite Reaction in the Late Stage Diagenesis, Am. J. Sci., Vol 291, p. 473-506.
6. Houde, R.F., 1979: Sedimentology, diagenesis, and source bed geochemistry of the Spraberry sandstone, subsurface Midland basin, west Texas. Unpub. MS thesis, U. Texas Dallas.
7. Boles, J., and Franks, S., 1979: Clay diagenesis in Wilcox sandstones of southwest Texas: implications of smectite diagenesis on sandstone cementation: J. Sed. Petrol. v. 49, p. 55-70.
8. Eslinger, E. and Pevear, D., 1988: Clay Minerals: SEPM Short Course Notes No. 22., SEPM, Tulsa OK.
9. Lorenz, J.C., Teufel, L. W. and Warpinksi, N.R., 1991: Regional fractures 1: A mechanism for the formation of regional fractures at depth in flat-lying reservoirs. AAPG Bull, V. 75, no. 11, p. 1714-1737.

Table 1.1-1— XRD Analysis, Parts in 10

Depth (ft)	illite	chlorite	kaolinite
7069.4	4	1	1
7081.6	2	1	1
7082.6	2	1	1
7083.5	3	2	1
7085.7	2	1	---
7087.4	4	1	1
7090.6	3	1	---
7092.1	3	1	---

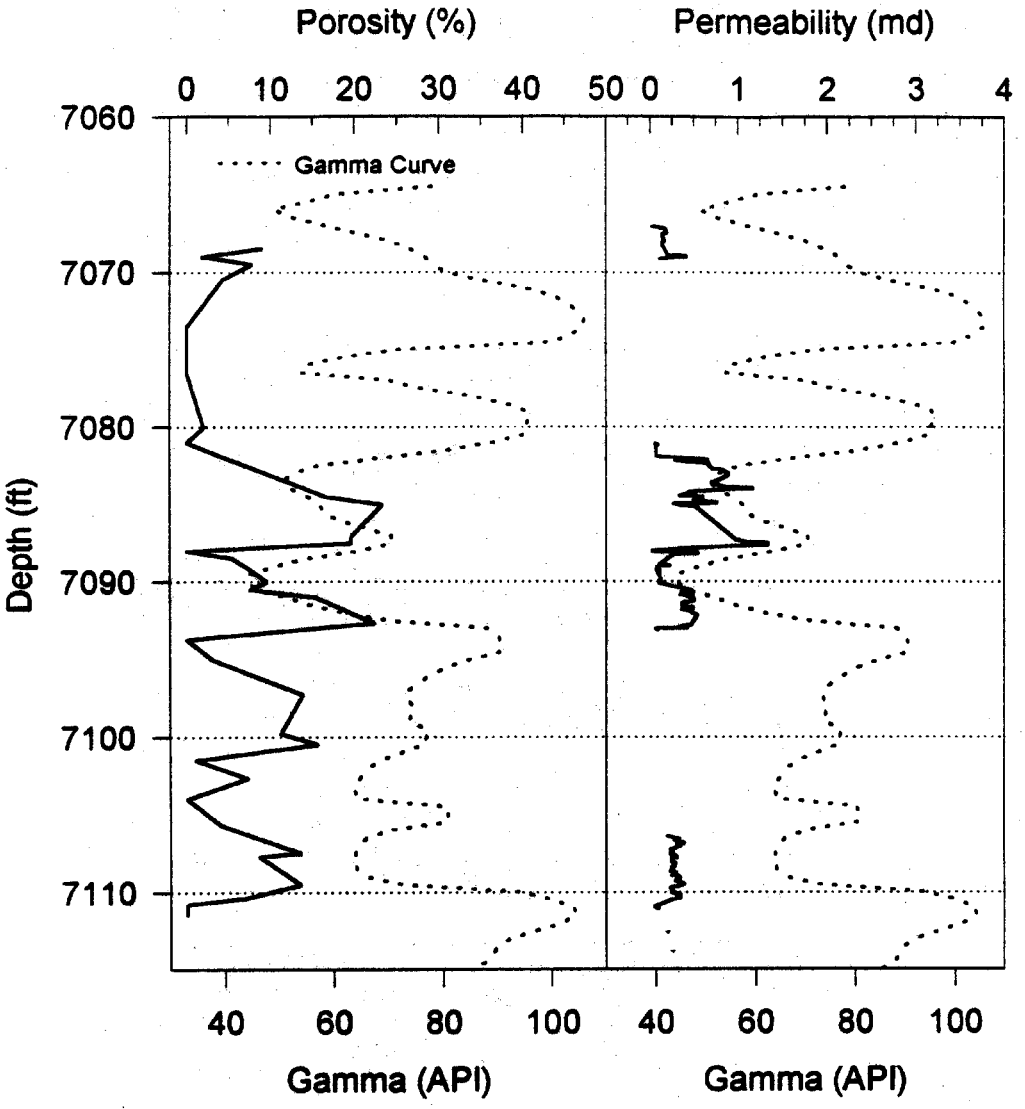

Fig. 1.1-1—Log tracks of permeability, porosity, and the gamma ray. 1U pay sand occurs from 7082-7092 ft.

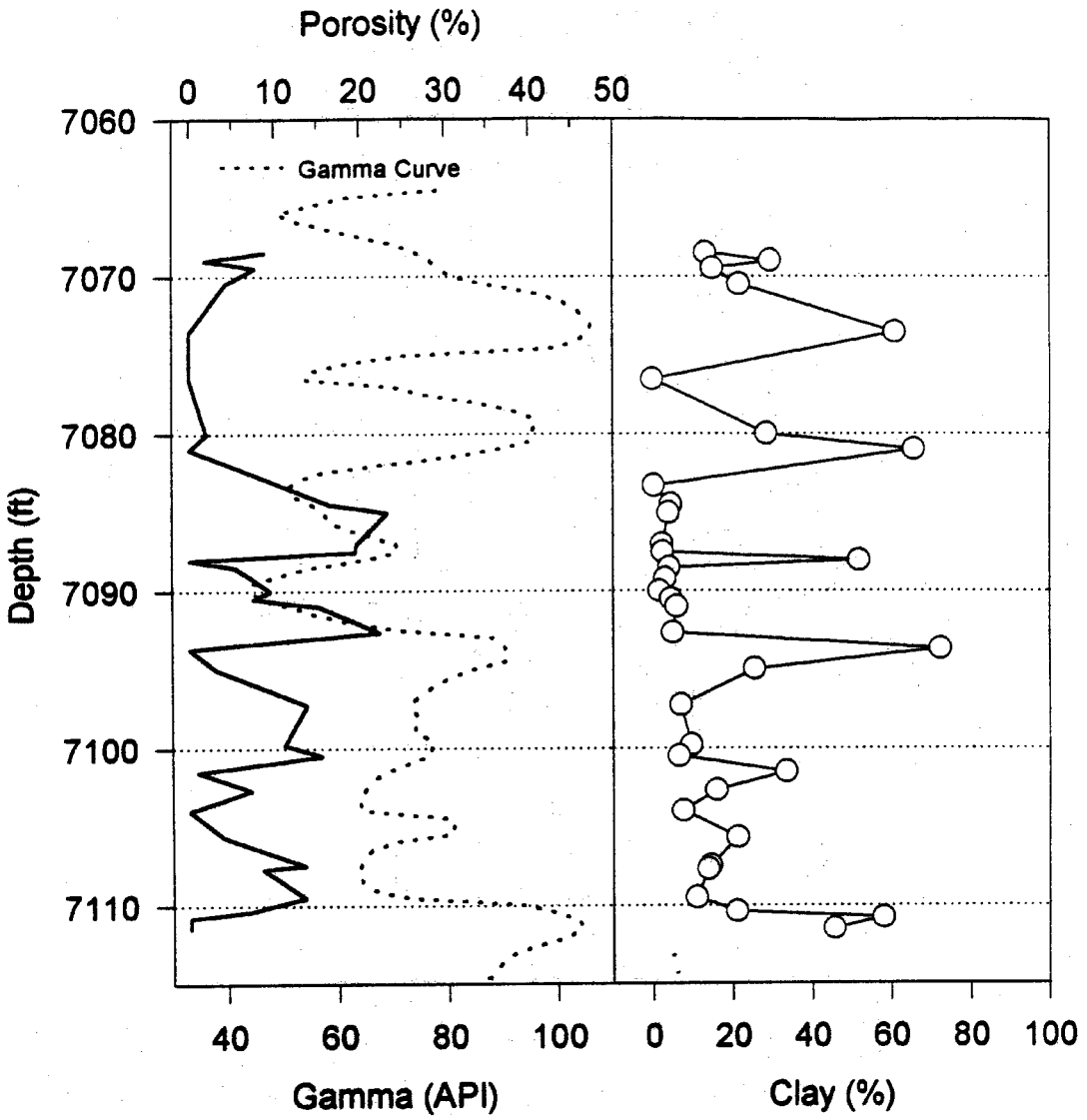

Fig. 1.1-2—Logs of porosity, gamma ray response, and percent clay (determined by point count)

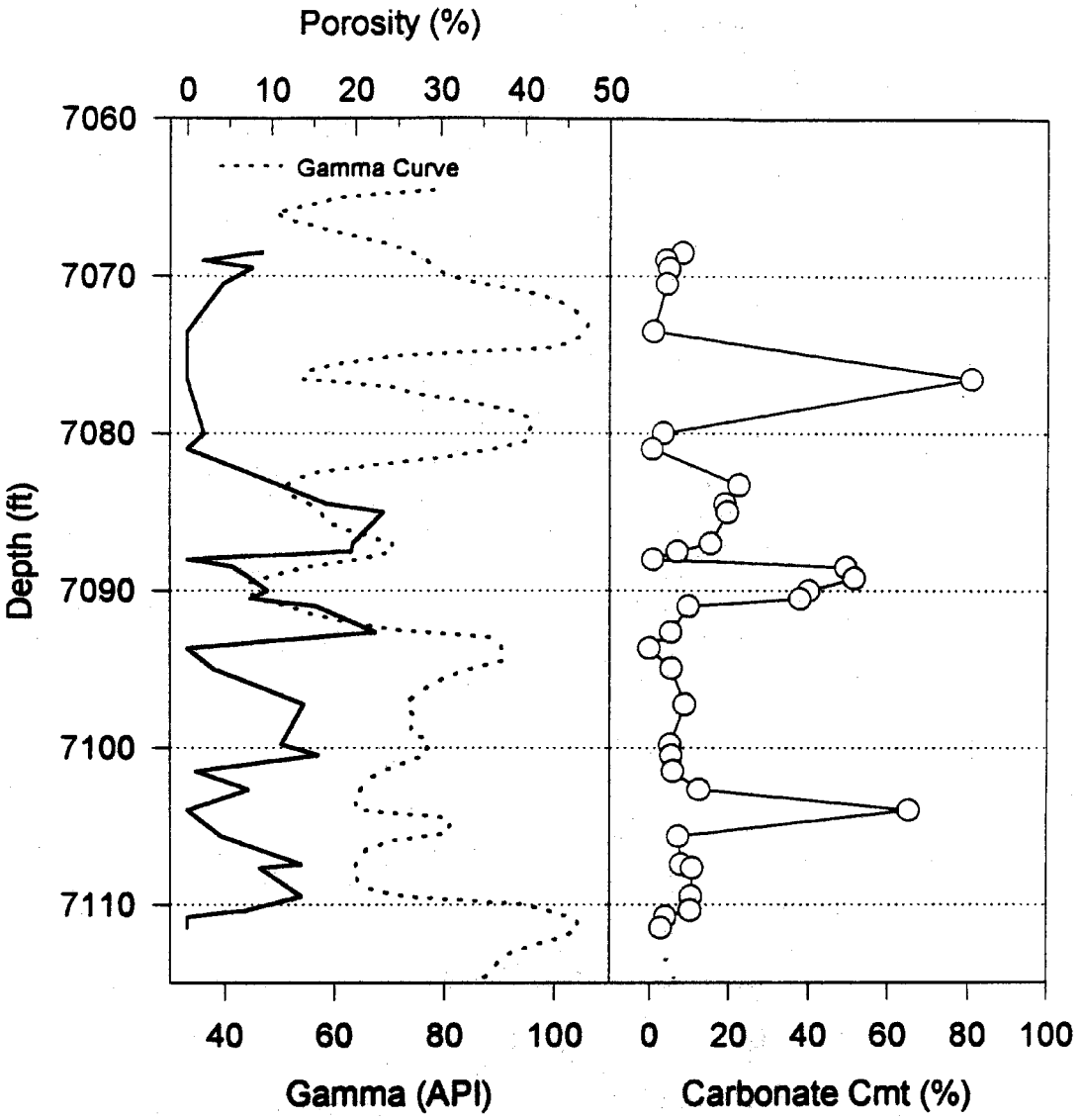

Fig. 1.1-3—A high percentage of carbonate cement is completely occluding the porosity at a depth of 7076 ft even though gamma-ray response indicates sandstone pay.

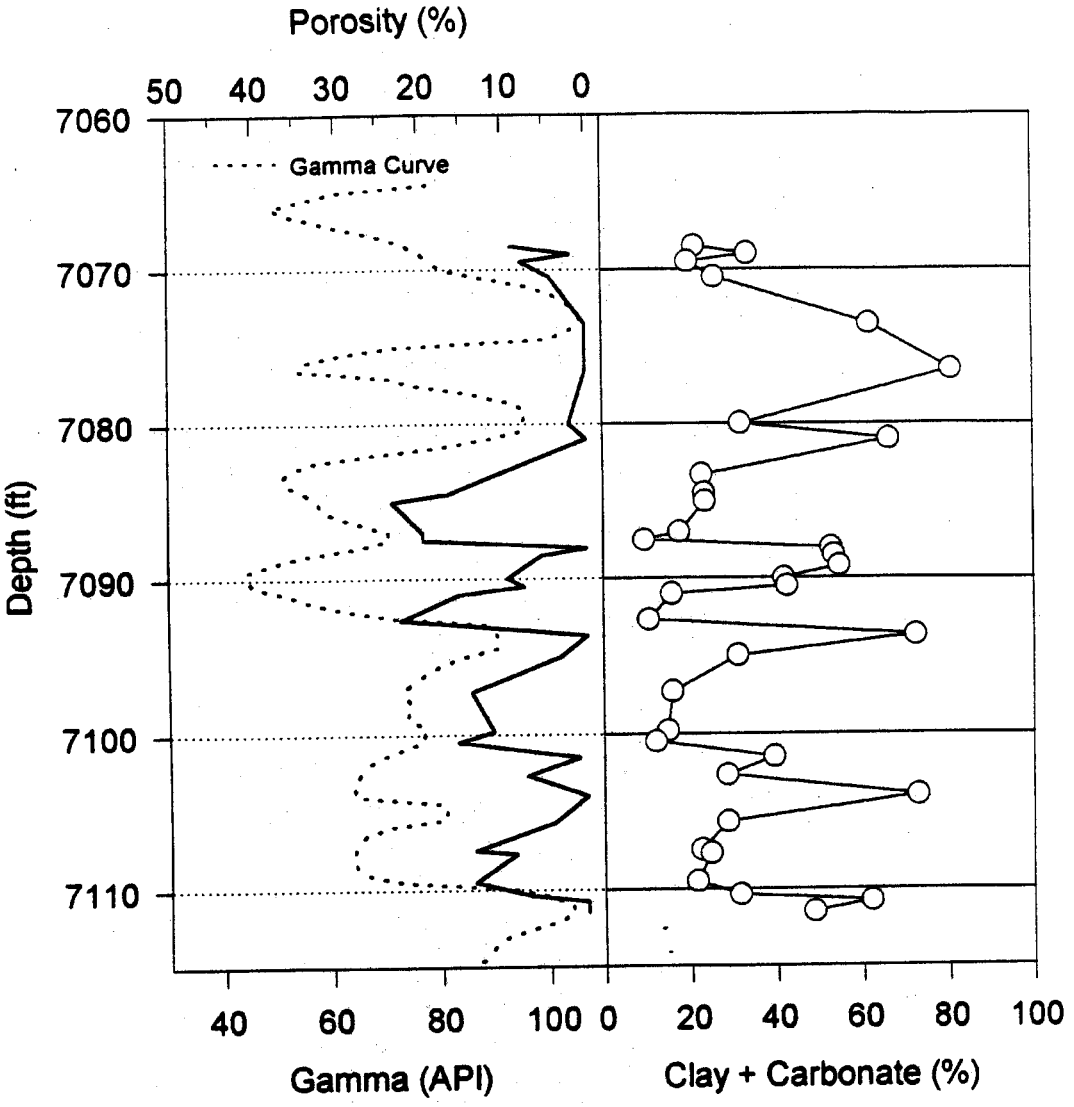

Fig. 1.1-4—Combination of the carbonate and clay matrix.

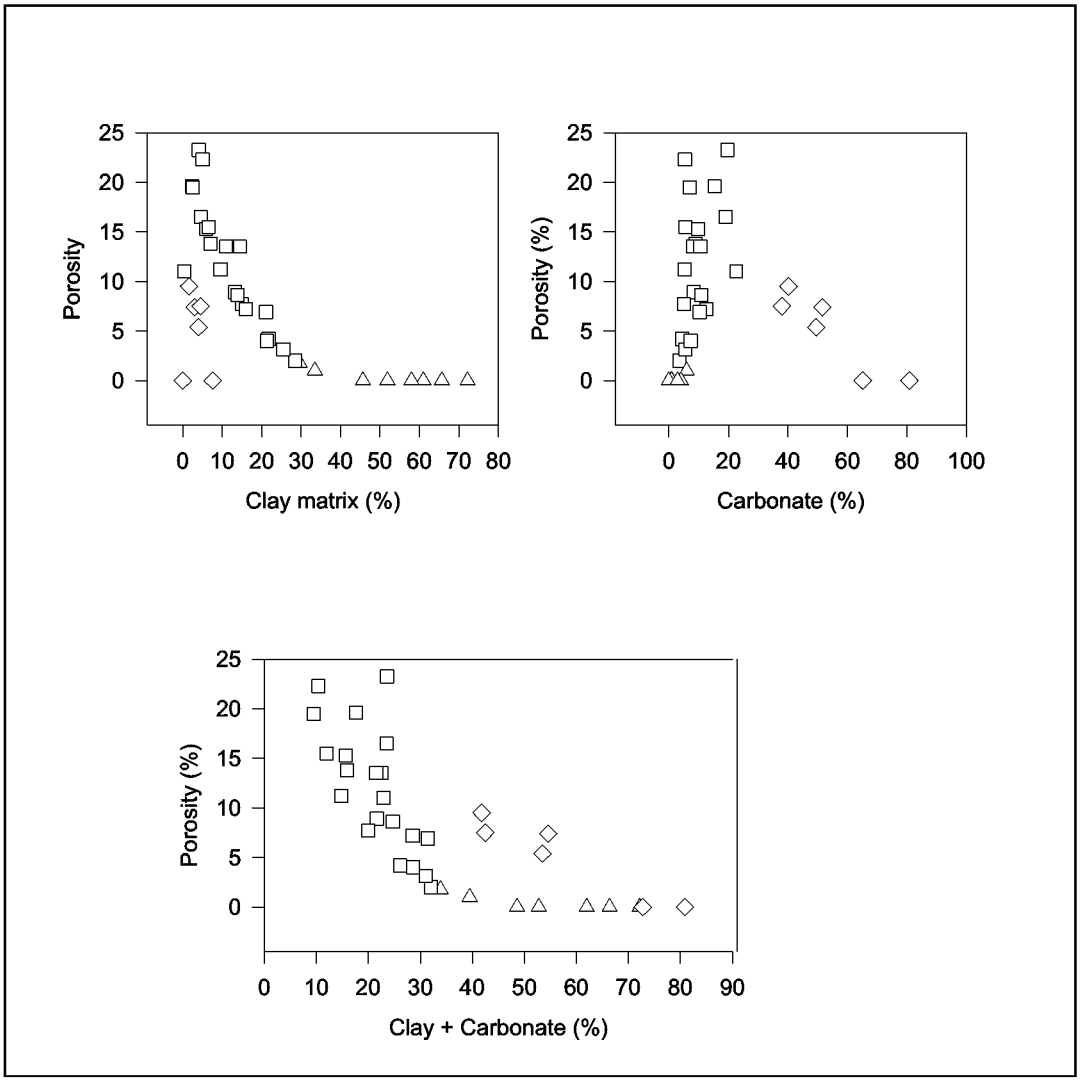

Fig. 1.1-5—A comparison of the relative contributions of percent clay matrix and percent carbonate cement to the overall reservoir porosity degradation.

1.2 Core-Log Integration for Characterization of the Spraberry Trend Shaly Sands

Abstract

In this section, Spraberry Trend Area reservoirs have been characterized with emphasis on identification of oil-bearing sands based on core-log correlation. Integration of extensive geological and petrophysical data presented in the previous section into a modern shaly-sand log interpretation model has been performed to characterize the Spraberry Trend. Quantitative cut-off criteria based on core-log integration was developed which allows log based identification of thin, oil-bearing intervals suitable for hydraulic fracture treatment. The Archie parameters (*a, m*, and *n*) have been derived from core data to improve log-derived water saturation. Core-derived porosity and water saturation have been compared with log-derived values for the purpose of identification of oil-bearing intervals. We present a log based rock model which distinguishes pay and non-pay zones. This allows definition of true net pay throughout the Trend regardless of depositional environment. The results from this investigation provide recommendations for logging suites that will allow a better description of thin pay sands which characterize the Spraberry Trend throughout the Midland Basin. The methodology developed may be used primarily to understand the areal extent and pinch-off of productive intervals and the water saturation within the pay intervals.

Introduction

The tremendous areal coverage and large amount of remaining oil warrant further investigation to expend all possible process options before large numbers of Spraberry wellbores need to be plugged and abandoned (Schechter *et al*[1,2]). Identification and mapping of the thin pay zones that comprise Spraberry Trend pay is an important first step when considering any IOR process in the future.

Mardock & Myers[14] and Lyttle & Ricke[15] first published techniques for evaluating the Spraberry Trend using radioactive and induction logs. These efforts provided reasonable results for distinguishing lithologies. However, quantitative analysis was not possible at that time. Since then, many interpretative techniques have been developed. Fairly recent studies of the Spraberry Trend were carried out by Tyler & Gholston[18] and Guevara[19]. These studies attempted to ascertain the distribution of the sedimentologic attributes of Spraberry Trend by analysis of the shape and magnitude of the gamma ray log. Quantitative shaly-sand log interpretation and core-log integration was not presented. Several authors[7, 20] provide a qualitative geological characterization of the Spraberry Trend depositional sequences, however no quantitative log analysis is available to map these sequences, especially the thin, oil-bearing pay zones.

On a lease basis, the pay sands are relatively easy to recognize yet correlation of pay sands throughout the Trend has not been attempted. Thousands of wells have been completed in the Spraberry Trend Area in the last 45 years. The logs run in many of these

wells are old, cased-hole gamma-ray, sometimes with a porosity log and in many cases, a porosity log may not be available. We therefore need to develop methodology whereby pay zones can be distinguished in areas where 1) no core is available, 2) a porosity log may or may not be available and 3) perhaps the only log available might be vintage, cased-hole gamma-ray.

In this investigation, we demonstrate the applicability of modern shaly-sand log analysis in determining net pay as observed in three recent core wells discussed in Section 1.1. We recommend a logging suite which provides the most reliable technique for net pay determination. This investigation will clearly show that true reservoir rock (primarily massive/clean siltstone) in the Spraberry Trend Area cannot be identified by gamma-ray response alone. We also provide the methodology to convert old cased-hole gamma-ray logs into porosity logs. Good agreement is demonstrated between generated porosity logs and actual porosity logs. Finally a rock-model is presented which identifies essentially three rock types:

- Rock Type **A** - massive, clean siltstone, low clay and dolomite content and strongly fluorescent, low water saturation
- Rock Type **B** - low clay, high dolomitic content with weak or no fluorescence and high water saturation, and
- Rock Type **C** - muddy clay rich zones that do not fluoresce.

The methodology presented provides the basis for mapping the extent, thinning and pinch-off of Rock Type A pay intervals throughout the Midland Basin for Upper Spraberry, Lower Spraberry (Jo-Mill) or Dean reservoirs. The methodology used in this investigation integrates the following data: ultraviolet photographs of whole core, thin-section analysis, minipermeameter measurements, whole core analysis, open and cased-hole logs.

Archie Parameter *a, m*, and *n*

Log interpretation models are sensitive to the uncertainity in both *m* and *n*. *m* and *n* are usually derived from core data. It was reported that the Archie parameter *a* is a weak-fitting parameter with no physical significance and can generally be set to unity (Maute *et al*[22]). According to Aguilera[28], *m* should be relatively small (ranging from about 1.1 to 1.3) for naturally fractured systems. *m* and *n* values were derived from Spraberry core data. Based on our analysis (Banik & Schechter[5,6]), we found that the value of *m* is 1.35 for the upper pay zone, 2.49 for the upper non-pay zones, 1.10 for the lower pay zones, 2.22 for the lower non-pay zones and 2.41 for the Dean zones. Similarly, the value of *n* is 1.74 for the lower pay zones, and 1.15 for the lower non-pay zones. Therefore overall *m* and *n* values for the Spraberry Trend Area are 1.66 and 1.46.

Core Analysis

Upper Spraberry core from the Shackelford 1-38A, Judkins "A" No. 5 and the first DOE pilot well the E.T.O'Daniel # 37 were available for this investigation. The cores were examined to determine gross lithologic properties and to correlate core properties with the wireline response in addition to development of a rock model. Thin-sections were made to determine the distribution of microscopically visible porosity and for investigation of diagenesis, cementation etc., as reported in Section 1.1. Porosity, water saturation and permeability were obtained from whole core analysis[8]. Permeability distribution in the main pay was measured by minipermeametry and found to correlate well with whole core analysis. Minipermeameter measurement of the entire pay zone indicated that the matrix by itself is relatively homogeneous, usually in the range of 0.1 to 1.0 md. The two main pay zones 1U & 5U (each is approximately 8-15 ft in thickness separated by 150 ft. of non-pay) were clearly identified by oil fluorescence and are indicated in the log shown in **Fig. 1.2-2**.

Core-Log Integration

Effective water saturation and effective porosity were calculated from shaly-sand log interpretation using both conventional m & n (m=2 & n=2) and core derived m & n (m=1.66 & n=1.46). It has been observed that conventional m & n values overestimate the water saturation, whereas water saturation calculated using core derived m & n values shows good agreement with core measured water saturation (**Fig. 1.2-1**). It has also been observed that for the Spraberry Trend, the Automatic Compensation Method (ACM)[9] and the Fertl[29] method of shaly-sand interpretation performs better than the Dual water method[30]. Effective water saturation calculated from the Dual Water method is much higher than the effective water saturation calculated from the ACM and the Fertl method.

Shaly-Sand Log Interpretation

Volume of shale was calculated from gamma-ray logs using the Larionov non-linear relationship[9]. The result was compared with ultraviolet observation of fluorescing intervals. The fluorescent intervals show a clear distinction between oil bearing sand and muddy zones containing no oil due to sharp contrast seen at the interface between these lithologies. Effective porosity was calculated from log data, and was cross-plotted along with volume of shale on a modified shaly-sand producibility chart to determine if the volume of shale is high enough to drastically reduce producibility. Based on fluorescing intervals observed in the core along with the modified shaly-sand producibility chart, we contend that shale volume less than 15% and effective porosity greater than 7% provide accurate cut-off criteria for identification of fluorescing intervals in Spraberry Trend Area reservoirs. Thin-section analysis confirms the cut-off criteria by observation of visible porosity in oil bearing intervals whereas no visible porosity is observed in the non-pay muddy zones.

Identification of the Pay Zones

We previously demonstrated[5,6] that classic shaly-sand analysis could accurately quantify thin fractured pay zones which characterize the Spraberry Trend. The acquisition of core data reaffirmed our analysis that Upper Spraberry net pay consists of two primary, thin (8-15 ft) pay zones, the 1U and 5U. We mentioned previously that sharp contrast is observed by fluorescence between shales containing no oil and the 1U and 5U pay zones. The 1U and 5U pay zones are easily identified by integrating whole core analysis and open-hole logs into a calibrated shaly-sand model. However, there is inconsistency with the 2U, 3U and 4U zones shown in Fig.1.2-2 through **Fig. 1.2-5**. Gamma-ray cut-off criteria indicate these zones are pay, yet core data demonstrates these zones are not pay. To resolve this dilemma, volume of shale was correlated with neutron-density, sonic and bulk-density porosity logs. It has been observed that the porosity of the 2U, 3U and 4U zones which have low gamma-ray response, is less than 7%. Thin-section point counts presented in Section 1.1 indicates a large concentration of dolomite in these zones. Thin section analysis also reveals that the porosity of the 2U, 3U and 4U zones is drastically reduced due to dolomitic cement, thus effectively rendering these zones as non-pay. A closer look at porosity logs is necessary to distinguish low gamma-ray zones which are oil saturated and those zones which contain no oil.

Effective Porosity from Different Log Suites

Thin section results indicated the necessity of refining porosity cut-off. Different porosity logs (both open-hole and cased-hole) have been investigated to confirm the above mentioned cut-off criteria for identification of the pay zones. Sonic, bulk-density and neutron-density cross-plot porosity along with gamma ray log were utilized in this study to isolate and differentiate pay and non-pay zones that demonstrate similar gamma ray response.

Open-Hole Logs

The E.T. O'Daniel lease consists of 2,100 acres in the middle of the Spraberry Trend Area. This relatively small lease is the site for the pilot CO_2 project. Fig. 1.2-2 is an example of open-hole log from the E.T. O'Daniel #37 (Upper Spraberry). Fig. 1.2-2 shows shale volume derived from gamma ray response using the non-linear Larionov relationship (Asquith[9]). Fig. 1.2-2 also shows neutron, density and bulk-density porosity logs along with the neutron-density cross-plot porosity. The effective porosity derived from the neutron-density cross-plot clearly identified 1U and 5U pay zones having porosity >7%, whereas the 2U, 3U, 4U zones which have low amounts of clay and porosity less than 7% due to dolomitic cement. This result correlates well with point count data presented in Fig. 1.2-3.

Fig. 1.2-3 is an example of an open-hole log from the E.T. O'Daniel # 26 (Upper Spraberry). Fig. 1.2-3 shows the gamma-ray and volume of shale as was seen in Fig. 1.2-2. A bulk-density log was run in this well. Bulk-density clearly indicates much greater

density in the 2U, 3U and 4U zones than in the 1U and 5U zones. Matrix density for sandstones and quartzites is 2.65, for limey-sands or sandy-limes is 2.68, for limestone 2.71 and for dolomites 2.87 (Dewan[10]). Higher bulk-density indicates lower porosity. Effective porosity, calculated from bulk-density accurately distinguishes between the 1U and 5U pay zones with porosity >7% and the 2U, 3U and 4U zones with porosity <7%. Fig. 1.2-3 also shows reduction of caliper log in the 1U and 5U pay zones whereas there are no changes are evident in the caliper log for the 2U, 3U and 4U non-pay zones. This indicates borehole diameter is reduced due to mudcake buildup. The presence of mudcake itself is proof of the presence of permeability in the 1U and 5U pay-zones. Mud losses are generally observed in the 1U and 5U pay zones. This observation correlates with the observation that natural fractures tend to occur in the pay zones and terminate at gradual or sharp non-pay contacts. This suggests that natural fractures tend to be concentrated in the pay zones. Mudcake is likely to accumulate within the fractures. Fracture indications may be obtained from the density correction curve[11]. Since the density correction curve corrects the density log for effects of rough borehole and mud cake, the density correction curve may be affected by mud in the fractures and indicate a correction in the 1U and 5U pay-zones, which tends to confirm the presence of open fractures in the 1U and 5U pay zones (Fig. 1.2-3).

Fig. 1.2-4 is an example of an open-hole log from the E.T. O'Daniel # 28 (Upper Spraberry). This log suite consists of gamma ray and sonic transit time. Volume of shale was derived from gamma ray log as before and porosity was derived from sonic transit time. Sonic transit time in the 2U, 3U and 4U is lower than in the 1U and 5U pay zones. Lower transit time indicates lower porosity. Sonic transit time is 1) 54 μsec/ft for sandstone, 2) 49 μsec/ft for limestone and 3) 44 μsec/ft for dolomite (Dewan[10]). Effective porosity calculated from sonic transit time also indicates high porosity (>7%) in the 1U and 5U pay zones and low porosity (<7%) in the 2U, 3U and 4U non-pay zones. Thus effective porosity cut-off of 7% accurately differentiate 1U and 5U pay zones from 2U, 3U and 4U non-pay zones.

Porosity Generation from Gamma Ray Log

We have shown that sandstone zones with low gamma-ray response and high percentage of carbonate cement can be distinguished from pay by effective porosity derived from 1) neutron-density cross-plots, 2) bulk-density log, and 3) sonic transit time log. However, it is possible that only old cased-hole gamma ray logs might be available. But for accurate log-based identification of pay zones, the minimum requirement is a gamma ray log and any porosity log. So we made an attempt to generate porosity logs from gamma ray logs using established cut-off criteria as presented in previous sections. Fig. 1.2-4 shows sonic transit time generated from the gamma ray log and is compared with the original sonic transit time log. Good agreement is observed between original sonic transit time log and the generated sonic transit time log from the gamma ray log.

Cased-Hole Log

Fig. 1.2-5 is an example of a cased-hole log from the O'Daniel "G" # 1. This log consists of gamma ray log and old neutron log (API). Fig. 1.2-5 shows that the neutron log accurately distinguishes the 1U and 5U pay zones from the 2U, 3U, and 4U non-pay zones. The neutron log shows high CPS (count per second) in the 2U, 3U and 4U non-pay zones. High neutron counts indicates low porosity.

Log Based Rock Model

A rock-log model[4] has been developed to identify the highest quality pay intervals using available open-hole well log data. Volume of shale was cross-plotted against effective porosity in **Fig. 1.2-6**. Three general rock types have been identified, of which only one can be classified as pay. Rock Type A has volume of shale <15%, and porosity >7% with little dolomitic cement and strongly fluoresces. Rock Type B has volume of shale <15%, yet the porosity <7% and primarily occluded by dolomitic cement and may be weakly fluorescent. Rock Type C has volume of shale >15% and does not fluoresce. Rock Type A is the primary reservoir rock (1U and 5U) in the Upper Spraberry. This rock type consist of mainly massive/clean siltstone. This rock type fluoresces strongly under ultraviolet light, has high oil saturations and visible porosity is observed as seen in thin section photographs. Rock Type B has low volume of shale and low porosity occluded by dolomitic cement as shown in Fig. 1.2-6., and is considered non-pay (2U, 3U and 4U zones). This rock type mainly consist of siltstone and dolomite and fluoresces weakly relative to the 1U and 5U. Rock Type C is non-pay mudstones with high shale volume. Rock Type C does not fluoresce under ultraviolet light. The schematic representation of the log based rock model is given in the Table 1.2-1.

Potential for Fractured Zone Identification

Fig. 1.2-7 shows the effective porosity derived from neutron-density cross-plot and compared with core derived porosity for the DOE pilot well E.T.O'Daniel # 37 (Upper Spraberry). Comparison of core measured porosity with log derived porosity may be helpful in determining the zones that may be fractured in the reservoir. In this method, it is assumed that the core represents porosity in the matrix. The neutron-density cross-plot is assumed to read total porosity (both matrix and fracture). Consequently, the difference between the two porosity curves is interpreted as near wellbore fracture porosity. From Fig. 1.2-7, it is observed that, in the intervals 7230-7240, there are indications of fractures due to the separation of the core-measured and log-derived porosity curves. It is also observed from Fig.1.2-7 that for the interval 7230-7240, log derived water saturation (total water saturation) is higher than core-measured water saturation (matrix water saturation), which may indicate the presence of water-filled fractures. These intervals were confirmed to be fractured by analysis of the whole cores and a FMI log. However, this analysis does not distinguish between drilling induced and natural fractures. Both coring induced and natural fractures were observed in the pay interval.

Conclusions

The success of shaly-sand analysis now provides quantitative methodology to map the thin pay sands that comprise the Spraberry Trend Area. This technique can be applied to the entire Trend to understand pinch-off and thinning of the sands near the fringe of the basin or channel sand development or disappearance. The following conclusions were reached based on a detailed investigation for identification of pay zones using core-log integration:

1. Volume of shale <15% and effective porosity >7% provides adequate cut-off criteria to identify and differentiate pay zones from non-pay zones.

2. Volume of shale is derived from gamma ray using the non-linear Larionov relationship and effective porosity can be derived from 1) neutron-density cross-plots, 2) bulk-density logs and, 3) sonic transit time, etc.

3. Porosity logs can be generated from cased hole gamma-ray logs where no porosity logs may be available.

4. In the E.T. O'Daniel area, the 1U and 5U are the pay zones in the Upper Spraberry.

5. The 2U, 3U and 4U, even though the gamma ray appears favorable, is composed of siltstone with dolomitic cement occluding the porosity thereby rendering these zones as non-pay.

6. Utilization of new values of m & n integrated with shaly-sand interpretation has proven effective for identification of thin fluorescing intervals and the water saturation within these intervals. The interpretation was confirmed by whole core analysis.

7. The Automatic Compensation Method and the Fertl method of shaly-sand analysis performs better than the Dual water method in the Spraberry Trend Area.

8. Porosity exponent m, separation between log-derived porosity and core-measured porosity, and separation between log-derived water saturation and core-measured water saturation may be a good fracture indicator for the Spraberry Trend.

9. The pay-zones are relatively homogeneous and composed predominantly of quartz and feldspar with some dolomite. Clay minerals are mostly illite.

10. The methodology presented allows basin-wide mapping of the thin, fractured siltstone intervals which are oil saturated.

Nomenclature

GR	= gamma ray log, API.
VSHL	= volume of shale.
CALI	= borehole caliper log, in.
RHOB, RHOZ	= bulk-density log, gm/cc.
DPHI, DPHZ	= density porosity log, pu.
INTT	= sonic transit time log, μsec/ft.
INTT (GR)	= sonic transit time log derived from the GR, μsec/ft.
NPHI	= neutron porosity log, pu.
PHIE	= effective porosity corrected for shale.
PHIEX	= effective porosity derived from the neutron-density cross-plots porosity.
BDPE	= effective porosity derived from the bulk-density logs.
NEUT	= old neutron logs, API.
m	= porosity exponent.
n	= saturation exponent.
a	= cementation factor.

References

1. Schechter, D.S., McDonald, P., Sheffield, T., and Baker, R.: "Integration of Laboratory and Field Data for Development of a CO_2 Pilot in the Naturally Fractured Spraberry Reservoir," SPE 36657 presented at poster session of the 1996 SPE Annual Technical Conference and Exhibition, Denver, Colorado, 6-9 October 1996.
2. Schechter, D.S., McDonald, P., Sheffield, T., and Baker, R.: "Reservoir Characterization and CO_2 Pilot Design in the Naturally Fractured Spraberry Trend Area," paper SPE 35469 presented at the SPE Permian Basin Oil & Gas Recovery Conference, Midland, Texas, 27-29 March 1996.
3. Sheffield, T.D., McDonald, P., Schechter, D.S., Baker, R., and Teufel, L.: "CO_2 Pilot Design in the Naturally Fractured Spraberry Trend: Project Update and Spraberry Rock Model," paper presented at the Annual Convention of the American Association of Petroleum Geologists, May 19-22, 1996.
4. Schechter, D.S., and Banik, A.K.: "What is Spraberry Pay?," report of investigation, PRRC Report # 96-28, New Mexico Petroleum Recovery Research Center, Socorro, NM, 1996.
5. Banik, A.K., and Schechter, D.S.: "Core-Log Integration for the Naturally Fractured Spraberry Trend Area," paper presented at the Naturally Fractured Reservoir Forum (Characterization & Fluid Flow), Socorro, New Mexico, April 19, 1996.
6. Banik, A.K., and Schechter, D.S.: "Characterization of the Naturally Fractured Spraberry Trend Shaly Sands Based on Core and Log Data," paper SPE 35224 presented at the SPE Permian Basin Oil & Gas Recovery Conference, Midland, Texas, 27-29 March 1996.

7. Saleta, C.J., Banik, A.K., Cather, M.E., and Schechter, D.S.: "Application of Analytical Techniques to Evaluate the Heterogeneities of the Upper Spraberry Formation (Permian) and its Influence on the Quality of the Midland Basin Reservoirs in West Texas," SPE 35225 presented at a poster session at the SPE Permian Basin Oil & Gas Recovery Conference, Midland, Texas, 27-29 March 1996.
8. "Geological and Petrophysical Analysis of the Upper Spraberry Formation in Midland County, Texas," report prepared by Reservoirs Inc. for Parker & Parsley Development Company, 1996.
9. Asquith, G.B.: *Log Evaluation of Shaly Sandstone Reservoirs: A Practical Guide*, AAPG, Tulsa, Oklahoma, 1982.
10. Dewan, J.T.: *Essentials of Modern Open-Hole Log Interpretation*, PennWell Book, Tulsa, Oklahoma, 1983.
11. Beck, J., Schultz, A., and Fitzgerald, D.: "Reservoir Evaluation of Fractured Cretaceous Carbonates in South Texas," paper presented at the SPWLA Eighteenth Annual Logging Symposium, June 5-8, 1977.
12. Elkins, L.F.: "Reservoir Performance and Well Spacing, Spraberry Trend Area Field of West Texas," Petroleum Transaction, AIME (1953) 198, 177-196.
13. Elkins, L.F., and Skov, A.M.: "Cyclic Water Flooding the Spraberry Utilizes End Effects to Increase Oil Production Rates," JPT (August 1963A) 877-884.
14. Mardock, E.S., and Myers, J.P.: "Radioactivity Logs Define Lithology in the Spraberry Formation," Oil & Gas Journal (November 29, 1951), 90.
15. Lyttle, W.J., and Ricke, R.R.: " Well Logging in Spraberry," Oil & Gas Journal (December 13, 1951), 92.
16. Archie, G.E.: "Electrical Resistivity Log as an Aid in Determining Some Reservoir Characteristics," Trans., AIME (1942) 146, 54-62.
17. Stalheim, S.O., and Eidesmo, T.: "Is The Saturation Exponent n A Constant?," SPWLA 36th Annual Logging Symposium, June 26-29, 1995.
18. Tyler, N., and Gholston, J.C.: " Heterogeneous Deep-Sea Fan Reservoir, Shackelford and Preston Waterflood Units, Spraberry Trend, West Texas," Report of Investigation No. 171, Bureau of Economic Geology, The University of Texas, Austin, 1988.
19. Guevara, E.H.: "Geological Characterization of Permian Submarine Fan Reservoirs of the Driver Waterflood Unit, Spraberry Trend, West Texas," Report of Investigation No. 172, Bureau of Economic Geology, The University of Texas, Austin, 1988.
20. Handford, C.R.: " Sedimentology and Genetic Stratigraphy of Dean and Spraberry Formations (Permian), Midland Basin, Texas," AAPG (1981), v. 65, No. 9, 1602-1616.
21. Worthington, P.F., and Pallatt, N.: "Effective of Variable Saturation Exponent Upon the Evaluation of Hydrocarbon Saturation," paper SPE 20538 presented at the 1990 SPE Annual Technical Conference and Exhibition, New Orleans, Sept. 23-26.
22. Maute, R.E., Lyle, W.D., and Sprunt, Eve S.: "Improve Data-Analysis Method Determines Archie Parameters From Core Data," JPT (January 1992) 103-107.
23. *QLA2-A Log Interpretation System*, GeoGraphix, Inc. 1994.
24. Log Interpretation Principles/Applications, Schlumberger Educational Services, Houston (1989).
25. Log Interpretation Charts, Western Atlas Logging Services, Houston (1985).

26. Doublet, L.E., Pande, P.K., Clark, M.B., Nevans, J.W., and Blasingame, T.A.: "An Integrated Geological and Engineering Reservoir Characterization of the North Robertson (Clearfork) Unit: A case Study, Part 1," paper SPE 29594, presented at the 1995 Joint Rocky Mountain Regional Meeting and Low-Permeability Reservoirs Symposium, Denver, Colorado, USA, 20-22 March 1995.
27. Davies, D.K., and Vessell, R.K.: "Flow Unit Characterization of a Shallow Shelf Carbonate Reservoir: North Robertson Unit, West Texas," paper SPE/DOE 35433, presented at the 1996 SPE/DOE Tenth Symposium on Improved Oil Recovery, Tulsa, OK, 21-24 April 1996.
28. Aguilera, R.: "Analysis of Naturally Fractured Reservoirs From Sonic and Resistivity Logs," JPT (November 1974).
29. Fertl, W.H.: "Shaly Sand Analysis in Development Wells," SPWLA 16th Annual Logging Symposium Trans., paper A, 1975.
30. Clavier, C., Coates, G., and Dumanoir, J: "The Theoretical and Experimental Basis for the 'Dual Water' Model for Interpretation of Shaly Sands," JPT (April 1984).
31. Gomez-Rivero, O.: "A Practical Method for Determining Cementation Exponents and Some Other Parameters As An Aid in Well Log Analysis," The Log Analyst (September-October 1976), 8-24.

Table 1.2-1—Log Based Rock Model

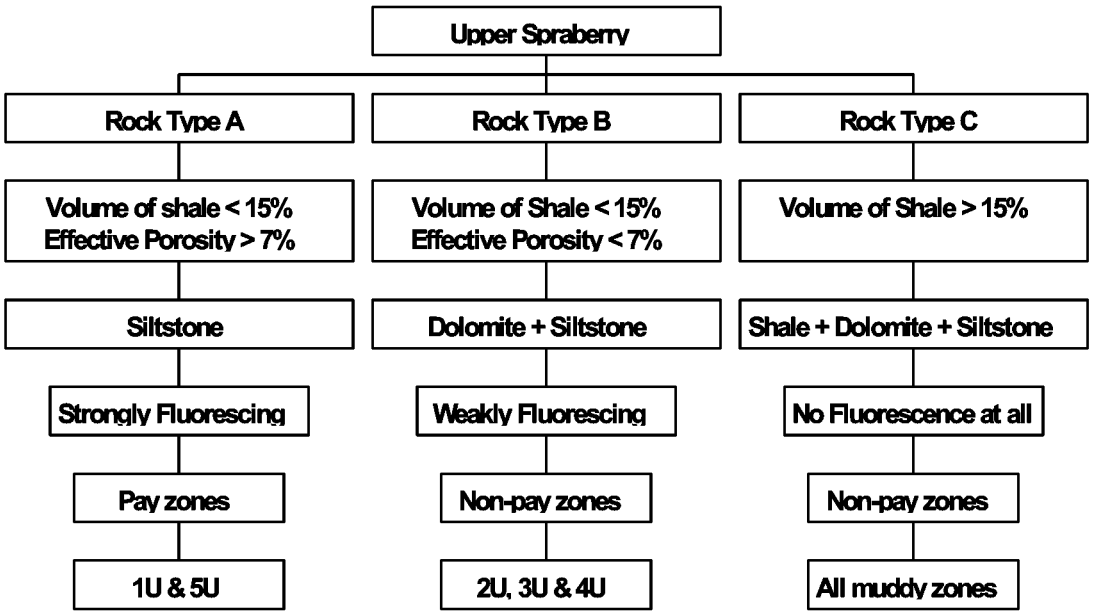

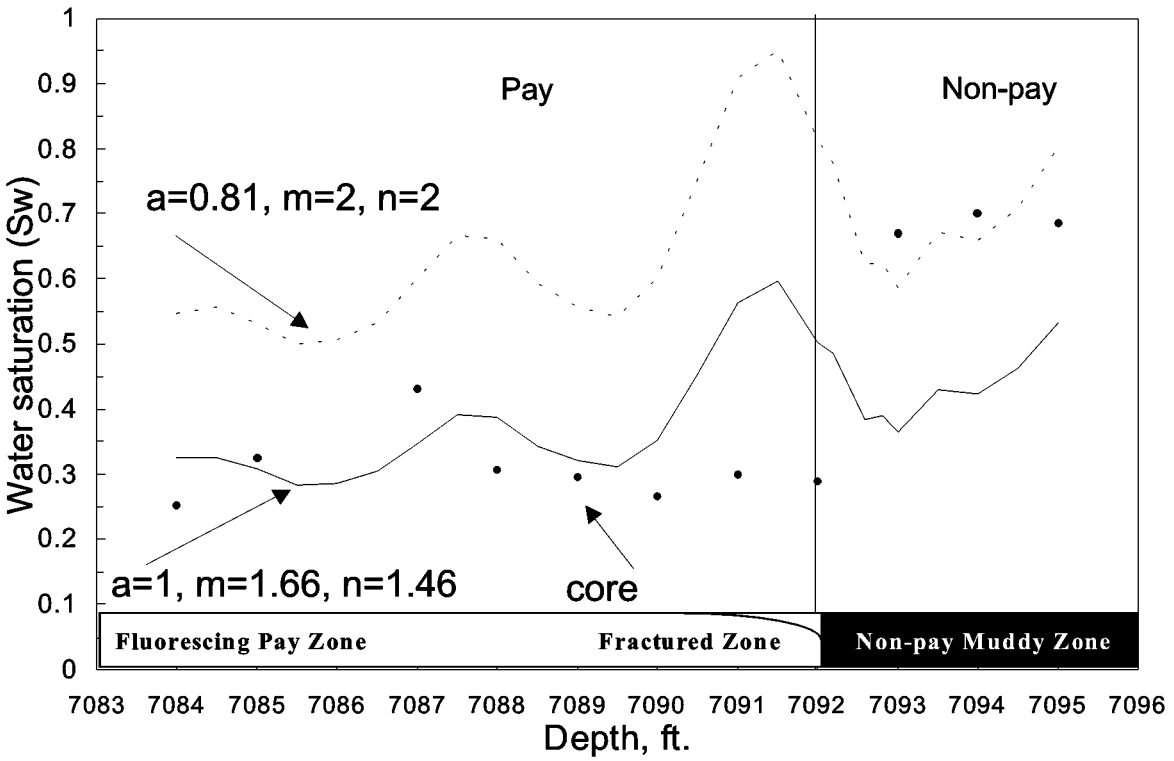

Fig. 1.2-1—Log-derived water saturation calculated using conventional and derived m and n values and compared with core-measured water saturation (Upper Spraberry, Shackelford 1-38 A). Sharp contrast between pay and non-pay is observed by fluorescence at a depth of 7092 ft. Geological characterization of this interval is found in Figs. 1.1-1 through 1.1-5.

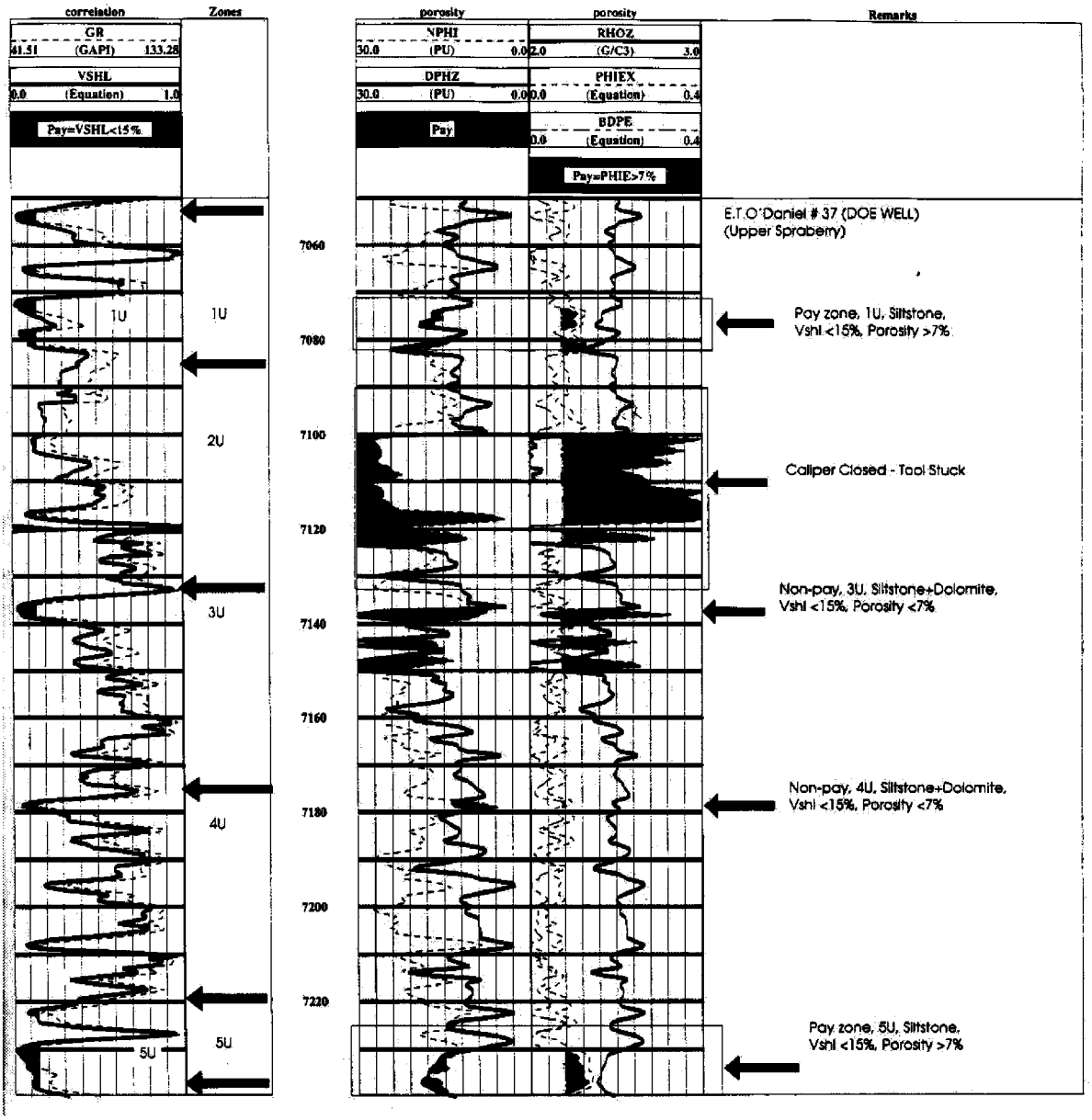

Fig. 1.2-2—Open-hole log for the DOE pilot well E.T.O'Daniel # 37 (Upper Spraberry)

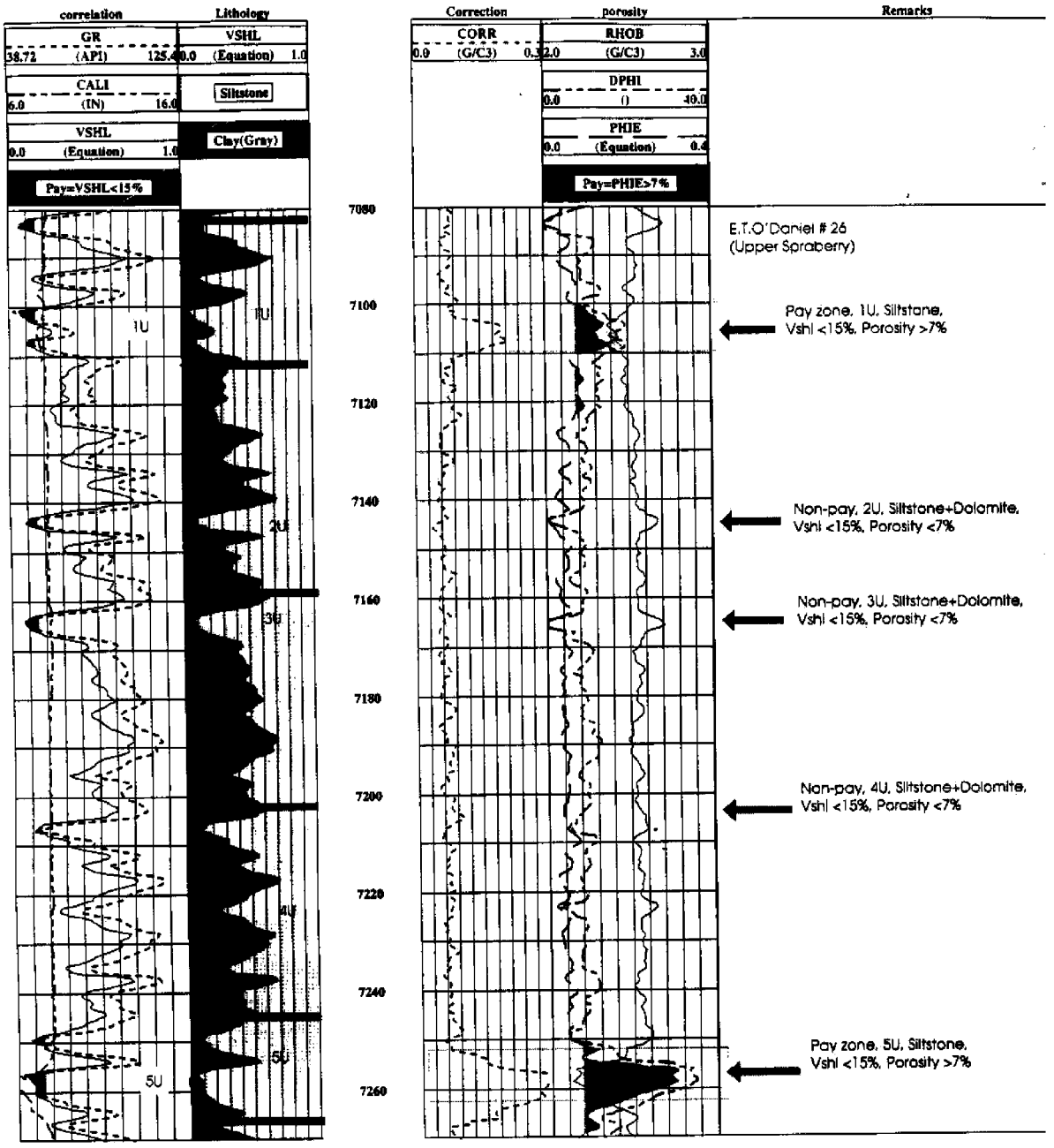

Fig. 1.2-3—Open-hole log for the DOE pilot well E.T.O'Daniel # 26 (Upper Spraberry)

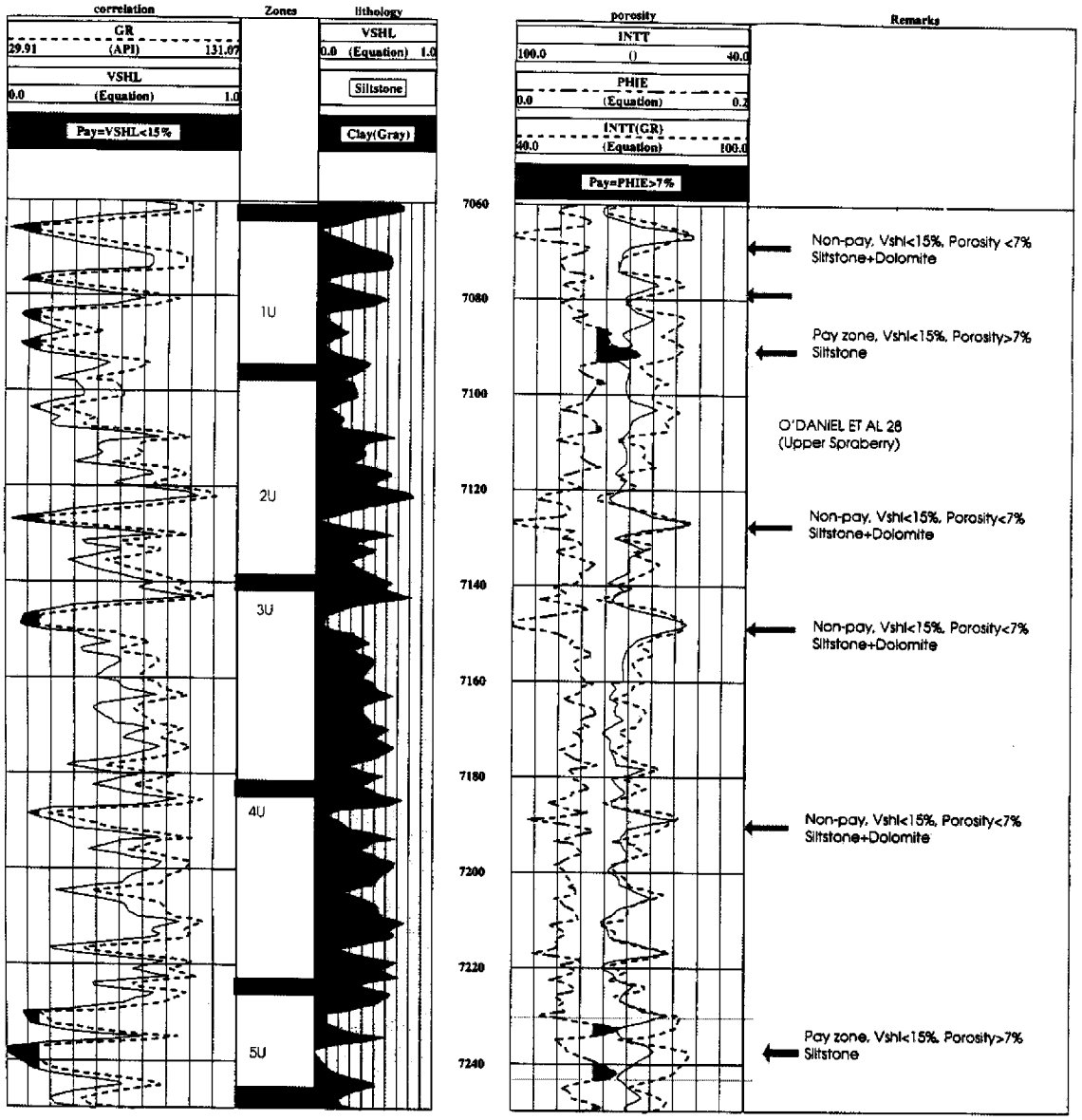

Fig. 1.2-4—Open-hole log for the DOE pilot well E.T.O'Daniel # 28 (Upper Spraberry). INTT is original sonic log and INTT (GR) is sonic log generated from gamma-ray log.

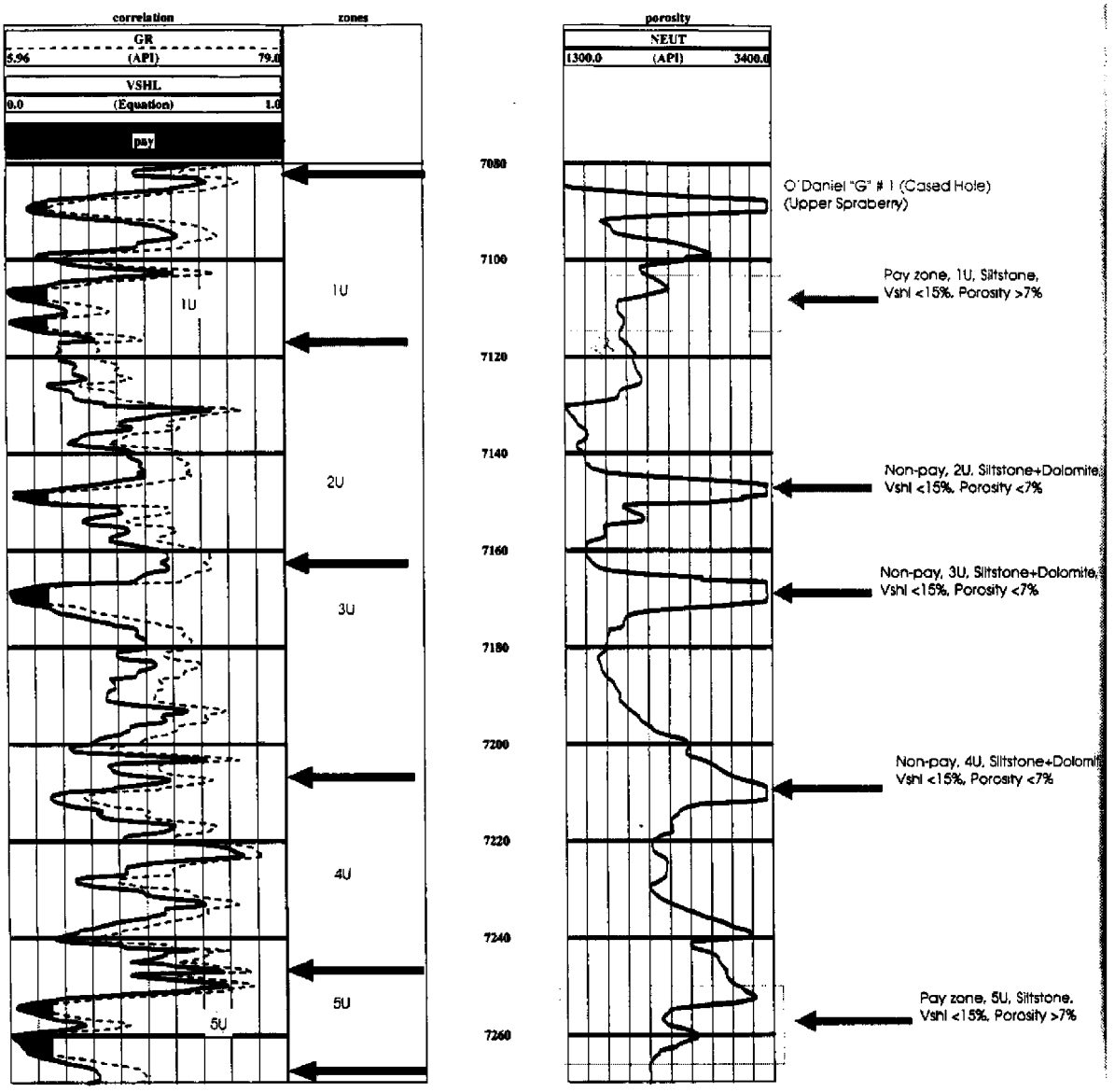

Fig. 1.2-5—Cased-hole logs from the E.T.O'Daniel "G" # 1 (Upper Spraberry)

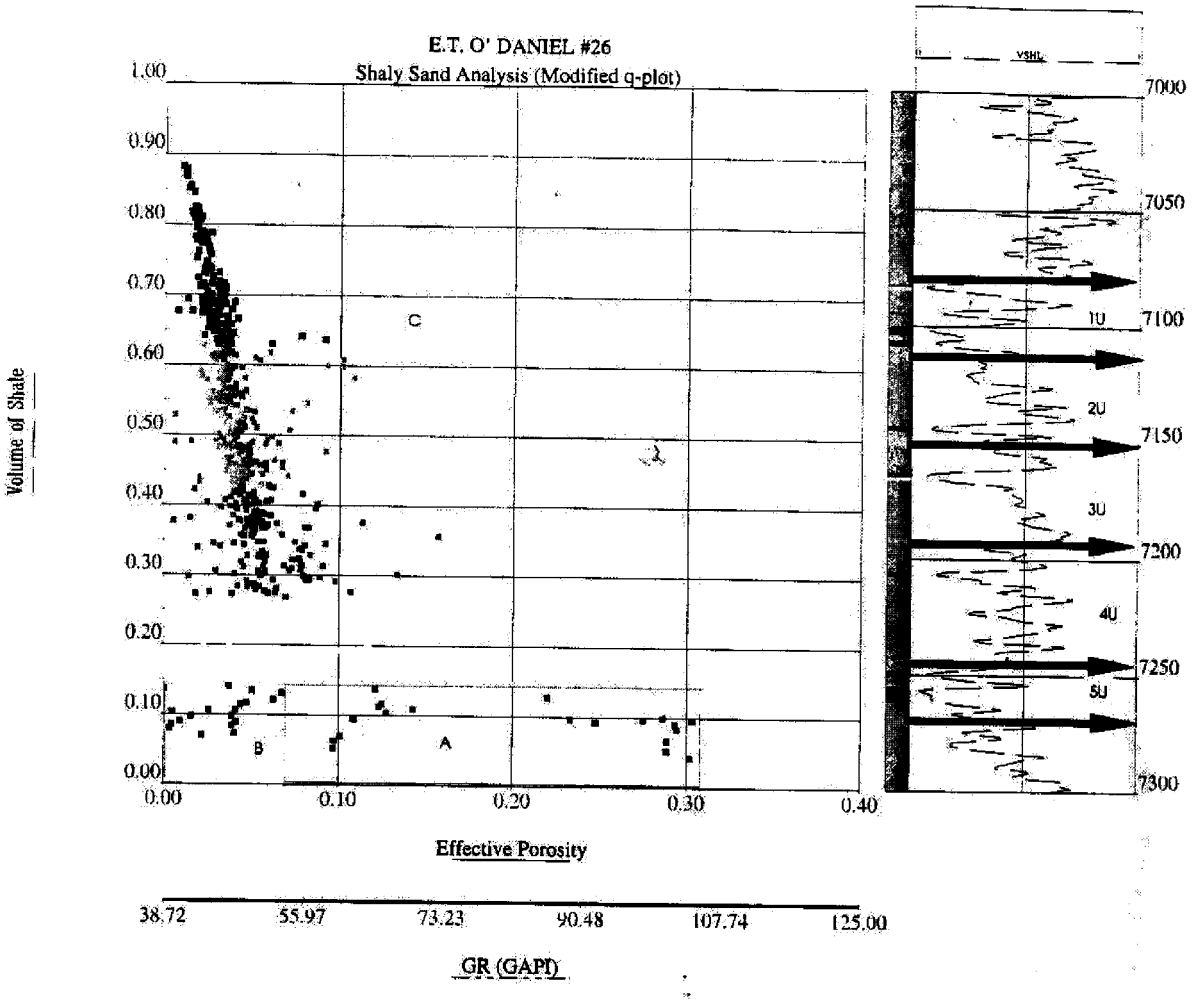

Fig. 1.2-6—Effective porosity vs. volume of shale for identification of rock type. Log based rock model for the Spraberry Trend Area. Data points in box A are from the 1U and 5U pay zones (rock type A, VSHL<15%, effective porosity >7%). Data points in the box B are from the 2U,3U and 4U non-pay zones (rock type C, VSHL >15%).

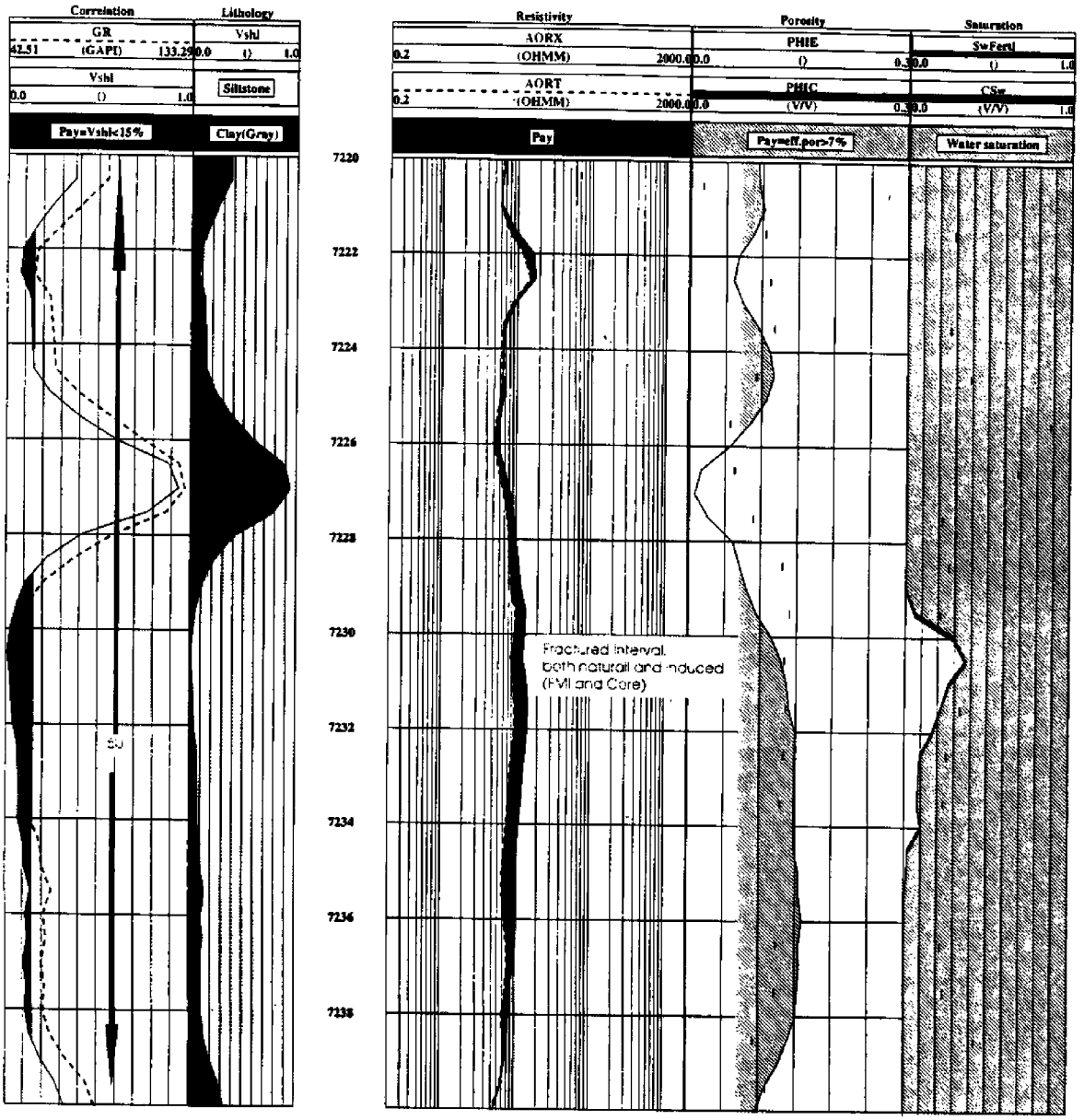

Fig. 1.2-7—Fractured zone identification from well logs for E.T.O'Daniel # 37. The present analysis shows that the fractured interval is from 7230 ft to 7240 ft based on difference between core-measured and log-derived porosity and water saturation, which is confirmed by FMI and core.

1.3 Acquisition of Horizontal Cores from the Dual Lateral E.T. O'Daniel #28

Introduction

Natural fractures existing over a regional area have long been known to dominate all aspects of performance in the Spraberry Trend Area[1]. However, there is little or no information on the actual fracture system other than: orientation, on a gross basis, from pulse and/or tracer tests in the 50's and 60's, and fracture spacing inferred from simulation and a few existing vertical cores. Previous descriptions and old core reports did not distinguish between natural and coring induced fractures, thus almost all information from the early years, when almost all Spraberry data was obtained, provides no detailed information on the natural fracture system. The first vertical core, taken as part of the current program in 1993 from the Shackelford Spraberry Unit #1-38A, intersected a vertical natural fracture with significant mineralization that had clearly grown into unoccupied space. This open, mineralized fracture was contained within a thin pay sand and was observed to terminate at a shale parting. This fracture was the first documented evidence of the existence of mineralized natural fractures within the pay sand.

The orientation, containment within zone, degree of mineralization, fracture aperture and spacing are important questions when considering fluid flow in naturally fractured reservoirs. However, after considerable data gathering, it became apparent that only superficial characterization of the natural fracture system was available. Recent acquisition of the horizontal core has radically altered understanding of the natural fracture system in the Spraberry Trend Area. This well, the E.T. O' Daniel #28, was cored with the intent of intersecting natural fractures in the thin sand streaks where oil saturation is found in the Upper Spraberry. Over 100 natural fractures were intersected from the 1U and 5U pay zones exhibiting an intriguing and diverse array of fracturing behavior.

Geology

The Spraberry formation was deposited during the Permian age within the Leonardian system in the Midland Basin, a part of the province known as the Permian Basin of west Texas and southeast New Mexico. The depositional environment consisted of a combination of turbidity and density currents sourced from the northwestern shelf area. The Spraberry formation facies can be characterized as submarine fan and basin plane deposits and consists of very fine grained sandstones to coarse grained siltstones and mudstones. The various fan complexes can be traced to the north in Dawson and Lynn counties and are considered the source material for the fan lobe sequences within the area of study in eastern Midland County.

Since its discovery, the Spraberry has been subdivided into three principal intervals, the lower, middle and upper Spraberry formations. In the late 1980's, Tyler and Gholston further subdivided the Spraberry intervals to represent distinct episodes, or operational units, within each of the submarine fan complexes (**Fig. 1.3-1**)[2]. Six of these units were

found in the Upper Spraberry and two in the Lower Spraberry. Only two of the six horizons in the Upper Spraberry (1U and 5U) have been identified as containing reservoir quality rock capable of making significant production contributions.

The proposed target of the horizontal core was the natural fractures within the main pay intervals of the 1U and 5U sands. Net pay within each of these zones averages between 8 and 14 ft. depending on location. Unfortunately, logs run following the coring of the 1U interval confirmed that the core had actually come from a thinner (2-3 ft.) pay section, within the 1U interval, located 6-8 ft. above the main pay. Further explanation is found in Section 1.4.

Core Acquisition

One of the primary objectives in obtaining horizontal core was to provide direct measurement of fracture orientation and spacing, therefore, the well plan called for both laterals to extend perpendicular to the assumed fracture trend in order to maximize the intersection of natural fractures. The mechanics of obtaining the core in a horizontal well proved to be not unlike that of coring a vertical well. In fact, the problems which hampered horizontal coring operations were typical of problems commonly encountered in coring vertical wells.

Curve Build Bottom Hole Assembly. The bottom hole assembly (BHA) utilized to drill the curve on both the Upper Spraberry 1U and 5U targets was as follows: 6-1/2" PDC bit, 5" O.D., 5/6 lobe 4 stage adjustable angle motor, flex sub, float sub with stainless steel insert float, UBHO (Universal Bottom Hole Orienting) sub, and 2 non-magnetic monel drill collars. The BHA was run on 3-1/2" IF drill pipe.

Coring Bottom Hole Assembly. The first BHA utilized to perform the coring operations was configured as follows: 6-1/8" diamond core bit, 6-1/8" O. D. scribe shoe with slip dog core catcher, 6-1/8" X 2-5/8" X 30' core barrel with aluminum inner barrel, 4-3/4" O. D. monel drill collar with electromagnetic survey (EMS) tool inside, and 2 monel drill collars (**Fig. 1.3-2**). The core bit was threaded onto the outer core barrel and was rotated by the power swivel at the surface. The inner barrel, located inside the outer barrel, was allowed to rotate independently through a bearing pack assembly. The scribe shoe, which has three scribe knives in a symmetrical position around the circumference of the shoe, was threaded onto the bottom of the inner barrel. The knives are used to keep the barrel from rotating with the outer barrel. The other function of the knives is to scribe the core with orientation lines as the core enters through the shoe into the inner barrel. The entire assembly was run in the hole on 3-1/2" IF drill pipe. After core run #1 in the 5U sand failed, the bit design was changed from a standard diamond design to a 6-1/8" X 2-5/8" PDC design. One monel collar was dropped from the drill string. After core run #4 in the 5U sand , the core catcher assembly was strengthened by adding a basket catcher and a split ring catcher. The basket catcher was dropped from the assembly after core run #5.

Orientation Tool And Procedure. The electronic survey instrument chosen to orient the recovered core is a three axis system utilizing accelerometers and magnetometers to determine well bore inclination, well bore direction, and core barrel scribe knife

orientation. Information obtained from the survey is stored in memory and downloaded at the surface after each core run. The tool is capable of storing over 7,700 readings, has no attitude or heading limitations, and is programmable over a wide range of timing intervals, allowing for greater flexibility. The orientation assembly consists of an instrument pressure barrel, rotating centralizers, and spacer bars to correctly space the tool inside the non-magnetic drill collar (Fig. 1.3-2). The survey instrument is calibrated electronically prior to its arrival on location.

Core barrel alignment is accomplished by placing an orientation mark on the assembly distinguishing the high side of the survey instrument and aligning it to the main scribe knife in the scribe shoe. To accomplish this, the outer barrel is suspended at the surface by the rig blocks. The inner barrel is then removed and a protractor is aligned with the main scribe knife. The inner barrel is then lowered and a mark is placed on an orientation rod attached to the top of the inner barrel. The survey instrument is threaded onto the orientation rod, the marks on the rod and the instrument assembly are aligned, and the tool is set in place through the use of set screws. The core barrel assembly is then screwed back together and run in the hole.

Well Plan And Coring Proposal. The well plan called for a curve with a dogleg severity (DLS) of less than 19^{o}/100 ft. to minimize deflection of the core. A radius of curvature of 400 ft., providing a DLS of 14.32^{o}/100 ft. was chosen to optimize drilling time and to allow maximum flexibility. The proposed hole diameter of the curve was 6-1/2" O. D. to increase tool string mobility if the DLS became critical. Planned weight on bit (WOB) was from 3,000 lbs. to 5,000 lbs. Rotary speeds were to operate in the range of 35 RPM minimum to a maximum of 65 RPM.

The Upper Spraberry 5U casing exit called for a section cut from 6,788' to 6,858' with a proposed kick off point (KOP) of 6,838'. The true vertical depth (TVD) of the 5U target was projected to be 7,238' TVD. The Upper Spraberry 1U casing exit called for a section cut from 6,639' to 6,709' with a proposed KOP of 6,689'. The 1U target was projected to be 7,089' TVD.

Original plans were to cut and retrieve 150 ft. of 2-5/8" diameter oriented core from each zone in 30 ft. increments. Clean out and TVD correction runs were to be performed as needed, based upon core recovery and mud log information.

Upper Spraberry 5U Casing Exit and Curve Summary. A 7- 5/8" cast iron bridge plug (CIBP) was run in the hole via electric wireline and set at a depth of 6,890 ft. A 75 ft. section of the 7-5/8" casing from 6,788 ft. to 6,863 ft. was then milled out using a 7-5/8" section mill. A caliper log was run across the interval to verify the actual amount of casing removed. For the cement kick off plug, a slurry of class "C" w/1% $CaCl_2$ was pumped and allowed to set for 24 hours to attain sufficient compressive strength for kick off. The plug was then tagged with the drill string to locate the top of cement. Upon tagging the plug, the top was found below the proposed KOP, necessitating pumping a second plug. After another 24 hour curing period, the plug was tagged and dressed off to the KOP of 6,838 ft.

The curve build BHA was made up on the surface and run in the hole to the KOP. Circulation was established with a fluid rate of 50 gallons per minute (gpm) and an air rate of 150 gallons per minute equivalent (gpm eq.) at the motor. The build section was drilled on an azimuth of 167 degrees from 6,838 ft. measured depth (MD) to 7,488 ft. MD resulting in a radius of curvature of 414 ft. with a DLS of 13.85 degrees/100 ft.

Upper Spraberry 5U Coring Summary. The first coring assembly was made up on the surface and run in the hole to the KOP. Circulation was established with the foamed air/brine mixture, the assembly was run to bottom, and coring operations were initiated.

The Upper Spraberry 5U sand was cored and drilled from 7,488 ft. MD to 7,931 ft. MD for a total of 443 ft. with a net core recovery of 169 ft. (**Figure 1.3-3**). Core run #1 resulted in zero recovery and an extremely low ROP of 35.3 min./ft. The bit design was changed from a standard diamond core bit to a 6-1/8" X 2-5/8" PDC design, increasing ROP tremendously. Core runs #2 and #3 resulted in 58 ft. of core recovery. Core run #4 was successful but the core was lost when the core catcher assembly failed at the surface during breakdown procedures. The catcher design was changed from a single slip dog catcher to a triple assembly consisting of a slip dog catcher, a basket catcher, and a split ring catcher. Core run #5 resulted in a 20 ft. recovery. Determining that the catcher assembly was too conservative, the basket catcher was dropped for subsequent core runs. Core run #6 resulted in only 6 in. of recovery due to rubble in the hole. After a clean up run, core runs #7 - #9 resulted in 89.5 ft. of recovery which terminated coring operations in the 5U.

Upper Spraberry 1U Casing Exit and Curve Summary. A 7- 5/8" retrievable bridge plug (RBP) was run in the hole via electric wireline to a depth of 6,750 ft. but set unsuccessfully. The plug and setting tool were removed from the hole and a second plug was successfully set at 6,750 ft. with two sacks of sand on top of the plug. A 30 ft. section of the 7-5/8" casing from 6,609 ft. to 6,639 ft. was milled out using a 7-5/8" section mill. A caliper log was then run across the milled interval to verify the actual amount of casing removed. For the cement kick off plug, a slurry of class "C" w/1% $CaCl_2$ was pumped and allowed to set for 24 hours to attain sufficient compressive strength for kick off. The plug was then tagged with the drill string to locate the top of cement. Upon tagging the plug, the top was found below the proposed KOP, necessitating pumping a second plug. After another 24 hour curing period, the plug was tagged and dressed off to the KOP of 6,612 ft.

The curve build BHA was made up on the surface and run in the hole to the KOP. Circulation was established with a fluid rate of 50 gpm and an air rate of 140 gpm eq. at the motor. The build section was drilled on an azimuth of 157.7 degrees from 6,612 ft. MD to 7,330 ft. MD resulting in a radius of curvature of 457 ft. with a DLS of 12.53° /100 ft.

Upper Spraberry 1U Coring Summary. The coring assembly consisting of a 6-1/8" X 2-5/8" PDC bit, scribe shoe with slip dog and split ring catchers, 6-1/8" X 2-5/8" X 30'

core barrel with aluminum inner barrel, 4-3/4" monel drill collar with EMS survey tool, 4-3/4" monel collar, and crossover sub was made up and run in the hole on 3-1/2" IF drill pipe to the KOP. Circulation was established with the foamed air/brine mixture, the assembly was run to bottom, and coring operations were initiated.

The Upper Spraberry 1U sand was cored and drilled from 7,330 ft. MD to 7,727 ft. MD for a total of 397 ft. with a net core recovery of 226 ft. (Fig. 1.3-3). Core runs #1 and #2 resulted in net core recovery of 62 ft. Core run #3 resulted in net recovery of 8 ft. before the core barrel jammed with black shale, indicating that the well path was out of zone. After a clean out and TVD correction run, core runs #4 - #8 resulted in a net recovery of 153 ft. Core run #9 resulted in a net recovery of 3 ft. before the barrel jammed and coring operations were terminated.

In summary, acquisition and orientation of the horizontal core was a mechanical success. Drilling procedures, in fact, proved to be not unlike that of coring a vertical well.

References

1. Schechter, D.S.: "Advanced Reservoir Characterization and Evaluation of CO_2 Gravity Drainage in the Naturally Fractured Spraberry Trend Area," First Annual Technical Progress Report, Contract No. DE-FC22-95BC14942, U.S. DOE (Dec 1996).
2. Tyler, N., and Gholston, J.C.: "Heterogeneous Deep-Sea Fan Reservoir, Shackelford and Preston Waterflood Units, Spraberry Trend, West Texas," Report of Investigation No. 171, Bureau of Economic Geology, The University of Texas, Austin, 1988.

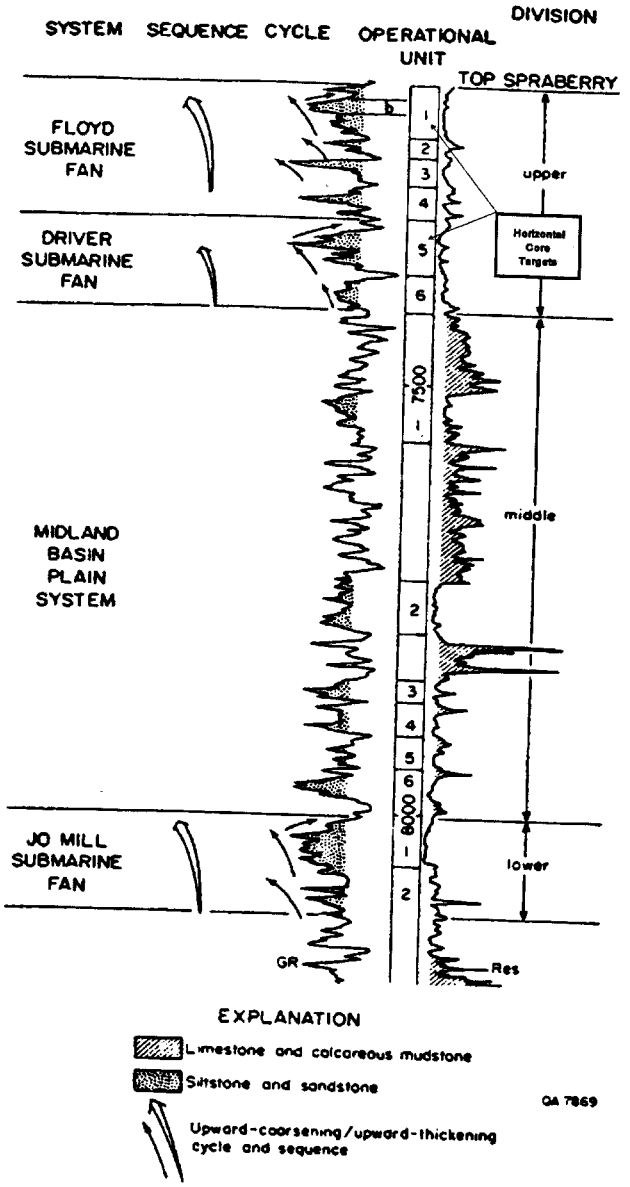

Fig. 1.3-1—Division of the Spraberry Formation in the central trend area, TXL Fee "B" No.1 well

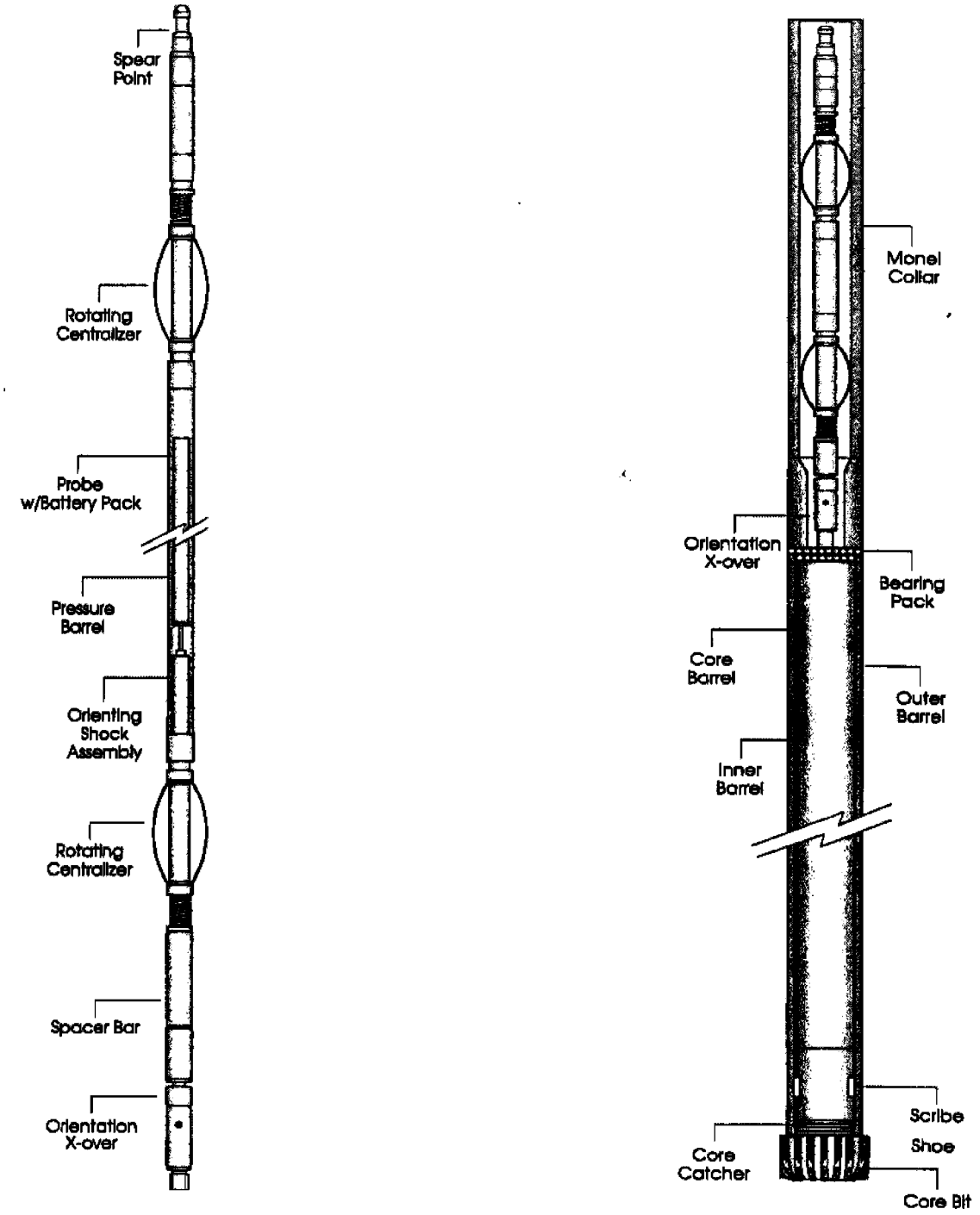

Fig. 1.3-2—Bottom hole coring and orientation assembly for horizontal coring of E.T. O'Daniel #28

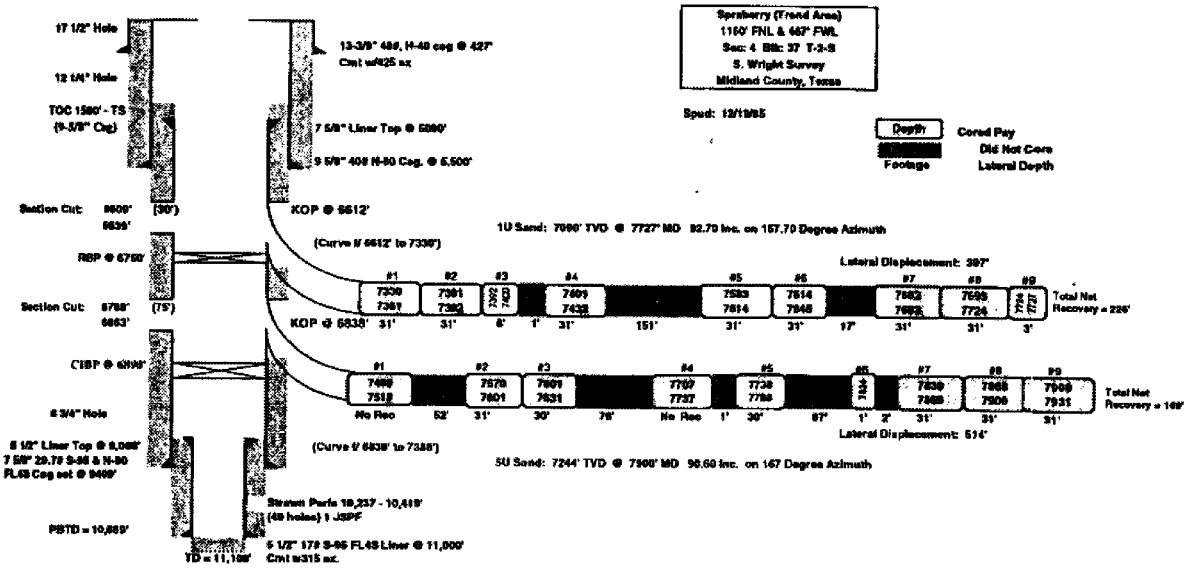

Fig. 1.3-3—A schematic diagram showing coring intervals in the E.T. O'Daniel #28

1.4 Fracture Analysis of the E.T. O'Daniel #28 Horizontal Core

Three distinct fracture sets, trending NNE, NE, and ENE, are present in cores from the 1U and 5U reservoirs.[1] NE fractures are commonly mineralized with barite and are found only in the 1U reservoir. Unmineralized NNE and ENE fractures occur in the 5U reservoir. Unmineralized ENE fractures are also more widely distributed within the black shales overlying both the 1U and 5U reservoirs, and locally near the top of the 1U unit. However, no fractures are present in the black shales underlying either reservoir. Each fracture set has its own characteristic and distinct patterns of 1) spacing, 2) mineralization, 3) distribution with respect to lithology, 4) surface characteristics, and 5) distribution of strikes. Therefore each fracture set is most likely to have resulted from a separate stress event. Aspects of these fractures that are important to production are as follows: 1) fracture strikes are segregated by reservoir unit 2) NE fractures are typically partially mineralized, but mineralization is absent in this set at the base of the 1U reservoir 3) none of the NNE or ENE fractures are mineralized 4) no fractures are present in the shales underlying both reservoirs, but ENE fractures occur in shales overlying both reservoirs.

Orientation. Three distinct natural fracture orientations are present in these horizontal cores, trending approximately NNE, NE, and ENE (Table 1.4-1).

Although the total range of strikes for each fracture set is about 25 degrees, the distribution of those strikes varies by set (**Figs. 1.4-1** and **1.4-2**). Most of the NE fractures occur within a narrow range (5 degrees) of distribution while most of the ENE fractures fall within a somewhat broader (20 degree) distribution of strikes. The ENE fracture strikes are relatively scattered within the total range of nearly 30 degrees.

Stratigraphic and Lithologic Controls. All 28 NNE fractures occur within the 5U reservoir, while the entire set of 46 NE-striking fractures is contained within the 1U reservoir. Fractures of the ENE fracture are not confined to either the 5U reservoir or to the sandy facies of either reservoir, although they are more common in the 5U unit. Eleven of the ENE fractures are present within the good 5U reservoir facies, seven ENE fractures are present near the top of the 1U reservoir in silty zones of poor florescence, and eleven more ENE fractures are present in the black shale facies overlying both the 1U and 5U reservoirs. No fractures of any set are present in any of the long cores taken from the black shale facies below either reservoir.

Spacing. The NNE fractures are very closely spaced. The average ENE fracture spacing is significantly larger, more than double that of the NNE fractures. NE fractures also have a wide average spacing similar to that of the ENE fractures (Table 1.4-2).

Each fracture set has a distinct pattern to its spacing distribution. The spacing distribution for the NNE fracture set (**Fig. 1.4-3**) conforms to the log-normal pattern typical of regional fractures; i.e., numerous closely spaced fractures and fewer widely

spaced fractures. The ENE fracture set (Fig. 1.4-3) has somewhat fewer of the fractures spaced less than one foot apart, but has a significant number of fractures within the one foot to three foot range. These ENE fractures are widely and irregularly scattered throughout the Spraberry formation, and the tail on the ENE fracture distribution histogram is significantly longer than that for either the NNE or NE sets, extending to 13 feet (Fig. 1.4-3).

In contrast, the NE fracture set is relatively regularly spaced (Fig. 1.4-3). The spacing distribution histogram for the NE fracture set shows relatively few and nearly equal numbers of both closely and widely spaced fractures, a narrow range of spacings, and a dominance of intermediate spacings of one to four feet. This fracture set is much more evenly distributed within the formation than either of the other two sets, or than is typical of regional fractures.

Apertures, Mineralization, and Surface Characteristics. Only fractures of the NE striking set (and thus only fractures in the 1U reservoir) contain obvious mineralization. This mineralization is inferred to be barite, and varies in extent from complete filling of original fracture apertures less than a millimeter wide to a complete absence of mineralization along hairline cracks in the intact rock. Most of the fractures of this set contain some mineralization with the average percentage of filling being on the order of 75%. Where fractures are incompletely mineralized, patches of barite with local crystal faces and rosettes are common, indicating open porosity and permeability pathways at depth. Most of the unmineralized NE fractures occur near the base of the 1U reservoir. This relationship is consistent in both intervals where the base of the 1U was cored. Although the reason for this local absence of mineralization is presently unclear, it may be related to local geochemical environments caused by segregation of hydrocarbons and formation waters.

In contrast, none of the ENE or NNE fractures contain mineralization, even in those few intervals where they occur in conjunction with mineralized NE fractures. Rather, the ENE and NNE fractures have gray or brown-stained surfaces that are distinct from the fresh, irregular, coring-induced breaks in the rock. Microscopic crystalline overgrowths may be present on some of the sand grains lining these surfaces.

The ENE fracture surfaces tend to be planar and smooth, whereas many of the NNE fractures occur as anastomosed or en echelon fracture segments with rough fracture surfaces and mm-scale en echelon fracture offsets. Preferred trend to the en echelon steps suggest incipient right-lateral shear.

The NNE and ENE fractures appear as hairline cracks in the core surface where the core has remained intact across the fracture surfaces. This is suggestive of significant in situ conductivity capability along the fractures.

Possible Fracture Origins. The average strikes of the NNE and ENE fractures are respectively 11 degrees counterclockwise and 27 degrees clockwise from the average strike of the NE fracture set. This initially suggests that these three fracture sets might be

interpretable as 1) a conjugate pair (the NNE and ENE fracture sets), with 2) a related NE fracture set sub-parallel to the bisector of the acute angle between the conjugate pair. Relatively small changes in stress conditions between the two reservoir units and/or subtle differences in the mechanical properties of the two units would have sufficed to create parallel vertical extension fractures in one bed and a related conjugate pair in the other bed.

However, in addition to the fact that the NE set does not precisely bisect the strike angle between the other two sets, there are several arguments against this interpretation:

1. Only the NNE set of the supposed NNE-ENE conjugate pair shows signs of the shear stress (the en echelon steps and offsets) that should accompany conjugate fracturing.
2. The ENE half of the pair occurs throughout the formation (except in the shales below the reservoirs), and commonly as the only fracture set present, rather than being limited in distribution to an association with the NNE half of the pair. The ENE fractures show no indications of a shear stress origin.
3. The NE set of fractures is mineralized whereas the other two sets are not: this suggests that the NE fracture set had formed and was mineralized prior to the formation of the other two sets under non-mineralizing conditions.
4. Each of the three fracture sets has its own distinguishing characteristics (including unique spacing and orientation distributions, surface characteristics, and distributions with respect to lithology), which separate the fracture sets and suggest that each formed under a different condition of stress and/or lithification.
5. One, albeit ambiguous, intersection between fractures of two sets was cored, this intersection suggesting that a NNE fracture terminates against, and is therefore younger than, an ENE fracture, rather than being part of a contemporaneous pair.

The conjugate sets theory is simple and clean and it has not been abandoned entirely, but it seems untenable based on these observations. An alternative but somewhat cumbersome interpretation is to suggest three separate fracture events, with the mineralized NE fractures being oldest, the ENE fractures of intermediate relative age, and the NNE fractures youngest. If the stress orientations have not changed since the formation of the youngest fractures, the maximum horizontal in situ compressive stress should then, theoretically, parallel the youngest fracture set. While this interpretation seems uncomfortably complex for this deep basin area of minimal structure, it would seem to best explain the data as presently understood.

Correlation of Core Fractures to Wellbore Image Log. A wellbore image log was run in the horizontal hole along the upper 1U interval. Although the images seem to be of good quality, there is an unsettling ambiguity in the correlation of log and core fractures (**Fig. 1.4-4**).

In order to analyze this ambiguity, a six inch tolerance was used (i.e., an imaged fracture is assumed to correlate to a fracture in core if it is within plus or minus six inches of the

measured core depth), and only the intervals where both core and log data are available were considered. In this interval, there are 24 fractures in core that have no correlative fractures at the equivalent depth in the image log, and 36 fractures in the image log that have no equivalents in the core. A maximum of only 15 fractures are definitively present in both the core and the image log, no matter what depth shifts are applied. Fracture swarms and isolated fractures in core, which should have made easily recognizable patterns in the image log and thus provided good core-log tie points, have not left similarly-obvious patterns on the image log.

Nevertheless, the overall fracture strike trend indicated by the image log is nearly aligned with the average of the fracture orientations measured in core. The secondary trend of ENE fractures in the core is also present in the image log, within the approximately correct measured-depth intervals.

The reasons for agreement in strike without a one-to-one correlation of individual fractures are unclear. Stretch during conveyance of the imaging tool and the common depth ambiguity of cores make exact depth determinations difficult and may explain some of the discrepancy. However these factors can not account for the significant over count of fractures (133%) made by the image log relative to the natural fractures in core. It has been suggested that the log is seeing fractures that were missed by the naked eye during minute core examination (unlikely, and which moreover would be insignificant to production if present). However, the images on the log do not indicate that any of the fracture apertures are significantly less than others. Coring induced fractures that formed in the wellbore but not in the core might also explain the apparent over count, but with the present images it is not possible to distinguish these from natural fractures. Moreover, this would not account for the mineralized fractures that are present in the core but not apparent in the image log.

In general, the patterns of fracture positions and the numbers of fractures in the core and image log are not compatible, although the average fracture strikes are. This suggests that image logs should be calibrated with core wherever possible.

Conclusion

Acquisition of this core unequivocally documents numerous, closely spaced natural fractures in the reservoirs of the Spraberry formation and led to the following major conclusions: 1) Three distinct fracture sets, trending NNE, NE, and ENE, are present in the cores from the 1U and 5U reservoirs. NE fractures are commonly mineralized with barite and are found only in the 1U reservoir. Unmineralized NNE and ENE fractures occur in the 5U reservoir. 2) Each fracture set has its distinct pattern of spacing, mineralization, distribution with respect to lithology, surface characteristics and distribution of strikes. Therefore each fracture set is most likely to have resulted from a separate stress event. 3) There was an unsettling ambiguity in the correlation of the fractures found in the core and the fractures found on the well bore image log. Orientation of the fracture sets from the core and logs were similar, however, there was a significant over count (133%) of fractures made by the image log relative to the natural fractures in the core.

References

1. Lorenz, John: "Summary of Observations and Interim Interpretations: Fractures in Horizontal Spraberry Cores, E.T. O'Daniel Well #28", Internal Memo to Project Team, December 12, 1996.

Table 1.4-1—Fracture Orientation		
Fracture Set	Average Strike (deg)	Total Range of Strikes (deg)
NNE	32	20-45
NE	43	35-50
ENE	70	50-85

Table 1.4-2 — Fracture Spacing		
Fracture Set	Spacing Range (ft)	Average Spacing (ft)
NNE	0.05-4.50	1.62
NE	0.73-5.75	3.17
ENE	0.04-13.0	3.79

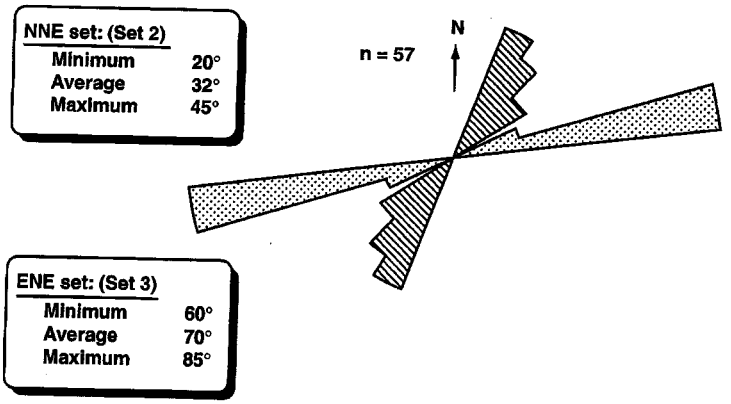

Fig. 1.4-1—Orientation of fractures in the 5U reservoir.

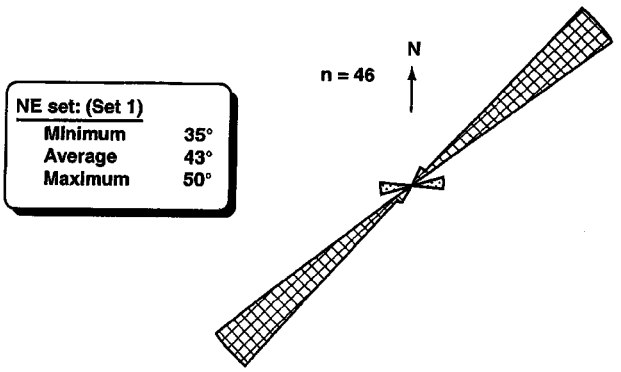

Fig. 1.4-2—Orientation of fractures in the 1U reservoir.

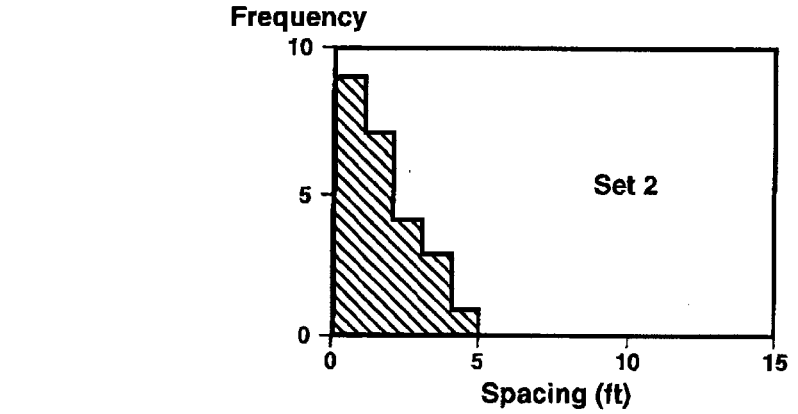

Set 2: NNE set
n=24 min 0.05'
avg 1.62'
max 4.5

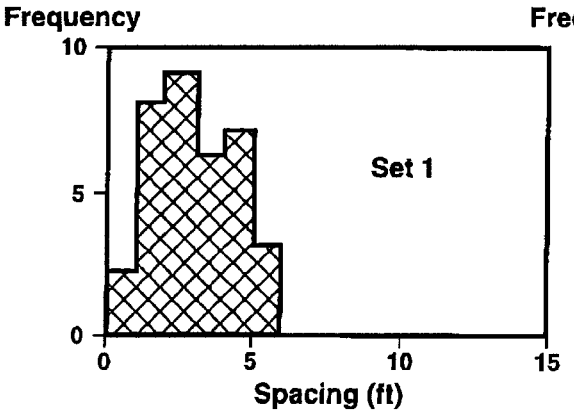

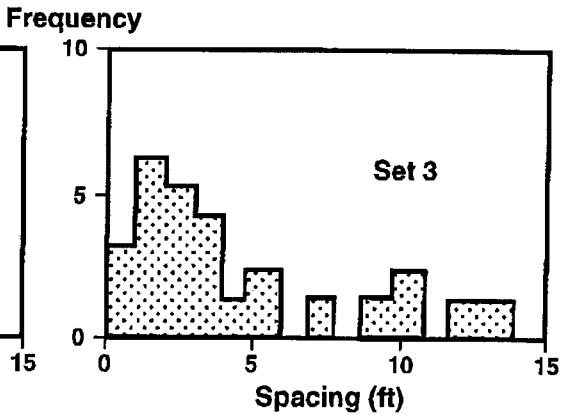

Set 1: NE set
n=35 min 0.73'
avg 3.17'
max 5.75'

Set 3: ENE set
n=28 min 0.04'
avg 3.79'
max 13.0

Fig. 1.4-3—Distribution of fracture spacing.

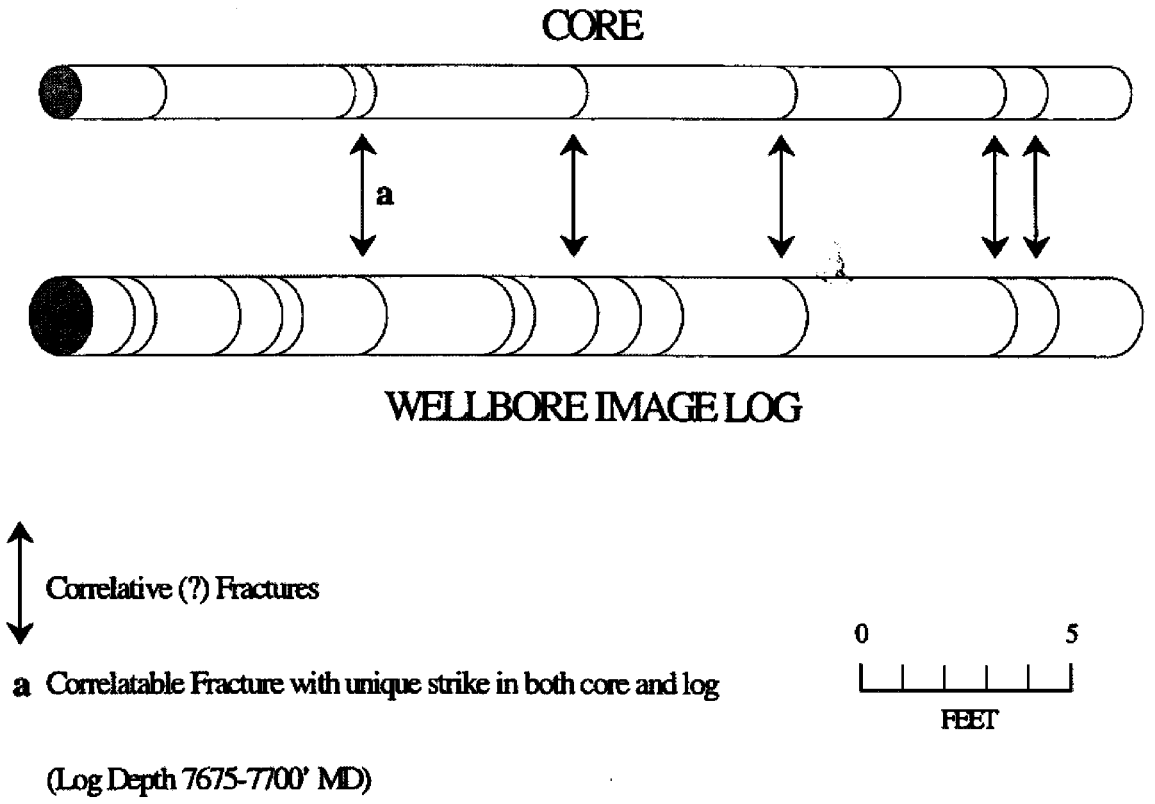

Fig. 1.4-4—Correlation between core fracture and wellbore image log fracture.

1.5 Investigation of Fracture Diagenesis from Core Spraberry Natural Fractures

This section summarizes diagenesis studies of the horizontal core and other fractures in the Spraberry database. We seek to answer a number of questions that have been posed about Spraberry fractures, including fracture spacing, fracture aperture, nature of mineralization, fracture paragenesis, relationship of fracture cements to diagenetic events within the rock matrix, what effect fractures and their diagenesis may have had on nearby rock matrix, and what controls, if any, the rock matrix exerts on the occurrence of the fractures.

Fractures have been examined in a number of cores at a variety of scales. Most work has been done at the core scale, where fracture spacing, orientation, vertical extent of fractures, and presence or absence of mineralization has been documented. Petrographic thin sections have been made from a number of fractures, both mineralized and unmineralized, and most recently, some fracture surfaces have been examined by SEM.

Results and Discussion

Descriptions of the various fractures from different wells follow. Refer to Table 1.5-1 for description of natural fractures, and **Fig. 1.5-1** for a type log from a Spraberry well showing units and stratigraphic position of the fractures discussed in this report.

Hutchinson #9

One length of fractured core was obtained from this well from a depth of 6850 ft. No log was available, but based on core depth and rock composition, this sample is believed to be from the Clearfork shale immediately overlying the upper Spraberry. The rock matrix is a very hard, dense, black dolostone. The fracture is unmineralized, but appears to be natural. Evidence for a natural origin of fractures in this core includes the presence of round microfossils that are broken sharply by the fracture and with no matching portion across the fracture. This implies either movement along the fracture (difficult to determine in this very homogeneous dolostone) or dissolution of material from within the fractured area. Additionally, fracture hackle plumes indicate an area of origin outside of and unrelated to the core itself. Fracture aperture is 0.05 to 0.08 mm.

Hutchinson #7

Two fractured cores were obtained from this well. Both were from the middle Spraberry (Fig. 1.5-1). One core from the middle Spraberry contains a mineralized fracture approximately 1 ft long from a depth of 7448-7449 ft. The fracture cuts across lithological boundaries between siltstones and mudstones, but terminates on both ends in zones that become increasingly clay-rich. Three thin sections were made from this interval. The uppermost thin section consists of a carbonate grainstone/packstone underlain at a sharp contact by a very fine-grained argillaceous siltstone to mudstone. There are three distinctive diagenetic zones noted in this thin section; the lowest, a terrigenous mudstone, the middle, a silicified grainstone, and the uppermost, a carbonate-cemented grainstone. Diagenetic zonation indicates that, at least locally, interbedded clay-rich units provide a source for silica cements in siltstones. The next thin section

downward in the core contains a fine siltstone that grades down into a very fine-grained siltstone interlaminated with argillaceous siltstones and mudstones. The lowermost thin section is a very fine siltstone/mudstone containing abundant detrital clays, micas, and organic matter. The fracture filling in all thin sections is calcite. Fracture width ranges from 0.06-0.08 mm wide up to about 0.16 mm at its widest, and length is about 250 mm long. The widest part of the fracture is in the uppermost thin section, in the coarsest grain-sized material. There are void spaces within the fracture filling; some are apparently open in the subsurface, as there are euhedrally terminated carbonate crystals growing in the pore space. There is an open crack within the fracture that parallels fracture boundaries in one of the thin sections, but it is not apparent whether this is open in the subsurface. The fracture cuts through several very different lithological boundaries, including boundaries between clean and dirty siltstones, siltstone and mudstone, and from a medium-grained fossiliferous grainstone that is strongly silicified to a very fine-grained terrigenous mudstone. Little change in fracture character is apparent at these lithological boundaries.

The finely-laminated siltstones have a few bedding plane fractures. These openings are partially occluded by very fine-grained gypsum. Some of these partings do break through the primary vertical fracture, but there is no mineralization at the juncture to determine relative timing of fractures or mineralization.

The other middle Spraberry fractured core is from a depth of 7645–7647 ft, and it contains a fracture set showing an intersection at a 60 degree angle. Both fracture directions are mineralized; again, the only fracture-filling phase appears to be calcite. Four thin sections were made from this fracture zone. The uppermost portion of the fracture is within a laminated mudstone siltstone unit, with laminae defined by increasing and decreasing amounts of detrital clay and organic matter. One fracture terminus is present in one of the thin sections. Fracture width at the tip is only about 0.004 mm wide and the fracture detours around harder framework grains, making a path through the less competent clays and micritic dolomite cement. As the fracture continues, it widens and begins to break through grains, and as less clay-rich laminae are encountered the fracture becomes straighter and wider, up to 0.04 mm wide. Fracture character does change somewhat as laminae are crossed, becoming narrower and more sinuous in the clay-rich layers and wider and straighter in harder, more quartz-rich layers. The fracture is multi-strand in places, and there are parts of the fracture that contain no mineralization. Calcite crystals look corroded in places, as if dissolution had occurred.

Hutchinson #1

There is one large mineralized fracture in the core from this well. The fracture is about 2 ft long and is from the depth interval 6945–6947 ft. No log was available for this well, but fracture characteristics and matrix lithology are consistent with that seen in the 1U Spraberry interval in other wells. Mineralization in the large fracture includes quartz and dolomite as the earliest-precipitated phases, a later-precipitated coarsely crystalline barite, and a very finely crystalline mineral identified using qualitative waveform dispersive spectroscopy (WDS) as finely crystalline dolomite. The fracture forms the edge of the core sample and the other side is not available, so information on fracture

aperture is not available. Parallel to the large mineralized fracture is a much less obvious fracture that appears unmineralized in hand specimen. Petrographic examination shows the presence of significant quartz mineralization in the form of euhedral quartz crystals within this fracture and along its edges. The fracture is wider and more meandering than the hairline fractures seen in the Hutchinson No. 7 well and contains many fragments of matrix rock. The maximum fracture width is about 0.45 mm, but the average aperture of a single strand is about 0.08 mm. This type of fracture would contribute a significant amount of porosity and permeability to a sample, and is almost invisible to the casual observer of a core. Matrix rock in this fractured interval is a clean, very fine sandstone/siltstone with some clay-rich layers and evidence of bioturbation.

E. T. O'Daniel #37

There are two principal fractured intervals noted in this core. The most easily-identified natural fracture set is at 7134–7136 ft, within the upper Spraberry 3U sand. Several calcite-filled hairline fractures were noted in the interval. Fracture width in thin section is about 0.16 mm, but there is a gap running along the fracture, and actual filling width is about 0.03 mm wide. Fracture length is about 250 mm (1 ft). There are small fracture strands parallel to the main fracture that are also calcite-filled; these are completely mineralized. The sides of the fracture do not match exactly, indicating that the gap may be open in the subsurface.

The other main zone of fracturing is in the interval from 7226 ft to 7234 ft. The fractures are above and within the 5U pay zone. Fractures are not mineralized, but were identified as natural fractures.[2] Several thin sections were made from this zone, some in the horizontal plane and some in the vertical plane. One feature that was noted from thin section analysis is that fractures are not simple planes, but zones, and an individual fracture is composed of short segments that may or may not be joined in the plane of the thin section. Connections between fracture segments may be simple or complex. Also, the fracture can split into bands or zones of disrupted rock. The widest single fracture is about 0.04 mm wide and zones of fracturing ranged from 0.14 to 0.5 mm in width.

E. T. O'Daniel #28 (horizontal core)

This well was originally drilled as a vertical well, but was redrilled as a horizontal well for this project as described in previous sections. Two intervals were cored within the upper Spraberry. Although it was believed that one of the cored intervals was the Spraberry 1U main pay zone, an increasing body of evidence indicates that this cored interval is mostly within one of the two small sands that overlie the main 1U pay zone (**Fig. 1.5-2**). This evidence will be presented in a following section. The other cored interval from this well was the 5U.

Both cores were logged for fracture orientation, fracture spacing, and large scale features. These are summarized in Figs. 1.4-1, 1.4-2, 1.4-3, and **1.5-3**. A few pieces of core were recently made available for detailed petrographic examination. One sample was obtained from each of the cored intervals.

Most fractures in the 1U cored interval are mineralized, and the average orientation of these fractures trends N43E. Fracture spacing is about 3.17 ft, and the fracture orientation is quite uniform. There are a small number of unmineralized fractures that trend N70E and are only seen in the overlying black shale intervals that were penetrated in this coring operation. Surfaces of both these fracture sets are smooth and show no sign of shear as described in Section 1.2.

SEM examination of one of the mineralized fractures shows that there are at least three fracture-lining mineral phases. Quartz and dolomite are the earliest deposited phases, and mineralization is nucleated on quartz grains and dolomitic cements that are adjacent to the fracture opening. The sample examined in SEM contained more quartz than carbonate cement, and approximately 30% of the fracture surface was lined with quartz cement. Crystal size is still fairly small, and there is still a significant amount of intergranular and intercrystalline porosity available to permit the flow of fluid between rock matrix and fracture. Barite forms a later fracture-filling phase and appears to form a much more significant barrier to fluid flow. Barite crystals are quite large, up to a millimeter or more in size, and they can completely cover the underlying matrix. Examination in SEM reveals almost no porosity within barite crystals. The paragenetic sequence exhibited by the fracture is similar to that seen in 1U sandstone from the Hutchinson #1 and Shackelford #1-38A.[3]

Fractures within the 5U appear to be mostly unmineralized. One fracture sample was selected because it did appear to have some mineralization, but examination by SEM revealed that the mineral was halite, probably left over from evaporation of reservoir brine. 5U fractures show two distinct orientations, N32E and N70E. Both sets are unmineralized. The N32E set is only seen within the coarser clastics of the 5U, while the N70E set is seen within the clastics and the fine-grained black shales that overlie the 5U. N70E fractures have a spacing of 3.79 ft on average (Fig. 1.4-3). The N32E fracture set has a spacing of 1.62 ft on average and distribution is log-normal. This fracture set has surfaces that are rougher and show evidence of a shear origin, unlike any of the other fracture sets.[4]

Conclusions

The examination of naturally-occurring fractures in several vertical Spraberry cores and the horizontal cores obtained from the E. T. O'Daniel #28 demonstrates unusual complexity for a fairly homogenous and structurally uncomplicated reservoir. Fractures were noted in three main orientations, with two different surface morphologies, and having two kinds of mineralization or none at all. Fracture aperture has not yet been measured for the horizontal core, but thin section measurements show widths of 0.05-0.08 mm in mineralized fractures. The horizontal core was invaluable in providing evidence on fracture orientation, spacing, aperture, and mineralization within the 1U and 5U, but many questions still remain to be answered concerning the origins of the various fracture sets, the relationship of the fracture network to rock matrix, and its effects on reservoir production.

References

1. Schechter, D.S.: "Advanced Reservoir Characterization and Evaluation of CO_2 Gravity Drainage in the Naturally Fractured Spraberry Reservoir," quarterly technical progress report, Contract No. DE-FC22-95BC14942, U.S. DOE (Dec. 1995) (PRRC 96-12).
2. Lorenz, J., 1997, "Horizontal Core Fracture Description," paper presented at the Spraberry Symposium, Parker & Parsley Development Company and U.S. Department of Energy, Midland, TX (Jan. 1997).
3. "Advanced Reservoir Characterization and Evaluation of CO_2 Gravity Drainage in the Naturally Fractured Spraberry Trend Area," The First Annual Technical Progress Report, Contract No. DE-FC22-95BC14942, U.S. DOE (Dec. 1996) (PRRC 96-42)
4. Nelson, R.A.: *Geologic Analysis of Naturally Fractured Reservoirs*, Gulf Publishing Co., Houston (1985).

Table 1.5-1—Summary of Naturally Fractured Cores

Well Name	Depth of Fracture Interval (ft)	Formation Zone	Pay/ Nonpay	Comments
Hutchinson #9	6850	Clearfork	NP	unmineralized
Hutchinson #7	7448	Middle Spraberry	NP	calcite
Hutchinson #1	7645	Middle Spraberry	NP	calcite, 60 set
Hutchinson #1	6945	Upper Spraberry 1U	P	barite
E.T. O'Daniel #37	7135	Upper Spraberry 3U	NP	calcite
E.T. O'Daniel #37	7226–7234	Upper Spraberry 5U	P	unmin.
E.T. O'Daniel #28 (horizontal core)	7330–7226 MD 7082–70892 TVD	Upper Spraberry 1U	P/NP	barite
E.T. O'Daniel #28 (horizontal core)	7851–7928 MD 7230–7250 TVD	Upper Spraberry 5U	P/NP	unmin.
Shackelford #138A	7088–89	Upper Spraberry 1U	P	barite

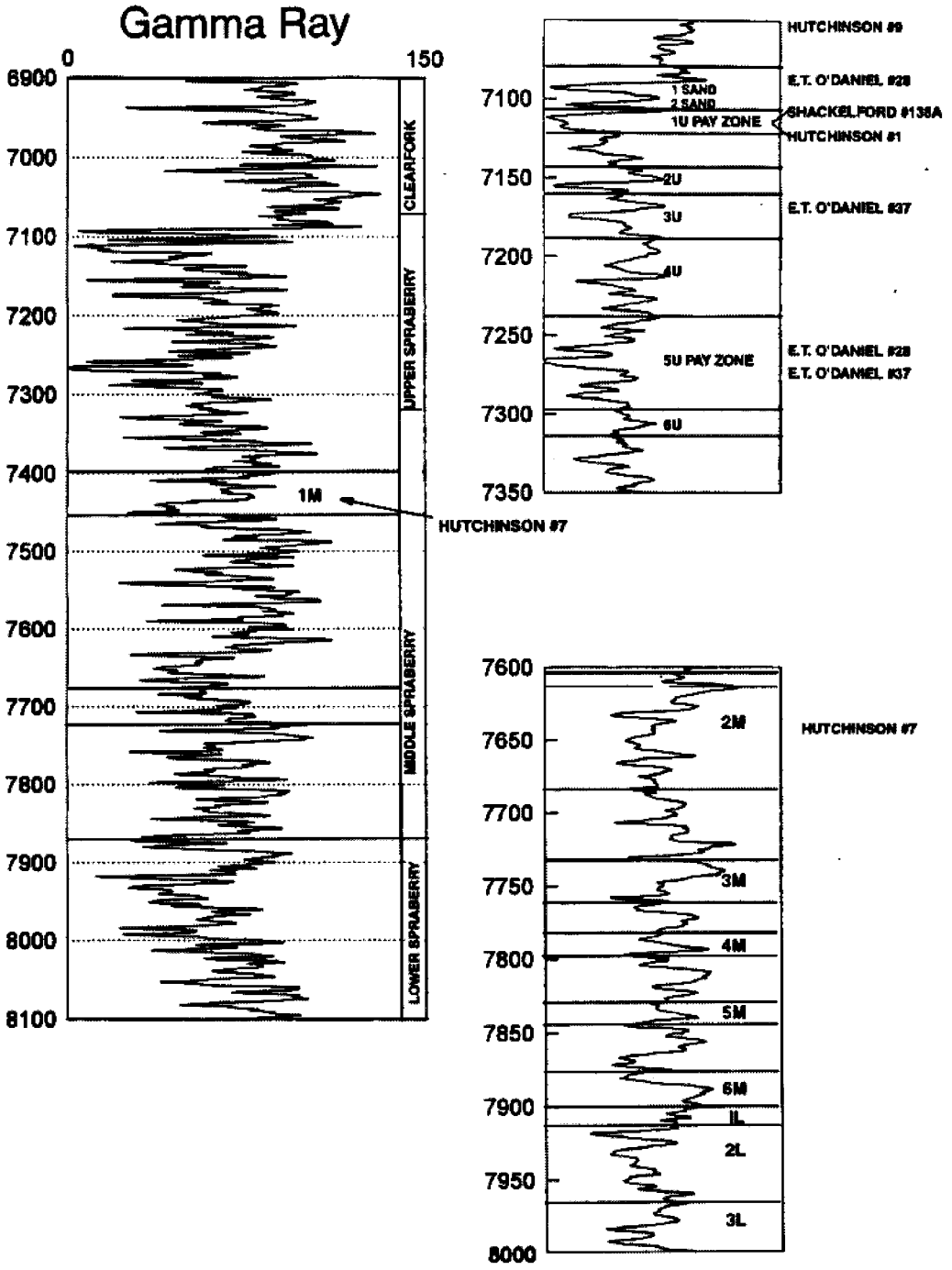

Fig. 1.5—Type log of Spraberry in the O'Daniel lease, showing various stratigraphic divisions and the approximate stratigraphic positions where various fractured core samples were obtained. Texas Bureau of Economic Geology subdivides the 1U of the Spraberry into several subunits, of which the b-c sand is the most important pay zone. We refer to this sand as the main 1U pay. Logs from our type log area (E.T. O'Daniel lease) show two small sands off center above the main pay. We refer to these as the first and second sands above the 1U.

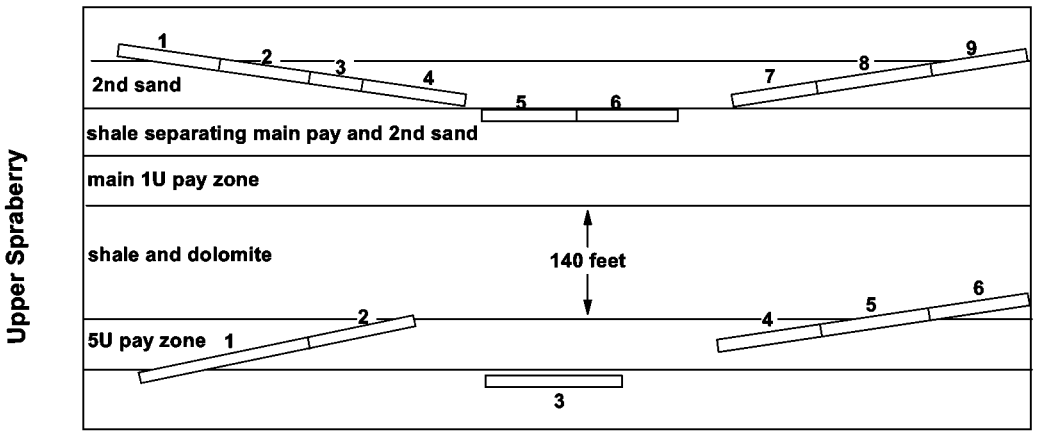

Fig. 1.5-2 —Schematic diagram of the horizontal cores from the E.T. O'Daniel #28 well (not to scale).

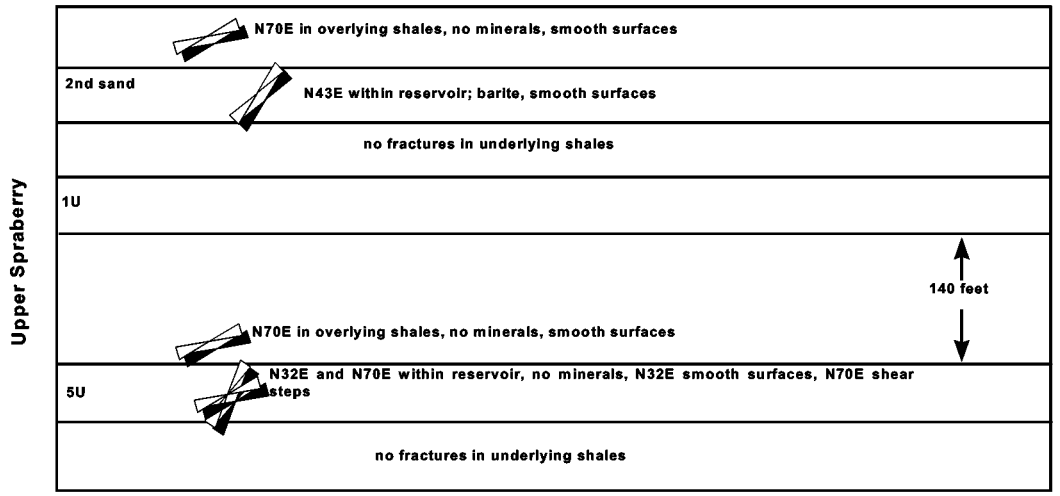

Fig. 1.5-3 —Summary of fracture characteristics noted in the two horizontal cores from the E. T. O'Daniel #28 well for both pay and non-pay lithologies.

1.6 Application of Rock-Log Model to the Horizontal Core Well

During the first year of this project, we developed a rock-log model for identification of pay zones in the Spraberry Trend Area reservoirs based on vertical cores and logs (reference 3 in section 1.3). This section demonstrates the capability of the rock-log model using logs from a horizontal well.

Log Analysis

Figure 1.6-1 shows the open-hole logs from the E.T.O'Daniel # 28 horizontal well (Upper Spraberry). The volume of shale was calculated from gamma ray (GR) logs using the Larionov non-linear relationship. Effective porosity was calculated from the bulk-density log and integrated with whole core porosity.

As previously mentioned, there is evidence indicating that the upper cored interval of the O'Daniel #28 horizontal well is not actually the main 1U pay zone, but is one of the two thin pay sands that immediately overlie this zone (Fig. 1.5-2). A detailed comparison of gamma logs from the vertical log of this well and the log that was made from the horizontal redrilling shows that there is good correspondence of gamma peaks between the two logs (**Fig. 1.6-2**). As the horizontal well begins its curve from vertical to horizontal, the depths do not correspond, and the gamma peaks in the horizontal log become broader and less sharp as the log reflects the increasing curvature of the hole. Still, peaks have a good one-to-one correspondence, and the peak that constitutes the major Spraberry sand encountered in the horizontal core does not correspond to the main pay zone of the 1U, but to the second small sand that is encountered *above* the 1U. A similar relationship can be seen when examining the lithodensity log. Dolomite zones, corresponding to intervals of high bulk density, can be compared. Again, the main "pay" interval is actually above the true 1U. We were unable to log the 5U lateral due to the continual problem of tools getting jammed in the 5U curve.

Examination of the lithodensity-neutron crossover log provides further confirmation (**Fig. 1.6-3**). Within the logged interval, there are only three zones of crossover. The first is small and occurs at a log depth of 7250 ft. The second zone of crossover is thicker, from 7360 ft to 7400 ft, and this corresponds to the second sand above the 1U. This is the zone that was cored. Based on the hole geometry, the sand interval is only about three feet thick, much thinner than the pay zone interval (10 ft) of the 1U sand as determined from application of the rock-log model to the vertical log.

A fourth line of evidence supporting the argument that the primary 1U pay zone was not actually cored in the horizontal drilling operation is the close correlation between the core description and the well log after depth correction. At the top of core #1, 7330 ft core depth and 7315 ft log depth, there is a 25-ft interval of non-pay, non-fluorescing material. At a depth of 7355 ft (7340 ft log depth) sand percentage begins to increase and the core has poorly developed fluorescence. This trend continues and corresponds with the decrease in gamma count and a decrease in percent dolomite. At a measured depth of 7380 ft (7365 ft core depth), good fluorescence and the lowest gamma and bulk density readings are encountered. This corresponds to the gamma low of the second thin sand above the main 1U pay zone. At a core depth of 7425 ft, a sharp contact between

fluorescing and non-fluorescing zones is encountered, again corresponding to the higher gamma counts seen in the well log, which indicate a zone of increased shale content.

The horizontal core well penetrated the two sand stringers that overlie the true main 1U pay zone. The reasonable production rates from this 3-ft thick zone are puzzling. The well has produced water-free oil for several months, which is rare in a 40 year old waterflood unit. There are two possible explanations. One explanation may be that the various sands within the 1U are not in direct communication with each other. No natural fractures were seen in the shaley zones below the cored sand; however, other fractures from other cores do show continuity of fractures through small zones of lithologic change, and it could be that such fractures were simply not encountered in the small section of core that was taken from between the shale overlying the main 1U pay zone (Fig. 1.5-3). Another possibility may be that production is controlled by fracture intensity, and fracture density is higher within thinner competent beds than in the thicker beds.

Also, crossplots of gamma ray vs. shale volume indicate that there is very little of the pay sand classified as rock type A, based on the our rock-log model[1] (**Fig. 1.6-4**). It can be observed from the Fig. 1.6-4 that cut-off criteria previously developed from vertical well logs can accurately quantify rock type in the horizontal well. Data points, where the volume of shale is less than 15% and the effective porosity is greater than 7% (Rock Type A) are sandiest part of the second sand above the 1U unit. Data points where the volume of shale is less than 15% and the effective porosity is less than 7% (Rock Type B) are from the marginal pay of the 1U sequence. Core data indicates these zones are marginal pay. The porosity of these zones is drastically reduced due to presence of dolomite cement. Data points where the volume of shale is greater than 15% are from muddy non-pay zones of the Upper Spraberry as the horizontal wellbore traverses shale zones (Rock Type C). Most data points from the 1U horizontal cores lie either in regions B (marginal pay) or C (nonpay), atypical of reservoir rock from the main 1U pay.

Core Data Analysis

The Upper Spraberry 1U sand was drilled and cored from 7,330 ft. MD to 7,727 ft. MD for a total of 397 ft. with a net core recovery of 226 ft. Core runs #1 and #2 resulted in net core recovery of 62 ft. Core run # 3 resulted in net recovery of 8 ft. before the core barrel jammed with black shale, indicating that the well path was out of zone. After a clean out and TVD correction run, core runs #4 - #8 resulted in a net recovery of 153 ft. Core run #9 resulted in a net recovery of 3 ft. before the barrel jammed and coring operations were terminated[2]. Core runs #1 & #2 are from 7,330-7,390 ft. Core runs #3 & #4 are from 7,390-7,430 ft. Core runs #5 & #6 are from 7,587-7,643 ft. Core runs #7 & #8 are from 7,662-7,693 ft. and Core run #9 are from 7,722-7,726 ft.

Core analysis of these cores were performed by Reservoirs Inc.[3] A surface gamma ray log of the each core was recorded for downhole correlation. Full diameter ultraviolet and natural photographs were taken for permanent record. Water and oil saturations were determined by Dean-Stark Extraction. Porosity was determined using Boyle's law.

Horizontal and vertical permeability to air was measured using the Hassler Sleeve Permeameter. Comparison of these cores are shown in Table 1.6-1.

Verification of Rock-Log Model

Integration of core and log data indicates that cut-off criteria for log-based Rock Type A are similar to the rock properties observed in core runs #3 & #4 and #7 & #8. Cut-off criteria for log-based Rock Type B are similar to the core runs #1 & #2 and #9, which are considered as non pay. Cut-off criteria for the log-based Rock Type C are observed in core runs #5 & #6, which are non-pay muddy zones. These core observations of oil saturation in porosities greater than 7% verify the rock-log model developed based on vertical wells.

Geological Steering

The correct placement of the wellbore within the pay zone has a crucial role in determining the subsequent commercial success of a horizontal well. However, accurate placement of horizontal wells in thin beds demands changes to present geometrical well planning and drilling techniques. Logging-while-drilling (LWD) formation evaluation in real time has opened up a powerful horizontal directional drilling technique-Geological Steering. Typical LWD tools include GR, dual resistivities, neutron porosity, density porosity, and ultrasonic caliper. Geological steering is the process of landing the well in the target zone prior to drilling horizontally and maintaining the drainhole at the optimum level within the pay.

Conclusions

The following conclusions were reached based on detailed integration and analysis of the Upper Spraberry horizontal open-hole logs and core data from the well E. T. O'Daniel # 28:

1. The rock-log model, previously developed from open and cased-hole logs from vertical wells, can be applied successfully to the new horizontal well drilled in the Spraberry Trend and can be used successfully for placement of horizontal wells within thin pay sands.

2. Horizontal core runs #3 & #4 and #7 & #8 from the upper part of the 1U main pay of the Upper Spraberry, have been found to exhibit characteristics of Rock Type A (massive clean siltstone, low shale volume, low bulk density, low water saturation and with strong oil fluorescence).

3. Core runs #1 & #2 and # 9 are classified as Rock Type B (porosity occluded by dolomitic cement and weak fluorescence).

4. Core runs #5 & #6 are Rock Type C (non-pay mudstones, high shale volume with no oil fluorescence).

Table 1.6-1—Comparison of Horizontal Cores Taken from the 1U Zone in the E.T. O'Daniel #28

Core Run No. (see Fig. 1.5-2)	Porosity	Oil Fluorescence	Permeability	Water	(md)	Oil
#1	< 0.07	No		< 0.1	High	No
#2	< 0.07	No		< 0.1	High	No
#3	> 0.07	Strong	> 0.1	< 0.20	< 0.15	
#4	> 0.07	Strong	> 0.1	< 0.20	< 0.15	
#5	< 0.07	No		< 0.1	High	No
#6	< 0.07	No		< 0.1	High	No
#7	> 0.07	Strong	> 0.1	< 0.20	> 0.10	
#8	> 0.07	Strong	> 0.1	< 0.20	> 0.10	
#9	< 0.07	No		< 0.1	High	No

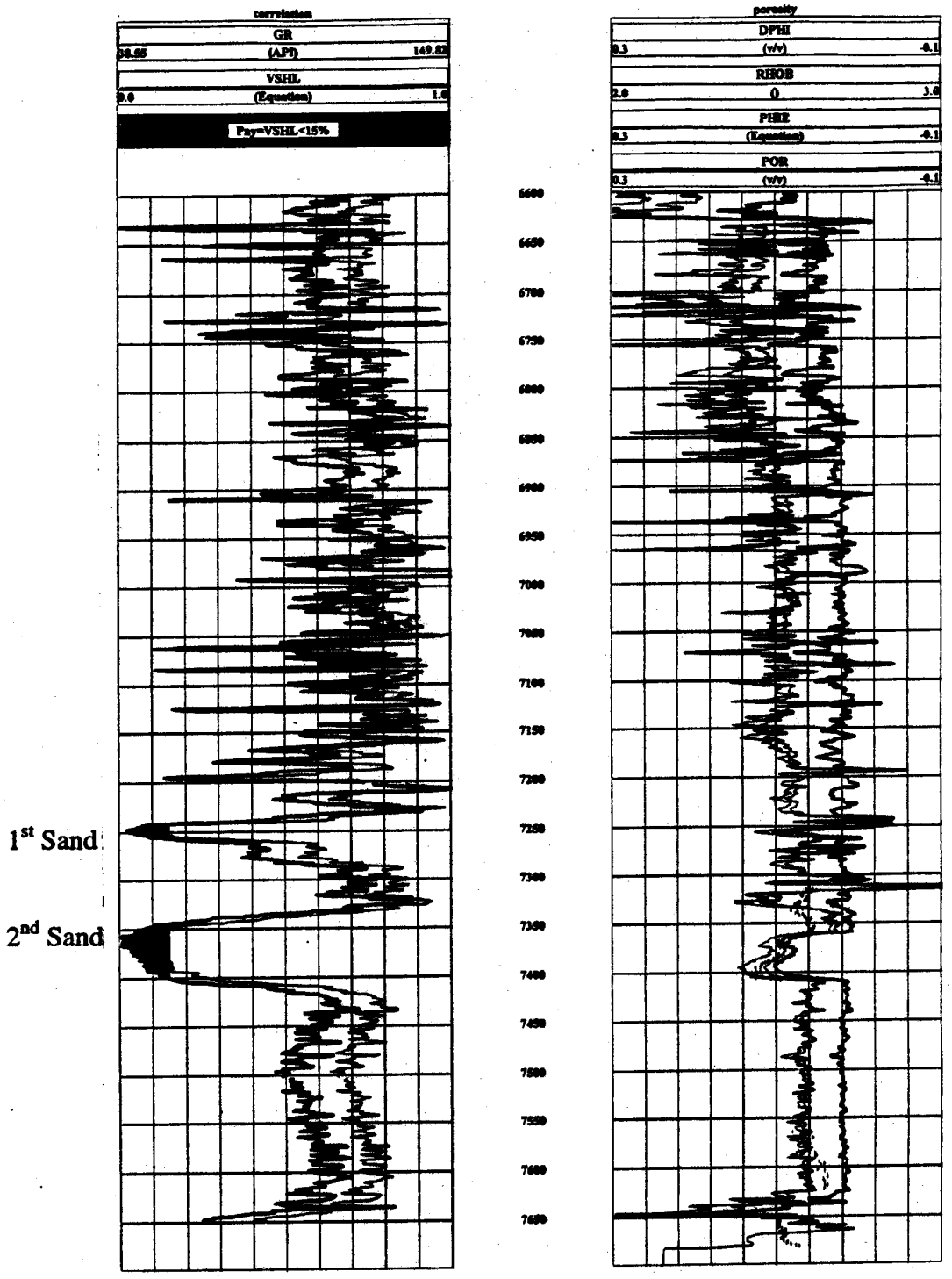

Fig. 1.6-1—Open-hole logs from the 1U zone in the horizontal well E.T. O'Daniel #28

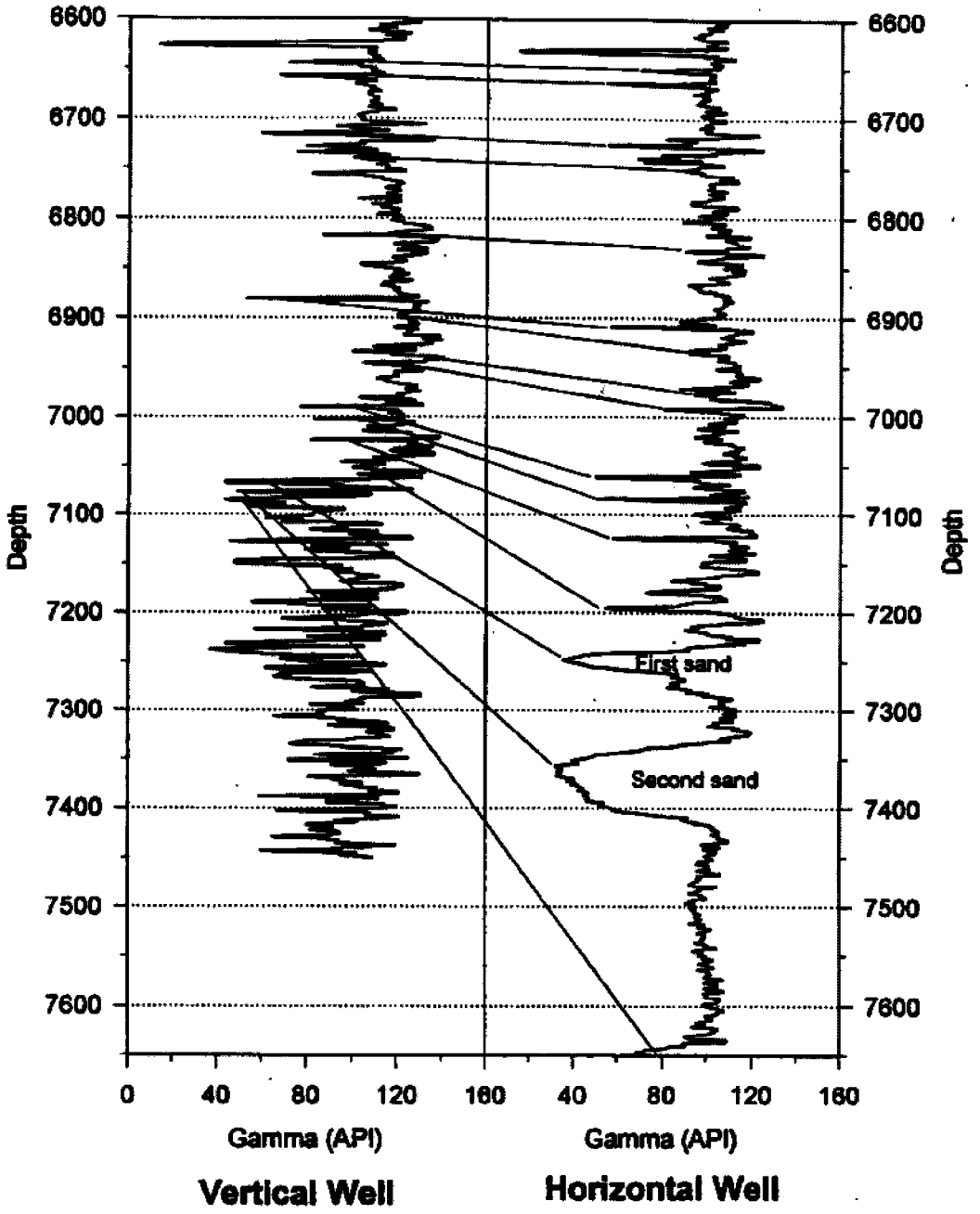

Fig. 1.6-2—Comparison of gamma ray log from vertical and horizontal logs in the E.T. O'Daniel #28 well. Note how individual beds appear to get thicker and more separated from each other as the curvature of the horizontal bore increases and approaches a horizontal line. Lines match various peaks within the Clearfork and demonstrate that the cored interval was not the main 1U pay zone but the sand immediately above.

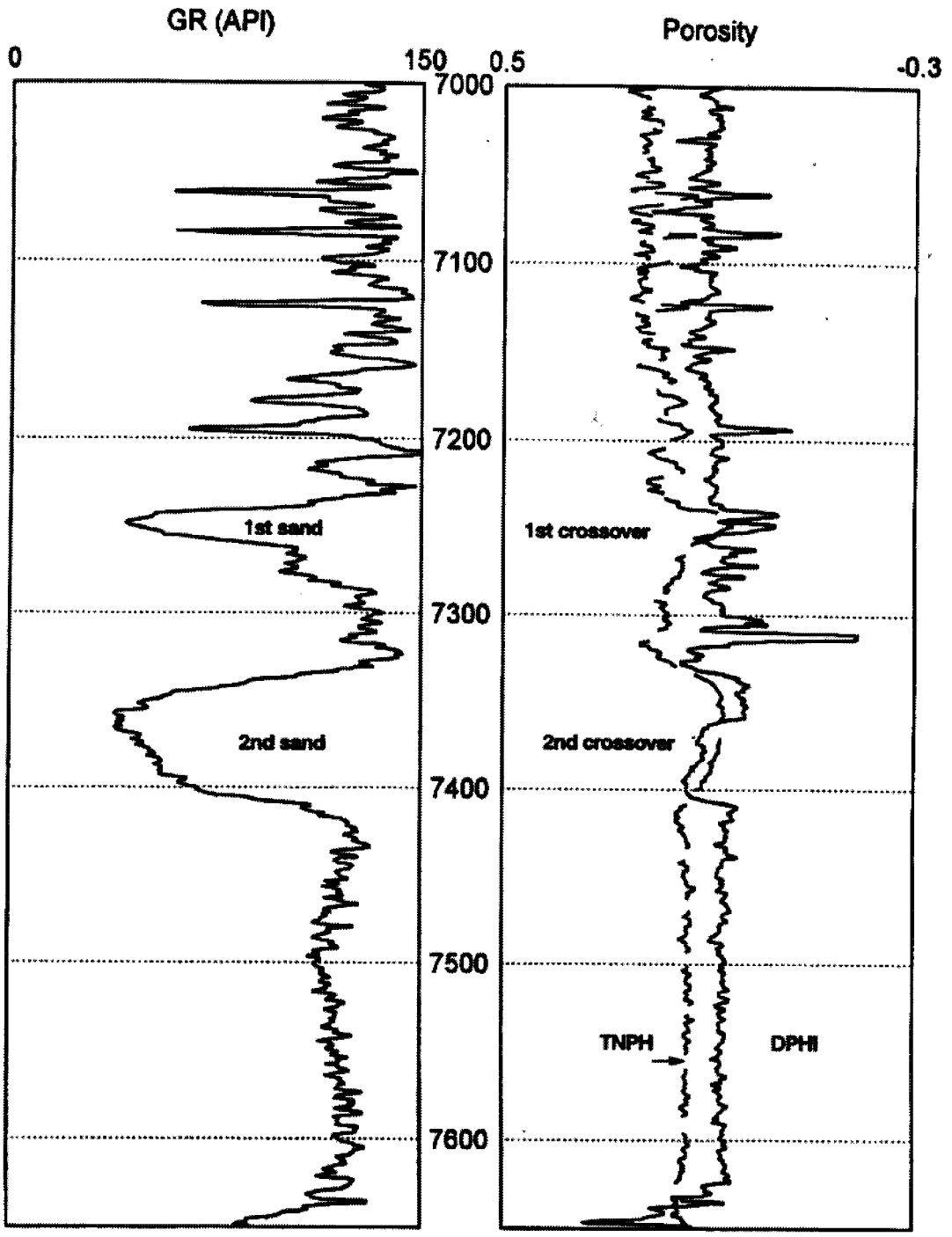

Fig. 1.6-3—Lithodensity/Neutron crossover log. This log shows only two pay zones, neither of which is as thick as the 1U was estimated to be in this area. The two minor pay zones correspond to the first and second sand above the 1U pay.

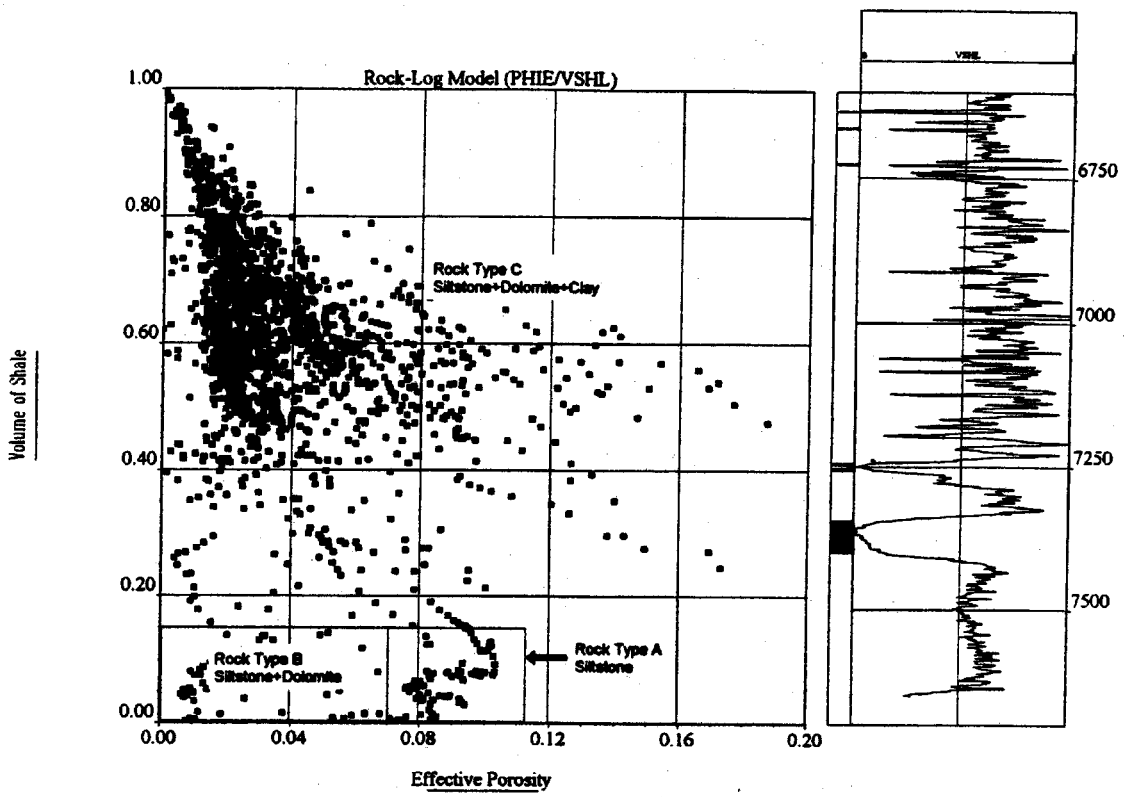

Fig. 1.6-4—Crossplot of volume of shale vs. effective porosity. Note that a relatively small amount of zones intersected by the horizontal wellbore are classified as Rock Type A, good reservoir rock. Most of the horizontal cores have been observed to be Rock Types B and C.

1.7 Pay Zone Identification Using Old Cased-Hole Logs

Introduction

We demonstrated in our first annual report[4] that classic shaly-sand analysis of open-hole logs from Spraberry wells could accurately quantify thin fractured pay zones which characterize the Spraberry Trend. Based on ultraviolet observations of fluorescing intervals along with whole core analysis and open-hole log interpretation, we reported that a shale volume less than 15% and an effective porosity greater than 7% provide accurate cut-off criteria for identification of fluorescing pay zones in the Spraberry Trend Area. We also reported a rock-log model developed for identification of the highest quality pay intervals of the Spraberry Trend Area, using available open-hole well log data. Volume of shale was cross-plotted against effective porosity. Three general rock types were identified, of which only one can be classified as pay. Rock type A (1U and 5U of the Upper Spraberry) has a volume of shale less than 15% and an effective porosity greater than 7%. This type of rock is the primary reservoir rock and consists of mainly massive, clean siltstone, fluoresces strongly under ultraviolet light, has low water saturation and visible porosity is observed in thin section analysis. Rock type B (2U, 3U and 4U of the Upper Spraberry) has a volume of shale less than 15% yet the effective porosity is less than 7%. This type of rock has a low volume of shale with porosity occluded by dolomite cement. Rock type B mainly consists of siltstone and dolomite, fluoresces weakly relative to the 1U and 5U and is considered marginal pay. Rock type C has a volume of shale greater than 15%. This type of rock is composed primarily of non-pay mudstones and has a high shale volume with no fluorescense under ultraviolet light.

In the second year of the project, we extended this open-hole log analysis to old cased-hole gamma ray and neutron (API, count per second or no units) logs. Good agreement is demonstrated between modern open-hole and old cased-hole logs for identification of Spraberry pay. A new method of normalizing neutron logs is also presented in this section.

Case-hole Log Analysis

Figure 1.7-1 is an example of a cased-hole log from the well O'Daniel "G" #1 from the Spraberry Trend Area, and consists of an old gamma ray and neutron log in API units. This figure shows that the old neutron (API) log accurately distinguishes the 1U and 5U pay zones from the 2U, 3U, and 4U marginal pay and non-pay zones. The neutron log shows high API in the 2U, 3U, and 4U marginal pay zones. High neutron API indicates low porosity. Accurate porosity calibration is necessary to apply the cut-off criteria derived from modern open-hole logs and core data to old cased-hole logs.

It is well known that for most old neutron logs, the counts per second or API unit is approximately an inverse linear relationship to the logarithm of porosity.[5] Calibration charts of neutron logs were available from some of the service companies but most analysts found that relative calibration methods worked best most of time. In this investigation, the neutron log was first normalized to a neutron index (NI). The NI is

defined as a linear scaling of the neutron log (API or counts per second) between neutron minimum and neutron maximum in the following form

$$NI = \frac{Neutron_{(\log)} - Neutron_{(\min)}}{Neutron_{(\max)} - Neutron_{(\min)}} \quad (1)$$

To obtain quantitative porosity values, a correlation was constructed using NI = 0 as 26% porosity and NI = 1 as 3% porosity on a semilog plot of porosity and NI, based on the cased-hole log from well O'Daniel "G" #1. A relationship was obtained through exponential regression and was used to calculate porosity from NI. The relationship is given below:

$$Porosity = 0.26e^{-2.16(NI)} \quad (2)$$

The porosity values were then corrected for matrix contribution (limestone matrix to sandstone matrix), shale effect and hydrocarbon effect to obtain effective porosity.[5]

Discussion

The volume of shale was calculated from gamma ray logs using the Larionov non-linear relationship. Figure 1.7-1 shows volume of shale (VSHL) and gamma ray (GR) on the left hand side, neutron, API (NEUT), and effective porosity (NIP) calculated from neutron API on the right hand side. **Figure 1.7-2** shows the cross-plot of volume of shale vs. effective porosity, both calculated from old cased-hole gamma ray and neutron (API) logs from the well O'Daniel "G" #1. Data points, where the volume of shale is less than 15% and the effective porosity is greater than 7%, are from 1U and 5U pay zones of the Upper Spraberry (Rock Type A). Data points where the volume of shale is less than 15% and the effective porosity is less than 7% are from 2U, 3U and 4U units. Core data indicates these zones are non pay. The porosity of the 2U, 3U, and 4U zones is drastically reduced due to dolomite cement, thus effectively rendering these zones as non-pay (Rock Type B). Data points where the volume of shale is greater than 15% are from muddy non-pay zones of the Upper Spraberry (Rock Type C).

This investigation shows that the cut-off criteria for identifying the Spraberry pay zones and log-based rock model that we developed from modern open-hole log suites and core data can be applied successfully to old cased-hole logs in the Spraberry Trend throughout the Midland Basin.

Conclusions

The following conclusions were reached based on detailed analysis of old cased-hole logs from the Spraberry Trend Area:

1. Old cased-hole gamma ray and neutron (API, counts per second or no units) logs can be used successfully for identification of the naturally fractured Spraberry pay zones.

2. Reliable quantitative porosity values obtained from careful calibration of open-hole logs and core data, can be obtained from old cased-hole neutron (API, counts per second or no units) logs.

References

1. Schechter, D. S., and Banik, A. K.: "Integration of Petrophysical and Geological Data with Open-Hole Logs for Identification of the Naturally Fractured Spraberry Pay Zones," paper SPE 38913 presented at the 1997 SPE Annual Technical Conference and Exhibition, San Antonio, Texas, 5-8 October 1997.
2. McDonald, P., Lorenz, J. C., Sizemore, C., Schechter, D. S., and Sheffield, T.: "Fracture Characterization Based on Oriented Horizontal Core From the Spraberry Trend Reservoir: A Case Study," paper SPE 38664 presented at the 1997 SPE Annual Technical Conference and Exhibition, San Antonio, Texas, 5-8 October 1997.
3. "E.T. O'Daniel # 28, 1U Horizontal Core," report prepared by Reservoirs Inc. for Parker & Parsley Development Company, March 10, 1997.
4. Schechter, D.S.: "Advanced Reservoir Characterization and Evaluation of CO_2 Gravity Drainage in the Naturally Fractured Spraberry Trend Area," The First Annual Technical Progress Report for Contract Number DE-FC22-95BC14942. PRRC Report 96-42.
5. Hilchie, D.W.: *Old Electrical Log Interpretation*, Douglas W. Hilchie Inc., Boulder, Colorado, 1979.

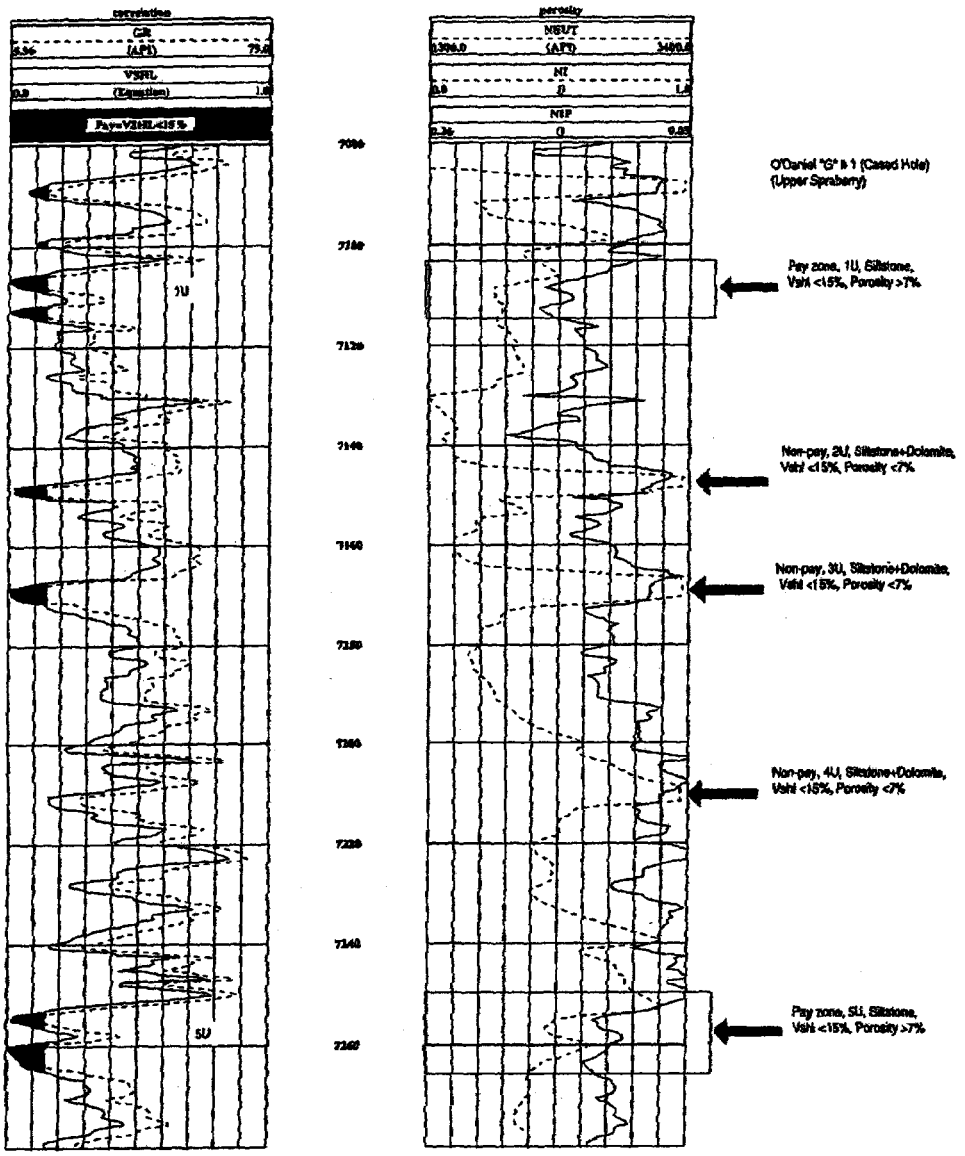

Fig. 1.7-1—Cased-hole logs from the E.T. O'Daniel "G" #1 (Upper Spraberry). Gamma Ray (GR) and volume of shale (VSHL) on the left hand side and neutron log (API) and effective porosity (NIP) on the right hand side.

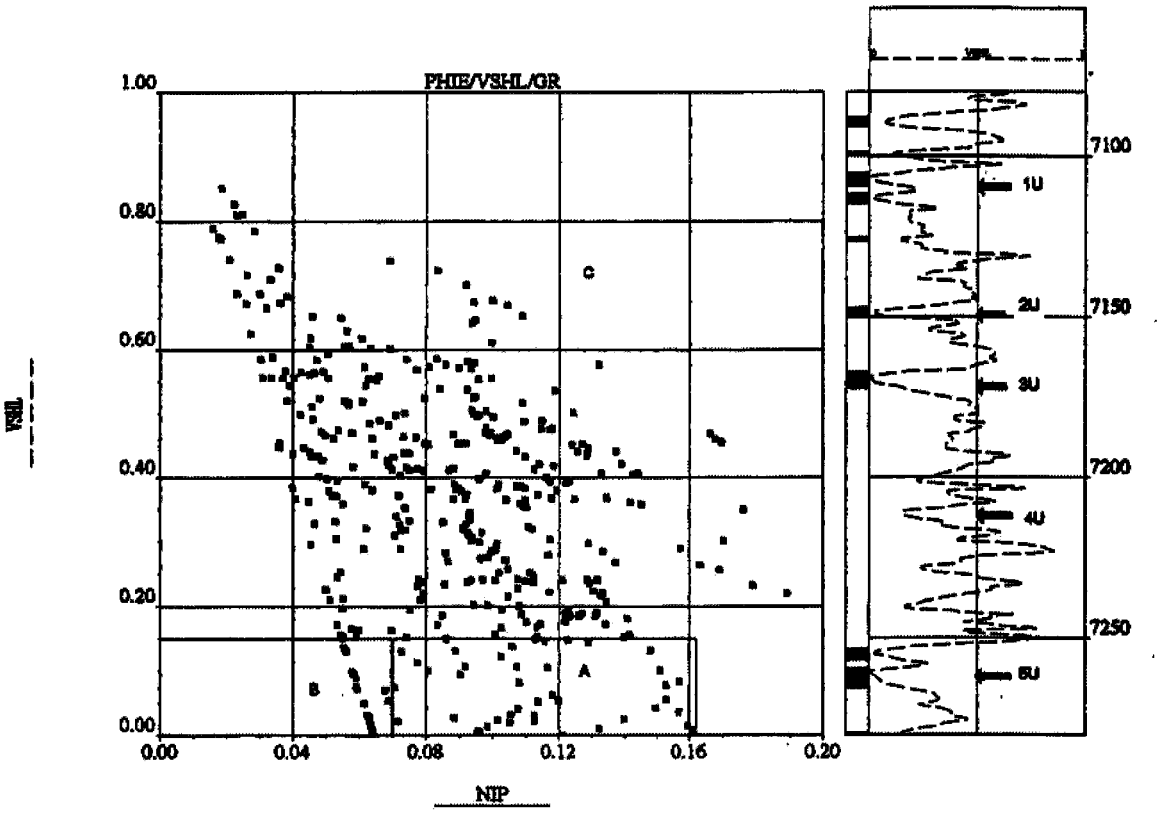

Fig. 1.7-2—Volume of shale vs. effective porosity (NIP) calculated from old cased-hole neutron log (API unit). Data points where VSHL < 15% and effective porosity > 7% are from 1U and 5U pay zones (Rock Type A). Data points where VSHL < 15% and effective porosity < 7% are from 2U, 3U and 4U marginal pay zones (Rock Type B). Data points where VSHL > 15% are from muddy non-pay zones (Rock Type C).

1.8 CORE INTERPRETATION AND SEDIMENTOLOGICAL ANALYSIS

Generalized Core Description

Two cores, E.T. O'Daniel 37 and Shackelford 138A, were examined in detail. Shown in Fig.1.8-1 is the core description for E.T. O'Daniel 37 correlated to the gamma ray log. A total of eight large-scale lithologic categories were delineated by this study. These lithofacies are based on distinguishable sedimentary structures, textures, grain size, primary mineralogy, and environment as inferred from these characteristics. The following list shows the different lithofacies defined by this core analysis:
Textural Lithofacies for Fine Grained Deposits: Lithofacies L1: Massive, silty dolostone and dolomite cemented siltstones. Lithofacies L2: Shales. Lithofacies L3: Thin bedded argillaceous siltstone with lenticular or convolute lamination. Lithofacies L4: Bioturbated argillaceous coarse-grained siltstone. Lithofacies L5: Parallel finely laminated siltstone.
Textural Lithofacies for Coarse Grained Deposits: Lithofacies L6: Thick bedded, massive, very fine sandstones and siltstones. Lithofacies L7: Thin bedded, massive, very fine sandstones and coarse siltstone. Lithofacies L8: Thin bedded, graded cross-laminated, very fine sandstones and siltstones.

Textural Lithofacies for Fine Grained Deposits

Low energy deposits consist of siltstones, shaly laminated siltstones, thin layers of black shale, and silty dolostone. These are volumetrically the most abundant lithofacies comprising the upper Spraberry formation. The following lithofacies are observed in Spraberry cores: *Lithofacies L1: Massive, silty dolostone and dolomite cemented siltstones.* These are dark gray to black, massive, very well indurated, silty dolomite mudstones and siltstones, which display massive or faint planar horizontal bedding. Ripple laminae and contorted bedding are rare. Dolomite occurs both as locally abundant or pervasive cement. Beds range from 1 to 3 ft thick and have sharp or scoured basal contacts or grade into underlying sandstones. Dolomite cement severely limits reservoir quality. Carbonate rocks are not very common in the analyzed cores. *Lithofacies L2: Shales.* Shale beds are typically less than 2 ft thick and also grade into underlying siltstones. The shales are structureless and are only locally disrupted by small, horizontal burrows. Thin, isolated lenses of silt occur infrequently; the black color of these shales is a function of their high organic carbon content. Organics occur in association with locally abundant pyrite; phosphatic nodules are common. Shales are relatively abundant in the Spraberry study cores:

Lithofacies L3: Thin bedded argillaceous siltstone with lenticular or convolute lamination - These rocks are medium to dark gray colored argillaceous siltstones and consist of thin (<0.5 ft) interbedded coarse siltstones and shales. They have poorly preserved lenticular lamination. The siltstones are moderately well sorted. Most of the original bedding within these rocks has been disrupted by soft sediment deformation. Convolute bedding and pillow structures are common. *Lithofacies L4: Bioturbated argillaceous coarse-grained siltstone.* These rocks are gray to black in color. The rock groundmass consists of detrital clays that support scattered silt-sized grains of quartz and feldspar. Bioturbation has destroyed original sedimentary structures. The intensity of bioturbation ranges from moderate to extreme. Fossil burrows from browsing or feeding

animals that leave traces generally parallel to bedding were evident in the cores. This trace fossil assemblage is indicative of deposition in deep-water (slope to basin) setting (Basan, et al., 1978). *Lithofacies L5: Parallel finely laminated siltstone.* This lithofacies is characterized by alternations of light and dark colored fine laminae, each a few millimeters (generally <5mm) in thickness. Light colored laminae are quartz-rich, coarse siltstone. Dark colored laminae consist of the same silt sized detrital grains mixed with organic detritus and small amounts of argillaceous material. Commonly laminae have sharp/erosional bases. Normal graded bedding is common. Lamination is generally parallel. A few tops of finely laminated sequences are ripple laminated.

Textural Lithofacies for Coarse Grained Deposits

The very fine-grained deposits described above are widespread along the Spraberry Trend. They form a depositional continuum and encase the more localized very fine-grained "clean" sandstones and coarse siltstones. These sandstones are very fine grained and moderately to well sorted. The following coarse-grained lithofacies are observed in the cores:

Lithofacies L6: Thick bedded, massive very fine sandstones and siltstones– This lithofacies consist of light gray to light brown colored, fine grained, well-sorted sandstones to coarse grained siltstones. These sandstones occur as individual beds, 1 to 3 ft in thickness that stack vertically to form much thicker composite units. Sand beds have scoured basal contacts, often marked by a thin layer of intraformational mud clasts (matrix supported). Beds are internally massive and lack sedimentary structures. There is evidence of bioturbation. *Lithofacies L7: Thin bedded, massive very fine sandstones and coarse siltstones* – These are light gray to light brown colored, very fine grained, moderately well sorted to sorted very fine sandstones and coarse grained siltstones. Individual sandstone beds are less than 1.5 ft thick. Beds are composites consisting of basal intervals of massive sandstones, which may grade vertically into parallel laminated or cross-laminated sandstones. The tops of some beds display dish structures or evidence of fluid escape. Individual beds have scoured bases often marked by thin layers of intraformational mud-clast conglomerate (matrix supported). Composite beds are often difficult to identify due to relatively uniform grain size.

Lithofacies L8: Thin bedded, graded, cross-laminated very fine sandstones and siltstones – This lithofacies consists of thin bedded (<1 foot) very fine grained, light gray to brown colored, moderately well to well sorted very fine sandstones interbedded with dark gray shales. Individual sand beds have sharp, erosive bases and are normally graded. A thin layer of shale rip-up clasts often overlies basal surfaces. Normally graded sandstone beds are characterized by vertical sequences of sedimentary structures indicative of deposition from waning flow (i.e. socalled Bouma sequence). Such sequences consist of a basal section of parallel laminated sandstones. Sand beds grade vertically into overlying beds of dark gray shale or lenticular 0laminated silty shale.

Lithofacies Interpretation

Sandstone beds display abundant evidence of deposition from waning traction currents including:

1) Erosional, scoured bases (often sole marked, with rip-up clasts) and gradational bed tops, which denote tractional currents with a subsequent decrease in the energy of the environment.
2) Normal graded bedding (individual beds fine upwards),
3) Common cross bedding or current lamination indicative of transport by high energy traction currents,
4) General lack of bioturbation,
5) Some fluid escape, load, or flame structures indicative of rapid deposition and subsequent dewatering and,
6) Vertical sequence of sedimentary structures recording gradation from high to low flow regime conditions ("Bouma" sequences). The total sedimentary package described above is interpreted as basinal deposits, based on:
1) Preservation of delicate, very fine scale, parallel lamination within non-burrowed sections, which is suggestive of anoxic conditions in very calm waters.
2) Local presence of abundant preserved organics, probably marine kerogens (suggestive of very slow rates of deposition in poorly oxygenated or deoxygenated bottom waters)
3) Preservation of very fine scale finely laminated graded bedding within individual siltstone laminae, very fine to fine grain size and abundant argillaceous sediments, probably due to distal location during deposition.

Depositional Setting for Low Energy Environment

The finely parallel laminated siltstones (L1) were formed by suspension settling of silt and very fine sized particles from submarine density currents. However, for the most part, they lack evidence of deposition from tractional currents. Handford (1981) proposed that such deposits result from density stratification of the water column when shelf derived density currents periodically move out over the basin as an interflow suspended above the basin floor. Suspension settling of thin layers of silt and very fine-grained sand resulted from eventual mixing of waters near the terminus of such flows. Normal hemipelagic sedimentation of shale and organics occurred between such flows:

Burrowed siltstone (L2) alternates with the parallel finely laminated siltstone (L1) and with thin shale beds. The transition from laminated to burrowed intervals or, less frequently into shales, is interpreted as recording periodic changes in bottom water chemistry, primarily in bottom water oxygen content. Such changes may have occurred in response to fluctuations in eustatic sea level through time.

Depositional Setting for High Energy Environment

Based on the association of traction current structures with the finer grained rocks, and evidence presented above for basinal deposits, the sandstones represent deposition in submarine channels and fans. The Spraberry sandstones analyzed in this study are interpreted as deposits of deepwater origin, specifically deposits of waning traction currents that were responsible for the filling of erosional channel cuts on the higher energy, inner/middle portions of submarine fans. Lithofacies L6 and L7 were formed from the channelized portions of the inner fan to nonchannelized middle submarine fan. They are associated with thinly bedded sandstone/shale sequences (with lenticular/wavy and convoluted bedding) of lithofacies L3, interpreted as basinal, fine-grained tail of

interflows. Sandstones of lithofacies L8 are classical turbidite deposits. These deposits occur within the upper portions of channel fills and within non-channelized portions of the middle fan. Thinly interbedded sandstones and mudstones of lithofacies L8 are traditional distal turbidites: deposits of low density turbulent flows on the outer portion of the fan.

References

1. Basan, P. B. et al., 1978, Trace Fossils Concepts, SEPM short course No.5. P. 142-143.
2. Handford, C. R., 1981, Deep-water facies of the Spraberry Formation (Permian), Reagan County, Texas; a core workshop (No. 2); Siemers, Tillman, and Williamson.

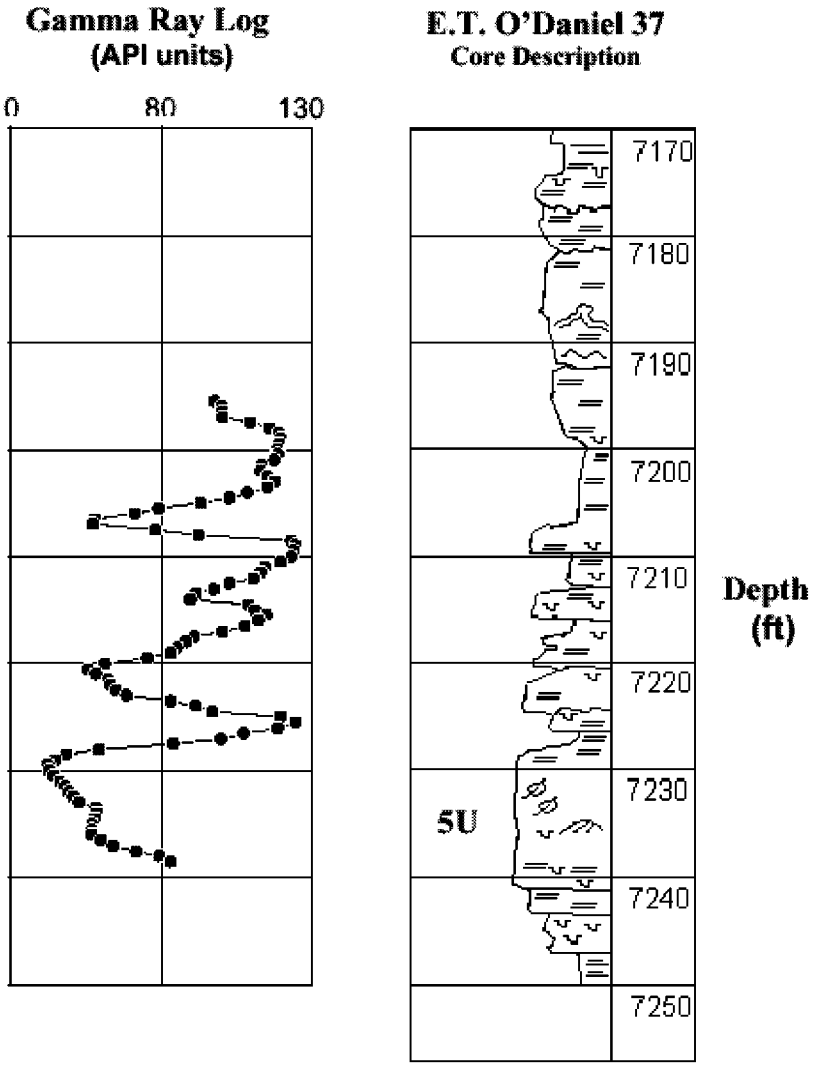

Fig. 1.8-1—Depth profiles showing the correlation of gamma ray log with core description for the E. T. O'Daniel 37 well.

1.9 PETROGRAPHY AND DIAGENESIS

Petrography

Thin section petrography, x-ray diffraction for clay mineralogy and fracture cements, and scanning electron photomicrographs were used to define mineralogy, rock fabric, texture, pore morphology and distribution, and diagenetic features and history for samples from three cores from the Spraberry Formation. The three cores analyzed are from the upper Spraberry Formation. Only the two most important productive zones, units 1U and 5U, were studied. Two of the three cores contain both zones, while the Shackelford 138-A core contains only the 1U unit. A list of the different techniques applied to each well per unit and depth of coring is shown in Table 1.9-1. Out of approximately 100 thin sections analyzed, 80 were point counted (see Table 1.9-1). Detailed point count analysis was conducted (300 points counted per thin- section) to determine the percentage amounts of detrital and authigenic minerals making the rock fabric, the amount and type of pore filling constituents, and the percentage of visible pore space. Based on this type of analysis, six small-scale lithofacies, referred to in this writing as rock types, have been described.

General Textures and Mineralogy

Spraberry reservoir rocks are typically low porosity, coarse siltstones to very fine sandstones that are intercalated with shaly non-reservoir rocks. Samples examined for this study cover a range of rock types from very fine and clay rich massive shales, through coarse laminated siltstones, to the very fine grained sandstones within the operational units 1U and 5U of the upper Spraberry Formation. Most of the carbonate muds and shales are matrix supported, while sandstones and siltstones display grain supported fabric. Spraberry reservoirs have grain size ranging from 45 to 66 μm with an average of 60-μm (Rock Type "A") (see Table 1.9-1). Grain sorting varies from moderately well sorted clayey coarse siltstones to very well sorted clean sandstones. Grain shape ranges from subrounded to angular. The rock fabric displays two main forms: massive and laminated. Mottled sedimentary fabric is not rare and it is associated with burrowing and/or dewatering action. Water escape pillars are commonly found within the Spraberry stratigraphic sequence. Burrowing produces patches of coarser grain size that look cleaner and sandier than surrounding shaly sediments. Other structures noted are cross stratification, which is fairly common in the very fine sandstones, and soft-sediment deformation. Monocrystalline quartz is the dominant type of detrital grain. Other abundant detrital grains are plagioclase, K-feldspar and muscovite mica. Rock fragments, heavy minerals, and carbonate fragments are present in minor amounts. Detrital clay matrix (laminar clays+dispersed clays+organics) averages 22.4% in argillaceous laminated siltstones (Rock Type "F") and 40.6% in shales (Rock Type "E") (see Table 1.9-1). Typically clays, organic debris, carbonate mud, and considerable amounts of mica flakes and pyrite form a fine laminae. Massive very fine sandstones and siltstones (Rock Type "A") contain only minor amounts of clay matrix. Authigenic minerals observed in variable amounts depending on the petrographic category include quartz, dolomite and ferroan dolomite, calcite and pyrite. Barite is also abundant as fracture-filling cement. Amounts of primary and secondary porosity also show variable values for the different mineralogical facies (see Table 1.9-1). In this study, XRD

diffractograms were recorded for samples along 60 ft of core (Shackelford 138A) in order to define clay mineralogy within the various lithologies. Table 1.9-2 shows the results of XRD analysis of clay samples (<2_m, grain size) from the Shackelford 138A. Relative amounts of different clays were calculated in a semiquantitative manner using a series of formulas developed by G. Austin (personal communication). Illite occurs as the dominant clay mineral followed by chlorite, kaolinite and traces of mix-layer illite/smectite. Illite clays are optically identified using SEM photomicrographs (Fig. 1.9-1*)*. X-ray diffractograms show the different characters of clay peaks that can be observed between clean very fine sandstone at a depth of 7087 ft, and an argillaceous sample at 7104 ft depth (Fig. 1.9-2*)*. The difference of peak intensity between these two lithologies is probably due to the fact that much of the clay in sample 7087 is diagenetic, while sample 7104 has dominantly detrital types of clays. The diffractogram for Shackelford 138A (7104 ft) presents sharper and longer peaks suggesting more abundance or probably better crystallinity of clay minerals than the sample at 7087 ft. (I) illite, (K) kaolinite and (CL) chlorite.

Porosity

Two major pore types and five subcategories were identified based on pore size, pore shape, and general pore morphology. Primary pores include intergranular macropores, intergranular mesopores, and micropores. Secondary pores are generally oversized (up to 50μm) and are a product of dissolution of precursor grains and cements. All pore types determined and discussed here are summarized in Table 1.9-3.

Small Scale Lithofacies – Rock Types

Six rock types were identified based on microscopically observable features. Characteristics used to define each group include porosity, amounts of clays and organics, amounts of carbonate mud and cements, textural features such as relative abundance of laminae or massive fabric, burrows, grain sorting and grain size.

Rock Type "A"

Moderately good porosity, very fine sandstones and coarse siltstones, reservoir rocks - Very fine sandstones and siltstones are distinguished as the best quality reservoirs within the upper Spraberry Formation. Of arkosic to subarkosic composition, these light colored, massive to poorly laminated sediments represent the highest porosity rocks among all six petrographic categories. Rock Type "A" sandstones contain most of the different types of pores noted in Spraberry rocks; however, there are significant amounts of secondary pores (Pore Type 5) and primary pore types 1 and 2 (see Table 1.9-3 for definition of pore types).

Rock Type "B"

Slightly shaly laminated and/or patchy siltstones and very fine sandstones; low quality reservoir rocks – Not as much dissolution porosity is observed within these rocks as within Rock Type "A" rocks. Quartz and feldspar grains are again the main mineral species (arkosic composition). Relatively higher amounts of clay, organic matter, carbonate matrix and cements, and relatively lower porosity characterize this facies. Rock Type "B" exhibits considerably more lamination and burrowing than Rock Type "A."

These silica-cemented, slightly laminated and patchy very fine sandstones are considered low quality reservoir rocks of secondary importance.

Rock Type "C"
Silty Dolomite mudstones "Dolostone" - From the observation of core macro-samples these sedimentary rocks are described as dark gray very fine grained dolomites; possibly mudstones in *"Lithofacies 5."* Thickness varies from a few centimeters to several tenths of centimeters. They are commonly massive but can show some laminae formed of a mixture of carbonate mud, clays, and organics. Thin section specimens show that a silty micritic dolomite is the major component of this facies. These rocks present a general lack of porosity and form non-reservoir rocks with good seal characteristics.

Rock Type "D"
Very "patchy" dolomitic siltstone – These samples, like Rock Types "A" and "B," are arkosic to subarkosic in composition. The major detrital grains are quartz, followed by feldspars and minor rock fragments. Dolomite and calcite are pervasive cements forming patches scattered throughout the rock. Porosity amounts are moderate to low. A higher percentage of dolomite cement distinguishes Type "D" siltstones from the similar, but less dolomitic, Type "B" rocks. Rock Type "D," calcareous "patchy" siltstones are marginal reservoirs.

Rock Type "E"
Shales and Silty Shales - Shales and silty shales, together with the silty dolomite mudstones (Rock Type "D") show the lowest amount of pore space among the six categories described, while clay matrix is abundant. Color varies from gray to black. Non-reservoir rocks, these were probably hydrocarbon host rocks from deposition until migration of oil to high porosity units, and presently they form excellent seal rocks.

Rock Type "F"
Argillaceous Highly Laminated Siltstones - Argillaceous highly laminated siltstones form a category that can grade from relatively clean laminated siltstones to very low reservoir quality laminated shaly siltstones. Depending on the relative amounts of clays, organics, pyrite and other argillaceous materials, sediments will present thinner or thicker laminae between silts and shales. This is the most common lithology occurring throughout the upper Spraberry Formation in the three cores examined. Laminated shaly siltstones are darker in color, and differ from the cleaner siltstones (Rock Type "B") in having significantly higher amounts of argillaceous matter. Laminated shaly siltstones tend to be matrix supported.

Diagenesis

Very fine sandstones and coarse siltstones of the upper Spraberry have been subjected to highly variable degrees of post-depositional alteration (diagenesis). Diagenesis has resulted in an overall reduction of original porosity and permeability. Variations in the extent of compaction, cementation and dissolution have overprinted the original rock

fabric, and asserted certain control to spatial variations in reservoir quality within the upper Spraberry Formation.

Quartz and Feldspar Overgrowth, Authigenic Feldspar, and Pressure Solution

Quartz overgrowths: Quartz overgrowths are noted as euhedral grain boundaries or by the presence of vacuoles or dust rims that separate grain from cement. Quartz cement is most abundant in Rock Type "A" and "B." In general, median values of quartz overgrowth percentages (from point count) vary from one category to another (see Table 1.9-1). The lower values of quartz cement found in Rock Type "B" suggests that the presence of larger amounts of clays and carbonate cements probably have somewhat inhibited growth of quartz cements.

Authigenic feldspar: Authigenic feldspar is a minor cementing agent occurring in quantities of 1% or less. Alteration and dissolution of weaker feldspar mineralogy is found repeatedly in the Spraberry Formation.

Pressure solution: Overpressuring during compaction in conjunction with several other factors can cause pressure solution. The effect of compaction is clearly observed within the matrix-free sandy petrographic categories and lithofacies. Flat and concave-convex grain suturing contacts are common in these lithofacies, denoting the pressure solution effect between quartz grains. It is possible that some of the silica in quartz overgrowths was derived from pressure solution processes.

Authigenic Clays

The Spraberry Formation contains abundant clay, although it is not an easy task to differentiate between depositional and authigenic clay. Detrital clays in the sand rich facies caused very low initial porosity and permeability, which were only decreased by compaction. Rock Type "E" and "F" presents a thick mixture of clays, organics, carbonate muds, and common associated pyrite precipitates and mica sheets that appear very well compacted. It seams that Rock Type "A" and "B" have gained from having more pore space available so hairy illite flakes have developed. Both forms of clay described above are presently diagenetic forms, either through recrystallization of large clumps of compacted clays or neoformation of fibrous flakes.

Pyrite

Authigenic pyrite occurs in small quantities in all lithologies and is especially abundant in shales and shaly samples. Nodules of pyrite, 1 to 0.5cm, flattened due to burial during compaction are visible in hand specimens. Framboidal pyrite is also noted in association with organic-rich facies.

Carbonate

Authigenic carbonates are the most abundant cementing agents in the Spraberry Formation. Utilization of proper staining, along with observation in scanning electron microscopy, helped identify dolomite cementation and replacement of microorganisms

and detrital grains. The authigenic character of the dolomite is quite clear when observed as large patches of poikilotopic cement and replacement of detrital grains.

Pore Space

Pore types have been identified on the basis of size, shape, origin and distribution using qualitative thin section and SEM photomicrographs of rock samples (see Table 1.9-3). These analytical procedures reveal that the pore systems of these rocks consist of varying proportions of five (5) pore types. Type 5 pores, secondary dissolution pores, are moderately abundant in some parts of the upper Spraberry Formation. The most common recognizable secondary porosity feature is the partial or total dissolution of feldspar grains. Remnants of partially dissolved grains within a pore space with typical grain shape are often found in thin sections from the very fine clean sandstones and siltstones (Rock Type "A"). Relict features of cleavage with the typical extinction patterns of plagioclase (probable Ca rich) are also commonly found. Dissolution is also observed in unstable carbonate grains and cements. One type of secondary pore is an oversized pore formed by dissolution of framework grains, patches of matrix, or cements. This type of pore has a greater diameter than the average detrital grain size. Moldic pores are also seen in thin sections from the Spraberry Formation, and are recognized by geometrical shapes of the precursor grains. Another very common secondary pore is the intra-constituent pore, which occurs mainly within framework grains, but also in cement and matrix. Secondary intergranular pores are very difficult to differentiate from primary intergranular pores due to their similar habit.

Paragenesis

Upper Spraberry sandstones have been subjected to several stages of diagenesis. Diagenesis has resulted in both the occlusion and, rarely, the enhancement of porosity and permeability. The relative timing of various diagenetic events may be deciphered by examination of the spatial relationship of cements in thin section or with the scanning electron microscope. The following diagenetic sequence has been determined for upper Spraberry sandstones examined in this study:

1. Deposition of sediments with initial primary intergranular porosity. Some interstitial space within more poorly sorted and lower energy deposits filled by detrital clay matrix.

2. Basinal sediments that were deposited in anoxic bottom waters conditions experienced varying degrees of pyrite precipitation due to the production of H_2S by sulfate reducing bacteria at the sediment-seawater interface prior to burial.

3. Shallow burial. Minor adjustments in grain packing in response to burial loading. Some rocks, particularly clean sandstones of submarine channel origin, were subject to an early stage of silica overgrowth cementation. While volumetrically insignificant in controlling reservoir quality variations, these overgrowths aided in arresting compactional effects and preservation of porosity and permeability.

4. Precipitation of calcite cement (a near surface event-precipitation from connate waters in equilibrium with seawater).

5. Precipitation of chlorite, illite and smectite.

6. Dolomite cement precipitation.

7. Late stage precipitation of silica overgrowth (individual euhedral crystals rather than more extensive and massive overgrowths). Minor development of K-feldspar overgrowths on framework feldspar grains.

8. Late stage precipitation of fibrous illite clay growths on pore walls and within pore throats. Illite clay cement, while volumetrically insignificant, bridges pore throat openings dramatically reducing formation permeability.

9. Fracture formation after enough unconfinement effect is produced.

10. Fracture mineralization, mainly calcite and barite.

Porosity, Dissolution and Reservoir Quality Preservation

Various diagenetic processes have enhanced or damaged the initial pore structure of Spraberry rocks. The interaction of compaction effects, cementation, dissolution and fabric rigidity within the original rock texture has resulted in highly variable pore structures in Upper Spraberry rocks. A number of factors affect the formation, preservation, and damage of pore space:

1. Original rock texture: this controls grain size and sorting. Very fine grained, poorly sorted sandstones of submarine channel abandonment, distal turbidite, and basinal origin have smaller pore and pore throat sizes than coarser grained and better-sorted sandstones of submarine channel origin. Pore size distribution is more heterogeneous within the low energy, basinal siltstones and sandstones: a function of lamination and bioturbation.

2. Compaction: this controls grain packing and the degree of deformation of ductile grains. Compaction has resulted in a reduction of the original size of pore bodies and pore throats, and therefore has contributed to a general reduction in porosity and permeability during burial. Compaction must have affected in a greater manner the more ductile composition of the various clay rich lithofacies and petrographic categories (L1, L2, L3 and L4 section 1.2; and RT "E" and RT "F" section 1.3-Petrography).

3. Cementation: this also results in reduced pore and pore throat size and increased pore system tortuosity (in the case of sandstones with microquartz, carbonate and clay cements). Precipitation of authigenic clay can produce a dramatic increase in pore surface area, and in partitioning of intergranular pore space near pore walls into micropores (pores<5μm in diameter). Additionally, the bridging effect of pore throats by fibrous illite has an effect far in excess of the small volume of clay present, dramatically reducing formation permeability.

4. Dissolution: Dissolution of chemically unstable grains produces secondary porosity within very fine-grained sandstones and siltstones, usually improving permeability (Lithofacies L6, L7, L8 section 1.2; RT "A" section 1.3-Petrography).

5. Fabric rigidity: Despite being subject to burial loading, some of the Spraberry lithofacies and petrography categories examined in this study (Lithofacies L6, L7, L8 section 1.2; RT "A" and RT "B" section 1.3-petrography) have retained significant amounts of original intergranular porosity, resisting grain slippage and packing adjustments. Petrographic analysis suggests that this is the result of non-ductile fabric composition and early silica cementation, which arrested grain slippage by increasing the mechanical strength (rigidity) of the rocks. An important event that perhaps followed the dissolution in the Spraberry Formation is the preservation of porosity due to significant increases in geopressures. High overburden effects are suggested by the pressure solution characteristics such as long and sutured grain boundaries found within the very fine sandy units of Spraberry Formation. The formation of regional vertical fracture systems, which are very important for fluid conductivity in the reservoirs, are also related in part to the occurrence of overpressure events within the reservoir sands (Lorenz, et al., 1991). Some characteristics of the Spraberry Formation are common to overpressured formations. Highly compressible shales, rich in organic fluids, are overwhelmingly more abundant in the Spraberry Formation than the rigid, fine, clean, and porous sandstones. In these clay-rich systems high amounts of fluids are gradually injected into the more porous sandstone and siltstones from the shales by compaction dewatering. After the lithification occurred, shaly rocks and carbonates that presently show a total lack of permeability formed a very good seal preventing escape of fluids from the enclosed sandy units. Very high pore pressure must have been preceded by periods of high lithostatic compression that promoted dissolution of silica at grain contacts. With the final buildup of overpressuring and due to reduction in effective stresses, both fracture formation and preservation of matrix porosity occurred. The influence of secondary porosity in reservoir quality is important, but that much porosity is simply redistributed rather than newly produced (Bloch, S., 1994). Material dissolved in one place may be redeposited only a short distance away. Pore space formed by the dissolution of framework grains in the Spraberry Formation can increase the total amount of porosity but it is understood that an equally considerable improvement of permeability rarely occurs. Dissolution of very small grain and intra-granular material may produce pores that are too small or isolated to increase effective porosity. Pore space formed by dissolution of pore filling cements is often more important in substantially improving porosity and permeability. Physically and chemically relatively stable arkosic and subarkosic compositions such as the Spraberry reservoirs are the type of lithology that can preserve high amounts of dissolution porosity.

Hydrocarbon Emplacement

An interesting relationship exists between the progressive increase in crystallinity (lattice order) and the amount of illite with the simultaneous thermal maturation of hydrocarbon in potential source rocks. Catagenesis, the action of generating oil at a given temperature

range during burial, seems to occur parallel to the abrupt transformation of illite/smectite sequences into the ordered R=1 polytype (Jadgozinski, H., 1949).

The relation between maturation of oil and alteration of clays is still not well understood. Temperature wise there is a range that goes from approximately 100°C (abrupt change to the ordered rectorite type of I/S; R=1) to 175°C where a higher stage of ordering of I/S is produced (R≥3) (Eslinger, et al., 1988). The "oil window," or temperature range where hydrocarbon maturation occurs (65° to 175°) roughly coincides with the rectorite range of illitization shown above. The temperature of oil maturation is above the random I/S (R=0), yet just below the range temperature for a very ordered "Kalkberg" (I/S, R≥3), and closely coincides with the rectorite (I/S, R=1) range of temperatures. Spraberry rocks coincide with the typical assemblage of clays for ordered polytypes; however, possible paleo-temperatures found by others (60°-77°C; Houde, 1979 and Dutton, 1980) may only reach the initial part of the oil maturation stage. These temperatures are not enough to account for the lack of expandable smectite layers noted in the Spraberry, unless the time and kinetics with rocks of Permian time have worked in favor of the illitization processes. Another possibility is that a relatively low amount of smectite was present in the initial composition of the sediments. The latter is not very probable due to the high amount of smectitic clays that is usually present in this type of sediments.

Fracture Model

In this section we explain a diagenetic model for the fracturing of the Spraberry Formation. Macro-observations of core samples, microscopic analysis of thin sections, and information extracted from XRD and SEM analysis of clays have helped construct a history of burial, compaction, lithostatic pressure buildup for vertical, and horizontal stresses, pore pressure increase, reduction of unconfinement and fracturing.

The gradual increase in burial depth produced an increase of compaction, pressure, and temperature. The clay-rich nature of the Spraberry, interbedded with only a minor amount of fine sands and siltstones, provides a typical environment for production of significant overpressuring. Clay sediments mixed with organic matter are characterized by having the highest initial porosity and contain large amounts of fluid. Burial compaction and diagenesis of this material usually results in almost total destruction of porosity within the clayey sediments accompanied by a tremendous loss of fluids. At the same time that the principal vertical stresses are being increased, the pore pressure mainly within the sandy part of the formation is increased due to the migration of huge amount of fluids into the sands. Pressure solution features, typical of overpressured sands, have been found during petrographic analysis. These conditions probably caused the necessary reduction of principal effective stresses to a level at which enough unconfinement (Lorenz et. al. 1991) effect is created to cause fracturing. Then mineralization of fractures occurred. Fracture cements analyzed by XRD, thin section observations, and SEM analysis have shown the presence of calcite, barite, and also quartz. Pressure solution of grain boundaries and quartz overgrowth are abundant in the majority of the thin-section examined. Matrix free sandy siltstones and very fine sandstones show the effect of compaction. Grains show both flat and concave-convex contacts.

The following is a brief account of the result encountered on examination of horizontal cores retrieved from the upper Spraberry Formation. Horizontal cores from upper Spraberry 1U and 5U units provided invaluable evidence on fracture orientation, spacing, aperture, and mineralization. However many questions still remain to be answered concerning the origins of the various fracture sets, the relationship of the fracture network to rock matrix, and its effect to rock production. At least three sets of fractures are found within the upper and middle Spraberry cores. These sets have distinct orientations, spacing, mineralization, distribution with respect to lithology, and surface characteristics (Lorenz, 1997).

1U Fractures:
Fractures found in the 1U zone of the upper Spraberry have a NE strike, and tend to be partly mineralized with barite, quartz, and dolomite. Fractures with NE orientation have a maximum of seven ft and an average of about 3.2 ft. In the megascopic view, this set of fractures has fairly smooth and planar surfaces that show no evidence of movement or shear. Microscopic examination of 1U fracture surfaces shows that barite occurs in large crystals (1mm or more) with very smooth tabular faces. Barite crystals can partly to completely cover the surfaces of 1U fractures and appears to occlude porosity and may be responsible for reducing the crossflow of fluids and gas between rock matrix and fracture porosity. Quartz and dolomite occur in varying abundance as authigenic minerals on 1U fracture surfaces; however, their size and morphology do not seem to have the same deleterious effect on porosity. Indeed, although quartz crystals seem insignificant in terms of abundance and size, they provide numerous asperities that may prevent these fractures from closing even at reservoir pressure conditions. The presence of abundant euhedrally-terminated quartz demonstrates that fractures were open during certain periods of diagenesis.

5U Fractures:
The 5U zone of the upper Spraberry contains fractures with NNE and ENE orientations. These are two separate sets of fractures. The NNE set of fractures has stepped fractures surfaces indicating a shear origin, and minor amounts of fracture mineralization. These fractures have a fairly narrow spacing, with an average of about 1.6 ft and a maximum of about 5 ft. The ENE fracture set has smooth planar surfaces of tension origin with some calcite mineralization present. Spacing between fractures in this set is quite different than seen in the other two sets. The spacing is about 3.79 ft, but the maximum spacing is over 14 ft and the most common spacing is less than 2 ft. Like 1U fractures, these have a smooth planar appearance with no indication of shear, but there appears to be no surface mineralization under visual examination. Closer examination of 5U fractures shows that surface mineralization is present on these fractures, but not in the abundance of 1U fractures. Quartz and dolomite are both fairly common, but barite is rare. Calcite cement was not seen in 1U fractures, however it has been observed in several 5U fractures of N70E orientation.

Other Fracture Sets:
Natural fractures in black shales overlying both the 1U and the 5U have an ENE orientation similar to unmineralized fractures in the 5U. No fractures were encountered in

similar shales underlying reservoir zones. A set of hairline fractures, most completely healed with calcite cement, was also found in some Middle Spraberry cores.

The unique nature of each of these fracture sets implies that fracturing probably occurred as separate events and indicates that the Spraberry Formation has undergone a more complex stress history than might be construed from its fairly flat-lying nature.

Fracturing Paragenetic Sequences:
The N42E fracture set probably occurred first, as there is no barite mineralization within the few N80E fractures that were noted. Following fracturing, minor dolomite quartz precipitation occurred. Based on preliminary scanning cathodoluminescence studies (CL), it is believed that these cements were being precipitated both within the rock matrix and the fractures themselves contemporaneously. The barite was formed at a later time, deduced from the fact that there is little or no barite within the rock matrix.

Paragenesis of 5U fractures is more complicated, as there are two sets of fractures. The N70E fracture set is believed to have formed first since there are a couple of examples of these fractures causing termination of N32E fractures. As in the 1U, diagenesis of matrix and fracture probably occurred near the same time. Later movement of fluids through the fractures caused at least local precipitation of calcite within fractures and nearby rock matrix. The N32E fracture set formed subsequent to this first fracture event, and there is minor precipitation of quartz and dolomite within these fractures. Barite precipitation probably occurred following the first fracture event, but there is not enough evidence to determine its relation to the second fracture event. The fact that barite is not abundant in any 5U fractures and was only noted in samples containing N70E fractures suggests that the precipitation of Barite occurred between the two fracture events.

The earliest stages of diagenesis and dolomitization were followed by a period of fracturing, possibly the N70E fracture set in the 5U. The stresses or events that caused this fracture set may have been stronger deeper within the Spraberry. This is suggested by the presence of calcitefilled fractures within the middle Spraberry and the 5U, but not within the 1U. Precipitation of calcite cement within the N70E fractures followed. The next event was probably fracturing within the 1U that caused the N42E fractures. At least three phases of carbonate are present in some 1U samples, with dolomite being the first-formed phase followed by ankerite, then a ferroan dolomite. Ferroan dolomite is the most common phase seen within the 1U fractures. Non-luminescent quartz cement is seen both within fractures and rock matrix, suggesting that fracturing and precipitation of quartz and ferroan dolomite were occurring at the same time.

Precipitation of barite within 1U fractures and possibly within the 5U followed. A third fracture event then affected the 5U and formed the N32E. This was the only event that involved any obvious signs of incipient shear stress. The other fractures are solely tension-type fractures. Precipitation of quartz and dolomite within this fracture set then followed.

Discussion:

Relationship Between Depositional Features, Textures, Mineralogy, Provenance, Pore-Filling Constituents, Pore Space and Reservoir Quality

The very fine grain size shown by the Spraberry sandstones reflects their distal depositional position within the Permian basin. The angularity of about half of the detrital grains and the presence of numerous strain shadows is described by Warn and Sidwell (1953) as a physical wear that can only occur due to impact during long reworking and transportation by water. Suspension settling, saline density currents, and turbidites are the main mechanisms of sediment transport (Handford, 1981; N.Tyler and Gholston, 1988; Guevara, 1988). Very fine sandstones and siltstones commonly form the coarser bottom part of fining upward sequences having sharp erosional contacts with underlying shales and muddy burrowed tops. Diagenetic processes have obviously overprinted original depositional characteristics. However, mineralogical composition due to provenance and depositional factors probably exerts the most important control on reservoir quality. For example, the dominantly arkosic composition of the Spraberry sandstones and siltstones helped maintain some reservoir quality because the rigid and low ductile character of the framework grains made these rocks more resistant to compression forces. Also, quartz rich rocks are more stable and resistant to chemical alteration. On the other hand, cleaner sandstones and siltstones tend to be more affected by precipitation of quartz and other types of cement into open pore spaces. Pressure solution is also more prevalent. To some extent, the presence of argillaceous materials may prevent nucleation of quartz or carbonate cements on grain surfaces. Spraberry reservoir rocks represent a balance between the mechanisms of pore space preservation and destruction.

In the Spraberry sands there are minor amounts of interstitial clay, silt, and organics that Warn and Sidwell (1953) tried to explain by considering deposition in mildly turbid waters, which do not allow for complete and final size sorting. Another possibility for the hydrodynamically unlikely occurrence of fine clay mixed with coarser silts and sands is the infiltration of detrital clays in sandstones (Walker et al. 1978). Thus, original low porosity after deposition with a moderately sorted grain fabric was further reduced by authigenic cements and compaction. Bloch and McGowen (1994) stated that "porosity is essentially independent of grain size but it is strongly controlled by sorting and decreases progressively from very well-sorted to poorly sorted sand."

Another indirect depositional control on quality is the very fine grain size of these sands and silts, which probably causes marginal permeability in Spraberry reservoirs (Bloch and McGowen, 1994). Reducing the size of grains produces a proportionally equal decrease in pore size. Total porosity for a given volume of rock does not depend on grain size. However,reservoir quality will rely less on total amount of porosity than it does on the pore size of the individual pores. Considerable reduction of grain size does cause a direct decrease in *pore throat aperture* and in the size of individual pores. A decrease in the pore throat aperture causes higher capillary pressures that further damage the conductivity of fluids throughout the reservoir. Bloch and McGowen (M. Wilson, 1994) have stated that at the reservoir scale, grain size is the primary control of permeability. A

decrease in grain size from proximal to more distal facies is generally accompanied by decreasing permeability.

Visual differences between the organic-rich clays of the shaly facies (Rock Type "E" and "F") and the much less abundant clays in the clean facies (Rock Type "A" and "B") are quite obvious too. Shaly facies present deposited laminae with a matrix mixture of clays, organics, carbonate muds, and common associated pyrite precipitates and mica flakes that are parallel or sub-parallel to the bedding. The more porous rock types "A" and "B" show well defined fibrous illite, which differs from the poorly developed and compacted clays of Rock Type "E" and "F." The amount of expandable clays was small and was restricted to minor quantities of interbedded smectite with illite. The possibility that the expansion effect and high cation exchange capacity of smectites damaged porosity or permeability is relatively low. Small amounts of expandable clays suggest that the bad effect on any type of electric log or porosity logs, from bound water in interlayer between successive lattices of smectite is very low. However, structural water contained in illite and chlorite should still affect the response of electric logs. The main effect of the clays present in the Spraberry rocks is in the damage of reservoir pore space and fluid conductivity, by forming pore lining, pore coating, and pore filling. Mineralogy, the presence of matrix-supported or grain-supported fabric, grain size, sedimentary structures, and ultimately, reservoir quality, vary with lithofacies type. This is, in turn, a product of deposition and diagenetic changes. The main controls over reservoir quality are clay matrix content, carbonate content, presence of quartz overgrowths, and pressure solution of grains by compaction. Very fine sandstones and siltstones (Rock Type "A") were observed to be very clean and present the highest level of porosity among the distinct lithofacies groups. However, the detrimental effect of silica cement was found to be most notable with these clean sandstones as well as in thinner intervals with lower reservoir quality (Rock Type "B"). Patchy dolomitic siltstones (Rock Type "D") that have relatively high amounts of carbonate cements form a second category of possible reservoir rock. Substantial dissolution has taken place in some of these rocks, thus, they are considered moderately good quality reservoir rocks. Shales and shaly laminated siltstones (Rock Types "E" and "F") are the dominant lithofacies present in most of the cores examined. These are seen as rocks of low to very poor reservoir quality as are Rock Type "C" micritic dolomitic mudstones.

References

1. Bloch, S., 1994, Secondary porosity in sandstones: Significance, origin, relationship to subaerial unconformities, and effect on pre-drill reservoir quality prediction. From Wilson M. D., Reservoir quality assessment and prediction in clastic rocks, 1994, SEPM short course 30, p. 137-162.
2. Bloch, S., and McGowen, J. H., 1994, Influence of depositional environment on reservoir quality prediction. From Wilson M. D., Reservoir quality assessment and prediction in clastic rocks, 1994, SEPM short course 30, p. 41-57.
3. Dutton, S. P., 1980, Petroleum source rock potential and thermal maturity, Palo Duro basin, Texas: Texas Univ. Bur. Econ. Geology Geol. Circ. 80-10, 48 p.

4. Eslinger, E., and Pevear, D., 1988, Clay Minerals for petroleum geologists and engineers: SEPM short course notes No. 22., SEPM, Tulsa OK.
5. Guevara, E. H., 1988, Geological characterization of Permian submarine fan reservoirs of the Driver Waterflood Unit, Spraberry Trend, Midland Basin, Texas; BEG, UT Austin; Report of Investigation No. 172.
6. Handford, C. R., 1981, Deep-water facies of the Spraberry Formation (Permian), Reagan County, Texas; a core workshop (No. 2); Siemers, Tillman, and Williamson.
7. Houde, R. F., 1979, Sedimentology, diagenesis, and source bed geochemestry of the Spraberry sandstone, subsurface Midland basin, West Texas, Unpub. MS thesis, UT Dallas.
8. Jadgozinski, H., 1949, Eindimensionale Felordnung in Kristallen und ihr Einfluss auf die Rontgeninterferenzen. I. Berechnung des Fehlordnungsgrades aus der Rontgenintensitaten: Acta Crystallogr. 2, 201-207.
9. Lorenz, J. C., Teufel, L. W., and Warpinski, N. R., 1991, Regional fractures 1: A mechanism for the formation of regional fractures at depth in flat-lying reservoirs. AAPG Bull, V. 75, no. 11, p. 1714-1737.
10. Lorenz, J. C., 1997, "Horizontal Core Fracture Description," paper presented at the Spraberry Symposium, Parker & Parsley Development Company and U.S. Department of Energy, Midland, TX (Jan. 1997)
11. Lorenz, J. C., 1997, Non-Congruent Natural Fracture Sets in Adjacent Beds at Depth: Data From Horizontal Cores from the Spraberry Formation, Midland Basin, TX, presented at: AAPG Hedberg Research Conference, Reservoir Scale Deformation – Characterization and Prediction, June 22-28, 1997, Bryce, Utah.
12. Tyler, N. and Gholston, J. C., 1988, Heterogeneous deep-sea fan reservoirs, Shackelford and Preston waterflood units, Spraberry Trend, West Texas; BEG, UT at Austin, Report of Investigation No. 171.
13. Walker, T. R., 1978, Deep-water sandstone facies and ancient submarine fans: Models for exploration of stratigraphic traps: AAPG Bull., v. 62, pp. 932-966.
14. Warn, F. G. and Sidwell, R., 1953, Petrology of the Spraberry Sands of West Texas: Jour. Sed. Petrology, v. 23, pp. 67-74.

Table 1.9-1— Mineralogical averages for point counts of thin sections for six categories of small-scale lithofacies. Summary of data from three cores from three different wells.

PETROGRAPHIC POINT COUNT SUMMARY BY ROCK TYPE																																
	TEXTURE		GRAIN COMPOSITION														MATRIX					CEMENT COMPOSITION					POROSITY					
	ROCK TYPE	GRAIN SIZE (mm)	MONOCRYSTALLINE QTZ.	POLYCRYSTALLINE QTZ.	SUMA QRTZ	CHERT	MUSCOVITE	K-FELDSPAR	PLAGIOCLASE	IRF	MRF	SRF	CARBONATE FRAGMENTS (CALCITE)	ACCESSORY MINERALS	LAMINAR	DISPERSED	ORGANICS	DEPOSITIONAL CARBONATE (DOLOMITE)	SUMA MATRIX	UNDIFFERENTIATED CLAY	QUARTZ OVERGROWTHS	CALCITE	DOLOMITE	PYRITE	PRIMARY	SECONDARY	MICRO	TOTAL POROSITY
MAXIMUM	A	66.0	44.7	6.0	47.0	1.7	2.7	16.7	14.7	2.0	4.0	2.7		3.0	4.3	4.3	2.3	7.7	12.3	8.3	7.0	0.3	7.3	2.0	13.3	7.7	1.3	18.7
MINIMUM		46.0	36.0	1.0	39.0	0.3	0.3	6.3	3.7	0.7				0.3			0.7	1.7	1.7	1.0	3.3	0.3	2.7	0.7	7.3	2.7		10.3
AVERAGE		60.0	40.2	2.7	42.8	1.0	1.4	11.8	6.8	1.2	0.5	0.2		1.6	1.5	1.2	1.6	3.7	6.6	3.6	5.2	0.3	4.9	1.1	9.8	4.4	0.2	14.3
MAXIMUM	B	66.0	47.0	5.7	52.0	1.3	4.7	17.3	11.7	1.7	1.7	2.7	1.0	4.3	13.0	3.0	5.3	7.7	25.0	12.7	7.0		8.7	4.0	8.7	4.7	1.7	13.0
MINIMUM		40.0	29.0	0.7	30.0	0.7	0.3	6.3	3.3	0.7	0.7	0.3	0.7	1.0	0.7	1.3	0.7	1.3	5.0	0.7	2.7		1.0	0.7	0.3	1.0	0.7	1.0
AVERAGE		57.3	40.2	2.5	42.5	1.0	1.9	11.5	6.3	1.0	1.1	1.3	0.8	2.1	5.2	1.7	2.5	4.0	11.6	5.1	4.5		4.4	2.0	4.9	2.9	1.1	7.5
MAXIMUM	C	60.0	23.7		23.7	0.3	2.0	5.7	2.7	0.7	0.7		7.7		2.7	2.7	8.7	38.3	41.0	4.3		3.3	31.3	3.7				
MINIMUM		50.0	19.7		19.7	0.3	0.3	3.3	1.0	0.3	0.3		3.7		1.3	2.7	0.3	25.0	33.0	4.3		1.7	21.3	0.7				
AVERAGE		54.8	22.3		22.3	0.3	1.2	4.1	1.8	0.5	0.5		5.7		2.0	2.7	4.2	30.7	36.1	4.3		2.5	26.4	2.1				
MAXIMUM	D	60.0	39.3	4.7	42.0		2.3	8.0	3.7	0.3	0.7	0.3	2.0		4.3	2.3	2.7	25.7	35.0	3.0	4.7	3.0	18.3	3.0	4.3	4.0		7.3
MINIMUM		56.0	27.3	1.0	27.3		1.0	5.0	2.0	0.3	0.3	0.3	0.7		1.7	1.3	1.3	9.3	14.0	1.0	2.3	1.7	13.7	3.0	2.0	1.3		3.3
AVERAGE		58.3	34.9	2.3	36.6		1.8	6.3	3.1	0.3	0.4	0.3	1.1		2.3	1.6	1.9	17.6	22.2	2.4	3.7	2.5	16.1	3.0	3.1	2.5		5.6
MAXIMUM	E	62.0	44.3	3.3	44.3	0.3	7.7	9.3	5.3	0.7	1.0	0.3	2.3	3.7	44.0	3.3	9.7	4.7	56.7	20.7	1.3	2.3	2.0	6.7			1.0	1.0
MINIMUM		26.0	21.0	3.3	21.0	0.3	1.0	1.3	0.7	0.3	0.3	0.3	2.0	0.3	25.0	0.7	4.3	1.3	34.0	4.3	1.3	2.3	0.7	0.3			0.3	0.3
AVERAGE		39.2	29.0	3.3	29.3	0.3	5.5	4.9	2.9	0.5	0.7	0.3	2.2	1.7	30.7	2.1	7.1	2.2	41.1	13.3	1.3	2.3	1.3	3.0			0.7	0.7
MAXIMUM	F	58.0	42.7	4.0	46.7		5.3	16.3	11.7	0.7	1.7	0.7	0.7	2.0	19.3	8.0	5.3	8.7	33.3	14.0	4.7	1.0	4.3	5.0	4.7	2.3	0.7	7.0
MINIMUM		40.0	34.0	1.0	35.0		1.3	7.3	1.3	0.3	0.3	0.7	0.7	0.7	3.3	1.0	0.7	2.0	7.3	1.0	2.0	1.0	1.7	2.3	1.0	0.7	0.7	1.0
AVERAGE		52.6	38.8	2.0	40.0		3.0	11.7	5.6	0.5	0.7	0.7	0.7	1.1	13.4	4.2	3.0	3.4	22.8	6.1	3.0	1.0	3.1	3.5	2.4	1.2	0.7	2.9

Table 1.9-2— X-ray diffraction data for clay mineralogy covering all lithologic types in the Spraberry Formation.

CLAY COMPOSITION from XRD ANALYSIS (parts in 10)				
Sample Depth (ft)	**Illite**	**Chlorite**	**Kaolinite**	**I/S**
7069	4	4	1	1
7076	10	--	--	--
7081	6	2	1	1
7082	6	2	1	1
7083	5	3	2	1
7085	7	2	1	--
7087	4	4	1	1
7290	6	3	1	--
7092	6	3	1	--

Table 1.9-3—A summary of the pore types encountered in SEM samples from the Spraberry Formation.

SUMARY OF PORE TYPES			
PORE TYPE	**PORE MORPHOLOGY**	**PORE SIZE**	**PORE CONECTIVITY**
PT1	Primary intergranular macropores with irregular shapes.	Relatively Large 30-40 µm	Relatively well interconnected, pore throats radius of 0.75-2 µm
PT2	Primary intergranular macropores with irregular shapes	15-30 µm	Moderately interconnected, pore throats radius of 0.4-1.0 µm
PT3	Primary intergranular mesopores generally Polyhedral pore shapes	5-15 µm	Poorly interconnected through pore throats <0.5 µm
PT4	Micropores. Pores are developed within clay cement rims on framework sand grains, between fibrous illite growths (often bridging pore throat), within partially dissolved grains, and within shale	Much less than 5 µm	No connectivity
PT5	Secondary dissolution pores crated by selective leaching of chemically unstable framework sand grains or cements. Usually polygonal in shape.	Oversized up to 40 µm	Very good connectivity

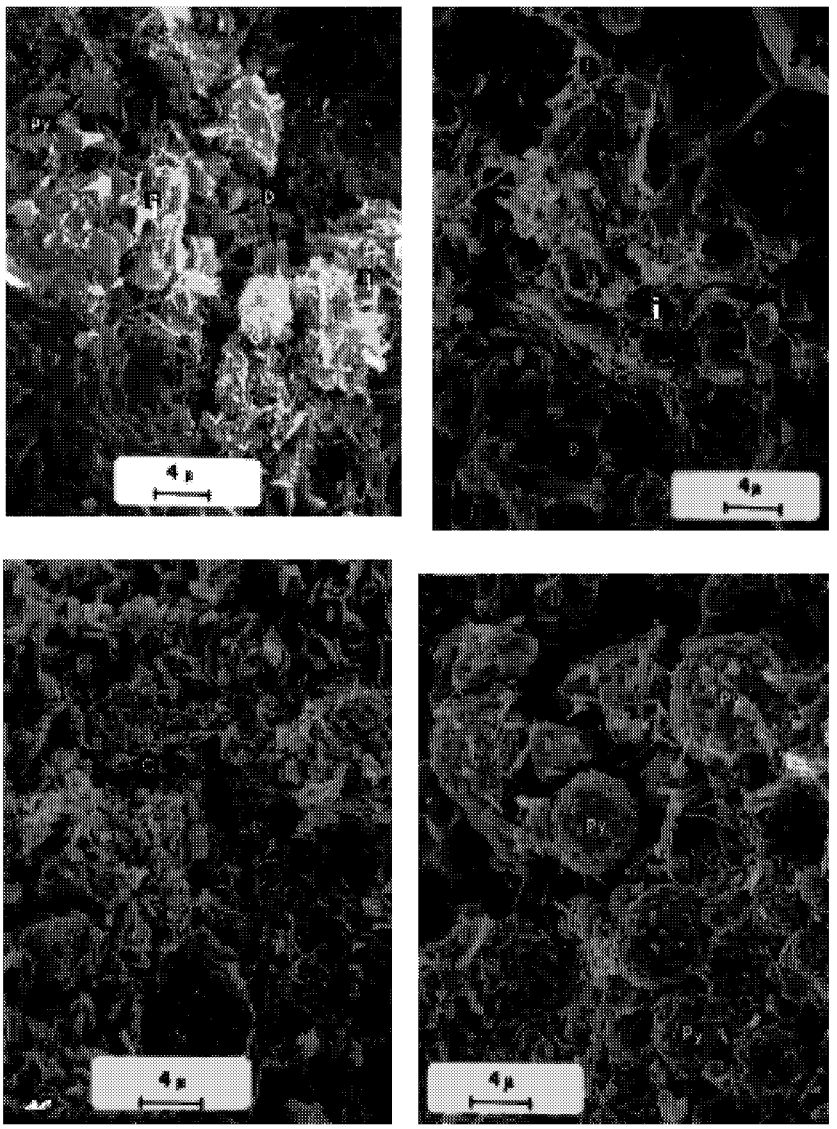

Fig. 1.9-1—SEM photomicrographs showing different types of illite clay accumulation, dolomite cement, and pyrite occurrence in the Spraberry Formations

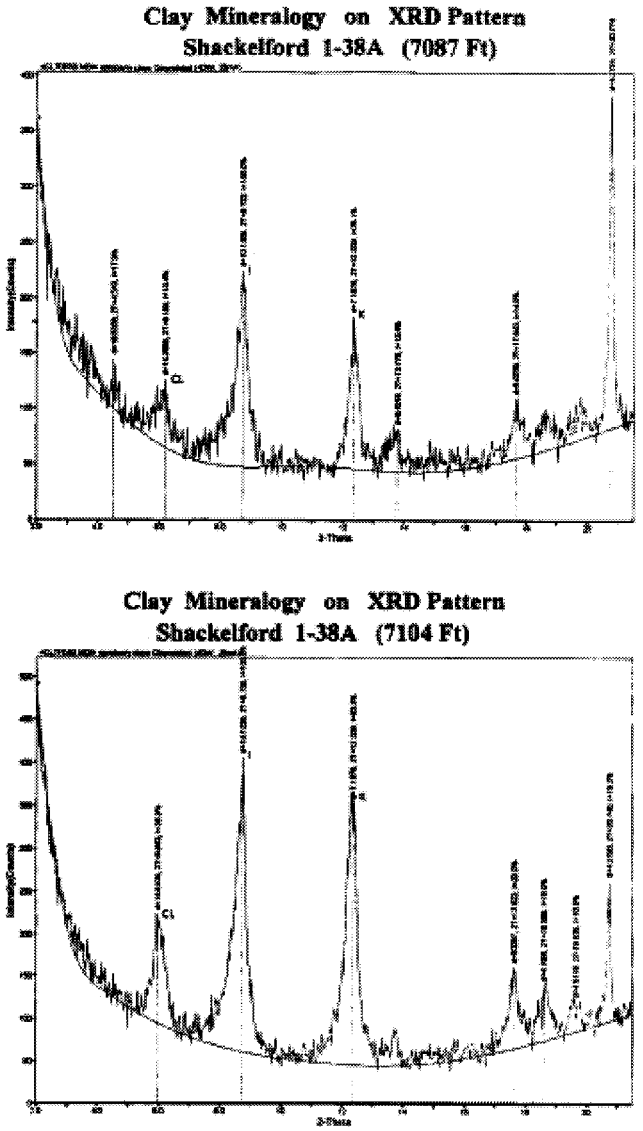

Fig. 1.9-2—Two X-ray diffractograms showing clay mineralogical composition (Cl, I, and K).

1.10 PETROPHYSICS: Combined Rock and Fluid Character

Integration of geological and petrophysical data allows development of a rock-fluid model for upper Spraberry rocks. This study identifies the different rock types that comprise the subject reservoirs, marginal reservoirs and non-reservoir rocks. A rock type is defined as an interval of rock with unique pore geometry, determined mineralogical composition and is related to certain specific fluid flow characteristics.

The rock-fluid model relates fluid flow characteristics to rock types defined in the previous section (1.3: Petrography and Diagenesis). Analytical techniques used to develop this model include porosity-permeability analysis of core plug samples, air minipermeameter measurements on core slabs, thin section analysis, scanning electron microscope analysis of the pore structures, air-mercury capillary pressure, pore body and pore throat size distributions and GR log of each well. Integration of results from these various analytical techniques reveals that the six (6) smallscale lithofacies described using thin-section analysis are consistent with the petrophysical model shown in this section.

Gamma Ray Log Resolution

A method of distinguishing between shales, clay rich siltstones and very fine sandstones units uses gamma-ray logs (Fig.1.10-1) and is widely implemented in the field practice. This method has shown to provide good differentiation between lithological characteristics in many investigations (Guevara, 1988; Tyler and Gholston, 1988). Data from different analytical techniques combined with the gamma-ray log response for the E.T. O'Daniel 37 core are shown in Fig. 1.10-1. The gamma-ray deflection curves show good correlation with core descriptions.

Thicknesses for sandy beds are fairly well predicted by the deflection to the left, however peak heights do not define facies quality very accurately. The later is due to the limited sensitivity of the gamma ray tool to differentiate mineralogical sources others than clay amount in the matrix.

Determination of Petrophysical Properties

Three different methodologies were used to analyze petrophysical properties: (1) A computercontrolled scanning air-minipermeameter (CCSAM), (2) imbibition experiments with air, oil and synthetic brine, and (3) petrophysical properties with injection of nitrogen, helium and mercury.

Computer-Controlled Scanning Air-Minipermeameter (CCSAM)

Although the air permeability curves show good relationship with gamma-ray curves and core descriptions, the vertical air permeability variation is much more complex in character (Fig. 1.10-1). A number of factors affect the formation heterogeneity: clay and organic rich laminae, burrowing, cementation, pore morphology, pore distribution, pore throat aperture, level of interconnection of pores and rock wettability.

Methodology for Obtaining Petrophysical Properties

Permeability determination with Nitrogen Flow Through Rock Type:
Core plug samples of 1 in. and 1.5-in. diameters were used to measure petrophysical properties of the different lithofacies for two cores from the Upper Spraberry Formation. Parameters measured include porosity (ϕ), permeability (k), and grain density (Reservoirs Inc., 1996). A core holder with a specific confining pressure is used. Formulas for the calculation of permeability, porosity and water saturation are given below. The permeability resulted from injection of nitrogen gas into the samples at a constant pressure until a constant flow rate of gas through the sample is attained (steady-state conditions). Permeability (k) is a function of flow rate (q), viscosity of the fluid (μ), length of the core plug (L), transversal area of core plug (A), and drop in flow pressure (ΔP):

$$k_b = \frac{q\mu L}{A\Delta P} \quad \text{.....(1)}$$

Helium Porosity Determination
Boyle's law was used to calculate the porosity for each core plug sample:

$$P_1 \times V_1 = P_2 \times V_2 \quad \text{.....(2)}$$

Helium was used as the gas phase. Two chambers of known volumes were connected, one containing helium at a given pressure (P_1) and another (matrix cup) with a core plug. The helium is expanded into the matrix cup and an equilibrium pressure (P_2) is recorded. The initial volume (V_1) of the sole helium chamber is known, thus the volume of the new system helium chamber and matrix cup (V_2) is determined using the Boyle's Law. By subtracting V_1 from V_2 the total pore volume (PV_t) for the given core plug is obtained. The porosity (ϕ) is simply the fraction between the total pore volume (PV_t) and the core plug bulk volume (V_b) determined from mercury immersion (*Archimedes principle*) and corroborated by measuring the core plug dimensions.

$$\phi = \frac{PV_1}{V_b} \quad \text{.....(3)}$$

Grain density (GD) for each core plug is a function of the grain volume and weight of the clean and dry core material. Grain volume (GV) is the result of subtracting the total pore volume (PV_t) from the bulk volume (V_b) for each plug sample:

$$GV = V_b - V_t \quad \text{.....(4)}$$

GD is then the amount of weight of grain or core material (*Wdry*) per volume of grain (*GV*) in the given sample:

$$GD = \frac{W_{dry}}{GV} \quad \text{.....(4)}$$

These sets of data are analyzed using cross-plots correlating pairs of data to define relationships and quality controls. For instance it is observed in Fig. 1.10-2 that porosity and permeability increase or decrease more or less simultaneously below a depth of 7195 ft, while the relationship of ϕ and K above this depth is more complex. Implications regarding variability and lithological controls on rock-fluid behavior will be further discussed in the following sections.

Mercury Injection Techniques: Capillary Pressure, Pore Distribution, Pore Throat and Connectivity

Mercury injection (Reservoirs Inc., 1996) into core plugs is used to determine capillary pressures, pore throat sizes, connectivity, relative quality of different rocks and Leverett's "J" function. This procedure utilizes a vacuumed injection chamber to hold a core plug. A specific distance between the injection of mercury and the core plug was allowed to avoid undesirable pressure changes. Mercury starts invading the core pore system specific applied pressure or threshold pressure. This specific threshold pressure remains constant until mercury intrusion ceases. At this point the pressure and the amount of mercury injected is recorded. The pressure is then increased incrementally and the same procedure is repeated. In this case the range of pressures selected was 0-2000 psia and 0-60,000 psia for high-pressure measurements. The test results were used to calculate pore throat radii and Leverett's "J" function.

Rock Types and Rock-Fluid Properties

The Rock Types previously described (see section 1.3) were defined based on their petrophysical properties. For each of these we found a rock-fluid model with unique pore geometry, a determined mineralogical composition and certain specific fluid flow characteristics. Each of these six rock-fluid models is directly related to their analogous previously described petrographic categories.

Discussion of Petrophysical Properties

Accurate representation of rock-fluid properties is necessary when obtaining petrophysical data. Laboratory techniques that implement injection of nitrogen, helium and mercury into core plug samples are very accurate in obtaining reservoir properties. This section presents permeability and porosity data from nitrogen and helium injection respectively (Reservoir Inc., 1996). Helium is capable of filling up all connected space inside a rock sample thus giving accurate porosity values. Mercury, a non-compressible fluid, is a non-wetting fluid that does not react with the rock and also possesses the ability to completely occupy pore space. Thus, measurements using mercury injection are very accurate in determining pore throat values. The goal of this work was to define reservoir

rock character and to distinguish it from all other types of rocks encountered within the Spraberry strata sequence. The different data sets were analyzed to determine correlations between porosity and permeability behavior and lithologic controls on reservoir quality. Capillary pressure analysis is presented to define pore throat systems for each rock type.

Permeability, Porosity and Water Saturation Relationships:
Core plug samples selected for detailed analysis in this study have a wide dynamic range of porosity (0.4 to 13.7%) and permeabilities (0.01 to 1.97 md). The dispersion of porosity– permeability data is such that permeabilities range over an order of magnitude for any given value of porosity (Figs. 1.10-3 and 1.10-4). This dispersion of porosity–permeability data reflects changes in the volumetric distribution of pore types within the reservoir.

The first striking point that can be drawn from the depth profile of porosity and permeability (Fig. 1.10-2) for E.T. O'Daniel is the difference in correlation match approximately below and above the depth of 7175 ft. Above this depth there is a poor match between porosity and permeability due to great variation in lithology. A number of heterogeneities at various scales tend to deteriorate fluid conductivity. These include dispersed and laminated clay matrix, abundant organic matter, bioturbation, soft sediment deformation within shaly laminae, and silica cement within sandy laminae. In this way pore interconnection is considerably reduced for many samples while its total porosity remains relatively high. However, the sandy areas that comprise the reservoir interval 5U unit (below 7175 ft) exhibit a better correlation between porosity and permeability. Better fluid conductivity is related to bigger pore spaces and pore throat radius present in Rock Types "A" and "B" within this area.

A set of six cross plots are presented in Figs. 1.10-3 and 1.10-4 relating porosity and permeability data (Reservoir Inc. 1996) to observable lithofacies (see section 1.2) as defined from core plug samples of Shackelford 138-A (Fig. 1.10-3) and E.T. O'Daniel 37 (Fig. 1.10-4). Strong evidence is presented for depositional controls on porosity and permeability. For instance, Lithofacies 6 (massive sandstone and siltstone), a product of high-energy deposition, shows the best reservoir properties in the porosity-permeability cross plot. Massive dolostone (Lithofacies 1) and shale (Lithofacies 2), from low energy environments, show very low reservoir quality. However the clusters of points for each lithofacies type are not totally distinct from each other. The overlapping of depositional lithofacies in these graphs is probably caused by a number of factors including diagenesis, similarity in pore-structure produced by different depositional environments and the somewhat subjective nature of specifying lithofacies based on hand specimens.

Presented in Figs. 1.10-5 and 1.10-6 are contiguous intervals of fluorescing pay zone and non-pay shaly zones with permeability, porosity and water saturation relationships that suggest strong mineralogical control. Areas of non-fluorescence ordinarily contain higher amounts of clays although they may appear quite similar to fluorescent rocks when viewed in normal light. Although some porous areas exist, non-fluorescent intervals exhibit much less permeability than fluorescent zones. The low permeability in these relatively porous intervals is probably related to higher amounts of clay minerals that

affect pore throat connectivity. Relatively similar sandy units do not show obvious evidence of major heterogeneity in core samples. Petrophysical properties measured in the lab show important variations between fluorescing pay zones and non-pay zones richer in clay content, as in the core analysis of the Shackelford 1-38A (see Fig 1.10-5).

Data from the, Shackelford 138A and E.T. O'Daniel 37 cores shown in Fig. 1.10-7 correlate porosity with S_w measurements. The linear relation with a negative slope clearly indicates the trend of decreasing water saturation with porosity increase. The variation of both variables along the depth profile is presented in Fig 1.10-1. This depth profile shows a strong increase of water saturation within the non-pay, low porous muddy zone. This depth profile of S_w and porosity further indicates that lithological control is strongly related to fluid-rock behavior.

Previous reports have analyzed wettability data from Spraberry core plug samples using brine and oil injection and spontaneous imbibition of brine. From these measurements, initial water saturation, core permeability, and core wettability have been determined. These are very important factors because of their effect on final oil recovery.

When some mineral facie are water-wet, it means that they posses a hydrophilic character; thus water will preferentially be attached to the surface of this mineral. If it were the case of a hydrophobic mineral facie, this would probably be preferentially and electrochemically related to the oil phase.

Pore walls in the Spraberry sands are formed by a variety of different minerals including quartz, different types of feldspar, micas, accessory minerals, carbonate cements, clays, organic matter, pyrite and other less abundant minerals. These different mineralogical species present distinct wetting behaviors at the microscopic level. The clay rich zones tend to be water-wet in the Spraberry formation, which contrast with the mixed oil-water-wettability behavior of clean siltstones and sandstones. Due to this characteristic, the argillaceous and less porous rocks within the studied intervals exhibit much higher water saturation than the cleaner siltstones and sandstones.

Due to variations in composition from one core plug to another, the behavior of the capillary pressure-S_w curve presents considerable differences (Fig. 1.10-9). The Amott wettability index to water (I_w) was determined to be between 0.22 and 0.35. As a result of this mineralogical heterogeneous character, the Spraberry reservoirs are considered weakly or moderately waterwet. The microscopic displacement efficiency during spontaneous water imbibition varies from 10% to 15% depending upon core permeability. In turn permeability depends on rock properties such as pore throat size, pore size distribution, pore connectivity, tortuosity, and rock-fluid properties such as capillary pressure and wettability.

Spraberry sandstones have been found to imbibe oil spontaneously without requiring any pressure input, due to the partially oil wet character of the rocks. This behavior does not favor oil recovery by conventional water flood techniques. At a certain point, water

injection would not be able to move any more of the oil that is trapped in hydrophobic intergranular pore cavities.

Grain Density and Porosity Relationships:
Presented in Fig.1.10-8 are additional analyses of lithological controls on reservoir quality. Grain density is strongly related to lithological character. There is a hyperbolic relation with a positive slope for porosity and grain density data from the core. A cluster of points in the top left corner can be discriminated as carbonate muddy rocks with their typical high grain density, very low porosity and petrographic characteristics. Table 1.10-1 summarizes the general trends found in the petrophysical data for three major subdivisions of rock types: 1) Clean sandy rocks, 2) Shaly and silty non-fluorescent rocks, and 3) Dolostones.

Notice that these three subdivisions represent the major trends that occur in the Spraberry Formation (i.e. Rock Types "A," "B," "C," "E," and "F"). Patchy dolomitic siltstone "Rock Type D" falls between "B" and "F" (see Fig.1.10-8). This category shows slightly higher grain density range and lower porosity than "B" due to the higher amounts of dolomite cement present.

Capillary Pressure and Pore Throat Relationships:
Mercury injection data from core plug samples from the Shackelford 138A and E.T. O'Daniel 37 is presented in this section. A set of cross plots that correlate porosity, permeability and pore throat data is shown in Fig. 1.10-10. The results show consistency between rock-fluid parameters and those obtained in the petrographic study. Summarized in Table 1.10-2 are the results (average values) for each rock type from helium, nitrogen and mercury injection.

The analysis of petrophysical data emphasizes the heterogeneous nature of the Midland basin deposits. From this data, one can see distinct differences among Rock Types occurring in the upper Spraberry Formation. As expected from thin section analysis, Rock Types "A" and "B" present the best potential reservoir rocks. These consist of very fine sandstones and siltstones with variable pore structures. Rock Types "C," "D" and "F" required higher pressures to pass fluid through tight pore systems with very small pores and pore throat radii. No measurements of Rock Type "E" (shale) samples were made due to its obvious poor reservoir quality. Rock Types "C," "D," "E" and "F" are considered to be marginal reservoirs to poor or non-reservoir rocks.

They are dolostones and patchy dolomitic siltstones, and shales and shaly siltstones with variable organic content. The following detailed enumeration of results for each Rock Type includes description of the different petrographical and petrophysical parameters affecting their pore system.

Description of Rock Types

Rock Type A – The average values of porosity and permeability are 11.07% and 0.445 md respectively. This rock type is dominated by intergranular macropores of Pore Type 1 (30-40μm), Pore Type 2 (15-30μm) and secondary dissolution Pore Type 5 (50μm). Intergranular macropores (PT1) are relatively large and are well interconnected through large pore throats of relatively uniform size. The rock is very fine to fine grained, well-sorted sandstone to coarse siltstone, with massive sedimentary fabric. Thin section analysis reveals that the hydrocarbon- bearing samples classified as Rock Type "A" have relatively well preserved intergranular pore systems. Quartz overgrowths, patchy dolomite cement, and dispersed pore-filling clays produce some reduction of total pore volume. Illite, chlorite and smectite have also reduced pore volume. These minerals have formed pore linings and caused pore throat bridging, which in turn has resulted in the partitioning of pore space near pore walls into micropores (Pore Type 4 <5 μm in diameter). Type 2 pores are much less abundant than Type 1 pores. Type 3 pores are not significant components of the pore system. Capillary pressure data shows a relatively high average value of 156.7 psia necessary to intrude the larger system of pore throat radii (0.53 μm) reflecting moderate obstruction of the intergranular pore system. Relatively high displacement pressures for sandstones with moderate porosity are the product of small pore throats and significant amount of pore lining and pore bridging illite clay and carbonate cements.

Rock Type B – These are lesser quality reservoir rocks with average values of 9.49% for porosity and 0.041md for permeability. They are very fine to fine grained, moderately to well sorted siltstones dominated by Type 2 pores (intergranular macropores 15-30 μm diameter). Type 3 (intergranular mesopores 5-15 μm diameter) are less abundant, but common within these rocks. Silica cement is present filling pore spaces. Carbonate and clay cementation has partitioned pore space near pore walls into micropores (Type 4 pores). Pore Types 1 and 5 are not significantly developed. The larger pore throat radii averages 0.15 μm and has displacement pressure of 629.9 psia.

Rock Type C – These are carbonate muds (dolostones) equivalent to the carbonate debris flow deposits of Lithofacies 1. These carbonates have very low porosity (0.70% avg.) and permeability (0.013 md avg.) and are not reservoir rocks. For this reason the pore structures of these rocks have not been studied in any detail (two samples studied). Very small pore throat apertures of 0.0035 μm need extremely high displacement pressures (10,464 psia) to intrude them. These are essentially moderate quality seal rocks rather than potential reservoirs.

Rock Type D – Porosity for these patchy dolomitic siltstones is 4.70% and very low permeability averages 0.01 md (one sample). Rocks of Type "D" are moderately well to well sorted siltstones and sandstones dominated by Type 3 pores (intergranular mesopores 15 μm diameter). They display poorly preserved pore systems and have massive, laminated, or disturbed sedimentary fabrics. Type 2 pores (intergranular macropores 15-30 μm diameter) are less abundant. Microporosity (Type 4 pores) is developed within clay cement rims on grains. The microporous clays tend to severely obstruct intergranular pores. Type 1 macropores scarcely occur within these rocks. Type 5 (dissolution) pores are also very rare. Pore throat radii (0.045 μm) are considerably obstructed; thus, moderately high displacement pressure (1,196 psia) is required to intrude them.

Rock Type E – Porosity found for these samples averages 3.14%, while average permeability is 0.025md. These are very tight rocks with very high amounts of clay, organic matter, and carbonate mud mixed within an argillaceous matrix. Type 5 rocks are shales characterized by micropores (Pore Type 4) and very small modal pore throat radii. Data from capillary pressure mercury injection was not recorded for these samples due to their extremely low reservoir quality. These rocks commonly form permeability seals, not reservoir rocks.

Rock Type F – Average porosity and permeability for five samples are 6.36% and 0.022 md, respectively. Rock Type "F" is moderately to poorly sorted clay rich siltstones. Samples display massive, laminated, or disturbed sedimentary fabrics, and are characterized by the virtual absence of visible porosity. Intergranular pore space is severely occluded by abundant detrital clays or dolomite cement. Estimated microporosity is high for clay–rich samples, but low for the dolomite-cemented samples. Main pore types present are mesopores of 5 to 15 μm. Though porosities and permeabilities are slightly higher than Rock Type D (patchy dolomitic siltstones), the average value for modal pore throat radii is considerably smaller (0.039 μm). Displacement pressure necessary to intrude the larger set of pore throats in Rock Type "F" is 2,637.8 psia, more than double that used in Rock Type "D."

Summary

Rock Types "A" and "B" are potential reservoir rocks. These are distinguished from one another by different pore structures. Rock Type "A" has the best reservoir quality and is characterized by the largest intergranular and dissolution macropores and largest interconnecting pore throats.

Rock Types "B," "D," and "F" are characterized by progressively poorer reservoir quality, the result of reduced pore and pore throat sizes. Rock Types "C" and "E" are carbonate muds and shales that completely lack reservoir properties and form moderate quality seal rocks.

The occurrence of the largest pores and pore throats in Rock Type "A" is a function of several factors including:

1. Rock Type "A" is the coarsest grained sandstones and siltstones.
2. Rock Type "A" is very fine sandstone and siltstones are better sorted than other Spraberry rocks and contain smaller amounts of depositional micritic mud, carbonate cements, clay matrix, clay cements, and organics.
3. Rock Type "A" is very fine sandstone and siltstones are characterized by relatively open grain packing (compactional effects are not pronounced).

The reservoir quality of Rock Type "A" and "B" is strongly tied to mineralogical and textural properties such as grain size, grain sorting, clay type and content, and carbonate cement. These are parameters that strongly control pore and pore throat size, permeability, capillary pressure, and wettability. Individual pores and pore throats in Spraberry sandstones are of relatively small sizes and this, in turn, is related to the very fine sand and siltstone grain size of these rocks (J. Neasham, 1977).

Rock Type "B" has more complex pore structure than Rock Type "A." This complexity is a function of finer grain size, increase occurrence of depositional shale laminae (as well as some organics), carbonate and silica cements, and increased effects of compaction. Owing to the presence of shale laminations in some samples, substantially reduced vertical permeability is noted when compared with Rock Type "A." These factors contribute to produce small pore size (these rocks are generally characterized by pores of less than 30 μm diameter) and pore throat size as well as a large standard deviation of pore and pore throat sizes. While varying little in total porosity from Rock Type "A" sandstones, reduced permeability in Rock Type "B" sandstones is a function of this smaller pore and pore throat size and slightly higher amounts of clays and carbonates.

Rock Type "D" and "F" siltstones present varying degrees of heterogeneities, as a result binary, skewed, and uniform pore size distributions are all noted. Lithologies are a mixture of: 1) Micropore-dominated, shale/organic layers (distorted in the case of bioturbated rocks) and; 2) Primary intergranular pore-dominated sand layers with dolomite patches, and dispersed clays.

The pore systems of Rock Type "D" differ from good reservoir rocks "A" and "B," in that most of the porosity in these rocks is poorly interconnected and consists of intergranular mesopores (generally 5-15 μm diameter).

Rock Types "C" and "E" are essentially nonporous and impermeable seal rocks. High pressure mercury injection capillary pressure data indicate that displacement pressures are very high, ranging from 1000 to 15,000 psia. These tightly cemented samples have very small modal pore throat radii, ranging from 0.004 to 0.05 microns.

References

1. Guevara, E. H., 1988, Geological characterization of Permian submarine fan reservoirs of the Driver waterflood Unit, Spraberry Trend, Midland Basin, Texas; BEG, UT Austin; Report of Investigation No. 172.
2. Neasham, John W., The morphology of dispersed clay in sandstones reservoirs and its effect on sandstones shaliness, pore space and fluid flow properties, Society of Petroleum Engineers, paper SPE 6858, Annual Technical Conference and Exhibition held in Denver, CO, October 9-12, 1977.
3. Reservoirs Inc., 1996, Internal report: Core analysis, Parker & Parsley Development, L. P. Midland County, Texas.
4. Tyler, N. and Gholston, J. C., 1988, Heterogeneous deep-sea fan reservoirs, Shackelford and Preston waterflood units, Spraberry Trend, West Texas; BEG, UT at Austin, Report of Investigation No. 171.

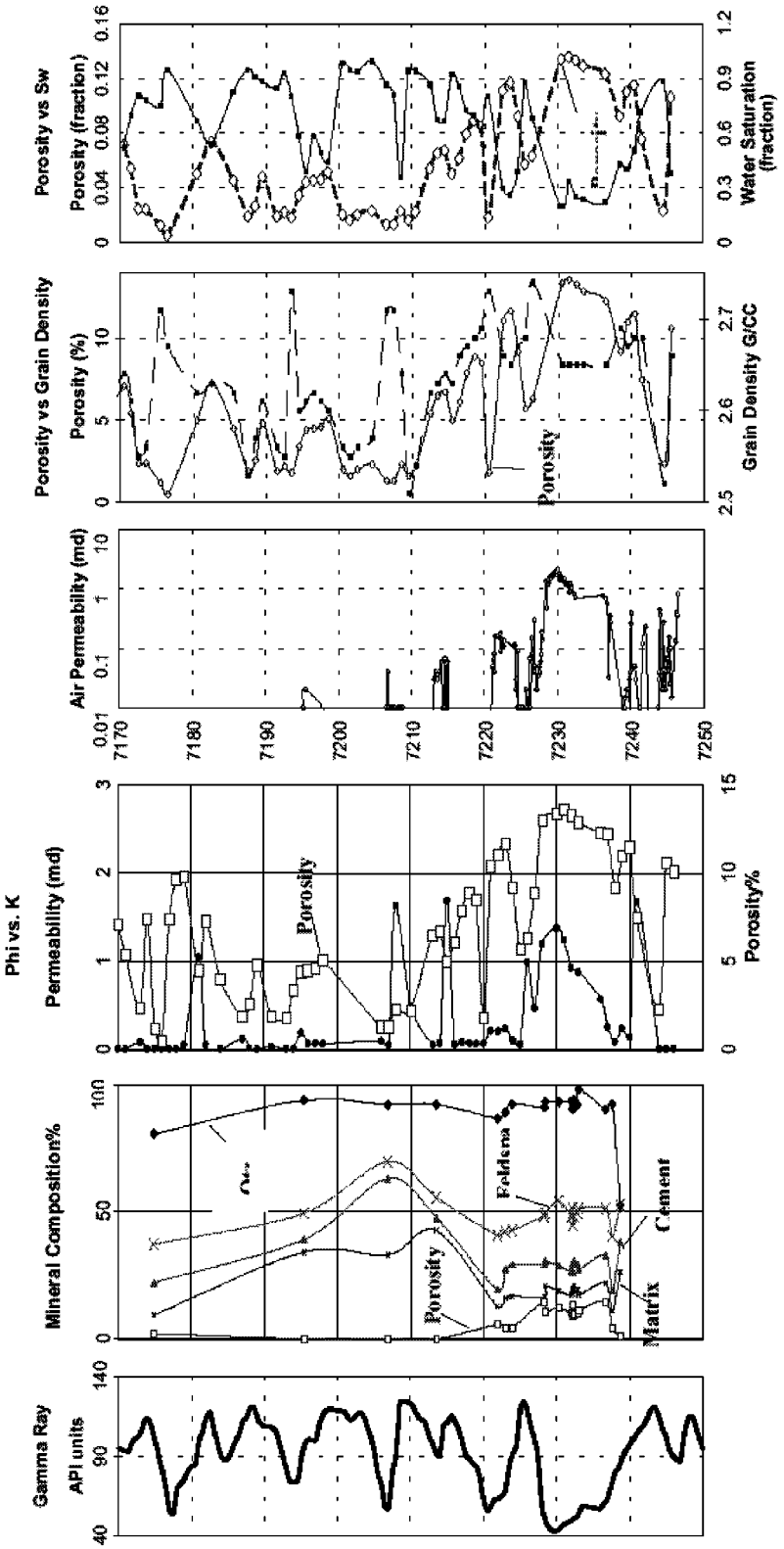

Fig. 1.10-1—Core E.T O'Daniel 37 - Integration of Petrographic and Petrophysics Data

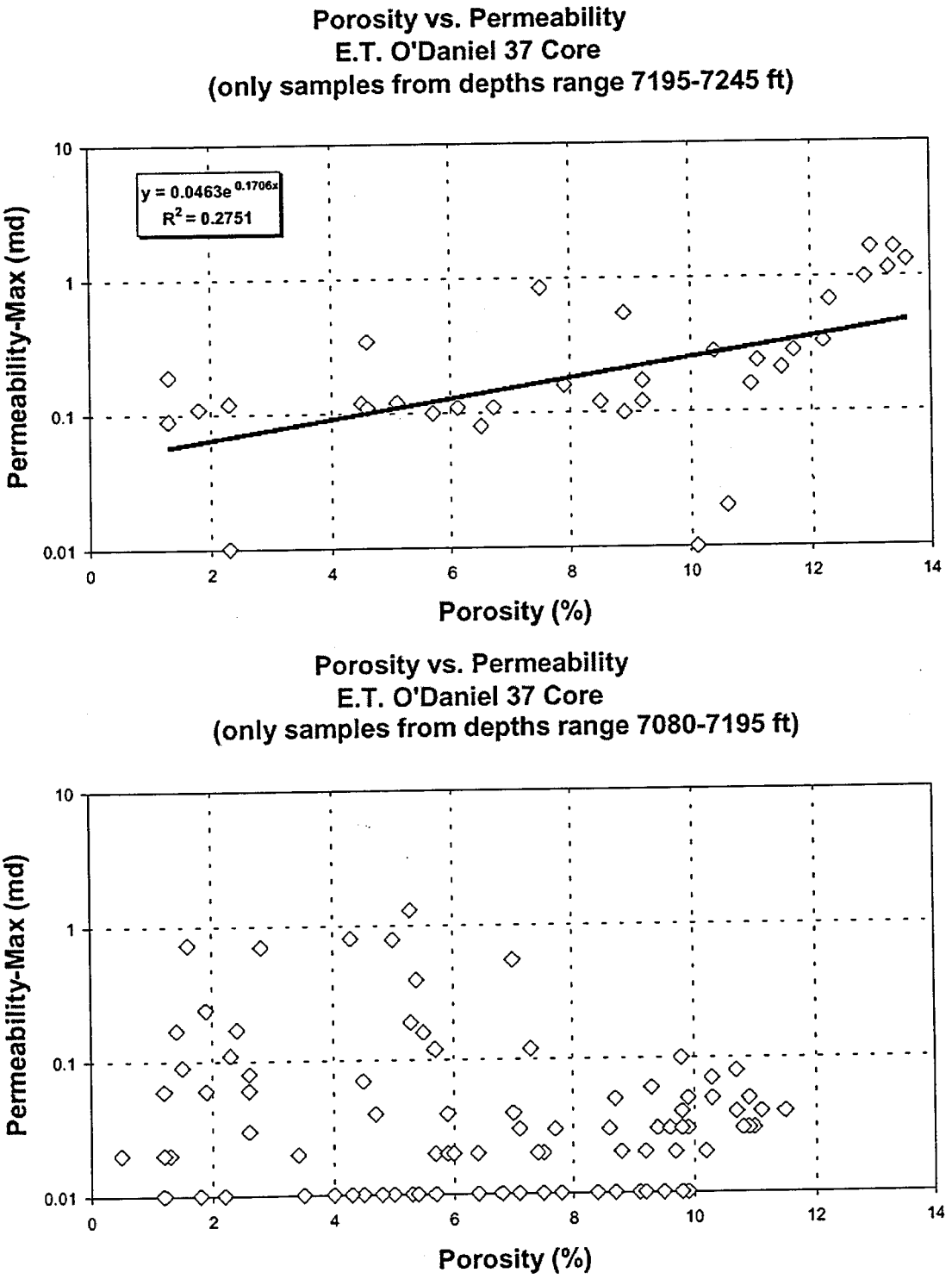

Fig. 1.10-2—Cross plots illustrate the differences in porosity-permeability correlation for samples above and below 7195 ft depth for E.T. O'Daniel 37 core

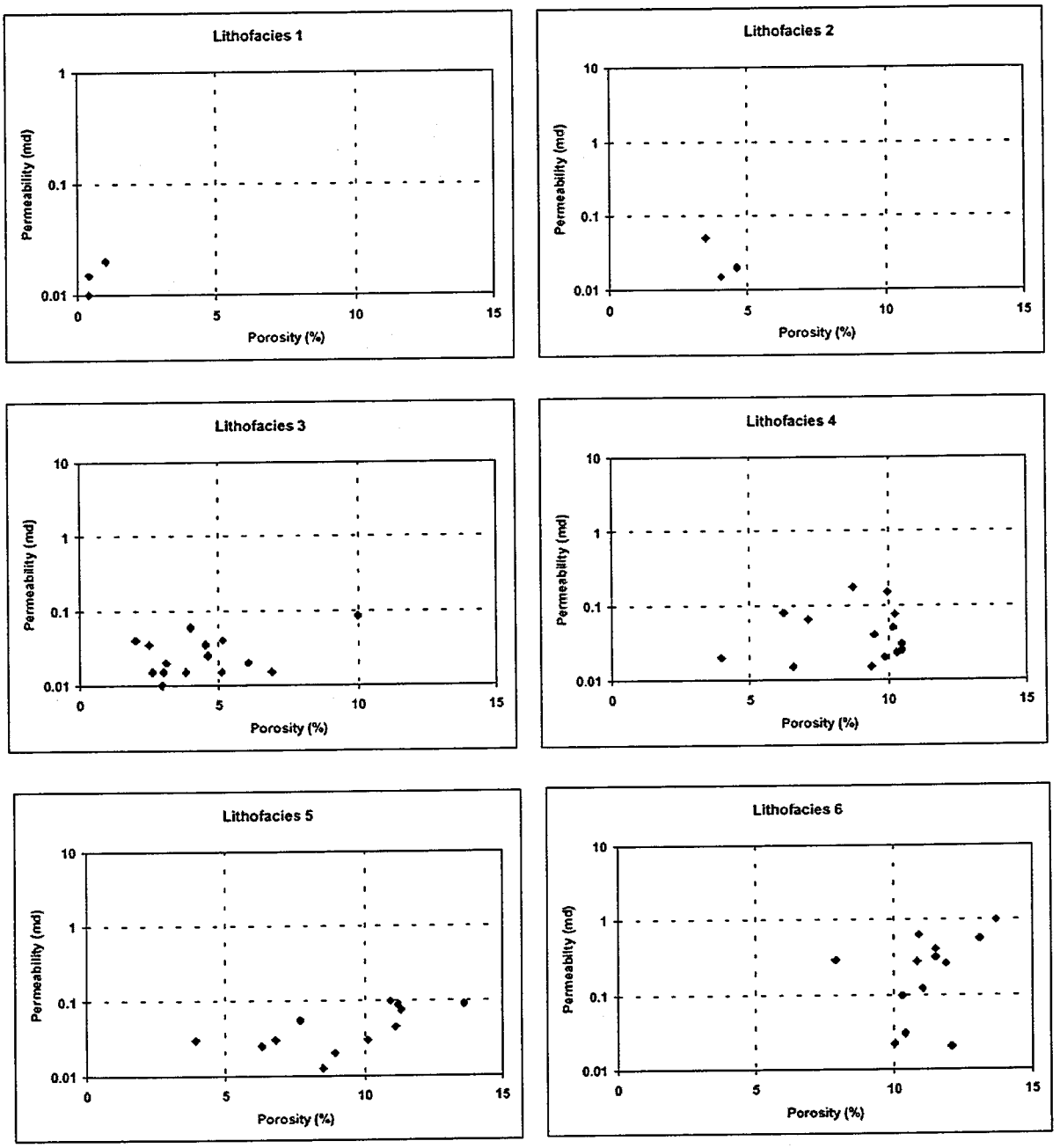

Fig. 1.10-3—Set of porosity-permeability cross plots shows the lithological control upon and k. Shackelford 138-A core *(Data compiled from Reservoirs Inc. internal report).*

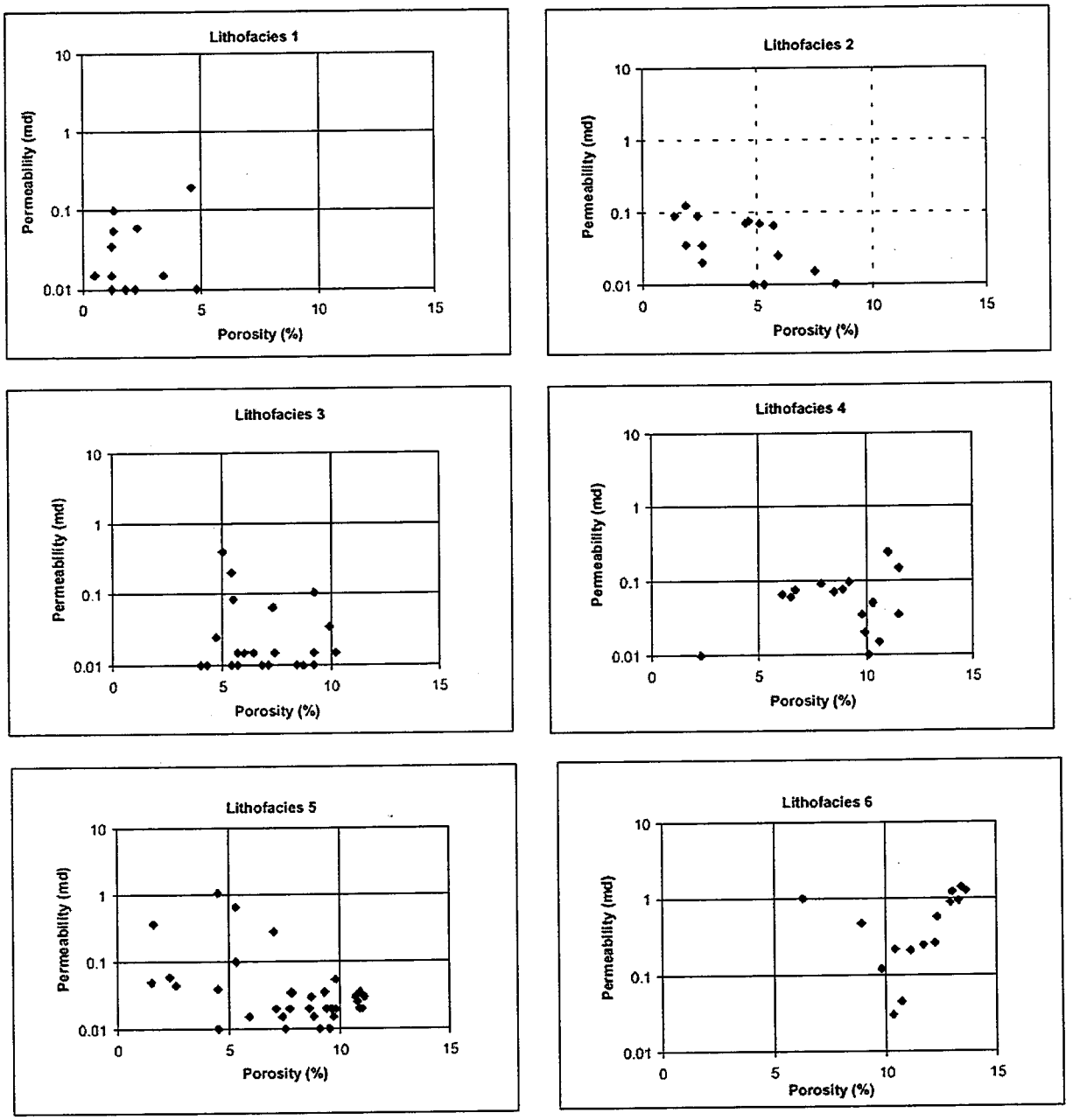

Fig. 1.10-4—Set of cross-plots showing the lithological control upon porosity and permeability for six large-scale lithofacies. Core E.T. O'Daniel 37.
(Data compiled from Reservoirs Inc. internal report)

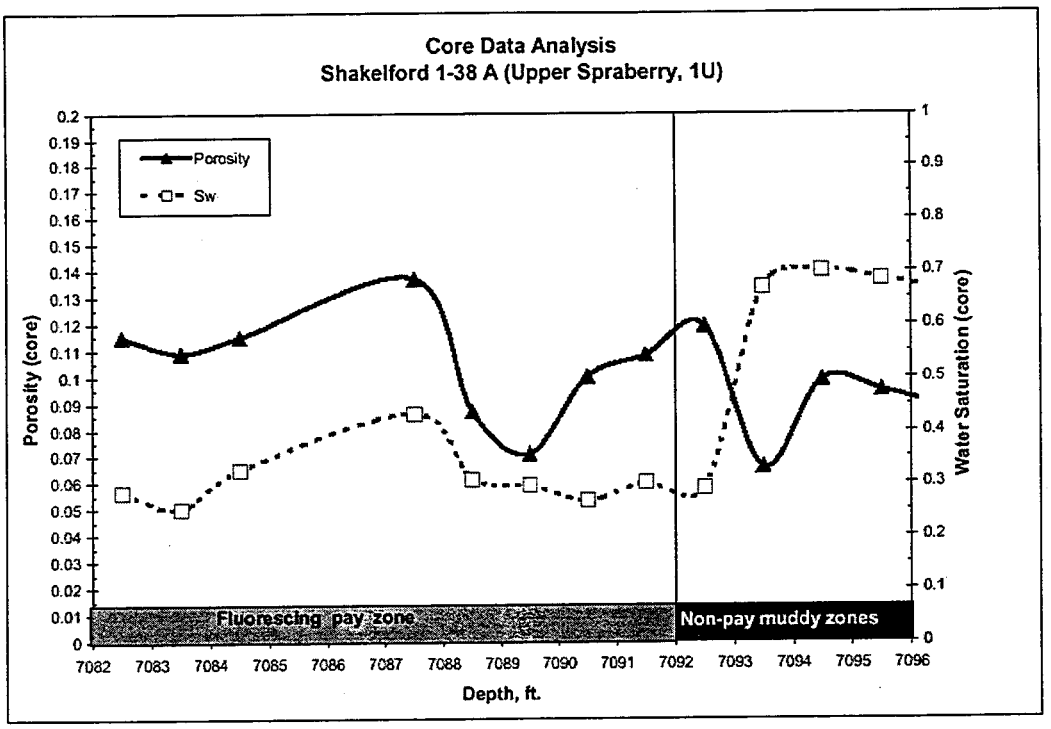

Fig. 1.10-5—Comparison of fluorescing pay zone and non-pay zones richer in clay content (Shackelford 1-38A)

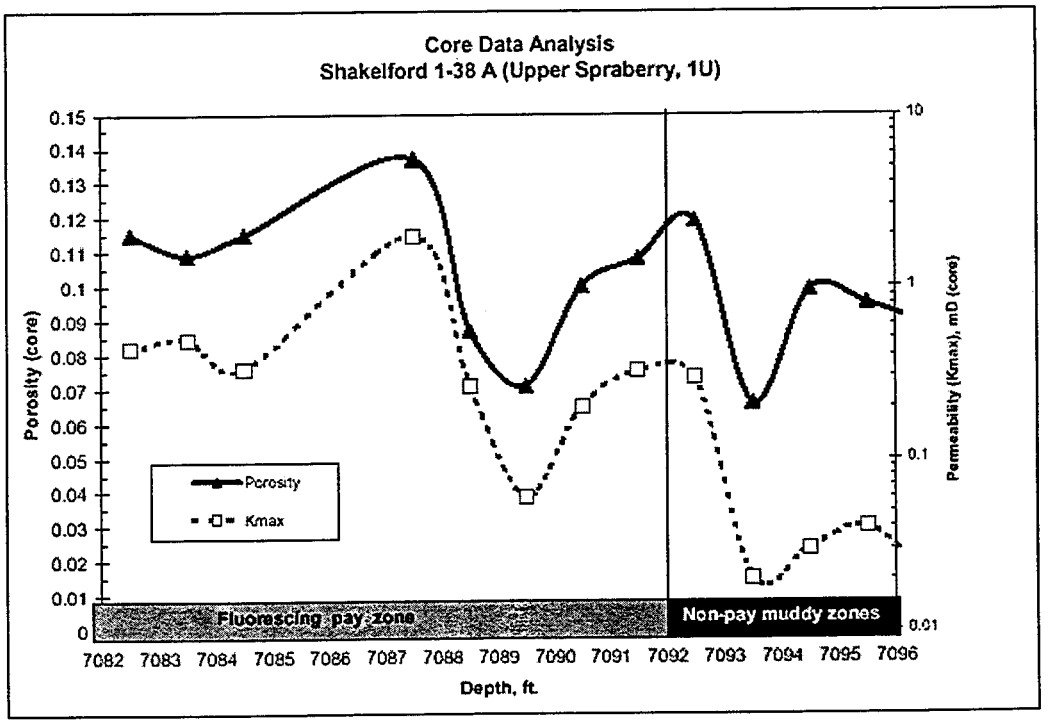

Fig. 1.10-6—Non-fluorescent zones are commonly lower quality reservoirs and non-reservoir rocks strongly affected by pore lining and pore bridging clays.

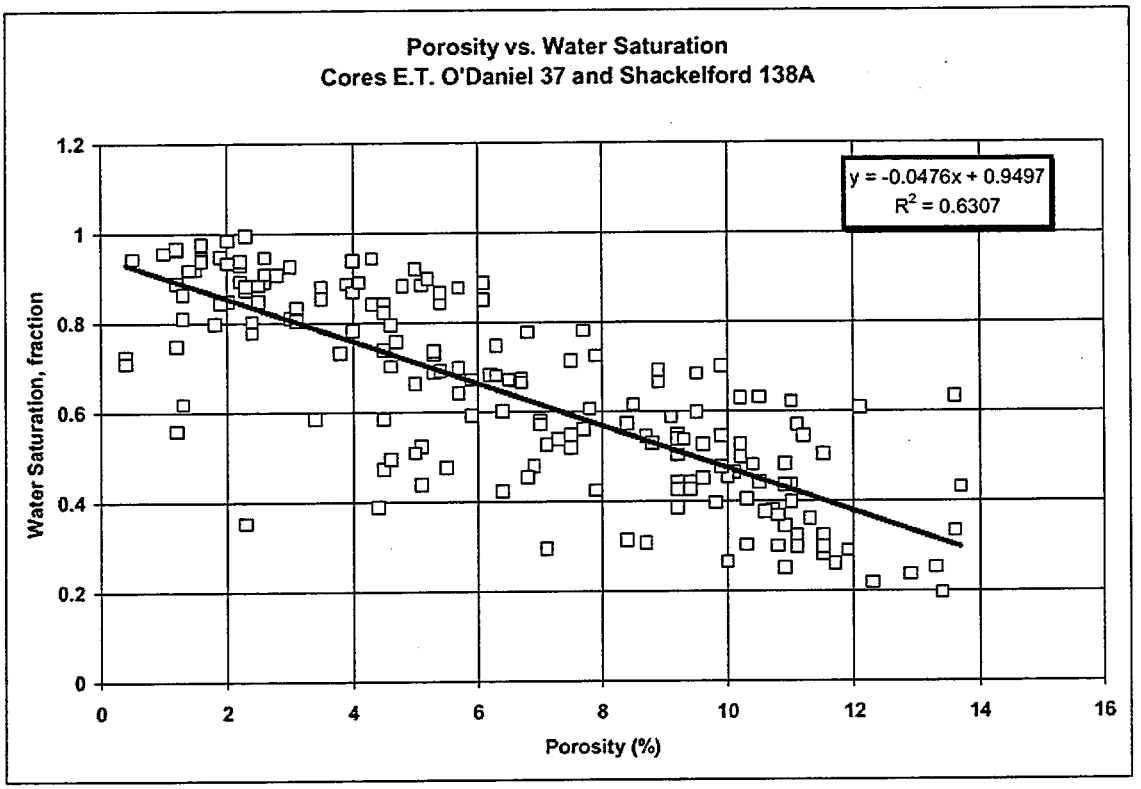

Fig. 1.10-7—Porosity vs. water saturation from the E.T. O'Daniel 37 and Shackelford 1-38A.

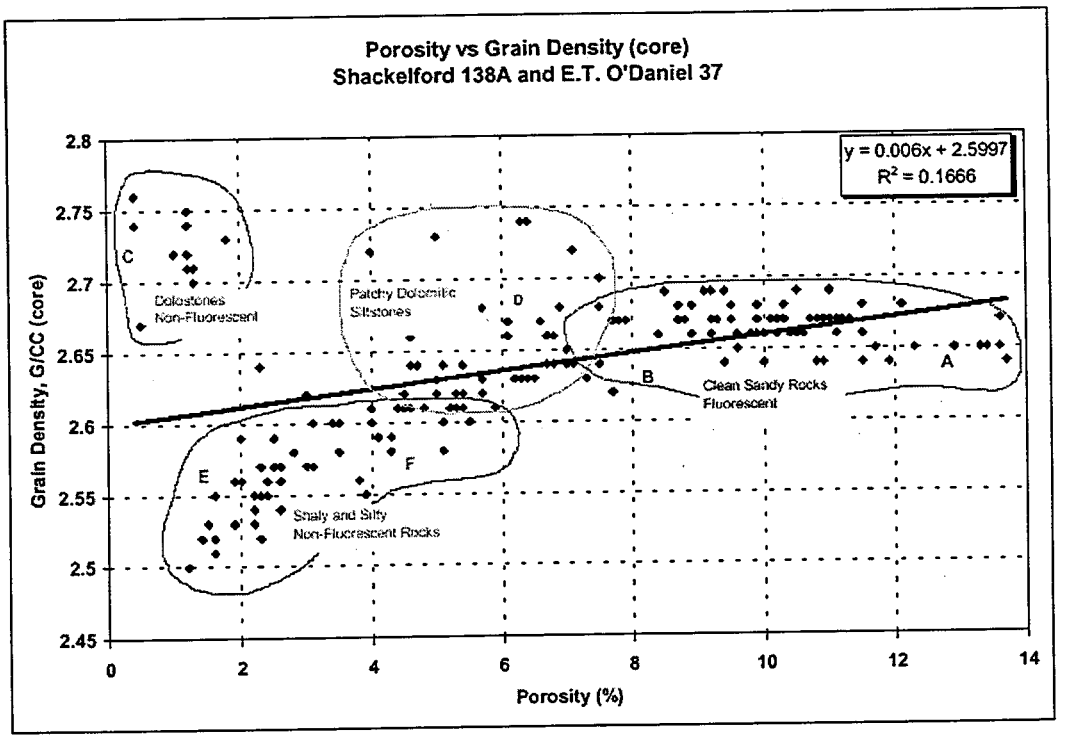

Fig. 1.10-8—Grain density vs. porosity cross-plot suggests strong lithological controls on reservoir quality.

Table 1.10-1— Summary of grain density data correlated with the major Rock Types.

Major lithologic types - small scale categories - upper Spraberry formation			
Main Group	Clean Sandy Rocks	Shaly and Silty Non-Fluorescent Rocks	Dolostones
Description	Mostly massive structure, low clay amounts, good porosity and pore throat radius, main mineral component is quartz. Include Rock Types "A" and "B"	Laminated, bioturbated, or convoluted, very low porosity, main mineral component are clays and quartz. Include Rock Types "E" and "F"	Mostly massive carbonate rich mudstones, poor porosity to total absence of pore space, main mineral components are dolomite mud, and quartz. Include Rock Type"C"
Fluorescent Capacity	Fluorescent	Non-Fluorescent	Non-Fluorescent
Grain Density	2.70 to 2.64 g/cc	2.60 to 2.51 g/cc	2.75 to 2.73 g/cc
Porosity (helium)	12% ("A") 9.95% ("B")	3.8% ("E") 7.3% ("F")	1.0%
Permeability (nitrogen, avg.)	0.64 md ("A") 0.12 md ("B")	0.056 md ("E") 0.034 md ("F")	0.048 md ("C")
Sw (from J-function)	35% ("A") 44% ("B")	75% ("E") 61% ("F")	79%

Table 1.10-2—Summary of helium, nitrogen and mercury injection data for plugs of different Rock Types that form the Spraberry Formation.

ROCK TYPE	POROSITY (%)	PERMEABILITY (md)	MODAL PORE THROAT RADIUS (μm)	DISPLACEMENT PRESSURE RANGE (psia)	AMOUNT OF SAMPLES
A	12	0.64	0.53	74.8-161	7
B	9.95	0.12	0.15	300-602	7
C	1.0	0.05	0.0035	11,943-4,980	2
D	8.0	0.18	0.045	987	1
E	3.8	0.06	0.0075	3,491	2
F	7.2	0.03	0.06	1,434	3

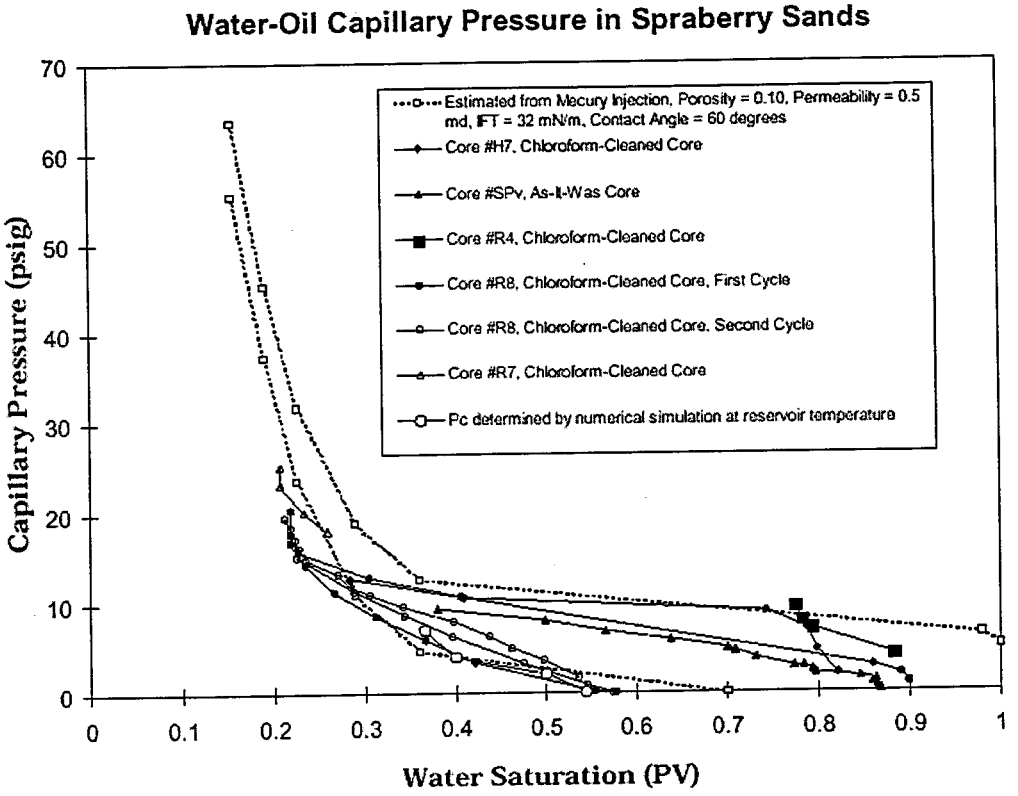

Fig. 1.10-9—Graph showing several curves for S_w and capillary pressure from imbibition experiments done with core plugs from various depths.

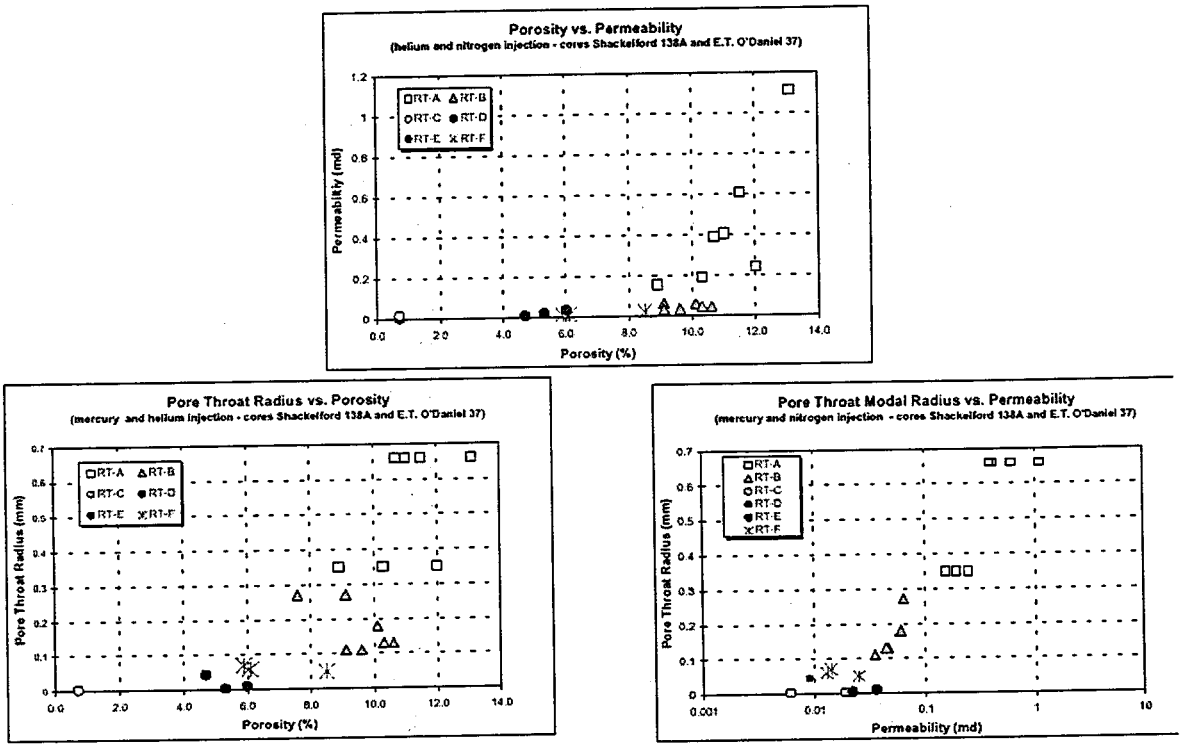

Fig. 1.10-10—Three cross-plots presenting mercury injection data correlated with porosity-permeability and pore throat radius. Cross-plots suggest that rock-fluid behavior is linked to lithological variability for the six Rock Types under study.

1.11 The Effects of Mechanical Stratigraphy on Fracture Variability and Reservoir Behavior

Abstract

Horizontal cores taken from two of the deep-marine, sandstone-siltstone reservoirs in the Spraberry Formation (Midland basin, west Texas) have documented two entirely different but related systems of vertical natural fractures. Each fracture system is capable of producing the long recognized, generally northeast-trending, strong permeability anisotropy in the Spraberry reservoirs. However, the two fracture systems offer potentially different degrees of permeability anisotropy, and different potentials for fluid deliverability. One fracture set consists of evenly spaced, well mineralized, northeast-striking fractures. The other fracture set, occurring in a similar lithology only 145 ft deeper in the section, consists of a poorly mineralized conjugate fracture pair, striking north-northeast and east-northeast. The geometry of these fracture sets suggests that the maximum compressive stress at the time of fracturing was in the horizontal plane. Subtle differences in the clay and quartz-overgrowth contents of the two layers produced important differences in the mechanical properties: although similar in appearance, the lower strata have a measured mechanical yield strength that is only half that of the upper layer. This caused the two layers to fracture differently under the same regional stress, with conjugate fractures forming in the weaker layer and extension fractures forming in the stronger layer. Such differences in the mechanical properties, caused by minor variations in the diagenetic and depositional histories of the strata, are probably widespread within the formation and may cause significant variations in the fracture system both across the basin and vertically within the formation.

Introduction

Background

Large reserves of oil were discovered in the Spraberry Formation in the Midland basin of West Texas in 1949. The area of Spraberry production (Fig. 1.11-1) comprises one of the largest plays in the world: it encompassed over 400,000 acres as early as 1953 (Elkins, 1953), and currently covers approximately 16,000,000 acres. Spraberry reservoirs occur at depths of approximately 7000-8000 ft, and consist of nearly 1000 ft of interbedded, fine-grained sandstones, coarse siltstones, and organic-rich shales. The main Spraberry reservoir units in the E.T. O'Daniel Unit described here are two 10-15 ft thick sandstones, designated the 1U and 5U reservoirs, within the sandier parts of the formation (Fig. 1.11-2).

The Spraberry strata were deposited in a deep-marine environment during the Leonardian stage of the Permian period. The formation is typically interpreted as the deposits of turbidity currents (e.g., Tyler and Gholsten, 1988; Guevara, 1988). The lateral continuity of small-scale bedding, sedimentary structures including sub-millimeter scale depositional-event laminae, and a high degree of size sorting, suggest that some of the Spraberry and related systems have resulted from eolian processes and dust-storm activity (Lorenz and Brooks, 1990; Kocurek and Kirkland, 1998).

Poor recovery efficiency has hampered the exploitation of the Spraberry resource. The play has had a cumulative production of 740 million barrels of oil to date, but oil recovery percentages and the daily production rates of individual wells are low. Daily production across the entire play currently averages 62,000 barrels of oil (and 25,000 cubic feet of gas), which is an average of only 7 BO/D from each of the 8,900 producing wells (Whigham, 1998). The estimated ultimate recovery of oil from the play is only 10-15% of the 6-10 billion barrels of oil originally in place. Spraberry reservoirs are underpressured, averaging only 800-900 psi. Porosities range from 6-15%, and restored-state matrix permeabilities are typically significantly less than 10 md.

All areas of the Spraberry Trend have indications of extensive natural fracturing despite their location in a stable, cratonic setting with minimal faulting and folding. Fracturing and a generally northeasterly-trending, fracture-controlled permeability anisotropy were recognized to be the dominant controls on reservoir plumbing early in the life of the field. However, the data necessary for three-dimensional characterization of this important fracture system, and for prediction of its variability and effects on the reservoir plumbing system, were lacking. The presence of fracturing was corroborated by early workers with limited amounts of core, including one deviated core (Wilkinson, 1953), although many of the fractures logged in those vertical cores would now be classified as coring-induced fractures. These induced fractures are parallel to many of the natural fractures and thus the proper inferences were made, albeit for the wrong reasons. Given the natural fracture spacing demonstrated by the horizontal cores as discussed below and the low probability of intersecting vertical natural fractures with vertical cores (e.g., Lorenz, 1992), only 10-20% of four-in diameter cores taken would be expected to intersect a natural fracture in any given Spraberry reservoir.

Much of the early recognition of the importance of fracturing was based on the results of well tests and notations of rapid interference or communication between adjacent wells (Elkins, 1953; Elkins and Skov, 1960, Schechter et al., 1996a,b.) However, these tests often give erratic results, and do not lead to a uniform picture of the fracture characteristics and their effects across the field. Horizontal permeability anisotropy due to fracturing was calculated to average 13:1 but locally ranged up to 1000:1 (Elkins and Skov, 1960). The early data indicated a generally northeast trend to this maximum horizontal reservoir permeability that has been assumed to be the average fracture strike, although the maximum-permeability axes observed locally sites ranges from N 36° E to N 76° E.

Early tracer tests, pulse tests, and pressure buildup and decline tests (Elkins and Skov, 1963; summarized by Putra, 1998) also suggested that the conductivity of the Spraberry fracture system is sensitive to changes in the in-situ stress. Decreased formation pressures during production may cause a partial or complete closing of fracture apertures, accounting in part for the observed rapid declines in production rates in fractured reservoirs. Likewise, increasing the local pressures during injection has caused a significant increase in local reservoir conductivity (see Lorenz, 1999). A sensitivity of the fractures to changes in stress has been confirmed by recent testing (Schechter et al., 1996a.) It is discussed further below.

Spraberry Project

A proposal to conduct experiments designed to improve recovery from Spraberry reservoirs was funded by the National Petroleum Technology Office of the U.S. Department of Energy in 1995. This was a cost-sharing proposal submitted to DOE's Class Reservoir program by 1) the Petroleum Recovery Research Center of the New Mexico Institute of Mining and Technology, and 2) Pioneer Natural Resources (then Parker and Parsley, Inc.). The goal of the project has been to assess the economic feasibility of CO_2 flooding in Spraberry reservoirs.

One of the initial tasks of the project was to perform a detailed characterization of the natural fractures and the in-situ stresses in Spraberry reservoirs through the use of oriented horizontal cores. Samples of the matrix rock would also be taken from these cores, to be tested in the laboratory for suitability for CO_2 flooding as the primary objective of the project (Schechter et al., 1996a). The horizontal cores are the first known cores from the Spraberry reservoirs in the Midland basin. This report discusses the characterization of the natural fractures, analyzes the fractures in the context of the geologic variables that produced them, and briefly outlines on their effects on the Spraberry reservoirs.

Nineteen horizontal core runs, recovering a total of 395 ft of core, were cut in 1996 from two horizontal sidetracks from the existing E.T. O'Daniel #28 well (McDonald et al., 1997). The principal reservoirs within the 1U and 5U intervals are ten-foot thick sandstone to siltstone units, which are separated vertically from each other at this site by 145 ft of interbedded sandstones, siltstones, and shales (Fig. 1.11-2). Although the two ten-foot thick units were targeted for coring, post-drilling analysis suggests that most of the cores were cut at near-horizontal angles across thinner, three- to four-ft thick sandy siltstones immediately above the two main-pay reservoirs. Several of the cores missed the reservoir units and were cut in the immediately over- and underlying shale beds, allowing for a comparison of fracture distributions with lithology. The cores were carefully pieced together immediately after recovery, and analyzed for natural fractures before being slabbed, plugged, or sampled (techniques described by Lorenz and Hill, 1992).

Natural Fracture Descriptions

An excellent data set characterizing the local subsurface Spraberry fracture system was obtained from the horizontal cores. Preliminary reports on the natural fracture data have been given in Lorenz (1997a, 1997b) and Malmanger et al. (1997), but the final data set and its in-depth analysis are presented here. The most surprising aspect of the data is the significant difference that exists, despite stratigraphic proximity and lithologic similarity, between the fracture populations of the two cored intervals (Table 1.11-1).

The upper cored interval contains forty-six mineralized, northeast-striking fractures (Set 1 fractures, having an average strike of 43°; Fig. 1.11-3). In contrast, the lower sandstone contains two poorly mineralized natural fracture sets, the strikes of neither set

corresponding to that of Set 1 (Fig. 1.11-3). The twenty-eight fractures of Set 2 strike generally north-northeast (average strike 32°), and twenty-nine fractures of Set 3 strike east-northeast (average 70° degrees).

Set 1 fractures have a low variability in strike (Fig. 1.11-3), and occur only in the sandstone and siltstone reservoir facies. These fractures are regularly and closely spaced; corrected spacing normal to fracture strike ranges from just under 1 ft to 5.8 ft and averages 3.2 ft (Figs. 1.11-4, 1.11-5). The fractures are partially to almost wholly mineralized with barite except for the four fractures nearest the base of the sandstone. The fractures of Sets 2 and 3 have irregular spacings (Fig. 1.11-6): spacings of fractures within Set 2 range from fractions of an inch to 4.5 ft (average 1.6 ft), whereas spacings of Set 3 fractures range from fractions of an inch up to 13 ft (average 3.8 ft). Analyzed together, Set 2 and Set 3 fractures in the lower core have a combined average spacing along a northeast trend (oblique to both fracture strikes) of about 2 ft. Although poorly mineralized, the surfaces of fracture sets 2 and 3 do not resemble the common surfaces of fresh, broken rock in the core. Moreover, minute euhedral crystals of quartz, dolomite, and barite are visible on the fracture surfaces under the microscope (Cather, 1997; Cather and Lorenz, 1998), proving that they are in fact natural.

Fractures of Set 2 occur only within the very fine-grained sandstones to coarse siltstones of the lower reservoir, and Set 1 fractures occur only within this facies in the upper reservoir. Set 3 fractures are more widespread, however. They occur predominantly in the sandstone-siltstone facies of the lower reservoir but are also present within higher, finer-grained zone of the upper sandstone. They are also widely spaced (about 10 ft) but present within the black shales that immediately overlie both upper and lower reservoirs. In contrast, no natural fractures are present within the 80 ft of core inadvertently taken from the black shales immediately below these two reservoirs.

The north-northeast trending fractures of Set 2 are distinct from fractures of the other two sets in several important ways. First, the average spacing of the Set 2 fractures is about half that of the two other fracture sets. Second, these fractures commonly have an irregular, stepped, surface morphology with an en echelon character. This stepping character suggests that these fractures formed by the coalescence of smaller extension fractures within an incipient, right-lateral, Riedel-type shear zone (Petit, 1987; Lorenz, 1997c,d). In contrast, fracture surfaces from the other two sets are typically planar, suggesting an origin in extension.

Although the data reported here from the horizontal Spraberry cores have documented an unexpected variability in the Spraberry natural-fracture system, they probably have not defined the total range of that variability. Moreover, these data should not be extrapolated uniformly as a natural-fracture template to the Spraberry strata in all other parts of the basin. Rather, the stress conditions and mechanical properties that produced the observed variability in fractures should be considered, as detailed below, when predicting local Spraberry fracture characteristics.

Possible Origins for Three Fracture Sets

The presence of significantly different fracture populations in the two cored Spraberry reservoirs in the E.T. O'Daniel #28 well, within this relatively non-structural province of the Midland basin (average dips less than 2°), begs explanation. Hole geometries suggest that both of the cored sandstones are between three and four ft thick, thus differences in bed thickness should not have caused significantly different fracture characteristics. The two most likely scenarios by which three such fracture sets may form are: Three fracture sets may result from three separate, sequential fracturing events, or Three fracture sets may form contemporaneously as parts of an integrated fracture system.

Although the distinctive characteristics of the three natural fracture sets initially favored the first option, the second option is the simplest and, by Occam's razor, the most likely. It is supported by the most plausible interpretations of the data, as discussed below. However, the first sequence cannot be entirely discounted without further comment.

Option 1 – Three Separate Fracturing Events

Each of the fracture sets has its own characteristic patterns of spacing (Fig. 1.11-6), distribution of fracture strikes (Fig. 1.11-3), fracture distribution with respect to lithology (Figs. 1.11-4, 1.11-5), and mineralization. Such variability initially suggested that each set formed in response to a different stress event and was mineralized during separate diagenetic events. The presence of better-developed mineralization in the northeast-striking fractures of Set 1 might even suggest a relative age relationship, i.e., that it formed and was mineralized prior to the formation of either of the other two unmineralized sets, accounting for their lack of mineralization.

However, reconstructions of the tectonic history of the basin (e.g., Ewing, 1991; Winfree, 1994, 1995) suggest that there have been very few post-depositional tectonic events likely to have produced stresses capable of fracturing the Spraberry strata. The only significant post-Permian tectonic events to affect the area have been the Laramide orogeny (Late Cretaceous to Eocene), followed by or possibly contemporaneous with gentle uplift and tilting of the strata and broad folding over basement faults.

Thus it is difficult to conceive of three or even of two separate, significant, structural-deformation events to account for three separate fracturing events. In fact, an even more convolute sequence would be required by the measurements showing that the maximum horizontal compressive stress now trends parallel to the fractures of Set 1 (Holcomb, 1997). This observation mandates that if the Set 1 fractures in fact represent a separate and oldest event, then an improbable, fourth, and final tectonic event is necessary to bring the maximum stress back again into coincidental alignment with these hypothetically oldest fractures. This would seem to be an overly contrived sequence of four stress events for this structurally simple province, and it is not supported by the tectonic history of the basin.

Option 2 – Conjugate Fractures with Related Extension Fractures

The preferred interpretation of the three fracture sets is suggested by their relative orientations. The geometry of the fractures is close to that of an ideal conjugate fracture pair (Sets 2 and 3) with an associated extension-fracture set (Set 1), the strike of the latter bisecting the acute conjugate angle (Fig. 1.11-7). The stepped surfaces of the fractures of Set 2 show the proper indications of incipient right-lateral shear and therefore support this interpretation, although in a perfect case complementary left-lateral shear indications would be found on the associated fractures of Set 3.

The formation of extension fractures in one bed contemporaneously with conjugate fractures in the other would require that there were significant differences in either the local effective stresses or in the mechanical properties of the two beds at the time of fracturing. The lithologic similarity and stratigraphic proximity of the two beds argue conclusively against significant local differences in stress magnitudes, in the stress differential, or in the formation pore pressures, thus local stress differences are not considered further here as a potential cause for the observed fracture variability. Rather, laboratory measurements suggest that a difference in the mechanical properties of the beds was the controlling factor.

Mechanical Properties

Strata of the two sandstone-siltstone reservoir units are similar in appearance and have similar, low, average Poisson's ratios (0.11). The elastic moduli of these strata are also nearly equal (about 2.4×10^4 MPa) (Cherney, 1998). However, the mechanical yield strength of the upper unit as measured by triaxial tests is, on average, nearly twice that of the lower unit (262.5 MPa and 150.2 MPa respectively; Fig. 1.11-8).

This important mechanical difference may result from subtle differences in the clay and quartz contents of the two units. Petrographic examinations (Reservoirs Inc, 1997; Saleta, 1998) show that the average total clay content of the lower unit is 10%, whereas it is only about half that (6%) in the stronger, upper unit. Moreover, the type of clay apparently varies between the units: the lower unit has more common diffuse clay laminae and "an unusually high amount of detrital clay" (Reservoirs Inc, 1997). Probably because of this difference in clay content and distribution, euhedral quartz overgrowths on the component sand grains are better developed in the strong upper unit where they comprise an average of 7% of the rock volume, compared to only 3% of the rock volume in the lower unit.

Low clay contents and better cementation by quartz overgrowths would both tend to strengthen a rock mechanically. Theoretical considerations (e.g., Griggs and Handin, 1960; Lorenz, 1997c) and empirical observations of other formations (e.g., Lorenz, 1997d) suggest that weaker rock may fail in conjugate shear under the same stress conditions that create extension fractures in stronger rock. Assuming that the rock properties at the time of fracturing were similar to those measured presently, this offers a plausible basis for the presence of different fracture sets in the two units since the rock of the lower unit has only half the strength of the upper unit. The assumption of similar properties since fracturing is tenable given that the rocks were deeply buried and lithified

at the time of fracturing, and considering the present depth of burial and the 200 million year hiatus between deposition and the inferred time of fracturing.

The measured yield strengths of the Spraberry samples are high, and fracturing such rock would require higher stresses than are generated in most tectonic settings. However, the strengths of these rocks would have been significantly less if formation pressures were high during fracturing, allowing fracturing under reduced differential stress conditions (see Lorenz et al., 1991). Despite the significantly underpressured nature of the current Spraberry reservoir system, it is very likely that the reservoir was overpressured at some point during its geologic history. Spraberry shales have relatively high total organic carbon contents (up to 5%; Dutton, 1980), and most of the formation has passed through the oil window. The maturation of kerogen to oil and of oil to gas produces significant volume increases that may result in significantly increased formation pore pressures (e.g., Barker, 1990; Meissner, 1980, 1981). Thus the most likely time of fracturing of the Spraberry Formation was during the coincidence of high pore pressures and regional tectonic activity, when it passed through the oil window during Laramide time (Winfree, 1995).

Mechanical property variations may also explain the observed absence of fractures in strata underlying the reservoirs. The upper zones of the shale beds underlying the reservoirs are the most clay-rich and therefore likely to be the most ductile zones in the shales, and devoid of fractures. In contrast, the widely spaced fractures in the lower zones of shale beds immediately overlying the reservoirs are likely to have a certain silt content. The distribution and nature of the shale mechanical properties is still under study.

Discussion

Some fracture characteristics that initially seemed to support the scenario requiring three sequential fracture events can be reinterpreted, with deeper insight, to support the conjugates-with-bisector model.

Fracture Spacing

The three cored Spraberry fracture sets have three unique spacing distributions (Fig. 1.11-6). This initially suggested that each set formed as a separate system under a different stress condition. However, such differences in spacing distribution can also be attributed to different modes of formation (i.e., extension vs. shear), to the common differential development of the sets of a shear-fracture pair, and to the variable numbers of fractures of each type required to accommodate equivalent amounts of strain.

The reported spacing distributions of most fracture sets (e.g., Lorenz and Laubach, 1994; Hanks et al., 1997; Lorenz and Hill, 1994) are log-normal, i.e., with numerous close spacings and significantly fewer wide spacings. This common log-normal pattern contrasts strongly with the regular, nearly Gaussian (normal) distribution of the spacings of Set 1 fractures, and, to a lesser extent, with the modified log-normal patterns of the Set 2 and Set 3 fracture spacings.

A Gaussian distribution of extension fracture spacings has been suggested to indicate that a fracture set is exceptionally well developed or "saturated" (Wu et al., 1994; Wu and Pollard, 1995). The fractures of such a population are typically long relative to their spacing. The production and interference characteristics of the Spraberry reservoirs are consistent with a well-developed and inter-connected system of long fractures, and therefore the Set 1 fractures are inferred to be saturated.
We are unaware of published distributions of shear-fracture spacings for comparison, although Wu (personal communication, 7/97) suggests that they might be expected to follow the same pattern of development (i.e., log-normal spacings early in fracture development history, becoming Gaussian with continued development and maturation.) If so, then the log-normal spacing distributions of fracture sets 2 and 3 suggest fracture sets that are less mature than fracture set 1. However, combined, the two less-mature fracture sets of the conjugate pair appear to have accommodated an amount of strain equivalent to that accommodated by the single, well developed set of Set 1 extension fractures. The average aperture of the Set 1 extension fractures and the average offset of the Set 2 and 3 conjugate fractures are estimated to be 0.5 mm, and the average spacing of Set 2 and Set 3 fractures (combined) is about two feet. Back-of-the-envelope calculations considering the geometries of these fractures suggest that both the extension and the conjugate fracture systems accommodated about 0.05% horizontal extension in the southeast-northwest direction. This supports an interpretation of the concurrent formation of different fracture types having different characteristics under the same stress system.

Shear

The shear offset across the fractures of many conjugate systems is minimal and therefore difficult to discern. However, the subtle, consistent, Riedel-type shear steps on Set 2 fracture surfaces are convincing evidence that incipient shear did in fact occur on these fractures.

The absence of obvious shear indicators on the complementary Set 3 fractures is problematic but not insurmountable. One member of a fracture pair is better developed than the other in many conjugate systems, although the reasons for this are usually obscure. We infer that local structures may have played an important role in the differential fracture development observed in the Spraberry reservoirs. Winfree (1994, 1995) has suggested that many of the flexures within the strata of the Permian basin formed contemporaneously with fracturing of the Spraberry in Laramide time. Extension across the east-west axis of the small nose at the O'Daniel site (Fig. 1.11-9) during folding would have superimposed a small amount of north-south extension on the developing fracture systems, leading to a hybrid shear-extension fracturing in the Set 3 fracture orientation. Moreover, the smaller average angle between the sheared Set 2 fractures and the inferred northeast-trending maximum horizontal compressive stress (compared to the angle between Set 3 fractures and the compressive stress) means that Set 2 fractures would have been more readily sheared than Set 3 fractures.

Mineralization

The differences in fracture mineralization that initially suggested sequential fracture development may actually be the result of differences in either the fluid flow capacities of the two fracture systems or of the differences in apertures of the three sets. Interconnected conjugate fractures should have had better conductivity and interconnectedness within the reservoirs, allowing for easy mineralization and/or its dissolution. A system of poorly-connected, sub-parallel extension fractures, on the other hand, may have become a relatively closed system early on during mineralization, minimizing subsequent fluid flow. Shear fractures also accommodate strain via slip on an incline with no aperture required, whereas extension fractures accommodate strain via the opening of void-space apertures along the fracture planes. Therefore, shear fractures, especially incipient shears, would typically have less aperture within which to deposit large volumes of mineralization such as are found in Set 1extension-fractures.

Stress

Detailed circumferential velocity-anisotropy measurements on the core indicate a northeast-trending present-day, in situ, maximum horizontal stress (Holcomb, 1997). This trend is parallel to the Set 1 fracture strikes and bisects the acute angle between Sets 2 and 3, as would be expected for stresses capable of concurrently forming both the Set 1 extension fractures and the Set 2-3 conjugate fractures (Fig. 1.11-7). This stress orientation provides strong support for an origin of the three fracture sets as an integrated system.

Microfracturing and Cathodoluminescence

Microfractures visible only under the microscope and illuminated by cathodoluminescence (CL) have been suggested to be predictors for larger-scale fracture trends (Laubach, 1997). Three samples of sandstones from the upper zone were analyzed for microfracturing using CL techniques. The results (BEG, 1997) do not predict the three fracture sets described above.

One CL sample, located midway between two mineralized fractures spaced 5.5 ft apart and having strikes of 40° and 45°, is reported to have a vector mean microfracture strike measured by cathodoluminescence of 25° degrees.
Two CL analyses from the second sample, located immediately adjacent to a fracture with a 45° strike, have reported vector mean microfracture strikes of 19° and 347°.
Three CL analyses of the third sample, located exactly midway between two fractures with 80° and 40° strikes and spaced 4.4 ft apart, have reported vector mean microfracture strikes of 25°, 42°, and 32°.

Most of the fractures from the interval sampled for cathodoluminescence are extension fractures, with an average strike of 43°. However, the reported average of 25° +_10° for all analyzed cathodoluminescence microfractures would appear to be best aligned with the average 32° strike of the Set 2 shear fractures in the other sandstone. Cathodoluminecence results do not reflect the average 70° fracture set (Set 3) that is also common in the other zone or the 80° extension fracture present 2.2 ft from the third sample. There is little or no field evidence (from vertical cores, from horizontal cores, or

from well tests,) for the 347° fracture trend inferred from cathodoluminescence, and this fracture trend does not affect the Spraberry reservoirs if it is present.

Implications for Regional Geology

Northeastward-directed Laramide compressive stresses have been suggested to be the source of much if not all of the post-Permian structural deformation in this basin (e.g., Hills, 1970; Price and Henry, 1985; Calhoun and Webster, 1983; Erdlac, 1993, Winfree, 1994, 1995). The closest of the Laramide thrust systems is only 300-350 km distant, located south of the El Paso region (Drewes, 1991). Its trend is northwest-southeast, consistent with a northeast-southwest directed compressive stress in the forelands as inferred from the geometries of the Spraberry fractures, and as measured in situ today.

Interestingly, the interpretation of fracture sets 2 and 3 as a system of conjugate fractures with a northeast-striking bisector mandates the unconventional interpretation that, at the time of fracturing, the vertical, overburden stress was not the maximum compressive stress. Rather, a conjugate fracture pair with this geometry (i.e., with a vertically oriented axis of fracture-plane intersection), records a stress system oriented such that the maximum compressive stress was northeast-southwest in the horizontal plane, the minimum stress was southeast-northwest, and the intermediate stress was vertical.

The interpretation that the vertical, overburden stress in the Permian basin was only the intermediate stress at the time of fracturing suggests that the horizontal stress magnitudes, and by implication the stress anisotropies, were large during Laramide tectonic events. A configuration where the maximum stress is horizontal rather than vertical is not a commonly recognized condition in basins distant from obvious sources of significant horizontal stress. However, Craddock and van der Pluijm (1989) have suggested that significant differential stresses can be derived from a thrust system and imparted to strata up to a thousand kilometers beyond a thrust front by measuring calcite twin lamellae in strata in front of the Appalachian-Ouachita thrust-belt. Conjugate shear fractures with similar geometries that indicate similar stress orientations have been documented elsewhere (e.g., in the Tertiary strata of the Piceance basin of Colorado; Lorenz, 1997d).

Although the present-day stresses are still aligned with this trend, the stress magnitudes are low. Differential velocity (P and S waves) and strain measurements made on samples from the horizontal and nearby vertical cores (Holcomb, 1997) suggest that there is presently only a 1-3% difference in the velocity anisotropy in these rocks, implying that the horizontal stress magnitudes in Spraberry reservoirs are similarly low. Measurements of stress in other formations of the basin (Nolen-Hoeksmema et al., 1992; Avasthi et al., 1991) are generally consistent with the northeast-trending maximum stress orientation measured at the O'Daniel site, although they suggest that a somewhat larger stress differential exists in other parts of the basin. These authors also report that the in-situ stresses may locally be reoriented over structures. If the above stress/fracture model is valid, then the present day stress field is a weaker, relaxed remnant of the fracturing stresses. Reduction of pore pressures over geologic time would have contributed to this diminution of the total stress magnitudes.

Similar relaxed stresses have been documented elsewhere. One example is the Mesaverde strata in the Piceance basin of Colorado. A low-magnitude, remnant, stress anisotropy has been measured within the lenticular sandstones in this formation. The remnant status of that stress is proven by measurements of stresses in the enclosing shales showing that they have completely relaxed to the overburden stress state, and are thus not transmitting an active stress to the sandstones to produce the measured anisotropy (Lorenz and Finley, 1991.)

Implications for Reservoirs

The natural fracture system in the Spraberry reservoirs creates a permeability anisotropy of up to 1000:1 despite the absence of a strong stress anisotropy. The permeability anisotropy is typically but not universally aligned along a northeast-southwest trend. This much has been known for some time. However, data from the horizontal, E.T. O'Daniel #28 cores highlight an unsettling variability in fracture characteristics, a variability that may be present within reservoirs despite seemingly homogeneous lithologies and an absence of major structure. Well tests and tracer tests in Spraberry reservoirs commonly give erratic results when measuring the magnitude and orientation of the horizontal permeability anisotropy in the formation, indicating that horizontal permeability ratios and their orientations are variable with location. As discussed below, this study suggests that both observations may be a function of subtle differences in lithology, which in turn control mechanical properties such that different types of fracture systems formed. Anisotropy ratios and orientations also change with time, as the in situ stresses are altered by production or injection and cause different fracture sets to open or close. Finally, variability in the production potential of different zones may be related to the different interconnectivity and conductivity of the different fracture systems. Such non-uniformity is explained by low horizontal stress differentials in combination with multiple fracture orientations.

The ratio of maximum to minimum horizontal permeability should be higher in zones that contain only the northeast-southwest (Set 1) fracture type. Reservoirs with weaker strata and the resulting conjugate fractures should have a less pronounced permeability anisotropy. Production potential from a conjugate fracture system should be greater, both because of the better fracture interconnection and because of the insignificant mineralization. Moreover, the sensitivity to changes in the in situ stresses during production should be different for the two fracture systems: increases in confining stress should close the apertures of extension fractures, but should initiate slip on shear fractures (see Lorenz, 1997c). Unfortunately, the lateral leg of the E.T. O'Daniel #28 well through the lower horizon containing conjugate fractures was lost before a comparison could be made between the production capabilities of the two fracture systems.

The horizontal permeability ratios and the trends of maximum permeability are also variable in this system. Extension fractures will provide little enhancement over matrix permeability in the transverse direction and will thus produce large anisotropy ratios. Conjugate fractures create drainage areas with less ellipticity. One leg of a conjugate

fracture pair may be better developed or may be preferentially held open by the in-situ stresses, creating unexpected deviations to the maximum permeability trend. Although the maximum permeability orientation within the Spraberry Trend is often close to N45°E, many operators have noted preferential east-west movement of fluids. The Humble pulse test from the 1960s in the Midkiff Unit (see Putra, 1998) illustrates this variability. A test in one section of the Midkiff Unit confirmed the known northeast-southwest directional permeability, but a pulse test conducted in less than one mile away yielded a faster pulse transmissibility in the east-west direction.

Anisotropy orientations and ratios in the Spraberry may change as a function of changes in stress. Hydraulic fractures tend to follow natural fractures below a threshold injection pressure, but are less constrained above this threshold because the low stress anisotropy is easily overcome by local injection pressures. Similarly, injections of tracers at relatively low pressures are capable of opening up communication pathways that are not aligned with the primary northeast-southwest trend. Humble's pulse test in the Midkiff Unit can also be used to illustrate this: water was injected into a pilot pattern during this test over a period of six months, and communication was established between wells along the northeast-southwest trend early in the test. No communication was apparent initially between the injection wells and production wells aligned perpendicular to this trend. Once injection water was recovered from wells along the off-trend direction, however, the volume of water recovered from these wells gradually increased as injection proceeded. A secondary, stress-sensitive fracture network was probably opened and exploited by the increased reservoir pressures created by continued water injection, decreasing the horizontal permeability anisotropy of the system. This "breathing" effect that is dependent on reservoir pressure is probably a large part of the reason for the wide variability in measured permeability anisotropy ratios and directions throughout the field.

Further evidence of stress-sensitive fractures was observed in 1993 during an 80-acre water-injection pilot in Upper Spraberry reservoirs, also in the Midkiff Unit (Schechter et al., 1996a). Production wells at this site, again oriented along the trend of the northeast-southwest fracture trend from an injection well, were monitored after initiation of water injection. No injected water was observed in the nearest offset well for nearly 300 days. However, a radioactive tracer injected once communication between the wells had been established reached the same production well within 24 hours. This change in conductivity of the reservoir system is a clear indication that permeability of the fracture system had increased as the local pressure increased.

The stresses and related resistance of the Spraberry Formation to fracturing are so low that mud weights and/or the piston action of tripping a core barrel into the hole are commonly sufficient to cause inadvertent hydraulic fracturing of the formation below the bit. This results in Spraberry cores that are intensely petal-fractured or that are split along one or more parallel planes along the core axis. Many such coring-induced fractures merely extend the existing plane of a natural fracture, obscuring the distinction between natural and induced fractures. This below-the-bit, inadvertent hydraulic fracturing is undoubtedly common but undocumented in uncored holes as well. So-called "vacuum fracs" are also a typical stimulation practice in the field: the formation is broken down

and stimulated by a hydraulic fracture created merely by the weight of a column of fluid in a wellbore.

Summary

Horizontal cores taken from two different levels of the Spraberry Formation show that significantly different systems of natural fractures are present in the two otherwise similar, closely adjacent sandstone-siltstone reservoirs. One fracture set consists of evenly spaced, mineralized, vertical, northeast-striking fractures. The other fracture set, occurring in strata only 145 feet deeper, consists of a poorly mineralized, vertical, conjugate pair, the members of which strike north-northeast and east-northeast. Both fracture systems formed during the same Laramide tectonic event, when the regional compressive stress was directed northeast-southwest and pore pressures in the formation were probably high. The conjugate geometry indicates that the maximum compressive stress was in the horizontal plane at the time of fracturing. Differences in the petrographic makeup of the two layers, primarily their clay content and the volume of quartz overgrowths, caused subtle but important differences in the mechanical properties, specifically the yield strengths, of the rocks. Conjugate fractures formed in the weaker strata at the same time that extension fractures formed in the stronger layer. This variability may be predictable to the extent that the subtleties in local diagenetic and depositional histories can be accurately reconstructed and integrated with subtle structural variations. The minimal differential between the present-day in situ horizontal stresses, as well as the low in-situ stress magnitudes, provide poor constraints on the azimuths of injections into the formation, and off-trend fracture permeability may be opened up at higher injection pressures.

Fracture characteristics may vary significantly between different Spraberry reservoir units: an understanding of the basis for this variability should lead to a rationale for designing and positioning development wells. The observed system of extension fractures in the upper zone with conjugate fractures in the lower Spraberry reservoir unit should *not* be extrapolated universally to the 1U and 5U Spraberry reservoirs across the Midland basin. Predictions of fracture characteristics will be most successful where subtle changes in depositional environments and the related petrologic characteristics can be delineated, and where good control exists on the structural configuration of the basin.

References

Avasthi, J.M., R.C. Nolen-Hoeksema, and A.W.M. Rabaa, 1991, In-situ stress evaluation in the McElroy field, West Texas: *SPEFE*, v. 6, p. 301-309.

Bureau of Economic Geology, 1988, Reservoir Characterization Research Laboratory, Sixth Quarterly Report, 58 p.

Bureau of Economic Geology, 1997, Determination of natural fracture orientation using scanned CL; Natural fracture analysis project progress report NM-004, March 14, 1997; 7 p., 2 figs.

Barker, Colin, 1990, Calculated volume and pressure changes during the thermal cracking of oil to gas in reservoirs: *AAPG Bull.*, v. 74, p. 1254-1261.

Calhoun, G.C., and R.E. Webster, 1983, Surface and subsurface expression of the Devils River Uplift, Kinney and Val Verde counties, Texas, *in* Kettenbrink, E.C., Jr. (ed.), Structure and stratigraphy of the Val Verde basin-Devils River Uplift, Texas: West Texas Geological Society Publication 83-77, p. 101-118.

Cather, Martha, 1997, Spraberry fracture diagenesis: The microscopic view of fractures; Third Naturally Fractured Reservoir Symposium, Petroleum Recovery Research Center, New Mexico Institute of Mining and Technology, Socorro, NM, October 28, 1997, (unpaged).

Cather, Martha, and J.C. Lorenz, Characterization of natural fractures in Spraberry trend area reservoirs, Permian basin, West Texas (abstract); AAPG annual convention, Salt Lake City, 17-28 May, 1998 (unpaged).

Cherney, J.L., 1998, Investigation of anisotropy from Spraberry horizontal cores: Fourth Annual Naturally Fractured Reservoir Symposium, Petroleum Recovery Research Center, New Mexico Institute of Mining and Technology, Socorro, NM, October 27, 1998 (unpaged).

Craddock, J.P., and B.A. van der Pluijm, 1989, Late Paleozoic deformation of the cratonic carbonate cover of eastern North America: Geology, v. 17, p. 416-419.

Drewes, Harald, 1991, Description and development of the Cordilleran Orogenic Belt in the southwestern United States and northern Mexico; US Geological Survey Professional Paper 1512, 87 p.

Dutton, S.P., 1980, Petroleum source rock potential and thermal maturity, Palo Duro basin, Texas: Bureau of Economic Geology Geological Circular 80-10, 32p.

Elkins, L. F., 1953, Reservoir performance and well spacing, Spraberry trend area field of West Texas: *Trans., AIME*, v. 198, p. 177-196.

Elkins, L.F., and A.M. Skov, 1960, Determination of fracture orientation from pressure interference: *Trans., AIME*, v. 219, p. 301-304.

Elkins, L.F., and A.M. Skov, 1963, Cyclic water flooding in the Spraberry utilizes "end effects" to increase oil production rate: *JPT*, v. 15, p. 877-884.

Erdlac, R.J., 1993, Small-scale structures in the Guadalupe Mountains region: Implication for Laramide stress trends in the Permian basin: New Mexico Geological Society Guidebook, 44th Field Conference, Carlsbad region, New Mexico and West Texas: p. 167-174.

Ewing, T.E., 1991, The tectonic framework of Texas; text to accompany the tectonic map of Texas: University of Texas at Austin, Bureau of Economic Geology, 36 p.

Griggs, D., and J. Handin, 1960, Observations on fracture and a hypothesis of earthquakes: Geological Society of America Memoir 79, p. 347-364.

Guevara, E.H., 1988, Geological characterization of Permian submarine fan reservoirs of the Driver waterflood unit, Spraberry Trend, Midland basin, Texas: Bureau of Economic Geology Report of Investigations No. 172, 44 p.

Hanks, C.L., Lorenz, J.C., Teufel, L.W., and Krumhardt, A.P., 1997, Lithologic and structural controls on natural fracture distribution and behavior within the Lisburne Group, northeastern Brooks Range and North Slope subsurface, Alaska: *AAPG Bull.*, v. 81, p. 1700-1720.

Hills, J.M., 1970, Late Paleozoic structural directions in southern Permian basin, West Texas and southeastern New Mexico: *AAPG Bull.*, v. 54, p. 1809-1827.

Holcomb, D.J., 1997, In situ stress from Core (E.T. O'Daniel #28): Third Naturally Fractured Reservoir Symposium, October 28, 1997, New Mexico Petroleum Recovery Research Center, New Mexico Institute of Mining and Technology, Socorro, NM, (unpaginated).

Kocurek, G., and B.L. Kirkland, 1998, Getting to the source: Aeolian influx to the Permian Delaware basin region: Sedimentary Geology, v. 117, p. 143-149.

Laubach, S.E., 1997, A method to detect natural fracture strike in sandstones: *AAPG Bull.*, v. 81, p.

Lorenz, J.C., and L.L. Brooks, 1990, Suspension- and current-deposit reservoirs in the Delaware basin: Trends and cycles in siltstones of the Permian Bone Spring Limestone (abstract), *AAPG Bull.*, v. 74, p. 708.

Lorenz, J.C., and R.E. Hill, 1992, Measurement and analysis of fractures in core; *in*, Geologic studies relevant to horizontal drilling: Examples from western North

America, Schmoker, J.W., E.B. Coalson, and C.A. Brown (eds.): Rocky Mountain Association of Geologists, p. 47-59.

Lorenz, J.C., and R.E. Hill, 1994, Subsurface fracture spacing: Comparison of inferences from slant/horizontal and vertical cores: *SPEFE*, v. 9, p. 66-72.

Lorenz, J.C., N.R. Warpinski, and L.W. Teufel, 1991, Regional fractures I: A mechanism for the formation of regional fractures at depth in flat-lying reservoirs *AAPG Bull.*, v. 75, p. 1714-1737.

Lorenz, J.C., and S.J. Finley, 1991, Regional Fractures II: Fracturing of Mesaverde reservoirs in the Piceance basin, Colorado: *AAPG Bull*, v. 75, p. 1738-1757.

Lorenz, J.C., and S.E. Laubach, 1994, Description and interpretation of natural fracture patterns in sandstones of the Frontier Formation along the Hogsback, southwestern Wyoming: Gas Research Institute Topical Report GRI-94/0020, 89p.

Lorenz, J.C., 1992, Well-bore geometries for optimum fracture characterization and drainage: West Texas Geological Society Bulletin, v. 32, p. 5-8.

Lorenz, J.C., 1997a, Horizontal core fracture description: Spraberry Symposium, Sponsored by Parker and Parsley Development Company and the U.S. Department of Energy, held at the University of Texas Permian Basin Center for Energy and Economic Diversification, Midland, TX, January 30, 1997, section K.

Lorenz, J.C., 1997b, Non-congruent natural fracture sets in adjacent beds at depth: Data from horizontal cores from the Spraberry Formation, Midland basin, TX (expanded abstract): *AAPG*, Hedberg Research Conference on Reservoir Scale Deformation - Characterization and Prediction: June 22-28, 1997, Bryce , UT.

Lorenz, 1997c, Conjugate fracture zones: Potential "sweet spot" reservoirs within regional parallel-fracture systems: SPE 38749 presented at SPE Annual Technical Conference and Exhibition, San Antonio, TX, 5-8 October, 1997, p. 481-484.

Lorenz, J.C., 1997d, Conjugate fracture pairs in the Molina Member of the Wasatch Formation, Piceance basin, Colorado: Implications for fracture origins and hydrocarbon production/exploration, *in*, Natural Fracture Systems in the Southern Rockies, Close, J.C., and T. A. Casey (eds.): Four Corners Geological Society, p. 97-104.

Lorenz, J.C., 1999, Stress-Sensitive Reservoirs: *JPT*, v. 51, p. 61-63.

Lorenz, J.C., S.J. Finley, and N.R. Warpinski, 1990, Significance of coring-induced fractures in Mesaverde core, northwestern Colorado: *AAPG Bull.*, v. 74, p. 1017-1029.

Malmanger, E.M., J.C. Lorenz, and L.W. Teufel, 1997, Fractures in horizontal core from the Spraberry Formation, Midland basin; Interpreted and modeled using data from analog outcrop fractures in the Brushy Canyon Formation (abstract), American *AAPG Bull.*, v. 81, p. 1228-1229.

McDonald, Paul, J.C. Lorenz, Charlie Sizemore,, D.S. Schechter, and Tom Sheffield, 1997, Fracture characterization based on oriented horizontal core from the Spraberry Trend reservoir: a case study: SPE 38664 presented at Annual Technical Conference and Exhibition, San Antonio, Texas, 5-8 October, 1997, p. 231-239.

Meissner, F.F. 1980, Examples of abnormal fluid pressure produced by hydrocarbon generation (abstract); *AAPG Bull.*, v. 64, p. 749.

Meissner, F.F. 1981, Abnormal pressures produced by hydrocarbon generation and maturation and their relation to processes of migration and accumulation (abstract); American Association of Petroleum Geologists Bulletin, v. 65, p. 2467.

Nolen-Hoeksema, R.C., J.M. Avasthi, W.C. Pape, and A.W.M. El Rabaa, 1992, Waterflood improvement in the Permian basin: Impact of in-situ stress evaluations: SPE 24873 presented at Annual Technical Conference and Exhibition, Washington, D.C., 4-7 October, 1992, p. 81-92.

Petit, J.P., 1987, Criteria for the sense of movement on fault surfaces in brittle rocks: Journal of Structural Geology, v. 9, p. 597-608.

Price, J.G., and C.D. Henry, 1985, Summary of Tertiary stress orientations and tectonic history of trans-Pecos Texas, *in*, Dickerson, T.W., and W.R. Muehlberger (eds.), Structure and tectonics of Trans-Pecos Texas; West Texas Geological Society Field Conference, p. 149-151.

Putra, Erwinsyah, 1998, Reservoir simulation issues in the Spraberry trend area: Fourth Annual Naturally Fractured Reservoir Symposium, Petroleum Recovery Research

Center, New Mexico Institute of Mining and Technology, Socorro, NM, October 27, 1998 (unpaginated).

Reservoirs Inc, 1997, Volume 2, Geological and petrophysical analysis of the upper Spraberry Formation in Midland County, Texas: E.T. O'Daniel No. 28 horizontal cores: Report RSH 3588, May, 1997.

Saleta, C.J., 1998, Geological and petrophysical analysis of reservoir cores: Fourth Annual Naturally Fractured Reservoir Symposium, Petroleum Recovery Research Center, New Mexico Institute of Mining and Technology, Socorro, NM, October 27, 1998 (unpaginated).

Schechter, D.S., Paul McDonald, Tom Sheffield, and R.O. Baker, 1996a, Reservoir characterization and CO_2 pilot design in the naturally fractured Spraberry trend area: SPE 36469 presented Permian Basin Oil and Gas Recovery Conference, Midland, TX, 27-29 March, 1996, p. 819-833.

Schechter, D.S., Paul McDonald, Tom Sheffield, and R.O. Baker, 1996b, Integration of laboratory and field data for development of a CO_2 pilot in the naturally fractured Spraberry trend; SPE 36657 presented at Annual Technical Conference and Exhibition, Denver, CO, 6-9 October, 1996, p. 939-944.

Tyler, N., and J.C. Gholston, 1988, Heterogeneous deep-sea fan reservoir, Shackelford and Preston waterflood units, Spraberry trend, West Texas: Report of Investigation No. 171, Bureau of Economic Geology, The University of Texas, Austin. 38 p.

Whigham, C.L., 1998, Overview of the CO_2 pilot in the Spraberry trend area: Fourth Annual Naturally Fractured Reservoir Symposium, Petroleum Recovery Research Center, New Mexico Institute of Mining and Technology, Socorro, NM, October 27, 1998 (unpaged).

Wilkinson, W.M., 1953, Fracturing in Spraberry reservoir, West Texas: *AAPG Bull.*, v. 37, p. 250-265.

Winfree, K.E., 1994, Post-Permian folding and fracturing of the Spraberry and San Andres formations within the Midland basin region of West Texas, *in*, Laroche, T.M., and J.J. Viveiros, (eds.), Structures and tectonics of the Big Bend and

southern Permian basin, Texas: West Texas Geological Society field trip guidebook, publication 94-95, p. 189-212.

Winfree, K.E., 1995, Post-Permian folding and fracturing of the Spraberry and San Andres formations within the Midland basin region of West Texas: West Texas Geological Society Bulletin, v. 35, no. 3, p. 5-20.

Wu, H., E.J.M. Willemse, and D.D. Pollard, 1994, Prediction of fracture density and drainage distance in layered rock masses using borehole data: Rock Mechanics in Petroleum Engineering, Society of Petroleum Engineers/International Society of Rock Mechanics International Conference, Eurock '94, 29-31 August 1994, Proceedings, p. 487-494.

Wu, H., and D.D. Pollard, 1995, An experimental study of the relationship between joint spacing and layer thickness: Journal of Structural Geology, v. 17, p. 887-905.

TABLE 1.11-1—FRACTURE DATA SUMMARY

	SET 1	SET 2	SET 3
SPACING (ft)*			
Range	0.8-5.8	0.05-4.5	0.04-13.0
Average	3.2	1.6	3.8
Shape	normal, regular	log-normal, narrow range	skewed; log-normal
ORIENTATION (degrees)			
Total Range	35-55	20-50	50-85
Typical Range	40-45	20-50	60-80
Average Strike	43	32	70
FRACTURE TYPE	extension	shear	(shear?)
MINERALIZATION	barite, most fracs w/ high percentage surface coverage	minimal	minimal
DISTRIBUTION	upper reservoir	lower reservoir	upper reservoir, plus shales that overlie upper and lower reservoirs
NUMBER OF FRACS	35	24	28

*Fracture spacing normal to the average fracture strike of that set, corrected from observed spacing in core

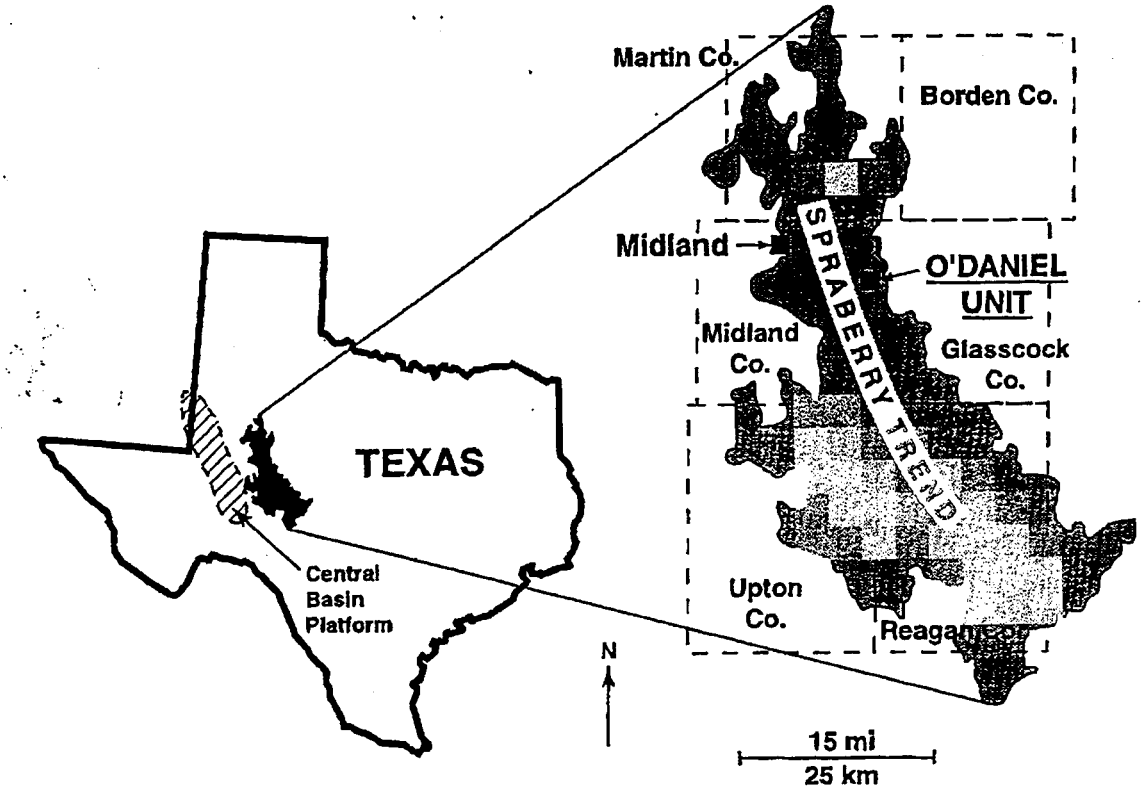

Fig.1.11-1—Location map, showing the Spraberry trend of West Texas.

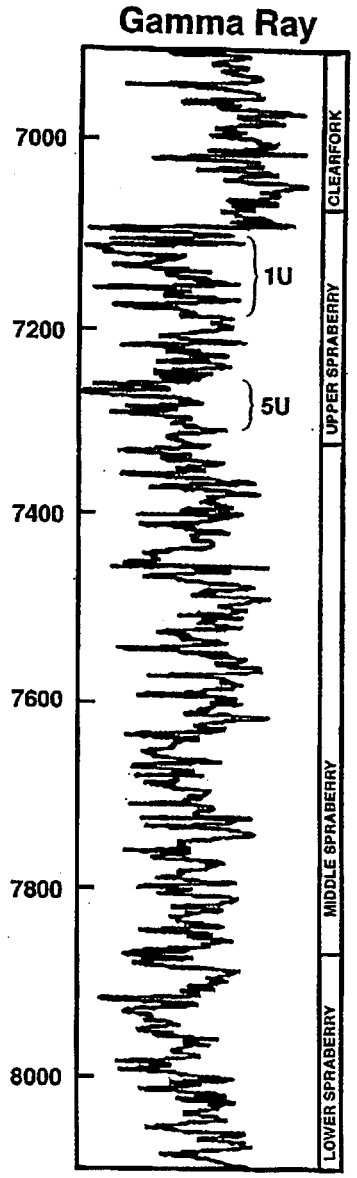

Fig. 1.11-2— Stratigraphic column/Gamma-Ray profile through the Spraberry formation in the O'Daniel unit, Midland basin, West Texas. IU and 5U intervals are the main producing reservoir units of the Spraberry trend. The horizontal cores were taken from the thinner sandstones near the tops of the 1U and 5U intervals.

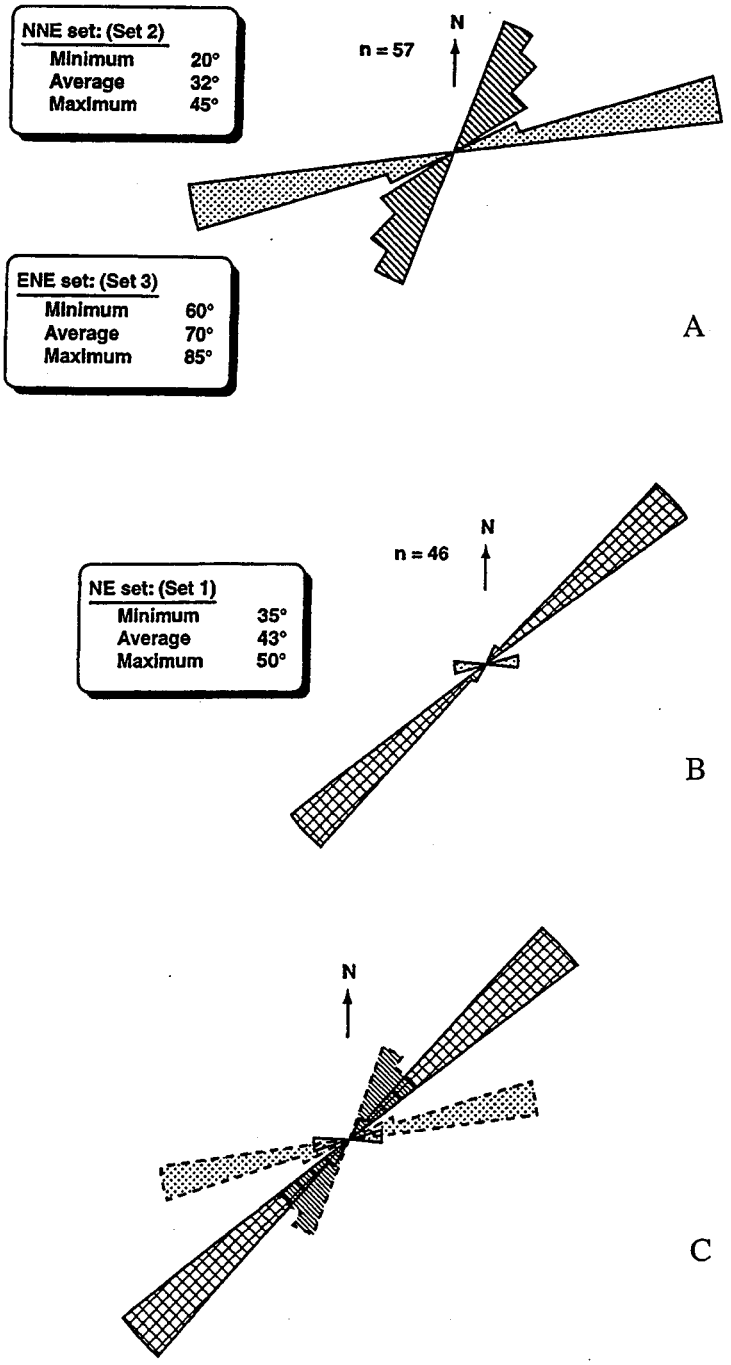

Fig. 1.11-3—Rose diagrams of fracture strikes in horizontal cores from the O'Daniel #28 well. a) Fractures from the lower cored unit associated with the 5U interval; b) Fractures from the upper cored unit associated with the 1U interval, c) Superimposed rose diagrams of fracture strikes from the upper and lower units.

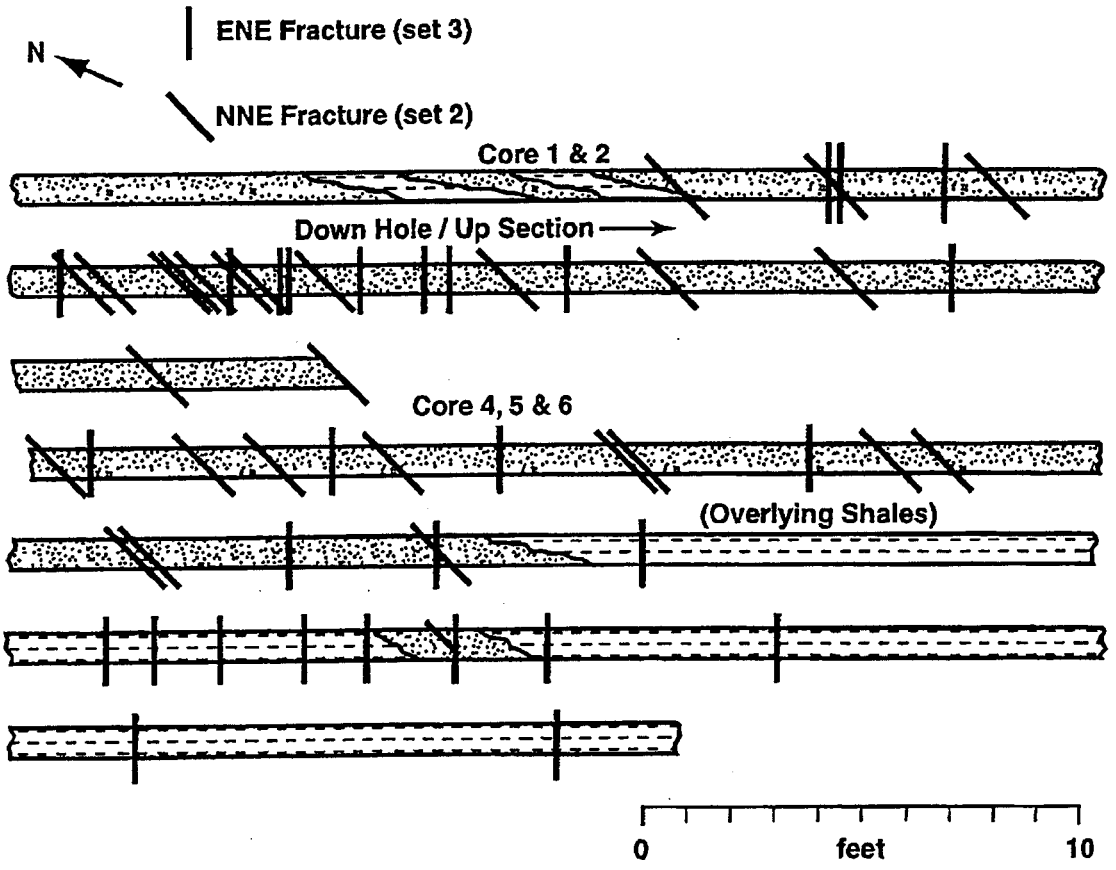

Fig. 1.11-4—Schematic planview of the locations of natural fractures in horizontal core from the upper Spraberry unit, O'Daniel #28 well. (Note: the bedding planes that define lithologic changes are portrayed in side view.)

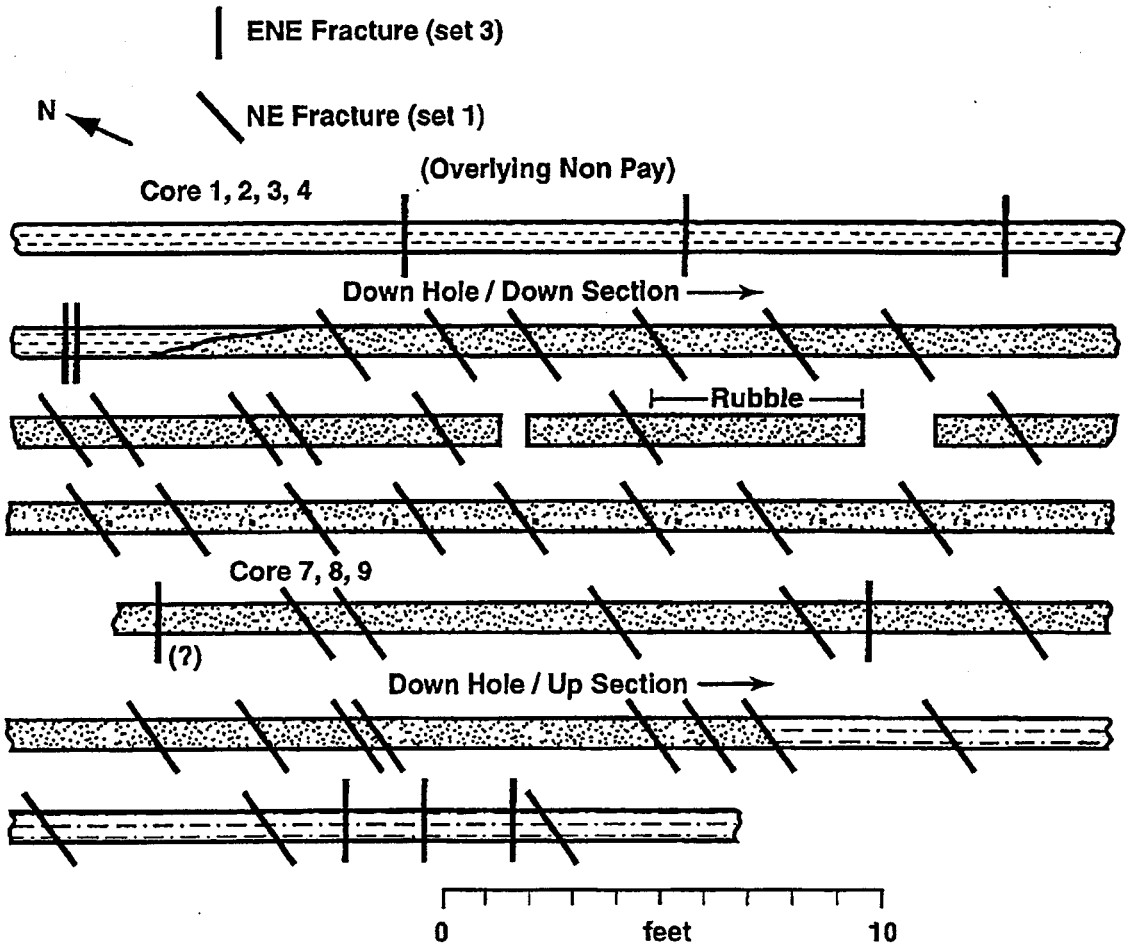

Fig. 1.11-5—Schematic planview of the locations of natural fractures in horizontal core from the lower Spraberry unit, O'Daniel #28 well. (Note: the bedding planes that define lithologic changes are portrayed in side view.)

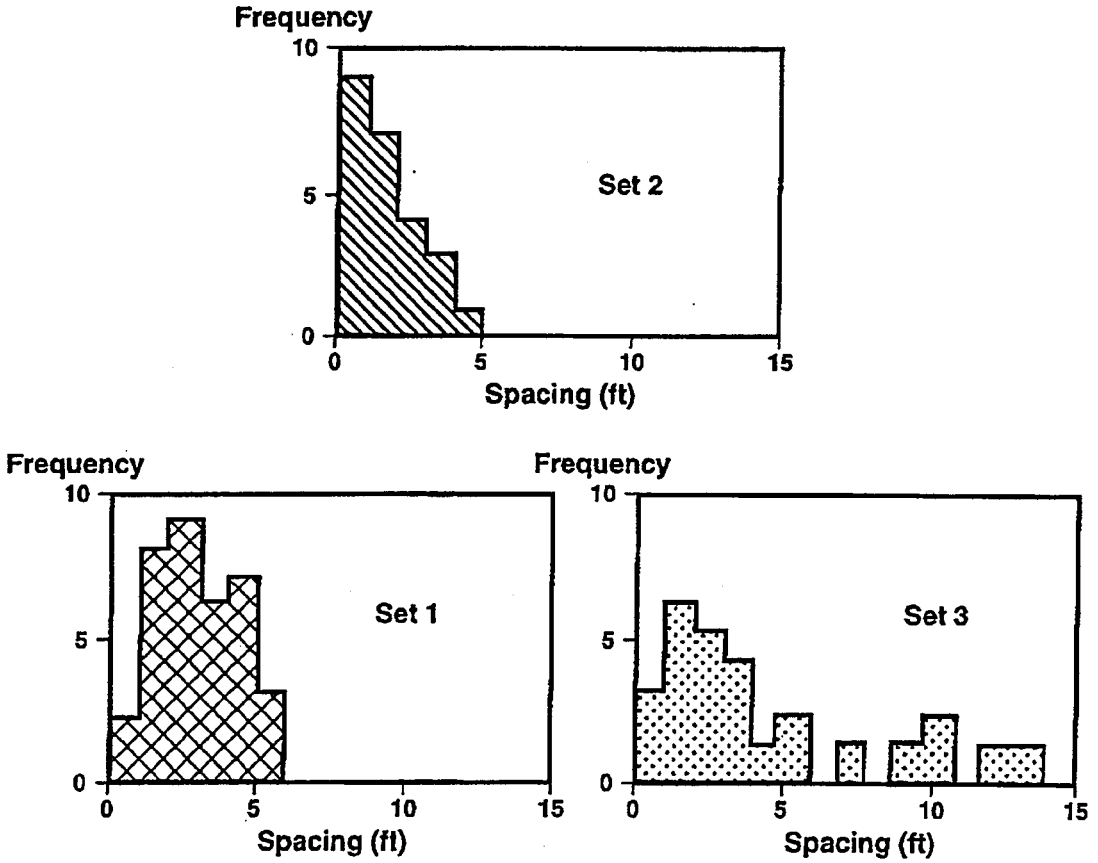

Fig. 1.11-6—Spacing histograms of the three cored Spraberry natural fracture sets. (Shading patterns are keyed to the shading of the rose diagrams in Fig. 1.11-3)

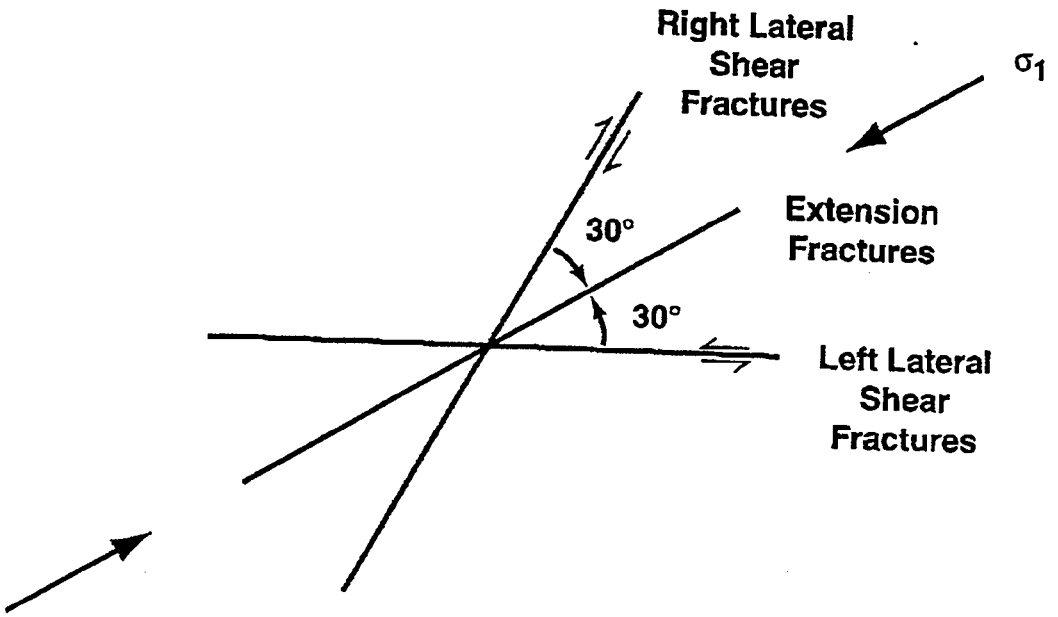

Fig. 1.11-7—Ideal geometry of a conjugate fracture pair with an extension fracture set that bisects the acute conjugate angle.

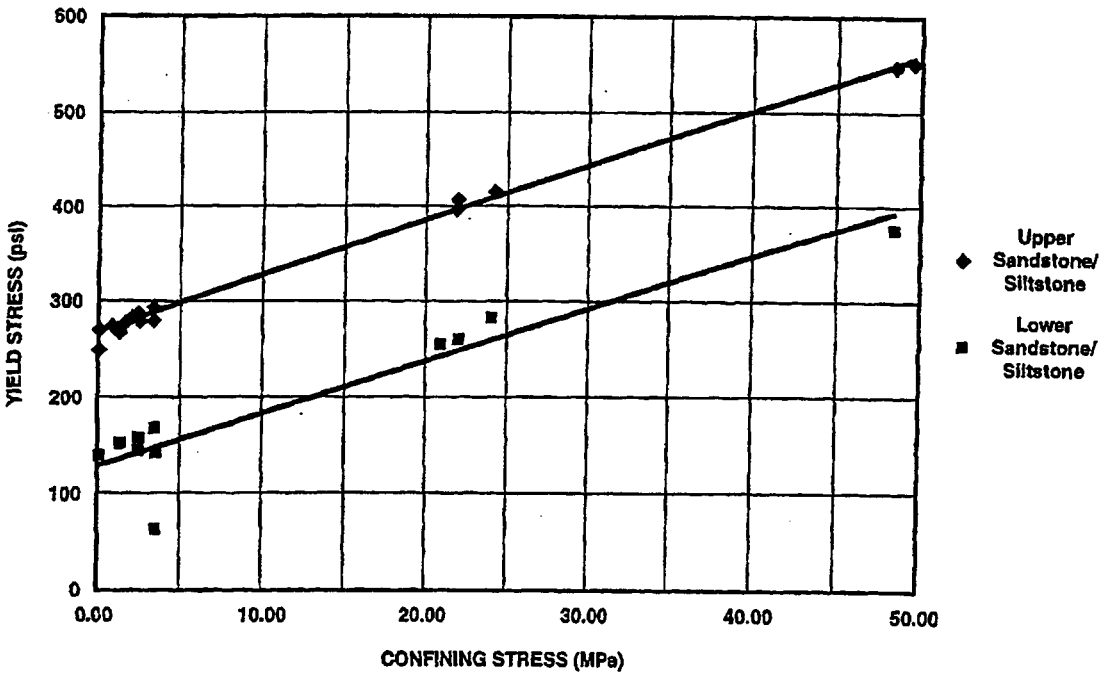

Fig. 1.11-8—Comparison of the yield strengths for different confining stresses for samples of the upper (1U) and lower (5U) Spraberry siltstone-sandstone units. The lower unit is significantly weaker, causing conjugate fractures to form in this interval whereas extension fractures formed concurrently in the stronger, upper unit.

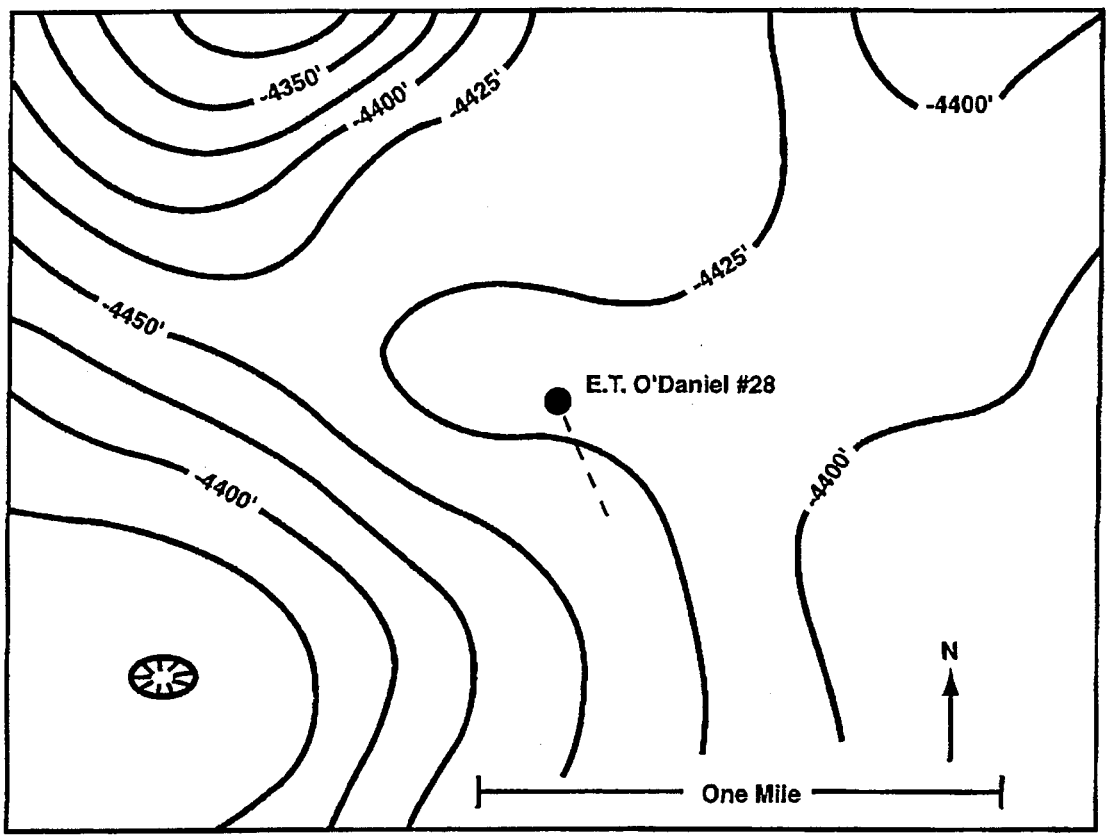

Fig. 1.11-9—Structure contour map on top of the Spraberry formation in the O'Daniel unit area, Midland basin, West Texas. Dashed line is the azimuth of the two horizontal side tracks of the O'Daniel #28 well.

1.12 Transcending Conventional Log Interpretation – A More Effective Approach for the Spraberry Trend Area

Introduction

Discovery of a potentially great source of oil reserves in the Spraberry sand section, a lower Permian sandstone of the Midland basin, unleashed a surge of leasing and wild catting in the 1950's that was scattered over an eight-county area. Although the Spraberry is considered highly overrated by many and its crude producing ability has been doubted, a close study of the production history and the reservoir characteristics proves the pay to be of greater importance both from an economic standpoint and from the standpoint of reserves. Sparaberry reservoirs are characterized by low recovery during rapid primary depletion, disappointing waterflood results and low ultimate recovery.

Thousands of wells have been completed in this region since its discovery. The logs in these wells are cased-hole gamma ray logs with a porosity log and in many cases a porosity log may not be available[1]. More recently well logging in this area has achieved new heights with the growing technology. Even though pay zones were recognized by applying cutoffs for volume of shale and effective porosity[2,3,4] , when it comes to evaluating reservoir parameters, log analysis has been difficult. This is partly due to the fractured nature of the formation, which has a dominant influence on the reservoir and the lack of a true formation water resistivity.

It is only appropriate that the fractured condition of the Spraberry sandstone be mentioned at this stage because this condition is more or less related to the accumulation of oil in the Spraberry sandstone[5]. The fracture nature of the formation annuls the use the Archie's model, since it hasn't been established that Archie's model would work in fractured formations.
This paper outlines a simple log interpretation model, which is very effective in this region. This paper also recommends the logging suite that should be used in Spraberry and also the correlation to the cores taken from this region.

Background

The Spraberry sandstone is a lower Permian sandstone, which occurs in the lower Leonard section and is generally restricted to the Midland basin province of the west Texas, New Mexico Permian basin[5]. The pay section consists primarily of a few fine-grained sandstone or siltstone units in a thousand-ft thick section of shale, limestone, and siltstone. All of the reservoir rocks in the Spraberry are characterized by both low porosity and low permeability. The better-developed sandstones exhibit porosities from 8 to 14 per cent, with the limestones and shaly sands grading down to exceedingly low 5 per cent. Since porosities average only 10 per cent and nearly all permeabilities are less than 1 md, coupled with the influence of natural fractures, conventional log analysis does not estimate the reservoir parameters within reasonable accuracy.

From the core studies and analysis conducted in the recent past, a model of the Upper Spraberry could be visualized[5]. The total section is divided into three parts, the upper, the middle, and the lower:

- Upper Spraberry - varying from 200-270 feet in thickness this section consists usually of two fairly well developed sand bodies (the 1Uand 5U) that can be correlated.
- Middle Spraberry - this section is predominantly composed of shale with some development of sandstones and limestones in the middle.
- Lower Spraberry - the sandstone units of this section are generally thicker than the sandstone layers of the upper Spraberry.

One of the aims of this simplified analysis was to recreate the model of the reservoirs in the Upper Spraberry region. In this paper we have shown that water and hydrocarbon zones can be detected by using a statistical parameter $P^{1/2}$, that is a function of the formation resistivity and porosity. This was earlier investigated by Porter *et al*[6] for the Cretaceous sands of the Illinois basin. Aguilera *et al*[6] later developed it in detail for fractured reservoirs. This paper incorporates their analysis and provides a detailed and simplified algorithm for the analysis for Spraberry reservoirs.

Discussion

The wells under observation are located in the O'Daniel Pilot Area of the Spraberry. In this paper we shall present the analysis of two of wells in the O'Daniel Pilot Area well #37 and well #39. From core analysis and studies in the past, we had determined that the Upper Spraberry was divided into five regions (1U,2U,3U,4U and 5U) and from core analysis it was found that 1U and 5U were the main pay zones. This paper mainly focuses on the two main pay zones. The methodology of interpretation is given in Fig.1.12-1. We shall detail each step in subsequent discussions.
Fig.1.12-2 represents the Upper Spraberry model established through core studies and results of the past.

Determination of lithology

The determination of lithology is basic to any log interpretation. This could be achieved through various cross plots available in the industry or thorough log interpretations. The photoelectric curve (Pe) would be ideal to identify the lithology to the best extent. But the dominant fractures in this trend might have an effect on the log curve response. So we are left with the crossplots to determine the lithology, although we could determine the value of the matrix density thorough various methods and then estimate the lithology. Fig 1.12-3. represents the cross plot determination of lithology. the lithology of Well #37 was found to be sandstone heavily interbedded by shale.

Determination of Matrix Density

One of the common problems encountered in log analysis is the failure to estimate the true rock
matrix density. This may not be a major factor while dealing with reservoirs of good formation porosity. But when encountering a formation with low porosities such as this

one, the accuracy of the matrix density is critical. Conventionally 2.65g/cc for sandstone, 2.71 g/cc for limestone 2.87g/cc for dolomite has been used in determining bulk-density-derived-porosity. In reality no mineral is found in its true form so by assuming the conventional values we may be underestimating or overestimating the porosities. Underestimating porosity values would be critical since it would later affect our water saturation calculations. So determining the true matrix density becomes important in order to estimate true effective porosity.

This can be established by

1. If the core data is available, we can plot core porosity vs. bulk density and determine the value of bulk density when the core porosity is zero. This would give the actual matrix density. From Fig. 1.12-4 the matrix density was estimated to be 2.678 g/cc.
2. We can also estimate the true matrix density by performing a complex lithology analysis. Software's such as PRIZM® can perform the complex lithology analysis with inputs from the log data. The matrix density in this case was fairly close to that of the above method, 2.675 g/cc.

Volume of Shale

Volume of shale was calculated by its definition, from the gamma ray log. Shale index is defined by [7]

$$I_{sh} = (GR_{log} - GR_{min})/(GR_{max} - GR_{min}) \quad (1)$$

The shale index is then formulated into volume of shale using Larionov Equation[2].

$$V_{sh} = 0.33(2^{2Ish} - 1) \quad (2)$$

From the analysis, the volume of shale was on the higher side. In determining the volume of shale for a naturally fractured reservoir, we should take into consideration the fact that uranium is soluble in water and it could potentially flow along with water and occupy the open fractures. So a gamma ray tool response would be high in those fractures, leading to a high value of shale volume. A more comprehensive shale index can be obtained from the Spectral Gamma Ray Log using Potassium readings defined by:

$$I_{sh} = (K_{log} - K_{min})/(K_{max} - K_{min}) \quad (3)$$

This would give fairly acceptable levels of shale indices. Incidentally by carefully observing the uranium curve for peaks, one could be able to detect fractures. However due to the lack of Spectralog data, volume of shale was calculated from the Gamma Log.

Q – Factor

Shaly sand reservoir rocks are classified in three categories: producible, non-producible and zones which require stimulation. The values of q(x) (shaliness factor) and total porosity can be cross plotted on a shaly sand producibilty chart to determine if the volume of shale is high enough to drastically reduce permeability. The zone will not

produce if the data does not fall in the producible part of the cross plot. Fig. 1.12-5 shows the distribution of data in a q (x) vs total porosity crossplot. From the figure we contend that q (x)=0.20 can provide accurate cut-off for identification of fluorescing intervals in Spraberrry Trend Area reservoirs.

Comparison of core data and log data

Comparison of log and core porosities reveal that density porosities corrected for shale is fairly close to core porosity as opposed to effective porosity, which is a combination of density and neutron porosity corrected for shale effects. Fig. 1.12-6 compares the core porosity with the density porosity and effective porosity. The reason for density porosity matching the core porosity could be attributed to the fact that the density-logging tool is very accurate and is not affected as easily as the neutron tool.

Determination of m component

Aguilera *et al*[6] proved that a plot of $(\Delta t_{log}-\Delta t_m)$ vs R_t on a log- log paper should result in a straight line with a slope of –m . Pickett indicated that a similar type of analysis can be made for density tool by crossplotting $\log(\rho_m-\rho_b)$ vs $\log R_t$ (Pickett plot).

Since sonic logging runs were not conducted frequently in this region, we had to rely more on density logging. In conclusion, the log-log plot of formation resistivity vs porosity tool response allows detection of fracture systems.

In this study we have used a simple interplay between Hingle and Pickett plot to determine the porosity exponent m and also estimate the true formation density at the same time. Fig. 1.12-7 illustrates this method of obtaining m and ρ_m through Hingle-Pickett interplay.

The m component was found to range from 1.1 and 1.3, which is consistent with the established values for a naturally fractured reservoir. The determined matrix density was found to correlate well with the value obtained earlier through core analysis and complex mineral plots.

Detecting hydrocarbon zones

Water and hydrocarbon zones can be detected in a naturally fractured reservoir by means of a parameter, P that is a function of formation resistivity and porosity tool response. This parameter was investigated by Porter *et al* [6] and later analyzed by Aguilera[6] for naturally fractured reservoirs. Porter *et al* found that P was a parameter with an approximately square root normal distribution for 100 percent water saturated zones. Later empirically it was proved that the same trend exists for a naturally fractured reservoir.

The parameter is defined by

$$P = R_t (\rho_m-\rho_b)^m \quad \text{.....(4)}$$

If sonic logging tool is used,

$$P = R_t (\Delta t_{log}-\Delta t_m)^m \quad \text{.....(5)}$$

From this analysis it appears that a plot on probability paper of $P^{1/2}$ vs cumulative frequency should result in a straight line for water zones. Hydrocarbon zones should deviate from this straight line. Fig. 1.12-8 shows a typical scheme using this technique.

Once the hydrocarbon zones have been detected , it is possible to determine the resisitivity index I, for each zone by taking the ratio of their P's to the mean value of P at the water-bearing trend (from Aguilera). To accomplish this, it is necessary to consider the water zones as a single distribution. This would result in a plot similar to Fig. 1.12-8. From such a plot the mean value of P is determined at a cumulative frequency of 50 percent.
Having obtained the necessary data the resistivity index is determined from the equation;

$$I = \frac{P_{hyd}}{P_{mean}} \quad \text{.....(6)}$$

Once the resisitivity index has been determined, the water saturation is calculated by the equation

$$S_w = (I)^{-1/n} \quad \text{.....(7)}$$

Example 1

Well #37 is located in the O'Daniel region and the litology consists of calcareous sandstones and shales. The Hingle – Pickett interplay resulted in a definite trend of points with a slope of 1.2. This small value of the slope indicated the presence of fractures. For the purpose of water saturation, the statistical parameter P was determined and S_w was determined by the use of the equation described earlier. Fig. 1.12-10 shows the complete log analysis. The zones 1U, 5U and 3U have been marked. Water saturations range from 45 to 60 per cent. Notice that this log model represents the fracture model described thorough earlier core studies.

There is a region in the log from 7080 to 7180 where high-density porosity is observed. This was due to the fact that there were problem running the density tool inside the well. So caliper arm had to be closed for around 100 feet. This resulted in density porosity being higher and thereby obscuring the saturation evaluation.
High porosity compounded by a more or less constant resistivity has resulted in logs indicating hydrocarbons in that region.

Example 2

Well #39 is also located in the O'Daniel region. The Hingle-Pickett interplay for the clean zones for this region gave a slope of 1.3, which also indicated the presence of fractures. The core-log integration showed that density log derived porosity correlates better than the effective porosity determined from the combination of neutron and density

log responses and the sonic log (Fig. 1.12-11). Fig. 1.12-12 shows the analysis for the 1U zone and Fig. 1.12-13 shows analysis for 5U.

Though the density tool is very effective in Spraberry Trend area, the sonic logging tool plays an important part in this analysis, since the $P^{1/2}$ values determined from sonic logs - are of a higher magnitude than the density derived one. This helps in clear demarcation between water bearing and hydrocarbon zones.

Conclusions

1. Correct matrix density must be obtained from complex lithology plots or by interplay between Hingle and Pickett plots ito be useful for calculating density porosity.
2. Density porosity corrected for shale can be used instead of effective porosity to derive water saturations since it correlates with the core porosities better.
3. Hydrocarbon zones can be detected effectively using the statistical parameter $P^{1/2}$.
4. The interpretation model is very effective in formations whose formation water resistivity Rw, is difficult to obtain.
5. The ideal logging suite for this trend will be spectral Gamma ray, density, induction and sonic tools.

Acknowledgements

This work was performed under DOE/NPTO contract No.DE-FC22-95BC1492. Support from Pioneer Natural Resources is also gratefully acknowledged.

References

1. Schechter D.S., and Banik A.K.: "What is Spraberry Pay?," Report of Investigation No. PRRC #96-28, New Mexico PRRC, New Mexico, 1996.
2. Banik A.K., and Schechter D.S.: "Core-log Integration for the Naturally Fractured Spraberry Trend Area," paper presented at the Naturally Fractured reservoir Forum (Characterization and Fluid Flow), New Mexico Tech, Socorro, New Mexico, April 19, 1996.
3. Banik A.K, Schechter D.S.:" Characterization of Naturally Fractured Spraberry Trend Shaly Sands Based on Core and Log Data," paper SPE 35224 presented at SPE Permian Basin Oil & Gas Recovery Conference, Midland, Texas, 27-29 March 1996.
4. Banik A.K. & Schechter D.S.:" Integration of Petrophysical and Geological Data with Open-Hole Logs for Identification of the Naturally Fractured Spraberry Pay Zones," paper SPE 38913 presented at the Annual Technical Conference and Exhibition, San Antonio, 5-8 October, 1997.
5. "Geological and Petrophysical Analysis of the UPPER Spraberry Formation in Midland County, Texas," report prepared by Reservoir Inc. for Parker & Parsley Development Company, 1996.
6. Aguilera R.: "Analysis of Naturally Fractured Reservoirs From Sonic and Resistivity Logs," paper SPE 4398 presented at the Annul Technical Conference and Exhibition, Nov, 1974.

7. Aguilera R.: Naturally Fractured Reservoirs, Petroleum Publishing Company, Tulsa, Oklahoma, 1980.
8. Dewan J.T.: Essentials of Modern Open-Hole Log Interpretation, PennWell Book, Tulsa, Oklahoma, 1983.

Nomenclature

GR_{log} = gamma ray reading from log, API
GR_{min} = minimum gamma ray reading, API
GR_{max} = maximum gamma ray reading, API
I = resisitivity index
I_{sh} = shale index
K_{max} = potassium curve reading from log, API
K_{min} = minimum potassium curve reading, API
K_{log} = maximum potassium curve reading, API
m = porosity exponent
P = statistical parameter with an approximated square-root normal distribution for 100-percent water saturation zones
P_{hyd} = value of P for hydrocarbon-bearing zones
P_{mean} = mean value of P for water zones
Sw = water saturation
Rw = formation water resistivity, ohm-m
Rt = true formation resistivity, ohm-m
Vsh = volume of shale , fractional
ρ_m = matrix density, gm/cc
ρ_b = bulk density, gm/cc
Δt_{log} = response of the sonic log, μsecs/ft
Δt_m = response of the sonic log in matrix, , μsecs/ft

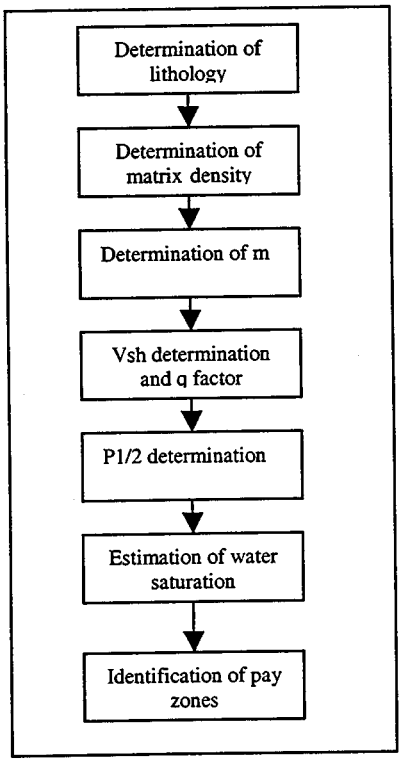

Fig.1.12-1— **Methodology of analysis**

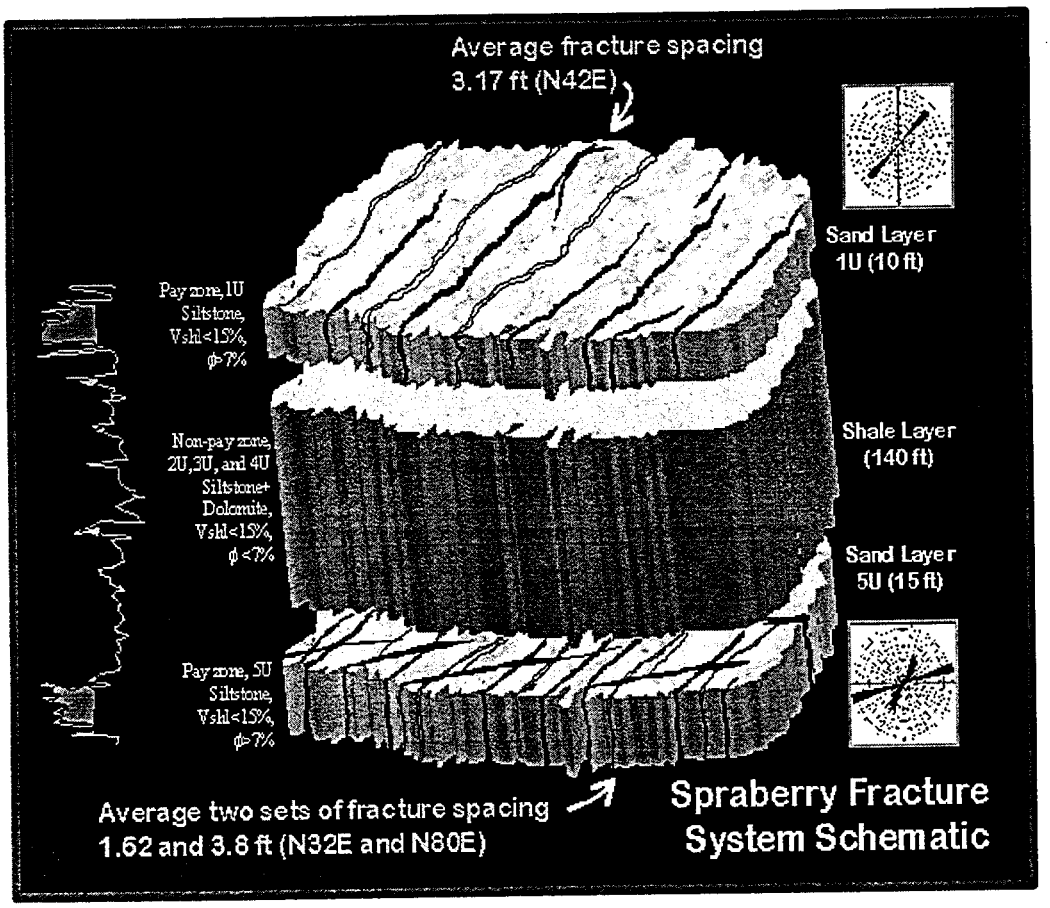

Fig.1.12-2 — **Upper Spraberry model from core studies**

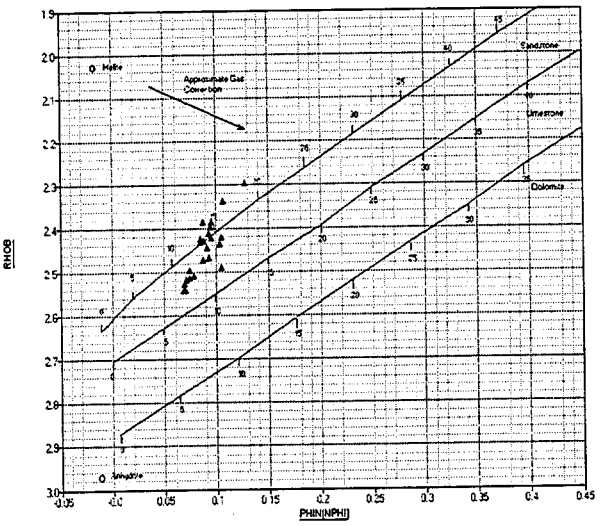

Fig.1.12-3—**Lithology analysis from density-neutron cross-plot in O'Daniel #37**

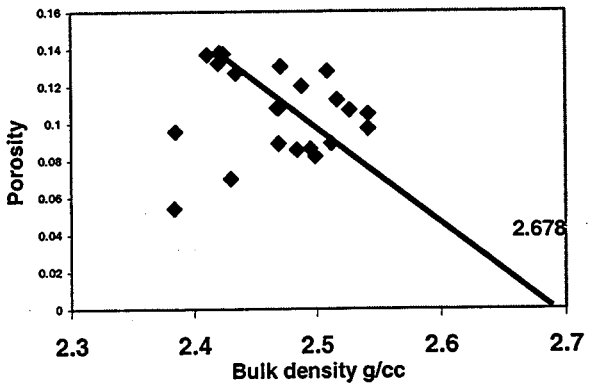

Fig.1.12-4—**Determination of matrix density from core**

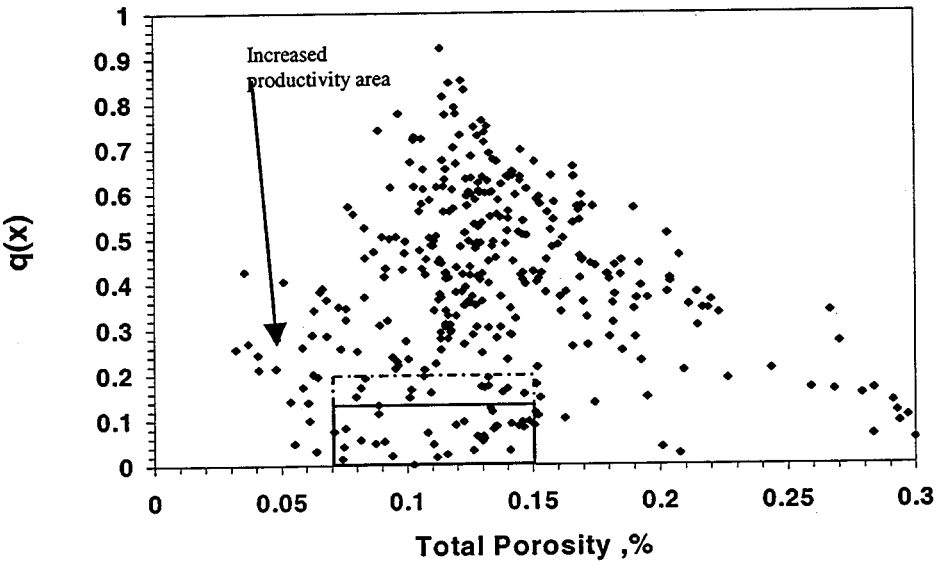

Fig. 1.12-5 — **q(x) vs. total porosity crossplot**

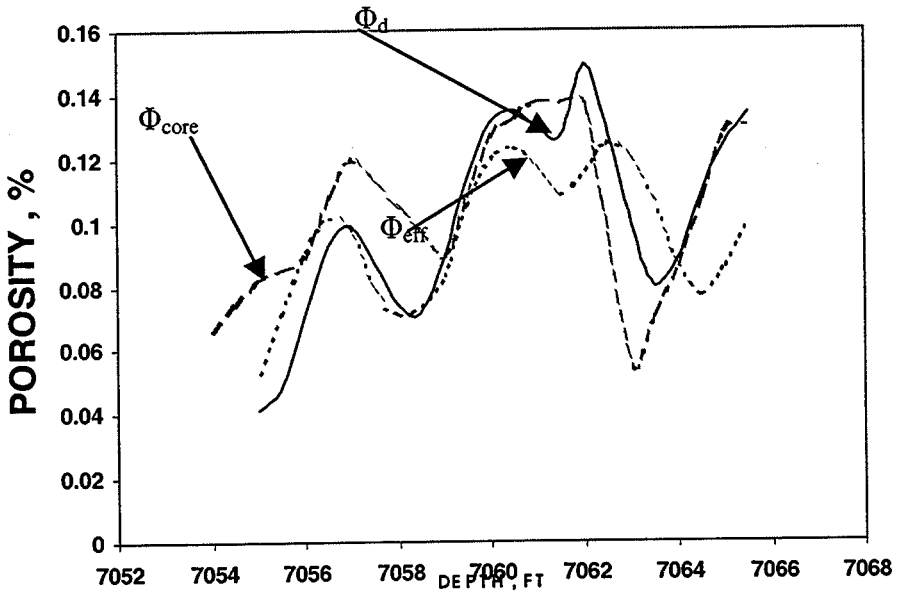

Fig. 1.12-6—**Correlation of porosities to core porosity**

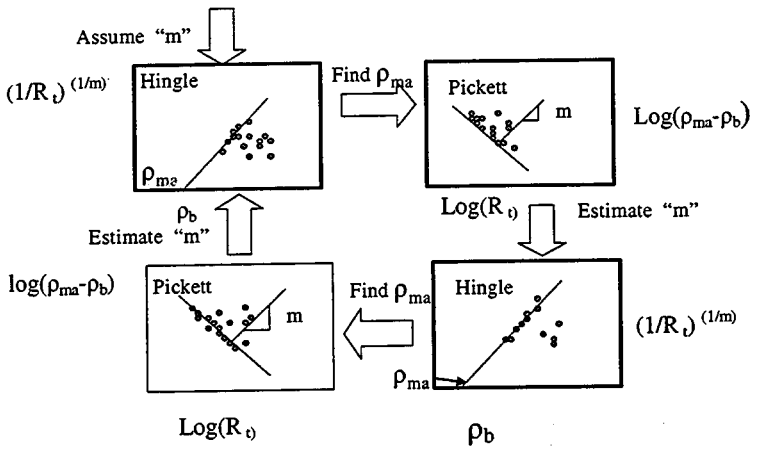

Fig. 1.12-7 —**Hingle-Pickett Interplay**

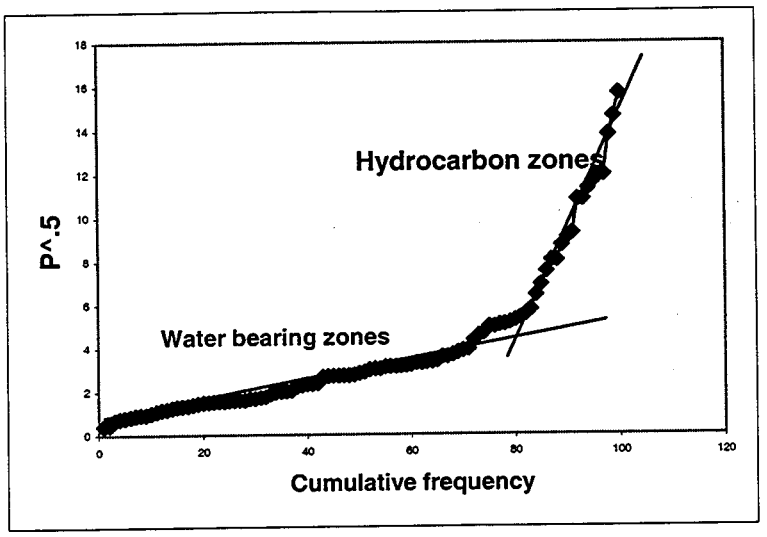

Fig. 1.12-8—$P^{1/2}$ vs. cumulative frequency(all zones)

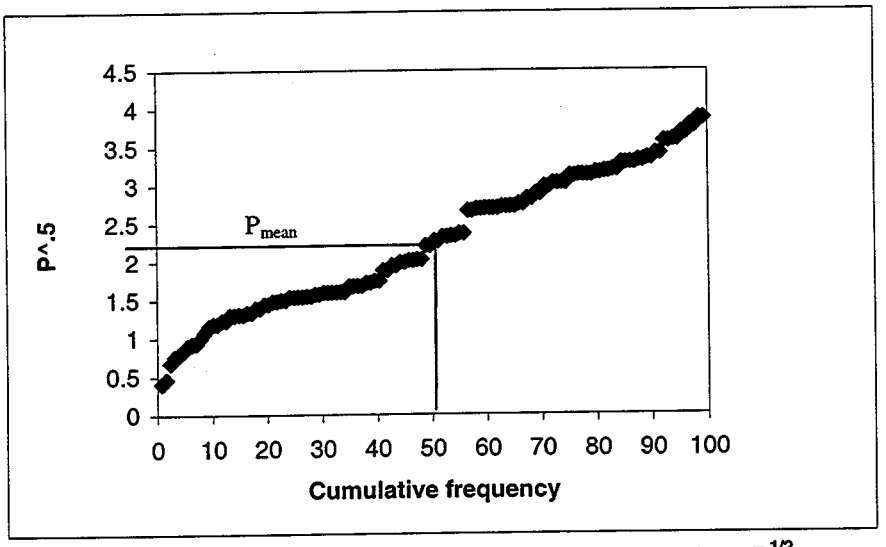

Fig. 1.12-9—Cumulative frequency (water zones) vs $P^{1/2}$

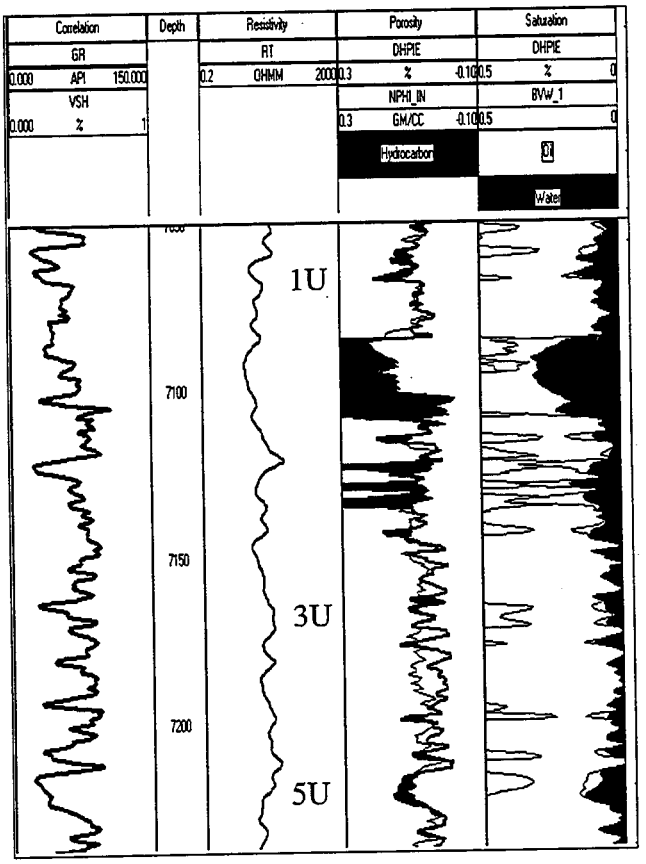

Fig. 1.12-10—**Log interpretation for well#37**

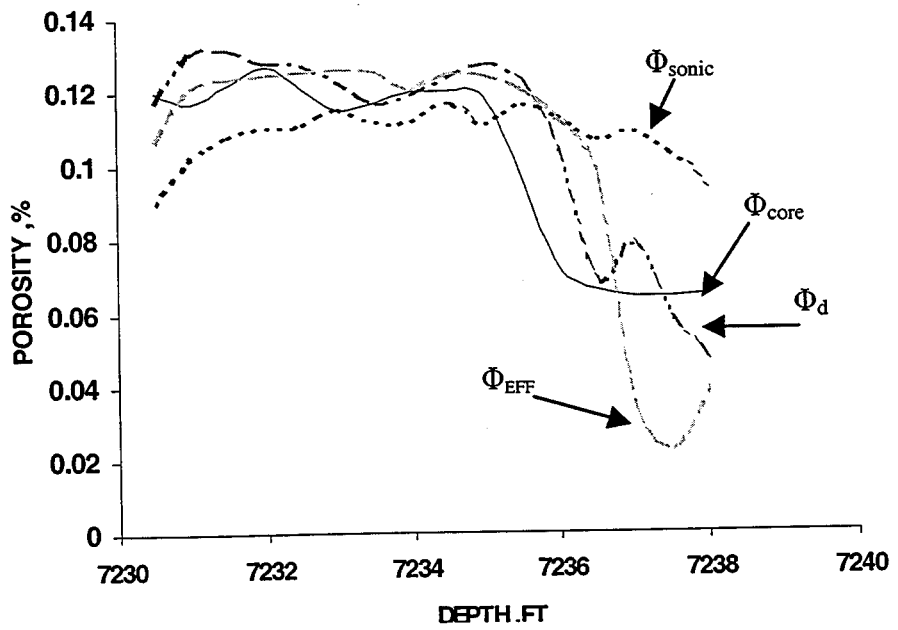

Fig. 1.12-11— **Correlation of core porosity with density, sonic and effective porosities from logs**

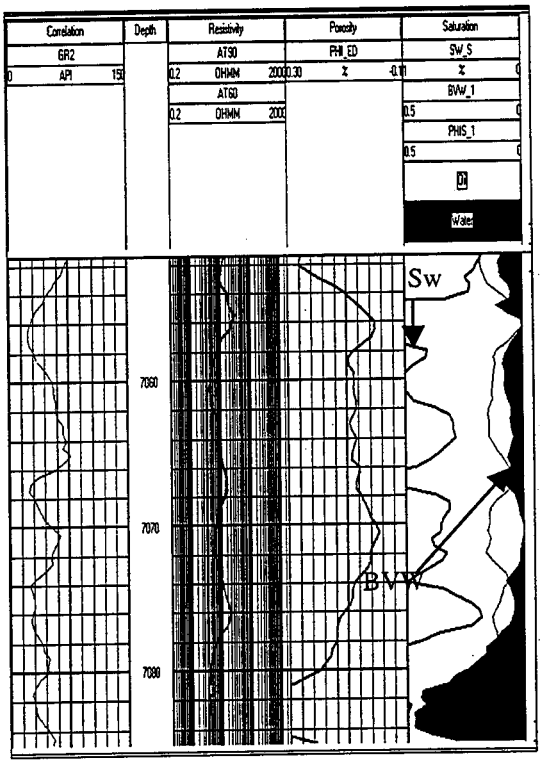

Fig. 1.12-12—**Log interpretation for 1U zone of well #39**

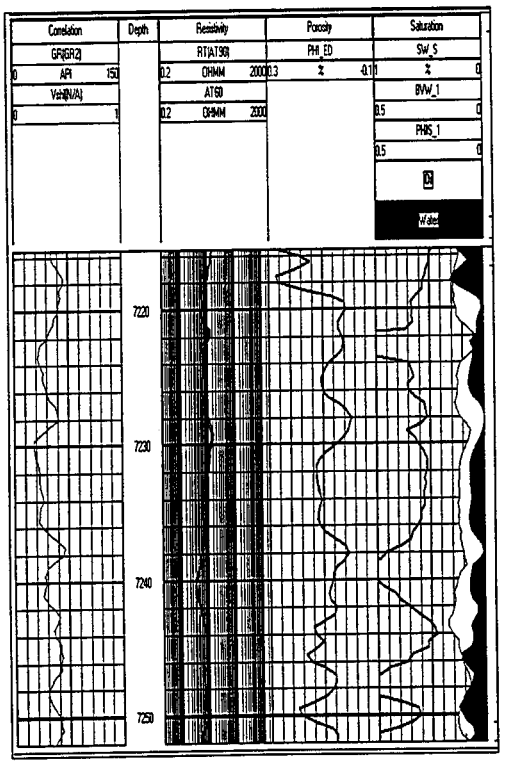

Fig. 1.12-13—**Log interpretation of 5U zone of well#39**

2. INVESTIGATION OF CRUDE OIL/BRINE/ROCK INTERACTION

2.1 Determination of Initial Water Saturation

The initial water saturation in the Spraberry Trend Area reservoirs has been carefully evaluated based on cores from 46 wells drilled before 1954. Fig. 2.4-1 shows a plot of the initial water saturation against air permeability of the cores. It is seen from the plot that the initial water saturation is above 0.20 pore volume (PV) for nearly all the cores. The saturation data is more scattered in the low permeability region as opposed to high permeability regions. The average water saturation can approximately be represented by the following correlation:

$$S_{wi} = 0.20 + 0.12\, e^{-0.6(k-0.1)} \quad \text{.....(2.1)}$$

where S_{wi} is the initial water saturation and k is air permeability of the core in milidarcies.

Using this correlation for the initial water saturation and laboratory determined water saturation of cores, macroscopic displacement efficiencies (E_{dm}) of waterflooding in the Spraberry cores at various times have been evaluated and summarized in Table 2.4-1. It is seen that the macroscopic displacement efficiencies (E_{dm}) of waterflooding in these cores are much higher than field observed water flooding oil recovery, which is between 5 % and 9 % in the Upper Spraberry sand. This indicates that the volumetric sweep efficiency in Spraberry Trend Area reservoirs is low.

2.2 Rock Wettability as Determined by Imbibition Experiments

Introduction

In order to understand the interaction between rock, crude oil and brine in Spraberry Trend Area reservoirs, we have performed water and oil imbibition experiments using Spraberry oil, synthetic Spraberry reservoir brine, and Spraberry reservoir rock. Macroscopic displacement efficiency of water to oil in core samples due to capillary forces has been determined by spontaneous imbibition tests. Effect of core cleaning and aging on the displacement efficiency and wettability has been investigated. Wettability of Spraberry cores taken from the Spraberry Shackelford 1-38A has been estimated based on spontaneous water and oil imbibition tests. It is concluded that the cores are weakly water-wet with mixed wetting behavior. The Amott wettability index to water (I_w) of the cores has been determined to be between 0.5 and 0.7. The macroscopic displacement efficiency during spontaneous water imbibition varies from 40% to 70% depending upon core permeability.

Experimental Procedure for Imbibition Tests

The whole cores we received are 4-inch-diameter cores taken from the Spraberry Shackelford 1-38A. We cut core plugs from whole cores to fit our core holders. The core

plugs are 1.5 inch in diameter and about 2 inches long. Core plugs were dried in an oven before initiation of imbibition experiments. The experimental procedure is as follows:

1. Measure core dimensions, weigh core in air, and measure permeability to air (k_a).

2. Vacuum core for 72 hours, then saturate core in vacuum with synthetic reservoir brine, let the core age in brine and measure core weight until the weight stabilizes. Estimate core porosity (ϕ).

3. Inject brine into the core under 200 psig of injection pressure and 500 psig of overburden pressure for 2 pore volumes. Estimate core permeability to brine (k_w).

4. Inject oil into the core under 200 psig of pressure. Measure brine and oil flow rate until initial brine saturation (S_{wi}) is established in the core. Estimate permeability to oil at initial brine saturation (k_o).

5. Age the fluid-saturated core in oil and weigh core until core weight stabilizes. The aging time should be at least 2 weeks before going to the next step.

6. Place core into a beaker filled with brine at ambient conditions. Weigh core in brine after removing produced oil from the core surface. Calculate oil recovery based on change in weight of the core as a function of imbibition time. Terminate imbibition experiment when recovery stabilizes.

7. Displace the residual oil in the core by waterflooding at 200 psig injection pressure. Calculate Amott wettability index to water (I_w).

In order to assure that reservoir conditions were established in the core prior to water imbibition, we cleaned some core plugs by injecting chloroform into them. To investigate the effect of cleaning on rock properties, chloroform was injected into the core after step 3 and followed by another water injection before proceeding to step 4.

Results and Discussion

Untreated Cores. Assuming that the whole cores we received were clean, the first 10 core plugs were not treated with chloroform. Oil recovery curves obtained from some of the uncleaned core plugs are presented in Fig. 2.4-2. It is seen from Fig. 2.4-2 that brine imbibition rate varies from core to core. Final oil recovery due to imbibition varies from 10% to 40%. Properties of the cores and fluids, final recoveries, and wettability indices to water are summarized in Table 2.4-2.

Cleaned Cores. In order to establish a wetting condition similar to that in the reservoir, some cores were cleaned with chloroform before imbibition tests. Oil recovery curves obtained from some of the core plugs are presented in Fig. 2.4-3. This figure also indicates that brine imbibition rate varies from core to core. Final oil recovery due to imbibition varies from 15% to 70%. Comparison between Fig. 2.4-2 and Fig. 2.4-3

reveals that the rate of water imbibition was significantly improved after cleaning the cores with chloroform. Final oil recovery by spontaneous imbibition was also improved. Rock properties before and after chloroform cleaning are shown in Table 2.4-3 indicating that both porosity and permeability increased. Comparison of the residual water saturation data in Table 2.4-2 and Table 2.4-3 indicates that the initial water saturation after oil injection under 200 psig increased from 18.6% to 42.2% due to chloroform cleaning. This result suggests that the cores became more water wet after the cleaning procedure. This was confirmed by the improved Amott wettability index to water (I_w) calculated after waterflooding the core. The average I_w was increased from 0.5 to 0.6.

Several factors may affect the final oil recovery during brine imbibition. These factors should include core permeability, initial water saturation, and core wettability. The final oil recovery is plotted in Fig. 2.4-4 against core permeability to brine. This figure indicates that the final oil recovery increases with core permeability. Scatter of data is probably due to variations in initial water saturation and wettability of the cores.

We have also investigated brine recovery during spontaneous imbibition of oil into a Spraberry core (core No. SP-10 in Table 2.4-2) fully saturated with brine. Fig. 2.4-5 shows the resultant recovery curve. This curve indicates that a small portion of the rock is oil wet since the core imbibes oil.

In order to exclude the effect of aging time in oil on the result, the final oil recoveries from completed tests with cleaned cores are plotted against aging time in Fig. 2.4-6. This figure indicates if the data beyond three weeks aging time is considered equilibrated, then the final oil recovery due to spontaneous water imbibition should be about 50% of original oil in place (OOIP). The Amott wettability indices to water for various cores are plotted versus the aging time in Fig. 2.4-7. This plot indicates that if the data below three weeks aging time are disregarded, the I_w of Spraberry reservoir rock should be about 0.55, which implies a weakly water wet system.

2.3 Water-Oil Interfacial Tension Measurements

Experimental Apparatus

Shown in Fig. 2.4-8 is a sketch of our experimental setup for IFT determination by pendant drop measurements. Up to 18 needles can be installed in a high pressure cell for forming pendant and sessile drops of different sizes. Fluids are circulated by a pump through the measuring cell, where pendant drops are formed, and then into a density meter to measure densities of the two phases. A circulating water bath is used to control the temperature of the measuring cell and the density meter. Pressure and temperature in the cell are measured by a pressure transducer and a thermometer. The temperature is regulated at measuring conditions. Pendant/sessile drops are imaged by a CCD video camera. Drop images are sent to the VCR, monitor and computer for data processing. IFT is calculated from the image profile by the computer. The density meter is a PAAR mPDS 2000. The video camera is a SANYO VCB-3524 with a 1.5X tele-conversion lens, C-Mount Lens Adapter, and a video monitor. The image processing software is EPIX

SVIP version 7.0 for Windows. The circulating pump is a high speed LDC analytical mini-pump. Needle sizes range from 0.23 mm to 0.90 mm outer diameter. For calibration uses, accurately cut metal collars are attached around the needles.

2.4 Water-Oil Capillary Pressure Determination

The water-oil capillary pressure in the Upper Spraberry 1U and 5U sands has been estimated by utilizing the Leverett J-function on previously measured mercury injection capillary pressure data. Plotted in Fig. 2.4-9 are mercury injection capillary pressure curves converted to Leverett J-function for 9 cores taken from the Shackelford # 138A. As can been seen from Fig. 24-9, the capillary pressure measurements for 6 low permeability (<0.1 md) cores were not complete in the low saturation region indicating these samples were from non-pay zones. Therefore, those curves for low permeability cores are disregarded in this analysis. Fig. 2.4-10 shows mercury injection capillary pressure curves converted to Leverett J-function for 5 cores taken from the Judkins A#5. The curve for core #5 was not complete in the low saturation region because of its low permeability, and therefore is disregarded. The seven completed curves presented in Figs. 2.4-9 and 2.4-10 appear to be identical. The average J-function of the seven cores is plotted in Fig. 2.4-11, which can be further used for estimation of water-oil capillary pressure. Assuming that water-oil interfacial tension is 42 mN/m and contact angle is 45 degrees, water-oil capillary pressures for a 0.5 md Spraberry core have been estimated as shown in Fig. 2.4-12. The imbibition capillary pressure curve was estimated by subtracting a pressure of 15 psia from the estimated drainage capillary pressure so that the curve intersects the S_w axis at a point corresponding to the Amott wettability index to water (I_w) of 0.55 as determined by imbibition tests. The water-oil capillary pressure of Spraberry core is currently being measured in the New Mexico Petroleum Recovery Research Center using Spraberry oil and synthetic Spraberry brine. Some of the experimental results are presented in Fig. 2.4-13 and compared with the above estimated capillary pressure from mercury injection tests.

Table 2.4-1 —Estimated Macroscopic Displacement Efficiency (E_{dm}) in Cores from Spraberry Trend Area Reservoirs

Year	Core Permeability (md)	Water Saturation (%PV)	E_d (%OOIP)	Well Cored
1963	0.4 - 1.3	32 - 40	10 - 16	Tippett #5
1974	0.3 - 0.5	35 - 45	20	Parish #7
1987	0.3 - 1.0	35 - 55	17 - 21	Judkins A#5
1990	0.6 - 1.2	31 - 52	15 - 26	Pembrook #9407
1995	0.2 - 1.6	20 - 50	12 - 28	E.T.O'Daniel #37

Table 2.4-2 —Properties of Rock and Fluids Used in 8 Completed Tests

Test No.	ϕ	k_a	k_w	k_o	S_{wi}	ρ_w	ρ_o	μ_w	μ_o	R_{im}	R_{wf} I_w
	(%)	(md)	(md)	(md)	(%)	(g/cc)	(g/cc)	(cp)	(cp)	(%)	(%)
SP-1	10.0	0.43	0.28	0.09	13.9	1.09	0.86	1.16	16.4	38	41	0.45
SP-2	10.0	0.45	0.22	0.10	18.4	1.09	0.87	1.18	22.4	38	38	0.50
SP-3	9.8	0.44	0.23	0.14	21.3	1.08	0.87	1.17	21.8	41	22	0.64
SP-4	10.0	0.46	0.14	0.06	14.3	1.08	0.87	1.17	19.5	40	27	0.59
SP-5	10.7	0.49	0.27	0.09	15.3	1.08	0.87	1.18	19.5	35	40	0.47
SP-6	9.8	0.43	0.22	0.06	17.2	1.08	0.87	1.18	19.5	>11	25	0.31
SP-7	10.4	0.34	0.20	0.08	22.0	1.08	0.75*	1.18	1.72*	>10		
SP-8	5.9	0.06	0.03		18.8	1.08	0.87	1.18	19.8			
SP-9	6.5	0.06	0.03		18.4	1.08	0.87	1.18	19.8			
SP-10	12.8	0.36	0.15	0.05	26.5	1.08	0.87	1.18	19.5	21	24	0.46
Average	10.4	0.43	0.21	0.08	18.6	1.08	0.87	1.18	19.8	32	31	0.50

* Soltrol 220

Table 2.4-3 —Rock Properties and Results of Water Imbibition Experiments

Test No.	Before Cleaning			After Cleaning			t_{oil}	R_{im}	Iw
	ϕ (%)	k_w (md)	S_{wi} (%)	ϕ (%)	k_w (md)	S_{wi} (%)	(Day)	(OOIP)	
SP-8a	5.9	0.03		9.9	0.12	52	14	>0.36	
SP-9a	6.5	0.03		9.0	0.18	47	21	>0.16	
SP-10	12.8	0.15		14.3	0.45	32		0.09*	
SP-11	10.0	0.11		13.2	0.31	38	6	0.71	0.76
SP-15	3.1	0.02		6.9	0.06	55	16	0.70	
SP-16	2.1	0.01		9.2	0.07	53	25	>0.14	
SP-17	3.1	0.02		7.7	0.08	54	7	0.40**	
SP-19	5.0	0.03		12.3	0.32	36			
SP-21	10.8	0.10		14.4	0.35	36	15	0.45	0.64
SP-22	5.0	0.03		10.1	0.25	42	49	0.42	0.49
SP-24	4.1	0.03		11.6	0.36	38	1	0.79	0.75
SP-25	4.0	0.02		10.4	0.27	40	20	0.72	
SP-27	6.8	0.04		10.6	0.29	39	30	0.57	0.66
SP-28	2.9	0.02		7.8	0.09	53	90	0.29	0.35
SP-30	7.0	0.04		9.7	0.26	41	41	0.48	0.52
SP-33	11.8	0.21		13.9	0.41	35	60	0.47	0.55
SP-34	11.1	0.17		13.2	0.34	40	28		
SP-1	10.0	0.28	13.9	12.0	0.34	37	21	0.50	0.55
SP-3	9.8	0.23	21.3	11.2	0.34	33	21	> 0.15**	
Average						42.2			

* Brine recovery during oil imbibition

** Imbibition performed at 138 F and 1250 psig

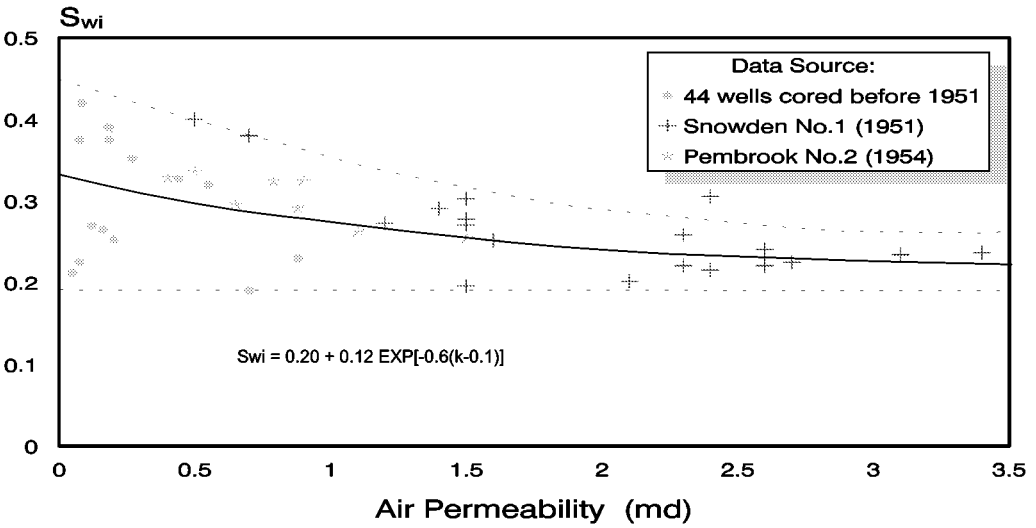

Fig. 2.4-1—Initial water saturation in Spraberry sandstone

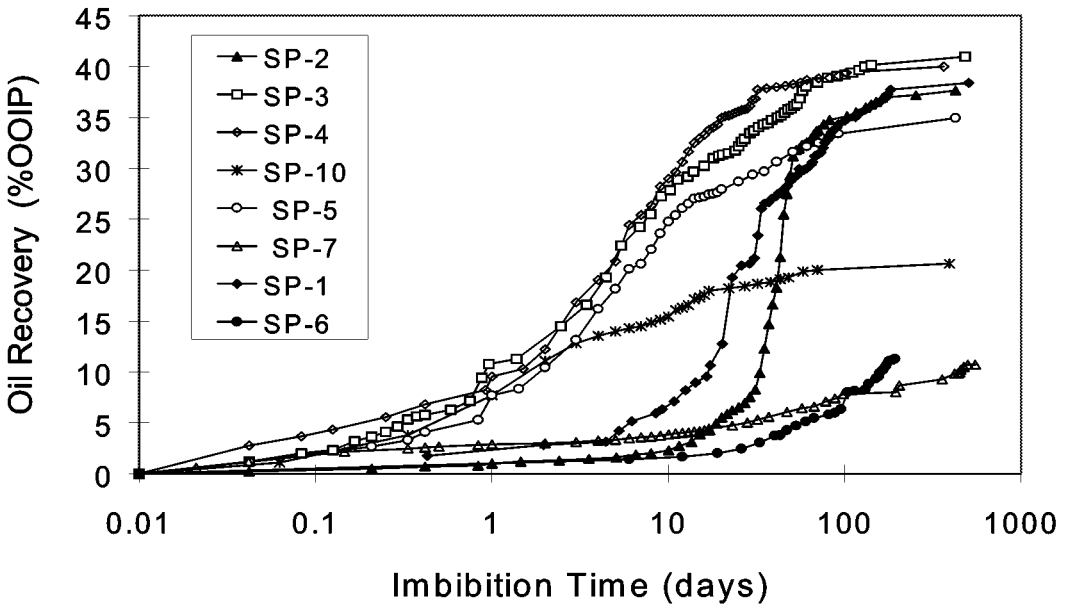

Fig. 2.4-2—Oil recovery from untreated Spraberry cores during brine imbibition

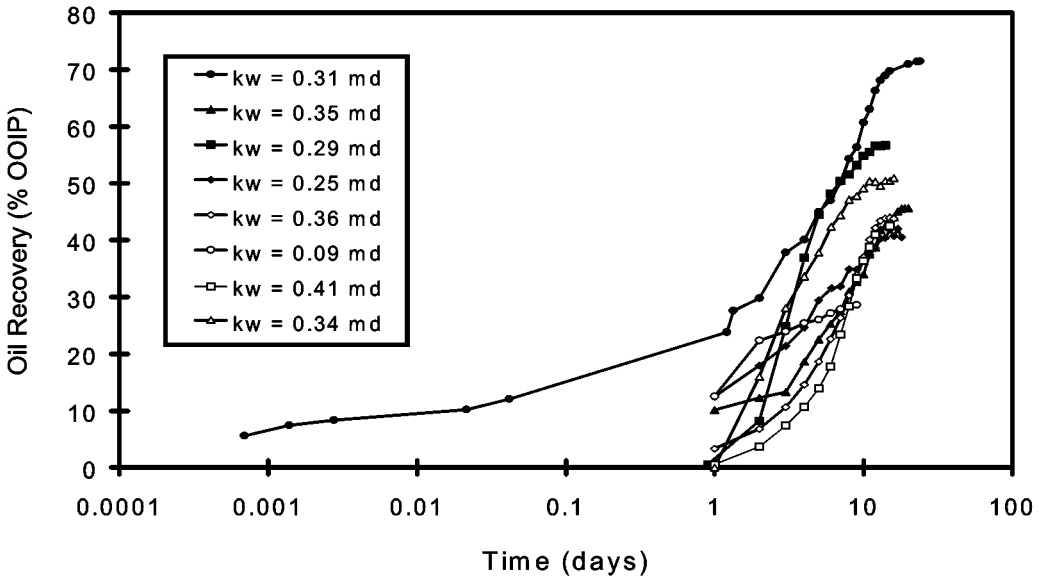

Fig. 2.4-3 —Oil recovery from cleaned Spraberry cores during water imbibition

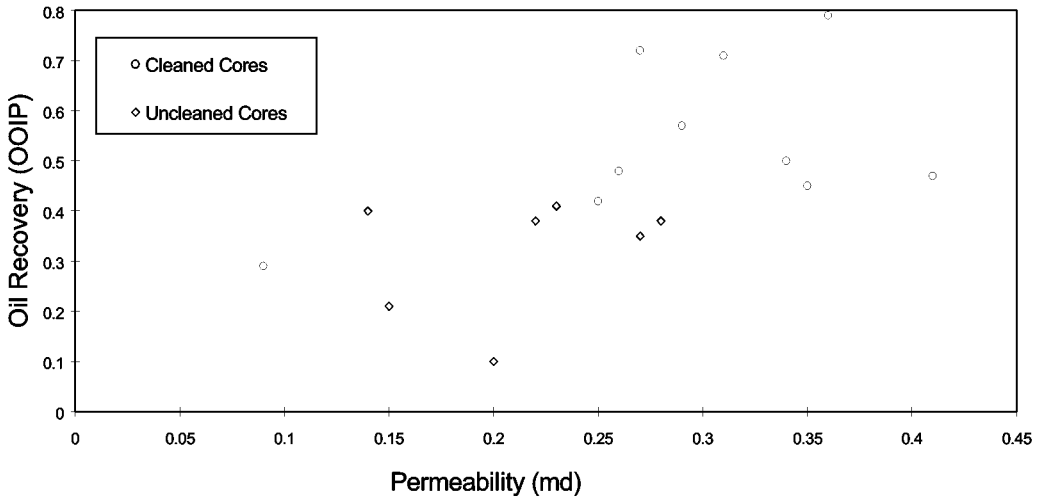

Fig. 2.1-4 —Effect of permeability on final oil recovery

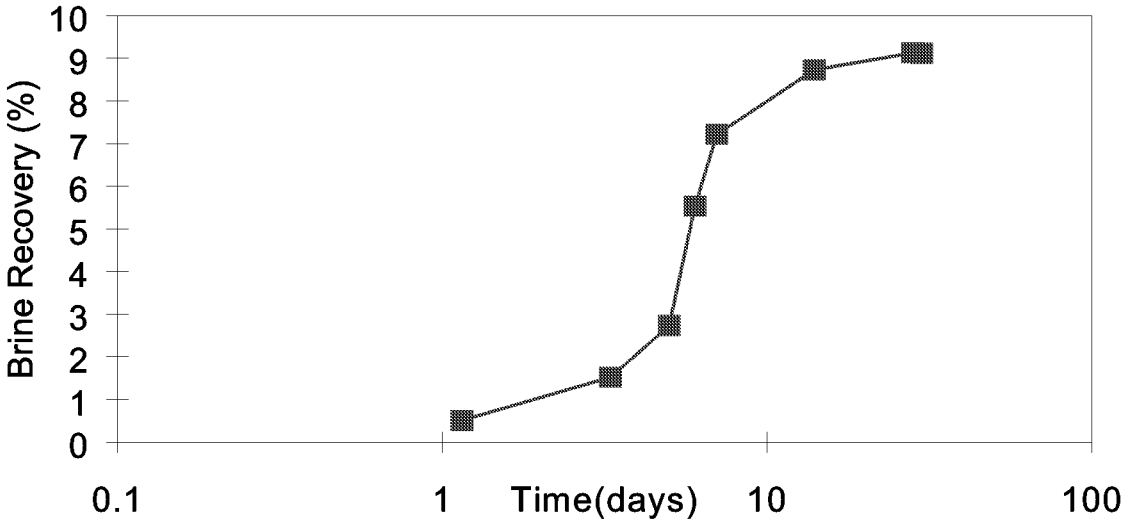

Fig. 2.4-5 —Brine recovery from a cleaned core during oil imbibition. Spontaneous oil imbibition indicates mixed wettability

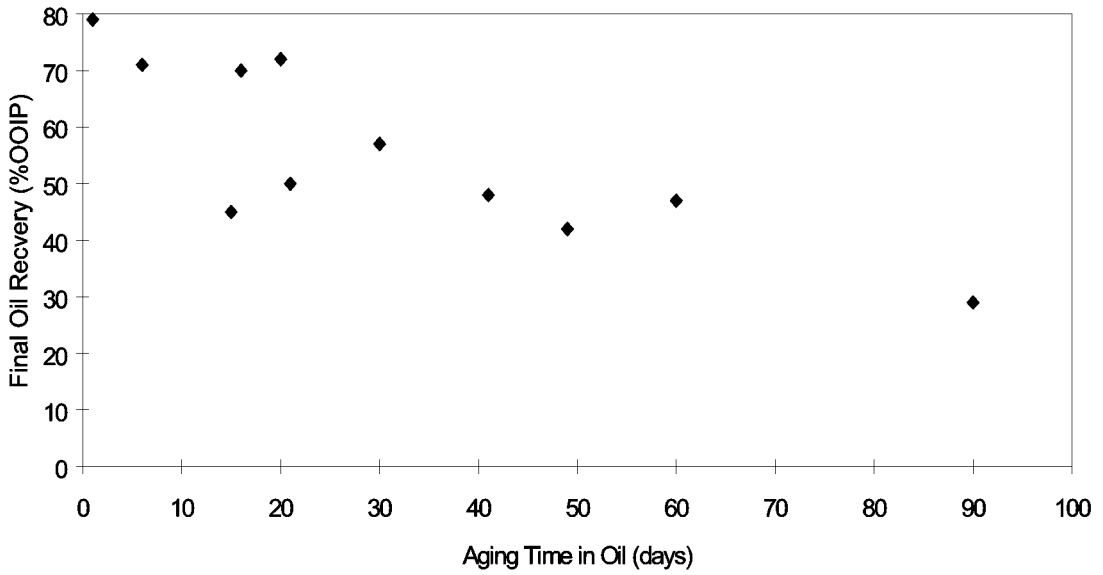

Fig. 2.4-6 —Final recovery versus corresponding aging time in oil.

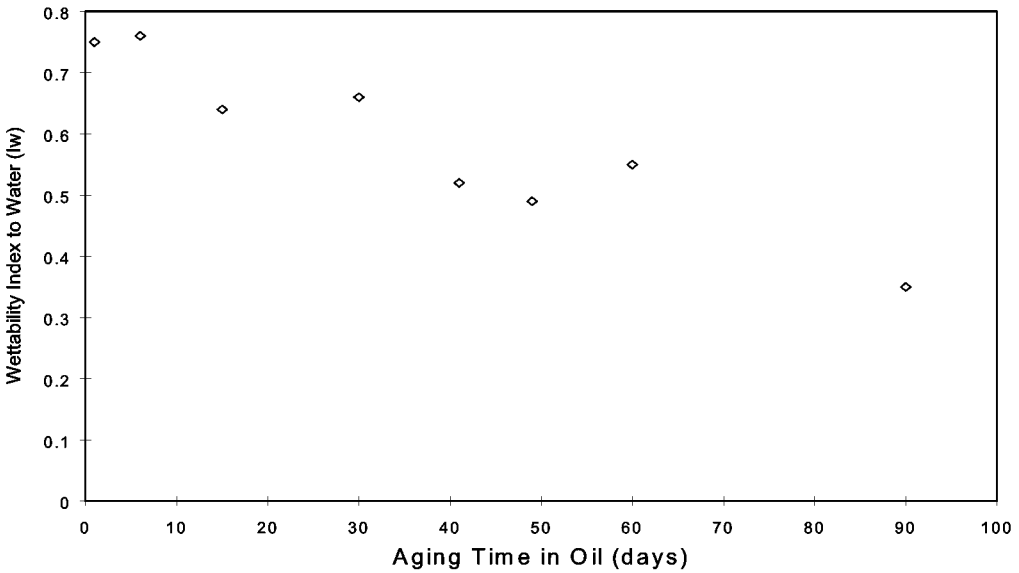

Fig. 2.4-7 —Effect of aging of core in oil on wettability to water

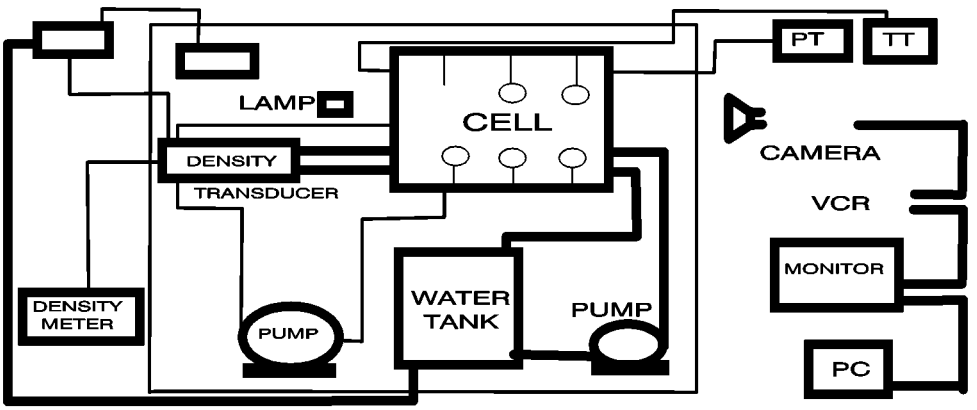

Fig. 2.4-8 —Diagram of experimental set-up for IFT measurements

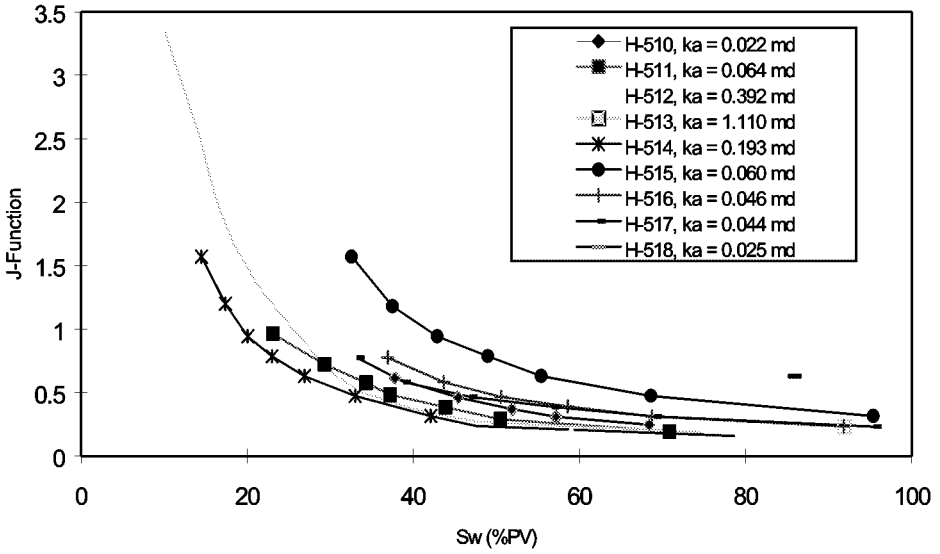

Fig. 2.4-9 —J-function calculated from mercury injection capillary pressure data, cores from Shackelford #1-38A

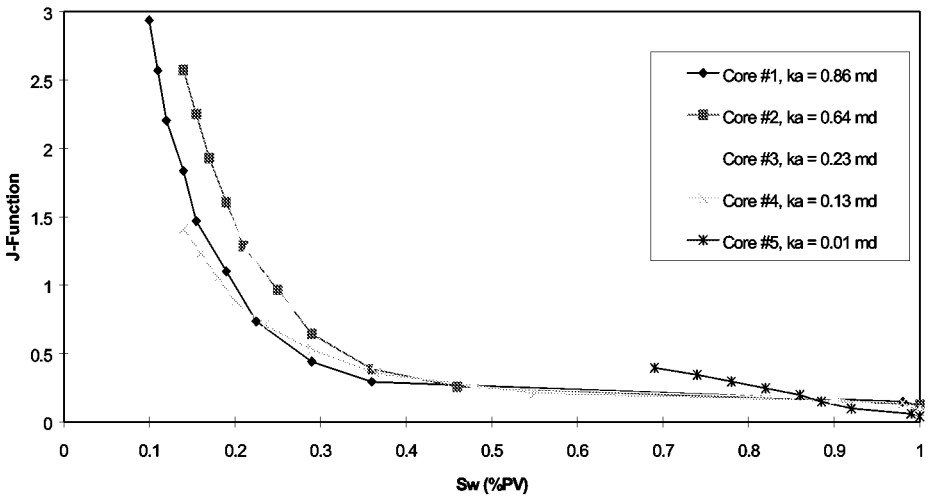

Fig. 2.4-10 — J-function calculated from mercury injection capillary pressure data, cores from Judkins A#5

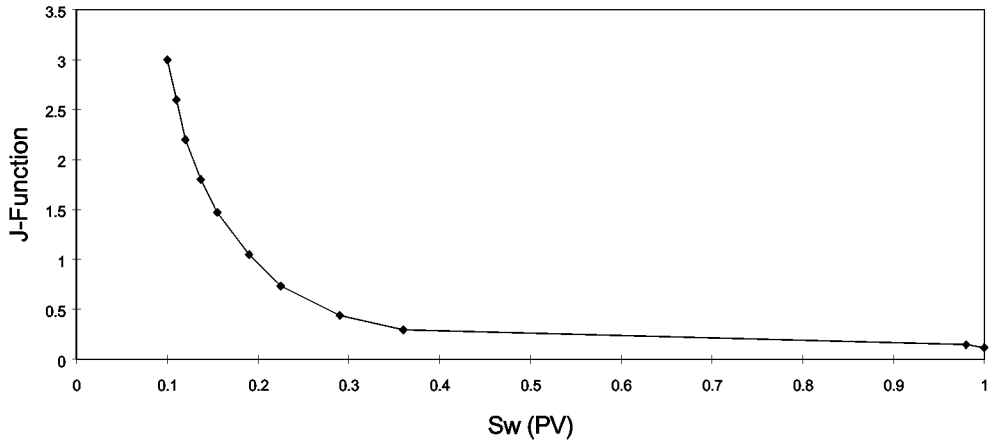

Fig. 2.4-11 —J-Function calculated from mercury injection capillary pressure data, cores from wells Judkins A#5 and Shackelford #1-38A

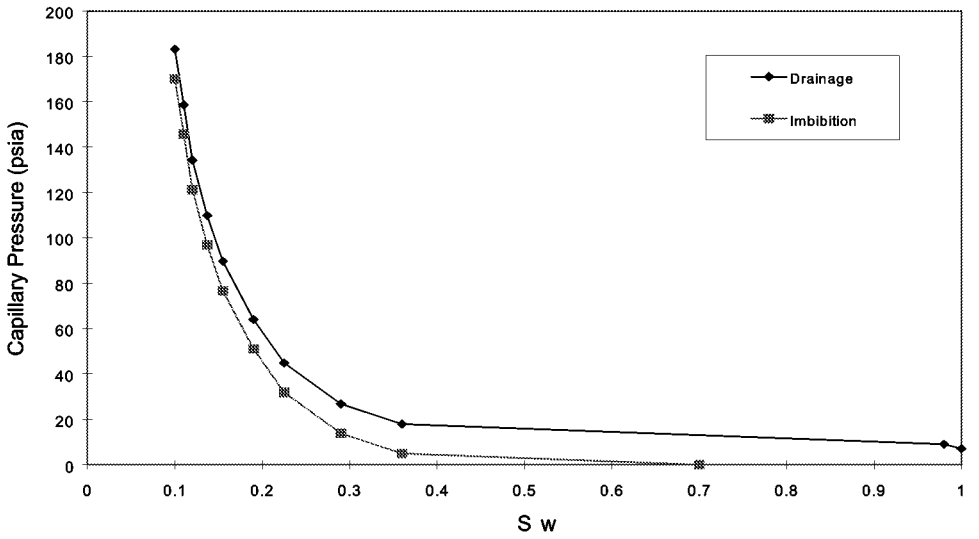

Fig. 2.4-12—Estimated water-oil capillary pressure in Spraberry sand, permeability = 0.5 md, porosity = 0.10, water-oil IFT = 42 mN/m, contact angle = 45 degrees. Imbibition capillary pressure curve is positioned based on Amott wettability index (Iw) evaluated from imbibition and coreflood tests

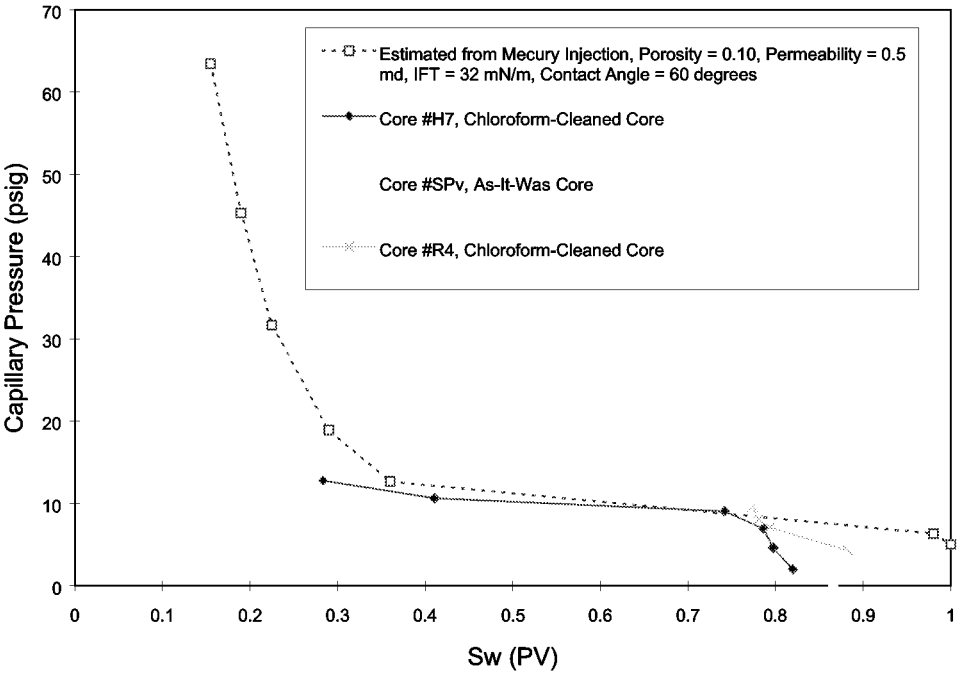

Fig. 2.4-13 —Measured and estimated (from mercury injection pressure data) drainage water-oil capillary pressure in Spraberry 1U and 5U pay sand

2.5 Comparison of Up-scaled Imbibition Results to Field Data

Introduction

The Spraberry Trend Area reservoirs are low permeability, naturally fractured siltstones, which present unusual problems for both primary production and waterflooding. After more than 40 years of waterflooding, the current oil recovery in most areas is still less than 15 per cent. The reasons for the low waterflood recovery have never been thoroughly understood. Various hypotheses have been proposed to explain the poor performance of wide-scale waterflooding.[1-3] These hypotheses include: lack of pattern confinement and injection well density, incorrect well pattern alignment, fracture mineralization which could restrict crossflow,[1] low permeability to oil after waterflooding a high GOR reservoir,[2] and stress-sensitive fracture conductivity.[3] This section emphasizes the importance of slow imbibition of water into the tight, weakly water-wet rock matrix during waterflooding.

The pioneering work on production decline analysis during primary production was performed by Arps[4] in 1944. Differential equations for pressure decline were formulated empirically based on statistical analysis of production data obtained from non-fractured reservoirs. Production decline was considered to be proportional to pressure decline through assumptions of constant wellbore pressure and constant productivity index. Exponential, hyperbolic and harmonic decline curves can be identified based on Arps' analysis. Fetkovich[5] developed decline curves using type curves, so that production decline in hydraulically fractured reservoirs, stratified reservoirs, and the effect of changing backpressure could be analyzed. Laustsen[6] presented an overview of methods and theory in decline curve analysis. He identified common misinterpretations and rules to avoid these misinterpretations. Two important conclusions were stated by Laustsen:[6] 1) an understanding of the principals of decline analysis, depletion mechanisms, and rock and fluid characteristics is essential to establish reliable decline interpretations; and 2) subtle changes to curve fits within the engineering accuracy of the data can result in large differences in estimated reserves.

In order to analyze production decline in naturally fractured reservoirs during waterflooding, it is essential to have a simple mathematical model. Unfortunately, such a model is not available in the literature. Therefore, it is desirable to develop simple models, based on principals which govern reservoir performance, for analyzing production decline in naturally fractured reservoirs during waterflooding.

On the basis of the rate law which governs mass transfer, oil production during imbibition waterflooding in naturally fractured reservoirs has been mathematically analyzed in this study. Analytical models for oil production rate and oil recovery schedule have been developed. Imbibition experiments have been conducted using reservoir oil, synthetic reservoir brine, and low-permeability reservoir cores under room and reservoir conditions. Remarkable consistency has been observed between experimental and field data utilizing the new model. This section demonstrates the models that match both production decline and oil recovery observed in the E.T. O'Daniel Unit waterflood and Humble pilot waterflood in the Spraberry Trend. This scaling analysis clearly indicates the link between laboratory measurements of

imbibition, capillary pressure and wettability and twenty years of reservoir performance in the imbibition mode. It is found that slow imbibition of water into the weakly water-wet rock matrix is the limiting step for oil recovery during waterflooding Spraberry reservoirs. Since the scaling model indicates that rock permeability and fracture spacing are key factors controlling imbibition rate, it is evident that waterflooding should be sought in areas of high matrix permeability and greater fracture intensity.

Physical Process

Primary oil production from the class of naturally fractured reservoirs where storage occurs in the matrix and fractures provide reservoir permeability may be divided into three stages: 1) production from the fracture network at early time; 2) production from the fracture network and rock matrix at intermediate time; and 3) production from the rock matrix at a later time. Waterflooding is usually initiated during the mature stage of primary production. Since permeability of the fracture network is usually much higher than that of the rock matrix, it is presumed that oil production rate during waterflooding essentially depends upon the matrix permeability.

The oil production process during the mature stage of a waterflood in a naturally fractured reservoir may be analogous to a bucket of fluid with a small hole in the bottom dripping liquid onto a conveyor belt, as is illustrated in Fig. 2.5-1. Liquid leaking from the bucket[7] is analogous to oil produced from the matrix due to water imbibition dominated by capillary forces, and the conveyor belt is analogous to water flow in the fractures that brings the produced oil to the production wellbore. Beyond a certain conveyor belt speed, increasing the speed of the conveyor belt does not matter because the limiting step is the slow discharge of liquid from the bucket. In naturally fractured reservoirs, high injection/throughput rates results in a greater amount of water production, but the imbibition process remains the rate limiting step. Since the oil rate is determined by the imbibition process, oil production is relatively constant and unaffected by injection/throughput rates above a certain threshold; thus, the only result of high injection/throughput rates is increased WOR's and reduced profitability. This production mechanism was observed from the Driver Unit waterflood in the Spraberry Trend Area, where after three cycles of high-rate water injection (during which sweep efficiency was improved), the cyclic water injection scheme produced a similar oil production rate as that produced by a steady low-rate water injection scheme.[8]

Mathematical Models

The imbibition process may be mathematically modeled using the following rate law governing mass transfer:

$$\frac{dV}{dt} = -\lambda V^{\alpha} \tag{2.2}$$

where V is the volume of oil in place recoverable by imbibition, t is time, λ is a proportionality coefficient, and α is an empirical exponent. Equation (2.2) is widely used

in chemical engineering and frequently employed by petroleum researchers such as Gupta and Civan[9] for analyzing mass transfer in naturally fractured reservoirs.

If an initial condition of $V=V_o$ at $t=0$ is used, where V_o is the volume of recoverable oil by imbibition, the following two solutions to Eq. (2.2) can be obtained:

$$V = V_o\, e^{-\lambda t} \tag{2.3}$$

for $\alpha = 1$, and

$$V = \left[V_o^{1-\alpha} - \lambda(1-\alpha)t\right]^{\frac{1}{1-\alpha}} \tag{2.4}$$

for α not equal to unity.

Recovery Equations. Dimensionless oil recovery due to imbibition is defined as

$$R_{imb} = \frac{V_o - V}{V_o} \tag{2.5}$$

Substitutions of Eqs. (2.3) and (2.4) into Eq. (2.5) result in

$$R_{imb} = 1 - e^{-\lambda t} \tag{2.6}$$

for $\alpha = 1$, and

$$R_{imb} = 1 - \left[1 - \frac{\lambda(1-\alpha)t}{V_o^{1-\alpha}}\right]^{\frac{1}{1-\alpha}} \tag{2.7}$$

for α not equal to unity.

Production Decline Equations. The volume of produced oil (cumulative oil production due to imbibition) is expressed as:

$$V_p = V_o - V \tag{2.8}$$

Substitution of Eq. (2.3) into Eq. (2.8) yields:

$$V_p = V_o(1 - e^{-\lambda t}) \tag{2.9}$$

An expression for oil production rate is obtained by taking the derivative of Eq. (2.9) with respect to time:

$$q_o = \frac{dV_p}{dt} = \lambda V_o e^{-\lambda t} \tag{2.10}$$

Eq. (2.10) represents an exponential decline model.

Other decline models can be derived from Eqs. (2.4) and (2.8). Substitution of Eq. (2.4) into Eq. (2.8) yields:

$$V_p = V_0 - \left[V_o^{1-\alpha} - \lambda(1-\alpha)t\right]^{\frac{1}{1-\alpha}} \tag{2.11}$$

Taking derivative of Eq. (2.11) with respect to time gives:

$$q_o = \frac{dV_p}{dt} = \frac{\lambda V_o^{1-\alpha}}{\left[1 + \frac{\lambda\alpha t}{V_o^{1-\alpha}\left(\frac{\alpha}{\alpha-1}\right)}\right]^{\frac{\alpha}{\alpha-1}}} \tag{2.12}$$

which is a hyperbolic decline model if $\alpha > 1$. If $\alpha >> 1$, Eq. (2.12) reduces to a harmonic decline model:

$$q_o = \frac{\lambda V_o^{1-\alpha}}{1 + \frac{\lambda\alpha t}{V_o^{1-\alpha}}} \tag{2.13}$$

It should be emphasized that if $\alpha < 1$, Eq. (2.12) becomes:

$$q_o = \lambda V_o^{1-\alpha}\left[1 - \frac{\lambda(1-\alpha)t}{V_o^{1-\alpha}}\right]^{\frac{\alpha}{1-\alpha}} \tag{2.14}$$

which is a power-law type decline model that has not been identified previously in performance analysis. The condition of $\alpha < 1$ represents a situation where the imbibition rate is not sensitive to oil volume in place. This may be the case when a very slow imbibition process occurs in a near-neutral wetting situation.

Experimental Studies

In order to understand the interaction between reservoir rock, crude oil and brine in Spraberry Trend Area reservoirs, we have determined rock wettability by performing water and oil imbibition experiments using Spraberry oil, synthetic Spraberry reservoir brine, and Spraberry reservoir rock under ambient and reservoir conditions. Water-oil interfacial tension and capillary pressure were also measured using reservoir oil, synthetic

reservoir brine, and reservoir rock. Some of the results are presented here. Detailed information has been documented in the First Annual Technical Progress Report.[10]

Procedure. The whole cores received are 4-inch-diameter cores taken from the Spraberry Shackelford Unit 1-38A. Core plugs were cut to 1.5 inch in diameter and about 2 inches long. The plugs were dried in an oven before initiation of imbibition experiments. The experimental procedure for imbibition tests is as follows:

1. Measure core dimensions, weigh dry core, and measure permeability to air (k_a).
2. Periodically inject chloroform into the core samples until the output is clear.
3. Place the chloroform-saturated cores into an oven set to 115°C, and let the core dry for at least 72 hours.
4. Vacuum core for 72 hours, then saturate core in vacuum with synthetic reservoir brine, let the core age in brine and measure core weight until the weight stabilizes. Calculate core porosity (ϕ).
5. Inject brine into the core at 200 psig with 500 psig of overburden pressure for 2 pore volumes. Estimate core permeability to brine (k_w).
6. Inject oil into the core at 200 psig. Measure brine and oil flow rate until the initial brine saturation (S_{wi}) is established in the core. Estimate permeability to oil at initial brine saturation (k_o).
7. Age the fluid-saturated core in oil and weigh the core until the core weight stabilizes.
8. Place core into an imbibition cell filled with brine at ambient or reservoir conditions. Collect produced oil and determine oil recovery. Terminate imbibition experiment when recovery stabilizes. Determine final oil recovery by imbibition (R_{imb}).
9. Displace the residual oil in the core by waterflooding at 200 psig. Determine additional oil recovery by waterflooding (R_{fld}).
10. Calculate Amott wettability index to water ($I_w = R_{imb} / (R_{imb} + R_{fld})$).

Water-oil interfacial tension was measured using a pendant drop apparatus. Water-oil capillary pressure was measured using a static equilibrium method similar, in principle, to that described by Honarpour *et al.*[11]

Results. Core properties and experimental conditions are summarized in Table 2.5-1. Oil recovery curves obtained from water imbibition experiments conducted at ambient conditions are presented in Fig. 2.5-2. A brine recovery curve obtained from an oil imbibition experiment is presented in Fig. 2.5-3. Oil recovery curves obtained from water imbibition experiments conducted at reservoir temperature (138°F) and representative pressures are presented in Fig. 2.5-4. The water-oil interfacial tension was measured to be 36 dynes/cm. Smoothed water-oil capillary pressure data are shown in Figs. 2.5-5 and 25-.6 for drainage and imbibition cycles, respectively.

Discussion. Figure 2.5-2 indicates that brine imbibition rate varied from core to core. The oil recovery at two weeks when the experiments were terminated ranged from 15% for low permeability cores to 70% for high permeability cores. The Amott wettability indices to water (I_w) for various cores was determined and the average value was about 0.55, indicating a weakly water-wet system.

Figure 2.5-3 demonstrates that a brine-saturated core spontaneously imbibed oil up to 9% of the pore volume. This implies that a small fraction of the rock surface is oil-wet, thus the reservoir rock exhibits mixed-wetting behavior.

Water imbibition for core sample SP-H8 was conducted under room temperature during the first three weeks of an extended test. As is shown in Fig. 2.5-4, no oil was recovered during the three weeks. The imbibition cell was transferred into an air bath at reservoir temperature. Oil recovery by water imbibition was initiated as the temperature increased. This indicates that water imbibiton rates are stimulated by increased temperature, possibly due to reduced oil viscosity. However, the final recovery due to imbibition does not seem to be affected by the viscosity reduction.

Imbibition test results from core samples SP-H2 and SP-H4, conducted at elevated pressure, indicate that pressure does not significantly affect imbibition rate.

Comparison between Figs. 2.5-2 and Fig. 2.5-4 indicate that final oil recovery due to water imbibition at reservoir temperature is lower than at room temperature. This is probably due to differences in the initial water saturations. This result could also be due to the reservoir rock becoming less water-wet at elevated temperatures. However, due to the limited amount of data, conclusions can not be drawn. In order to minimize uncertainties in the experiments and speed the investigation, more experiments were conducted to verify the temperature and pressure effects using Berea cores. The results are presented in Section 2.2.

In addition to the capillary pressure curves measured using the static equilibrium method, Figs. 2.5-5 and 2.5-6 also include capillary pressure curves obtained using the centrifuge method[12] and mercury injection.[13,14] It is seen from Figs. 2.5-5 and 2.5-6 that the capillary pressure curves obtained from centrifuge measurements are significantly higher than those obtained from the static equilibrium measurements. These two figures also show that the capillary pressure curves from the static equilibrium measurements are near to those scaled from mercury injection data when a contact angle of 50° is assumed.

Figure 2.5-5 corroborates the interpretation of mixed wetting behavior. Note that oil spontaneously imbibes at zero capillary pressure during the drainage cycle. This result is consistent with the oil imbibition experiment shown in Fig. 2.5-3.

Scale-up of Laboratory Data to Match Reservoir Performance

In order to apply the experimental data to field scale imbibition waterflooding using the developed mathematical models, dimensionless time (t_D) initially proposed by Mattax and Kyte[15] and modified by Ma *et al.*[16] is used:

$$t_D = t\sqrt{\frac{k}{\phi}}\frac{\sigma\cos(\theta)}{\mu_g L_c^{\,2}} \tag{2.15}$$

where t is imbibition time, k is permeability, ϕ is porosity, σ is interfacial tension, μ_g is the geometric mean of water and oil viscosities, L_c is the characteristic length defined by Ma *et al.*,[15] and θ is contact angle. The characteristic length for a matrix block in the reservoir is half the fracture spacing.

The experimental data presented in Fig. 2.5-2 are plotted in Fig. 2.5-7 using dimensionless variables. The dimensionless oil recovery is defined by Eq. (2.5). Also plotted in Fig. 2.5-7 is the scaled oil recovery curve for Berea cores[15] under varying conditions. It is seen from Fig. 2.5-7 that although the recovery data are plotted against dimensionless time, they still do not collapse in a narrow band as do recovery curves obtained using Berea cores.[16] However, to best utilize the experimental data, an average recovery curve was established and shown in Fig. 2.5-8. The scaled oil recovery curve for Berea cores is also reproduced for comparison. For the purpose of simplicity, Eq. (2.6) is used for analyzing imbibition data from Spraberry cores. A curve fit of Eq. (2.6) to the experimental data shown in Fig. 2.5-8 is obtained when the following relation is used for Spraberry cores:

$$\lambda t = 6.2\times10^{-4} t_D \tag{2.16}$$

Substituting Eq. (2.15) into Eq. (2.16) and solving the latter for λ yields the following result:

$$\lambda = 6.2\times10^{-4}\sqrt{\frac{k}{\phi}}\frac{\sigma\cos(\theta)}{\mu_g L_c^{\,2}} \tag{2.17}$$

Substituting Eq. (2.17) into Eqs. (2.7) and (2.10) yields:

$$R_{imb} = 1 - e^{-6.2\times10^{-4} t\sqrt{\frac{k}{\phi}}\frac{\sigma\cos(\theta)}{\mu_g L_c^{\,2}}} \tag{2.18}$$

and

$$q_o = 6.2\times10^{-4} V_o\sqrt{\frac{k}{\phi}}\frac{\sigma\cos(\theta)}{\mu_g L_c^{\,2}} e^{-6.2\times10^{-4} t\sqrt{\frac{k}{\phi}}\frac{\sigma\cos(\theta)}{\mu_g L_c^{\,2}}} \tag{2.19}$$

The above equations are valid when consistent units are used.

Production data from the E.T. O'Daniel Unit and Humble pilot in the Spraberry Trend

Area are used to test the imbibition scaling procedure.

Case 1 - E.T. O'Daniel Unit Waterflood. This unit is located at the northern part of the Spraberry Trend Area Field. The unit covers 2,160 acres, and contains two zones.[17] The upper zone is responsible for the vast majority of the production from the unit, while the lower zone is productive in only a few areas and does not significantly contribute to the overall production.[16] The reservoir is known to be highly fractured. The porosity varies from 7% to 15%, with the matrix permeabilities being less than 1.0 md. The original oil in place (OOIP) was estimated to be 14.3 MM STB. Well spacing in the unit is 40 acres. Primary production by solution gas drive began in 1951. At the initiation of waterflood in 1959, 7.4% of OOIP had been recovered. Currently there are 16 active producing wells in the unit giving a total production rate of about 130 STB/day.

Production Decline. The match between observed production rate and the production rate calculated with Eq. (2.19) is shown in Fig. 2.5-10. This match indicates an exponential decline rate of λ=0.00357 per month. It can be seen from Fig. 2.5-9 that the observed production rate is significantly lower than the calculated production rate for the time period between 1959 and 1971. This is probably due to low sweep efficiency during the early time of waterflooding. This decline curve is extrapolated into the future to determine when the economic limit would be reached. For this case, if nothing was changed and the unit was left to reach its economic limit, it would do so at the end of 2020. This projection is based on the limit of 3 STB/day/active well (48 STB/day for the lease).

Parameters used in the calculations are summarized in Table 2.5-2. No forced matching between the observed and calculated decline curves was necessary. Interfacial tension, viscosity, oil formation volume factor, and porosity were measured in laboratories. Matrix permeability was determined based on a current well test.[18] The total contributing pay thickness was estimated based on a shaly-sand rock model[10] and the fact that the upper zone is responsible for the vast majority of the production from the unit.[17] The initial water saturation in the reservoirs was estimated by Guo and Schechter.[3] The gas saturation after reservoir repressurization by waterflooding was assumed to be 5% on average. Average fracture spacing of 2.86 ft was observed from horizontal core data.[19]

As was mentioned earlier, a contact angle of 50° was estimated by scaling the mercury injection data to the water-oil capillary pressure curve measured using the static equilibrium method. The contact angle can also be estimated directly from this water-oil capillary pressure curve. In fact, based on the Leverett[20] relation, capillary pressure can be expressed as:

$$P_c(S_w) = \sigma \cos(\theta) \sqrt{\frac{\phi}{k}}\ J(S_w) \tag{2.20}$$

The measured water-oil capillary pressure curve shown in Fig. 2.5-6 indicates that P_c is about 5 psig, or 19.7 psia, at the average initial water saturation, S_{wi} = 0.4. If $J(S_w)$ is assumed to be equal to C, where C is 0.4 for the capillary tube model,[21, 22] the contact

angle θ can be estimated from Eq. (2.20). Substituting P_c = 19.7 psia, σ = 36 mN/m, ϕ = 0.10, k = 0.35 md, and $J(S_w)$ = 0.4 into Eq. (2.20) results in θ = 57 degrees. Considering the difference between the capillary tube model and reservoir rock, a C value of less than 0.4 should be used. If C values of 0.35 and 0.30 are used in the equation, the calculated values for θ are 52 degrees and 44 degrees, respectively. These calculations tend to confirm the estimated contact angle of 50 degrees obtained from scaling the mercury injection data to the water-oil capillary pressure curve.

Recently, we built an apparatus for contact angle measurements. A cubical stainless steel cell was constructed with a three-inch diameter circular internal cavity. Inside this cavity is a horizontal disk on the end of a vertical shaft. The disk can be rotated in a horizontal plane through a handle on top of the shaft. Extending from the bottom of the cavity is a hollow needle mounted on a valve apparatus. The apparatus enables the needle to extend and retract vertically. The cell has a water-heated jacket to enable it to be heated to reservoir temperatures. It can also be pressurized to several thousand psia using an external piston pump. Contact angles on a mica surface using reservoir brine and crude oil were measured at the reservoir temperature of 138°F and a pressure of 15 psig. A sheet of mica was attached horizontally to the disk. The cell was filled with synthetic Spraberry brine. A drop of Spraberry separator oil was deposited and advanced on the bottom surface of the mica by using the needle, as shown in Figure 2.5-10. The oil was then retracted back into the needle. The process was recorded in both analog and digital forms using a VCR and SVIP video software. The water receding and advancing contact angles were measured using the digital images and found o be 49.9 degrees and 52.4 degrees, respectively. These values are very close to the assumed contact angle of 50 degrees. The combination of imbibition capillary pressure and contact angle measurements tends to confirm that Spraberry reservoirs are not strongly water-wet.

Although our experimental data indicates that 15% to 70% of OOIP can be recovered by water imbibition, it was found that use of the average imbibition efficiency of 32% gives the best match between the observed decline data and the calculated decline curve. It was recognized that the imbibition capillary pressure curve measured using the static equilibrium method corroborates very well with this number. In fact, Table 2.5-1 shows that the average initial water saturation in the core samples is 40%. The average initial oil saturation is then 60%. The imbibition capillary pressure curve measured using the static equilibrium method, as is shown in Fig. 2.5-6, indicates that water imbibition ceased at 60% water saturation, leaving an oil saturation of 40% in the core. The efficiency of water imbibition is determined to be (0.6-0.4)/0.6=0.33, which is very close to the value of 0.32 obtained from decline-curve matching.

Oil Recovery. Oil recovery from the unit is presented in Fig. 2.5-11. Calculated imbibition oil recoveries using Eq. (2.18) are also plotted in Fig. 2.5-11. Again, no matching effort was attempted between the observed oil recovery and calculated oil recovery curves. Figure 2.5-11 indicates that the ultimate recovery is about 36% of the OOIP by the end of 2020.

Discussion. Figure 2.5-11 shows that the actual oil recovery is slightly lower than the

model calculated recovery. Reasons for this discrepancy are not clearly understood. It is speculated that one of the reasons is mineralization of the fractures that hinders mass transfer during water imbibition. This hypothesis is partially supported by recent horizontal core data that indicates an average percentage of mineral filling being on the order of 75% in one of the primary fracture sets.[19]
It is important to note that the match shown in Figs. 2.5-9 and 2.5-11 can be made using other combinations of matrix permeability and fracture spacing. Some of the combinations are presented in Table 2.5-3. This means that the uncertainty about one of the parameters may be narrowed through the match if the other parameter is known with confidence.

Case 2 - Humble Pilot Waterflood. This pilot waterflood program was inaugurated on Humble's L.H. Shackclford B lease in the west central portion of the Spraberry Trend in March, 1955. This pilot was considered a successful Spraberry waterflood. Full-scale waterflooding did not emulate the results of the Humble pilot. Understanding the difference between this pilot and field-wide waterflooding is vitally important for improving waterflood performance in the Spraberry Trend Area.

The Humble pilot area is located in the west central portion of the Spraberry Trend Area. The pilot flood consisted of a single 80-acre five-spot. Four injection wells and one center producing well were completed in the Upper Spraberry sand.[23]

Oil Recovery. Oil recovery from the Humble pilot is presented in Fig. 2.5-12. Calculated imbibition oil recoveries using Eq. (2.18) are also plotted in Fig. 2.5-12. Matching was achieved using the same parameters presented in Table 2.5-2 except for a confinement factor of 40% and a fracture spacing of 0.6 ft.

Production Decline. The comparison between observed production rate and the production rate calculated with Eq. (2.19) is shown in Fig. 2.5-13. No further matching effort was made after oil recovery match. It can be seen from Fig. 2.5-13 that the observed production rate is significantly lower than the calculated production rate for the early time of waterflooding. This is probably due to low sweep efficiency during the early time of waterflooding. Figure 2.5-13 indicates an exponential decline rate of λ=0.08891 per month.

Discussion. The production decline rate of λ=0.08891 per month indicated by Fig. 2.5-13 is much higher than the long-term decline rate of λ=0.00357 per month in the E.T. O'Daniel Unit. Reasons for this discrepancy are not understood. It is speculated that one of the reasons is poor fluid confinement due to natural fractures. Some of the oil released from the rock matrix during water imbibition was probably washed out of the pilot area due to excess water injection. Quick response of water injection was observed in the wells out of the pilot area in the on-trend direction,[23] which tends to support this argument.

It is indicated by Eqs. (2.18) and (2.19) that oil recovery and oil production rate from the rock matrix are controlled by reservoir properties. Among these reservoir properties,

matrix permeability and fracture intensity have major influences on waterflood performance. In fact, comparison between the matching parameters shows that the major differences in achieving the match between the two waterfloods are matrix permeability and fracture spacing. Other properties such as matrix porosity, and water and gas saturations also affect oil rate performance. Since reservoir properties can not be altered during the waterflood, the best waterflood performance should be expected in areas of high permeability, high porosity, high fracture intensity, thick pay zones, and low water and gas saturations.

Conclusions

An integrated study of imbibition waterflooding in the naturally fractured Spraberry Trend Area reservoirs has been performed. The imbibition process was investigated both experimentally and analytically, and scaled-up to match reservoir performance. Based on experimental results and comparison to field data, the following conclusions can be drawn:

1. Water imbibition in Spraberry reservoir rock samples is significantly slower than that in strongly water-wet Berea sandstone samples after scaling with dimensionless time (t_D). This indicates that the Spraberry reservoir rock is not strongly water-wet.
2. The Spraberry Trend Area reservoir rock tends to be weakly water-wet with mixed-wetting behavior. The estimated average water-rock contact angle used in the scaling analysis is about 50 degrees. This value is fortified by imbibition, capillary pressure, and contact angle measurements.
3. Low rate water imbibition is the dominating mechanism for oil production during the waterflooding in the E.T. O'Daniel Unit and Humble pilot in the Spraberry Trend Area. The scaling model applied to the E.T. O'Daniel Unit and Humble pilot indicates that fracture spacing and matrix permeability may vary from area to area in the Spraberry Trend Area field.
4. The scaling model indicates that the best waterflood performance should be expected in areas of better permeability and porosity, high fracture intensity, thick pay zones, and low water and gas saturations.
5. Production decline models have been derived from a description of imbibition mechanisms. The decline models demonstrate exponential and hyperbolic (including harmonic) declines. A power-law type decline may exist in the case of very slow imbibition.

Nomenclature

I_w =Amott wettability index to water
k =permeability, md
k_a =air permeability, md
k_o =effective permeability to oil at initial water saturation, md
k_w =water permeability, md
L_c =characteristic length, ft

P_c =capillary pressure, psig
q_o =oil production rate, STB/day
R_{imb} =scaled imbibition oil recovery, dimensionless
R_{fld} =scaled waterflood oil recovery, dimensionless
t =time, day
t_D =scaled time, dimensionless
V =oil in place recoverable by imbibition, bbl
V_o =original oil in place recoverable by imbibition, bbl
V_p =oil recovered by imbibition, bbl
α =rate exponent, dimensionless
θ =contact angle, degrees
λ =rate coefficient in exponential decline, day^{-1}
μ_g =effective fluid viscosity (geometric average of water and oil viscosities), cp
σ =interfacial tension, mN/m
ϕ =porosity, dimensionless

References

1. Schechter, D.S., McDonald, P., Sheffield, T., and Baker, R.: "Reservoir Characterization and CO_2 Pilot Design in the Naturally Fractured Spraberry Trend Area," paper SPE 35469, presented at the SPE Permian Basin Oil & Gas Recovery Conference held in Midland, Texas, 27-29, March 1996.
2. Baker, R.O.: "Reasons for the Relatively Low Recovery of the Spraberry Waterfloods," PRRC Spraberry Database, June, 1996.
3. Guo, B. and Schechter, D.S: "Use of a Simple Mathematical Model for Estimating Formation Damage in Wells Intersecting Long Fractures," paper SPE 38178 presented at the 1997 SPE European Formation Damage Conference held in The Hague, The Netherlands, 2-3 June 1997.
4. Arps, J.J.: "Analysis of Decline Curves," paper T.P. 1758 in Petroleum Technology, AIME, September 1944.
5. Fetkovich, M.J.: "Decline Curve Analysis Using Type Curves," *JPT* (June 1980), pp. 1065-1077.
6. Laustsen, D.: "Practical Decline Analysis, Part 1 --- Uses and Misuses," *JCPT* (November 1996), pp. 34-38.
7. Baker, R.O.: "Practical Implications of Imbibition and Fracture Characterization to Spraberry Waterflood Operations," memorandum from the Epic Consulting Services Ltd., PRRC Spraberry Database, January 1997.
8. Elkins, L.F., Skov, A.M., and Gould, R.C.: "Progress Report on Spraberry Waterflood Reservoir Performance, Well Stimulation and Water Treatment and Handling," *JPT* (September 1968), pp. 1039-1049.
9. Gupta, A. and Civans, F.: "Correlation of the Imbibition Drive Matrix-to-Fracture Oil Transfer," paper SPE 28929 submitted for publication in the SPE Journal, January 30, 1996.
10. Schechter, D.S.: "Advanced Reservoir Characterization and Evaluation of CO_2 Gravity Drainage in the Naturally Fractured Spraberry Trend Area," First Annual

Technical Progress Report to DOE under Contract No. DE-FC22-95BC14942, PRRC Report 96-42, Dec. 17, 1996.
11. Honarpour, M.M., Huang, D.D., and Al-Hussainy, R.: "Simultaneous Measurements of Relative Permeability, Capillary Pressure, and Electrical Resistivity with Microwave System for Saturation Monitoring," paper SPE 30540, presented at the SPE Annual technical Conference and Exbibition held in Dalas, Texas, 22-25 October, 1995.
12. Reservoirs Inc.: "Oil-Water Capillary Pressure Data, Parker & Parsley E.T. O'Daniel No. 37 Well, Midland County, Texas," PRRC Spraberry Database, January 1997.
13. Parker & Parsley: "Upper Spraberry Capillary Pressure, Judkins A#5," PRRC Spraberry Database, July 1995.
14. Parker & Parsley: "Mercury Injection Capillary Pressure, Parker & Parsley Shackelford No. 1-38A Well, SRS 2097/RSH 3300A," PRRC Spraberry Database, June 1996.
15. Mattax, C.C. and Kyte, J.R.: "Imbibition Oil Recovery from Fractured, Water Drive Reservoirs," *SPEJ* (June 1962), pp. 177-184.
16. Ma, S., Zhang, X., and Morrow, N.R.: "Influence of Fluid Viscosity on Mass Transfer between Rock Matrix and Fractures," paper CIM 95-94, presented at the 46th Annual Technical Meeting of the Petroleum Society of CIM held in Banff, Alberta, Canada, May 14-17, 1995.
17. Baker, R.O.: "Parker & Parsley Waterflood Surveillance E.T. O'Daniel Unit," PRRC Spraberry Database, February 1997.
18. Baker, R.O. and Spenceley, N.K.: "Pre and Post Hydraulic Fracture Buildup tests on E.T. O'Daniel #37," Correspondence with Parker and Parsley, PRRC Spraberry Database, December 1996.
19. Lorenz, J.: "Summary of Observations and Interim Interpretations: Fractures in Horizontal Spraberry Cores, E.T. O'Daniel Well #28," PRRC Spraberry Database, Dec. 12, 1996.
20. Leverett, M.C.: "Capillary Behavior in Porous Solids," *Trans.* AIME (1941) **142**, 152-169.
21. Zhou, D. and Stenby, E.H.: "Immiscible Displacement in a Porous Medium Simulated by a Statistical Model. In: Buller et al. (Editors). North Sea Oil and Gas Reservoirs --- II. Graham and Tortman, London, UK, 271-280.
22. Schechter, D.S., Zhou, D., and Orr, Jr., F.M.: "Low IFT Drainage and Imbibition," *J. of Petroleum Science and Engineering*, 11 (1994), 283-300.
23. Barfield, E.C., Jordan, J.K., and Moore, W.D.: "An Analysis of Large-Scale Flooding in the fractured Spraberry Trend Area Reservoir," JPT (April 1959), 15-19.

Table 2.5-1 - Rock Properties and Conditions for Imbibition Experiments

Core No.	ϕ (%)	k_w (md)	S_{wi} (%)	Experimental Condition
SP-11	13.2	0.31	38	Ambient
SP-21	14.4	0.35	36	Ambient
SP-22	10.1	0.25	42	Ambient
SP-24	11.6	0.36	38	Ambient
SP-27	10.6	0.29	39	Ambient
SP-28	7.8	0.09	53	Ambient
SP-33	13.9	0.41	35	Ambient
SP-1	12.0	0.34	40	Ambient
SP-10*	14.3	0.45	32	Ambient
SP-H8	9.5	0.46	53	Ambient and 138°F
SP-H9	10.4	0.45	65	138°F
SP-R4	9.3	- - -	22	138°F
SP-R5	9.6	0.07	22	138°F
SP-H2	11.0	0.58	40	138°F/1040 psig
SP-H4	10.5	0.55	49	138°F/1040 psig
Average 11.2	0.35	40		

* Oil imbibition into a brine-saturated core

Table 2.5-2 - Reservoir Properties of the E.T. O'Daniel Unit, Spraberry Trend Area, West Texas

		Source
Total pay zone thickness, ft	20	Ref. 10
Matrix permeability, md	0.03	Ref. 18
Matrix porosity	0.11	Table 2.1
Initial water saturation	0.40	Table 2.1
Gas saturation after repressurization	0	Assumed
Advancing contact angle, degrees	50	Imbibition P_c
Effective fluid viscosity, cp	0.95	Ref. 10
Oil-water interfacial tension, mN/m	36	Ref. 10
Oil formation volume factor, rb/STB	1.2	Ref. 10
Efficiency of water imbibition, %	32	Imbibition P_c
Fracture spacing, ft	2.86	Ref. 19

Table 2.5-3 - Alternative Matching Parameters

Effective Matrix Permeability (md)	Fracture Spacing (ft)
0.03	2.86
0.06	3.40
0.12	4.05
0.24	4.81
0.36	5.32
0.48	5.72

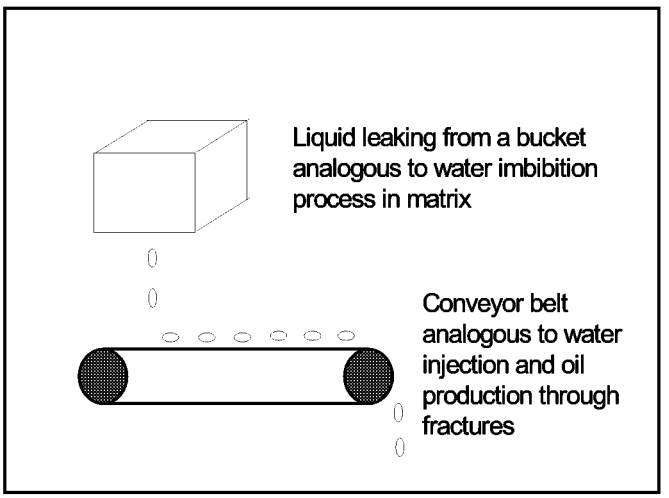

Fig. 2.5-1—An analogue model for imbibition waterflooding in naturally fractured reservoirs with spontaneous imbibition acting as the rate-limiting step

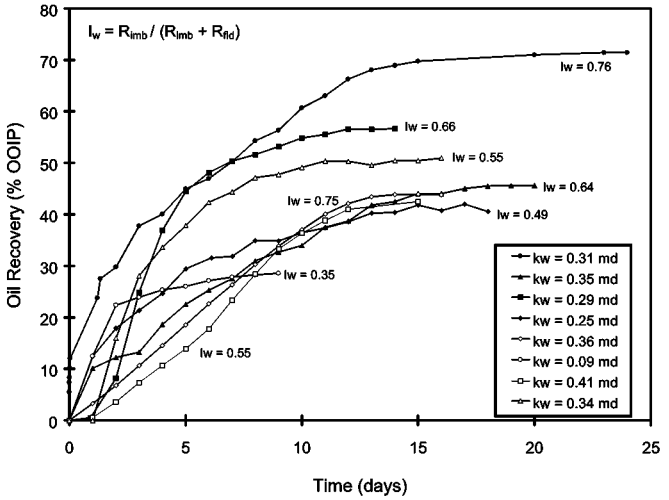

Fig. 2.5-2 —Oil recovery curves obtained from water imbibition under ambient conditions. Values of wettability index, I_w,, are shown for each experiment

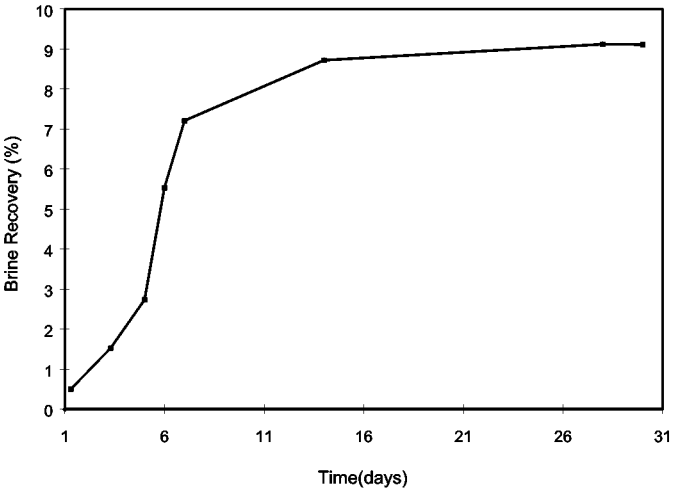

Fig. 2.5-3 —Brine recovery curve obtained during oil imbibition on a core sample from the Spraberry Trend Area

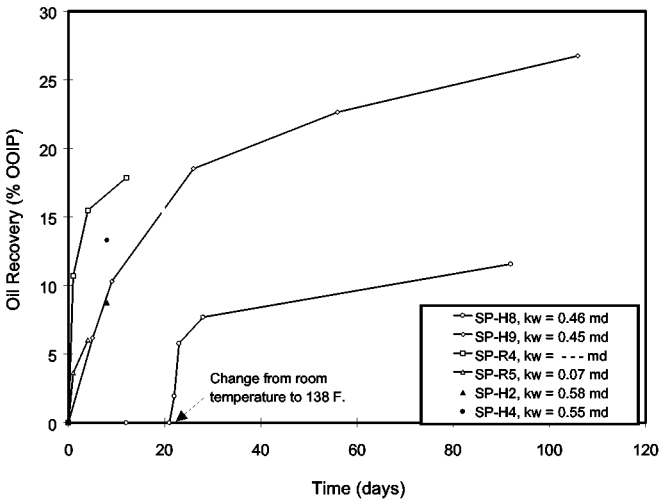

Fig. 2.5-4 —Oil recovery curves obtained from water imbibition under reservoir temperature and pressures. Experimental conditions are summarized in Table 2.5-1

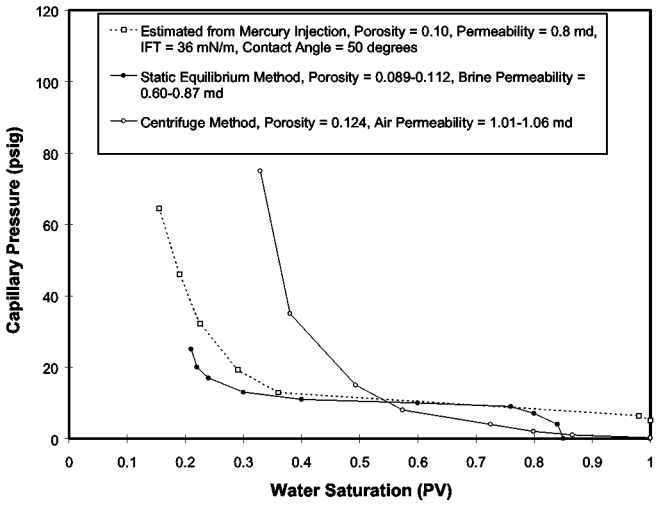

Fig. 2.5-5 —Comparison of drainage capillary pressure curves obtained using various methods for core samples from the Spraberry Trend Area

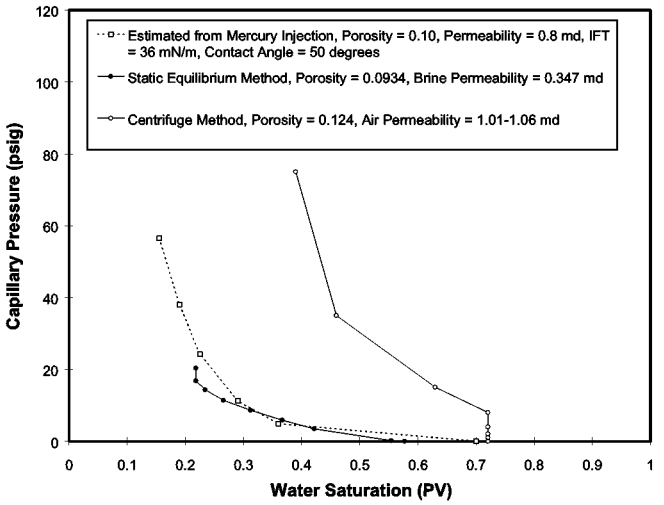

Fig. 2.5-6 —Comparison of imbibition capillary pressure curves obtained using various methods for core samples from the Spraberry Trend Area

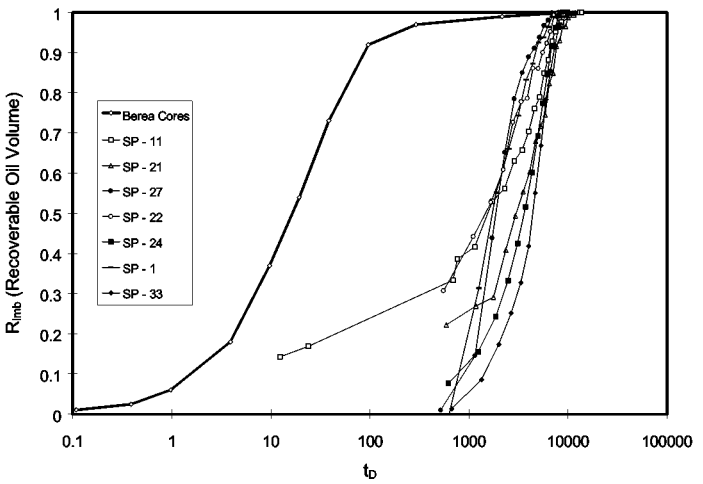

Fig. 2.5-7 —Oil recovery curves from Fig. 2.5-2 plotted using dimensionless variables and compared with a strongly water-wet composite curve measured from Berea cores

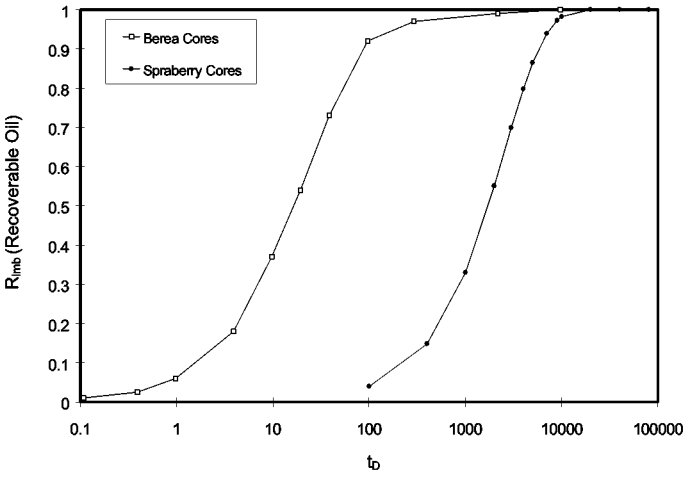

Fig. 2.5-8 —Comparison between composite imbibition oil recovery curves obtained from Berea sandstone and Spraberry Trend Area reservoir sandstone

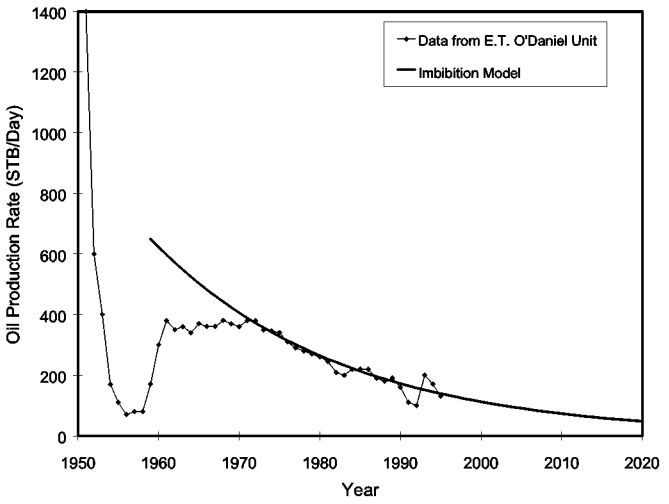

Fig. 2.5-9 — Match between imbibition scaling model and production decline data from the E.T. O'Daniel Unit, Spraberry Trend Area.

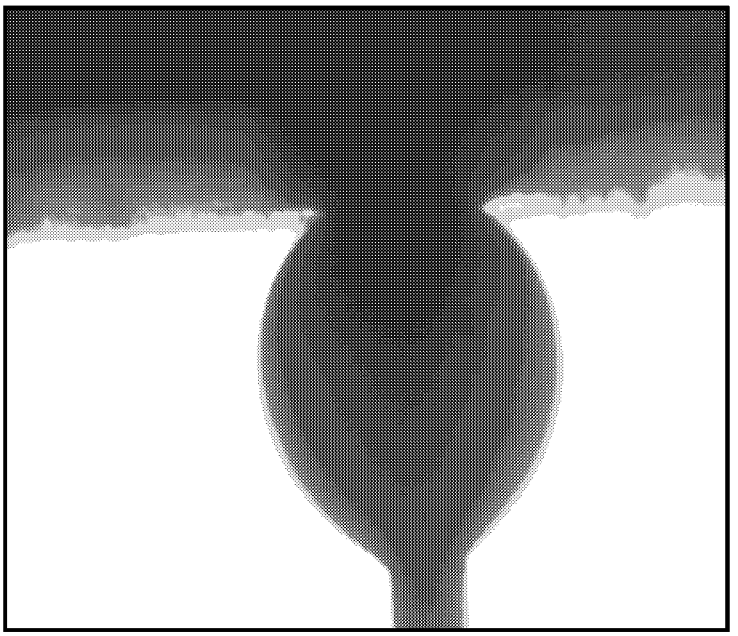

Fig. 2.5-10—A typical image of oil drop attachment during contact angle measurement.

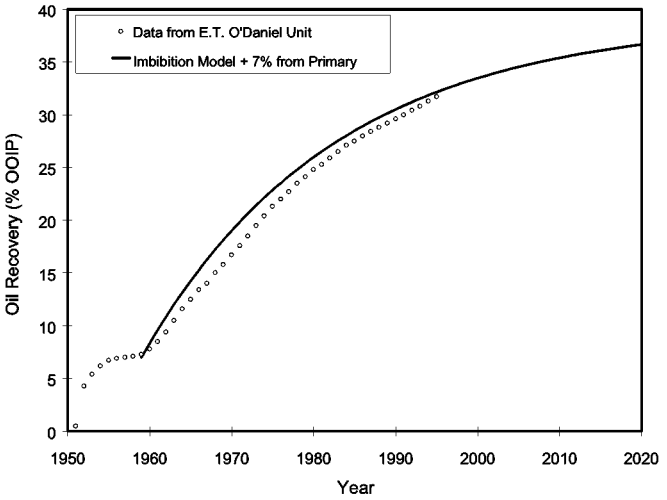

Fig. 2.5-11—Comparison between imbibition model calculated oil recovery and observed oil recovery from the E.T. O'Daniel Unit, Spraberry Trend Area

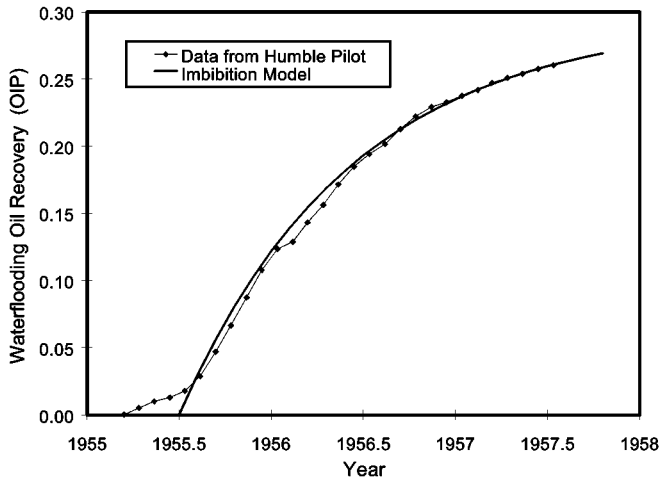

Fig. 2.5-12—Match between imbibition model calculated oil recovery and observed oil recovery from the Humble pilot, Spraberry Trend Area

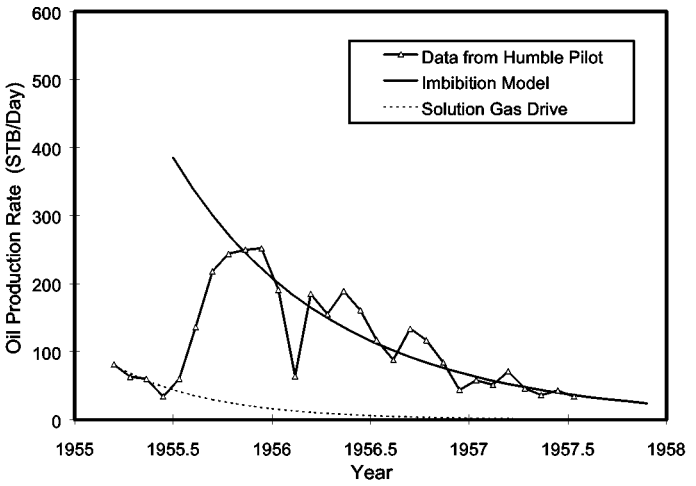

Fig. 2.5-13—Comparison between imbibition scaling model and production decline data from the Humble pilot, Spraberry Trend Area

2.6 Crude Oil/Brine/Rock Interaction at High-Temperature and Pressure Conditions

Introduction

As mentioned in the previous section, because data from imbibition experiments on reservoir rocks was both limited and inconsistent, it was difficult to draw conclusions regarding the effects of temperature and pressure on rock wettability and imbibition efficiency. In order to minimize uncertainties in the experiments and decrease investigation time, more experiments were conducted to verify the temperature and pressure effects using Berea cores.

Experimental results for Berea cores seem to indicate that elevated temperature increased the rate of water imbibition while rock wettability was not significantly affected. However, aging of cores in oil at different temperatures reduced the water imbibition rate and hence wettability to water to differing degrees. Increased pressure seems to slow down the water imbibition process. The experimental work has not been sufficient to date to draw a conclusion. This section presents the results of our experimental investigations on the effect of temperature and aging on water imbibition and rock wettability using Berea cores.

Core and Fluid Properties

Berea cores were utilized in this laboratory investigation. Dimensions and physical properties of the core plugs are presented in Table 2.6-1. Core porosity ranges from 0.16 to 0.21. Permeability to brine varies between 215 md and 243 md. Initial brine saturations ranging from 25% to 39% was achieved by displacing brine with oil.

Synthetic Spraberry brine was used in the experiments. It contains 122.7 g/L of N_aCl and 7.5 g/L of $C_aCl{\cdot}2H_2O$. Density, viscosity, and interfacial tension (IFT) with oil at room and reservoir temperatures are summarized in Table 2.6-2.

Spraberry separator oil was used in the investigation. Oil density, viscosity, and IFT with the brine at room and reservoir temperatures are summarized in Table 2.6-2. Density, viscosity, IFT and thermal expansion data at various temperatures are presented in Figs. 2.6-1, 2.6-2, and 2.6-3 respectively.

Experimental Results

Experimental procedures were similar to those described in Section 2.1 except that the core cleaning process using chloroform was not necessary for Berea cores and the oil injection pressure was 10 to 12 psig. Results of the investigations with Berea are presented hereafter.

Effect of Temperature

Presented in Fig. 2.6-4 are oil recovery curves obtained from brine imbibition tests conducted at room and reservoir temperatures. It is seen that elevated temperature increased the rate of brine imbibition but did not change the final recovery. The reason

may be that the reduced oil viscosity at high temperature made the oil easily displaced by brine.

Effect of Pressure

A brine imbibition test was conducted under room temperature and 1,200 psig in a pressure vessel. Oil recovered from the core was displaced from the vessel periodically and the recovered oil volume was recorded. The oil volume was utilized to determine oil recovery during the experiment. The calculated oil recovery curve is plotted in Fig. 2.6-5 and compared with recovery curves shown in Fig. 2.6-4. It is seen from Fig. 2.6-5 that the oil recovery rate at 1,200 psig is much lower than that at room pressure. One of the possible explanations is that the oil recovered from the core was not fully washed out from the pressure vessel. Another possible reason is the increased oil viscosity due to elevated pressure, although this effect is not likely to be significant. More experiments are being performed to resolve this conflict.

Effect of Aging

The effect of aging in oil before brine imbibition was investigated using two Berea cores. One core was aged for 6 hours at room temperature, the other was aged for 6 hours at 138°F. Oil recovery curves during brine imbibition for the two cores are compared with that obtained without the aging process in Fig. 2.6-6. This comparison indicates that aging at room temperature caused reductions in both imbibition rate and final oil recovery. However, aging at the reservoir temperature of 138°F caused a reduction in the imbibition rate. It appears that aging caused the rock surface to become less water-wet for one core. However, these inconsistent results made it difficult to draw a quantitative conclusion. In order to quantitatively characterize the effect of aging on rock wettability, oil imbibition experiments were run with the same cores after termination of brine imbibition tests. Wettability index to water (I_w), index to oil (I_o) and Amott-Harvey wettability index (I_{w-o}) were determined. The results are shown in Table 2.6-1. These data are also inconclusive regarding the effect of aging on rock wettability.

The effect of aging in oil on wettability was also investigated using the standard adsorption method developed by a group of researchers[1,2] at the New Mexico Petroleum Recovery Research Center. Advancing and receding contact angles of a Muscovite Mica/Spraberry brine/Spraberry oil system were measured at different aging conditions. The results are summarized in Table 2.6-3. It is seen from the table that aging at 60°C for one day increased contact angles, while aging at the same temperature for 21 days made the contact angles lower. These data are again inconclusive regarding the effect of aging time and temperature on rock wettability.

Effect of Initial Water Saturation

Imbibition experiments were performed using Berea cores with different initial water saturations. The oil recovery curves are plotted in Fig. 2.6-7. This figure appears to indicate that water imbibition rates are higher in cores with higher initial water saturations during the early time of the experiments. To eliminate the inconsistencies due to other factors, these oil recovery curves are normalized and plotted in Fig. 2.6-8 using

dimensionless time (t_D) defined by Eq. (2.15) assuming zero contact angle in the water phase. It is seen from Fig. 2.6-8 that the water imbibition rate increases with initial water saturation for initial water saturations between 25% and 39%.

Summary

Water and oil imbibition experiments were conducted using Berea cores, synthetic reservoir brine, and reservoir oil under elevated temperatures and pressure. Water imbibition rate increased with temperature and decreased with pressure. While aging of cores in crude oil caused the rate of water imbibition to decrease, its effect on rock wettability was not fully evidenced due to a limited amount of data.

References

1. Buckley, J.S. and Morrow, N.R.: Characterization of Crude Oil Wetting Behavior by Adhesion Tests," paper SPE/DOE 20263 presented at the 1990 SPE/DOE EOR Symposium held in Tulsa, OK, April 23-25.
2. Liu, Y. and Buckley, J.S.: "Evolution of Wetting Alteration by Adsorption from Crude Oil," paper SPE 28970 presented at the 1995 International Symposium on Oilfield Chemistry held in San Antonio, TX, Feb. 14-17, 1995.

Table 2.6-1 —Summary of Results of Imbibition Experiments with Berea Cores and Spraberry Fluids

Core No.	d	L	ϕ	k_w	S_{wi}	S_{or}	R_{total}	I_w	I_o	I_{w-o}
	(cm)	(cm)		(md)			(OOIP)			
B-A5*	3.60	5.16	0.16	236	0.33	0.44	0.34	1.00	0.29	0.71
B-A6	3.60	4.97	0.21	227	0.39	0.40	0.34	1.00	0.20	0.80
B-A7	3.79	4.65	0.19	215	0.39	0.41	0.33	1.00	0.17	0.83
B-A8	3.79	4.93	0.18	228	0.41	0.24	0.60	1.00	0.13	0.87
B-A9	3.80	4.91	0.17	226	0.37	0.42	0.33	1.00	0.23	0.77
B-A10	3.79	5.46	0.19	225	0.36	0.45	0.30	1.00	0.20	0.80
B-A11	3.80	6.17	0.20	233	0.25	0.40	0.47	0.98	0.41	0.57
B-A12	3.80	6.19	0.19	233	0.33	0.36	0.47	1.00	0.35	0.65
B-A13	3.79	6.41	0.17	243	0.31	0.23	0.66	0.99	0.38	0.61

* Note: Imbibition test was performed at room temperature for core B-A5. Imbibition tests were performed at 138°F for the rest of cores.

d = diameter; L = length; ϕ = porosity; k_w = permeability to brine; S_{wi} = initial brine saturation; S_{or} = residual oil saturation after brine imbibition; R_{total} = total oil recovery after waterflood; I_w = wettability index to water; I_o = wettability index to oil; I_{w-o} = Amott-Harvey wettability index.

Table 2.6-2 —Properties of Fluids Used in the Experiments

Fluid Property	Temperature (°F)	Brine	Crude Oil
Viscosity (cp)	75	1.184	10.380
	138	1.170	7.930
Density (gr/cc)	75	1.091	0.870
	138	1.076	0.834
Interfacial Tension (mN/m)	75	30.75	
	138	24.13	

Table 2.6-3 — Contact Angles Measured Using Standard Adsorption Method for a Muscovite Mica/Spraberry Brine/Spraberry Oil System

Aging Time (days)	Aging Temperature (°C)	Advancing Angle (Deg.)	Receding Angle (Deg.)
1	Room Temp.	22	16
1	60	40	19
21	Room Temp.	34	20
21	60	24	17

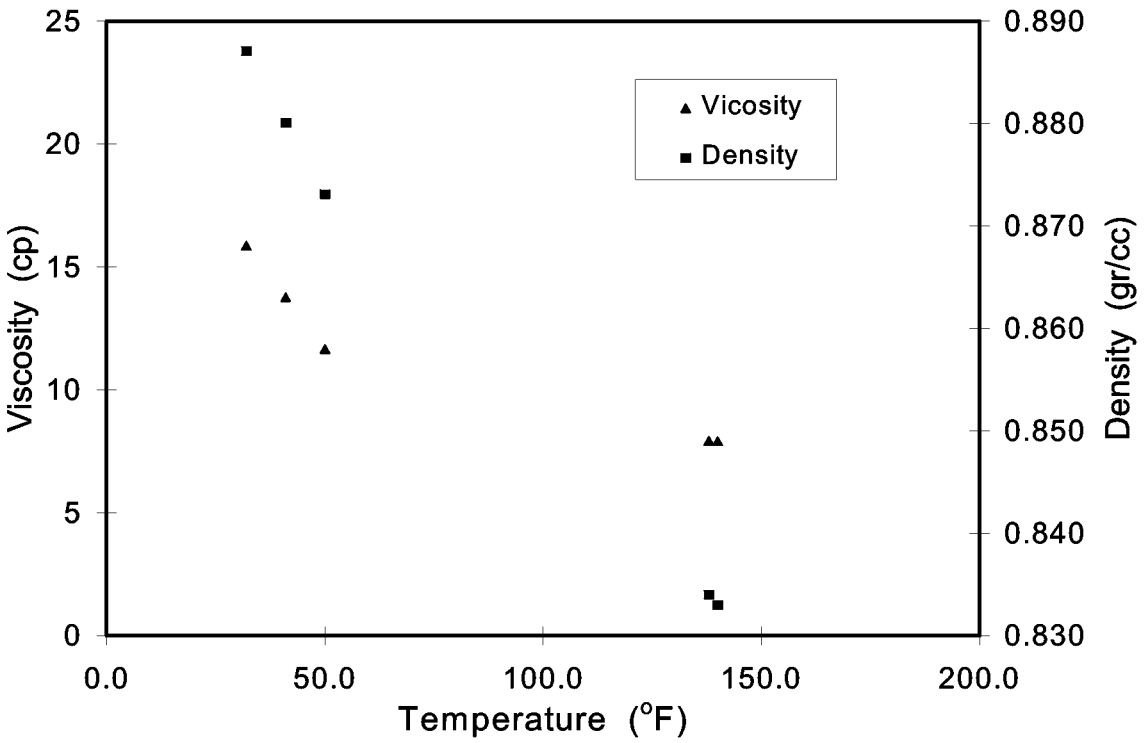

Fig. 2.6-1 —Density and viscosity of Spraberry crude oil versus temperature

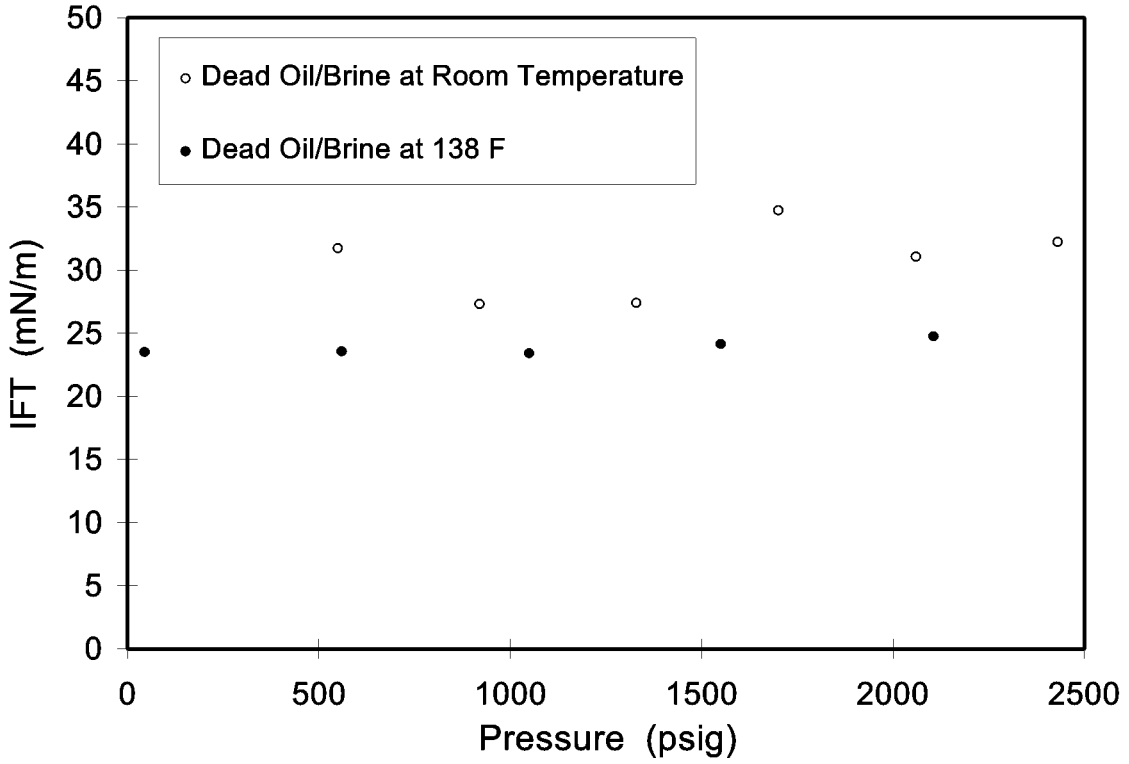

Fig. 2.6-2 - IFT of Spraberry brine/cruide oil at elevated pressures

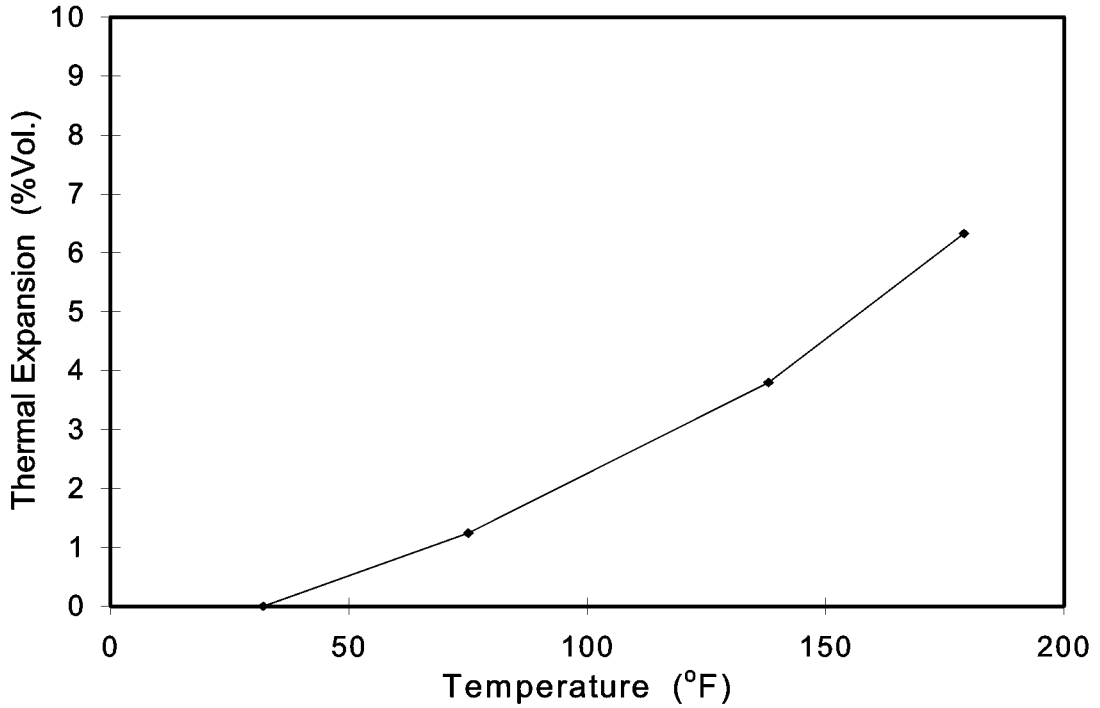

Fig. 2.6-3 —Thermal expansion of Spraberry crude oil

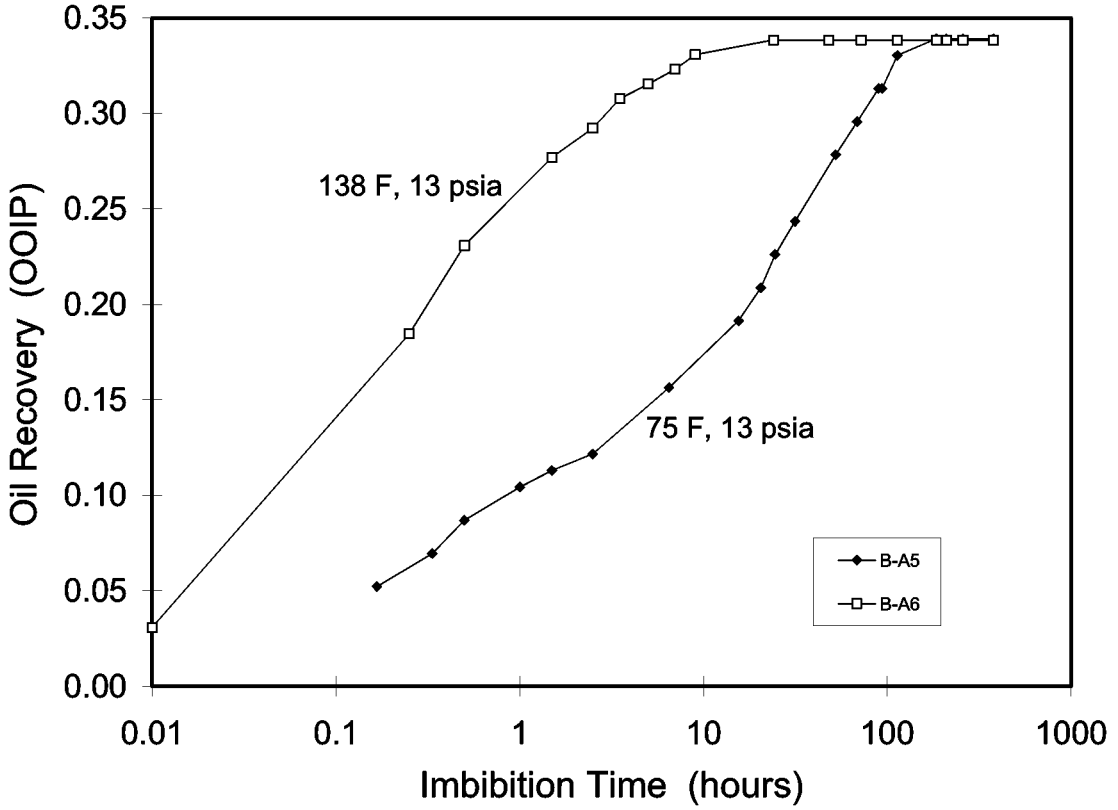

Fig. 2.6-4 —Imbibition oil recovery at different temperatures

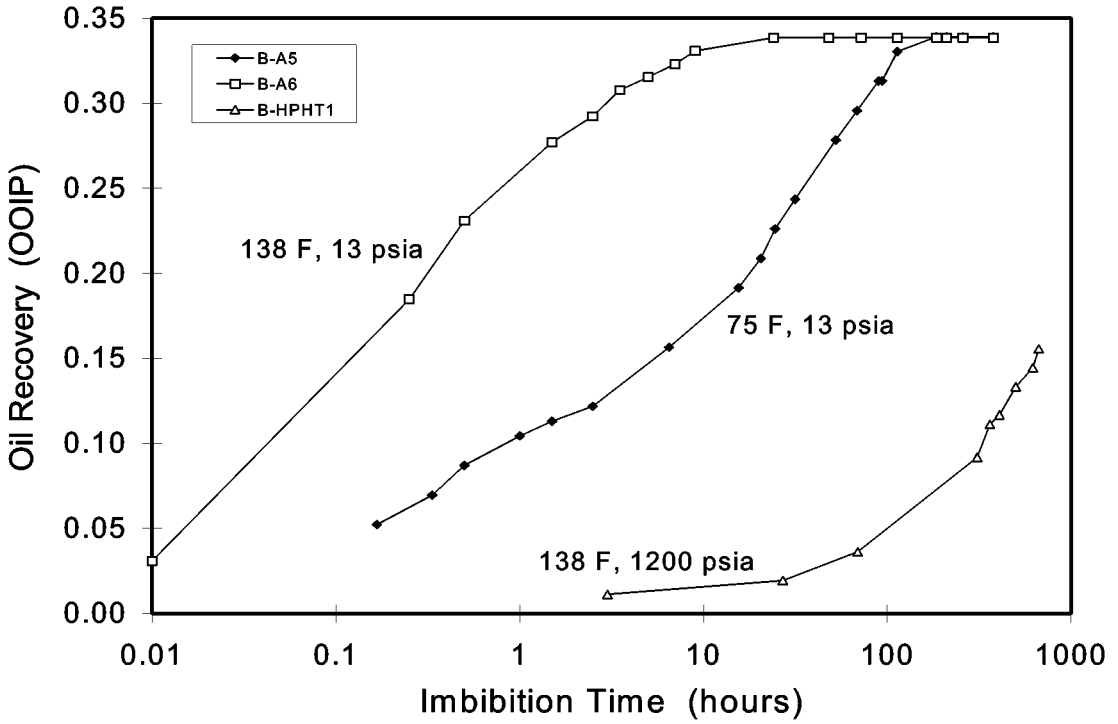

Fig. 2.6-5 — Imbibition oil recovery at different pressures

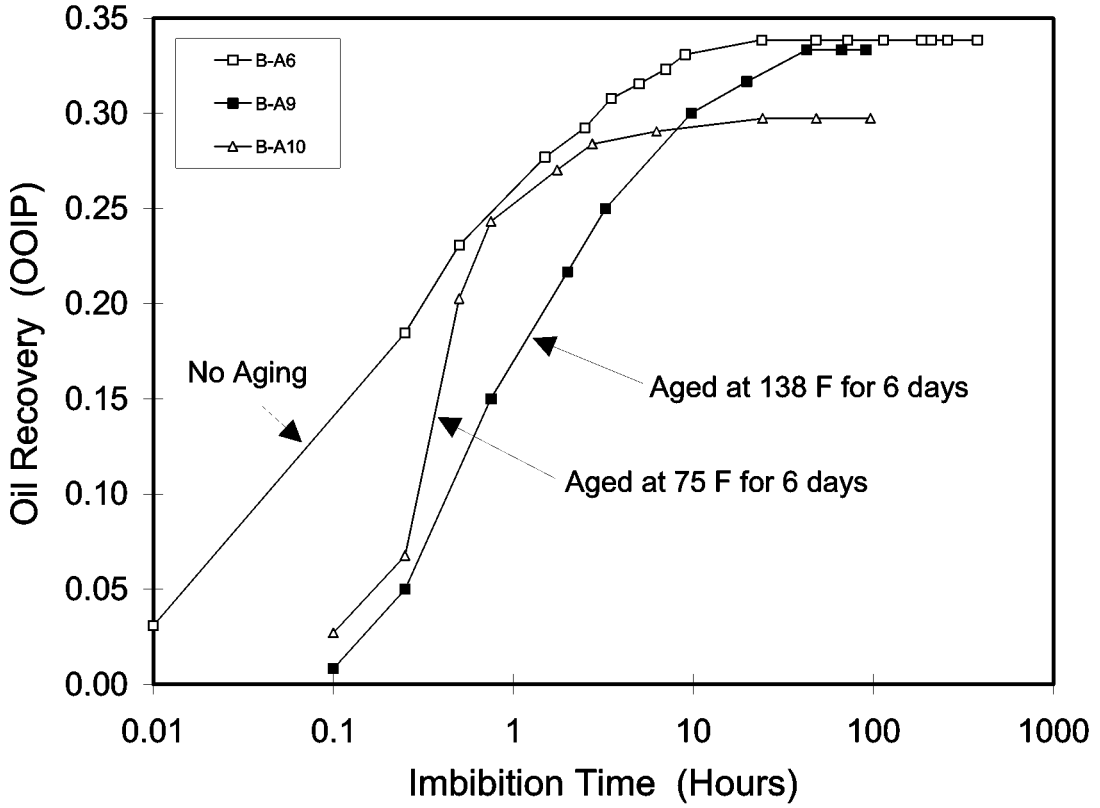

Fig. 2.6-6—Imbibition oil recovery under different aging conditions

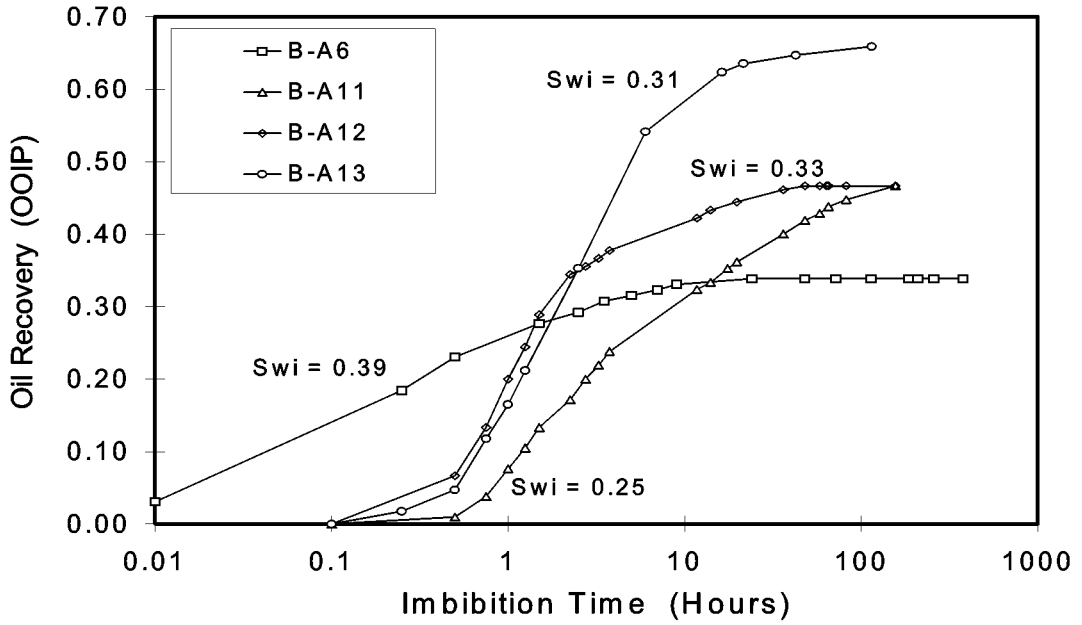

Fig. 2.6-7 — Imbibition oil recovery from Berea cores with different initial water saturations without core aging.

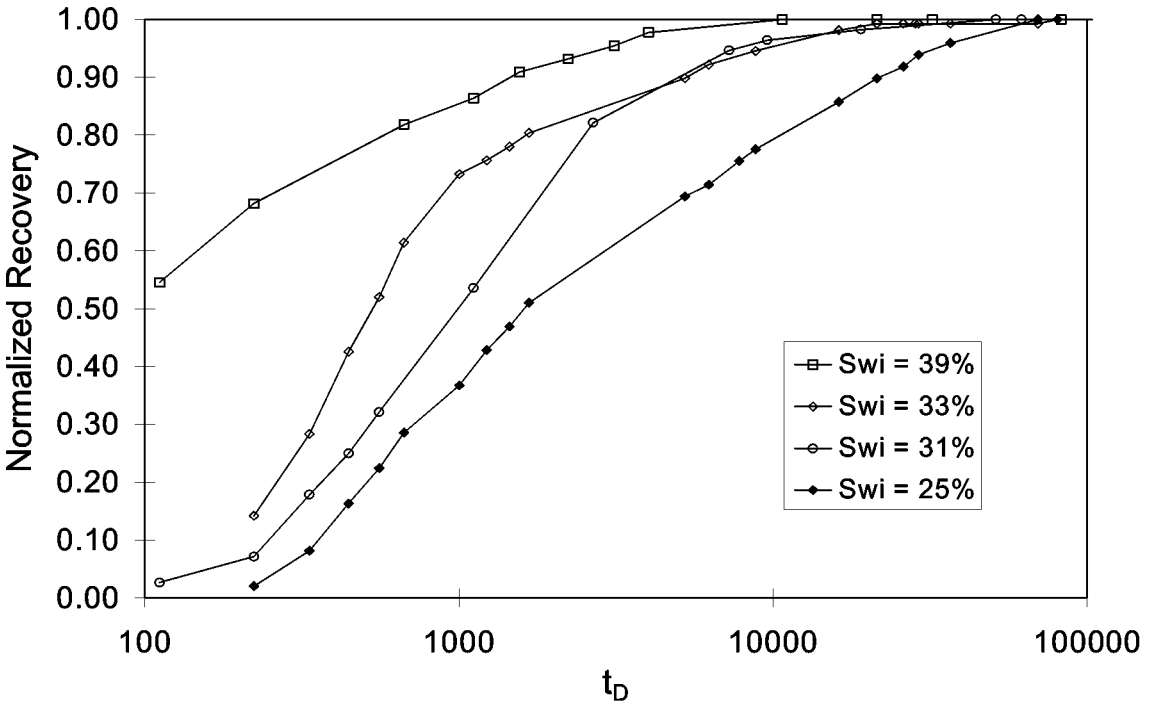

Fig. 2.6-8 - Normalized imbibition oil recovery curves from cores with different initial water saturations without core aging

2.7 EXPERIMENTAL STUDY OF CRUDE/BRINE/ROCK INTERACTION AT RESERVOIR CONDITIONS

Introduction

In the previous section, the fluid/rock interactions were described from a geological/petrophysical perspective. We further define this interaction in this section and expand the understanding of the interactions of the Spraberry reservoir rock, oil and brine. Spraberry rock-wetting behavior was determined by performing water imbibition experiments. The experiments used Spraberry oil, synthetic reservoir brine and Spraberry core at reservoir temperature (138°F). This section presents the experimental results on the effect of temperature and aging on brine imbibition, brine displacement and rock wettability using low permeability Spraberry cores.

A schematic of the experimental program is presented in Fig. 2.7-1. Briefly, the water imbibition rate was found to increase with temperature and the ultimate recovery was also affected by the temperature condition, becoming higher as the temperature increased. The aging of low permeability cores saturated with oil had little effect in the rate of imbibition or oil production rate, particularly after seven days or more aging time with oil. However, the ultimate oil recovery after 21 days of imbibition decreased with the increase in aging time. Increasing the temperature during the brine displacement process appears to increase the displacement recovery.

The experimental data under reservoir conditions also confirm that the Spraberry reservoir rock are weakly water-wet with an Amott wettability index to water of 0.24 to 0.35, depending on the temperature of the brine during displacement. Heterogeneity in rock properties, such as initial water saturation and permeability of the cores used in the experiment, causes less influence than the aging time on the recovery mechanism.

Experimental Material

Core samples. The reservoir cores used in this study were core plugs prepared from 4-in. diameter cores taken from the Spraberry Shackelford Unit 1-38. The cores were cut to 3.80 cm in diameter and about 5.10 cm in length. The air permeabilities of the Spraberry cores were measured, varying from 0.1 to 1.5 md and the porosity ranged from 9.5 to 12%. The absolute permeabilities to brine ranged from 0.10 to 0.51 md.

A traditional toluene Dean-Stark extraction method was used to clean the very tight core samples from the Spraberry formation. The method removes water and light components by raising the temperature of the core and boiling off the light end components. To ensure the core sample is sufficiently clean, injecting chloroform into the core sample under a pressure of 200 psi until the output of the chloroform was clear followed this step. The Spraberry cores were heated in an oven at 100°C for at least two days to dry completely. After cleaning the core porosities were determined to be about 10%, and the absolute permeabilities to brine ranged from 0.10 to 0.33 md. The physical properties of the reservoir core samples after cleaning are presented in Table 2.7-1.

Brine composition. Synthetic Spraberry brine was used in the experiments and was prepared by dissolving NaCl and $CaCl_2$_$2H_2O$ in distilled water. The brine composition is shown in Table 2.7-2. The viscosity and density of the synthetic brine at elevated temperature are presented in Fig.2.7-2 and Fig.2.7-3, respectively.

Oil samples. Spraberry dead oil is used in the investigation. Table 2.7-3 (as given by Chang and Buckley (1997)) summarizes the physical and chemical properties of the oil samples. The composition of the sample, determined by gas chromatography analysis, is listed in Table 2.7-4 (Siagin, 1997). The viscosity of Spraberry oil was determined using a Cannon-Fenske routine viscometer and the density was determined using a digital density meter. The plots of oil viscosity and density at elevated temperature are shown in Fig. 2.7-4 and Fig. 2.7-5, respectively. The interfacial tensions (IFT) of the oil/brine system was also measured using a pendant drop instrument and de Nouy Ring (see Fig. 2.7-6). The plot of IFT at different elevated temperature is presented in Fig. 2.7-7. Both methods show agreement in the measured IFT at room and reservoir temperature. However, pressure is shown to influence the IFT little if any at all. In addition, the volumetric expansion with temperature increase was also measured and is shown in Fig. 2.7-8.

Experimental Procedures

Saturating Spraberry Core with Brine. The dry core sample was weighed on a balance after measuring its air permeability. The core sample was then saturated with deaerated brine, using a vacuum pump, for 24 hours. Porosity and pore volume (PV) were determined from the dry and saturated weights of core samples, from bulk volume, and from brine density. After saturating the core samples with brine, a period of about three days was allowed for the brine to achieve ionic equilibrium with the rock. The core sample was then inserted into a Hessler core holder. A confining pressure of 500 psig was used to measure the core's absolute permeability to brine.

Saturating the Core with Oil. The core sample was saturated with oil by flowing oil through the core confined in a Hassler core holder with a confining pressure of 500 psig. The oil was injected into a brine-saturated core to establish initial water saturation. Injection was stopped after 2 to 5 PV oil effluent from the core. The lowest initial saturation achieved was 32%.

Aging Procedure. In an oil reservoir, the adsorption equilibrium between the rock surface and the oil is established over geologic time of the rock-oil system. In an effort to restore the adsorption equilibrium, the Spraberry core samples were aged prior to each of the imbibition tests by saturating and immersing the core samples in an oil bath at the reservoir temperature (138°F) for a certain period of time. To investigate the effect of adsorption equilibrium level on the imbibition process, the aging period was varied from zero to thirty days.

Spontaneous Imbibition Test. The spontaneous imbibition experiments were performed using the imbibition apparatus schematically shown in Fig. 2.7-9. As can be seen from this figure, the apparatus basically is a simple glass container equipped with a graduated

glass cap. To perform an imbibition test, a core sample was immersed in the glass container filled with preheated brine solution. The container was then covered with the graduated cap. After fully filling the cap with brine solution, the container was then stored in an air bath that had been set at a constant temperature of 138°F. Due to capillary imbibition action, oil was displaced from the core sample by the imbibing brine. The displaced oil accumulated in the graduated cap by gravity segregation. During the experiment, the volume of produced oil was recorded against time. Before taking the oil volume reading, the glass container was gently shaken to expel oil drops adhering to the core surface and the lower part of the cap so that all of the produced oil accumulated in the graduated portion of the glass cap. At an early stage of the test the oil volume was recorded every half-hour while toward the end of the test the oil volume reading was made every 24 hours. Excluding the core preparation, one series of tests was usually completed within 21 days.

Brine displacement. After the spontaneous imbibition in brine was completed, the core sample was subjected to forced displacement by water using a pressure ranging from 120 to 200 psi depending on the wetting condition. The injections were performed under room and reservoir conditions. At the conclusion of the imbibition test under reservoir temperature, the core and apparatus was cooled several hours to achieve an equilibrium temperature before brine displacement under room temperature performed. Brine displacement was performed under reservoir condition. Once the imbibition test was stopped, the core was flushed by preheated brine right away. The amount of oil produced was used to determine the wettability index for water (I_w).

Results and Discussion

In considering the spontaneous imbibition experiments performed under reservoir conditions, a series of imbibition experiments were performed at reservoir temperature (138°F) and elevated pressure (13.5 psi and 1000 psi). Berea sandstone cores were used in this experiment to verify the effect of pressure on the imbibition process. During spontaneous imbibition more oil is recovered using a homogeneous and high permeability porous medium, as would be expected. The results as presented in Fig 2.7-10 shows that changes in pressure give small effects on imbibition rate and recovery. An additional imbibition reference recovery curve for very strongly water-wet conditions is also plotted in Fig. 2.7-10. Performing a spontaneous imbibition experiment under reservoir temperature using refined oil (Soltrol-130) generated the reference curve. This behavior has also been confirmed by previous studies (Mugan, 1972; Hjelmeland, 1986, Anderson, 1986; Cuiec, 1995). The temperature effects shown in Fig 2.7-11 are considered more critical to imbibition than the pressure effects.

Effect of Temperature on Spontaneous Imbibition

A series of experiments were run to investigate the effect of temperature on spontaneous imbibition using a volumetric method. Four Spraberry cores were used to investigate the effect of temperature during imbibition tests. Two of these cores were prepared for spontaneous imbibition under reservoir temperature (138°F). The other two cores were prepared for spontaneous imbibition under ambient conditions (70°F). All cores were established at almost the same initial water saturation of about 34%. The preparations to

establish initial water saturation were made at room temperature condition and the cores were not aged in oil for this test.

During the test sequences, the distinction between the aging temperature (T_a), the imbibition temperature (T_{imb}), and the displacement temperature (T_d) is necessary. The aging temperature is the temperature condition applied when the core is aged in oil. The imbibition temperature is the temperature condition when spontaneous imbibition is performed. Finally, the displacement temperature is applied during brine displacement after the imbibition test is conducted.

The effect of temperature on the rate of brine imbibition in low permeability Spraberry cores is presented in Fig. 2.7-12. Two measurements were carried out for each temperature condition and good reproducibility is indicated in Fig. 2.7-12. The results demonstrate that during the process of brine imbibition into low permeability core the water is imbibed by the rock quicker at reservoir (elevated) temperature than at room temperature. The ultimate recovery is also affected by temperature. Higher ultimate recovery can be expected if the temperature is increased with all other parameters remaining constant. These results agree with previous studies (Handy, 1960; Anderson (1986); Reis (1990); Babadagli, 1995; Tang, G.Q., et al., 1996). Handy stated that the rate of imbibition increased with an increase in temperature due to oil/water interfacial tension, oil viscosity and water viscosity. This is true if the contact angle is not affected by changes of temperature. In addition, based on the surface physical chemistry (Anderson, 1986), an increase in temperature tends to increase the solubility of wettability-altering compounds and desorb from the surface. A decrease in the viscosity ratio of oil and water due to increasing temperature result in oil being displaced more easily and the ultimate recovery being improved.

A sensitivity test of the imbibition mechanism to temperature was performed. After oil recovery ceased at the end of the imbibition test performed under ambient temperature, the experiment temperature was changed to reservoir temperature (see Fig. 2.7-13). As indicated in Fig. 2.7-13, changing the temperature from ambient to reservoir results in a dramatic increase in the rate of spontaneous imbibition, just as was shown in the Berea core in Fig. 2.7-11. The increase in imbibition rate results in an improvement in recovery. The result approaches the ultimate recovery for imbibition under reservoir temperature since the beginning of the test.

According to Tang (1996), in contrast to the large change in imbibition recovery for crude oil, increasing the temperature during the course of imbibition had essentially no effect on refined oil. Therefore, the crude oil/brine/rock interactions are responsible for the dramatic increase in oil recovery with temperature increase rather than changes related to the rock properties alone. Dangerfield, et al, (1985) performed a similar study using chalk core samples and the results were comparable. Changes in temperature using refined oil was not verified in this study.

Effect of Aging Time

The effect of aging commencement of the imbibition process was investigated using 11 cores aged in oil at 138°F. The aging time varied from 0 to 30 days. For comparison two cores were not aged in oil. Oil recovery from spontaneous imbibition tests plotted against time in hours shows that the rate of imbibition for cores without aging is faster than that for the aged cores (see Fig. 2.7-14). Slightly different imbibition rates at the beginning of the imbibition test are observed for Spraberry cores aged from seven to 30 days. However, oil recovery after 21 days of imbibition decreases substantially from 15% to 10% IOIP with increase in aging time for no aging to 30 days of aging (Fig. 2.7-15). A more representative reservoir condition is obtained when the Spraberry core is aged before the imbibition test under reservoir temperature.

The effects of aging become less important to the recovery mechanism if forced imbibition or brine displacement takes place after spontaneous imbibition. Figure 2.7-16 shows a plot of total recovery (i.e., recovery after imbibition plus recovery after brine displacement) versus aging time. The total oil recoveries appear to remain constant for core aged more than seven days. For the Spraberry, a reasonable time to start the brine imbibition and displacement test is after the core has aged in oil at reservoir conditions for at least seven days.

Effect of Temperature on Brine Displacement

After imbibition tests, all core plugs were displaced by brine. As shown in the experimental program presented in Fig. 2.7-1, brine displacements were performed under two different temperatures (i.e. room and reservoir temperature). Total recovery (recovery after imbibition plus recovery after brine displacement) versus aging time at elevated temperatures during the displacement process is shown in Fig. 2.7-17. The total recoveries for Spraberry cores aged more than seven days and flooded by brine at room temperature after imbibition at reservoir temperature remained constant at an average of about 35% IOIP. When brine displacement was performed at reservoir temperature, the total oil recoveries improve to 65% IOIP for Spraberry cores with and without aging in oil. Increases in temperature during the brine displacement process appear to increase the displacement recovery, thus significantly increasing total recovery. Also evident is that total recovery of 44% after brine imbibition and displacement occurred at room temperature, with no aging effect from Spraberry cores tested under this condition.

Wettability Index

The wettability index is determined on the basis of oil recovery by imbibition and from brine
displacement. The relationship is expressed as:

$$I_w = \frac{R_{imb}}{R_{imb} + R_{bf}} \quad \text{.....2.21}$$

where R_{imb} is oil recovery by imbibition and R_{bf} is oil recovery by brine displacement flooding. A high index indicates a more water-wet system, a lower index indicates a less

water-wet rock.

A plot of wettability index to brine versus aging time for brine displacement at different temperatures is shown in Fig. 2.7-18. This figure shows that the wettability index is about 0.35 for brine imbibition at reservoir temperatures with brine displacement at room temperature. The wettability index is 0.24 for brine imbibition and displacement both at reservoir temperature. This result can be explained as the effect of the low viscosity ratio between oil and brine at high temperatures. As the temperature rises, the viscosity ratio of oil to brine decreases. The decrease in viscosity at higher temperatures is much greater for oil than that for brine. Thus, an increase in temperature can result in a substantial decrease in viscosity ratio of oil to brine.

When brine is injected to displace oil at high temperature, a decrease in the viscosity ratio of oil and water due to increasing temperatures results in oil being recovered more easily from the core and produces an improvement in the ultimate recovery, due to the higher temperature brine displacement. As observed previously, the oil recoveries after brine imbibition decreased corresponding to longer aging time. If the oil recovery resulting from brine displacement experiments performed at reservoir temperatures is higher than the recovery with brine at room temperatures, then the wettability index will be lower. As a comparison, Fig. 2.7-18 also shows the plot of the wettability index versus aging time for both brine imbibition and displacement at room temperature. Without aging the cores in oil, the wettability index is about 0.22. This low value is due to low oil recovery obtained with brine imbibition. This result is close to the wettability index for brine imbibition and displacement both at reservoir temperatures.

Heterogeneity in Rock Properties

The initial water saturation and permeability of different low permeability Spraberry cores were not the same. The effects of initial water saturation and core permeability on the recovery mechanisms are also needed. Initial water saturations were found to vary over a range of 32% to 43%, due to the difficulty of establishing constant values for initial water saturation in a low permeability matrix. The initial water saturations of these cores do not provide a great enough variance to conclusively state the initial water saturation does not have an effect on the recovery. However, the initial water saturation data in this experiment does indicate for the range under discussion that both imbibition and total recovery are affected only slightly if at all by the initial water saturations in these cores (see Fig. 2.7-19 and 2.1-20). If the initial water saturations have a great enough variance or range then an increase in initial water saturation will decrease capillary pressure, which results in a decrease of the ultimate oil recovery. Cores used in this study have variable permeabilities, which ranged from 0.1 to 0.5 md. To investigate the effect of core permeability on the recovery mechanism, oil recoveries from imbibition were plotted against permeability as shown in Fig. 2.7-21. The results show that the imbibition recoveries were slightly affected by core heterogeneity. Total recovery values indicate no effect by heterogeneity (Fig. 2.7-22). In summary, the results show that aging time has a large influence on imbibition recovery with permeability affecting the imbibition recovery slightly.

Conclusions

1. This study using Spraberry oil, brine and Berea sandstone shows that the effect of pressure is much less important than the effect of temperature.
2. Low permeability Spraberry core imbibes water more readily at higher temperature (i.e. reservoir temperatures).
3. Ultimate recovery is higher at greater temperatures (i.e. reservoir temperature).
4. Spontaneous imbibition rate is increased at higher temperature resulting in higher ultimate recovery.
5. This study using Spraberry crude oil shows temperature to have substantial effect on recovery mechanism.
6. The oil/brine/rock interactions are responsible for dramatic increase in oil recovery with temperature rather than changes to rock properties alone.
7. A more representative reservoir condition is obtained when the core is aged at reservoir conditions before the imbibition test is performed.
8. Oil recovery by imbibition decreased from 15% of IOIP at no aging to 10% of IOIP after 30 days of aging.
9. Aging become less important to recovery if forced imbibition or displacement is to be used.
10. The wettability index at reservoir temperature is 0.24 indicating the Spraberry to be a very weakly water-wet rock.
11. Wettability index does not appear to be affected by aging time at reservoir temperature.
12. Higher permeability increases the imbibition recovery slightly. The permeability range used in these experiments does not affect total recovery.

References

1. Anderson, G. W., "Wettability Literature Survey- Part 1 : Rock/Oil/Brine Interaction and the Effects of Core Handling on Wettability," *JPT*, (Oct. 1986).
2. Babadagli, T., "Temperature Effect on Heavy-oil Recovery by Imbibition in Fractured Reservoirs," *Journal of Petroleum Science and Engineering* 14 (1996), 197-208.
3. Chang, V., and Buckley, J.S., "COBR Interaction of Some Medium Gravity Crude Oils," PRRC internal report, PRRC 98-4 (1997).
4. Cuiec, L., "Wettability Laboratory valuation Under Reservoir Conditions: A New Apparatus," paper 9529 presented at the 1995 SCA, Calgary.
5. Dangerfield, J.A., and Brown, D.A., "The Ekofisk Field," North Sea Oil and Gas Reservoirs, J. Klepe et al (eds.), Graham and Trotman, London (1985).
6. Handy, L.L., 1960, "Determination of Effective Capillary Pressure For Porous Media from Imbibition Data," Petroleum Transaction of AIME, 219, p. 75.
7. Hjelmeland, O.S. and Larrondo, L.E., "Experimental Investigation of the Effects of Temperature, pressure and Crude Oil Composition on Interfacial Properties," SPERE (July 1986), 321.
8. Mugan, N., "Relative Permeability Measurements Using Reservoir Fluids," *SPEJ*, (Oct. 1972), 398-402.

9. Reis, J.C., "Oil Recovery Mechanisms in Fractured Reservoirs during Steam Injection," SPE 20204 presented at the SPE/DOE Seventh Symposium on Enhanced Oil Recovery, Tulsa, April 22-25, 1990.
10. Siagian, W.U., "A Laboratory Study of the Extraction of Hydrocarbons from Crude Oil by High Pressure Carbon Dioxide," MS thesis, New Mexico Institute of Mining and Technology, Socorro, NM (1997).
11. Tang, G.Q., and Morrow, N.R., "Effect of Temperature, Salinity and Oil Composition on Wetting Behavior and Oil," paper SPE 36680 presented at the SPE Annual Technical Conference and Exhibition, Denver, Oct. 6-9, 1996.

Table 2.7-1— The Physical Properties of the Reservoir Core Samples

Core No.	Diameter, (cm)	Length, (cm)	k_{brine}, (md)	PoreVolume, (cc)	Porosity, (%)	S_{wi} (%)
SPR-1HR	3.608	6.579	0.22	6.55	9.74	34.36
SPR-2HR	3.607	6.579	0.34	7.11	10.58	43.72
SPR-3HR	3.607	5.842	0.51	7.08	11.86	40.66
SPR-4HR	3.607	5.669	0.30	6.93	11.97	33.62
SPR-5HR	3.607	5.702	0.24	6.94	11.92	36.59
SPR-6HR	3.607	5.563	0.21	5.65	9.94	38.03
SPR-7HR	3.607	5.433	0.14	5.61	10.11	32.22
SPR-8H	3.608	6.487	0.17	7.28	10.98	34.04
SPR-9H	3.607	6.502	0.33	6.81	10.26	41.29
SPR-10H	3.607	5.804	0.12	6.66	11.24	39.96
SPR-11H	3.607	5.842	0.10	6.39	10.71	40.55
SPR-12H	3.607	5.685	0.38	6.42	11.05	34.54
SPR-13R	3.594	5.829	0.10	6.16	10.42	35.03
SPR-14R	3.594	5.723	0.13	6.03	10.38	33.62
SPR-15R	3.594	6.111	0.22	5.13	8.28	41.53

Table 2.7-2— Composition of Synthetic Spraberry Reservoir Brine

Salts Content	Concentrations (mg/L)
NaCl	122,699
$CaCl_2 \cdot 2H_2O$	7,497
Total Dissolved Solids	130,196

Table 2.7-3— Properties of Spraberry Crude Oil*

API Gravity @ 60°F	31.1
Acid Number (mg KOH/g oil)	0.085 ± 0.022
Base Number (mg KOH/g oil)	2.65 ± 0.040
Density @ 25°C (g/ml)	0.8635
Refractive index @ 20°C	1.47824 ± 0.00007
PRI with n-C7	n/a
Asphaltene ppt with n-C_5 (wt%)	0.39
Asphaltene ppt with n-C_7 (wt%)	0.16
Molecular Weight	180

* Chang, V., and Buckley, J.S., (1997)

Table 2.7-4— Spraberry Crude Oil Composition**

Components	Mole fractions
C_1	0.0211
C_2	0.0172
C_3	0.0351
C_4	0.0212
C_5 - C_{10}	0.5137
C_{11} - C_{20}	0.2151
C_{21} - C_{30}	0.0710
C_{30} - C_{36}	0.0302
C_{37}^+	0.0740
Total	1.0000

** *Siagian, W.R., (1997)*

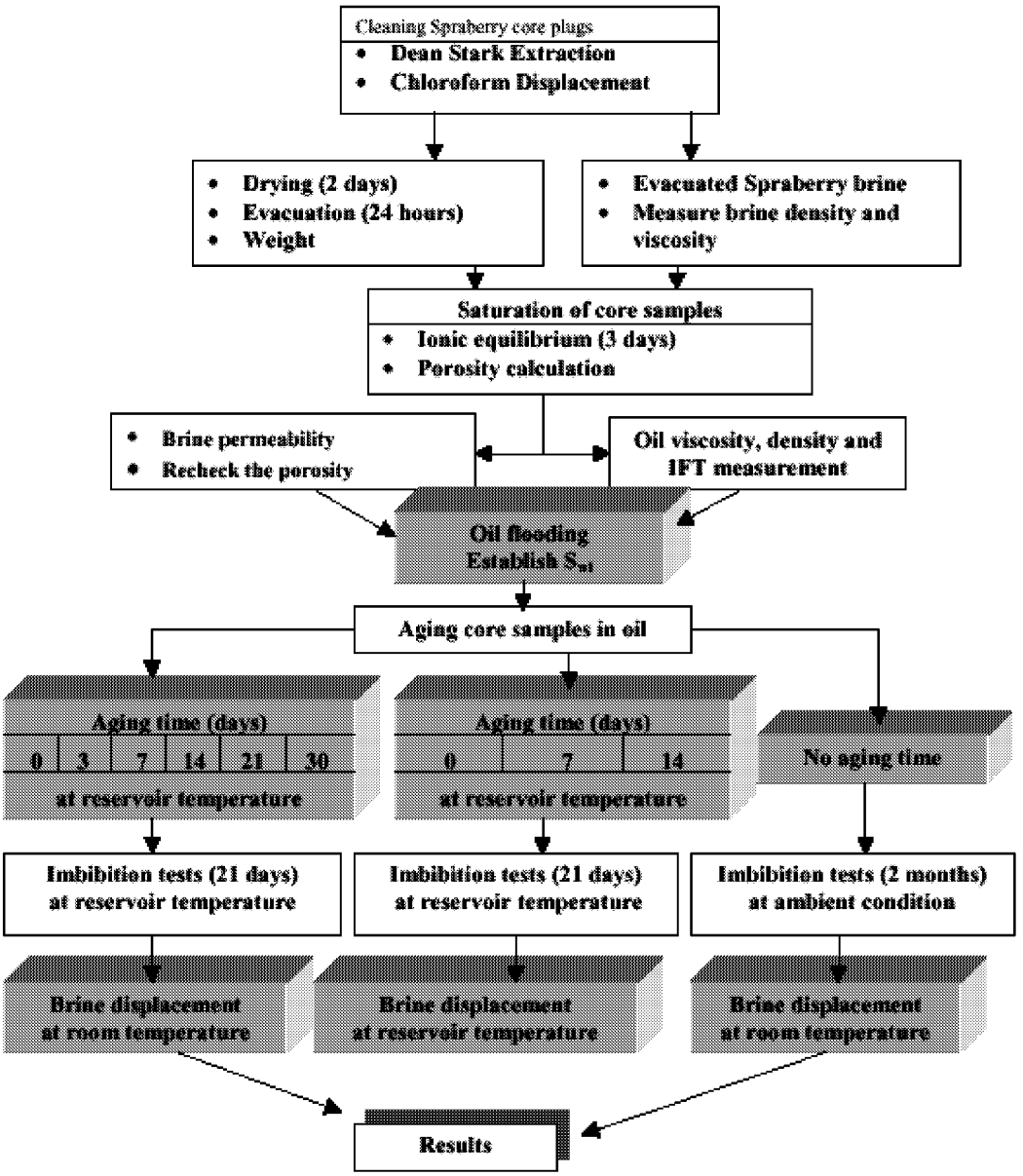

Fig. 2.7-1— Schematic experimental program

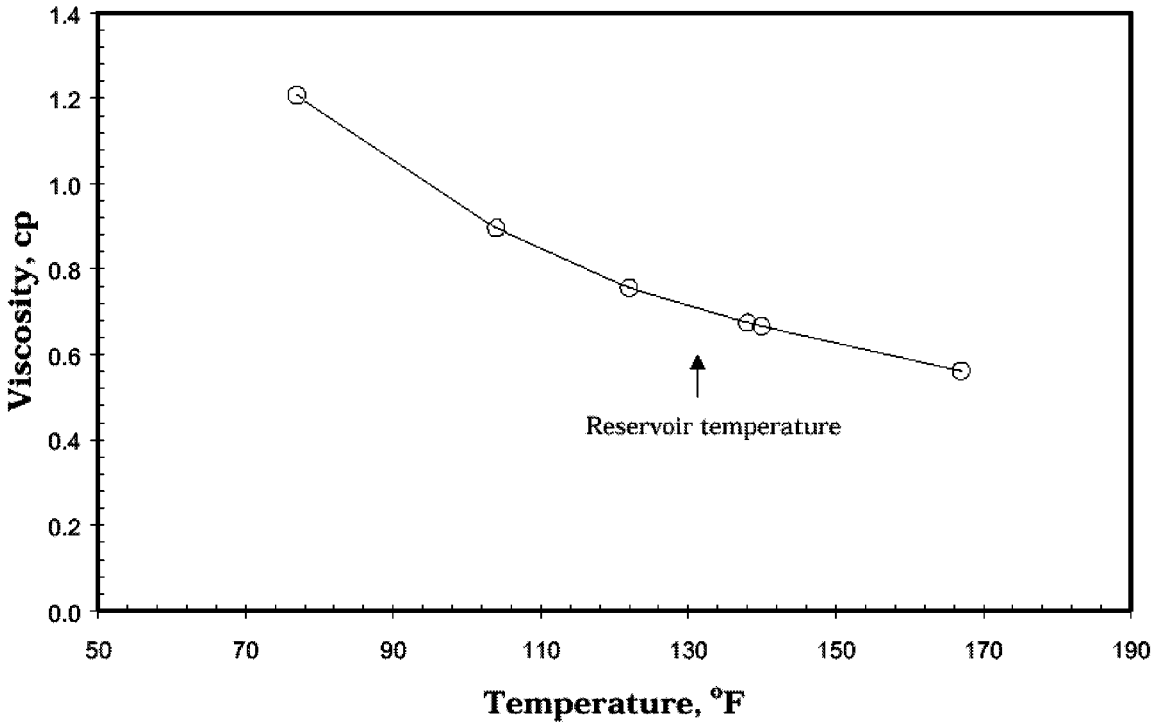

Fig. 2.7-2— Variation in viscosity of synthetic Spraberry brine with temperature increase

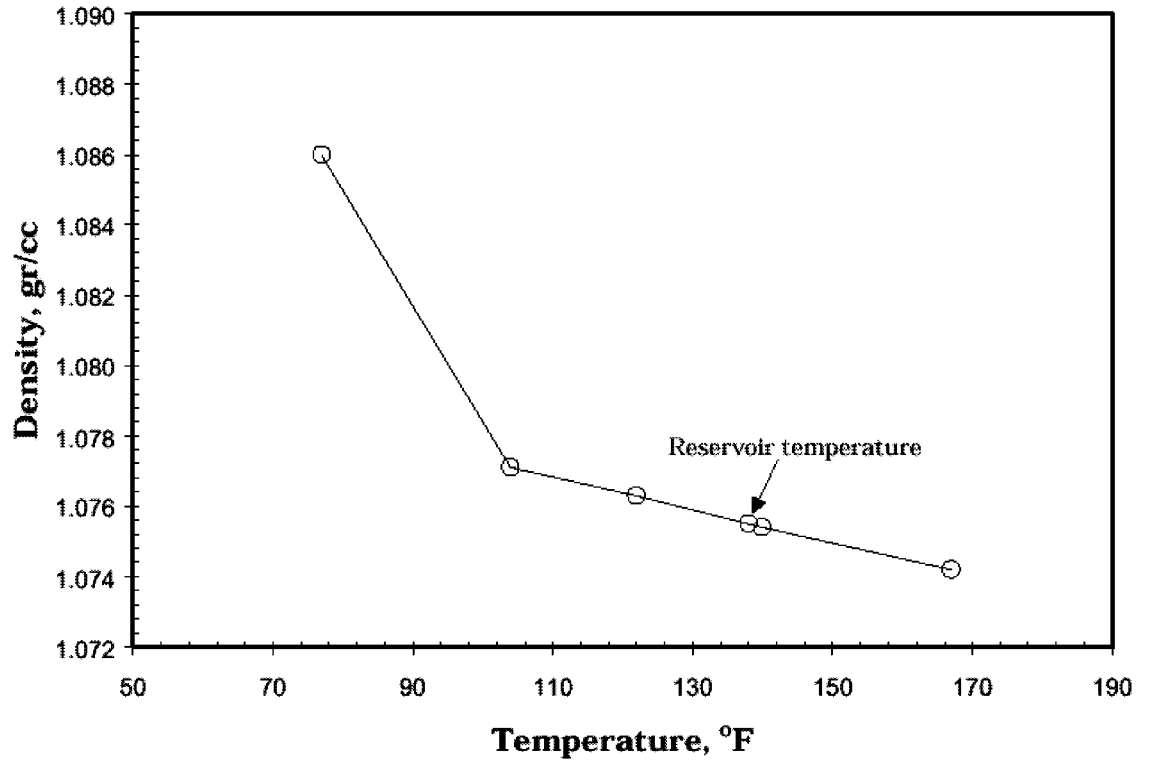

Fig. 2.7-3— Variation in density of synthetic Spraberry brine with temperature increase

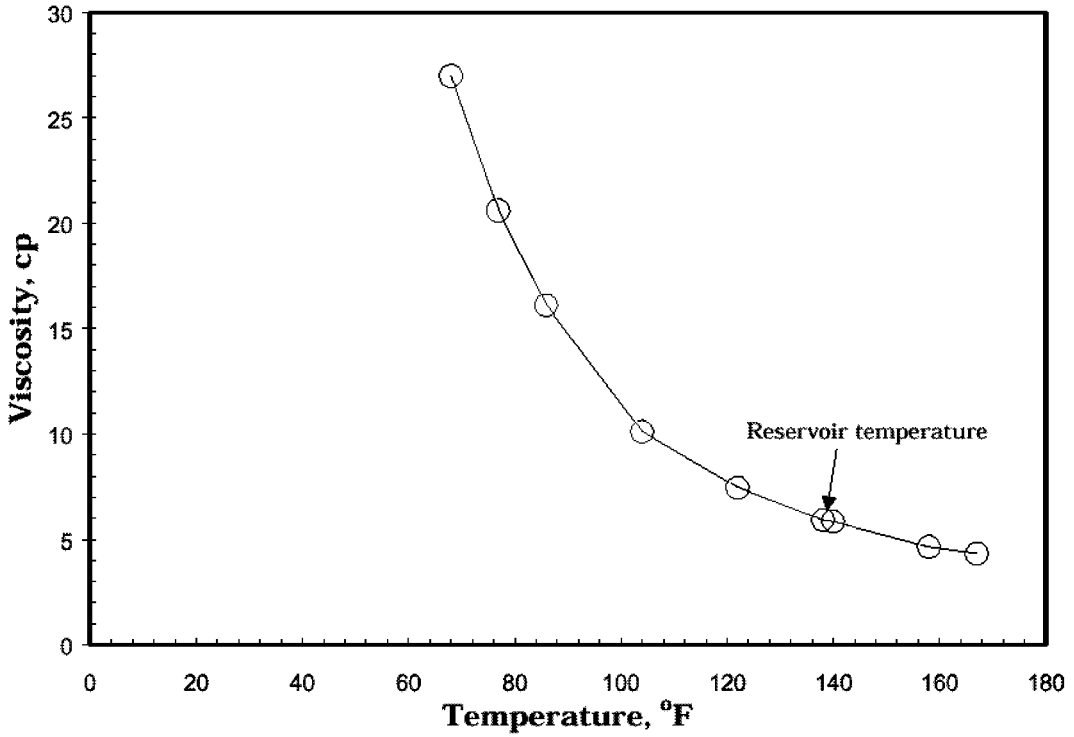

Fig. 2.7-4 —Variation in viscosity of Spraberry oil with temperature increase

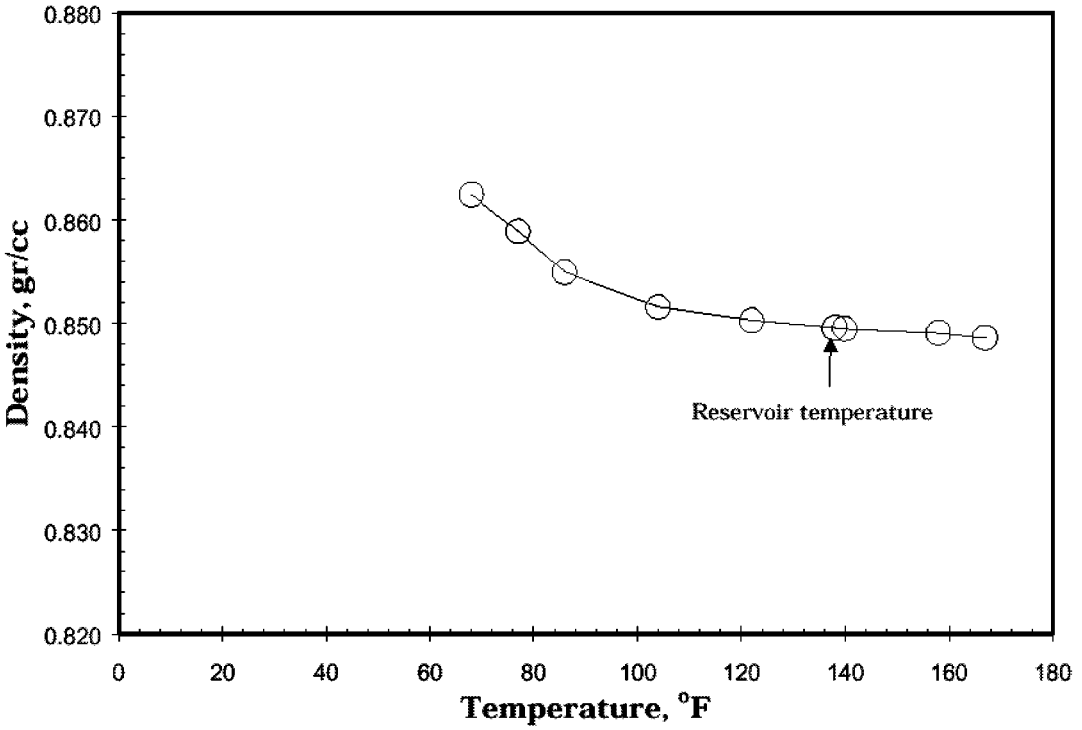

Fig. 2.7-5—Variation in density of Spraberry oil with temperature increase

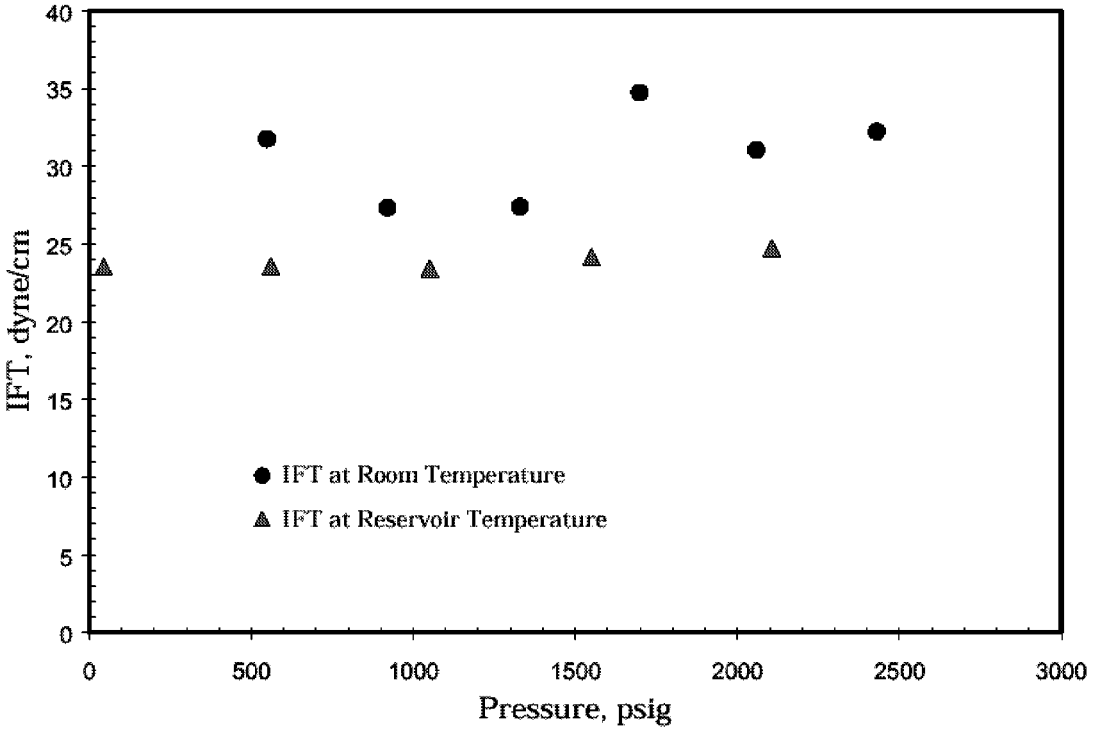

Fig. 2.7-6—Interfacial tension of Spraberry oil – brine at elevated pressure

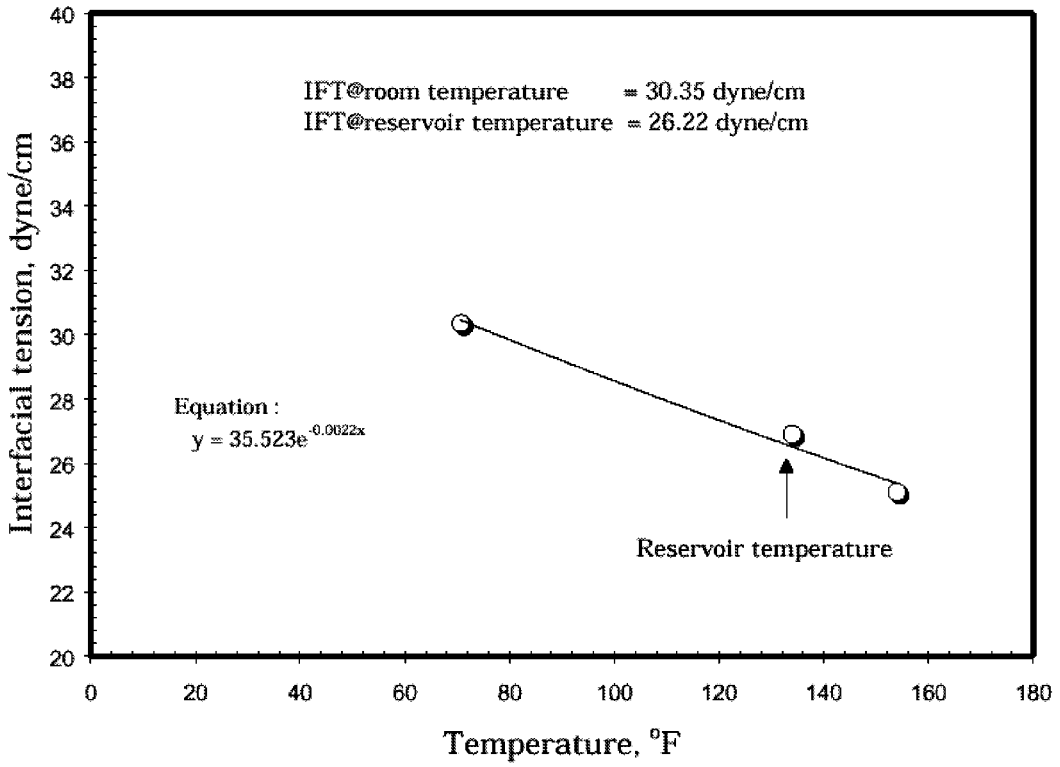

Fig. 2.7-7— Interfacial tension of Spraberry oil – brine at elevated temperature

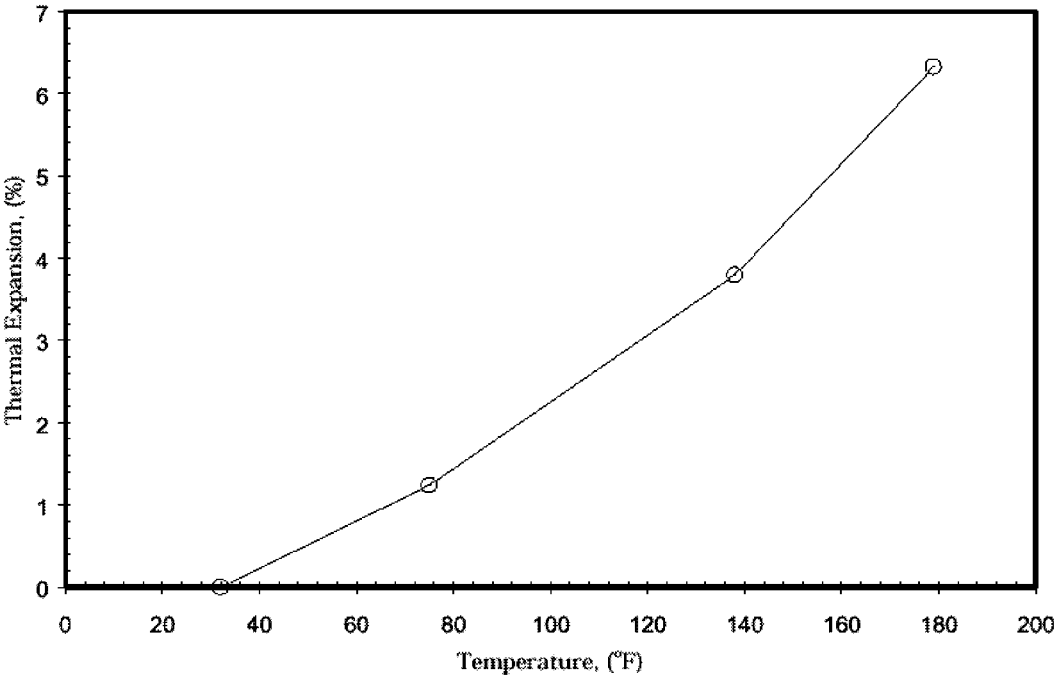

Fig. 2.7-8—Thermal expansion of Spraberry oil

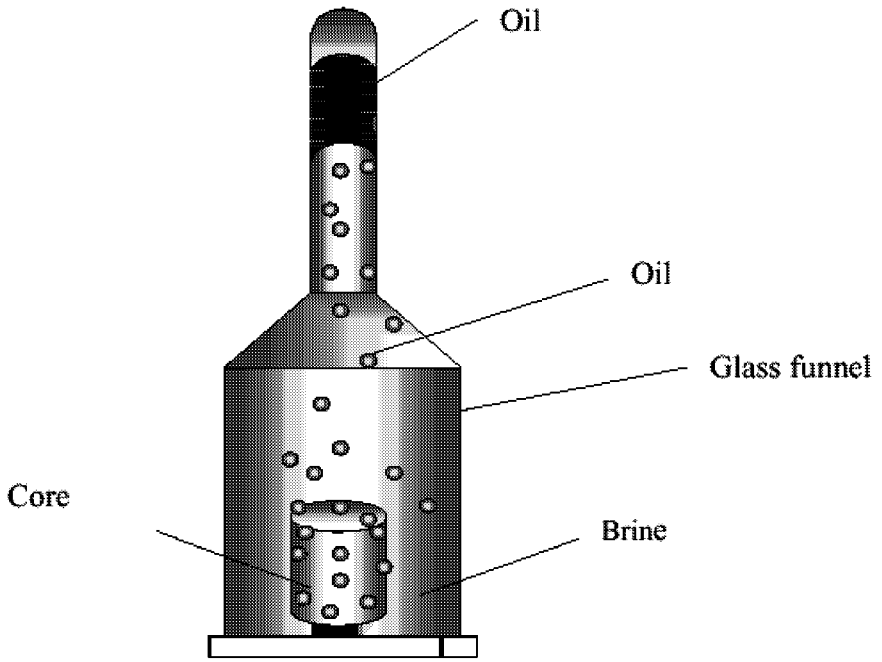

Fig. 2.7-9—Spontaneous imbibition apparatus

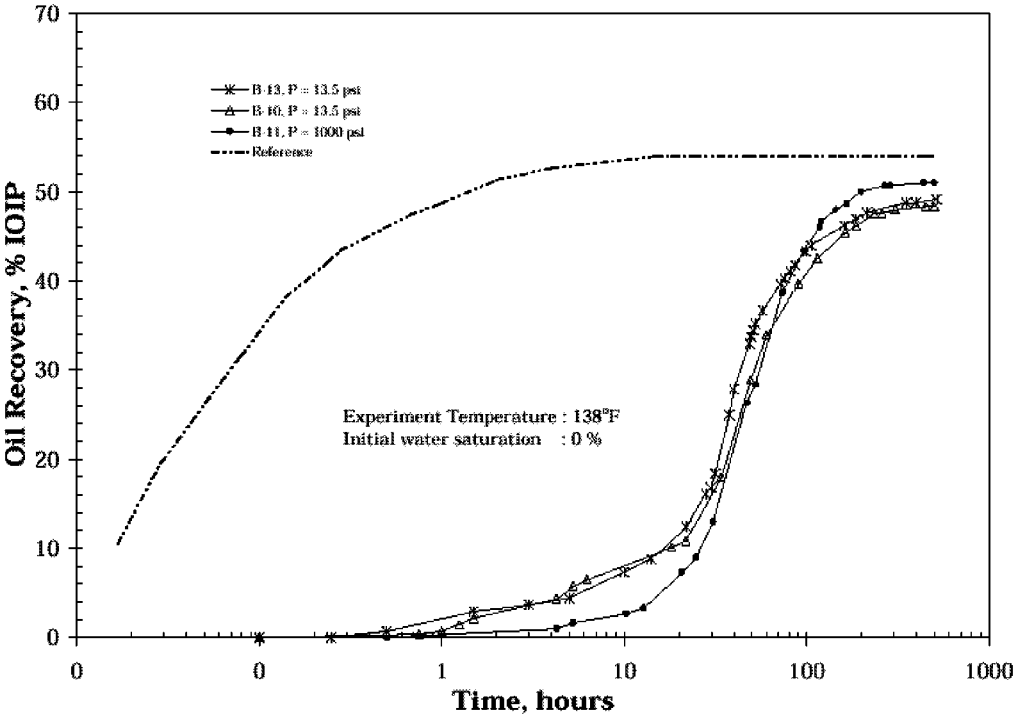

Fig. 2.7-10—Effect of elevated pressure on rate of imbibition and recovery using Berea sandstone

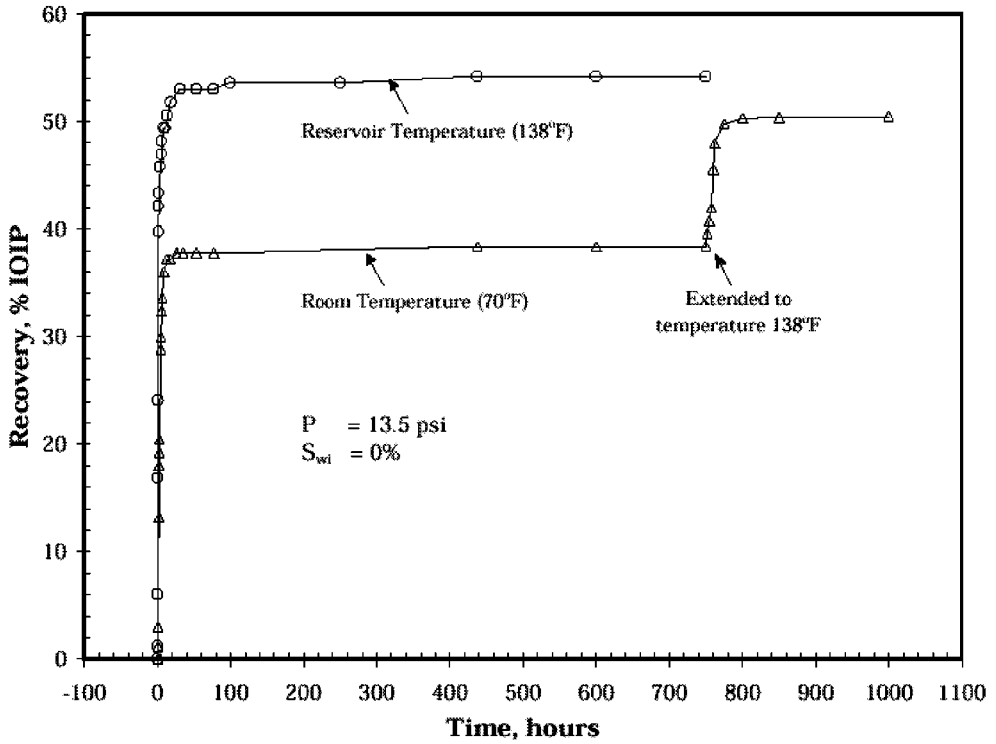

Fig. 2.7-11— Effect of changing temperature on rate of imbibition and recovery using Berea sandstone

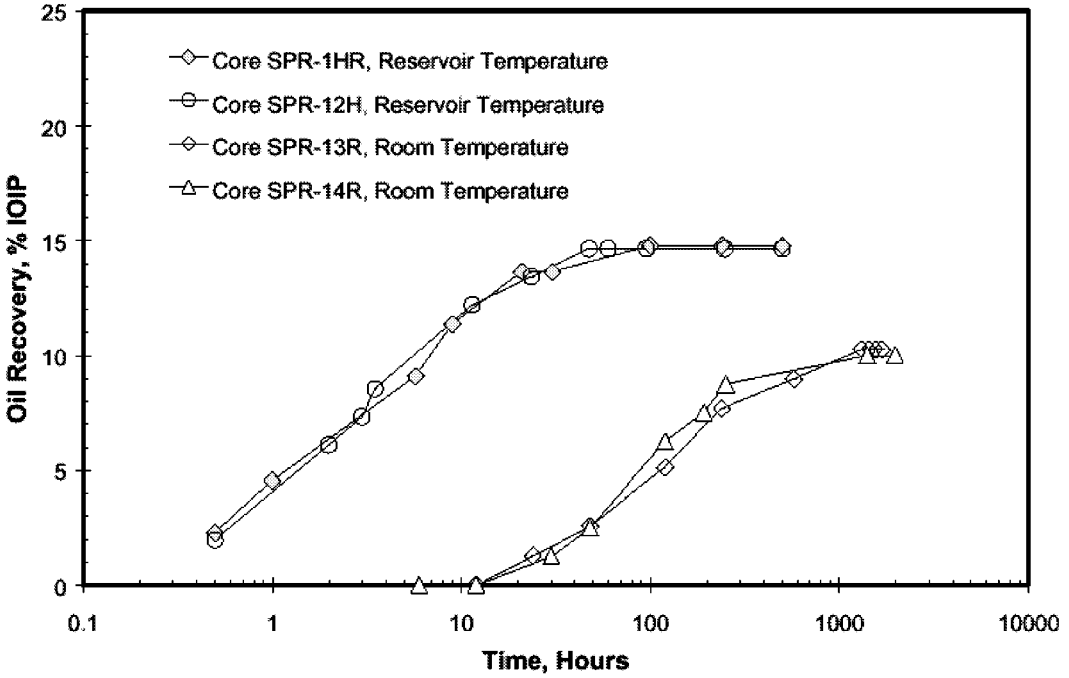

Fig. 2.7-12— Effect of temperature in imbibition tests

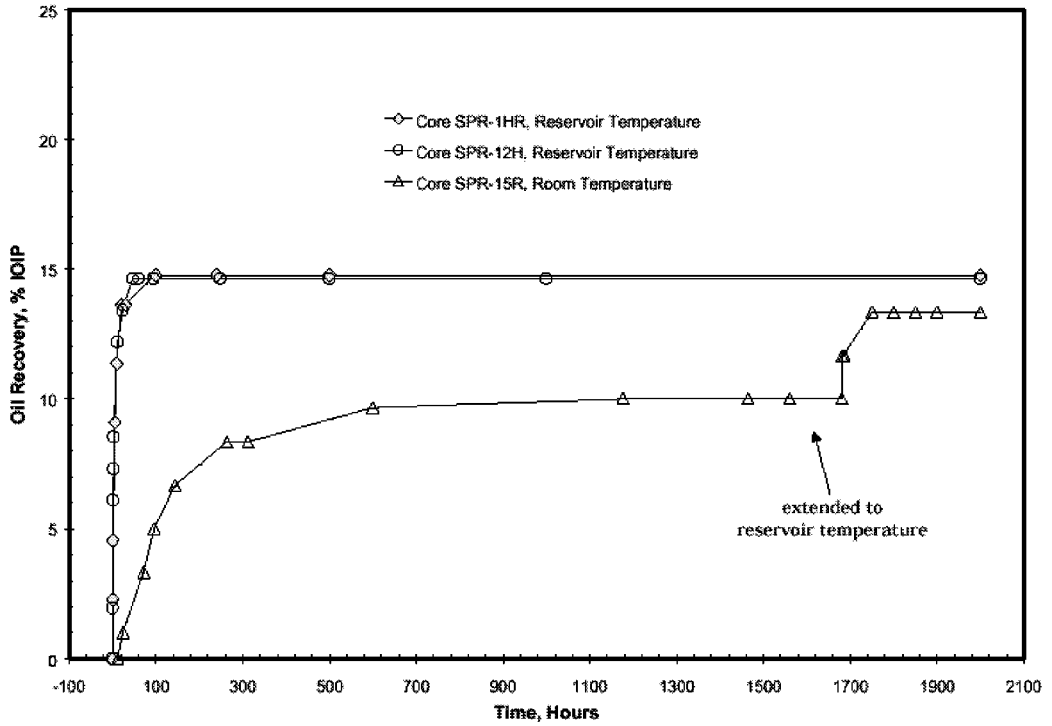

Fig. 2.7-13—Effect of temperature changes on oil recovery by imbibition

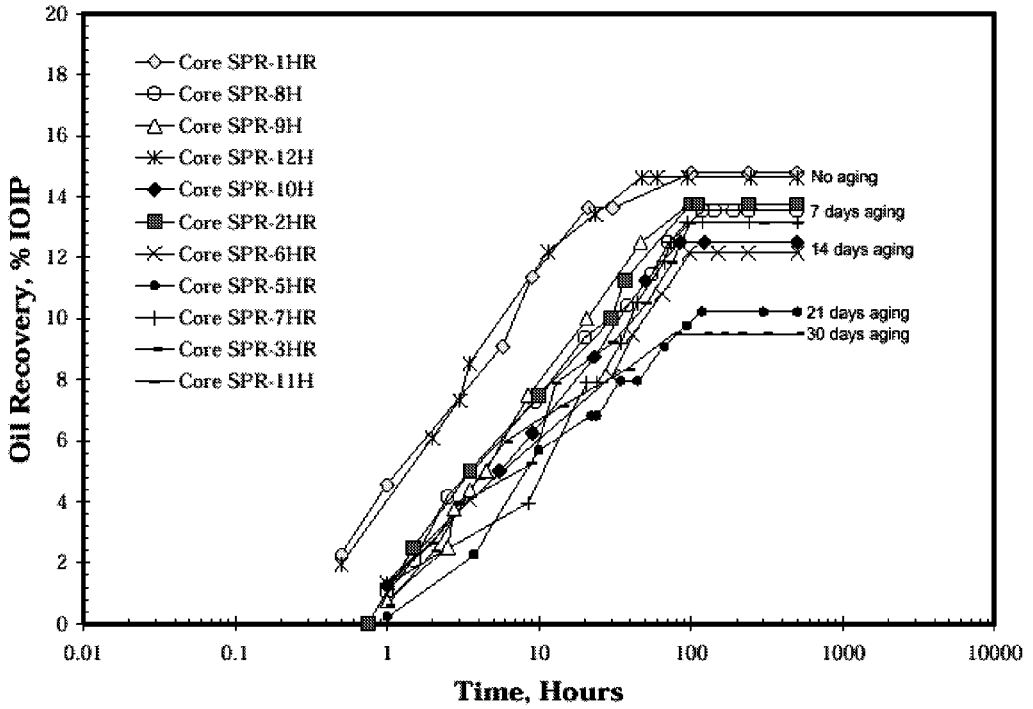

Fig. 2.7-14— Oil recovery curve obtained from imbibition experiment performed at reservoir temperature

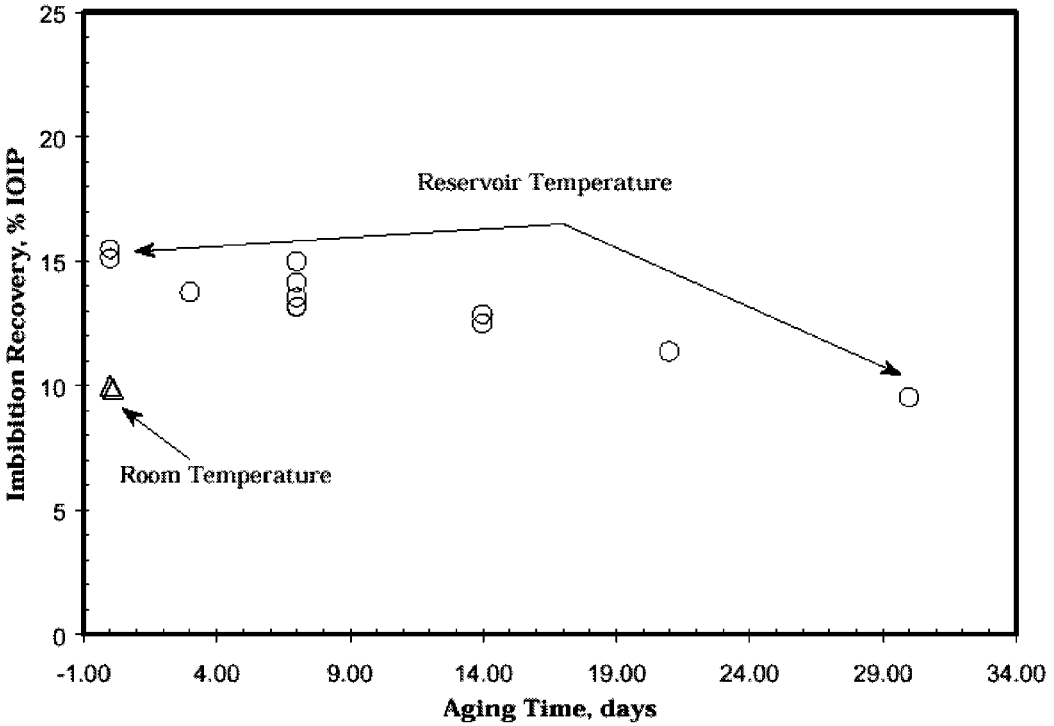

Fig. 2.7-15—Effect of aging time on the recovery of oil by imbibition

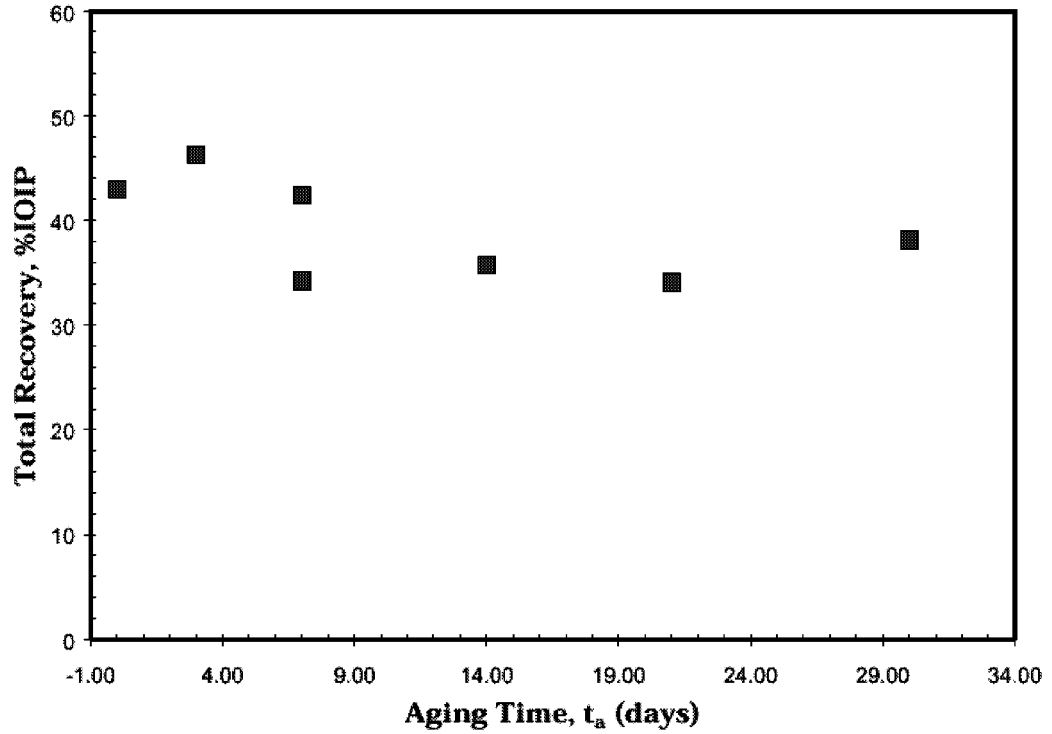

Fig. 2.7-16—Total recovery (imbibition plus displacement) versus aging time to exclude the effects of aging time on the recovery mechanism

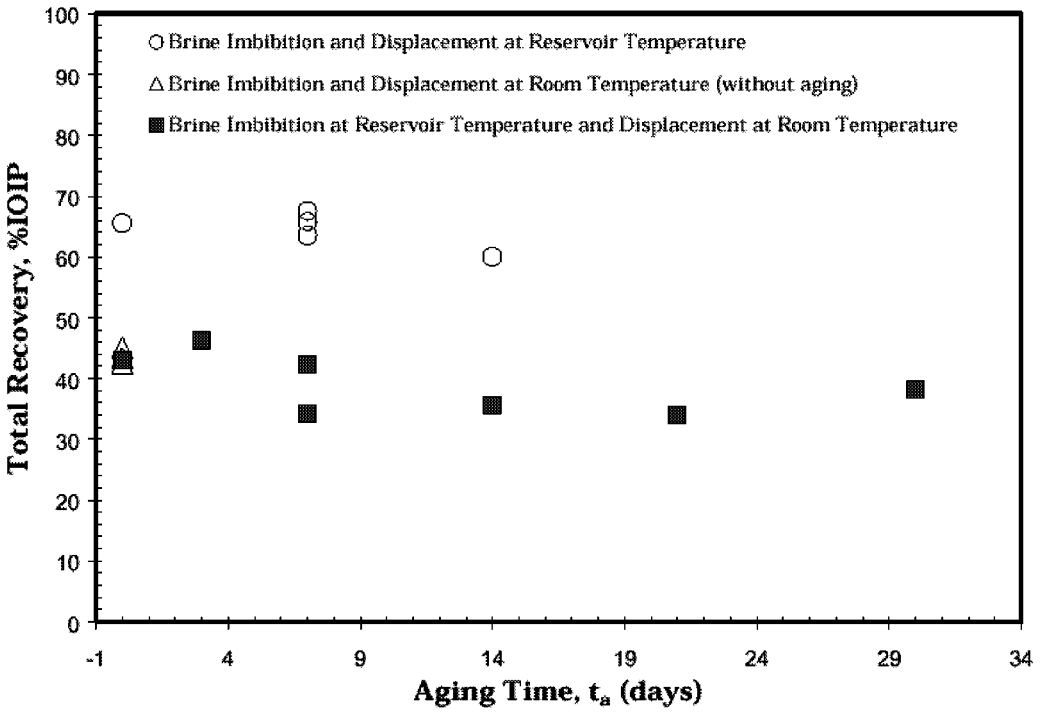

Fig. 2.7-17— Effect of aging time on total recovery at elevated temperatures

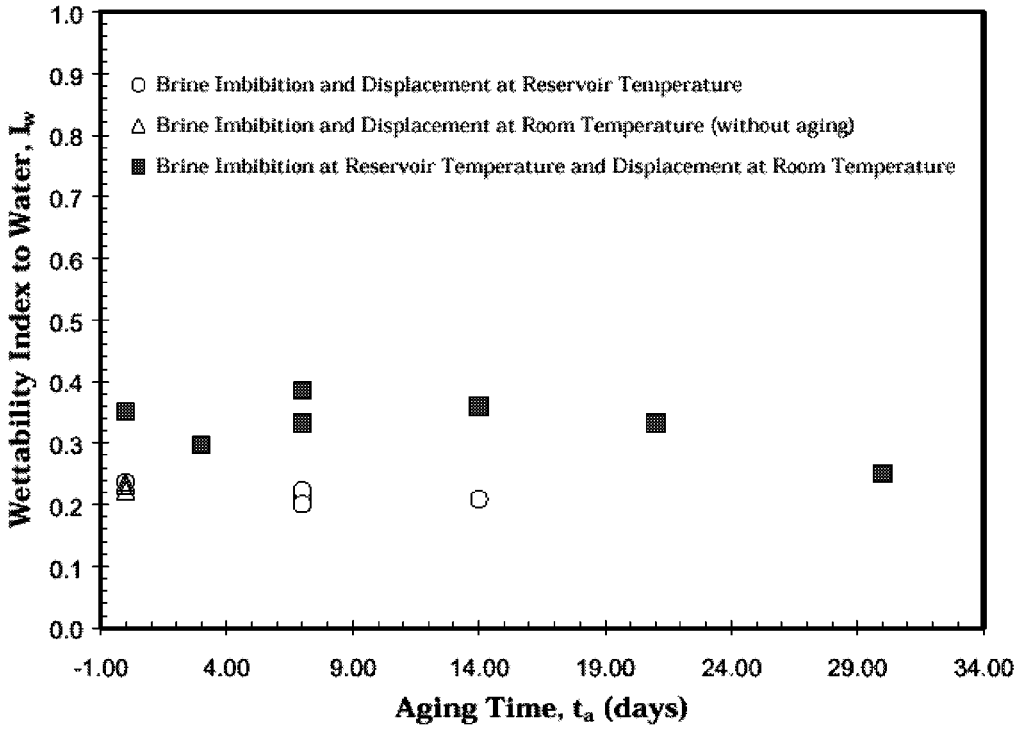

Fig. 2.7-18— Wettability index to water versus aging time for the different experiment temperatures

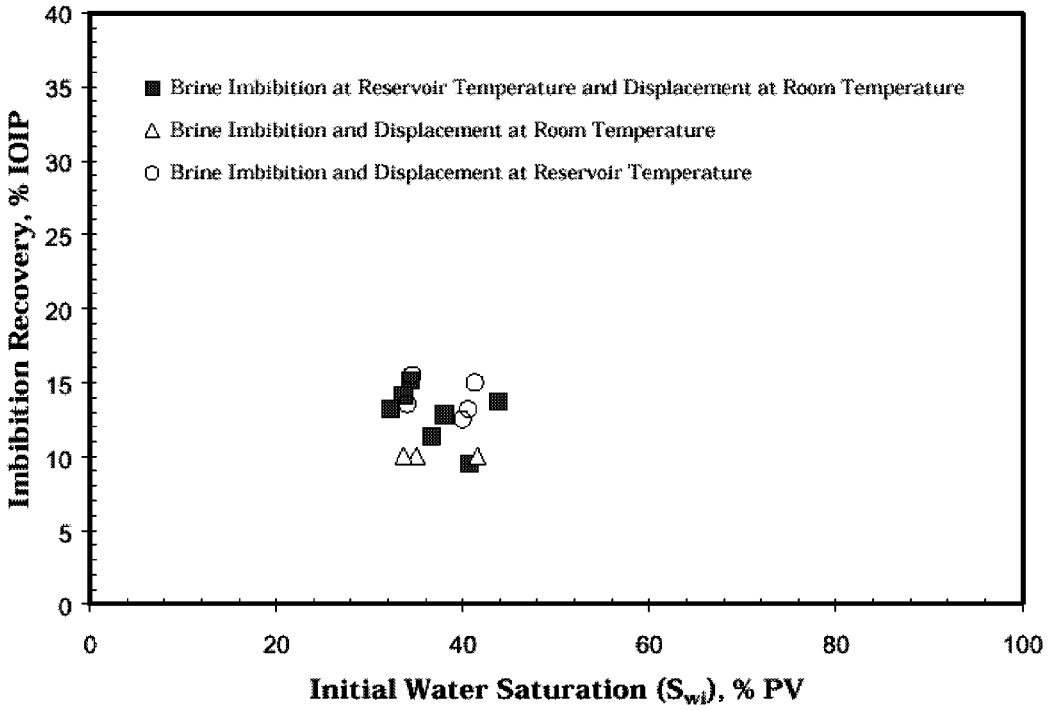

Fig. 2.7-19—Effect of initial water saturation on oil recovery by imbibition

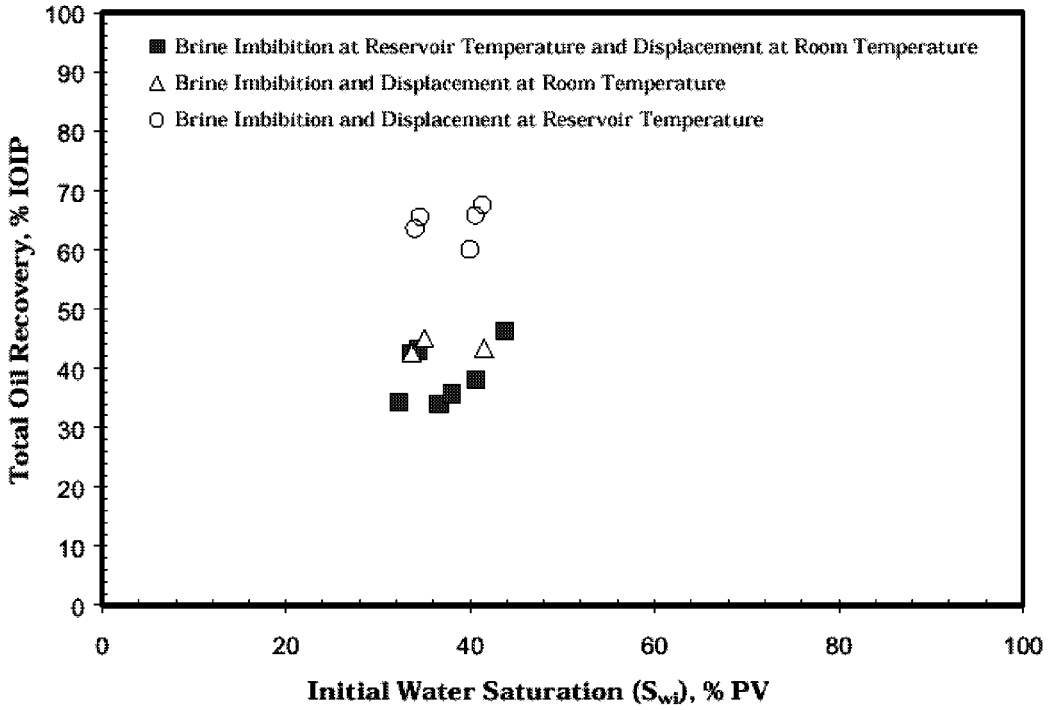

Fig. 2.7-20—Effect of initial water saturation on total recovery

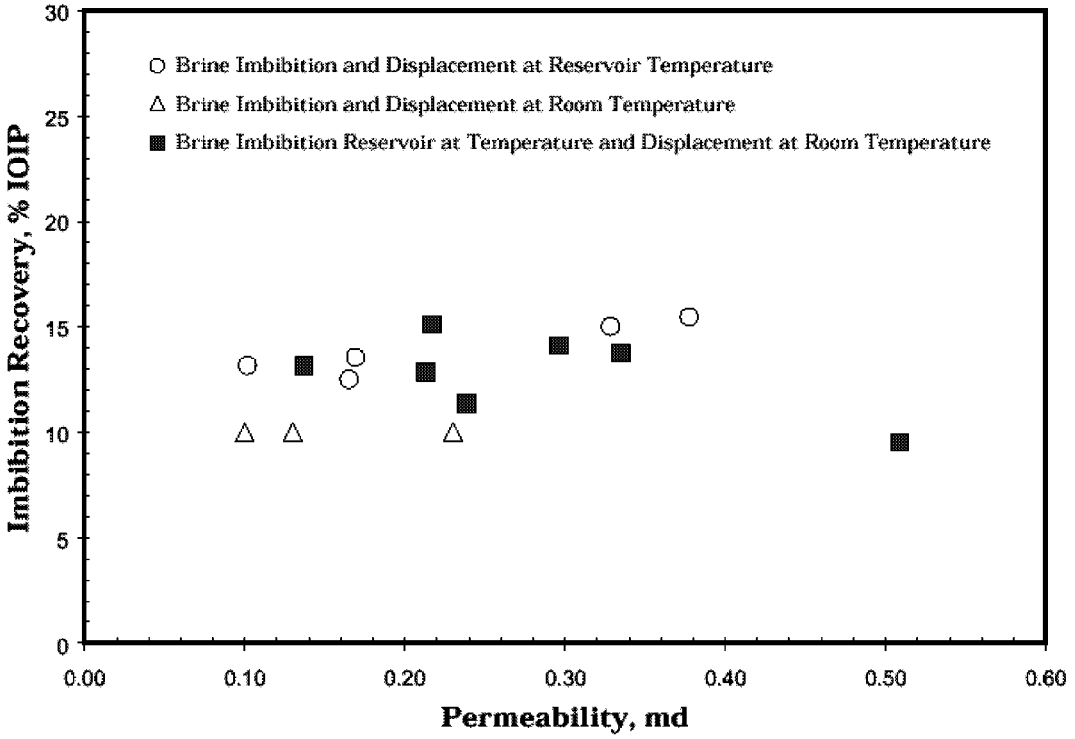

Fig. 2.7-21—Effect of permeability on recovery by imbibition

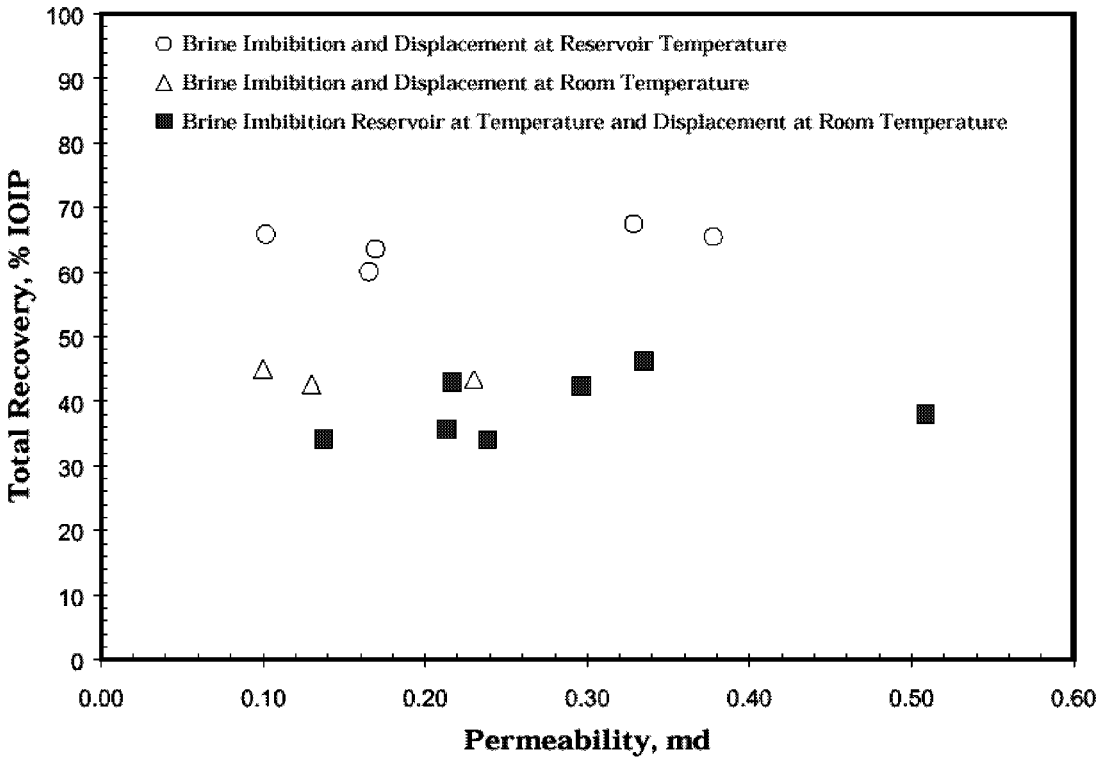

Fig. 2.7-22—Effect of permeability on total oil recovery

2.8 SPONTANEOUS IMBIBITION MODELING OF SPRABERRY CORES USING A FINITE DIFFERENCE SCHEME

Introduction

This section presents the numerical modeling of the spontaneous imbibition experiment presented in the previous section. A fully finite-difference implicit scheme was developed to solve non-linear diffusion of the spontaneous imbibition equation. The objectives of this study were to simulate and to understand the imbibition process in low permeability Spraberry core. The numerical results satisfactorily matched the laboratory spontaneousimbibition experiment data. By matching the experimental data with the simulation output, the matrix capillary pressure was determined. Once the important capillary pressure parameter is determined, then key variables of relative permeability, oil and water viscosities and initial water saturations, on the imbibition rate can be evaluated. Also, the sensitivity of the capillary pressure on imbibition in the Spraberry rock could be evaluated.

Background

Imbibition plays a very important role in the recovery of oil from the naturally fractured Spraberry area. An understanding of the imbibition process and the key parameters that control the imbibition process are crucial. To understand the physical process of imbibition, the spontaneous imbibition experiment was conducted using core, oil and synthetic brine. When oil saturated core contacts with brine, the imbibition process starts immediately. The amount of oil produced is recorded against time. Spontaneous imbibition experiments usually take a long time. Sensitivity studies to investigate the effect of some parameters on imbibition rate can become very lengthy. Two parameters present a problem. The capillary pressure is difficult to determine and the water saturation profiles at different times and locations can be difficult and time consuming to determine. To quantify the effects of these two parameters on the imbibition process in a reasonable and effective length of time, numerical modeling or simulation is used.

Several studies have been conducted to simulate the spontaneous imbibition process in a core plug. These studies were concerned primarily with the capillary pressure as the only driving force in the spontaneous imbibition process. Blair (1964) presented 1D-numerical solutions describing the imbibition of water and the countercurrent flow of oil in porous rocks. Blair concluded that the rate of imbibition varies with capillary pressure, relative permeability curves, oil viscosity, and initial water saturation.

Beckner *et al* (1987) proposed modeling imbibition as a diffusion process with anonlinear diffusion coefficient. They assumed that the oil phase gradient ahead and behind the front is negligible. In other words, no countercurrent oil flow exists. Knowing this weakness, they used equations for imbibition with countercurrent flow described by Blair (1964). They set total velocity equal to zero in the fractional flow equation and ignored gravity and source terms. Bech *et al* (1989) and Dutra *et al* (1991) have used this diffusion equation.

Chen *et al* (1995) used the diffusion equation to conduct numerical experiments of countercurrent imbibition in a single matrix block to identify flow characteristic. They used the nonlinear diffusion equation describing countercurrent flow derived by Blair (1964). They solved that equation numerically by using a semi-implicit method.

Baker and Wilson (1997) used a "black oil" DRS Ver. 3.5 simulator to study numerical simulation of a laboratory scale imbibition experiment. They used a radial coordinate and modeled the matrix and fracture systems explicitly. The fracture system simulated the shock front that provided the driving mechanism for the initiation of the imbibition process, while the matrix system represented the core plug. They studied the variation of relative permeability and matrix capillary pressure on the behavior of the recovery curve by matching the laboratory imbibition data. They concluded that imbibition recovery was sensitive to relative permeability and capillary pressure.

In this study, the spontaneous imbibition tests were conducted under reservoir conditions using core plugs taken from low permeability Spraberry formation (see Section 2.1). Spraberry oil and synthetic Spraberry brine were used as wetting and non-wetting fluids. The work described in this section was performed to develop the mathematical model for matching the laboratory imbibition data. The matching data can be used to study the spontaneous imbibition process in detail and to investigate the effect of key variables on the imbibition rate.

Experimental Data

Based on results of previous imbibition experiments as presented in Section 2.7, four representative core samples were used as a comparison of the simulation data. The physical properties of the reservoir core samples and fluids are presented in Table 2.8-1. The experimental procedure is described in Section 2.7.

Mathematical Formulation

A mathematical formulation of the spontaneous imbibition process is described here. In deriving the governing equations, some assumptions are used:

- gravity terms are negligible,
- capillary pressure is the only driving force where total velocity is zero, and
- fluid and rock are incompressible.

The simultaneous flow of two-phases in a porous media is described in four basic flowequations (Eqs. 2.22 to 2.25) as described below:

$$\nabla \cdot \vec{u}_w + \phi \frac{\partial S_w}{\partial t} = 0 \quad \text{.....2.22}$$

$$\nabla \cdot \vec{u}_o + \phi \frac{\partial S_o}{\partial t} = 0 \quad \text{.....2.23}$$

$$p_o - p_w = p_c(S_w) \quad \text{.....2.24}$$

$$S_o + S_w = 1 \quad \text{.....2.25}$$

By using Darcy's law, the water and oil velocities can be written as

$$\vec{u}_w = -\frac{k}{\mu_w} k_{rw} \nabla p_w \quad \text{.....2.26}$$

$$\vec{u}_o = -\frac{k}{\mu_o} k_{ro} \nabla p_o \quad \text{.....2.27}$$

The total flow for countercurrent imbibition is defined as

$$\vec{u}_T = \vec{u}_o + \vec{u}_w \quad \text{.....2.28}$$

Combining Eqs. 2.24,2.26,2.27 and 2.28 gives

$$\vec{u}_w (1 + \frac{k_{ro}}{\mu_o} \frac{\mu_w}{k_{rw}}) = \vec{u}_T + \frac{k}{\mu_o} k_{ro} \nabla p_c \quad \text{.....2.29}$$

Implementing the assumption that the capillary pressure is the only driving force, then the total velocity can be set to be zero and Eq. 2.29 becomes

$$\vec{u}_w = \frac{k}{\mu_o} k_{ro} f_w \nabla p_c \quad \text{.....2.30}$$

Where water fractional flow is defined as

$$f_w = \left(1 + \frac{k_{ro}}{\mu_o} \frac{\mu_w}{k_{rw}} \right)^{-1} \quad \text{.....2.31}$$

Substituting Eq. 2.30 into Eq. 2.22, a governing equation for describing the spontaneous imbibition process is obtained as follows:

$$\nabla \cdot D(S_w) \frac{\partial S_w}{\partial x} = -\phi \frac{\partial S_w}{\partial t} \quad \text{.....2.32}$$

Where the non-linear capillary diffusion coefficient is defined as

$$D(S_w) = \frac{k}{\mu_o} k_{ro} f_w \frac{\partial p_c}{\partial S_w} \quad \text{.....2.33}$$

Because of the non-linear capillary diffusion coefficient, Eq. 2.32 must be solved by numerical methods.

Finite-Difference Scheme

In order to solve Eq. 2.32 numerically, discretization in 2D finite-difference form was implemented. The left-hand side was discretized by applying Taylor series using central difference and the right-hand side using backward difference. The superscript indicates the time level. *n* is the old time level for which we have a complete solution and all variables and properties. *n+1* is the new time level for which the solution is unknown. With this notation, our finite-difference approximations to the 2D spontaneous imbibition equation is

$$\begin{bmatrix} & D_{i,j+1/2} & \\ D_{i-1/2,j} & -D_{i-1/2,j} - D_{i+1/2,j} - D_{i,j-1/2} - D_{i,j+1/2} & D_{i+1/2,j} \\ & D_{i,j-1/2} & \end{bmatrix} \begin{bmatrix} \\ S_{w_i} \\ \\ \end{bmatrix}^{n+1}$$

$$= -\frac{\phi h_x h_y}{\Delta t} \left[S_{w_i}{}^{n+1} - S_{w_i}{}^{n} \right] \quad \text{.....2.34}$$

$D_{i-1/2,j}$ and $D_{i+1/2,j}$ are evaluated using arithmetic averaging as below

$$D_{i-1/2,j} = \frac{D_{i,j} + D_{i-1,j}}{2} \quad \text{.....2.35}$$

$$D_{i+1/2,j} = \frac{D_{i,j} + D_{i+1,j}}{2} \quad \text{.....2.36}$$

Note that the relative permeabilities and capillary pressure are functions of water saturation, thus, Eq. 2.34 must be solved iteratively. Once the new saturations are solved using the initial guess, these new water saturations are compared with the old water saturations until acceptance convergence has been reached.

The core plug is totally immersed in the water and therefore, boundary conditions are set to be 1-S_{or}. This implies that instantaneous imbibition occurs at the matrix-fracture interface. Initial conditions are required to begin the time step sequence. In this study, initial conditions are specified equal to initial water saturation.

Results and Discussions

In order to match the recovery from the imbibition experiments, only capillary pressure was altered and other parameters were kept constant. The following relative permeability correlations from Honarpour *et al* (1986) as inputs:

$$k_{ro} = k_{ro}^{o}(1 - S_w^*)^3 \quad \text{.....2.37}$$

$$k_{rw} = k_{rw}^{o}(S_w^*)^3 \quad \text{.....2.38}$$

For the base case, the maximum oil relative permeability (k^o_{ro}) was set to 1.0 and the maximum water relative permeability (k^o_{rw}) was set to 0.3. In these relationships, the S_w* is expressed as $S_w^* = \frac{(S_w - S_{wi})}{(1 - S_{or} - S_{wi})}$. The residual oil saturation (S_{or}) was set to 0.5437 and irreducible water saturation (S_{wi}) was set to 0.37. Those average values of S_{or} and S_{wi} values are obtained from Table 2.8-1. The average of residual oil saturations after spontaneous imbibition experiments was still very high. Therefore, the water saturation changes during the simulation are very small, which causes the numerical solution to become unstable and the result cannot be obtained. In order to approach this problem, three higher residual oil saturations of 0.2, 0.3 and 0.4 were used. Once the numerical solution matched with the experimental data, the matrix capillary pressures from different residual oil saturations were obtained. Then, the matrix capillary pressure for 0.54 residual oil saturation was estimated as shown in Fig. 2.8-1. The low-capillary pressure curve obtained indicates that the Spraberry matrix is weakly water-wet. The weakly water-wet indication is also found by the measurement of wettability index (average Amott index is 0.3, see section 2.1). Figure 2.8-2 shows four experimental data and numerical solution matches for recovery against time using residual oil saturation of 0.2.

The diffusion coefficient as shown in Fig. 2.8-3 is strongly non-linear due to varying capillary pressure and relative permeability curves as functions of water saturation. Therefore, using constant capillary pressure and relative permeability curves to solve the spontaneous imbibition equation, which is always solved by an analytical solution, may fail to predict oil recovery by spontaneous imbibition.

The Effect of Capillary Pressure

In order to investigate the sensitivity of imbibition capillary pressure on the imbibition rate, three different capillary pressures were used with multiplication in order of 0.1, 1 and 10 to the matching result of capillary pressure. Capillary pressure is assumed to be the only driving force in the spontaneous imbibition process. Thus, increasing the capillary pressure will increase the imbibition rate as shown in Fig. 2.8-4.

The Effect of Oil and Water Relative Permeabilities

In order to investigate the sensitivity of relative permeability curves on the imbibition rate, three cases of oil relative permeability and water relative permeability curves were used. The results in Figs. 2.8-5 and 2.8-6 show that oil recovery by imbibition is sensitive to the oil relative permeability curves while no significant effect was observed in

changing the water relative permeability curves. The imbibition rate was sensitive to the oil relative permeability. The capillary diffusion coefficient as given by Eq. 2.33 is a function of the square of the oil relative permeability and thus affects the imbibition process much more strongly.

The Effect of Oil and Water Viscosity

To examine the effect of oil viscosity on the imbibition rate, simulation runs were made for three different oil viscosities, 0.59, 5.9 and 59 cp and three different water viscosities of 0.068, 0.68 and 6.8. In each case the fluid and rock properties were the same as those described in Table 2.8-1. The effect of different oil viscosities on the imbibition rate is shown in Fig. 2.8-7, where the oil volumes recovered as a function of time for three oil viscosities are plotted. The lower the oil viscosity, the easier for counter-current flow of oil and water in the porous matrix as water imbibes into the core plug. Increasing or decreasing water viscosity has no effect on the imbibition rate as shown in Fig. 2.8-8. The viscosities for water are exaggerated, but were made to delineate effects of this parameter. Again, like the oil relative permeability, the oil viscosity is squared in the capillary diffusion term of Eq. 2.33, causing any changes to magnify by that power.

The Effect of Initial Water Saturation

The effect of initial water saturation on the imbibition rate is studied using four initial water saturation of 0, 0.2, 0.34, and 0.4. The results indicated that the imbibition rate is sensitive to the changes of initial water saturations. As initial water saturation decreases, the capillary pressure is greater, resulting in higher imbibition rate and in turn, higher oil volume recovered as shown in Fig. 2.8-9.

Conclusions

1. A 2D fully implicit numerical model has been developed to simulate the laboratory static spontaneous imbibition experiment.
2. The spontaneous imbibition equation might only be solved by the numerical method due to strong non-linear capillary diffusion.
3. The imbibition model developed here predicts a low imbibition capillary pressure for the Spraberry core. The capillary pressure was obtained by matching experimental oil recovery data. Results indicate that the wettability of the Spraberry core plug was weakly water-wet.
4. The rate of imbibition was sensitive to capillary pressure, oil relative permeability, oil viscosity and initial water saturation.
5. The rate of imbibition was not sensitive to water relative permeability and water viscosity.

Nomenclature

D = diffusion coefficients, ML^3T^{-2}
f = fractional flow, dimensionless
h = distance, L
k = permeability, L^2
kr = relative permeability, dimensionless

p = pressure, MLT^{-2}
Pc = capillary pressure, MLT^{-2}
S = saturation, fraction
t = time, T
u = velocity, LT^{-1}
ϕ = porosity, fraction

Subscripts
i = initial condition
i,j = integer denoting cell location in the x- and y- directions.
o = oil
w = water
x,y = x-,y- direction, respectively

Superscripts
n = integer indicating time level

References

1. Baker, R and Wilson, G.: " Numerical Simulation of Laboratory Scale Imbibition Experiment," Internal Report, Epic Consultant Services Ltd., (April 1997).
2. Bech, N., Jensen, O.K., and Nielsen, B.: "Modeling of Gravity-Imbibition and Gravity-Drainage Processes," *SPERE*. (Feb. 1991) 129-136.
3. Beckner, B. L., Ishimoto, K., Yamaguchi, S., A. Firoozabadi and Azis, K.: "Imbibition-Dominated Matrix-Fracture Fluid Transfer in Dual Porosity Simulators," paper SPE 16981 presented at the 1987 SPE Annual Technical Conference and Exhibition, Dallas, TX., Sept. 27-30.
4. Blair, P.M.: "Calculation of Oil Displacement by Countercurrent Water Imbibition," SPEJ Sept. 1964, 195-202; *Trans.,* AIME, **231**.
5. Chen, J., Miller, M.A. and Sepehrnoori, K.: "Theoretical Investigation of Countercurrent Imbibition in Fractured Reservoir Matrix Blocks," paper SPE 29141 presented at the 1995 Symposium on Reservoir Simulation, San Antonio, TX., Feb. 12-15.
6. Honarpour, M., Koederitz, L. and Harvey, A. H.: Relative Permeability of Petroleum Reservoirs, CRC Press, Inc., Boca Raton, FL, (1986).
7. Dutra, T. V. and Aziz, K.: "A New Double-Porosity Reservoir Model for Oil/Water Flow Problems," paper SPE 21248 presented at the 1991 SPE Sypmosium on Resrvoir Simulation, Ca., Feb 17-20.

Table 2.8-1—Core and Fluid Properties

Core Properties						Fluid properties at 138°F	
Cores #	Length, (cm)	Diam., (cm)	Perm. to brine, (md)	ϕ, (%)	S_{wi}, (%)	μ_o, (cp)	5.92
SPR-8H	6.487	3.608	0.17	10.98	34.04	μ_w, (cp)	0.68
SPR-9H	6.502	3.607	0.33	10.26	41.29	ρ_o, (gr/cc)	0.850
SPR-10H	5.433	3.607	0.14	10.11	39.96	ρ_w, (gr/cc)	1.076
SPR-11H	5.842	3.607	0.10	10.71	40.55	IFT, (dyne/cm)	26.22

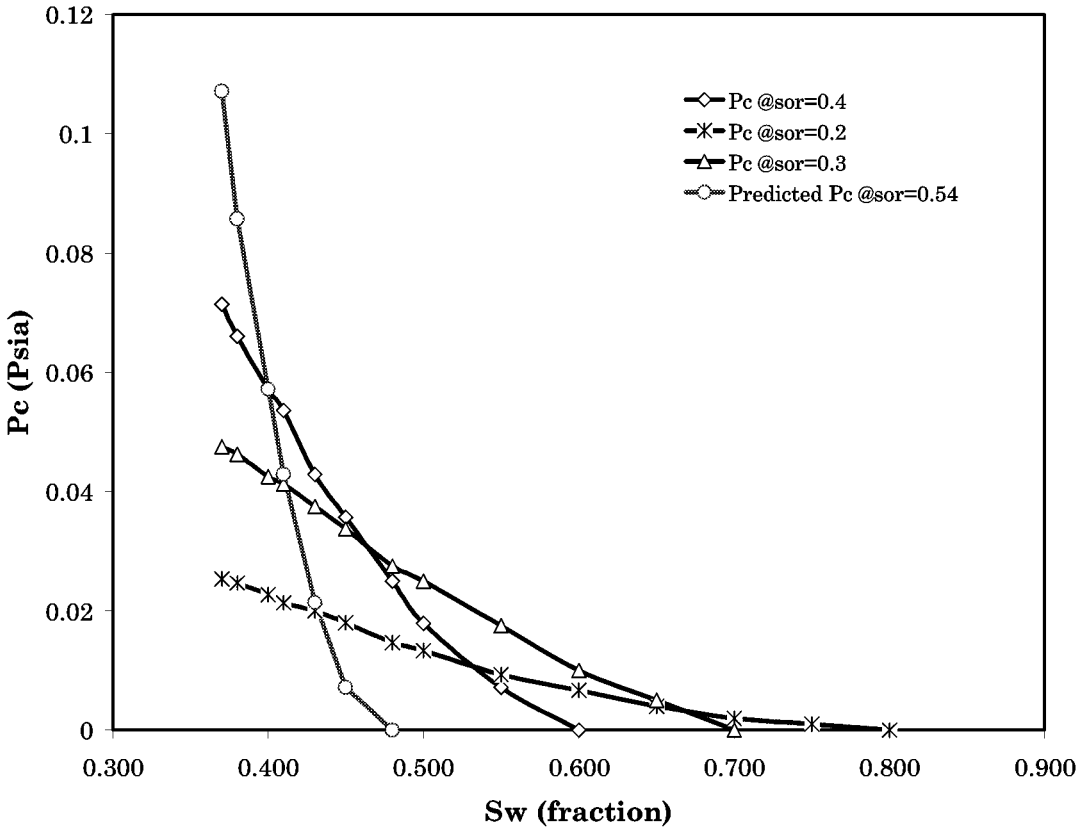

Fig. 2.8-1—Imbibition capillary pressure obtained from matching spontaneous imbibition data

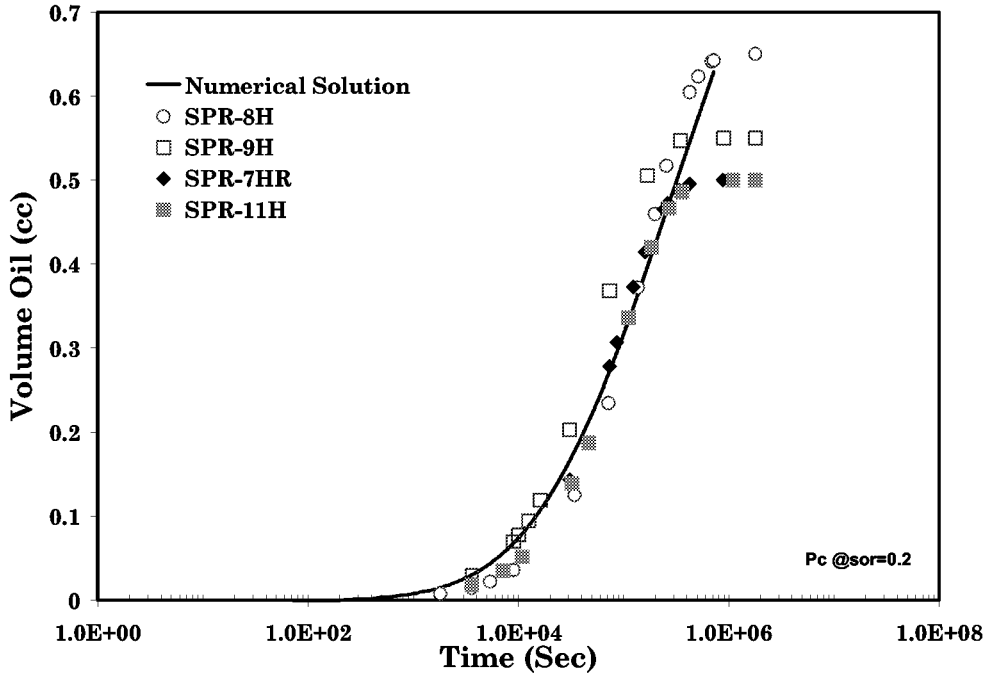

Fig. 2.8-2—Matching between spontaneous-imbibition experiments with numerical solution

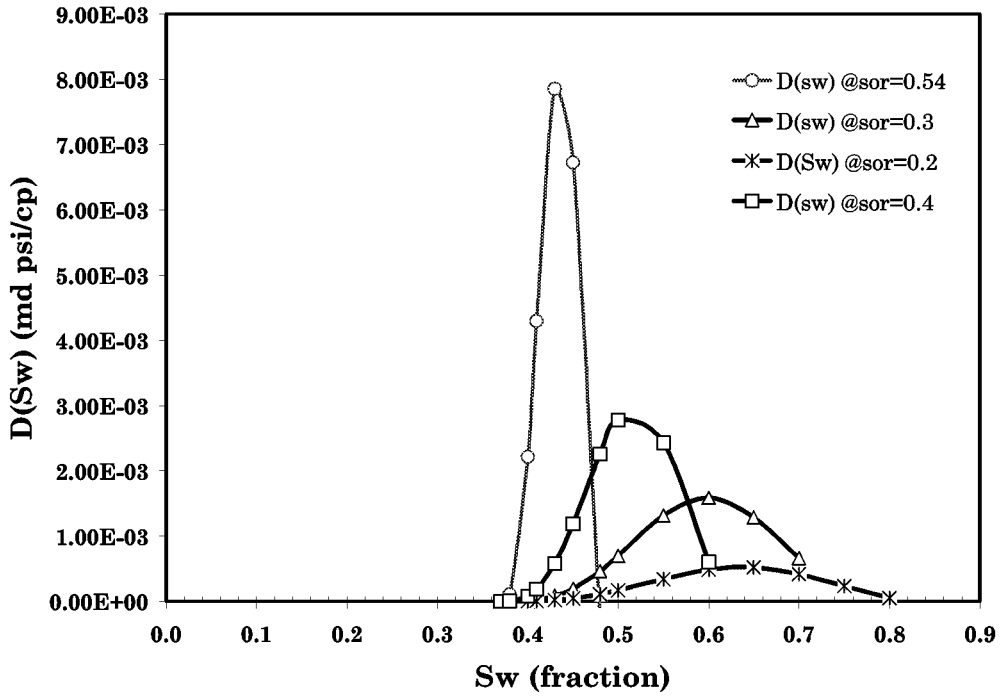

Fig. 2.8-3—Non-linear difusion coefficient

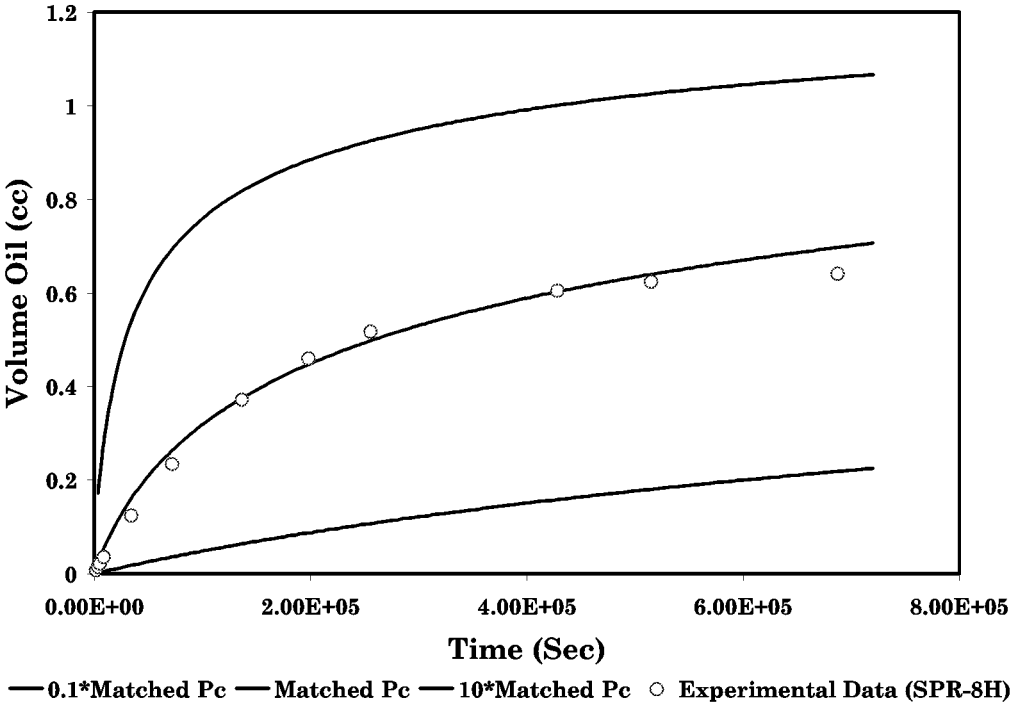

Fig. 2.8-4—Effect of different capillary pressures on oil volume recovered

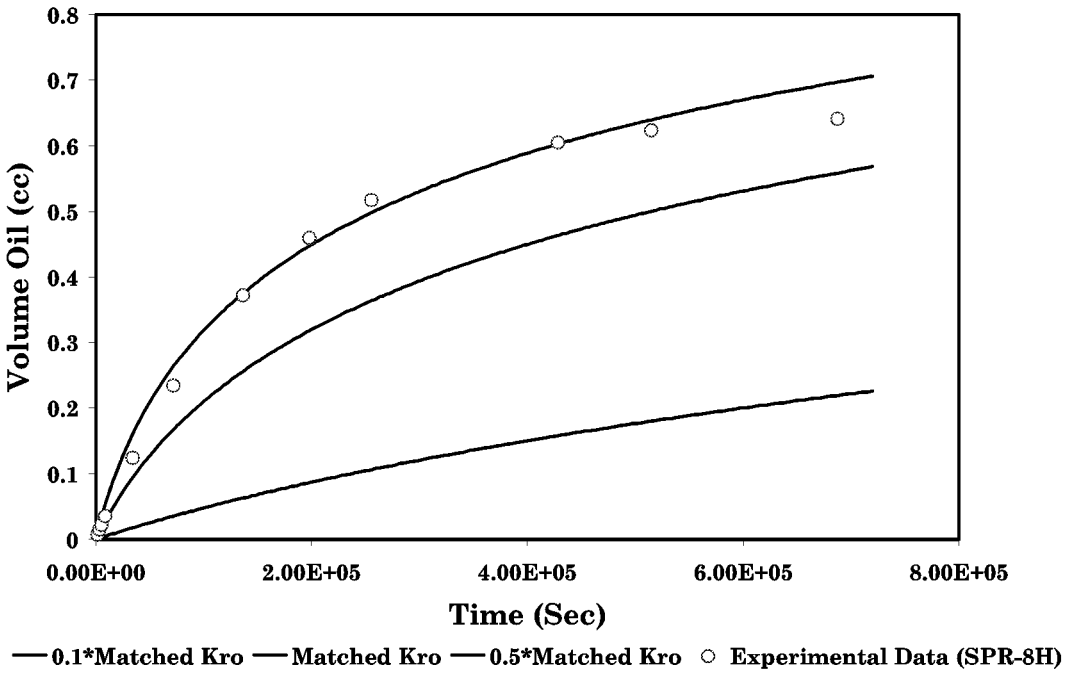

Fig. 2.8-5—Effect of different oil relative permeabilities on oil volume recovered

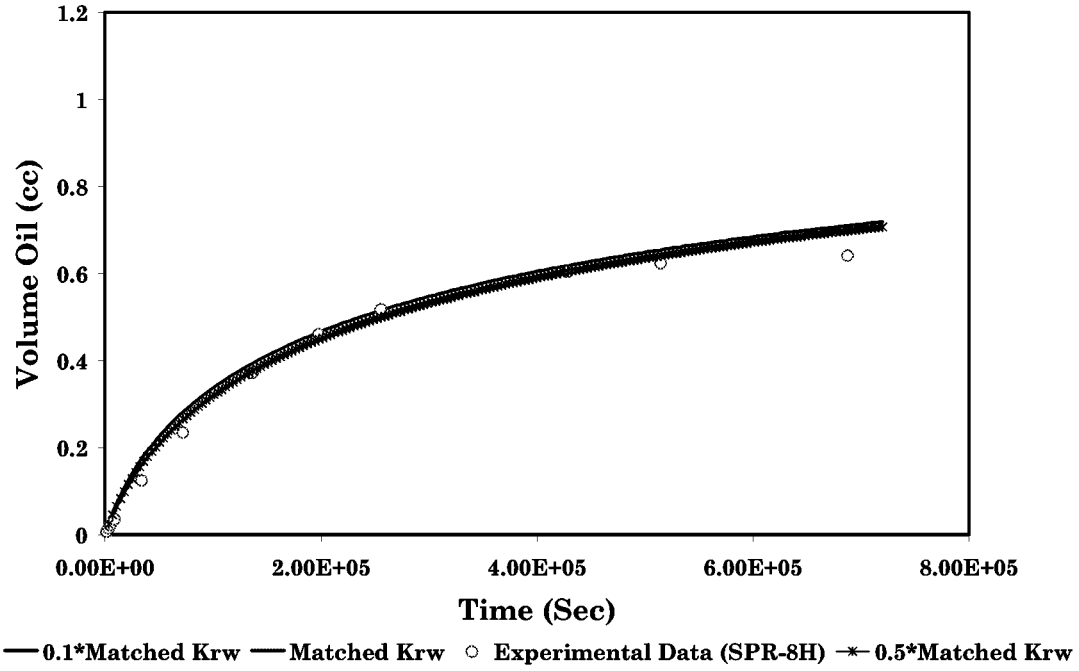

Fig. 2.8-6—Effect of different water relative permeabilities on oil volume recovered

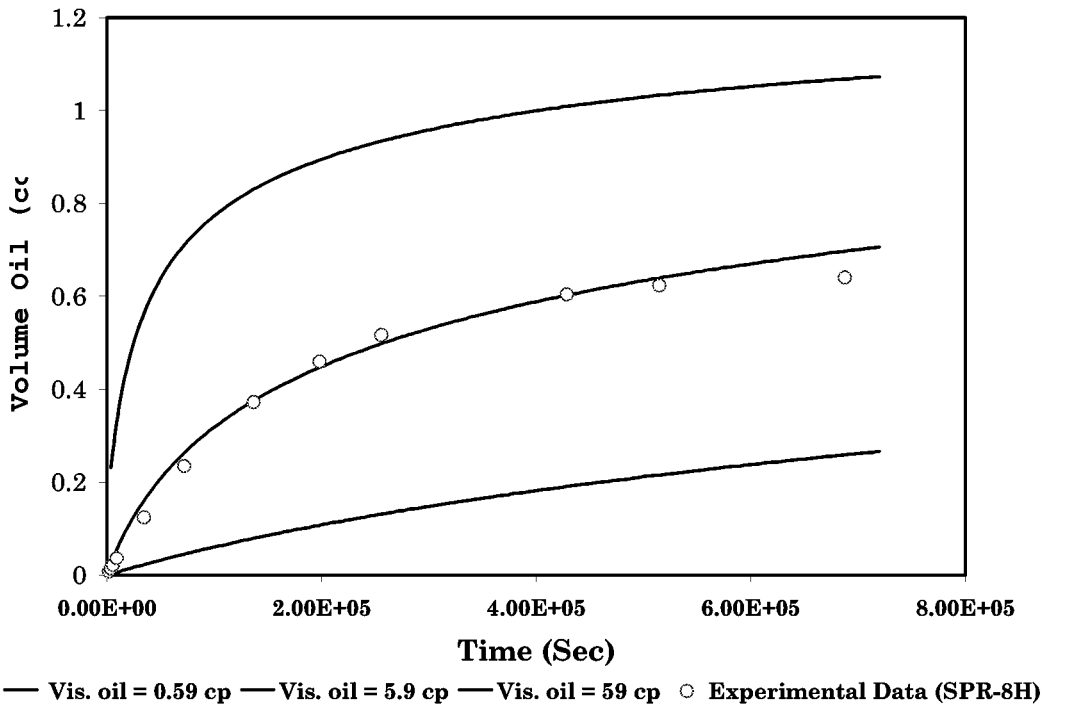

Fig. 2.8-7—Effect of different oil viscosities on oil volume recovered

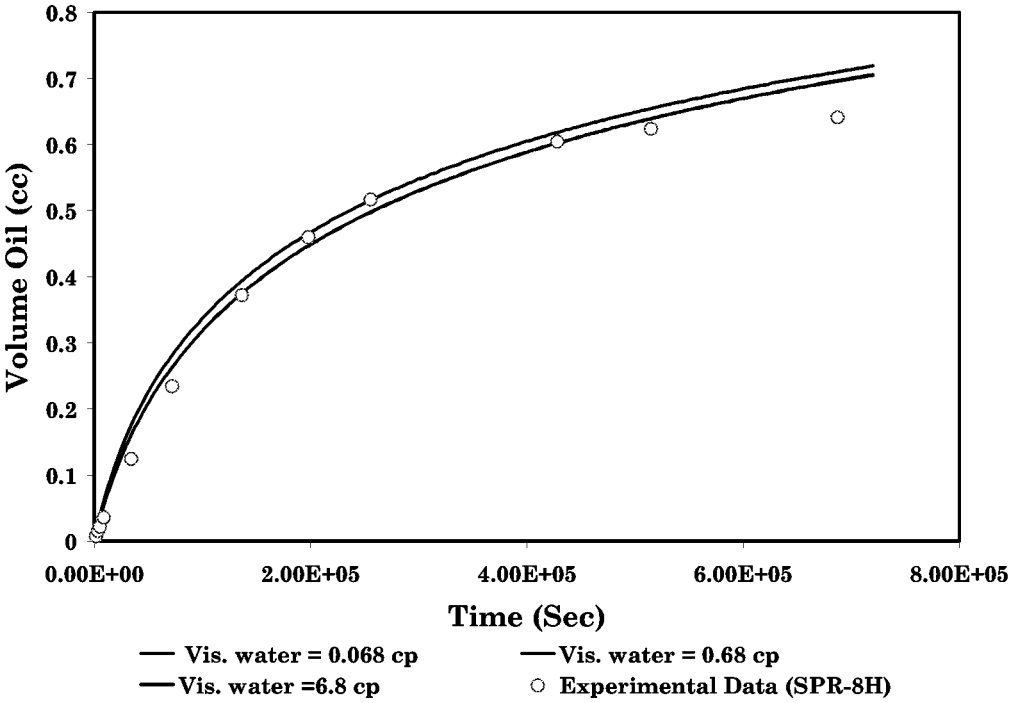

Fig. 2.8-8— of different water viscosities on oil volume recovered

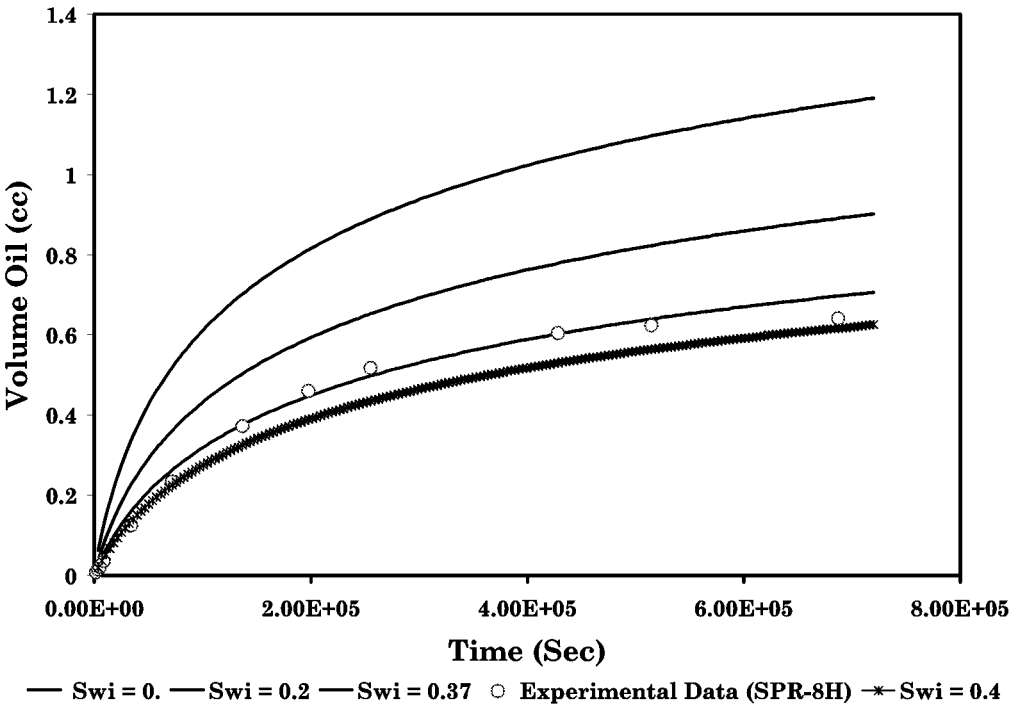

Fig. 2.8-9—Effect of different initial water saturations on oil volume recovered

2.9 IMBIBITION-FLOODING MODELING OF ARTIFICIALLY FRACTURED CORE

The capillary force is the only force to recover oil during static imbibition tests. However, there are two processes involved during producing oil by waterflooding in naturally fractured reservoirs, spontaneous imbibition (capillary force) and displacement processes (viscous force). During spontaneous imbibition, water imbibes into the matrix and oil is expelled from the matrix to the fracture (counter current mechanism). The oil that reaches the fracture is displaced by injected water to the production end of the fracture, as shown in Fig. 2.9-1. Several laboratory and numerical studies have been conducted regarding this subject (Brownscobe and Dyes [1952], Mannon and Chilingar [1972], Kleppe and Morse [1974], Kazemi and Merrill [1977], Babadagli [1994]).

In order to understand the imbibition process in an artificially fractured core, a coreflood experiment at low water injection rate was performed at reservoir temperature. A low-permeability Berea core sample was cut in cylindrical shape, 3 in. long and 1.5 in. diameter. The fracture pattern on the core sample was generated along the long axis using a hydraulic cutter. The cut sections were put back together without polishing the cut surfaces and without spacers. Synthetic Spraberry brine and Spraberry crude oil were used as wetting and non-wetting phases. The properties of rock and fluids for both cores used in this experiment are shown on Tables 2.9-1 and 2.9-2.

In general, the experimental process was started by saturating the core sample with 100% Spraberry oil. This process was followed by brine imbibition flooding as the wetting phase. The experimental procedure is described in detail as follows:

- Dimensions of core sample were taken and the core sample then weighed.
- The core sample was inserted into a Hassler-type core holder using a confining pressure of 500 psi to saturate the core by oil. Approximately 2-5 PV of Spraberry crude oil were passed through the core sample using a constant pressure of 30 psi supplied by a nitrogen tank. The volume of oil produced then was measured to determine the oil rate. By using Darcy's law, the absolute matrix permeability to oil was then calculated.
- After permeability measurement, oil-saturated core was taken from the core holder and covered with aluminum foil to prevent air penetration into the core sample. Then it was cut in half using a hydraulic cutter to generate fracture horizontally along the axis of the core. The oil-saturated artificially fractured core was then weighed to determine core pore volume and porosity.
- The core was inserted back into the Hassler-type core holder. The effective permeability of the fractured core was determined by injecting oil into the fractured core in the core holder. The fracture permeability (Guo and Svec, 1998) was calculated based on the following equation by assuming the fracture porosity of 1%:

$$k_e = k_m + \phi_f k_f \quad \text{.....2.39}$$

where k_e(mD), k_m(mD) k_f(mD)and ϕ_f(fraction) are the effective reservoir permeability, matrix permeability, fracture permeability and fracture porosity, respectively.

- The fracture width, w_f(cm), was calculated based on the correlation developed by Seright *et al* (1996):

$$w_f = 0.000131\sqrt{k_f} \quad \text{.....2.40}$$

- The oil-saturated artificially fractured core was taken again from the core holder to clean oil from the core surface. Then, the core was inserted back into the core holder to start the experiment. The face of the matrix was sealed off by wrapping plastic and aluminum foil, in order to allow brine injection flow only through the fracture. This set-up was stored in an air bath with constant temperature of 138°F, as shown in Fig. 2.9-2.
- During the experiment, the oil-saturated core sample was flooded by injecting synthetic Spraberry brine into the fracture with constant brine injection rate of 4.0 cc/hour. The oil and brine produced were collected against time at the producing end of the fractured core for about 48 hours, until zero oil production rate was achieved.

Dynamic Imbibition Modeling

Single porosity simulation was used instead of dual porosity simulation, because single porosity is more representative for modeling a single fracture from the artificially fractured core. However, this single porosity simulation has to be able to duplicate the behavior of dual porosity simulation, which has different properties for matrix and fracture media. Thus, the properties of a fracture should be added in the single porosity simulator, such as porosity, permeability, relative permeability, and capillary pressure.

The rectangular grid block was used to overcome the difficulty of modeling the cylindrical core shape. The pore volume of the rectangular shape was set to be the same as the cylindrical core pore volume. Three layers were used in the model with the fracture layer between the matrix layers. In addition, 10 x 10 grid blocks were used in x and y direction. The fracture layer was injected at one end with low constant water injection rate of 4.0 cc/hour (Berea core). Oil and water were produced at the opposite end of the fracture layer. The rest of the boundary blocks had a specified no-flow boundary condition.

Relative permeability for the matrix layer was calculated from the following relationships (Kazemi and Merrill, 1977).

$$k_{rw} = S_w^{\,3} \quad \text{.....2.41}$$

$$k_{ro} = (S_o - S_{or})^3 \quad \text{.....2.42}$$

while relative permeability for the fracture layer was assumed to be a straight line for both k_{rw} and k_{ro}.

Similar procedures were carried out with the Spraberry core, except for using a more refined grid block in the vertical direction and Spraberry relative permeability curves (Fig. 2.9-3). The refined grid block was used to avoid numerical instability because the grid blocks representing the fracture are very small and the matrix permeability is very low (0.1 md) compared to that of Berea core (28.09 md). As with the Berea core, relative permeability was fixed and the main adjusted parameter was the matrix capillary pressure. Zero capillary pressure was used as the base case in fracture layer for both Berea and Spraberry cores.

The initial condition from the reservoir simulator is obtained from the hydrostatic equilibrium calculation. For instance, initial water saturation is determined by capillary pressure, which is based on the difference between oil pressure and water pressure. Thus, it is difficult to use the equilibrium option to represent initial conditions for the laboratory experiment. Instead of using the equilibrium option, initial water saturation and pressure were input directly, since those initials were known from laboratory experiments.

Fracture Capillary Number

Naturally fractured reservoirs are characterized by two distinct media, a low permeability matrix and a high permeability fracture system. This distinction in permeability may result in rapid water breakthrough during water injection, depending on the wettability of the matrix.

Fluid displacement in a fracture network occurs due to the fracture system's higher conductivity compared to that of the matrix when an exchange of fluids occurs between matrix and fracture system. The fluid transfer process is controlled by the flow of water under naturally imposed pressure gradients (viscous force) and the spontaneous movement of water into the matrix under capillary forces (imbibition). During spontaneous imbibition, water imbibes into the matrix and oil is expelled from the matrix to the fracture (countercurrent mechanism). The oil that reaches the fracture is displaced by injected water to the production end of the fracture, as illustrated in Fig. 2.9-1.

High water injection rate is one of the causes of low productivity in the Spraberry Trend Area. Water breakthrough occurred in most producing wells without any flush production of oil after waterflooding was initiated (Schechter *et al*, 1996). Elkin (1963) proposed to stop water injection temporarily to permit the reservoir to equalize between capillary and viscous forces. Water injection was ceased and within five days oil production increased threefold. In the months following, cyclic pressure pulsing was performed during injections, which increased the recoveries above those observed during continuous water injection.

Several papers were published on dynamic imbibition experiments using fractured cores to illustrate the actual waterflooding mechanism in naturally fractured reservoirs. These

papers were concerned primarily with developing mathematical models to match the results of experimental work (Kazemi and Merrill [1977], Babadagli [1994]).

Few studies have been conducted to optimize water injection rates at field dimensions scaled up from coreflood experiments. A recent study conducted by Babadagli (1994) addressed this subject. He concluded that the injection rate should be adjusted depending on the matrix permeability and maximum matrix capillary pressure to obtain the efficient capillary imbibition transfer. Using a similar basic equation as derived by Babadagli (1994), we propose the fracture capillary number (FCN) equation to scale up laboratory data to field dimensions. Derivation of our FCN equation is not based on dimensionless analysis, but on the geometry and properties of the matrix and fracture system (Fig. 2.9-4). Therefore, it is not universal, even though it is dimensionless. The dynamic imbibition data from different cores do not superimpose onto one curve as is characteristic of a dimensionless equation. However, the use of this equation provides an estimate of the injection rate necessary to avoid early breakthrough during waterflooding in naturally fractured reservoirs.

The parameters that affect the viscous and capillary forces can be grouped into a fracture capillary number (FCN) equation, which is used to determine the critical injection rate. It is defined as the ratio between the viscous force (parallel to the fracture direction) and the capillary force (perpendicular to the fracture direction). The viscous force is defined as a function of water velocity, water viscosity and fracture volume and is assumed to occur only in the fracture (Fig. 2.9-4). The capillary force that occurs only in the matrix is defined as a function of interfacial tension, contact angle and matrix volume (Fig. 2.9-4). Thus, the fracture capillary number can be written below:

$$N_{f_{VC}} = \frac{Viscous\ Force}{Capillary\ Force} = \frac{v\,\mu_w\,A_f}{\sigma\cos\theta\,A_m} \quad \text{.....2.43}$$

where v is the velocity of the injected fluid in the fracture, defined as $\frac{q_{inj}}{A_f}$, where q_{inj} is the volumetric injection rate, and A_f is the fracture cross-sectional area. A_f is the fracture area, where the viscous force occurs, and can be defined as $A_f = w \times dz$. dz is the height of the core, μ_w is the water viscosity, σ is the interfacial tension and θ is the contact angle. σ $cos\theta$ can be substituted with $\frac{P_{c,\max}}{J(S_{wi})}\sqrt{\frac{k_m}{\phi_m}}$, where $P_{c,max}$ is the maximum capillary pressure at S_{wi}, k_m is the matrix permeability, ϕ_m is the matrix porosity, and $J(S_{wi})$ is the J-function at S_{wi}. A_m is the matrix area, where the capillary force occurs that can be defined as $A_m \approx dy \times dz$, where dy is the length of the core in the y-direction.

By rearranging and substituting all those parameters into Eq. 2.43, it can be rewritten as follows:

$$N_{f_{VC}} = \frac{q_{inj}\mu_w}{\frac{Pc,\max}{J(S_{wi})}\sqrt{\frac{k_m}{\phi_m}}A_m} \quad \text{.....2.44}$$

For laboratory units, Eq. 2.44 can be written as

$$N_{f_{VC}} = \frac{1.27e-5 * q_{inj}(cc/hr)\mu_w(cp)}{\frac{Pc,\max(psi)}{J(S_{wi})}\sqrt{\frac{k_m(md)}{\phi_m}}A_m(cm^2)} \quad \text{.....2.45}$$

In the same way, laboratory units can be scaled to field units as written below:

$$N_{f_{VC}} = \frac{9.05e-5 * q_{inj}(STB/Day)\mu_w(cp)}{\frac{Pc,\max(psi)}{J(S_{wi})}\sqrt{\frac{k_m(md)}{\phi_m}}A_m(ft^2)} \quad \text{.....2.46}$$

Results and Discussion

In numerical modeling of the dynamic imbibition process, the matrix capillary pressure controlling the imbibition mechanism was the primary parameter adjusted to match the experimental data. Meanwhile, the fracture capillary pressure was set to be zero. The cumulative water production, oil production rate, cumulative oil production, oil recovery and watercut were parameters used to match between the observed experimental data and the numerical model. The best matches between experimental data and numerical solution (only cumulative water production and cumulative oil production are presented) can be seen in the Figs. 2.9-5 through 2.9-8.

The cumulative water production of Berea core shows that once brine injection was started with a constant rate of 4.0 cc/hr, oil was produced simultaneously. However, the water still was not produced. This indicated that the water was imbibing into the rock and oil was expelled from the matrix to the fracture. After two hours of brine injection, water breakthrough occurred because the maximum matrix capillary pressure was reached. Consequently, water started to produce before being completely imbibed. Water was produced until 100% watercut was reached. Similar behavior was also shown by the performance of cumulative water production of Spraberry core.

The matrix capillary pressures for Berea and Spraberry cores generated, after matching was obtained, are shown in Fig. 2.9-9. Although matrix capillary pressure for Berea core is lower than for Spraberry core, oil recovery for Berea core is higher than for Spraberry core. The higher cumulative oil production is because of capillary imbibition transfer for Berea core is higher than for Spraberry core.

Satisfactory reproducibility of the dynamic imbibition procedure using Berea cores was obtained when two series of dynamic imbibition tests with different cores at the same experimental conditions were performed, as shown in Fig. 2.9-10. Then, different water injection experiments were conducted at different rates (*i.e.*, 1, 2, 4, 8, 16 and 40 cc/hr). The results were plotted on oil recovery curves versus total production for continuous flow in the fracture as shown in Fig. 2.9-11. The oil recovery curves seen in this figure imply that once capillary imbibition is initiated (*i.e.*, the first drop of water penetrates the matrix), imbibition is continuous until the recoverable amount of the oil in the matrix is displaced by capillary imbibition. However, the oil recovery rate of this process is different at each injection rate. As the injection rate is increased, the brine tends to flow in the fracture because of the high fracture-matrix permeability ratio, which results in slower oil recovery because faster injection rate results in shorter residence time for water to contact the matrix. The water cuts at different injection rates were also plotted against time as shown in Fig. 2.9-12. The plot indicates that an increase in the injection rate causes high water cut and results in significantly faster water breakthrough.

An extension of the dynamic imbibition experiment was performed using four low-permeability Spraberry cores. Three cores were designated as fractured cores with dynamic imbibition investigated at different injection rates. The other core was designated as an unfractured core. The experiments were carried out for 70 hours. The results are presented in Fig. 2.9-13. If unfractured core is compared with fractured core at the same injection rate of 0.2 cc/hr, brine displaces oil in a piston-like process in the unfractured core with an ultimate recovery of about 55% IOIP at the production end. The ultimate recovery of the fractured core was lower than that of the unfractured core. Obviously, this is due to a difference in the displacement mechanisms. The experiment using unfractured core was a piston-like displacement, while countercurrent imbibition and viscous displacement were involved in the fractured core.

For fractured cores with different injection rates (*i.e.*, 0.2, 0.5 and 1.0 cc/hr), the results were similar to those of experiments using fractured Berea cores. Faster injection rates resulted in a slower rate of oil recovery, while the ultimate recovery approached the same value as shown in Fig. 2.9-13. However, higher injection rates are associated with faster water breakthrough (Fig. 2.9-14).

According to Babadagli [1994] when the injection rate increases and reaches a certain value, there is no capillary imbibition because the contact time with the matrix was not long enough. Based on this mechanism, the limiting value of injection rate can be defined as a critical injection rate. The critical injection rate is the maximum injection rate at which the capillary imbibition is not effective. At this point the injected fluid does not contact the matrix long enough to initiate capillary imbibition. Thus, water flows only in the fracture, displacing the oil, and no matrix interaction occurs.

To determine the critical injection rate, the ultimate oil recovery at a certain total fluid production at different injection rates for both Berea and Spraberry cores (Figs. 2.9-11 and 2.9-13) was chosen. The results were then plotted in the form of injection rate against the ratio between total oil produced and total fluid produced (TOP/TFP) called an oil cut,

as shown in Fig. 2.9-15. The results show that the oil cut produced from Berea core is higher than that from Spraberry core. At lower (2.0 cc/hr) injection rates used in fractured Berea core, the capillary force (static imbibition mechanism) was the only force in the coreflooding process. Thus, oil recovery took a substantial amount of time. When using injection rates between 2.0 and 16.0 cc/hr, both capillary pressure and viscous forces were dominant (dynamic imbibition mechanism). This means that when water imbibed into the matrix and released oil from the matrix to the fractures, the oil in the fracture was pushed out by the volume of the water injected (viscous forces). However, at a higher injection rate (more than 16 cc/hr), coreflooding was inefficient because the viscous force was the only dominant mechanism. After the maximum capillary pressure was reached, the producing end only produced water. Thus the oil cuts from 16 cc/hr injection rate were about the same as the oil cut using injection rate of 40 cc/hr. However, the field cost of a higher injection rate is greater since more water must be processed to achieve the same recovery. The results also suggest that the critical injection rate, which also can defined as the maximum injection rate in which the capillary and viscous forces are still dominant, was determined to be 20 cc/hr for this set of experiments. The critical injection rate is the point where the curves bend. Beyond this point, the curves are essentially constant and steadily approach zero oil cut.

An exponential correlation was used to fit the experimental data. Then, the injection rate beyond experimental points could be approximated. The critical injection rate for Spraberry reservoir rock was found to be approximately 10 cc/hr.

In order to upscale the critical injection experiments to field dimensions, Eq. 2.45 and Spraberry rock properties (Table 2.9-2) were used. The critical injection rate of 10 cc/hr from Spraberry core was converted to N_{fvc} of 1.0e-7. Using this N_{fvc} number, the critical injection rate for field dimensions can be calculated using a rearranged version of Eq. 13. The upscaling of laboratory data to field dimensions is tabulated in Table 2.4, with Berea sandstone used as a comparison. For the Spraberry waterflood case, the waterflood pilot consisted of four injection wells with a center producer for creating a confined 40-acre five-spot pattern, 0.1 md matrix permeability, 10% porosity and 10 ft net pay. The critical injection rate is about 393 bbl/day water. Meanwhile, the critical injection rate for the more permeable rock (Berea sandstone) is about 1013 bbl/day.

This fracture capillary number concept was also applied for the O'Daniel Pilot area, assuming the same properties as in the Spraberry core case. This pilot area consists of six water injection wells, four CO_2 injection wells, three oil production wells, and two logging-observation wells. The well location is shown in Fig. 2.9-16. The distance between the center production well (well 39) and the seven water injection wells (well 41, 42, 43, 44, 45, 47, and 48) that are parallel to fracture orientation is tabulated in Table 2.9-4 along with the critical injection rate for each well. Meanwhile, the critical injection rate for well 46 cannot be determined because its orientation with respect to well 39 is perpendicular to the fracture direction.

Conclusions

1. Imbibition transfer is more effective for low injection rates due to lower viscous forces and longer contact time with the matrix.
2. Optimization of the injection rate is important prior to conducting waterflooding in naturally fractured reservoirs. As the flow rate increases, contact time between matrix and fluid in fracture decreases, thereby reducing the effectiveness of capillary imbibition.
3. Increasing injection rate beyond the critical injection rate causes high watercut, which results in significantly faster water breakthrough (the displacement process is inefficient).
4. The critical injection rate depends on the properties of the rock. The critical injection rate for Berea core in lab experiments and 40-acre field dimensions is 20 cc/hr and 1013 STB/D, respectively, and for Spraberry core, the critical injection rate is 10.0 cc/hr and 393 STB/D, respectively.

Nomenclature

A = area, L^2
dy = length of the core in y-direction, L
dz = height of the core, L
D = capillary diffusion coefficient, ML^3T^{-2}
f = fractional flow, dimensionless
$J(S_{wi})$ = J-function at S_{wi}, dimensionless
k = permeability, L^2
k_r = relative permeability, dimensionless
$P_{c,max}$ = maximum capillary pressure, $ML^{-1}T^{-2}$
q_{inj} = volumetric injection rate, L^3T^{-1}
S = saturation, fraction
t = time, T
v = velocity of the injected fluid in the fracture, LT^{-1}
w = fracture width, L
x = spatial coordinate, L

Greek letters

σ = interfacial tension, MT^{-2}
θ = contact angle, degree
ϕ = fracture porosity, fraction
μ = viscosity, $ML^{-1}T^{-1}$

Subscripts

e = effective
f = fracture
i = initial

m = matrix
o = oil
r = residual
w = water

References

1. Brownscobe, E.R. and Dyes, A.B.: "Water-Imbibition Displacement-A Possibility for the Spraberry," *Drill. and Prod. Prac.* API (1952), 383-390.
2. Mannon, R.W. and Chilingar, G.V.: "Experiment on Effect of Water Injection Rate on Imbibition Rate in Fractured Reservoirs," paper SPE 4101 presented at the 1972 Annual Fall Meeting of the SPE of AIME, San Antonio, Oct. 8-11.
3. Kleppe, J. and Morse, R.A.: "Oil Production from Fractured Reservoirs by Water Displacement," paper SPE 5084 presented at the 1974 SPE Annual Meeting, Houston, Oct. 6-9.
4. Kazemi, H. and Merrill, L.S.: "Numerical Simulation of Water Imbibition in Fractured Cores," paper SPE 6895 presented at the 1977 SPE Annual Technical Conference and Exhibition, Denver, Oct. 9-12.
5. Babadagli, T.: "Injection Rate Controlled Capillary Imbibition Transfer in Fractured Systems," paper SPE 28640 presented at the 1994 SPE Annual Technical Conference and Exhibition, New Orleans, Sept. 25-28.
6. Guo, B. and Svec, R.: "A Preliminary Analysis of Permeabilities in the Teague-Blinbay Reservoir based on Step-Rate Test on Well Lamunyon Federal #62 and Whole Cores from Well Lamunyon Federal #50," PRRC internal report, January 29, 1998.
7. Seright, R., *et al.*: "Gel Placement Technique," unpublished manuscript, PRRC internal report (1996).
8. Kazemi, H., Merrill, L.S., Porterfield, L.K., and Zeman, P.R.: "Numerical Simulation of Water-Oil Flow in Naturally Fractured Reservoirs," *SPEJ* (Dec. 1976), 317-26.
9. Schechter, D. S., McDonald, P., and Sheffield, T.: "Reservoir Characterization and CO_2 Pilot Design in the Naturally Fractured Spraberry Trend Area, " paper SPE 35469 presented at the 1996 SPE Permian Basin Oil and Gas Recovery, Midland, March 27-29.
10. Elkins, L. F.: "Cyclic Water Flooding the Spraberry Utilizes 'End Effect' to Increase Oil Production Rate," *JPT* (August 1963), 877-884.

Table 2.9-1—Core and Fluid Properties for Berea Core

Core Properties		**Fluid Properties**	
D (cm)	3.786	Oil	Spraberry oil
L (cm)	6.8936	Water	Spraberry brine
k_m (md)	28.09	μ_o (cp)	3.52
ϕ_m (%)	17.16	μ_w (cp)	0.68
k_f (md)	3429	S_{wi} (%)	0
ϕ_f (%)	1.0	S_{or} (%)	40
w_f (cm)	0.0076		

Table 2.9-2—Core and Fluid Properties for Spraberry Core

Core Properties		**Fluid Properties**	
D (cm)	3.607	Oil	Spraberry oil
L (cm)	5.842	Water	Spraberry brine
k_m (md)	0.5	μ_o (cp)	5.92
ϕ_m (%)	10.84	μ_w (cp)	0.68
k_f (md)	335	S_{wi} (%)	36.6
ϕ_f (%)	1.0	S_{or} (%)	42.51
w_f (cm)	0.0024		

Table 2.9-3—Rock Properties of Spraberry and Berea Cores

	Spraberry Core		**Berea Core**	
Parameter	Lab unit	Field unit	Lab unit	Field unit
μ_w	0.68	0.68	0.68	0.68
A	-	40	-	40
$L_{inj\text{-}prod}$	6.8	933.4	7.1	933.4
H	3.6	10	3.7	10
A_m	24.8	9333.81	25.807	9333.81
K	0.1	0.1	63.41	63.41
ϕ	0.1	0.1	0.166	0.166
P_{cmax}	7	7	1.2	1.2
θ	0	0	25	25
σ	26.2	26.2	26.2	26.2
J	0.27	0.27	0.99	0.99
q_{crit}	10	393.22	20	1013.26
Nfvc	1.010^{-7}	-	2.8210^{-7}	-

Table 2.9-4—Critical Injection Rates for Wells in O'Daniel Pilot Area

Injection Well	Distance to well 39 (ft)	Critical injection rate (STB/D)
w-41	1020	430
w-42	1040	438
w-43	1040	438
w-44	1020	430
w-45	1420	598
w-47	1450	610
w-48	1460	615

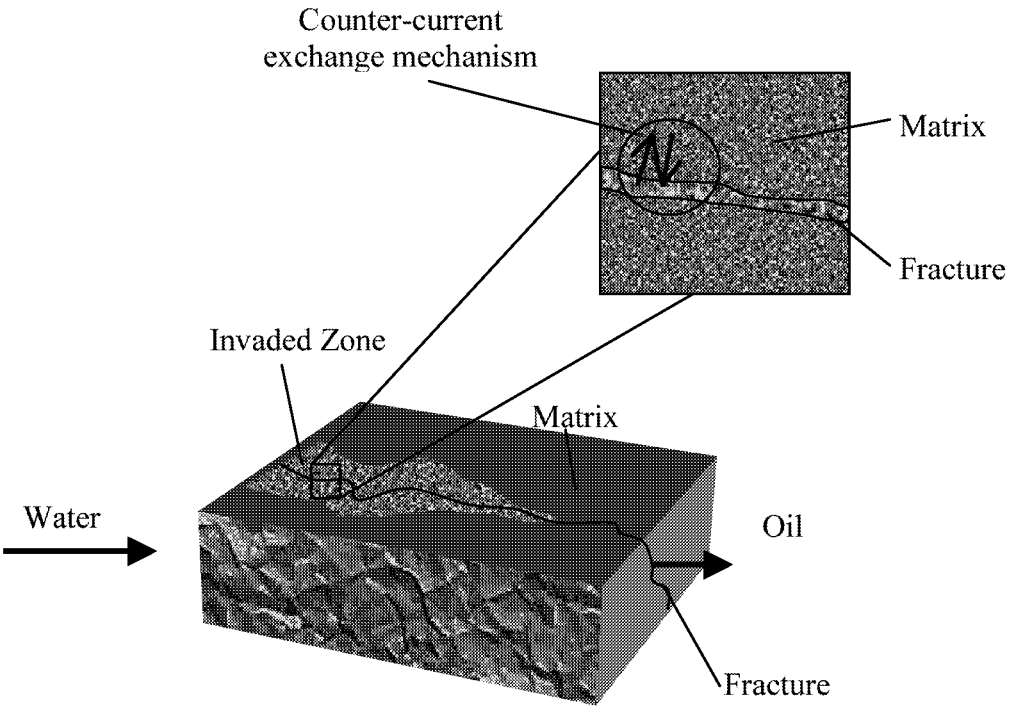

Fig. 2.9-1— Concept of dynamic imbibition process

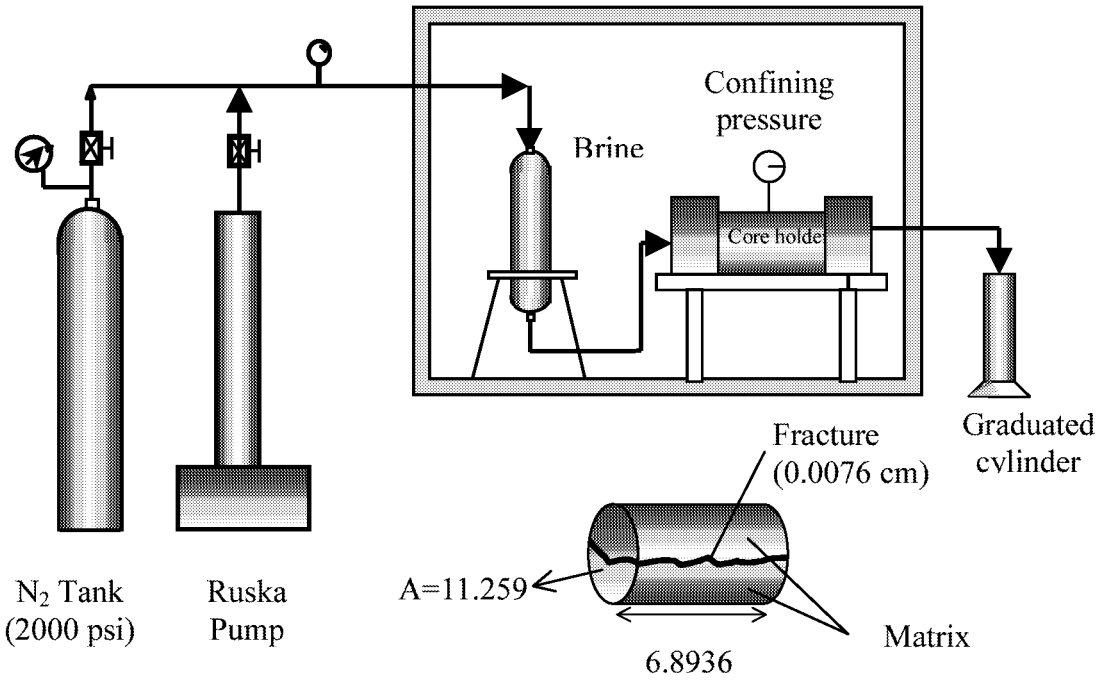

Fig. 2.9-2—Experimental setup of dynamic imbibition

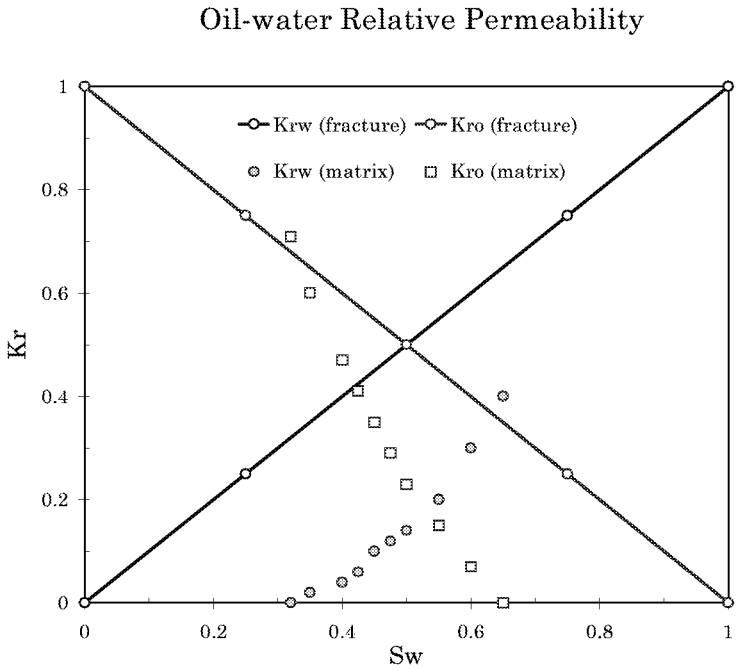

Fig. 2.9-3—Relative permeability curves

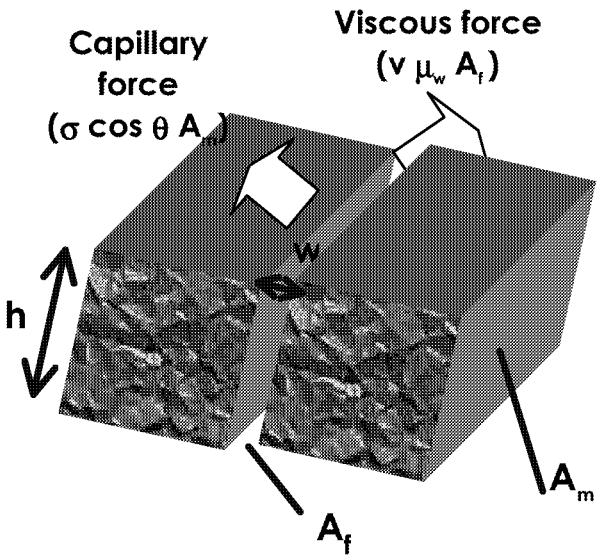

Fig. 2.9-4—Schematic representation of matrix and fracture where the viscous and capillary forces are effective

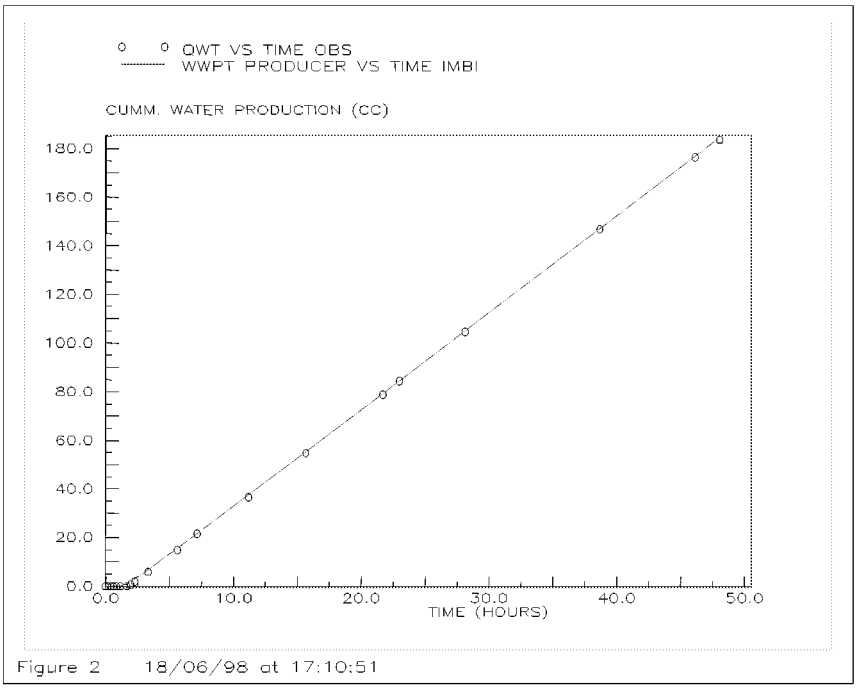

Fig. 2.9-5—Matching between experimental data and the numerical solution (Berea core - cumulative water production, injection rate = 4.0 cc/hr)

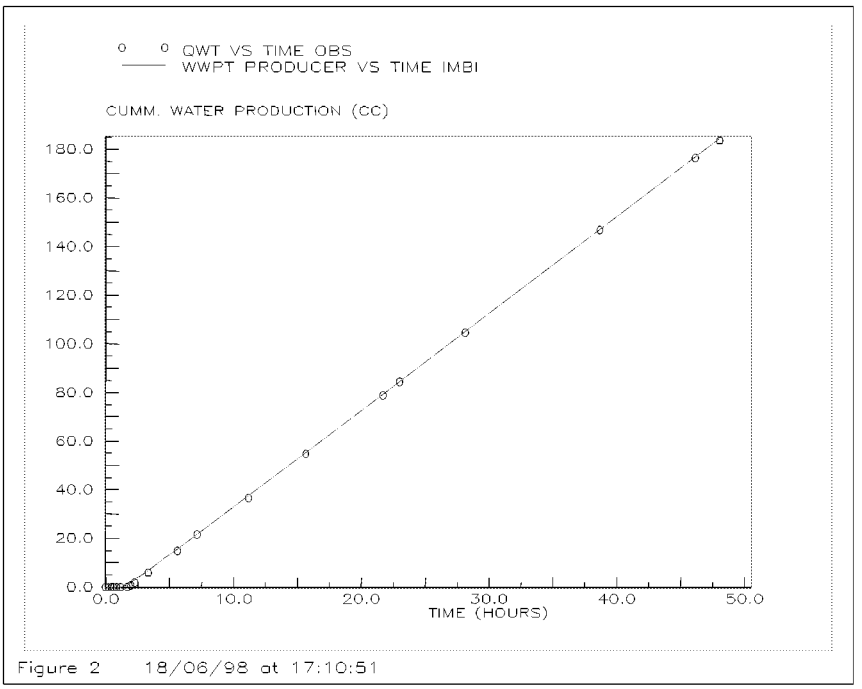

Fig. 2.9-6—Matching between experimental data and the numerical solution (Berea core-cumulative oil production, injection rate = 4.0 cc/hr)

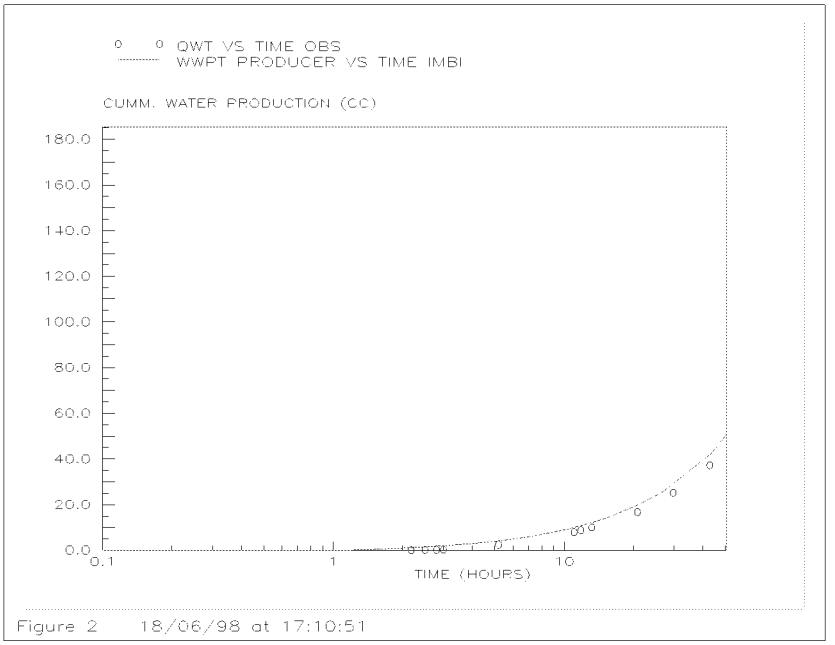

Fig. 2.9-7—Matching between experimental data and the numerical solution (Spraberry core-cumulative water production, injection rate = 1.0 cc/hr)

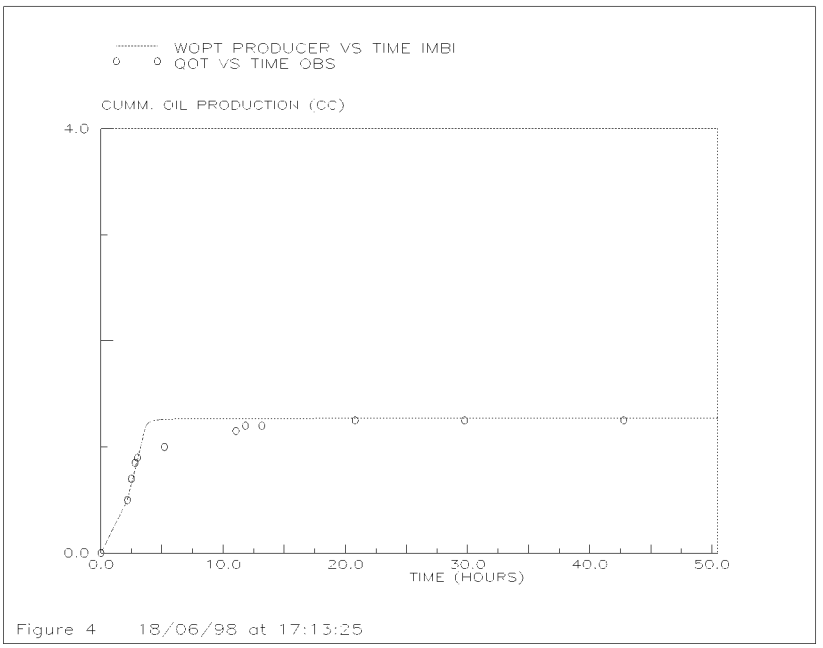

Fig. 2.9-8—Matching between experimental data and the numerical solution (Spraberry core-cumulative oil production, injection rate = 1.0 cc/hr)

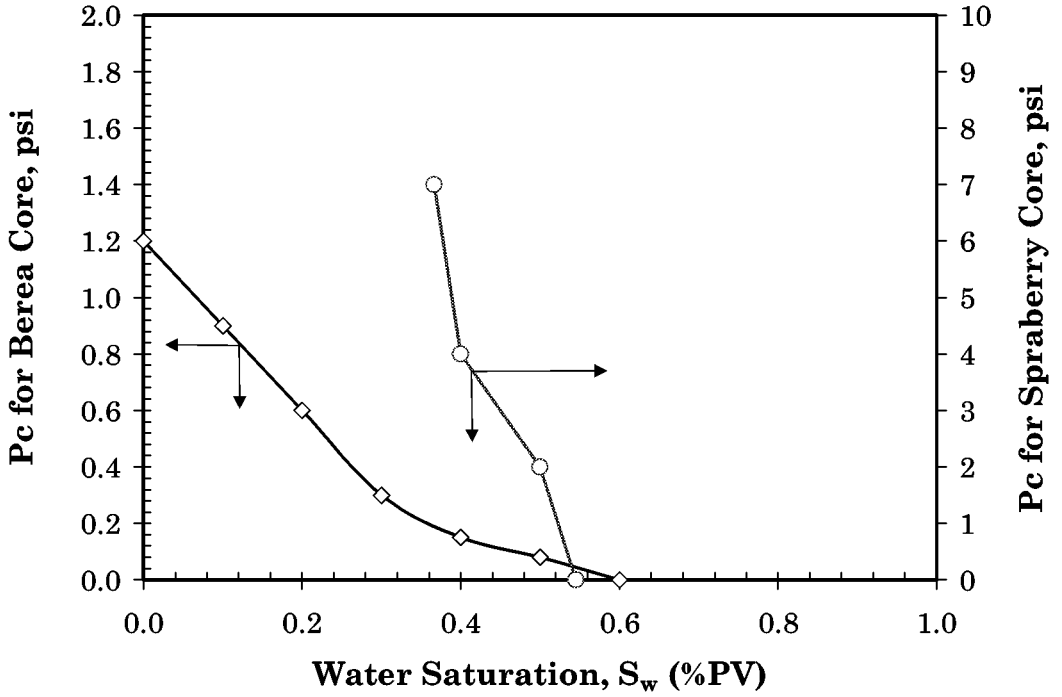

Fig. 2.9-9—Capillary pressure obtained as a result of matching experimental data (Berea and Spraberry cores)

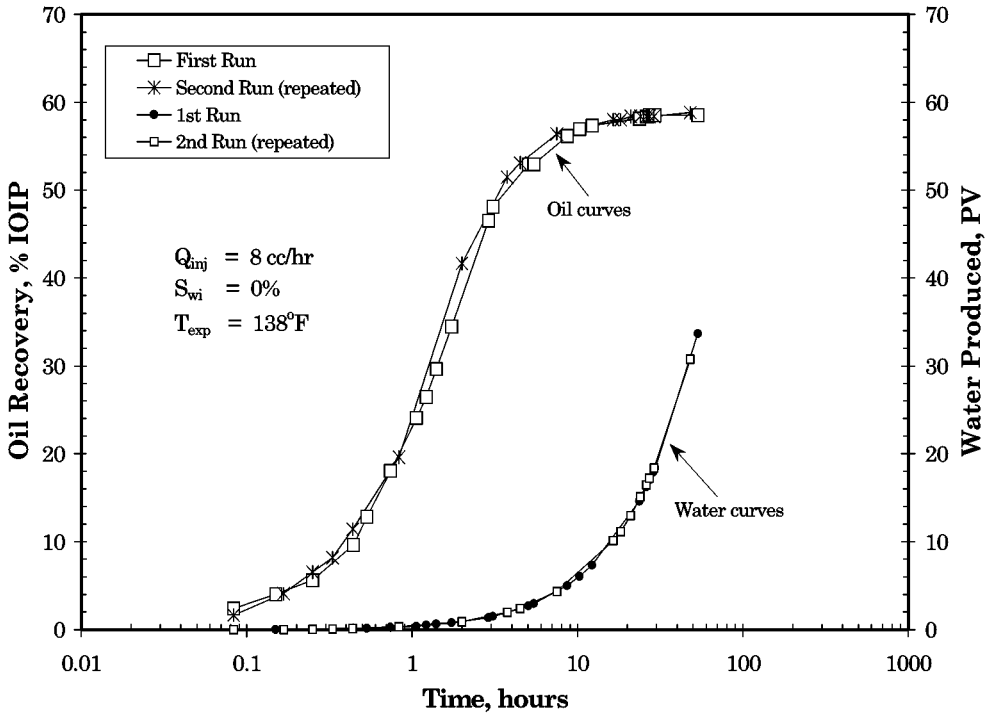

Fig. 2.9-10—Reproducibility of the dynamic imbibition flooding results in Berea sandstones

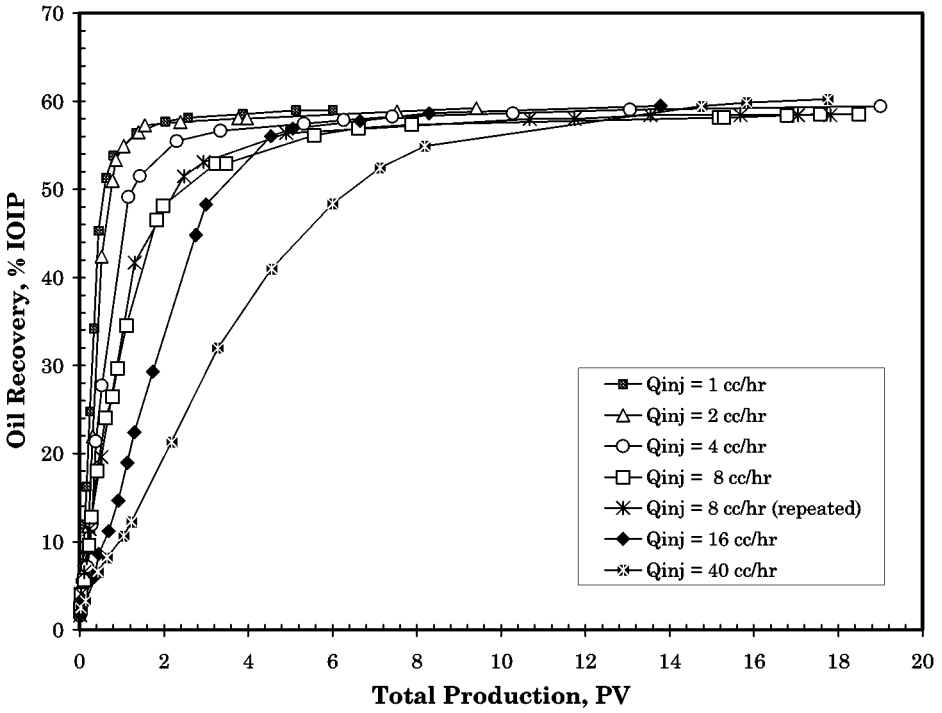

Fig. 2.9-11—Oil recovery from fractured Berea cores during water injection using different injection rates

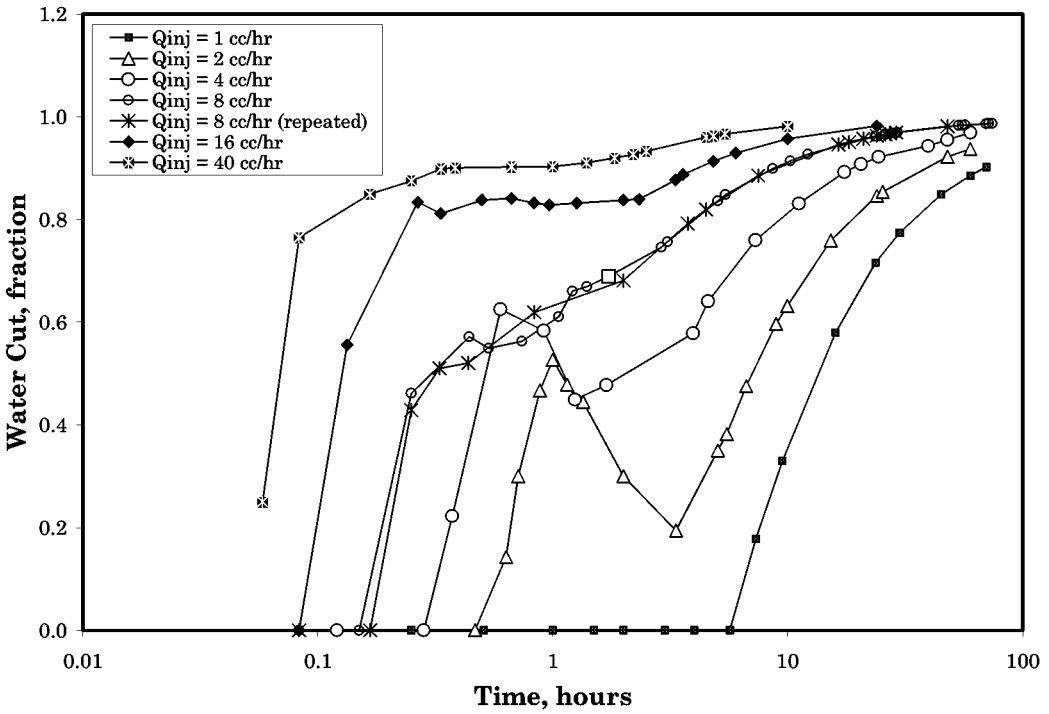

Fig. 2.9-12—Watercut during the dynamic imbibition experiments for fractured Berea cores

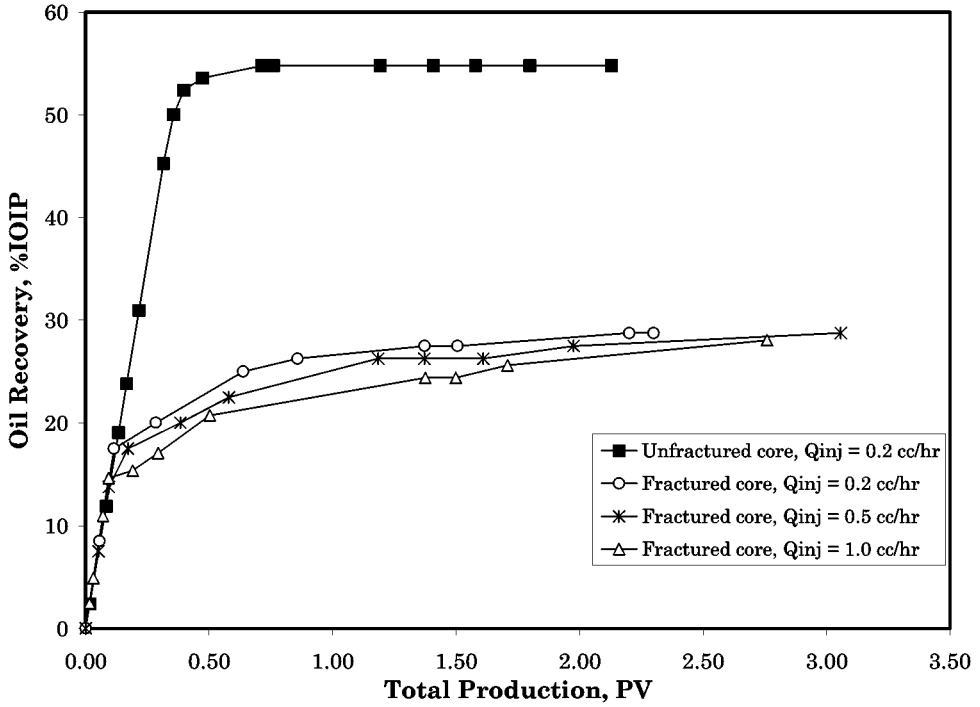

Fig. 2.9-13—Oil recovery from fractured and unfractured Spraberry cores during water injection, using different injection rates

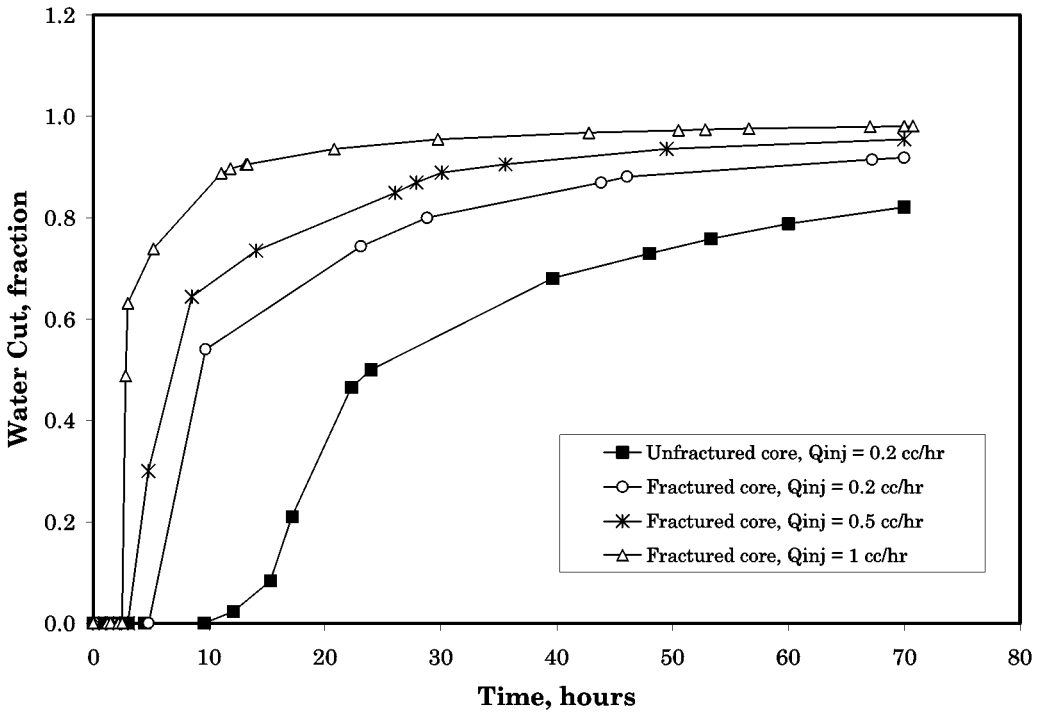

Fig. 2.9-14—Watercut during the dynamic imbibition experiments for fractured and unfractured Spraberry cores

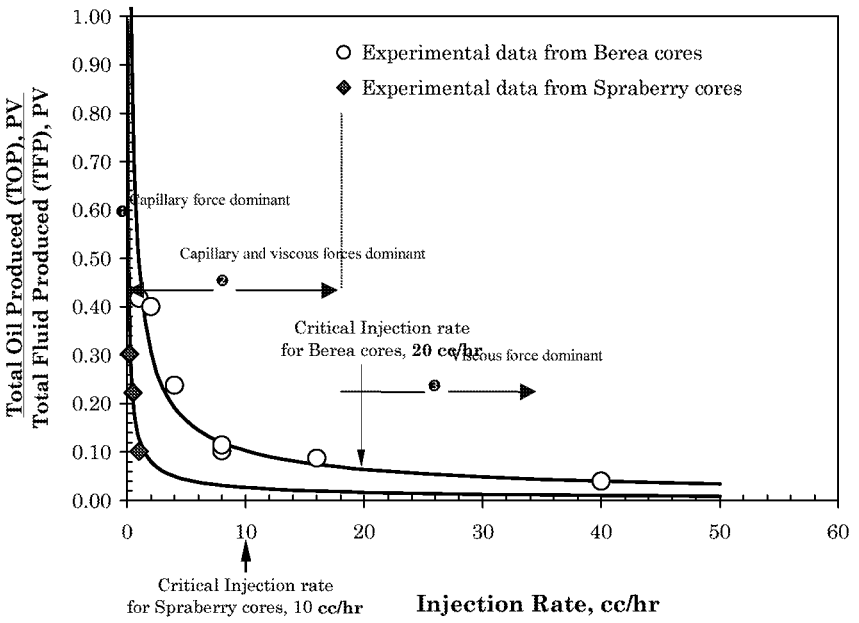

Fig. 2.9-15—Injection rate vs. oil cut (TOP/TFP)

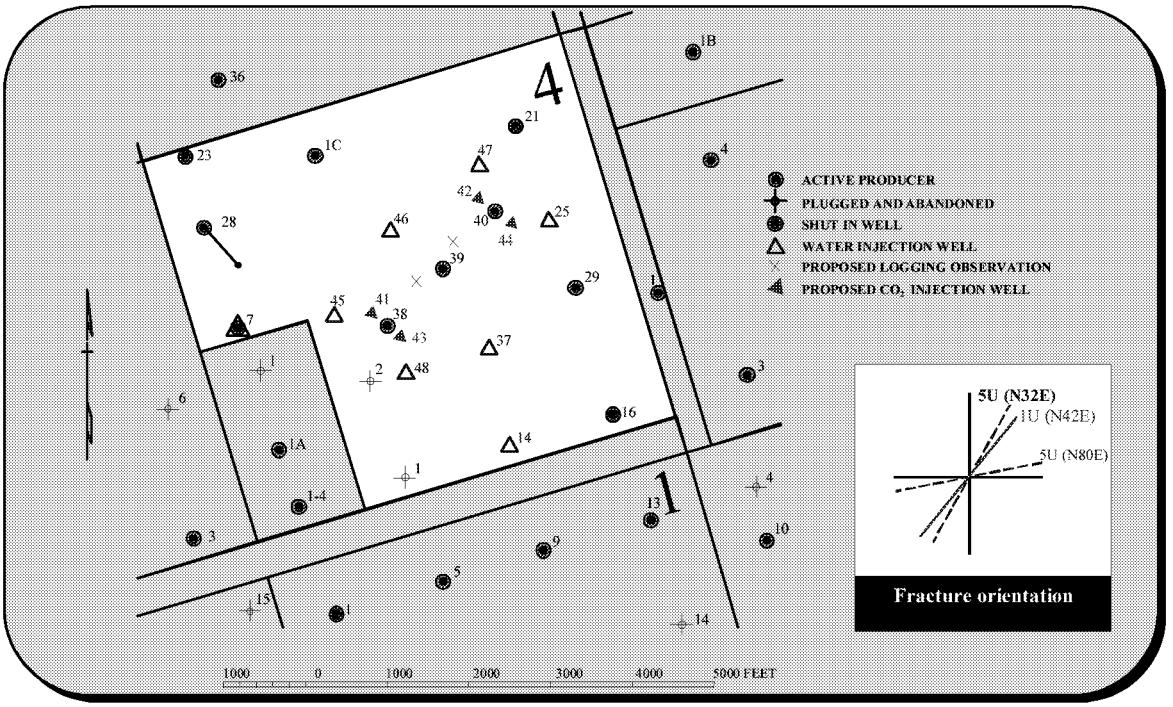

Fig. 2.9-16—E.T. O' Daniel pilot area

3. RESERVOIR PERFORMANCE ANALYSIS

3.1 Scaling Analysis of Water Imbibition Results

Introduction

In order to understand the interaction between rock, crude oil and brine in Spraberry Trend Area reservoirs, water imbibition experiments have been performed using Spraberry oil, synthetic Spraberry reservoir brine, and Spraberry reservoir rock under ambient conditions. Macroscopic displacement efficiency of water to oil in core samples due to capillary forces has been determined by spontaneous imbibition tests. Wettability of Spraberry cores taken from the Spraberry Shackelford #1-38A and E.T. O'Daniel #37 has been estimated based on spontaneous water and oil imbibition tests. It is found that Spraberry reservoir rock is weakly water-wet with mixed wetting behavior. The Amott Wettability index to water (I_w) has been determined to be on average about 0.55, based on 29 imbibition tests. The macroscopic displacement efficiency during spontaneous water imbibition is on the order of 50%. Using 50% for the maximum recoverable oil, scaling from core geometry to matrix block geometry (assuming a fracture spacing of 4 feet) in the 5U Unit of the Upper Spraberry zone resulted in oil recovery after 44 years of waterflood of between 8% and 15.5% depending upon sand permeability. Integration of the recovery profile along the depth of the pay zone resulted in an estimate of imbibition oil recovery from the 5U zone to be about 11%. This is higher than the observed 5-9% of waterflood oil recovery from the Upper Spraberry sand. One of the reasons for overestimation is believed to be wettability alteration of the sand under reservoir conditions. It has been observed that the oil recovery process is slower in our on-going imbibition experiments at reservoir temperature. When the effective oil permeability is used in the scaling equation, scaling from core geometry to matrix block geometry in the 5U Unit of the Upper Spraberry zone resulted in oil recovery after 44 years of waterflood of between 5.5% and 11% with an average of 7.7%, which is close to the observed 5-9% of waterflood oil recovery from the Upper Spraberry sand. However, it is unclear if the effective oil permeability should be used in the scaling equation because the scaling equation was derived on the basis of absolute permeability.

Experimental Results

Experimental procedure and results for imbibition experiments have been presented in Chapter II. Results from 9 complete runs are plotted in Fig. 3.1-1 in dimensionless form. The dimensionless time (t_D) is defined by Ma *et al.* as[2]

$$t_D = t\,(k/\phi)^{0.5}\,\sigma/\mu_g L_c^2 \quad \text{.....(3.1)}$$

where t is the imbibition time, k is the permeability, ϕ is the porosity, σ is the interfacial tension, μ_g is the geometric mean of water and oil viscosities, and L_c is the characteristic length defined by Ma *et al.*[2] Also plotted in Fig. 3.1-1 is the scaled oil recovery curve established by Ma *et al.*[2] using Berea cores under varying conditions. It is seen from Fig.

3.1-1 that although the recovery data are plotted against dimensionless time, they still do not collapse in a narrow band as do recovery curves obtained using Berea cores.[2]

Scaling Equation

In order to apply experimental imbibition data to reservoir development, it is desirable to develop an simple equation relating experimental oil recovery through core geometry to matrix geometry in fractured reservoirs. Such an equation can be established based on Gupta and Civan's work[3] and Eq. (3.1). Assuming that the mass transfer rate is proportional to the available mass of oil in place, the following governing equation is formulated:

$$dV/dt = -\lambda V^{\alpha} \tag{3.2}$$

where V is the volume of oil in place to be recovered by imbibition, t is the time, λ is a proportionality coefficient, and α is an empirical exponent. If an initial condition of $V=V_o$ at $t=0$ is used, where V_o is the volume of recoverable oil by imbibition, the following two solutions to Eq. (3.2) can be obtained:

$$V = V_o e^{-\lambda t} \tag{3.3}$$

for $\alpha = 1$, and

$$V = [V_o^{1-\alpha} - \lambda(1-\alpha)\, t\,]^{1/(1-\alpha)} \tag{3.4}$$

for α not equal to unity. Dimensionless oil recovery due to imbibition is defined as

$$R_{im} = (V_o - V)/V_o \tag{3.5}$$

Substitutions of Eqs. (3.3) and (3.4) into Eq. (3.5) result in

$$R_{im} = 1 - e^{-\lambda t} \tag{3.6}$$

for $\alpha = 1$, and

$$R_{im} = 1 - [1 - \lambda(1-\alpha)\, t / V_o^{1-\alpha}\,]^{1/(1-\alpha)} \tag{3.7}$$

for α not equal to unity, respectively.

Equation (3.6) was assumed by Aronofsky *et al.*[41] in 1958 without derivation.
For the purpose of simplicity, Eq. (3.6) is used for analyzing imbibition data from Spraberry cores. A curve fit of Eq. (3.6) to the experimental data shown in Fig. 3.1-1 is obtained when the following relation is used:

$$\lambda t = 0.0001\, t_D \tag{3.8}$$

Substituting Eq. (3.8) into Eq. (3.6) yields:

$$R_{im} = 1 - e^{-0.0001\, tD} \tag{3.9}$$

Fig. 3.1-2 shows that the shape of the recovery curve given by Eq. (3.8) for the Spraberry cores is similar to the recovery curve established for Berea cores as established by Ma *et al.*[2]

Application

Eq. (3.9) may be utilized for analyzing 44-years of waterflood performance in the Spraberry Trend Area. Assuming fracture spacing of 4 feet, imbibition oil recoveries from the two pay sands have been calculated using Eq. (3.9) and the absolute permeability. The result is plotted in Fig. 3.1-3, which indicates that permeability is one of the key factors affecting imbibition oil recovery. Using log-derived porosity and absolute permeability,[4] an oil recovery profile in the 5U Unit of the Upper Spraberry zone has been estimated and found to be between 8% and 15.5% as shown in Fig. 3.1-4. Integration of the recovery profile along the depth of the pay zone resulted in an estimate of imbibition oil recovery from the 5U zone to be about 11%. This is higher than the 5-9% observed waterflood oil recovery from the Upper Spraberry sand.[6] One of the reasons for the overestimation is believed to be wettability alteration of the sand under reservoir conditions. It has been observed that the oil recovery process is slower in our on-going imbibition experiment at reservoir temperature. Another reason may be the significant difference between the absolute permeability and the effective permeability for the very tight Spraberry sand. Yet another reason for the discrepancy may be the experimental conditions are not representative of reservoir conditions.

The oil-water relative permeability for cores taken from the Tippett #5 was utilized in this analysis.[5] Relative permeability data has been correlated to the reduced water saturation as shown in Fig. 3.1-5. Empirical equations for relative permeability to water (k_{rw}) and relative permeability to oil (k_{ro}) are expressed in this study as follows:

$$k_{rw} = S_{wD}^{3.5} \tag{3.10}$$

and

$$k_{ro} = 0.71\,(1-S_{wD})^{9} \tag{3.11}$$

where the reduced water saturation (S_{wD}) is defined as

$$S_{wD} = S_w - S_{wi} \tag{3.12}$$

where S_w and S_{wi} are water saturation and initial water saturation, respectively. With known relative permeabilities, effective permeability to each phase (oil and water) can be estimated because the absolute permeability of the sand is known from core analysis and well logs. Using the effective oil permeability in the scaling equation, the result is shown in Fig. 3.1-6. It is indicated by Fig. 3.1-6 that oil recovery after 44 years of waterflood in

the 5U Unit of the Upper Spraberry zone should be between 5.5% and 11% with an average of 7.7%. This value is close to, but still a little higher than the observed recovery (5-9%) from the Upper Spraberry.[6] However, it is unclear if the effective oil permeability should be used in the scaling equation because the scaling equation was derived on the basis of absolute permeability.

Summary

Imbibition experiments conducted under ambient conditions suggest that the maximum recoverable oil by water imbibition is about 50% of original oil in place. The experimental imbibition data has been scaled to reservoir dimensions using the absolute and effective oil permeabilities respectively. Analysis for the 5U Unit of the Upper Spraberry zone indicates that the scaling result using the absolute permeability is higher than the observed oil recovery, while a good match between the scaled oil recovery and the field observed oil recovery was obtained using the effective oil permeability. More experiments are being conducted to verify the validity of our wettablity determination procedures.

References

1. "Advanced Reservoir Characterization and Evaluation of CO_2 Gravity Drainage in the Naturally Fractured Spraberry Reservoir," PRRC Report No. 96-18, Quarterly Technical Report to DOE, DOE Contract No. DE-FC22-95BC14942. 1996
2. Ma, S., Zhang, X., and Morrow, N.R.: "Influence of Fluid Viscosity on Mass Transfer between Rock Matrix and Fractures," paper CIM 95-94, presented at the 46th Annual Technical Meeting of the Petroleum Society of CIM held in Banff, Alberta, Canada, May 14-17, 1995.
3. Gupta, A. and Civans, F.: "Correlation of the Imbibition Drive Matrix-to-Fracture Oil Transfer," paper SPE 28929.
4. Banik, A.K. and Schechter, D.S.: "Characterization of the Naturally Fractured Spraberry Trend Shaly Sands Based on Core and Log Data," paper SPE 35224 presented at the SPE Permian Basin Oil & Gas Recovery Conference held in Midland, Texas, 27-29 March, 1996.
5. Humble Oil & Refining Company: "Analysis of Cores from Well Tippett #5," Core Analysis Data Report 431, August 12, 1963, PRRC Spraberry Database.
6. Epic Consulting Services Limited: "Reasons for the Relatively Low Recovery of the Spraberry Waterfloods," PRRC Spraberry Database, 1996.
7. Buckley, J.S., Bousseau, C., and Liu, Y.: "Wetting Alteration by Brine and Crude Oil: From Contact Angles to Cores," paper SPE 30765 presented at the Ann. Tech. Conf. and Exhib., Dallas, Oct. 22-25, 1995.

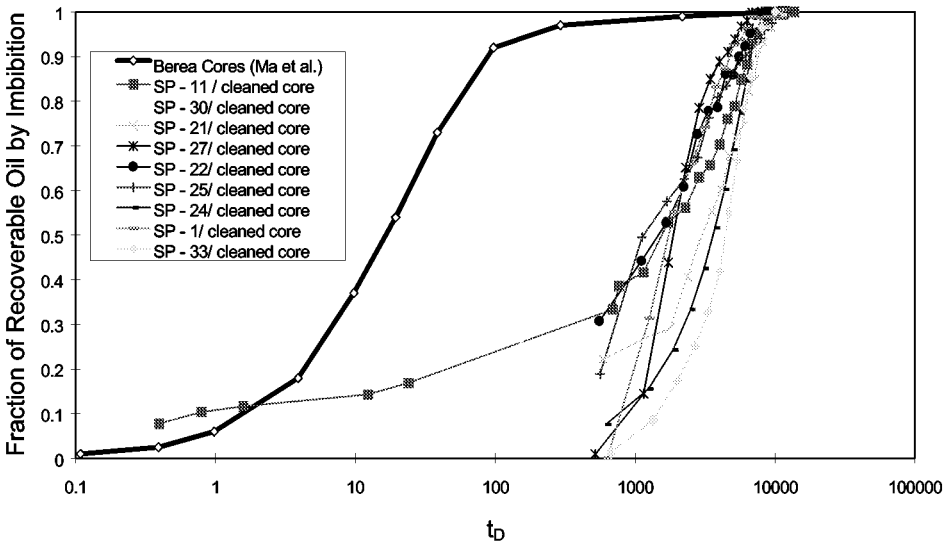

Fig. 3.1-1—Imbibition oil recovery from cleaned Spraberry cores compared with scaling curve for Berea presented by Ma *et al.*

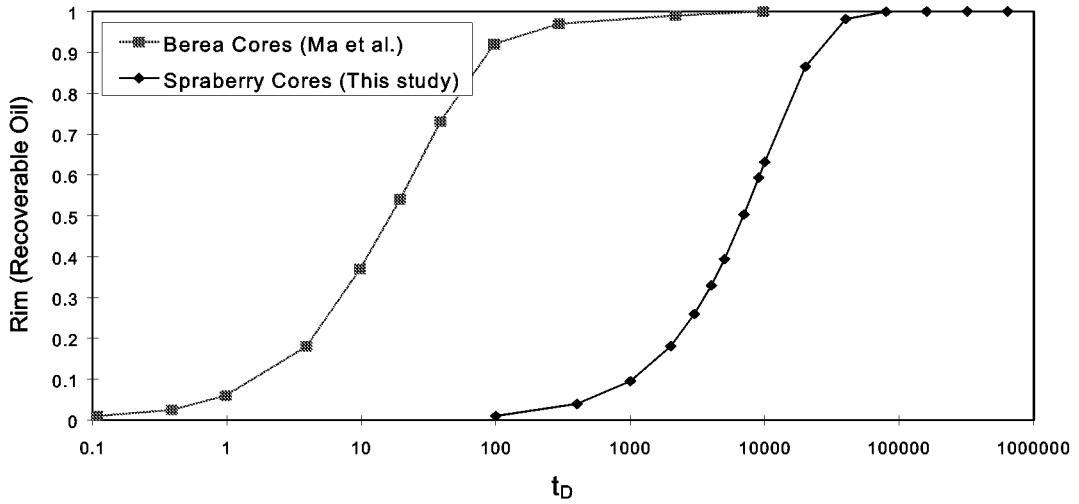

Fig. 3.1-2 —Dimensionless imbibition oil recovery curves from Ma *et al.* compared with Spraberry data

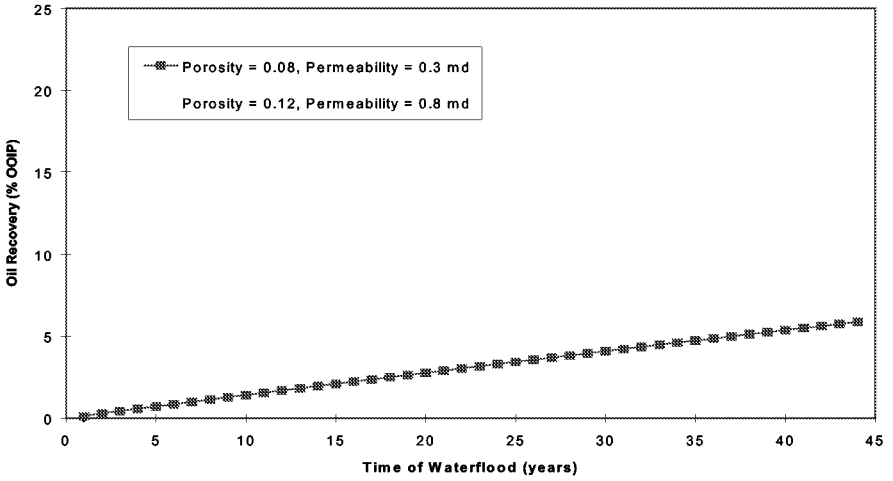

Fig. 3.1-3 —Calculated imbibition oil recovery from Spraberry reservoir based on scaling of experimental data and fracture spacing 4 feet

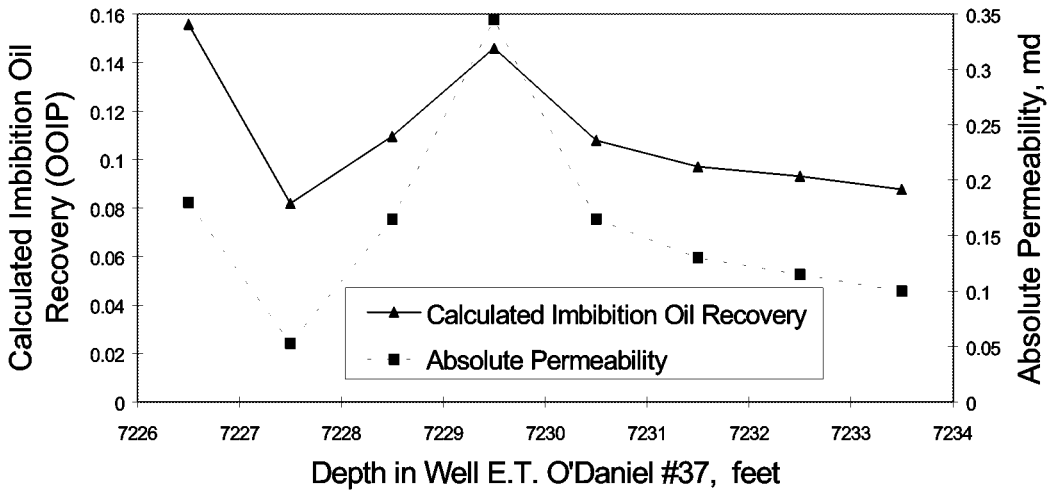

Fig. 3.1-4 —Calculated imbibition oil recovery from the 5U Unit, Upper Spraberry based on absolute permeability

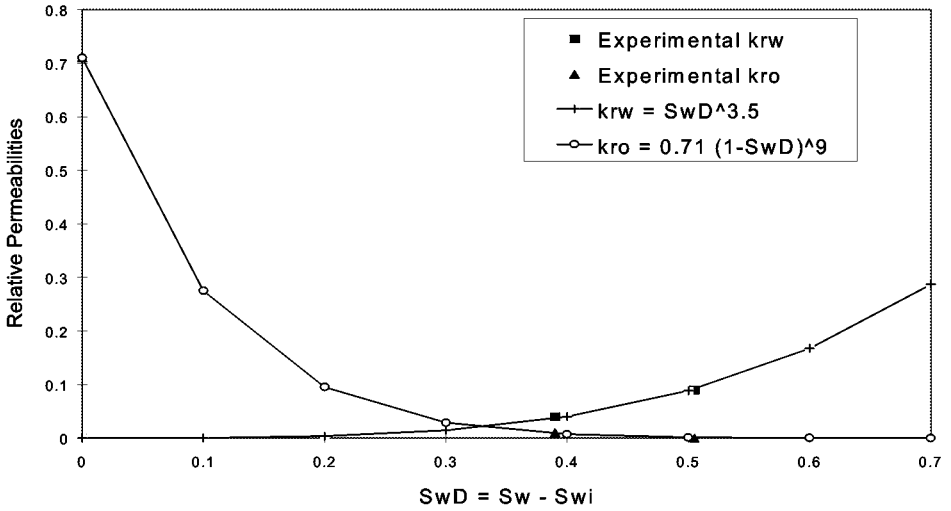

Fig. 3.1-5 —Oil water relative permeability curves for Spraberry sand

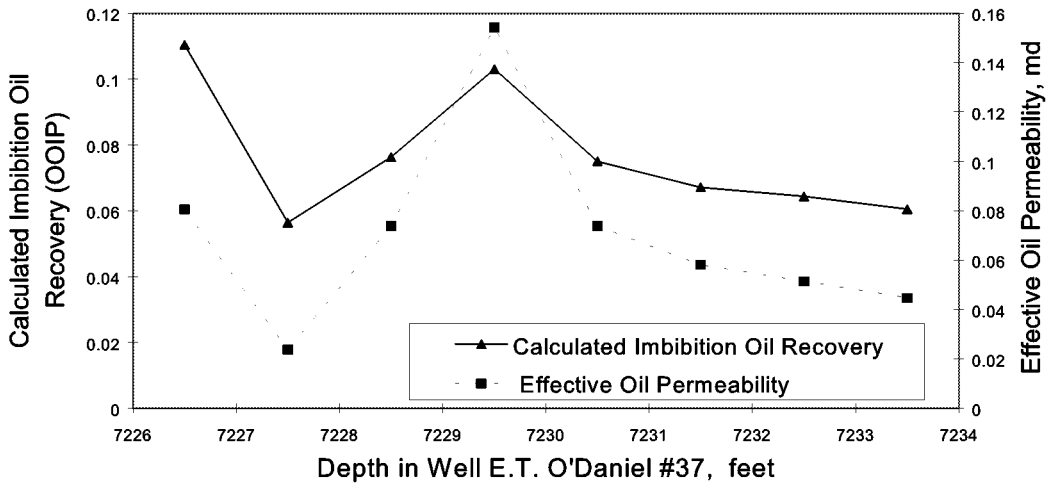

Fig. 3.1-6 —Calculated imbibition oil recovery from the 5U Unit, Upper Spraberry based on effective oil permeability

3.2 ANALYSIS OF IMBIBITION MECHANISM IN THE NATURALLY FRACTURED SPRABERRY RESERVOIR

Introduction

There are several mechanisms that can contribute to oil recovery in naturally fractured reservoirs. Spontaneous imbibition is particularly important in the recovery of oil by water injection from fractured reservoirs with low matrix permeability. A rock's ability to imbibe water spontaneously is dependent on its water-wetness quality. This imbibition property is a dominant factor in the rate of oil recovery. The rate of spontaneous imbibition in a porous medium is basically determined by the net effect of the capillary pressure driving force and the opposing viscous resistance to flow. Understanding imbibition and capillary phenomena is critical to develop the interactions and efforts between these parameters and other key parameters in the oil recovery mechanism (i.e., matrix permeability, fracture spacing and rate of imbibition).

In this section, the contribution of spontaneous imbibition to the oil recovery mechanism in the West Texas Spraberry reservoir is evaluated. Waterflood recovery in the Spraberry reservoir is dominated by counter-current imbibition of water. The imbibition experiments conducted under reservoir conditions suggest that the oil recovery by water imbibition is only 13% of the original oil in place. The scale-up of imbibition experimental results to field scale imbibition flooding uses several assumptions of the rate law that governs mass transfer (Guo, *et al.*, 1998). The developed scaling equation is then applied to evaluate scaling up from core geometry to matrix block geometry in the 1U and 5U Units of the Upper Spraberry zone. The results are in agreement with the observed 8 to 15% IOIP for 40 years of waterflooding in the Upper Spraberry sand. Fluid saturation, waterflooding efficiency, and recovery are also reviewed in this section. Based on analysis of fluid saturation of the field, the volumetric sweep efficiency in the Spraberry reservoir is much higher than the displacement efficiency. This characteristic suggests that the waterflood failed primarily because of very poor imbibition displacement efficiency. A sensitivity study of the imbibition model after 40 years of waterflooding in the Spraberry Trend with oil recovery of only 13% IOIP shows that the imbibition mechanism has not been affected. The degrees of heterogeneity in the matrix and the fracture system control recovery during waterflooding in the Spraberry.

Concept of Process

In the Spraberry reservoir, oil is stored in a very tight matrix, with virtually all permeability concentrated in a large number of natural fractures. Due to these fractures, oil cannot be displaced from the matrix by means of conventional waterflooding. Channeling and bypassing through the fractures would result in extremely poor recovery. Based on Brownscombe and Dyes's (1952) study, waterflood performance in the Spraberry reservoir is believed to be dominated by counter-current imbibition of water. The counter-current imbibition occurs when a liquid-filled, porous rock is contacted by another fluid that preferentially wets the rock (wetting fluid). The capillary pressure

gradient mechanism causes the wetting fluid to invade the rock pore, with less-wetting phases being displaced at the same time in the opposite direction. In the Spraberry, the wetting phase is water and the less-wetting phase is oil. When waterflooding is performed in this type of reservoir, the intent is to fill the fractures with water to initiate spontaneous counter-current imbibition, displacing the oil from the matrix block into the surrounding fractures.

As mentioned previously, the rate of imbibition is governed primarily by capillary pressure (i.e., corresponding to the wettability of the matrix rock), matrix permeability and fracture spacing (i.e., the amount of surface area exposed to imbibition). The rate of imbibition and the rate of water injection then govern the producing water-oil ratio. The oil production process during the mature stage of a waterflood in a naturally fractured reservoir may be considered analogous to a bucket of fluid with a small hole in the bottom dripping liquid onto a conveyor belt (Guo. *et al.*, 1998). Liquid leaking from the bucket is analogous to oil produced from the matrix by the imbibition process, and the conveyor belt is analogous to water flow in the fracture that brings the produced oil to the production well. Above a certain threshold, if one increases the speed of the conveyor belt, the rate of the oil produced from the matrix does not increase. In naturally fractured reservoirs, high injection rates result in a greater amount of water production, but the imbibition process remains the rate-limiting step. In this case, understanding the imbibition mechanism provides a tool to narrow the range of key parameters, i.e., matrix permeability, fracture spacing, fracture orientation, ultimate recovery, and the rate of imbibition. Some of these parameters will be utilized for scaling of imbibition data.

Scaling of Imbibition Data

The analytical model for describing oil recovery by water imbibition was developed by Aronofsky *et al* (1958). This recovery model can be applied using small reservoir core samples to scale the laboratory imbibition data to field dimensions. All laboratory parameters are converted into dimensionless forms (Mattax and Kyte, 1962). The following conditions must be met for scaling imbibition:

1. The gravity effects are negligible.
2. The shape and the rock type used in the laboratory must be identical to that of the matrix block of the reservoir.
3. The wettability and relative permeability represents the matrix block.
4. The capillary pressure functions for the matrix block and the laboratory model must be related by direct proportionality through Leverett's dimensionless *J*-function.
5. The viscosity ratio of oil to water must be duplicated.
6. The equations used in this study refer to the above assumptions.

Imbibition Recovery Model

In order to apply the experimental imbibition data to field scale imbibition waterflooding, the dimensionless time (t_D) initially proposed by Mattax and Kyte (1962) and then modified by Ma *et al.* (1995) is used:

$$t_D = Ct\sqrt{\frac{k_m}{\phi}}\frac{\sigma}{\mu_g}\frac{\cos(\theta)}{L_c^2} \quad \text{.....3.13}$$

where t is imbibition time, C is a constant, k_m is permeability, ϕ is porosity, σ is interfacial tension, μ_g is the geometric mean, and θ is the contact angle. The characteristic length, L_c, of the matrix block is given in another relation defined by Ma *et al* (1995):

$$L_c = \sqrt{\frac{V}{\sum_{i=1}^{n}\frac{A_i}{X_{Ai}}}} \quad \text{.....3.14}$$

In the above equation V is the volume of a matrix block where there are n fracture faces exposed to imbibition, A_i is the surface area of face i and X_{Ai} is the distance from the fracture face to the center of the matrix block.

Aronofsky (1958) showed that for a reservoir experiencing recovery due to imbibition, the recovery versus time curve could be approximated by the following equation:

$$R_{imb} = R_\infty(1-e^{-\lambda t}) \quad \text{.....3.15}$$

Then, the recovery equation is normalized as:

$$R_n = \frac{R_{imb}}{R_\infty} = 1-e^{-\lambda t} \quad \text{.....3.16}$$

where R_∞ is the ultimate recovery and λ is a curve fitting parameter, which can take any real numerical.

Based on laboratory imbibition experiments conducted under reservoir temperature using Spraberry cores and oil, recoverable oil by water imbibition can be up to 13% of IOIP. In analysis of the imbibition data from Spraberry cores, all of the imbibition experimental data are plotted in Fig. 3.1-1 using the dimensionless time variable, defined by Eq. (3.13). As a comparison, the experimental data from imbibition tests under ambient conditions are also plotted in Fig. 3.1-1. In these experiments, the rate of imbibition at reservoir temperature is greater than the rate of imbibition at ambient condition.

A composite imbibition curve is shown in Fig. 3.1-2. A curve-fitting imbibition data obtained for a very strongly water-wet Berea sandstone with zero initial water saturation is also shown for reference. Ma and Morrow (1997) derived a correlation for this curve as:

$$R = R_{\infty}\left(1-\frac{1}{(1+0.04t_D)^{1.5}}\right) \quad \text{.....3.17}$$

where R_{∞} is the ultimate recovery by spontaneous imbibition data and t_D is dimensionless time. The composite imbibition curves obtained from Berea sandstone were then used to compare the imbibition curves obtained from Spraberry rock as shown in Fig. 3.1-2. To achieve the best match of the experimental data from Spraberry cores, an average recovery curve was established using Eq.(3.16) by adjusting the value of λ. A curve fit of Eq.(3.16) for the experimental data as shown in Fig. 3.1-2 is obtained when the following relation is used for Spraberry cores as:

$$\lambda t = 0.0053\, t_D \quad \text{.....3.18}$$

Substituting Eq. (3.18) into Eq. (3.16) and the recovery curve fit presented in Fig. 3.1-2 can be expressed as:

$$R_n = \frac{R}{R_{\infty}} = 1 - e^{-0.0053 t_D} \quad \text{.....3.19}$$

Using the dimensionless time t_D defined by Eq. (3.13), the decline rate or the rate coefficient, which has unit 1/days, can be expressed as:

$$\lambda = 0.0053C\sqrt{\frac{k_m}{\phi}}\frac{\sigma}{\mu_g}\frac{\cos(\theta)}{L_c^2} \quad \text{.....3.20}$$

The experimental data was then normalized and fit to an empirical model using Eq. (3.13) and substituting into Eq. (3.19). Then, the recovery can be expressed as:

$$R_n = \frac{R}{R_{\infty}} = 1 - e^{-0.0053Ct\sqrt{\frac{k_m}{\phi}}\frac{\sigma\cos(\theta)}{\mu_g L_c^2}} \quad \text{.....3.21}$$

The characteristic length (L_c) for a matrix block in the reservoir is assumed to be half of the fracture spacing (L_s). Equation (3.21) can be used for analysis of the recovery mechanism in a naturally fractured reservoir during waterflooding.

Production Decline Model

Guo *et al.*, (1998) modified an analytical model for decline curve analysis based on imbibition theory and the rate law that governs mass transfer as developed by Gupta and Civan (1996). Decline of oil production rate is expressed as:

$$q_o = 0.0053 C V_o \sqrt{\frac{k_m}{\phi}} \frac{\sigma}{\mu_g} \frac{\cos(\theta)}{L_c^2} e^{-0.0053 Ct \sqrt{\frac{k_m}{\phi}} \frac{\sigma \cos(\theta)}{\mu_g L_c^2}} \quad \text{.....3.22}$$

where V_o is the original oil in place recoverable by imbibition. The above equations are valid when consistent units are used. The derivation of Eq. (3.22) is presented elsewhere (see Schechter, 1997).

Analysis of Recovery Mechanism

Recovery Based on Laboratory Scaling of Imbibition Data

The oil recovery in the 1U Unit (data from Well Shackleford 138) and 5U Unit (data from Well E.T. O'Daniel 37) of the Spraberry reservoir were calculated using log-derived porosity and permeability (Banik and Schechter, 1996) as shown in Fig.3.1-3 and 3.1-4. In Figs. 3.1-5 and 3.1-6 show the plot of oil recovery together with pore size of rocks versus well depth. The pore size is the square root of ratio of permeability and porosity k/ϕ, which is proportional to a macroscopic radius in porous medium. The characteristic length (L_c) for a matrix block in the reservoir core, which is half of the maximum fracture spacing of 3.79 ft as determined from fractured core analysis (Lorenz, 1996), was used in the scaling equation (Eq. (3.13)). The calculations of imbibition recovery were performed using Eq. (3.21) on the basis of 13% ultimate oil recovery from imbibition data. In the analysis of five years' waterflooding performance, pore size of 1U and 5U Units is plotted versus well depth as presented in Fig. 3.1-5 and 3.1-6, respectively. The oil recoveries are then plotted in the same figures, respectively. As shown in these figures, the integration of recovery profiles along the depth of the pay zone resulted in an estimation of average oil recovery of about 9% IOIP for 1U sand and 11% IOIP for 5U sand.

The effect of time on recovery profiles was investigated. Several scenarios were performed at 1, 5, 10, 20 and 40 years waterflood. The recovery calculations based on the imbibition model are plotted against well depth for Upper Spraberry 1U and 5U sands as presented in Fig. 3.1-7 and 3.1-8, respectively. Within 10 years of waterflood initiation, the average recovery is 11% and 13% for oil recovered from 1-U Sand and 5U sand, respectively. When the waterflooding is extended up to 20 years, the recovery improves to 12.5% for the 1-U sand. At 20 years there is no more oil recovered from 5U sand indicating that the waterflooding performance in the 5U sand has reached ultimate

recovery. After 40 years of waterflooding, there is no increase in oil recovery from both 1U and 5U sands. Thus, the scaling from coreflood geometry to reservoir matrix block geometry in the 1U and 5U Units of the Upper Spraberry zones resulted in oil recovery of only 13% IOIP for 40 years waterflooding.

On further analysis, the calculated recovery of 1U and 5U sands were plotted versus time. The average permeability and porosity for both sand units (1U and 5U) as input data in the calculation is tabulated in Table 3.1-1. Waterflooding in this field has been practiced for 40 years, the recovery analysis is performed on the basis of this time period. Equation (3.21) was then utilized to analyze 40 years of waterflood performance in the Spraberry Trend Area reservoir. The result is plotted in Fig. 3.1-9. This figure indicates that the time required to recover oil on the basis of the contribution of imbibition mechanism from 5U Unit sand is almost double that of the permeability of the 1U Unit sands. Based on Table 3.1-1, the average porosity for both sand units are almost the same. However, the average permeability in 5U Unit is higher than that in 1U Unit. Figure 3.1-9 shows that the matrix permeability is one of the key factors affecting this oil recovery mechanism.

As expected the higher permeability results in faster recovery of oil, until an ultimate recovery of about 13% IOIP is reached. For the Spraberry, this was achieved within 11 years' waterflooding. This suggests that the imbibition process cannot induce the production of oil after 11 years of waterflooding in the Spraberry. This also confirms that the calculated imbibition oil recoveries are in agreement with the observed 8 to 15% IOIP after 40 years of waterflooding in the Upper Spraberry sand. The ultimate recovery for each zone is indicated to be the same for each zone in Fig. 3.1-9.

Recovery Field Performance

Evaluation of the fluid saturation of the Spraberry field is an important parameter to be determined. The initial water saturation (S_{wi}) and current oil saturation (S_{or}) are crucial data for estimating waterflood performances, i.e., displacement efficiency and volumetric sweep efficiency. These data can be used to explain the low recovery in Spraberry Trend Area reservoir.

Fluid Saturation

Water saturations have been evaluated on the basis of permeability cutoff criteria to determine the oil saturation of the Spraberry field. In 1953, Elkin used a cutoff of S_{wi} = 60%, which roughly corresponds to a permeability of 0.1 md. Baker (1996a) determined the average water saturation of cores taken from four wells in the Spraberry field. He used an absolute permeability cutoff value of 0.3 and 0.8 md for these cores. The average water saturation was determined to be 49.3% and 52.6% for cutoff of 0.3 md and 0.8 md, respectively. These values corresponded to 50.7% and 47.4% oil saturation (assuming no gas saturation to be present).

By reviewing all methods of analysis to estimate initial water saturation, Baker concluded that the initial water saturation in the Spraberry rock is about 30% to 40%. The water saturation data and reservoir oil recovery by waterflood were used to determine the displacement efficiency and volumetric sweep efficiency. Initial water saturation was established based on cores taken from 46 wells drilled prior to waterflooding were evaluated before 1954 Schechter (1996b). Core data were gathered from wells before waterflooding was initiated. In this study, the initial water saturations that were obtained based on equation derived by Guo (1995) were re-plotted against the absolute permeability of cores, as presented in Fig. 3.1-10. The correlation of the average initial water saturation used was (Guo, 1995):

$$S_{wi} = 0.20 + 0.13e^{-0.6(k-0.1)} \quad \text{.....3.23}$$

Where S_{wi} is the initial water saturation and k is absolute permeability of the core in millidarcies. From the plot, the high water saturations in the higher permeability rock are probably associated with a microporosity system in which both the oil and the water are immobile (Baker, 1996a).

Current water saturations (S_w) were obtained by analyzing cores taken from wells that were waterflooded (data from Guo, 1995). By assuming there is no gas saturation, the current oil saturation can be determined. The results of this analysis are presented in Table 3.1-2. These data will be used later to determine the displacement efficiency and volumetric sweep efficiency.

Displacement Efficiency ($E_{displ.}$)

The displacement efficiency is the ratio between the amount of oil displaced and amounts of oil contacted by displacing fluid (Lake, 1989). Initial water saturation and current water saturation of the rock can determine the displacement efficiency. Assuming that the oil and gas are produced during waterflooding (no gas saturation in the rock after waterflooding), the displacement efficiency can then be determined using the following equation:

$$E_{displ.} = \frac{1 - S_{wi} - S_{or}}{1 - S_{wi}} = \frac{\bar{S}_W - S_{wi}}{1 - S_{wi}} \quad \text{.....3.24}$$

Where S_{wi} is initial water saturation, S_{or} is residual oil saturation, and S_w is current water saturation.

Volumetric Sweep Efficiency (E_{vol})

The volumetric sweep efficiency is defined as the ratio between the volume of oil contacted by the displacing fluid and the volume of oil originally in place (Lake, 1989). It can be calculated using the correlation between oil recovery (E_R) and displacement efficiency. The equation can be defined as:

$$E_R = E_{displ.} \times E_{vertical} \times E_{areal} \quad \text{.....3.25}$$

if $E_{vol} = E_{vertical} \times E_{areal}$

therefore,

$$E_{vol} = \frac{E_R}{E_{displ.}} \quad \text{.....3.26}$$

Oil recovery in the Spraberry field after more than 40 years of waterflooding is estimated in the range of 8 to 15% IOIP. Thus, the displacement and volumetric sweep efficiency in the Spraberry can be determined using the water saturation data presented in Table 3.1-2 and the estimated oil recovery from waterflooding. The results are presented in Table 3.1-3. The results show that the volumetric sweep efficiency in the Spraberry reservoir ranges from 47 to 83%, which is much higher than the displacement efficiency (15 to 26%). The high volumetric sweep efficiencies are also supported by infill drilling and pressure interference testing data. The infill drilling programs in Spraberry tend to produce wells with high water cuts indicating that water has contacted a large portion of the reservoir fracture system (Baker, 1996a), and pressure interference test during waterflooding showed conclusively that pressure communication was very good (Elkin, 1960). Low displacement efficiency is indicated by the low recovery from imbibition experiments. The results show that the waterflood was less successful than typical waterfloods primarily because of low imbibition displacement efficiency, not because of poor volumetric sweep efficiency. However, the maximum recovery by imbibition, as indicated previously, is about 13%.

Sensitivity Study of Imbibition Model

Previously, several key parameters involved in the analysis of the oil recovery mechanism based on the imbibition model have been described. Understanding the individual parameters of the recovery mechanism helps define the effects, interaction, and range of these key parameters. Matrix permeability and fracture spacing are used in this study to define and limit the uncertainty of the reservoir model. The imbibition process has a dominant effect on oil production. The imbibition process is analyzed here by performing sensitivity studies in the Humble Pilot Waterflood.

A pilot waterflood program was inaugurated on Humble's L.H. Shackelford B lease in the west central portion of the Spraberry Trend Area in March 1955. The pilot consisted of four injection wells with a center producer, creating a confined 80-acre, five spot pattern. Oil production from the center well increased within six months initiating of water injection. The water injection was then stopped and the center well still produced oil at a higher rate than prior to injection.

The reservoir performance in this pilot study demonstrated non-conventional waterflood characteristics according to observed Spraberry area response. Injected water appeared to displace oil from the fractures and simultaneously imbibed into the matrix. When injection was stopped, the water continued to imbibe into the matrix rock and displace oil from the matrix, which resulted in improvement of oil production. The imbibition mechanism is believed to strongly affect the waterflood recovery mechanism in the Spraberry trend.

The Humble pilot was considered a successful Spraberry waterflood. Subsequently, full-scale waterflood was initiated. However, the performance did not emulate the results of the Humble pilot. Understanding the difference between this pilot and field-wide waterflooding is vitally important for improving waterflood performance in the Spraberry Trend Area.

Reservoir Parameters

The initial oil in place (IOIP) in the Humble pilot area was estimated to be about 724,181 reservoir barrels. The mechanism of primary oil production in the Spraberry Trend Area is believed to be dominated by solution gas drive (Elkin, 1953). The gas saturation after reservoir repressurization by waterflooding was assumed to be zero because gas dissolved into the fluid during production. The reservoir parameters used in the calculation of oil recovery based on the experimental data and imbibition model are summarized in Table 3.1-4.

A recent horizontal core study by Lorenz (1996) showed three distinct fracture sets. The fracture sets present in cores from the 1U and 5U reservoir trend NNE, NE and ENE Table 3.1-5 presents the spacing of these sets. As shown in Table 3.1-5, the arithmetic average of the fractures spacing is 2.86 ft. All data were then used as the input for performing the sensitivity analysis of oil recovery for 15 years of waterflooding experience.

Matrix Permeability

Matrix permeability is an important parameter in modeling imbibition data. The higher the permeability the less time required for the water to imbibe into the matrix block and displace oil. In this study, to investigate the effect of matrix permeability on field recovery mechanisms, four values of permeability (i.e., 0.01, 0.03, 0.10 and 0.30 md) are used. Based on the experimental imbibition results from core plugs, the imbibition efficiency is 13% and the constant rate of imbibition (λ) is 0.0053. Using initial water saturation as a function of absolute permeability (Eq. 3.23), an average fracture spacing of 2.86 ft, and an average porosity from logs of 10.02%, the oil recovery using the imbibition model for 15 years of waterflooding is simulated and the result is presented in Fig. 3.1-11. From Figure 3.1-11, the recovery rates of this pilot field, as expected, are dependent on the matrix permeability. An increase in the matrix permeability results in an increase in the rate of recovery. It takes approximately six years for the reservoir with the highest matrix permeability to reach the ultimate recovery of 13%. The production rate

drops from 185 Bpd to below 10 Bpd within six years of production (see Fig. 3.1-12). Reservoirs that have low matrix permeability, even after 15 years of waterflooding recoveries still have not reached ultimate recovery of 13%.

Fracture Spacing

Effective permeability is a function of fracture spacing. A decrease in fracture spacing results in an increase in fracture density and therefore an increase in the fracture permeability. To investigate the effect of fracture spacing on the recovery of 15 years of waterflooding, the four sets of fracture spacing shown in Table 3.1-5 was used in a sensitivity study. The calculated matrix permeability was 0.1 md while the other parameters were held constant as in the previous calculation in the sensitivity of matrix permeability. The model assumes that all fractures are evenly spaced, perpendicular and extend the full length of the zone.

The results presented in Fig. 3.1-13 shows that recovery is sensitive to fracture spacing. Increasing the fracture spacing yields improvement in recovery. For example, ultimate recovery is achieved within five years for the shortest fracture spacing, while ultimate recovery is not yet reached for the longest spacing after 15 years of waterflooding. When the average fracture spacing is 2.86 ft, ultimate recovery will be reached after 15 years of waterflooding.

Production Decline

The sensitivity analysis for the production decline parameters is presented in Fig. 3.1-14. Figure 3.1-14 shows that the decline rate constant increases with matrix permeability and also increases with decreasing fracture spacing. This figure shows that for the lowest fracture spacing (1.62 ft), the decline rate constant increases rapidly with small increases in permeability. The matrix permeability and the fracture spacing apparently affect the decline rate constant.

Conclusions

The imbibition experiments conducted under reservoir conditions suggest the following conclusions as follows:

1. Spraberry oil recoverable by water imbibition could be up to 13% of original oil in place.
2. Imbibition data from laboratory core experiments can be scaled to reservoir dimension. 3. The results of the scaling from core geometry to matrix block geometry in the 1U and 5U Units of the Upper Spraberry zone is in agreement with the observed 8 to 15% IOIP or 40 years of waterflooding in the Upper Spraberry sand.
3. Analysis of field fluid saturation indicates that the volumetric sweep efficiency in the Spraberry reservoir is much higher than the displacement efficiency. This indicates that the waterflood in Spraberry trend was less successful than typical waterfloods, primarily because of very poor imbibition displacement efficiency.

4. A sensitivity study of the imbibition model presents a convincing argument that the effect of the imbibition mechanism on oil recovery resulted in only 13% IOIP after 40 years of waterflooding.
5. The degree of heterogeneity in the matrix and natural fractures controls the Spraberry waterflooding recovery process.

Nomenclature

A_i = Area of imbibition, L^2
C = Constant = 0.018849
k_m = Matrix permeability, L^2
L_c = Characteristic length, L
L_s = Effective fracture spacing, L
n = Number of fracture surfaces exposed to imbibition
R_{imb} = Imbibition recovery at time t (%IOIP)
R_∞ = Ultimate recovery at economic limit (%IOIP)
t = time, T
t_D = Dimensionless time
V = Volume of oil in place recoverable by imbibition, L^3
V_o = Volume of original oil in place recoverable by imbibition, L^3
X_{Ai} = Distance from fracture face to no-flow boundary, L
ϕ = Porosity
λ = Empirical constant from Aronofsky's model, T^{-1}
μ = Viscosity,
σ = Interfacial tension
θ = Contact angle

Reference

1. Aronofsky, J.S., Masse, L., and Natanson, S.G., "A Model for the Mechanism of Oil Recovery from the Porous Matrix due to Water Invasion in Fractured Reservoirs," paper T.P. 4703 in Petroleum Technology, *AIME*, vol. 213, 1958.
2. Baker, R., memo from Epic Consulting Service Limited, March 6, 1996a.
3. Baker, R., "Reasons for the Relatively Low Recovery of the Spraberry Waterfloods," memo from Epic Consulting Service Limited, June, 1996b.
4. Elkin, L.F., "Reservoir Performance and Well Spacing, Spraberry Trend Area Field of West Texas," *Trans. AIME*, Volume 198, 1953.
5. Elkin, L.F. and Skov, A.M., "Determination of Fracture Orientation from Pressure Interference," *Trans. AIME* , Volume 219, 1960.
6. Guo, B., "Imbibition and Drainage Studies in Spraberry Reservoir Rock," in Proceedings of Characterization and fluid Flow, Naturally Fractured Reservoir Forum, Petroleum Recovery Research Center New Mexico Tech, Socorro, NM, April 19, 1995.

7. Guo, B., and Schechter, D.S., and Baker, R.O., "An Integrated Study of Imbibition Waterflooding in the Naturally Fractured Spraberry Trend Area Reservoirs," SPE Permian Basin Oil and Gas Recovery Conference, Midland, 25-27 March 1998.
8. Gupta, A. and Civans, F., "An Improved Model for Laboratory Measurement of Matrix to Fracture Transfer Function Parameters in Immiscible Displacement," paper SPE 28929 presented at the 69th Annual Technical Conference and Exhibition, New Orleans, Sept. 25- 28, 1994.
9. Lake, L.W., "Enhanced Oil Recovery," Prentice-Hall, Inc., New Jersey, 1989.
10. Lorenz, J., "Summary of Observations and Interim Interpretations: Fractures in Horizontal Spraberry Cores, E.T. O'Daniel Well #28," Dec. 12, 1996.
11. Ma, S., and Morrow, N.R., "Mathematical Modeling of Spontaneous Imbibition Data for Strongly Water-Wet Systems," unpublished manuscript, (1997).
12. Schechter, D.S., McDonald, P., Sheffield, T., and Baker, R., "Reservoir Characterization and CO_2 Pilot Design in the Naturally Fractured Spraberry Trend Area," paper SPE 35469 presented at the SPE Permian Basin Oil & Gas Recovery Conference Midland, 27-29, March 1996, (a).
13. Schechter, D.S., "Advanced Reservoir Characterization and Evaluation of CO_2 Gravity Drainage in the Naturally Fractured Spraberry Trend Area," First Annual Technical Progress Report to DOE under Contract No. DE-FC22-95BC14942, Dec. 17, 1996, (b).
14. Schechter, D.S., "Advanced Reservoir Characterization and Evaluation of CO_2 Gravity Drainage in the Naturally Fractured Spraberry Trend Area," Second Annual Technical Progress Report to DOE under Contract No. DE-FC22-95BC14942, Oct. 1997.

Table 3.2-1—The Average Absolute Permeability and Porosity For Both Sand Units (1u And 5u) in Spraberry Trend Area Reservoir

Sand Units	Absolute Permeability (md)	Porosity (%)
1U Sand	0.34	10.10
5U Sand	0.70	9.93

Table 3.2-2—Evaluation of Water Saturation and Current Oil Saturation

Source of Data	Year	k_{air}(md)	S_{wi}[(b)](%)	S_w(%)	S_{or}(%)
Tippett 5	1963	0.76 – 1.31	26 – 29	37 – 40	63 – 60
Nannie Parish 7	1974	0.13 – 0.40	31 – 33	43 – 50	50 – 57
Judkin A5	1987	0.15 – 0.70	29 – 33	40 – 50	50 – 60
Pembrook 9407	1990	0.06 – 0.80	29 – 33	42 – 50	50 – 58
Shackleford-138	1993	0.01 – 0.15	33 – 34	45 – 50	50 – 55

Table 3.2-3—Evaluation of Displacement Efficiency (E_d) and Volumetric

Source of Data	Year	S_{wi}(%)	S_w(%)	E_{displ}[(c)](%)	E_{vol}[(d)](%)
Tippett 5	1963	26 – 29	37 – 40	15 – 16	76 – 83
Nannie Parish 7	1974	31 – 33	43 – 50	18 – 26	47 – 68
Judkin A5	1987	29 – 33	40 – 50	15 – 26	47 – 78
Pembrook 9407	1990	29 – 33	42 – 50	19 – 25	48 – 64
Shackleford-138	1993	33 – 34	45 – 50	18 – 25	49 – 65

Average of reservoir oil recovery is 12% IOIP

Table 3.2-4—Reservoir parameters as input data

Area	80 acre
Net Pay	20 ft
Bulk Volume	69,696,000 ft^3
Porosity	10.02%
Pore Volume	6,983,539.20 ft^3
Water saturation	31.53 – 33.72%
Gas Saturation (assumed after waterflood initiated)	9.0 – 9.3%
Oil Saturation	57.3 – 59.2%
Initial Oil In Place	712,404 – 735,957 rb
Imbibition Efficiency	13%
Recoverable Oil	92,613 – 95,674 rb
Oil Formation Volume Factor	1.294 rb/STB
Interfacial Tension	26.22 dyne/cm
Viscosity	2.01 cp

Table 3.2-5—Fracture Spacing

Fracture Set	Spacing Range (ft)	Average Spacing (ft)
NNE	0.05 - 4.50	1.62
NE	0.73 - 5.75	3.17
ENE	0.04 – 13.00	3.79
Average		2.86

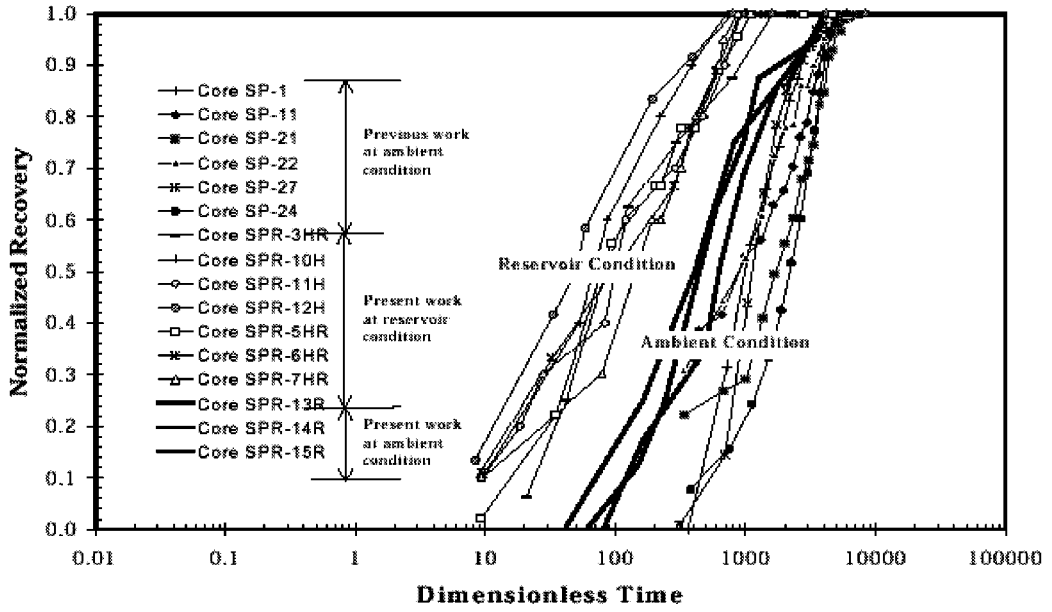

Fig. 3.2-1—Oil recovery curves obtained under reservoir condition plotted using dimensionless variables and compared with oil recovery curves obtained under ambient condition

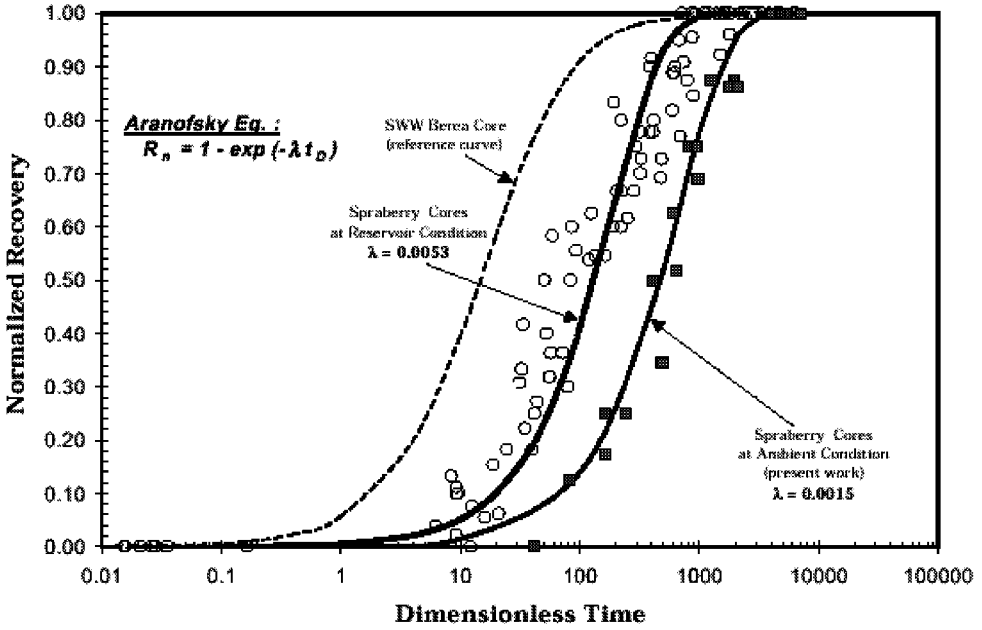

Fig. 3.2-2—Averaging of imbibition curves using the Aranofsky equation to fit the imbibition experimental data by adjusting empirical constant λ

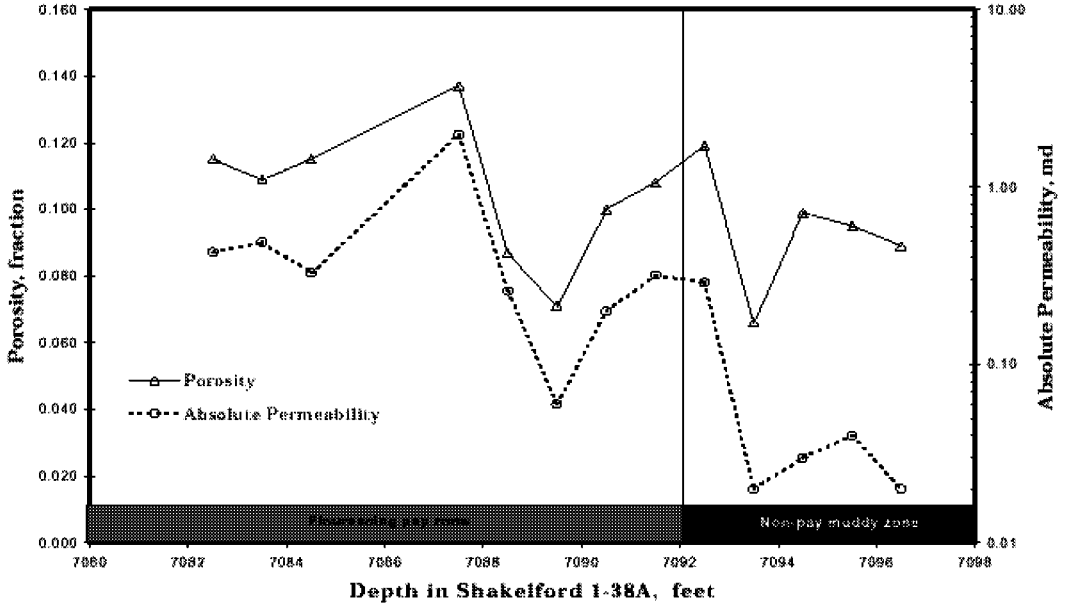

Fig. 3.2-3—Porosity and absolute permeability of Upper Spraberry 1U Unit versus depth (data taken from Well Shackleford 1-38A)

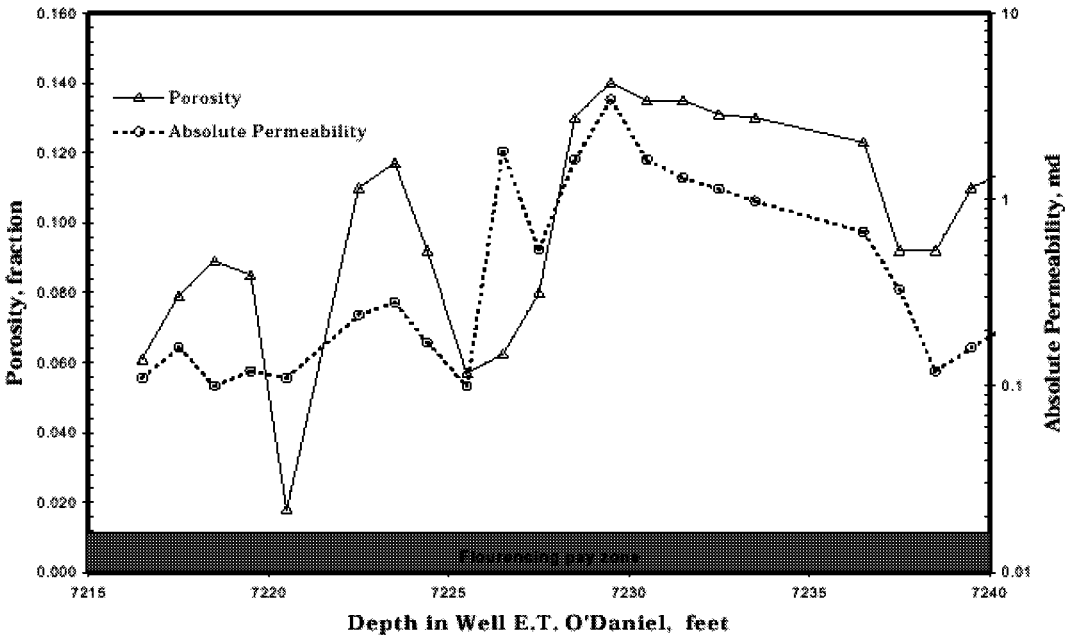

Fig. 3.2-4—Porosity and absolute permeability of Upper Spraberry 5U Unit versus depth (data taken from Well E.T. O'Daniel 37)

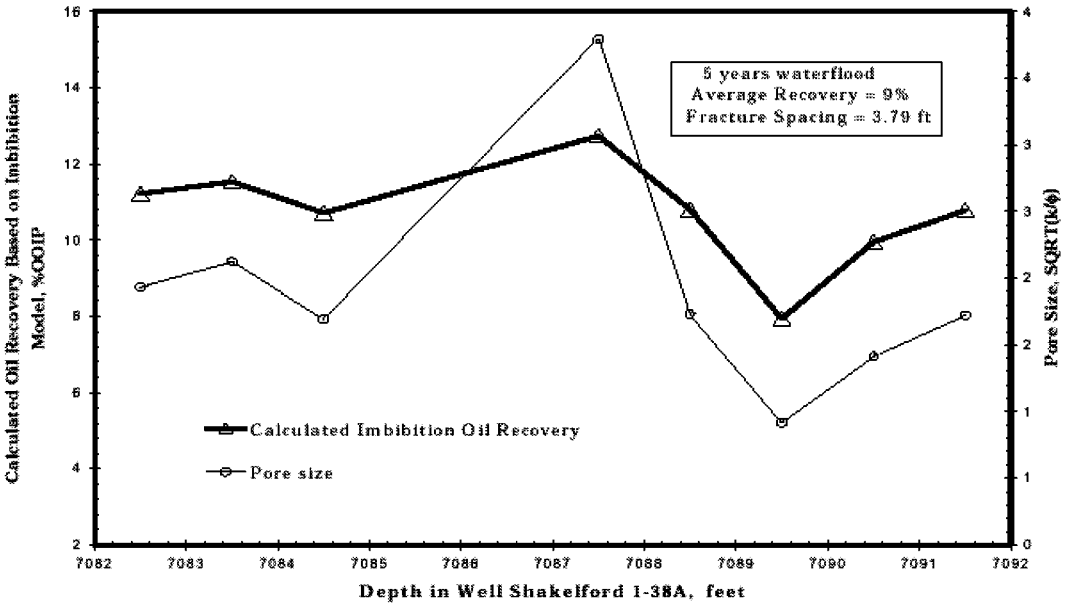

Fig. 3.2-5—Calculated imbibition oil recovery for five years of waterflooding from Upper Spraberry 1U formation, based on scaling of experimental data and fracture spacing of 3.79 ft.

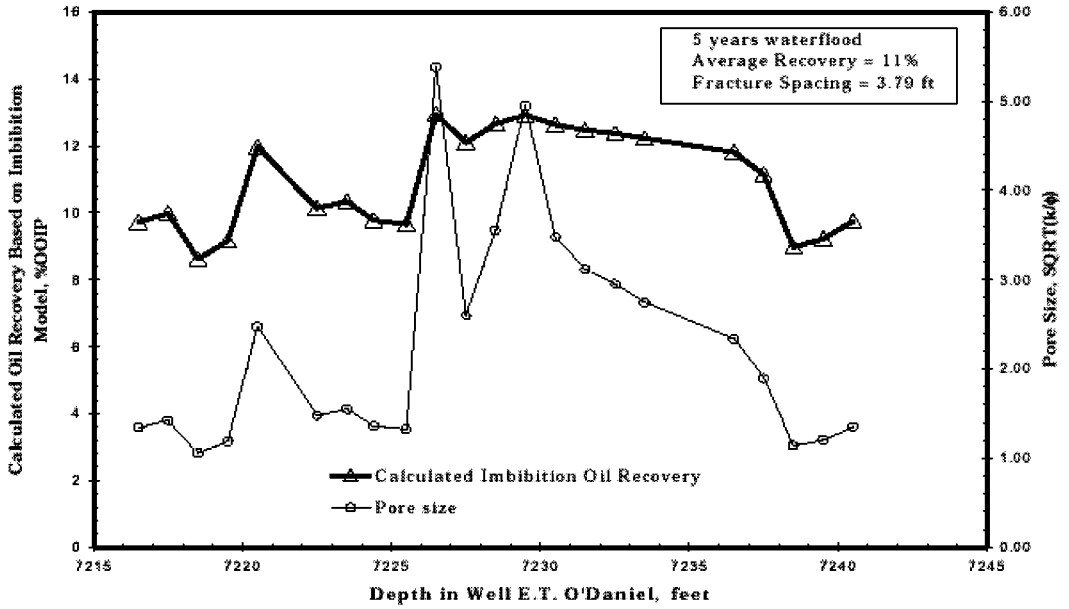

Fig. 3.2-6—Calculated imbibition oil recovery for five years of waterflooding from Upper Spraberry 5U formation, based on scaling of experimental data and fracture spacing of 3.79 ft

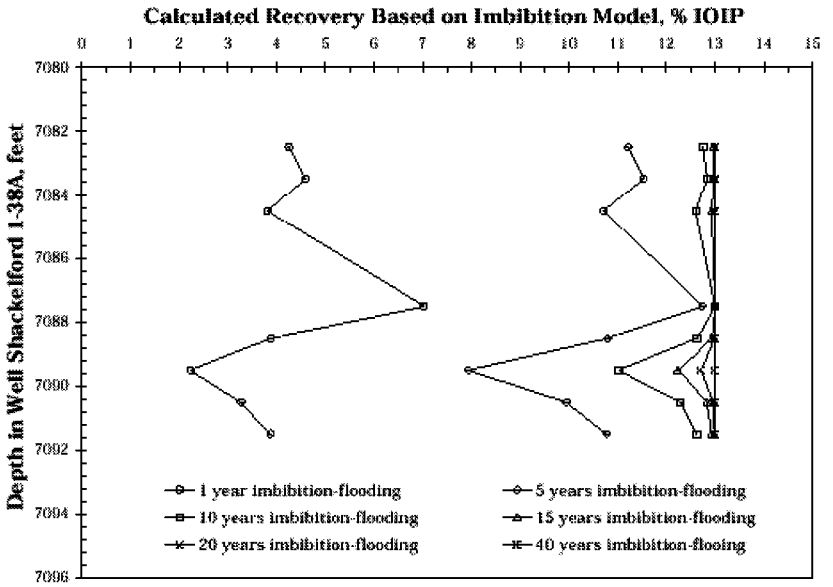

Fig. 3.2-7—History of waterflood recovery profiles from Upper Spraberry 1U formation, based on scaling of experimental data and fracture spacing of 3.79 ft Fig.

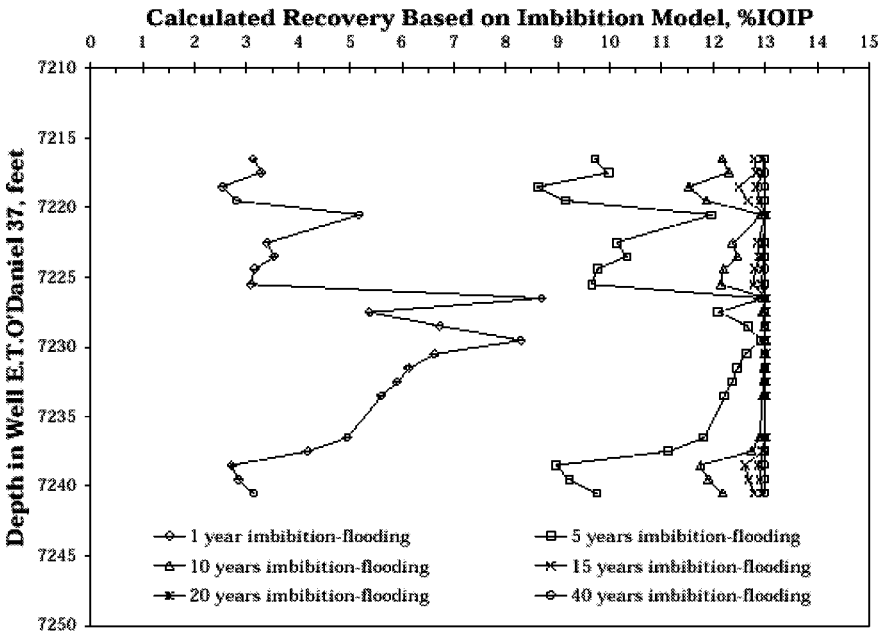

Fig. 3.2-8—History of waterflood recovery profiles from Upper Spraberry 5U formation, based on scaling of experimental data and fracture spacing of 3.79 ft

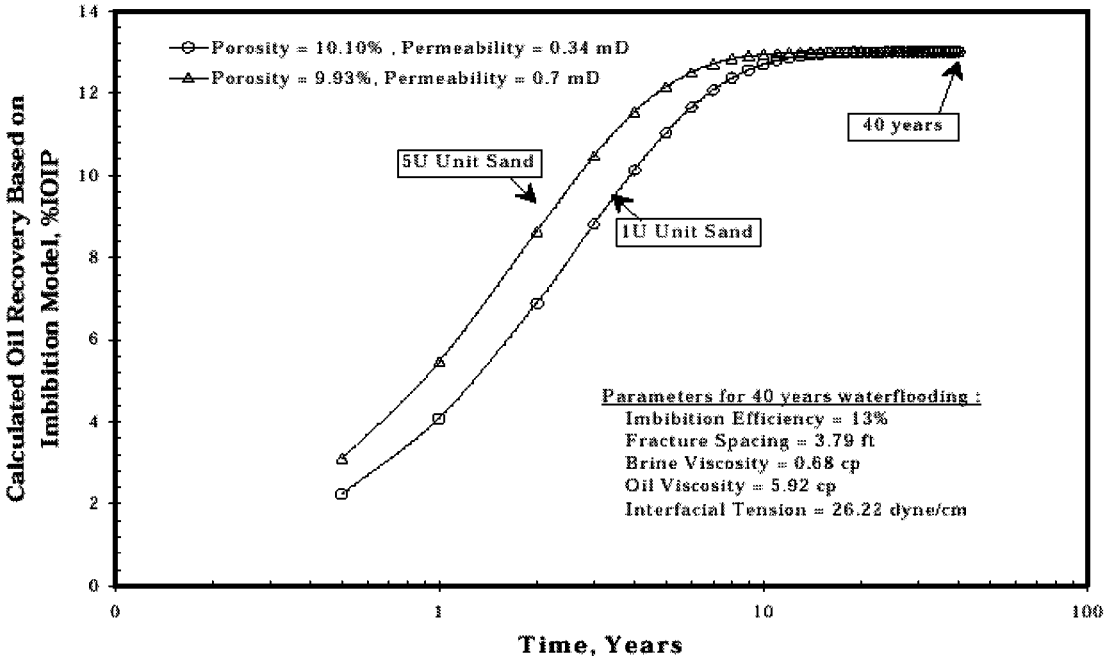

Fig. 3.2-9—Calculated imbibition oil recovery for 40 years of waterflooding from Spraberry 1U and 5U formation, based on scaling of experimental data and fracture spacing of 3.79 ft

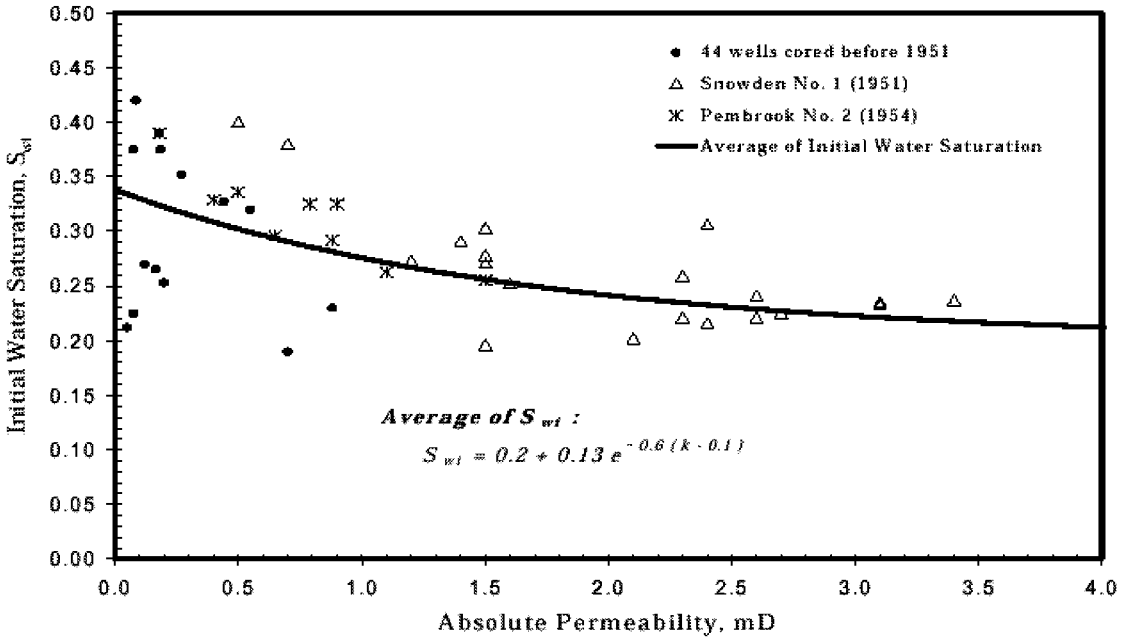

Fig. 3.2-10—Initial water saturation in the Spraberry reservoir

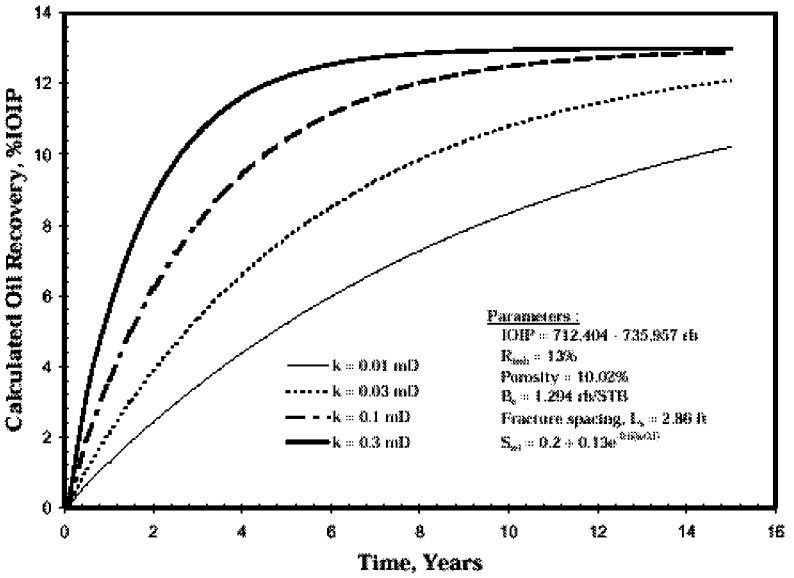

Fig. 3.2-11—Effect of matrix permeability on oil recovery mechanism

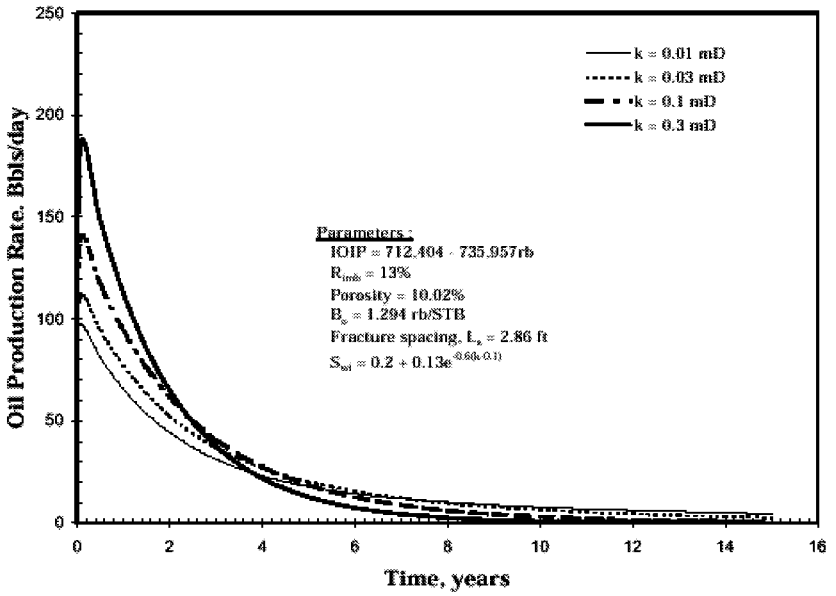

Fig. 3.2-12—Effect of matrix permeability on calculation of production rates

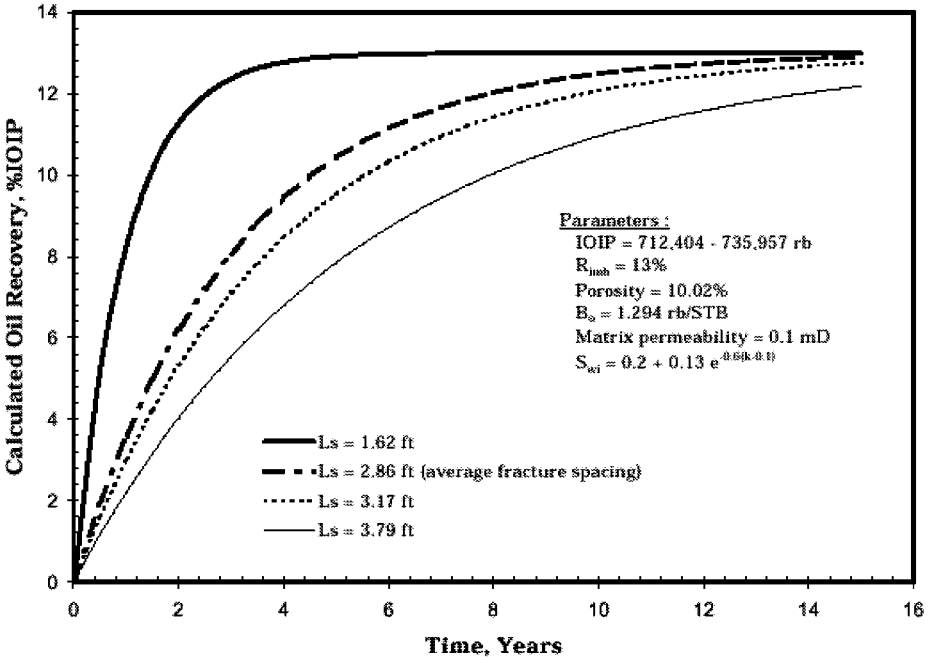

Fig. 3.2-13—Effect of fracture spacing on recovery mechanism

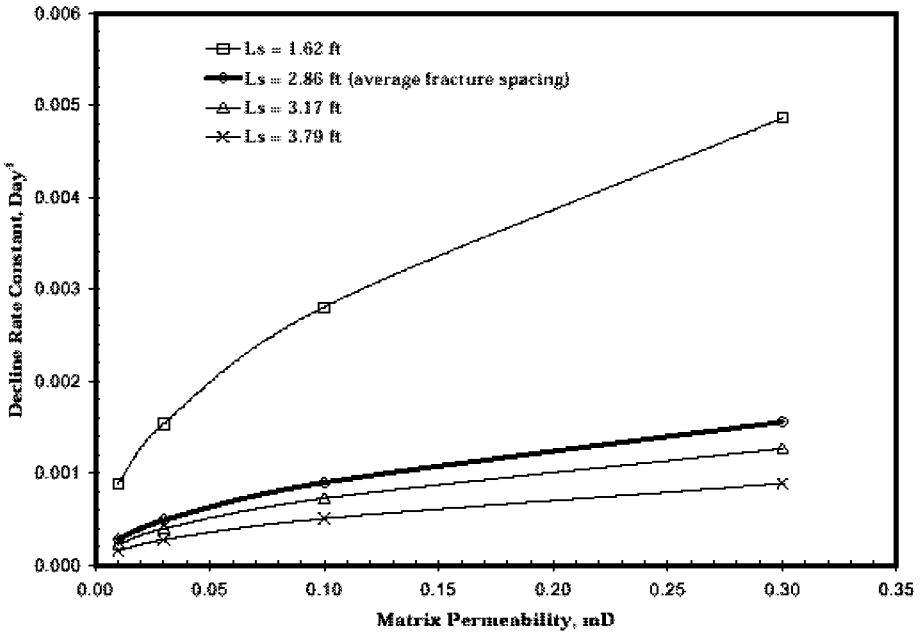

Fig. 3.2-14—Effect of matrix permeability and fracture spacing on decline rate constant

3.3 Analysis of Inflow Performance of Spraberry Trend Area Wells

Introduction

A model study of a waterflooding pilot in Spraberry Trend Area indicated a NE-SW trend of the major fractures.[1] A contrast of 144/1 was required for the major/minor fracture trend permeability to match the pilot response. This strong anisotropic effective permeability implies the existence of well inter-connected, long natural fractures in the Spraberry reservoir. A characteristic of flow in long natural fractures is the pressure variation along the fracture should be significantly higher compared to that in a hydraulic fracture or a short natural fracture. Unfortunately, a method for analyzing flow behavior in reservoirs with long fractures is not readily available from the literature. This section presents a more rigorous analysis on productivity of wells intersecting long fractures. Equations presented in this paper are general and useful for estimating inflow performance relationship (IPR) of vertical and horizontal wells intersecting long fractures.

Several analytical solutions have been presented for transient flow in fractured reservoirs.[2-8] Numerical models have also been developed for simulating fluid flow in fractured reservoirs.[9,10] However, it is still customary for reservoir engineers to use equations derived for steady flow conditions. This is not only because the analytical transient-flow solutions and numerical simulators are not convenient to use in construction of IPR, but also because steady or pseudo-steady flow prevails as the dominating flow mechanism in the lifetime of most oil wells. Therefore, steady flow equations are more attractive rather than transient flow equations and numerical models for productivity analysis.

The first mathematical model for analyzing productivity of horizontal wells intersecting fractures was presented by Giger *et al.*[11,12] Two solutions were proposed for short horizontal wells and long horizontal wells respectively. For both cases, flow in the rock matrix and flow in the fractures were formulated separately, and then combined to obtain an equation for flow in both regimes (from external boundary to wellbore). Radial flow was assumed in the fracture for both short and long well cases. For the case of a short horizontal well, they employed a radial flow equation presented by Muskat[13] for matrix flow from external boundary to a small fracture. For the long horizontal well case, a flow equation developed by Houpeurt[14] for flow in matrix from external boundary to an extended fracture was utilized. The drawback of Giger's approach is that the equations for flow from external boundaries to the fractures were derived based on the assumption that the pressure in the fracture is uniform (invariant along the fracture length and height). Karcher *et al.*[9] calculated productivity increase of fractured horizontal wells over fractured vertical wells using equations presented by Giger.[12] Consistent results were obtained. They also investigated issues of increasing productivity, reducing coning, and improved sweep efficiency by multi-fractured horizontal wells using their numerical simulation for infinite conductivity fractures. Joshi[15] proposed a steady state flow equation for analyzing productivity of horizontal wells. His equation for flow in the matrix was also derived based on the assumption of constant pressure in the fracture (infinite conductivity fracture). Joshi[16] presented a review of horizontal well technology. He pointed out that in most fracture jobs it is difficult to obtain infinite conductivity and, moreover, fracture conductivity decreases over time. Mukherjee and Economides[17]

developed a simplified steady-state approach to calculate the number of infinite conductivity fractures equivalent to a drainhole. Their model was developed on the basis of the inflow performance relationship suggested by Joshi[15] with Prats'[18] correlation of dimensionless wellbore radius. Economides et al.[10] performed a comprehensive simulation of horizontal-well performance. Their results agree well with Joshi's[15] equation. Raghavan and Joshi[19] presented a steady flow solution based on uniform flux along the fracture length. This solution was presented as valid for finite-conductivity fractures with a specific dimensionless fracture conductivity value of C_{fD}=4.4. Guo and Evans[20] performed analyses similar to that of Giger's[12] except that direct flow from matrix to wellbore, reservoir anisotropy, and multi-phase flow were included in the mathematical models. Like Giger's[12] model, Guo and Evans'[20] models were also derived assuming uniform pressure in the fracture when the flow in matrix was formulated using Darcy's law. Recently, Li et al.[21] presented an approximate formula for predicting performance of fractured horizontal wells. It was assumed that oil first flows linearly from the external reservoir boundary to the vicinity of a vertical fracture, then turns 90 degrees and flows linearly to the fracture face while pressure in the fracture is equal at all points. Flow in the fracture was assumed to be linear away from the wellbore and radial near the wellbore. The drawback of their formulation is similar to that of Giger's and Guo and Evans'.

In summary, most steady flow equations presented by previous investigators for productivity analysis of fractured horizontal wells rely on the assumption of infinite conductivity fractures (invariant pressure in the fracture) when the flow from external boundary to the fracture was formulated. While the mathematical problems were very much simplified by using this assumption, reliability of the solutions is questionable. Only one analytical solution dealing with horizontal wells in finite-conductivity fractures was reported in the literature.[19] This solution is applicable to fractured reservoirs where fractures have dimensionless conductivity of 4.4 and the flux in the fractures is uniform, which may not occur in practice.

This paper presents a simple and more rigorous mathematical model for predicting performance of vertical and horizontal wells intersecting fractures fully penetrating reservoir sections. An important feature of the new model is that it was derived by rigorous coupling of flow in the matrix and flow in the fracture, where a unique pressure distribution was consistently used both for flow in the matrix and for flow in the fracture. Another feature of the new model is simplicity of use by reservoir engineers. This is because the equations in the model are closed and in a very simple form. However, this model was derived for wells intersecting long fractures where 1-dimensional flow to the fracture face dominates in the matrix. Care needs to be taken when this model is used for estimating performance of wells intersecting short, highly conductive fractures where significant 2-dimensional (in x and y directions as discussed in Appendix A) flow may exist in the matrix. It is probable that both long and relatively short fractures contribute in Spraberry.

This mathematical model has been utilized for analyzing performance of wells intersecting natural fractures in the Spraberry Trend Area, West Texas. Use of the model to match production data aided in the understanding of the unusual primary behavior of Spraberry Trend Area reservoirs.

Mathematical Model

A simple and more rigorous mathematical model has been derived in this study for estimating productivity of vertical and horizontal wells intersecting long fractures, where pressure variation in the fracture is of significance. While derivation of the model is presented in detail in Appendix A, resultant equations for flow of an incompressible fluid in a fracture wing are summarized in this section.

Pressure in a Fracture

Pressure distribution in a fracture may be estimated using Eq. (3.27):

$$p_f(x) = p_e - (p_e - p_w)e^{\sqrt{c}(x-x_f)} \tag{3.27}$$

where x is the distance from the fracture tip, $p_f(x)$ is fracture pressure at point x, p_e is the pressure at the drainage boundary, p_w is the flowing bottom hole pressure, x_f is the length of a fracture wing (from fracture tip to wellbore), and c is defined as a group of variables:

$$c = \frac{2k_z}{z_e w k_f} \tag{3.28}$$

where k_z is the permeability of the rock matrix in the direction perpendicular to the fracture face, z_e is the distance from the fracture to the drainage boundary of the fracture, w is the average fracture width (aperture), and k_f is the fracture permeability. Consistent units should be used in Eqs. (3.27) and (3.28) so that the exponential function is dimensionless.

Inflow Performance Relationship (IPR)

Production rate Q from a fracture wing is given by Eq. (3.29) in field units:

$$Q = \frac{0.00254k_z h}{B_o \mu z_e \sqrt{c}}(p_e - p_w)(1 - e^{-\sqrt{c}x_f}) \tag{3.29}$$

where h is the fracture height, B_o and μ are formation volume factor and viscosity of oil, respectively. Productivity index PI for the fracture wing is given by

$$PI = \frac{Q}{p_e - p_w} = \frac{0.00254k_z h}{B_o \mu z_e \sqrt{c}}(1 - e^{-\sqrt{c}x_f}) \tag{3.30}$$

It must be noted that these inflow equations were derived assuming that one-dimensional flow dominates the flow from the drainage boundary to the fracture face in the rock matrix. This is an ideal situation where the fracture extends to no-flow boundaries. If the fracture is not long enough to reach no-flow boundaries, pressure drawdown at the fracture tip may not be negligible compared to drawdown in the wellbore, and significant two-dimensional flow may exist near the fracture tip. In such cases, results from this mathematical model may be erroneous. To ensure the applicability of the mathematical model to a given fractured reservoir, the minimum fracture length should be checked

before using the equations. This is discussed as follows. A conservative estimation of the minimum length of the fracture above which this model is applicable can be determined using Eq. (3.27). The relative pressure drawdown at the fracture tip (x=0) can be determined from Eq. (3.27) to be

$$\frac{p_e - p_{x_f}}{p_e - p_w} = e^{-\sqrt{c}x_f} \tag{3.31}$$

where p_{xf} is the pressure at the fracture tip. The fracture half length x_f can be solved from Eq. (3.31):

$$x_f = -\frac{1}{\sqrt{c}} \ln \frac{p_e - p_{x_f}}{p_e - p_w} \tag{3.32}$$

Eq. (3.32) can be utilized to estimate the minimum required fracture length for a given relative pressure drawdown (p_e - p_{xf})/ (p_e-p_w) at the fracture tip. For example, if the maximum allowable relative pressure drawdown at the fracture tip is 5% , the drainage boundary for the fracture is 2 feet, matrix permeability is 0.5 md, fracture width and permeability are 0.002 inch and 20 Darcies respectively, the minimum required length of the fracture wing is calculated to be 7.74 feet.

Relation between Fracture Width and Permeability

Application of the new mathematical model requires information regarding fracture width w and fracture permeability k_f . However, these two parameters should not be used independently because they are closely related. Similar to the cubic law[22] which describes the relationship between fracture width and fracture conductivity, a simple relation between fracture width and fracture permeability is derived analytically in Appendix B and summarized as follows:

$$k_f = \frac{\phi_f{}^3 w^2}{12} \tag{3.33}$$

where ϕ_f is the fracture porosity accounting for volume of minerals, crushed rock, and proppant introduced during hydraulic fracturing operations. If the fracture porosity and permeability are known, fracture width can be estimated using Eq. (3.34):

$$w = \sqrt{\frac{12k_f}{\phi_f{}^3}} \tag{3.34}$$

Stress-Sensitive Fractures

It has been reported that productivity of some wells intersecting naturally fractured reservoirs decline rapidly as wellbore/reservoir pressure declines.[23] It has been postulated that partial closure of fractures is responsible for this behavior. As the pressure in the fracture decreases, fracture aperture could conceivably decrease and effective stress at the

fracture face would thus increase to support the matrix. The partially closed fracture should have a much lower conductivity resulting in lower productivity of the well. Walsh's model[24] for conductivity in a fracture is frequently employed for correlating both laboratory and field data.[23] Since conductivity and permeability are equivalent, both representing flow resistance of the medium for given fluid properties, the following simplified relation similar to Walsh's model may be utilized for fracture permeability analysis:

$$k_f{}^n = A + B\ln(\sigma - \alpha p) \tag{3.35}$$

where k_f is fracture permeability, A and B are constants, σ is the confining stress, p is the pore pressure, α is the poroelastic parameter defining the effective-stress law, and the exponent n is 1/3 according to Walsh. The (σ-αp) term represents the effective stress. Assuming that the fracture permeability is k_{fo} at unit effective stress, the constant A can be determined to be $k_{fo}{}^n$, and Eq. (3.35) becomes

$$k_f{}^n = k_{fo}{}^n + B\ln(\sigma - \alpha p) \tag{3.36}$$

Substituting of Eq. (3.36) into Eq. (3.34) yields

$$w = \sqrt{\frac{12}{\phi_f{}^3}}\left[k_{ko}{}^n + B\ln(\sigma - \alpha p)\right]^{\frac{1}{2n}} \tag{3.37}$$

Combination of Eqs. (3.36) and (3.37) gives the following expression for the product of fracture width and fracture permeability that appears in Eq. (3.28):

$$wk_f = \sqrt{\frac{12}{\phi_f{}^3}}\left[k_{fo}{}^n + B\ln(\sigma - \alpha p)\right]^{\frac{3}{2n}} \tag{3.38}$$

If the fracture width and porosity at unit effective stress are denoted by w_o and ϕ_{fo}, Eq. (3.38) can be simplified as

$$wk_f = w_o k_{fo}\left[1 - D\ln(\sigma - \alpha p)\right]^{\frac{3}{2n}} \tag{3.39}$$

where D is a constant and its value reflects sensitivity of fracture conductivity to the effective stress.

It can be shown that if the cubic law[22] for a fracture, rather than Eq. (3.33), is used in the derivation, the exponent 3/2n in Eq. (3.39) is 4. This exponent is 4.5 if Walsh's n=1/3 is used. Warpinski and Teufel showed that the value of n varies for different rocks and an n value of 0.515 for chalk was reported. This corresponds to an exponent 3/2n of 2.91 for chalk.[23]

Applications

The newly developed mathematical model can be used for analyzing and understanding the unusual behavior of Spraberry Trend Area reservoirs. The Spraberry Field of West Texas was discovered in 1949 and was considered the largest field in the world. The Spraberry encompasses a productive area greater than 2,500 square miles and consists of

a 1,000-ft section of sandstones, shales and limestones. The productive sands are relatively thin as was demonstrated in Section 1. All sands have matrix permeabilities of 1 md or less and porosities of 8-15 per cent. Initial water saturation varies from 0.25 to 0.60 in productive sands. Initial reservoir pressures were approximately 2,300 psi in the Upper Spraberry. Bubble point pressure of Spraberry oil is about 1,900 psi.[26] Oil viscosity at the saturation pressure is about 0.71 cp.[27] Spraberry wells typically produced 100-400 bopd initially after hydraulic fracture treatment. Primary oil recovery by solution gas drive is less than 10 per cent of oil in place. Waterflooding in the Spraberry was initiated after two pilot tests conducted by Atlantic and Humble.[28] While the unconfined Atlantic pilot was disappointing, the Humble pilot was promising. Oil production of the center well increased from 50 bopd to 256 bopd in four months. A model study of the Humble pilot indicated a NE-SW (N50°E) trend for the major fractures.[27] A major/minor fracture trend permeability contrast of 144/1 was required to match the pilot response.

The Spraberry Field presents unusual problems for both primary production and waterflooding. After more than 40 years of waterflooding, the current oil recovery is still less than 15 per cent. The reasons for the low productivity of Spraberry wells and disappointing imbibition waterflooding remain a mystery to this day. Various hypotheses have been proposed to explain the poor behavior of waterflooding. These hypotheses include: lack of pattern confinement and injection well density, incorrect well pattern alignment, weak wettability to water of the reservoir rock and fracture mineralization which could restrict crossflow,[28] and low permeability to oil after waterflooding of the gas-saturated reservoir, etc.[29] The new mathematical model presented in the previous section is used here for analyzing performance of Spraberry wells. This analysis may be helpful for understanding Spraberry reservoir performance.

According to interpretations of a tracer test,[30] fracture lengths in Spraberry are probably less than the interwell distance (<1,800 feet). Schechter *et al.*[28] found that the fractures vanish at shale-sand interface. It may be a good assumption that the fracture height is equal to the thickness of the pay zone. Elkins[27] summarized fracture analyses and reported that fracture spacing varies from a few inches to a few feet. Schechter *et al.*[28] estimated that fracture spacing in the 1U Unit of the Upper Spraberry is about 4 feet. Based on 111 measurements of fracture openings, Elkins[27] reported that the fracture width ranged up to 0.013 inch and averaged 0.002 inch. This number agrees with Christie's[26] estimation of fracture width of 0.002-0.004 inch based on flow rates and measurement of the fractures in cores. Browscombe and Dyes[31] reported 0.002-0.003 inch fracture width and 3-4 foot fracture spacing. All of these numbers are applied with caution since there was no distinction between coring induced and natural fractures when all of this data was accumulated. The in-situ fracture width in the reservoir may be estimated based on well tests. Well testing[32,33] has not shown dual porosity pressure transient behavior. This indicates that the fracture volume is less than 1/1000 of the matrix volume.[28] Assuming that matrix volume is on the order of 8,000 bbl/acre then the fracture volume should be less than 8 bbl/acre, or 45 cubic feet in a square area of 209 ft by 209 ft assuming a 10-feet-thick pay zone. If a fracture spacing of 4 feet is assumed in the area, at most 52 fractures exist in the area. The maximum fracture width can then be estimated to be 0.005 inch. However, if the fracture spacing is 2 feet in the area, the maximum fracture width should then be about 0.0025 inch.

Primary Production

Initial Production: The mechanism of primary oil production in the Spraberry Trend Area is believed to be dominated by solution gas drive.[27] Initial potential of wells was estimated to be 5 to 10 bopd before hydraulic fracture treatment. Eq. (3.29) has been used to calculate productivity of a Spraberry well under primary production. Data used in the calculations are presented in Table 3.3-1. This table shows that Eq. (3.29) gives a capacity of 5.01 bopd from each fracture. Comparison of this oil rate with actual production rate indicates that the wellbore might intersect one or two natural fractures due to extension of drilling induced fractures.

Hydraulically Fractured Well: Initial potential of a typical Spraberry well was 100 to 400 bopd after hydraulic fracture treatment. Table 3.3-1 also shows calculated production rate of a hydraulically fractured well using Eq. (3.29). The calculated production rate from each fracture is 31.45 bopd. Comparison with actual production rate of 100-400 bopd indicates that the hydraulic treatment might intersect 3 to 13 natural fractures depending upon the scale of the treatment. It appears that hydraulic fracturing probably caused more natural fractures to become connected to the wellbore, rather than opening and extending an existing natural fracture.

Productivity Decline: Eqs. (3.29) and (3.39) have been used for matching the production data from a 1951 shut-in test in the X.B. Cox A-4 in the Driver Unit of the Spraberry Trend Area. Based on a micro-fracture test in the E.T. O'Daniel #37,[34] the minimum horizontal stress in the Upper Spraberry formation is about 3200 psi (0.447 psi/ft). Rapid productivity decline of the well could not be matched by the equations when this minimum stress was utilized. However, when the drawdown, instead of the effective stress, was used in Eq. (3.39), a match to the production data was achieved. The stress sensitivity factor (D in Eq. (3.39)) has been determined to be about 0.1. Table 3.3-2 shows data used for matching. Matched production rate and productivity index is plotted in Fig. 3.3-1. The matched parameters have been used for estimation of productivity of 5 shut-in tests in the Driver Unit. Figures 3.3-2 through 3.3-6 show the comparison between the calculated oil production rates and actual oil production rates observed from the 5 shut-in wells. These figures indicate that calculated and actual oil rate match well at most points except at the point corresponding to the time of April 1952. The reason for the discrepancy is not clear. Fig. 3.3-7 shows a comparison between the calculated oil production rates and actual oil production rates observed from 6 regularly producing wells. Consistency between calculated and actual productivity index of the 6 wells is also observed as shown in Fig. 3.3-8. However, direct application of the stress sensitivity factor of 0.1 to some of the regularly producing wells under-estimated decline of productivity. The result in Figs. 3.3-7 and 3.3-8 was obtained assuming that stress-sensitivity factor increases with time slightly. For example, to match data from the Davenport B-14, the stress-sensitivity factor D was increased from 0.1 to 0.105 for a three month time.

Waterflooding

Unusual Behavior: Large scale waterflooding in the Driver Unit was initiated in July, 1960. It was found that oil production rate was very sensitive to whether the water injection wells were shut-in or not.[25,35] Oil rate was low during water injection and high

when injection wells were shut-in. Consequently, a high-rate cyclic waterflooding (pressure pulsing) scheme was adopted in the Sohio-operated Driver Unit. This production scheme was very successful in the beginning. However, after three cycles of water injection, it was found long-term performance of the cyclic waterflood to be no better than that achieved with much slower steady water injection in a Mobil cooperative waterflood.[36] The interpretation of the mechanism of cyclic water injection has never been satisfactory. Elikins and Skov[25] presented a hypothesis for explaining the behavior of the reservoir subjected to cyclic water injection. It was written in their paper that "over-injection might have been responsible for the absence of waterflood oil at water breakthrough. It appeared that cessation of water injection to permit capillary forces to become dominant and expansion of the rock and its contained fluids during pressure reduction might aid in expulsion of oil from the rock matrix into the fractures." It is possible that the sensitivity of fracture conductivity to effective stress in the fracture dominates the mechanism of cyclic water injection. Fig. 3.3-9 shows calculated pressure distributions along a stress-insensitive fracture. It is seen that if the fracture width is 0.015 inch, the drainage distance in the fracture may be up to 300 feet from the wellbore. Fig. 3.3-10 shows calculated pressure distributions along a stress-sensitive fracture. The stress sensitivity factor used in the calculation is 0.1. It is seen from Fig. 3.3-10 that if the fracture width is 0.015 inch, the drainage distance in the fracture may be only 30 feet from the wellbore, which is 10 times less than 300 feet. This concept of stress-sensitivity may be used to explain cyclic waterflooding behavior. Consider a wellbore intersecting several natural fractures after hydraulic fracture treatment. Let us divide these fractures into two groups: group A and group B. Let fractures in group A represent fractures situated near the line between an injection well and a production well, and let fractures in group B represent fractures located far from the line between the injection well and the production well, as depicted in Fig. 3.3-11. Obviously, the flow resistance from the injection well to the production well through fractures in group A is less than that through fractures in group B. This is because the flow path in group B fractures is longer than that in the group A fractures. During high-rate water injection, fractures in both group A and group B should open, and a higher proportion of water flows from the injector to the producer through path A rather than through path B. Since path A contains less oil expulsed from the rock by capillary pressure than path B, high water cut is expected from the producer. However, when the injector is shut-in, the pressure in path A should drop faster than the pressure in path B. As a result, fractures in path A close (to some degree) faster than that in path B. Since path B contains more oil, lower water-cut is expected at the producer. After resumption of water injection, more water should enter path B because some of the fractures near the injector in group B should still be open, and low water cut production is expected to remain for a certain time before path A opens for water influx. This phenomenon was observed from all the three cycles of water injection in the Driver Unit (see Figure 4 in reference 35). As the number of cycles increase, oil supply from path B decreases due to low rate of water imbibition. Oil production rate should also decrease, and eventually, the cyclic water injection scheme should be no better than steady low rate water injection scheme. This was also observed from the Driver Unit waterflood.

Productivity: After three cycles of waterflooding, productivity in the Driver Unit declined to a level equivalent to low rate waterflooding. Since then low rate waterflooding has

been carried out over many years. Well performance has been poor although pattern injections are sparse. Large volume hydraulic fracturing treatments were conducted on several wells.[35] The results were unsatisfactory as large-scale treatments improve productivity only very little.

Table 3.3-3 shows a comparison between actual production rate and calculated production rate for three wells before and after hydraulic treatments. Results indicate that the calculated pre-fracture oil rates match the actual pre-fracture oil rates when tight natural fractures are assumed, indicating that compacted natural fractures exist in the reservoir under high drawdown conditions. Table 3.3-3 also indicates that calculated post-fracturing oil rates match the actual post-fracturing oil rates if improvement in fracture conductivity is poor. This may be an indication that proppant was pumped into existing natural fractures rather than hydraulically induced fractures. This is evident based on Ogden and Locke's[37] analysis indicating that the high leakoff encountered is unlikely to be a result of the matrix permeability. If this is true, proppant in the natural fractures may have been crushed during production because of a low concentration in the fractures. As a result, well productivity has remained low. This hypothesis is also consistent with the observation by Barba et al.[38] It was written in their paper that "although it is apparent that the natural fractures were open during drilling, logging, and stimulation operations, they were clearly no longer open when normal reservoir condition were restored." However, to what degree the fractures are open needs further investigation.

Possible Solutions: Tremendous oil reserves in the Spraberry reservoir keeps operators searching for better methods of producing oil. The above analysis implies that probably there is no proppant that is strong enough to withstand the stress in the fracture under low reservoir pressure conditions because of low proppant concentration. However, several possible solutions to the low productivity problem in the Spraberry reservoir exist. Schechter and Guo[39] have demonstrated that CO_2 gravity drainage may be a promising method to recover oil from the Spraberry reservoir. The second solution might be acidizing fractures while waterflooding. Significant mineralization has been found on fracture surfaces in core taken from the Spraberry. Saleta et al.[40] found that the composition of the minerals on the fracture surface is primarily calcite or barite. Thin section analysis indicates that it is impossible for water to imbibe into the rock across layers of minerals on the surface of the fractures. If a large portion of natural fractures are found to be mineralized, acidizing fractures while waterflooding should be investigated. Another possible solution is to fracture hydraulically the pay zones with porous cement, which should be stronger than low concentration proppant to keep fractures open, at least around wellbore. The combination of the three measures may lead to performance enhancement.

Conclusions

1. A simple and more rigorous mathematical model has been developed for estimating productivity of wells intersecting long fractures. The model reveals that pressure variation is significant in tight fractures.

2. This model helps to understand the unusual performance of Spraberry reservoirs. Matching of the new model to production data indicates that:

   i) During primary production, a Spraberry wellbore interconnected 1 to 2 natural fractures due to extension of drilling induced fractures before hydraulic treatment.

   ii) A Spraberry wellbore interconnects several natural fractures after hydraulic fracture stimulation.

   iii) Stress-sensitive fracture conductivity may be partially responsible for the decline of well productivity in the Spraberry Trend Area. However, other factors, such as gas saturation, can similarly affect the decline of well productivity in the area. Further investigations need to be conducted.

   vi) Currently natural and hydraulic fractures in the Spraberry reservoir may, or may not, be closed depending upon local pore pressures in the fractures. Fractures near high-drawdown wellbores may be compacted and closed to some degree.

   v) Large scale hydraulic fracturing treatments were not helpful probably due to low concentration of proppant spread in a large volume of natural fractures. Horizontal wells may not provide significant help if a high pressure drawdown is utilized during oil production.

3. Cyclic waterflood performance in the Spraberry can be interpreted based on the theory of stress-sensitive fracture conductivity.

4. Integration of CO_2 flooding, fracture acidizing and utilization of porous cement as a fracturing fluid may be potential measures for improving well productivity in the Spraberry Trend Area.

Nomenclature

A = constant in Walsh's equation.
B = constant in Walsh's equation
B_o = formation volume factor of oil
c = a group of variables defined by Eq. (3.28)
c_1 = integration constant
c_2 = integration constant
C_{fD} = specific dimensionless fracture conductivity
D = stress-sensitivity factor
f = friction factor
h = fracture height
k_f = permeability of fracture
k_{fo} = permeability of fracture at unity effective stress
k_z = permeability of matrix in z-direction
L = fracture length

n = conductivity exponent
p = pore pressure
p_d = pressure drawdown in fracture
p_d* = pressure drawdown in wellbore
p_d' = derivative of pressure drawdown with respect to distance
p_e = pressure at drainage boundary
$p_f(x)$= fracture pressure at point x
PI = productivity index
p_w = flowing bottom hole pressure
p_{xf} = fracture pressure at point $x=x_f$
Q = total oil flow rate from one wing of fracture
$Q(x)$= flow rate in fracture at point x
R_e = Reynold's number
v = interstitial velocity
v_D = Darcy velocity
v_z = velocity in z-direction
w = fracture width (aperture)
w_o = fracture width (aperture) at unity effective stress
x = distance from fracture tip
x_f = length of a fracture wing
y = vertical distance
z = distance in the direction perpendicular to fracture face
z_e = distance between fracture and drainage boundary
α = poroelastic parameter defining effective stress law
Δp = pressure drop across fracture length L
μ = oil viscosity
ρ = oil density
σ = confining stress
ϕ_f = fracture porosity
ϕ_{fo} = fracture porosity at unity effective stress

References

1. Barfield, E.C., Jordan, J.K. and Moore, W.D.: "An Analysis of Large-Scale Flooding in the Fractured Spraberry Trend Area Reservoir," *J. Pet. Tech.* (April 1959) 15-19.
2. Soliman, M. Y., Hunt, J.L., and El Rabaa,W.: "Fracturing Aspects of Horizontal Wells," *JPT* (Aug. 1990) 966-73.
3. Chen, C.C., Ozkan, E., and Raghavan, R.: "A Study of Fractured Wells in Bounded Reservoirs," paper SPE 22717 presented at the 1991 SPE Annual Technical Conference and Exhibition held in Dallas, Texas, Oct. 6-9, 1991.
4. Cinco-L., H., Samaniego-V., F., and Dominguez-A., N.: "Transient Pressure Behavior for a Well with a Finite-Conductivity Vertical Fracture," SPEJ (Aug. 1978) 253-64.

5. Ozkan, E., and Raghavan, R.: "New Solutions for Well-Test-Analysis Problems: Part 1 - Analytical Considerations," *SPEFE* (Sept. 1991) 359-65.
6. Chu,W., and Shank, G.D.: "A New Model for a Fractured Well in a Radial, Composite Reservoir," *SPEFE* (Sept. 1993) 225-32.
7. Beier, R.A.: "Pressure-Transient Model for a Vertically Fractured Well in a Fractal Reservoir," *SPEFE* (June 1994) 122-28.
8. Chen, C., and Raghavan, R.: "Modeling a Fractured Well in a Composite Reservoir," *SPEFE* (Dec. 1995) 241-46.
9. Karcher, B.J., Giger, F.M., and Combe, J.: "Some Practical Formulas to Predict Horizontal Well Behavior," paper SPE 15430, presented at the 1986 SPE Annual Technical Conference and Exhibition held in New Orleans, Louisiana, Oct. 5-8, 1986.
10. Economides, M.J., Delmbacher, F.X., Brand, C.W., and Heinemann, Z.E.: "Comprehensive Simulation of Horizontal-Well Performance," *SPEFE* (Dec. 1991) 418-26.
11. Giger, F.M., Reiss, L.H., and Jourdan, A.P.: "The Reservoir Engineering Aspect of Horizontal Drilling," paper SPE 13024 presented at the 1984 SPE Annual Technical Conference and Exhibition in Houston, Texas, Sept. 16-19, 1984.
12. Giger, F.M.: "Horizontal Wells Production Techniques in Heterogeneous Reservoirs," paper SPE 13710, presented at the SPE 1985 Middle East Oil Technical Conference and Exhibition held in Bahrain, March 11-14, 1985.
13. Muskat, M.: *The Flow of Homogeneous Fluids through Porous Media*, I.H.R.D.C., Boston, 1982.
14. Houpeurt, A: *Elements de mecanique des fluides dans les milieux poreux*, Editions Technip, Paris, 1975.
15. Joshi, S.D.: "Augmentation of Well Productivity with Slant and Horizontal Wells," SPE 15375, 1986; *JPT* (June 1988) 729-39; Trans. AIME, **285**.
16. Joshi, S.D.: "A Review of Horizontal Well and Drainhole Technology," paper SPE 16868, presented at the 1987 SPE Annual Technical Conference and Exhibition held in Dallas, Texas, Sept. 27-30, 1987.
17. Mukherjee, H., and Economides, M.J.: "A Parametric Comparison of Horizontal and Vertical Well Performance," *SPEFE* (June 1991) 209-16.
18. Prats, M.: "Effect of Vertical Fractures on Reservoir Behavior -- Incompressible Fluid Case," *SPEJ* (June 1961) 105-16; *Trans.* AIME, **222**.
19. Raghavan, R., and Joshi.,S.D.: "Productivity of Multiple Drainholes or Fractured Horizontal Wells," *SPEFE* (March 1993) 11-16.
20. Guo, G., and Evans, R.D.: "Inflow Performance of a Horizontal Well Intersecting Natural Fractures," paper SPE 25501, presented at the SPE Production Operations Symposium held in Oklahoma City, Oklahoma, March 21-23, 1993.
21. Li, H., Jia, Z., and Wei, Z.: "A New Method to Predict Performance of Fractured Horizontal Wells," paper SPE 37051, presented at the 1996 SPE International Conference on Horizontal Well Technology held in Calgary, Canada, November 18-20, 1996.
22. Van Golf-Racht, D.T.: *Fundamentals of Fractured Reservoir Engineering*, Elsevier Scientific Publishing Co., New York, 1982.

23. Warpinski, N.R., and Teufel, L.W.: "Effect of Stress and Pressure on Gas Flow Through Natural Fractures," paper SPE 22666, presented at the 1991 SPE Annual Technical Conference and Exhibition held in Dallas, Texas, Oct. 6-9, 1991.
24. Walsh, J.B.: "Effect of Pore Pressure and Confining Pressure on Fracture Permeability," *Int. J. Rock Mech., Min. Sci. & Geomech. Abstr.*, **18**, 1981, 429-35.
25. Elkins, L.F., and Skov, A.M.: "Cyclic Water Flooding the Spraberry Utilizes 'End Effects' to Increase Oil Production Rate," *JPT* (Aug. 1963) 877-84.
26. Christie, R.S., and Blackwood, J.C.: "Production Performance in Spraberry," *Oil & Gas Journal* (April 7, 1952) 107-15.
27. Elkins, L.F.: "Reservoir Performance and Well Spacing, Spraberry Trend Area Field of West Texas," *Trans.* AIME, **198**, (1953) 177-96.
28. Schechter, D.S., McDonald, P., Sheffield, T., and Baker, R.: "Reservoir Characterization and CO_2 Pilot Design in the Naturally Fractured Spraberry Trend Area," paper SPE 35469, presented at the SPE Permian Basin Oil & Gas Recovery Conference held in Midland, Texas, 27-29, March 1996.
29. Epic Consulting Services Limited: "Reasons for the Relatively Low Recovery of the Spraberry Waterfloods," (July 1996) PRRC Spraberry Database.
30. Howell, W.D., Armstrong, F.E., and Watkins, J.W.: "Radioactive Gas Tracer Survey Aids Waterflood Planning," *World Oil (*Feb. 1961).
31. Browscombe, E.R. and Dyes, A.B.: "Water Imbibition Displacement - Can It Release Reluctant Spraberry Oil?" *Oil & Gas Journal* (November 3 1952) 264-65.
32. Baker, R.: "Pressure Test Analysis for Midkiff 25-08 ," (April 1994) PRRC Spraberry Database.
33. Baker, R.: "Vertical Pulse Test Analysis of Shackelford 1-38A," (April 1994) PRRC Spraberry Database.
34. Pedersen, S.H.: "In-Situ Stress Evaluation in the Spraberry Trend," presentation at the Naturally Fractured Reservoir Forum held 19 April 1995 in Socorro, New Mexico. PRRC Spraberry Database.
35. Elkins, L.F., Skov, A.M., and Gould, R.C.: "Progress Report on Spraberry Waterflood Reservoir Performance, Well Stimulation and Water Treating and Handling," *JPT* (Sept. 1968) 1039-49.
36. Guidroz, G.M.: "E.T. O'Daniel Project -- A Successful Spraberry Flood," *JPT* (Sept. 1967) 1137-40.
37. Ogden, V. and Locke, J.: "What Are the Facts and Figures for Spraberry Trend Core Analysis," *Oil & Gas Journal* (Jan. 14, 1952) 97-99.
38. Barba, R.E. Jr., and Cutia, A.S.: "Evaluating Horizontal Well Potential in the Spraberry Trend," paper SPE 23949, presented at the SPE Permian Basin Oil & Gas Recovery Conference held in Midland, Texas, 18-20, March 1992.
39. Schechter, D.S., and Guo, B.: "Mathematical Modeling of Gravity Drainage After Gas Injection into Fractured Reservoirs," paper SPE 35170, presented at the SPE Improved Oil Recovery Symposium held in Tulsa, Oklahoma, 22-24 April, 1996.
40. Saleta, C.J., Banik, A.K., Cather, M.E., and Schechter, D.S.: "Application of Analytical Techniques to Evaluate the Heterogeneities of the Upper Spraberry Formation (Permian) and Its Influence on the Quality of the Midland Basin Reservoir in West Texas," SPE 35225, presented in the poster session at the SPE Permian Basin Oil & Gas Recovery Conference held in Midland, Texas, 27-29, March 1996.

41. Aronofsky, J.S., Masse, L., and Natanson, S.G.: "A Model for the Mechanism of Oil Recovery from the Porous Matrix due to Water Invasion in Fractured Reservoirs," *Trans.* AIME, **213**, (1958) 17-19.

Table 3.3-1—Well Productivity Before and After Hydraulic Fracturing Treatment for Primary Production

	Before Treatment	After Treatment
Matrix permeability, md	0.8	0.8
Water saturation	0.38	0.38
Residual oil saturation	0.15	0.15
Oil viscosity, cp	0.71	0.71
Formation volume factor	1.385	
Fracture spacing, ft	3	3
Fracture length, ft	200	600
Fracture height, ft	15	15
Initial fracture width, in	0.002	0.007
Initial fracture porosity	0.56	0.58
Reservoir pressure, psig	2400	2400
Flowing bottom hole pressure, psig	1900	1900
Stress sensitivity factor	0.1	0.1
Calculated oil production rate per fracture, bopd	5.01	31.45
Typical oil production rate per well,[25] bopd	5 - 10	100 - 400

Table 3.3-2 —Data Used for Matching Productivity Decline of X. B. Cox A-4

Month during 1952	March	April	May	June
Matrix permeability, md	0.8	0.8	0.8	0.8
Water saturation	0.38	0.38	0.38	0.38
Residual oil saturation	0.15	0.15	0.15	0.15
Oil viscosity, cp	0.90	0.95	1.0	1.0
Formation volume factor, v/v	1.310	1.295	1.285	1.285
Fracture spacing, feet	3	3	3	3
Fracture length, feet	600	600	600	600
Fracture height, feet	15	15	15	15
Initial fracture width, inch	0.005	0.005	0.005	0.005
Initial fracture porosity	0.6	0.6	0.6	0.6
Number of fractures	5	5	5	5
Reservoir pressure, psig	1650	1600	1500	1400
Flowing bottom hole pressure, psig	1000	1000	800	750
Stress sensitivity factor	0.1	0.1	0.1	0.1
Calculated oil production rate, bopd	101	89	84	75
Actual oil production rate, bopd	100	85	80	75

Calculated productivity index, B/D/psi	0.156	0.149	0.119	0.115
Actual productivity index, B/D/psi	0.160	0.140	0.099	0.087

Table 3.3-3 —Productivity of Depleted Wells in Driver Unit Before and After Large Scale Hydraulic Treatment

	Well 385		Well 389		Well 397	
	Pre-Frac.	Post-Frac.	Pre-Frac.	Post-Frac.	Pre-Frac.	Post-Frac.
Matrix permeability, md	0.8	0.8	0.8	0.8	0.8	0.8
Initial water saturation	0.38	0.38	0.38	0.38	0.38	0.38
Water saturation	0.50	0.50	0.50	0.50	0.50	0.50
Residual oil saturation	0.20	0.20	0.20	0.20	0.20	0.20
Oil viscosity, cp	1.5	1.3	1.5	1.3	1.7	1.6
Formation volume factor	1.18	1.22	1.18	1.22	1.16	1.16
Fracture spacing, feet	3	3	3	3	3	3
Fracture length, feet	600	600	600	600	600	600
Fracture height, feet	15	15	15	15	15	15
Initial fracture width, inch	0.003	0.005	0.003	0.004	0.002	0.0025
Initial fracture porosity	0.60	0.63	0.59	0.57	0.45	0.49
Number of fractures	4	4	3	3	4	4
Reservoir pressure, psig	1575	1480	1725	1565	1885	1635
Flowing bottom hole pressure, psig	370	530	350	505	180	190
Stress sensitivity factor	0.1	0.1	0.1	0.1	0.1	0.1
Calculated oil production rate, bopd	16	39	11	17	7	10
Actual oil production rate, bopd	15	39	11	17	7	10

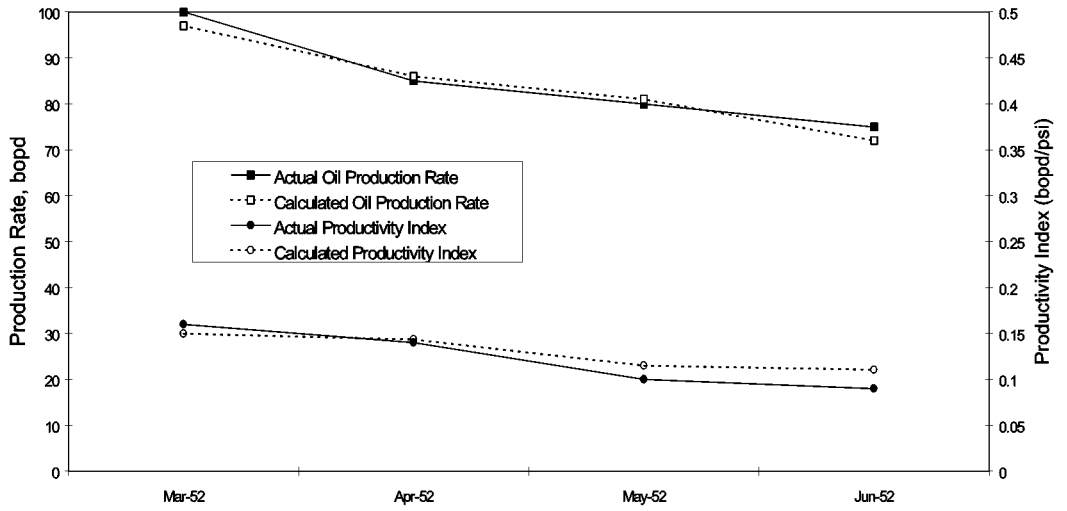

Fig. 3.3-1—Match for calculated and actual productivity for X.B. Cox A-4 (Driver Unit)

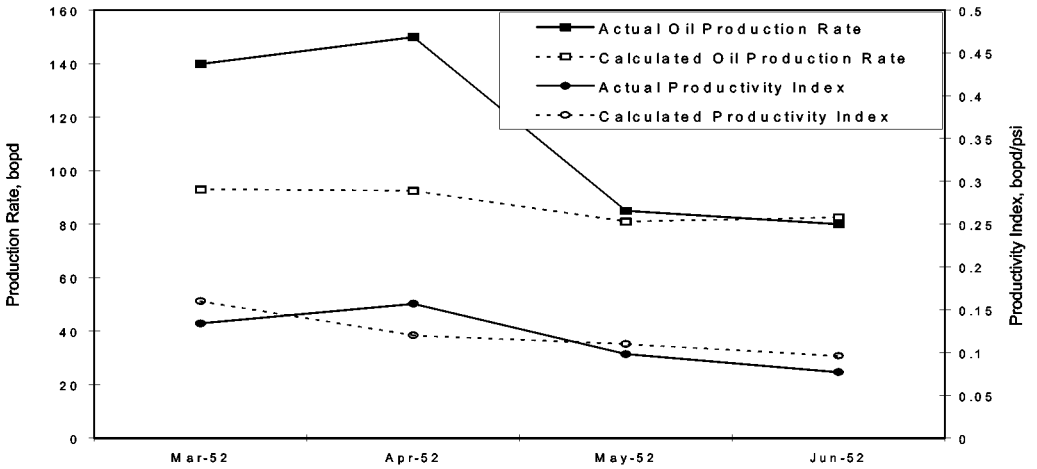

Fig. 3.3-2—Comparison between calculated and actual productivity for Davenport B-5

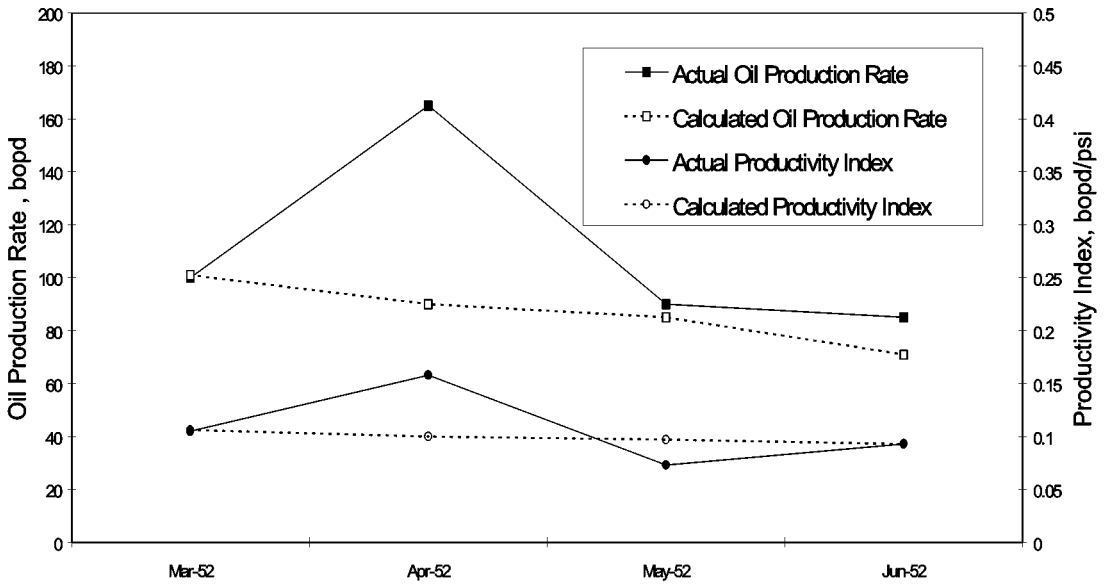

Fig. 3.3-3 —Comparison between calculated and actual productivity for Davenport B-7

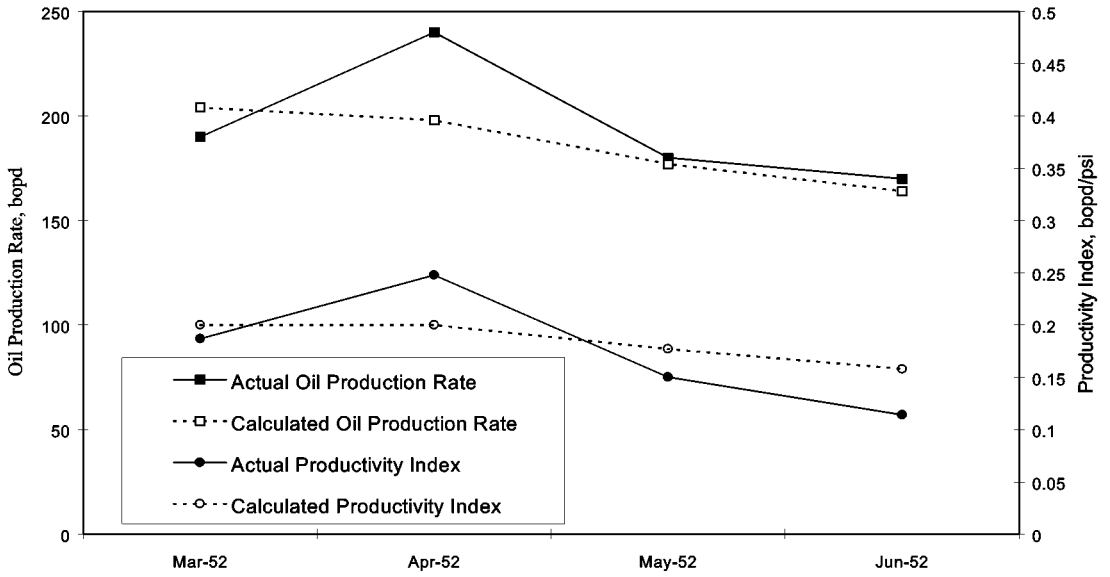

Fig. 3.3-4—Comparison between calculated and actual productivity for Davenport C-6

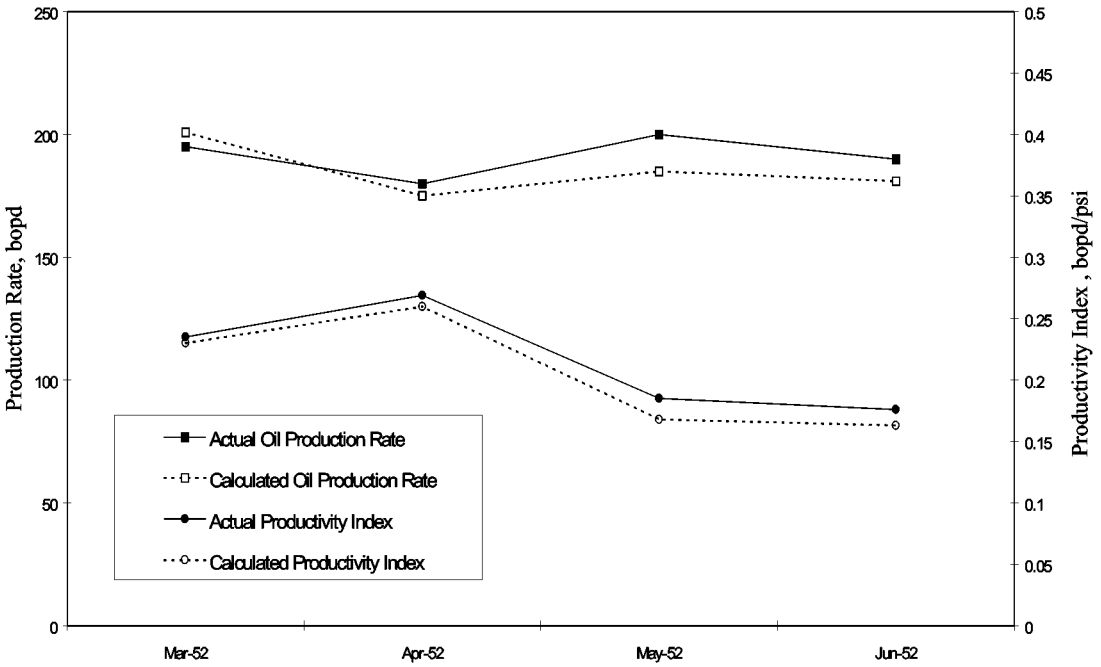

Fig. 3.3-5 —Comparison between calculated and actual productivity for Davenport C-8

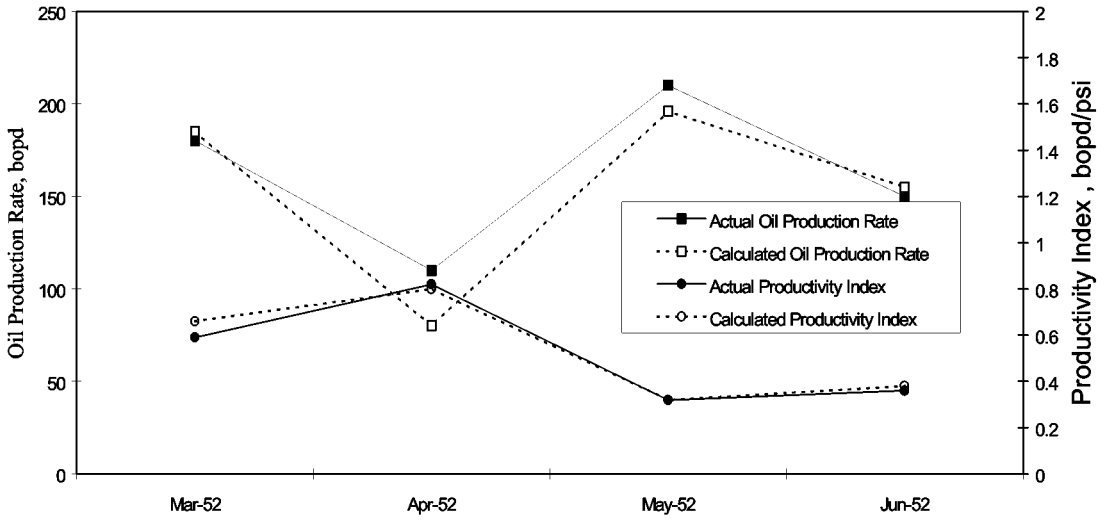

Fig. 3.3-6—Comparison between calculated and actual productivity for Bryans A-2

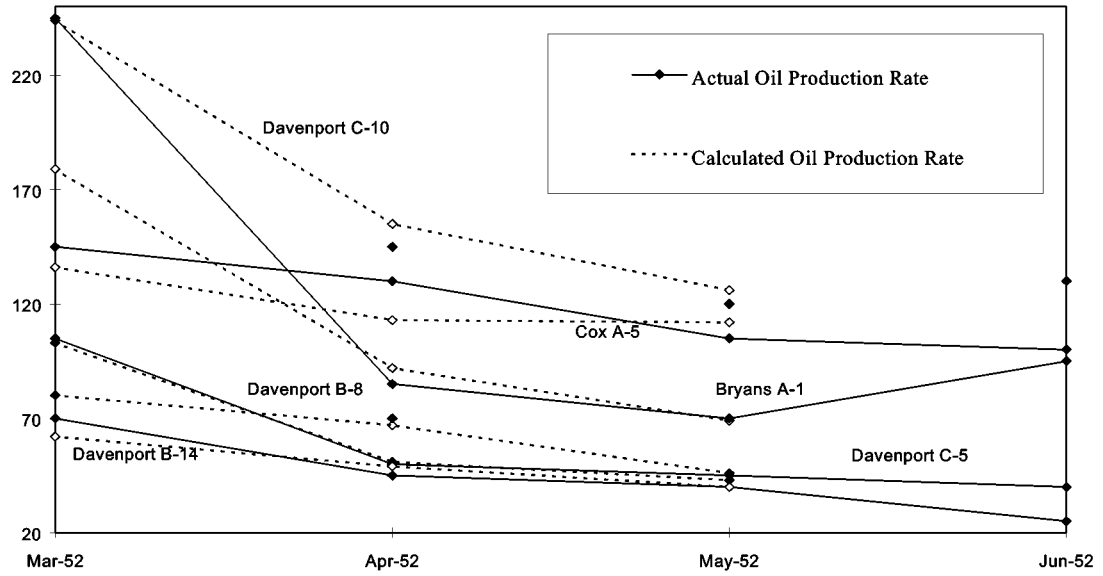

Fig. 3.3-7—Comparison between calculated and actual oil production rates in Driver Unit waterflood

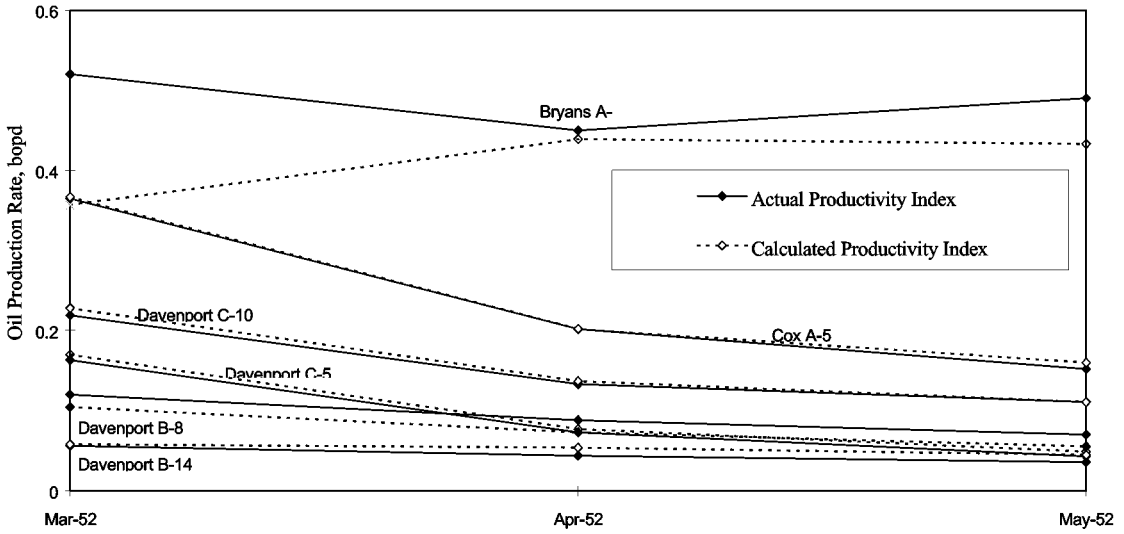

Fig. 3.3-8 —Comparison between calculated and actual productivity indices

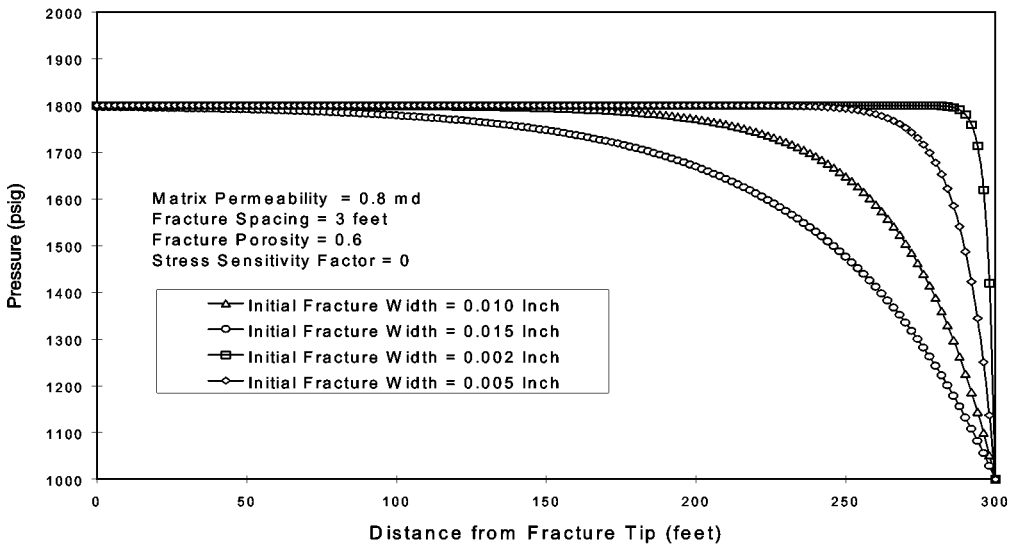

Fig. 3.3-9 —Calculated pressure distribution along a stress-insensitive fracture

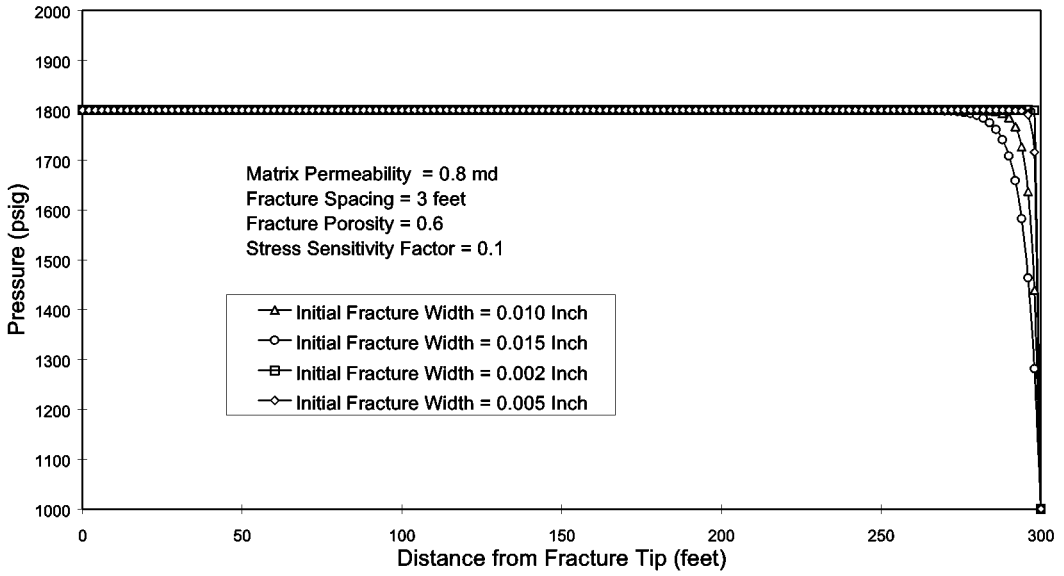

Fig. 3.3-10—Calculated pressure distribution along a stress-sensitive fracture

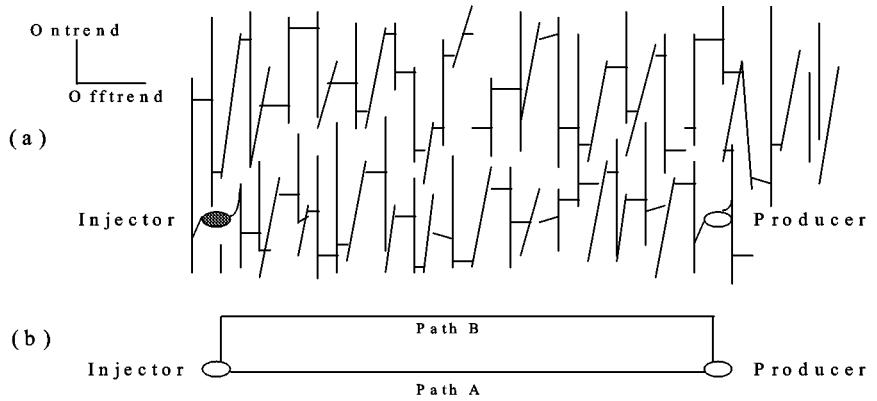

Fig. 3.3-11—A model to interpret cyclic waterflooding performance

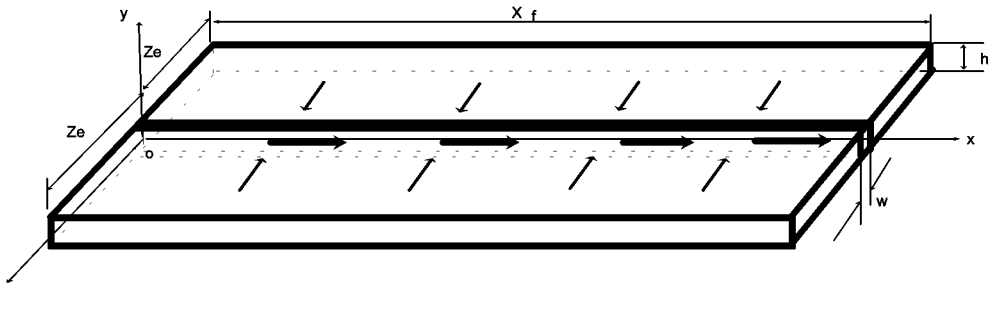

Fig. 3.3-12—Geometry of a reservoir drained by a wing of a fracture

Appendix III.A - Matrix-to-Fracture Cross Flow in Fractured Oil Reservoirs

Assumptions

A major assumption in this analysis is that the fracture is long enough to reach no-flow boundaries in the drainage area. Such no-flow boundaries exist at the borders of drainage areas of production wells. Oil flow in the neighborhood of such a long fracture may be analyzed with the following assumptions:

1. One-dimensional flow in the matrix.
2. One-dimensional flow in the fracture.
3. Pseudo steady flow prevails.
4. Oil is treated as an incompressible fluid.
5. Darcy flow dominates.

Governing Equation

The geometry of a reservoir section drained by a fracture wing is depicted in Fig. 3.3-12. Oil flows within the drainage boundaries ($z = \pm z_e$) to the fracture face in z-direction. Darcy velocity of oil in the matrix can be described by Darcy's law:

$$v_z(x) = \frac{k_z}{\mu z_e}[p_e - p_f(x)] \tag{A.1}$$

where $v_z(x)$ is Darcy velocity in z-direction at lateral distance x from the fracture tip, k_z is matrix permeability in z-direction, μ is oil viscosity, z_e is drainage distance of the fracture, p_e is the pressure at the drainage boundary, and $p_f(x)$ is the pressure in the fracture at the point x. The volumetric flow rate of oil in the fracture at point x can be determined based on $v_z(x)$:

$$Q(x) = 2h\int_0^x v_z(x)dx \tag{A.2}$$

where Q(x) is the volumetric flow rate in the fracture at point x, h is the height of the fracture which is assumed to be equal to reservoir thickness. Substituting Eq. (A.1) into Eq. (A.2) gives:

$$Q(x) = \frac{2hk_z}{\mu z_e} \int_0^x \left[p_e - p_f(x) \right] dx \tag{A.3}$$

If the average width (aperture) of the fracture is w, Darcy velocity in the fracture $v_f(x)$ can be obtained by dividing Eq. (A.3) by the cross sectional area of the fracture:

$$v_f(x) = \frac{Q(x)}{hw} = \frac{2k_z}{\mu w z_e} \int_0^x \left[p_e - p_f(x) \right] dx \tag{A.4}$$

Application of Darcy's law in the fracture gives:

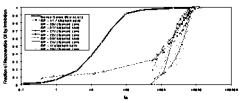

(A.5)

where k_f is the permeability of the fracture when it is treated as a porous medium. Substituting of Eq. (A.4) into Eq. (A.5) yields:

$$\frac{dp_f(x)}{dx} = -\frac{2k_z}{w z_e k_f} \int_0^x \left[p_e - p_f(x) \right] dx \tag{A.6}$$

Differentiation of Eq. (A.6) with respect to x gives:

$$\frac{d^2 p_f(x)}{dx^2} = -\frac{2k_z}{w z_e k_f} \left[p_e - p_f(x) \right] \tag{A.7}$$

which is the governing equation for the fracture pressure function $p_f(x)$. This equation can be further simplified using the definitions

$$p_d = p_e - p_f(x) \tag{A.8}$$

and

$$c = \frac{2k_z}{w z_e k_f} \tag{A.9}$$

where p_d is pressure drawdown in the fracture at point x, and c is a dimensionless variable describing the contrast between matrix and fracture conductivities. Substituting Eqs. (A.8) and (A.9) into Eq. (A.7) results in:

$$\frac{d^2 p_d}{dx^2} = c p_d \tag{A.10}$$

Boundary Conditions

The first boundary condition for Eq. (A.10) assumes that at any point where the drawdown is zero, the variation of the drawdown with respect to distance is negligible. This boundary condition is expressed as

$$\left(\frac{dp_d}{dx}\right)_{p_d=0} = 0 \tag{A.11}$$

The second boundary condition is that the drawdown at the exit of the fracture wing is equal to drawdown in the wellbore, or

$$p_d = p_d^{\,*} = p_e - p_w \tag{A.12}$$

Pressure distribution in a fracture may be estimated using Eq. (1):

Solution

Let

$$p_d^{\,'} = \frac{dp_d}{dx} \tag{A.13}$$

then

$$\frac{d^2 p_d}{dx^2} = \frac{dp_d^{\,'}}{dx} = \frac{dp_d^{\,'}}{dp_d}\frac{dp_d}{dx} = p_d^{\,'}\frac{dp_d^{\,'}}{dp_d} \tag{A.14}$$

Substituting Eq. (A.14) into Eq. (A.10) yields:

$$p_d^{\,'}\frac{dp_d^{\,'}}{dp_d} = cp_d \tag{A.15}$$

By separation of variables, a solution to Eq. (A.15) is obtained:

$$\frac{1}{2}p_d^{\,'2} = \frac{1}{2}cp_d^{\,2} + c_1 \tag{A.16}$$

where c_1 is an integration constant and can be determined using the boundary condition expressed by Eq. (A.11) as

$$c_1 = 0. \tag{A.17}$$

Substituting $c_1 = 0$ into Eq. (A.17) and rearranging the latter yield:

$$p_d^{\,'} = \sqrt{c}\,p_d \tag{A.18}$$

Substituting of Eq. (A.13) into Eq. (A.18) gives:

$$\frac{dp_d}{dx} = \sqrt{c}\, p_d \tag{A.19}$$

which has a solution of

$$\ln(p_d) = \sqrt{c}x + c_2 \tag{A.20}$$

The integration constant c_2 can be determined using boundary condition Eq. (A.12) to be

$$c_2 = \ln(p_d^*) - \sqrt{c}x_f \tag{A.21}$$

Substituting Eq. (A.21) into Eq. (A.20) and rearranging the latter yield:

$$\ln(\frac{p_d}{p_d^*}) = \sqrt{c}(x - x_f) \tag{A.22}$$

or

$$p_d = p_d^* e^{\sqrt{c}(x-x_f)} \tag{A.23}$$

Substitution of Eqs. (A.8) and (A.12) into Eq. (A.23) result in an equation for pressure drawdown distribution in the fracture:

$$p_e - p_f(x) = (p_e - p_w)e^{\sqrt{c}(x-x_f)} \tag{A.24}$$

The equation for pressure distribution in the fracture is then:

$$p_f(x) = p_e - (p_e - p_w)e^{\sqrt{c}(x-x_f)} \tag{A.25}$$

Based on Eq. (A.3), the oil flow rate at the exit of the fracture wing can be expressed as

$$Q = \frac{2hk_z}{\mu z_e}\int_0^{x_f}[p_e - p_f(x)]\, dx \tag{A.26}$$

Substituting Eq. (A.24) into Eq. (A.26) yields:

$$Q = \frac{2hk_z}{\mu z_e}\int_0^{x_f}(p_e - p_w)e^{\sqrt{c}(x-x_f)}dx \tag{A.27}$$

which can be integrated resulting in the following inflow performance relationship:

$$Q = \frac{2hk_z}{\mu z_e\sqrt{c}}(p_e - p_w)(1 - e^{-\sqrt{c}x_f}) \tag{A.28}$$

The productivity index for the fracture wing is then

$$PI = \frac{Q}{p_e - p_w} = \frac{2hk_z}{\mu z_e\sqrt{c}}(1 - e^{-\sqrt{c}x_f}) \tag{A.29}$$

If field units are used, Eqs. (A.28) and (A.29) take the following form:

$$Q = \frac{0.00254 k_z h}{B_o \mu z_e \sqrt{c}} (p_e - p_w)(1 - e^{-\sqrt{c} x_f}) \tag{A.30}$$

and

$$PI = \frac{Q}{p_e - p_w} = \frac{0.00254 k_z h}{B_o \mu z_e \sqrt{c}} (1 - e^{-\sqrt{c} x_f}) \tag{A.31}$$

where B_o is the formation volume factor of oil.

Appendix III.B - Relationship between Fracture Width and Permeability

Application of the mathematical model derived in Appendix A requires information concerning the fracture width *w* and fracture permeability k_f . However, these two parameters should not be used independently because they are closely related. Similar to the cubic law[22] for the relationship between fracture width and fracture conductivity, a simple relation between fracture width and fracture permeability is derived analytically in this section.

For flow of a liquid in a fracture at a practical rate encountered in petroleum reservoirs, laminar flow should prevail. Pressure drop (Δp) across a fracture length (L) can be written as[23]

$$\Delta p = \frac{f \rho v^2 L}{w \phi_f} \tag{B.1}$$

where f is the friction factor, ρ is the fluid density, v is fluid velocity, and ϕ_f is fracture porosity. The fracture porosity characterizes volume of solid materials including minerals, crushed and uncrushed rock within the fracture aperture. The friction factor for laminar flow in a fracture can be expressed as[23]

$$f = \frac{24}{R_e} \tag{B.2}$$

where R_e is the Reynold's number and is expressed as[23]

$$R_e = \frac{2 \rho v w \phi_f}{\mu} \tag{B.3}$$

where μ is fluid viscosity. Substituting Eqs. (B.2) and (B.3) into Eq. (B.1) yields:

$$\Delta p = \frac{12 \mu v L}{w^2 \phi_f{}^2} \tag{B.4}$$

If the fracture is treated as a porous medium, the pressure drop can also be expressed in Darcy equation:

$$\Delta p = \frac{\mu v_D L}{k_f} \tag{B.5}$$

where v_D is Darcy velocity and is related to interstitial velocity (v) through fracture porosity (ϕ_f):

$$v_D = \phi_f v \tag{B.6}$$

Equating the right-hand-side of Eqs. (B.4) and (B.5) gives the interrelationship of fracture width, fracture porosity and fracture permeability as

$$k_f = \frac{\phi_f{}^3 w^2}{12} \tag{B.7}$$

3.4 WELL PRODUCTIVITY DURING PRIMARY PRODUCTION

Introduction

During the first year of this project, we analyzed the productivity behavior of Spraberry wells using a newly developed mathematical model. We concluded that stress-sensitive fracture conductivity may be partially responsible for the decline of well productivity in the Spraberry Trend Area. In the second year of this project, we modified the mathematical model with consideration of mechanical skin due to fluid damage to the matrix permeability. This section addresses the possibility of the effect of formation damage on well productivity in the Spraberry Trend Area during the primary oil production.

The Spraberry Trend Area presents unusual problems for both primary production and waterflooding. After more than 40 years of waterflooding, the current oil recovery is still less than 15 per cent. A model study of a waterflood pilot in the Spraberry Trend Area indicated a NE-SW trend of the major fractures.[1] A contrast of 144/1 was required for the major/minor fracture trend permeability ratio to match the pilot response. This strong anisotropic effective permeability implies the existence of well inter-connected, long natural fractures in the Spraberry reservoir. A characteristic of flow in long natural fractures is that the pressure variation along the fracture should be significantly higher compared to that in a hydraulic fracture or a short natural fracture. Unfortunately, a method for analyzing flow behavior in reservoirs with long fractures is not readily available from the literature.

Several analytical solutions have been presented for transient flow in fractured reservoirs.[2-8] Numerical models have also been developed for simulating fluid flow in fractured reservoirs.[9,10] However, it is still desirable for reservoir engineers to use steady flow equations for identification of formation damage in fractured reservoirs. This is not only because the analytical transient-flow solutions and numerical simulators are not convenient to use, but also because steady or pseudo-steady flow prevails as the dominating flow mechanism in the lifetime of most oil wells. Therefore, steady flow equations are attractive for formation damage analysis.

This section demonstrates that use of a modified steady-flow model for matching production data aided in understanding of the unusual behavior of Spraberry Trend Area reservoirs. The use of the model has captured the characteristics of rapid decline in productivity of Spraberry vertical wells. The results indicate that even though high gas saturation could hinder the productivity of the Spraberry wells, the wells should still have higher oil production rates if the formation was not damaged. Comparison between the effects of matrix skin and fracture conductivity reduction due to pressure drawdown indicates that the stress-sensitive fracture conductivity is probably responsible for the productivity loss of these wells during primary production.

Existing Models

Van Poollen[11] investigated productivity versus permeability damage in hydraulically induced fractures by means of mathematical analyses of electrical-model analogs. The maximum simulated fracture length was 0.6 times the drainage radius. Productivity of

fractured wells was graphically presented in terms of ratio of oil production rate with fractures and without fractures. Van Poollen[11] concluded that damage to the formation immediately surrounding the fracture has only a minor effect on the productivity of the well, while the damage to the fracture flow capacity has a major effect on the productivity of the well.

Dyes *et al.*[12] reported the influence of fracturing in well productivity based on experimental results obtained from a Carter Electric Analyzer. The maximum simulated fracture length was 0.75 times the drainage distance between the well and the element boundary. McGuire and Sikora[13] provided more experimental data obtained from the Carter Electric Analyzer. The maximum simulated fracture length was equal to the drainage distance between the well and the element boundary. The effect of vertical fractures on well productivity was graphically presented in terms of ratio of well productivity with fractures to that without fractures.

Raymond and Binder[14] presented their mathematical analyses on productivity of wells in vertically fractured, damaged formations. Their mathematical models were formulated assuming pressure at any given radial position is the same throughout the entire drainage area so that the isobars form a set of concentric circles. Since the models did not consider the pressure drop necessary to move fluid from a point in the formation to the fracture, excessive error was observed[14] at large ratios of fracture length to drainage radius, as compared to the results given by McGuire and Sikora.[13]

The first mathematical model for analyzing productivity of horizontal wells intersecting fractures was presented by Giger *et al.*[15,16] Two solutions were proposed for short horizontal wells and long horizontal wells respectively. For both cases, flow in the rock matrix and flow in the fractures were formulated separately, and then combined to obtain an equation for the entire flow path from external boundary to wellbore. Radial flow was assumed in the fracture for both short and long wellbore cases. For the case of a short horizontal well, they employed a radial flow equation presented by Muskat[17] for matrix flow from external boundary to a small fracture. For the long horizontal well case, a flow equation developed by Houpeurt[18] for flow in matrix from an external boundary to an extended fracture was utilized. Giger's approach may be considered to be less rigorous because the equations for flow from external boundaries to the fractures were derived based on the assumption that pressure in the fracture is uniform, or invariant, along the fracture length. Karcher *et al.*[9] calculated productivity increase of fractured horizontal wells over fractured vertical wells using equations presented by Giger.[16] They also investigated issues of increasing productivity, reducing coning, and improving sweep efficiency by multi-fractured horizontal wells using their numerical simulator for infinite conductivity fractures. Joshi[19] proposed a steady state flow equation for analyzing productivity of horizontal wells. His equation for flow in the matrix was also derived based on the assumption of constant pressure in the fracture. Joshi[20] presented a review of horizontal well technology. He pointed out that in most fracture jobs it is difficult to obtain infinite conductivity and, moreover, fracture conductivity decreases over time. Mukherjee and Economides[21] developed a simplified steady-state approach to calculate the number of infinite conductivity fractures equivalent to a drainhole. Their model was developed on the basis of the inflow performance relationship suggested by Joshi[19] with Prats'[22] correlation for dimensionless wellbore radius. Economides *et al.*[10] performed a

comprehensive simulation of horizontal-well performance. Their results agreed well with Joshi's[19] equation. Raghavan and Joshi[23] presented a steady flow solution based on uniform flux along the fracture length. This solution was presented as valid for finite-conductivity fractures with a specific dimensionless fracture conductivity value of C_{fD}=4.4. Guo and Evans[24] performed analyses similar to that of Giger's[16] except that direct flow from matrix to wellbore, reservoir anisotropy, and multi-phase flow were included in the mathematical models. Like Giger's[16] model, Guo and Evans'[24] models were also derived assuming uniform pressure in the fracture when flow in matrix was formulated using Darcy's law. Li *et al.*[25] presented an approximate formula for predicting performance of fractured horizontal wells. It was assumed that oil first flows linearly from the external reservoir boundary to the vicinity of a vertical fracture, then turns 90 degrees and flows linearly to the fracture face while pressure in the fracture is equal at all points. Flow in the fracture was assumed to be linear away from the wellbore and radial near the wellbore. The drawback of their formulation is similar to that of Giger's and Guo and Evans'.

It is seen that most steady flow equations presented by previous investigators for productivity analysis of fractured horizontal wells rely on the assumption of infinite conductivity fractures when the flow from the external boundary to the fracture face was formulated. While the mathematical problems were very much simplified by using this assumption, accuracy of the solutions is questionable. Only one analytical solution dealing with horizontal wells intersecting finite-conductivity fractures was reported in the literature.[23] This solution may be applicable to fractured reservoirs where fractures have dimensionless conductivity of 4.4 and the flux in the fractures is uniform, which may not occur in practice. Therefore, Guo and Schechter[26] proposed a simple and more rigorous mathematical model for predicting performance of vertical and horizontal wells intersecting fractures fully penetrating reservoir sections.

New Model

Derivation of the mathematical model was presented in detail in Guo and Schechter's paper.[26] Resultant equations are summarized in this section.

Inflow Performance Relationship (IPR). Production rate Q from a well intersecting N fractures is given by Eq. (3.40) in field units:

$$Q = \frac{0.00508 N k_m h (1 - e^{-\sqrt{c} x_f})}{B_o \mu (z_e \sqrt{c} + S)} (p_e - p_w) \tag{3.40}$$

where k_m is the matrix permeability, h is fracture height (assumed to be equal to pay thickness), x_f is fracture half-length, p_e is the pressure at the drainage distance (z_e), p_w is the flowing bottom hole pressure, B_o and μ are formation volume factor and viscosity of oil respectively, S is skin factor for rock matrix, and c is defined as a group of variables:

$$c = \frac{2 k_m}{z_e w k_f} \tag{3.41}$$

where w and k_f are fracture width (aperture) and permeability respectively. Productivity index (PI) for the well is given by

$$PI = \frac{Q}{p_e - p_w} = \frac{0.00508 N k_m h (1 - e^{-\sqrt{c} x_f})}{B_o \mu (z_e \sqrt{c} + S)} \tag{3.42}$$

The productivity index can also be defined using the average reservoir pressure ($\bar{p}$) as:

$$J = \frac{Q}{(\bar{p} - p_w)} = \frac{0.00508 N k_m h}{B_o \mu (z_e \sqrt{c} + S)\left[\frac{1}{1 - e^{-\sqrt{c} x_f}} - \frac{1}{2 x_f \sqrt{c}}\right]} \tag{3.43}$$

If the reservoir is not fractured, the productivity index, J_o, is defined in a similar way as Eq. (3.43):

$$J_o = \frac{0.00708 k_m h}{\mu B_o (\ln \frac{r_e}{r_w} - \frac{3}{4} + S_o)} \tag{3.44}$$

where r_e is the radius of drainage area, r_w is wellbore radius, and S_o is the skin factor for the unfractured well. Dividing Eq. (3.43) by Eq. (3.44) yields:

$$\frac{J}{J_o} = \frac{0.72 N\left(\ln \frac{r_e}{r_w} - \frac{3}{4} + S_o\right)}{(z_e \sqrt{c} + S)\left[\frac{1}{1 - e^{-\sqrt{c} x_f}} - \frac{1}{2 x_f \sqrt{c}}\right]} \tag{3.45}$$

which is an equation for estimating productivity improvement of a fractured well over an unfractured well. Guo and Schechter[26] showed that upon comparison to the McGuire-Sikora model, Eq. (3.45) gives higher J/J_o values in the low fracture conductivity region and lower J/J_o values in the high fracture conductivity region.

Model Studies on Driver Unit Wells in the Spraberry Trend

The new mathematical model has been used for productivity analyses of twelve wells in the Driver Unit of the naturally fractured Spraberry Trend Area, west Texas.

Reservoir Parameters. The thickness of the productive sands varies from 8 to 16 feet. All productive sands have porosities of 7-15 per cent.[27] Initial reservoir pressures were approximately 2,300 psi in the Upper Spraberry. Bubble point pressure of Spraberry oil is about 1,900 psi.[28] Spraberry wells typically produced 100-400 bopd initially after hydraulic fracture treatment. Primary oil recovery was less than 10 per cent of the oil in place.

The mechanism of primary oil production in the Spraberry Trend Area is believed to be dominated by solution gas drive.[29] Performance of twelve wells drilled in the Driver Unit is evaluated using the mathematical model. Six of the wells were shut-in test wells and the other six were regularly producing wells. In order to make such an evaluation, the values of parameters that appear in Eqs. (3.40) and (3.42) are determined as follows and summarized in Table 3.4-1.

A composite plot between core permeability and initial water saturation is shown in Fig. 3.4-1 for the Spraberry reservoir sands. Data are based on analyses of selected core samples from 46 wells obtained during the early time of field development. Although air permeability of these cores varies from 0.1 md to 3.4 md, production history indicates that major oil production was from Spraberry sands having matrix permeabilities of 1 md or less.[27,29] An average matrix absolute permeability of 0.8 md is assumed for the Upper and Lower Spraberry sands in the Driver Unit. For a 0.8 md sand, an initial water saturation of 0.30 is estimated based on Fig. 3.4-1.

The water-oil relative permeability curves shown in Fig. 3.4-2 were constructed based on analyses of cores taken from well V.P. Tippett #5 in 1963. Gas-oil relative permeability curves were determined based on numerical reservoir simulation,[30] and are presented in Fig. 3.4-3. Gas saturation in the Spraberry sands during primary production was estimated by Elkins[31] to be about 0.24. However, this number may vary from area to area depending upon reservoir pressure. The following empirical relation between production gas-oil-ratio (GOR) and gas saturation (S_g) is used in this analysis based on data presented by Elkins[31]:

$$S_g = 0.24 + 0.10 \log(GOR). \tag{3.46}$$

Corresponding to practical GOR's of 1 to 12 MCF/STB in the Driver Area, Eq. (3.46) yields gas saturation values between 0.24 and 0.34, which are comparable to that given by Elkins.[31] The effective matrix and fracture permeabilities to oil are estimated based on the absolute permeability, relative permeability curves and saturations.

According to interpretations of a tracer test,[32] fracture lengths in Spraberry are probably less than the interwell distance (<1,800 feet). Since the well spacing is 40 acres, the average fracture half-length is assumed to be 660 feet. As shown by Guo and Schechter,[26] the fracture half-length does not significantly affect the result as long as it exceeds a minimum value. This is because the value of the exponential function in Eq. (3.40) is much smaller than 1 when fracture half-length (x_f) is long.

Based on recent fracture characterization,[33] three distinct fracture sets, trending NNE, NE, and ENE, are present in cores from the 1U and 5U units in the Upper Spraberry zone. The average fracture spacing of the three fracture sets are 1.62, 3.17, and 3.79 feet, respectively, as was shown in Section 1.2. The unmineralized NNE and ENE fractures appear as hairline cracks in the 5U unit, while the NE fractures are commonly mineralized with barite and only found in the 1U unit. Although it is unclear which set of fractures plays a more important role in fluid transport within Spraberry Trend Area reservoirs, recent studies on waterflooding[34] tend to support that the NNE fractures are less dominant in fluid transport. If the conductivity of the NNE fractures are assumed to

be much lower than that of the ENE fractures in the 5U unit, the average fracture spacing in the Upper Spraberry sands (1U and 5U units) is 3.48 feet.

Based on 111 measurements of fracture openings, Elkins[29] reported that the fracture width ranged up to 0.013 inch and averaged 0.002 inch. This number agrees with Christie's[28] estimation of fracture width of 0.002-0.004 inch based on flow rates and measurement of the fractures in cores. Browscombe and Dyes[35] reported 0.002-0.003 inch fracture width and 3-4 foot fracture spacing. The in-situ fracture width in the reservoir may be estimated based on well tests. Well testing[36,37] has not clearly demonstrated dual porosity pressure transient behavior in the Spraberry Trend. This indicates that fracture volume is less than 1/1000 of the matrix volume.[38] Assuming that matrix volume is on the order of 8,000 bbl/acre then the fracture volume should be less than 8 bbl/acre, or 45 cubic feet in a square area of 209 ft by 209 ft assuming a 10-foot-thick pay zone. If fracture spacing of 3.48 feet is assumed in the area, at most, 60 fractures should exist in the area. The maximum fracture width can then be estimated to be 0.004 inch. Based on these data, the average initial (before oil production) fracture width is assumed to be 0.0025 inch in this analysis.

Mineralized fractures were found in the 1U unit of the Upper Spraberry[31] with an average percentage of mineral-filling in the fractures of about 75%. Fractures found in the 5U unit of the Upper Spraberry are not mineralized. It is believed that the conductivities of non-mineralized fractures are more sensitive to stress. An average initial (before oil production) fracture porosity of 0.7 is used in this analysis.

Similar to the cubic law[40] which describes the relationship between fracture width and fracture conductivity, a simple relation between fracture width and fracture permeability was derived analytically by Guo and Schechter as:[26]

$$k_f = \frac{\phi_f{}^3 w^2}{12} \tag{3.47}$$

where ϕ_f is the fracture porosity accounting for volume of minerals, crushed rock, and proppant introduced during hydraulic fracturing operations. From the initial fracture porosity and width, the initial fracture permeability is estimated with Eq. (3.47) to be about 115 darcies.

It has been reported that productivity of some gas wells intersecting naturally fractured reservoirs declines rapidly as wellbore/reservoir pressure declines.[39] It has been postulated that partial closure of fractures is responsible for this behavior. As the pressure in the fracture decreases, fracture aperture decreases and effective stress at the fracture face increases to support the matrix. The partially closed fracture should have a lower conductivity resulting in lower productivity of the well. Walsh's model[40] for conductivity of a fracture is frequently employed for correlating both laboratory and field data.[39] Similar to Walsh's model, Guo and Schechter[26] proposed the following relation for estimating stress-sensitive fracture conductivity:

$$wk_f = w_o k_{fo}\left[1 - D\ln(\sigma - \alpha p)\right]^{\frac{3}{2n}} \tag{3.48}$$

where w_o and k_{fo} are initial (before oil production) fracture width and permeability at unity effective stress respectively, σ is total stress, p is pore pressure, α is the poroelastic

parameter defining the effective-stress law. The (σ-αp) term represents the effective stress. The constant D is referred to as stress factor, and its value reflects sensitivity of fracture conductivity to the effective stress. The exponent n is a constant for a given rock type.

As observed by Guo and Schechter,[26] pressure drawdown (p_e-p_w) gives better results than the effective stress (σ–αp) in Eq. (3.48) for history matching, thus (p_e-p_w) is employed to replace (σ–αp) in this analysis for determination of fracture conductivity under varying pressure drawdown.

It can be shown that if the cubic law[38] for a fracture is used, the exponent $3/2n$ in Eq. (3.48) is 4. Warpinski and Teufel showed that the value of n varies for different rocks and an n value of 0.515 for chalk was reported. This corresponds to an exponent $3/2n$ of 2.91 for chalk.[39] A value of 1/3 for n is used in this analysis, based on Walsh's equation.

The number of fractures interconnected by a well is estimated based on fracture spacing and an overall permeability anisotropy ratio, which is obtained from pressure analysis. In the Driver unit, the average overall permeability anisotropy ratio is 13/1 based on pressure analysis data.[29] Using this number and fracture spacing of 3.48 feet, it is estimated that each well interconnects 14.6 fractures on average.

Reservoir pressure and flowing bottom hole pressure for twelve wells in the Driver unit were provided by Elkins.[29] For the given pressure range, oil viscosity varies from 0.9 cp to 1 cp. Oil formation volume factor is between 1.285 and 1.310. Estimated properties of reservoir rock, fracture, and fluids are summarized in Table 3.4-1. Production data are presented in Table 3.4-2 and Table 3.4-3 for the six shut-in test wells and six regularly producing wells, respectively.

Results. Using the parameters determined above, oil production rates from twelve wells in the Driver unit were first calculated assuming constant fracture conductivity (D=0) and zero skin factor. Although the effect of gas saturation on oil production rate was considered in the calculation, the calculated oil production rates are still 2 to 10 times greater than the actual oil production rate of these wells. This calculation appears to disprove the hypothesis[32] that high gas saturation may be responsible for poor performance of Spraberry wells. The discrepancy between the actual oil production rate and the calculated rate is then attributed to formation damage. Two types of formation damage may exist in Spraberry reservoirs: 1) damage to matrix permeability as a result of drilling and/or fracturing fluids, and 2) damage to fracture conductivity as a result of partial closure of fractures during oil production. While the damage of rock matrix permeability by drilling/fracturing fluid is reflected by the positive skin factor S in Eq. (3.40), the loss of fracture conductivity (to some degree) due to production drawdown may be inferred by the positive value of the stress factor D in Eq. (3.48). The poor performance of Spraberry wells may be due to combination of the two types of formation damage. Although it is difficult to distinguish their effects quantitatively, the maximum effect of each type of damage may be estimated by assuming the other type of damage is null. Figures 3.4-4 through 3.4-15 demonstrate matching between actual oil production rates and calculated oil production rates for the twelve wells. Figs. 3.4-4 through 3.4-8 are for the six shut-in test wells, and Figs. 3.4-9 through 3.4-15 are for the six regularly producing wells.

Discussion. Figs. 3.4-4 through 3.4-15 indicate that the low production rates of Spraberry wells during primary production may be due to stress-sensitive fracture permeability. If this is true, the maximum stress factor (D) is about 0.095 (well Davenport B-14). However, the low performance may also be attributed to matrix skin. If this is the case, the maximum skin factor is about 0.85 (Davenport B-14). Although it is not clear which type of formation damage is more important in the Spraberry wells, it appears that stress-sensitive fracture conductivity may dominate. This is inferred by comparison of production rate and drawdown for these wells. It is generally believed that a higher draw down (lower flowing bottom hole pressure) usually yields a higher production rate. However, this is not true in the Driver Unit. For example, although the pressure drawdown for well J.C. Bryans A-2 was relatively low compared to that for other shut-in test wells, this well still produced oil at a higher rate. Also, the pressure drawdown for well X.B. Cox A-5 was relatively low compared to that for other regularly producing wells, this well again produced oil at a higher rate. This phenomenon can be explained by the theory of stress-sensitive fracture conductivity: less reduction in fracture conductivity at low drawdown resulted in higher productivity of the two wells. Comparison of production rates of shut-in test wells with those of the regularly producing wells shows a similar effect. The former is generally higher than the latter, because the reservoir pressures are higher around the shut-in test wells, although pressure drawdown is within the same range. These observations indicate that stress-sensitive fracture conductivity is the more dominant factor that affects productivity of Spraberry wells.

Conclusion

Application of a new mathematical model to analysis of inflow performance of Spraberry Trend Area wells indicates that the rapid decline of well productivity during the primary oil production may be mainly attributed to stress-sensitive fracture conductivity.

Nomenclature

B_o =formation volume factor of oil, L^3/L^3, rb/STB
c =a group of variables defined by Eq. (3.41), L^{-2}, ft^{-2}
C_{fD} =specific dimensionless fracture conductivity
D =stress-sensitivity factor, dimensionless
h =fracture height, L, ft
J =productivity index of fractured well, L^4 t/m, bopd/psi
J_o =productivity index of fractured well, L^4 t/m, bopd/psi
k_f =permeability of fracture, L^2, md
k_{fo} =permeability of fracture at unity effective stress, L^2, md
k_m =permeability of matrix, L^2, md
N =number of fractures interconnected to wellbore
n =conductivity exponent, dimensionless
p =pore pressure, m/Lt^2, psia
p_e =pressure at drainage boundary, m/Lt^2, psia
PI =productivity index, L^4t/m, bopd/psi
p_w =flowing bottom hole pressure, m/Lt^2, psia
Q =oil production rate, L^3/t, bopd
r_e =radius of drainage area, L, ft

r_w =radius of wellbore, L, ft
S =skin factor of fractured well, dimensionless
S_o =skin factor of unfractured well, dimensionless
w =fracture width (aperture), L, in
w_o =fracture width (aperture) at unity effective stress, L, in
x_f =length of a fracture wing, L, ft
z_e =distance between fracture face and drainage boundary, L, ft
α =poroelastic parameter defining effective stress law, dimensionless
μ =oil viscosity, m/Lt, cp
σ =confining stress, m/Lt^2, psi
ϕ_f =fracture porosity, dimensionless
ϕ_{fo} =fracture porosity at unity effective stress, dimensionless

References

1. Barfield, E.C., Jordan, J.K. and Moore, W.D.: "An Analysis of Large-Scale Flooding in the Fractured Spraberry Trend Area Reservoir," *J. Pet. Tech.* (April 1959) 15-19.
2. Soliman, M. Y., Hunt, J.L., and El Rabaa,W.: "Fracturing Aspects of Horizontal Wells," *J. Pet. Tech.* (Aug. 1990) 966-73.
3. Chen, C.C., Ozkan, E., and Raghavan, R.: "A Study of Fractured Wells in Bounded Reservoirs," paper SPE 22717 presented at the 1991 SPE Annual Technical Conference and Exhibition held in Dallas, Texas, Oct. 6-9, 1991.
4. Cinco-L., H., Samaniego-V., F., and Dominguez-A., N.: "Transient Pressure Behavior for a Well with a Finite-Conductivity Vertical Fracture," *SPEJ* (Aug. 1978) 253-64.
5. Ozkan, E., and Raghavan, R.: "New Solutions for Well-Test-Analysis Problems: Part 1 - Analytical Considerations," *SPEFE* (Sept. 1991) 359-65.
6. Chu,W., and Shank, G.D.: "A New Model for a Fractured Well in a Radial, Composite Reservoir," *SPEFE* (Sept. 1993) 225-32.
7. Beier, R.A.: "Pressure-Transient Model for a Vertically Fractured Well in a Fractal Reservoir," *SPEFE* (June 1994) 122-28.
8. Chen, C., and Raghavan, R.: "Modeling a Fractured Well in a Composite Reservoir," *SPEFE* (Dec. 1995) 241-46.
9. Karcher, B.J., Giger, F.M., and Combe, J.: "Some Practical Formulas to Predict Horizontal Well Behavior," paper SPE 15430, presented at the 1986 SPE Annual Technical Conference and Exhibition held in New Orleans, Louisiana, Oct. 5-8, 1986.
10. Economides, M.J., Delmbacher, F.X., Brand, C.W., and Heinemann, Z.E.: "Comprehensive Simulation of Horizontal-Well Performance," *SPEFE* (Dec. 1991) 418-26.
11. Van Poollen, H.K.: "Productivity vs. Permeability Damage in Hydraulically Produced Fractures," API, *Drilling and Production Practice* (1957), 103.
12. Dyes, A.B., Kemp, C.E., and Caudle, B.H.: "Effect of Fractures on Sweep-Out Pattern," *Trans.* AIME (1958), **213**, 245.
13. McGuire, W.J. and Sikora, V.J.: "The Effect of Vertical Fractures on Well Productivity," *Trans.*, AIME (1960), **219**, 401.
14. Raymond, L.R. and Binder, G.G. Jr.: "Productivity of Wells in Vertically Fractured, Damaged Formations," *J. of Pet. Tech.* (January 1967), 121.

15. Giger, F.M., Reiss, L.H., and Jourdan, A.P.: "The Reservoir Engineering Aspect of Horizontal Drilling," paper SPE 13024 presented at the 1984 SPE Annual Technical Conference and Exhibition in Houston, Texas, Sept. 16-19, 1984.
16. Giger, F.M.: "Horizontal Well Production Techniques in Heterogeneous Reservoirs," paper SPE 13710, presented at the SPE 1985 Middle East Oil Technical Conference and Exhibition held in Bahrain, March 11-14, 1985.
17. Muskat, M.: *The Flow of Homogeneous Fluids through Porous Media*, I.H.R.D.C., Boston, 1982.
18. Houpeurt, A: *Elements de mecanique des fluides dans les milieux poreux*, Editions Technip, Paris, 1975.
19. Joshi, S.D.: "Augmentation of Well Productivity with Slant and Horizontal Wells," SPE 15375, 1986; *JPT* (June 1988) 729-39; *Trans.* AIME, **285**.
20. Joshi, S.D.: "A Review of Horizontal Well and Drainhole Technology," paper SPE 16868, presented at the 1987 SPE Annual Technical Conference and Exhibition held in Dallas, Texas, Sept. 27-30, 1987.
21. Mukherjee, H., and Economides, M.J.: "A Parametric Comparison of Horizontal and Vertical Well Performance," *SPEFE* (June 1991) 209-16.
22. Prats, M.: "Effect of Vertical Fractures on Reservoir Behavior -- Incompressible Fluid Case," *SPEJ* (June 1961) 105-16; *Trans.* AIME, **222**.
23. Raghavan, R., and Joshi.,S.D.: "Productivity of Multiple Drainholes or Fractured Horizontal Wells," *SPEFE* (March 1993) 11-16.
24. Guo, G., and Evans, R.D.: "Inflow Performance of a Horizontal Well Intersecting Natural Fractures," paper SPE 25501, presented at the SPE Production Operations Symposium held in Oklahoma City, Oklahoma, March 21-23, 1993.
25. Li, H., Jia, Z., and Wei, Z.: "A New Method to Predict Performance of Fractured Horizontal Wells," paper SPE 37051, presented at the 1996 SPE International Conference on Horizontal Well Technology held in Calgary, Canada, November 18-20, 1996.
26. Guo, B. and Schechter, D.S.: "A Simple and Rigorous Mathematical Model for Estimating Inflow Performance of Wells Intersecting Long Fractures," paper SPE 38104 presented at the 1997 SPE Asia Pacific Oil and Gas Conference and Exhibition held in Kuala Lumpur, Malaysia, 14-16 April, 1997.
27. Elkins, L.F., and Skov, A.M.: "Cyclic Water Flooding the Spraberry Utilizes 'End Effects' to Increase Oil Production Rate," *J. Pet. Tech.* (Aug. 1963) 877-84.
28. Christie, R.S., and Blackwood, J.C.: "Production Performance in Spraberry," *Oil & Gas Journal* (April 7, 1952) 107-15.
29. Elkins, L.F.: "Reservoir Performance and Well Spacing, Spraberry Trend Area Field of West Texas," *Trans.* AIME, **198**, (1953) 177-96.
30. Schechter, D.S.: "Advanced Reservoir Characterization and Evaluation of CO_2 Gravity Drainage in the Naturally Fractured Spraberry Trend Area," First Annual Technical Progress Report to DOE under Contract No. DE-FC22-95BC14942, PRRC Report 96-42, Dec. 17, 1996.
31. Elkins, L.F.: "Spraberry CO_2-Gravity Drainage," Condensed Report, PRRC Spraberry Database, May 14, 1996.
32. Howell, W.D., Armstrong, F.E., and Watkins, J.W.: "Radioactive Gas Tracer Survey Aids Waterflood Planning," *World Oil (*Feb. 1961).

33. Lorenz, J.: "Summary of Observations and Interim Interpretations: Fractures in Horizontal Spraberry Cores, E.T. O'Daniel Well #28," PRRC Spraberry Database, Dec. 12, 1996.
34. Beshry, M.: "Possible Fracture Orientation Based On Waterflood Surveillance for the O'Daniel Unit," PRRC Spraberry Database, August 26, 1996.
35. Browscombe, E.R. and Dyes, A.B.: "Water Imbibition Displacement - Can It Release Reluctant Spraberry Oil?" *Oil & Gas Journal* (November 3 1952) 264-65.
36. Baker, R.: "Pressure Test Analysis for Midkiff 25-08," (April 1994) PRRC Spraberry Database.
37. Baker, R.: "Vertical Pulse Test Analysis of Shackelford 1-38A," (April 1994) PRRC Spraberry Database.
38. Van Golf-Racht, D.T.: *Fundamentals of Fractured Reservoir Engineering*, Elsevier Scientific Publishing Co., New York, 1982.
39. Warpinski, N.R., and Teufel, L.W.: "Effect of Stress and Pressure on Gas Flow Through Natural Fractures," paper SPE 22666, presented at the 1991 SPE Annual Technical Conference and Exhibition held in Dallas, Texas, Oct. 6-9, 1991.
40. Walsh, J.B.: "Effect of Pore Pressure and Confining Pressure on Fracture Permeability," *Int. J. Rock Mech., Min. Sci. & Geomech. Abstr.*, **18**, 1981, 429-35.

Table 3.4-1—Parameters Used for Analyzing Performance of Spraberry Trend Area Reservoir Wells in the Driver Unit

Matrix permeability, md	0.80
Pay zone thickness, ft	15
Initial water saturation	0.30
Water saturation during primary production	0.30
Average initial fracture porosity	0.70
Average initial fracture width, in	0.0025
Average fracture spacing, ft	3.48
Average fracture half-length, ft	600
Fracture height, ft	15
Fracture conductivity exponent	0.33
Overall permeability anisotropy ratio	13/1
Number of fractures interconnected to wellbore	14.6
Oil viscosity, cp	0.9 - 1
Formation volume factor	1.285 - 1.310

Table 3.4-2—Production Data of Six Shut-In Test Wells in the Driver Area, Spraberry Trend Area Field, Texas

	Month during 1952			
	March	April	May	June
Davenport C-6:				
Reservoir pressure, psig	1850	1780	1700	1640
Bottom hole pressure, psig	800	800	700	600
Gas oil ratio, MCF/BBL	0.8	0.8	1.0	1.5
Oil production rate, bopd	190	250	180	175
Davenport C-8:				
Reservoir pressure, psig	1970	1930	1910	1860
Bottom hole pressure, psig	1100	1250	800	740
Gas oil ratio, MCF/BBL	0.85	0.65	0.65	0.75
Oil production rate, bopd	195	220	255	245
Davenport B-5:				
Reservoir pressure, psig	1680	1600	1500	1400
Bottom hole pressure, psig	1100	840	760	550
Gas oil ratio, MCF/BBL	2.8	1.2	1.3	2.1
Oil production rate, bopd	140	150	90	85
Davenport B-7:				
Reservoir pressure, psig	1600	1470	1390	1060
Bottom hole pressure, psig	600	570	510	510
Gas oil ratio, MCF/BBL	3.6	1.2	2.8	1.8
Oil production rate, bopd	110	170	85	85
X.B. Cox A-4:				
Reservoir pressure, psig	1650	1600	1500	1400
Bottom hole pressure, psig	1000	1000	800	750
Gas oil ratio, MCF/BBL	1.5	1.4	2.2	1.9
Oil production rate, bopd	100	85	80	75
J.C. Bryans A-2:				
Reservoir pressure, psig	1830	1740	1640	1605
Bottom hole pressure, psig	1560	1650	1010	1205
Gas oil ratio, MCF/BBL	1.35	1.2	1.5	1.0
Oil production rate, bopd	180	110	205	160

Table 3.4-3 —Production Data of Six Regularly Producing Wells in the Driver Area, Spraberry Trend Area Field, Texas

	Month during 1952		
	March	April	May
Davenport C-5:			
Reservoir pressure, psig	1750	1600	1540
Bottom hole pressure, psig	1250	740	600
Gas oil ratio, MCF/BBL	2.0	3.9	12.2
Oil production rate, bopd	80	60	40
Davenport C-10:			
Reservoir pressure, psig	1860	1740	1730
Bottom hole pressure, psig	780	620	590
Gas oil ratio, MCF/BBL	1.0	1.75	2.4
Oil production rate, bopd	250	150	125
Davenport B-8:			
Reservoir pressure, psig	1600	1530	1430
Bottom hole pressure, psig	640	850	660
Gas oil ratio, MCF/BBL	5.0	9.7	10.0
Oil production rate, bopd	110	50	50
Davenport B-14:			
Reservoir pressure, psig	1600	1530	1430
Bottom hole pressure, psig	530	610	530
Gas oil ratio, MCF/BBL	3.8	5.1	7.1
Oil production rate, bopd	60	40	35
X.B. Cox A-5:			
Reservoir pressure, psig	1750	1620	1510
Bottom hole pressure, psig	1380	1010	820
Gas oil ratio, MCF/BBL	1.65	1.85	3.05
Oil production rate, bopd	145	130	105
J.C. Bryans A-2:			
Reservoir pressure, psig	1710	1620	1590
Bottom hole pressure, psig	1220	1400	1430
Gas oil ratio, MCF/BBL	1.4	2.9	2.2
Oil production rate, bopd	250	85	70

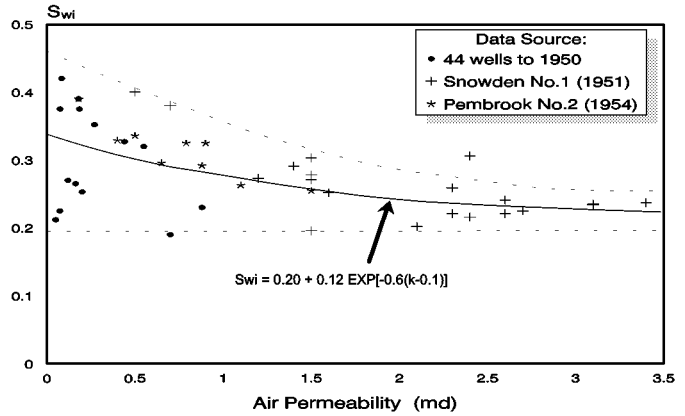

Fig. 3.4-1—Initial water saturation in the Spraberry Trend Area as a function of rock permeability

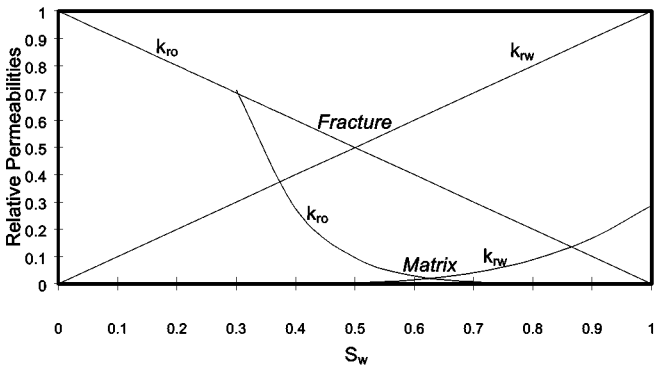

Fig. 3.4-2 —Water-oil relative permeability curves for the Spraberry Trend Area

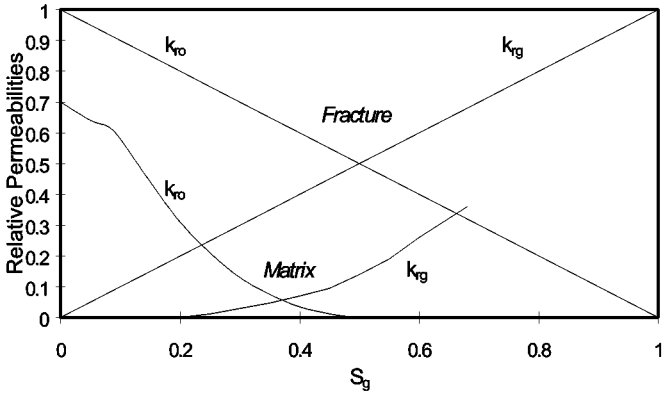

Fig. 3.4-3 —Oil-gas relative permeability curves for the Spraberry Trend Area

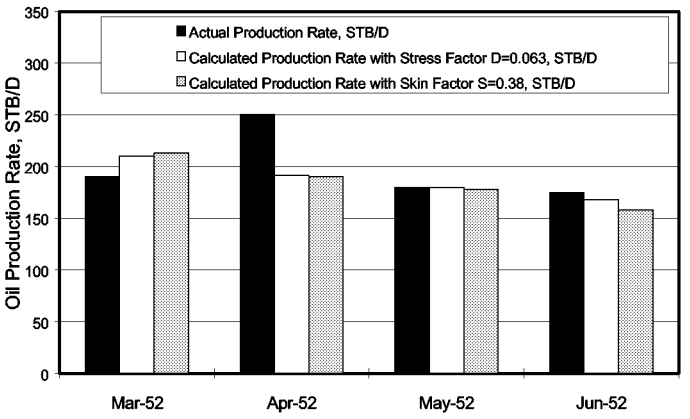

Fig. 3.4-4 —Comparison between calculated and actual oil production rates for Davenport C-6, Driver Unit, Spraberry Trend Area Field, west Texas.

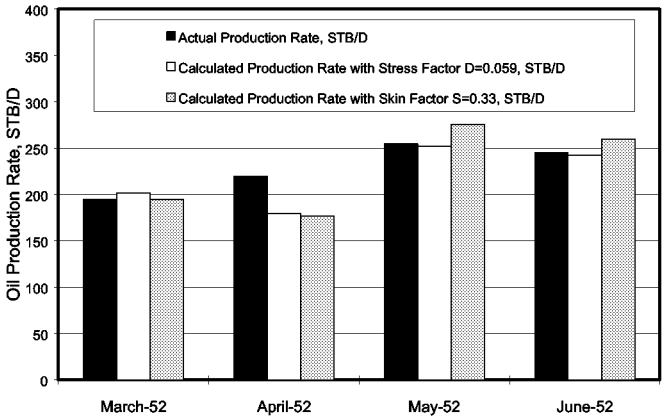

Fig. 3.4-5 —Comparison between calculated and actual oil production rates for Davenport C-8, Driver Unit, Spraberry Trend Area Field, west Texas.

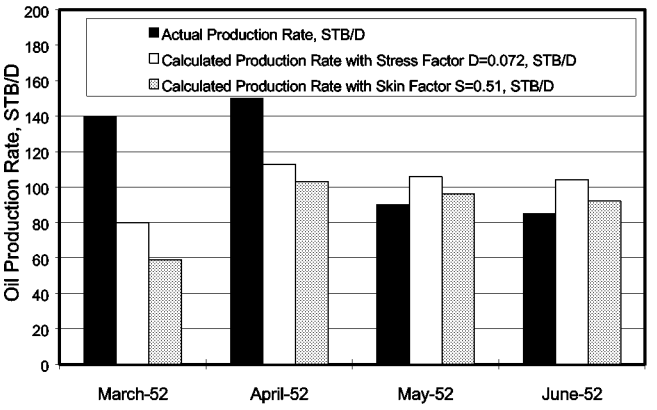

Fig. 3.4-6 —Comparison between calculated and actual oil production rates for Davenport B-5, Driver Unit, Spraberry Trend Area Field, west Texas.

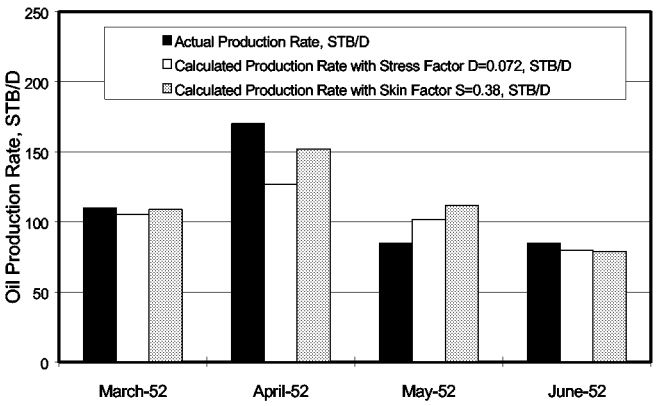

Fig. 3.4-7 —Comparison between calculated and actual oil production rates for Davenport B-7, Driver Unit, Spraberry Trend Area Field, west Texas.

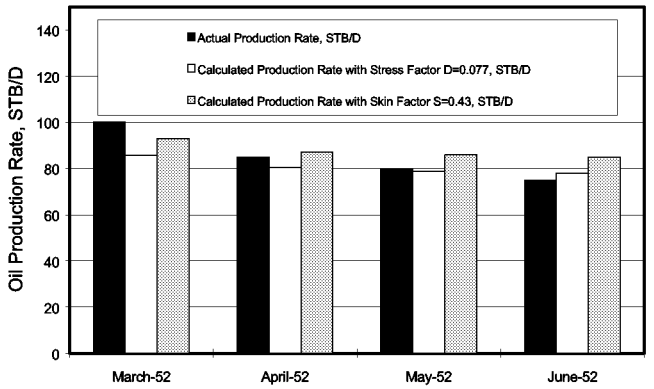

Fig. 3.4-8 —Comparison between calculated and actual oil production rates for X.B. Cox A-4, Driver Unit, Spraberry Trend Area Field, west Texas.

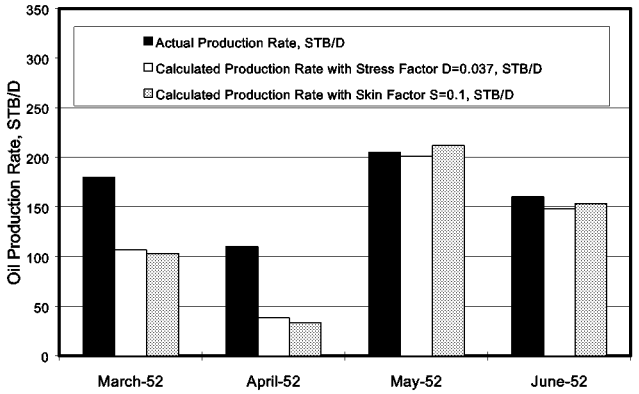

Fig. 3.4-9 —Comparison between calculated and actual oil production rates for J.C. Bryans A-2, Driver Unit, Spraberry Trend Area Field, west Texas.

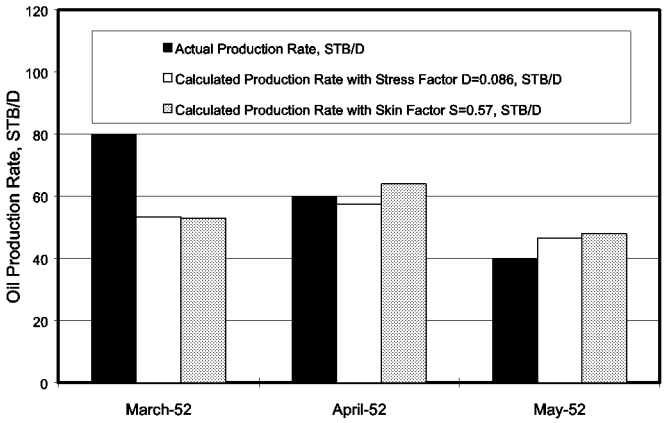

Fig. 3.4-10 —Comparison between calculated and actual oil production rates for Davenport C-5, Driver Unit, Spraberry Trend Area Field, west Texas.

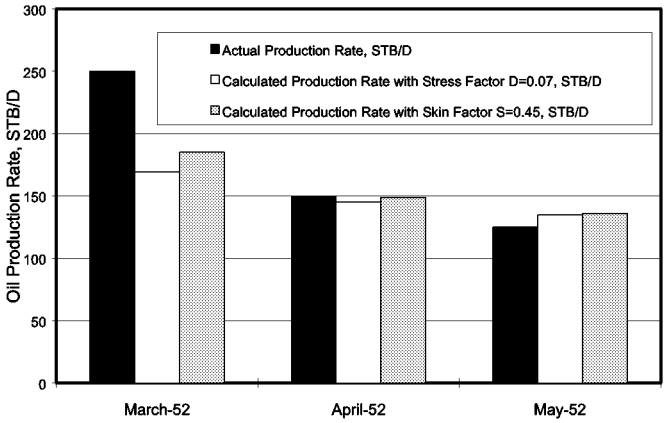

Fig. 3.4-11 —Comparison between calculated and actual oil production rates for Davenport C-10, Driver Unit, Spraberry Trend Area Field, west Texas.

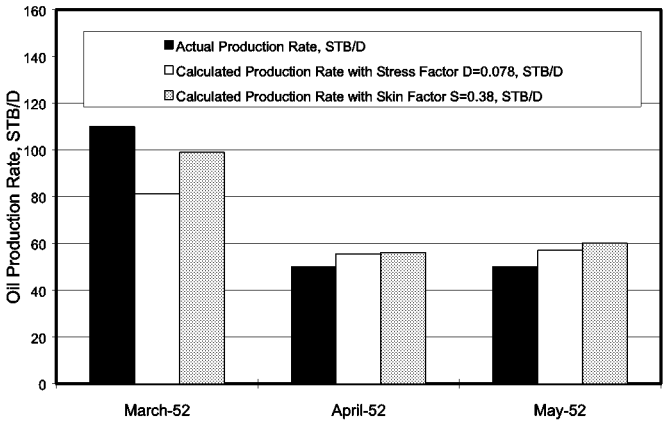

Fig. 3.4-12 —Comparison between calculated and actual oil production rates for Davenport B-8, Driver Unit, Spraberry Trend Area Field, west Texas.

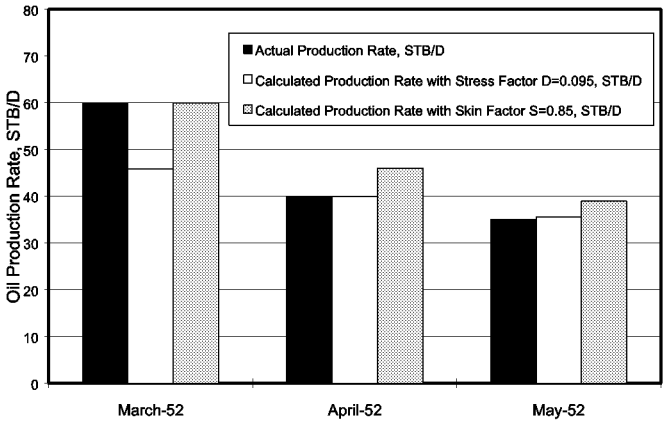

Fig. 3.4-13 —Comparison between calculated and actual oil production rates for Davenport B-14, Driver Unit, Spraberry Trend Area Field, west Texas.

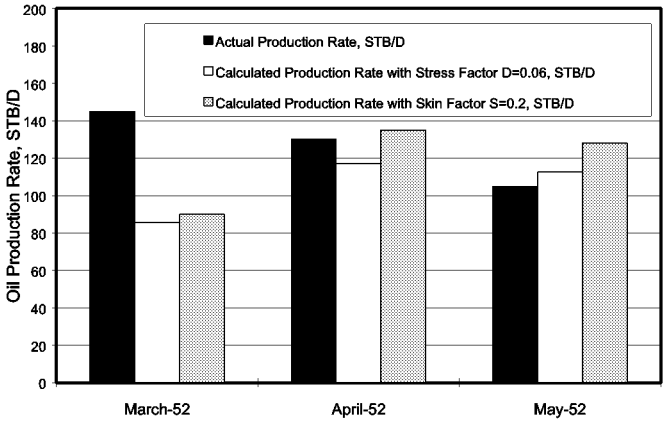

Fig. 3.4-14 —Comparison between calculated and actual oil production rates for X.B. Cox A-5, Driver Unit, Spraberry Trend Area Field, west Texas.

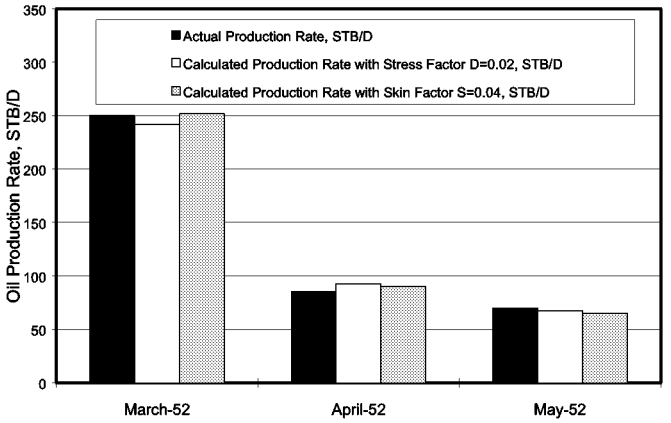

Fig. 3.4-15 —Comparison between calculated and actual oil production rates for J.C. Bryans A-1, Driver Unit, Spraberry Trend Area Field, west Texas.

3.5 WELL TESTING ANALYSIS OF THE E.T. O'DANIEL WELLS

Introduction

The production equipment facilities are complete and currently in use. All six proposed water injection wells and three producers for the 10-acre field demonstration pilot have been drilled and completed. The four CO_2 injection wells will be completed in 1999 along with the two logging observation wells.
The first water injection well completed was the O'Daniel No. 47. Water injection into this well initiated the beginning of the pulse test March 10, 1999. The pulse test consists of injecting water in a single well and monitoring the pressure response in the three producing wells. During the pulse test, only one well will be injecting. Projected length of the pulse test is four to six months but depends on observing breakthrough or response timing.

Buildup Tests

Epic Consulting Services Ltd. provided analyses of the E.T. O'Daniel Wells 38, 39, and 40 buildup tests using the FAST WellTest package. The buildup tests were taken prior to the SRIT. Both the single porosity and dual porosity model were used. The length of the buildup test and quality of data indicate that Well 39 is the most reliable analysis. The following results were obtained from the analyses:

Single Porosity Model

Parameter	**Well 38**	**Well 39**	**Well 40**
Permeability to oil, k (md)	0.014	0.014	0.033
Skin, s	-2.844	-3.305	-3.411
Storage coefficient, C_D	461.5	846.9	2167
Current average pressure (psi)	1318	1344	1024

Dual Porosity Model

Parameter	**Well 38**	**Well 39**	**Well 40**
Permeability to oil, k (md)	0.014	0.014	0.033
Skin, s	-3.57	-3.93	-4.24
Storage coefficient, C_D	620	1312	2892
Interporosity coefficient, λ	1.34E-4	4.6E-5	4.0E-5
Storativity ratio, ω	2.85E-6	3.9E-5	1.6E-5
Current average pressure (psi)	1090	1081	874

Wellbore storage is high and dominates the majority of the tests. The storage masks the early pressure transient flow in the fracture system, which causes the calculated permeability to be low and representative of the matrix rather than an effective permeability. The pressure determined from these tests are low and below the MMP necessary for the CO_2 flood. However, as the pulse test proceeds and more water is injected, the pressure is expected to increase. The transition to pseudo-steady-state (PSS) from radial flow apparently did not occur because the tests were not long enough (1000 hours for well 39). The dual porosity parameters of λ (interporosity flow coefficient) and ω (storativity ratio) are small. A small λ indicates the permeability is in the fractures and a small ω indicates most of the storage capacity is in the matrix. This seeming contradiction is due to the length of the test and the domination by wellbore storage.

Step Rate Testing (SRT)

Step rate injection tests to obtain formation parting pressures were conducted in the new injection wells O'Daniel 46 (Figs. 3.5-1 and 3.5-2) and 47. The conventional SRT analysis assumes a steady-state Darcy flow into the injection well and is based on the steady-state solution of the diffusivity equation[4] given by

$$\bar{p} - p_{wf} = 141.2\frac{qB\mu}{kh}\left[\ln\left(\frac{r_e}{r_w}\right) + s\right] \quad \text{.....(3.49)}$$

If a steady-state condition is achieved, then the external drainage radius, r_e, and average pressure at r_e will be constant and a linear relationship will exist between the p_{wf} and q at the end of each rate. Normally the rates are not long enough to reach steady-state conditions. However, the drainage radius or radius of influence of the rate change can be used if we assume that the $\ln\frac{r_d}{r_w}$ is insensitive to small changes in r_d. A plot of p *vs* q will yield a straight line prior to the formation parting. After formation parting pressure has been exceeded, the resulting fracture acts as an additional fluid conductor and causes a change in the slope. There is no theoretical basis for drawing a second straight line through the points above the parting pressure. However, conventional analysis suggests this and the intercept of the pre-parting straight line and post-parting straight line is assumed to be the parting pressure. Singh, Agarwal and Krase[4] showed that this may lead to erroneous parting or propagation pressure. To try to quantify the actual parting pressure and thus lend a theoretical basis to the determination of the formation parting or fracture propagation pressure, the multirate superposition analysis technique introduced by Odeh and Jones[5] and suggested and extended by Singh and Agarwal[4] is used.

The Odeh and Jones method assumes transient radial flow into the reservoir during each constant rate period. Figure 3.5-3 shows the radial Odeh and Jones plot for well 46. For data below parting pressure and in true radial flow, the Odeh and Jones method should provide a single straight line for all data below parting pressure. In addition the slope and

intercept of this line provide a method to obtain formation flow capacity, *kh*, and wellbore skin, *s*, before fracturing (Fig. 3.5-4). The method breaks down after fracturing. Figure 3.5-3 shows a downward shift for each rate after the first rate indicating fracture length is increasing. From the above it is apparent that radial type flow may not be completely valid. Therefore the data was analyzed using the Odeh and Jones superposition linear flow equation.[4,6] Figure 3.5-5 shows the resulting plot for Well 46. Like the radial analysis, this shows a definite shift in the data for each subsequent step after the second step and possibly during the second step also. This indicates propagation pressure for fractured wells where linear flow is occurring. Note that the first and second curves in Fig. 3.5-5 are fairly close, indicating that the fracture lengths may not have extended much during the second step. This can also be seen in the radial analysis in Fig. 3.5-3. In addition, Agarwal's equivalent time was employed to see if this would lend the possibility of using type curves to the analysis and if manipulation of the time function in this way would formulate any overlay of the data. The parting pressure or extension pressure is difficult to ascertain since no radial flow is seen; therefore, the end of the first step is conservatively estimated to be the parting pressure or 2215 bottomhole for the specific gravity of water obtained prior to the SRT of 0.452 psi/ft.

Using the equivalent wellbore radius concept determining the fracture length can be done for each step above FPP.[4] This type of calculation may not be possible if the fracture is still extending during the rate or the data is not in the bilinear flow regime and preferredly in pseudoradial flow. Similarly, using a simulation program, the fracture length was obtained for each step. The results are shown in Table 3.5-1.

Inconsistencies appear to exist in the above table in regards to the effective permeability and the fracture length. Calculated finite conductivity hydraulic fractures in a fissured formation have been shown to exhibit significantly smaller lengths than the real length.[7] As the fracture becomes longer and perhaps intersects more of the natural fracture system the total response of the system becomes that of the fissures. Because each step rate is not long enough to be outside of bilinear flow (and propagation may be continuing during each rate) and certainly has not attained pseudo-steady-state, the information is qualitative at best and any additional conclusions would be conjecture. The first few step rates exhibit early time behavior of a fissured system.

The MRT analysis of O'Daniel Well 47 is masked by significant afterflow (see Figs. 3.5-6-10). The first step is actually not part of the SRT design, but is an attempt to fill up the tubing prior to the SRT. As a result the first rate severely distorts the test and makes analysis difficult or impossible; thus, the parting pressure is suggested to have been exceeded in the first step.

Conclusions

1. Except for Well 39, the buildup data is generally poor and dominated by wellbore storage because of the low permeability and flow rates. The storage masks early pressure transient flow in the fracture system, and hence the permeability calculated is very low and representative of the matrix rather than an effective

permeability.

2. These same effects appear to limit the multirate analysis of the SRTs also.
3. The skin calculated from the buildup tests is negative and in the range of -2.8 to -3.4 for the singe porosity model and -3.5 to -4.2 for the dual porosity model.
4. The current average reservoir pressure is 1331 psi based on the single porosity model and 1100 psi based on dual porosity model. Both of these pressures are below the MMP for CO_2 but the average pressure is expected to continually increase during the interference/pulse test.
5. The transition to pseudo steady-state flow probably did not occur in either the buildup and SRT since the buildup tests and SRT rates were not long enough to get beyond domination of wellbore storage effects.

References

1. Schechter, D.S.: "Advanced Reservoir Characterization and Evaluation of CO_2 Gravity Drainage in the Naturally Fractured Spraberry Trend Area," quarterly technical progress report to DOE under contract No.: DE-FC22-95BC14942, U.S. DOE (October 5, 1998).
2. Schechter, D.S.: "Advanced Reservoir Characterization and Evaluation of CO_2 Gravity Drainage in the Naturally Fractured Spraberry Trend Area," quarterly technical progress report to DOE under contract No.: DE-FC22-95BC14942, U.S. DOE (January 13, 1999).
3. Schechter, D.S.: "Advanced Reservoir Characterization and Evaluation of CO_2 Gravity Drainage in the Naturally Fractured Spraberry Trend Area," third annual technical progress report to DOE under Contract No.: DE-FC22-95BC14942, U.S. DOE (December1998).
4. Singh, P.K., Agarqal, R.G., and Jrase, L.D.: "Systematic Design and Analysis of Step-Rate Tests To Determine Formation Parting Pressure," paper SPE 16798 presented at the 1987 Annual Technical Conference and Exhibition, Dallas, Tx., September 27-30.
5. Odeh, A.S. and Jones, L.G.: "Pressure Drawdown Analysis, Variable Rate Case," *JPT* (aug. 1965) 960.
6. Earlougher, R.C., Jr.: *Advances in Well Test Analysis*, Monograph Series Volume 5, Society of Petroleum Engineers, Dallas (1977)
7. Naceur, K.B. and Economides, M.J.: "Production From Naturally Fissured Reservoirs Intercepted by a Vertical Hydraulic Fracture," SPE 17425, *SPERE* (December 1989) 550.

Table 3.5-1—Fracture Propagation

k_{eff} (md)	L_f (ft)
4.308	11.389
12.968	12.374
21.867	13.783
37.625	19.027
42.276	20.062
54.642	21.9
142.41	10.099
201.1	6.44
268.92	5.1217

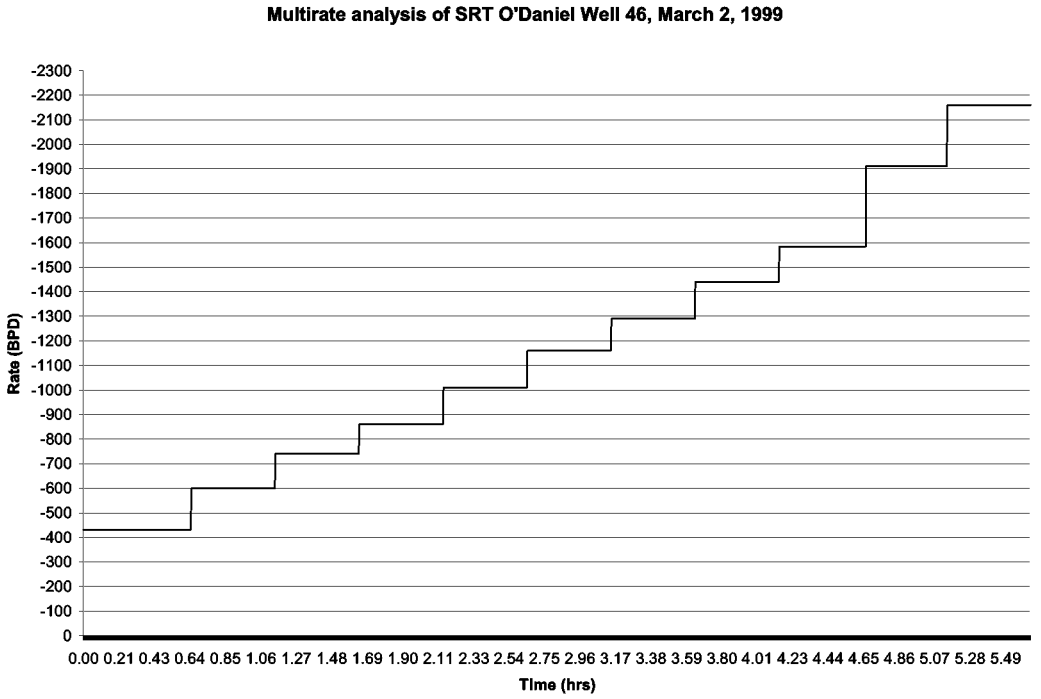

Fig. 3.5-1—Step rate test (SRT) design for O'Daniel injection Well 46.

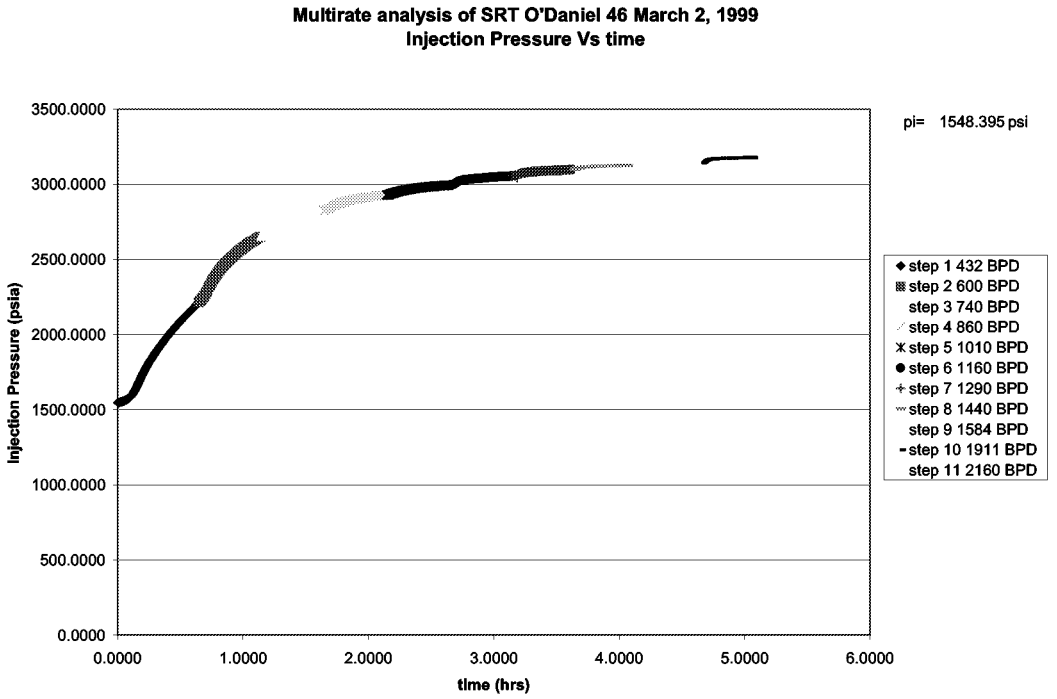

Fig. 3.5-2—Plot of injection pressure versus cumulative time for O'Daniel Well 46.

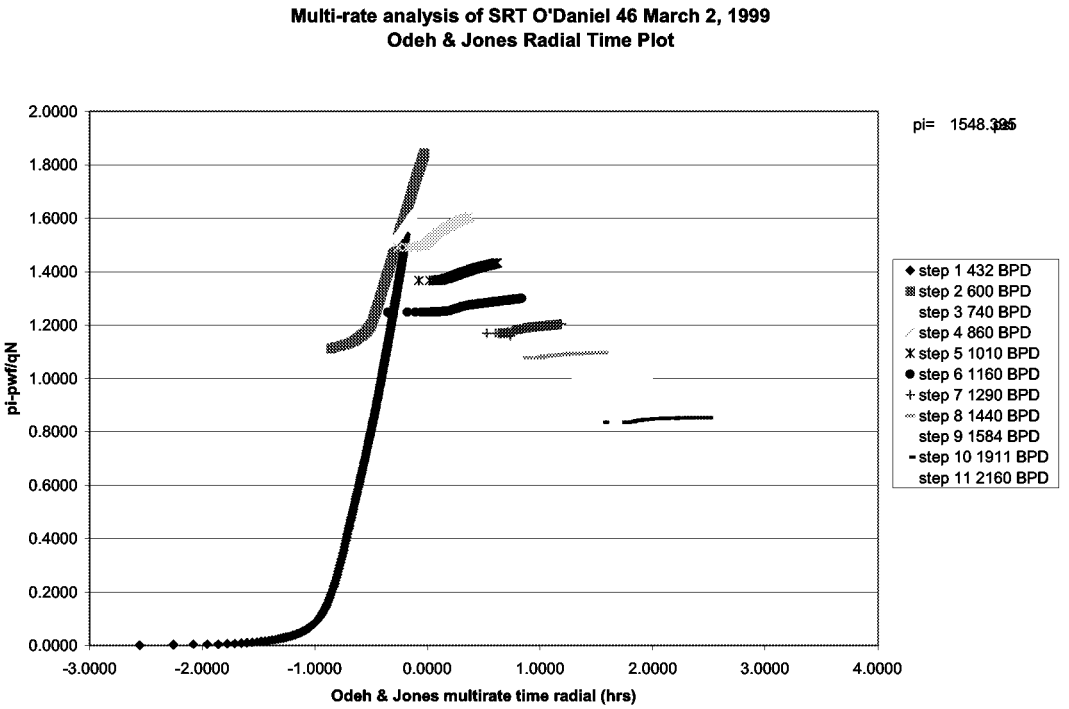

Fig. 3.5-3—Radial Odeh & Jones plot for Well 46.

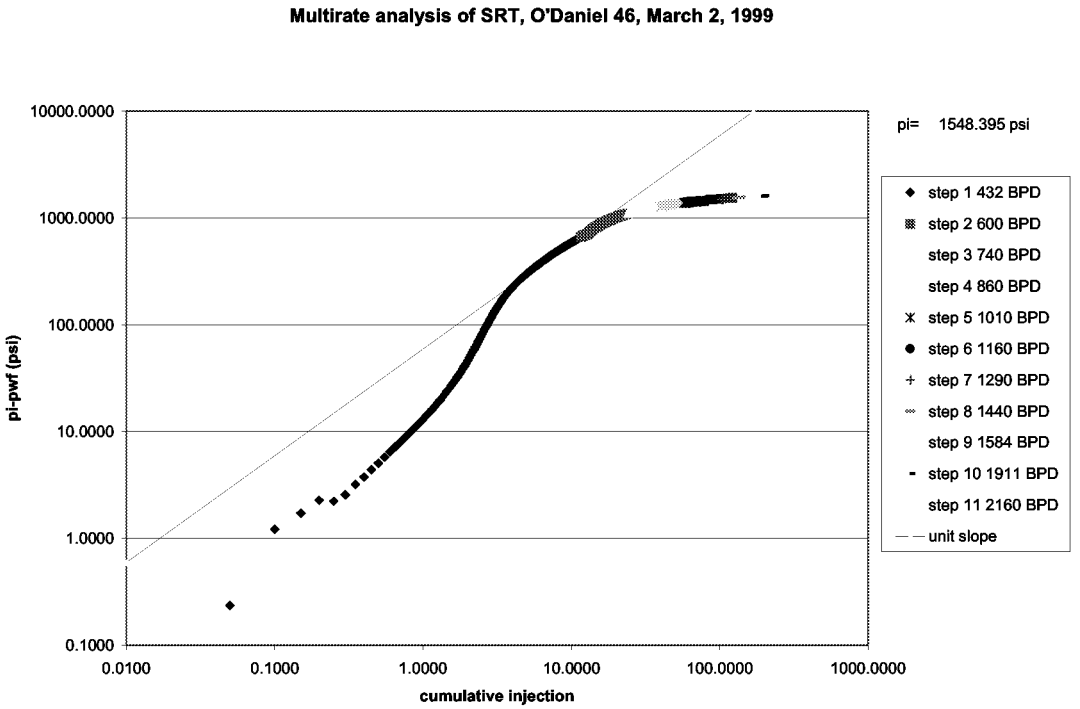

Fig. 3.5-4—Pressure vs. cumulative injection during SRT O'Daniel Well 46 with unit slope line to determine effects of wellbore storage on rates.

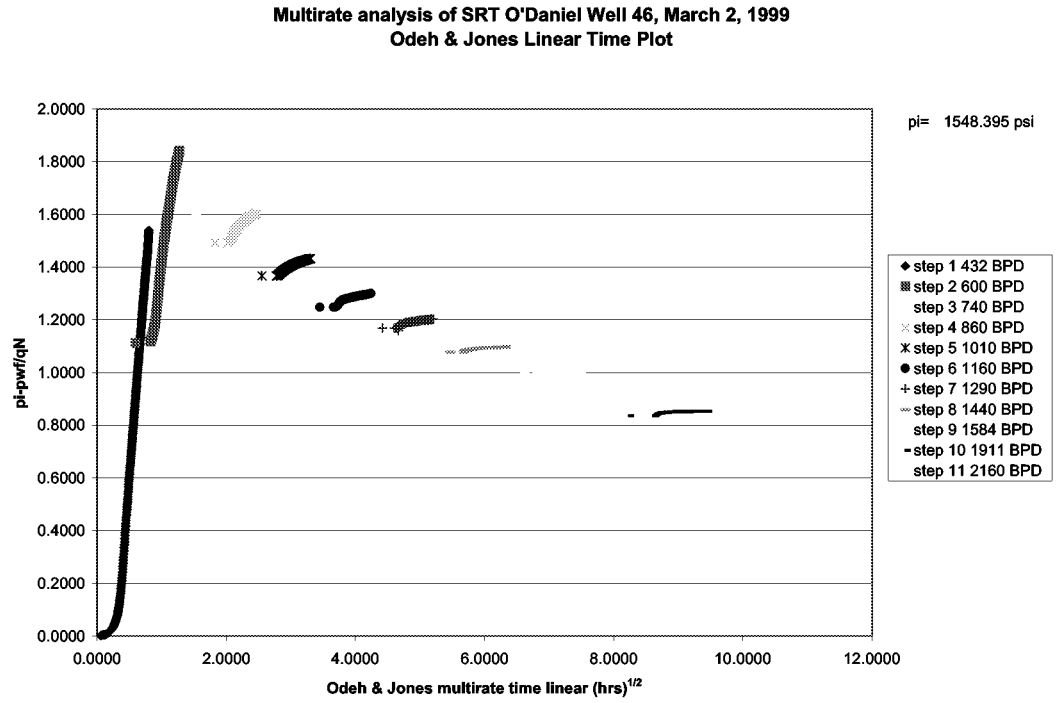

Fig. 3.5-5—Odeh & Jones linear time plot for O'Daniel Well 46.

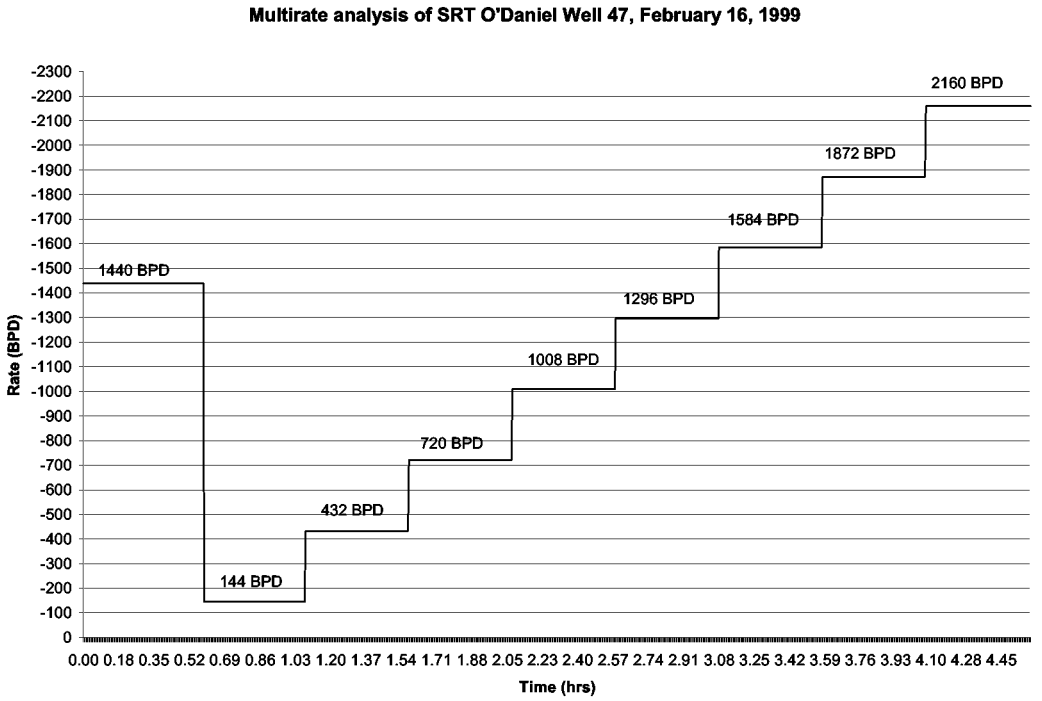

Fig. 3.5-6—Step rate test history of O'Daniel Well 47.

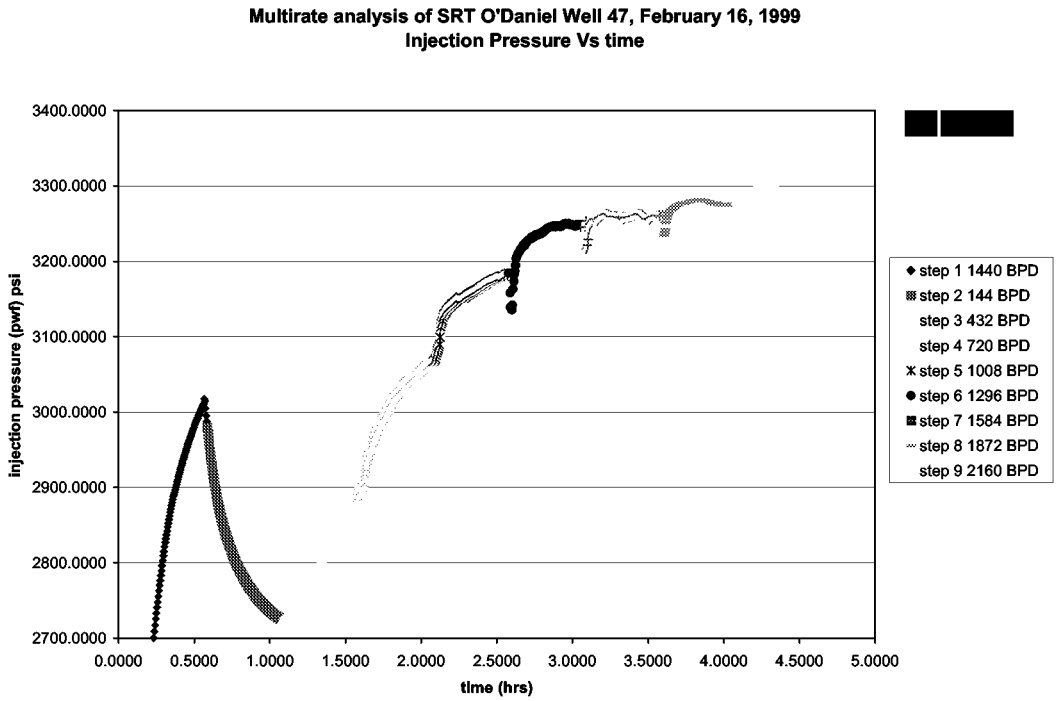

Fig. 3.5-7—Pressure/time history plot of O'Daniel Well 47.

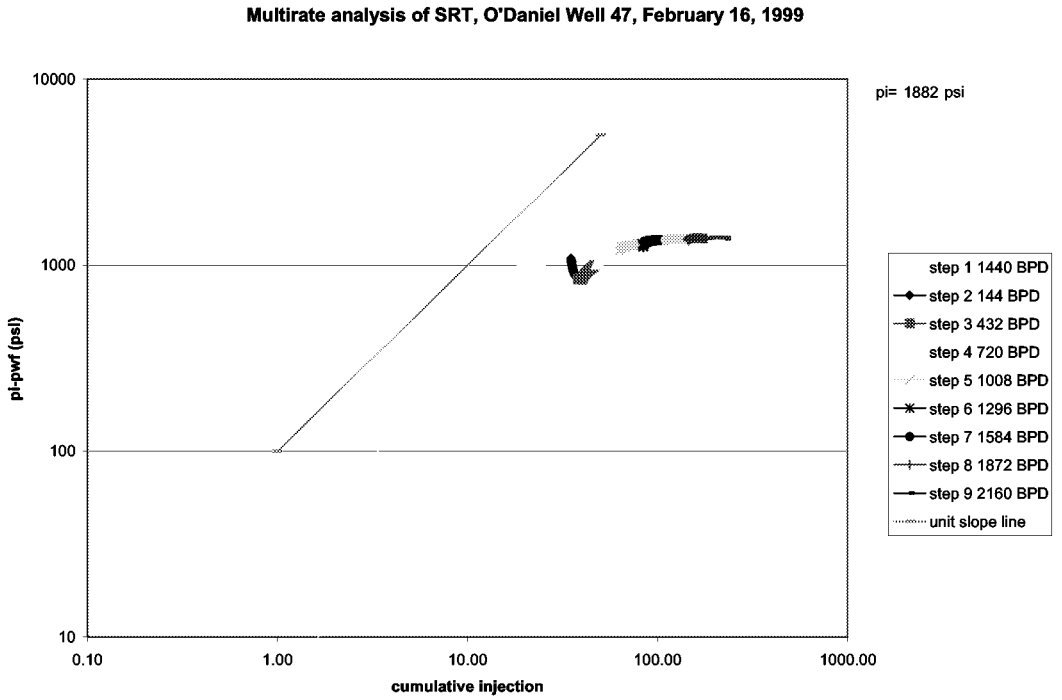

Fig. 3.5-8—Cumulative injection plot during SRT on O'Daniel Well 47.

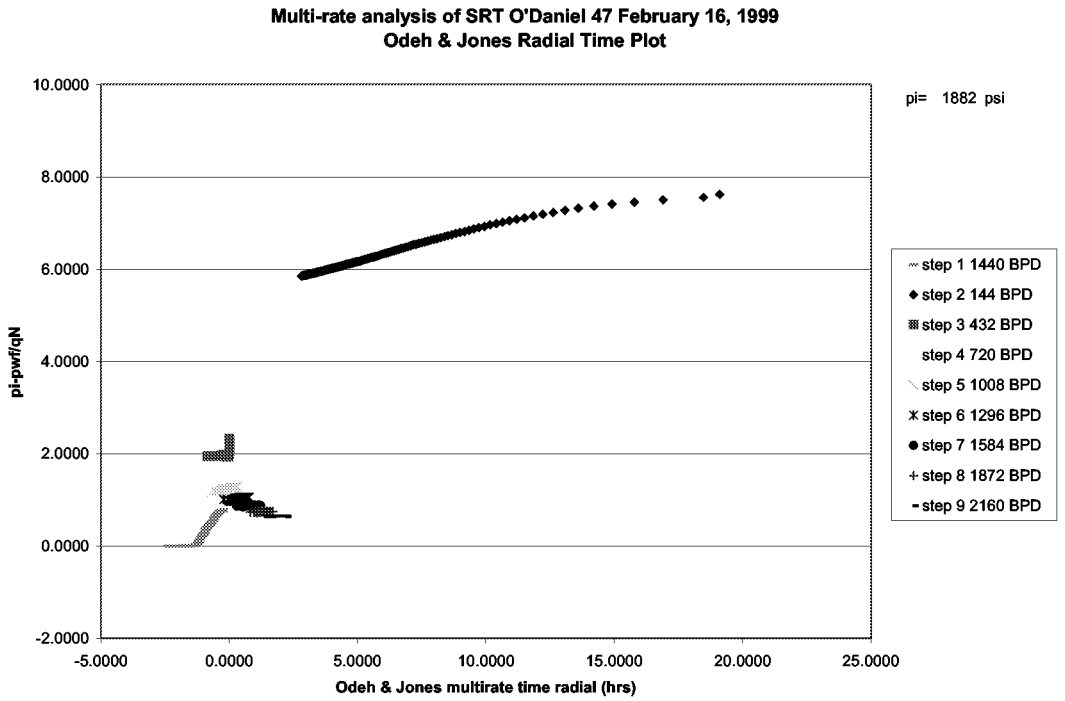

Fig. 3.5-9—Odeh & Jones multirate radial plot for O'Daniel Well 47.

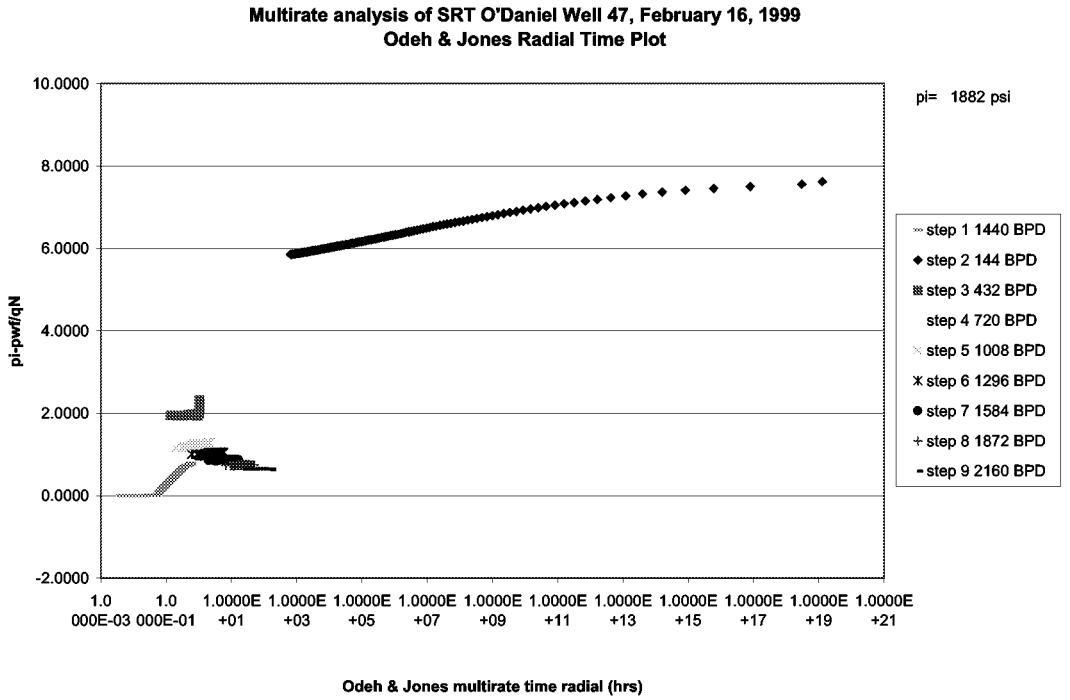

Fig. 3.5-10—Odeh & Jones multirate linear time plot for O'Daniel 47.

3.6 ANALYSIS OF STEP RATE INJECTION TESTS IN THE O'DANIEL PILOT AREA

Introduction

Step rate injection tests (SRIT) were conducted in new water injection wells #46 and #47 (Fig. 3.6-1) to determine the maximum safe injection pressure without fracturing the reservoir rock. This pressure is referred as to formation parting pressure. Determination of formation parting pressure is useful to avoid creating artificially induced fractures during CO_2 flooding from injection wells directly to production wells. Artificially induced fractures can result in premature CO_2 break-through, poor sweep efficiency, reduced oil recovery, and the loss of costly injection fluids due to uncontrolled fracture extension.

The step rate injection test was conducted prior to the multi-well interference tests in Well 46 (Fig. 3.6-2), with 11 different injection rates, from 432 BWPD stepping up to 2160 BWPD, for a total injection time of 5.6 hours. Fewer and shorter injection tests were performed in Well 47 (Fig. 3.6-3) with nine different injection rates, from 1440 BWPD stepping up to 2160 BWPD for total time of 4.5 hours injection. The first step (1440 BWPD) was actually not part of the SRIT design, but a procedure to fill up the tubing prior to the SRIT.

The SRIT's were analyzed using two flow models, the analytical and numerical models. Both models were used to estimate the parting pressure. The analytical model employed a multiple-rate transient technique derived by Odeh and Jones.[1] A computer-simulated step-rate injection test was used to confirm the initiation of the parting. The model can also be used to estimate the fracture permeability.

In addition, pressure transient analysis using type curve analysis was applied to determine the effective permeability and fracture half-length for each injection test. This analysis clearly demonstrates stress-sensitive behavior, one of the phenomena that influences the performance of waterflooding in Spraberry Trend Area.[1]

Analytical Flow Model

The tests were analyzed using the Odeh and Jones method[2] in which data from each injection rate were plotted on a Cartesian plot between $\frac{p_i - p_{wf}}{q_n}$ vs $\sum_{i=1}^{n} \frac{(q_j - q_{j-1})}{q_n} \log(t - t_j)$. This plot yields a straight line prior to formation parting. After formation pressure has been exceeded, the line shifts downward for each rate indicating that fracture length is propagating. The line shifts downward because the resulting fracture acts as an additional fluid conductor, thereby resulting in a change of the slope. There is no theoretical basis for drawing a second straight line through the points above the parting pressure. However, conventional analysis suggests that the intercept of the pre-parting straight line and the post-parting straight line is assumed to be the parting

pressure.[3] Singh *et al* showed that this may lead to erroneous parting propagation pressure.[4]

Figures 3.6-4 and 3.6-5 show the linear flow of Odeh and Jones plot for Wells 46 and 47, respectively. The plot for well 46 shows that the parting pressure occurs during the third step, as indicated by shifting the straight line downward. Therefore, the parting pressure is estimated to be 2730.54 psia. Meanwhile, the parting pressure that is predicated by the conventional analysis is about 2712 psia, as shown in Fig. 3.6-6.

On the other hand, the step rate injection test analysis for Well 47 shows that the parting pressure occurred at the first step when the high injection rate of 1440 BWPD was used to fill up the tubing. Therefore, the parting pressure cannot be estimated for this well and no further analysis will be performed.

Numerical Flow Model

A commercial black-oil simulator, *ECLIPSE*, was used to match the well performance data during the step injection-rate tests in Well 46. This enables confirmation of the result from the analytical model that a formation part definitely occurred during the third step injection-rate test. A single phase, radial-homogeneous reservoir model was developed with a single existing fracture. The developed model is similar to the model for simulating hydraulic fracturing, except for assigning a value of fracture permeability. The reservoir data used in this model can be seen in Table 3.6-1.

To represent reservoir behavior as infinite-acting in the model, a large volume with porosity to 1e12 was set up in the last cell. The original reservoir pressure of 1550 psia was given for all cells. A porosity of 1 and a permeability of 100,000 mD at cell number one were set up to represent an empty pipe and no flow resistance in the wellbore, respectively.

Equally spaced grids on a logarithmic basis were used for our radial grid system, applying the equation below:

$$\beta = \left(\frac{r_e}{r_w}\right)^{1/IMAX} \quad \text{.....(3.50)}$$

$$r_{i+1/2} = \beta\, r_{i-1/2} \quad \text{.....(3.51)}$$

Assigning a half-length fracture of 50 ft and fracture permeability of 100 md, the pressure response for the first two injection rates can be matched as shown in Fig. 3.6-6. The observation data is taken at the end of each injection step. The result indicates that the fracture propagation occurred during the third injection test. The pressure for the rest of the injection tests cannot be matched because the model is developed for a static fracture model. Current available simulators cannot be used to model the dynamic fracture (the

fracture propagation) model in naturally fractured reservoirs. Further research is needed to simulate fracture propagation in a naturally fractured reservoir.

Type Curve Matching

A commercial pressure transient analysis was used to analyze data with a dual porosity option and an infinite conductivity fractured reservoir. Type curve analysis was performed to determine the fracture half-length and the effective permeability at each step-rate injection test.

Figure 3.6-7 shows that at the first three-injection steps the fracture lengths propagates a few feet, and the effective permeability increases as the injection rate increases, indicating that the fractures are stress-sensitive. Then, fracture propagation and effective permeability abruptly increases as more fractures are intersected. After this period, fractures stop propagating and the fracture length becomes even shorter because the high injection rates create more fractures around the wellbore. Thus, effective permeability increases dramatically during this period.

Conclusions

1. Using the Odeh and Jones method, the parting pressure for the SRIT is estimated to be 2730 psia.
2. The numerical and analytical flow models confirm that parting pressure in Well 46 occurs during the third injection step.
3. The SRIT tests reveal that the pressure responses were dominated by fracture propagation and stress sensitivity.

References

1. Schechter, D.S.: "Advanced Reservoir Characterization and Evaluation of CO_2 Gravity Drainage in the Naturally Fractured Spraberry Trend Area," Fourth Annual Technical Progress Report to DOE under Contract No.: DE-FC22-95BC14942, U.S. DOE (December 1998).
2. Odeh, A.S. and Jones, L.G.: "Pressure Drawdown Analysis, Variable Rate Case," *JPT* (aug. 1965) 960.
3. Earlougher, R.C., Jr.: *Advances in Well Test Analysis*, Monograph Series Volume 5, Society of Petroleum Engineers, Dallas (1977)
4. Singh, P.K., Agarwal, R.G., and Jrase, L.D.: "Systematic Design and Analysis of Step-Rate Tests To Determine Formation Parting Pressure," paper SPE 16798 presented at the 1987 Annual Technical Conference and Exhibition, Dallas, Tx., 27-30 September.

Table 3.6-1—Reservoir Parameters

Parameter	Value
k_m	0.1 md
ϕ	10 %
h	30 ft
p_i	1550 psia
L_f	50 ft

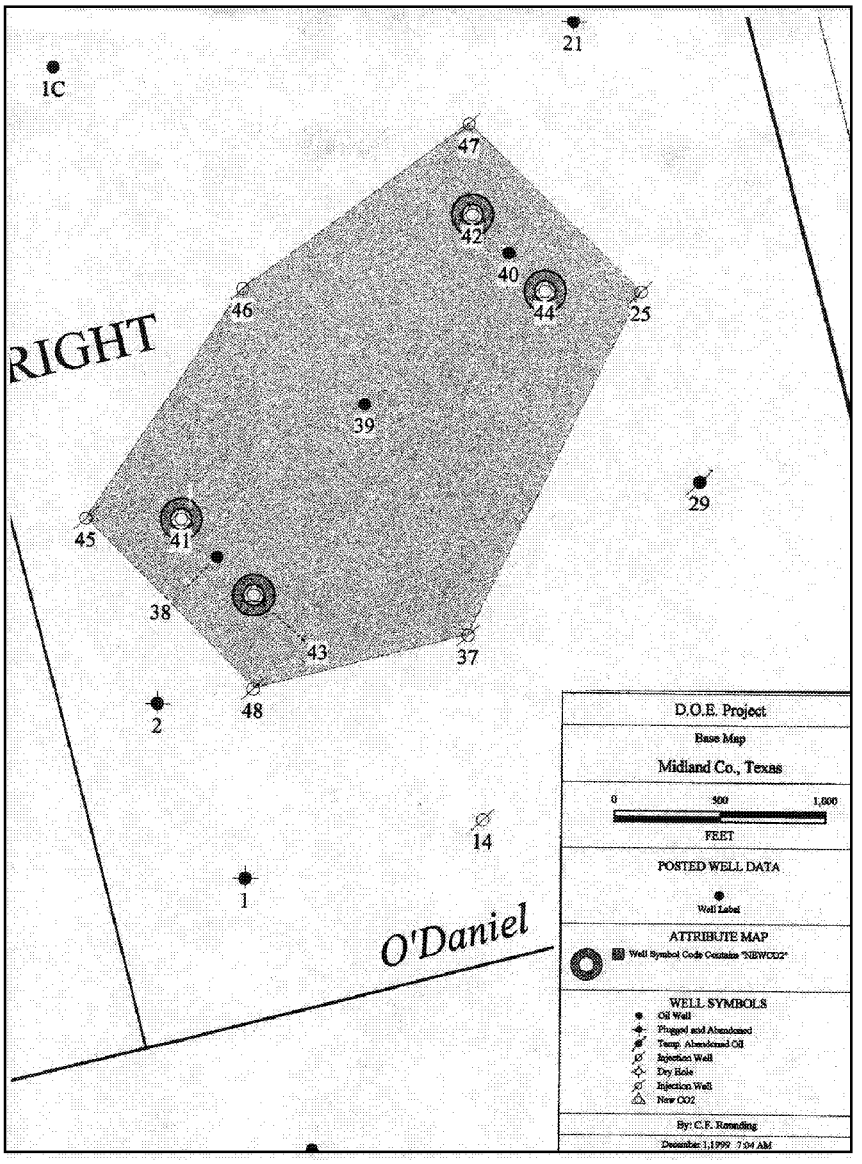

Fig. 3.6-1—Well configuration in E.T. O'Daniel Pilot, Spraberry Trend Area, West Texas

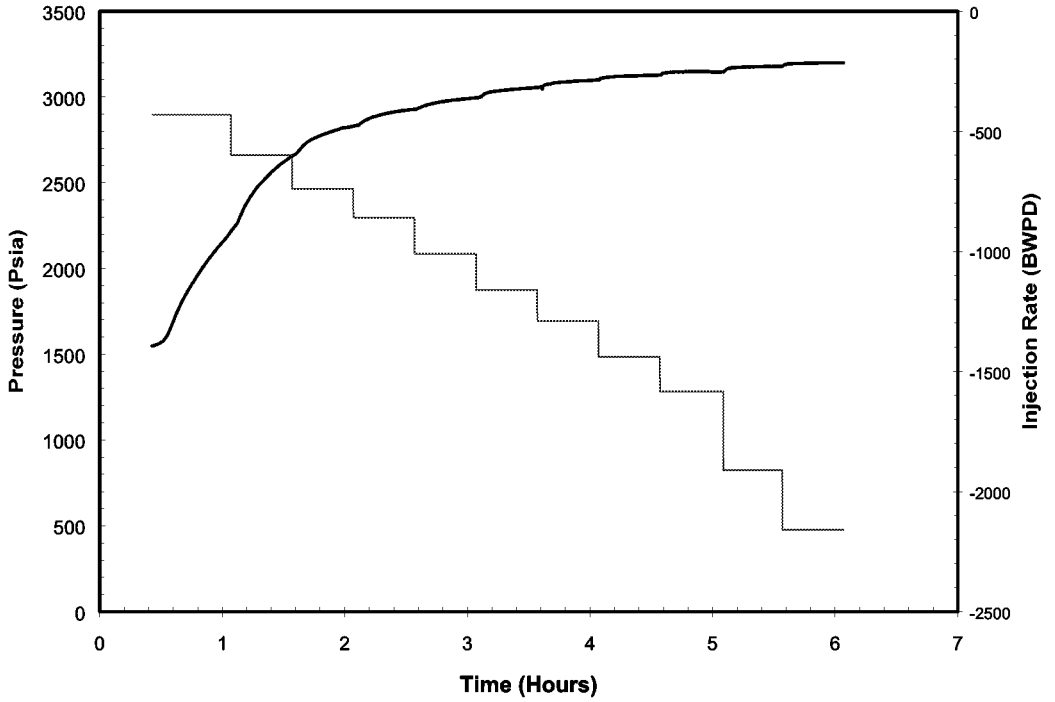

Fig. 3.6-2 —Step rate injection test for O'Daniel injection Well 46

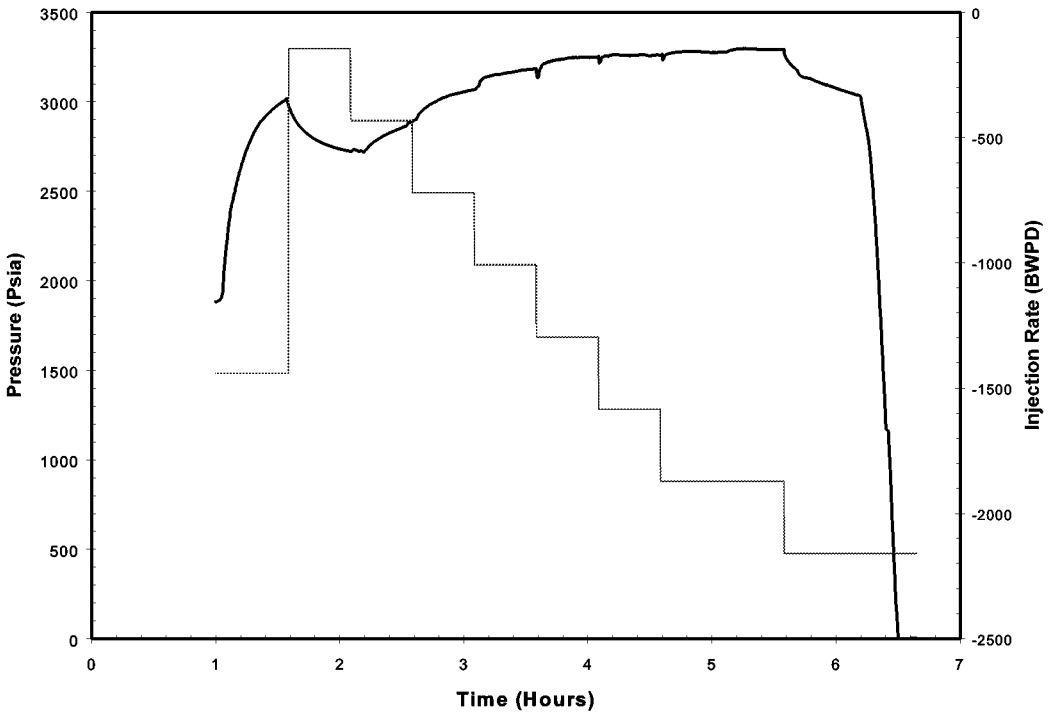

Fig. 3.6-3 —Step rate injection test for O'Daniel injection Well 47

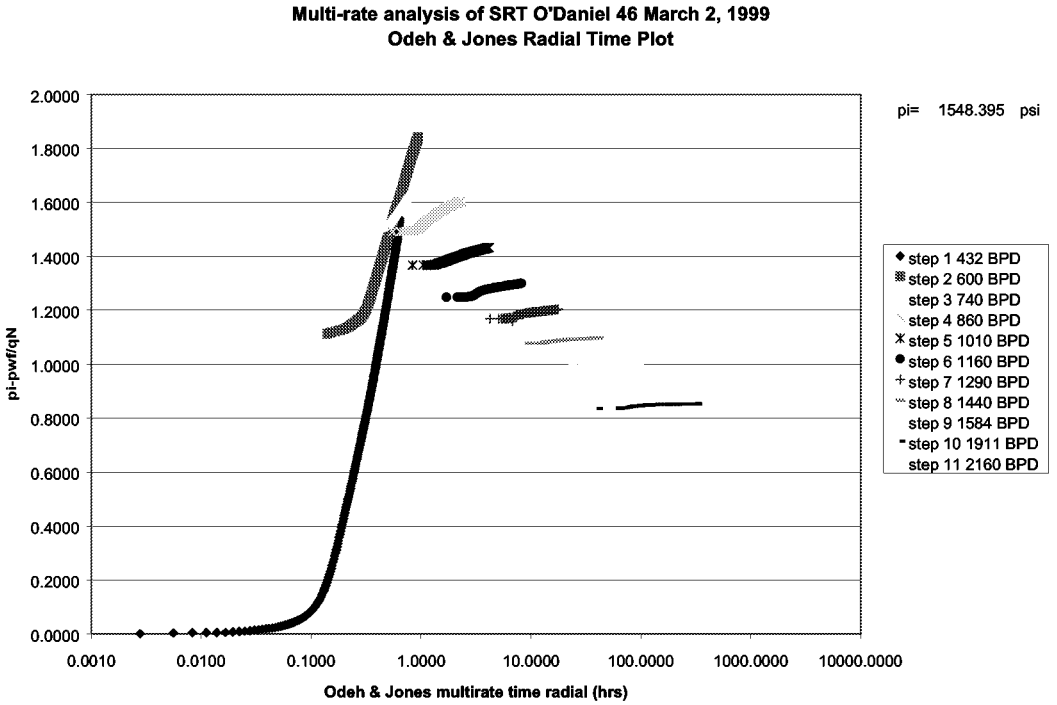

Fig. 3.6-4 —Multi-rate analysis of SRIT O'Daniel Well 46

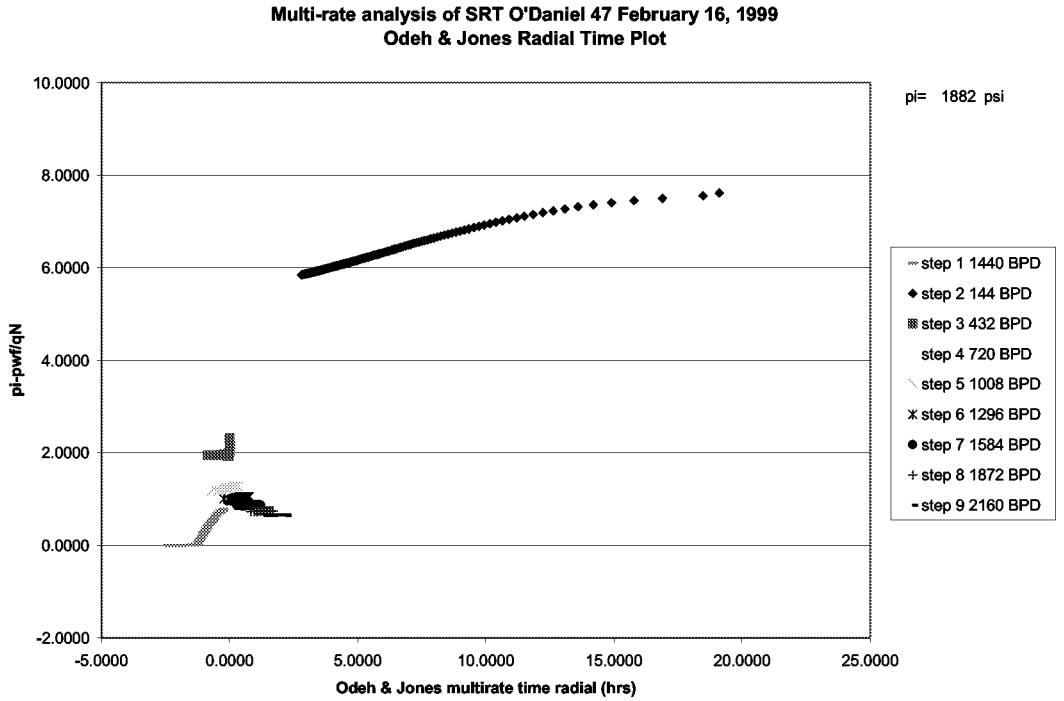

Fig. 3.6-5 —Multi-rate analysis of SRIT O'Daniel Well 47

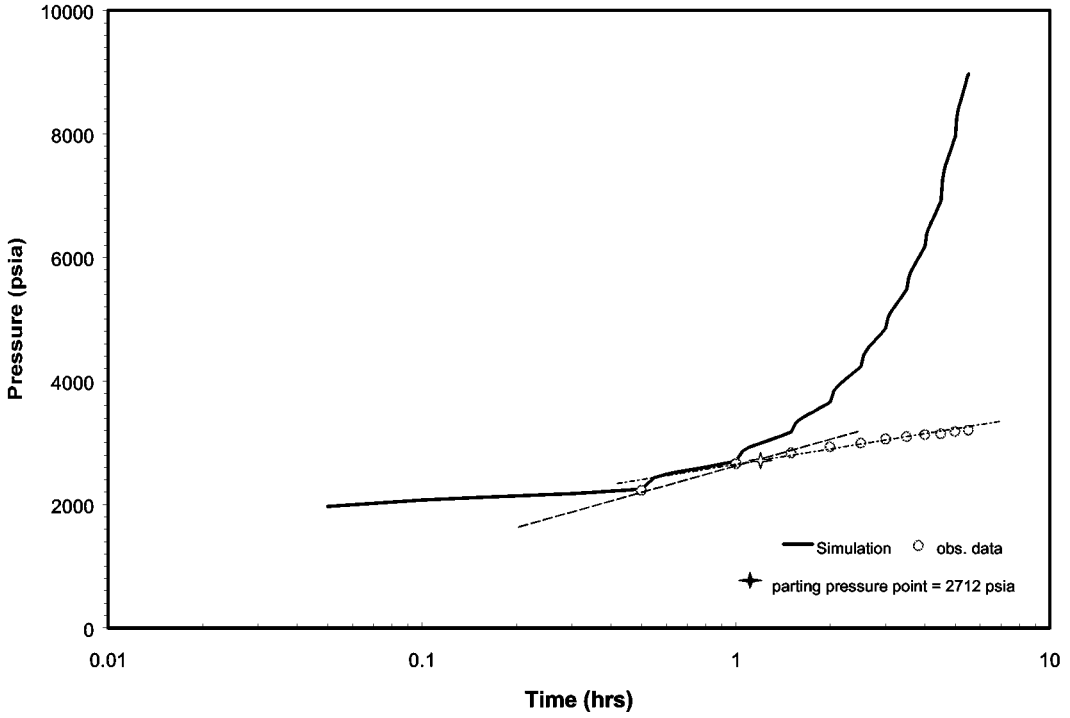

Fig. 3.6-6 —Match beween simulation result and observation data for SRIT O'Daniel Well 46

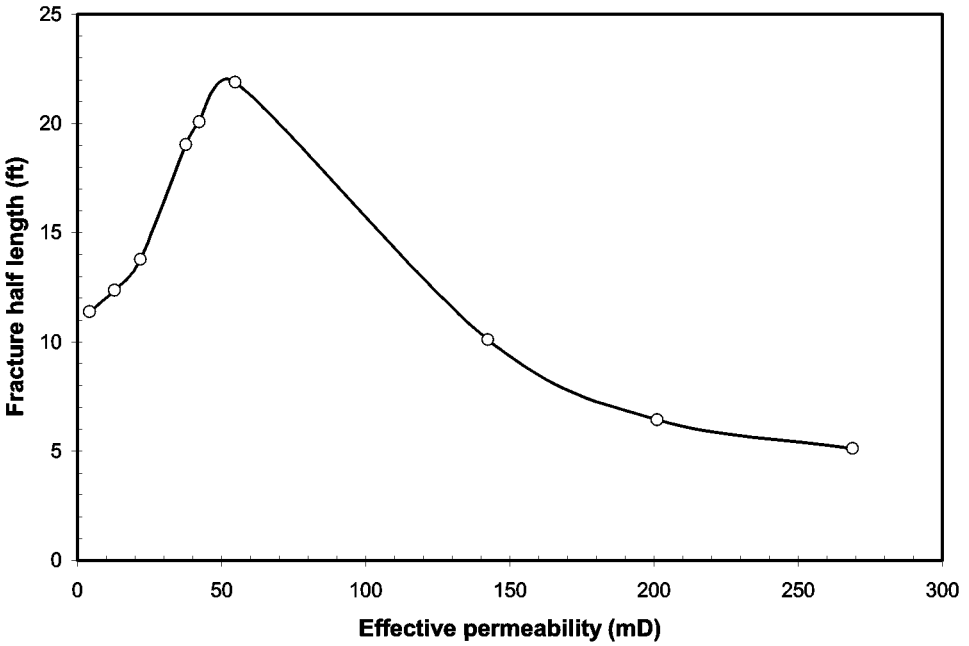

Fig. 3.6-7 —Effect of injection rate on fracture propagation and stress sensitivity

3.7 NUMERICAL MODELING OF SOLID DEFORMATION AND STRESS-DEPENDENT PERMEABILITY IN NATURALLY FRACTURED RESERVOIRS

During the first year of this project, we analyzed the productivity behavior of Spraberry wells using a newly developed mathematical model. In the second year of this project, we modified the mathematical model with consideration of mechanical skin due to fluid damage to the matrix permeability. In the third year of this project, the stress-sensitive permeability was studied in detail including the effect of deformation. A model coupling the solid deformation and the motion of fluid flow was developed using a fully implicit finite-difference scheme. A comparison between conventional dual-porosity and stress dual-porosity simulators has been made. The effect of stress-sensitive permeability to the well productivity is demonstrated.

Introduction

Fractures are the main fluid flow paths in naturally fractured reservoirs. Therefore, the productivity of naturally fractured reservoirs relies on the magnitude of fracture permeability. When the pore pressure depletes due to oil/gas production rates in highly stress-sensitive naturally fractured reservoirs, the confining stresses on the reservoir rock increase over the hydraulic pressure in the pores of the rock causing compaction of the rock. The interaction between fluid flow and rock volumetric deformation causes significant reduction in fracture permeability. This, in turn, may reduce the reservoir productivity. In current conventional dual-porosity simulators the stress-sensitive reservoir is simulated by using pressure-sensitive permeability, where permeability is treated as a function of pore pressure and the effect of rock deformation due to changes of the stress-state is neglected. Hence, productivity predictions obtained using conventional dual-porosity simulators in reservoir with stress-sensitive characteristic may be misleading. Therefore, in this study numerical modeling of a stress dual-porosity simulator was developed to take into account the effect of solid deformation in the naturally fractured reservoir.

Although naturally fractured reservoirs have been the subject of much research, not many studies cover the effect of solid deformation on the changes in fluid pressure. Uncertainties still exist in the governing equation describing this process as found in the cited references (Huyakorn and Pinder, 1983, Unger and Aifantis, 1990, Bai et al., 1993, Chen and Teufel, 1997). The governing equation used in this research is adopted from Chen and Teufel (1997), which is considered conceptually more consistent than other references cited.

The main thrust of this study is to develop numerical simulation schemes to simulate naturally fractured reservoirs having solid deformation and stress-sensitive permeability.

Technical approach

In this section, governing equations for coupled fluid flow and poroelastic models in porous media are presented. The development of governing equations involves the mathematical representation of conceptual models, the process underlying the conceptual models and the assumption of governing equations.

Dual-porosity/dual-permeability fluid flow model

The concept of the dual-porosity system considered in this study is identical to the single-phase flow equations given by Barenblatt *et al* (1960). These equations were derived under the following assumptions: (1) Fluid flow is single-phase laminar (2) Fluid is slightly compressible (3) Gravity effects are negligible and pressure gradients are small (4) Transfer of fluid from matrix to fractures occurs under pseudo-steady state conditions. The governing equations for the conventional dual-porosity model is presented below:

$$\nabla\cdot(\frac{k_1}{\mu}\nabla p_1)=(c_1+\phi_1 c_f)\frac{\partial p_1}{\partial t}-\Gamma \quad \text{.....(3.52)}$$

$$\nabla\cdot(\frac{k_2}{\mu}\nabla p_2)=(c_2+\phi_2 c_f)\frac{\partial p_2}{\partial t}-\Gamma \quad \text{.....(3.53)}$$

where c, ϕ, c_f and Γ are medium compressibility, porosity, fluid compressibility and interporosity flow, respectively. Subscripts 1 and 2 denote matrix and fracture, respectively.

Meanwhile, the fluid flow governing equation for dual-porosity was modified to include the effect of solid displacement. Three basic principles constituting this model are mass conservation, Darcy's law and equation of state.

Mass conservation:

Fluid: $\nabla\cdot(\rho\phi_n v_n)+\frac{\partial(\phi_n\rho)}{\partial t}+(-1)^n\rho\Gamma=0$ .....(3.54)

Solid: $\nabla\cdot(\rho_s(1-\phi_t)v_s)+\frac{\partial(1-\phi_n\rho_s)}{\partial t}=0$ .....(3.55)

Darcy's law: $\phi_n(v_n-v_s)=-\frac{k_n}{\mu}\nabla p_n$ .....(3.56)

Equation of state (isothermal fluid compressibility):

$$c_n=\frac{1}{\rho}\frac{\partial\rho}{\partial p_n} \quad \text{.....(3.57)}$$

The subscript n = 1 denotes the matrix block while n=2 for the fractures and s for solid phase. By combining those three principles, the governing equation for fluid flow and the effect of solid deformation on the change of fluid pressure can be written as:

For the matrix system:

$$\nabla\cdot(\frac{k_1}{\mu}\nabla p_1)=b_{11}\frac{\partial p_1}{\partial t}+b_{12}\frac{\partial p_2}{\partial t}+b_{13}\frac{\partial(\nabla.u)}{\partial t}-\Gamma \quad \text{.....(3.58)}$$

For the fracture system:

$$\nabla\cdot(\frac{k_2}{\mu}\nabla p_2)=b_{21}\frac{\partial p_1}{\partial t}+b_{22}\frac{\partial p_2}{\partial t}+b_{23}\frac{\partial(\nabla.u)}{\partial t}+\Gamma \quad \text{.....(3.59)}$$

where the coefficients are represented by:

$$b_{11}=\phi_1 c_1+\phi_1 c_{p1}(\beta_1-\alpha_1) \qquad b_{12}=\phi_1 c_{p1}(\beta_2-\alpha_2)$$

$$b_{13}=\frac{\phi_1 c_{p1}}{c_b} \qquad b_{21}=\phi_2 c_{p2}(\beta_1-\alpha_1)$$

$$b_{22}=\phi_2 c_{p2}(\beta_2-\alpha_2) \qquad b_{23}=\frac{\phi_2 c_{p2}}{c_b}$$

$$c_{p1}=\frac{\alpha^* c_b^*}{\phi_1} \qquad c_{p2}=\frac{\phi_t}{\phi_2}(c_p-c_p^*)$$

$$c_p=\frac{\alpha c_b}{\phi} \qquad \alpha_1=\frac{\alpha^* c_b^*}{c_b}$$

$$\alpha_2=\alpha-\frac{\alpha^* c_b^*}{c_b} \qquad \alpha=1-\frac{c_s}{c_b}$$

$$\beta=1-\frac{c_s}{c_p} \qquad \beta_1=\frac{c_p^*\beta^*}{c_p}$$

$$\beta_2=\beta-\beta_1$$

In equations 3.52 through 3.57, ρ is the fluid density, ϕ_n is the effective porosity, ϕ_t is the total effective porosity, v_n is the fluid velocity vector, p_n is the fluid pressure, k_n is the permeability, μ is the viscosity, c_n is the fluid compressibility, t is time, b_{nm} is the porosity-compressibility coefficients, c_p is the pore compressibility, c_b is the bulk compressibility, c_s is the solid compressibility, β_n is the effective stress coefficient associated with the pore volumetric change, α is the effective stress coefficient associated with the bulk volumetric change, ∇ and $\nabla\cdot$ denote gradient and divergence, respectively. The interaction between the matrix and fracture systems is governed by interporosity flow between these media that occurs under pseudo-steady state conditions (Barenblatt *et al.*, 1960, Warren and Root, 1963):

$$\Gamma = \frac{\sigma}{\mu} k_1 (P_1 - P_2) \quad \text{.....(3.60)}$$

where Γ is the volumetric flow rate from the matrix to the fractures per unit of bulk volume. For dual-porosity/dual-permeability, both the fracture and matrix systems have the ability to transport fluid to the wellbore. Fluid may also be transferred from the matrix system to the fracture system. Therefore, the production or injection well must be added in equations 3.58 and 3.59. In the dual-porosity case, where the matrix permeability is small and only acts as a source term, the fluid flow is transferred only through the fractures to the wellbore. Therefore, the left-hand term of equation 3.58 is negligible compared to the right-hand term. Using this assumption, equation 3.58 reduces to

$$b_{11} \frac{\partial p_1}{\partial t} + b_{12} \frac{\partial p_2}{\partial t} + b_{13} \frac{\partial (\nabla . u)}{\partial t} = \frac{\sigma}{\mu} k_1 (P_1 - P_2) \quad \text{.....(3.61)}$$

The above statement expresses that the matrix permeability is a function of both macroscopic and intrinsic properties. For example, when we refer to the dual-porosity case, setting macroscopic matrix permeability equal to zero, this formulation only implies that no fluid is produced at the wellbore via the matrix system. It does not imply that intrinsic matrix permeability in the interporosity flow is zero.

The parameter σ is a shape factor that reflects the geometry of the matrix block (Gilman and Kazemi, 1982). This parameter controls the flow between the fractures and matrix and is defined as

$$\sigma = 4\left(\frac{1}{L_x^2} + \frac{1}{L_y^2} + \frac{1}{L_z^2}\right) \quad \text{.....(3.62)}$$

where L_x, L_y, and L_z are the characteristic dimensions of the matrix blocks that correspond to fracture spacing in the x-, y- and z- direction respectively. This shape factor was derived from a finite-difference approximation of flow between fractures and matrix systems for a grid block shown in **Fig. 3.7-1**. Two-dimensional mass conservation is expressed as

$$\frac{\partial}{\partial x}\left(T_{i,j} \frac{\partial p}{\partial x}\right) + \frac{\partial}{\partial y}\left(T_{i,j} \frac{\partial p}{\partial y}\right) = \frac{\partial (\phi S)_{i,j}}{\partial t} \quad \text{.....(3.63)}$$

Assuming the length of the matrix block is much larger than the fracture width, $L_x >> W_f$, thus the fracture width can be ignored. Then the discretization of finite difference equation of **Fig. 3.7-1** would be

$$\frac{1}{L_x}(T_{i+1/2,j}\frac{p_{fi+1,j}-p_{ma_{i,j}}}{L_x/2}-T_{i-1/2,j}\frac{p_{ma_i,j}-p_{f_{i,j}}}{L_x/2})+$$

$$\frac{1}{L_y}(T_{i,j+1/2}\frac{p_{fi,j+1}-p_{ma_{i,j}}}{L_y/2}-T_{i,j-1/2}\frac{p_{ma_i,j}-p_{f_{i,j}}}{L_y/2})=\frac{(\phi S)_i^{n+1}-(\phi S)_i^n}{\Delta t} \quad \text{.....(3.64)}$$

If fracture pressure and transmissibility changes between matrix block are negligible, then the mass conservation can be written as

$$4(\frac{1}{L_x^2}+\frac{1}{L_y^2})(T)(p_{ma}-p_f)=\frac{(\phi S)_{i,j}^{n+1}-(\phi S)_{i,j}^n}{\Delta t} \quad \text{.....(3.65)}$$

Therefore, the flow from matrix to fractures is expressed by the left-hand side of equation 3.65 and the shape factor for one-dimensional flow is written as

$$\sigma=4(\frac{1}{L_x^2}+\frac{1}{L_y^2}) \quad \text{.....(3.66)}$$

The other important parameter to emphasize is the representation of the production or injection well in a particular gridblock. The well is located in the center of the grid block and the grid block pressure, p_{ij}, is not the wellbore flowing pressure, p_{wf}. In addition, the grid block at the well location is not normally the well drainage-boundary pressure. Additional expressions are required to compute the p_{wf} and to calculate an equivalent radius from the block center. The wellbore flow rate can be represented in terms of pressure drop at the well as shown in equation 3.67 below:

$$q=J(p_{ij}^{n+1}-p_{wf}) \quad \text{.....(3.67)}$$

For pseudo-steady state flow into a wellbore, the productivity index (J) is defined by

$$J=\frac{7.08x10^{-3}\,k_{eff}h}{\mu\,ln(\frac{r_e}{r_w}-\frac{3}{4}+S)} \quad \text{.....(3.68)}$$

where k_{eff} is the effective permeability, h is the formation thickness, μ is the viscosity, r_e is the equivalent grid block radius, r_w is the wellbore radius, $-\pi/2$ is the value if J is based on grid block pressure and S is the skin factor.

For anisotropic permeabilities, effective permeability is defined as

$$k_{eff} = \sqrt{k_x \times k_y} \quad \text{.....(3.69)}$$

Assuming isotropic permeabilities, square grid blocks, single phase flow and a well at a center of interior block, Peaceman (1978) showed that the equivalent radius, r_e, is about

$$r_e = 0.2\Delta x \quad \text{.....(3.70)}$$

or, in the case of anistropic permeabilities, the equivalent radius is defined as

$$r_e = \frac{0.28\left(\sqrt{\frac{k_y}{k_x}}\Delta x^2 + \sqrt{\frac{k_x}{k_y}}\Delta y^2\right)^{1/2}}{\left(\frac{k_y}{k_x}\right)^{1/4} + \left(\frac{k_x}{k_y}\right)^{1/4}} \quad \text{.....(3.71)}$$

Around the wellbore, two inner boundary conditions can be specified: constant wellbore flow rate and constant wellbore flowing pressure. When constant wellbore flow rate is specified, the wellbore flowing pressure is determined after the grid block pressure at the well location is obtained. This grid block pressure is used to recalculate the p_{wf} from equation 3.64. When the wellbore flowing pressure other than rate is specified, the finite-difference equations must be modified. The rate is replaced by equation 3.64. This means that $J(p^{n+1})$ is added to the center coefficient while $J(p_{wf})$ is added to the right-hand side. After pressure changes converge from specified tolerance at each time step, the equation 3.64 is applied to obtain the rate.

Poroelastic model

In the poroelastic model, the rock can be assumed to behave in a linear elastic fashion for the stress change and rock deformation induced within the reservoir. Furthermore, the rock mass is assumed to be isothermal and the governing equation comprises three parallel basic principles as in fluid flow modeling: stress equilibrium, strain-displacement and strain-stress pressure relations.

In the absence of body forces, the stress equilibrium equation is:

$$\sum_{j=1}^{3} \frac{\partial \tau_{ij}}{\partial x_j} = 0 \quad \text{.....(3.72)}$$

where τ_{ij} is the total stress on the medium, which can be expressed as

$$\tau_{ij} = \sigma_{ij} - (\alpha_1 p_1 + \alpha_2 p_2)\delta_{ij} \quad \text{.....(3.73)}$$

where σ_{ij} is referred to as the effective stress acting on the solid skeleton, p is the fluid pressure, and α is the effective stress coefficient. The solution of the effective stress is in incremental form and after an elapsed time t can be expressed as

$$\sigma_{ij} = \sigma_{ij}^{0} + \Delta\sigma_{ij} \quad \text{.....(3.74)}$$

where σ_{ij}^{0} is the initial effective stress and $\Delta\sigma_{ij}$ is the effective stress increment. Similar expressions apply for incremental forms of displacement, strain and pressure. The strain components are defined by the average displacement components as

$$\varepsilon_{ij} = \frac{1}{2}\left(\frac{\partial u_i}{\partial x_j} + \frac{\partial u_j}{\partial x_i}\right) \quad \text{.....(3.75)}$$

where ε_{ij} is the strain of the solid skeleton. The increment of strain is assumed equal to the strain since the initial strain can be negligible. The initial strain may be caused by such factors as temperature changes and shrinkage. u is defined as the incremental displacement vector. For isotropic porous material, the linear elastic of strain-stress-pressure equations takes the form

$$\sigma_{ij} = 2G\varepsilon_{ij} + \frac{2G\nu}{1-2\nu} e\delta_{ij} - (\alpha_1 p_1 + \alpha_2 p_2)\delta_{ij} \quad \text{.....(3.76)}$$

where G is the shear modulus, ν is poisson's ratio, e is volume strain of solid skeleton and δ_{ij} is kronecker's delta (δ_{ij} =1 for i = j, δ_{ij} = 0 for i ≠ j). The volume strain of solid skeleton, e, relates to the divergence of solid displacement as

$$e = \nabla \cdot u \quad \text{.....(3.77)}$$

Combining those three basic principles through equations 3.72, 3.76 and 3.77, the governing equation for solid displacement on the change of fluid pressure can be written as:

$$G\nabla^2 u_i + \frac{G}{1-2\nu}\frac{\partial(\nabla \cdot u)}{\partial x_i} = \alpha_1 \frac{\partial p_1}{\partial x_i} + \alpha_2 \frac{\partial p_2}{\partial x_i} \quad \text{.....(3.78)}$$

For the two dimensional case, equations 3.58, 3.59 and 3.78 are a set of a system of partial differential equations that lead to four equations in four unknowns, p_1, p_2, u_x, and u_y

So far, the governing equations used to describe fluid flow and poroelasticity in a fractured reservoir have been presented. Next, these equations are solved using the appropriate initial and boundary conditions.

Initial and boundary conditions

The initial conditions are implemented by assigning the value of both matrix and fracture pressures for the fluid flow model and stress or displacement for the poroelastic model to each grid block. At times greater than zero, boundary conditions for fluid flow and poroelastic models must be specified. There are two boundary conditions for the fluid flow model; inner and outer boundary conditions. The inner boundary is used to specify the boundary condition around the wellbore. The simulator allows for two conditions, either constant rate or constant bottomhole pressure. Outer boundary conditions reflect the far field boundary condition. Two outer boundary conditions are considered, Dirichlet-type and Neumman-type boundary conditions. The first boundary condition is applied for an infinite boundary condition or constant pore pressure at the boundary system. The second boundary condition is applied for a close outer boundary condition or zero flow-rate at the boundary system.

In addition, two outer boundary conditions also exist for the poroelastic model, Dirichlet-type and Neumman-type boundary conditions. The Dirichlet-type boundary condition refers to solid displacement at the boundary. Zero solid displacements are considered for nondeformable boundaries while the Neumman-type boundary refers to imposing normal stress at the boundary. A mixed boundary condition can be modeled in the simulation in which the displacement components are prescribed over part of the boundary and the stress components over the rest of boundary.

Results and discussions

Our purpose was twofold: (1) develop a rigorous, robust dual porosity simulator incorporating effects of stress sensitivity in a fractured reservoir (2) compare the simulator against commercial dual-porosity simulators.

In order to make a comparison between conventional dual-porosity and stress dual-porosity simulators, the correlation of permeability as the function of pore pressure was used. The correlation was obtained from the Humble waterflood simulation (Putra and Schechter, 1997) as seen in **Fig. 3.7-2**. Constant permeability-porosity and variable permeability-porosity were two cases used in both simulators. Constant permeability-porosity was used to verify the stress dual-porosity simulator while the variable permeability-porosity was used to verify the conventional dual-porosity simulator.

The discretization grid consisted of 25 blocks in the x-direction and 25 blocks in the y-direction with 100-ft length of each grid block. In order to simulate a closed system and nondeformable outer boundary conditions, the flow rate and the displacement were set

equal to zero. The model parameters used here are presented in Table 3.7-1. The well was located in the middle of the model and produced with a constant flow rate of 100 bbl/d. The simulation was run using a time step of 10 days. Initial conditions are set to zero for both displacement and pore pressure.

Fig. 3.7-3 shows the solid displacement distribution in the x-direction. The maximum displacement for the x-direction will be to the right-hand side and minimum displacement will be in the opposite direction. The direction of magnitude is different because the inner boundary condition for displacement is set to be zero.

Fracture pressure distribution at 10 days is shown in **Fig. 3.7-4**. Constant rate of 100 b/d was used as the inner boundary condition and there is no flow boundary condition is for outer boundary condition. At this time, pressure distribution in y-direction still acts as infinite acting reservoir, but pressure distribution in x-direction has reached boundary condition. This is because of different magnitude of permeability in x- and y-directions.

As mentioned earlier, once fluid production is initiated, pore-pressure starts to decrease causing deformation of the solid part, which, in turn, increases the effective stress as seen in **Fig. 3.7-5**. The maximum effective stress is observed to occur close to the wellbore and decreases as the distance from the wellbore increases. Thus, the maximum reduction of fracture permeability due to stress-sensitive permeability occurs near the wellbore and will disappear as distance from the wellbore increases as shown in **Figs. 3.7-6** and **3.7-7**. Once the pore pressure reaches the outer boundary system, the pore pressure at that boundary starts decreasing because zero flow-rate was set up in the boundary system.

Both simulators were used to predict the flow rate as a function of wellbore pressure with two cases; (1) constant permeability-porosity and (2) variable permeability-porosity. Several constant flow-rates from 300 bbl/d to 10 bbl/d were simulated at 10 days. The grid block pressure at the well location obtained at the various rates was used to back calculate the bottom hole pressure using equation 3.64. For the variable permeability-porosity case, a significant reduction in predicted flow rates is seen as wellbore pressure decreases in both simulators (**Figs. 3.7-8** and **3.7-9**). This is because in the stress and pressure-sensitive permeability, both simulators allow fracture permeability and porosity changes as pressure changes. Due to fracture permeability decreases, a high-pressure gradient has to be maintained at the well to sustain the same flow rate as the constant permeability case. This results in a lower bottomhole pressure.

Fig. 3.7-10 shows the interesting results that occurred when constant permeability-porosity was applied. Both simulators gave similar bottomhole pressures because stress transfer effect did not show any significant contributions. However, when variable permeability-porosity was used, bottomhole pressure from the conventional dual-porosity simulator deviated from the stress dual-porosity simulator after using a high constant flow-rate above 100 b/d. This deviation results from neglecting the stress transfer effect. If the stress transfer is neglected at high production rate, then the interpretation of stress sensitivity in natural fractured reservoirs can be erroneous.

Conclusions

Conclusions drawn based on the present study are summarized below:

1. A numerical model of solid deformation and stress-pressure dependent permeability in naturally fractured reservoirs has been developed.

2. The comparisons of constant and variable permeability-porosity performances between conventional and stress dual-porosity simulator were made.
3. The variable permeability-porosity shows a significant reduction in the production rate as compared to constant permeability-porosity.
4. Both conventional and stress dual-porosity simulators with constant permeability-porosity can be used to predict reservoir performance.
5. Conventional dual-porosity with variable permeability cannot be used for high production rates in naturally fractured reservoirs.
6. The stress transfer effect in naturally fracture reservoirs has been demonstrated to be important.

Nomenclature

b	=	porosity-compressibility coefficients, Lt^2/m
c	=	compressibility, Lt^2/m
e	=	volumetric strain, dimensionless
E	=	Young's modulus, m/Lt^2
G	=	shear modulus, m/Lt^2
h	=	formation thickness, L
J	=	productivity index, L^2t/m
k	=	permeability, L^2, md
L	=	characteristic dimension of matrix block, L
p	=	fluid pressure (positive for compression), m/Lt^2
q	=	source/sink term, L^3/t
r	=	radius, L
S	=	skin factor, dimensionless
t	=	time, t
u	=	displacement, L
v	=	fluid velocity vector, L/t
V	=	volume, L^3
x,y,z	=	spatial coordinates, L
α	=	effective stress coefficient associated with the bulk volumetric change, dimensionless
β	=	effective stress coefficient associated with the pore volumetric change, dimensionless
δ_{ij}	=	Kronecker's delta (δ_{ij}=1 for i=j, δ_{ij}=0 for i≠j)
ε	=	strain, dimensionless
ϕ	=	porosity, fraction
Γ	=	interporosity flow, $L^3/t/L^3$
μ	=	fluid viscosity, m/Lt
ν	=	Poisson's ratio, dimensionless
ρ	=	fluid density, m/L^3
σ	=	shape factor, L^{-2}
∇	=	gradient
$\nabla\cdot$	=	divergence

Subscripts

b	=	bulk
c	=	confining
eff	=	effective
f	=	fluid
ij	=	grid block location in i- and j-directions
n	=	index of primary and secondary pores
p	=	pore
s	=	solid
t	=	total
w	=	wellbore
1	=	primary pores
2	=	secondary pores

Superscripts

$*$	=	single porosity nonfractured system
^{0}	=	initial condition

References

1. Bai, M., Elshworth, D., and Rogiers, J.C.: "Modeling of Naturally Fractured Reservoirs Using Deformation Dependent Flow Mechanism," *Int. J. Rock Mech. Min. Sci. & Geomech.* (1993), 1185-1191.
2. Barenblatt, G.I., Zehltov, Iu, P., and Kochina, I.N.: "Basic Concepts in Theory of Seepage of Homogeneous Liquids in Fissured Rocks (Strata)," *Priklad. Mat. Mekh.* (1960) 24 (5), 825-864.
3. Chen, H.-Y. and Teufel, L.W.: "Coupling Fluid Flow and Geomechanics in Dual-Porosity Modeling of Naturally Fractured Reservoirs," paper SPE 38884 presented at the 1997 SPE Annual Technical Conference and Exhibition, San Antonio, TX, Oct. 5-8.
4. Gilman, J.R. and Kazemi, H.: "Improvements in Simulation of Naturally Fractured Reservoirs," paper presented at the 6th SPE Symposium on Reservoir Simulation in New Orleans, LA, Jan. 31-Feb. 3, 1982.
5. Huyakorn, P.S. and Pinder, G.: *Computational Methods in Subsurface Flow*, Academic, San Diego, CA (1983) 229-288.
6. Kazemi, H. *et al.*: "Numerical Simulation of Water-Oil Flow in Naturally Fractured Reservoirs," *SPEJ*, December 1976, 317-26, *Trans., AIME*, 261.
7. Peaceman, D.W.: "Interpretation of Well-Block Pressures in Numerical Reservoir Simulation," *SPEJ*, June 1978, 183-94, *Trans., AIME*, 265.
8. Putra, E. and Schechter, D.S.: "Numerical Simulation of a Waterflood Pilot in the Naturally Fractured Spraberry Trend," paper submitted at the 2nd Annual Technical Progress Report (DOE Contract No.: DE-FC22-95BC14942), PRRC Report No. 97-29.
9. Unger, D.J. and Aifantis, E.C.: "Notes: Completeness of Solutions in Double Porosity Theory," Acta Mechanica 75, 269-274 (1988).

10. Warren, J.E. and Root, P.J.: "The Behavior of Naturally Fractured Reservoir," *Soc. Petrol. Engr. J.* (Sept. 1963) 245-255; *Trans., AIME*, 228.

Table 3.7-1 —Model Parameter Employed

Young's modulus, psi	10^6
Poisson ratio	0.2
Fluid viscosity, cp	10
Initial pore pressure, psi	0
Initial stress, psi	0
Thickness, ft	50
Flow rate, B/D	100
No. of grid block in x-direction, ft	25(100 ft each)
No. of grid block in y-direction, ft	25(100 ft each)
Matrix rock compressibility, psi^{-1}	10^{-8}
Matrix bulk compressibility, psi^{-1}	10^{-6}
Matrix fluid compressibility, psi^{-1}	10^{-5}
Fracture rock compressibility, psi^{-1}	10^{-8}
Fracture bulk compressibility, psi^{-1}	10^{-6}
Fracture fluid compressibility, psi^{-1}	10^{-5}
Matrix porosity, fraction	0.1 or (0.1exp(-0.0004*dp))
Fracture porosity, fraction	0.01 or (0.01exp(-0.0004*dp))
Matrix permeability, mD	0.1 or (0.1exp(-0.0004*dp))
Fracture Spacing, ft	5
Fracture permeability in x-dir, mD	2.5 or (2.5exp(-0.0004*dp))
Fracture permeability in y-dir, mD	150 or (150exp(-0.0004*dp))

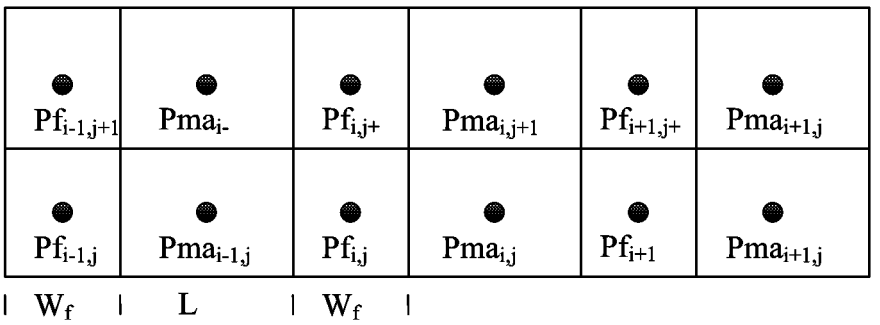

Fig. 3.7-1—Two-dimensional fracture-matrix idealization

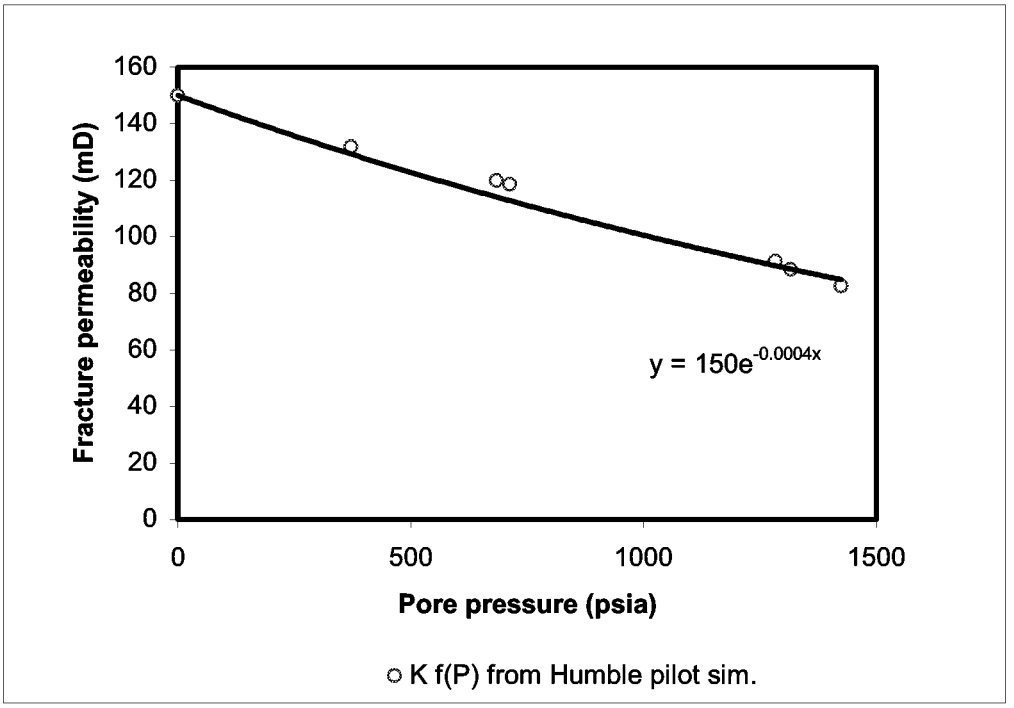

Fig. 3.7-2 —Permeability reduction curve as function of pore pressure obtained from Humble pilot simulation

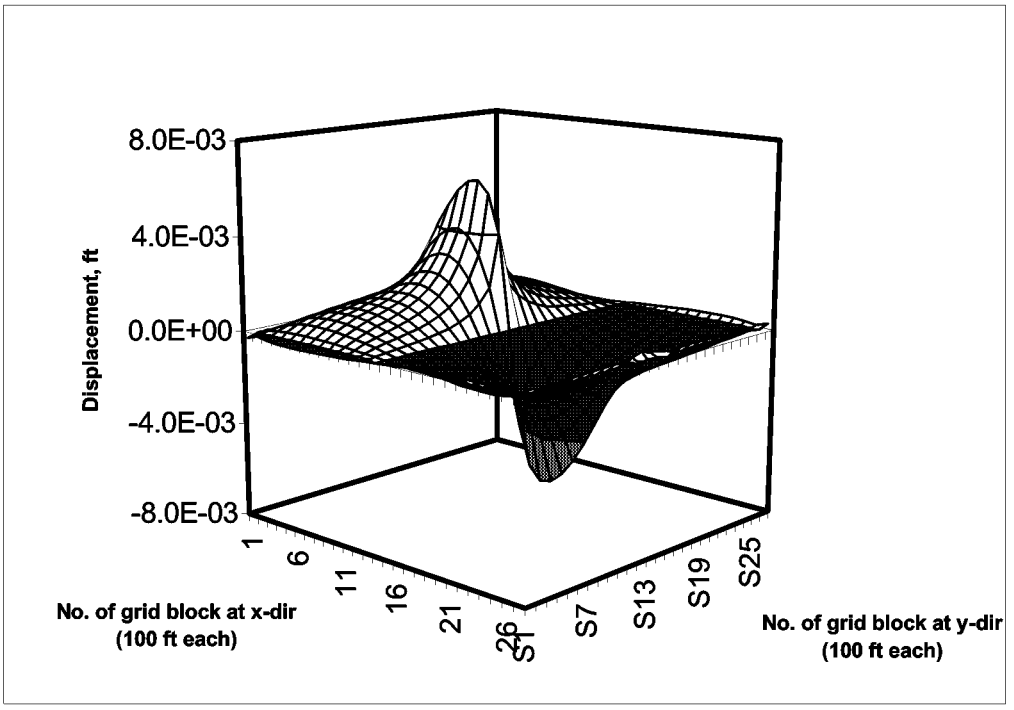

Fig. 3.7-3 —Solid displacement distribution in x-direction at 20 days

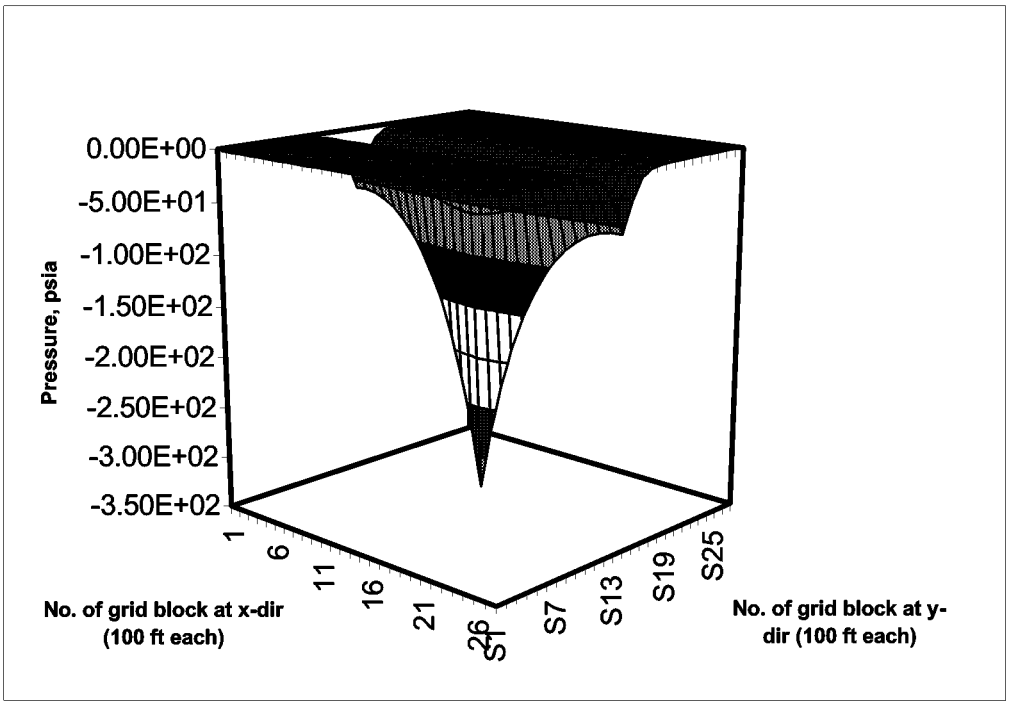

Fig. 3.7-4 —Fracture pressure distribution at 20 days

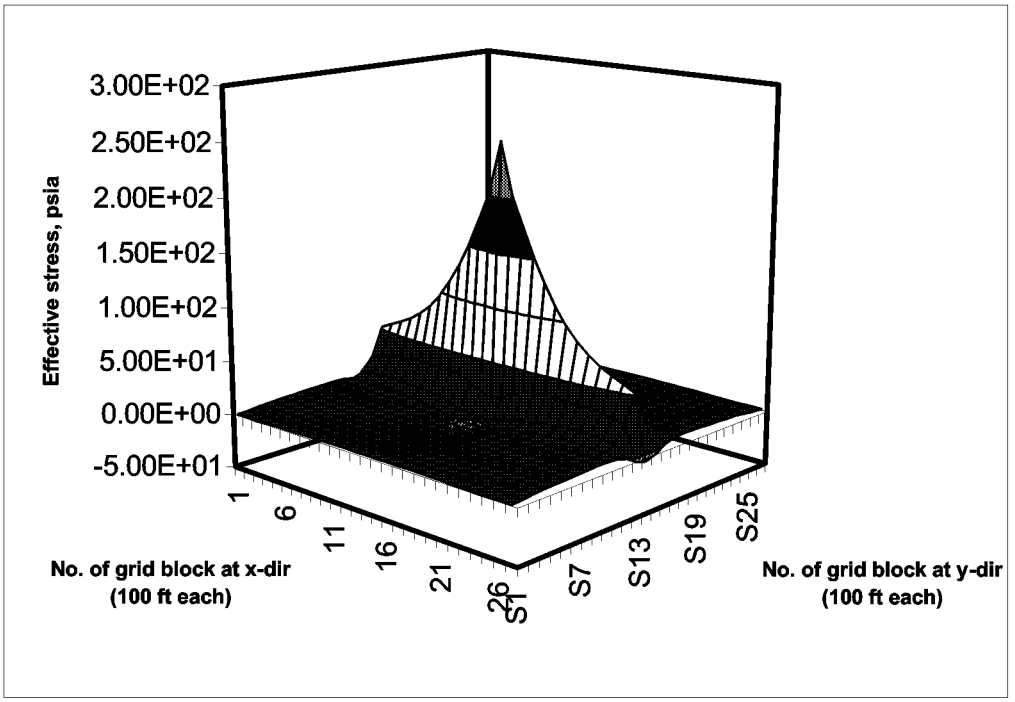

Fig. 3.7-5 —Effective stress distribution in x-direction at 20 days

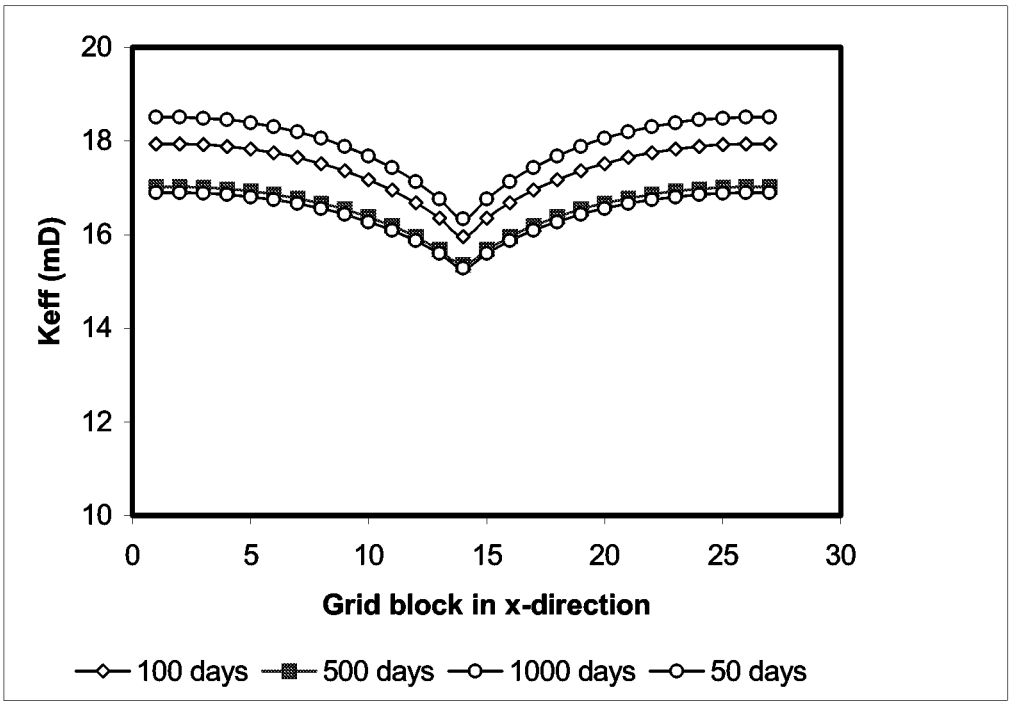

Fig. 3.7-6 —Reduction of effective fracture permeability at the grid blocks in the x-direction intersect through the grid block containing the well

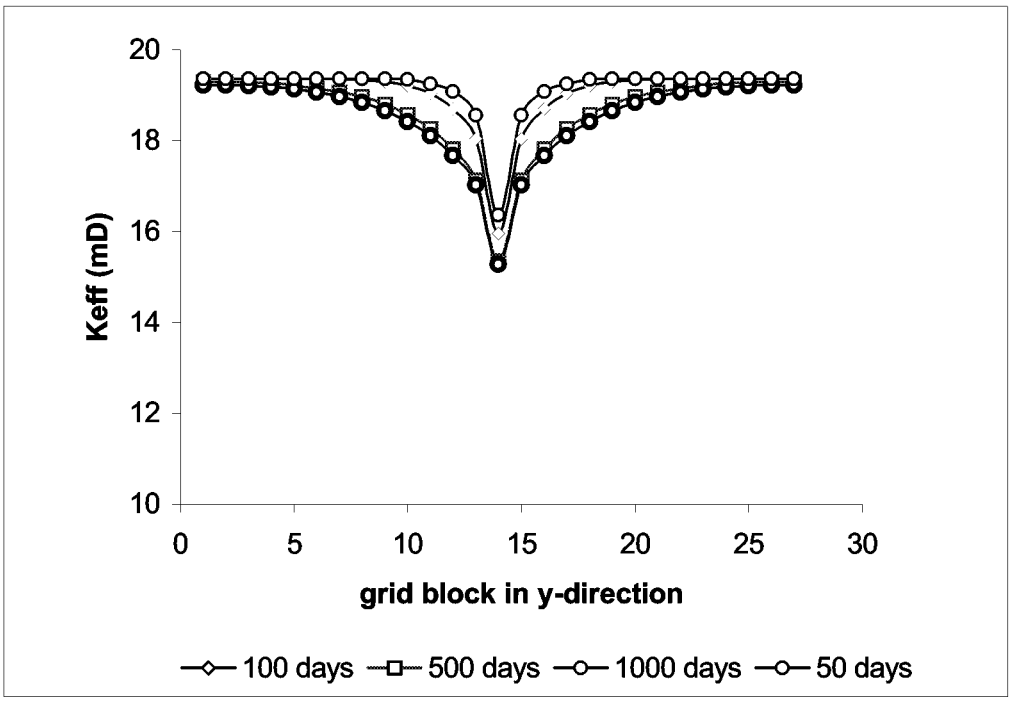

Fig. 3.7-7 —Reduction of effective fracture permeability at the grid blocks in the y-direction intersect through the grid block containing the well

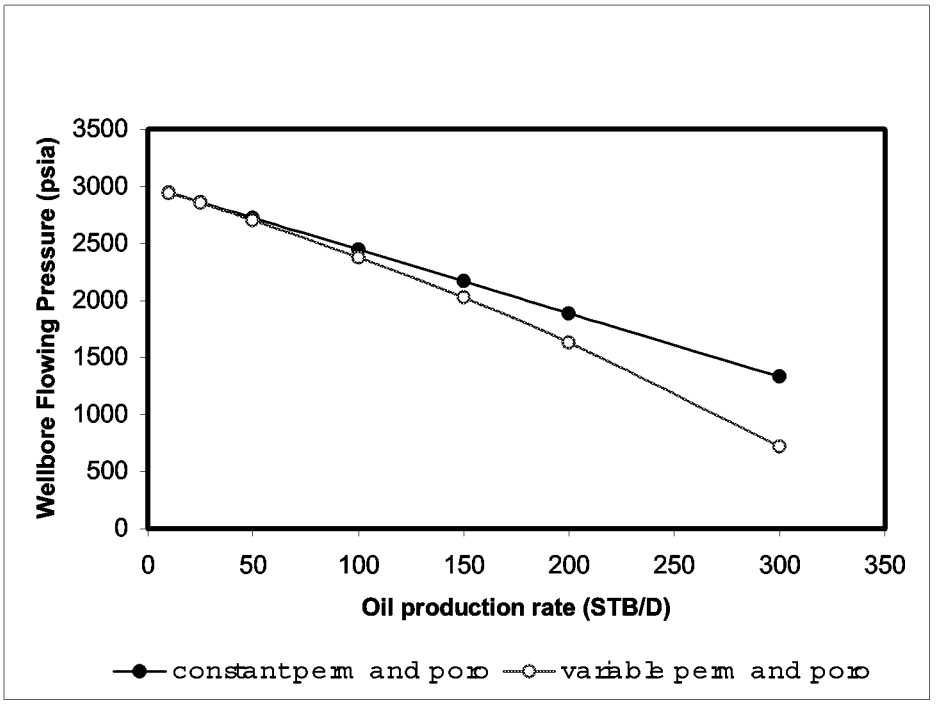

Fig. 3.7-8 —Flow rate as a function of bottomhole pressure from the conventional dual-porosity simulator

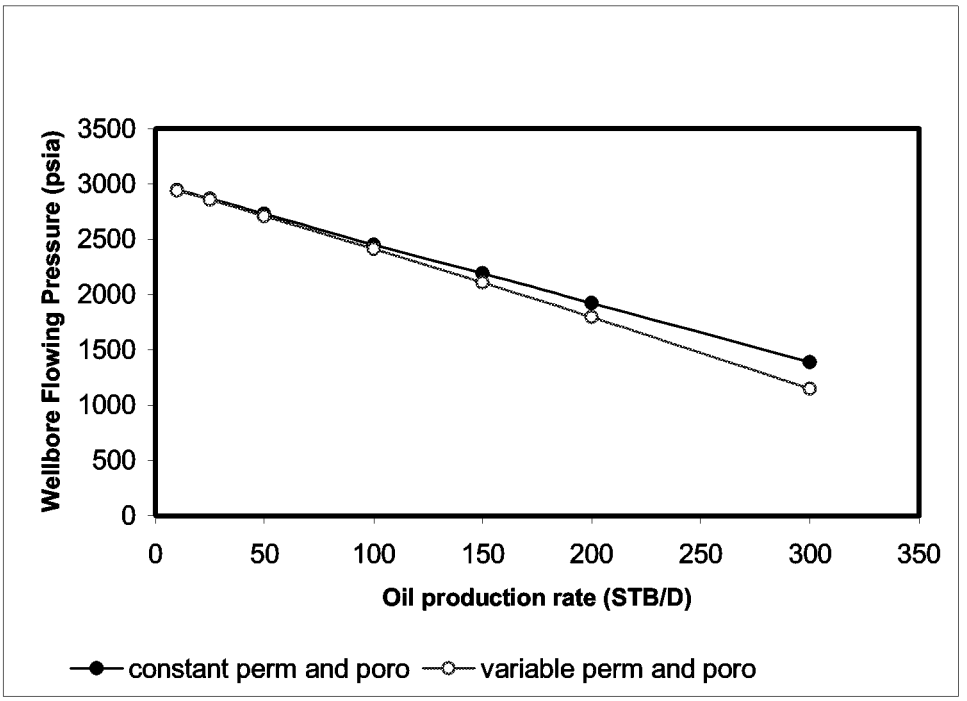

Fig. 3.7-9 —Flow rate as a function of bottomhole pressure from the stress dual-porosity simulator

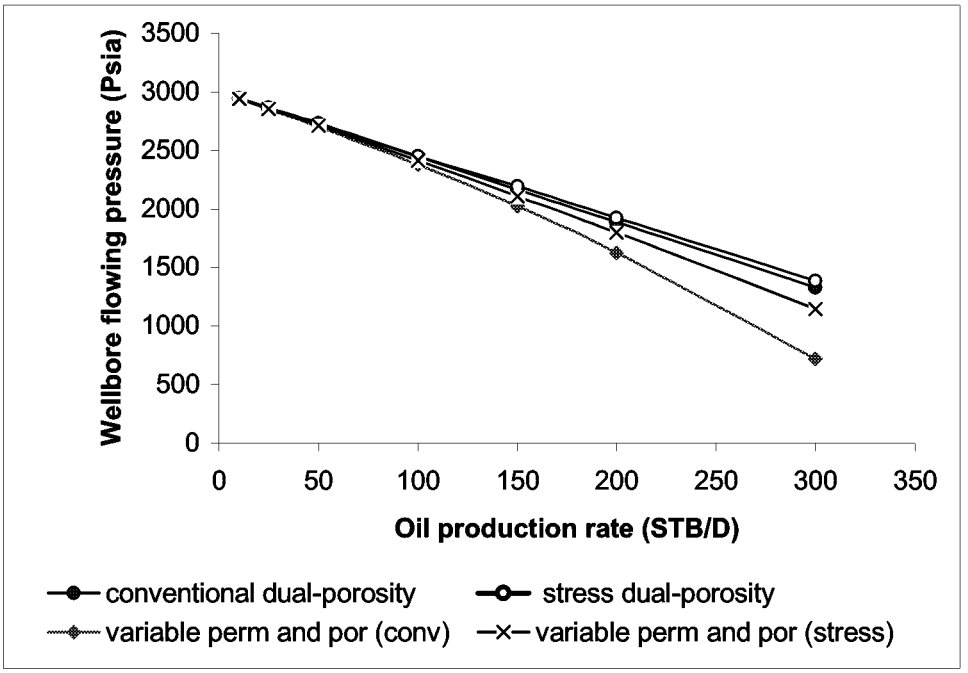

Fig. 3.7-10 —Comparison of performance between conventional and stress dual-porosity simulators

3.8 INTERFERENCE TEST ANALYSIS IN E.T. O'DANIEL PILOT

Introduction

Considerable work has been done to establish a reasonable technical basis for expecting that CO_2 injection may improve recovery from fractured Spraberry reservoirs. The work includes selecting a pilot area, characterizing reservoir properties, and designing and installing pilot facilities. Prior to the implementation of the CO_2 flood, several single well and multi-well pressure tests were conducted in a 60-acre pilot area of the E.T. O'Daniel Unit (Fig. 3.8-1). These included constant pressure decline rate tests, buildup tests, step-rate injection tests (SRIT), falloff tests and multi-well interference tests. The tests have been used to determine permeability, skin, fracture connectivity, average reservoir pressure, formation parting pressure and orientation of maximum permeability.

Production data for several vertical wells were analyzed using a decline analysis technique.[1] Peak production rates ranged from 20 to 90 BOPD.

Buildup tests to the E.T. O'Daniel wells 38, 39, and 40 were performed prior to the SRIT. The tests showed that the effective permeability ranges from 0.01 to 0.03 mD, with skins of –4.5 to –5.6. The average reservoir pressure was approximately 1300 psia. No classic dual porosity behavior was noted.[1] The signature of classic dual porosity shows two parallel semilog straight line on a semilog plot, where first straight line shows a response from fracture system only and second straight line shows a response from a total system (fracture and matrix).

Step-rate injection tests were conducted in the new injection wells O'Daniel 46 and 47. The tests indicate that the fractures are very stress- and pressure-sensitive.[1,2] The parting pressure occurred at 3017 psia when injection rates were at 200 bbl/d. This pressure is reached during the first injection rate, and subsequent higher injection rates merely extend the fracture length.[1,2] As the fracture becomes longer and perhaps intersects more of the natural fracture system, the total response of the system becomes that of the natural fracture system.

A falloff test was conducted after the SRIT to determine effective permeability and waterflood-induced fracture characteristics. The falloff test showed effective water permeability ranged from 2.6 to 14 mD, with a fracture half-length of 73 ft.[1]

The interference tests were conducted to test communication of the 1U and 5U between the wells. The test could provide information about direction and degree of permeability. The main objective of the interference test performed in the E.T. O'Daniel pilot area is to determine the location of well candidates for CO_2 injectors. The interference test consisted of sequential injection of 2000 BWPD in wells 47, 45, 25 and 48. Water was injected for four to five weeks into one well at a time, with a field stabilization period (two to three weeks) between each injection period. The bottomhole pressure response was observed at wells 38, 39, and 40. The bottomhole profile at each of the observation wells is shown in Fig. 3.8-2.

This report describes the schematic procedures used to analyze the interference test by diagnostic plots and the calculation methods using two observation wells. The results from this study reveal that the E.T. O'Daniel pilot area exhibits both isotropic and anisotropic behavior, depending on the degree of permeability ratio calculated at a particular position within the pilot area.

Data Analysis

This section describes the methods used to interpret the interference test. Two methods are used to analyze the interference test, the diagnosis plot and the calculation methods.
In order to analyze the interference test by the diagnosis plot, the pressure change (Δp) against normalized time (t/r^2) from all observation wells are plotted on log-log curves in the same graph (Fig. 3.8-3). The well coordinates are transformed based on reference point (0,0) as shown in Table 3.8-1. The active well or injection well serves as a reference point. The normalized time is used to eliminate the effect of differing distance between monitoring wells. All the pressure responses are compared to obtain a qualitative idea about the existence of anisotropy.

The pressure responses show that this reservoir behaves as a homogeneous and anisotropic reservoir in which the pressure responses will superimpose if those responses are shifted horizontally. Even though the Spraberry field is well known as a naturally fractured reservoir, no dual porosity masks are indicated from the pressure responses. It is probable that the pressure responses were still in the earlier time (only from fractures) or had reached the later time, where responses were from fissures and matrix.

The magnitude of permeability anisotropy is shown by the magnitude of separation of pressure responses of those observation wells. In the homogeneous isotropic reservoir case, those three pressure responses will superimpose for all wells, which the means same Δp-match (i.e., same transmissivity, $\frac{k_e h}{\mu}$) and the same t/r^2-match (i.e., same diffusivity, $\frac{k_r}{\mu\phi c}$) for all wells.
Anisotropic analysis requires pressure data from at least two observation wells located on different straight lines to the active well. In order to analyze the responses using two observation wells, the value of porosity and compressibility are required.

The model assumes that there are two values of permeability, denoted by k_{max} and k_{min}, and they are perpendicular in direction. The pressure responses from an anisotropic reservoir will be the same for the Δp-match, which means the same average permeability for all wells, but different for the t/r^2-match, which reflects the different interwell permeability, k_r. The larger the k_r, the quicker the response.

Knowledge of directional permeability obviously would have important effect on planning reservoir development, particularly for fluid injection operations. The pressure

responses against normalized distance from observation well as shown in Fig. 3.8-4 indicates that the maximum permeability trend measured from reference point (well 47) would be in the direction of well 39. The quicker the pressure response, the higher the permeability. No pressure response due to water injection is observed in well 38. Therefore only two pressure responses, wells 39 and 40 will be used in analyzing the interference test. Also only two pressure responses are observed during subsequent injection performed in wells 45 and 25, as shown in Fig. 3.8-4. A similar diagnosis is applied for observation wells with difference active wells (injector). The diagnosis indicates that the maximum permeability trends are expected to be in the direction of well 38 with injector 45 and of well 39 with injector 25.

Only one pressure response from observation well 38 was recorded during injection performed in well 48. Therefore neither diagnosis nor calculation is possible for the response with injection in well 48.

In analyzing the interference test by the calculation method, the method used in this study is similar to that used in a study conducted by Ramey[3] (1975) based on infinite-acting and homogeneous assumptions. This report presents procedures for using an interference type-curve in a form readily useable for interference test analysis. The pressure response of a heterogeneous reservoir at an early time is different from that of a homogeneous reservoir since the pressure response in a heterogeneous reservoir is a result of the fractures. The same phenomenon occurs with pressure response at the wellbore where wellbore storage exists. After the system is filled, the pressure response will be the same as in the homogeneous reservoir case. Therefore, the late time data will be selected to undergo further analysis.

The analysis of the interference test is performed by type-curve matching against analytical techniques based on the line source solution in a homogeneous anisotropic infinite reservoir (Fig. 3.8-5). The dimensionless form of the line source solution for pressure at any location and time can be written as follows[3-5]:

$$p_D = -\frac{1}{2} Ei(-r_D{}^2 / 4t_D) \quad \text{.....(3.79)}$$

where the dimensionless pressure drop, p_D, and the dimensionless time, $t_D / r_D{}^2$ are defined as:

$$p_D = \frac{k_e h[p_i - p(r,t)]}{141.2 q \mu B} \quad \text{.....(3.80)}$$

$$\frac{t_D}{r_D{}^2} = \frac{0.0002637 k_r t}{\mu \phi c_t r^2} \quad \text{.....(3.81)}$$

where the average permeability, k_e, and the interwell permeability, k_r are defined as

$$k_e = \sqrt{k_{max} k_{min}} = \sqrt{k_{xx} k_{yy} - k_{xy}^2} \quad \text{.....(3.82)}$$

$$\frac{1}{k_r} = \frac{\cos^2 \theta}{k_{max}} + \frac{\sin^2 \theta}{k_{min}} = \frac{1}{r^2}\left(\frac{x^2}{k_{max}} + \frac{y^2}{k_{min}}\right) \quad \text{.....(3.83)}$$

$$= \frac{1}{r^2}\left(\frac{k_{yy} x^2 + k_{xx} y2 - 2k_{xy} xy}{k_{xx} k_{yy} - k_{xy}^2}\right) \quad \text{.....(3.84)}$$

The pressure data from three observed wells are analyzed by type-curve matching data to the line source solution with a log-log type curve. The type-curve matching is accomplished by placing the exponential-integral curve on top of the observed data. Then, the exponential-integral curve is moved horizontally with the axes of both graphs kept parallel until the best-match fit is obtained between the observed data and the type curve. A match point is chosen and the reservoir properties are calculated by using the procedure as described below.

Three equations and three unknowns, as can be seen in step 5 below, are solved using the Newton-Raphson method with tolerance of 1.e-5 and maximum iteration of 100 times. A computer program for this procedure is given in Appendix-A. The best match is chosen by how well each of the two curves fit the type curve (Table 3.8-2). Using well reservoir data from E.T. O'Daniel pilot (Table 3.8-3), the anisotropic permeability ratio and directional maximum permeability are obtained as shown in Table 3.8-4.

Procedures of Interference Testing for Homogeneous Anisotropic Reservoir Using Two Observations Wells

After matching the exponential integral curve to the observed data, the calculation was made to estimate the direction and degree of permeability by the following procedures:

1. Plot log-log curve, Δp vs. time (same scale as the type-curve), for each observation well j
2. Perform type-curve matching and obtain pressure and time matches for each observation well:

$$\left[\frac{p_D}{\Delta p}\right]_{Mj} \quad \text{and} \quad \left[\frac{t_D / r_D^2}{t}\right]_{Mj}$$

3. Estimate average and radial-directional permeability from pressure and time-distance matches, respectively. Value of porosity and compressibility are required.

$$k_{ej} = \frac{141.2qB\mu}{h}\left[\frac{p_D}{\Delta p}\right]_{Mj} \quad \text{.....(3.85)}$$

$$k_{rj} = \frac{\mu\phi c}{0.0002637} r_j^2 \left[\frac{t_D / r_D^2}{t}\right]_{Mj} \quad \text{.....(3.86)}$$

4. Choose a representative value or take an average value for k_e for all observation wells (N is number of observation wells).

$$k_{ej} = \frac{\sum k_{ej}}{N} \quad \text{.....(3.87)}$$

5. Set up the following equation for two observation wells,

$$y_1^2 k_{xx} + x_1^2 k_{yy} - 2x_1 y_1 k_{xy} = r_1^2 k_e^2 / k_{r1} \quad \text{.....(3.88)}$$

$$y_2^2 k_{xx} + x_2^2 k_{yy} - 2x_2 y_2 k_{xy} = r_2^2 k_e^2 / k_{r2} \quad \text{.....(3.89)}$$

$$k_{xx} k_{yy} - k_{xy}^2 = k_e^2 \quad \text{.....(3.90)}$$

Use Newton-Raphson method to solve three equations above.

6. Compute maximum and minimum permeabilities using the permeability components obtained from step 5.

$$\left.\begin{matrix} k_{max} \\ k_{min} \end{matrix}\right\} = \frac{k_{xx} + k_{yy}}{2} \pm \sqrt{\left(\frac{k_{xx} - k_{yy}}{2}\right)^2 + k_{xy}^2} \quad \text{.....(3.91)}$$

7. Determine the orientations of maximum and minimum permeabilities. First, determine two values α from the following equation.

$$tan\ 2\alpha = 2k_{xy} /(k_{xx} - k_{yy}) \quad \text{.....(3.92)}$$

These two angles are 90° apart, one between 0 and 90° and the other between 90 and 180°. One is α_1 (the angle associated with k_{max}) and the other is α_2 (associated with k_{min}). α_1 is the one satisfying both of the following two equations.

$$\cos 2\alpha_1 = (k_{xx} - k_{yy})/(k_{max} - k_{min}) \quad \text{.....(3.93)}$$

$$\sin 2\alpha_1 = 2k_{xy}/(k_{max} - k_{min}) \quad \text{.....(3.94)}$$

Results and Discussions

Using the overlay technique and procedures as discussed above, the pressure responses at observation wells with injection in well 47 and 45 show good agreement with the calculation result shown in Fig. 3.8-6 and 3.8-7. Therefore, the results obtained from this calculation can be used to estimate the ratio and direction of permeability anisotropy of the E.T. O'Daniel pilot from those particular reference points. However, the matching effort for the observation wells with injection in well 25 cannot be obtained. It is probable that the pressure responses from the observation wells, 39 and 40, are still in the early and transition times. Thus, this method cannot be applied to this kind of response. No calculation is made for the observation wells with injection in well 48. In this case, the pressure response is only from well 38, while no response is recorded from wells 39 and 40.

The permeability ratio with injection in well 47 and 45 obtained using this procedure is 1.87 and 69.5, respectively. The orientation of maximum permeability from reference points of well 47 and 45 is 10° EN and 38° EN, respectively, as shown in Figs. 3.8-8 and 3.8-9. Previous studies of injection profiles showed 70 per cent in 5U and 30 per cent in 1U and horizontal cores showed direction of maximum permeability is average of 20° EN in 5U and 47° EN in 1U.[2] The permeability ratio can indicate the permeability distribution of the reservoir. The permeability ratio at reference point of well 47 is low; thus, the location can be considered isotropic. On the other hand, at the reference point of well 45, the permeability ratio is about 69.5, thereby demonstrating anisotropic behavior. From this analysis, the CO_2 injection wells should be aligned to the maximum permeability of 10° from the reference point of well 47 and 38° EN from the reference point of well 45.

Conclusions

1. The pressure responses from the interference testing indicated that this pilot exhibits both homogeneous isotropy and anisotropy depending on the degree of permeability ratio calculated at a particular position. At the reference point of well 47 the reservoir shows isotropic behavior while at reference point of well 45 the reservoir is anisotropic.
2. The homogeneous reservoir procedure can be used to analyze interference tests in heterogeneous reservoirs if utilizing the late time data for the calculation.
3. The CO_2 injection wells should be aligned to the maximum permeability of 10° from the reference point of well 47 and 38° EN from the reference point of well 45.

Nomenclature

B = formation volume factor, rb/stb
c_t = total compressibility, 1/psia
Ei = exponential integral
h = formation thickness, ft
k = permeability, md
k_e = average permeability, md
k_r = interwell permeability, md
k_{xx}, k_{yy}, k_{xy} = components of permeability tensor, md
k_{max}, k_{min} = maximum and minimum principal permeability, respectively, md
$(p_D)_M$ = dimensionless pressure at the match point for the type-curve analysis, psi
$(\Delta p)_M$ = pressure change at match point for the type-curve analysis, psi
q = flow rate, stb/d
r = distance between wells, ft
t = time, hour
t_D = dimensionless time = $0.0002637 \dfrac{k_r t}{\phi \mu c r^2}$
$(t_D / r_D^2)_M$ = dimensionless time at the match point for the type-curve matching
$(t)_M$ = time at match point for the type-curve analysis, hours
α = angle, degrees
μ = viscosity, cp
ϕ = porosity, fraction

References

1. Baker, R., Contreras, R.A., and Sztukowski, D.: "Characterization of the Dynamic Fracture Transport Properties in a Naturally Fractured Reservoir," paper SPE 59690 presented at the 2000 SPE Permian Basin and Gas Recovery Conference, Midland, Texas, 21-23 March.
2. Schechter, D.S: "Advanced Reservoir Characterization and Evaluation of CO_2 Gravity Drainage in the Naturally Fractured Spraberry Trend Area," Fourth Annual Technical Progress Report to DOE under contract No.: DE-FC22-95BC14942, U.S. DOE (October 1999).
3. Ramey, H.J., Jr.: "Interference Analysis for Anisotropic Formations - A Case History," *JPT* (Oct. 1975) 1290-1298; Trans., AIME, **259**.
4. Kamal, M.M.: "Interference and Pulse Testing - A Review," *JPT* (Dec. 1983), 1525.
5. Earlougher, R.C. Jr.: Advances in Well Test Analysis, Monograph Series, SPE, Richardson, Texas (1977).

Appendix A - A computer program to solve interference testing with two observation wells.

```
clear all
clg
load d:\project\welltest\inj47.txt;
hrs=inj47(:,1);
well39=inj47(:,6);
well40=inj47(:,7);
%
%     Input Parameters
 B=1.008;                  % factor volume formation, RB/STB
 vis=0.472;                % water viscosity, cp
 rw=0.33;                  % well radius, ft
 s=0.;                     % skin factor
 h=33;                     % thickness of injection well
 por=0.10;                 % porosity, %
 d=pi/180;                 % conversion to radian
 q=2000;                   % injection rate, STB/D
 ti=1;
 tf=1000;
% well position
%     w39   w40
 x =[-492   197  ];
 y =[-1319  -591 ];
 r =[1408    622 ];

% Matched Points, (1)=w39, (2)=w40
     tm(1) =9.8455e3;    tD(1) = 2; pm(1) = 50; pD(1)=1e-2;
   tm(2) =0.9745e4;    tD(2) = 9; pm(2) = 50; pD(2)=1e-2;

 % input/output via menu
  meth = menu ('Choose well is being plotted',...
  'Well-39',...
  'Well-40');
   if meth ==1, w=1; end
   if meth ==2, w=2; end
disp('please wait, the plot is being generated...');
%

  close all
  for i = 1:2
     ke(i)=141.2*q*B*vis*pD(i)./(h*pm(i));
     end
     keave=(sum(ke))./2;

% storage (por*Ct*h) as input data
```

```
%*************************
     storage=3.1e-5;
%*************************

for i=1:2
   Kr(i)=(vis*storage/h)*r(i).^2/0.0002637*tD(i)/tm(i);
       rhs(i)=r(i).^2.*keave^2./Kr(i);
     end

  % Newton Raphson Method
    NN=100;
    tol=1.e-5;
    g=[2 2 2]';
  % compute J(x)
    jj=1; kk=2;
    disp(' ');
    disp('   Iteration No.   Kxx      Kyy      Kxy');
    disp('   ------------------------------------');
    for iter=1:NN
     J=[y(jj).^2   x(jj).^2   -2*x(jj)*y(jj)
        y(kk).^2   x(kk).^2   -2*x(kk)*y(kk)
        g(2)      g(1)      -2*g(3)];

% compute -F
     F=[-(y(jj).^2*g(1)+x(jj).^2*g(2)-2*x(jj)*y(jj)*g(3)-
rhs(jj))
        -(y(kk).^2*g(1)+x(kk).^2*g(2)-2*x(kk)*y(kk)*g(3)-
rhs(kk))
        -(g(1)*g(2)-g(3).^2-keave.^2)];

     Y=inv(J)*F;
% R = Infinity norm of Y
    R=0;
    if (abs(Y) > R) R=abs(Y);
     g=g+Y; end
     if(R < tol)
     break, end
     disp([iter, g']);
    end
    if iter==NN
    disp('Linear System has no solution');
    break, end
 Kxx=g(1);
 Kyy=g(2);
 Kxy=g(3);
```

```
      Kmax = (Kxx+Kyy)./2+(((Kxx-Kyy)./2).^2+Kxy.^2).^0.5;
      Kmin = (Kxx+Kyy)./2-(((Kxx-Kyy)./2).^2+Kxy.^2).^0.5;

      alpha = 0.5*atan(2*Kxy./(Kxx-Kyy))*1/d;
      alpha1=0.5*acos((Kxx-Kyy)/(Kmax-Kmin))*1/d;
      alpha11=0.5*asin(2*Kxy./(Kmax-Kmin))*1/d;
      alpha2=atan((Kmax-Kxx)/Kxy)*1/d;

      theta(1)=atan(y(1)/x(1))*1/d+alpha;
      theta(2)=atan(y(2)/x(2))*1/d+alpha;

      c1=141.2*B*vis./(keave*h);
   %  Do superposition
          time=ti:2:tf;
            kr=
1/((cos(theta(w))).^2/Kmax+(sin(theta(w))).^2/Kmin);
            tD =0.0002637*kr*time./(vis*storage/h*rw*rw);
            rD =r(w)/rw;
            y1=tD./rD.^2;
            dp=c1*q*0.5*expint(1./(4*y1));
% Print results
  disp(' ');
  disp('  Output for Anisotropy Permeability');
     disp('       2 wells combination');
     disp(' -------------------------------');
     disp('   Storage Term ');
     disp( storage);
     disp('   Kxx        Kyy      Kxy');
     disp([Kxx; Kyy ; Kxy;]');
     disp('   Kmax       Kmin');
     disp([Kmax; Kmin;]');
     disp('   Angle of Max. Permeability');
     disp(alpha);
%
     if w==1,  w=well39; well='well 39'; end
     if w==2,  w=well40; well='well 40'; end
% Plot results
  loglog(hrs,w,'o',time,dp,'+');
  title(['Matching of Pressure Response for
',num2str(well)]);
  legend('observed data', 'simulated data');
  xlabel('Injection Time, hrs');
  ylabel('Pressure Response, Psia');
  text(1000,1000,'2 wells combination');
  axis([1 10000 1 10000]);
```

Table 3.8-1 —Well Coordinates

Well	Injection in Well-47 (0,0)		Injection in Well-45 (0,0)		Injection in Well-25 (0,0)	
	x	y	X	y	x	y
38	-1201	-2047	630	-197	-2018	-1250
39	-492	-1319	1329	531	-1319	-531
40	197	-591	2028	1240	-630	177

Table 3.8-2 —Time and Pressure Matches from Exponential-Integral Curve and Observed Data

Injection Well	Observation Well	t_D/r_D^2	t	p_D	Δp
47	39	2	9845.5	0.01	50
	40	9	9745	0.01	50
45	38	100	92500	0.01	9
	39	100	59200	0.01	9
25	39	-	-	-	-
	40	-	-	-	-

Table 3.8-3 — Well Reservoir Data from E.T. O'Daniel Pilot

Total thickness (ft)	33
Water viscosity (cp)	0.472
Porosity (%)	10
Water FVF (bbl/stbw)	1.008
Total compressibility (psi^{-1})	9.5e-6
Welbore radius (ft)	0.33 ft
Average injection rate (BWPD)	2000

Table 3.8-4 —Interference Test Results

Parameter	Injector		
	Well-47	Well-45	Well-25
K_{xx}	1.0961	23.4948	-
K_{yy}	0.6120	14.7683	-
K_{xy}	0.0876	18.0696	-
K_{max}	1.1115	37.7205	-
K_{min}	0.5966	0.5426	-
α	9.95°	38.2°	-

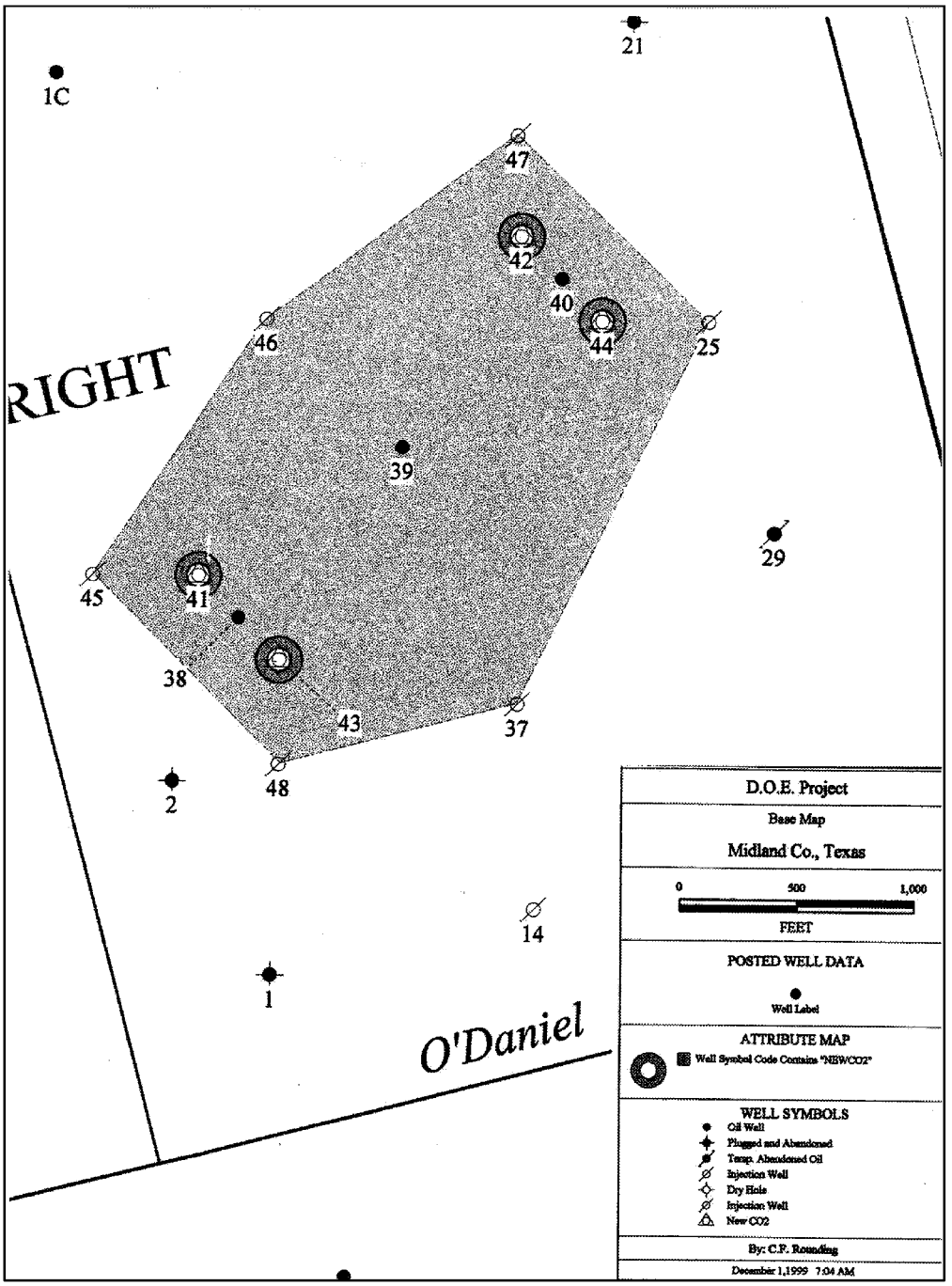

Fig. 3.8-1 —Well configuration in E.T. O'Daniel pilot, Spraberry Trend Area, west Texas

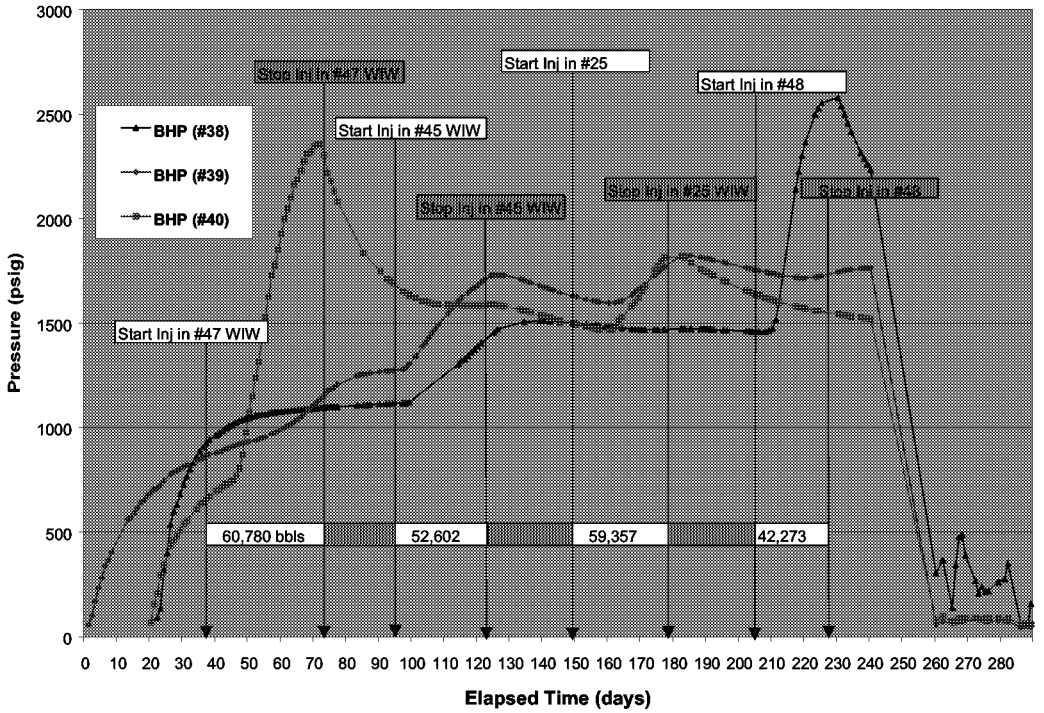

Fig. 3.8-2 —E.T. O'Daniel pilot producers BHPBU overlay during pulse and interference tests

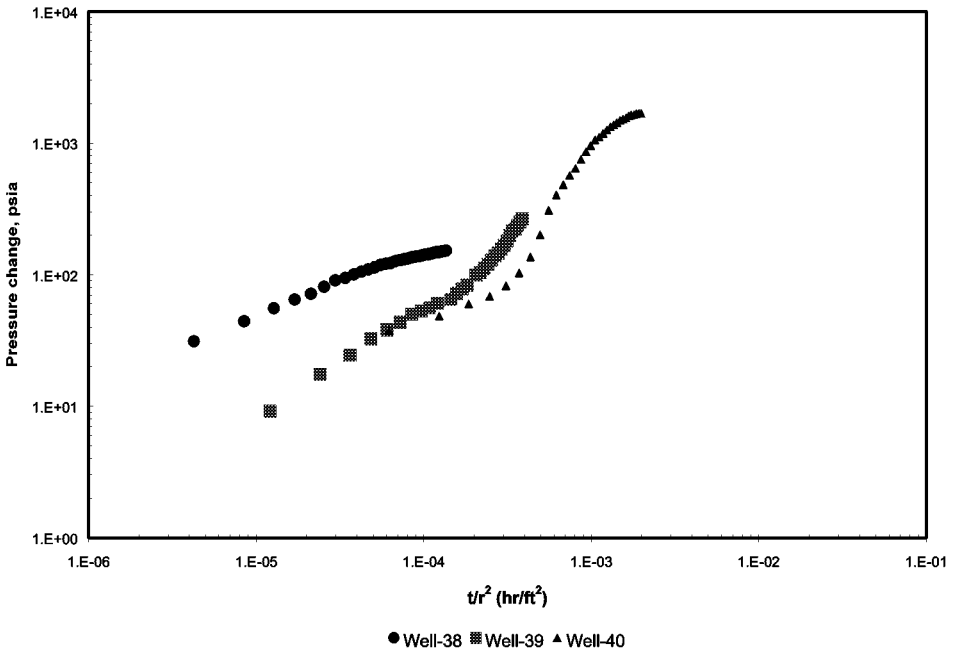

(a)

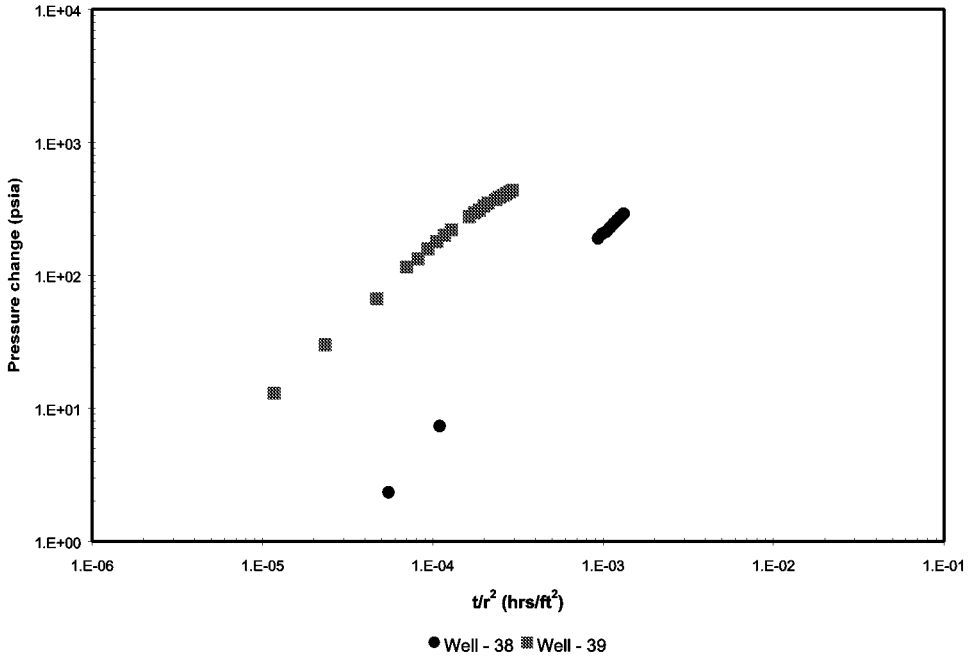

(b)

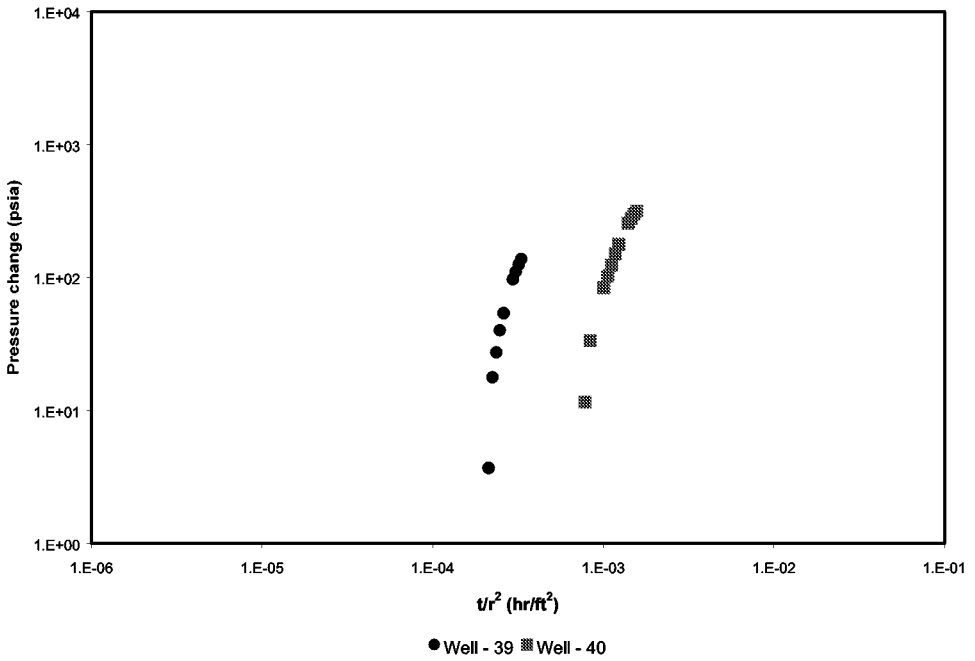

(c)

Fig. 3.8-3 —The pressure responses against normalized distance from observation wells for diagnosis plot (a) injection in well 47 (b) injection in well 45 (c) injection in well 25

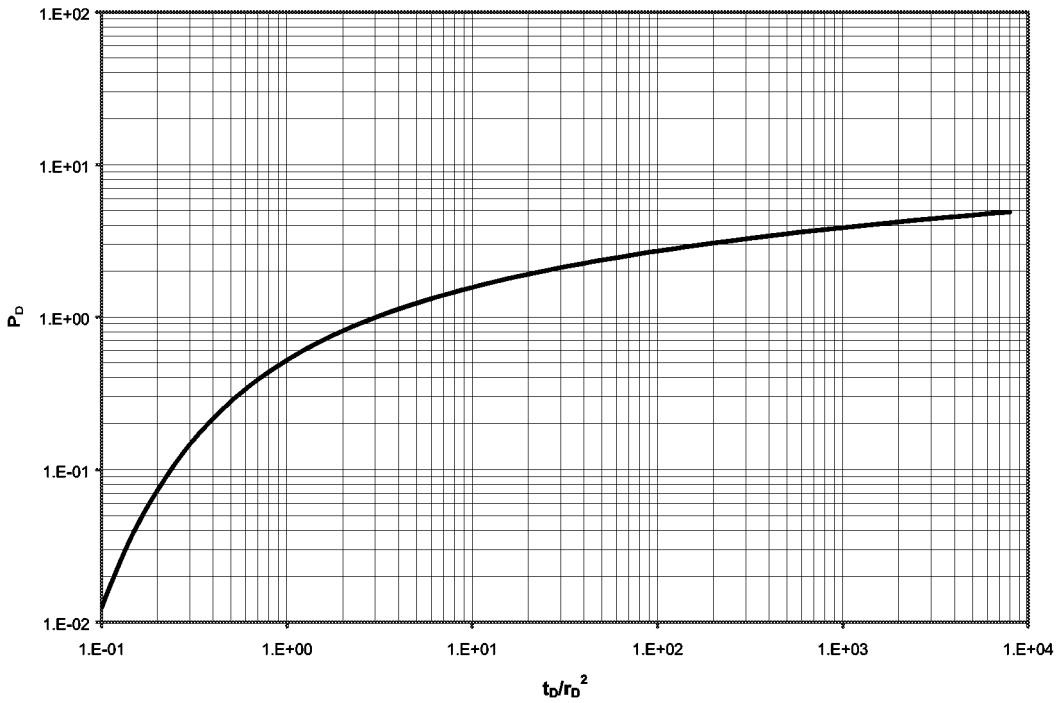

Fig. 3.8-4 —Dimensionless pressure for a single well in an infinite system, no wellbore storage and skin (line source solution)

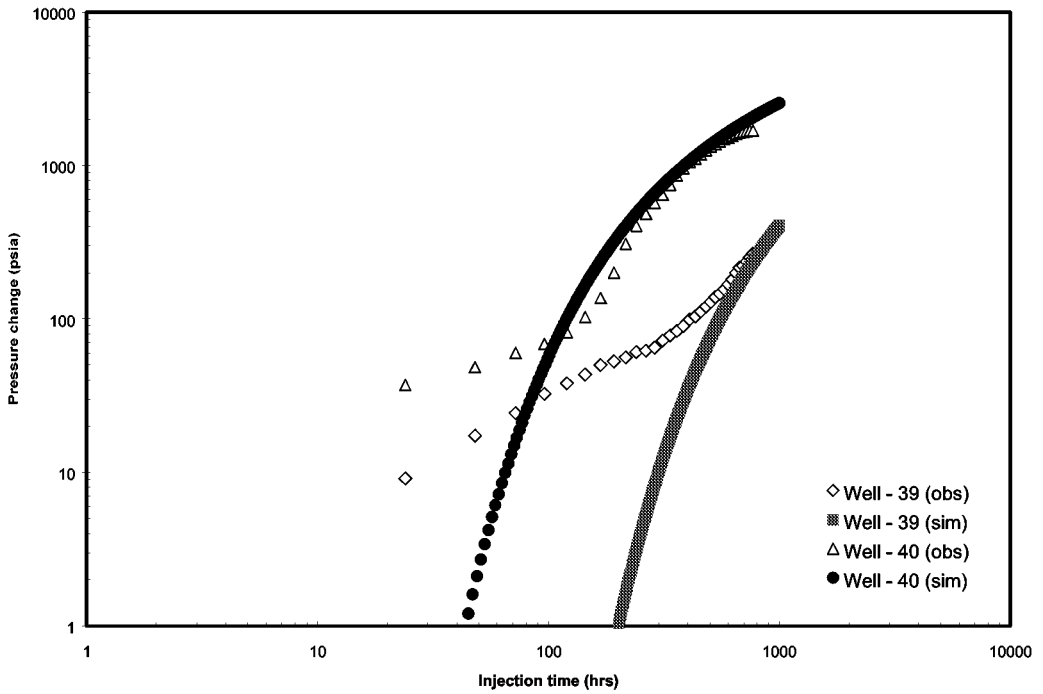

Fig. 3.8-5 —Type curve matches of data from observed wells (injection in well 47) and the line source solution

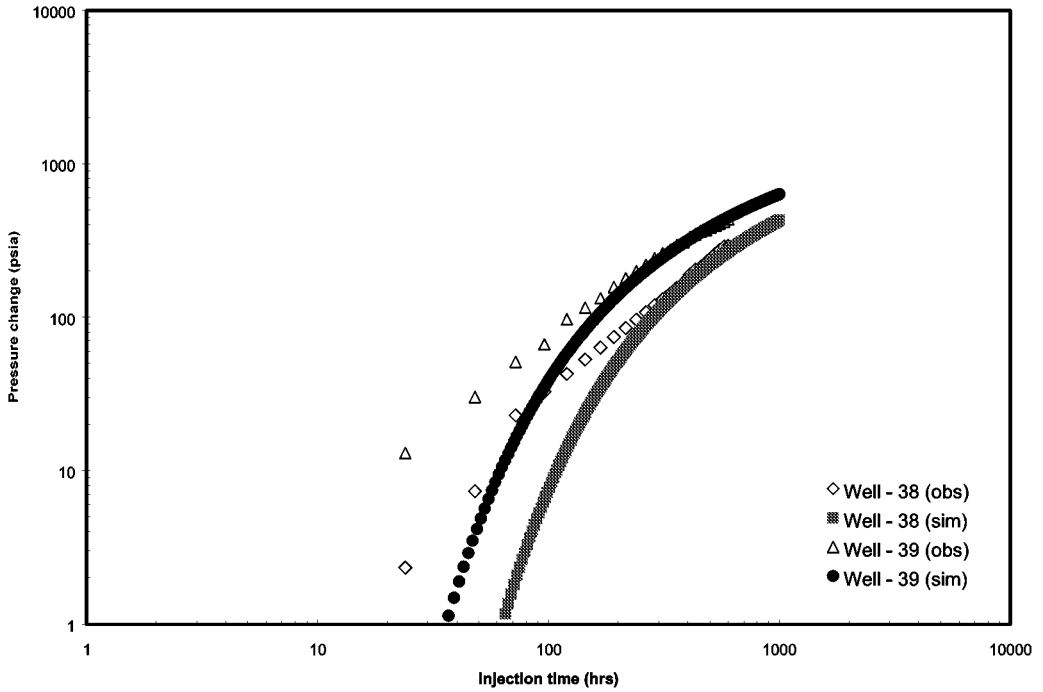

Fig. 3.8-6 —Type curve matches of data from observed wells (injection in well 45) and the line source solution.

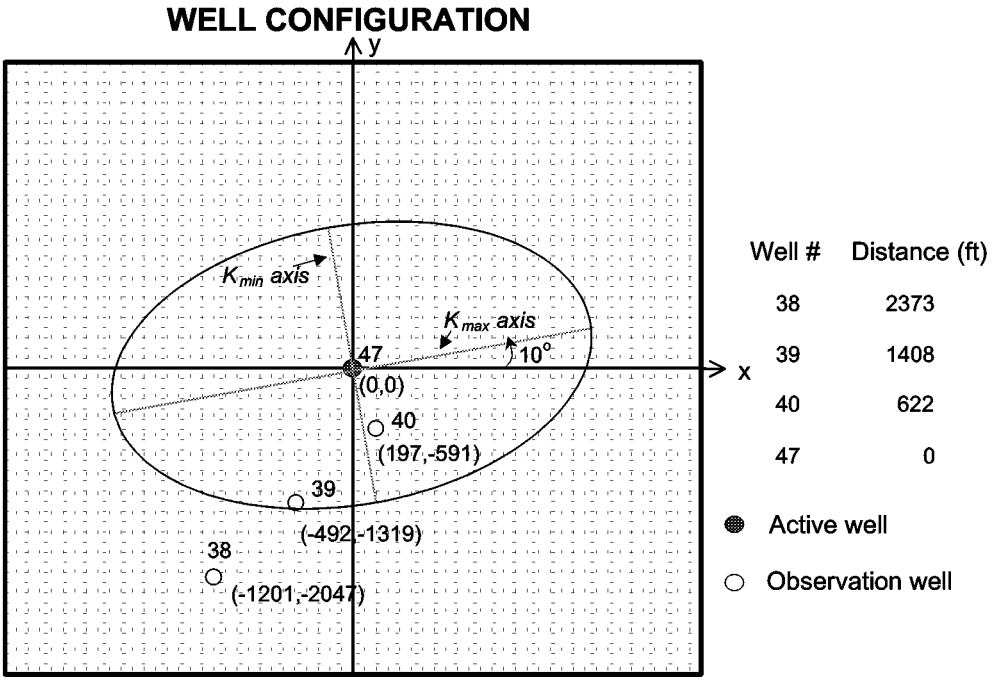

Fig. 3.8-7 —The anisotropic trend estimated from active well 47 is N65W after 15° adjustment to true north

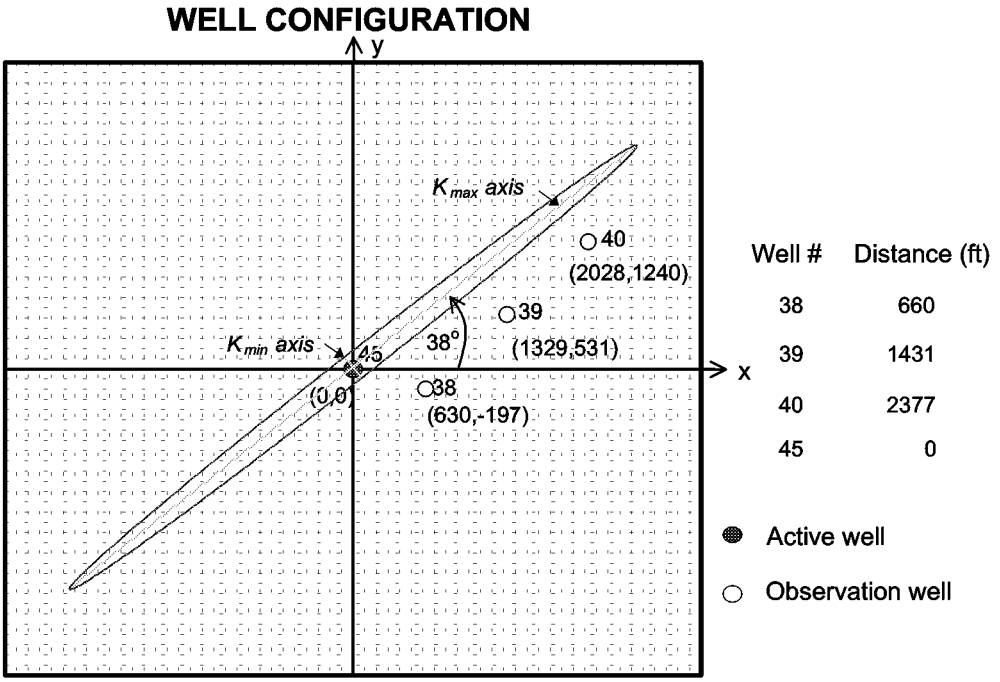

Fig. 3.8-8 —The anisotropic trend estimated from active well 45 is N37W after 15° adjustment to true north

3.9 CHARACTERIZATION OF THE DYNAMIC FRACTURE TRANSPORT PROPERTIES IN THE SPRABERRY TREND AREA

Introduction

In characterizing and modeling the performance of naturally fractured reservoirs (NFR), fracture length and fracture connectivity (permeability) are often assumed to be constant. A number of field tests done on Spraberry Trend wells suggest this assumption is *not* always true for NFR.

Pressure transient tests and decline analyses have been used to determine permeability, skin, connectivity of the fracture system and average reservoir pressure for the Spraberry Trend reservoir of West Texas. L. Elkins[1] hypothesized that fractures open and close due to pressure and rock mechanical properties. In order to better understand these effects and fluid movement pathways, a number of specialized pressure transient tests have been conducted and analyzed in the E.T. O'Daniel Unit of Spraberry. This included constant pressure decline rate tests, build up tests, step-rate tests, falloff tests and a multi-well interference test, carried out so as to minimize the risk of induced fractures which can cause reduced sweep efficiency and fluid losses to other non pay zones. Results indicate that fracture systems are very stress sensitive in the Spraberry formation, with fractures opening and the effective permeability increasing at high injection rates (in addition, reservoir flow simulation has also confirmed that permeability is stress sensitive).

Field Characteristics

The Spraberry Trend of West Texas is a naturally fractured reservoir (NFR). A map of the Spraberry area is shown in Figure 3.9-1. This Permian age formation is divided into the Upper, Middle and Lower formations (see type log depicted in Figure 3.9-2). The Upper Spraberry, at a depth of approximately 7200 ft, is further divided into six units of which the 1U and 5U are productive. The rock is characterized by low matrix permeability (less than 0.1 mD, often ~ 0.05 mD) and a 10% average porosity. The combined 1U and 5U net pay is approximately 30 ft.

Effective permeability is essentially equal to fracture permeability in the Spraberry reservoir, since the matrix permeability is so low. Dyes and Johnston[2] report a range of 2 to 183 mD oil permeability, based on build up tests done in the Driver unit in the early 1950's. These tests were done during the initial depletion of the field. Previous interference testing shows ontrend (NE-SW) effective permeability of 108 md and offtrend (NW-SE) permeability of 8 md[3]. Our current work indicates an effective water permeability of about 2 to 14 mD in the E.T. O'Daniel Lease, but values of effective permeability vary widely as shown in Table 3.9-1.

Fracture orientation was studied by means of several horizontal well cores and field performance[4]. In general, the accepted main fracture orientation is N50°E. However, other non-orthogonal fracture sets are also present. Outcrop studies indicate natural fracture lengths of about 25 ft.[5]

Historical Perspective

The Spraberry Trend was first developed in the 1950s. Although many wells had initial production rates of more than 500 BOPD, the well productivity rapidly decreased. Waterflooding commenced in 1956.

Generally, waterflooding in Spraberry has not been successful due to the reservoir's low matrix permeability and natural fracture characteristics, as well as a lack of pattern confinement, low injection well density, weak imbibition forces and low reservoir pressures during startup of waterflood. In fact, compared to analogous NFR fields such as Weyburn/Midale (16 to 25% incremental waterflood recovery), the Spraberry experiences only a 2 to 5% incremental recovery through waterflooding[4]. The one exception to the generally poor waterflood recovery is the E.T. O'Daniel Lease in which total recovery has exceeded 25% and thus incremental waterflood recovery exceeds 15%.

For the entire Spraberry Trend, to date, only about 10% of the 10 MMMbbls OOIP have been recovered. Despite the fact that many wells have been abandoned due to low productivity as a result of fracture depletion, the large remaining oil in place represents a tremendous EOR target. Due to the success of CO_2 flooding the naturally fractured Midale reservoir, it was proposed that a CO_2 flood may be successful in Spraberry.

One Possible EOR Process: CO_2 Flooding

The success of a CO_2 miscible flood in Spraberry will be highly dependent on proper reservoir characterization of this low matrix permeability, but highly fractured rock. In order to best characterize the reservoir, it is important to try to narrow uncertainty in parameters such as fracture location, fracture orientation, fracture extent and effective permeability.

Prior to the implementation of the CO_2 flood, several single well and multi-well pressure tests were conducted in a 60 acre pilot area of the E.T. O'Daniel Lease (Figure 3.9-3). Through analyses of these pressure transient tests, we can now state several highly relevant conclusions about hydraulic fracturing, waterflood management and fracture characterization in this field. Among these is the key conclusion that fractures are very stress sensitive, meaning that injection pressures at reasonable injection rates significantly influence the extent of fractures as well as the effective permeability. Water injection widens existing fracture systems and connects otherwise discontinuous natural fractures.

Field Observations

The following pressure interference tests and decline analyses were done in the pilot area of the E.T. O'Daniel Lease:

Advanced Decline Analysis

Production data for several vertical wells in the Spraberry Trend were analyzed using an Advanced Decline Analysis technique in which decline characteristics were tied to reservoir parameters such as effective permeability and fracture half-length. The effective permeability ranged from 0.17 to 0.9 mD, while the fracture half-length varied

from 600 to 1300 ft. Peak production rates ranged from 20 to 90 BOPD. Comparative results are in Table 3.9-1.

Pressure Buildup Tests on Wells 38, 39 and 40

In contrast to early buildup tests, later tests show a marked decrease in oil permeability. Simulation studies show that a combination of relative permeability and stress effects are responsible for low oil permeability. Wells 38, 39 and 40 serve as the observation wells for the multi-well interference test, so buildup tests were done prior to injection in the pulse wells. The tests showed that the effective permeability ranges from 0.01 to 0.03 mD, with skins of –4.5 to –5.6. The average reservoir pressure was approximately 1300 psia. Wellbore storage was found to dominate the early time data and calculations showed that pressure transients traveled only approximately 50 ft away from each well. No classic dual porosity behavior was noted, probably because of wellbore storage effects. These results are similar to other recent buildup test analyses performed in the Spraberry area[6].

Step Rate Test on Wells 46 and 47

The step rate test (SRT) was conducted on well 47 prior to the multi-well interference test, with injection rates from 144 BWPD stepping up to 2160 BWPD. Primarily, the SRT is used to identify the fracture breakdown and/or propagation/extension pressure. The fracture extension pressure was calculated to be 3140 psia, while the breakdown pressure was found to be 3017 psia for well 47[7]. As shown in Figures 3.9-4 and 3.9-4a, there is good correspondence between the fracture extension pressure and the instantaneous shut in pressure (ISIP). Figures 3.9-5 and 3.9-6 show that the fracture extension/parting pressure was 2861 and 3231 for wells 46 and 47, respectively. Earlougher's technique[8] yields a fracture gradient pressure of 0.40 to 0.45 psi/ft, which is close to hydrostatic pressure.

Pre-interference Falloff Test

A falloff test was conducted after the SRT to determine effective permeability and waterflood induced fracture characteristics. The falloff test showed an effective water permeability anywhere from 2.6 to 14 mD, with a fracture half-length of 73 ft (assuming full fracture height of 31 ft). Note that this water permeability is markedly higher than the water or oil permeability as measured on buildup testing. This difference is greater than expected from relative permeability considerations. Once the SRT was completed and shutin, fluid dissipation caused the pressure around the wellbore to decrease below fracture extension pressure and in turn the fractures closed, reducing the permeability of the near wellbore system.

Multi-well Interference Testing with Analysis during Well 47 Injection

The interference test consists of sequential injection of 2000 BWPD in wells 47, 45, 25 and 48. Water is injected for 4 to 5 weeks in one well at a time, with a field stabilization period (2 to 3 weeks) between each injection period. Figure 3.9-7 shows the bottomhole pressure profile at each of the four observation wells (38, 39, 40 and 46) for the data

available. Figure 3.9-8 is a summary map of interference tests. Table 3.9-2 shows lag times and pressure response for interference tests

Although strong NE-SW pressure response is observed from well pair 45 to 46, substantial response is also seen in a north south direction, from well pairs 47 to 40 and 48 to 38.

The data was analyzed primarily using a method described by Earlougher[9], in which it is assumed that a single fracture, penetrating the full pay, exists directly between the injection and observation wells. The diagnostic plot used for this method is the Square Root Plot (as shown for Well 40 in Figure 3.9-9), in which pressure difference versus square root of time is plotted. The pressure difference refers to the difference between observed field pressure and an extrapolated pressure had the system remained at equilibrium with no injection. The slope calculated from Figure 3.9-10 can be used to find the fracture half-length through the following equation:

$$kx_f^2 = \left(\frac{-4.064 q_w B_w}{m_{vf} h} \right)^2 \frac{\mu_w}{\phi c_t} \quad \text{..... (3.95)}$$

This technique concludes that a fracture of half-length 275 to 385 ft exists between wells 40 and 47 (depending on how the slope m_{vf} is drawn). However, the minimum fracture half-length would have to be the interwell distance, or 660 ft (see 3.9-11) to intersect wells 40 and 47. Keeping the fracture capacity constant by using the same slope from Figure 3.9-11 used to calculate the 275 to 385 ft half-length, the fracture height must be 14 to 20 ft (i.e., less than full formation thickness of 31 ft) for a 660 ft fracture half-length.

An alternate analysis technique is that based on the type curves prepared by Raghavan et al[10]. This technique assumes that a single, vertical fracture intersects the injector wellbore located in an infinite, isotropic or anisotropic porous medium. This approach allows us to calculate the fracture orientation, fracture half-length and effective permeability. The technique is different from Earlougher's approach in that it does not assume that the fracture is directly oriented between injector and observation well. By analyzing the responses at wells 39 and 40, it was concluded that the fracture half-length varies anywhere from 1200 to 1900 ft, with an effective permeability of 0.5 to 1 mD. The orientation was 15° offset from wells 40-47 (towards well 39).

Subsequent interference testing was done with injectors 45, 25 and 48, and with pressure observation at wells 38, 39 and 40. The trends of data were very similar to that of the well 47 interference test as shown on Table 3.9-2 and Figure 3.9-12. In all those tests, there was an initial lag in response, then a definite pressure response. After injection was terminated, a more rapid response occurred at the producer communicating with the injector. This occurred even though there was an initial delay at the same well. These conclusions are based on examining the magnitude of pressure response, the rate of pressure rise and the lag time. As with similar previous pressure and well tests

interpretations, as well as outcrop observations at Spraberry, the permeability derived from these tests demonstrates the orientations of all fractures are not necessarily N50°E [1,4,5]

Post-interference Falloff Test on Well 47

The falloff test was conducted immediately following the interference test in well 47. The data is shown in Figure 3.9-13. Two models were considered: 1) infinite fracture conductivity and 2) composite. The effective permeability concluded from both models was 5 mD. The infinite fracture conductivity model showed a fracture half-length of 120 to 160 ft. Note that the fracture length was larger than the initial falloff test. Also, based on Lee's[11] definition of effective fracture half-length as a function of skin (Equation 3.96), the effective fracture half-length was calculated to be 150 ft, consistent with the falloff test results.

$$s = -\ln\left(\frac{x_f}{2r_w}\right) \quad (3.96)$$

Both the pre- and post-falloff tests indicate negative skins despite that the well had never been hydraulically fractured or acidized. A fact that the negative skin is typical of wells completed in naturally fractured reservoirs[12].

Discussion

Based on the pressure transient tests summarized above, several important observations and conclusions can be made. Most importantly, we discuss:

- The stress sensitive nature of fractures/"matrix" in the Spraberry Trend.
- The impact and consequences stress sensitive fractures have on waterflooding a naturally fractured reservoir (NFR).

Stress Sensitive Fractures

The conclusions about fracture half-length and effective permeability obtained from the pressure transient tests indicate that fractures are very stress and pressure sensitive.

The breakdown fracture pressure at Spraberry or in any NFR is primarily a fracture initiation pressure through unfractured rock. In unstimulated, unfractured wells the fracture breakdown pressure is substantially higher than the fracture propagation pressure. In Spraberry's case, however, it is fracture initiation through drilling damage near the wellbore that allows for connection of natural fractures. In this case the clearly developed hydraulic fracture is due to water injection. Even after the water injection is stopped, the mechanically closed fracture will have high fracture conductivity due to mismatched fracture surfaces and formation particles propping open the fractures.

The step rate test (Figures 3.9-4 and 3.9-4a) showed that the formation breakdown pressure occurred at 3017 psia when injection rates were at 200 bbl/day. This pressure is reached during the first injection rate, and subsequent higher injection rates merely

extend the fracture length. Note the decrease in pressure after the breakdown pressure is reached, despite the constant injection rate. Figures 3.9-4 and 3.9-4a also clearly show that, when the injection rate increased from 1000 bbl/d to 2200 bbl/d (a 120% increase), the injection pressure rose by only 30 psi. As described earlier, this is due to the opening and connecting of natural fractures. Secondary fracturing occurs when primary fractures cross secondary fracture offtrend systems as shown in Figure 3.9-12. Therefore, the fluid can penetrate relatively deeply into the ontrend (NE-SW) and offtrend (NW-SE) natural fractures when the bottomhole injection pressure gradients are close to hydrostatic gradient (0.43 psi/ft).

The results of the buildup/falloff tests further substantiate the stress sensitive nature of Spraberry fractures. During the buildup tests, the bottomhole pressures at wells 38, 39 and 40 did not exceed about 1000 psia. This pressure is much lower than fracture extension pressure, so rather than being dilated and connected, the fractures are probably constricted and unconnected. Because of this, the matrix is the dominant system through which pressure transients can travel, and hence an effective matrix (water/oil) permeability such as the 0.01 to 0.03 mD measured here is actually more representative of the matrix permeability. Note that constant pressure tests (decline rate analysis) showed lower permeabilities of 0.2 to 0.9 md. Yet during the interference and falloff tests, the tests determined effective "matrix" permeability was much higher -- in the 5 md range. It is probable that injection pressure opened both offtrend and ontrend fractures, leading to higher effective permeability. This phenomenon is similar as noted by Exxon in their 1970 analysis of the Spraberry Midkiff Unit[4].

Impacts of Waterflooding

We have observed the effects that high injection rates and pressures have on the effective permeability and fracture characteristics in the Spraberry reservoir. We have also seen the effects of poorly connected systems on measurements of effective permeability during buildup tests. These observations lead us to conclude that the injection pressures and rates present during a waterflood will have significant effects on the fracture half-lengths and permeabilities measured.

The SRT and pre-interference falloff test analyses have shown that an effective permeability of 2.6 to 14 mD is expected. At lower injection rates, the effective permeability was 2.6 md; this is representative of the falloff test. Once the pressure falls below the fracture extension pressure, the fractures begin to close and hence a relatively small fracture half-length of 73 ft is measured during the pre-interference falloff test. The 14 mD permeability is representative of the latter portions of the SRT at higher injection rates.

Once injection is resumed as in the interference test with 2000 BWPD in well 47 for 5 weeks, the fractures, already partly dilated and susceptible to connection and extension, are further able to grow. Earlougher's Square Root plot technique showed a 14 ft high, 660 ft long fracture. This is based on the 2.6 mD effective permeability measured from the SRT. These values show that with lengthy injection, fractures can significantly grow and increase in capacity.

This lengthening of fractures is shown in comparing lag time of response to start of injection compared to lag time of response to shut-in of injection. In actual fact, as shown in Table 3.9-1, there is a delay between the time that injection starts in a particular well and the lag time at which the pressure starts to increase rapidly and significantly. For example, observation well 40 experiences a 10 day delay during well 47 injection, while observation well 39 experiences a 4 day delay during well 45 injection. Conversely, the response to shutin of injection has no delay.

Conclusions

In summary, we can make the following conclusions regarding hydraulic fracturing and fracture characteristics in the Spraberry reservoir:

1. Assuming a constant permeability for this reservoir leads to very poor reservoir description.
2. Fractures are definitely stress sensitive. At reasonably high injection rates, fractures open up and the effective permeability of the system is in the 2 to 15 mD range. The fracture permeability is what is dominating the analysis of "matrix" permeability.
3. During production or in low pressure areas, effective permeability is governed primarily matrix permeability. The matrix permeability is generally in the range of 0.01 to 0.1 mD.
4. Generally, the Spraberry formation's parting pressure (opening and closing pressure) is in the range of 2900 to 3200 psia. Continued waterflooding at pressures near that range open up and connect short, regional fractures. The fracture gradient is generally quite close to hydrostatic pressure gradient.
5. Long term water injection does create very long fracture systems in which water can move very fast. However, many shorter fractures also interconnect to form a well-connected, extended fracture system. Once water injection is stopped, fractures can close and disconnect to some degree.

Nomenclature

B_w = *water formation volume factor (rb/stb)*
c_t = *total compressibility (psi^{-1})*
h = *fracture height (ft)*
k = *permeability (mD)*
m_{vf} = *slope from Square Root Plot ($psi/hr^{1/2}$)*
q_w = *water injection rate (Bbl/d)*
r_w = *wellbore radius (ft)*
s = *skin*
x_f = *fracture half-length (ft)*

Greek Symbols

μ_w = *water viscosity (cp)*

ϕ = *porosity*

References

1. Elkins, L.F. and Skov, A.M.: "Cyclic Water Flooding the Spraberry Utilizes End Effects to Increase Oil Production Rate," *JPT*, August 1963.
2. Dyes, A.B. and Johnston, O.C.: "Spraberry Permeability from Build up Curve Analyses," AIME Vol. 198, 1953.
3. Elkins, L.F. and Skov, A.M.: "Determination of Fracture Orientation from Pressure Interference," *Trans*, AIME (1960). **219,** 301.
4. Schechter, D.S., McDonald, P., Sheffield, T. and Baker, R.: "Reservoir Characterization and CO_2 Pilot Design in the Naturally Fractured Spraberry Trend Area," SPE paper 35469, presented at the SPE Permian Basin Oil and Gas Recovery Conference, Midland, Texas, March 27 – 29, 1999.
5. Malmanger, E.M.,: "Statistical Analysis and Simulation of Stress Sensitive Natural Fracture Networks," Master of Science in Petroleum Engineering, New Mexico Institute of Mining and Technology, Socorro, NM, March 1997
6. Barba, R.E.: "Optimizing Hydraulic-Fracture Length in the Spraberry Trend," *SPE Formation Evaluation*, September 1989.
7. Fekete Associates Inc.: "Fast Well Test User Manual," 1989.
8. Earlougher, R.C.: "Advances in Well Test Analysis," Monograph Vol. 5, pp. 87-88, 1977.
9. Earlougher, R.C.: "Advances in Well Test Analysis," Monograph Vol. 5, pp. 151-152, 1977.
10. Raghavan, R., Uraiet, A., Thomas, G.W.: "Determination of the Orientation of a Vertical Fracture by Interference Tests," SPE 5845, 1977.
11. Lee, J.: "Well Testing," SPE Textbook Series, Vol. 1, p. 34, 1982.
12. Gringarten, A.C.: "Interpretation of Tests in Fissured and Multilayered Reservoirs with Dual Porosity Behaviors: Theory and Practice," *JPT*, April 1984.

Table 3.9-1—Summary of Recent Spraberry Permeability Analyses

TEST	PERMEABILITY MEASURED (md)	COMMENT
Initial buildup tests on wells 37 to 40	0.01 to 0.03	• Believed to reflect only matrix permeability (closely conforms to core stress and initial water saturated corrected matrix permeability measurements). Sample areas near wellbore of producer with partially closed fractures (r_{inv} ~ 50ft).
Constant pressure (decline analysis)	0.2 to 0.9	• Reflects average effective permeability of both natural fractures and matrix [1,4]
Step rate tests on well 47	2.6 to 14	• Higher injection rates have higher effective permeability. In other words, higher injection rates were matched by higher effective permeability.
Pre-interference falloff test on well 47	2.6	• Reflects average effective permeability of partially extended natural fractures
Interference test	Very high	• Well pairs show long fracture lengths that are injection volume dependent.
Post-interference analysis falloff test	5.0	• Reflects average effective permeability of partially extended natural fractures and matrix.

Table 3.9-2 —Spraberry Interference Tests Results

Well Pair		Time Lag from Start Inj. to First Response (days)	ΔP (psi)	Time Lag from End Inj. to First Response (days)
Injector	Observer			
47	38	∞	Nil	∞
47	39	27	250	4
47	40	10	1600	0
45	38	4	425	4
45	39	4	425	3
45	40	∞	Nil	∞
45	46	4	700	N/A
25	38	∞	Nil	∞
25	39	13	300	5
25	40	13	300	4
48	38	5	1200	3
48	39	13	100	10
48	40	∞	Nil	∞

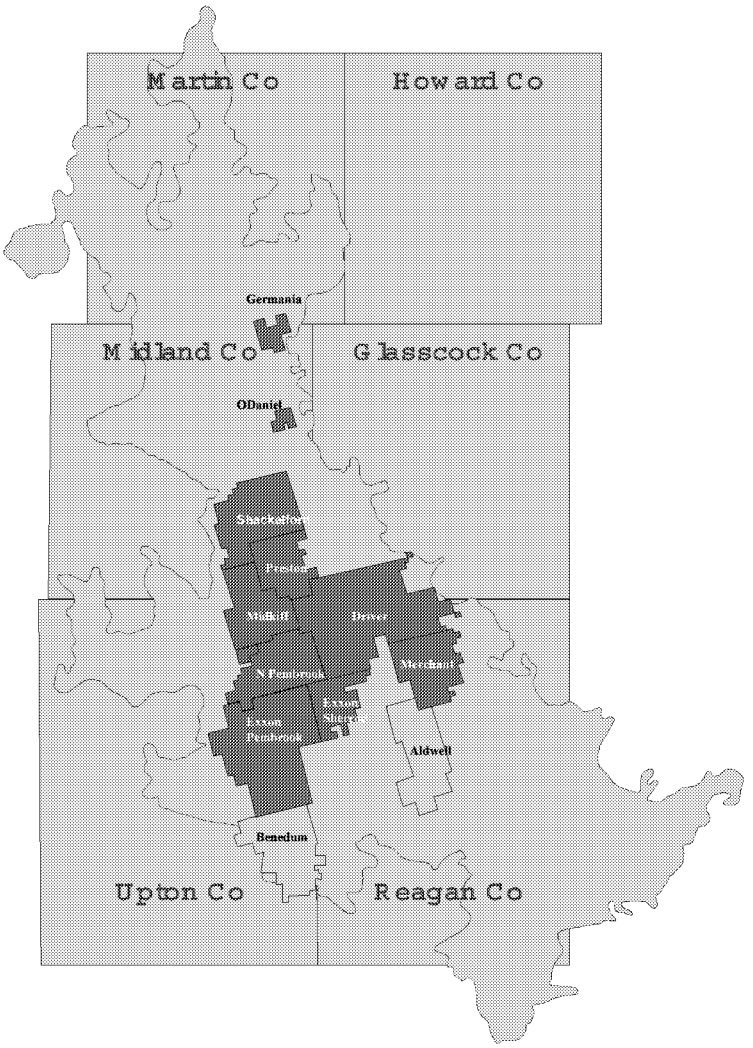

Fig. 3.9-1 —Map of Units Local to Midkiff and E.T. O'Daniel

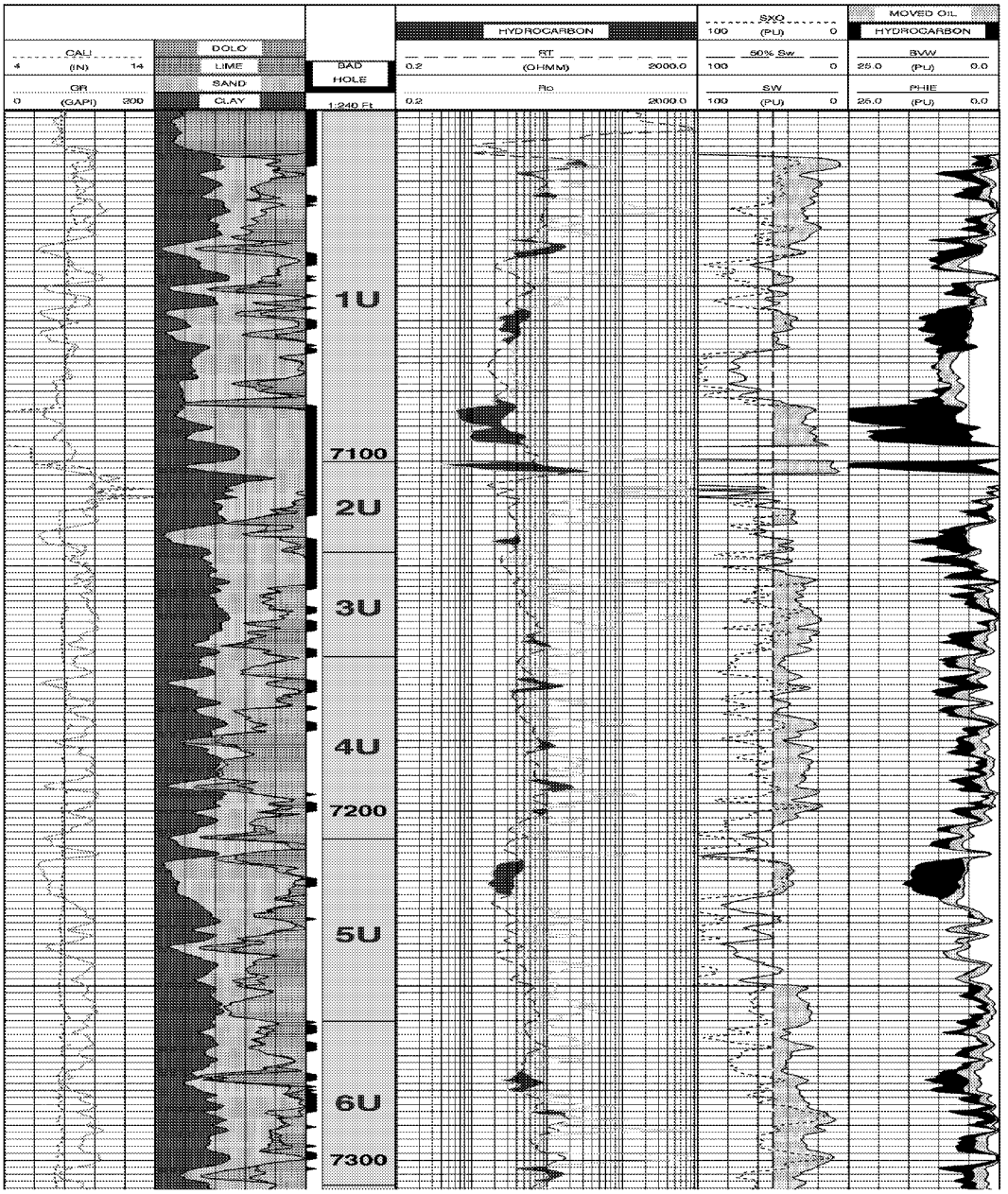

Fig. 3.9-2 —Petrophysical Analysis

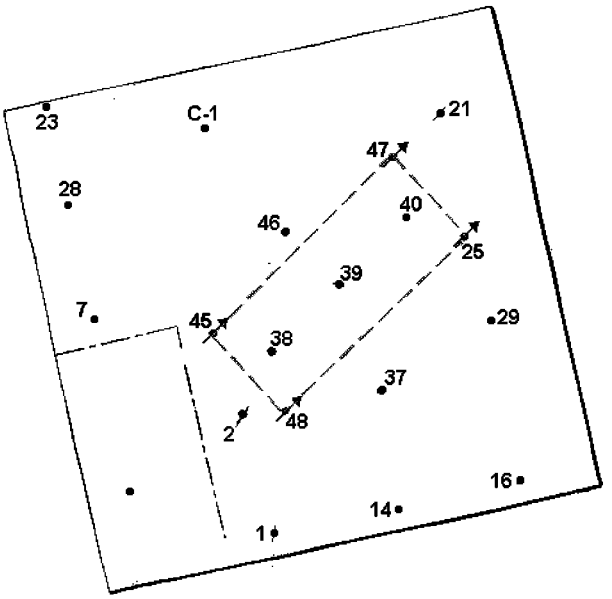

Fig. 3.9-3 —Section 4 of the E.T. O'Daniel Lease
(Pilot Area = 60 acres, Total Area = 1 sq. mile

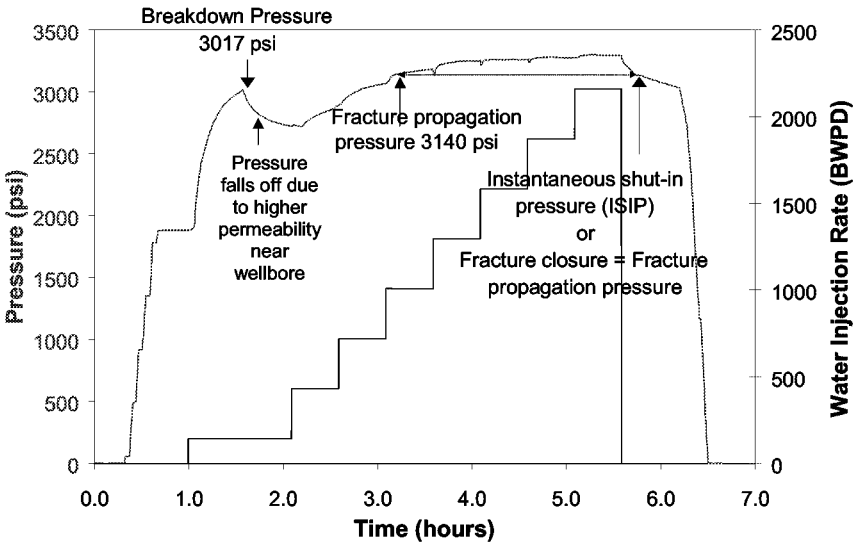

Fig. 3.9-4 —Well 47 Step Rate Test Profiles showing breakdown pressure, fracture propagation pressure and fracture closure (instantaneous shut-in pressure)

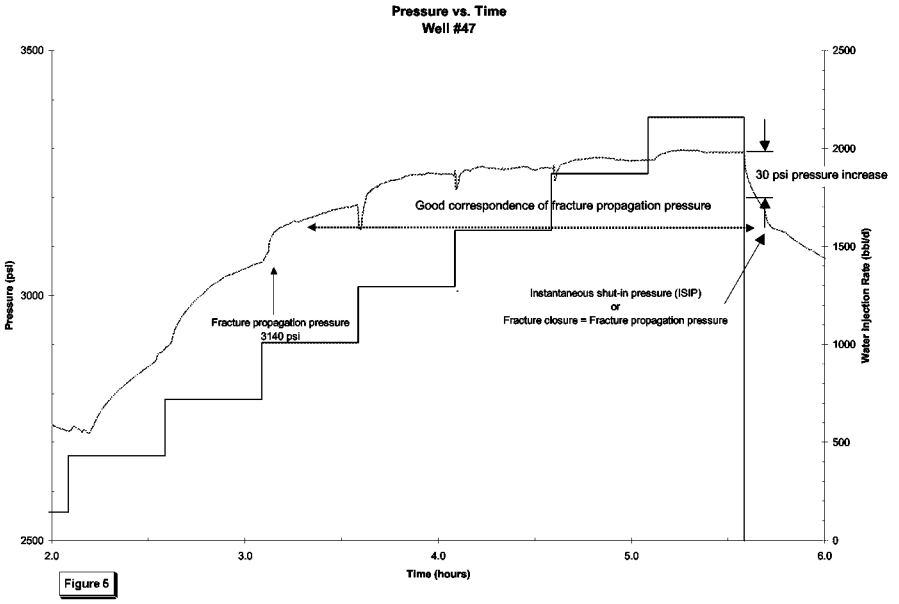

Fig. 3.9-4a —Zoom in of last half of Step Rate Test from Fig. 3.9-4

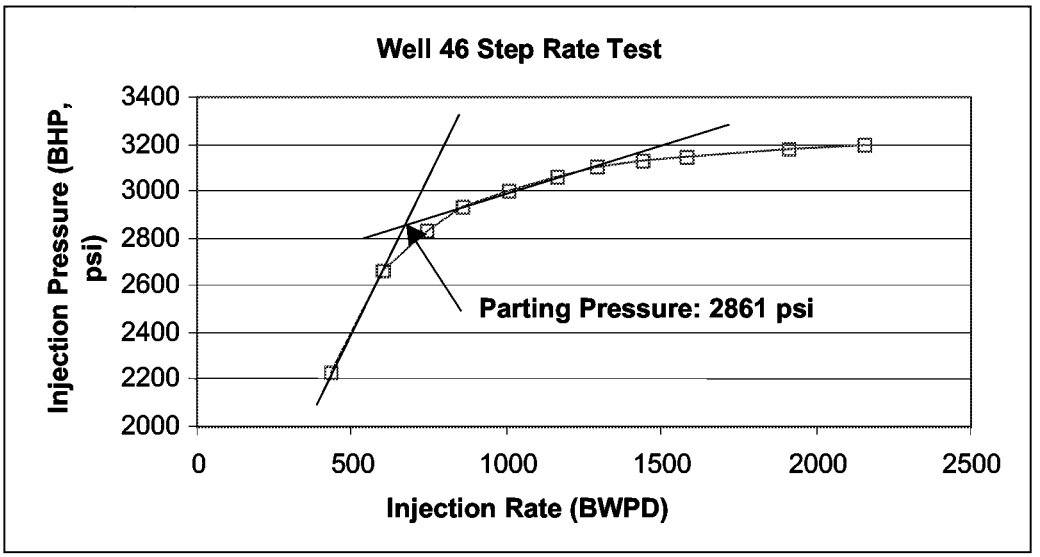

Fig. 3.9-5 —Well 46 Earlougher Step-Rate-Test Analysis

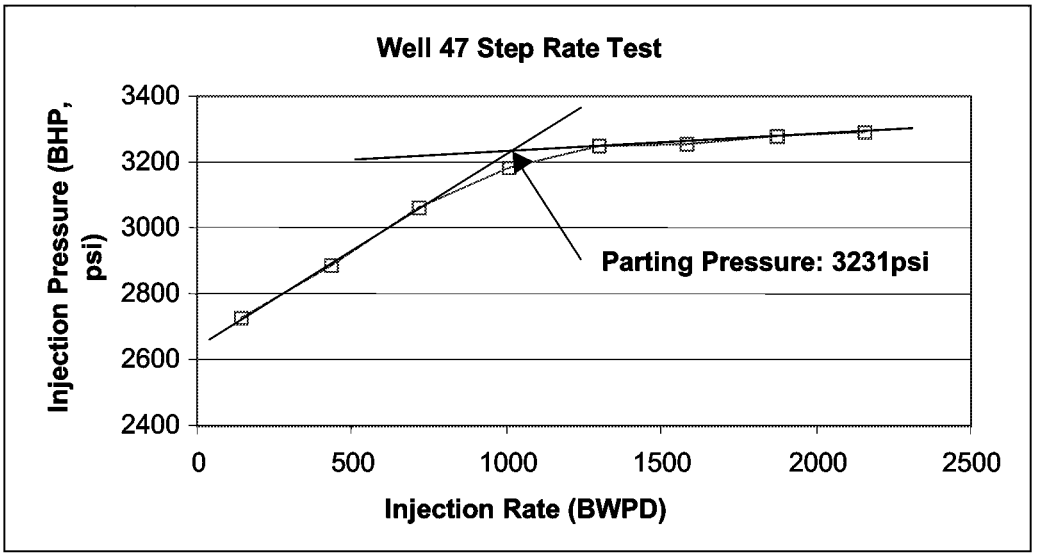

Fig. 3.9-6 —Well 47 Earlougher Step-Rate-Test Analysis

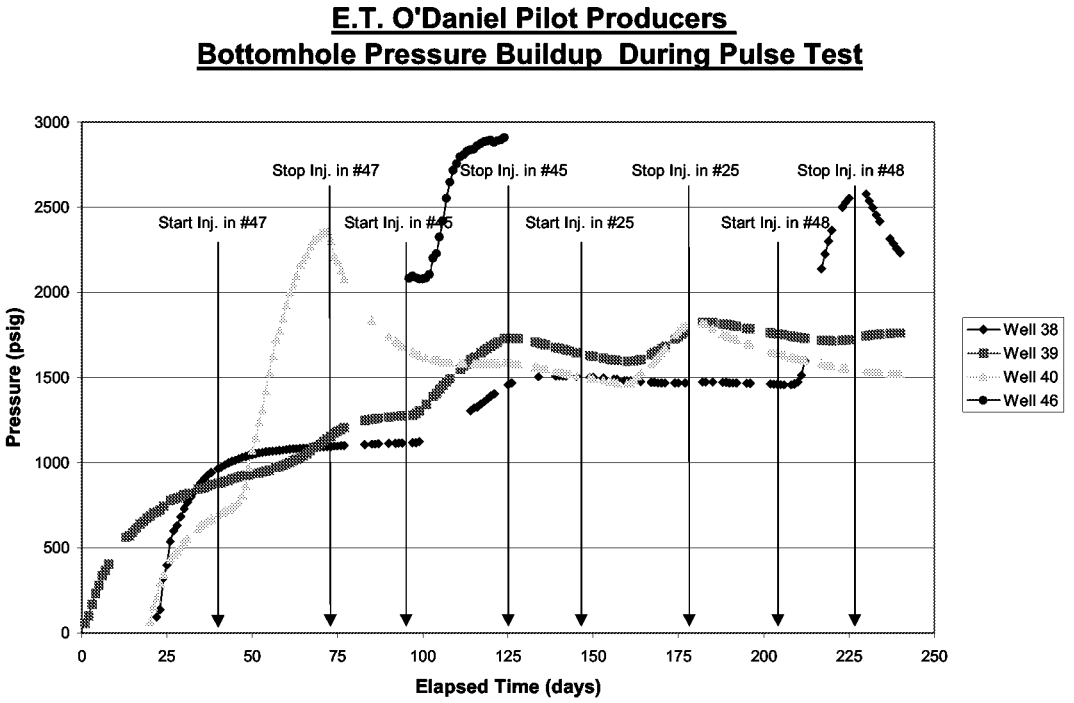

Fig. 3.9-7 —Bottomhole Pressures at each of the Observation Wells

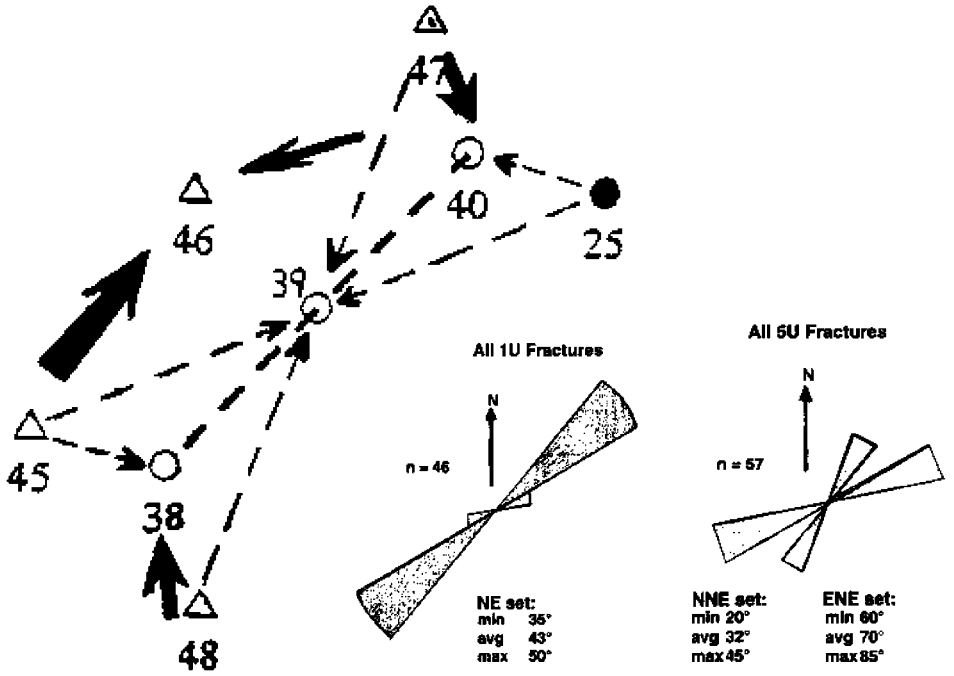

Fig.3.9-8 —Map of Communication Path

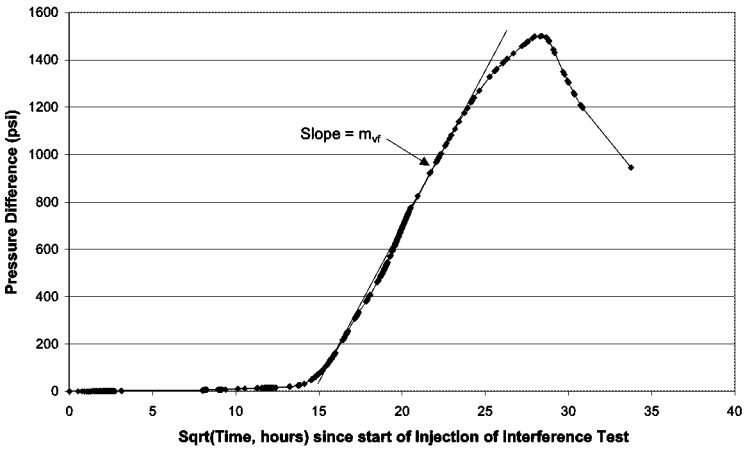

Fig. 3.9-9—Well 40 Square-Root Plot for Earlougher, Direct-Fracture Analysis

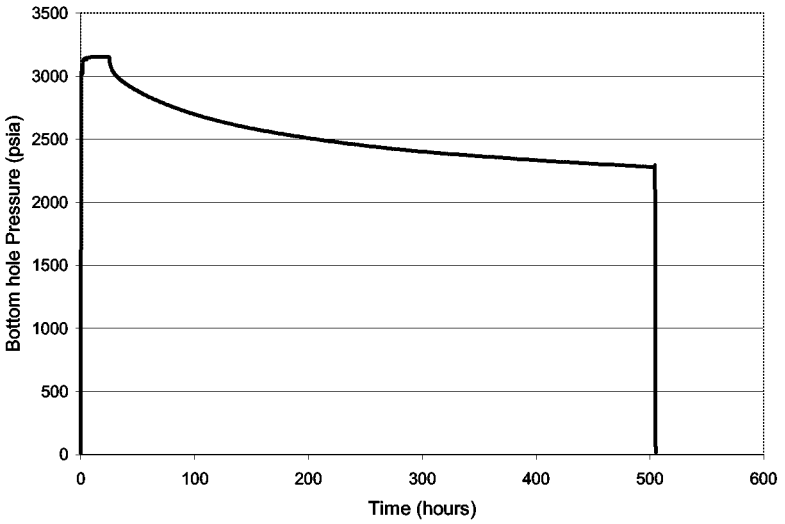

Fig. 3.9-10 —Well 47 Post-interference Falloff Test

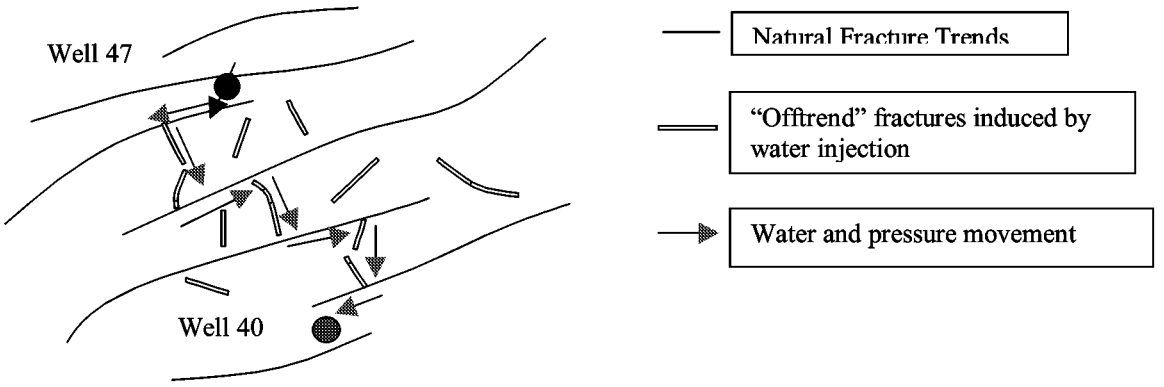

Fig. 3.9-11 —Direct Fracture Causes Pressure Response at Well 40

3.10 REVIEW OF WATER INJECTION PERFORMANCE IN THE NATURALLY FRACTURED SPRABERRY TREND AREA, WEST TEXAS

Introduction

The Spraberry Trend Area in west Texas was discovered in 1949 and continues to produce 60 Mbopd from more than 7,500 wells from an eight county area encompassing over 2,500 square miles. Spraberry reservoirs originally contained some 10 Bbbls OOIP of which less than 10% has been recovered.

The Spraberry Trend Area has proven to be elusive to engineers since discovery. Half a century later, the reservoir has maintained the status of one of the more complicated naturally fractured reservoirs to understand or forecast. There are three sets of highly permeable fractures distributed among the two pay intervals in the Upper Spraberry, the 1U and 5U sand (there is the lower Spraberry that is not discussed here). The fractures are stress-sensitive and the fracturing pressure of shales zones are very near fracturing pressure for Spraberry oil sands. Oil recovery is dominated by the imbibition mechanism, however Spraberry sands are weakly water-wet and the matrix permeability is very low. Waterflooding has not been widely applied in the Spraberry Trend Area. In the past, water injection wells were aligned parallel to the major NE-SW fracture trend and perpendicular to a line of production wells (line-drive). Line-drive pattern configuration in anisotropic reservoirs is commonplace as is shown in Fig. 3.10-1 However, aligning injectors along the same fracture trend with producers was viewed as unwise since the fractures would rapidly conduct injected water to the production well.

The general idea was to build interference between injectors along the fracture trend and force injected fluid to a line of producing wells, also aligned along the primary fracture trend. We believe this de facto approach to water injection in Spraberry has been the primary reason this tremendous resource is so underutilized. The fractures are highly anisotropic[1], and the matrix permeability is very low[2,3] thus requiring high rate fluid injection to force fluids to a line of production wells. The injection rate required to achieve this communication probably creates hydraulic fractures with variable orientation. The small difference in stress anisotropy between adjacent sand and shale layers (as measured in a mini-frac test) and the unquestionable stress sensitivity of the fracture system may result in preferential channeling in non-pay resulting in poor sweep efficiency.

The tremendous size of the reservoir, large number of active and plugged wells, lack of historical production/injection data, and fluid migration across lease boundaries have hampered assessment of water injection over the years. This has resulted in a lack of confidence in the application of water injection in Spraberry reservoirs.

In this paper, we will review the five most documented water injection tests in order to reach stage of development practices that could eventually unlock the key to successful water injection. We will review the results of water injection in the current CO_2 pilot area in order to use this information for development of widespread waterflooding throughout the Spraberry Trend Area. The documented waterflood projects in Spraberry are listed below:

1. Atlantic Richfield Pilot (1952)
2. Humble Pilot (1955)
3. Mobil O'Daniel Co-op Flood (1959)
4. SOHIO Driver Unit Waterflood Expansion (1960)
5. Pioneer Natural Resources O'Daniel DOE/NPTO project (1995)

Atlantic Richfield Pilot (1952)

Figure 3.10-2 shows locations of unitized areas waterflooded in the 60's and location of the current water/CO_2 pilot. In 1952 Atlantic Richfield Pilot developed an 80-acre pilot based on imbibition experiments that indicated spontaneous imbibition could recover oil in strongly water-wet rock.[4] The pilot area consisted of 3 injection wells on an 80-acre pattern. The debut of waterflooding in Spraberry demonstrated that wells would respond along the perceived fracture orientation of N50°E.

Figure 3.10-3 shows that wells along this orientation responded by a significant decrease in GOR's from 10,000 down to 2,000 scf/bbl accompanied by a modest increase in oil production in the range of 10 – 30 bopd per well. A good example was the Magnolia Bowles #2 in Tract 40 directly southeast of the Schrock #5 injection well as shown in Fig. 3.10-3. In the 2½ months from the middle of September to the first of December of 1952, production from this well was averaging 29 bopd. Production increased erratically but steadily from the first of December on. By the first of February 1954, production had increased to 78 bopd and GOR dropped from 2,400 to 400 scf/bbl.

Since much of the Spraberry was still being produced under primary depletion in 1952, few major operators were interested in pursuing waterflooding for the modest increases noted in production, especially with more water to process. Explanations were provided for the "poor" performance of this pilot, usually related to the unconfined nature of the pilot since only 3 injection wells were utilized.

Figure 3.10-3 demonstrates positive response from water injection outside the pilot area. However, it should be noted that the primary observation well, the Atlantic Schrock #7, observed a decrease in GOR yet there was almost no production response. The following is taken verbatim from May 17th, 1954 edition of the Oil and Gas Journal.[5]

"Through an unexplained quirk, Atlantic #7 W.M. Schrock, located on the base of the triangle equidistant from each injection well and pre-selected as the observation well for the experiment, showed absolutely no evidence of injected water or increase in oil production… If a fourth injection well were in place, the Atlantic #7 W.M. Schrock would have been the central production well in a classic 80-acre 5-spot pattern."

Humble Pilot (1955)

Humble Oil Co. embarked upon another 80-acre pilot[6] beginning in 1955 in the Midkiff Spraberry Unit (Fig. 3.10-4). At this point there were over 2,000 producing wells and pressure/production in the Spraberry Trend Area had declined significantly.

Once again, the idea of the pilot waterflood was to inject into wells aligned along the primary fracture trend, build interference and force water perpendicular to the primary fracture trend to a center production well. The Humble 80-acre pilot was completely confined with four injection wells as opposed to the Atlantic pilot where only 3 injection

wells were utilized. This difference in confinement for the two pilots would eventually result in many sources believing that confinement made the difference between the results of the Humble pilot and the unsuccessful Atlantic pilot. This observation added more ambiguity to the question of water injection in Spraberry.

Twelve surrounding wells were monitored for fluid production and reservoir pressure as is shown in Fig. 3.10-4. The numbers above the well symbol indicate production of oil (barrels) before and after injection of water. The numbers below the well symbol represent the reservoir pressure (psi) before and after the initiation of water injection.

Unlike the center well in the Atlantic pilot, the center production well in the Humble pilot, the Shackelford #9, demonstrated a sharp increase in oil production. A summary of injection and production data for the Humble pilot is shown in Fig. 3.10-5. A sharp oil bank is seen to arrive at the central production well and as is noted in Fig. 3.10-4. Production in the center well increased from 70 to 250 barrels of oil per day. The response of this single well (Shackelford #9) in the Humble pilot dictated future development of waterflood patterns. As we shall demonstrate in this report, basing field-wide waterflood development on the results of this single well may have created erroneous expectations for future water injection projects.

There are many explanations and hypotheses why this center production well performed far above previous and future waterflood producers. It should be noted however, the important difference that existed between the Humble pilot and all other Spraberry waterflood projects. The center well was a newly completed well flowing at 80 bopd. A flowing Spraberry well implies the reservoir was still under primary depletion. After initiation of water injection, the well was converted to a pumping well. During the time that a sharp increase in oil production was observed, as noted in Fig. 3.10-5 (August 1955), a larger pumping unit was installed. This information was not reported in Barfield and Jordan's paper[6] but was retrieved from internal company memorandum. [7] The fact that the well was still on primary and a larger pumping unit was installed during water injection obscures the interpretation since the dramatic increase in oil rate is not a result of water injection alone.

Since the center well responded in a dramatic fashion, the surrounding wells were ignored however as one can see from Fig. 3.10-4, all wells oriented along the NE-SW direction demonstrated an increase in oil production and/or pressure as the result of water injection.

Mobil O'Daniel Co-op Flood (1959)

In 1959, Mobil Oil Co. injected water in the E.T. O'Daniel cooperative waterflood (Fig. 3.10-6). This was a "dump flood" where water from the Santa Rosa Sand, at about 1,000 feet of depth was injected by gravity into the Spraberry sands at 7,000 feet. Initial injection rates were measured close to 1,500 bwpd and declined to 400 bwpd as the Santa Rosa aquifer was depleted. Guidroz[7] published a paper demonstrating a "successful Spraberry waterflood as measured by a significant increase in oil production in the O'Daniel Unit Co-op flood." It is known that the O'Daniel Unit waterflood far out-performed other waterfloods in Spraberry, especially the large-scale Driver Unit waterflood. Upon closer inspection, it appears that the O'Daniel Unit performed very similar to the Atlantic and Humble pilots. Wells outside the area of confinement yet along the dominant fracture trend responded favorably.

Figure 3.10-6 shows that several injection wells were aligned along the N50°E line in the adjacent Floyd, Powell and Leach leases, south of the O'Daniel Unit. The N50°E orientation was the generally accepted orientation of the fracture system by this point in the development of the reservoir, however, this was the result of pressure transient testing[8]. No verification of this orientation was pursued prior to injection in the co-op flood. This line of injectors terminated with the injection well E.T. O'Daniel #14.

Fifty five percent of the oil recovered as a result of water injection in the O'Daniel pilot came from wells in section four. [8] As is shown in Fig. 3.10-6, Section 4 was essentially parallel to the line of injection wells to the south of the O'Daniel lease, yet still within the co-op area. The injection/production profile shown in Fig. 3.10-7 shows a substantial increase in oil production near the end of 1959 and throughout 1960. Guidroz stated in his paper, "The greatest pressure increases were noted in wells 1 and 16. Correspondingly, the increase in oil production from Nov. 1959, through Dec. 1960 is due largely to waterflood response in wells 1, 2 and 16." As is shown in Fig. 3.10-6, the wells that Guidroz describes were outside an area of significant injection well density and generally along an orientation of N32°E, shown as a series of parallel lines drawn through water injectors in Fig. 3.10-6. One may presume that much of the rapid increase in oil production and incremental waterflood recovery described by Guidroz was a result of injection south of the O'Daniel lease and rapid movement of injected fluids in a northeasterly direction towards the lease line wells in Section 4 of the O'Daniel Unit.

Other company records reported that outside the co-op area the best performing section was the Powell lease to the south of Section 4 of the O'Daniel Unit. Fig. 3.10-6 demonstrates this is consistent with on-trend production as opposed to building interference between injection wells and forcing fluid to a line of production wells. Results from the early O'Daniel waterflood provides strong evidence that on-trend injection wells aligned with production wells are capable of producing significant improvements in well productivity.

SOHIO Driver Unit Waterflood Expansion (1960)

The dramatic increase from 70 to 250 bopd in the Humble pilot resulted in a new fervor of activity in the Spraberry Trend in the late 50's and early 60's. The immediate result of the Humble Midkiff pilot was development of a 9-section test of wide-scale waterflooding by Sohio in the Driver Unit of the Spraberry Trend Area shown in Fig. 3.10-8. This was and still remains the largest unitized area in the Spraberry Trend comprising approximately 60,000 acres.

Injection wells were aligned along the main fracture trend as determined by interference tests[9] (N50°E) and production wells were aligned along the same orientation as previously described and shown in Fig. 3.10-1. The alignment of injection wells in a line drive configuration was a result of the Humble pilot with the belief that large production increases would be noted in the line of injection wells, as was the case in the Humble pilot. Figure 3.10-8 shows the configuration of wells in the Driver Unit. There is little data in the public domain describing well-to-well response in the Driver Unit flood so it is difficult to discern any patterns of wells that responded to water injection. It is known that there was no "flush production" of oil in the line of production wells perpendicular to the line of injection wells, unlike the central production well in the Humble pilot. There

was a clear increase in oil production due to injection of water in the Unit as a whole[10], but the lack of "flush" production dampened enthusiasm for water injection in Spraberry sands.

Elkins did mention that Area 3 performed better than Area 2 although the geological conditions are not as favorable in Area 3. Furthermore, there was about half the injection wells in Area 3 as opposed to Area 2 yet Area 3 performed better under water injection. Once again, it may be possible that there were insufficient production wells oriented along the fracture trend with injection wells to provide a rapid increase in production that may have instilled a level of confidence in early waterflood trials. A secondary hypothesis is the good response seen in Area 3 was a result of more injection wells located in Area 1 that mobilized oil into Area 3.

The injection wells were oriented along the N50°E line as shown in Fig. 3.10-8. Earvin[11] later reported that an N32°E fracture orientation was a possibility. His evidence was based on the response of wells 376, 385, 389, 394 and 398 that are aligned an N32°E orientation with injection wells. It remains undocumented whether the "possible trend" described by Earvin was a result of pressure or production data. As is often the case in Spraberry, reconstruction of historical data is a crucial constraint to developing waterflood reserves.

Results of Water Injection in the E.T. O'Daniel Pilot Project (1995)

The E.T. O'Daniel Pilot is located in Section 4 T2S Block 37 of the E.T. O'Daniel lease in Midland County, Texas (Fig. 3.10-2). This site was selected due to the high oil recovery that occurred from primary and secondary operations in this particular area.

The pilot configuration is shown in Fig. 3.10-9. 15 wells have been completed with four CO_2 injection wells, three central production wells and two logging observation wells. The well pattern is oriented along the major trend with the three producers forming a line parallel to the primary fracture trend. The producers are flanked by four CO_2 injectors and surrounded by six water injections in an approximate regular hexagonal pattern. The overall area confined by six water injectors is sixty-seven acres while the area enclosed by the four CO_2 injectors is twenty acres. Such a configuration is believed to provide an adequate confinement in most directions although some on trend CO_2 losses in a NE-SW direction could occur.

Stable water injection was initiated in October of 1999 in order to increase the reservoir pressure above the minimum miscible pressure (MMP). Also, another goal was establishment of a waterflood baseline decline so that all produced oil as a result of CO_2 injection can be quantified. Since this is a 40-year-old waterflood area, it was assumed the area was at residual oil saturation and there would be minimal response from water injection. Production has been recorded in 37 wells in and around the pilot area as shown by the green dashed curve in Fig. 3.10-9. We have divided oil production into 23 off-trend and 7 on-trend wells. The 7 on-trend wells are located along the NE-SW natural fracture orientation as determined by horizontal core. [12]

The three central production wells 38, 39, and 40 have shown small incremental oil production after initiation of water injection. However, wells oriented parallel to the primary fracture trend responded with a significant increase in oil production. Some of the wells over one mile from the injection wells have responded whereas wells oriented

perpendicular to injection wells at a fraction of distance from injection wells have shown little response, similar to that observed in the tracer survey. It is possible that off-trend wells will respond in the future but the unexpected increase in production wells along the fracture trend clearly indicate the presence of un-swept oil even though the area has been previously waterflooded.

The composite performance of the "expanded" pilot area shows that oil production has steadily increased from 200 bopd before water injection to a current level near 400 bopd with an additional cumulative production of > 75,000 bbls after 1.5 years of water injection (Fig. 3.10-10). Thus, the seven on-trend wells are responsible for 150-200 barrels of incremental oil per day. This represents an incremental gain of 20-30 barrels for each seven on-trend wells. The results also dispel the notion that on-trend injection wells will channel via the fractures and rapidly water-out production wells without producing incremental oil via the imbibition mechanism.

Conclusions

1. Even though waterflooding in Spraberry Area has been documented as a poor recovery mechanism, recent results of low rate water injection has revealed that waterflooding can dramatically increase oil production.
2. On-trend well responded favorably in almost all waterflood pilots in the Spraberry Trend Area. The results oppose previously held notions that production wells aligned on-trend with injection wells will experience rapid channeling via fractures, thereby watering-out production wells with no incremental oil production.
3. High water injection rates were able to restore pressure in the O'Daniel Pilot area from about 1000 psia to pressure levels between the Minimum Miscible Pressure (MMP) of 1550 psia and Formation Parting Pressure (FPP) of 2730 psia.
4. The imbibition mechanism coupled with high permeability anisotropy and heterogeneity in the fracture system facilitated the increase oil production rate observed in the on-trend wells during steady, low rate water injection. This unexpected result implies that water is contacting unswept rock in an area that has been previous waterflooded.

References

1. "Radioactive Gas Tracer Survey Aids Waterflood Planning," World Oil (Feb. 1961).
2. Dyes, A.B. and Johnston, O.C.: "Spraberry Permeability from Build-Up Curve Analyses," Trans., *AIME* (1953) 198, 135-138.
3. Christie, R.S., and Blackwood, J.C.: "Production Performance in Spraberry," *OGC* (April 7, 1952) 107-15.
4. Brownscombe, E.R. and Dyes, A.B.: "Water-Imbibition Displacement...Can It Release Reluctant Spraberry Oil?" *OGC* (Nov.17, 1952) 264-265 & 377-378.
5. Enright, R.J., "Imbibition – Newest Producing Technique" OGC (May 17, 1954) 104 – 107.
6. Barfield, E.C., Jordan, J.K. and Moore, W.D.: "An Analysis of Large-Scale Flooding in the Fractured Spraberry Trend Area Reservoir," *JPT* (April 1959) 15-19.

7. "Waterflood Possibilities Spraberry Trend Area Field," Sohio Production Company Internal Report, (Sep. 1957).
8. Guidroz, G.M.: "E.T. O'Daniel Project- A Successful Spraberry Flood," *JPT* (September 1967) 1137 – 1140.
9. Elkins, L.F. and Skov, A.M.: "Determination of Fracture Orientation from Pressure Interference," Trans., *AIME* (1960) **219**.
10. Elkins, L.F.: "Cyclic Water Flooding the Spraberry Utilizes 'End Effect' to Increase Oil Production Rate," *JPT* (August 1963) 877-884.
11. Earvin, S. "Waterflood Performance in Spraberry" Internal Memorandum, Spraberry Database, Harold Vance Dept. PE, Texas A&M University (1988).
12. McDonald, P., Lorenz, J. C., Sizemore, C., Schechter, D.S., and Sheffield, T.: "Fracture Characterization Based on Oriented Horizontal Core From the Spraberry Trend Reservoir: A Case Study" paper SPE 38664 presented at the 1997 Annual Technical Conference and Exhibition, San Antonio, Tx, 5-8 October.

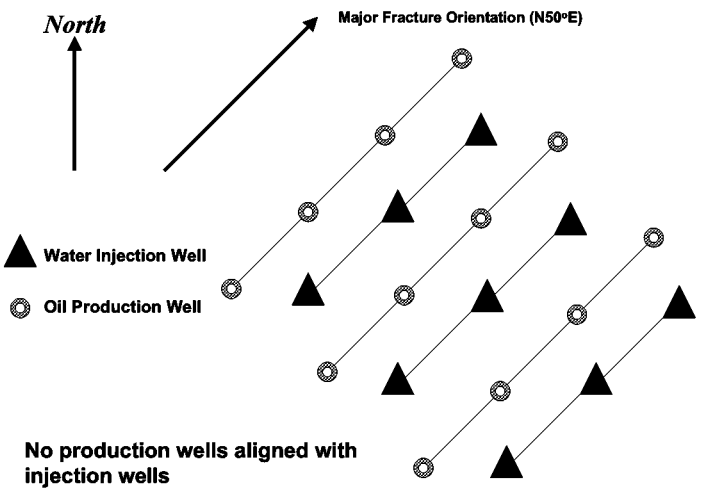

Fig. 3.10-1 —Line-drive pattern configuration in anisotropic reservoirs

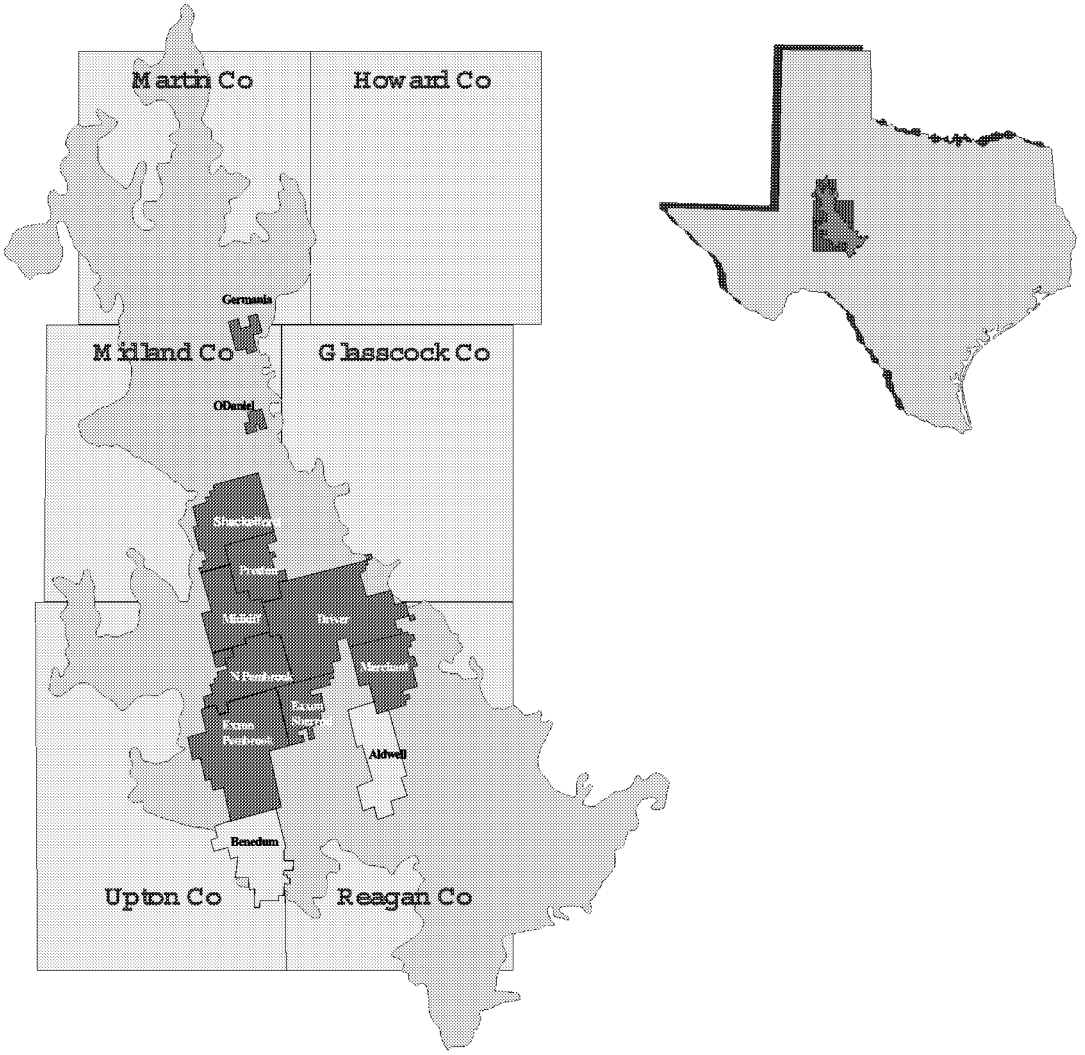

Fig. 1.10-2 —Units and reservoir extent in the Spraberry Trend Area

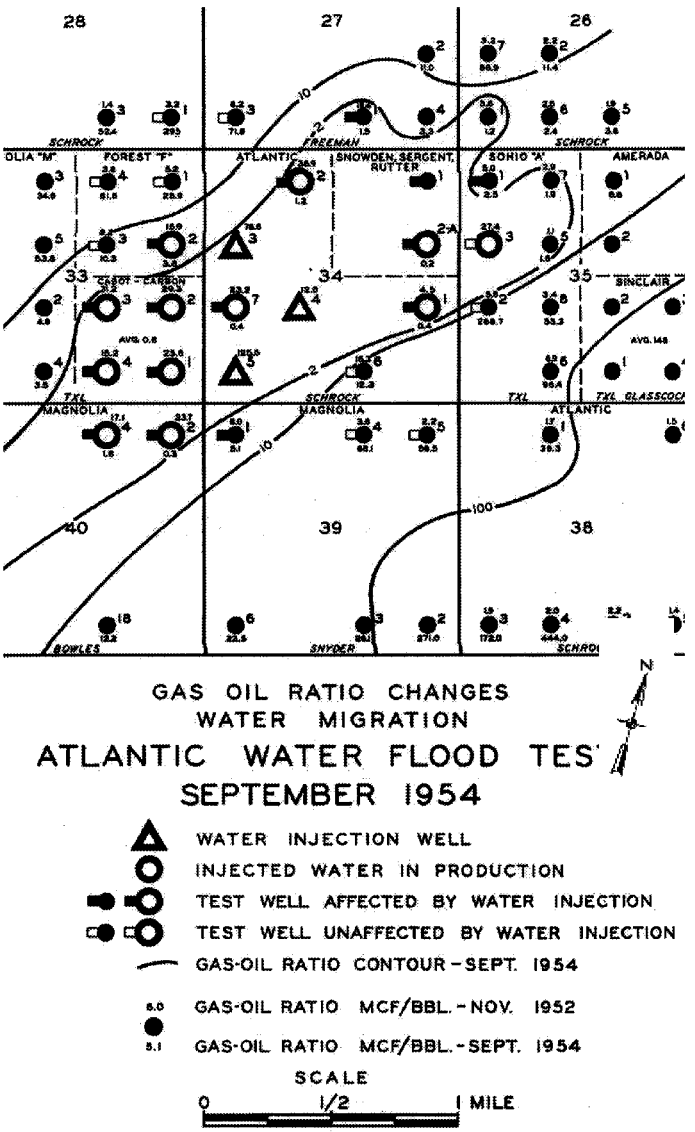

Fig. 3.10-3 —Atlantic Richfield waterflood pilot 1952

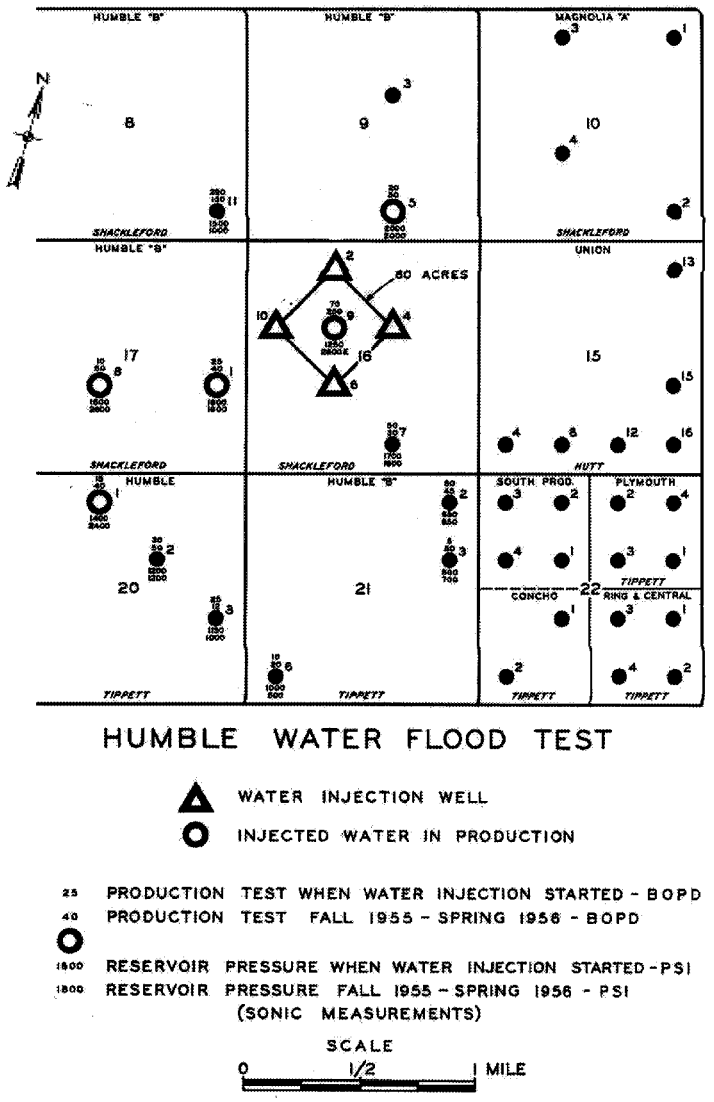

Fig. 3.10-4 —Humble water injection pilot in the Spraberry Midkiff Unit 1955

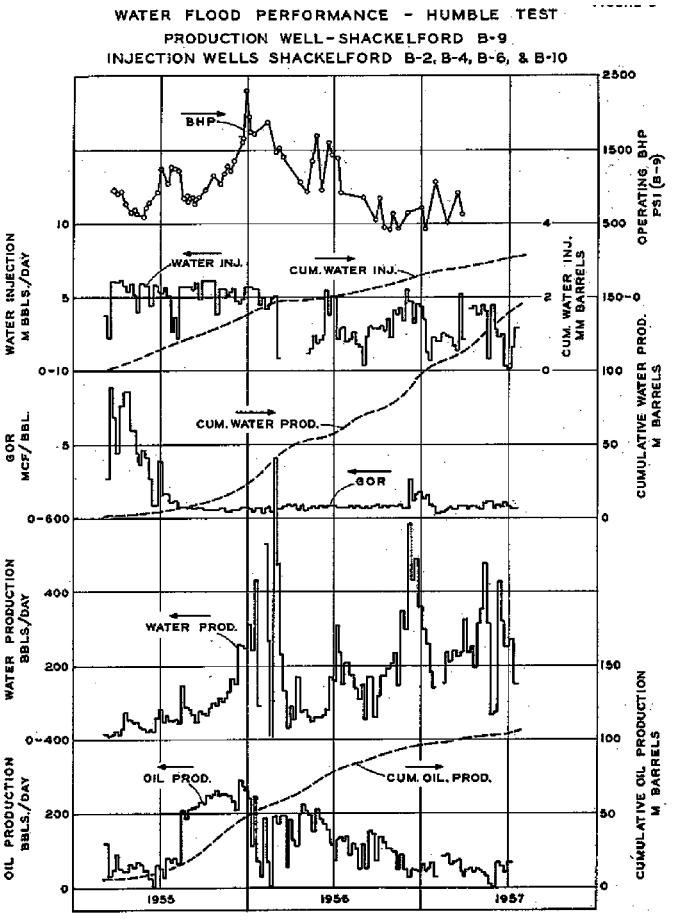

Fig. 3.10-5 —Production and injection data for the Humble pilot

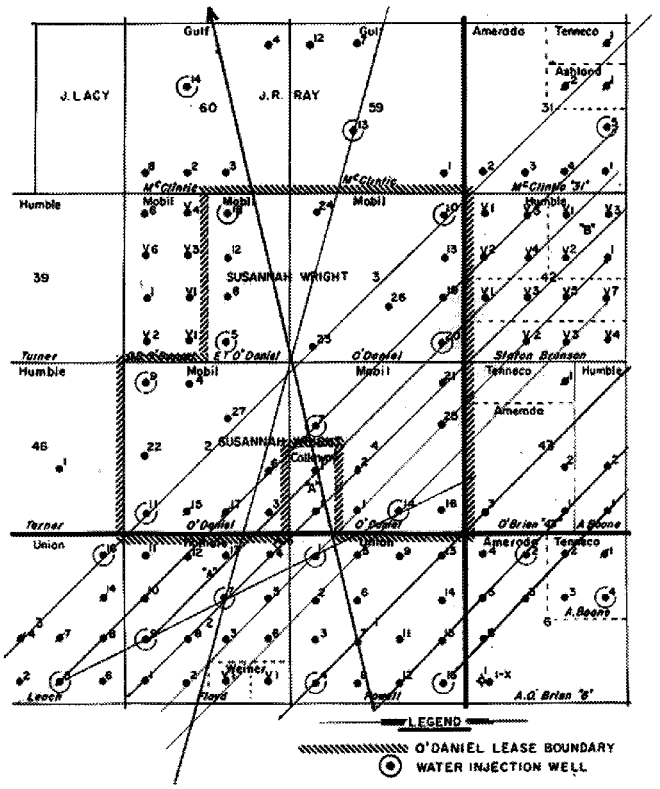

Fig. 3.10-6 —Waterflood Map, O'Daniel Unit Co-op Flood 1959: Injection wells originally aligned N50°E, series of lines indicates current fracture orientation as determined by waterflood response (approximately N32°E)

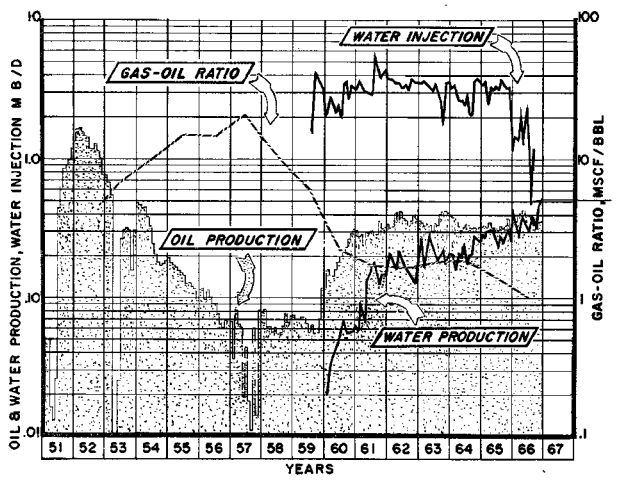

Fig. 3.10-7 —Performance of O'Daniel Unit co-op waterflood

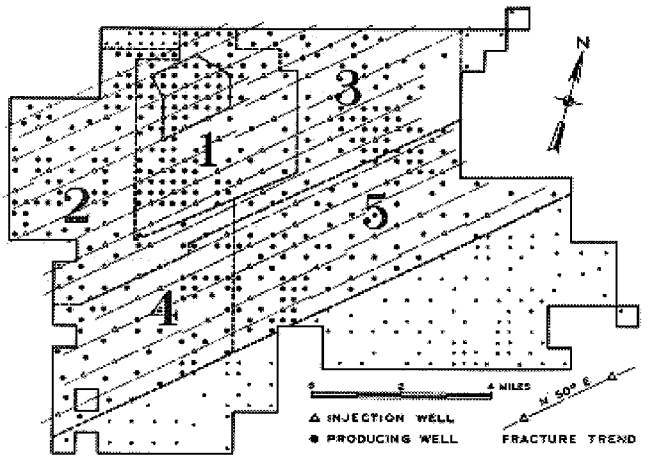

Fig. 3.10-8 —Areas developed for waterflood expansion in Spraberry Driver Unit, 1960

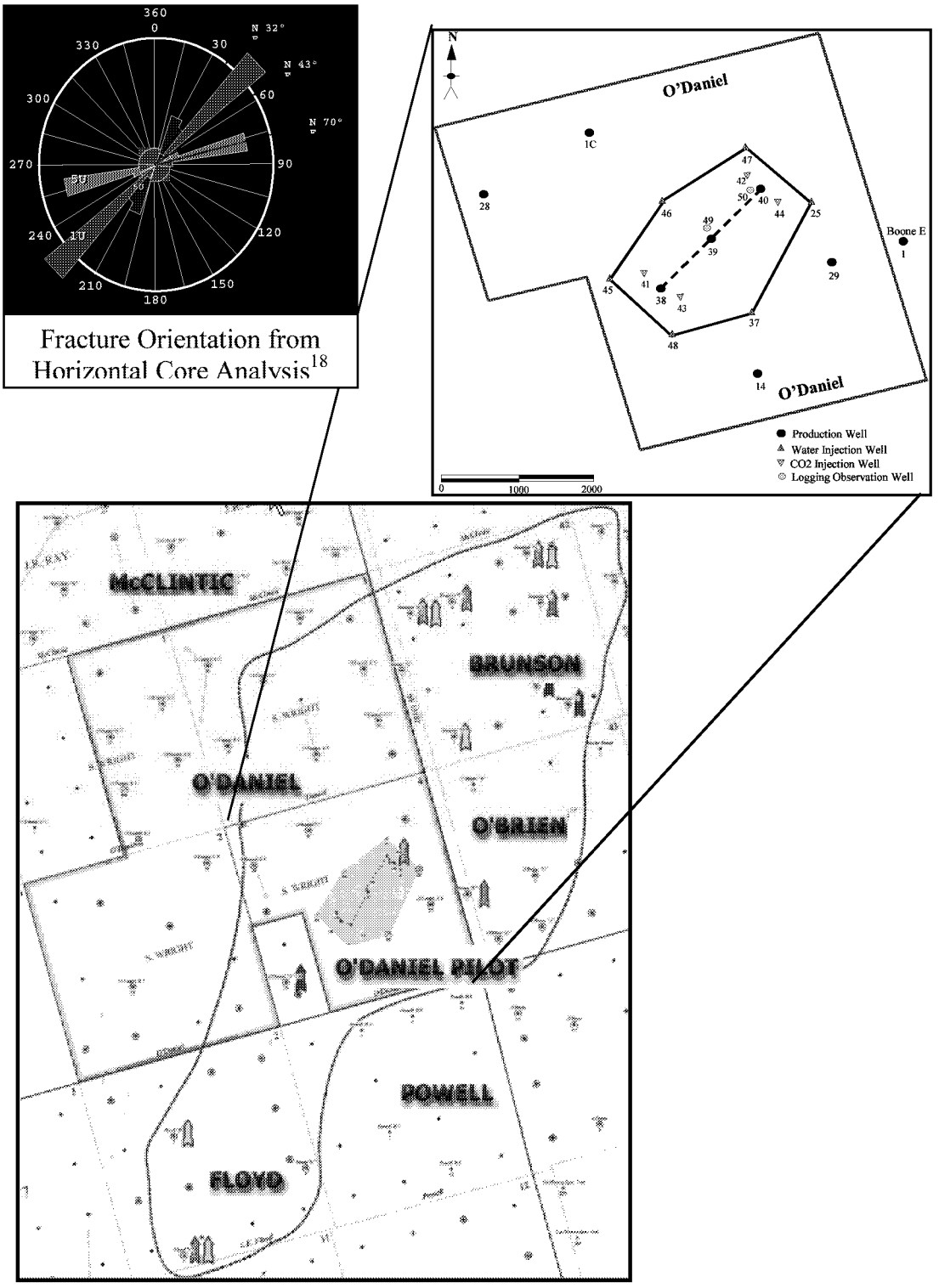

Fig. 3.10-9 —Map of O'Daniel pilot area and pilot well configuration

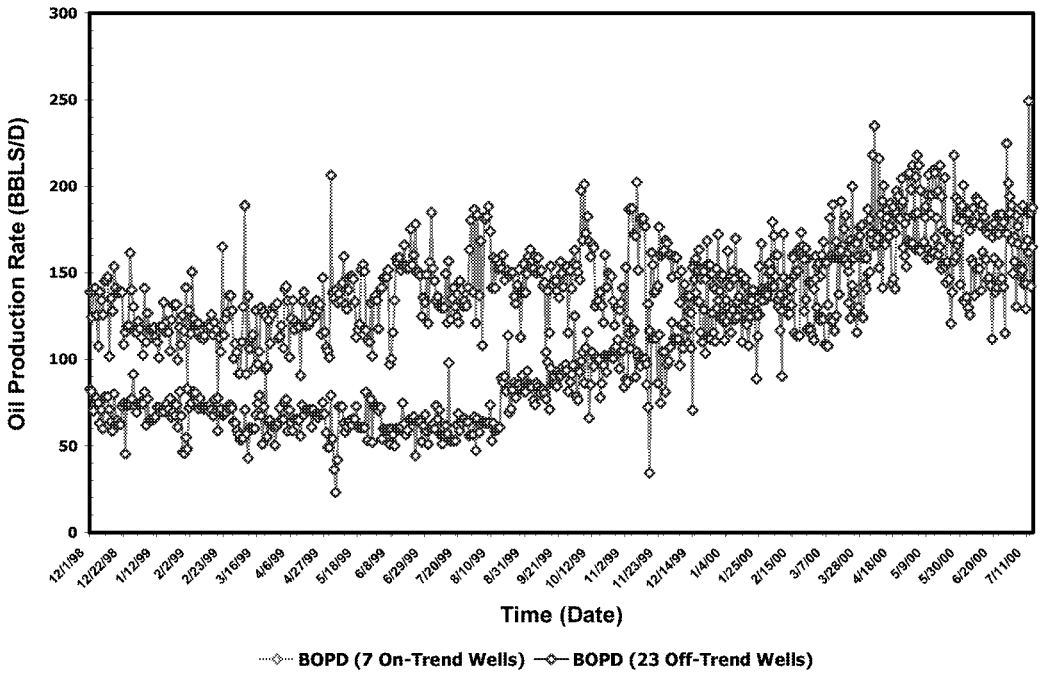

Fig. 3.10-10 —Response to water injection for 7 on-trend and 23 off-trend wells outside the pilot area

3.11 DEVELOPMENT OF A FRACTURE MODEL FOR SPRABERRY FIELD, TEXAS USA

Introduction

At the time of its discovery in 1949 the Spraberry Trend (Fig. 3.11-1) was considered the largest oil field in the World. The original primary recovery factor was anticipated to be less than 10%. In an effort to increase recovery, several areas of Spraberry were placed on waterflood beginning in the late 1950's. Waterflooding, for the most part, has been only moderately successful. The noted exception to this is the waterflood performance on the E.T. O'Daniel lease. The waterflood recovery in this lease has exceeded 25% of the original oil in place. Failure of waterflooding in Spraberry has been attributed to the low matrix permeability and extensive fracturing [1]. Many studies have been conducted to understand the Spraberry fracture characteristics[2-21]. However, the characteristics of the fracture network and its interaction with the supporting matrix framework remains poorly understood.

Over the last seven years, interference, step rate, inter-well tracer, salt tracer, buildup tests, fall-off tests, horizontal core, discrete fracture modeling, outcrop studies, fracture logs, production tests and profile logging data have been integrated to improve understanding of the Spraberry fracture system.

Geology

The Spraberry formation was deposited during Permian age in the Midland Basin, a geological province of the Permian Basin. The formation is comprised of submarine fans and basin plane deposits with a complex stratigraphy composed of sandstone, shale, siltstone and limestone interbedding. Core analyses and well logs show that the reservoir is characterized by both low porosity and low matrix permeability. Matrix permeabilities are in the order of 0.05 md or less with porosities ranging from 6 to 14 percent. The effective permeability of the reservoir, as determined from pressure buildup tests, step rate tests or advanced decline analysis, ranges from 1 to 200 md. We interpret that the primary contribution to the effective permeability is from the fracture systems, as opposed to the matrix. The formation has been subdivided into three principal intervals including the Lower, Middle and Upper Spraberry formations with average depths of about 7,200, 7,400 and 8,000 feet, respectively. These principal intervals have been further subdivided to different units (Fig. 3.11-2). Of these, only two units in the Upper Spraberry (1U and 5U) have been identified as containing reservoir quality rock capable of making significant production contributions.

Objectives

The overall objective of this report is to illustrate how a representative reservoir model was constructed by ***integrating*** the static geological data (core, fracture log and outcrop) with the dynamic engineering data (tracer test, production and pressure transient data).

Fracture Characterization

Effectively, the Spraberry trend can be characterized as a "triple component" system. The first component is the long, well-connected fractures, the second is a combination of matrix and smaller, more discontinuous fractures with some micro fracturing, and finally,

the third component is comprised of the low permeability matrix. A schematic view of the discontinuous fracture system is shown in Fig. 3.11-3. Figure 3.11-3 shows a diagram of more discontinuous fractures. The spacing of set 1 continuous fractures is not known.

The first component, the long fracture systems, or fracture clusters, are stress sensitive and greater than ~1000 feet in length. A secondary 'background' network of much shorter, partially connected (set 2) fractures, have an inter-fracture spacing in the two to four foot range.

The system of long, well-connected fractures initially controls flow in the reservoir and dictates which areas are invaded by injected fluids. In any short-term transport test (< 1 month), this component totally dominates the response, provided the wellbore area is not already pressure depleted. For example, if an individual producer intersects a well-connected fracture cluster, then that producer will have high initial fluid productivity, providing the reservoir is not depleted. The first component of the fracture system, although important initially, transports a relatively small proportion (<5%) of the flow over the well's total productive life.

The longer-term production response is controlled by both fracture sets and matrix crossflow. As water injection continues, water invades into the secondary, more discontinuous fracture system. The average fracture spacing, imbibition rate and matrix permeability then plays a more important role in controlling the production profile and recovery factors.

Data Types and Information

As is the case with a large number of naturally fractured reservoirs, there is limited direct fracture observation data available for the Spraberry trend. There is, however, plenty dynamic data that gives us some guidance for constructing a representative fracture model. The following is a review of this data.

Data from Direct Observation

1. Vertical core data show vertical fractures with fracture heights of one to four feet. Typically, vertical cores in Spraberry show NE-SW or East-West directionality[5, 9,20] as shown in Fig. 3.11-4. Fractures usually terminate against the shale barriers at the top or base of undisturbed geological events.
2. Recently, a horizontal core was acquired to better characterize the fracture system[14]. A lateral core was taken in each Upper Spraberry unit (1U and 5U). Figure 3.11-3 shows a schematic diagram of the Spraberry fracture distribution and orientation.
3. The Humble Unit Midkiff, deviated well [2,7] data shows that fractures are predominantly in the sand and not the shale, as shown in Fig. 3.11-5. From a mechanical strength perspective, this makes sense considering the ductility of shales whereas the sands are more brittle. As the fraction of shale content increases, fracture intensity decreases because the rock is more ductile, decreasing the brittle strain. Shale content in some reservoirs can therefore strongly control fracture intensity.

4. Study on an outcrop of an "analogous" reservoir[13] yielded information on fracture lengths, stress sensitivity, and orientation. A comparison of three analogous outcrops showed large variations in fracture characteristics. Figures 3.11-6 and 3.11-7 show the fracture images, fracture maps and average fracture lengths, for these outcrops. Fracture clustering and some fracture branching are observed in some outcrops but not in others. What is interesting about the outcrop is that ***most fractures are short (< 30ft).***

Indirect Hydraulic Data

5. A large volume of production /injection data is available for many of the Spraberry Units. Portions of the field have been flooded, intermittently, since 1951. The waterflood behavior (i.e., water breakthrough timing) indicates an average N50°E fracture trend. However it is expected that there is some overall variability of this trend [5,9]. The production and injection data show a variation in fracture orientation as shown in Table 3.11-1.
6. Constant pressure tests (and advanced decline analyses) indicated an effective permeability to oil in the range of k_{oe} = 0.4 to 0.9 md[18]. Note that the effective matrix permeability, based on core analysis, is less than 0.05md. The effective permeability, within the well drainage area, is therefore greatly enhanced by the second component fractures. These tests (and pressure buildup tests) can be interpreted as wells producing from a single hydraulic fracture in a low permeability reservoir. The data for these constant pressure tests were collected over a ten-year period and therefore represent a large radius of investigation.
7. A multi-well interference test, run during the year 2000 (Fig. 3.11-8) confirmed pressure communication existed between wells within the CO_2 pilot area as shown in Fig. 3.11-9. These tests have been analyzed using both single porosity and dual porosity methods. Regardless of how these test were analyzed the effective permeability was determined to be in the 10md range. These tests, performed within a 67-acre pilot area, confirmed the presence of heterogeneous fracture permeability.
8. Multi-well interference tests were run in the 1960's, at varying water injection rates in the Midkiff Unit. Rates were varied as shown in Fig. 3.11-10. The test results showed a stress sensitivity of fracture permeability to injection pressures. The test results also showed that a strong NE-SW fracture trend as well as East-West and NNE-SW trends prevailed. An interesting observation to note is that tests with higher injection rates yielded higher values of permeability.
9. Early build up tests (prior to 1960) yielded higher initial effective permeability values, in the 2 md to 200 md range[4] when reservoir pressure was near original pressures.
10. Approximately ten single-well pressure transient tests (falloff & buildup tests) were run[18]. In recent years, these tests have been analyzed using both single porosity and dual porosity models. Each of the evaluated wells had been stimulated with hydraulic fractures. All single well tests show negative skins and linear flow periods. The more recent buildup tests typically show low permeability (<1 md) whereas falloff tests yield a much higher permeability (>1 md), again confirming the probable stress sensitivity of the effective permeability (i.e., particularly of the fracture

system). The falloff tests measure higher permeability because these tests are conducted in water injectors with higher 'reservoir' pressures.

11. Mini-frac and step rate tests have shown that hydraulic fracturing occurs at relatively low pressures (i.e., close to a hydrostatic pressure gradient).
12. Average fracture spacing was derived from decline analyses and laboratory imbibition data. From this data it was determined that the average effective fracture spacing was 3.1 feet[16]. This agreed very well with the direct sample from the horizontal core on fracture spacing.
13. An interwell tracer test was conducted in late 2000 where six injectors had six tracers injected into them[25] and 37 offset wells were sampled. These tests showed NE-SW, NNE-SW and E-W rapid communication paths. Many wells experienced tracer breakthrough within a week of injection.
14. Numerous simulation models and waterflood analyses completed for the O'Daniel Unit, indicated East-West and NE-SW communication paths.
15. Salt-water tracer tests confirm communication in the NE-SW direction from the pilot area. Salt-water tracer tests at wells 28 and O'Daniel C1 also show that very poor communication exists in the north-westerly direction from the pilot area.
16. Production logging tests (PLTs) were run on three water injectors (Wells 45, 47 and 48 of the O'Daniel Unit). A figure of the profile log for Well 45 is presented in Fig. 3.11-11. The results show a relatively uniform distribution of flow within the 1U and 5U sands.

Some of the dynamic data seems to suggest the presence of a single fracture system, comprised of long fractures (points 6, 10 and 13). The dynamic data also emphasizes that the effective permeability in the reservoir, at any distance away from the wellbore, is higher than the matrix permeability (points 6, 7, 8, 9, 10 and 12). The shorter semi-continuous fractures enhance the 'matrix' permeability and are a major contributor to flow. Evidence of the stress sensitivity of both on-trend and off-trend fractures is shown by points 7,8, 10 and 11.

Fracture Length and Lateral Connectivity

Outcrop data and buildup/interference test data tend to indicate that the majority of fractures are short and not well connected. ***Individual*** fracture lengths appear to be short, in their natural state, as observed from outcrop data. Later stage buildup data also supports the concept of laterally semi-disconnected fractures in the reservoir. Most late stage buildup tests and constant pressure tests, yield a low effective permeability (k_{eff} < 1md). Even then, however, the permeability is higher than matrix permeability observed from core data.

It must be realized that the majority (i.e., >80%) of the fractures are probably not in hydraulic communication. The numerous small, disconnected fractures probably don't contribute that much to the effective permeability[22]. The small proportion of hydraulically connected fractures has been noted in numerous mining and ground water flow studies[23, 24].

On the other hand, some of the hydraulic data, such as tracer and production data, supports the theory of a well-connected fracture system. Well-connected fracture

systems (extending > 1000 feet) were evident in both the on-trend (N50°E) direction and off-trend direction (N30°E and N70°E), in the tracer tests and fall off test studies. Falloff tests on the well 47 and well 25 water injectors strongly suggest that the tests are dominated by linear flow as exhibited by the long duration linear flow periods (> 3 weeks).

These effective fracture system lengths are longer when water is injected. However it is believed that fractures close somewhat during depressurization of the reservoir. The systems of fractures are stress sensitive. Moderate water injection rates/pressures easily aggravate these systems. This observation made by comparing the falloff test results (permeability and fracture length) with build-up test results. The fracture lengths and permeabilities, determined from the falloff tests[18], are much greater.

Recent inter-well tracer tests conducted in the CO_2 pilot area, in the ET O'Daniel Unit, exhibit rapid water breakthrough times ranging from 1 to 99 days, corresponding to tracer velocities of 12,137 ft/day to 59 ft/day, respectively[25]. Six tracers were used in six injectors and sampling from 37 producing wells was done over a 100 day period. This implies that the waterflood tracer response was dominated by fracture flow and the first component (set 1) of the fracture system. However, the tracer recoveries during these tests were low, with maximum produced tracer concentrations of ~0.10 percent of injected tracer concentration, indicating low volumes of the highly connected fractures (set 1). Because of the high retention of tracer, it is believed that the bulk of the tracer is moving through the more tortuous pathways (set 2 fractures and matrix network). An example of fracture pathways inferred from tracer injection in Wells 46 and 47 is presented in Fig. 3.11-12. Figure 3.11-13 shows the tracer production response in well Brunson D-1. From tracers injected at well #46 and well #47, it was observed that tracer production declines sharply after breakthrough (peak concentration) and then gradually tapers off. The lag time and similar response pattern between injectors 46 and 47 is noteworthy. This echo of tracer response from injectors 46 and 47 suggest tracers are flowing in similar pathways

The results of salt tracer tests are summarized in Fig. 3.11-14. The salt tracer was sampled over a one-year period with 37 wells being sampled. Because of the earlier breakthrough of injected water, before salt-water tracer sampling, most wells do not show a marked change in sulfate concentration with time. Fig. 3.11-14 gives an estimation of the fraction of water produced by the well that comes directly from water injection. It **assumes** a background sulfate reading of zero. Clearly, on trend (NE-SW) producers such as Floyd "D1" and Brunson "D1" are strongly affected by the water injection.

Comparing results from the three interference tests, the salt-water tracer tests and the inter-well tracer tests, give insight into the nature of the long fracture systems. The Midkiff Unit interference test revealed a NE-SW as well as an East-West permeability trend. The O'Daniel interference test, within the 67-acre pilot area, showed that there was heterogeneous behavior. The O'Daniel tracer tests confirm all three trends: NNE-SSW, NE-SE and East-West (confirming once again the prevailing reservoir heterogeneity). Tracer breakthrough was observed from Well 47 to O'Brien 10, in a NW-SE direction. With the exception of this observation, all other pressure and tracer measurements confirm a fracture orientation that is in excellent agreement with fractures observed in the core data.

Fracture Porosity, Aperture and Fracture Volume

The volume of these fracture systems is in the order of 1 to 1000 Bbls or 25 - 50 Bbls/acre. These volumes are based primarily on the Midkiff Tracer Test and water breakthrough response[6]. This results in a fracture porosity of 0.04 to 0.08%.

Measured fracture apertures are expected to have a large range due to the stress (i.e., pressure) sensitivity of fractures. Measured apertures in un-stressed raw core averages ~50 microns, with a range of 10 to 320 microns. Near the injection wells, fracture aperture is likely to be wider compared to the regions near producers due to the injection of high-pressure water that opens and extends some of the pre-existing fractures.

Discussion of Fracture Height

The height of the fractures as seen in the vertical core is limited (1-4 ft). However, the number of vertical cores is also limited. Therefore sample totals are small. As mentioned earlier, fractures generally terminate at shale barriers (see Fig. 3.11-5). Injection logging data on water injectors show a relatively uniform distribution of flow within 1U and 5U sands. The profiles taken to date do not show that there is any single fracture taking a very high proportion of flow, as shown in Fig. 3.11-11. However, despite termination of natural fractures at shale boundaries, temperature logs suggest that fracturing out of the pay zone is likely. Note that Fig. 3.11-11 shows lower temperatures well above the perforation interval confirming the presence of cooler, injected water. The water likely migrated to this position via fractures, propagating out of zone. Note, this water injector was not intentionally hydraulically fractured.

Discrete Fracture Network (DFN) Modeling

A discrete fracture network (DFN) model was developed for the E.T. O'Daniel Unit using commercial software[26]. This DFN model was developed to improve the understanding of the Spraberry fracture network and to better integrate the results obtained from various sources, such as core, logs, outcrop, tracer tests, pressure transient data and multi-well interference tests. The DFN model developed in this study is based on data from outcrop studies[13] and core data [9,14]. The steps involved in development of a DFN model for the E.T. O'Daniel lease is outlined in Fig. 3.11-15. The modeling approach is to assume a permeability and anisotropy ratio (roughly known) and investigate combinations of fracture parameters that would agree with these assumptions.

Different sensitivities were carried out using different fracture aperture and average fracture lengths. Results for some of the runs are presented in Table 3.11-2. An example of directional permeability, calculated using fracture orientation from the Spraberry 5U Unit, is illustrated in Fig. 3.11-16. Assuming that the measured fracture spacing and orientation is correct, the following observations can be made from DFN modeling:

- Fracture length has tremendous impact on effective fracture permeability
- Fracture length must be greater than 10 ft (as there is no connectivity with smaller length fractures)
- Fracture height has a relatively moderate impact on horizontal permeability, at least when the fracture length/connectivity is low
- Fracture height has significant impact on vertical permeability

- Fracture height varies between 2 ft and 5 ft (i.e. fractures do not extend through the entire pay thickness)
- With long or moderate fractures (~ 100 ft), fracture aperture (or transmissivity) strongly controls permeability
- Given the observed 'cross-fracturing', the anisotropy ratio (k_{max}/k_{min}) is low (~ 10 or less)

Modeling Spraberry fractures indicates that these fractures are not well connected. These set 2 fractures can be considered as "stochastic fractures". The set 1 fractures are classified as "deterministic fractures".

Fracture Flow Mechanics

Creating a viscous pressure drop across the fracture will be important in both waterfloods and CO2 flooding. However, large pressure gradients in either the on-trend or off-trend direction will not be possible because of the "check valve" or "pressure relief valve" effect that the fractures have (especially in the off-trend fracture sets). Fluids injected at high pressure will enhance fracture connectivity thus increasing both the on-trend and off-trend fracture permeability of the system.

Any short-term hydraulic (pressure or rate) response is likely to be dominated by the large-scale fractures if they are reasonably close to the observation or signal wells. For these wells, the high lateral-connectivity fractures will control flow direction and thus pressure and rate response (water breakthrough or pressure pulse response).

However, ultimate waterflood recovery factors and production are controlled by the average fractures spacing between both the short fractures and by the long fracture system pathways. The long fracture system establishes where water is initially distributed (initial volumetric sweep) but with time, and increasing injected water volumes, many of the small and more discontinuous fracture systems become invaded by water. At this time imbibition rate, fracture spacing and matrix permeability control waterflood production response.

Conclusions

We have proposed a fracture model that seems to fit all available data, consistently. Initially the longer fractures dominate production performance of individual wells or areas. Some fracture systems determine initial well deliverability (flush production). Fracture connectivity of long fracture systems determine initial water/tracer breakthrough in waterfloods. However, with continued production and injection the importance of shorter, less connected fracture systems and the matrix, are felt. At later stages of waterflooding, average fracture spacing, average effective permeability and imbibition processes dictate recovery profiles. For solution gas drive scenarios, the long term deliverability is largely controlled by effective permeability.

References

Guidroz, G.M.: "E.T. O'Daniel Project – A Successful Spraberry Flood," JPT, September 1967, pp. 1137-40.

Carlson, R.F.: "Special Directional Drilling in West Texas," Oil and Gas Journal, September 1 1952, pp. 99-101.

Brownscombe, E.R. and Dyes, A.B.: "Water Imbibition Displacement – Can It Release Reluctant Spraberry Oil?" Oil and Gas Journal, November, 1952.

Dyes, A.B. and Johnston, O.C.: "Spraberry Permeability from Build up Curve Analyses," AIME Vol. 198, 1953.

Elkins, L.F. and Skov, A.M.: "Determination of Fracture Orientation from Pressure Interference," *Trans*, AIME (1960). **219,** 301.

Elkins, L.F. and Skov, A.M.: "Cyclic Water Flooding the Spraberry Utilizes End Effects to Increase Oil Production Rate," *JPT*, August 1963.

"Midkiff Pulse Testing – Results of Spraberry Final Pulse Testing Experiments July 1 August 6, 1963," Humble Oil Internal Memo, PRRC Spraberry Database, September 1963.

Epic Consulting Services Ltd.: "Parker & Parsley Waterflood Surveillance E.T. O'Daniel Unit," correspondence with Parker & Parsley (now Pioneer Natural Resources USA, Inc.), February 1996.

Schechter, D.S. et al.: "Reservoir Characterization and CO_2 Pilot Design in Naturally Fractured Spraberry Trend Area," paper SPE 35469 presented at the 1996 SPE Permian Basin Oil and Gas Recovery Conference held in Midland, Texas, 27-29 March.

Schechter, D.S.: "Advanced Reservoir Characterization and Evaluation of CO_2 Gravity Drainage in the Naturally Fractured Spraberry Trend Area," First Annual Technical Progress Report to DOE under Contract No. DE-FC22-95BC14942, PRRC Report 96-42, Dec. 17, 1996.

Baker, R.O. and Spenceley, N.K.: "Pre and Post Hydraulic Fracture Buildup tests on E.T. O'Daniel #37," correspondence with Parker & Parsley (now Pioneer Natural Resources USA, Inc.), December, 1996.

Guo, B. and Schechter, D.S.: "An Integrated Study of Imbibition Waterflooding in the Naturally Fractured Spraberry Trend Area Reservoirs," paper SPE 39801 presented at the 1997 SPE Permian Basin Oil and Gas Recovery Conference held in Midland, Texas, 25-27 March.

Malmanger, E.M., Statistical Analysis and Simulation of Stress Sensitive Natural Fracture Networks, M.S. Thesis, New Mexico Institute of Mining and Technology, Socorro, NM, March 1997.

McDonald, P., Lorenz, J.C., Sizemore, C., Schechter, D.S. and Sheffield, T.: "Fracture Characterization Based on Oriented Horizontal Core From the Spraberry Trend Reservoir: A Case Study," paper SPE 38664, presented at the SPE Annual Technical Conference and Exhibition held in San Antonio, Texas, 5-8 October, 1997.

Schechter, D. et al.: "An Integrated Investigation for Design of a CO_2 Pilot in Naturally Fractured Spraberry Trend, West Texas," paper SPE 39881 presented at the SPE International Conference and Exhibition held in Villa Hermosa, Mexico, March 3-5,

1997.
Baker, R.O. et al.: "Using An Analytical Decline Model to Characterize Naturally Fractured Reservoirs," paper SPE 39623 presented at the 1998 SPE/DOE Improved Oil Recovery Symposium held in Tulsa, OK, 19-22 April.
Putra, E. et al.: "Use of Experimental and Simulation Results for Estimating Critical and Optimum Water Injection Rates in Naturally Fractured Reservoir," paper SPE 56431 presented at the 1999 SPE Annual Technical Conference and Exhibition held in Houston, Texas, 3-6 October.
Baker, R.O. et al.: "Characterization of the Dynamic Fracture Transport Properties in a Naturally Fractured Reservoir," paper SPE 59690 presented at the 2000 SPE Permian Basin Oil and Gas Recovery Conference held in Midland, Texas, 21-23 March.
Baker, R.O. et al.: "Reservoir Characterization of Naturally Fractured Reservoir," paper SPE 63286 presented at the SPE Annual Technical Conference and Exhibition held in Dallas, Texas, 1-4 October, 2000.
Wilkinson, W.M.: "Fracturing in Spraberry Reservoir, West Texas, Bulletin of the AAPG, Vol. 37, No. 2, February 1953, pp. 250-65.
Tyler, N. and Gholston, J.C.: "Heterogeneous Deep-Sea Fan Reservoir, Shackelford and Preston Waterflood Units, Spraberry Trend, West Texas," Report of Investigation No. 171, Bureau of Economic Geology, The University of Texas, Austin, 1988.
Baker, R.O. et al.: "An Integrated Fracture Characterization of a Heavy Oil Naturally Fractured Carbonate Reservoir," paper CIM 2001-13 presented Petroleum Society's Canadian International Petroleum Conference held in Calgary, June 12-14, 2001.
Olsson, O. et al: "Site Characterization and Validation, Stage 2 – Preliminary Predictions," Swedish Geological Co., Report ID No. 88.
Long, J.C.: "Construction of Equivalent Discontinuum Models for Fracture Hydrology," Lawrence Berkley Laboratory, Berkley, CA.
Epic Consulting Services Ltd.: "Analysis of E.T. O'Daniel Tracer Study: Spraberry Formation," correspondence with Pioneer Natural Resources USA, Inc., April 2001.
User Documentation, FracWorks/95, Discrete Fracture Network Simulator, Version 1.3, Golder Associates Inc., 1999.

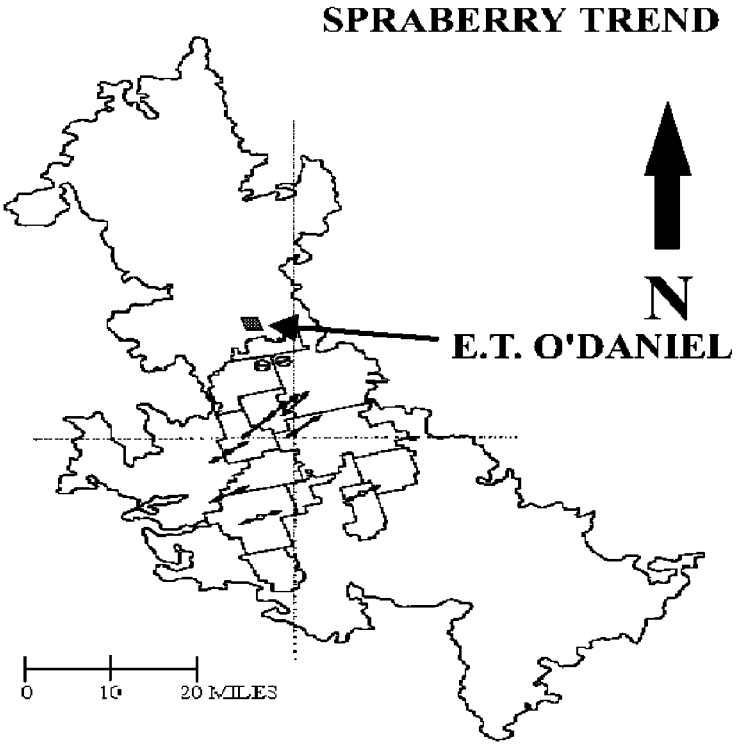

Fig. 3.11-1 —Map of Spraberry Trend illustrating location of the E.T. O'Daniel lease

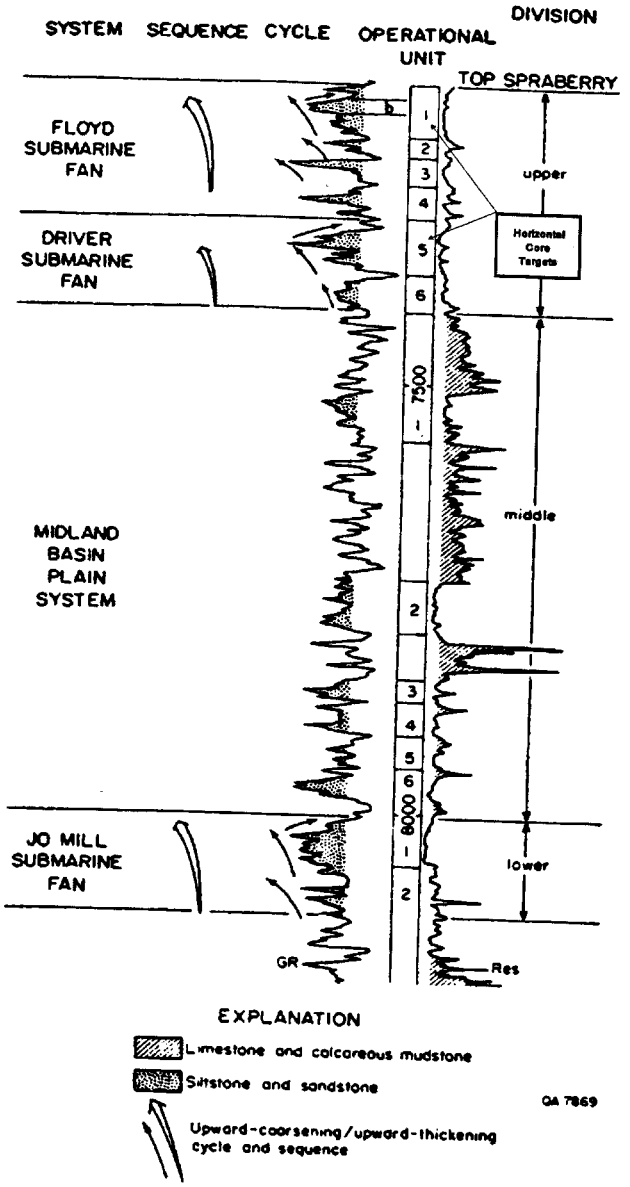

Fig. 3.11-2—Division of Spraberry Formation in the central trend area, TXL Fee "B" No. 1 Well

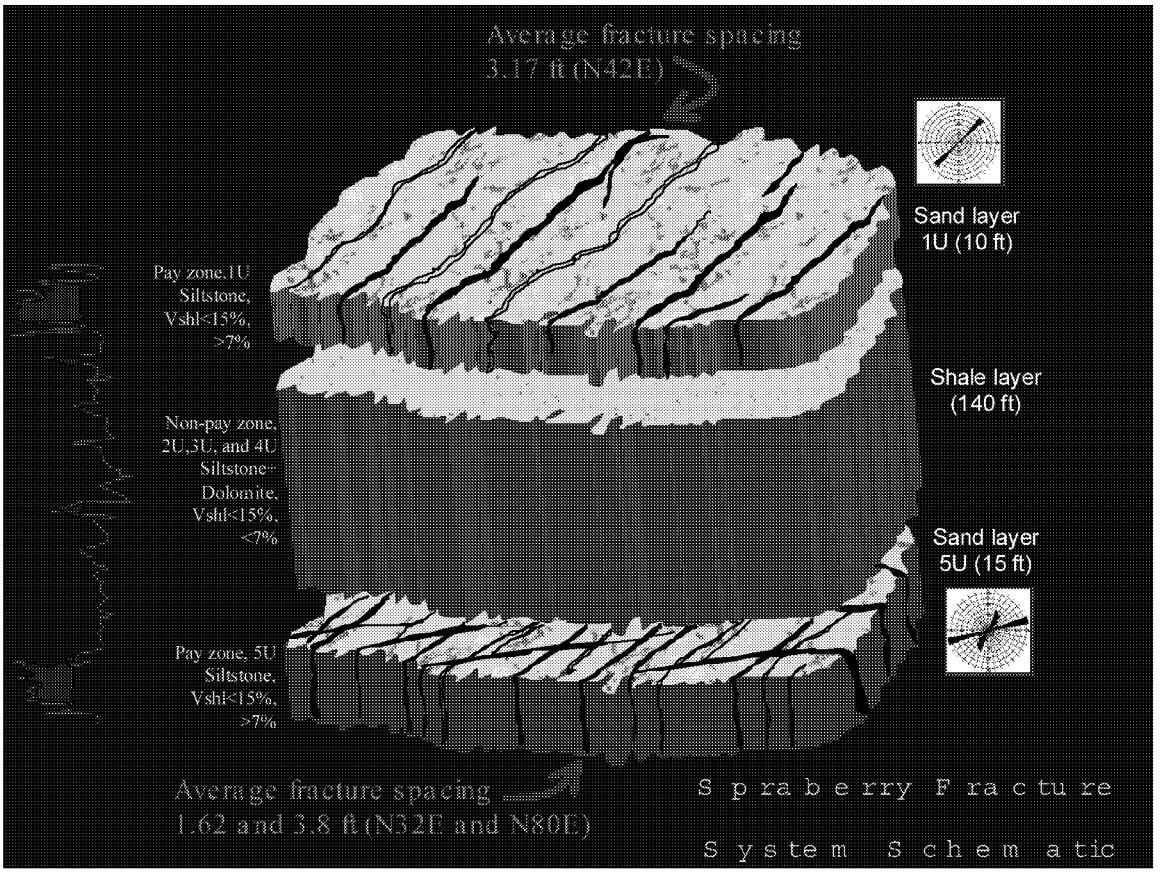

Fig. 3.11-3 —Schematic diagram of Spraberry fracture system

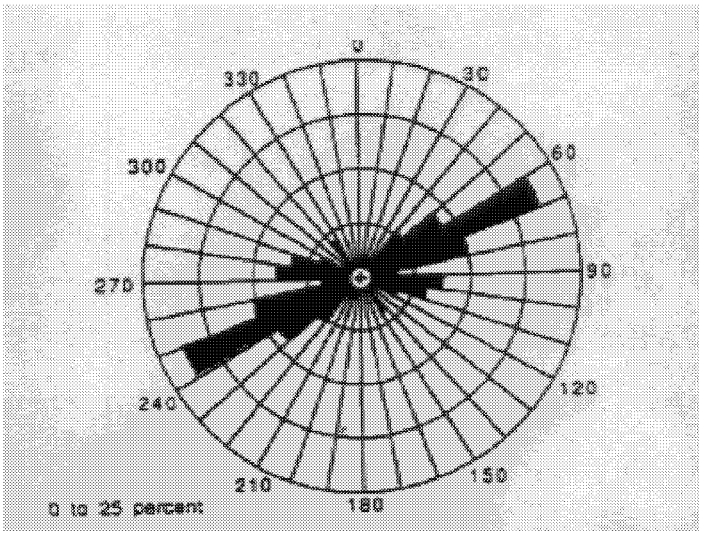

Fig. 3.11-4 —Azimuth of FMS Anomalies from Judkins A#5 and Preston #37 wells. This rose diagram indicates a conjugate fracture direction in the East-West direction.

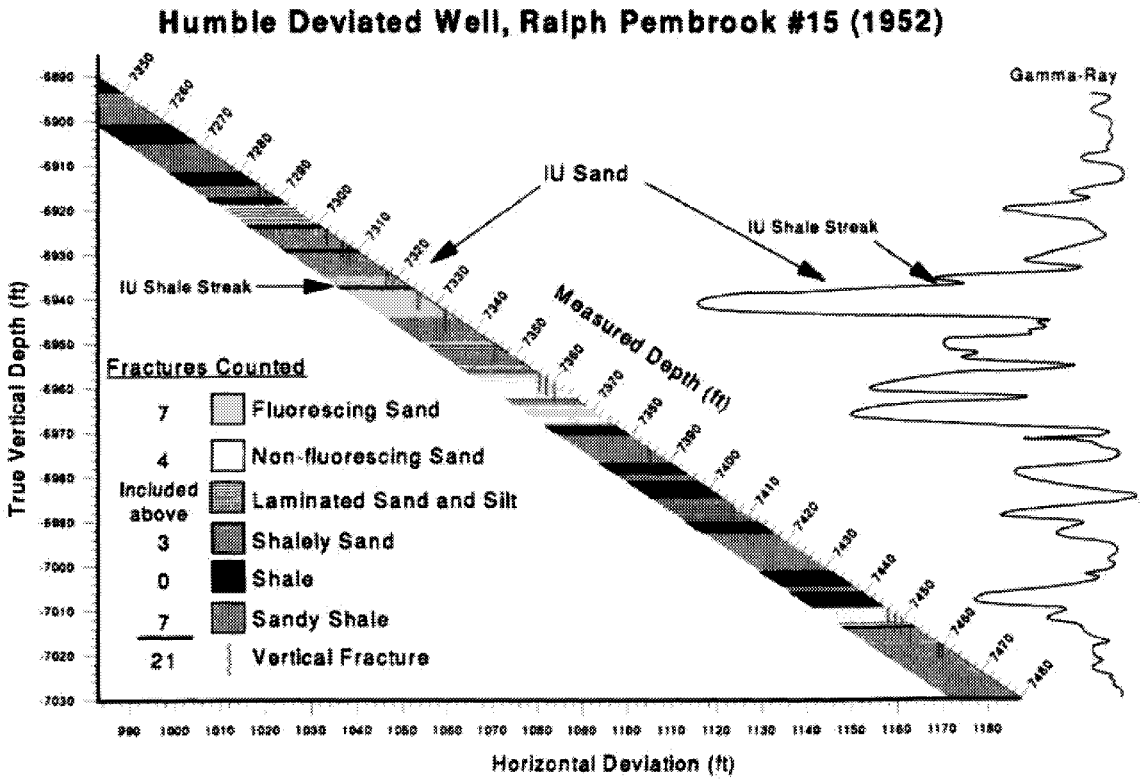

Fig. 3.11-5 —Humble deviated well showing fracture behavior and pattern

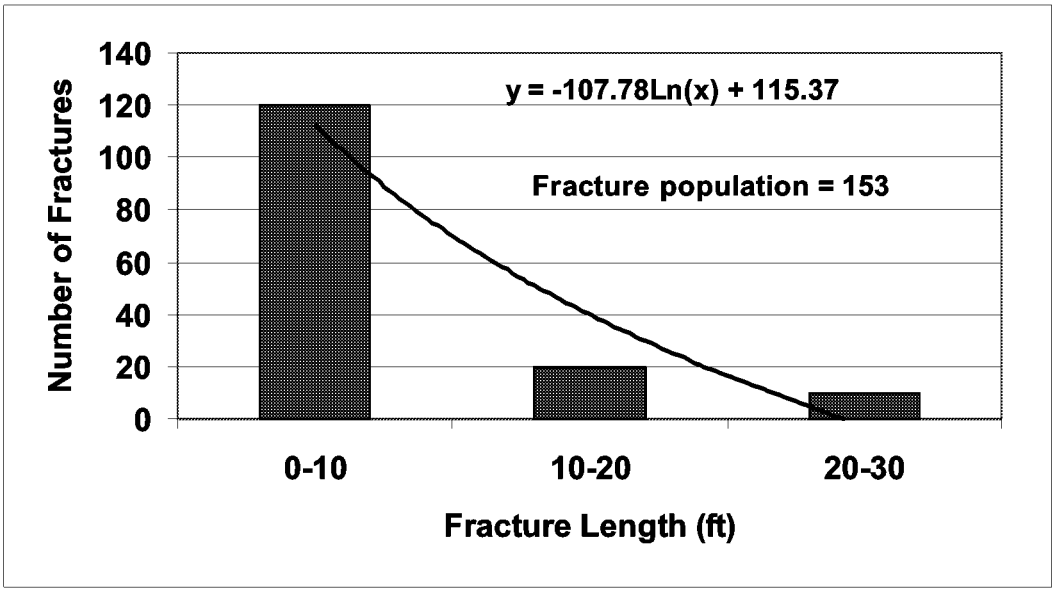

Fig. 3.11-6 —Fracture length frequency of Delaware outcrop data, West Texas

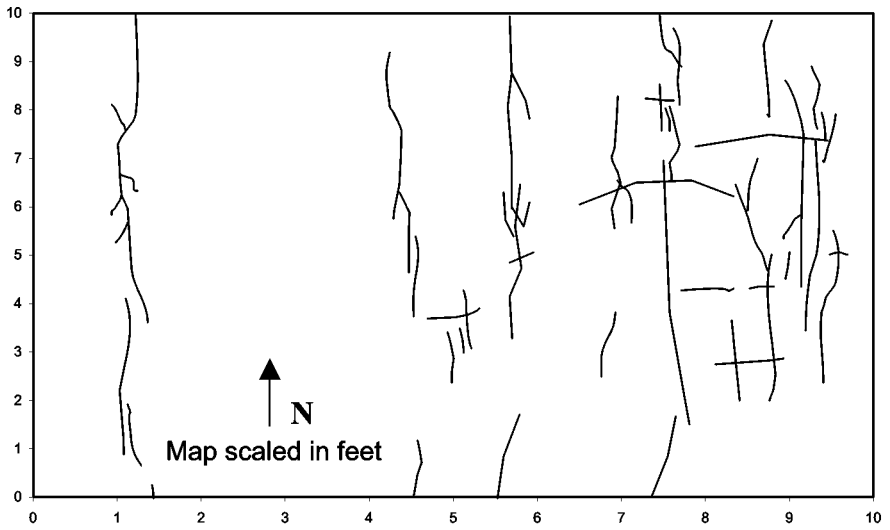

Fig. 3.11-7 —Fracture map of the Delaware outcrop data, West Texas

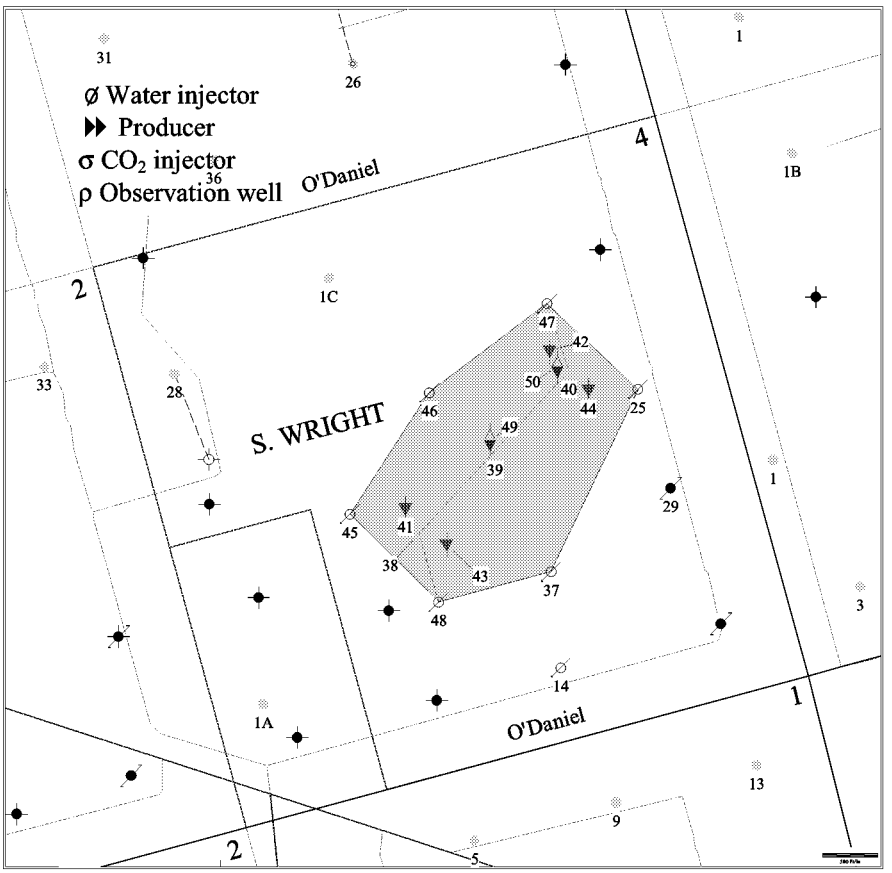

Fig. 3.11-8 —O'Daniel Interference Test; Wells 47,48,45 and 24 were injected into at high rates (2000 bbl/d) and wells 38,39,40,45 were observation wells; shaded pilot area is 67 acres in area

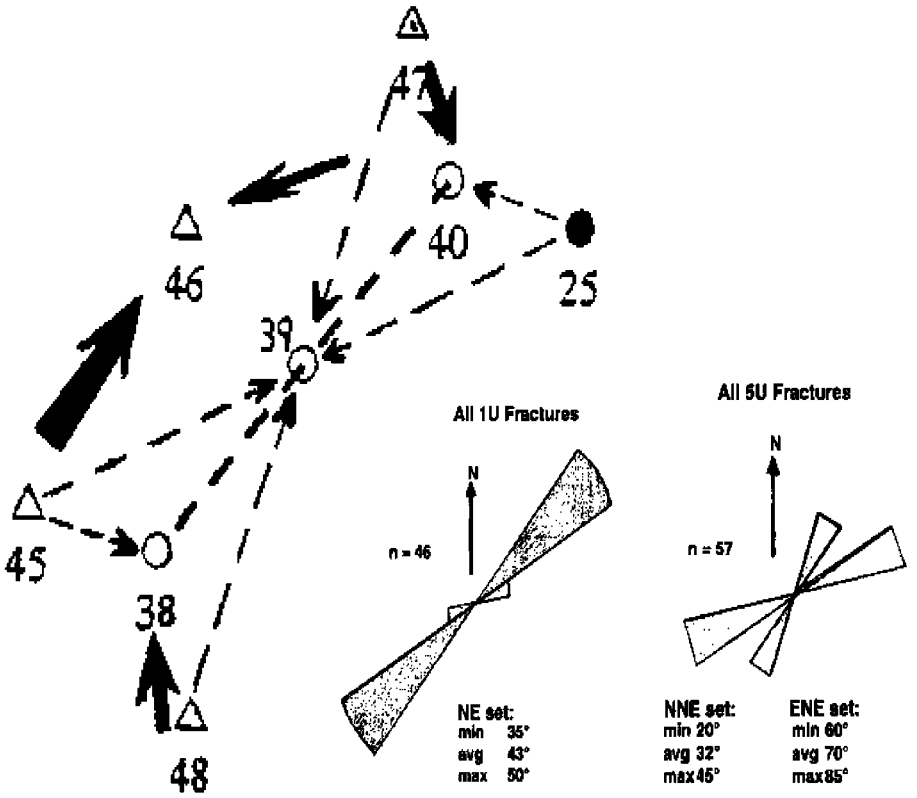

Fig. 3.11-9 —O'Daniel interference test map with arrows noting the strength of the response and horizontal well fracture (Rose Diagram)

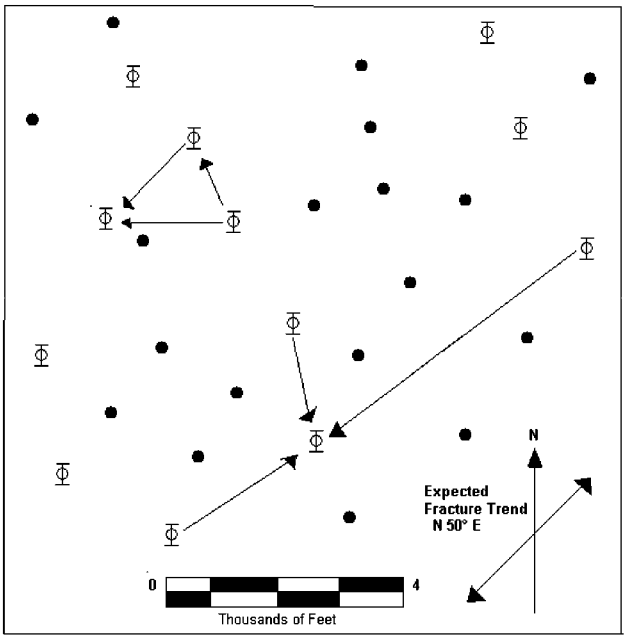

Fig. 3.11-10 —Humble interference test in Midkiff unit demonstrating the variability in direction of main fracture trend (NE and E-W) arrow indicate communication

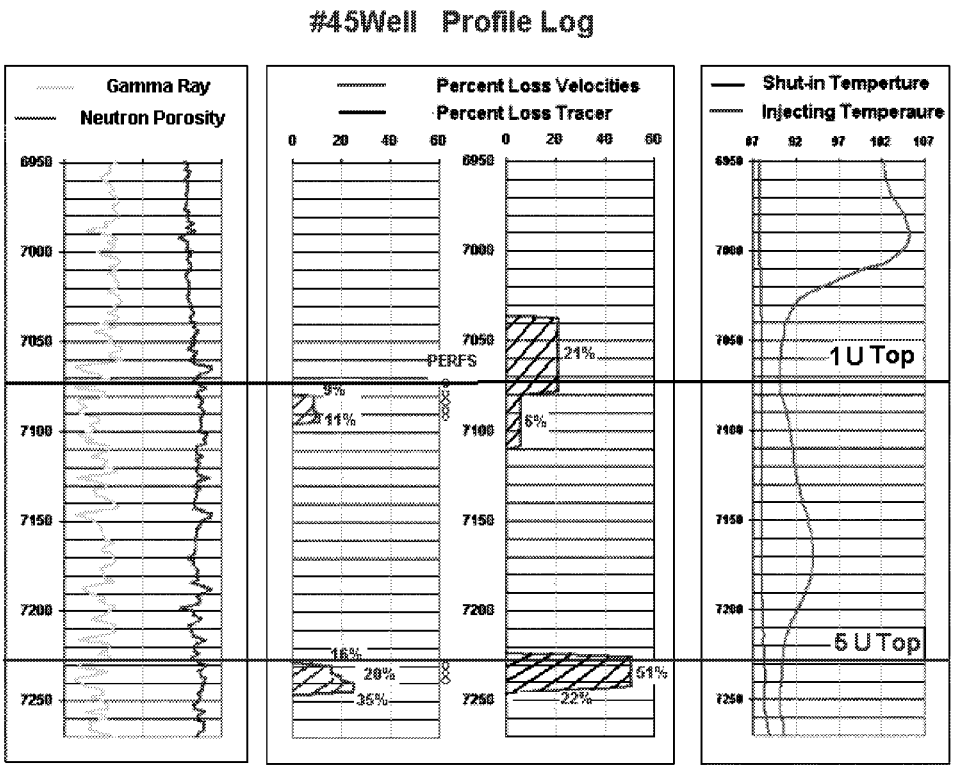

Fig. 3.11-11 —Injection profile log on Well 45

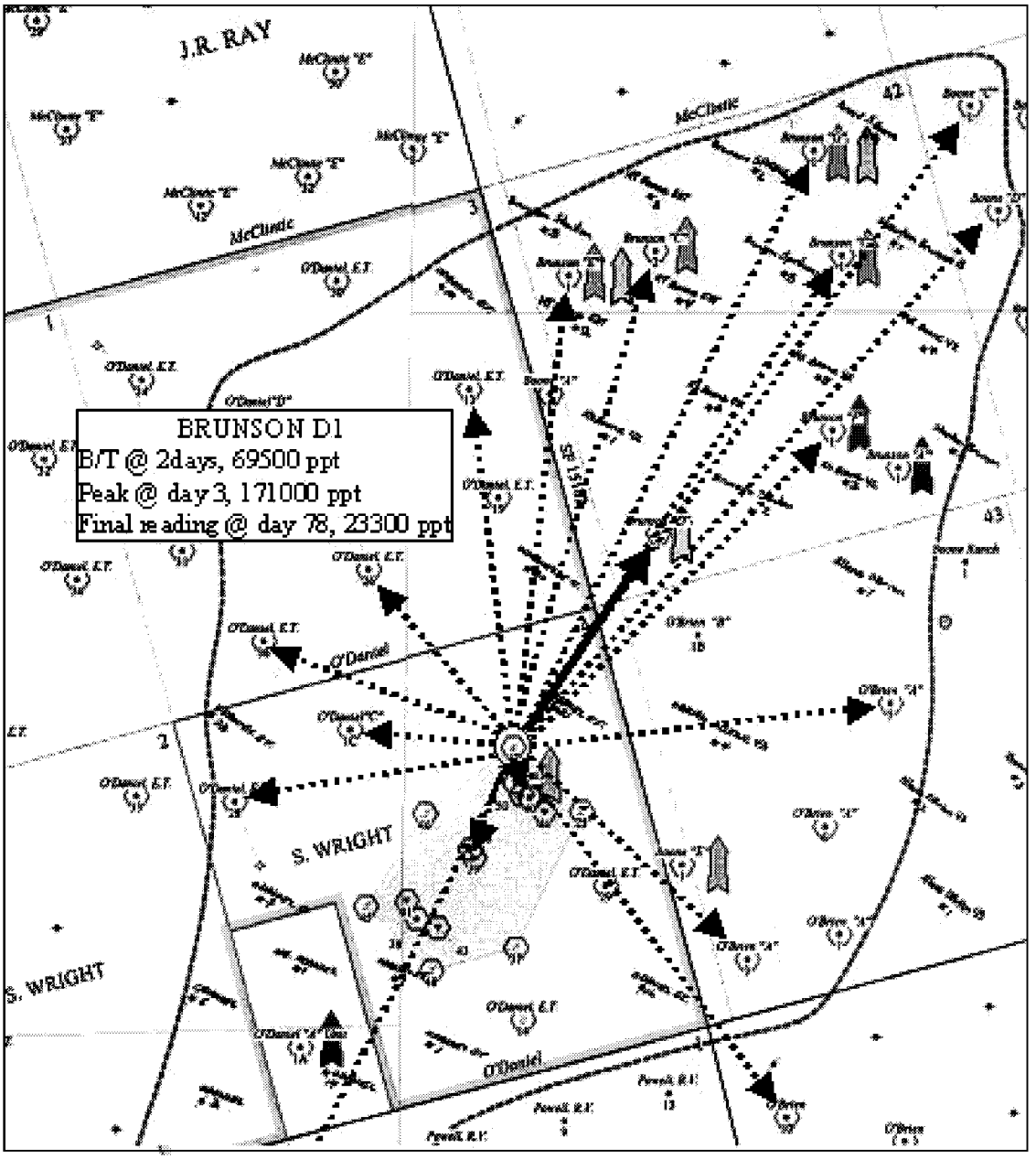

Fig. 3.11-12 —Fracture Pathways Inferred From Tracer Tests

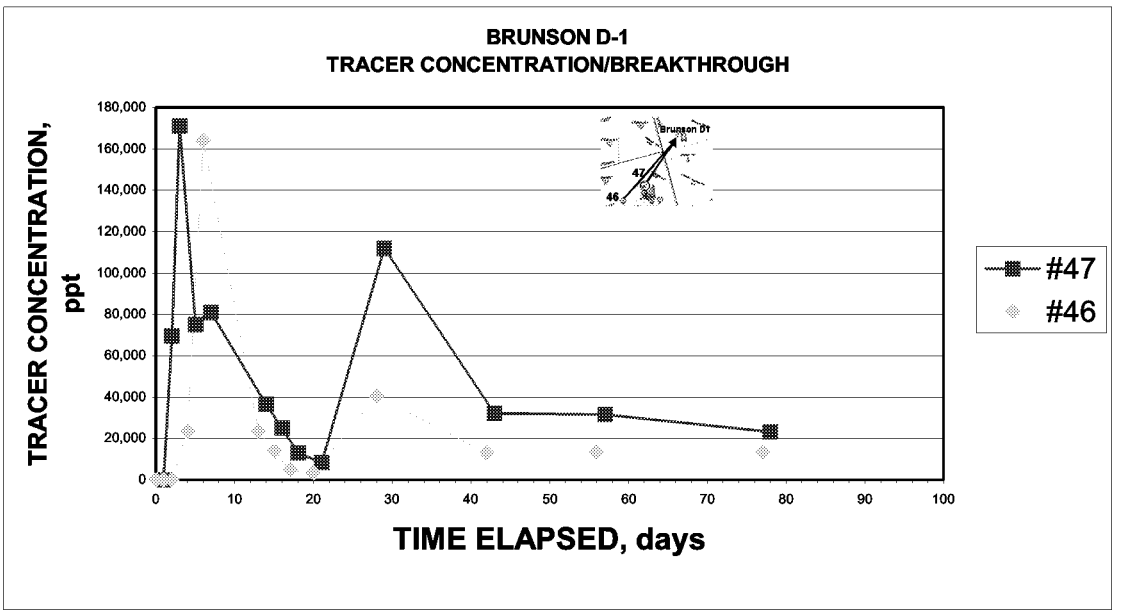

Fig. 3.11-13 —Brunson D1 tracer produced vs. time

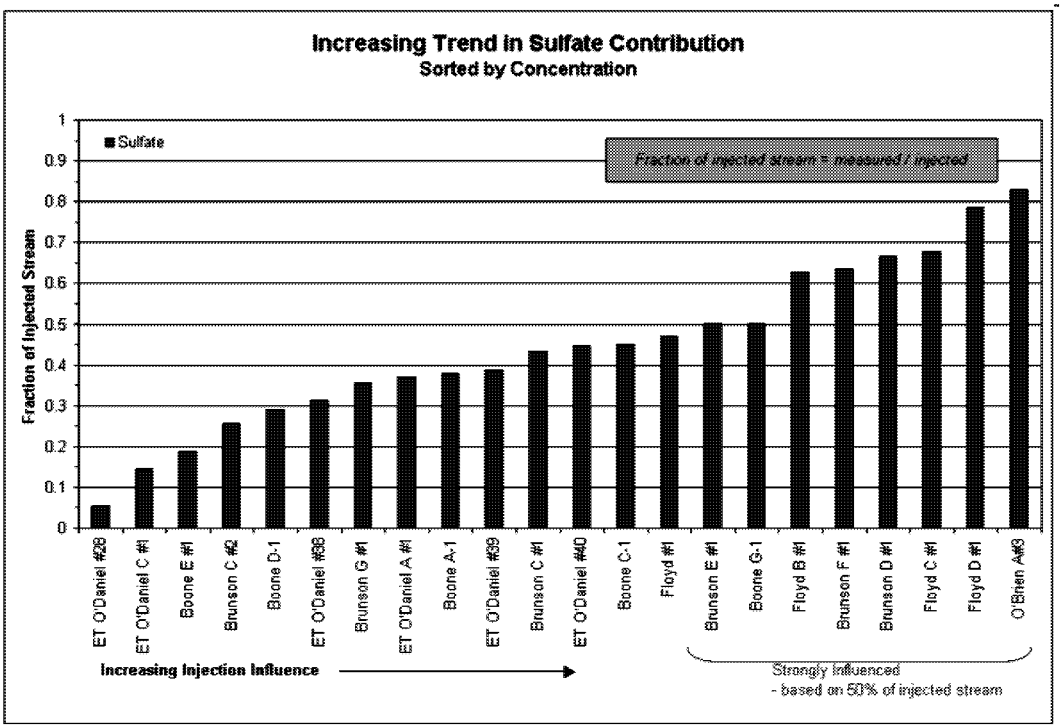

Fig. 3.11-14 —Fraction of Injected Stream Influencing Production Wells Based on Sulfate Sampled

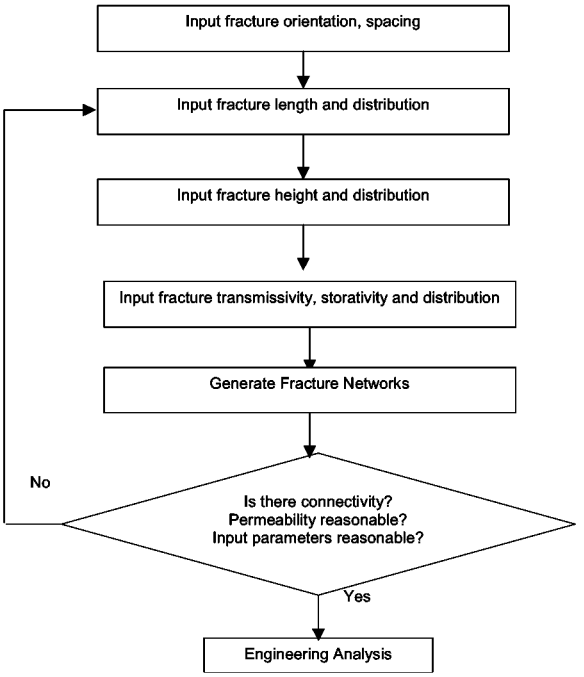

Fig. 3.11-15 —Steps Involved in Development of a DFN Model

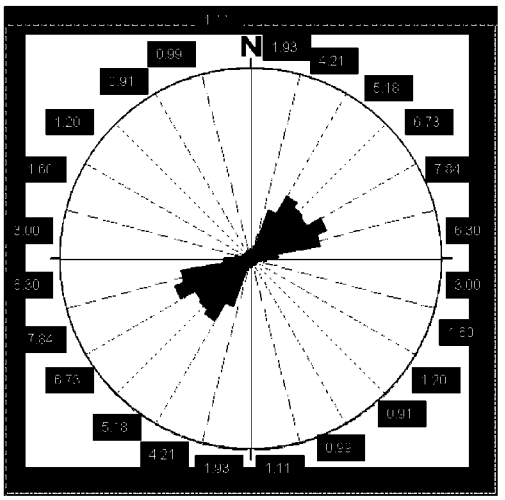

Fig. 3.11-16 —Calculation of Directional Permeability Using FRACMAN for Average Length = 100 ft, Height = 2ft, Transmissivity = 2 10^{-6} m^2/s (Using Fracture Orientations from 5U). Note k_{max}/k_{min} = 8.60.

Table 3.11-1 —Fracture characteristics and permeability contrast, Spraberry Trend area Field

	Fracture Trend	Ratio Permeabilities[b]	Avg. Deviation Calculated vs. Measured Pressures	Equivalent Permeability[a] (m/d f/t)
Midkiff Area				
Humble Water Flood	N50°E	144		
Pressure analysis (17 Wells)	N43°E	100 to 1000	78.4	443
North Driver Area				
Atlantic Water Flood[c]	N42°E	--		
Pressure Analysis (21 Wells)	N36°E	9	53.3	406
Pembrook Area				
Gas Injection test	N48°E	--		
Pressure Analysis (16 Wells)	N62°E	49	60.6	446
Aldwell Area				
Radioactive Gas Tracer	N53°E	~ 16	--	
Driver Area				
Pressure Analysis				
55-Well Composite	N56°E	13	31.6	888
14-Well Davenport A Lease	N76°E	36	24.7	1130
15-Well Davenport B Lease	N52°E	6	28.4	965
13-Well X. B.Cox and J.C. Bryans Leases	N76°E	36	15.2	1020
12-Well C.J. Cox and T.X.L. Leases	N36°E	7	14.7	481

a. $h\sqrt{k_x ky}$

b. Ratio of permeability along major fracture trend to permeability perpendicular to fracture trend

c. Orientation determined by general pattern of reduction of gas-oil ratio and water breakthrough

Table 3.11-2 —Results of Sensitivity Runs; Effect of Different Fracture Aperture and Fracture Height (Using Fracture Orientations from 5U)

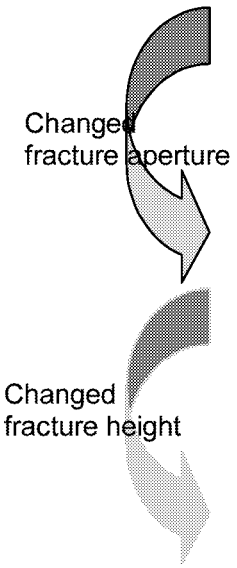

	Mean fracture height = 5 ft ***Mean transmissivity = 0.40 10^{-7} m^2/s***		
Mean Fracture Length	10 ft	100 ft	500 ft
k_x (md)	0	0.22	0.50
k_y (md)	0	0.14	0.39
k_z (md)	0	0.01	0.13
	Mean fracture height = 5 ft Mean transmissivity = 1.00 10^{-6} m^2/s		
Mean Fracture Length	10 ft	100 ft	500 ft
k_x (md)	0	5.40	12.48
k_y (md)	0	3.47	9.63
k_z (md)	0	0.37	3.37
	Mean fracture height = 2 ft Mean transmissivity = 1.00 10^{-6} m^2/s		
Mean Fracture Length	10 ft	100 ft	500 ft
k_x (md)	0	3.00	4.47
k_y (md)	0	1.93	4.74
k_z (md)	0	0.07	0.07

3.12 SPRABERRY RESERVOIR SIMULATION MODEL

Introduction

Waterflooding in the Spraberry Trend Area has always been subject to discussion resulting from ambiguity of performance after waterflooding. In every case of water injection, wells far away from injection wells and located on-trend direction have responded favorably. This behavior did not follow the common waterflooding practice in naturally fractured reservoirs. The practice dictated that all water injection should be aligned along major fracture trends and production wells are located perpendicular to the injection wells (off-trend direction). The reason is to produce oil, which flows in a direction perpendicular to the fractured trend towards a line of production wells, from strongly water-wet rock by force imbibition and to avoid rapid water breakthrough in the production wells.

The behavior of well in the on-trend direction is investigated through the Humble waterflood performance. A five-spot pilot waterflood was initiated in March 1955 in the Midkiff Spraberry Unit. The Humble 80-acre pilot was completely confined with one center production well, Shb-9 and four injection wells, B-2, B-4, B-6 and B-10 as illustrated in Fig. 3.12-1. During the waterflooding process, extensive data was collected on the center production well as well as on 19 observation wells in the vicinity of the pilot.

The center well responded in a dramatic fashion with the oil production increasing from approximately 50 to 135 B/D. Production continued to increase and reached a maximum of 256 B/D during December 1955. During the time that there is a sharp increase in oil production, a larger pumping unit was installed. The installation of pumping during the water injection clearly obscures the interpretation since the dramatic increase in oil recovery was not by water injection alone. Because of this reason, water injection response on the center production well cannot be used as our waterflood interpretation. Meanwhile, the observation wells located in the vicinity of the pilot area demonstrated a response to water injection. Observation wells located on a northeast-southwest trend received production responses and also had water breakthrough, while wells located perpendicular to this trend demonstrated no response to water injection. To simplify the analysis, it was decided to use only two wells, injection well (Shb-10) and observation well (Shb-8), that demonstrated a good response to water injection with the following assumptions:

- Only two wells were included in the basic model, one is injector (SHB-10) and the other is producer (SHB-8) as shown in Humble Pilot map.
- The production well was located in the same line with injection well (in the on-trend direction).
- The response of oil production rate in the Shb-8 well was only affected by water injection from the Shb-10 well.

The distance between these two wells is 3465.4 ft with number of grid blocks of 25x25x3, which covers about 275 acre. All known reservoir characteristics have been

done in the previous work as well as actual production and injection rates were included in the reservoir model.[1,2] With this flood behavior as criterion for the analysis, the water breakthrough time, ratio of off-trend and on-trend fracture permeability, the proper size of simulation area and effect of fracture orientation on oil recovery were determined.

Matching Process

Provision was made to allow changes in the value of important variables such as the on-trend and off-trend fracture permeability values and the size of the reservoir model.
Even though the permeability was changed to very high number for both on trend and off trend directions and the grid blocks had been refined at the same size of model area, the water injection rate constraint cannot be maintained during the injection rate period. The water injection rate constraints were changed to the BHP constraints because the boundary created high-pressure build up in that confined area.

To compensate the problem, the reservoir model was increased to 3 times in x and y directions from the original model. The injection rate constraints were still shifted to BHP constraints, but it was only at later injection rate constraints period. Thus, the model was increased to 5 times original reservoir model. The simulation run was able to maintain the water injection rate constraints as shown from the simulation result in Fig. 3.12-2 and the oil production rate constraints as well (Fig. 3.12-3).

Figure 3.12-4 shows that the simulated BHP pressure can be maintained below 3000 psia when using a large simulation area of 6890 acre. This large area is used to take into account very high permeability in the on-trend direction and to avoid a pressure build up because of limited area. The work does not intend to match the observed bottom hole pressure (BHP) because it is a static bottom hole pressure while BHP obtained from the simulation is the flowing bottom hole pressure. However, the observed bottom hole pressure is useful to give a BHP range of values for our simulation result.

Constant production and injection rates were used as simulation constraints during the simulation run. The fracture permeability values in the on-trend and off-trend directions were altered until the best matches were obtained. The fracture permeability values in the on-trend and off-trend directions are determined to be approximately 15000 and 100 md with the ratio of fracture permeability of 150:1. This ratio of fracture permeability is almost similar to the ratio permeability obtained from the previous study.[3,4] Figure 3.12-5 compares the observed water cut with the water cut obtained from the simulation result. A satisfactory match of water breakthrough time was achieved. From the magnitude of on-trend and off-trend fracture permeability, the values indicate that the permeability is highly anisotropy and the sweep area forms elongated ellipse trending in the major fracture trend.

Sensitivity Analysis

Because the fracture permeability is high only in y-direction, the grid blocks in the x-direction were optimized. After grid blocks in the x-direction were changed several times by keeping similar grid block in y-direction, we finally obtained at least 50 grid blocks

needed in x- direction. Thus, to properly simulate the two wells that has area of 275-acre we need at least 50 and 125 grid blocks in x- and y- directions, respectively, which covers simulation area of 2756 acre (Fig. 3.12-6).

The well performances of using 25 x 25 grid blocks are shown in Fig. 3.12-7. The peak water cut cannot be matched because the bottom hole pressure has reached the pressure limit of 3200 psi, which corresponds to the fracturing pressure. Thus, the simulator automatically reduces the given injection rates to maintain the bottom hole pressure below the fracturing pressure.

The next sensitivity study was conducted on altering fracture permeability. This study was conducted to see the effect of altering this parameter on well performance. Two simulation cases were conducted as follows,
Case 1: Kfx = 10 md and Kfy = 1500 md
Case 2: Kfx = 100 md and Kfy = 20000 md

The well responses were compared to the matched parameter. Herein we called it the base case (Kfx = 100 md and Kfy = 15000 md). The results are presented on Fig. 3.12-8. The fracture permeabilities in both x- and y- directions (Case 1) are one-tenth the permeability of the base case. Reducing the fracture permeabilities in both directions cause the reservoir to become less permeable causing lower injectivity. Due to lower injectivity, the simulator increases reservoir pressure as well as bottom hole pressure to maintain the constant production rates. However, the reservoir pressure is limited to the fracturing pressure of 3200 psi, therefore, the simulator cuts water injection rate constraints to maintain the pressure bellow the fracture pressure. The result also shows that the water cut response in Case 1 is faster than that in the base case due to lower fracture permeability in x-direction. In Case 2, the permeability in y-direction was changed to higher number (20000 md), and the permeability in x-direction was kept a similar value. The permeability change causes the water cut response is faster than that in the base case. The higher permeability yields faster water cut response in the production well.

Six wells with different orientations were included in the model that had matched parameters to simulate the effect of different fracture orientation on oil recovery during high water injection rate of 1000 STB/D. The six different orientations are 0, 18, 36, 54, 72 and 90 degrees, respectively. All the wells have similar distance to the injection well. The well located at 0 degree is the on-trend well, which is parallel (the same fracture line) to the injection well. Meanwhile the well located at 90 degree is the off-trend well, which is perpendicular to the injection well. The wells were produced with constant flowing pressure of 2000 psi for 15 years. The simulation results are presented in Fig. 3.12-9.

After injecting water for 2 years, the on-trend well had the highest cumulative oil production, because this well had the fastest response to water injection (co-current). However, this well simultaneously produces a high water production rate that significantly reduces the oil production rate. The wells located at 18 and 36 degrees have favored of slowing water production rate in both counter-current and co-current

imbibitions. Therefore, the cumulative oil productions from those wells are much higher than that produced from the on-trend well after 2 years producing time. Even though the wells are located at higher than 36 degrees from the fracture trend, they have favored both counter-current and co-current imbibitions. However, the response on water injection rate takes very long time. The off-trend well has the same cumulative production as the on-trend wells at about 13^{th} year. The long time response of production wells due to water injection remains uneconomic in the life span of waterflood project.

Conclusions

1. Because of high permeability in the on-trend direction, the size of the simulation area must be large enough to avoid a pressure buildup in the confined area.
2. The fracture permeability values in the on-trend and off-trend directions of 15000 and 100 md, respectively, indicate that the reservoir permeability is highly anisotropy.
3. It is recommended to place the production wells between 0 and 36 degrees relative to fracture trend to have efficient waterflood response.

References

1. Schechter, D.S., McDonald, P., Sheffield, T., Baker, R.O.: "Integration of Laboratory and Field Data for Development of CO2 pilot in the Naturally Fractured Spraberry Trend," paper SPE 36657 presented at the 1996 SPE Annual Technical Conference and Exhibition, Denver, Colorado, 6-9 October.
2. Putra, E. and Schechter, D.S.: "Reservoir Simulation of Waterflood Pilot in Naturally Fractured Spraberry Trend Area," paper SPE 54336 presented at the 1999 SPE Asia Pacific Oil and Gas Conference and Exhibition, Jakarta, Indonesia, 20-22 April.
3. Barfield, E.C., Jordan, J.K., and Moore, W.D.: "An Analysis of Large-Scale Flooding in the Fractured Spraberry Trend Area Reservoir," *JPT* (1959), Vol.11, No. 4, p.15-19.
4. Elkins, L.F., and Skov, A.M.: "Determination of Fracture Orientation from Pressure Interference," *Trans*. AIME (1960), Vol. 219, p.301-304.

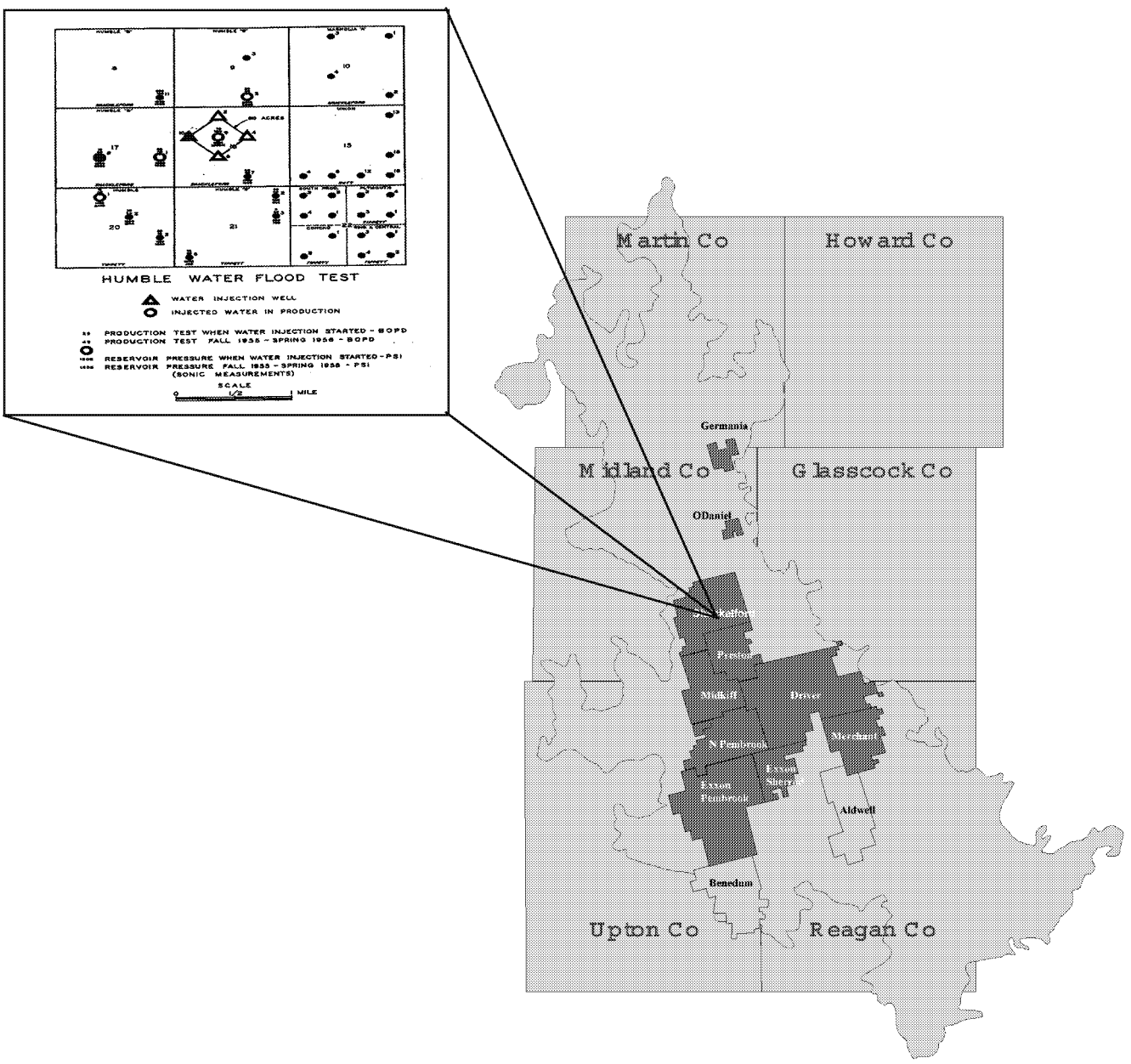

Fig. 3.12-1 —The Spraberry map shows the location of the Humble waterflood pilot

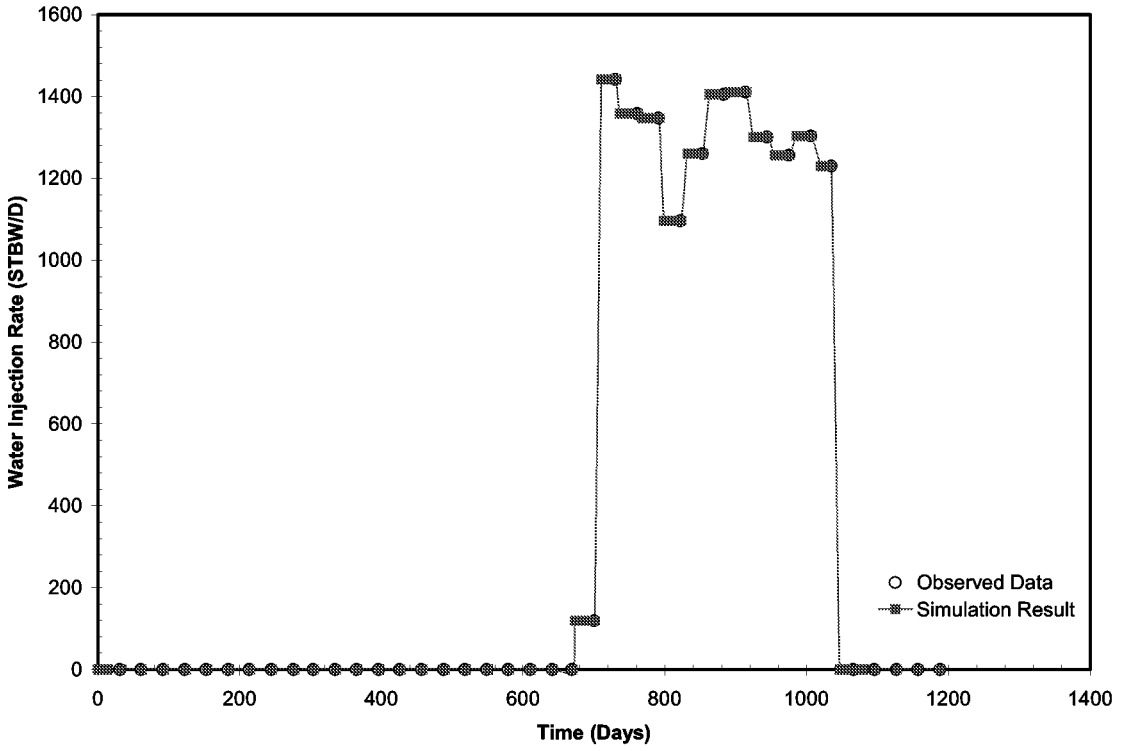

Fig. 3.12-2 —Comparison between observed water injection rate and simulation result

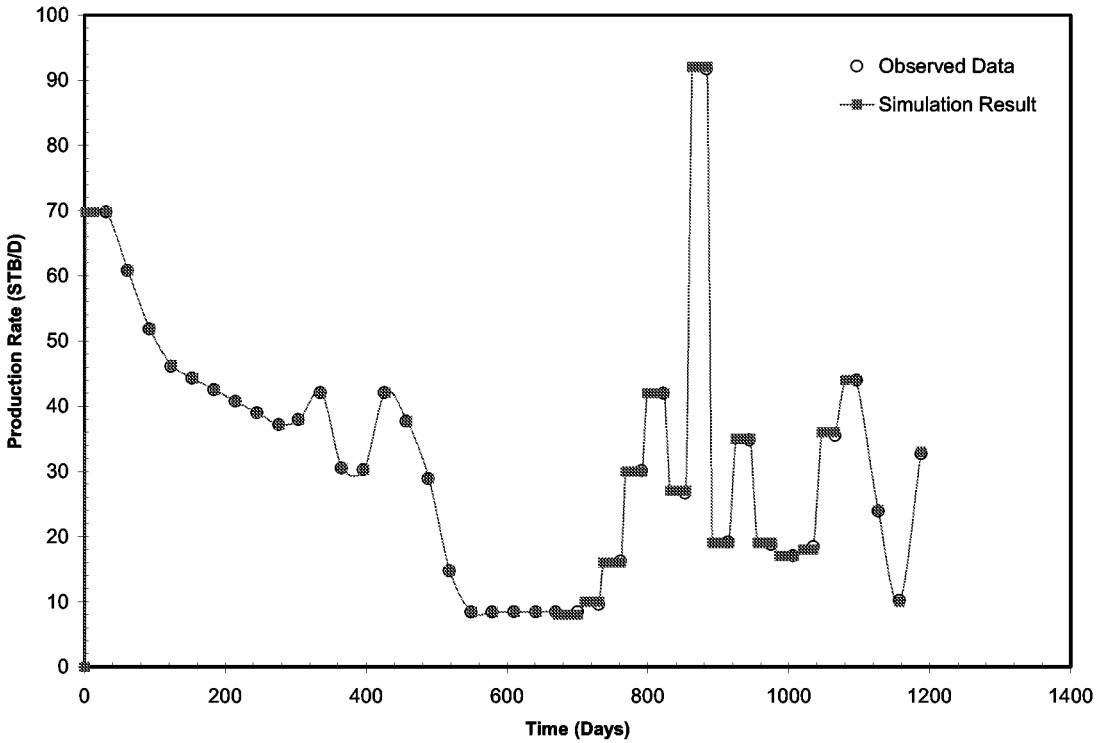

Fig. 3.12-3 —Comparison between observed oil production rate and simulation result

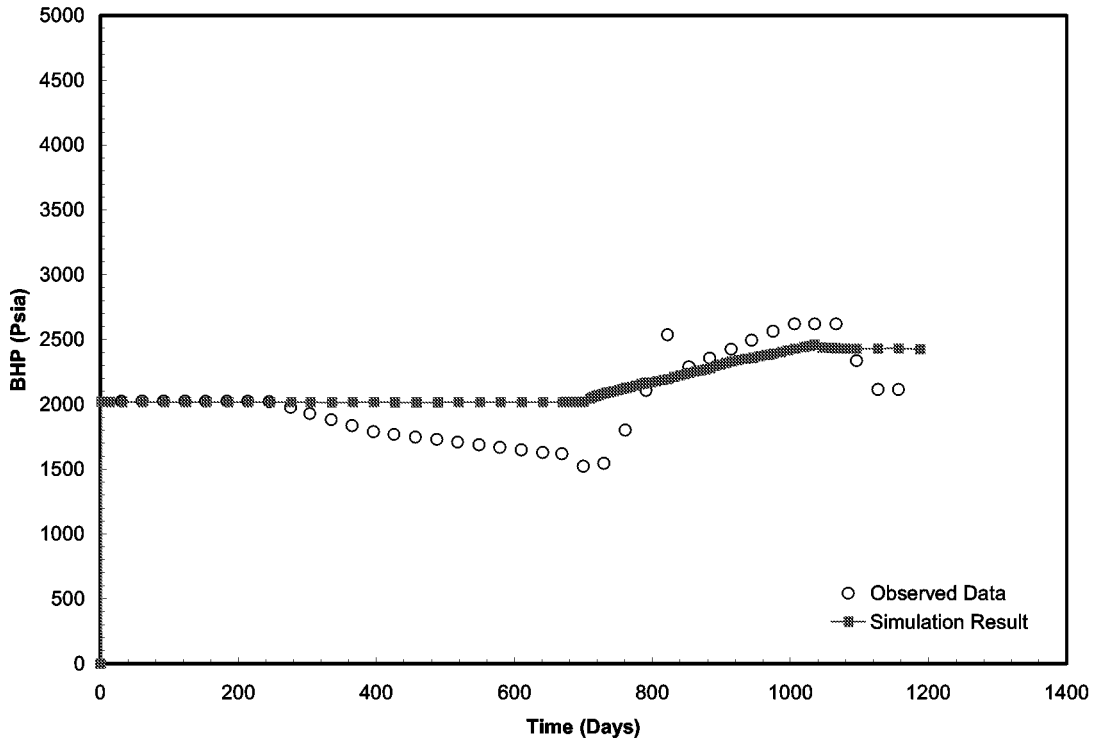

Fig. 3.12-4 —Comparison between observed bottom hole pressure (BHP) and simulation result

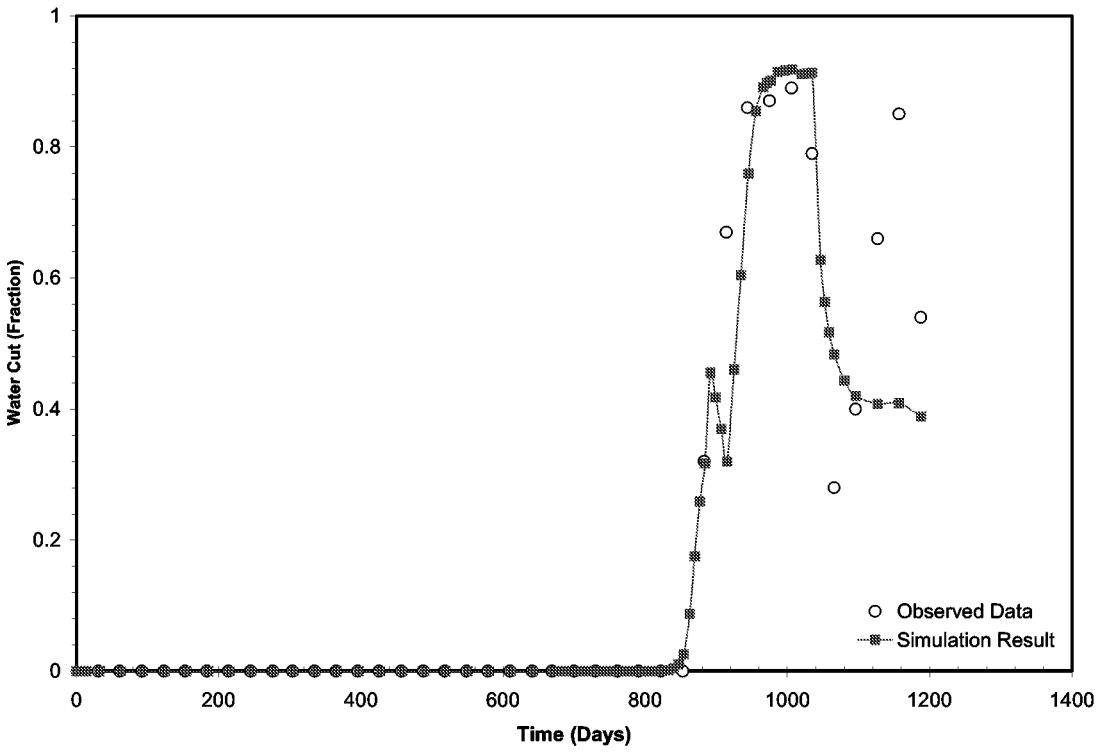

Fig. 3.12-5 —Match between observed water cut and simulation result

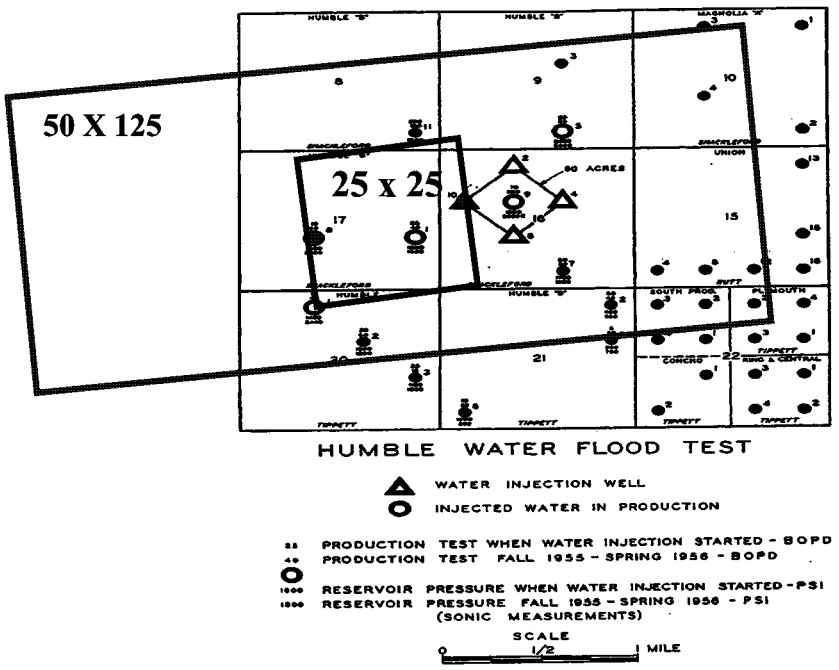

Fig. 3.12-6 —Effect of reservoir size on simulating two wells in Humble waterflood pilot

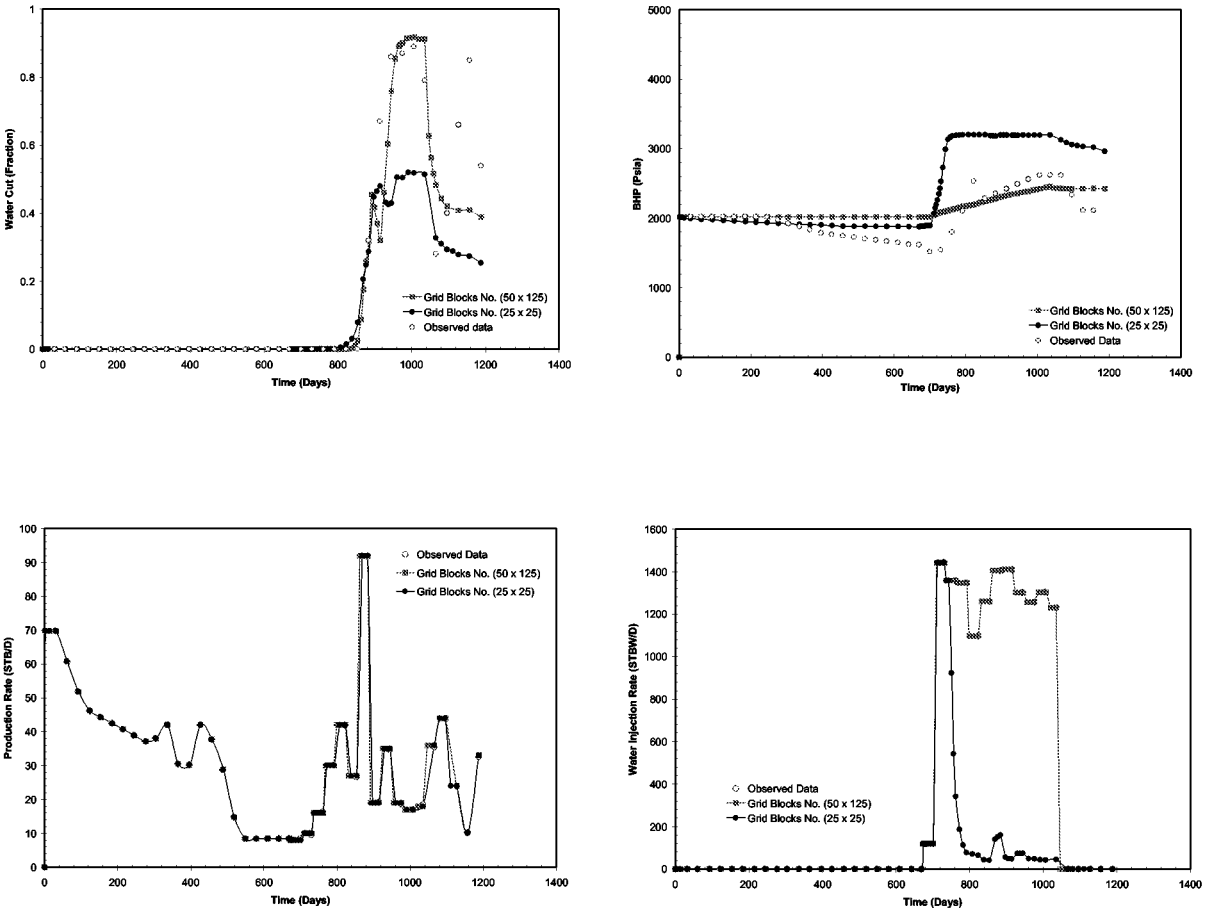

Fig. 3.12-7 —Effect of reservoir size on well performance during high water injection rate

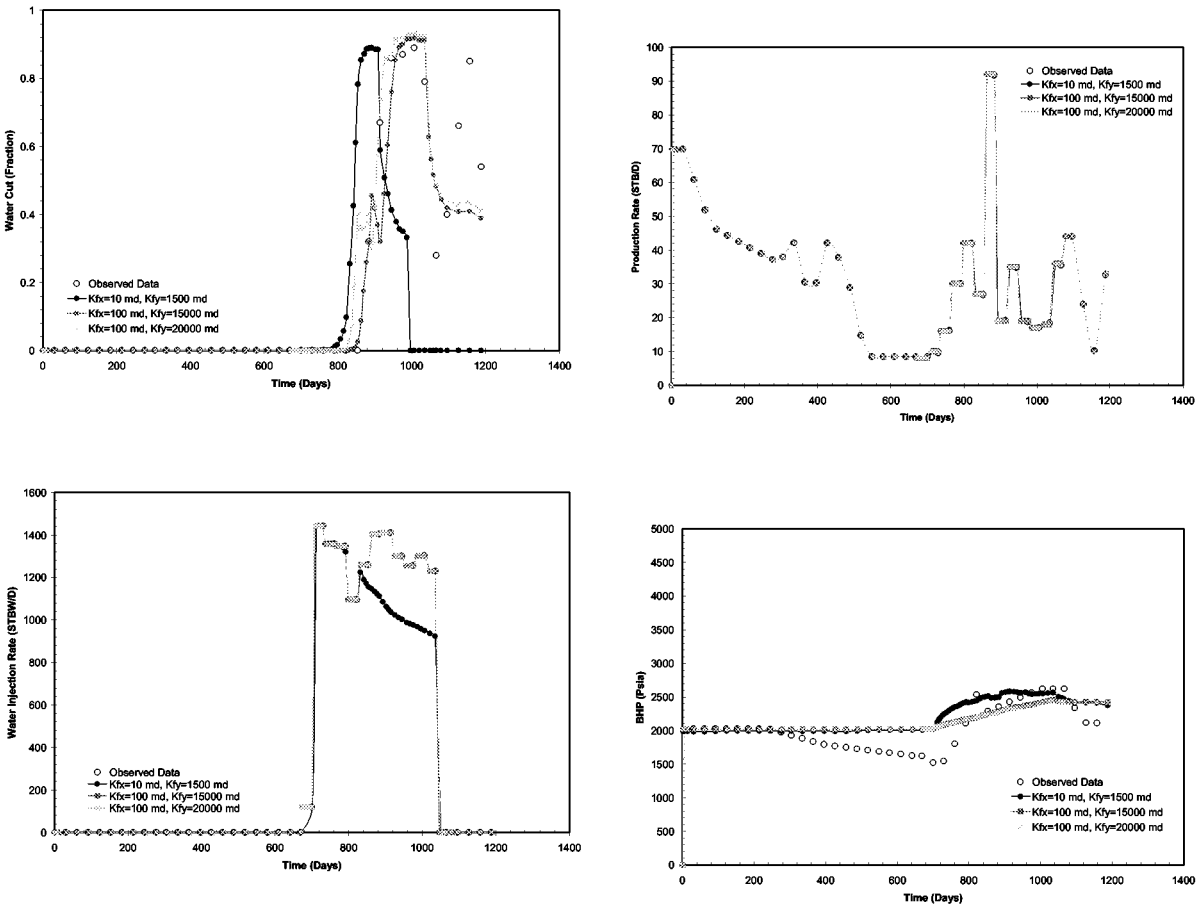

Fig. 3.12-8 —Effect of fracture permeability on well performance during high water injection rate

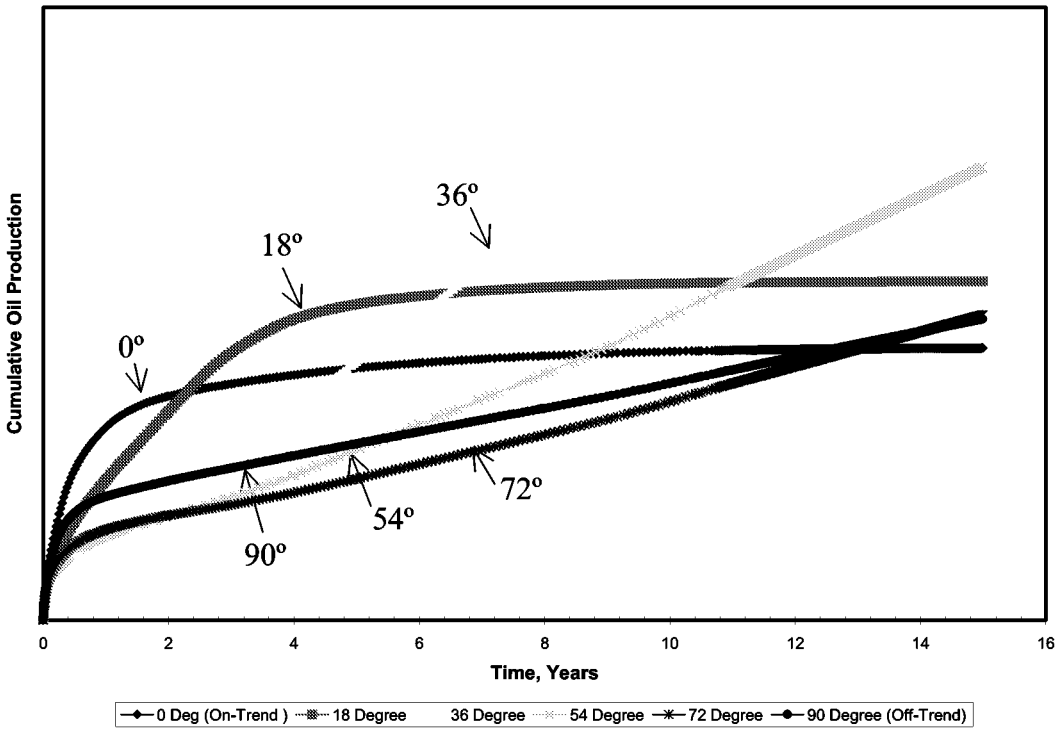

Fig. 3.12-9 —Effect of different well orientation on oil recovery during high water injection rate

3.13 SIMULATION OF TRACER RESPONSE IN E.T O'DANIEL PILOT AREA

Introduction

Six water phase inter-well tracers were injected into the six ring fence wells of the E. T. O'Daniel Lease in the middle of Aug. 2000. The injection schedule is shown in Table 3.13-1. Analysis was performed on the collected water samples from the twenty-nine producing wells in the O'Daniel Tracer Program. The result of the tracer program is presented in Fig. 3.13-1. The analysis indicates that tracer has arrived at twenty-seven of the twenty-nine producing wells. The result shows that there are four tracer concentrations near or exceeding 100,000 ppt in observation wells due to tracer injection, which are:

1. WIW #47 to Brunson D-1
2. WIW #46 to Brunson D-1
3. WIW #48 to O'Daniel A-1
4. WIW #45 to Pilot Well #38

The remaining wells have only shown weak tracer response or the tracer wave is just beginning to arrive at the well. In the three wells with high peak tracer concentration, tracer shows up in a few days after tracer injection. Tracer breakthrough in this short time is usually indicative of communication in the reservoir via isolated natural fractures or extremely high permeability, thin intervals. The breakthrough time and the peak concentration are presented in Table 3.13-2. From the tracer test analysis it is observed that the wells mentioned above have a very high velocity of tracer transport, which is presented in Table 3.13-3. These wells, which are very far from the injection wells, are subject to very fast breakthrough because of this extremely high tracer velocity. So it is assumed that there is a very high permeability path between each pairs of injection and production wells.

Analyzing the Tracer Response

A simple two well simulation model is chosen to analyze the tracer test. First an optimum number of grid blocks were selected by performing a grid sensitivity analysis. Then the sensitivity analysis was performed to obtain the ranges where the match might exist. The results found during a previous simulation (the Humble Pilot simulation) were used as a basis to start the sensitivity analysis.[1] The process of matching the simulation results with the observed data began after getting a good understanding of the model with the help of sensitivity results.

It is observed that there are several peak concentrations in the inter-well tracer response between the injection well WIW#47 and the production well O'Daniel D-1. Fig. 3.13-2a shows a typical tracer response curve. The observed data of WIW#47 to O'Daniel D-1 is shown in Fig. 3.13-2b. With this simulation model only the first peak of Fig. 3.13-2b was matched because different simulation models are necessary to match the second and all other successive peaks in the observed data. It is assumed that all the successive peaks are

due to the contribution of tracer from the secondary fracture trend i.e. from different fracture sets.

Simulation Model

The behavior of naturally fractured reservoirs is considerably different from conventional reservoirs. This difference arises from the existence of two interconnecting paths for fluid flow having totally different properties, which communicate with each other. The tracer test was performed and analyzed to understand the fracture system of the naturally fractured Spraberry Trend Area. To simplify the analysis a two well model was chosen with one injection well (O'Daniel#47) and one observation well (Brunson D-1). The two wells have a very good inter-well tracer response indicative of a continuous fracture path. The model is shown in Fig. 3.13-3.

The distance between these two wells is 3200 ft. The size of the model is 100x100x3 grid, which covers some 602 acre area. Of these three layers only the first and the third layers are pay layers. The model is assumed to have dual porosity behavior. The size of each grid block is 51.2 ft. The rock, fluid properties and reservoir characteristic data were taken from the Humble pilot. Actual injection rate, tracer concentration and the duration of tracer injection were used in this simplified model. Finally a model of 100x100 grid size was chosen with 3 layers.

Sensitivity Analysis

The 602 acre model has 5120 ft in both x and y directions. Grid block sensitivity was performed in this area with 55x55, 100x100 and 150x150 grid sizes. For a fixed orientation and a given on-trend and off-trend permeability, it is observed that a model with 100x100 grid gives a similar response to a model with 150x150 grid as shown in Fig. 3.13-4. So, to optimize the simulation run time the model with 100x100 grid was utilized for history matching the tracer test.

The grid orientation effect on the tracer response was analyzed by varying the on-trend and off-trend permeability for different orientations. When the grid is oriented at 33°, which makes the injection well in the on-trend direction towards the production well, there is no significant effect of the off-trend permeability (K_x) on the tracer response from the production well. Tracer response from this on-trend production well will be very much affected if the on-trend permeability (K_y) is varied. An increase in K_y gives a faster breakthrough (Fig. 3.13-5) and higher peak concentration (Fig. 3.13-6). If the grid is rotated so that the production well D-1 becomes 43° off-trend from the injection well O'Daniel#47, then the off-trend permeability K_x should have a significant effect on the tracer response. For the off-trend well, an increase in K_x gives a faster breakthrough (Fig. 3.13-7) and a higher peak concentration (Fig. 3.13-8). The production well in the off-trend direction (43° for this case) will also be affected by the on-trend permeability. This is observed in Fig. 3.13-5, where an increase in K_y gives a faster breakthrough. When K_y is increased, unlike the on-trend well, the off trend well experiences a decrease in the

peak tracer concentration (Fig. 3.13-6). When K_y is increased, much tracer goes to the on-trend direction relative off-trend. This will reduce the amount of tracer reaching the off-trend production well. If the production well is located further from the off-trend direction then the tracer breakthrough is delayed and the concentration becomes very small.

Matching

After performing the sensitivity analysis the reservoir parameters, such as on-trend, off-trend permeability and fracture orientation, were identified. The effect of these parameters on the tracer performance (breakthrough time and peak concentration) gives us guidance towards the matching process.

The variables used for the matching process are: 1) on-trend, off-trend permeability and 2) fracture orientation. During the simulation runs, tracer was injected into the O'Daniel#47 at a constant rate, with a tracer concentration of 158.9 ppm for 11.67 hours. Different simulation runs were performed for various orientations starting from the on-trend to farther off-trend directions. The permeability values in the on-trend and off-trend directions were changed for each orientation to match the observed data. In the best-fit match, the on-trend and off-trend permeability were found to be 15000 md and 84 md. This result is very close to that of the Humble Pilot simulation[1] where the permeability was 15000 and 100 md in the on-trend and off-trend directions respectively. The comparison between the observed data and simulation result is shown in Fig. 3.13-9. A very satisfactory match was found for the breakthrough time, the peak concentration and the width of the tracer performance plot.

Furthermore, the best match for fracture orientation was N43°E which is the average fracture orientation measured for horizontal core taken in the O'Daniel area.[2,3] Thus, the tracer results confirm the NE-SW fracture set in the 1U pay zone is responsible for tracer breakthrough in the Brunson D-1.

Conclusions

1. The fracture permeability values in the on-trend and off-trend directions were found to be 15000 and 84 md respectively. This result confirms the reservoir permeability is highly anisotropy.
2. The on-trend and off-trend permeability obtained in this study is very close to the values obtained for a history match of water in the Humble Pilot simulation[1] where the result was 15000 and 100 md in the on-trend and off-trend directions respectively.
3. A finite difference, dual porosity simulation indicates the primary fracture orientation is N43°E similar with the average orientation obtained from natural fracture counts in horizontal core acquired in a near-by well. [2,3]
4. The off-trend permeability has no significant effect on tracer response in production wells that are located along the on-trend fracture orientation.
5. Increasing the permeability in the simulation for on-trend orientation will reduce the tracer concentration in the off-trend production wells.

References

1. Schechter, D.S: "Advanced Reservoir Characterization and Evaluation of CO2 Gravity Drainage in the Naturally Fractured Spraberry Trend Area," First Quarterly Technical Progress Report, 2001 (DOE Contract No.: DE-FC22-95BC14942).
2. Schechter, D.S., Putra, E., Baker, R.O, Knight, W.H., McDonald, W.P., and Leonard, P.: "CO_2 Pilot Design and Water Injection Performance in the Naturally Fractured Spraberry Trend Area, West Texas," Paper SPE 71605 will be presented at the 2001 SPE Annual Technical Conference and Exhibition, New Orleans, Louisiana, 30 September–3 October.
3. McDonald, P., Lorenz, J. C., Sizemore, C., Schechter, D.S., and Sheffield, T.: "Fracture Characterization Based on Oriented Horizontal Core From the Spraberry Trend Reservoir: A Case Study" paper SPE 38664 presented at the 1997 Annual Technical Conference and Exhibition, San Antonio, Tx, 5-8 October.

Table 3.13-1 — Schedule of Tracer Injection

Injection Well	Tracer Material	Date of Injection	Duration of Injection (hours)	Injection Concentration (ppm)
ET O'Daniel #37	3-FBA	8/15/00	9.88	178.2
ET O'Daniel #47	4-TFMBA	8/15/00	11.67	158.9
ET O'Daniel #45	4-FBA	8/16/00	9.35	188.4
ET O'Daniel #46	3-TFMBA	8/16/00	10.25	171.8
ET O'Daniel #25	2-FBA	8/17/00	9.03	194.9
ET O'Daniel #48	2345-Tetra FBA	8/17/00	9.02	200.9

Table 3.13-2 —Summary of Result for the Four High Interwell Responses

Well Name	Breakthrough Time (Days)	Peak Concentration (ppt)
WIW#47 to Brunson D-1	1	171000
WIW#46 to Brunson D-1	3	164000
WIW#48 to O'Daniel A-1	3	180000
WIW#45 to Pilot Well#38	4	83200

Table3.13-3 —Tracer Breakthrough Velocity for Injector Producer pairs

Well Name	Breakthrough Velocity (ft/day)
WIW#47 to Brunson D-1	1559
WIW#46 to Brunson D-1	1103
WIW#48 to O'Daniel A-1	1843
WIW#45 to Pilot Well#38	642

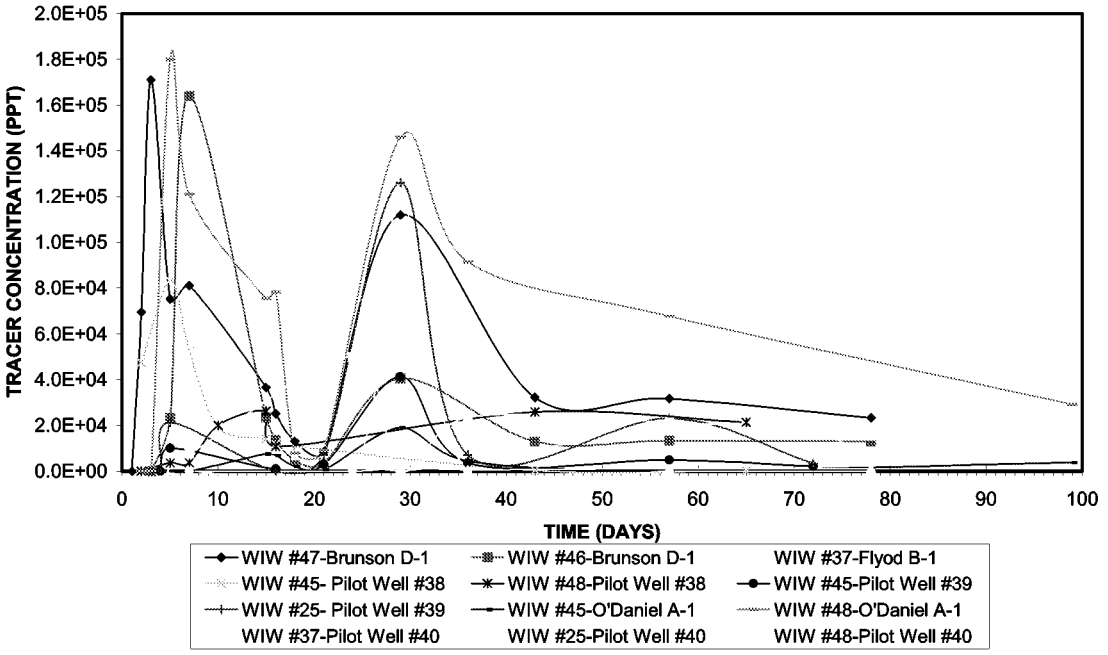

Fig. 3.13-1 —Response of Surrounding Wells on Tracer Injection at E.T O'Daniel Pilot Area.

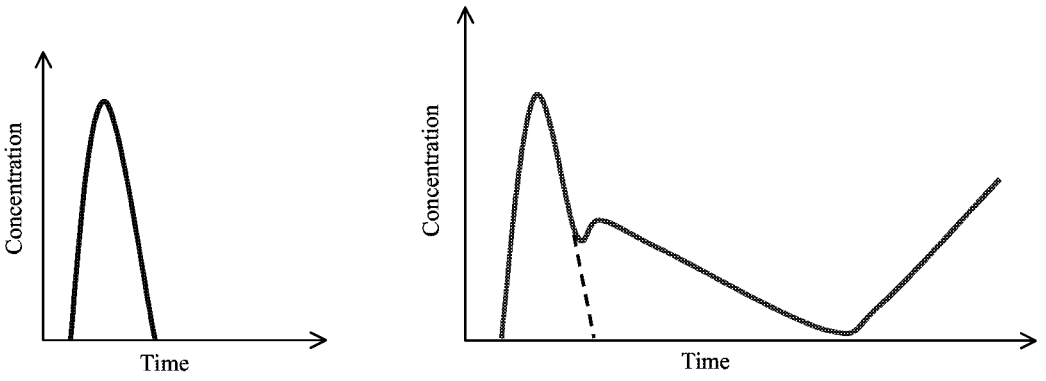

a) Typical Response

b) The Shape of Actual Response From WIW#47 to O'Daniel D-1

Fig. 3.13-2 —Typical and Actual Tracer Responses

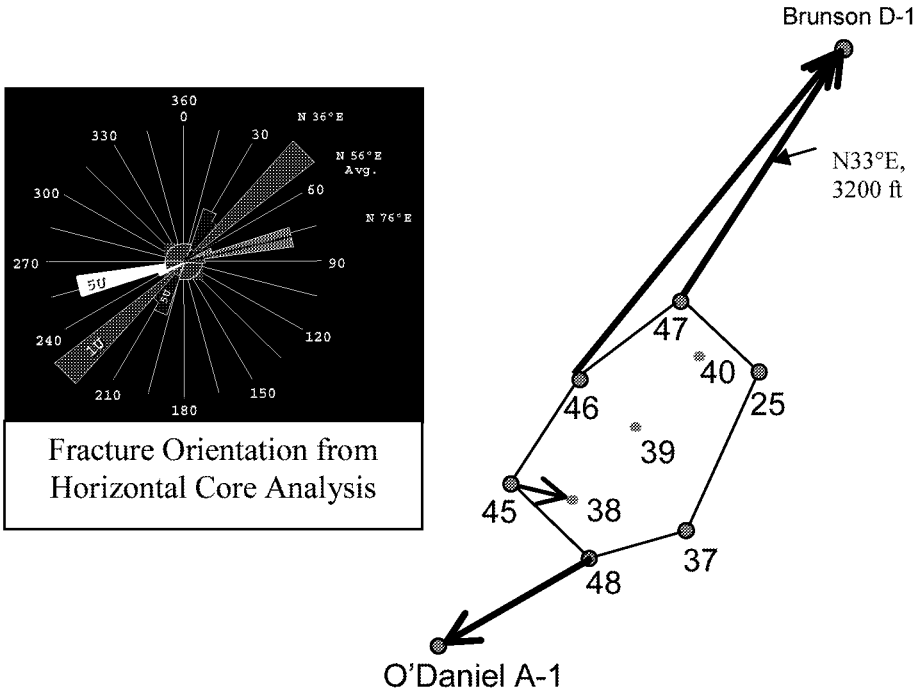

Fig. 3.13-3 - Schematic of Fracture Orientation as a Result of Tracer Injection

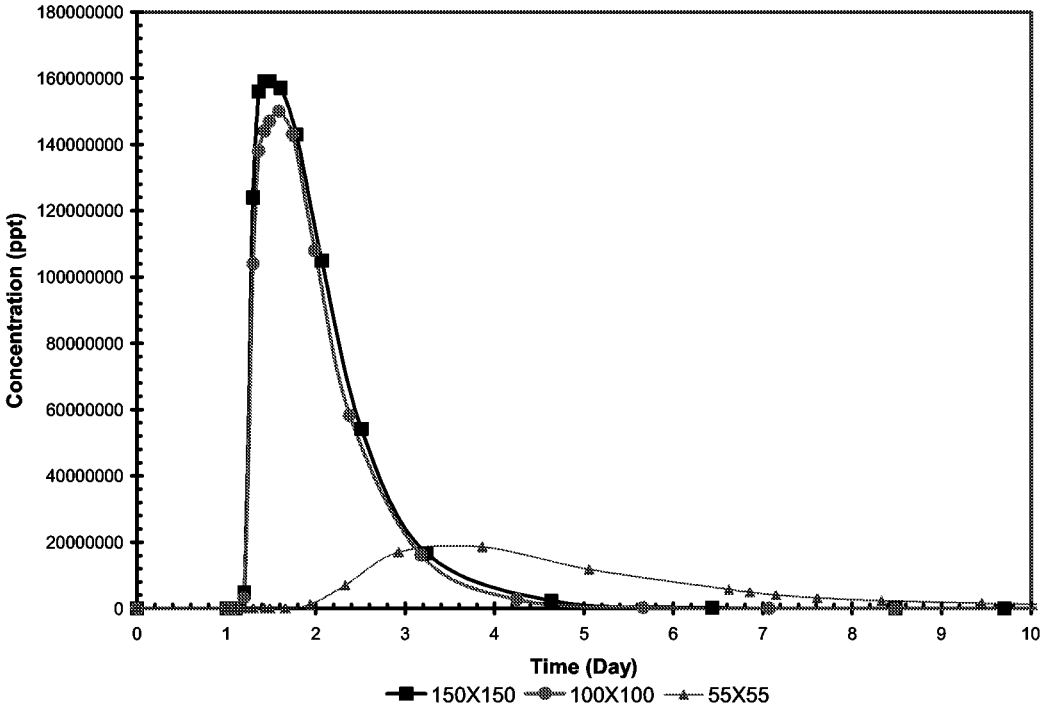

Fig. 3.13-4 —Effect of Grid Size in 35° Orientation With Kx/Ky = 100/15000 (WIW#47-D1)

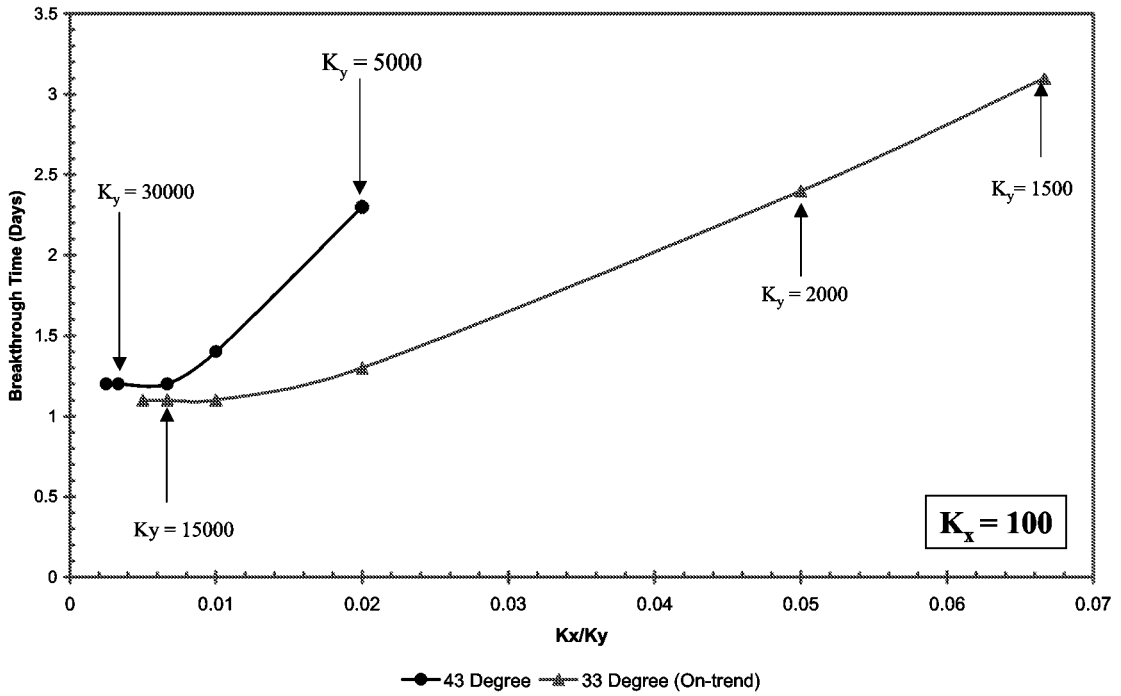

Fig. 3.13-5 —Effect of On-trend Permeability (K_y) on Breakthrough Time

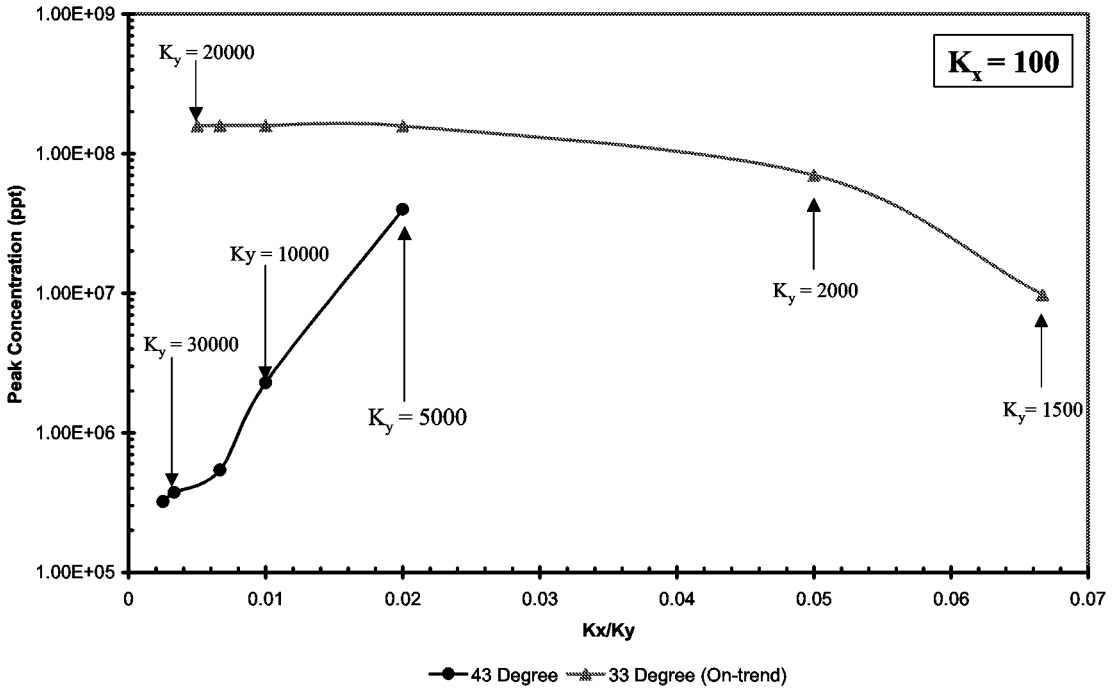

Fig. 3.13-6 —Effect of On-trend Permeability (K_y) on Peak Concentration

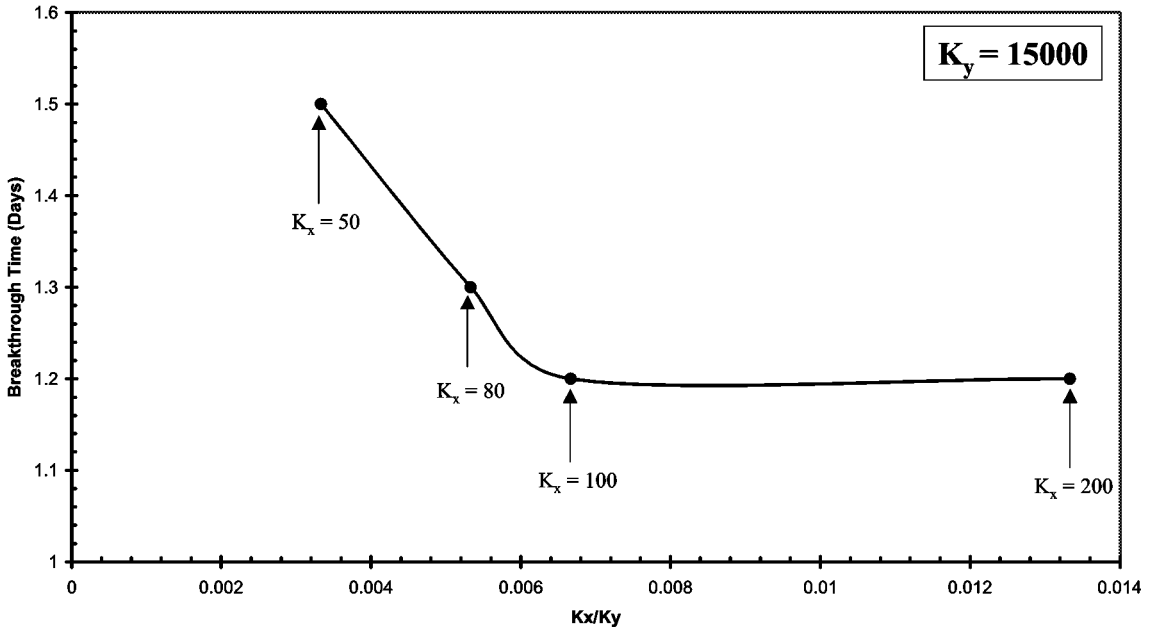

Fig. 3.13-7 —Effect of Off-trend Permeability (K_x) on Breakthrough Time for 43°Orientation

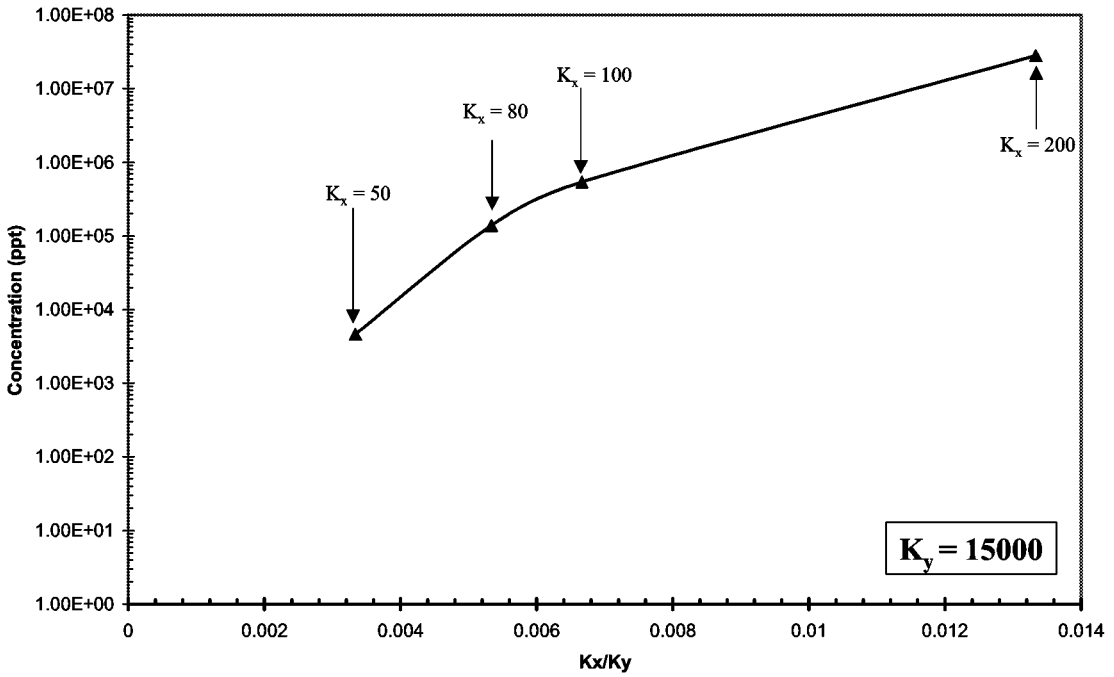

Fig. 3.13-8 —Effect of Off-trend Permeability (K_x) on Peak Concentration for 43° Orientation

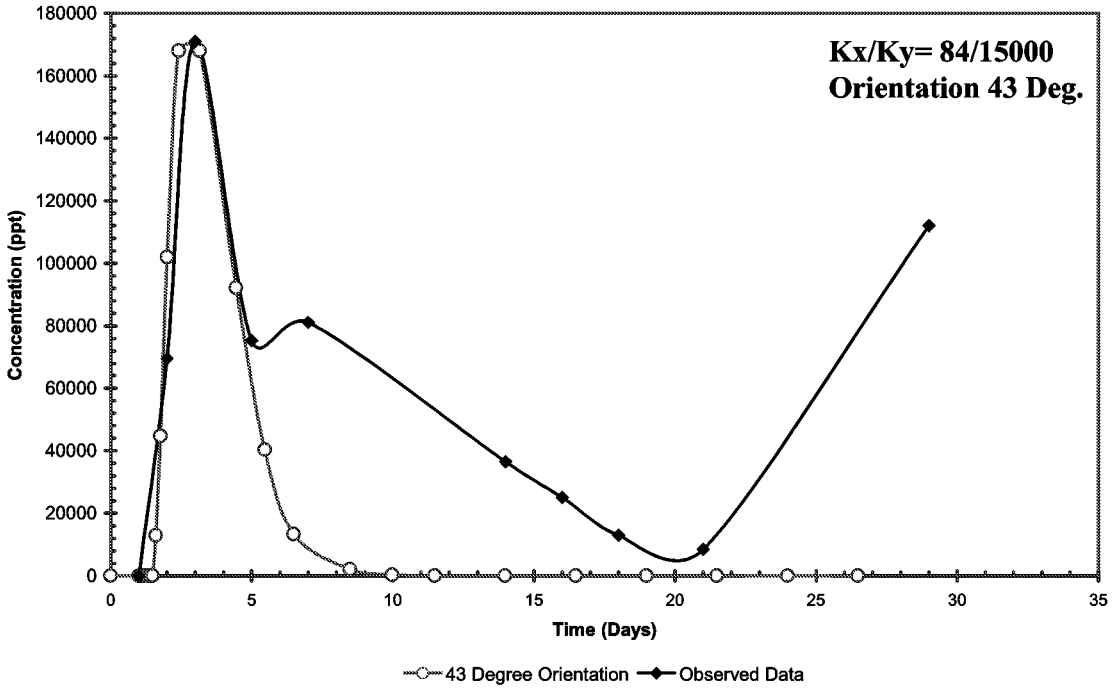

Fig. 3.13-9 —History Match Result

3.14 HYPOTHETICAL TWO WELLS AND MULTI-WELL SIMULATIONS OF E.T-O DANIEL PILOT AREA

The purpose of this study is to create a simple and small model as a precursor to model entire E.T O Daniel Pilot Area. To achieve the objective, two simulation models were created, hypothetical two wells simulation and multi well simulation with a portion of pilot area.

Hypothetical Two Wells Simulation

A hypothetical simulation was created to model and describe the behavior of production well during water injection in ET O'Daniel Pilot Area. This model was used as a precursor to multi-well simulation. Figure 3.14-1 shows the location of Brunson "C"-2 and Brunson "E-1" in the O'Daniel Lease. These wells were selected because of having good production and injection data. The production performance of the Brunson "C" - 2 and Brunson "E" –1 indicates that the trend of gas and water rates follow the trend of oil rate (Figs. 3.14-2 and 3.14-3). However, after performing pilot waterflooding the water trend of the Brunson "C" 2 becomes biased. When the oil rate increases sharply, the water rate suddenly disappears as shown in Fig. 3.14-2. This phenomenon still cannot be explained. It may be because of an active imbibition process or simple inaccurate water rate measurement.

A dual porosity option was used to model extensive fractured system in the hypothetical 40-acre area. The model consists of one injector and one producer. The rock and fluid input data were listed in our previous report. We used a $1/8^{th}$ area pattern to accelerate the simulation runs (Fig. 3.14-4). The oil and water rates that were used as a constraint and observed data, respectively, are thus $1/8^{th}$ time of the actual rate (Figs. 3.14-5 and 3.14-6). The volume modifier is applied to create the size of area pattern along with zeroing the porosity of inactive cells. The water injection rate applied here is not the actual water injection rate but it is one of matching parameters. The purpose is to check whether we have a realistic water rate measurement or not. Later on in the multi well simulation, all the water injection and production rates used the actual rates.

The water injection rate is started at the same time as oil production rate while the observed water rate data in Fig. 3.14-6 shows that the water saturation is not in the initial water saturation condition. So we adjusted water saturation in the beginning of the simulation to match the first water rate response. By changing the fracture permeability, matrix relative permeability and water injection rate we match the observed water and gas rates as shown in Figs. 3.14-6 and 3.14-7. The line indicates the simulation result and the point indicates the observed data.

Using the same input data as in Brunson "C"-2, The Brunson "E"-1 was simulated. Only the injection rate constraint was altered to match the water rate (Fig. 3.14-8). The injection rate was reduced because we knew that this well is closer to the actual injection well compared to Brunson "C"-2. A good match was achieved between actual data and simulation result as shown in Fig. 3.14-9.

The results from this single well study provide the knowledge of relative permeability and the behavior of dual porosity simulation in this field. This study also gives us a confidence to simulate the multi well simulation with the actual production and injection rates as discussed in the next section.

Multi Well Simulation

A multi well simulation was developed to mimic the production response during water injection in the ET O'Daniel Pilot Area. The simulation model consists of one injector with seven producers. They are ET O Daniel-10W, Brunson "E"-1, Brunson "C"-2, McClintic "E"-1, McClintic "E"-32, ET O Daniel-30, ET O Daniel-13 and Boone "A"-1. The top structure and well location in the simulation model is presented in Fig. 3.14-10. A 50x50x3(2) grid blocks with dual porosity option was used in CMG™ simulator. Only two of Upper Spraberry (1U and 5U) layers have been identified as containing reservoir quality rock capable of making significant production contributions with extensive fracture system. Three layers were created in the reservoir model. First and third layers consist of pay zone with thickness of 11 and 7.5 ft, respectively. The second layer consists of shale layer with 140 ft thickness. There is no communication between the first and third layers. The oil rate of individual wells and the injection rate of ET O'Daniel 10W are used as the constraints. The objective is to match the water rate of observed wells. The original fracture permeability was set to be 100 md in x- and y- directions. Using this permeability the Brunson "C"-2, Boone "A"-1 and McClintic "E"-32 did not produce any water at all. The trend of observed water rate of Brunson "C-2", Brunson "E-1", Boone "A"-1 and McClintic "E"-32 depicts the fracture orientation. Therefore we altered the fracture permeability to the orientation of those wells following the direction of fracture orientation obtained from the horizontal core analysis.[1] The new fracture permeability value was set to be 17000 md similar value as obtained from the tracer study.[2]

The fracture permeability enhancements were applied in the first layer (1U) to NE-SW trend and in the third layer (5U) to two fracture directions (NE-SW and NW-SE) as shown in Fig. 3.14-11. Then, we tuned end point of relative permeability and the fracture permeability around each well to match the individual well performance. The result of water saturation distribution at the end of the simulation run is presented in Fig. 3.14-12. The water saturation distribution shows the fractures situated along NE-SW trend and NW-SE trend. The match results for individual wells are presented in Figs. 3.14-13 to 3.14-27.

Conclusions

1. The waterflood analysis on the ET O'Daniel Pilot Area shows that the fracture permeability has strong NE-SW in the 1U and NE-SW as well as NW-SE in the 5U.
2. The results show that production performance is favorable to waterflood.
3. The matrix relative permeability and fracture permeability adjustment were applied to match the water rate.

4. The quality of water rate history match on individual basis is reasonably good.

Future work

1. Because simulation run of entire field requires a long CPU time especially in the matching process, we will construct another portion pilot before simulating entire E.T Daniel Area.
2. The portion pilot will be used as parametric studies to determine the best location of injector(s) and producer(s) during Waterflooding and/or CO_2 flooding.
3. Two portions pilot area will be combined to construct large area as our final goal.

References

1. McDonald P., Lorenz, J.C., Sizemore, C., Schechter, D.S. and Sheffield, T.: "Fracture Chracterization Based on Oriented Horizontal Core From the Spraberry Trend Reservoir: A Case Study," paper presented at the 1997 SPE Annual Technical Conference and Exhibition, San Antonio, Texas, Oct. 5-8.
2. Schechter, D.S.: "Advanced Reservoir Characterization and Evaluation of CO_2 Gravity Drainage in the Naturally Fractured Spraberry Trend Area," Sixth Annual Technical Progress Report, Contract No. DE-FC22-95BC14942, U.S. DOE, (Oct., 2001).

Hypothetical Two Wells Simulation

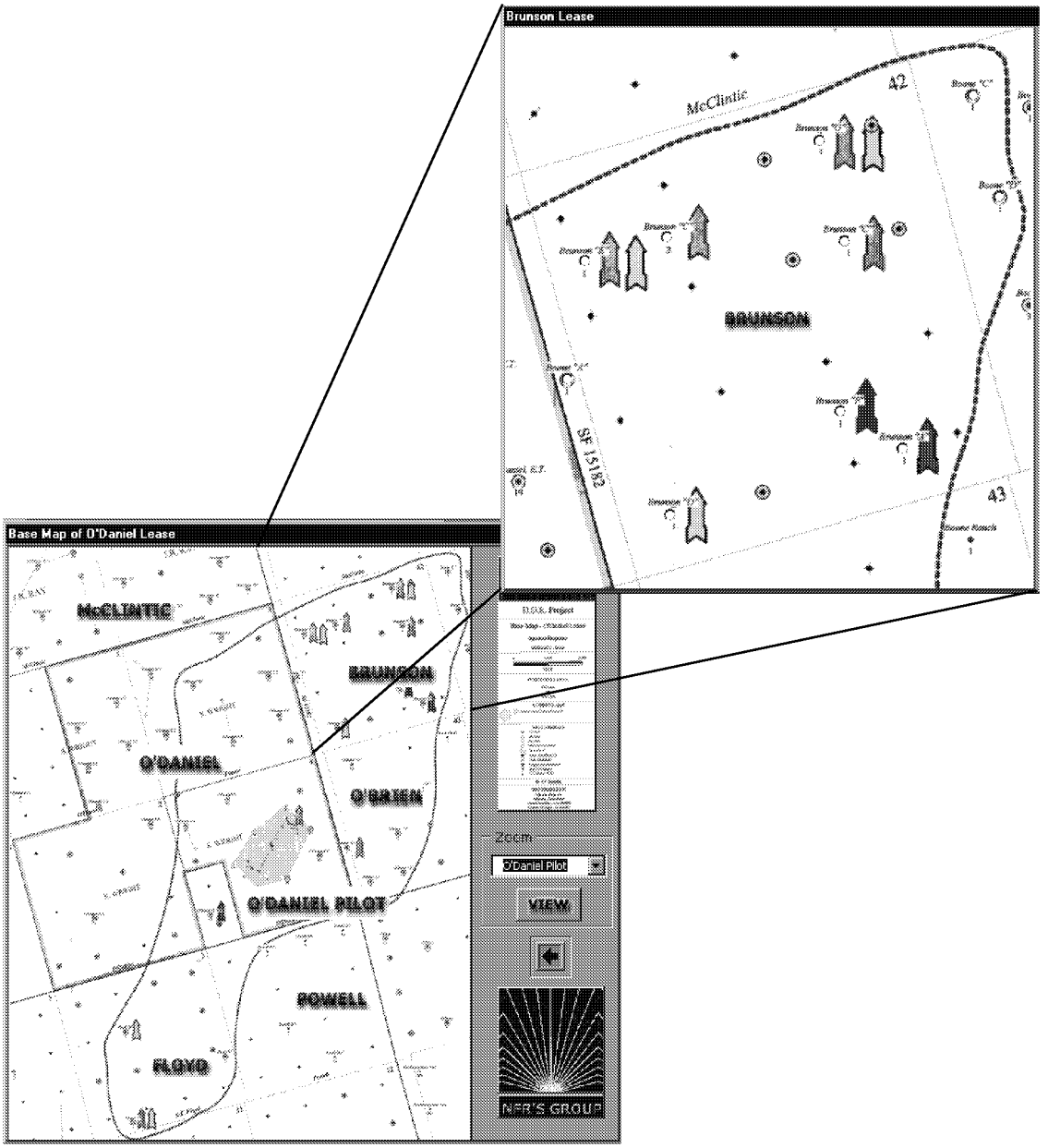

Fig. 3.14-1 —Location of Brunson “C” - 2 and Brunson “E” - 1 in the O’Daniel Lease

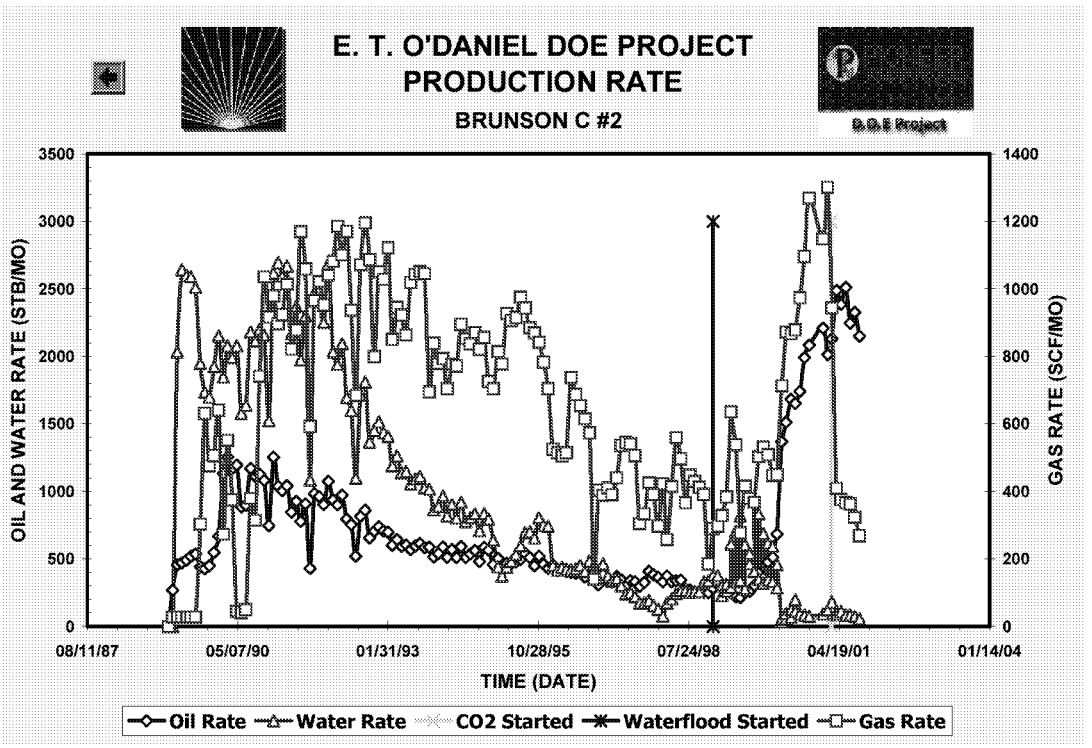

Fig. 3.14-2 —Production performance of Brunson "C" – 2

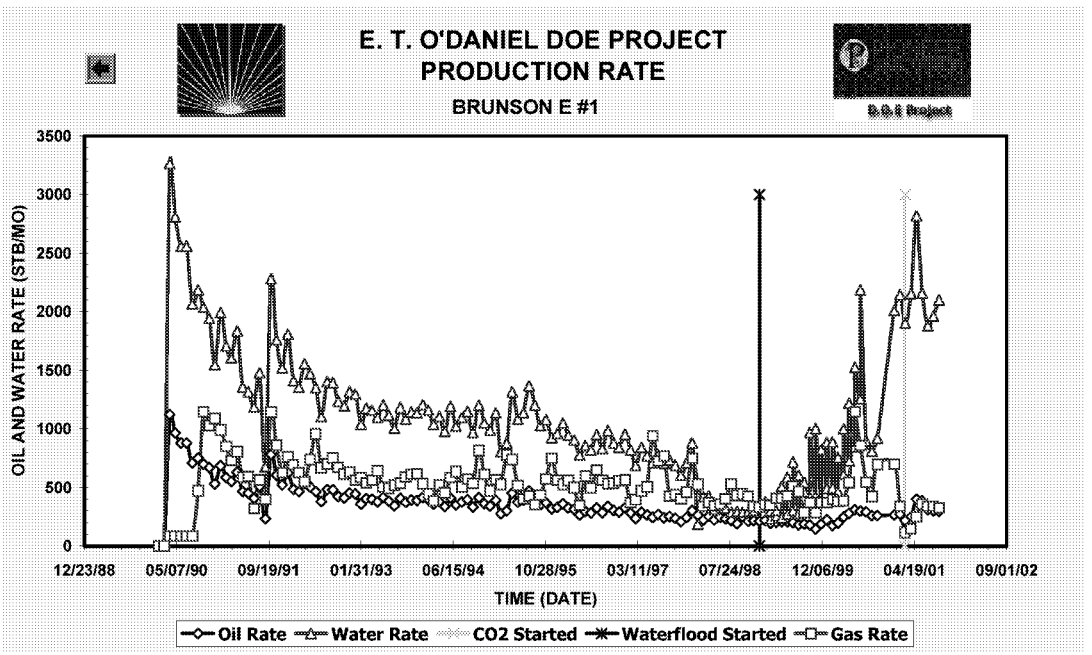

Fig. 3.14-3 —Production performance of Brunson "E" – 1

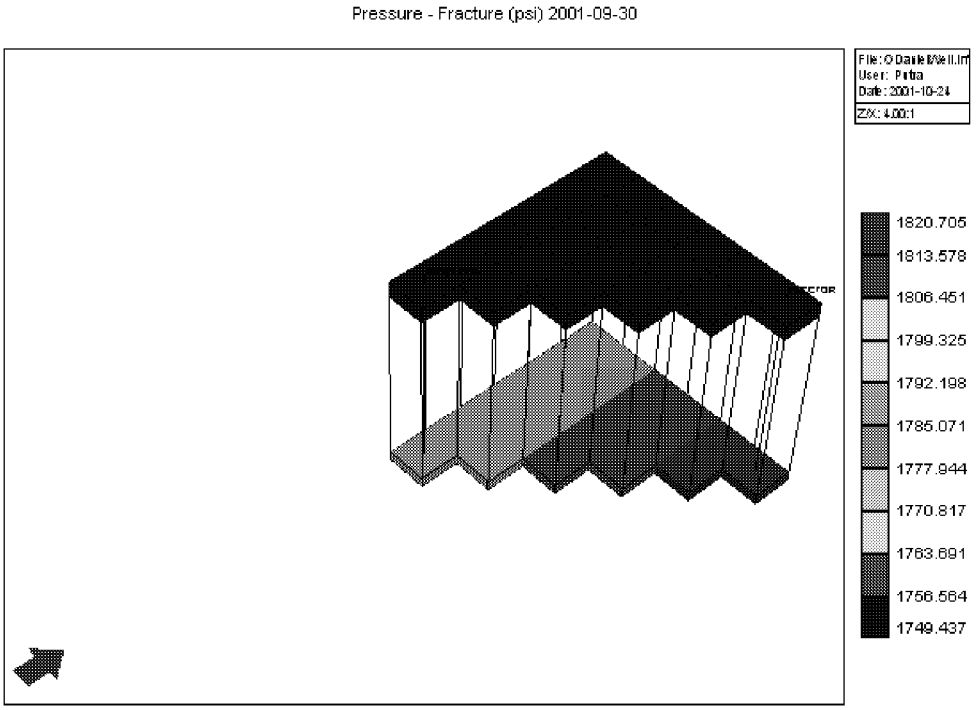

Fig. 3.14-4 —1/8th area pattern grid block used in the simulation

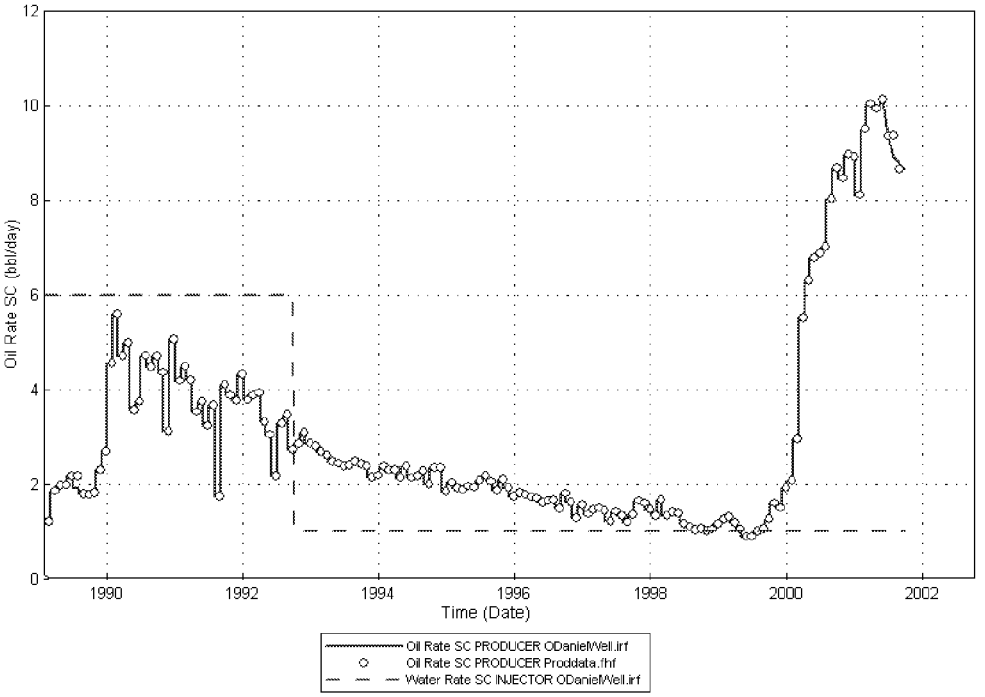

Fig. 3.14-5 —Oil rate and injection rate constraints of Brunson "C" – 2

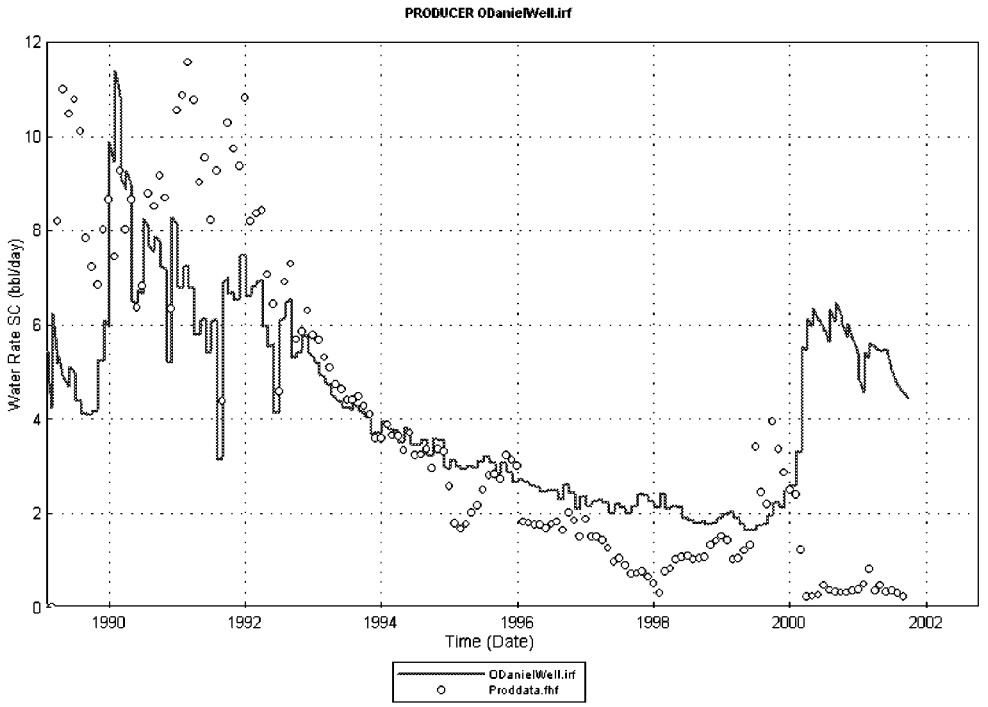

Fig. 3.14-6 —Water rate match between actual data and simulation result of Brunson “C” – 2

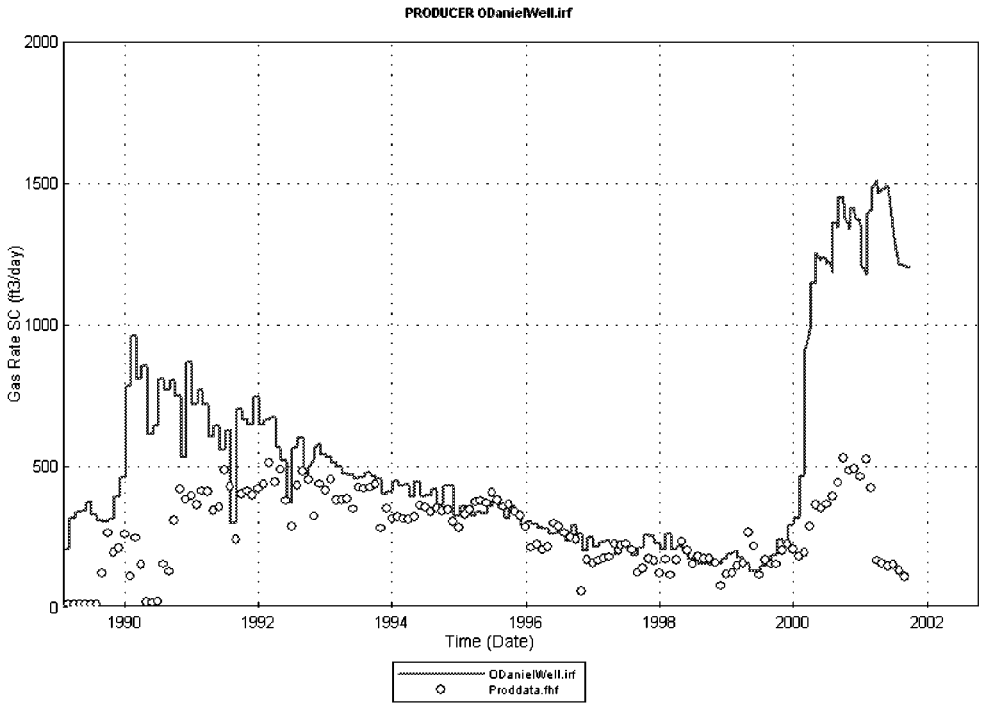

Fig. 3.14-7 —Gas production rate match between actual data and simulation result of Brunson “C” – 2

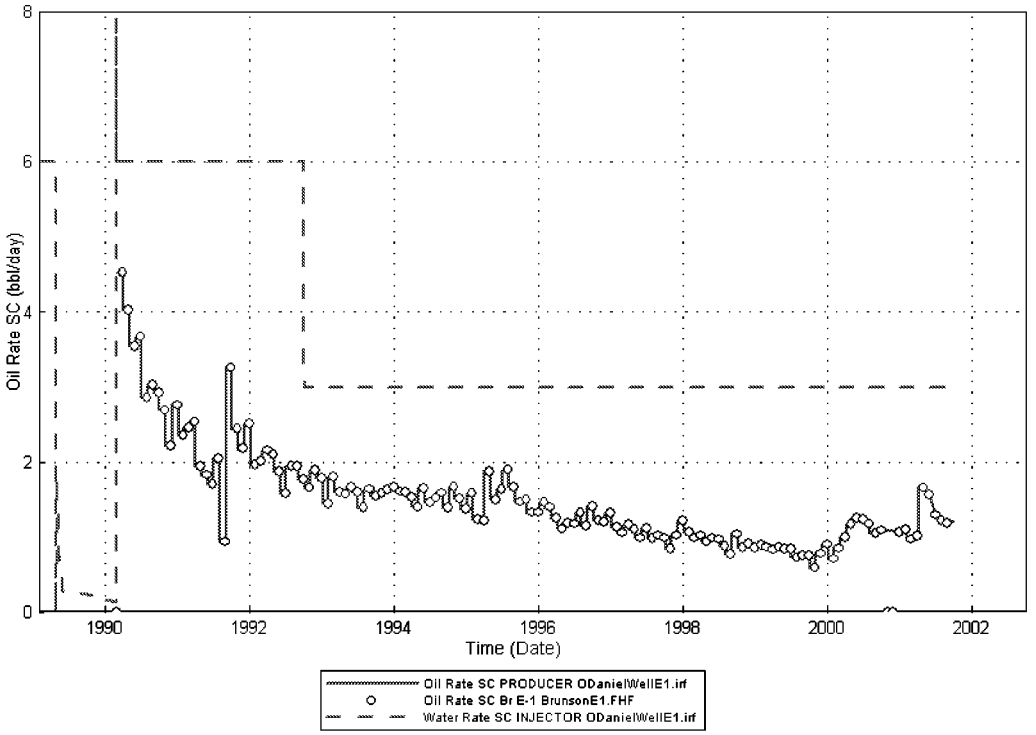

Fig. 3.14-8 —Oil rate and injection rate constraints of Brunson “E” – 1

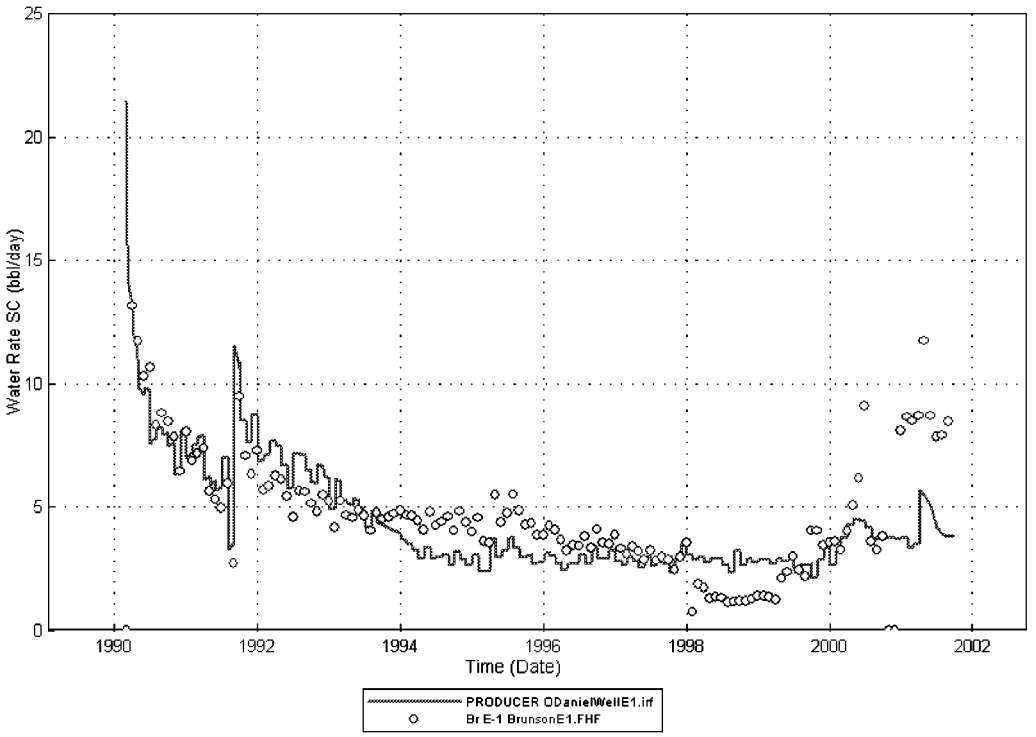

Fig. 3.14-9 —Water rate match between actual data and simulation result of Brunson “E” – 1

Multi-Well Model Simulation

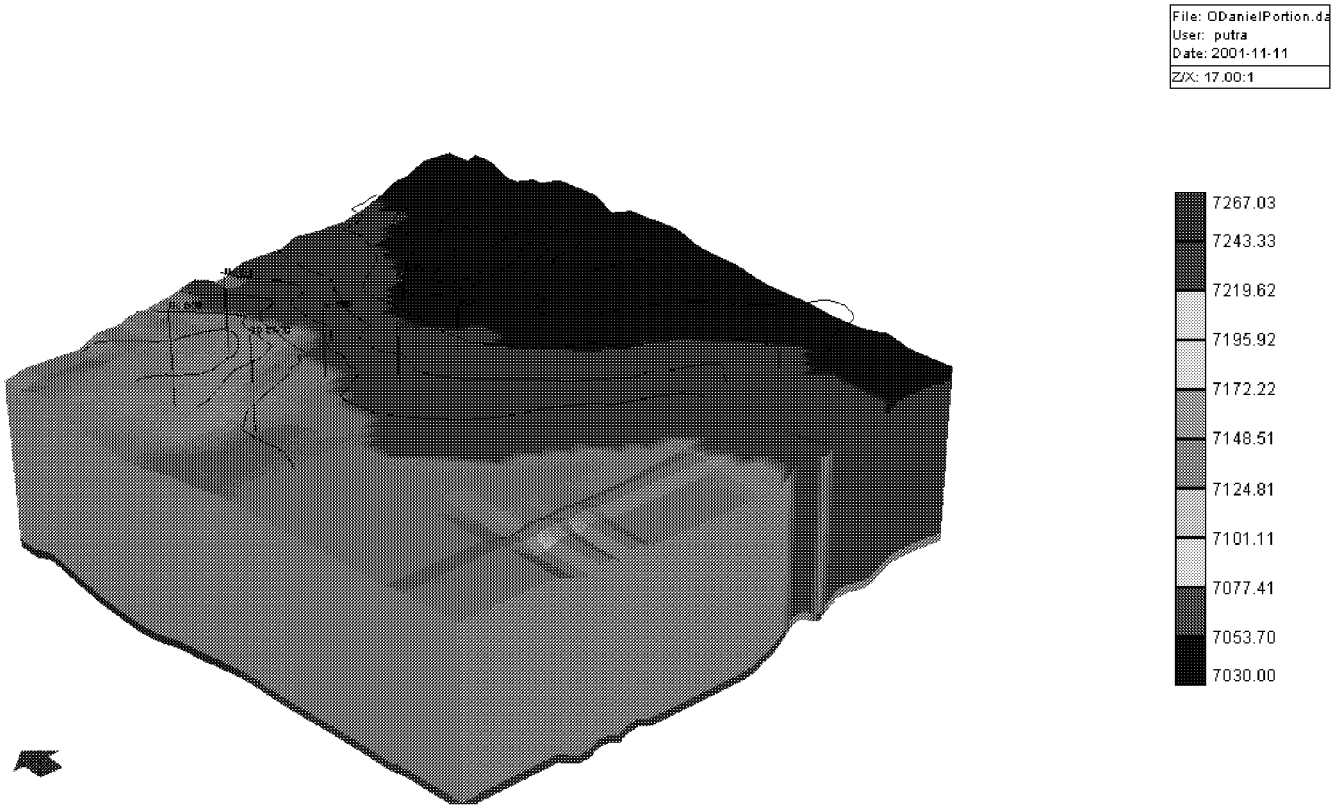

Fig. 3.14-10—Top structure and well location

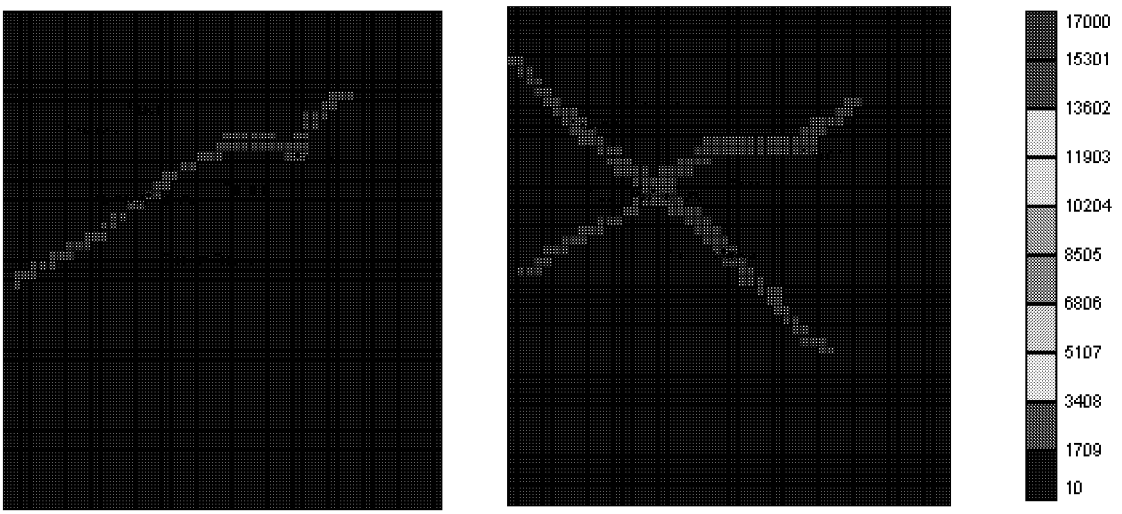

Fig. 3.14-11 —Fracture permeability enhancements to match the performance of the individual wells

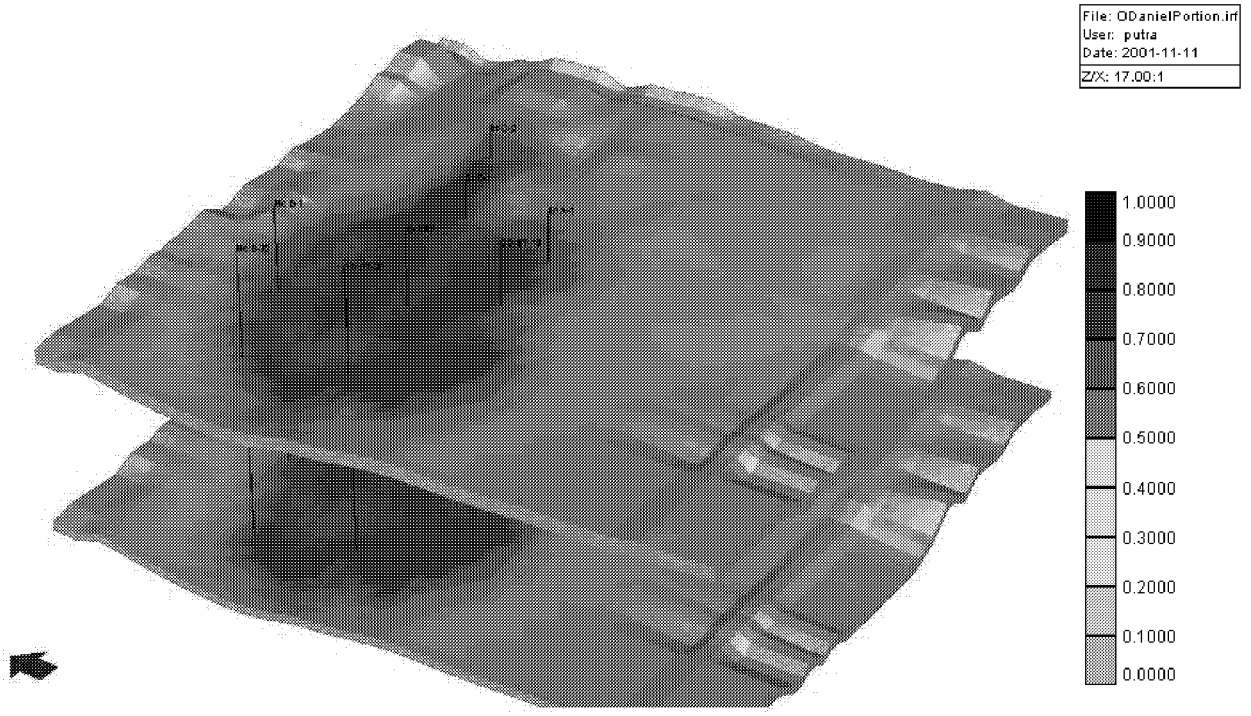

Fig. 3.14-12 —Water saturation distribution at the end of the simulation

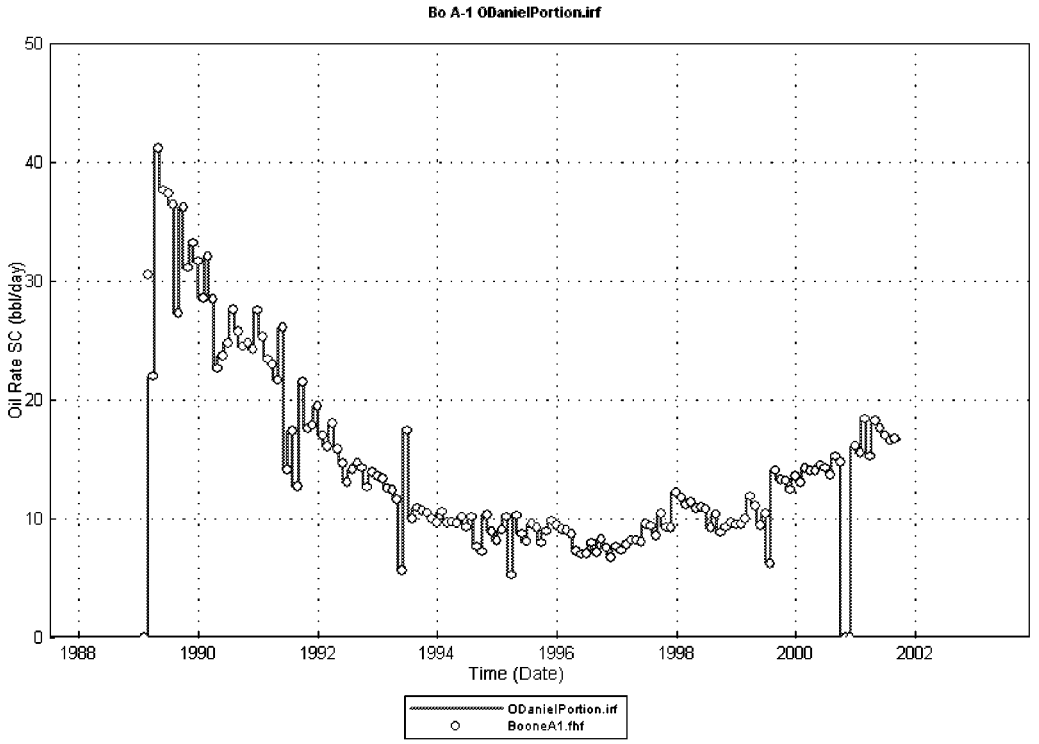

Fig. 3.14-13 —Oil rate constraint of Boone "A" – 1

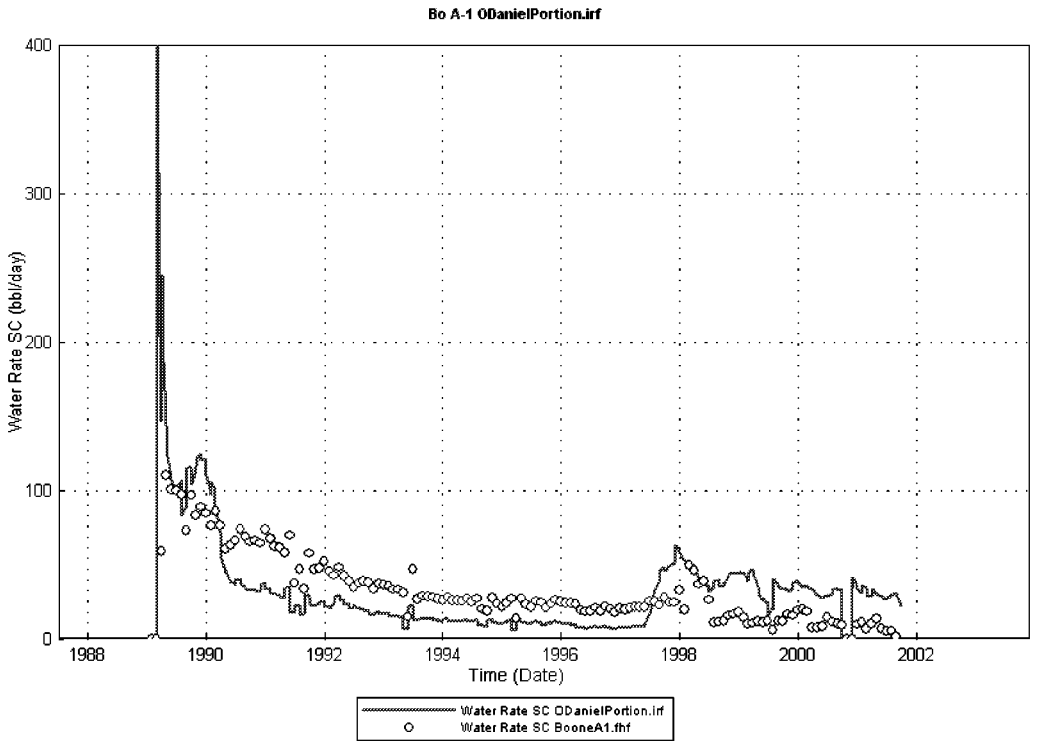

Fig. 3.14-14 —Water rate match between actual data and simulation result of Boone "A" – 1

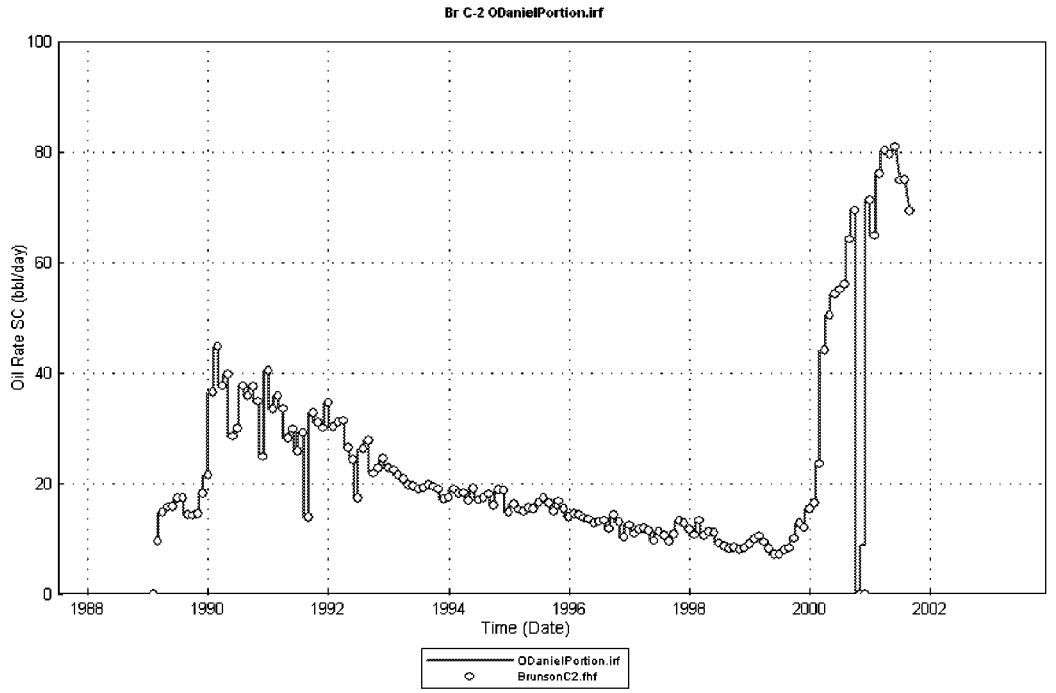

Fig. 3.14-15 —Oil rate constraint of Brunson "C" – 2

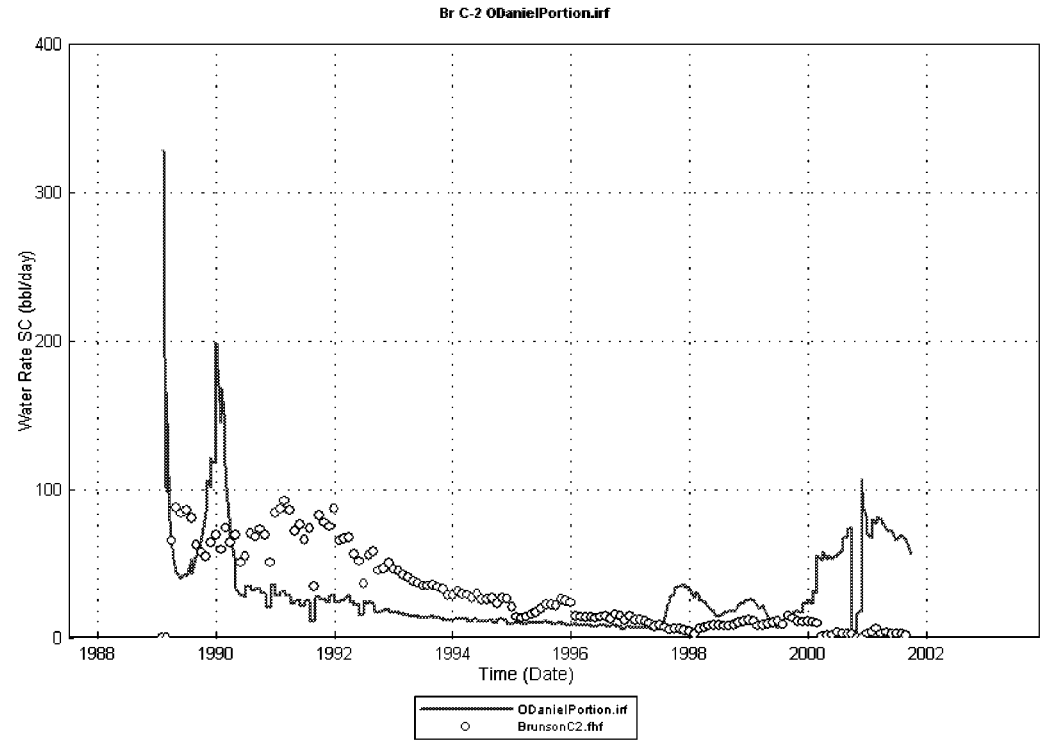

Fig. 3.14-16 —Water rate match between actual data and simulation result of Brunson "C" – 2

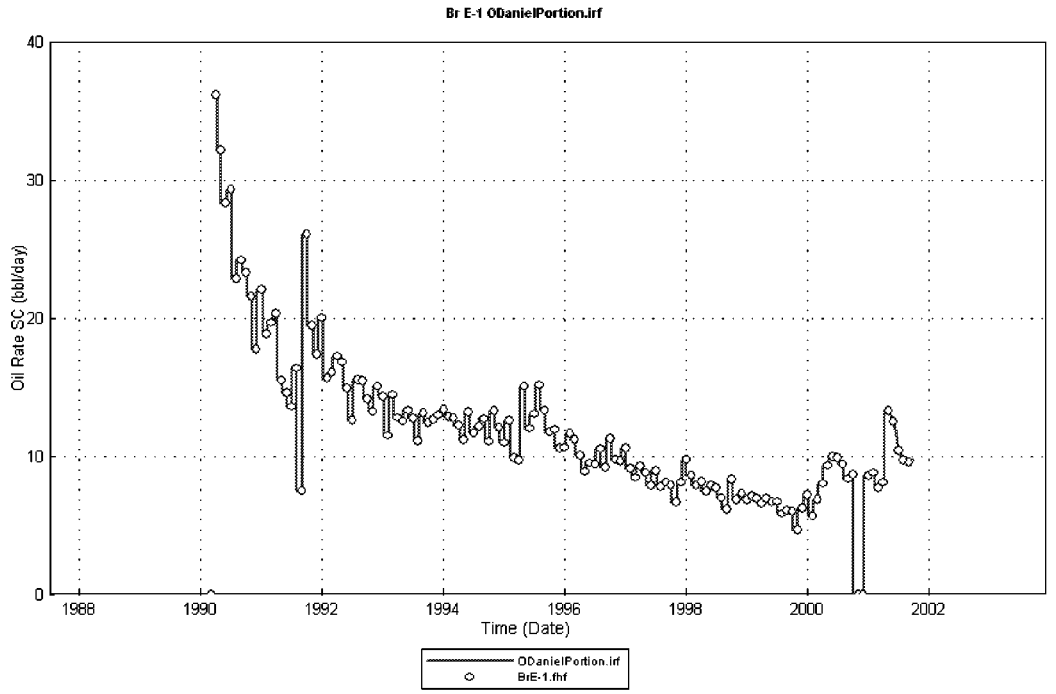

Fig. 3.14-17 —Oil rate constraint of Brunson “E” – 1

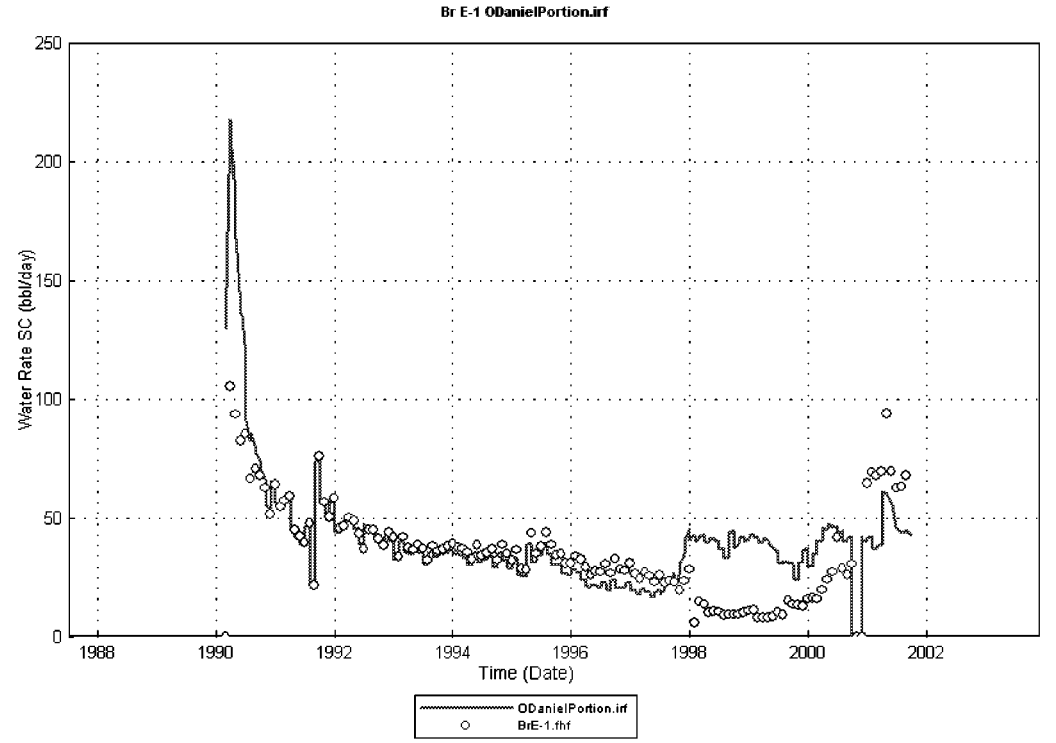

Fig. 3.14-18 —Water rate match between actual data and simulation result of Brunson “E” – 1

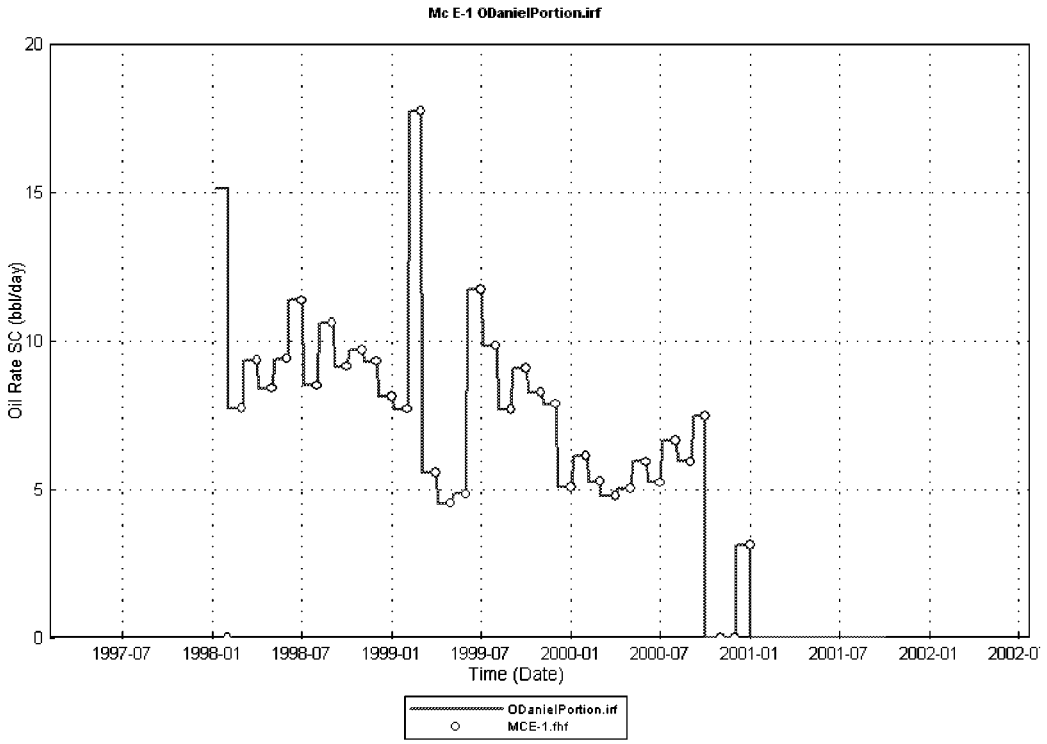

Fig. 3.14-19 —Oil rate constraint of McClintic "E" – 1

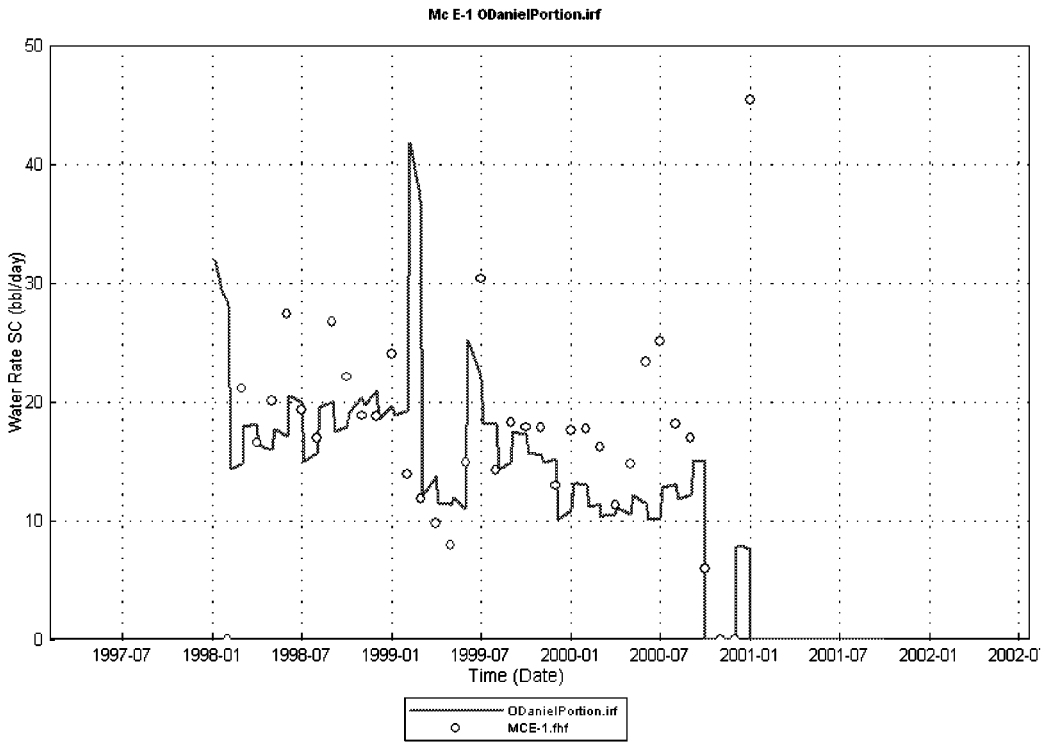

Fig. 3.14-20 —Water rate match between actual data and simulation result of McClintic "E"–1

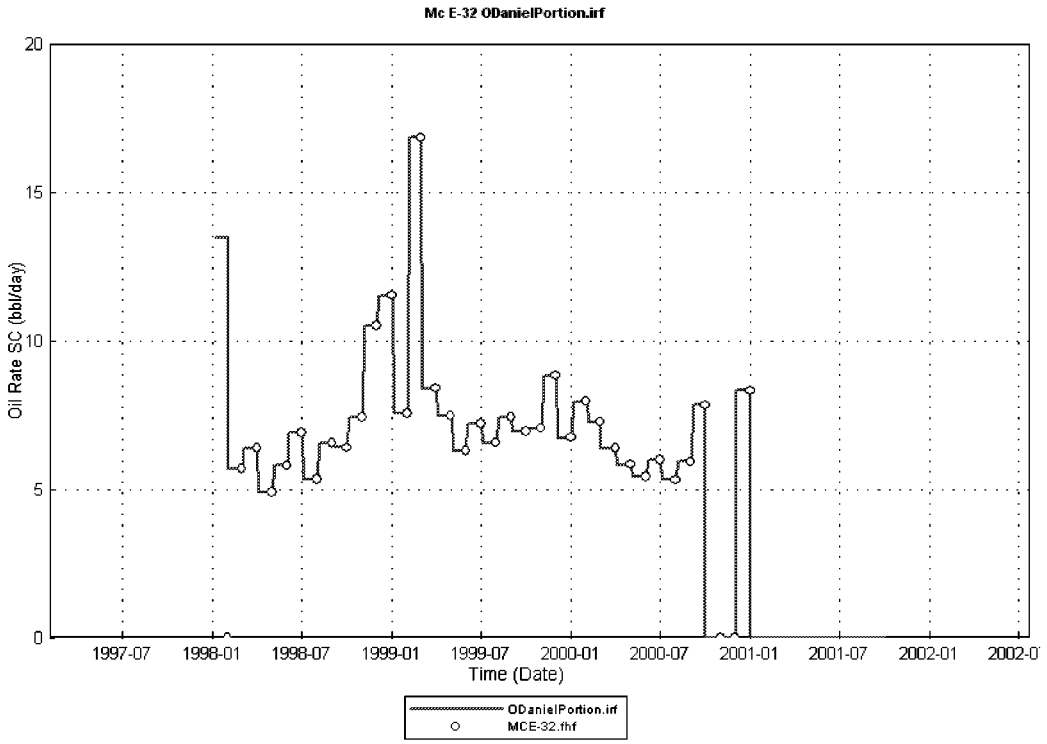

Fig. 3.14-21 —Oil rate constraint of McClintic "E" – 32

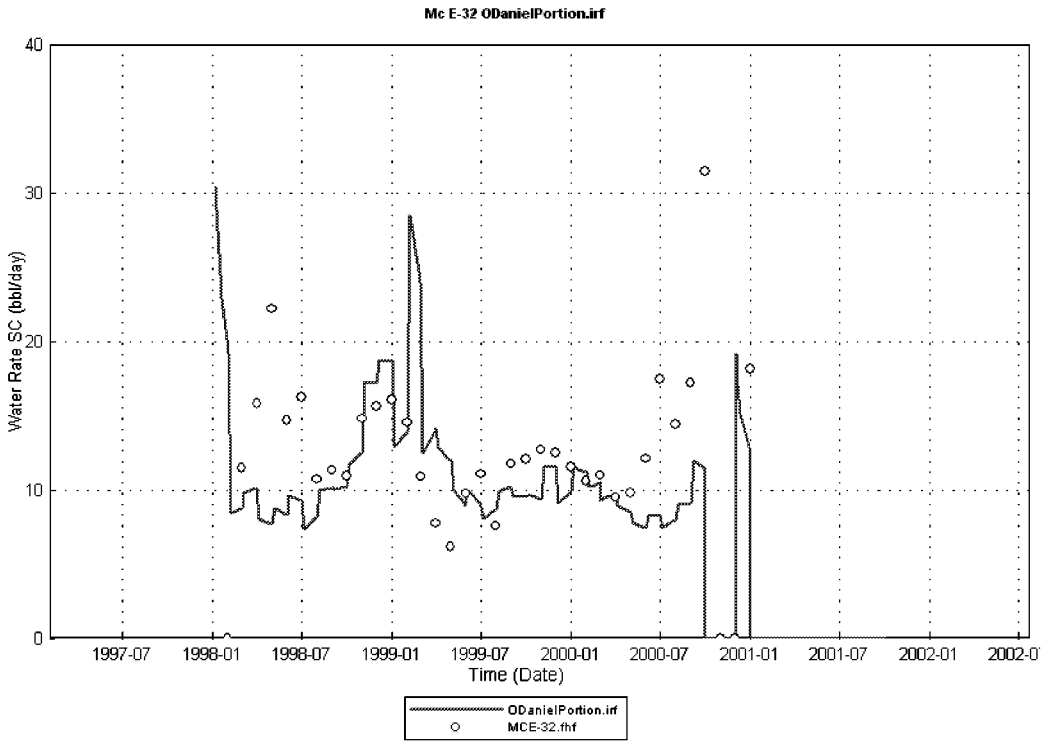

Fig. 3.14-22 —Water rate match between actual data and simulation result of McClintic"E"–32

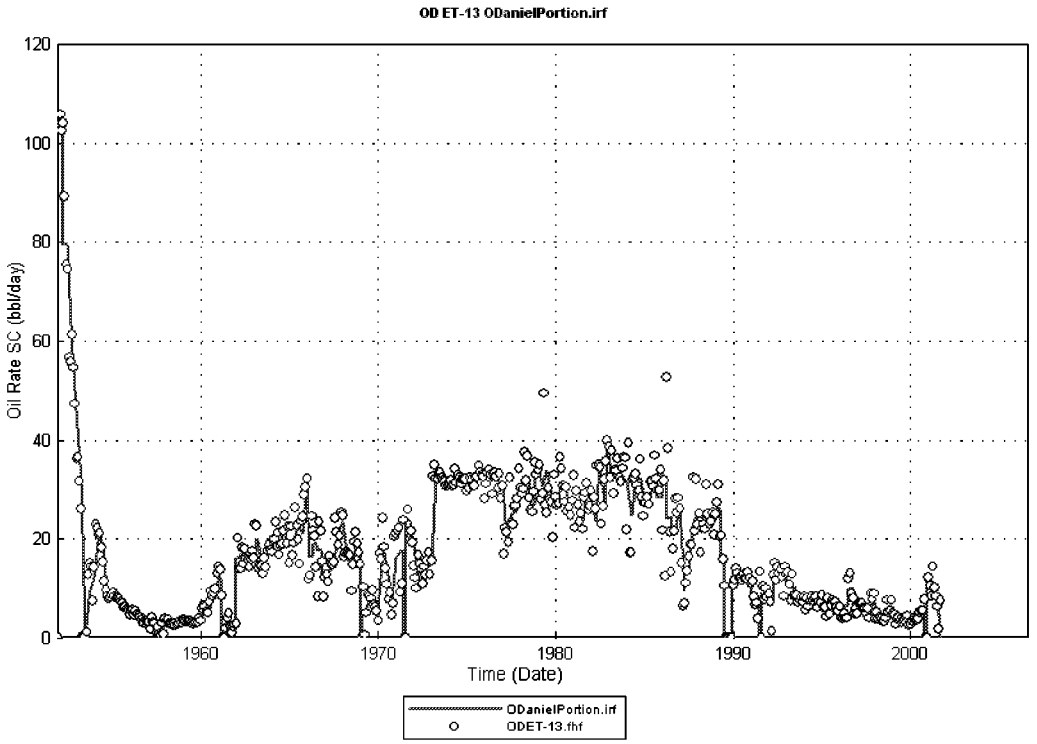

Fig. 3.14-23 —Oil rate constraint of ET O Daniel – 13

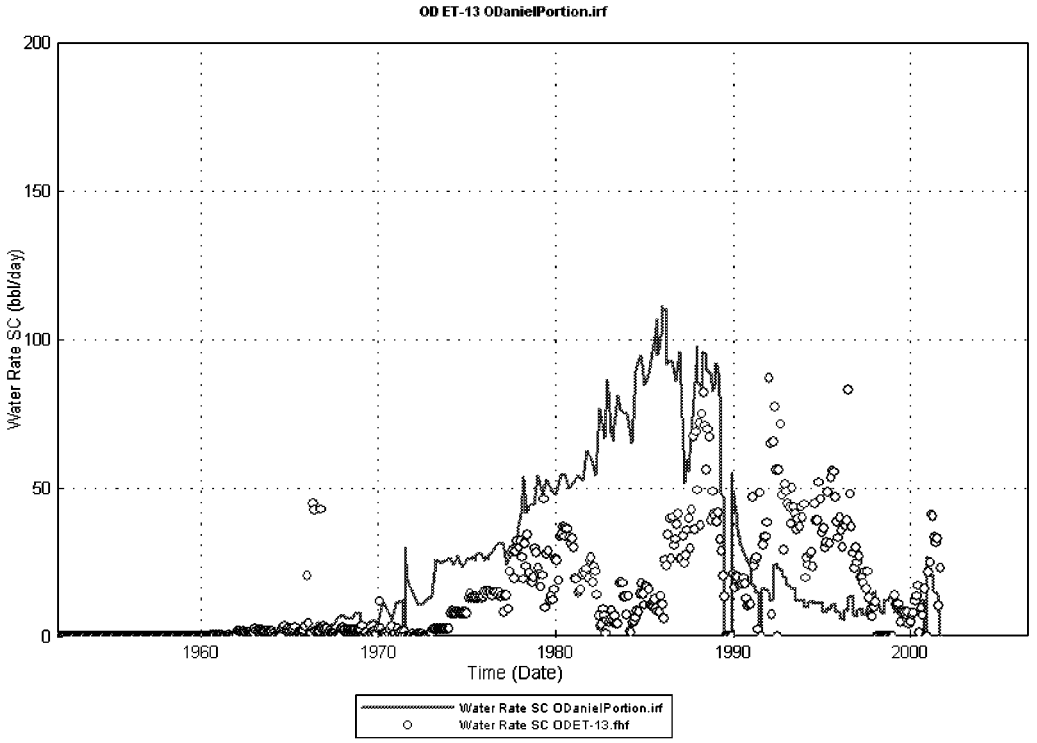

Fig. 3.14-24 —Water rate match between actual data and simulation result of ET O Daniel-13

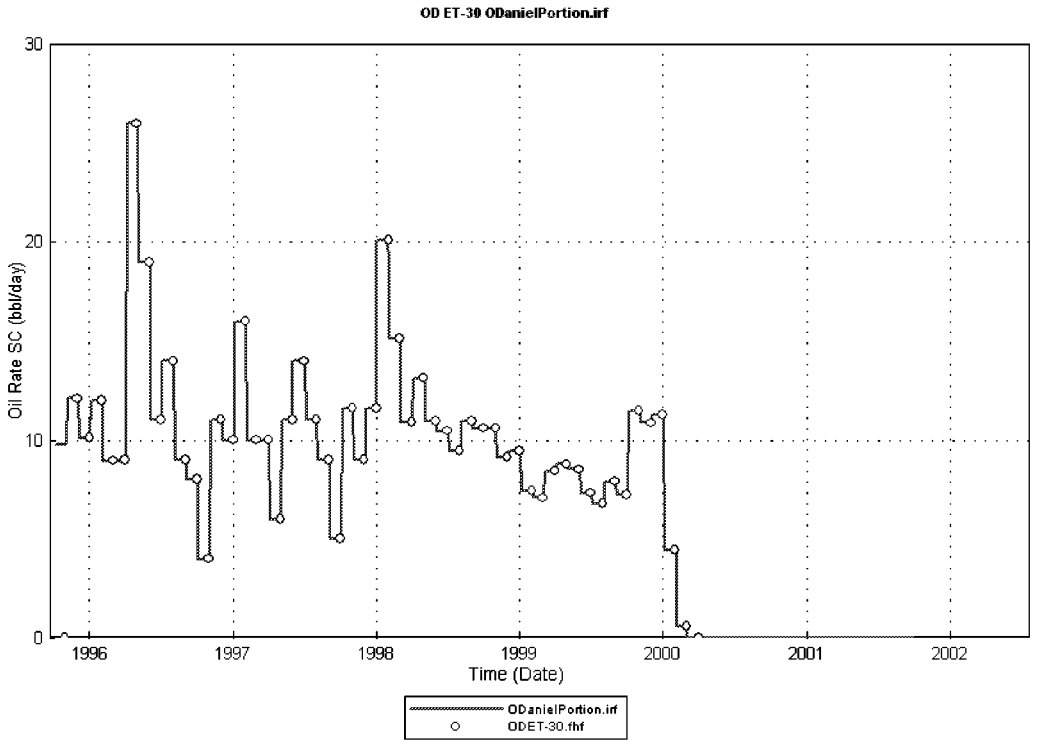

Fig. 3.14-25 —Oil rate constraint of ET O Daniel – 30

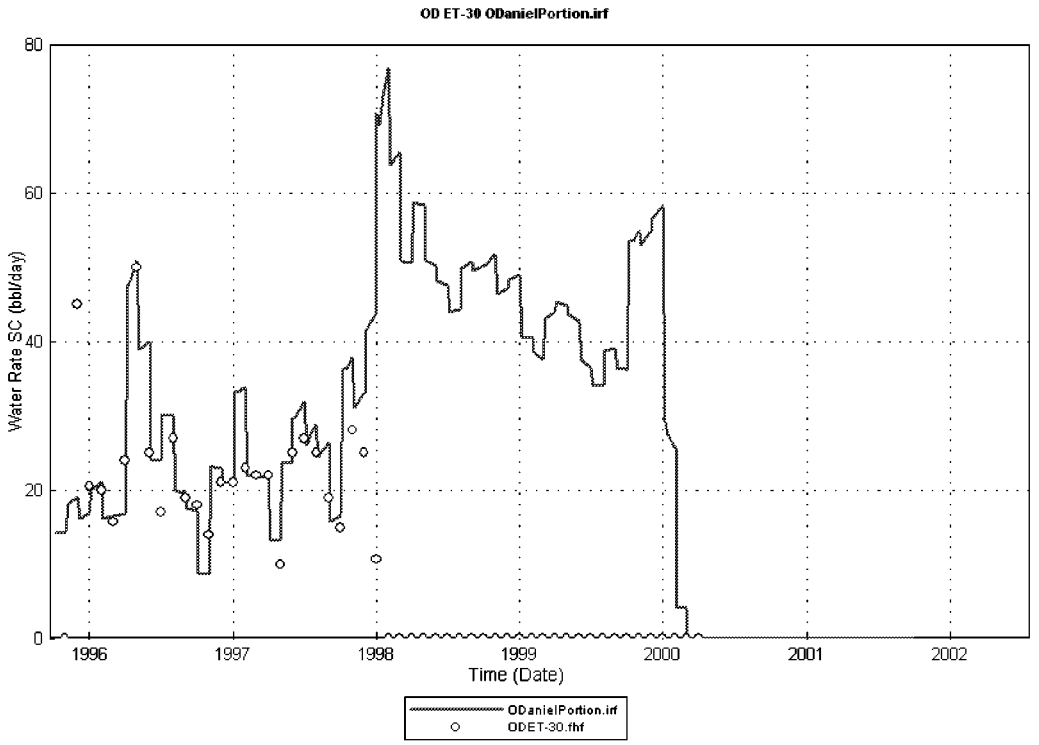

Fig. 3.14-26 —Water rate match between actual data and simulation result of ET O Daniel-30

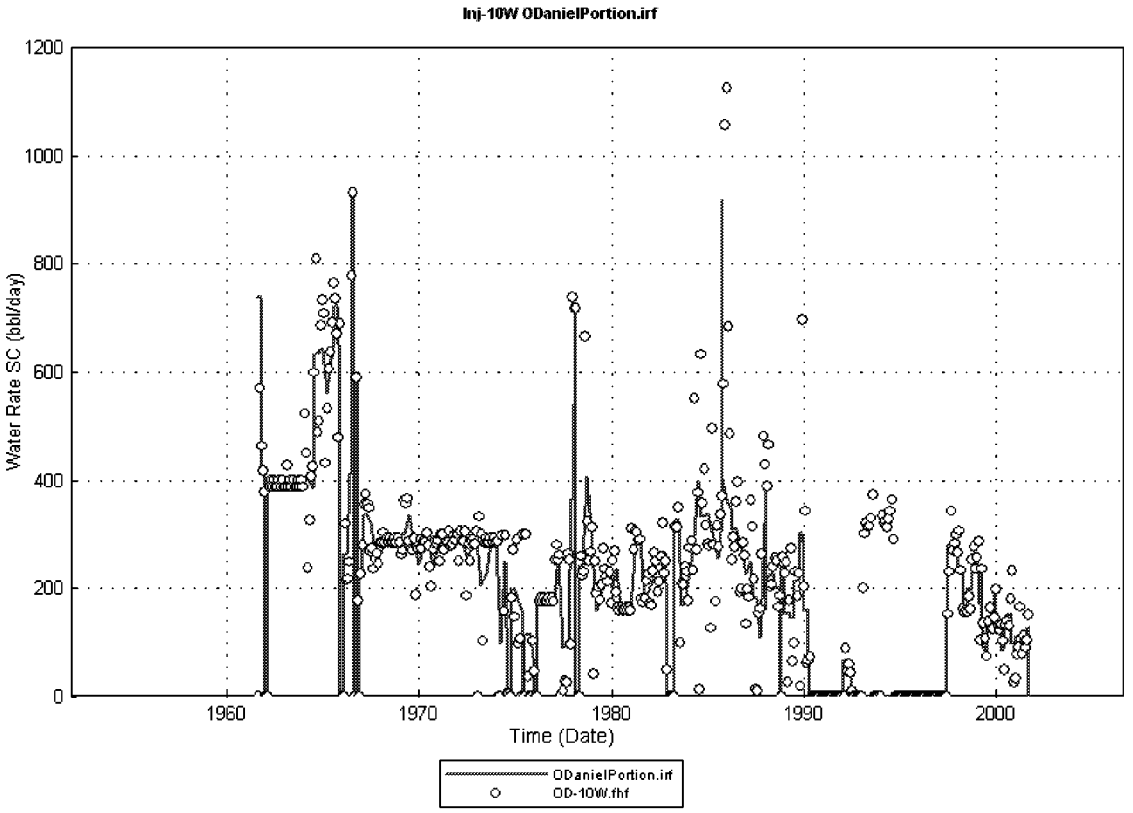

Fig. 3.14-27 —Water Injection rate constraint of ET O Daniel – 10W

3.15 FULL FIELD SIMULATION OF E.T.O'DANIEL PILOT AREA

Introduction

The E.T. O'Daniel Pilot is located in Section 4 T2S Block 37 of the E.T. O'Daniel lease in Midland County, Texas (Fig. 3.15-1). This site was selected due to the high oil recovery that occurred from primary and secondary operations in this particular area.

Stable water injection was initiated in the six ring fence wells in October of 1999 (Fig. 3.15-2) in order to increase the reservoir pressure above the minimum miscible pressure (MMP). Since this is a 40-year-old waterflood area, it was assumed the area was at residual oil saturation and there would be minimal response from water injection. Production has been recorded in 30 wells in and around the pilot area as shown in Fig. 3.15-2. We have divided oil production into 23 off-trend and 7 on-trend wells. The 7 on-trend wells are located along the NE-SW natural fracture orientation as determined by horizontal core.[11]

The three central production wells 38, 39, and 40 have shown little or no response to water injection as expected prior to initiation of CO_2 injection. However, wells oriented parallel to the primary fracture trend responded with a significant increase in oil production. Some of the wells over one mile from the injection wells have responded whereas wells oriented perpendicular to injection wells at a fraction of distance from injection wells have shown little or no response, similar to that observed in the tracer survey. It is possible that off-trend wells will respond in the future but the unexpected increase in production wells along the fracture trend clearly indicates the presence of un-swept oil even though the area has been waterflooded for about 40-years long.

The oil rate increase in the on-trend wells during waterflood (Fig. 3.15-3) confirms our conclusion after the Humble Pilot simulation, where it was recommended that production wells should be placed between 0 to 36 degree from the fracture trend to have fast and good waterflood response (Fig. 3.15-4).

Based on the information obtained in Humble Pilot simulation and tracer analysis in the O'Daniel Pilot, the reservoir model for the O'Daniel Pilot area (Fig. 3.15-2) was developed using three-phase, 3-D and dual porosity options in CMG. The dual porosity model was used, since the Spraberry formation is very tight, so no significant fluid flow in the matrix can be assumed. The main flow in the reservoir occurs through the exchange of fluid from the matrix to the fractures and from the fractures towards the production wells. As we have mentioned earlier, the magnitude and orientation of fracture permeability are the major parameters obtained from the Humble Pilot simulation and tracer analysis. These previous two studies also reveal that, placing the production wells between 0° and 36° from fracture trend gives fast and better waterflood responses. Thus, the knowledge that we have obtained after performing the two-well simulation studies were used to create a model for multi-well waterflood/ CO_2 pilot in the E.T. O'Daniel Area.

Fifteen wells have been completed with four CO_2 injection wells, three central production wells and two logging observation wells. The well pattern is oriented along the major trend with the three producers forming a line parallel to the primary fracture trend. The

producers are flanked by four CO_2 injectors and surrounded by six water injections in an approximate regular hexagonal pattern. The overall area confined by six water injectors is sixty-seven acres while the area enclosed by the four CO_2 injectors is twenty acres. Such a configuration is believed to provide an adequate confinement in most directions although some on trend CO_2 losses in a NE-SW direction could occur.

Simulation Model

Pioneer Natural Resources provided the structural map of the O'Daniel Pilot and its surrounding area (Fig. 3.15-5). The top structure and well locations for the simulator were digitized from this map. The resulting Windig file was then used by CMG during building and gridding the geological model. The 8383-acre area was gridded to 130X130X3 gridblocks. The simulation model in 3-D is shown in Fig.3.15-6. There are 15 injection wells and 44 production wells in the model. Similar to the Humble Pilot and tracer simulation models, the two main zones, the 1U and 5U, were modeled with one large intervening shale layer. It was assumed that there was no vertical communication in the matrix and fracture between the two different sand zones, by setting the transmissibilities of matrix and fracture in the intervening shale to be zero. This assumption agrees with recent horizontal core analysis. All of the wells are perforated only in the first and the third layer.

The main similarity between the O'Daniel Pilot simulation and the simple, two-well models (the Humble Pilot simulation and simulation of tracer test in the O'Daniel Pilot) is that in all the cases dual porosity option was used to create the models. The O'Daniel field was simulated using the CMG simulator, whereas, ECLIPSE was used for the two-well models. Both in the Humble Pilot and the tracer test simulation, the model was rotated in different orientations during the matching process in order to determine the actual orientation of the fracture trend. The field model of the O'Daniel Pilot has 59 wells and three different sets of fractures in the first and the third pay zones, so, it is not possible to orient the grids along a major fracture trend determined from the previous two simple models. However, we attempted to orient the field model along a major fracture orientation but after performing the simulation runs the resulting model produced excessive amount of water from the producer to match the observed data. To overcome this limitation the concept of permeability enhancement was used in the O'Daniel field model.

In order to get a feeling of the fluid movement in our simulation model an initial run was performed. During this simulation run, we have assumed a homogeneous fracture of 100 md in both x and y direction of the model. The simulation was run from 1951 to 2001. From the results obtained after this run we have observed that the six ring fence injectors are not able to inject the required amount of water. This is due to lack of injectivity offered by the homogeneous and isotropic (k_x: k_y = 100:100) fracture permeability introduced during the initial run. Figure 3.15-7 shows the wells included during the initial run. It was assumed in a simulation study conducted earlier that the on-trend and off-trend fracture permeability around the O'Daniel Pilot Area to be 100 md and 1 md respectively (i.e. k_x: k_y = 1:100). The low injectivity resulting from the low fracture permeability disqualifies this assumption.

In order to increase the injectivity in and around the pilot area, the fracture orientation and permeability anisotropy (k_x: k_y) obtained from the tracer test were used in the field simulation. Using tracer analysis result as guidance, a set of fractures was introduced over the O'Daniel Pilot Area as shown in Fig. 3.15-7. The grid-blocks where the fractures are introduced have on-trend and off-trend permeability of 17000 md and 100 md respectively. So, after introducing the fractures a very high permeability anisotropy is created in and around the hexagonal pilot area, which makes the fluid to move mostly along the NE-SW direction. Then the simulation was run from March 1, 1951 to September 30, 2001. This time we have found improved injectivity as shown in Fig. 3.15-8 and Fig. 3.15-9. After the end of simulation we have found acceptable improvement in water-cut performance (simulation results close to the observed data) for the 3 central producers and also for the 2 producers surrounding the O'Daniel Pilot Area (the asterisks in Fig. 3.15-7).
The improved injectivity has a significant role in the response of the 3 central producers. The enhanced permeability in the pilot area (Fig. 3.15-7) increases the injectivity (Figs. 3.15-8 and 3.15-9). So, the 3 central producers get more water from the hexagonal injectors and thus the simulation response gets close to the observed data. Fig. 3.15-10 shows the response of the central producer O'Daniel 37 before and after applying permeability enhancement.

In order to get improved history match results in more wells, the method of permeability enhancement was applied in other parts of the O,Daniel Unit (Fig. 3.15-11). We were able to get better match in 4 more wells (O'Daniel 12, 32, 31 and 36) when permeability enhancement was introduced on the injector O'Daniel 8W. Similarly, improved response was obtained for 5 more producers (O'Daniel. 30, McClintic.E-1, McClintic.E-32 and Brunson. E-1, Brunson .C-2) after permeability enhancement was applied to the injector O'Daniel 10W (Fig. 3.15-12). The method of permeability enhancement can be applied to different injectors to other parts of the unit to get improved waterflood performance from neighboring producers. The final simulation model with permeability enhancements (fractures) is shown in Fig. 3.15-13. Because of the limitations of this study, attempting to match the production histories of all the wells of the model is not the main priority here.

The average water saturation map for fractures, at the end of simulation, is shown in Fig. 3.15-15. Similar maps are also available for matrix water saturation, oil saturation, pressure distribution etc. These maps could be used as a baseline to differentiate the performance between waterflood and CO_2 flood for the economic purpose. The model could also be used to forecast oil production with different scenarios such as, infill drilling, CO_2 injection, horizontal wells.

Conclusions

The methods described here can be used to investigate areas of Spraberry where little or no water injection has occurred. The results of this work will provide a method to assess the economic feasibility of large-scale water injection in the remainder of the field. It is possible to match most of the wells in the O'Daniel field simulation by using the permeability anisotropy (k_x/ k_y), permeability enhancement and fracture orientation

obtained from the tracer simulation in the O'Daniel field model. It was also observed that the fracture trend obtained from this study show similar direction as obtained from the interference test and horizontal core analysis.

References

1. Schechter, D.S., McDonald, P., Sheffield, T., Baker, R.O.: "Integration of Laboratory and Field Data for Development of CO_2 pilot in the Naturally Fractured Spraberry Trend," paper SPE 36657 presented at the 1996 SPE Annual Technical Conference and Exhibition, Denver, Colorado, 6-9 October.
2. Putra, E. and Schechter, D.S.: "Reservoir Simulation of Waterflood Pilot in Naturally Fractured Spraberry Trend Area," paper SPE 54336 presented at the 1999 SPE Asia Pacific Oil and Gas Conference and Exhibition, Jakarta, Indonesia, 20-22 April.
3. Barfield, E.C., Jordan, J.K., and Moore, W.D.: "An Analysis of Large-Scale Flooding in the Fractured Spraberry Trend Area Reservoir," *JPT* (1959), Vol.11, No. 4, p.15-19.
4. Elkins, L.F., and Skov, A.M.: "Determination of Fracture Orientation from Pressure Interference," Trans. AIME (1960), Vol. 219, p.301-304.
5. Kindem, E.: "Characterization of Reservoir Simulation of a Waterflood Pilot in the Naturally Fractured Spraberry Trend," MS Thesis, New Mexico Institute of Mining and Technology, Socorro, New Mexico, May 1996.
6. Putra, E.: "Numerical Modeling of Laboratory Experiments for Waterflooding Simulation in Naturally Fractured Reservoirs: A Case Study from Spraberry Trend Area, West Texas," Ph.D. Dissertation, New Mexico Institute of Mining and Technology, Socorro, New Mexico, December 1998.
7. Epic Consulting Services Ltd.: "Reservoir Characterization and Simulation for Optimizing Hydrocarbon Reservoirs, Book 1," unpublished, May 1999.
8. Warn, G.W. and Sidwell, R.: "Petrology of The Spraberry Sands of West Texas," *Journal of Sedimentary Petrology*, Vol.23, No.2, p 67-74, June 1953.
9. Elkins, L.F.: "Determination of Fracture Orientation from Pressure Interference" Trans., AIME, Vol.219, October 1960.
10. Lytle, W.J. and Rieke, R.R.: "Well Logging in The Spraberry," *Oil and Gas Journal*, Vol.50, No.32, p 92-96 and 105, December 13, 1953.
11. Core Analysis Report 431, Humble Oil Company, July 12, 1963. (10)
12. Dyes, A.B. and Johnson, O.C.: "Spraberry Permeability from Build-up Curve Ananlysis," Trans., AIME, Vol.198, October 1953.
13. Banik, A.K. and Schechter, D.S.: "Charachterization of Naturally Fractured Spraberry Trend Shaly Sands Based on Core and Log Data, " SPE, Midland, TX, March 1996.
14. Elkins, L.F.: "Reservoir Performance and Well Spacing, Spraberry Trend Area Field of West Texas," Trans., AIME, Vol.198, February 1953.

15. Christie, R.S. and Blackwood, J.C: "Production Performance in Spraberry," *Oil and Gas Journal*, April 7, 1952, pp. 107-116.

16. Elkins, L.F. and Skov, A.M.: "Cyclic Water Flooding the Spraberry Utilizes "End Effects" to Increase Oil Production Rate," *JPT*, Vol.15, No. 8, pp. 877-884.

17. Brownscombe, E.R and Dyes, A.B.: "Water-Imbibition Displacement....Can It Release Reluctant Spraberry Oil?," *Oil and Gas Journal*, November 17, 1952, pp. 264-265 & 377-378.

18. Carlson, R.F.: "Spraberry Spacing Report," *Oil and Gas Journal*, October 20, 1952, Vol.51, No. 24, pp. 102-111.

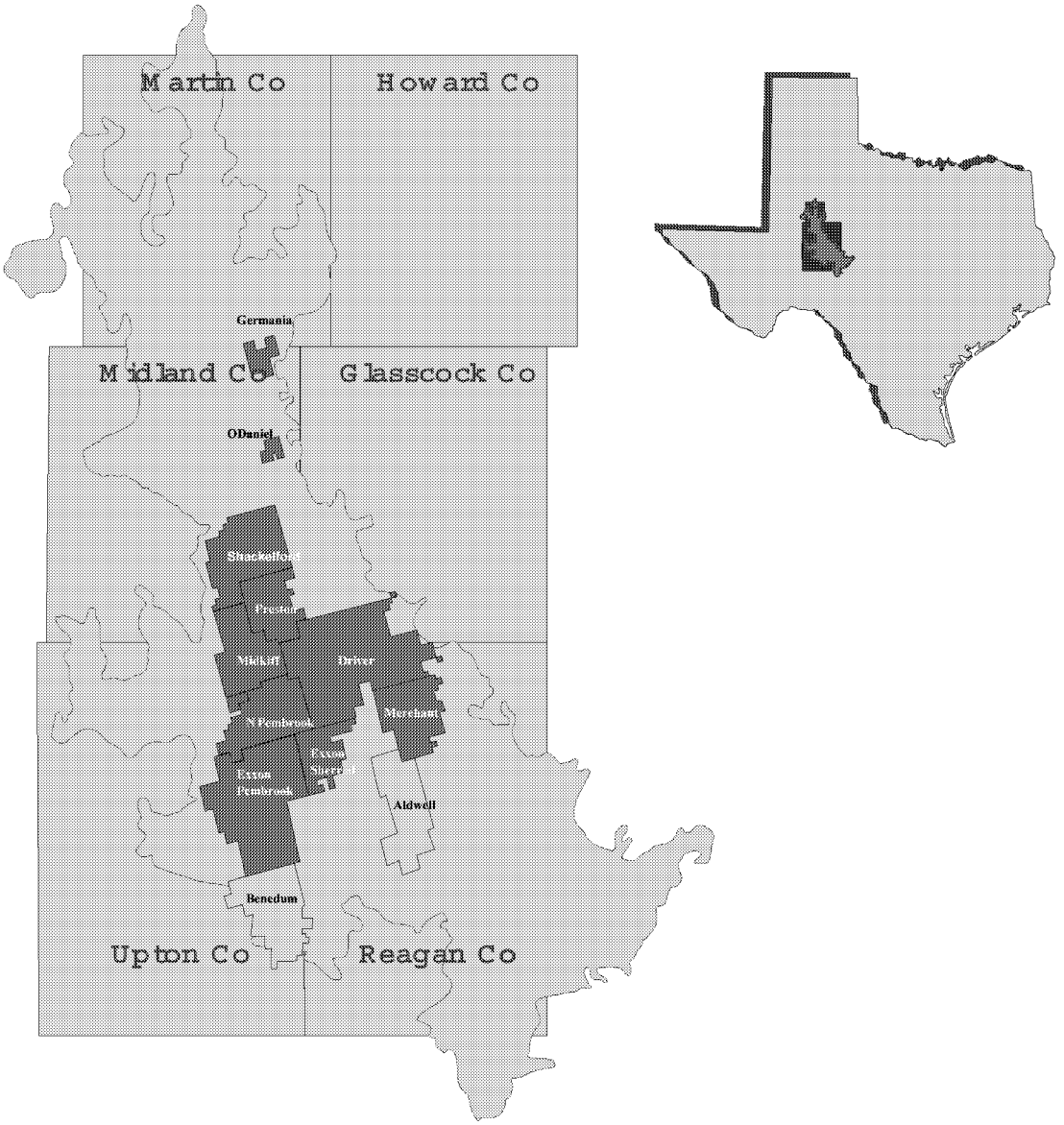

Fig. 3.15-1 —Units and Reservoir Extent in the Spraberry Trend Area

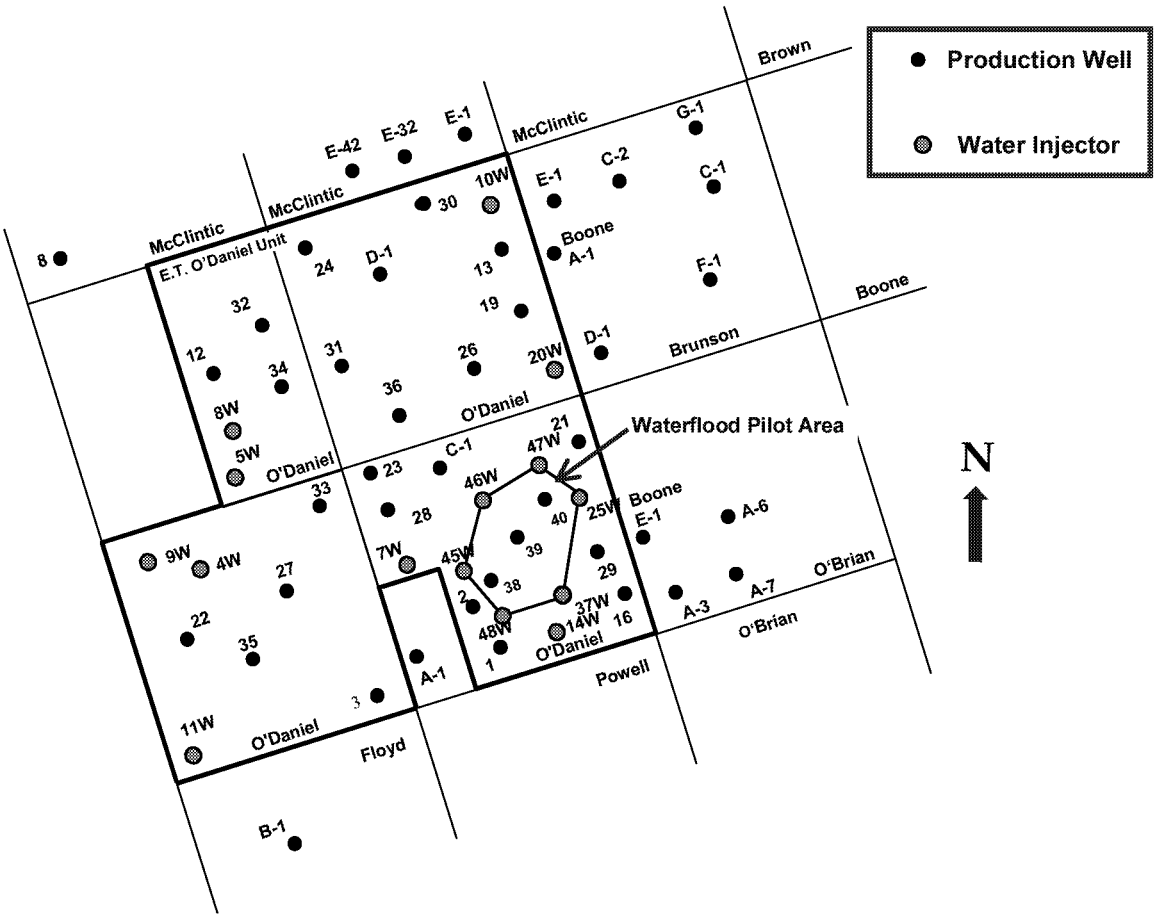

Fig. 3.15-2 —Map of O'Daniel Pilot Area and Pilot Well Configuaration

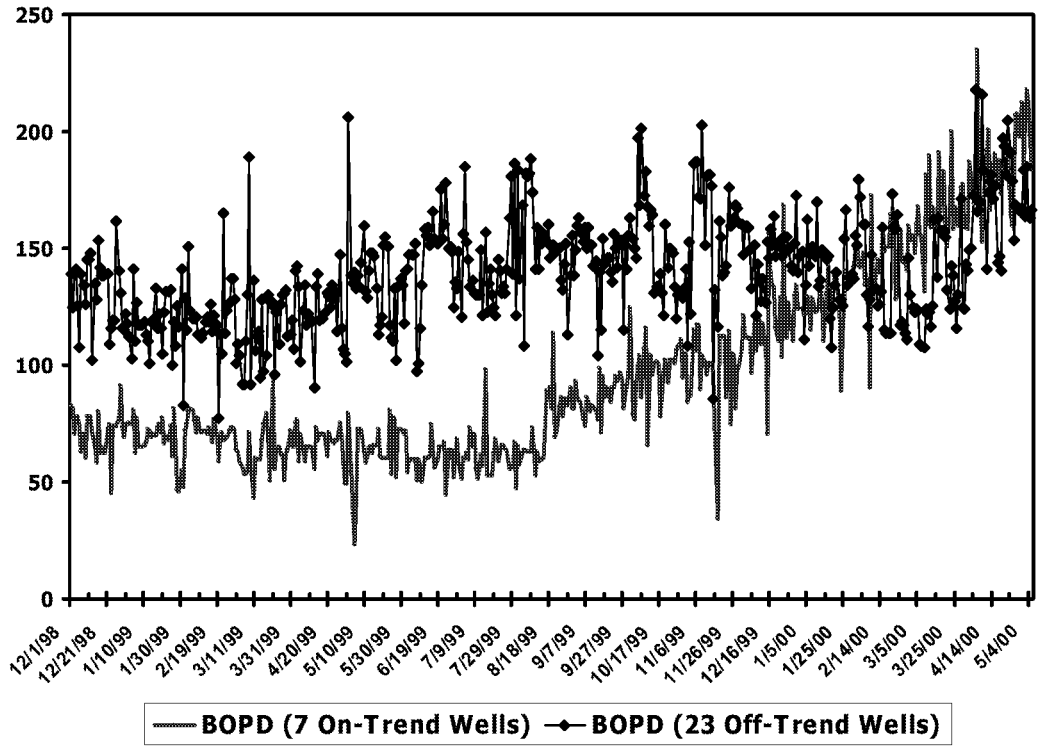

Fig. 3.15-3—Response to Water Injection for On-trend and Off-trend Wells Outside the O'Daniel Pilot Area

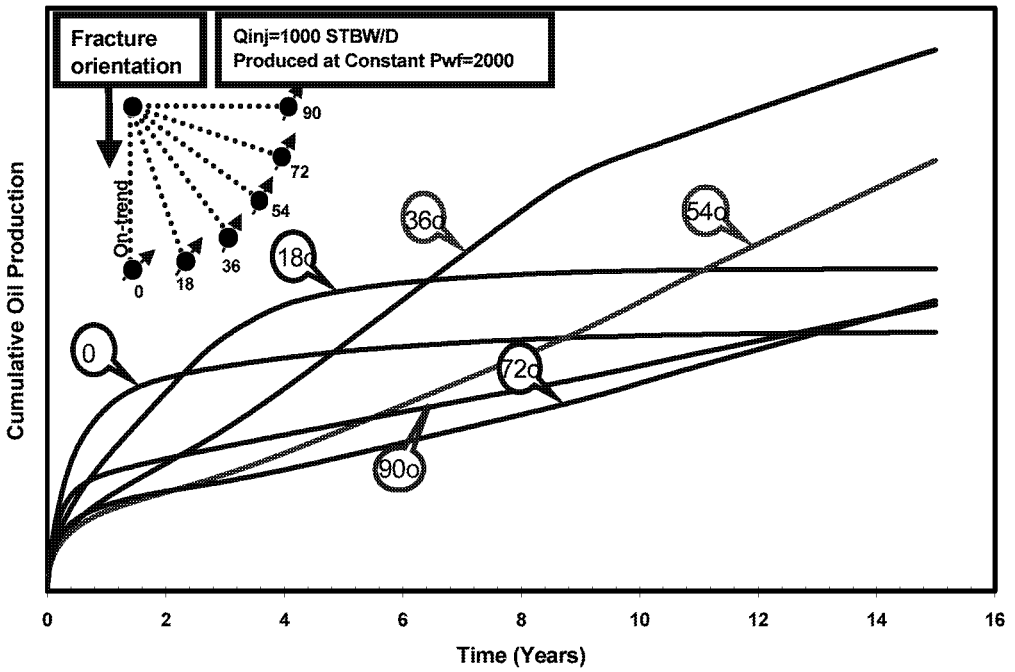

Fig. 3.15-4—Simulation Result from the Hypothetical Model Shows the Effect of Different Well Orientation on Oil Recovery during High Water Injection Rate

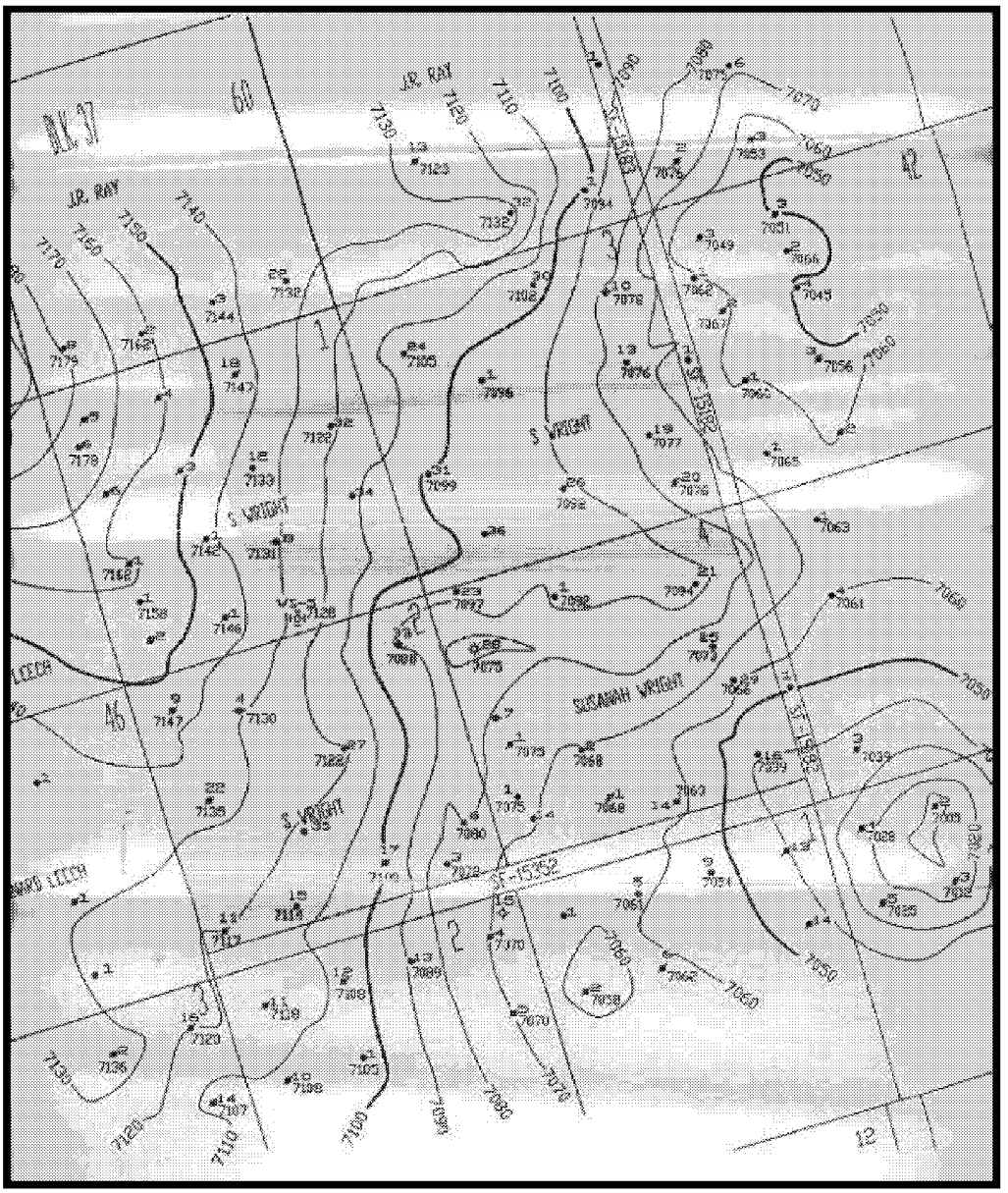

Fig. 3.15-5 —Structural Map for the Simulation Model.

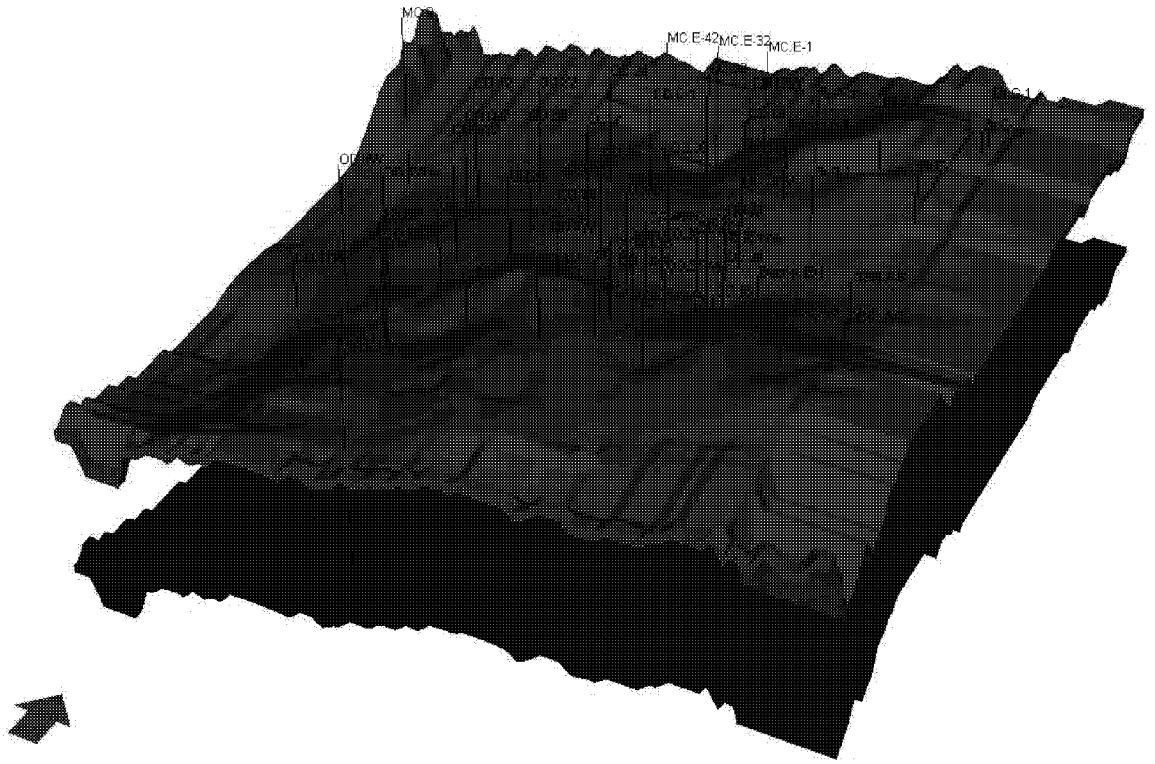

Fig. 3.15-6 —3D Simulation Model for the O'Daniel Waterflood Pilot

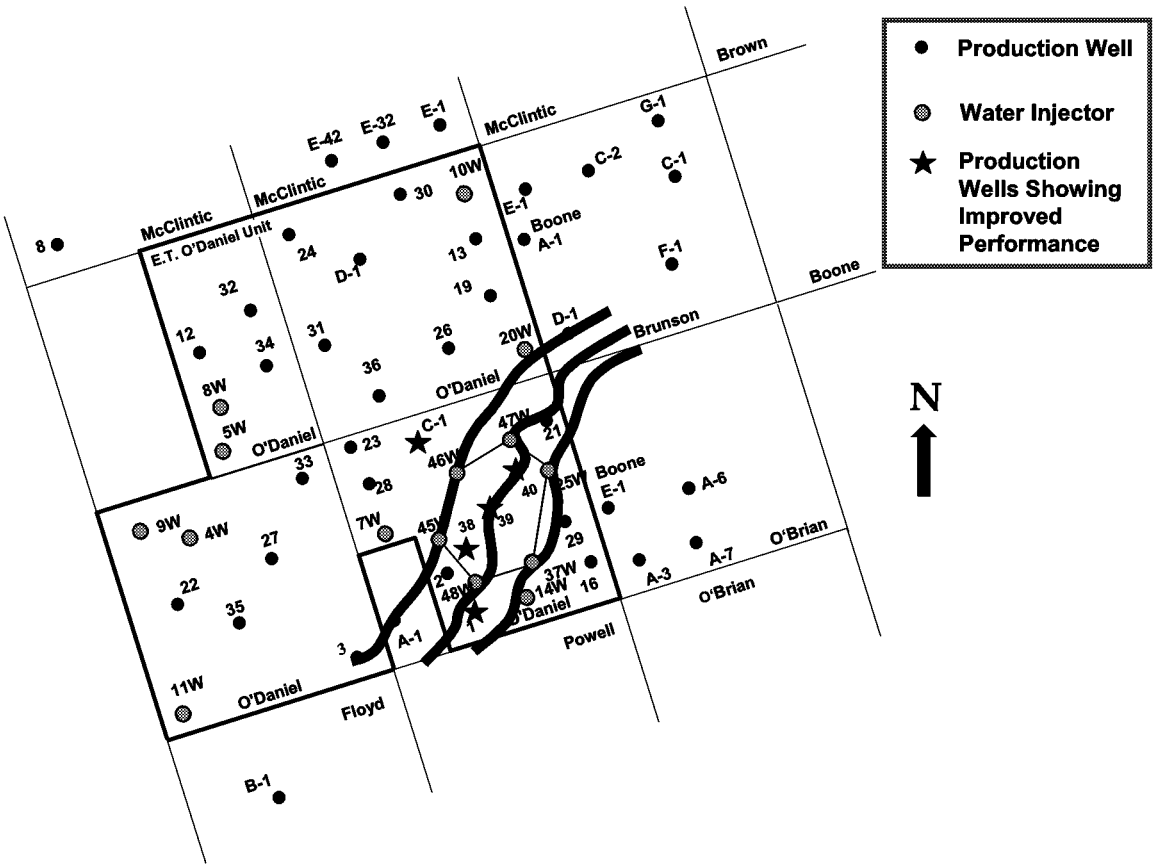

Fig. 3.15-7 —Wells Matched in and Around the Pilot Area After Introducing the Fractures

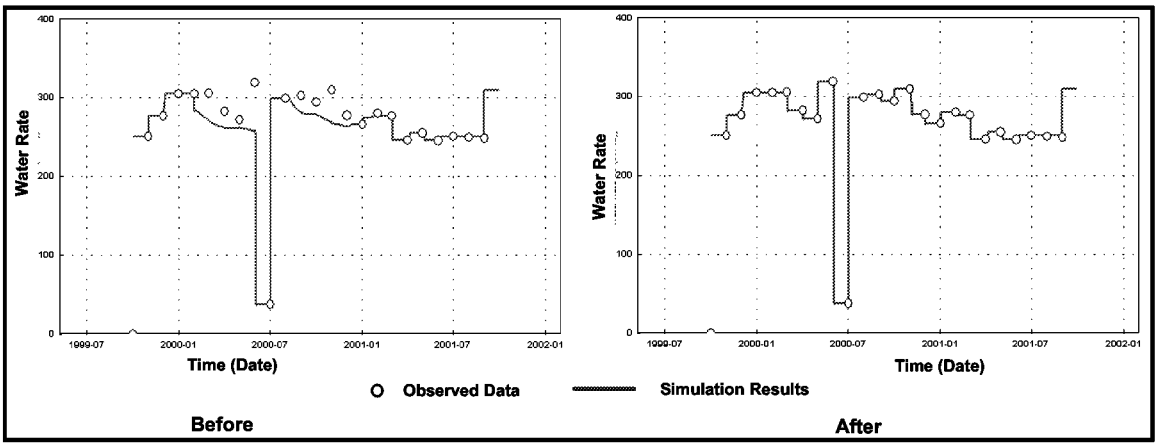

Fig. 3.15-8 —Injectivity Improved for the Injector O'Daniel 37W after Introducing Permeability Enhancement

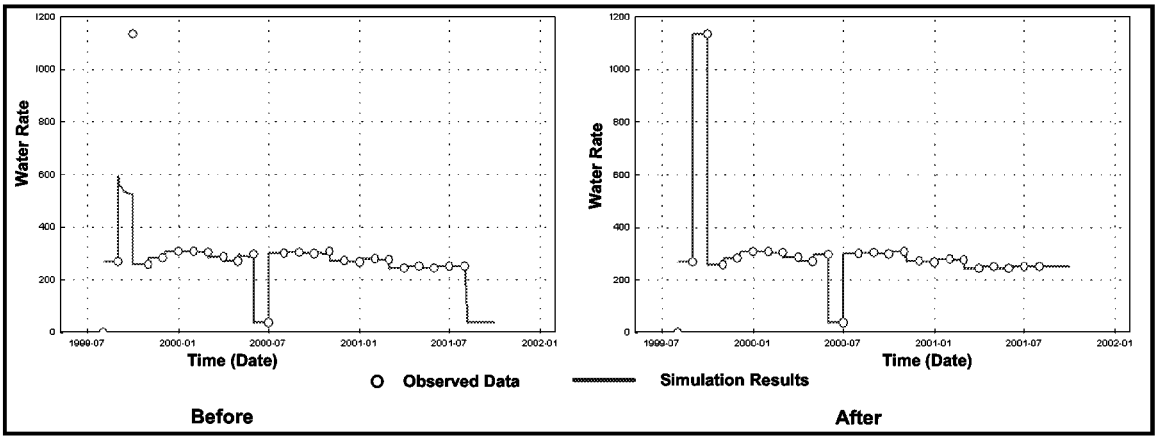

Fig. 3.15-9 —Injectivity Improved for the Injector O'Daniel 48W after Introducing Permeability Enhancement

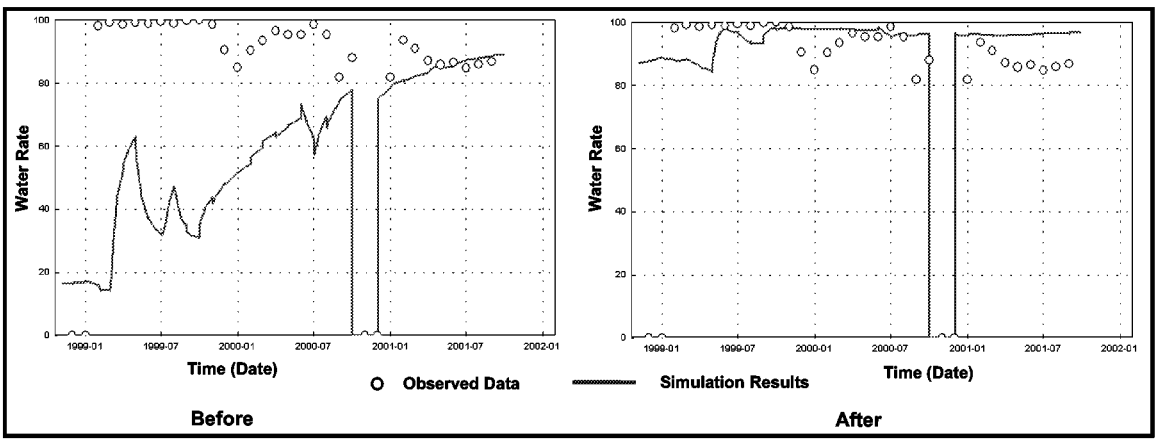

Fig. 3.15-10 —Improved Injectivity Gives Improved Water-cut Response for the Producer O'Daniel 38 after Introducing Enhanced Permeability

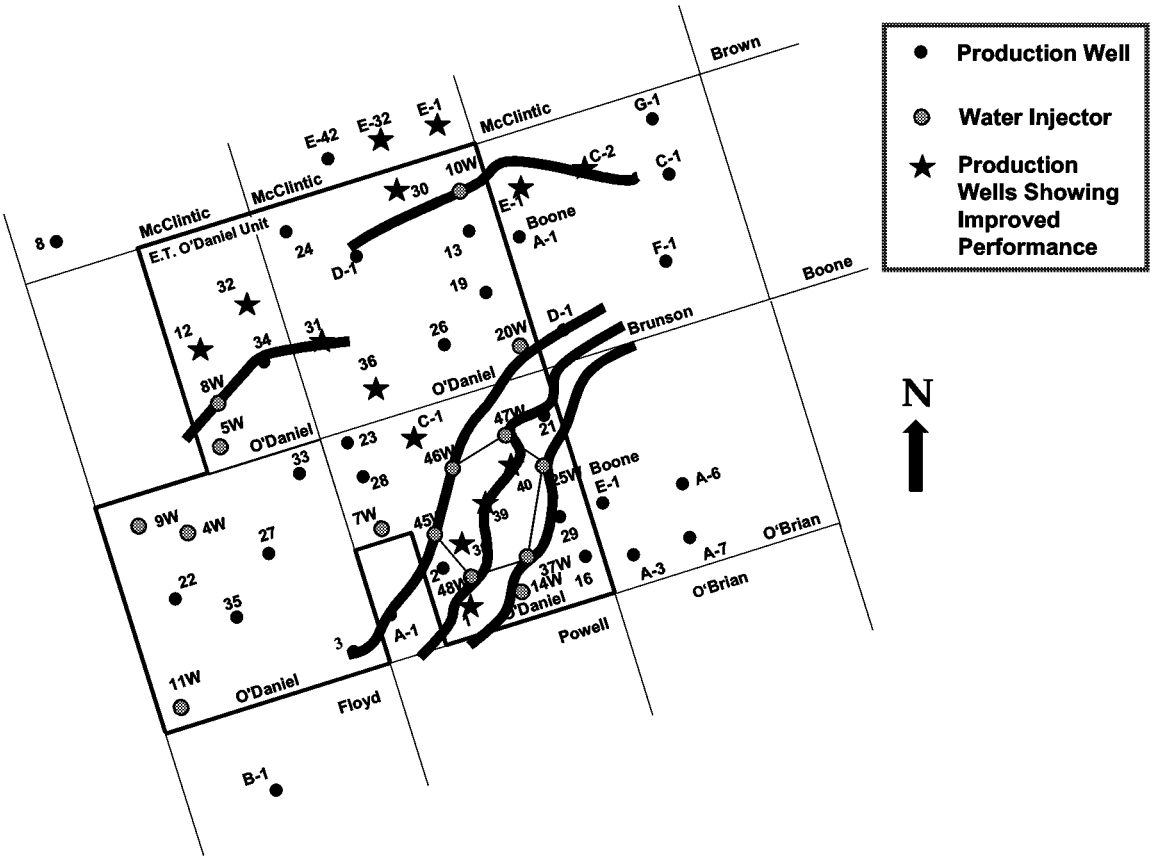

Fig. 3.15-11 —Wells Matched after Introducing Existing Fractures

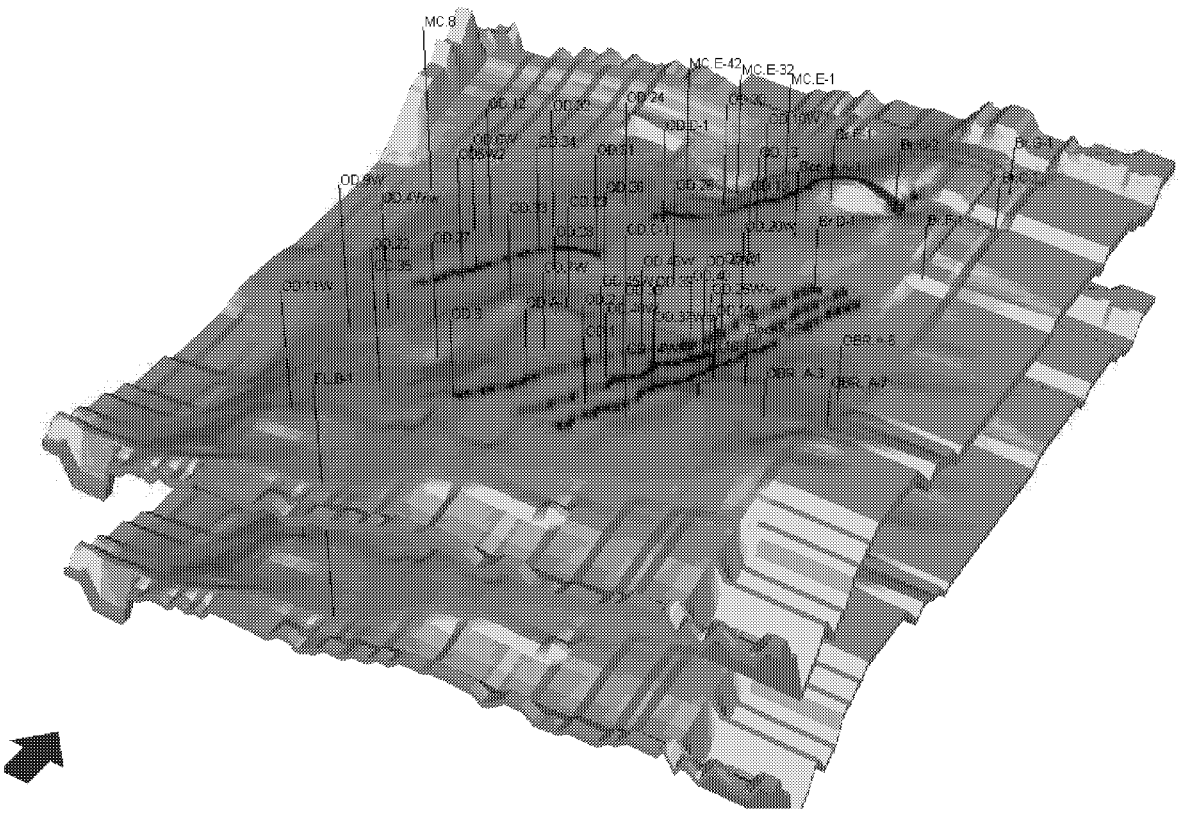

Fig. 3.15-12—Simulation Model after Introducing Existing Fractures

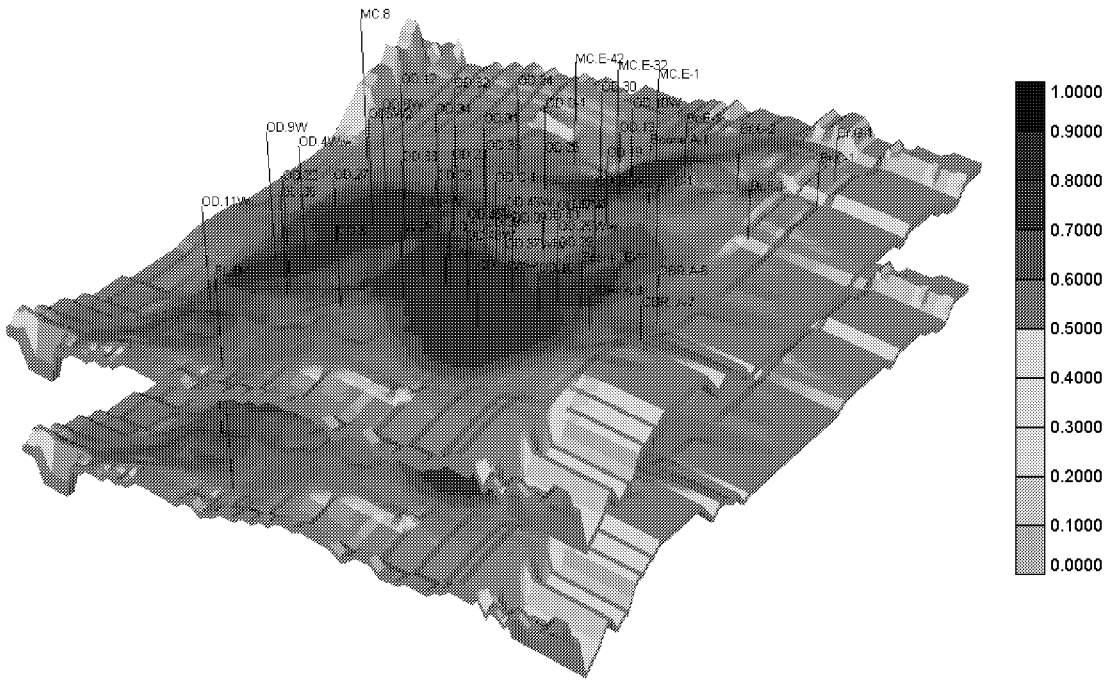

Fig. 3.15-13—Map of Fracture Saturation After the End of Simulation

3.16 ANALYSIS OF LOGGING OBSERVATION WELLS (LOW) IN E.T O'DANIEL PILOT

Introduction

This report discusses the progress of the CO_2 pilot project through interpretation of logs from the logging observation wells in the Spraberry CO_2 flood pilot. A background of the Spraberry reservoir and the events leading to the initiation of CO_2 flood has been presented elsewhere.[1-5] The purpose is to monitor the movement of CO_2 and saturation changes of oil, water and gas in the upper Spraberry interval of E.T O'Daniel wells by utilizing logs from two observation wells. Table 3.16-1 shows well inventory of this pilot.

To this date seven logging runs have been conducted to monitor the movement of CO_2 (Table 3.16-2). Schlumberger™ has conducted all the logging for the Spraberry Unit CO_2 Flood pilot. A review of logging tools used to evaluate reservoir fluid movements is presented below:

Compensated Neutron Log Tool (CNL-T)
This tool responds primarily to hydrogen present in the oil and brine. Although natural gas contains hydrogen, the hydrogen density in gas is very small compared with oil or brine. A decrease in compensated neutron porosity between logging runs indicates an increase in gas porosity, either hydrocarbon gas or CO_2. The Schlumberger CNL tool was used primarily for taking compensated neutron logs.

Array Induction Log Tool (AIT)
The array type induction tool is a high-resolution instrument used to measure the resistivity of the formation. This instrument investigates the median formation at radial depths of 10, 20, 30, 60, 90 and 120 inches from the wellbore. Identical readings of 90 inch and 120-inch depth measurements provide direct indication of deep resistivity (R_t). A higher value of resistivity indicates the presence of hydrocarbons or CO_2. In conjunction with the porosity measurements, a saturation profile can be obtained at different depths.

Natural Gamma Spectrometry tool (NGT)
The Natural Gamma Tool is used to measure the natural gamma ray radiation of the formation from the three most common components of the naturally occurring radiation: potassium, thorium, and uranium.

Methodology

A two-fold analysis was carried out to give a more effective interpretation of available log data

1. Analysis of log data using PRIZM™
2. Analysis of log data using statistical tools

Analysis of log data using PRIZM™

The following procedure was followed to analyze the log data obtained from the field:

1. The LAS files of each logging run from both the observation-wells (#49 and#50) for different run times were obtained.
2. For our case, natural gamma ray, neutron porosity and resistivity data was required. Hence only this information was sought from the LAS files.
3. The modified LAS file was imported to GEOGRAPHIX and the suite of log curves was obtained by using PRIZM.

Our preliminary analysis includes two log tracks, compensated neutron log and the array induction log.

Logging Observation Well #49

Fig 3.16-1 shows two log tracks, the neutron porosity log and the array induction log. These two curves have been obtained from logging runs carried out on Jan 31st 2001, which was taken as the base log for our analysis as it was conducted before the CO_2 injection started and March 16th 2001. The change in neutron porosity is evident in all the layers and the decreasing trend indicates the presence of hydrocarbon gas or CO_2.The change in resistivity is more pronounced in the 2U, 3U and 4U layers from the logs. But in 1U and 5U there is little change in the resistivity values even though there is a marked changed in porosity. This might be due to inadequate movement of CO_2 in these layers as compared to 2U, 3U and 4U. It can also be noted that there is excellent vertical conformance of the CO_2 flood as evidenced in the neutron log suppression.

Fig. 3.16-2 depicts a change in resistivity and neutron porosity in August as compared to January logging run. The neutron porosity shows a decreasing trend hinting the possibility of CO_2. The resistivity does not decrease in layers 1U and 5U hinting no movement of CO_2 in these layers but there is a definite change in saturations in the other layers as seen by the change in resistivity. Again it is clearly evident of movement of CO_2 in the all layers.

Logging Observation Well #50

In the case of Well 50 the base log is taken as the March 16th 2001 logging run and in Fig 3.16-3 this log is being compared with the log taken on June 12th. The trends in both resistivity and porosity logs are not very convincing to show a definite movement or presence of CO_2.The gamma ray also shows a shift. Unlike Well 49, the non-pay zones do not show convincing decrease in neutron porosity to warrant the presence of CO_2.
Fig 3.16- 4 shows the log tracks from the March 16th and August 18th logging runs. Even here the resistivity and porosity logs do not show a definite change to determine the presence or movement of CO_2. The gamma ray also shows a decreasing shift.

The observation made from the logs of this well is very inconclusive and more investigation has to be carried out. Some of the reasons for such anomalous readings might be attributed to:

1. High Logging Speed
2. Inconsistent CNL reading
3. Inaccurate data during the February logging run in Well 50
4. Very few logging runs

Analysis of log data using statistical tools

The emphasis of using statistical tools is to confirm the findings from the log interpretations as well as provide graphic representations (pictures) to make the data easier to comprehend. The analysis has been carried out to track the decrease in the neutron porosity index (NPHI) with respect to time.

The statistical exercise involves two steps:

- Computation of the relative frequency and cumulative frequency of NPHI of all zones
- Computation of the relative frequency and cumulative frequency of NPHI of only clean zones

Histograms are the statistical tools used for depicting the decrease in NPHI.

Relative and Cumulative Frequency of Neutron Porosity

The porosity readings (NPHI) from all zones in both the wells were divided into classes (NPHI intervals). A statistical software, SPSS^{TM}, was used to compute the relative frequency and cumulative frequency of the distribution. Analogous to the comparison of logs, Jan 31st logging run was taken as the base log for well 49 and Mar 16th log run was taken as the base log for well 50. The frequencies of the subsequent log runs were compared with the base log frequency.

The frequency distribution comparison for the zones 1u and 5u of wells 49 are shown in Figs. 3.16-5 and 3.16-6. The difference in cumulative curves shows a decrease in neutron porosity. The result may indicate the movement of CO_2 in this layer. However unexpected result was obtained in well 50 where the base curve overlaps with subsequent curves as shown in Figs. 3.16-7 and 3.16-8. The result indicates no CO_2 breakthrough through the layer. Meanwhile the nearby production wells (39 and 40) had produced significant high CO_2 percentage. The small different in cumulative frequency curve may be because of less of CO_2 volume being injected.

Even though the cumulative frequency of well 49 in all zones shows decrease in porosity but the decrease is not consistent with time lapse as shown in Fig. 3.16-9. The cumulative frequency of well 50 in all zones shows almost overlapping in all depths as depicted in Fig 3.16-10.

Clean zones imply those zones in which volume shale is less than 15% and porosity is greater than 7%.[2] These zones were chosen because they contain mostly sandstone and a clear distinction between the different cumulative frequency curves was expected. Even though there is a more clear discrepancy in frequency curves but the performance shows similar with the performance in all zones (Figs. 3.16-11 and 3.16-12).

Conclusions

The observations made from the logs of the two observation wells are contrary and more investigation has to be carried out to draw a firm conclusion. However, the following preliminary conclusions can be made based on presence results:

1. Comparison between the NPHI values from LOW #49 before and after injection of CO_2 confirms that there are decrease in compensated neutron density (NPHI) and increase in resistivity logs at different depths hinting the presence of a hydrocarbon gas or CO_2.
2. Even though CO_2 is going into all the layers as indicated in LOW #49 by the changes in resistivity and density logs, but those changes are not seen in LOW#50.
3. Even though the statistical analysis has been employed the observations made from the logs of two observation wells are still not clear. More CO_2 volume needs to be injected and more logging runs has to be carried out.
4. Even though nearby production wells (39 and 40) had produced significant high CO_2 percentage but the observation wells still can not capture the change of CO_2 saturation indicating the CO_2 volume passing through the layers is very small.

To facilitate an accurate interpretation and decrease uncertainty the following recommendations can be made:

1. Maintain a lower logging speed
2. Make two logging passes at this speed.
3. Use other tools such as MWD neutron, Dual Porosity to get a better and more consistent estimate of porosity

References

1. Schechter, D.S, Banik, B.S.: "Intergration of Petrophysical and Geological Data with Open Hole Logs for Identification of the Naturally Fractured Spraberry Pay Zones," paper SPE 38913 presented at the 1997 Annual Technical Conference and Exhibition held at San Antonio, TX, October 5-8.
2. Guidroz, M.G.: "E.T.O'Daniel Project-A Successful Spraberry Flood," paper SPE 1791 presented at the 1967 Permian Basin Oil and Gas Recovery Conference, Midland, TX, July 18.
3. Li H., Putra E., Schechter, D.S. Grigg, B.R.: "Experimental Investigation of CO_2 Gravity Drainage in a Fractured System," paper SPE 64510 presented at the 2000 Asia Pacific Oil and Gas Conference and Exhibition held at Brisbane, Australia, October 16-18.

4. Baxter, W.A, Harvey, P.A.: "Log Monitoring at the Midale CO_2 Flood Pilot" Internal report on CO_2 flood at the Midale Unit, Texas A&M University.
5. WZI Inc.: Design and Operating Policy E.T. O'Daniel Pilot CO_2 Flood, report prepared for Pioneer Natural Resources Company (Feb 2001), Texas A&M University.

Table 3.16-1 — Well Inventory

Type of Well	O'Daniel Well I.D No	Number of wells
Water Injector	#45,#46,#47,#25,#37,#48	6
CO_2 Injector	#41,#43,#44,#43	4
Producer	#38,#39,#40	3
Observer	#49,#50	2
Total		15

Table 3.16-2 — Logging Runs Conducted

Date Conducted	Logging Runs	Type of Logs Used for Study	
		Well#49	Well#50
Jan 31 2001	1	AIT*, GR, CNL**	AIT*, GR, CNL**
Feb15 2001	2	AIT*, GR, CNL**	AIT*, GR, CNL**
Feb18 2001	3	AIT*, GR, CNL**	AIT*, GR, CNL**
Mar16 2001	4	AIT*, GR, CNL**	AIT*, GR, CNL**
Apr 16 2001	5	AIT*, GR, CNL**	AIT*, GR, CNL**
Jun 12 2001	6	AIT*, GR, CNL**	AIT*, GR, CNL**
Aug 18 2001	7	AIT*, GR, CNL**	AIT*, GR, CNL**

AIT* = AO 10, 20, 30, 60, 90
AT 10, 20, 30, 60, 90
AF 10, 20, 30, 60, 90
AHFCO 60, AHTCO 90
CNL** = NPHI

NOTE: AT 90 HAS BEEN USED AS THE DEEP RESISTIVITY READING (R_t) FOR ALL CALCULATIONS

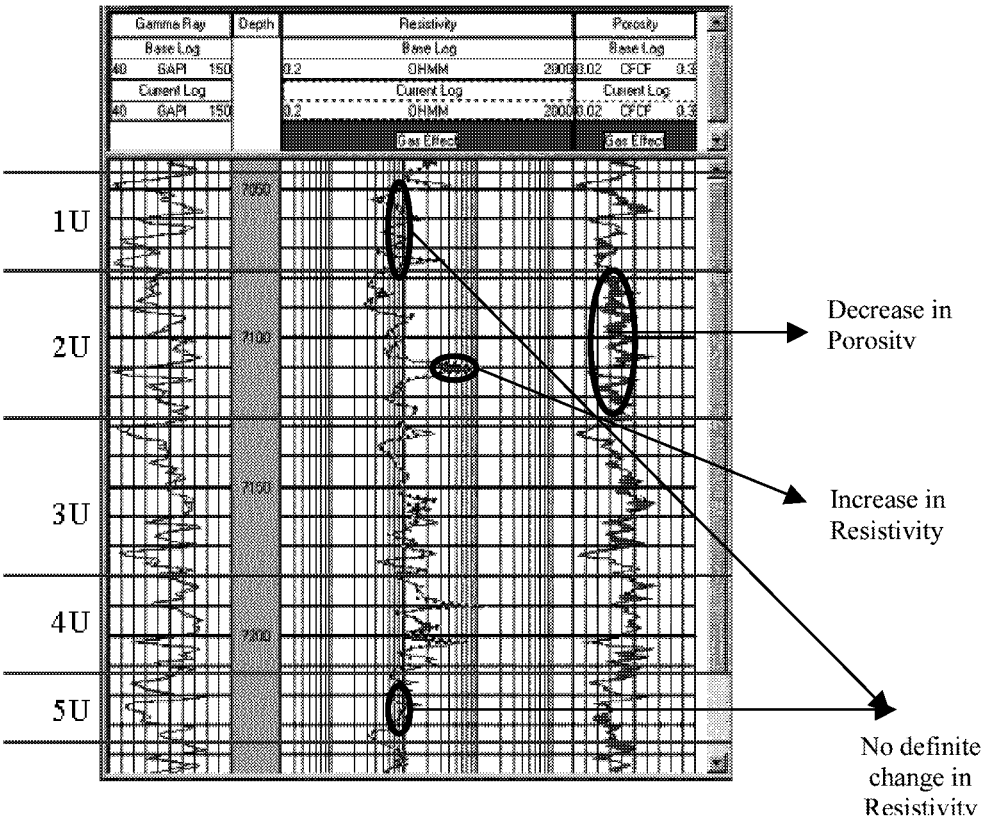

Fig. 3.16-1 —Neutron Porosity and Resistivity Profile of Well 49 (Jan-Mar)

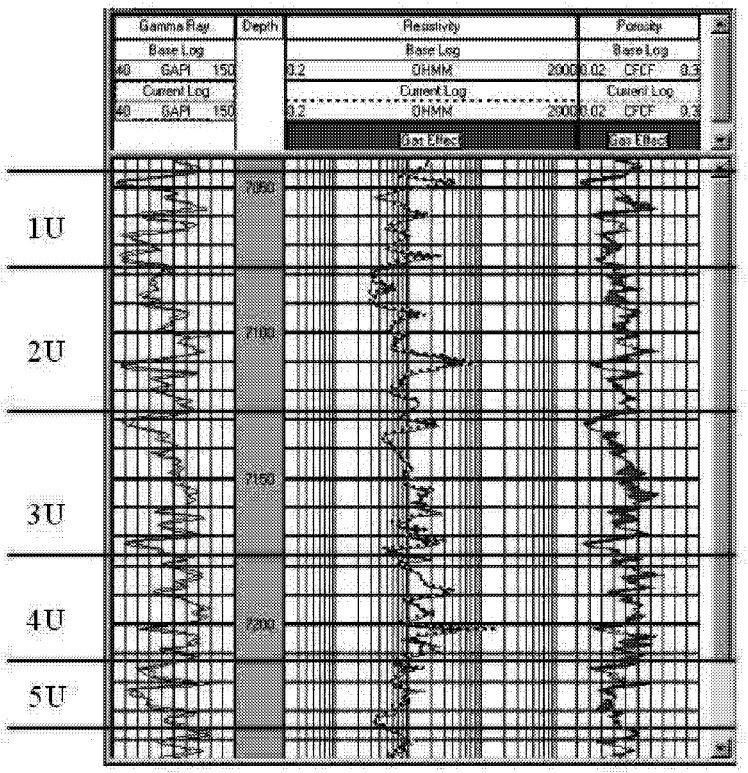

Fig. 3.16-2 —Neutron Porosity and Resistivity Profile of Well 49 (Jan-Aug)

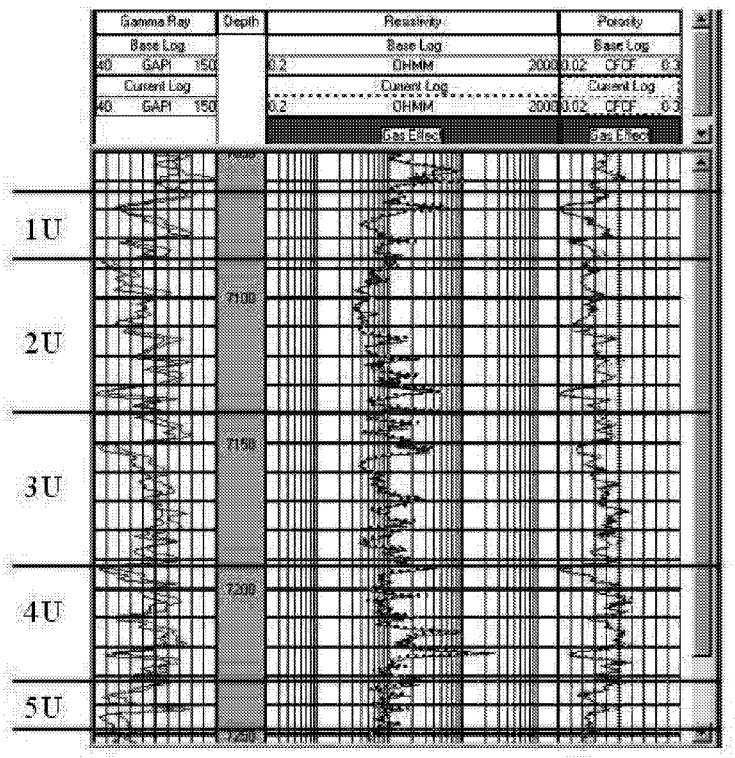

Fig. 3.16-3 —Neutron Porosity and Resistivity Profile of Well 50 (Mar-Jun)

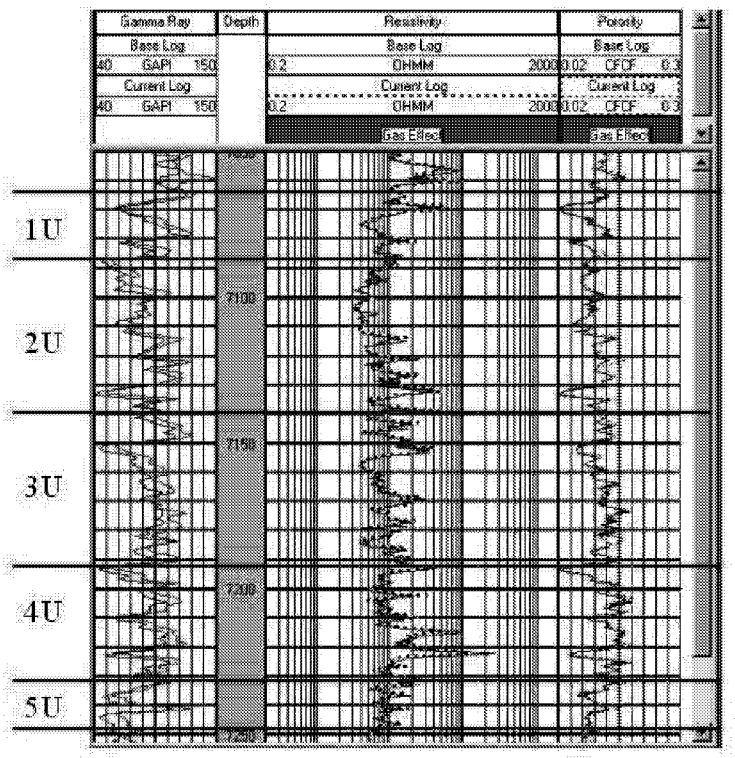

Fig. 3.16-4 —Neutron Porosity and Resistivity Profile of Well 50 (Mar-Aug)

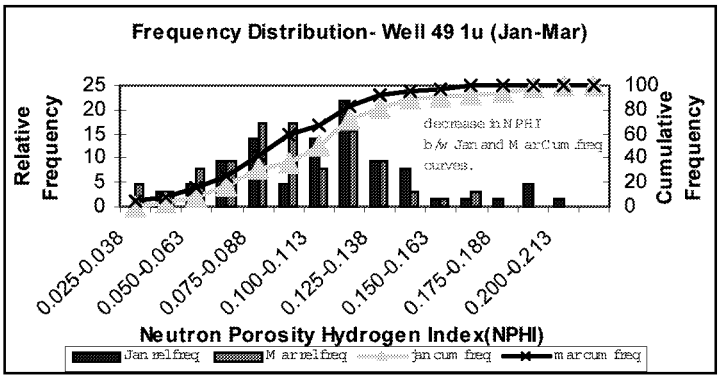

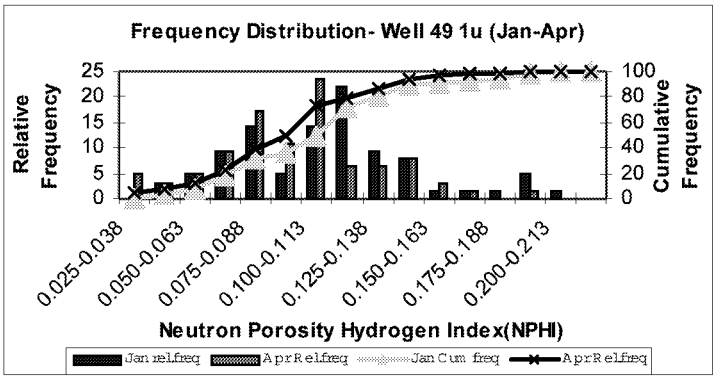

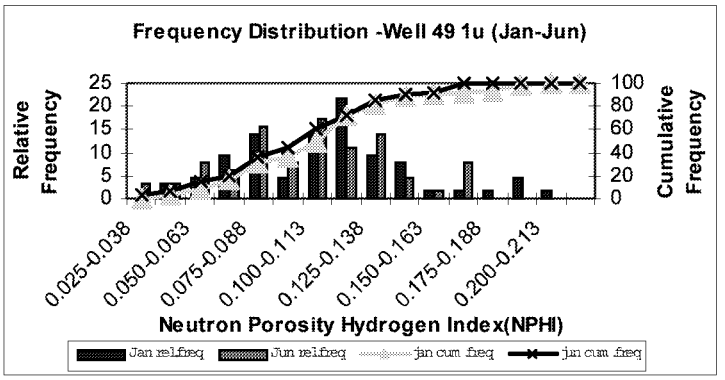

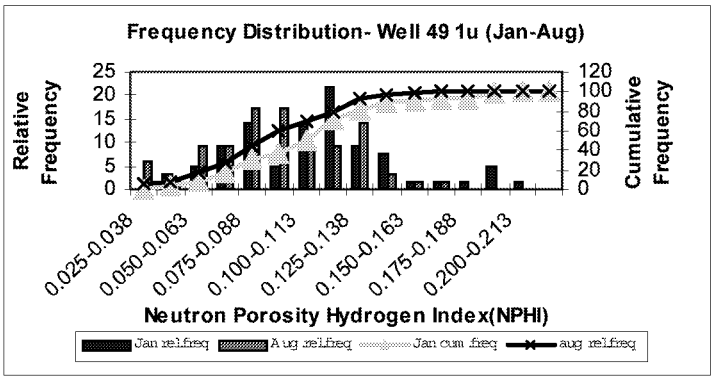

Fig 3.16-5— Relative and cumulative frequency of well 49 in 1U layer

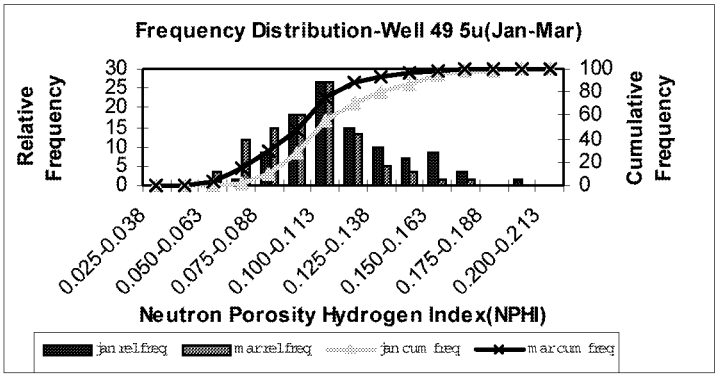

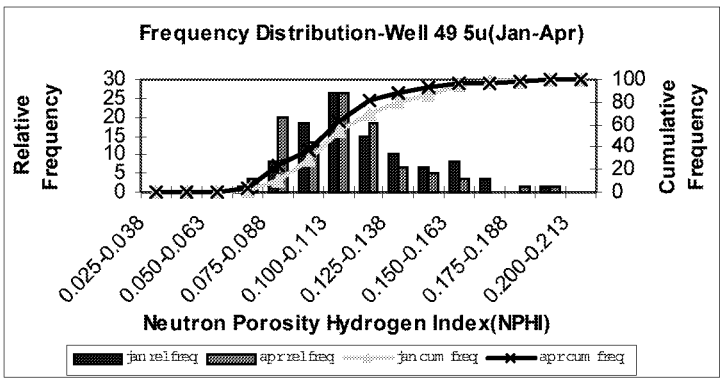

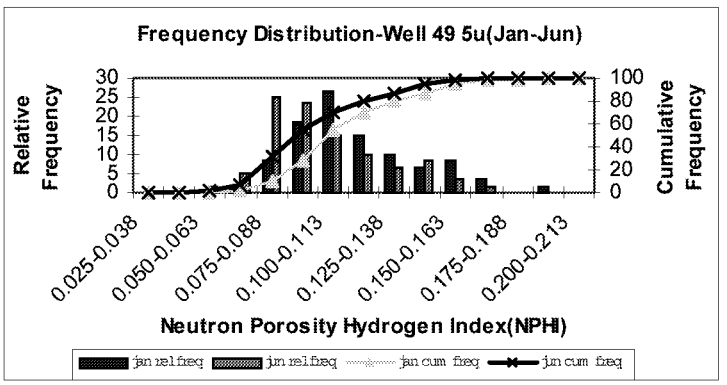

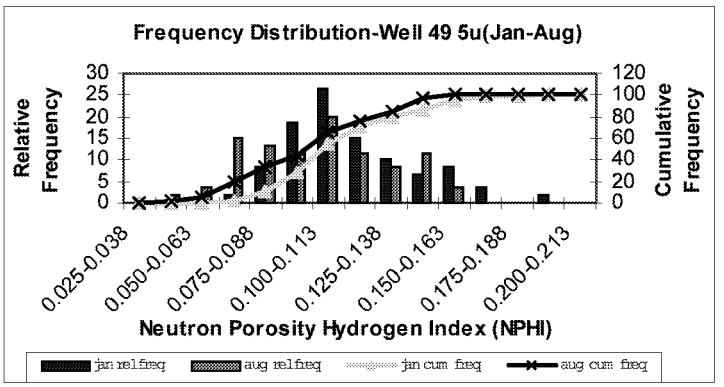

Fig 3.16-6— Relative and cumulative frequency of well 49 in 5U layer

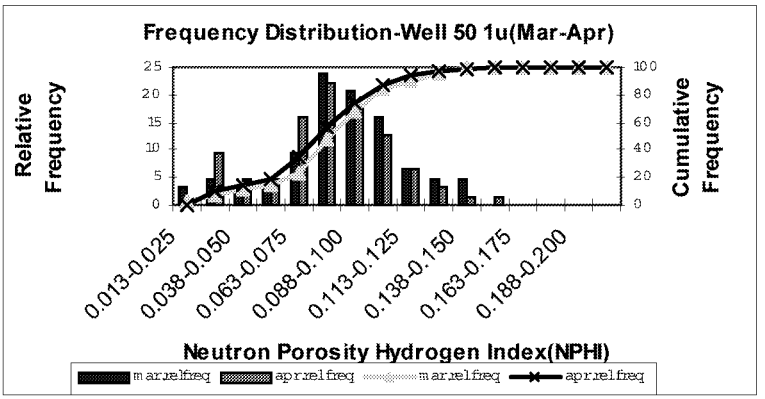

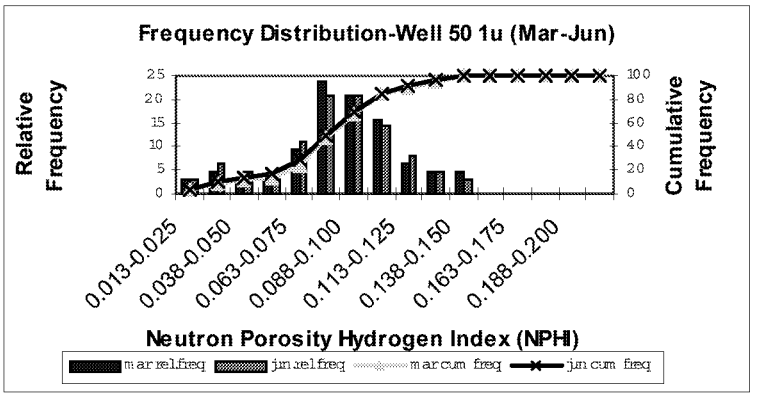

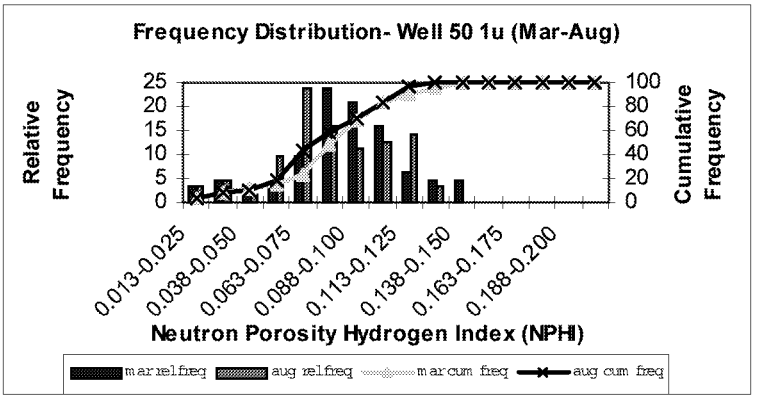

Fig 3.16-7—— Relative and cumulative frequency of well 50 in 1U layer

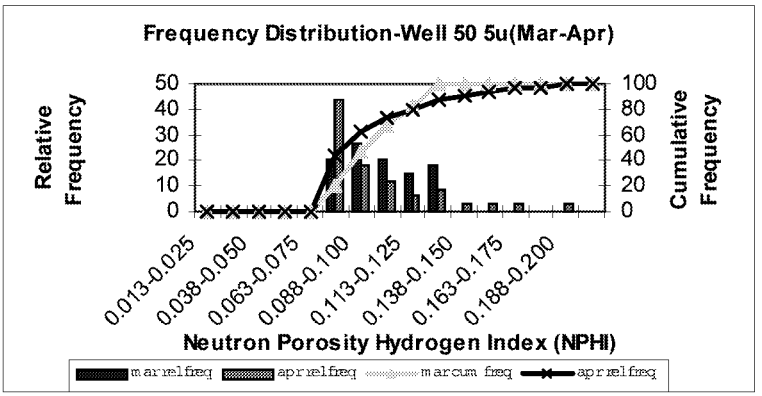

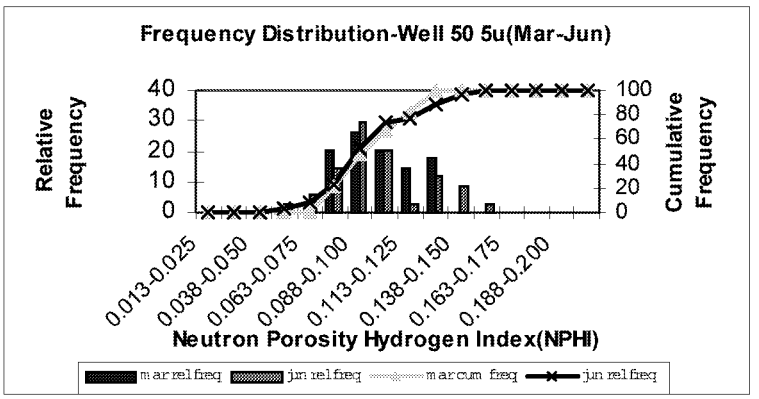

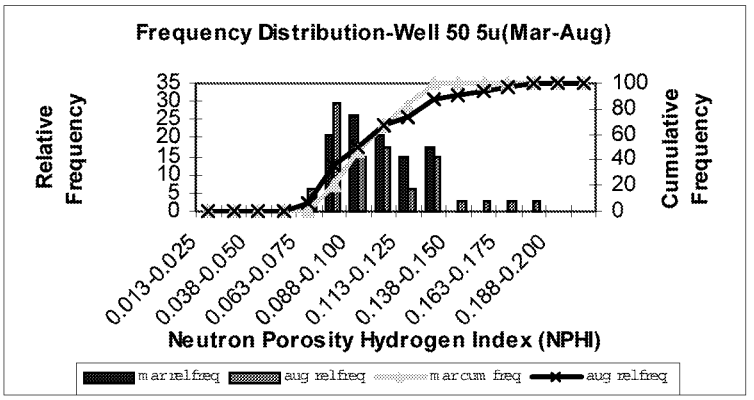

Fig 3.16-8—Relative and cumulative frequency of well 50 in 5U layer

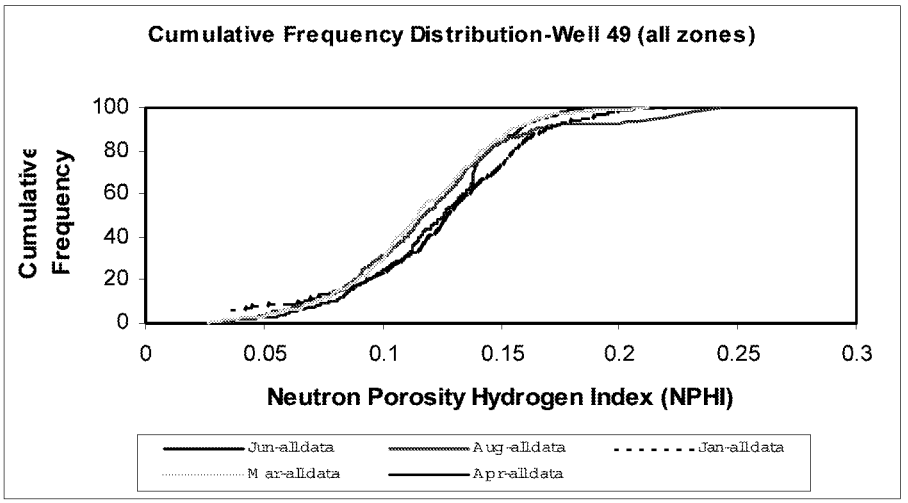

Fig. 3.16-9—Cumulative frequency distribution of NPHI from well 49 in all zones

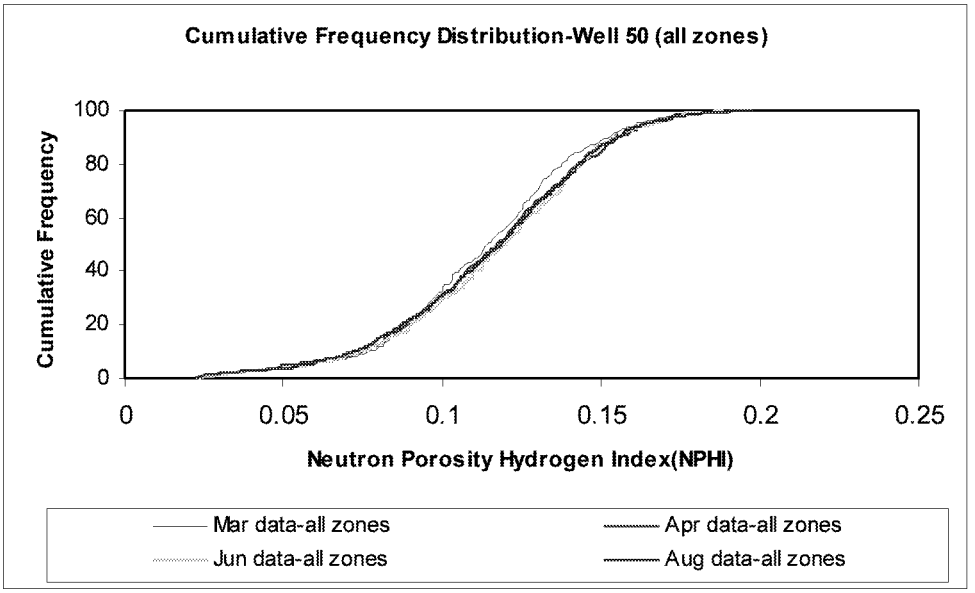

Fig. 3.16-10—Cumulative frequency distribution of NPHI from well 50 in all zones

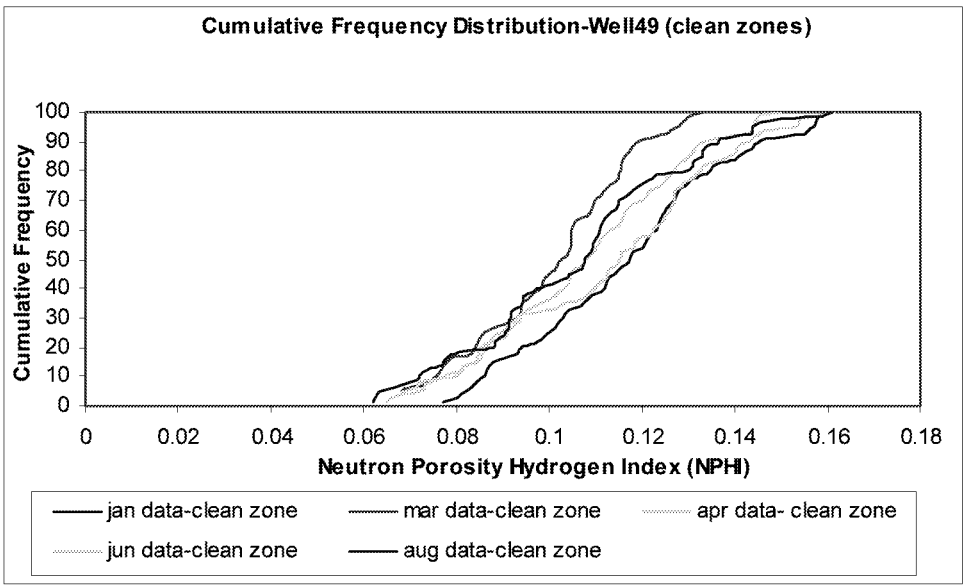

Fig. 3.16-11—Cumulative frequency distribution of NPHI from well 49 in clean zones only

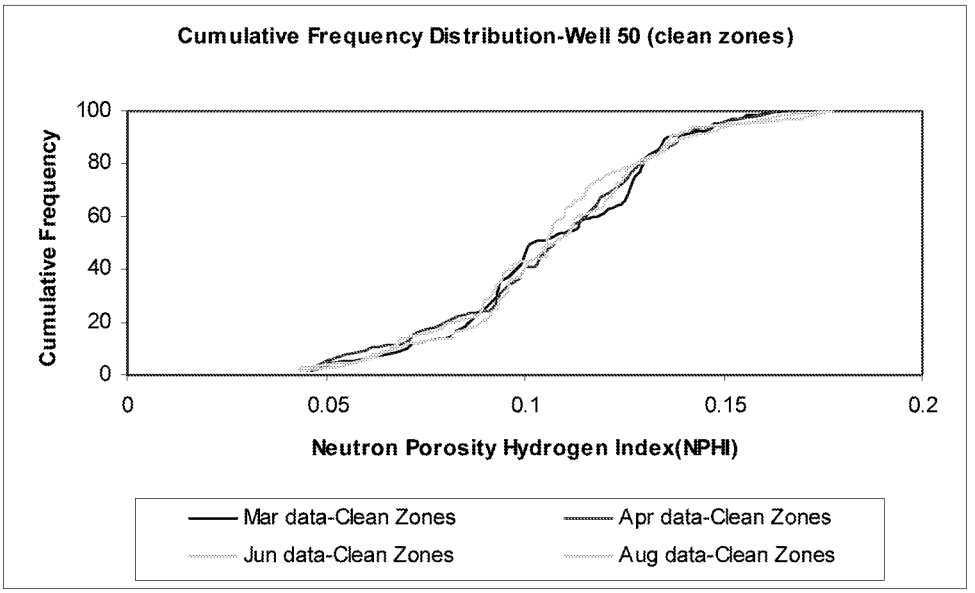

Fig. 3.16-12— Cumulative frequency distribution of NPHI from well 50 in clean zones only

3.17 A 10-ACRE FIELD DEMONSTRATION PILOT PROJECT

Introduction

The E.T. O'Daniel Pilot is located in Section 4 T2S Block 37 of the E.T. O'Daniel lease in Midland County, Texas (Fig. 3.17-1). This site was selected due to the high oil recovery that occurred from primary and secondary operations in this particular area, as well as the regional structure height, which should assist during CO_2 injection (i.e. via gravity drainage).

The pilot configuration is hexagonal pattern shown in gray color (Fig. 3.17-1). A total of 15 wells have been completed with six water injection, four CO_2 injection wells, three central production wells and two logging observation wells. The well pattern is oriented along the major fracture trend with the three producers forming a line parallel to the primary fracture trend. The producers are flanked on either side by four CO_2 injectors and surrounded by six water injectors in an approximate regular hexagonal pattern. The overall area confined by six water injectors is sixty-seven acres while the area enclosed by the four CO_2 injectors is twenty acres. Such a configuration is believed to provide an adequate confinement in most directions although some on trend CO_2 losses in a NE-SW direction could occur.

The water injection wells in hexagonal pattern are aligned approximately to N43°E fracture trend as determined by the horizontal cores. Water injection was initiated after completion of a multi-well interference test. Stable water injection was initiated in October of 1999 in order to increase the reservoir pressure above the minimum miscible pressure for Spraberry crude and CO_2. Also, establishment of a waterflood baseline decline so that all produced oil resulting from CO_2 injection can be quantified.

The step-rate, buildup and pulse tests have been performed prior to commencing water injection. The analysis of these tests to further characterize the reservoir and the proper reservoir management strategy has been completed.[1-3] The step-rate injection test indicates the fractures are stress- and pressure sensitive. The parting pressure occurred at 3017 psia and the fracture propagated as higher injection rates. [3,4] The pulse tests consisted of four sequential injection with total water injection rate of 2000 bwpd in wells #47, #45, #25 and #48. The result indicates the orientation of maximum permeability from reference points of well #47 and #45 is 10 °EN and 38 °EN.[2]

The main purpose of this chapter is to describe the field activity and pilot performance during waterflooding and CO_2 flooding periods.

Waterflood Performance

The three central production wells, the O'Daniel #38, #39, and #40 have shown little or no response to water injection as anticipated earlier since this is a 40-year-old waterflood area. It was assumed there would be minimal response from water injection and the area was at residual oil saturation. However, a rapid increase in oil production was noted in

several wells directly along an N32°E orientation. Some of wells located over one mile from the injection wells responded within days of initiation of water injection whereas wells oriented perpendicular to injection wells at fraction of the distance from injection wells have shown little or no response. The counter-current and co-current imbibition mechanisms along with high permeability anisotropy facilitated the oil production rate to increase on the on-trend wells during high water injection. Due to low matrix permeability, the off-trend wells continued to produce at low rate similar to pre-injection rates. It might be possible that the off-trend wells will respond in the future.

We have divided the overall oil production as that being produced from twenty-three off-trend and seven on-trend wells. The composite performance of the pilot is shown in Fig. 3.17-2. After initiation of water injection, rapid increase in oil production was noted in the seven on-trend wells whereas the twenty-three off-trend wells continued to produce at rates almost similar to pre-injection values. Oil production has steadily increased in the on-trend wells from 50-75 bopd prior water injection to a level of nearly 200 bopd. Thus, the seven on-trend wells are responsible for 100-150 barrels of incremental oil per day (Fig. 3.17-3). These results clearly show that the on-trend wells outside the Pilot Area are mainly responding to water injection as compared to the off-trend wells closer to the Pilot Area.

Rapid increase in oil production rate at Brunson F and water-out at Brunson A located about 500 ft away from the pilot area clearly indicates the presence of un-swept oil. This shows that the injected water can spread towards the Brunson field in the matter of few days indicating that the permeability ratio is highly anisotropic. It also indicates that the fractures are continuous and might have multiple orientations. The response from chemical tracers injection also indicates that the fracture system has very high permeability. Of the 29 wells sampled, 15 wells showed tracer breakthrough within the first two days after tracer injection started. The fracture system facilitates transport of fluids through long distances in short times (more than 3,000 ft in two days), reaching from Floyd "B1" to Brunson "D1".

The result also reveals that placement of the production wells along the fracture orientation could significantly increase oil production if water injection could be optimized. The results oppose the previous belief that on-trend injection wells will channel via fractures and rapidly water-out production wells. The water injection rate can be optimized by applying the Fracture Capillary Number (FCN) that we derived based on dynamic imbibition experiments for on-trend production wells.[5] By optimizing the water injection rate, the balance of viscous and capillary forces can be achieved, thus avoiding early water breakthrough at the on-trend wells and resulting higher oil recovery.

CO_2 Flooding Performance

CO_2 injection into the Spraberry formation was officially commenced on Monday, February 26th 2001 after remedial action was taken on cement problems at one of the logging observation wells.

In order to maintain a target of 200 RVB/D of CO_2 injection, the water injection rate was revised from 280 to 245 BWPD. A few minor glitches such as the CO_2 turbine meters getting clogged with debris were encountered.

Each CO_2 injector has experienced some unique problem during start-up but there have been no problem, which has warranted serious remedial action. The battery monitoring the four wells closest to the pilot shows that the interior producers (wells #38, #39 and #40) have experienced increased percentage of CO_2 in about 3 weeks of CO_2 injection. Surprisingly, at well "A" #1 (Fig. 3.17-4), which lies directly along the NE-SW fracture orientation, has observed a moderate CO_2 break-through. This might be due to high pressure around the six-ring fence that restricts the movement of CO_2 outside the pilot area. The line of production wells experiencing high CO_2 fraction are along the natural fracture trend and perpendicular to the CO_2 injection wells. This clearly indicates that there a direct communication exists between injection wells and production wells due to induced fractures that may have been created during step rate or pulse testing periods.

Due to high rate of gas production at the interior wells, a cyclic injection scheme of water alternating gas (WAG) was initiated in order to retain the injected CO_2 inside the reservoir for a longer period of time and thereby facilitate extraction of oil. The CO_2 injectors were converted to water injectors periodically while keeping up the total injection volume intact to keep up the reservoir pressure in-between that of MMP and minimum parting pressure (Fig. 3.17-5). A closer look at the rate of gas production at the interior wells reveal that at the end of every CO_2 injection cycle the gas production rate at the producers decreased but the next CO_2 cycle produced CO_2 at a higher rate than the previous one and the cyclic progression of CO_2 injection reveals that O'Daniel A-1 also started producing the gas from a later period (Fig. 3.17-6). In spite of CO_2 breakthrough, no immediate oil response was observed in the interior production wells as shown in Fig. 3.17-7.This could be due to the movement of CO_2 in the shale layers or movement of CO_2 above 1U or 5U as concluded from the logging observation wells and temperature log analyses.

Till date there has been no indication of CO_2 being produced at wells farther away from the pilot area. Even though the rate of gas production has been high at the interior wells the total volume of CO_2 produced is still less compared to the amount of CO_2 remaining in the reservoir. Number 1 in Fig. 3.17-8 indicates the amount of CO_2 (41000MSCF) that has been produced, while number 2 indicates the amount of CO_2 (87000MSCF) that has been injected. This indicates that a considerable amount of CO_2 (about 52 %) still remains in the reservoir and we could expect mobilization of extracted oil to the production wells at a later period. In addition, Fig. 3.17-9 shows that only 19% of the total water that has been injected through the confined six injection wells has been produced which further strengthens our premise that more oil could be produced at a later date.

In order to get a good response from a multiple contact CO_2 miscible displacement, a good proportion of CO_2 has to be injected. As of 2/10/02, the volume of CO_2 injected is still very small (about 47,000 bbls) when compared to the volume of water injected.

Wells such as Brunson F-1, Brunson C-2 and Brunson G-1 located at distances more than 5,000 feet away from the pilot area along naturally fractured trend started responding only after a water volume at least equivalent to about three times that of CO_2 volume was injected (Fig. 3.17-10). This shows that more CO_2 has to be injected in order to produce oil at far off wells. Most of the oil (other than the interior wells) that has been produced is mostly from O'Daniel A-1 (Fig. 3.17-11).

Figure 3.17-12 shows the comparison between the oil rate and gas rate observed at O'DANIEL A-1. Each time there has been an increase in gas production rate, the oil production rate has simultaneously increased. But an increase in water rate at O'DANIEL A-1 (Fig. 3.17-13) has produced less oil in O'DANIEL A-1 if both Figs. 3.17-12 and 3.17-13 are compared at the same time periods.

In order to confirm the production of oil due to CO_2 at O'Daniel A-1 and Brunson F1 and distinguish the oil response due to CO_2 injection instead of water injection a change in the injection pattern was initiated on 03/16/2002. In the new scheme the two interior producer wells (ET O'Daniel #38 and #39), one water injector (ET O'Daniel #48) and two CO_2 injectors (ET O'Daniel #42 and 44) were shut in. This was done to facilitate the movement of CO_2 without any restrictions through main fracture trend. The oil response was only observed in the well #40 and O'Daniel A-1.The results (Fig. 3.17-11) show that oil production rate O'DANIEL A-1 has drastically increased and the CO_2 % at O'DANIEL A-1 has increased (from Fig 3.17-4) when compared to well#40.

In order to closely monitor the change in composition at the interior wells and O'DANIEL A-1, Figs. 3.17-14 through 3.17-17 depict the different hydrocarbon mole fractions (C1 to C6+) being sampled at different dates. On breakup of the gas sampling study, it is observed that all the battery wells produce a high fraction of light components with a accompanying high fraction of CO_2. On comparison of all the on-trend wells outside the pilot area only O'DANIEL A-1 produces the greatest change in composition over the time of CO_2 injection.

The favorable response at O'DANIEL A-1 can be gauged by the extent of C1 enrichment by the CO_2 gas as evident from Fig. 3.17-18. This figure shows that CO_2 is extracting a higher fraction of C1 at O'DANIEL A-1 than at the interior wells. This shows that all the light fractions from the pilot area are being driven outside towards O'DANIEL A-1 by the larger pressure differential occurring across the periphery of the pilot area. Figure 3.17-19 shows no major change in the relative enrichments of C2, C3, N-C4 at any of the wells but a higher fraction of C6+ is observed at the interior producers compared to O'daniel O'DANIEL A-1.

The extent of the spread of CO_2 in the off-trend wells can be seen in Fig. 3.17-20. A pathetically low fraction (<1 mol fraction) of CO_2 fraction is observed at all off trend wells where gas samples have been taken. This again could be due to high retention of CO_2 in the pilot area. Also the WAG does not seem to improve the sweep efficiency or improve oil recovery.

On the other hand, a glance at the amount of CO_2 fraction observed at on-trend wells reveal that only two wells OD O'DANIEL A-1 and Brunson F1 are 'seeing' CO_2 when compared to the other on-trend wells. To make this more clear, the plot (Fig. 3.17-22) of C1 relative enrichment by CO_2 in the on-trend wells confirm that the produced samples at O'DANIEL A-1 and Brunson F1 contains a high fraction of CO_2 gas along with corresponding high fraction of C1.All other on-trend wells produce very less of C1 and this can be seen by the amount of CO_2 actually reaching them. But on the contrary O'DANIEL A-1 which is directly oriented along the known natural fracture trend from the CO_2 injection wells has produced a very low total volume of CO_2.

A scrutiny (Fig. 3.17-23) of the relative enrichments of C2, C3 and n-C4 by CO_2 show a familiar pattern. The flat profile with the exception of O'DANIEL A-1 of each of the above fractions tells us that a very low fraction of lights and intermediates are being produced at any of the wells. Even though a high CO_2 fraction is obtained at the interior wells, O'DANIEL A-1 and Brunson F1, there is very little change in mole fractions with increasing CO_2 mol %. Only the relative enrichment of C6+ due to CO_2 shows a linear increase in the interior producers, depicting that heavier fractions are being extracted inside the pilot area.

In order to obtain a sound basis for determining the production of oil due to CO_2 alone a decline curve analysis was carried out. The best indicator of CO_2 flood response until now at Spraberry reservoir has been at O'DANIEL A-1. Figure 3.17-24 shows an increase in oil recovery after the CO_2 injection was started as compared to the earlier years of waterflood. Figure 3.17-25 shows the depletion of Spraberry reservoir before the waterflooding was started. The decline of oil production was assumed to have started from the date of highest oil production (which falls just before the waterflooding started). Various decline scenarios (50%, 20%, 150%, 200%) have been attempted and this has been depicted in Fig. 3.17-26. Here, the cumulative oil production from the different decline scenarios reveals that a combined recovery in the range of 700-2500 bbls was projected with CO_2 flooding conducted in the time period between Feb 2001 and Feb 2002.

Continuing on the decline curve analysis, the depletion of the reservoir due to waterflooding of the pilot area alone is depicted in Fig. 3.17-27. Again a similar set of decline rates have been used to project the performance of CO_2 flood in the pilot area. The range of recovery estimated is around 2100 to 2800 bbls in the stipulated period between Feb 2001 and Feb 2002.

Further, LOW response and temperature logs (Figs. 3.17-28 and 3.17-29) indicate CO_2 injection occurs throught the Upper Spraberry interval, consistent with the notion that hydraulic fractures dominate CO_2 movement in the interior pilot. Also most of the CO_2 being produced at the interior wells are probably breaking through from the non-pay shaly zones. The fact that large volumes of CO_2 are being retained in the reservoir, as observed during water injection and a relatively small total volume of CO_2 has been injected on a HCPV basis warrants continuation of CO_2 injection. The two watered-out wells (Brunson D-1 and O'Daniel A-1) and one on-trend well (Brunson F-1) are observed

as potential key wells. Future reports will transfer the results of this ongoing Field Demonstration.

Conclusions

1. Placing the production wells at on-trend direction could significantly increase the oil production if the water injection can be optimized.
2. The on-trend production wells at Brunson and Flyod Fields that response to water injection indicates that the permeability ratio is highly anisotropy and the fracture is continuous and there is a presence of un-swept oil.
3. LOW response and temperature logs indicate CO_2 injection occurs through the Upper Spraberry interval, consistent with the notion that hydraulic fractures dominate CO_2 movement in the interior of the pilot.
4. Most of the produced CO_2 is from the interior pilot wells, the 38, 39 and 40, probably through the non-pay shaly zones.
5. To the contrary, the O'Daniel A-1 which is oriented directly along the known naturally fracture trend from the CO_2 injection wells has produced a very low total volume of CO_2.
6. Oil has been mobilized to ET O'Daniel A-1 as indicated by C1 enrichment and incremental oil response.
7. The total volume of CO_2 injected to date compared to the volume of water required for incremental waterflood recovery is still considerably low
8. WAG does not improve sweep efficiency or improve oil recovery

Reference

1. Schechter, D.S.: "Advanced Reservoir Characterization and Evaluation of CO_2 Gravity Drainage in the Naturally Fractured Spraberry Trend Area," Quarterly Technical Progress Report, PRRC Report No. 99-09 (DOE Contract No.: DE-FC22-95BC14942).
2. Schechter, D.S.: "Advanced Reservoir Characterization and Evaluation of CO_2 Gravity Drainage in the Naturally Fractured Spraberry Trend Area," Quarterly Technical Progress Report, PRRC Report No. 00-5 (DOE Contract No.: DE-FC22-95BC14942).
3. Schechter, D.S.: "Advanced Reservoir Characterization and Evaluation of CO_2 Gravity Drainage in the Naturally Fractured Spraberry Trend Area," Quarterly Technical Progress Report, PRRC Report No. 00-7 (DOE Contract No.: DE-FC22-95BC14942).
4. Baker, R., Contreras, R.A., and Sztukowski, D.: "Characterization of the Dynamic Fracture Transport in a Naturally Fractured Reservoir," paper SPE 59690 presented at the 2000 SPE Permian Basin and Gas Recovery Conference, Midland, Texas, 21-23 March.
5. Putra, E., Fidra, Y., and Schechter, D.S.: "Use of Experimental and Simulation Results for Estimating Critical and Optimum Water Injection Rates in Naturally Fractured Reservoirs," paper SPE 54336 presented at the 1999 Annual Technical Conference and Exhibition, Houston, TX, Oct. 3-6.

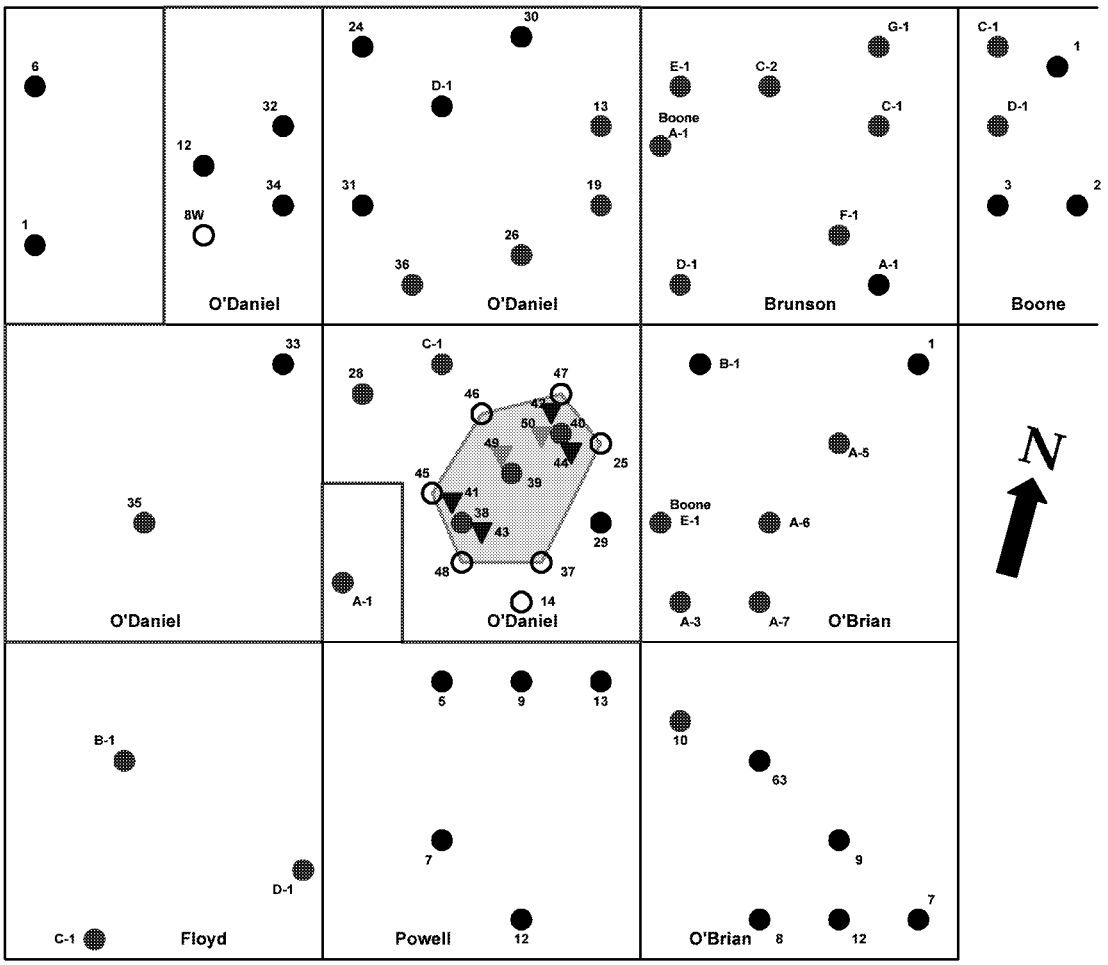

Fig. 3.17-1— E.T O'Daniel Pilot Map Area (The gray color shows location of the CO_2 pilot)

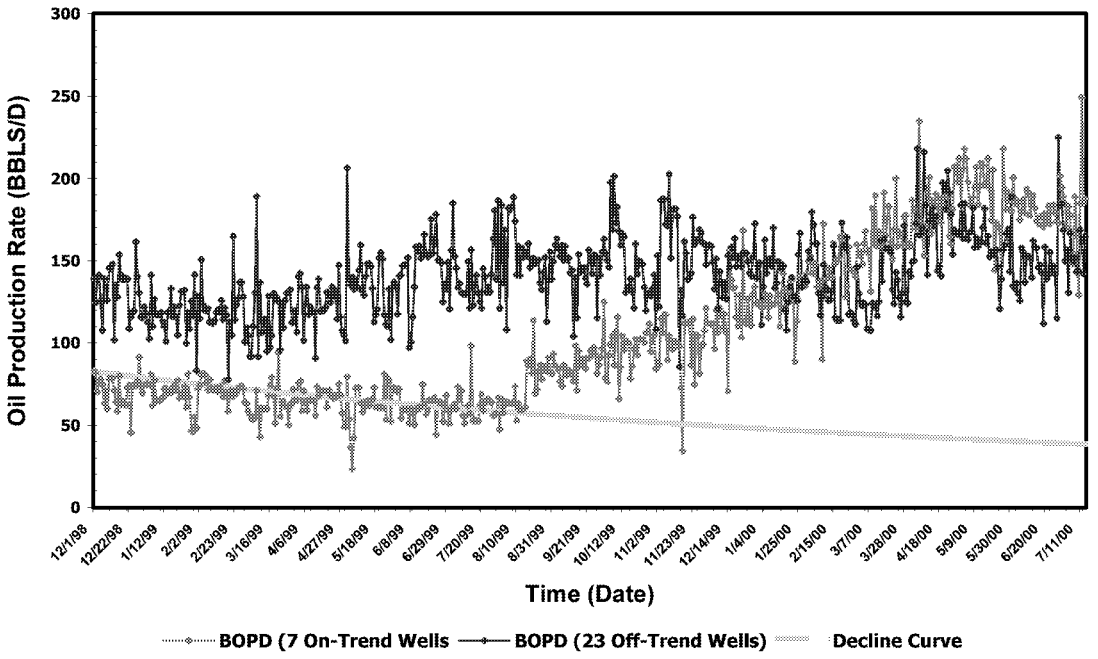

Fig. 3.17-2 —Comparison between on-trend and off-trend production rate of Upper Spraberry in the ET O'Daniel Pilot

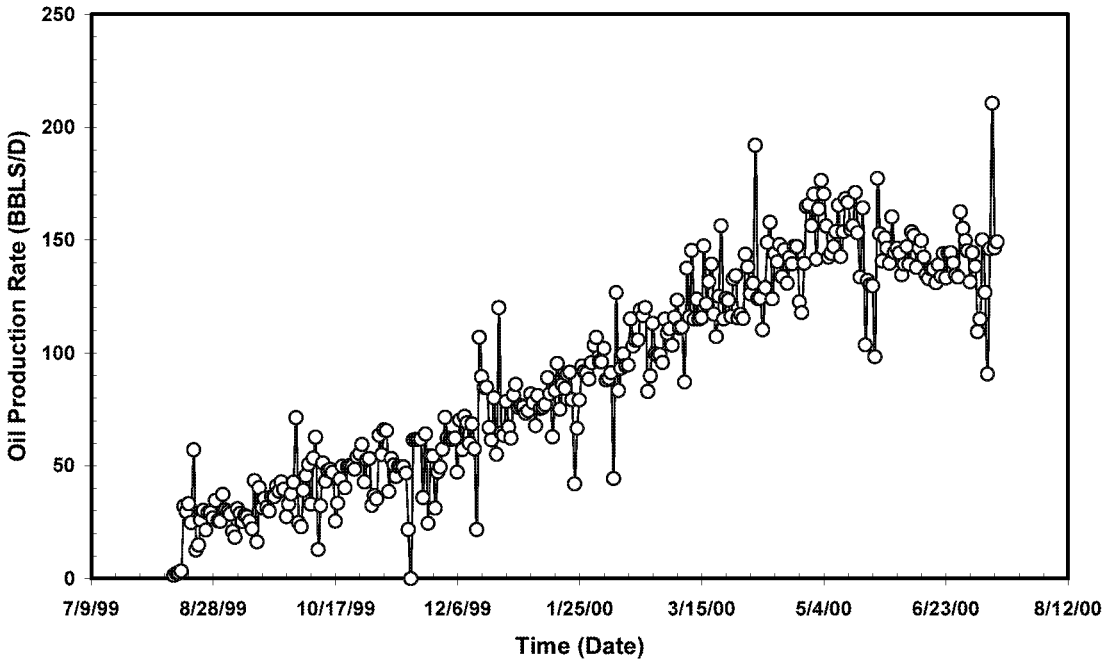

Fig. 3.17-3 — On-trend incremental oil recovery of Upper Spraberry in the ET O'Daniel Pilot

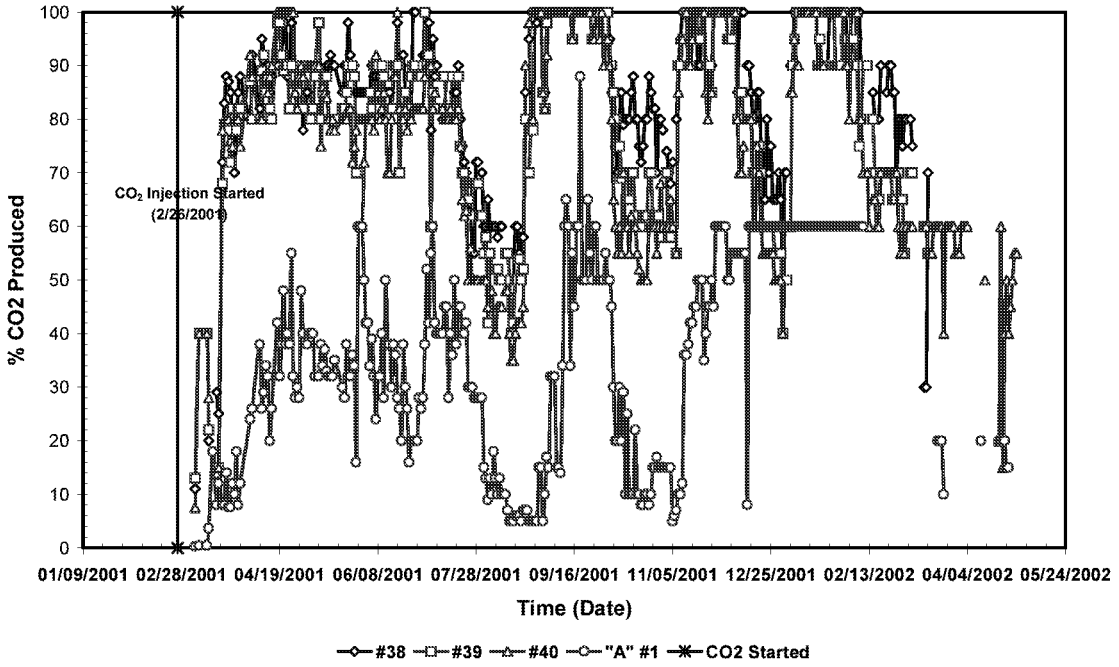

Fig. 3.17-4 —The percentage of CO_2 produced in the interior wells and ET O'Daniel A-1

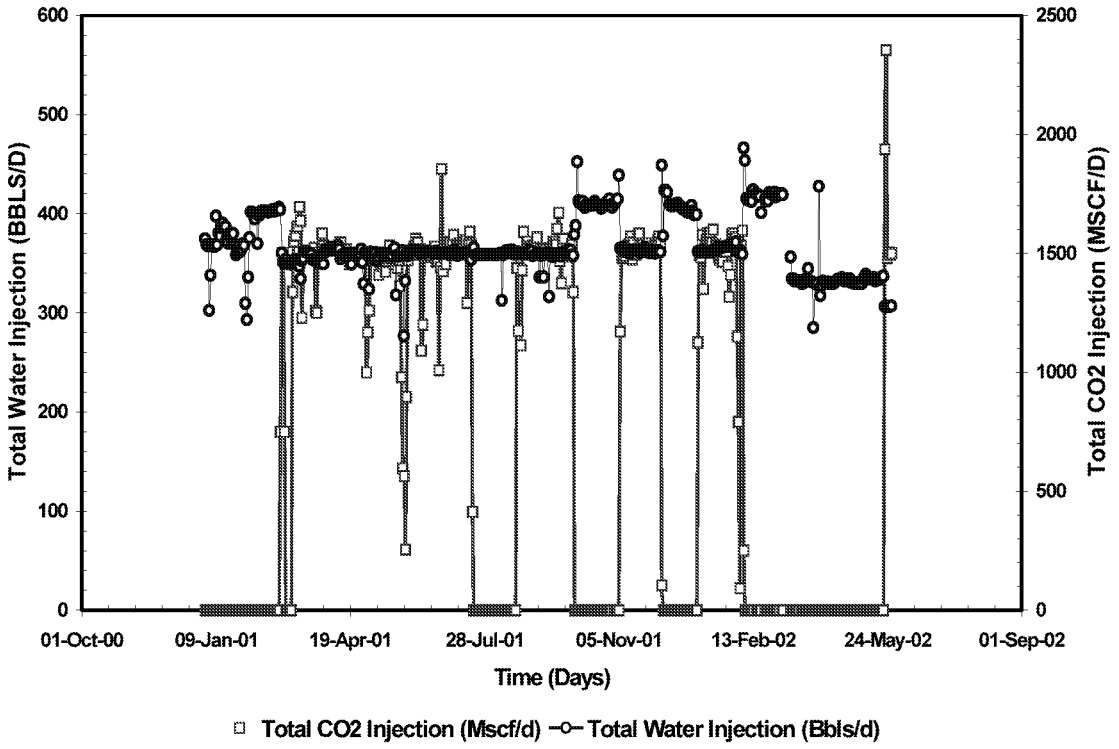

Fig. 3.17-5—The total water injection is maintained during water and CO_2 injection

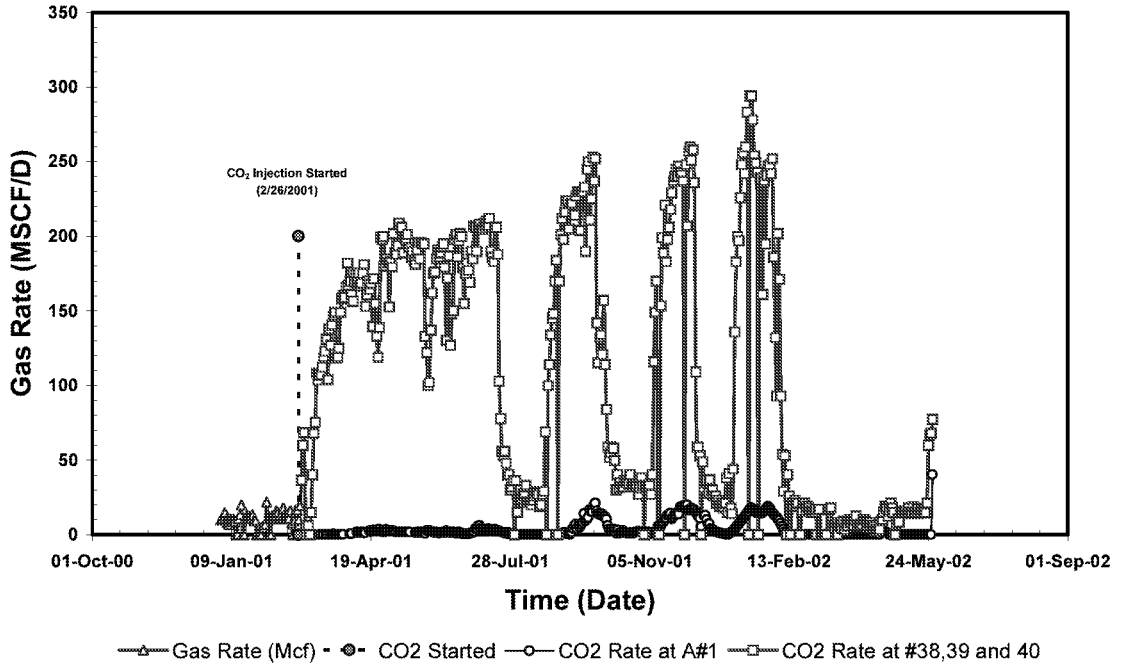

Fig. 3.17-6—The gas production rate in the interior wells and ET O'Daniel A-1

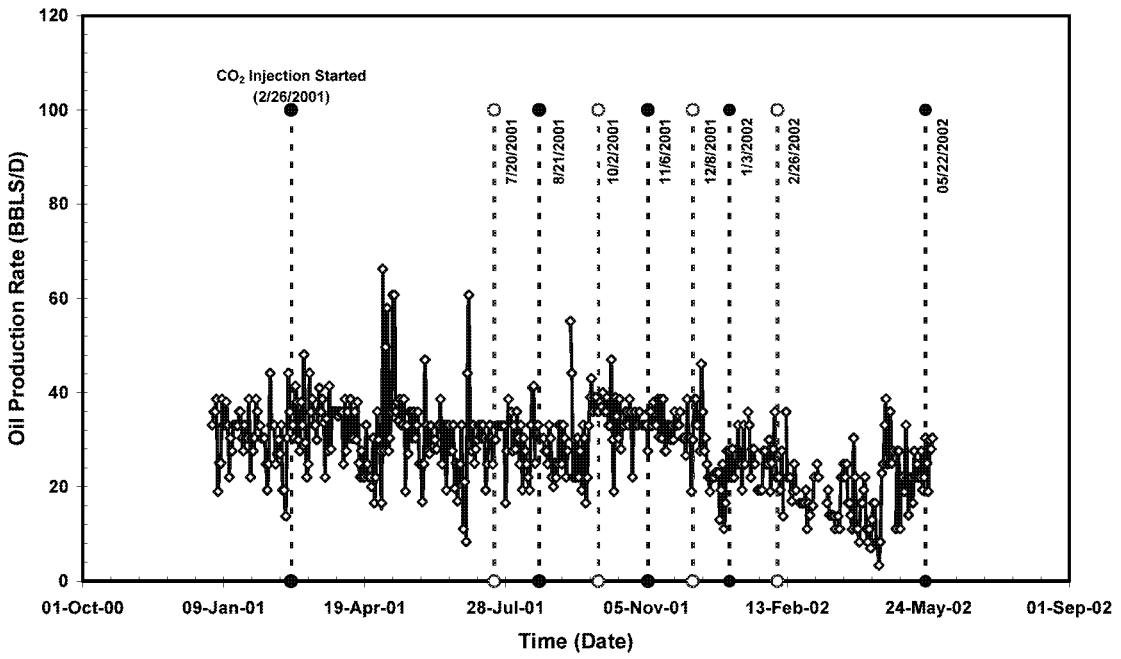

Fig. 3.17-7 —Total production rate from the interior wells and ET O'Daniel A-1

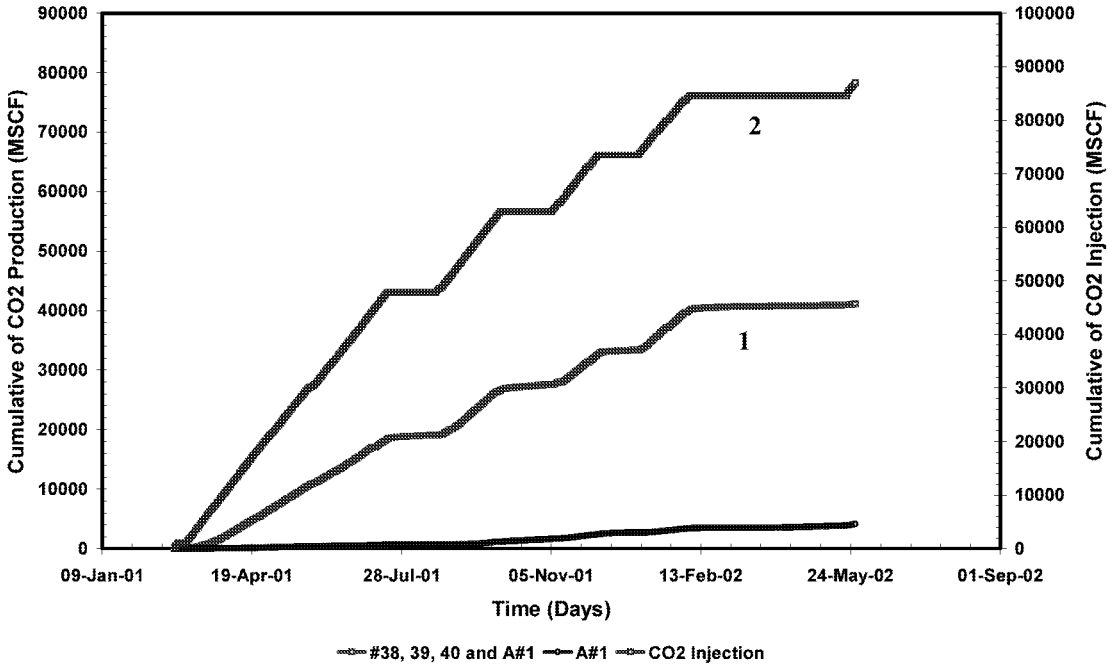

Fig. 3.17-8—The comparison between the amount of CO_2 injection and CO_2 production from the interior wells and ET O'Daniel A-1

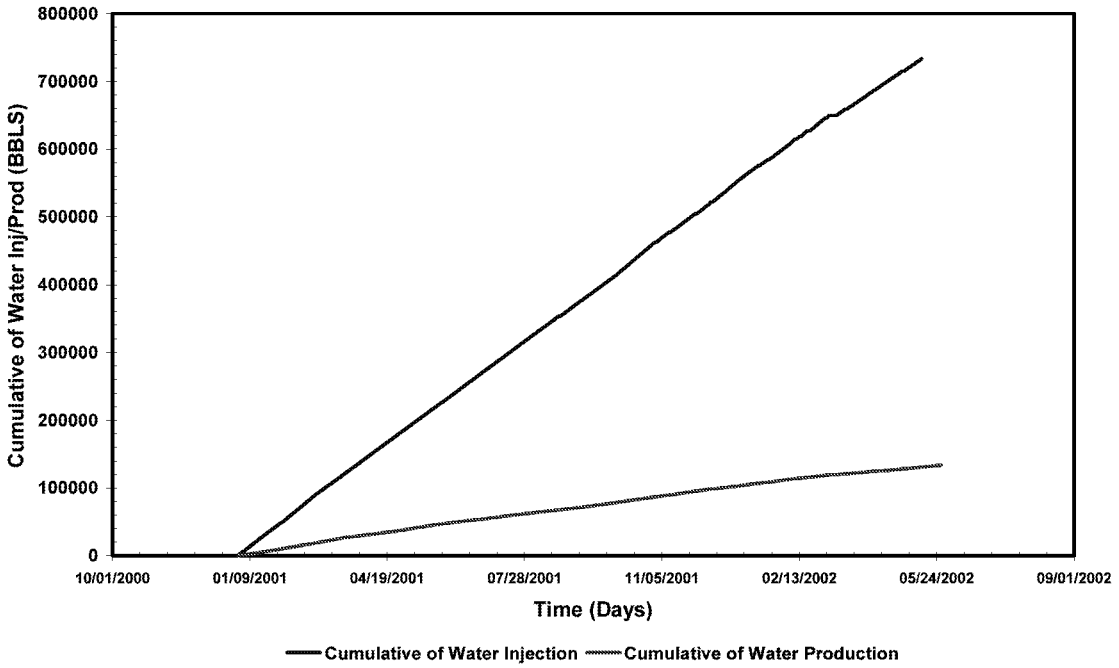

Fig. 3.17-9—The comparison between the amount of water injection and water production from the interior wells and ET O'Daniel A-1

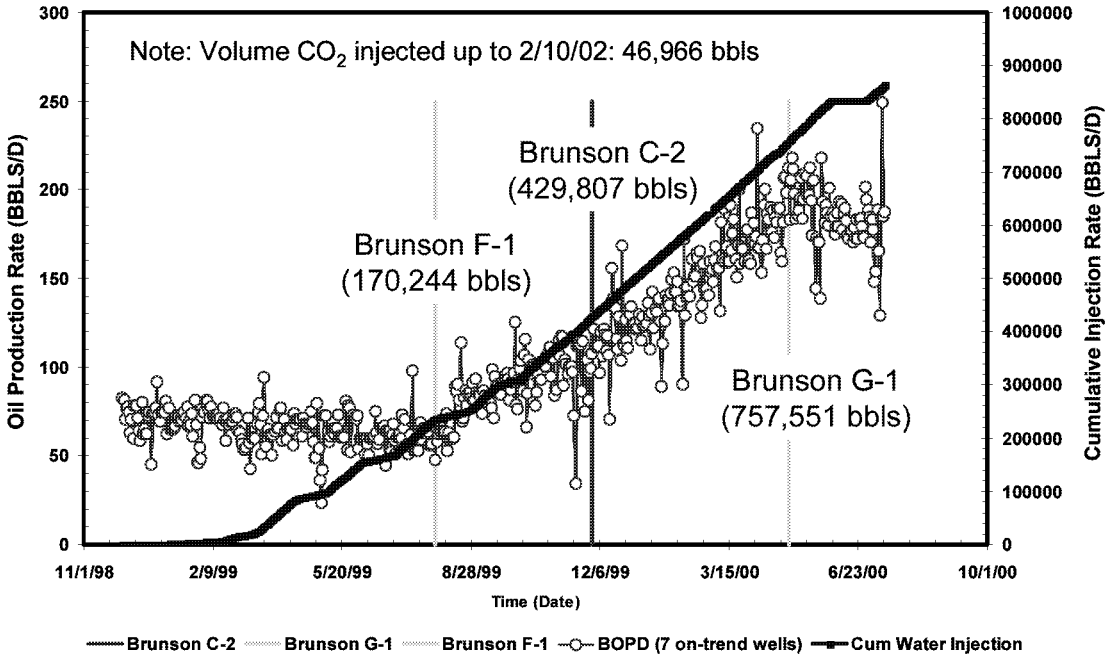

Fig. 3.17-10—Volume of water injection until on-trend production wells start responding

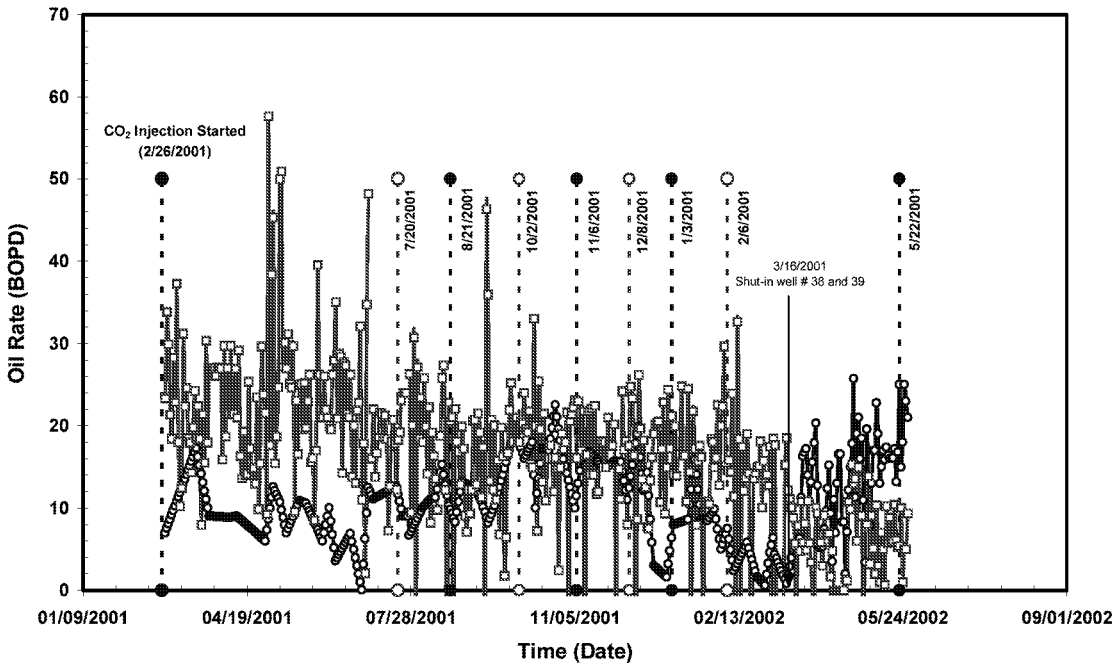

Fig. 3.17-11—Comparison between the oil produced from interior wells and ET O'Daniel Well

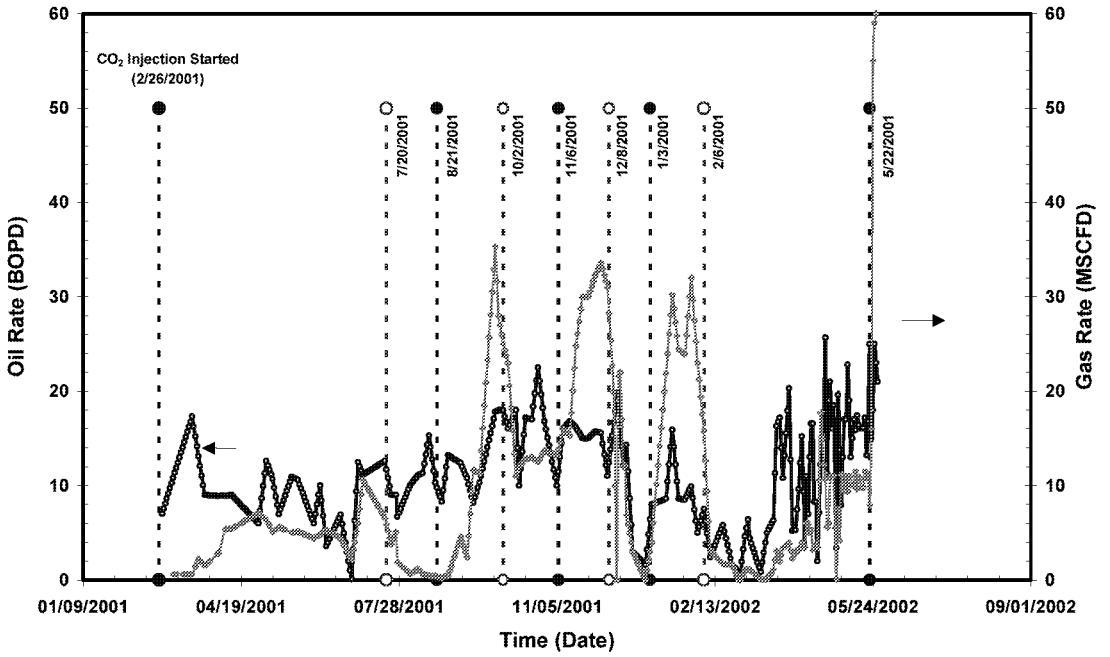

Fig. 3.17-12— Oil rate and gas rate performances of ET O'Daniel A-1

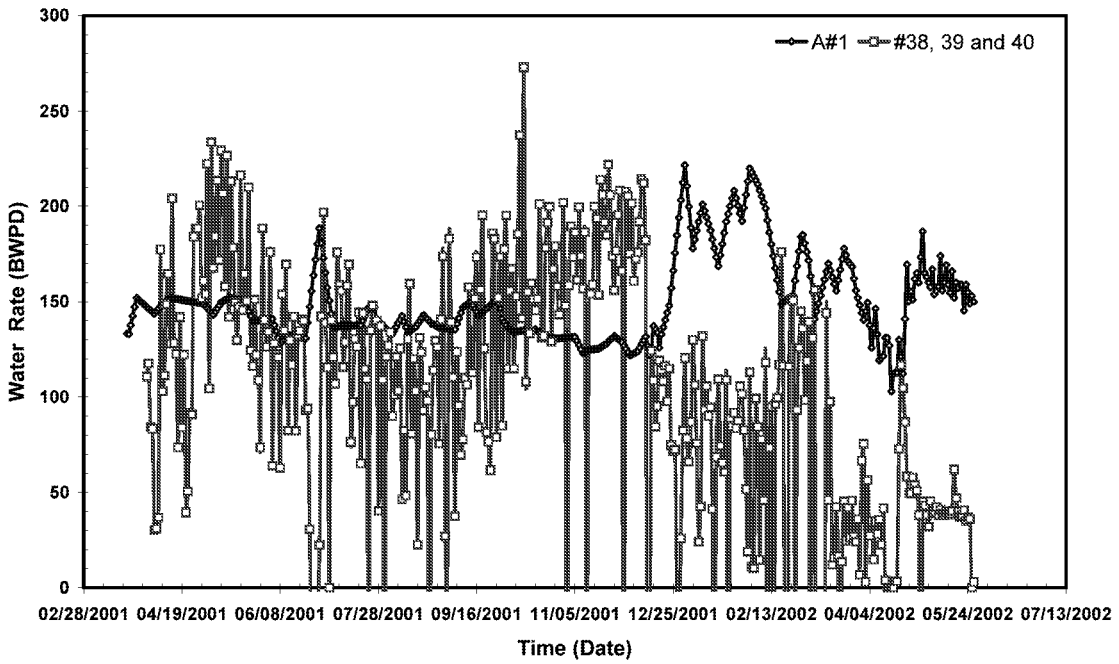

Fig. 3.17-13—Water rate performances produced from interior wells and ET O'Daniel A-1

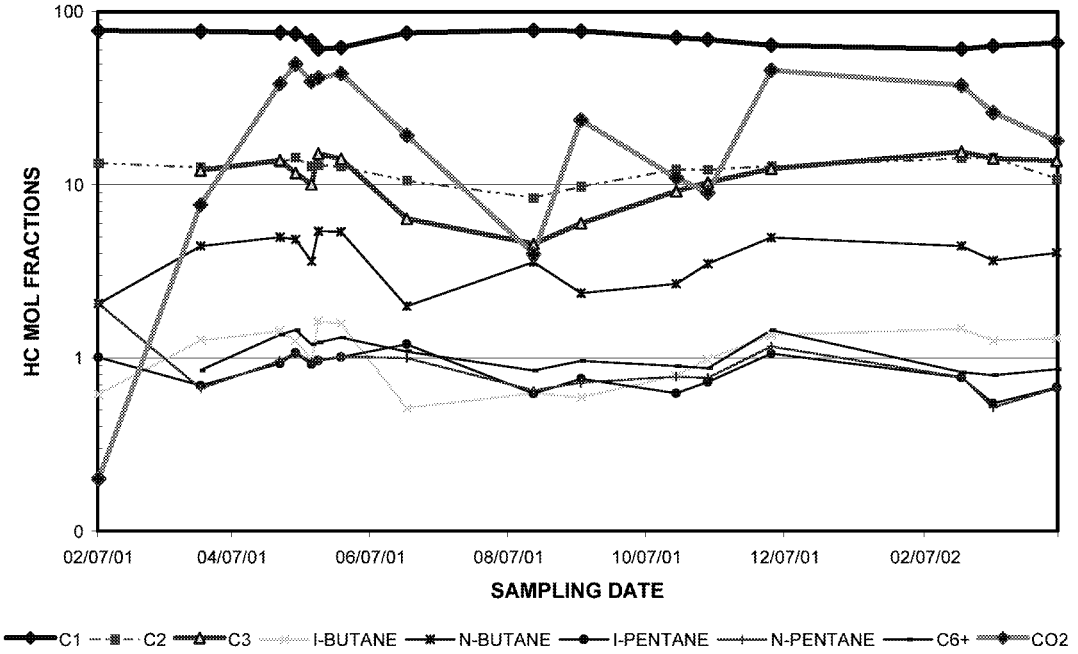

Fig. 3.17-14— Hydrocarbon mol fractions of the OD A-1 at different sampling date

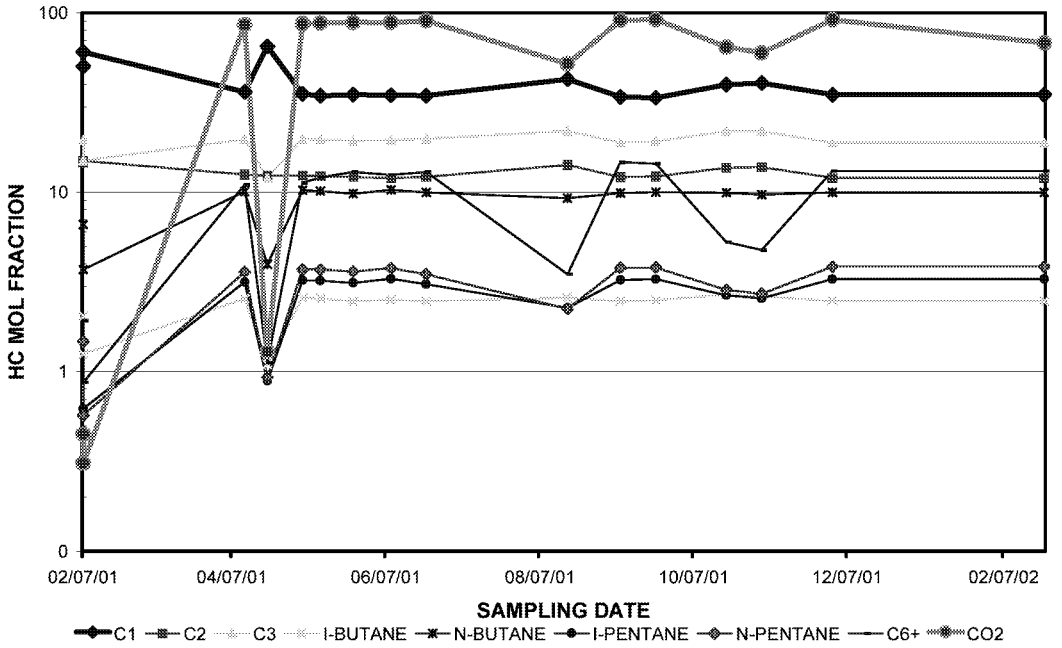

Fig. 3.17-15— Hydrocarbon mol fractions of the ET O'Daniel #38 at different sampling date

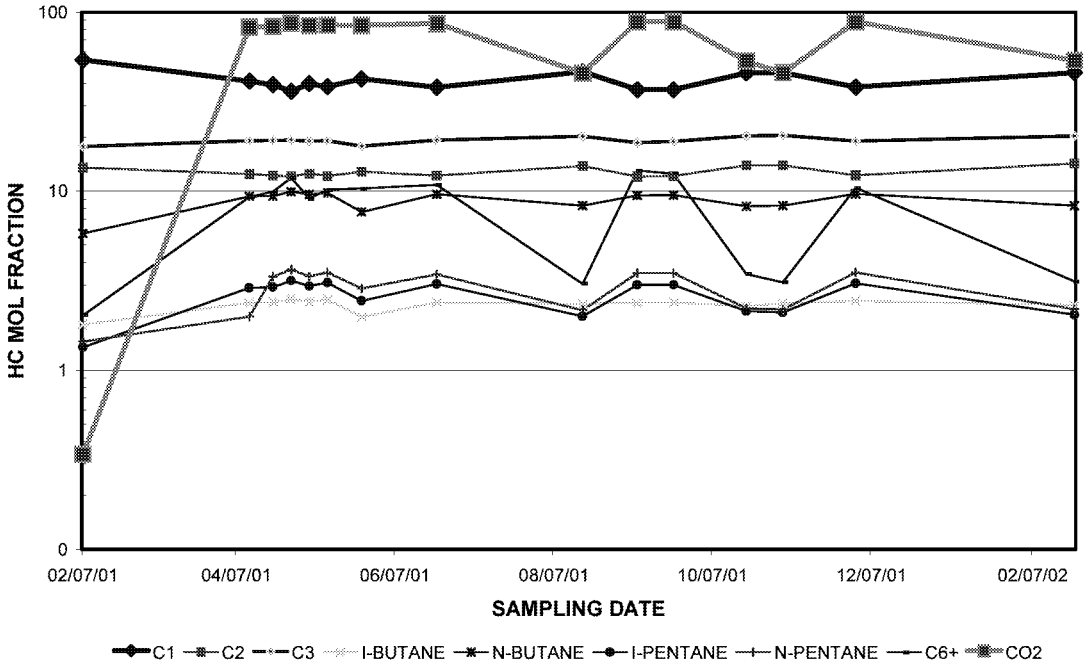

Fig. 3.17-16—Hydrocarbon mol fractions of the ET O'Daniel #39 at different sampling date

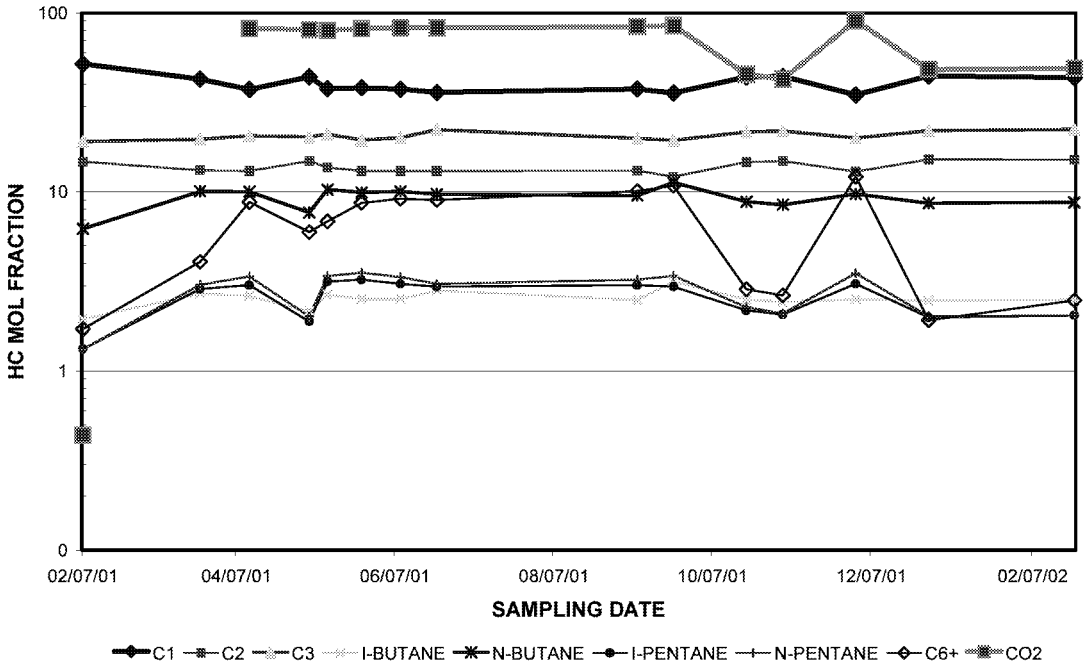

Fig. 3.17-17 —Hydrocarbon mol fractions of the ET O'Daniel #40 at different sampling date

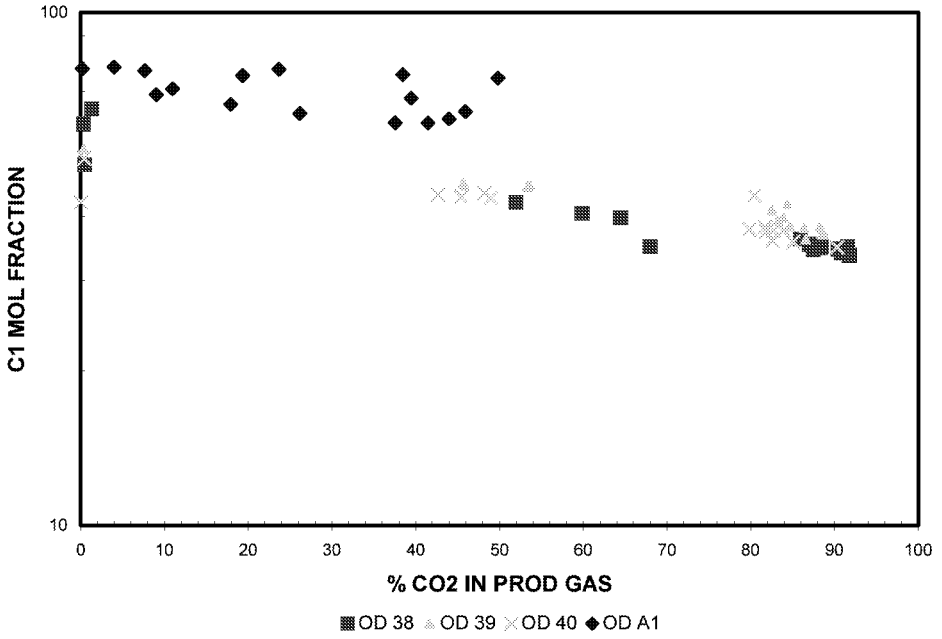

Fig. 3.17-18 —Relative enrichment of the C-1 component in interior wells and O'Daniel A-1

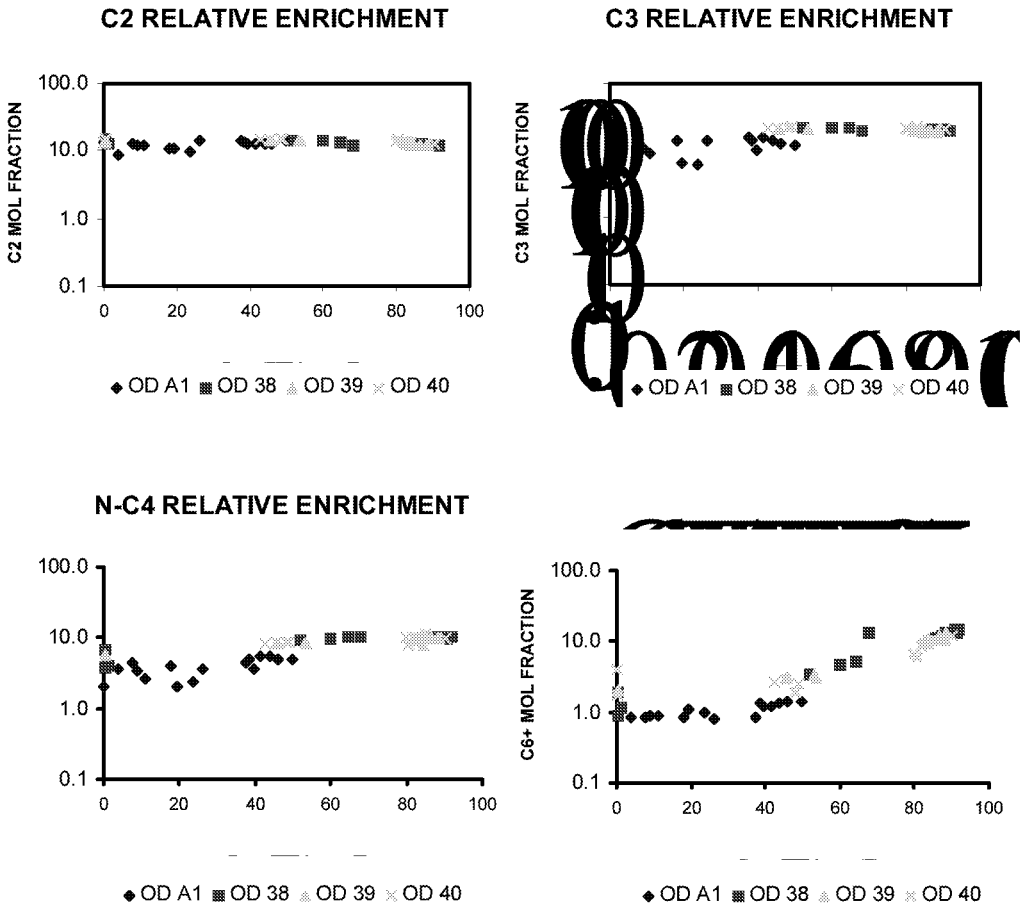

Fig. 3.17-19 —Relative enrichment of the gas component in interior wells and O'Daniel A-1

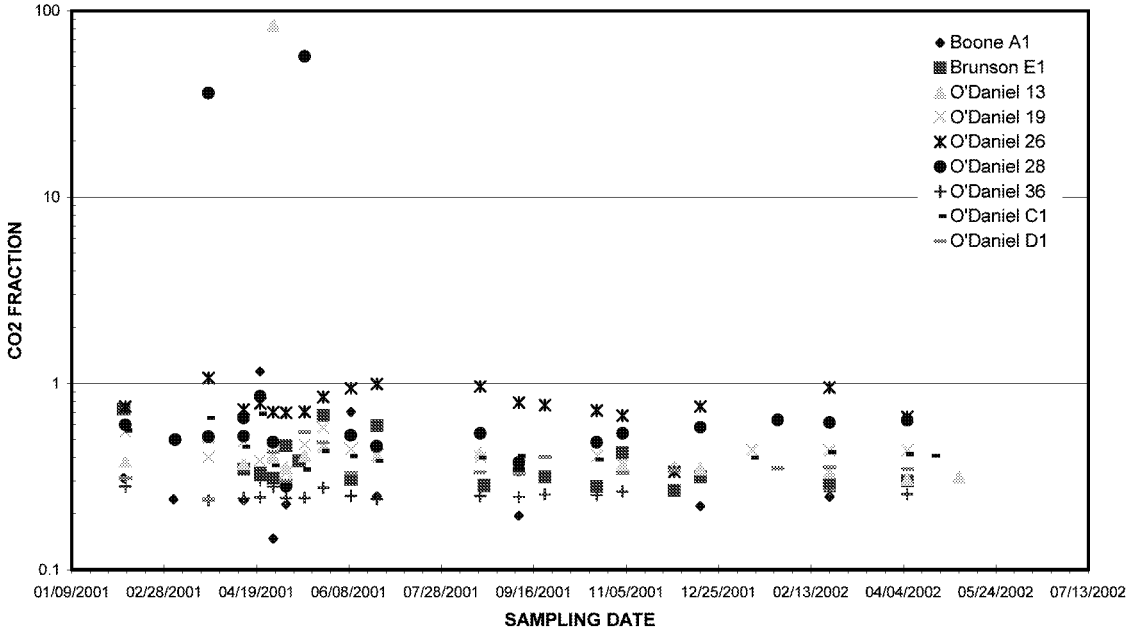

Fig. 3.17-20 —Amount of CO_2 fraction in off-trend wells during CO_2 injection

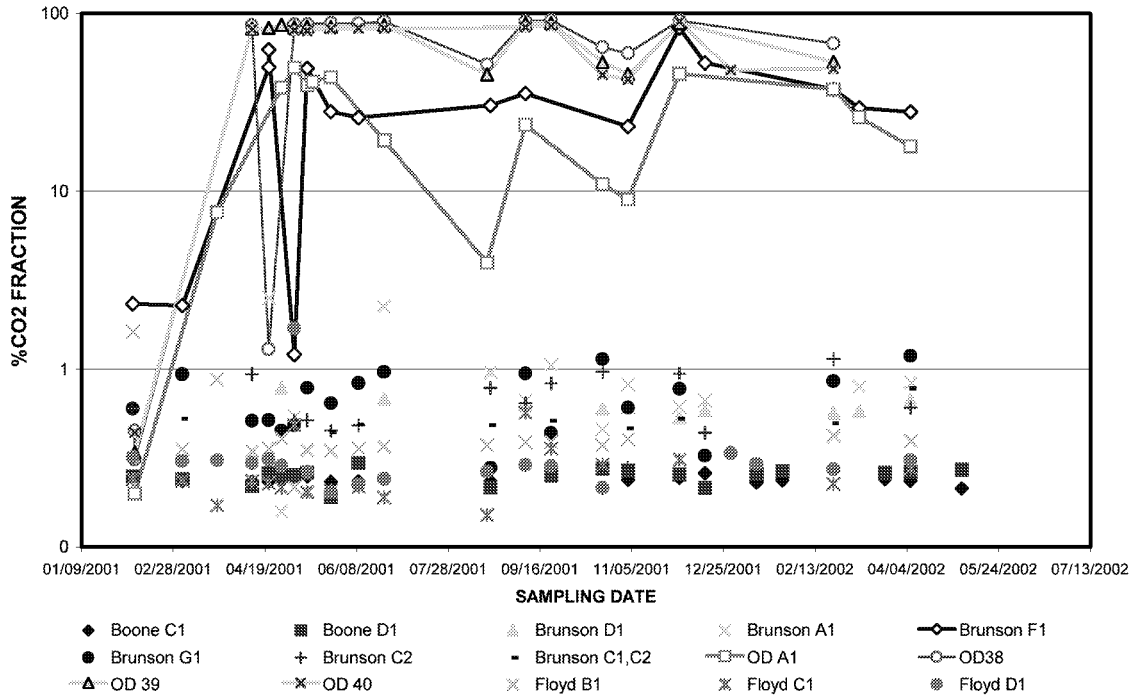

Fig. 3.17-21— Amount of CO_2 fraction in on-trend wells during CO_2 injection

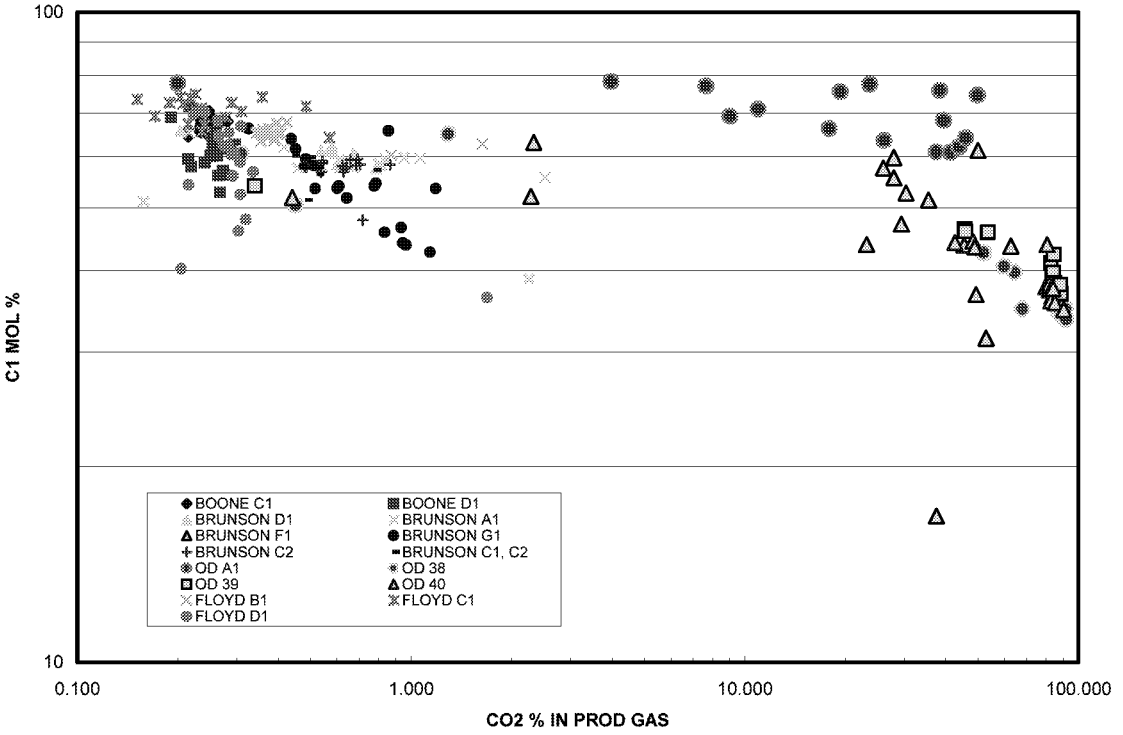

Fig. 3.17-22—Relative enrichment of the C-1 component in on-trend wells

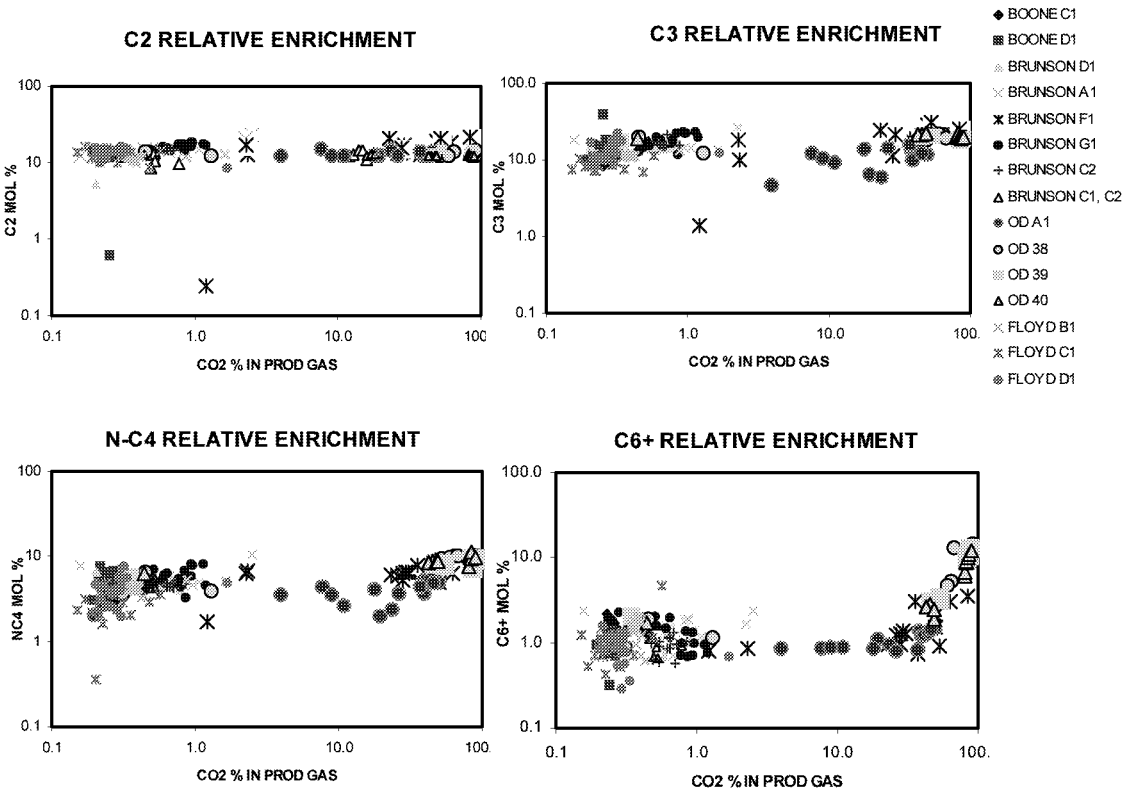

Fig. 3.17-23— Relative enrichment of the gas component in on-trend wells

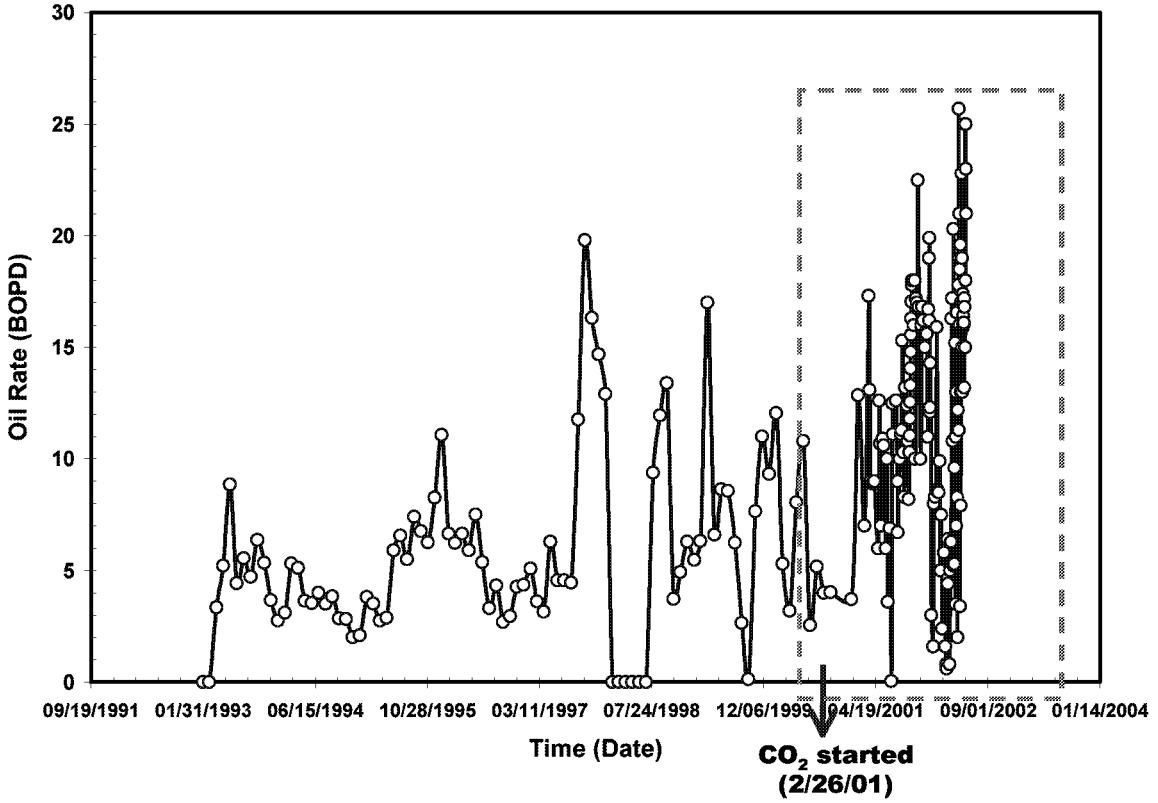

Fig. 3.17-24— The oil rate history in ET O'Daniel A-1 before and after CO_2 injection

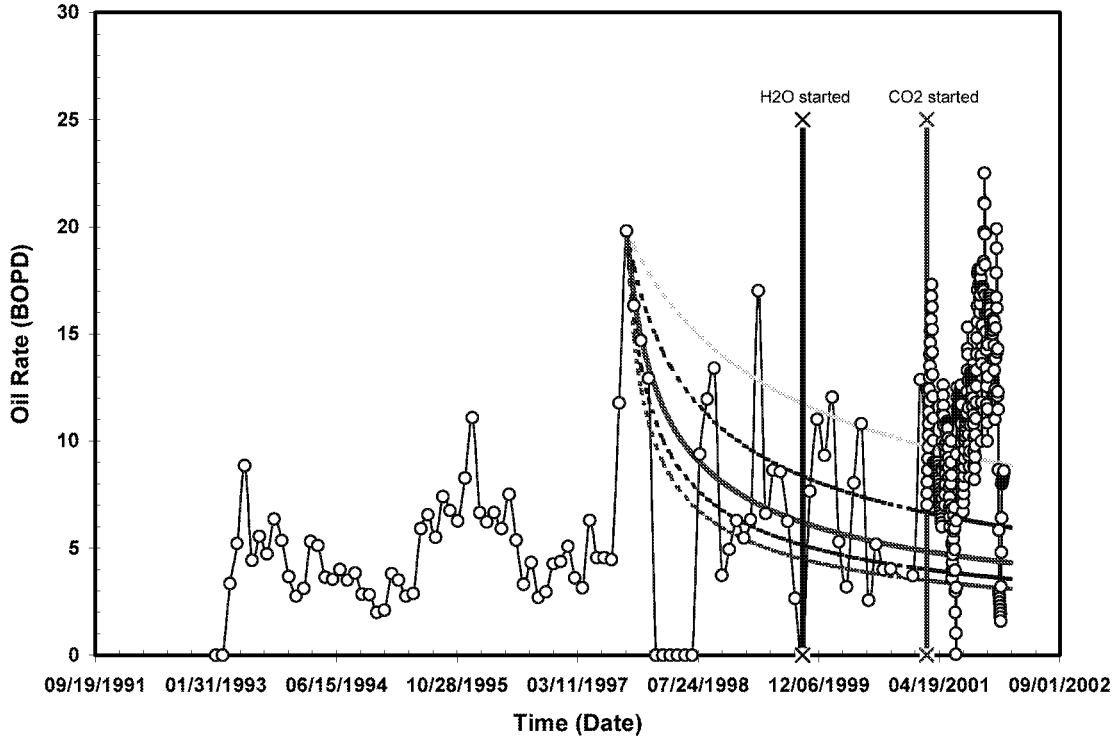

Fig. 3.17-25—Decline curve analysis is taken from the highest oil rate before waterflood started in the pilot area

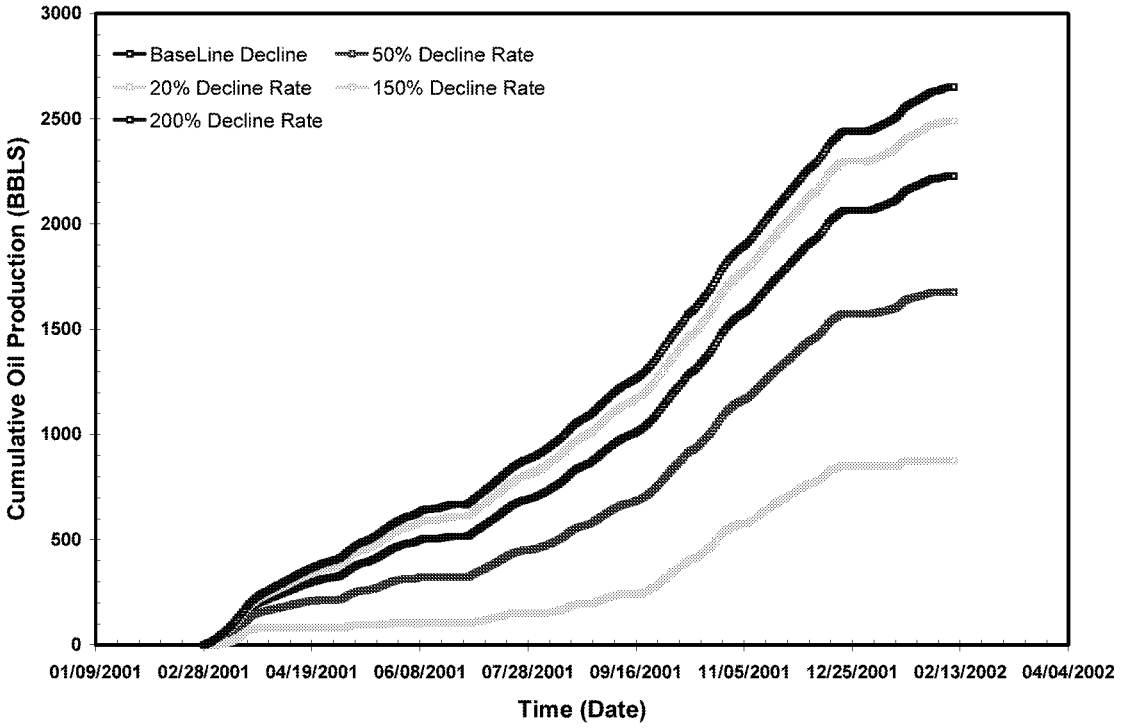

Fig. 3.17-26—The cumulative oil production after the base line with different decline rate taken before waterfloding conducted in the pilot area

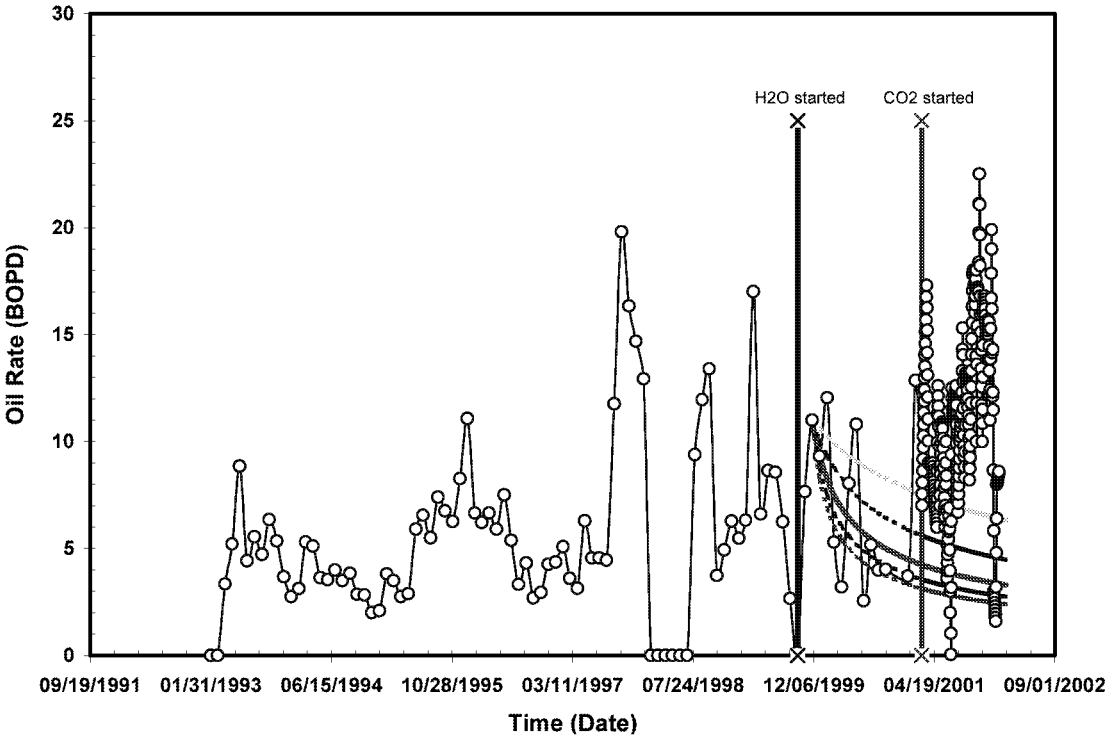

Fig. 3.17-27—Decline curve analysis taken after waterflooding started in the pilot area

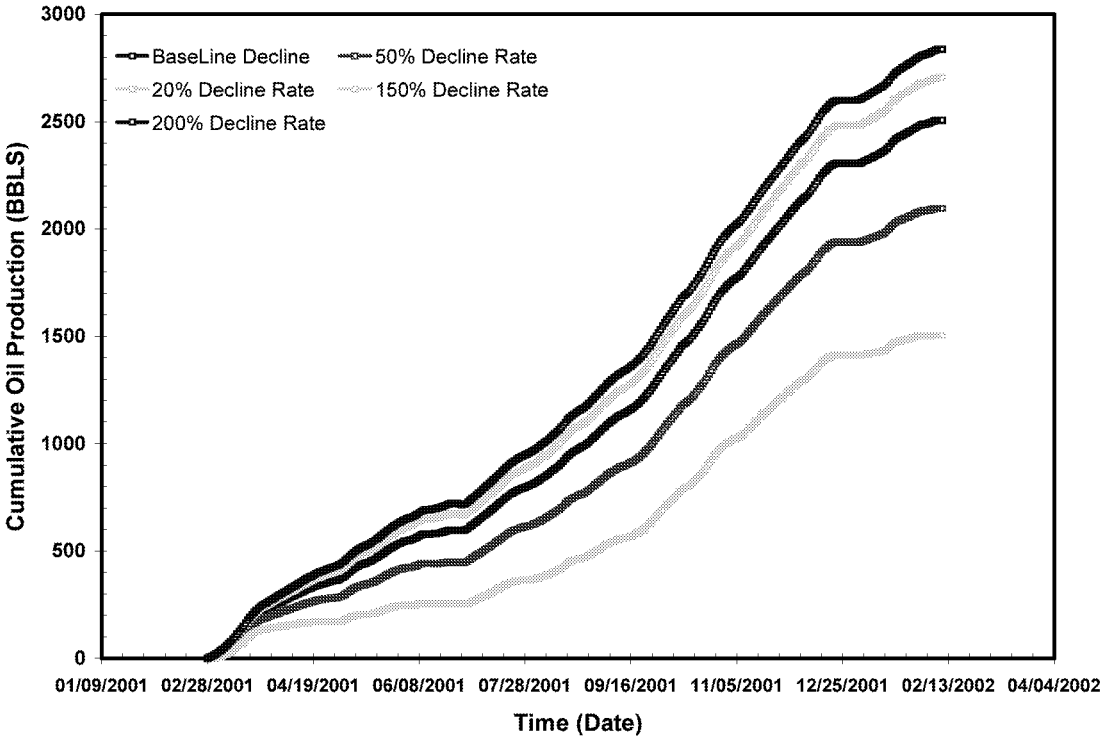

Fig. 3.17-28—The cumulative oil production after the base line with different decline rate taken after waterfloding conducted in the pilot area

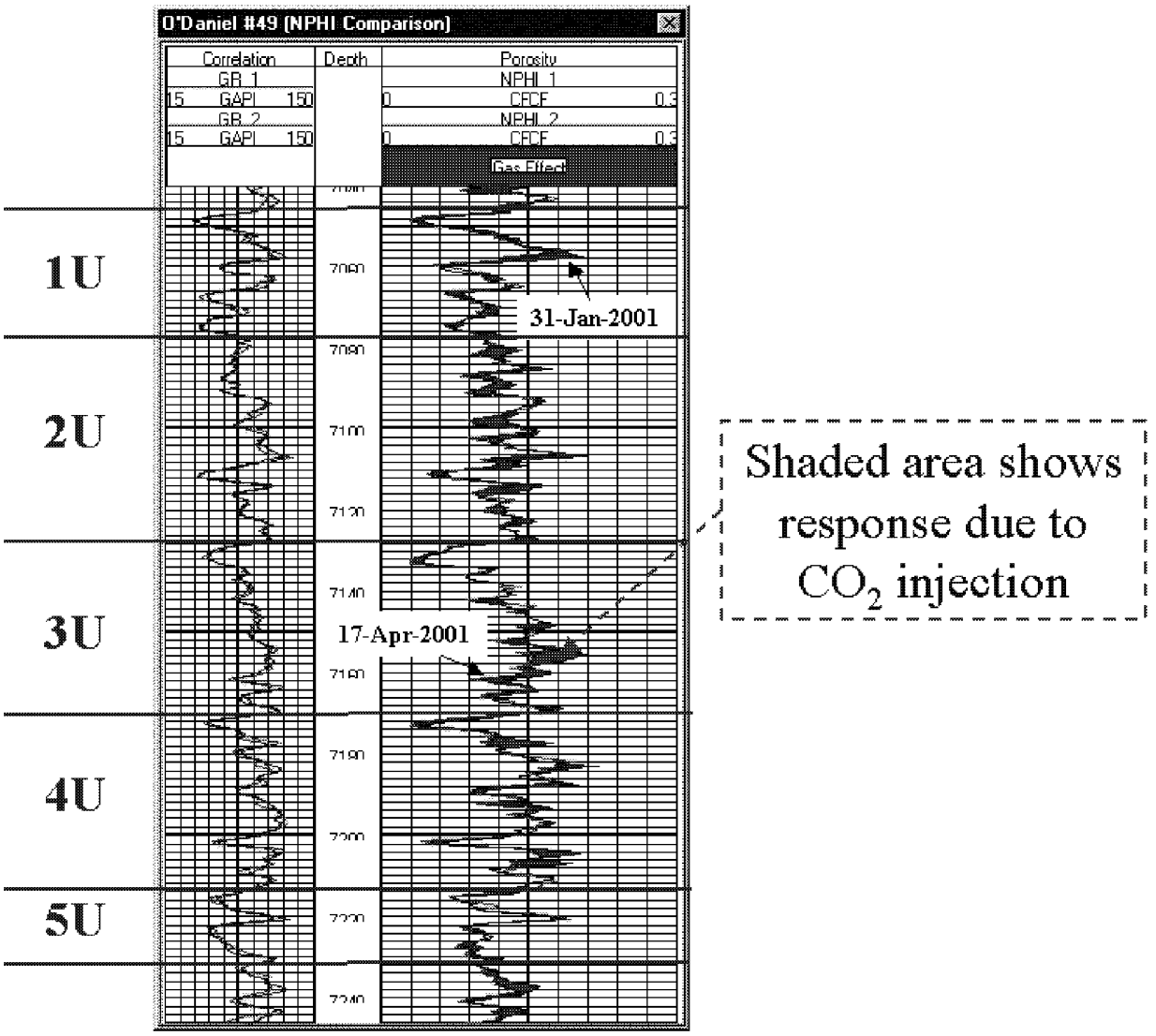

Fig. 3.17-29—Logging Observation Well Response (LOW)

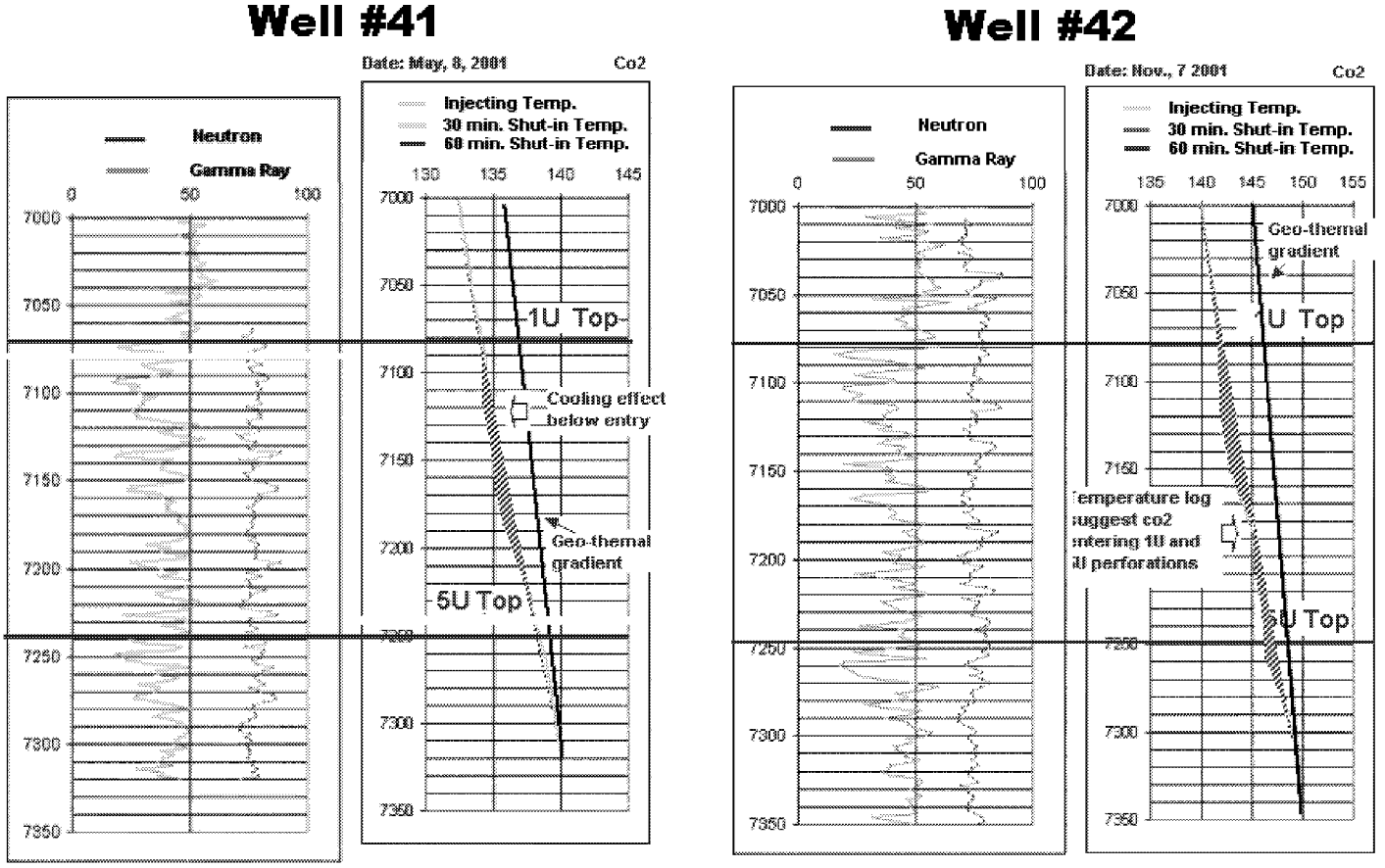

Fig 3.17-30—Temperature Log Response indicating the regions at which CO_2 is entering the formation

4. INVESTIGATION OF CO_2/CRUDE OIL PHASE BEHAVIOR AND RECOVERY MECHANISM BY CO_2 INJECTION IN FRACTURED SYSTEMS

4.1 MINIMUM MISCIBILITY PRESSURE (MMP)

We have measured the MMP of Spraberry separator oil in our laboratory. Figure 4.1–1 shows oil recovery versus pressure. The MMP is estimated to be about 1,550 psig. The interstitial velocity in our slim tube was calculated to be 0.094 cm/s. Viscosity of CO_2 was estimated to be 0.03 cp under experimental conditions. IFT was estimated using the Peng-Robinsion Equation of State (PREOS) to be about 1.8 mN/m, which is consistent with recently measured values near 2 mN/m (shown in the next section). The MMP value of 1,550 psig corresponds to a capillary number of 5.5×10^{-5}.

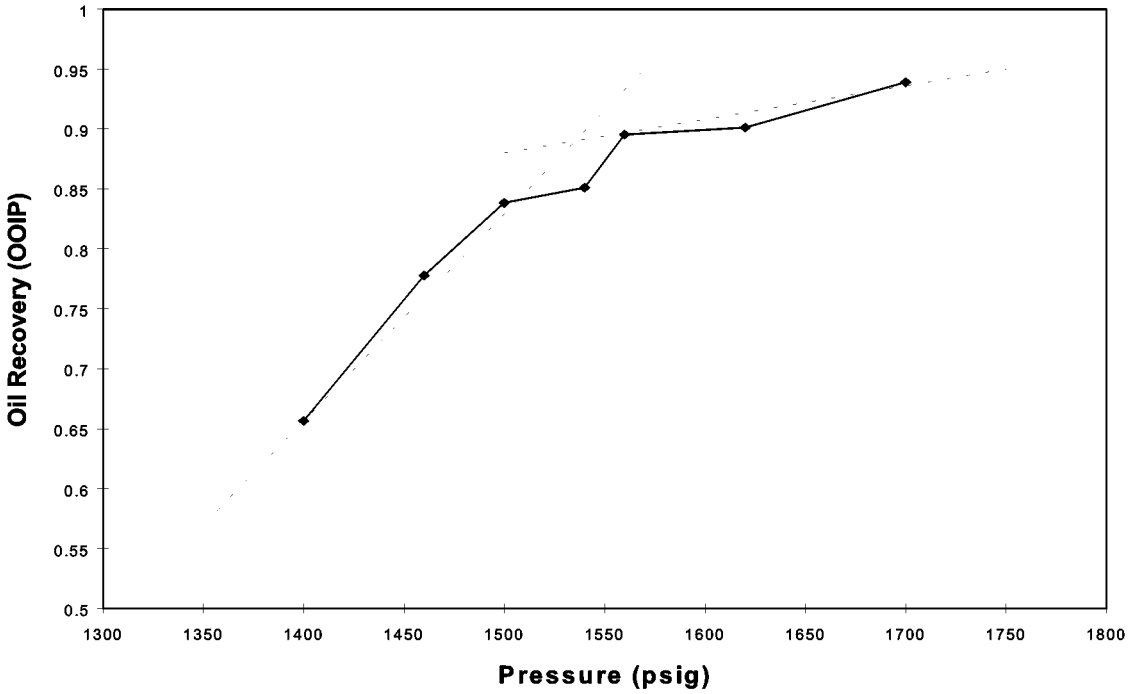

Fig. 4.1–1 —Results from slim-tube indicate the minimum miscibility pressure for Spraberry separator oil is approximately 1540 psig

4.2 INTERFACIAL TENSION MEASUREMENTS

Interfacial tension (IFT) of two CO_2/crude oil systems were measured versus pressure at 138 °F using the pendant drop apparatus in our laboratory. The first sample investigated was Spraberry separator oil which was tested to have a Minimum Miscibility Pressure (MMP) of about 1,550 psig. The second sample was recombined Spraberry reservoir oil with an MMP of about 1,565 psig which is within experimental variation of the separator oil. Phase densities of the two systems were also measured versus pressure. Fig. 4.2–1 shows measured density data for the two systems. This figure demonstrates that the presence of light components in the recombined reservoir oil causes the density of the liquid and gaseous phases of the recombined oil to be lower than that of the separator oil. Measured first-contact IFT data are plotted against pressure in Fig. 4.2–2. A composite plot of density difference against IFT is illustrated in Fig. 4.2–3 for the two systems.

It can be seen from Fig. 4.2–2 that the IFT of the CO_2/separator oil declines rapidly with pressure until about 1,550 psig which is close to the MMP. At pressures above the 1,550 psig, the IFT drops slowly with pressure. The CO_2/recombined oil demonstrates a similar trend with IFT declining rapidly with pressure before 2,000 psig is reached. This was higher than the measured MMP of 1,565 psig.

Although Fig. 4.2–1 and Fig. 4.2–2 demonstrate significant difference in IFT and density between the two systems, Fig. 4.2–3 clearly indicates that their first-contact IFT's have the same density-dependent behavior as they follow the same trend in the plot. However, as shown in Fig. 4.2–3, the slope deviates from the slope of 3.88 especially at high pressures. The 3.88 slope is defined by critical scaling law for pure substances[37], rather than for multi-component systems. However, it should be noted that the measured IFT are for first-contact fluids and this may not reflect the IFT during the multi-contact process.

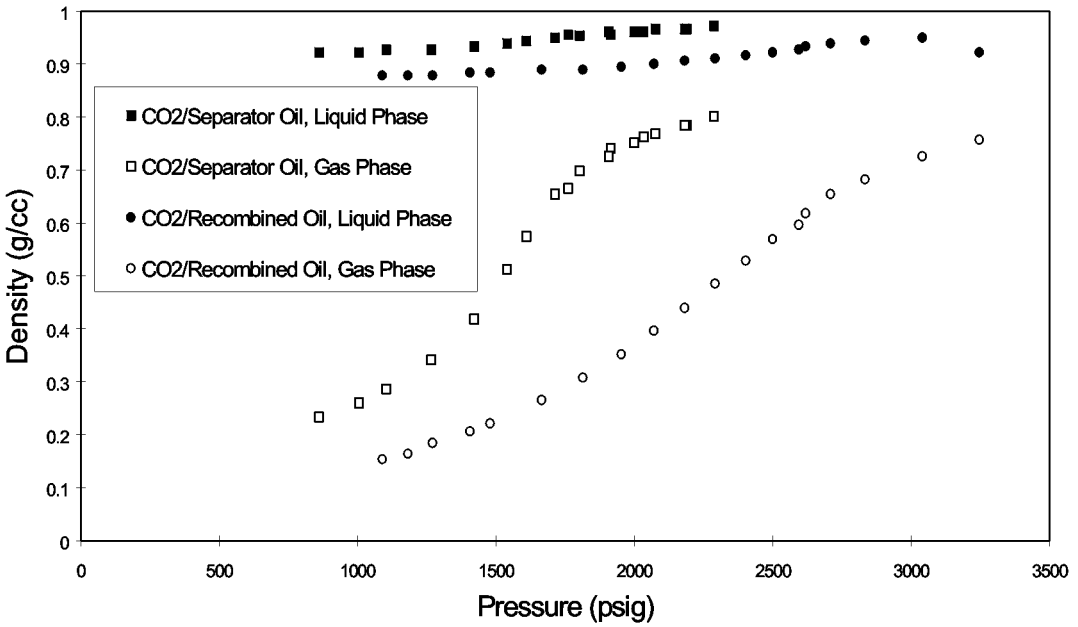

Fig. 4.2–1 —Measured densities of CO_2/Spraberry oil systems at 138 °F

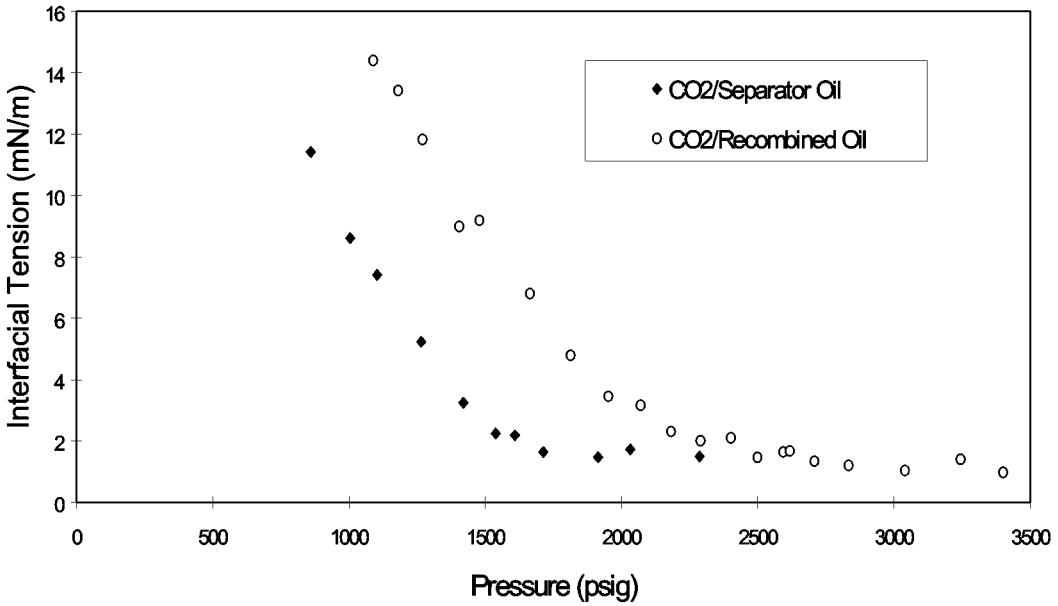

Fig. 4.2–2 —Effect of pressure on IFT of two CO_2/Spraberry crude oil systems at 138 °F

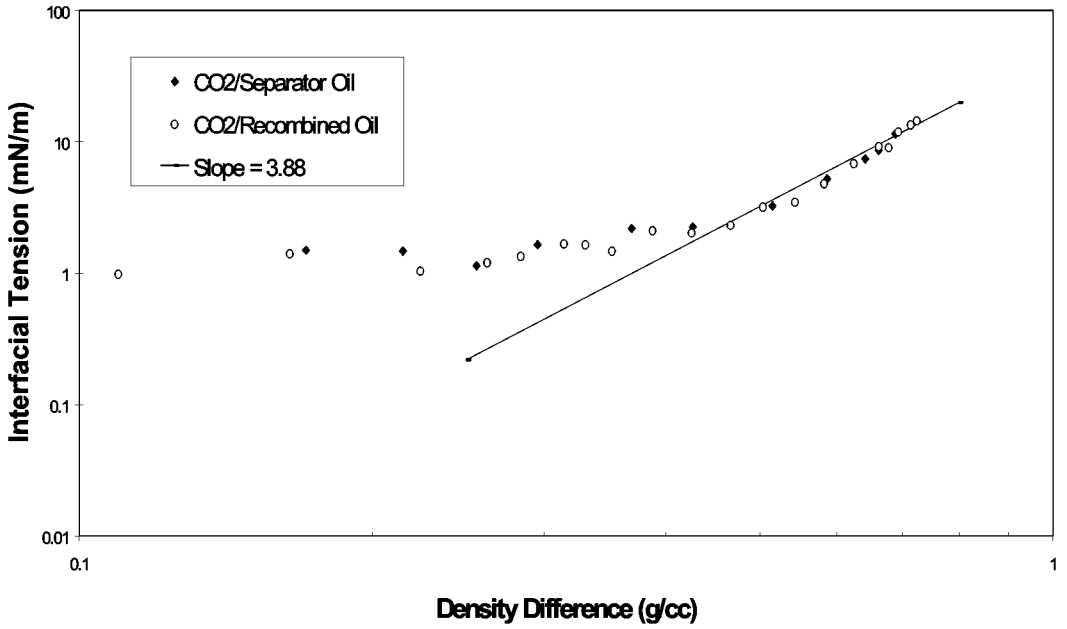

Fig. 4.2–3 —Relationship between density difference and IFT for two CO_2/Spraberry crude oil systems at 138 F

4.3 EXPERIMENTAL INVESTIGATIONS ON CO_2 GRAVITY DRAINAGE IN A FRACTURE SYSTEM

Introduction

During the first three years of this project, five experiments were performed on two 4 in Berea cores, one 4 in reservoir core, one 3.5 in reservoir core and two 2.5 in reservoir cores. The cores were taken from the Spraberry reservoir. The permeabilities to brine of 4in and 3.5 in Spraberry cores, are 0.01 md and 0.38 md, respectively. The absolute permeabilities of the two 4 in Berea cores are 500 md and 50 md, respectively. The two 2.5 in reservoir cores, which were stacked vertically during the experiment, have air permeabilities of 0.16 md and 0.13 md, respectively, while an average permeability to brine of 0.057 md was measured for the whole stack during the experiment. Table 4.3-1 summarizes the physical properties of those whole cores.

All five experiments were conducted to investigate the efficiency of CO_2 gravity drainage and the effect of initial water saturation during CO_2 gravity drainage experiments. The last experiment, which used a stack of two 2.5in Spraberry cores, was also performed to investigate the effects of core discontinuity and impermeable layers at the top and the bottom of the pay zone on the efficiency of the CO_2 gravity drainage. The partial results are also presented in Table 4.3-1.

Figure 4.3-1 summarizes the results (oil recovery curves) of all five experiments, which were given in the Third Annual Technical Progress Report. The results are redrawn in Figs. 4.3-2 and 4.3-3 as curves of oil recovery vs. rock permeability and oil recovery vs. initial water saturation. It is clearly seen from the figures that the efficiency of CO_2 injection decreases as permeability decreases and initial water saturation increases. It appears that core discontinuity and impermeable layers at the top and bottom of the pay zone affects the efficiency of the CO_2 gravity drainage, as can be seen by comparing the result of the last experiment (stacked core, K= 0.05 md and Sw_I = 0.376) with that of the third experiment (continuous core, K= 0.01 md and Sw_I = 0.386). The permeability and the water saturation of the cores are almost similar for that experiment but the recovery from stacked core (19% IOIP) is lower than the continuous core (31% IOIP) as shown in Table 4.3-1. Figures 4.3-2 and 4.3-3 show that the effect of initial water saturation on oil recovery is more pronounced than the effect of permeability.

In order to optimize the CO_2 pilot design in the E.T. O'Daniel Unit of the Spraberry Trend Area, the previous experimental results were scaled up to field scale using the mathematical model proposed by Schecter and Guo (1996). The modeling results indicate that significant amounts of oil can be recovered from the pilot area by CO_2 flooding in a relatively short time period, depending on matrix permeability, initial water saturation and fracture intensity.

During the fourth year of this project, another experiment was performed to model the actual field experience of first flooding and then CO_2 recovery in the naturally fractured

Spraberry Trend Area. The objective of the experiment is to investigate the effect of water imbibition followed by CO_2 gravity drainage on oil recovery under reservoir conditions. The effects of temperature and cyclic CO_2 injection were also investigated during the experiment. The experiment was initially designed to use a Berea core and a reservoir core from the Spraberry Trend Area. As the experiment on the Spraberry core has not been completed at the time of this writing, only the results from the experiment of the Berea core are presented in this report.

Laboratory Experiment

Materials used in the experiment

Core Sample. A 4in Berea core with 21.75in long was used in this experiment. The total bulk volume is 4476.62 cm^3 and the pore volume is 1004.0 cm^3. Thus the calculated porosity is 22.43%. The permeability of the Berea core was measured under room temperature (26°C) using synthetic Spraberry brine. Permeabilities to brine measured were 625.97, 619.78, 609.45, 600.50 and 593.68 md, corresponding to the pressure drops of 3.2, 5.5, 7.4, 9.5 and 13.2 psia. Therefore, the average permeability of the core to brine is 610 md. The physical properties are given in Table 4.3-2.

Brine. Synthetic Spraberry brine was used in the experiment. Density and viscosity of the brine is 1.08 g/cm^3 and 1.21 cp, respectively, measured under room temperature (26°C) and ambient pressure (12.6 psia).

Oil. Spraberry dead oil was used in the experiment. The composition of the oil was obtained from GC analysis as shown in Table 4.3-3. The average molecular weight of the dead oil is 230.4, oil density is 0.865 g/cm^3 and oil viscosity is 2.956 cp measured under room conditions.

Core preparation

Cleaning. The core was put into a core holder and cleaned under room temperature by injecting methanol, toluene, THF and chloroform. Methanol was at first injected in order to remove potential salts in the core. Then the four solvents were alternatively injected. Finally, methanol was injected once again to remove all other solvents. The core was first flushed with N_2 to remove methanol inside of the core and then with moist N_2 in order to recover its wettability. The core was then vacuum-pumped. After being cleaned, it was taken from the core holder and put into another oven under high temperature for drying.

Saturation. The core was put back into the core holder and air was removed from inside of the core using a vacuum pump. Synthetic Spraberry brine was injected from the bottom of the core. A total of 1004 cm^3 brine was put into the core, so the porosity, ϕ, can be estimated at about 22.43 %. The synthetic brine then was flushed through the core. The permeability of the core was measured under room temperature (26°C) after the flow was stable.

Spraberry dead oil was injected into the core from the top under reservoir temperature of 58.9°C (138°F). The oil flow rate was 0.0225 cm^3/s (81 cm^3/hr) at the pressure difference

of 2.2 psi, and later increased to 0.0451 cm^3/s (162 cm^3/hr) at the pressure drop of 5.1 psi. Oil broke through when 525 cm^3 of brine was produced. The total amount of dead oil injected was 1169 cm^3 (1.16 PV). The water saturation, S_w, and the oil saturation, S_o, were 42.6% and 57.4%, respectively. After aging core for 10 days under reservoir temperature 58.9 °C (138 °F) with pressure above 1600 psia, the core was flushed by injecting1350 cm^3 (1.35 PV) dead oil. Another 5.3 cm^3 brine was produced. Therefore, the total volume of oil within the core increased to 581.3 cm^3 and the initial oil saturation, S_{oi}, was 57.9 %. The initial water saturation, S_{wi}, decreased to 42.1%.

Procedure and experimental results

Figure 4.3-4 schematically illustrates the set-up used in this experiment. Basically, it consists of a drainage cylinder, a visual cell, a BPR, a pump, two accumulators for storing CO_2 and brine, an oil-gas separator and some glassware for measuring oil, gas and brine produced. Reservoir temperature is 58.9°C (138°F). The experiment was conducted in a drainage cylinder.

Water imbibition. The injection rate was 20 cm^3/hr and the backpressure was set above 1650 psia. A total of 194.38 cm^3 oil was produced during the water imbibition, which decreased the oil saturation from the initial oil saturation, 57.9% to 38.5%. The oil recovery was 33.44 % OOIP. The water saturation increased to 61.5%.

During water imbibition, a total of 138.9 cm^3 gas was produced at 12.6 psia. The gas volume was about 1.389 cm^3 under 1600 psia and temperature of 58.9°C (138°F). If we assume a gas factor equal to 0.85, the gas volume is only 0.13% the pore volume. Therefore, the gas saturation effect can be ignored.

CO_2 gravity drainage/injection. CO_2 gravity drainage was performed in two stages: dynamic gravity drainage (open system) and static gravity drainage (closed system). For both stages, the backpressure was set above 1700 psia and the temperature was set at 58.9°C (138°F). The total time for conducting CO_2 imbibition was 858 hours.

In the first stage, CO_2 was pumped into the drainage cylinder from the top and the injection rate was set up between 20 ~ 30 cm^3/hr. About 50 cm^3 black oil was produced approximately 40 hours after CO_2 injection initiated. Light oil was produced but the oil rate decreased significantly. This stage ran for about 330 hours after injecting about 7105 cm^3 (7.08 PV) CO_2.

In the second stage, the outlet was closed and CO_2 injection was stopped. The core, the CO_2 and the visual cell formed a closed system. The visual cell was connected to the bottom of the drainage cell to collect oil and water produced from the core. This stage ran for 528 hours. Not much CO_2 was used in this stage because CO_2 remained in the cell (closed system).

Thirteen oil samples were taken from the oil produced during CO_2 gravity drainage for a GC analysis. The colors of the oil samples changed from black to yellow and back to black.

A total of 93.2 cm^3 oil and 228.3 cm^3 water were produced during CO_2 gravity drainage. The oil recovery increased 16.03% OOIP, which made the total oil recovery increase to 49.4% OOIP. The oil saturation within the core decreased to 29.3% and the water saturation dropped to 39.0%. Assuming that only water and oil existed in the core before CO_2 drainage began, CO_2 saturation within the core was 31.7 %.

Temperature effect. To investigate the effect of temperature on CO_2 drainage, temperature was increased gradually to 180°F in two days. The pressure in the drainage cell increased to above 2300 psia. This process lasted 167 hours. Only 0.5 cm^3 of oil and 1.0 cm^3 of water were produced.

Cyclic CO_2 injection. The last step was cyclic CO_2 injection, where the CO_2 was injected at elevated pressure, and after a certain period of time, the injection was stopped, with CO_2 being released to a lower pressure. During the pressure decrease stage, CO_2 injection was stopped and CO_2 was slowly released from the drainage cylinder until the pressure went down to 1450 psia. Then, the outlet was closed and CO_2 was injected into the cylinder with the pressure kept above 1750 psi. Then the pressure decrease stage was run again. One cycle took about 24 hours. Oil and water were collected during the pressure decrease stage. A total of five cycles were run.

The volume of oil produced in this process was 13.1 cm^3, which increased oil recovery from 49.5 to 51.8% OOIP. The residual oil saturation dropped from 29.2 to 28.0%. The volume of water produced was 23.5 cm^3, which decreased water saturation to 36.5%.

Table 4.3-4 summarizes the experimental results. The oil and water producing histories are also plotted in Fig. 4.3-5. Figures 4.3-6 and 4.3-7 present the oil recovery and oil/water saturations vs. time, while Fig. 4.3-8 shows oil recovery and amount of CO_2 used during CO_2 injection/gravity drainage.

Analysis and Discussion

Our objective is to investigate effects of CO_2 gravity drainage after water imbibition on oil recovery under reservoir conditions. Thus, the discussion and analysis are concentrated on results obtained from CO_2 gravity drainage.

Nine of the 13 oil samples were analyzed using gas chromatograhy (GC). These oil samples were taken at different times. Table 4.3-5 shows the mole fraction and weight percent of different component groups in the oil samples. For convenient analysis, we divided the components of the oil samples into four groups: C1 ~ C10, C11 ~ C20, C21 ~ C30 and $C31^+$. The results are shown in Fig. 4.3-11 and 4.3-12. For more details, see Table 4.3-7 and 4.3-8. The results are also presented in Figs. 4.3-9 and 4.3-10.

The CO_2 extracted most of middle components, C11 ~ C20, from the oil during CO_2 gravity drainage. The oil samples from this component group were about 85 % by mole fraction and about 80 % by weight percent (Figs. 4.3-11 and 4.3-12). While more mole

fraction of light components were extracted at the beginning of the experiment the mole fraction of heavy components increased at the end of CO_2 injection/gravity drainage.

Oil sample densities were also measured at room temperature and ambient pressure. The average molecular weights of the samples obtained from GC analysis are presented in Table 4.3-6 and plotted in Fig. 4.3-13. The oil sample at time 0 was Spraberry dead oil. Both density and average molecular weight increased with time except at the beginning of the experiment. At that point, heavier components were flooded by CO_2 and then CO_2 extracted the light component about 40 hours later, which indicated that CO_2 drainage initiated.

Temperature seemed to have no significant effect on CO_2 drainage process in this experiment (Fig. 4.3-5), because CO_2 may have a more pronounced effect than temperature on increasing the mobility of oil and decreasing the interfacial tension (IFT).

Cyclic CO_2 injection may prove effective in improving the oil recovery during CO_2 gravity drainage, as displayed in Fig. 4.3-5. A cyclic injection scheme in this experiment enhanced oil recovery up to 2.3% OOIP. Considering that cyclic CO_2 injection was performed at low oil saturation (29.2%), the oil increment may be considered significant.

Figure 4.3-8 shows the volume of CO_2 used during CO_2 injection/drainage. A large quantity of CO_2 was used in this experiment. It should be noted also that the rate of pumping CO_2 into the drainage cell did not significantly affect the final oil recovery from the core, but only increased the amount of CO_2 usage as shown in Fig. 4.3-8. The oil production rate did not decrease when CO_2 injection was stopped. The only significant effect of the CO_2 injection rate may be on the oil production rate at the beginning of the CO_2 process. However, CO_2 injectivity studies need to be performed to clarify this issue.

Figure 4.3-14 shows that water imbibition followed by CO_2 injection may achieve higher oil recovery than using CO_2 injection alone. That comparison was made between Core No. 1 (k = 500 md) and this experiment (k = 500 md) (see Table 4.3-1) because of almost similar rock properties.

Conclusions

From the results obtained in this experiment, the following conclusions can be drawn:

1. CO_2 gravity drainage could significantly increase oil recovery after waterflooding in the naturally fractured Spraberry Trend Area.
2. Water imbibition followed by CO_2 injection may be more efficient than injecting CO_2 alone.
3. The efficiency of CO_2 injection decreases as permeability decreases and initial water saturation increases.
4. The effect of initial water saturation may have more effect on oil recovery than permeability.

5. Cyclic CO_2 injection may enhance oil recovery during a CO_2 gravity drainage process.
6. Temperature does not have a significant effect on oil recovery during the CO_2 gravity drainage process.

References

1. Schechter, D.S.: "Advanced Reservoir Characterization and Evaluation of CO_2 Gravity Drainage in the Naturally Fractured Spraberry Trend Area," Third Annual Technical Progress Report, Contract No. DE-FC22-95BC14942, U.S. DOE, (Dec 1998).
2. Schechter, D.S. and Guo, B.: "Mathematical Modeling of Gravity Drainage after Gas Injection into Fractured Reservoirs," paper SPE 35170 presented at the 1996 SPE Improved Oil Recovery Symposium Tulsa, April 22-24, 1996.

Table 4.3–1—Physical properties of the core samples used in previous experiments and partial results obtained

Core No.	1	2	3	4	5
Core Type	Berea	Berea	Spraberry	Spraberry	Spraberry
Configuration	continuous	continuous	continuous	continuous	stacked
Length, cm	55.52	55.25	55.0	55.245	24.77 25.08
Diameter, cm	10.16	10.16	10.16	8.89	6.53 6.58
Porosity, %	18.7	13.0	10.0	11.1	10.7
Brine Permeability, md	500	50	0.01	0.38	0.057
Water Saturation, %	35.0	29.3	38.6	45.0	37.6
Residual Oil Saturation, %	37.5	32.5	42.5	41.8	50.5
OOIP, cc	544.5	411.1	273.8	209.3	111.0
OWIP, cc	293.2	171.2	172.1	171.3	67.0
Oil Recovery, %	42.0	54.0	30.8	24.0	19.1
Time of Experiment, (day)	6	220	190	167	331

Table 4. 3–2—Physical properties of the core sample used in this experiment

Properties of the Berea Core	**Value**
Length, cm	55.25
Diameter, cm	10.16
Bulk Volume, cm^3	4476.62
Pore Volume, cm^3	1004.0
Porosity, %	22.43
Brine Permeability, md	610.0
OOIP, %	581.3
OWIP, %	422.7
Initial Water Saturation, %	42.1
Initial Oil Saturation, %	57.9

Table 4. 3–3—GC results of the Spraberry dead oil used in the experiment

Carbon No.	Molec. wt.	Weight %	Moles	Mole fract.	Molec. wt. %
1	16.04303	0	0	0	0
2	30.07012	0	0	0	0
3	44.09721	0	0	0	0
4	58.12430	0	0	0	0
5	72.15139	0.084064563	0.001165114	0.002683957	0.193651205
6	86.17848	0.761713828	0.008838794	0.020361054	1.754684680
7	100.20557	4.299808405	0.042909874	0.098847226	9.905042626
8	114.23266	5.136605594	0.044966173	0.103584119	11.832689410
9	128.25975	4.251297195	0.033145996	0.076355148	9.793292159
10	142.28684	5.343655162	0.037555512	0.086512913	12.309648980
11	156.31393	3.725624838	0.023834247	0.054904594	8.582352830
12	170.34102	3.498245901	0.020536720	0.047308408	8.058562498
13	184.36811	3.682212712	0.019972070	0.046007678	8.482348616
14	198.39520	3.928306014	0.019800409	0.045612239	9.049249375
15	212.42229	3.053448865	0.014374428	0.033112945	7.033927635
16	226.44938	2.829626878	0.012495627	0.028784937	6.518331098
17	240.47647	3.067010969	0.012753892	0.029379878	7.065169311
18	254.50356	2.735307623	0.010747620	0.024758228	6.301057176
19	268.53065	1.868650564	0.006958798	0.016030294	4.304625171
20	282.55774	2.671345541	0.009454158	0.021778607	6.153714065
21	296.58483	2.231717507	0.007524719	0.01733395	5.140986518
22	310.61192	2.097276207	0.006752079	0.015554095	4.831287414
23	324.63901	1.886004976	0.005809545	0.013382874	4.344602811
24	338.66610	1.820107843	0.005374343	0.012380342	4.192802113
25	352.69319	4.814449489	0.013650531	0.031445377	11.09057030
26	366.72028	1.758789839	0.004795998	0.011048066	4.051549904
27	380.74737	1.765568922	0.004637114	0.010682060	4.067166205
28	394.77446	1.273149915	0.003225006	0.007429126	2.932829323
29	408.80155	1.844834162	0.004512787	0.010395659	4.249761686
30	422.82864	1.735618455	0.004104780	0.009455775	3.998172280
31	436.85573	3.053084504	0.006988771	0.016099339	7.033088293
32	450.88282	1.873150914	0.004154407	0.009570097	4.314992181
33	464.90991	2.543647873	0.005471270	0.012603624	5.859549596
34	478.93700	1.597259782	0.003335010	0.007682533	3.679449114
35	492.96409	1.604971432	0.003255757	0.007499966	3.697213677
36	506.99118	2.651509536	0.005229893	0.012047586	6.108019825
C37+	563.09954	14.51193399	0.025771525	0.059367309	33.429704590
Total/Average		100	0.434102968	1	230.3600927

Table 4. 3–4—Experimental results during different stages

	Water Imbibition	CO_2 Drainage	Temperature Increase	Cyclic CO_2 Injection
Initial Oil Saturation, %	57.9	33.5	29.3	29.2
Final Oil Saturation, %	33.5	29.3	29.2	28.0
Initial Water Saturation, %	42.1	66.5	39.0	38.9
Final Water Saturation, %	66.5	39.0	38.9	36.5
Gas/CO_2 Saturation, %	0.1	31.7	31.7	35.5
Oil Recovery, %	33.44	49.4	49.5	51.8
Time of Experiment, day	22	36	7	5

Table 4.3–5—GC results of different group components of oil samples obtained from CO_2 gravity drainage/injection

Time	*C1 ~ C10*		*C11 ~ C20*		*C20 ~ C30*		*C31+*	
(hr)	Mole frac.	Weight %	Mole frac.	Weight %	Mole frac.	Weight %	Mole frac.	Weight %
0	0.388344	19.87714	0.347678	31.05978	0.139107	21.22752	0.124870	27.83556
10	0.266333	16.76627	0.600432	58.15009	0.094344	15.58787	0.038891	9.495767
37	0.438436	29.86307	0.475120	51.93866	0.060512	11.19651	0.025932	7.001758
42.5	0.055843	3.423766	0.854845	83.13537	0.088145	13.17068	0.001167	0.270184
50.5	0.049993	3.011592	0.847875	81.78595	0.099050	14.51070	0.003082	0.691760
89	0.072391	4.696062	0.857835	84.41236	0.068740	10.64875	0.001034	0.242836
209.5	0.085529	5.485306	0.801255	77.32346	0.111675	16.83614	0.001541	0.355099
301	0.012867	0.709839	0.875925	83.48775	0.109502	15.46458	0.001705	0.337837
330	0.017890	1.042006	0.836478	75.82748	0.109121	15.46735	0.036511	7.663163
359.5	0.106067	4.144405	0.346742	23.13898	0.280836	30.83610	0.266355	41.88052

Table 4.3–6—Properties of oil samples obtained from CO_2 gravity drainage/injection

Time, hr	0	10	37	42.5	50.5	89	209.5	301	330	359.5
Ave. Molec. Weight	230.4	206.3	181.0	217.6	221.7	208.5	210.5	233.6	235.4	322.4
Density	0.865	0.864	0.852	0.823	0.844	0.833	0.832	0.848	0.870	0.901

Table 4.3–7—Mole fraction of oil samples obtained from CO_2 gravity drainage/injection

Sample Carbon#	Dead oil	sample #1	sample #2	sample #3	sample #4	sample #5	sample #6	sample #7	sample #8	sample #9
1	0	0	0	0	0	0	0	0	0	0
2	0	0	0	0	0	0	0	0	0	0
3	0	0	0	0	0	0	0	0	0	0
4	0	0	0	0	0	0	0	0	0	0
5	0.00268	0.00035	0.00042	0.00020	0.00008	0.00008	0.00006	0.00014	0.00048	0.00015
6	0.02036	0.00182	0.00871	0.00024	0.00017	0.00026	0.00023	0.00009	0.00002	0.00135
7	0.09885	0.01982	0.07283	0.00288	0.00237	0.00042	0.00302	0.00114	0.00009	0.01425
8	0.10358	0.04912	0.11511	0.00694	0.00620	0.00875	0.00853	0.0025	0.00080	0.02440
9	0.07636	0.06911	0.10832	0.01098	0.01049	0.01598	0.01714	0.00279	0.00226	0.02563
10	0.08651	0.12612	0.13305	0.03460	0.03069	0.04690	0.05654	0.00619	0.01424	0.04030
11	0.05491	0.09859	0.08972	0.05517	0.04488	0.07254	0.07913	0.01046	0.03824	0.03361
12	0.04731	0.09426	0.07957	0.09314	0.07964	0.10944	0.11267	0.02908	0.07255	0.03436
13	0.04601	0.09301	0.07277	0.11257	0.12060	0.14581	0.14459	0.07278	0.11012	0.04649
14	0.04561	0.09138	0.06381	0.11886	0.11265	0.16095	0.14222	0.16015	0.15203	0.03780
15	0.03311	0.05536	0.04199	0.15125	0.14637	0.10333	0.08909	0.14729	0.13196	0.03719
16	0.02879	0.04670	0.03544	0.09859	0.09721	0.08595	0.07213	0.14002	0.09595	0.03495
17	0.02938	0.04856	0.03695	0.08987	0.09316	0.07572	0.06834	0.13411	0.10036	0.03868
18	0.02476	0.03627	0.02705	0.05721	0.07329	0.04658	0.04525	0.09675	0.06479	0.03498
19	0.01603	0.02027	0.01581	0.04884	0.04328	0.03596	0.02917	0.05222	0.04226	0.02473
20	0.02178	0.01603	0.01201	0.02936	0.03680	0.02158	0.01867	0.03308	0.02823	0.02396
21	0.01733	0.01684	0.01564	0.02717	0.02752	0.02196	0.01971	0.02465	0.02986	0.03582
22	0.01555	0.01280	0.00847	0.01612	0.02323	0.01466	0.06393	0.02396	0.01816	0.03686
23	0.01338	0.00731	0.00620	0.01025	0.01238	0.00849	0.00727	0.01041	0.01285	0.02739
24	0.01238	0.00494	0.00353	0.00681	0.00827	0.00595	0.00488	0.00688	0.00958	0.02740
25	0.03145	0.03647	0.01744	0.02204	0.01975	0.01271	0.01165	0.03466	0.01572	0.03173
26	0.01105	0.00376	0.00238	0.00283	0.00354	0.00241	0.00195	0.00351	0.00593	0.02604
27	0.01068	0.00382	0.00154	0.00165	0.00218	0.00135	0.00117	0.00205	0.00519	0.02562
28	0.00743	0.00237	0.00149	0.00068	0.00095	0.00055	0.00046	0.00113	0.00329	0.01875
29	0.01040	0.00302	0.00191	0.00045	0.00089	0.00066	0.00056	0.00216	0.0077	0.02707
30	0.00946	0.00302	0.00192	0.00014	0.00035	0.00000	0.00010	0.00009	0.00086	0.02416
31	0.01610	0.00177	0.0039	0.00022	0.00026	0.00012	0.00030	0.00052	0.00613	0.04041
32	0.00957	0.00160	0.00335	0.00003	0.00008	0.00006	0.00009	0.00029	0.00192	0.02395
33	0.01260	0.00149	0.00179	0.00009	0.00005	0.00003	0.00005	0.00030	0.00558	0.01168
34	0.00768	0.00423	0.00270	0.00002	0.00064	0.00004	0.00006	0.00020	0.00386	0.04292
35	0.0075	0.01136	0.00622	0.00006	0.00047	0.00039	0.00054	0.00031	0.00422	0.02009
36	0.01205	0.01087	0.00396	0.00041	0.00122	0.00034	0.00046	0.00008	0.00642	0.01773
C37+	0.05937	0.00759	0.00401	0.00034	0.00037	0.00004	0.00006	0.00001	0.00837	0.10957

Table 4.3–8—Weight percent of oil samples obtained from CO_2 gravity drainage/injection

Sample Carbon#	Dead oil	sample #1	sample #2	sample #3	sample #4	sample #5	sample #6	sample #7	sample #8	sample #9
1	0	0	0	0	0	0	0	0	0	0
2	0	0	0	0	0	0	0	0	0	0
3	0	0	0	0	0	0	0	0	0	0
4	0	0	0	0	0	0	0	0	0	0
5	0.08407	0.01216	0.01675	0.00673	0.00247	0.00287	0.00222	0.00444	0.01473	0.00327
6	0.76171	0.07585	0.41457	0.00937	0.00654	0.01073	0.00944	0.00345	0.00057	0.03595
7	4.29981	0.96277	4.03216	0.13275	0.10711	0.02030	0.14357	0.04907	0.00384	0.44291
8	5.13661	2.71991	7.26451	0.36444	0.31964	0.47932	0.46298	0.12226	0.03883	0.86451
9	4.25130	4.29653	7.67572	0.64724	0.60674	0.98283	1.04470	0.15344	0.12309	1.01941
10	5.34366	8.69903	10.4594	2.26324	1.96909	3.20002	3.82240	0.37719	0.86095	1.77836
11	3.72563	7.47039	7.74821	3.96434	3.16355	5.43733	5.87671	0.69977	2.53889	1.62927
12	3.49825	7.78327	7.48817	7.29323	6.11800	8.93982	9.11862	2.12040	5.24956	1.81537
13	3.68221	8.31264	7.41246	9.54002	10.0280	12.8916	12.6647	5.74429	8.62417	2.65816
14	3.92831	8.78818	6.99383	10.8393	10.0795	15.3126	13.4050	13.6026	12.8124	2.32592
15	3.05345	5.70065	4.92830	14.7685	14.0220	10.5257	8.99132	13.3942	11.9075	2.45002
16	2.82963	5.12607	4.43446	10.2621	9.92809	9.33387	7.75970	13.5738	9.22973	2.45478
17	3.06701	5.66027	4.90898	9.93368	10.1037	8.73180	7.80800	13.8070	10.2522	2.88520
18	2.73531	4.47492	3.80324	6.69294	8.4122	5.68459	5.47126	10.5409	7.00441	2.76140
19	1.86865	2.63826	2.34560	6.02793	5.24131	4.63128	3.72143	6.00357	4.82074	2.05921
20	2.67135	2.19545	1.87542	3.81336	4.68968	2.92379	2.50668	4.00121	3.38793	2.09967
21	2.23172	2.42092	2.56221	3.70379	3.68095	3.12359	2.77740	3.13000	3.76143	3.29470
22	2.09728	1.92768	1.45368	2.30184	3.25395	2.18332	9.43365	3.18612	2.39594	3.55070
23	1.88601	1.15016	1.11231	1.52891	1.81258	1.32244	1.12068	1.44671	1.77158	2.75749
24	1.82011	0.81124	0.66065	1.06033	1.26245	0.96598	0.78458	0.99729	1.37755	2.87761
25	4.81445	6.23558	3.39843	3.57371	3.14109	2.14898	1.95245	5.23260	2.35507	3.47088
26	1.75879	0.66769	0.48276	0.47751	0.58559	0.42432	0.33983	0.55094	0.92360	2.96196
27	1.76557	0.70482	0.32340	0.28952	0.37409	0.24591	0.21212	0.33435	0.83997	3.02536
28	1.27315	0.45331	0.32402	0.12309	0.16967	0.10420	0.08706	0.19171	0.55115	2.29597
29	1.84483	0.59749	0.43134	0.08423	0.16386	0.12918	0.10844	0.37818	1.33719	3.43259
30	1.73562	0.61899	0.44773	0.02775	0.06647	0.00084	0.01994	0.01670	0.15388	3.16885
31	3.05309	0.37378	0.94125	0.04500	0.05143	0.02524	0.06187	0.09774	1.13757	5.47525
32	1.87315	0.34855	0.83466	0.00647	0.01627	0.01376	0.01854	0.05651	0.36835	3.34928
33	2.54365	0.33505	0.45840	0.01954	0.01053	0.00768	0.01035	0.06003	1.10272	1.68472
34	1.59726	0.98137	0.71374	0.00340	0.13761	0.00978	0.01318	0.04057	0.78533	6.37557
35	1.60497	2.71556	1.69478	0.01277	0.10382	0.09320	0.12560	0.06440	0.88457	3.07171
36	2.65151	2.67109	1.11019	0.09621	0.27864	0.08236	0.11099	0.01735	1.38304	2.78763
C37+	14.5119	2.07037	1.24874	0.08680	0.09347	0.01083	0.01460	0.00124	2.00158	19.1364

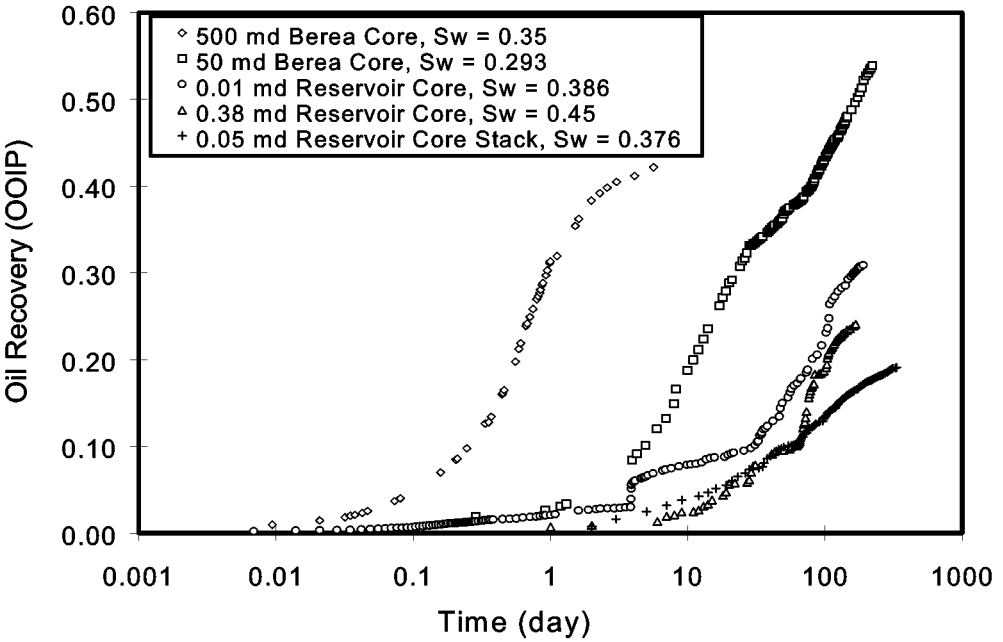

Fig. 4.3–1—Oil recovery curves obtained from the five experiments with different permeabilities and initial water saturations

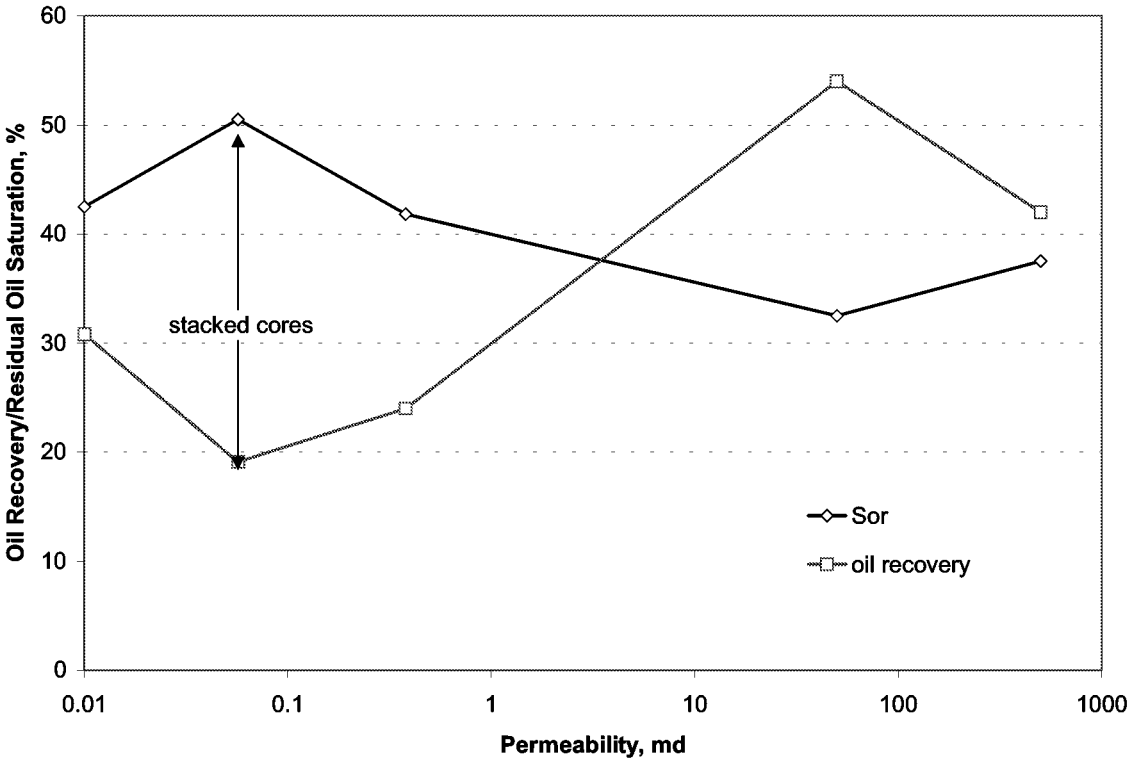

Fig. 4.3–2—Effect of permeability on oil recovery of CO_2 injection

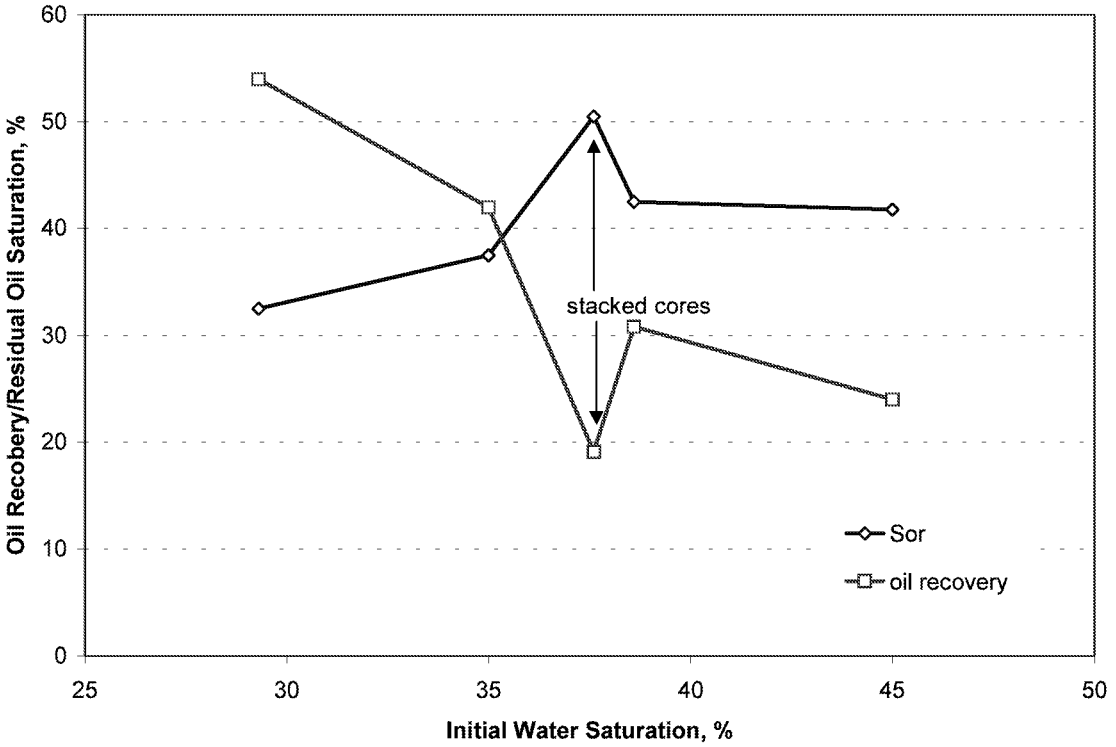

Fig. 4.3–3—Effect of initial water saturation on oil recovery of CO_2 injection

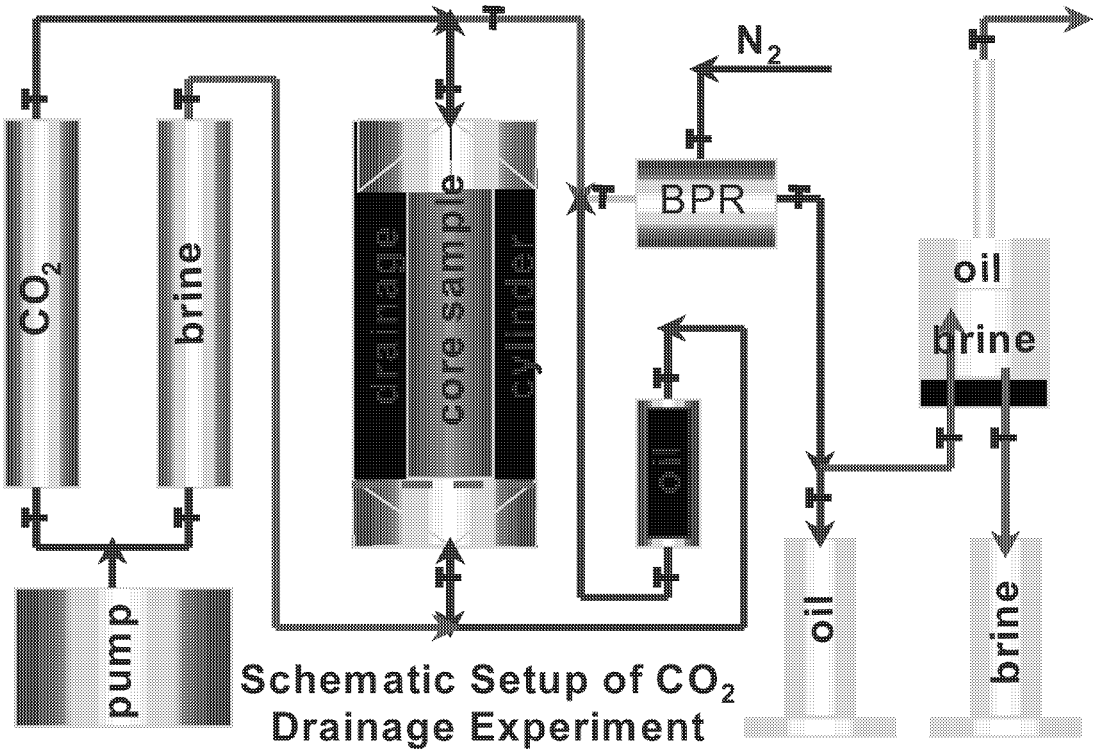

Fig. 4.3–4—Set up for water and CO_2 gravity drainage experiment

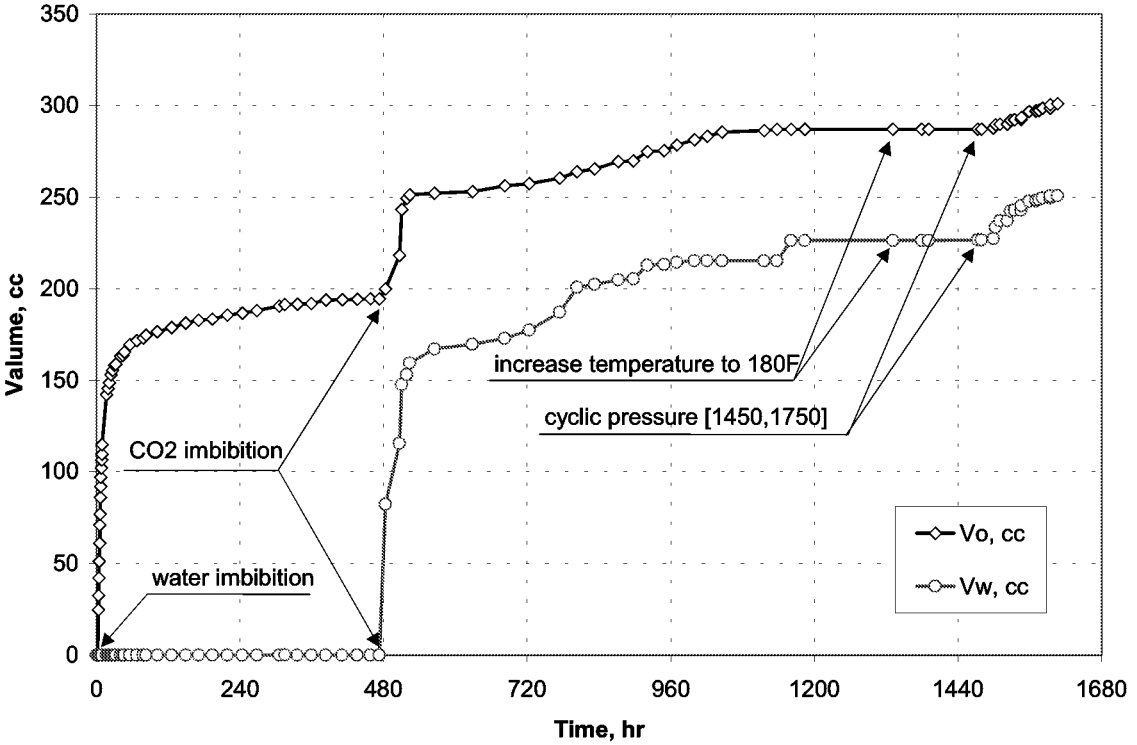

Fig. 4.3–5—Oil and water producing history during the experiment

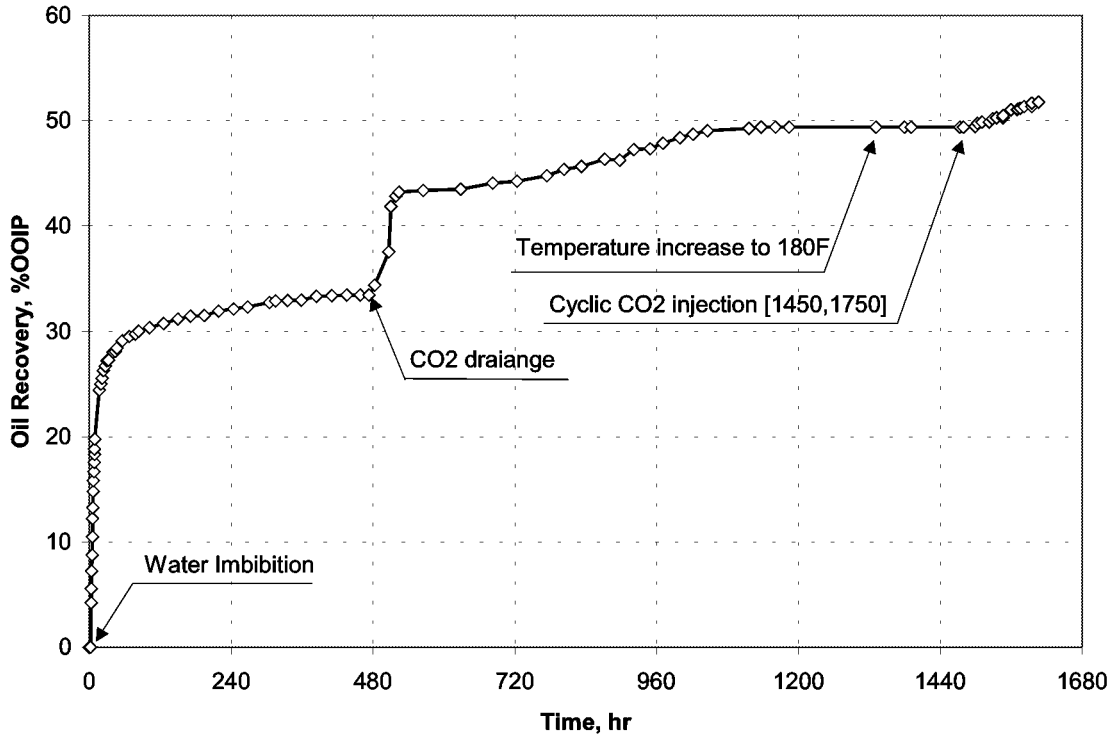

Fig. 4.3–6—Oil recovery curve for the whole experiment

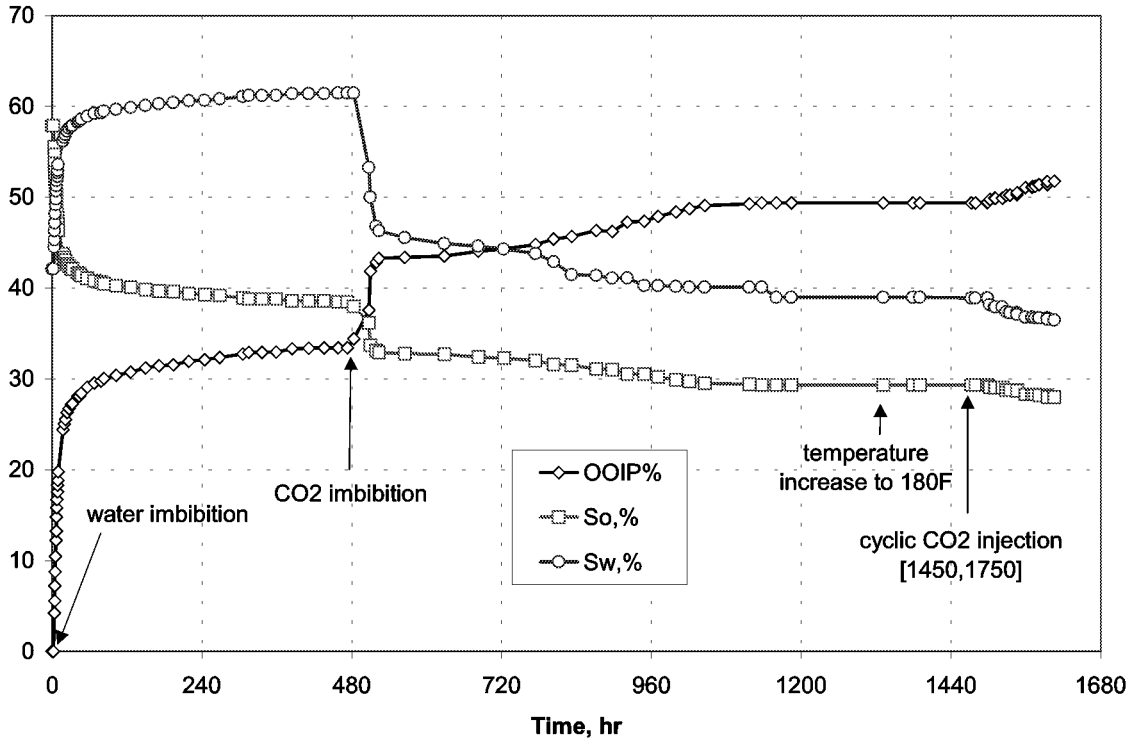

Fig. 4.3–7—Oil and water saturation history and oil recovery curve

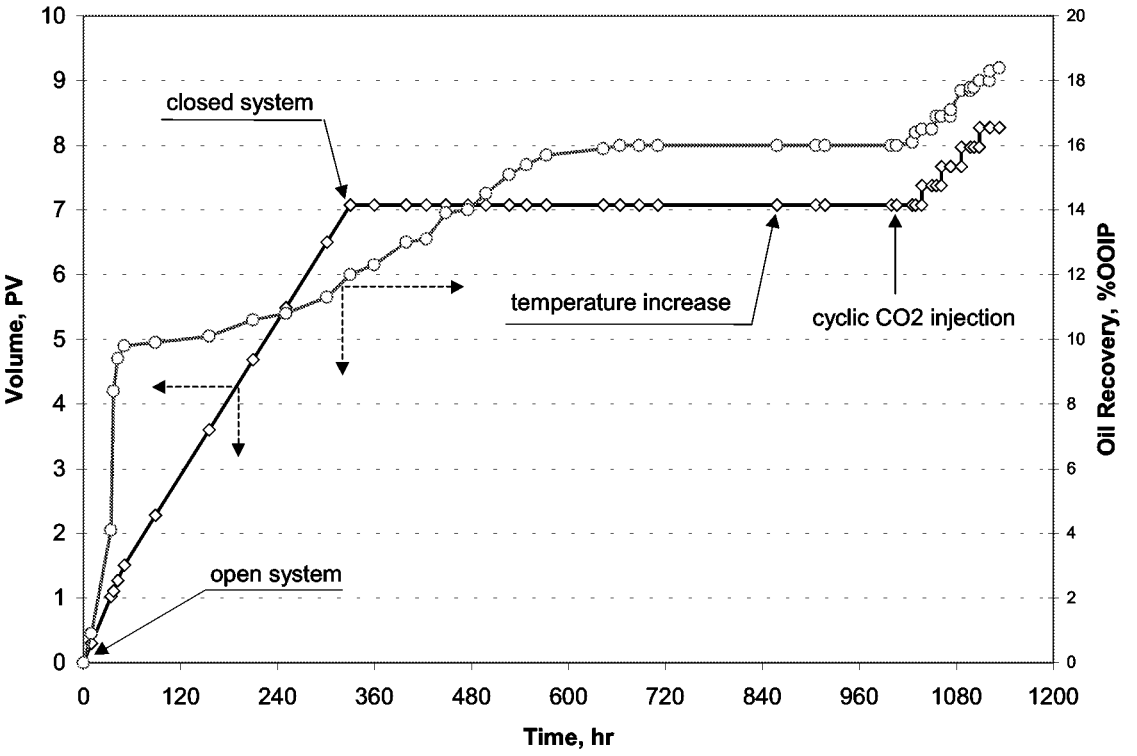

Fig. 4.3–8—Oil recovery and volume of CO_2 used during CO_2 drainage

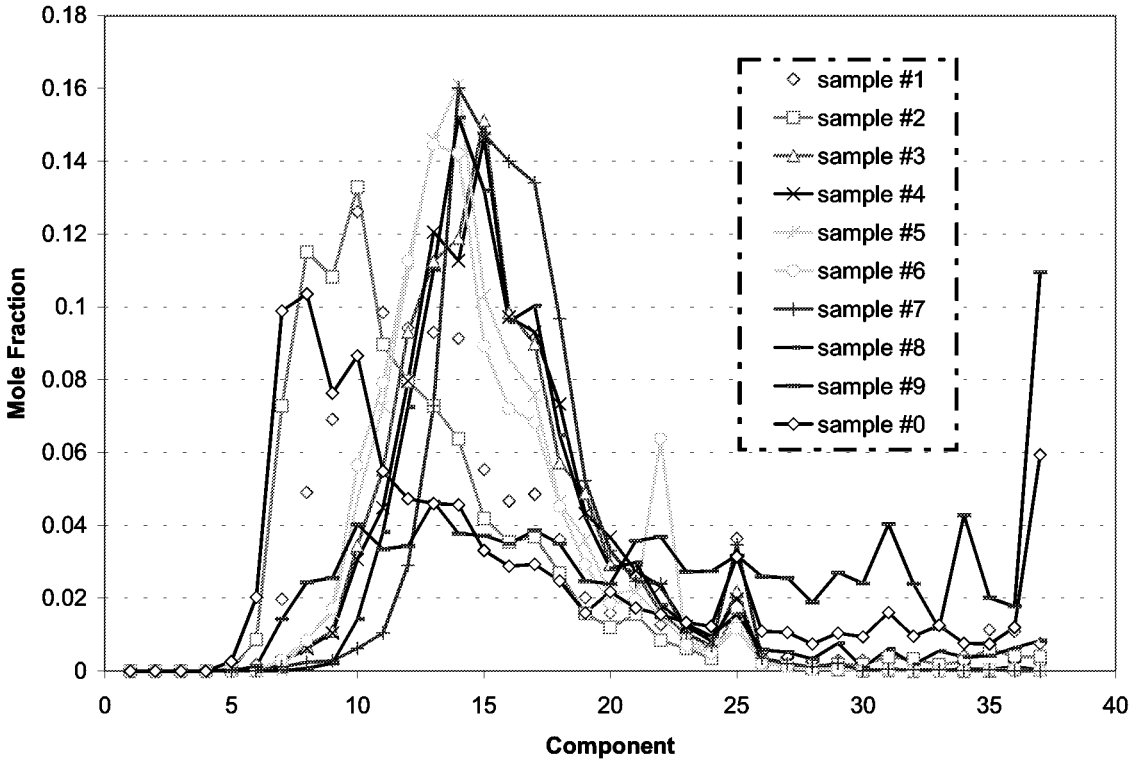

Fig. 4.3–9—Mole fraction of oil samples from CO_2 gravity drainage

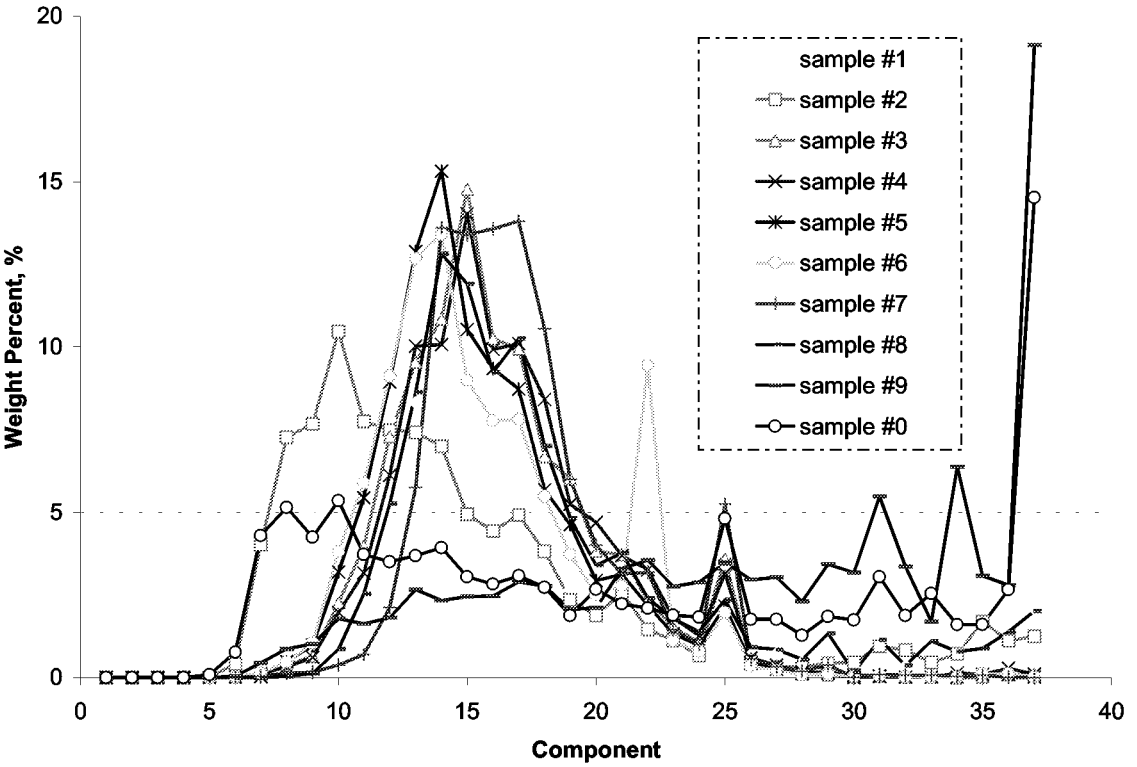

Fig. 4.3–10—Weight percent of components of oil samples from CO_2 drainage

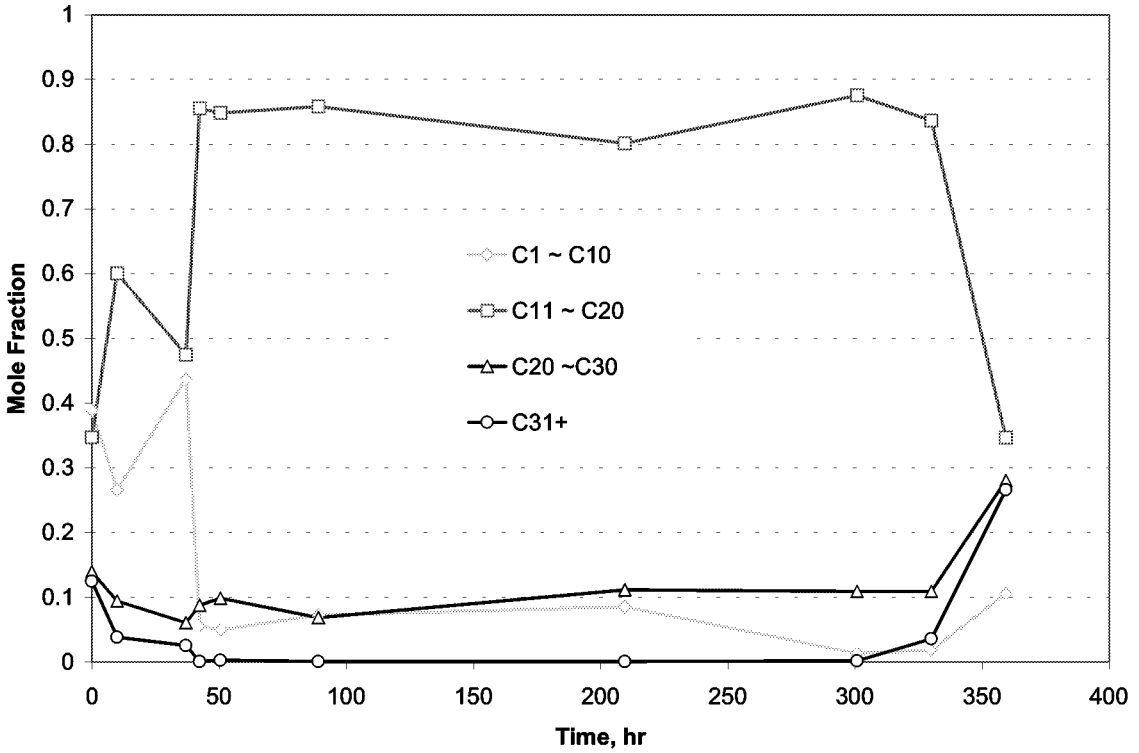

Fig. 4.3–11—Mole fraction of component groups of oil samples during CO_2 drainage

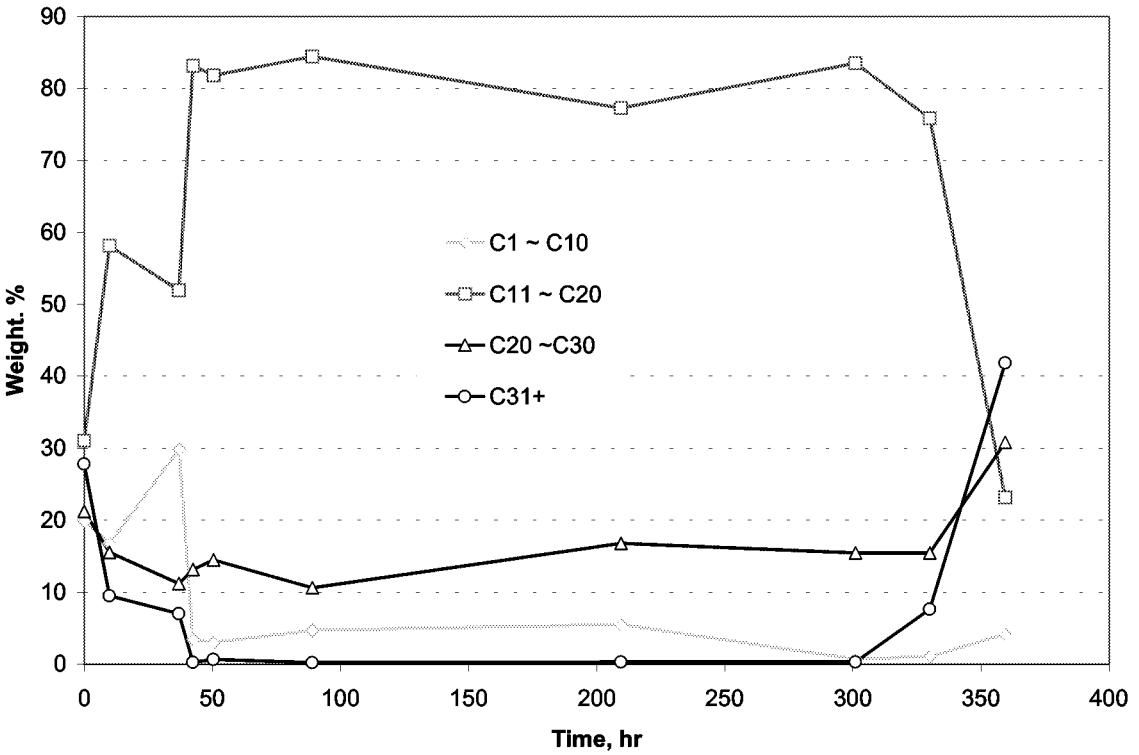

Fig. 4.3–12—Weight percent of component group of oil samples during CO_2 drainage

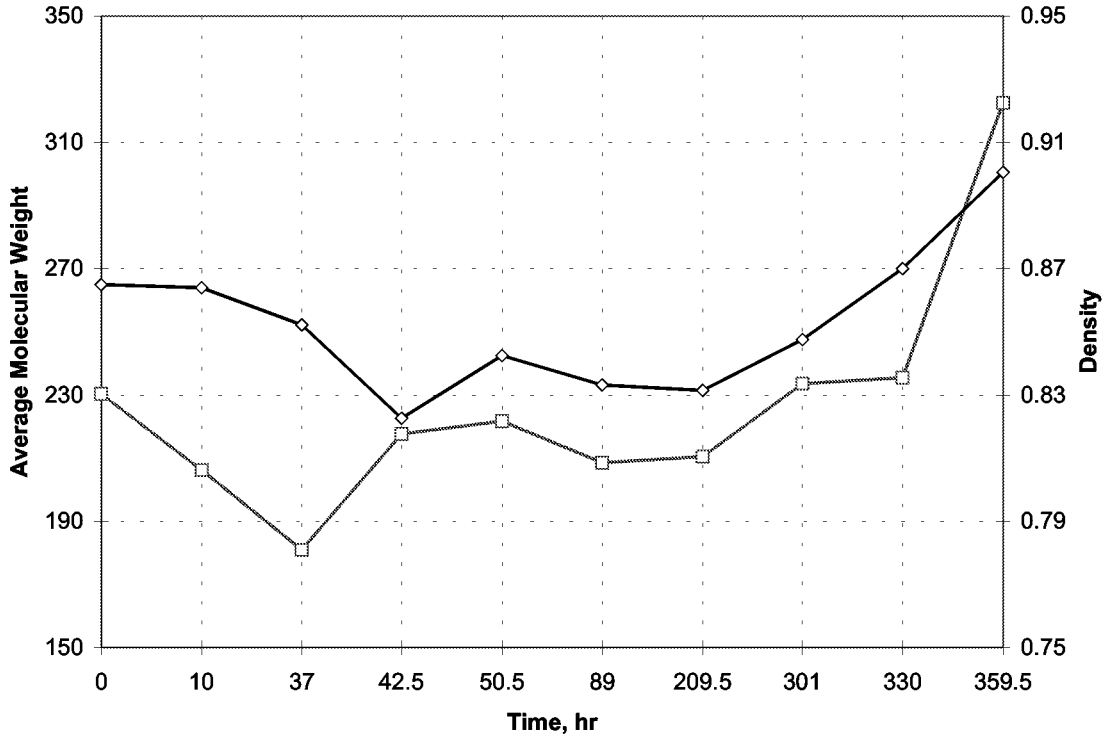

Fig. 4.3–13—Average molecular weight and density of oil samples from CO_2 drainage

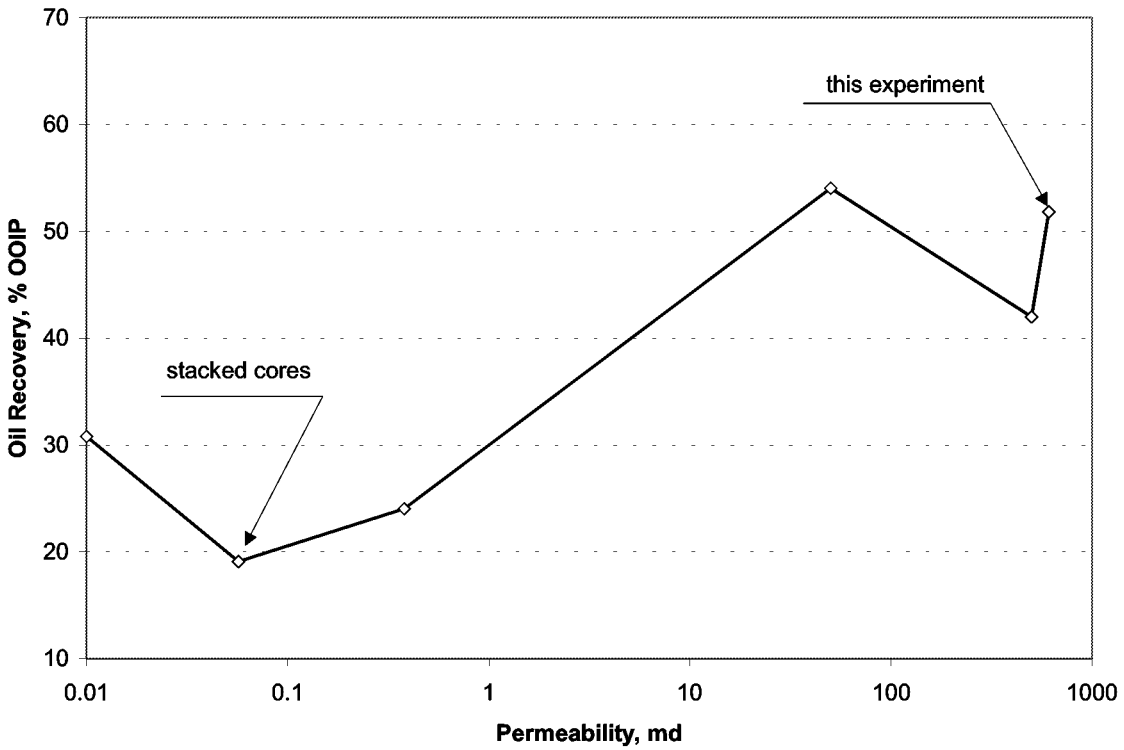

Fig. 4.3–14—Oil recovery curves vs. rock permeability of the six experiments

4.4 INVESTIGATION OF CO_2 GRAVITY DRAINAGE AFTER WATER INJECTION IN FRACTURED SYSTEMS

Introduction

A series of experimental investigations were performed to understand the mechanism of water imbibition followed by CO_2 gravity drainage in the Spraberrry Trend Area. Various experiments were conducted on whole diameter Berea cores and Spraberry cores under the conditions of reservoir temperature and pressures above the MMP of Spraberry crude oil and CO_2. The experiments were designed to simulate the process of CO_2 gravity drainage after water imbibition. One of the main goals was to estimate the efficiency of CO_2 gravity drainage after water injection.

Effects of other critical parameters (temperature, pressure, injection rate, injection pattern, rock permeability and initial water saturation) on CO_2 gravity drainage were also the goal of the investigation. Oil samples produced in the experiments were analyzed using gas chromatography to aid in understanding the mechanism of CO_2-improved oil production from tight matrix blocks.

In order to optimize the CO_2 pilot design in the E.T. O'Daniel Unit of the Spraberry Trend Area, previous experimental results were scaled up to field scale using the mathematical model proposed by Schechter and Guo (1996).[2] The modeling results indicate that significant oil can be recovered from the pilot area by CO_2 flooding in a relatively short time period, depending on matrix permeability, initial water saturation and fracture intensity. A decline curve analysis was also performed to compare the up-scaled experimental data to the CO_2 pilot performance and to investigate the effect of the important parameters on CO_2 gravity drainage.[1]

This paper concentrates on the experimental investigation of CO_2 gravity drainage on artificially fractured Berea cores. Comparisons with results from non-fractured Berea and Spraberry cores that were presented in detail in previous studies[1,3] will also be given in this paper.

Experimentation and Results

Prior to this experimental investigation of CO_2 gravity drainage on artificially fractured cores, five experiments had been performed on Berea and Spraberry reservoir cores. The properties of the cores and partial results are given in Table 4.4-1. Previous experiments were conducted to investigate the efficiency of CO_2 gravity drainage as well as the effects of initial water saturation, Swi and rock permeability on the efficiency under various conditions. In addition, the effects of other parameters on the efficiency of CO_2 gravity drainage were investigated during the earlier experiments. For example, one experiment conducted on a stack of two 2.5-in diameter Spraberry cores was also used to investigate the effects on recovery efficiency of core discontinuity and impermeable layers at the top

and bottom of pay zones. Figure 4.4-1 illustrates the results obtained from the previous experiments.

The experiments performed on an artificially fractured Berea core and an artificially fractured Spraberry core are described below. The Spraberry cores used in the experiments were taken from O'Daniel Well 37 and Shackelford Well 1-38A in Spraberry Trend Area, west Texas.

Description

A series of experimental investigations was designed to model the actual field experience of waterflooding followed by CO_2 injection in the naturally fractured Spraberry Trend Area. The objective of the experiments is to investigate the effect of water imbibition followed by CO_2 gravity drainage on oil recovery under reservoir conditions. Two experiments have been conducted on Berea cores.

Brine

Synthetic brine made using a measured Spraberry composition was used in the experiments. The density and the viscosity of the brine are 1.08 g/cm^3 and 1.21 cp, respectively, at ambient temperature (26 °C) and pressure (12.6 psia).

Oil

Dead Spraberry oil was used in the experiments. The average molecular weight of the dead oil was 230, the oil density was 0.85 g/cm^3 and the oil viscosity was 2.96 cp, measured at ambient temperature and pressure. The composition of the dead oil was measured by gas chromatography and was used as a base for comparing produced oil samples in the experiments.

Core samples

Two Berea cores were used in the experiments. Core #7 was 24.45 cm long, 10.16 cm diameter, 1971 cm^3 bulk volume, 348 cm^3 pore volume (PV), and 17.7%
porosity. Rock permeability to brine was measured seven times at ambient temperature, using three different constant pressure drops and four different flow rates. The permeabilities ranged from 196 to 215 md. with an average of 210 md. Core #8 was 48.74 cm long, 10.16 cm diameter, 3949 cm^3 bulk volume, 781 cm^3 pore volume, and 9.8% porosity.

The rock permeability to brine was also measured at various constant pressure drops and flow rates at ambient temperature. The permeabilities ranged between 394 and 413 md with an average of 404 md. The physical properties of those cores are presented in Table 4.4-2.

Procedure

Figure 4.3-4 (previous chapter) schematically illustrates the setup used in the experiments: drainage cylinder or core holder, visual cell for collecting produced fluids, back-pressure regulator (BPR), pump, CO_2 and brine accumulators, oil-gas separator, and

graduated glassware used to measure oil, gas and brine produced. The whole system was placed in an oven at the reservoir temperature of 58.9 °C.

Core Preparation

The cores were first put into a core holder and cleaned by following the procedure described in previous reports.[1,3] After cleaning, it was taken from the core holder and put into an oven for drying at reservoir temperature (58.9 °C). The core and core holder were oriented vertically and the system evacuated to about 0.6 psia. The bottom valve of the core holder was then opened to synthetic brine. After the core was saturated with brine, additional brine was flushed through the core. Permeability was then measured at various constant pressure drops and flow rates at ambient temperature.

Dead Spraberry oil was then injected into Core #7 from the top of the core at 50 cm^3 /hr. Oil broke through after 215 cm^3 of brine had been produced. The total dead oil injected into the core was 1003 cm^3 (2.88 PV) and the total volume of brine produced from the core was 264 cm^3. Thus, the initial water saturation, Swi, and the initial oil saturation, Soi, were 24.1% and 75.9%, respectively (Table 4.4-2).

After the core was aged five days at reservoir temperature, it was artificially fractured into two pieces, see Fig. 4.4-2. The fracture went through the middle on one side, and deviated from the center by about one-fourth of a radius to the other side. The two ends of the core were then sealed with PT-7 epoxy, to leave only the fracture open for fluid flow.

Core #8 was prepared in a similar way. After the core was cleaned and dried, it was put into a core holder in an oven at 58.9 °C. Dead Spraberry oil was injected into the top of the core at 50 cm^3 /hr and then flow was reversed by injecting oil into the bottom of the core holder at 20 cm^3 /hr. The total volume of brine produced from the core was 518 cm^3. The initial water saturation (Swi) and the initial oil saturation (Soi) were 33.7% and 66.3%, respectively. See Table 4.4-2 for more details. After the core was aged for 55 days at the reservoir temperature, it was artificially fractured into six pieces with two horizontal and three vertical fractures, shown in Fig. 4.4-3.

Water Imbibition

Water injection was performed for Core #7 at reservoir temperature for 28 days. The core holder was vertically placed in the oven. Brine was injected into the bottom of the core at 10 cm^3 /hr for 15 days and then at 50 cm^3 /hr for the last 13 days. The system backpressure was set above 1750 psig. A total of 43.7 cm^3 or 16.6% initial oil in the core (IOIC) was produced. For water imbibition IOIC equals the original oil in place (OOIP). The oil saturation decreases from 75.9% to 63.3% and the water saturation increases to 36.7%.

Water imbibition was similarly conducted for Core #8 at reservoir temperature for 31 days. Brine was injected into the bottom of the core at 1.0 cm^3 /hr for three days and then at 0.5 cm^3 /hr for 28 days. The system backpressure was again set above 1750 psig and 242 cm^3 or 46.9% IOIC was produced.

The oil saturation decreased from 66.3% to 35.3% and the water saturation increased to 64.8%. During water imbibition, 427 cm^3 (0.55 PV) of water was injected with 199 cm^3 of water was produced. Additional results obtained from water imbibition are presented in Table 4.4-3.

CO_2 Gravity Drainage

For Core #7, CO_2 gravity drainage was conducted at reservoir temperature for 38 days. The core holder was placed vertically in the oven. The system backpressure was initially set at 1750 psig and later increased to 1950 psig. CO_2 was injected vertically into the core with flow from top to bottom. The initial flow rate was 10 cm^3 /hr, which was decreased to 5 cm^3 /hr after six hours. After CO_2 gravity drainage continued for 806 hours, the backpressure in the system was decreased gradually from 1950 psig to 0 psig (Fig. 4.4-4). The total volume of oil produced from the core was 90.5 cm^3 (including captured liquids and estimated gas produced with CO_2, note a later discussion) and the volume of water produced was 98.6 cm^3. Oil recovery with CO_2 gravity drainage was 41.1 % IOIC. For CO_2 gravity drainage, IOIC is the amount of oil within the core before CO_2 gravity drainage began or oil left in the core after water imbibition ends (Fig. 4.4-5). The residual oil saturation was 34.0%. The total oil recovery was 50.8% during water imbibition and CO_2 gravity drainage.

CO_2 gravity drainage was conducted at reservoir temperature for 18 days for Core #8. The core holder was also placed vertically in the oven at a backpressure of 1700 psig. CO_2 was injected into the core from the top at flow rates between 0.5 cm^3 /hr and 1.0 cm^3/hr. The total volume of oil produced from the core was 65.6 cm^3 and the total volume of water produced was 137 cm^3 (Fig. 4.4-6). Oil recovery by CO_2 gravity drainage was 23.8 % IOIC (Fig. 4.4-7). The residual oil saturation was 22.8 %. The total oil recovery was 59.5 % during water imbibition and CO_2 gravity drainage. The results obtained from CO_2 gravity drainage are summarized in Table 4.4-3.

Comparisons and Analysis

A series of experimental tests were designed to aid in optimizing the CO_2 pilot design in the E.T. O'Daniel Unit of the Spraberry Trend Area in west Texas. Six experiments were performed, three on Berea and three on reservoir cores. The reservoir cores were from either Spraberry O'Daniel Well 37 or Shackelford Well 1-38A. The experiments were performed to investigate the effects of initial water saturation, Swi, and rock permeability on the efficiency of CO_2 gravity drainage. The properties of core samples used in the experiments and the experimental results are summarized in Table 4.4-1 and plotted on Fig. 4.4-1.

These studies show that CO_2 gravity drainage could significantly enhance oil recovery in the naturally fractured Spraberry Trend Area. The efficiency of CO_2 gravity drainage decreases as rocks become tighter and water saturation increases. The effect of water saturation on oil recovery seems to be more significant than rock permeability. Core discontinuity and impermeable layers at the top and bottom of the pay zone could affect

the efficiency of CO_2 gravity drainage. Changes of CO_2 injection rate could help in enhancing oil recovery during CO_2 gravity drainage process.

The experiments presented in this paper were designed and performed to investigate CO_2 gravity drainage after water injection in an artificially fractured core. These were done because reservoirs in the Spraberry Trend area are naturally fractured with very tight matrices. Initial investigations used Berea cores. The properties of Cores 6, 7, and 8 are given in Table 4.4-2. For comparison, Core #6 has no fractures, but was placed in the gravity drainage cell during water imbibition and CO_2 drainage where all the surfaces were exposed to either water or CO_2. The results obtained in the experiments are presented in Table 4.4-3, and are plotted in Figs. 4.4-8 and 4.4-9. The following analyses are based on these results.

Efficiency of CO_2 Gravity Drainage

The experimental results show the efficiency of CO_2 gravity drainage after water injection is significant, which is consistent with previous results.[1,3] The water saturations of the cores are high after water injection with IOIC reduced well below OOIP. The oil recovery, however, is improved by more than 20% OOIP, by CO_2 gravity drainage. This is explained by the low interfacial tension between oil and CO_2 in the core.

Much of the higher oil recovery for Core #7 was from production during system pressure blowdown just before the experiment was terminated as shown in Figs. 4.4-5 and 4.4-8. This action produced 12% IOIC. In addition, brine was displaced during CO_2 drainage. This indicates that some water would be produced during CO_2 gravity drainage in the Spraberry Trend when CO_2 injection is proceeded by water flooding.

Six oil samples were taken during CO_2 gravity drainage and analyzed using gas chromatography (GC). The results are shown in Fig. 4.4-10. The injected oil was dead Spraberry oil, with which the core was saturated. Figure 4.4-10 shows that most of the oil produced during CO_2 gravity drainage consists of the component group C_{11} - C_{20} (~80 weight %). This figure shows that there were essentially no C_{10}- components in the produced oil samples, as found in the dead oil injected into the core. As explained in a earlier paper, the C_{10}- components were produced with the high volume of CO_2 separated at the separator, and thus not collected in the oil samples.[2] For this reason the reservoir (core) condition produced oil volume was corrected for the C_{10}- loss or produced with the CO_2 gas. Theresidual oil saturation and the oil recovery during CO_2 gravity drainage process were both appropriately adjusted. The shrinkage factor of 1.25 was used to correct the data.[2]

The GC results are re-plotted as the weight percent of component groups with time in Fig. 4.4-11. The figure shows that the C_{11-20} components were being disproportionally extracted from the oil by the second sample that was taken during the forth day after the start of CO_2 injection. The C_{11}-C_{20} component group was roughly 80 wt% of the C_{11+} oil production until near the end of the test. The last two samples were taken during blowdown and had compositions closer to that of the original oil, but with higher heavier ends. These last two samples were probably a combination of oil that had the lighter components stripped by CO_2 and oil that had not been contacted or at least stripped by

CO_2. Figure 4.4-12 shows the changes in the average molecular weight of the oil samples versus time.

Effect of Fractures

Figure 4.4-8 shows that the oil recovery curves of the three cores are similar. IOIC was used to calculate the oil recovery curves in each. The results were unexpected as we anticipated higher oil recovery from the fractured cores. Since different conditions were used in each experiment, the unexpected results can be explained.

Core #6 was placed in a gravity drainage cell where all the outside surface area was exposed to CO_2 during CO_2 drainage, thus exposing greater surface area. Because of the fractures in Cores #7 and #8, they were not placed in the gravity drainage cell, but separately in a core sleeve in a core holder. The two ends on Core #7 were sealed so that only the fracture surfaces were exposed to CO_2. As Core #8 did not have the two ends sealed, it had a greater area exposed to CO_2. However, the experiment on Core #8 was terminated before production ended. Oil was only produced for 18 days, which was about half the time allowed in the other two experiments.

Allowing equal exposure surface area and drainage time should result in a higher oil recovery for the fractured systems.

Effect of Initial Water Saturation

Comparing the initial water saturations before CO_2 injection and the oil recoveries for the three cores, it appears that lower water saturation at the start of CO_2 injection results in higher oil recovery. This result is consistent with our previous conclusion.[1,3] It should be noted that Core #7 had a lower water saturation when water injection was terminated. The probable reason is that water flow occurred only in the fracture. If allowed to go to termination, Core #8 could well have achieved a higher oil recovery by CO_2 drainage. Oil recovery, however, may not be as high as Core #7, because of the higher water saturation at the start of CO_2 drainage, see Table 4.4-3 for details.

Effect of Permeability

There appears to be a simple relationship between oil recovery and rock permeability (Tables 4.4-2 and 4.4-3). Fractures in a core introduce more complexity into the analysis; however, it seems that initial water saturation when CO_2 drainage starts affects oil recovery more than does permeability.

Conclusions

From the series of experiments performed, we believe that CO_2 gravity drainage could significantly enhance oil recovery after waterflooding in the naturally fractured Spraberry Trend Area. The results from these experimental investigations support our previous conclusions.[1,3] This study supports previous indications that the efficiency of CO_2 gravity drainage is significantly affected by the water saturation at the start of CO_2 drainage. Fractures in a core could improve the efficiency of CO_2 flooding, but more investigations

using reservoir rocks need to be performed to clarify our concepts of the effects of fractures on the efficiency of CO_2 gravity drainage.

Oil produced during much of the CO_2 gravity drainage process, yields an increased concentration of components C_{11} -C_{20}. This indicates significant extraction by CO_2 during the CO_2 gravity drainage process.

During CO_2 gravity drainage after waterflooding, water in rock is moveable because of high water saturation indicating that water would be produced during CO_2 gravity drainage in the Spraberry Trend if waterflooding was performed before CO_2 injection.

Nomenclature

IOIC = initial oil in core, cm^3
IWIC = initial water in core, cm^3
OOIP = original oil in place (core), cm^3
S_{oi} = initial oil saturation, %
S_{wi} = initial water saturation, %
CO_2 = Carbon Dioxide
PV = pore volume
BPR = back pressure regulator

References

1. Schechter, D.S., *et al*: "Advanced Reservoir Characterization and Evaluation of CO_2 Gravity Drainage in the Naturally Fractured Spraberry Trend Area," Third Annual Technical Progress Report, Contract No. DE-FC22-95BC14942, U.S. DOE (Dec. 1998).
2. Schechter, D.S. and Guo, B.: "Mathematical Modeling of Gravity Drainage after Gas Injection into Fractured Reservoirs," paper SPE 35170 presented at the 1996 SPE Improved Oil Recovery Symposium, Tulsa, April 22-24.
3. Li, Hujun, "Experimental Investigation of CO_2 Gravity Drainage in Spraberry and Berea Whole Core," the Fifth Naturally Fractured Reservoir Symposium, Socorro, NM, USA, October 28, 1999.
4. Conway, P.I., Damm, M., and Andersen, P.M.: "Full Field Dual Porosity Modeling of a Complex Fractured Chalk Oil Reservoir Subject to Both Gas and Water Injection," paper SPE 36931 presented at the 1996 SPE European Petroleum Conference, Milan, October 22-24.
5. Elkins, L.: "Condensed Report: Spraberry CO_2–Gravity Drainage" Telephone Conference Call, May 14, 1996.
6. Luan, Z.: "Some Theoretical Aspects of Gravity Drainage in Naturally Fractured Reservoirs," paper SPE 28641 presented at the 1994 SPE Annual Technical Conference and Exhibition, New Orleans, September 25-28.

7. Horle, T.: "Laboratory Studies of Capillary Continuity in Fracture/Matrix Systems," *SPERE* (August 1990).
8. Suffridge, E.E. and Renner, R.A.: "Diffusion and Gravity Drainage Tests to Support the Development of a Dual Porosity Simulator," paper presented at the 6th European IOR-Symposium, Stavanger, May 21-23, 1994.

SI Metric Conversion Factors

cp x 1.0* *E*–03	= Pa.s	ft x 3.048* *E* +01	= cm
ft^2 x 9.290 304* *E* +02	= cm^2	ft^3 x 2.831 685 *E* +04	= cm^3
inch x 2.54* *E* +00	= cm	md x 9.869 233 *E*–04	= mm^2
psi x 6.894 757 *E* +00	= kPa		

*Conversion factor is exact.

Table 4.4-1 — Physical properties of the core samples used in the previous experiments and partial results obtained

Core Sample Number	1	2	3	4	5	6
Core Type	Berea	Berea	Spraberry	Spraberry	Spraberry	Berea
Configuration	Continuous	Continuous	Continuous	Continuous	Stacked	Continuous
Time of CO_2 injection	From begin	From begin	From begin	From begin	From begin	After water injection
Length, *L*, cm	55.52	55.25	55.0	55.25	24.77 & 25.08	55.25
Diameter, *D*, cm	10.16	10.16	10.16	8.89	6.53 6.58	10.16
Porosity, ϕ, %	18.7	13.0	10.0	11.1	10.7	22.43
Permeability, k_{brine}, md	500	50	0.01	0.38	0.057	610.0
S_{wi}, %	35.0	29.3	38.6	45.0	37.6	66.5
S_{or}, %	37.5	32.5	42.5	41.8	50.5	28.0
IOIC, cm^3	544.5	411.1	273.8	209.3	111.0	336.3
IWIC, cm^3	293.2	171.2	172.1	171.3	67.0	667.7
Oil Recovery, η_r, %	42.0	54.0	30.8	24.0	19.1	18.5
Time, *t*, day	6	220	190	167	331	36

Table 4.4-2 —Properties of the artificially fractured and non-fractured Berea core samples

Core Sample Number	6	7	8
Core Type	*Berea*	*Berea*	*Berea*
Number of Fractures	*0*	*1*	*5*
Sealed End-Sections	*No*	*Yes*	*No*
Core Orientation	*Vertical*	*Vertical*	*Vertical*
Length, L, cm	*55.25*	24.45	48.74
Diameter, D, cm	10.16	10.16	10.16
Bulk Volume, V_b, cm^3	4476.6	1971.3	3949.2
Pore Volume, V_p, cm^3	1004.0	348.0	781.0
Porosity, ϕ, %	22.43	17.65	19.80
k_{brine}, md	610.0	210.0	404.0
S_{wi}, %	42.1	24.1	33.7
S_{oi}, %	57.9	75.9	66.3
IOIC, cm^3	581.3	264.0	518.0
IWIC, cm^3	422.7	84.0	263.0
Aging Time, t, day	10	5	55

Table 4.4-3 —Comparison of results from the artificially fractured and non-fractured Berea core samples

	Core Sample Number	6	7	8
	S_{wi}, %	42.1	24.1	33.7
Water Imbibition	S_{oi}, %	57.9	75.9	66.3
	IOIC, cm^3	581.3	264.0	518.0
	IWIC, cm^3	422.7	84	263.0
	S_{we}, %	61.5	36.7	64.8
	S_{oe}, %	38.5	63.3	35.2
	V_{op}, cm^3	194.4	43.7	242.7
	Oil Recovery, η_w, %	33.4	16.6	46.9
	Time, t, day	20	28	31
	S_{wi}, %	61.5	36.7	64.8
CO_2 Gravity Drainage	S_{oi}, %	38.5	63.3	35.2
	IOIC, cm^3	386.5	220.3	275.3
	IWIC, cm^3	617.5	127.7	505.7
	S_{wr}, %	38.8	8.4	47.2
	S_{or}, %	29.2	42.5	28.5
	V_{op}, cm^3	93.2	72.5	52.6
	Oil Recovery, η_c, %	24.1	32.9	19.1
	Time, t, day	36	38	18
	Total Oil Recovery, η_t, %	49.4	44.0	57.0

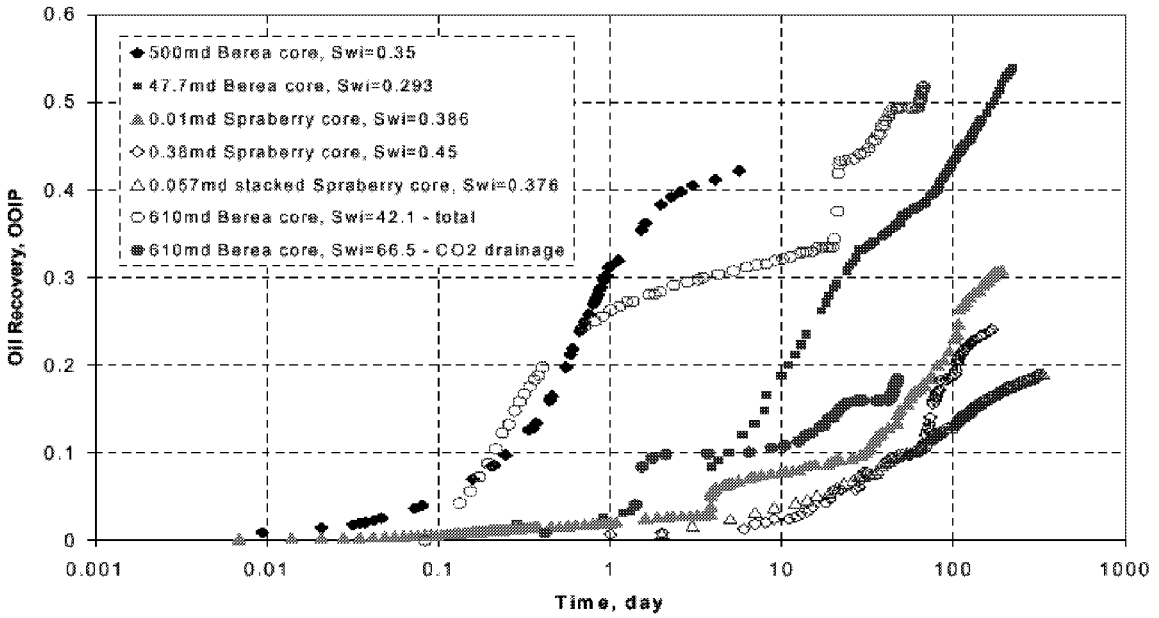

Fig. 4.4-1 —Oil recovery curves obtained from the previous six experiments with different permeabilities and initial water saturations

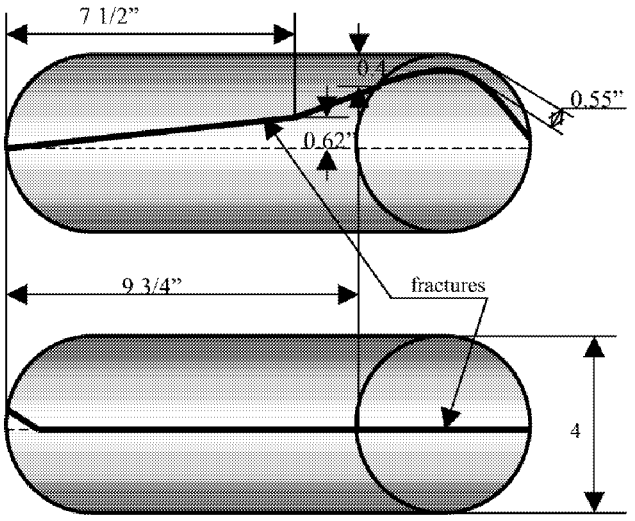

Fig. 4.4-2 —Sketch of the fractures split on Core #7

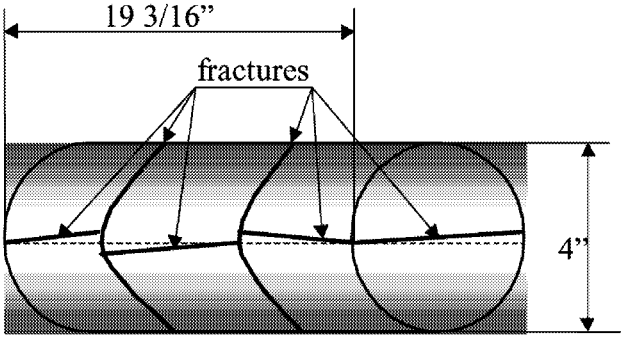

Fig. 4.4-3 —Sketch of the fractures split on Core #8

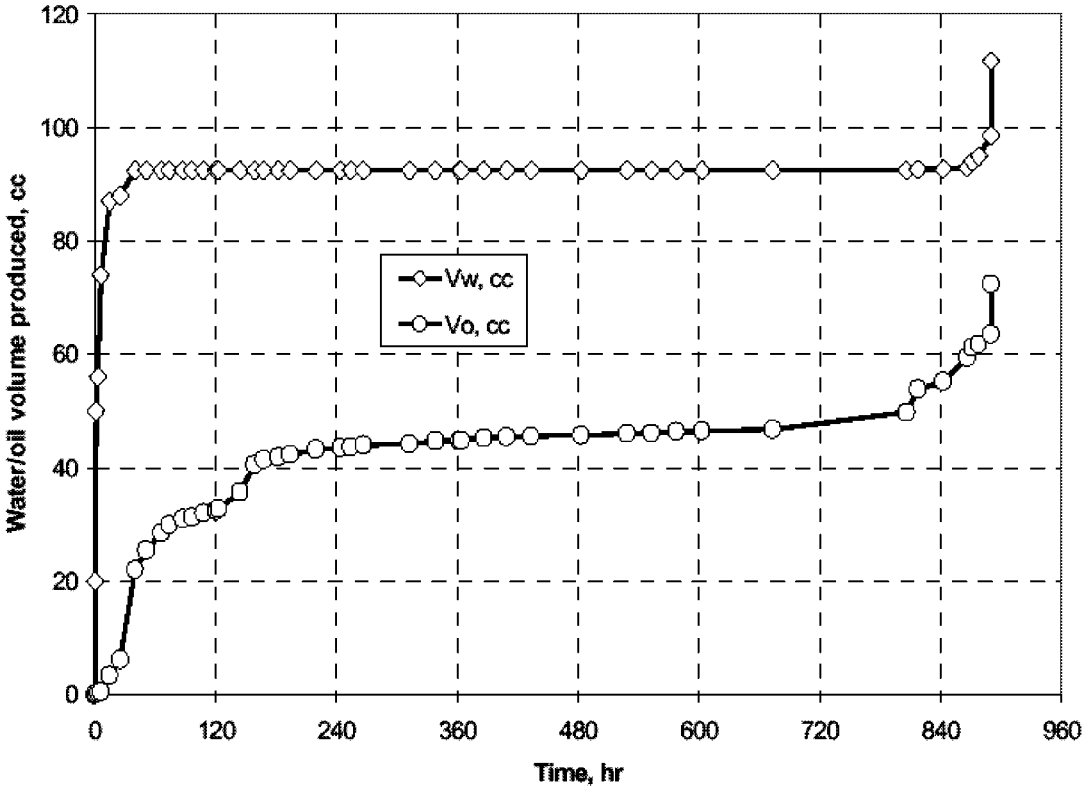

Fig. 4.4-4 — Water and oil produced during CO_2 gravity drainage for Core #7

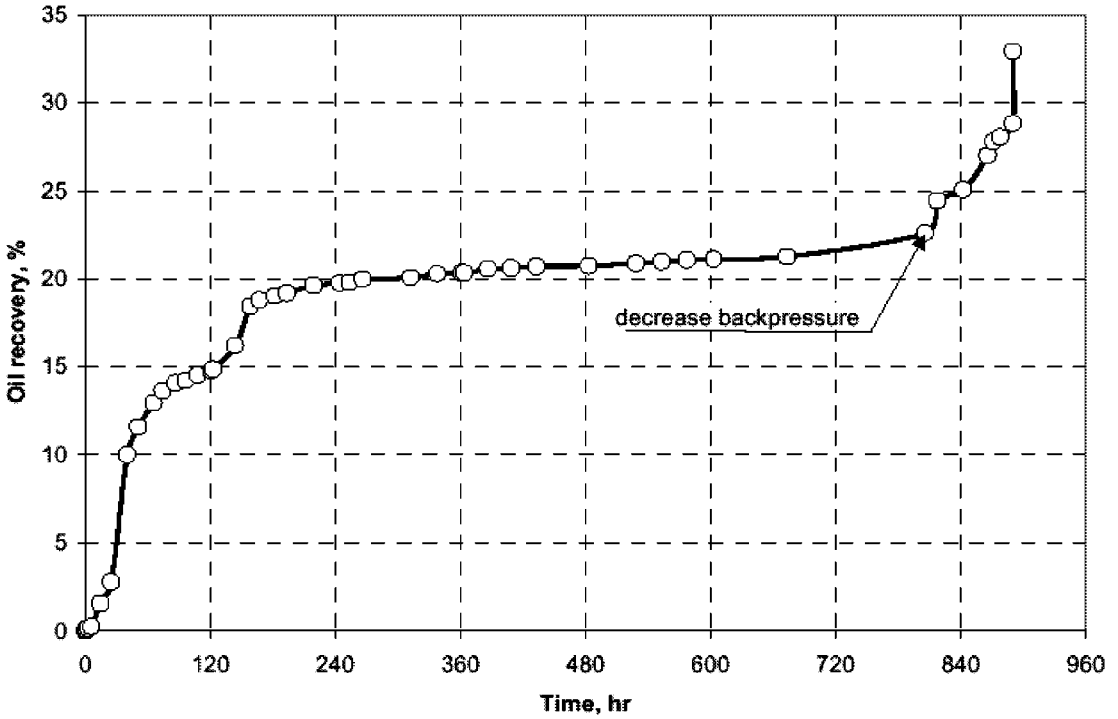

Fig. 4.4-5 —Oil recovery by CO_2 gravity drainage for Core #7

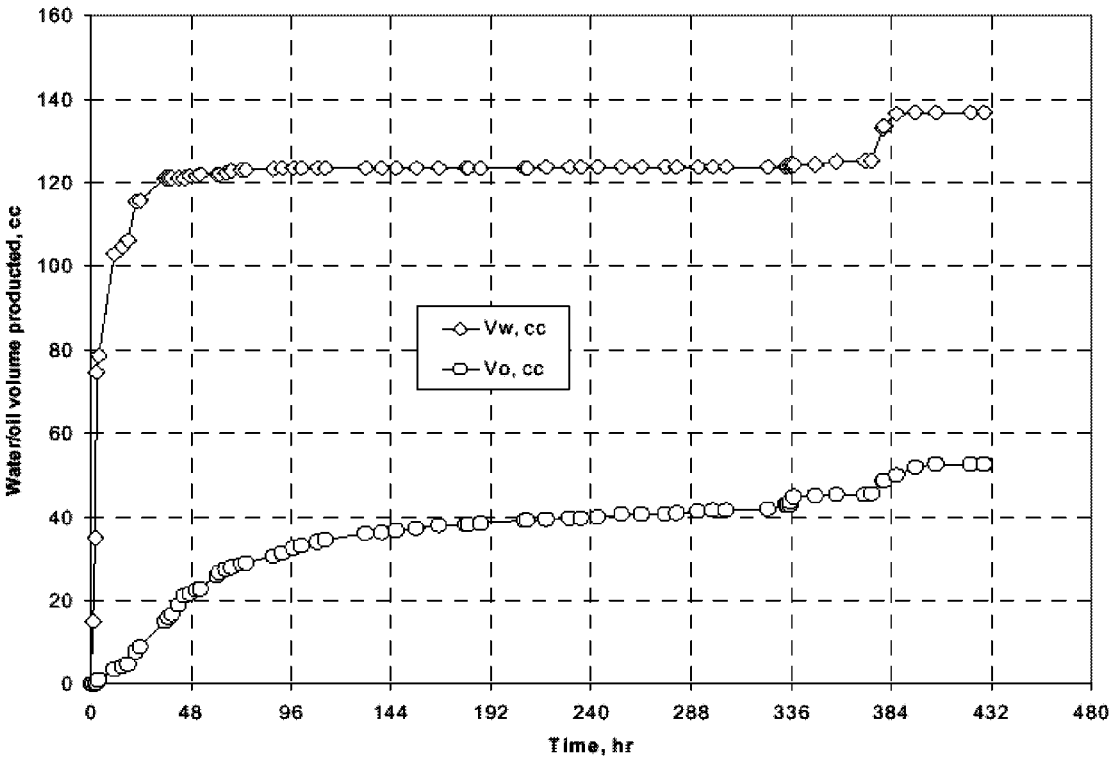

Fig. 4.4-6 — Water and oil produced during CO_2 gravity drainage for Core #8

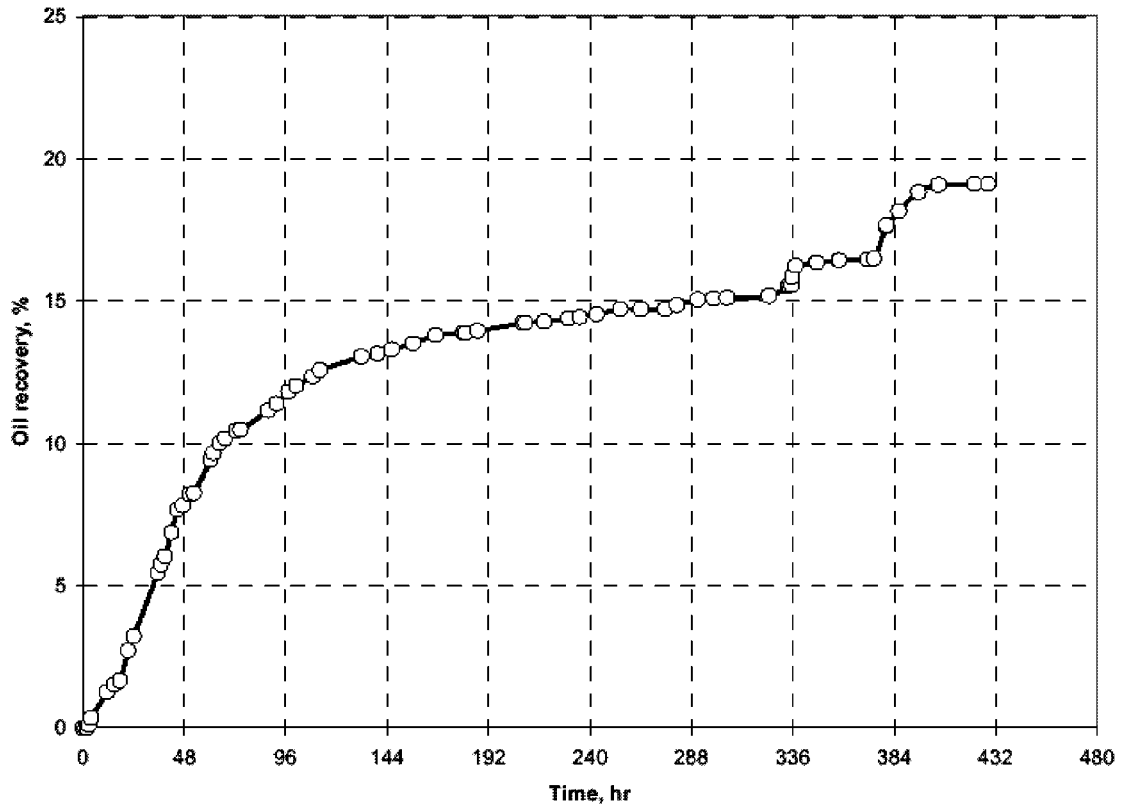

Fig. 4.4-7 — Oil recovery by CO_2 gravity drainage for Core #8

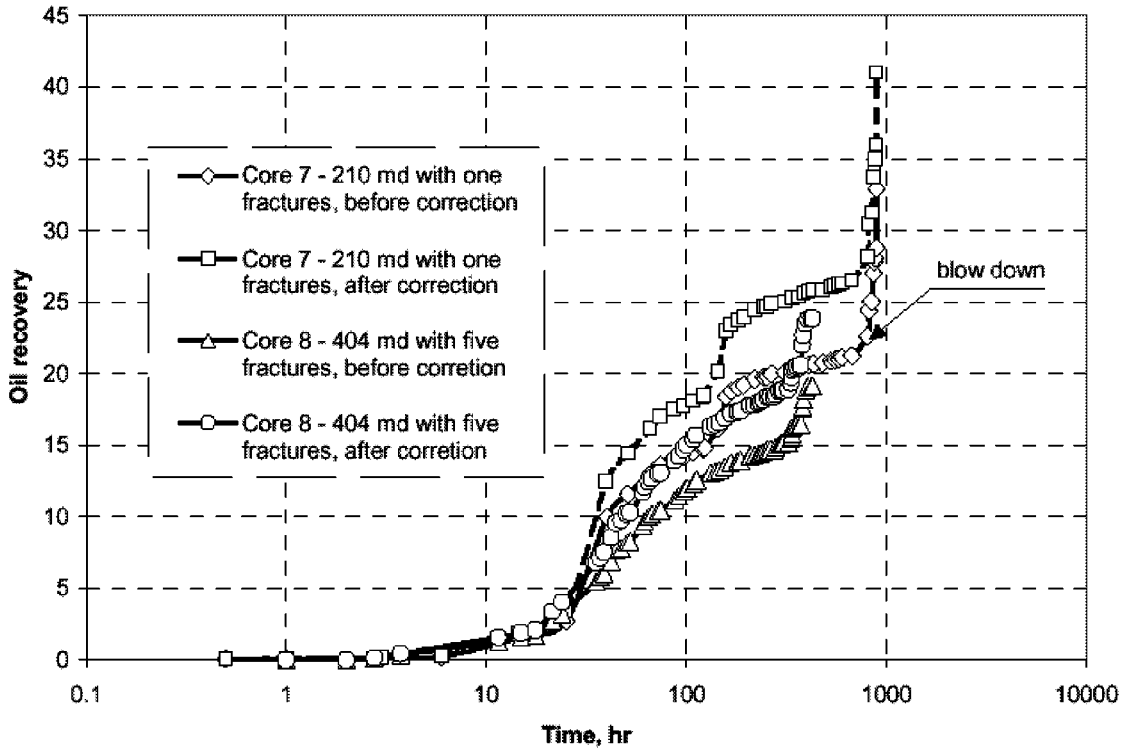

Fig. 4.4-8 —Oil recovery with correction of Cores #7 and #8

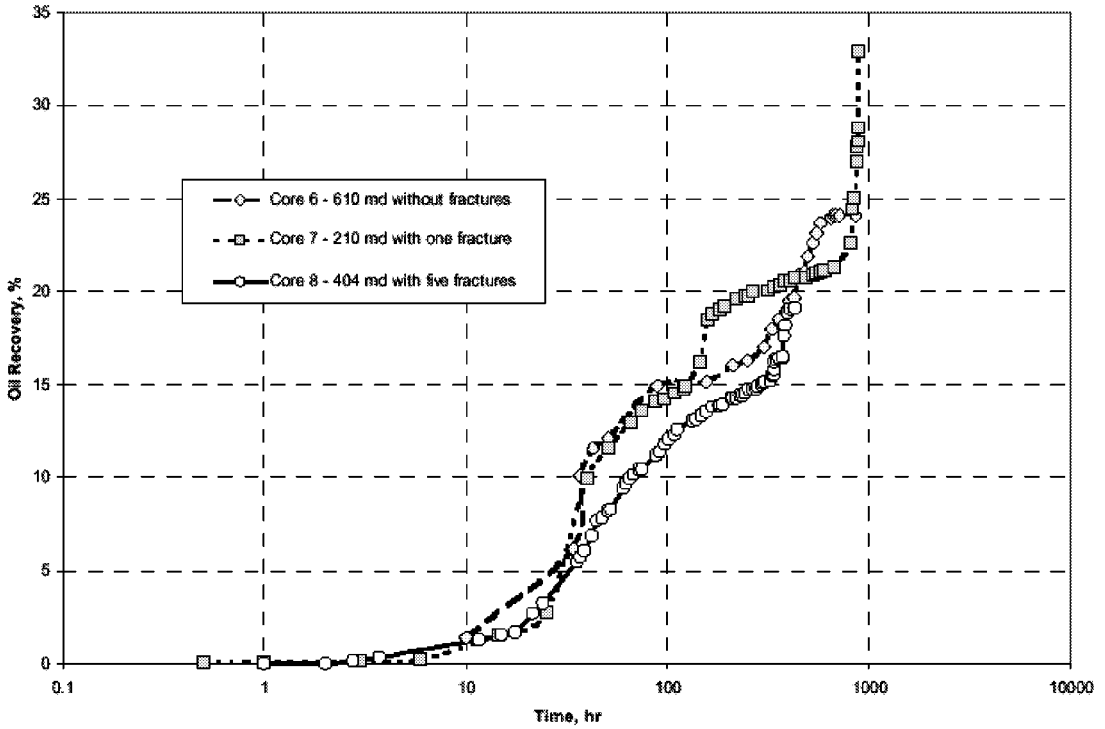

Fig. 4.4-9 —Comparison of oil recoveries obtained during CO_2 gravity drainage from the artificially fractured cores and non-fractured core

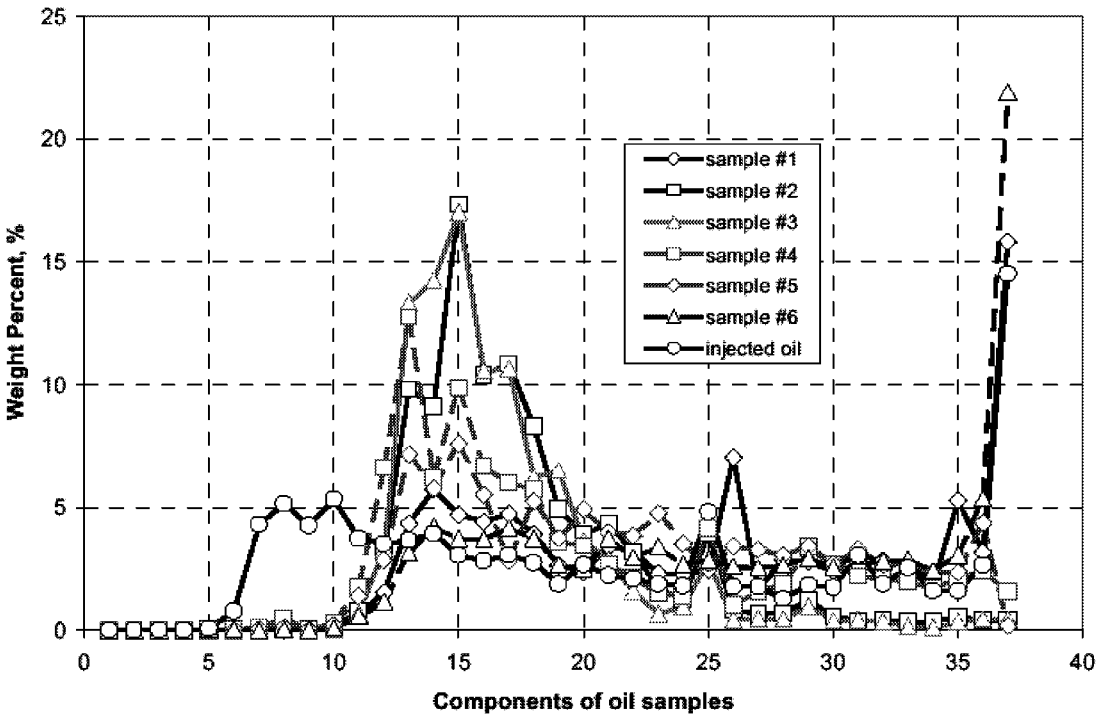

Fig. 4.4-10 — Weight composition of oil samples produced during CO_2 drainage

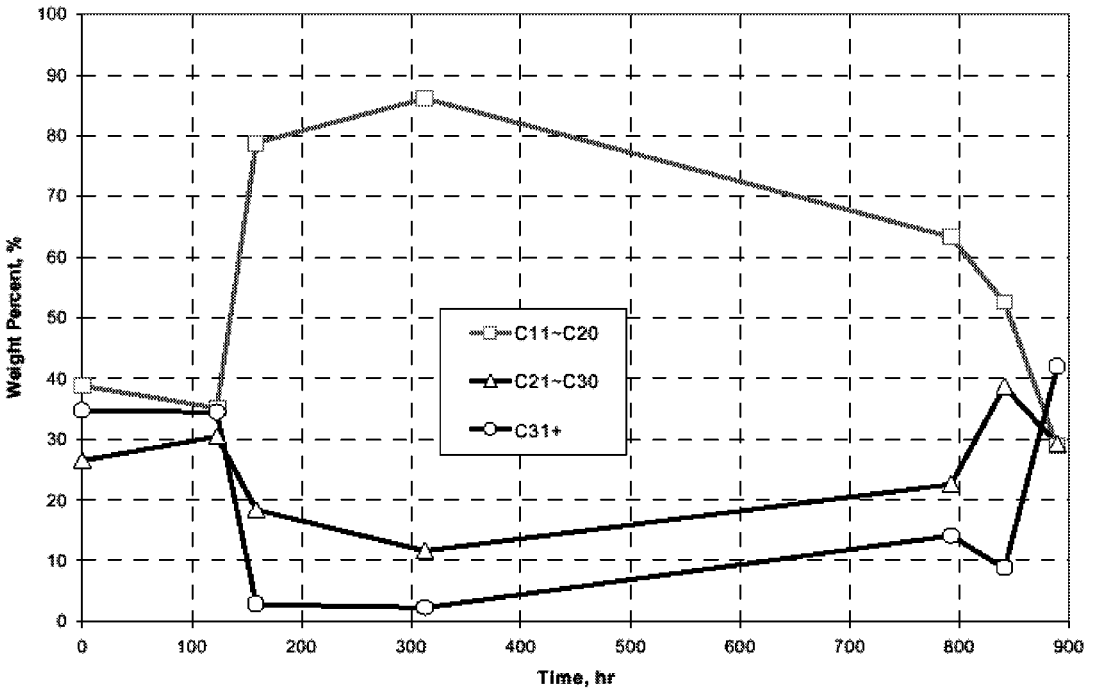

Fig. 4.4-11 —Changes of C_{11+} component distribution in weight % versus CO_2 injection time

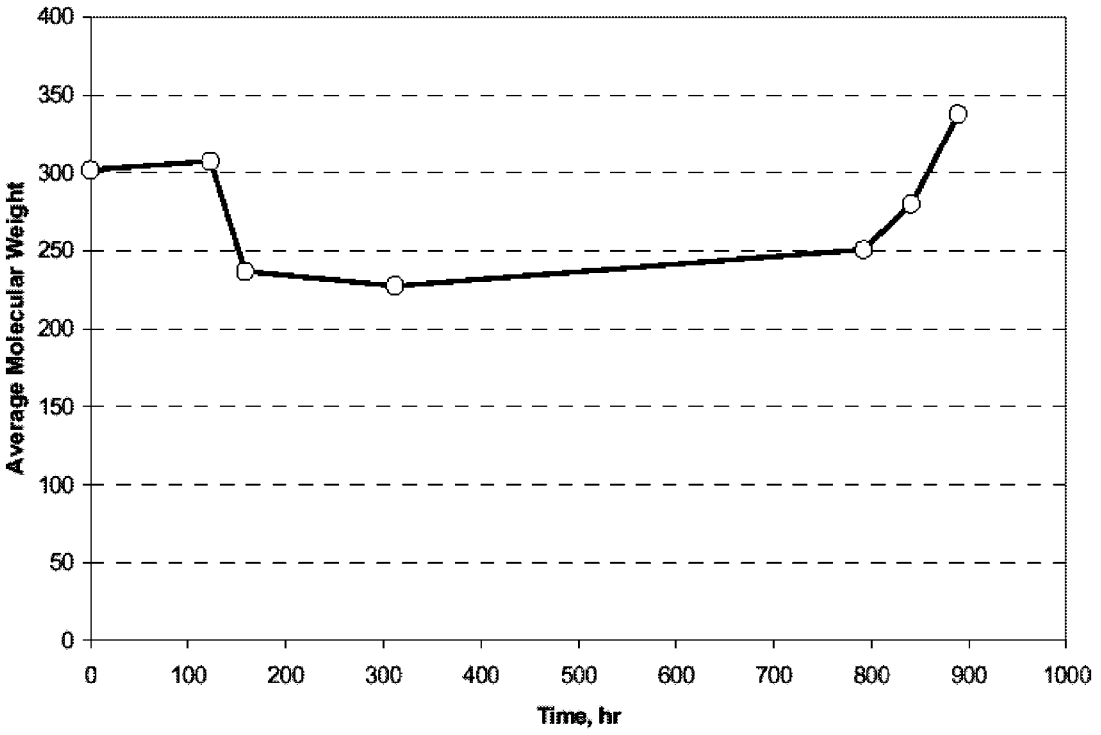

Fig. 4.4-12 —Changes of average molecular weights of C_{11+} components with time

4.5 MATHEMATICAL MODELING OF CO_2 GRAVITY DRAINAGE

Introduction

Because fractures are highly conductive to gas and gas is the non-wetting phase in the rock matrix, gas injection into fractured reservoirs has been traditionally considered as an inefficient method for enhancing oil recovery from fractured reservoirs. However, the Midale Pilot[1] indicated that the efficiency of CO_2 injection into fractured reservoirs is not as low as expected. The only explanation is that when a non-equilibrium gas is injected into the fractured system at elevated pressure, compositional effects become active between the gas in the fractures and oil in the matrix. Due to multi-contact mechanism, light hydrocarbons in the oil can be extracted from the virgin oil bank forming a ``gas"-rich light liquid phase and an oil-rich heavy liquid phase. This kind of phase split has been reported by several investigators including Lansangan and Smith[2]. The interfacial tension (IFT) between phases is low compared to that between virgin oil phase and gas phase. Therefore, the capillary pressure threshold may be overcome by gravity resulting in gravity drainage of oil from the matrix blocks. In order to understand the mechanism of gravity drainage and predict the response of fractured reservoirs to gas injection, a mathematical model of the process is desirable.

Equilibrium Gravity Drainage. Studies on gravity drainage were conducted a century ago when King[3] investigated the principles and conditions of aquifer motion. Investigations of gravity drainage of oil in oil reservoirs were initiated in early 40's of this century. Leverett[4] and Katz[5] presented data and discussed the theory relating capillary and gravitational forces acting on liquids contained in a sand body. Stahl *et al.*[6] conducted experiments to investigate behavior of free-fall gravity drainage of water and oil in an unconsolidated sand. Elkins *et al.*[7] presented a simplified theory of regional drainage of oil from an up-structure location to a down-structure location due to gravity assuming zero capillary pressure gradient. Cardwell and Parsons[8] presented a governing equation for the free-fall gravity drainage process. They could not solve the equation because of its non-linearity. By neglecting the term involving the product of permeability and variation of capillary pressure with saturation, they derived a solution for the simplified cases using the concept of a demarcator. Terwilliger *et al.*[9] conducted experimental and theoretical investigations on gravity drainage performance under controlled flow rates. Their theory was based on a Buckley and Leverett[10] approach. Nenniger and Storrow[11] presented an approximate series solution for free-fall gravity drainage based on film flow theory. The results accurately matched experimental data obtained from a highly permeable pack of glass beads. Essley *et al.*[12] analyzed the gravity drainage process and final oil recovery in a steeply dipping reservoir. Templeton and Nielsen[13] experimentally investigated the counterflow segregation of fluids under gravitational force field using glass beads. Dumore and Schols[14] performed experimental studies of free-fall gravity drainage of oil in the laboratory and developed a drainage capillary pressure function. Dykstra[15] generalized the approximate theory presented by Cardwell and Parsons. His mathematical model matched some experimental data with assumed permeability values. Hagoort[16]

theoretically analyzed vertical displacement efficiencies of forced and free-fall gravity drainage processes. He derived a governing equation for saturation during free-fall gravity drainage, which is identical to that given by Cardwell and Parsons except that he used the Leverett *J*-function for expressing capillary pressure. He again did not solve the saturation equation because of its non-linearity. Haldorson *et al.*[17] evaluated the gravity drainage mechanism in an oil field using compensated neutron logs, centrifugal displacements and an analytical stochastic approach. Nectoux[18] investigated the velocity influence on sweep efficiency in oil drainage experiments. Compositional effects were also discussed in his paper. Jacquin *et al.*[19] investigated gravity drainage with fluids not in equilibrium. Their laboratory experiments show that the oil recovery by gravity drainage increases if the content of intermediate components in the gas or in the liquid phase increases.

Low IFT and Non-equilibrium Gravity Drainage. Pavone *et al.*[20] conducted experiments to investigate free-fall gravity drainage at low IFT. The IFT of the C_1/C_7 mixture utilized in their experiments was 0.53 dyne/cm. They found that a drainage process can be divided into two phases. During the first phase, almost 50% of the oil in place was produced. The second phase began suddenly at a breakpoint or smoothly on the semilog plot. The second-phase production rate was low but led to more than 20 % additional oil production. They also presented a non-linear governing equation for gas saturation during drainage. Their governing equation is similar to the one given by Cardwell and Parsons. They linearized the governing equation by assuming straight-line permeability curve and logarithmic capillary pressure curve. They solved the linearized governing equation analytically assuming that the minimum gas saturation is always at the outlet of the core (the demarcator is always at the bottom of the core). They matched some experimental data by dual use of the analytical solution, i.e., the analytical solution was used twice for early and later times, respectively, to match the same set of experimental data. Stensen *et al.*[21]performed experiments for analyzing the effect of IFT on gravity drainage. They employed brine and a C_1/n-C_7 mixture having IFT ranging from 76 (reported in the paper) to 0.5 dyne/cm. Suffridge and Renner[22] investigated gravity drainage experimentally under constant and varying IFT in fractured and non-fractured cores. The varying IFT was obtained by first placing C_{10} in the core, and then letting C_1 to diffuse into the core. Vilva and Meyer[23] resented a formulation for oil desaturation curves used for reservoir simulation. Schechter *et al.*[24] reported experimental results of investigations on low IFT imbibition and drainage. They utilized brine/IPA/i-C_8 systems with IFT's of 0.1, 1.07, and 38.1 dynes/cm and density differences of 0.11, 0.21, and 0.33 g/cc, respectively. They also presented analyses of imbibition and drainage mechanisms. It was concluded that gravity drainage of wetting phase from fully saturated vertical cores occurs for inverse Bond numbers less than 1. Luan[25] discussed theoretical aspects of free-fall gravity drainage in naturally fractured reservoirs. He solved the governing equation given by Hagoort[16] analytically and numerically. However, he used the same boundary condition as that utilized by Pavone *et al.*, that is, the demarcator is assumed to be always at the bottom of the core. Espie *et al*[26] investigated gravity drainage/waterflood interaction in the laboratory. They found that injection of water into a gravity drained oil column with high gas saturations improves the mobilization of a dry oil bank. Catalan *et al.* [27] reported their results of investigations on the effects of

wettability and heterogeneities on the recovery of waterflood residual oil with low pressure inert gas injection assisted by gravity drainage. Experiments on forced gravity drainage by gas injection under varying pressures were performed and analyzed. They concluded that tertiary gravity drainage in water-wet systems is most efficient when the oil can spread on water in the presence of gas. Blunt *et al.*[28] presented a theoretical and experimental treatment of three phase flow in water-wet porous media from the molecular level upwards. They found that oil spontaneously spreads as a layer between water and gas in most three-phase systems. Their experimental data on gravity drainage in a capillary matched prediction by their theoretical model. Recently Oyno *et al.*[29] conducted laboratory experiments on composite cores at reservoir conditions using recombined reservoir fluids to investigate the potential of secondary and tertiary recovery using gas injection, where gravity drainage is regarded as an important recovery mechanism. Although they recognized that the time required to reach capillary/gravity equilibrium depends on oil/gas density difference, gas/oil IFT, and molecular diffusion in both gas and oil phases, they could not identify conditions under which each factor dominates.

In summary, the literature reveals that three different gravity drainage processes in porous media have been investigated: (i) forced gravity drainage by gas injection and controlled flow rate, which occurs when gas is injected into steeply dipping reservoirs, (ii) simulated gravity drainage by centrifuging, which exists only in the laboratory, and (iii) free-fall gravity drainage, which takes place in naturally fractured reservoirs after depletion of oil in the fractures or gas injection into the fractures. The free-fall gravity drainage, which is representative of gas injection into a depleted fractured reservoir, has been investigated by Leverett[4], Stahl *et al.*[6], Cardwell and Parsons[8], Nenniger and Storrow[11], Templeton and Nielsen[13], Dumore and Schols[14], Dykstra [15] , Hagoort[16], Jacquin *et al.*[19], Pavone *et al.* [20], Stensen *et al.*,[21] Suffridge and Renner,[22] Schechter *et al.*,[24] Luan,[25] and Oyno *et al.*[29]

Unlike forced gravity drainage, free-fall gravity drainage cannot be modeled using a Buckley-Leverett approach because flow rate is not pre-specified. A survey of the literature reveals four mathematical models that have been developed for describing the process of free-fall gravity drainage of equilibrium fluids. They are the Cardwell-Parsons-Dykstra (C-P-D) model, Nenniger-Storrow (N-S) model, Pavone-Bruzzi-Verre (P-B-V) model, and Luan Model. The accuracy of these models are found to be poor based on our comparisons with experimental data. Therefore, we have developed a new mathematical model to simulate equilibrium and non-equilibrium gravity drainage. Comparison of recovery data computed using the new model to experimental data found from both the literature and experiments conducted in our laboratory indicate that the new model can better describe the process of free-fall gravity drainage of both equilibrium and non-equilibrium fluids.

Mathematical Models

There is no mathematical model available from literature to describe non-equilibrium gravity drainage process after gas injection into fractured reservoirs (free-fall gravity

drainage). In this study, we simulate the process using mathematical models developed for equilibrium gravity drainage with modifications considering molecular diffusion during gravity drainage. We first tried to select one model among the four existing models: Nenniger-Storrow (N-S) model, Pavone-Bruzzi-Verre (P-B-V) model, and Luan Model. Unfortunately, we found none of them accurate enough to be adopted, even for equilibrium gravity drainage. Comparisons of these models are presented elsewhere.[30] Then we decided to develop a new model to simulate equilibrium and non-equilibrium gravity drainage processes. Derivation of the new model is detailed in SPE 35170.[31] Only the resultant equations are summarized here.

Based on the fact that the volumetric drainage rate is equal to the derivative of draining-phase volume in the porous media with respect to time, the following governing equation for wetting/non-wetting phase demarcator has been formulated:

$$\phi\left[S_{wi}-S_{wr}-\sqrt{\frac{F_s\phi z_D}{5t_D}}\right]\frac{dz_D}{dt_D}+\frac{\phi z_D}{3t_D}\sqrt{\frac{F_s\phi z_D}{5t_D}}-\left[1-\frac{H_D}{1-z_D}\right]=0 \tag{4.1}$$

where the dimensionless groups are defined as

$$z_D=\frac{z_d}{L} \tag{4.2}$$

$$H_D=\frac{H}{L} \tag{4.3}$$

and

$$t_D=\frac{k_e\,\Delta\rho\,g\,t}{\mu\,L} \tag{4.4}$$

Equation (4.1) is non-linear and is difficult, if not impossible, to solve analytically. Therefore, we solved the equation numerically by rearranging it into the following form:

$$\Delta z_D=\frac{-\frac{\phi z_D}{3t_D}\sqrt{\frac{F_s\phi z_D}{5t_D}}+\left[1-\frac{H_D}{1-z_D}\right]}{\phi\left[S_{wi}-S_{wr}-\sqrt{\frac{F_s\phi z_D}{5t_D}}\right]}\,\Delta t_D \tag{4.5}$$

Using initial condition of 0.001 for z_D at a very small time t_D (0.0001 for example) and a small time step Δt_D, the increment of the demarcator Δz_D can be calculated from this equation. Then z_D and t_D can be updated by

$$z_{D_{new}} = z_{D_{old}} + \Delta z_D \tag{4.6}$$

and

$$t_{D_{new}} = t_{D_{old}} + \Delta t_D \tag{4.7}$$

Repeated use of Eqs. (4.5), (4.6) and (4.7) gives a numerical solution to Eq. (4.1). Based on the position of the demarcator and the volume distribution of the liquid above the demarcator, the draining-phase recovery as a function of time is calculated utilizing Eq. (4.8).

$$R_D = \left(1 - \frac{S_{wr}}{S_{wi}}\right) z_D - \frac{2z_D}{3S_{wi}} \sqrt{\frac{F_s \phi z_D}{5t_D}} \tag{4.8}$$

Two typical solution curves are presented in Figs. 4.5-1 and 4.5-2 for $\phi = 0.1$, $S_{wr} = 0.1$, $H_D = 0.1$, and $F_s = 1$ and 0.5, respectively. It is clearly seen from Figs. 4.5-1 and 4.5-2 that the equilibrium gravity drainage process can be divided into two periods. During the first period, the demarcator drops and the total drainage rate is a combination of rate of full-pore flow and that of film flow. During the second period, the demarcator is stabilized and the total drainage rate is the rate of film flow only. It is interesting to note the effect of the correction factor to the Kozeny equation F_s (discussed in detail in reference 32) on the shape of demarcator and recovery curves indicated by the two figures. When F_s is greater, as shown in Fig. 4.5-1, the demarcator stabilizes gradually during bulk flow leaving more recoverable fluid behind for pure film flow to occur. When F_s is small, as shown in Fig. 4.5-2, the demarcator stabilizes sharply at the end of bulk flow leaving less recoverable fluid behind for pure film flow.

Non-equilibrium gravity drainage occurs when a porous medium saturated with one phase is surrounded by another phase not in equilibrium, for instance, injected gas and resident oil. In this case, the surrounding phase migrates into the porous medium due to molecular diffusion causing the IFT of the fluid in the porous medium to change with time. For example, when an oil-saturated, vertically oriented core is surrounded by CO_2 during gravity drainage, the CO_2 diffuses into the core resulting in continuous reduction of IFT between the CO_2-rich phase and the oil phase as CO_2 moves into the interior of the core. Thus the IFT at any point in the core is time dependent.

Although the new mathematical model is derived assuming that the wetting phase and non-wetting phase are in thermodynamic equilibrium, it is possible to apply the model to simulation of a non-equilibrium gravity drainage process if some modifications are made to account for the non-equilibrium effect due to diffusion. If we divide the core length into many elements along the direction of diffusion, then it is possible to apply the mathematical model to each individual element where uniform fluid properties are assigned to that element. We have developed the following step-wise procedure to simulate non-equilibrium CO_2 gravity drainage in our three cores:

1. Divide the core in the radial (horizontal) direction into 50 cylindrical elements, and estimate the concentration of the gas phase in each element at a given diffusion/drainage time;

2. Estimate the average fluid viscosity, density, IFT and capillary pressure in each element at the time based on the composition of the fluid mixture;

3. Apply the mathematical model to each element to estimate liquid recovery from the element at a given time;

4. Sum up the recoveries calculated from each element to get the total liquid recovery at a given time;

5. Update the time by adding a time step and repeat 1, 2, 3, and 4 until a desired ultimate drainage time is reached.

In order to estimate gas concentration in each element, it is necessary to solve the diffusion equation (Fick's second law). Different analytical solutions to the diffusion equation are available from literature such as Crank[31] and Carslaw and Jaeger[32]. It is not clear yet as which of the solutions is more suitable for analyzing gas diffusion into reservoir matrix. To avoid difficulties involved in programming these solutions, a simple numerical solution to the diffusion equation is used in this study. It has been found that the numerical result matches the analytical solution given by Crank[32] when the time step is less than 0.5 day for a diffusion coefficient less than 10^{-7} cm^2/s. This comparison is shown in Fig. 4.5-3. The numerical procedure to the solution is detailed in reference 31.

Comparisons

Equilibrium Gravity Drainage. The new mathematical model is derived assuming constant capillary pressure at the demarcator, i.e., the wetting phase and non-wetting phase are in thermodynamic equilibrium. This model is compared with existing models and 20 sets of experimental drainage data obtained under thermodynamic equilibrium. In these experiments, the IFT varies between 76 and 0.1 mN/m, the density difference changes from 1.25 to 0.11 g/cc, the effective permeability to the wetting phase covers a wide range, from 6,602 Darcies to 6.1 mD, porosity from 42.72% to 18.4 %, and connate water saturation from 0 to 15.8%. Fig. 4.5-4 shows comparisons of model calculated and observed C_1/C_7 recoveries from a Fontainebleau sandstone core.[20] Other comparisons similar to Fig. 4.5-4 have been presented in a separate document[30]. These comparisons indicate that the new model yields better accuracy than other models. The Cardwell-Parsons-Dykstra model and Nenniger-Storrow (N-S) model consider a moving demarcator, while the Pavone-Bruzzi-Verre (P-B-V) model and Luan model assume fixed a demarcator at the bottom of the porous media, which is not a true physical representation of drainage behavior. The C-P-D model neglects a capillary term that appears in the governing equation. The N-S model is an approximate series solution, and the accuracy depends on number of terms (the paper provides expressions for only three terms). The P-B-V model was obtained by assuming a straight-line relative permeability

and a logarithmic capillary pressure curve, which also may not be representative of the true behavior. It is believed that these unrealistic assumptions used in model development cause inaccuracies of these models in describing free-fall gravity drainage processes.

Non-equilibrium Gravity Drainage. The concentration of CO_2 in the simulated fracture (annular space around core sample) was estimated based on an Equation of State (EOS):

$$c_f = \frac{p}{zRT} \tag{4.9}$$

CO_2 concentration in each matrix element was obtained by multiplying c_f by dimensionless concentration calculated from the numerical solution to the diffusion equation presented in Appendix B. Then EOS was used again to determine volume of CO_2 in each element. Oil production due to horizontal diffusion was assumed to be equal to the volume of CO_2 that had diffused into the rock.

The viscosity data provided by Lansangan and Smith[2] for CO_2/West Texas oil was utilized in our model. Density and IFT data used in the model were from our measurements as presented in the previous sections. The capillary pressure threshold was calculated using Eq. 4.10.

$$H = \frac{0.2\sigma}{\Delta\rho\ g}\sqrt{\frac{\phi}{k_e}} \tag{4.10}$$

Based on Renner's measurements[34], the molecular diffusion coefficient of CO_2 in a decane-saturated Berea core at 100 °F and 850 psig varies from $5.05\text{x}10^{-5}$ to $1.08\text{x}10^{-4}$ cm^2/s. The molecular diffusion coefficient of CO_2 in the pure decane may be back calculated from the following equation:

$$D = \frac{D_0}{F\phi} \tag{4.11}$$

Using $0.81/\phi^2$ as an approximation to the formation factor F and 0.20 porosity for the Berea core, the molecular diffusion coefficient of CO_2 in the pure decane is estimated to be $D_0=2\text{x}10^{-4}$ to $4\text{x}10^{-4}$ cm^2/s. This value may be optimistic if applied to CO_2/STO system at 138 °F and 2,000 psig. In the petroleum industry, a practical value of $D_0=2\text{x}10^{-5}$ cm^2/s for a molecular diffusion coefficient for reservoir liquids is commonly used in simulation of CO_2 miscible flooding.[35] However, we have found that the $D_0=2\text{x}10^{-5}$ cm^2/s results in an over-estimation of oil recovery by our mathematical model. The oil recoveries from our CO_2 gravity drainage experiments were matched by our mathematical model when the molecular diffusion coefficient was tuned to $D_0=6\text{x}10^{-7}$ cm^2/s.

Figure 4.5-5 demonstrates the comparison of our experimental data with the recovery curve calculated by the mathematical model for a high permeability Berea core. Figure 4.5-6 shows the comparison of our experimental data with the recovery curve calculated

by the mathematical model for the low permeability Berea core. Figure 4.5-7 illustrates the comparison of our experimental data with the recovery curve calculated by the mathematical model for the low permeability Spraberry core.

Conclusions

1. A literature survey reveals that four mathematical models have been developed by previous investigators for describing free-fall gravity drainage of equilibrium phases in porous media. They are C-P-D Model, N-S Model, P-B-V Model and Luan Model. Comparison of wetting phase recoveries calculated by these models with experimental data indicates these models to be inaccurate. Discrepancies are believed to be due to unrealistic assumptions made in formulation of these models.

2. Based on Darcy's law and film flow theory, a new mathematical model has been developed to describe free-fall gravity drainage with equilibrium fluids. Comparisons of wetting phase recoveries given by the new model with 20 sets of experimental data obtained under thermodynamic equilibrium show better accuracy of the model over existing models.

3. The diffusion equation has been solved numerically to estimate gas concentration in the porous media. A procedure has been developed to couple equilibrium gravity drainage with diffusion in order to describe non-equilibrium gravity drainage. Using this procedure and empirical correlations for fluid properties, experimental data obtained under thermodynamic non-equilibrium conditions has been matched.

Nomenclature

c_f	=	fractional concentration, mol/cm^3.
D	=	effective diffusion coefficient, cm^2/s.
D_0	=	molecular diffusion coefficient, cm^2/s.
F	=	formation factor, dimensionless.
F_s	=	correction factor to Kozeny equation.
G	=	gravitational acceleration, cm/s^2.
H	=	capillary pressure threshold, cm.
H_D	=	dimensionless capillary pressure threshold.
k_e	=	effective permeability, md.
L	=	core length, cm.
p	=	pressure, atm.
R	=	universal gas constant, 8.314 J-mol^{-1}-K^{-1}
R_D	=	dimensionless fluid recovery, OOIP
S_{wi}	=	initial wetting phase saturation, fraction.
S_{wr}	=	residual wetting phase saturation, fraction.
T	=	time, s.
t_D	=	dimensionless time.

Δt = time step size, s.
z_d = demarcator depth, cm.
z_D = dimensionless demarcator depth.
$\Delta\rho$ = density difference, g/cm^3.
μ = viscosity, cp.
σ = interfacial tension, dyne/cm.
ϕ = porosity, fraction.

References

1. Beliveau, D., Payne, D.A., and Mundry, M.: "Waterflood and CO_2 Flood of the Fractured Midale Field," *Journal of Petroleum Engineering*, September 1993, 881.
2. Lansangan, R.M. and Smith, J.L.: "Viscosity, Density and Composition Measurements of CO_2/West Texas Oil Systems," *SPE Reservoir Engineering*, August 1993.
3. King, F.H.: "Principles and Conditions of the Movements of Ground Water," Annual Report, USGS (1899), **19**.
4. Leverett, M.C.: "Capillary Behavior in Porous Solids," *Trans. AIME* (1941), **142**, 152.
5. Katz, D.L.: "Possibilities of Secondary Recovery for the Oklahoma City Wilcox Sand," *Trans. AIME* (1942), **146**, 28.
6. Stahl, R.F., Martin, W.A., and Huntington, R.L.: "Gravitational Drainage of Liquids from Unconsolidated Wilcox Sand," *Petroleum Technology*, January 1943.
7. Elkins, L.F., French, R.W., and Glenn, W.E.: "Lance Creek Sundance Reservoir Performance --- a Unitized Pressure-Maintenance Project," *Petroleum Tech.*, July 1948.
8. Cardwell, W.T. and Parsons, R.L.: "Gravity Drainage Theory" *Trans.AIME* (1949), **179**, 199.
9. Terwilliger, P.L., Wilsey, L.E., Hall, H.N., Bridges, P.M., and Morse, R.A.: "An Experimental and Theoretical Investigation of Gravity Drainage Performance," *Petroleum Transactions, AIME* (1951), **192**.
10. Buckley, S.E. and Leverett, M.C.: "Mechanism of Fluid Displacement in Sands," *Trans. AIME* (1942), **146**, 107.
11. Nenniger, E. and Storrow, J.A.: "Drainage of Packed Beads in Gravitational and Centrifugal-Force Fields," *AIChE* (1958), **4**, No. 3, 305.
12. Essley, P.L., Hancock, G.L., and Jones, K.E.: "Gravity Drainage Concepts in a Steeply Dipping Reservoir," paper SPE 1029-G, 1958.
13. Templeton, E.E. and Nielsen, R.E.: "A Study of Gravity Counterflow Segregation," *SPE Journal*, June 1962.
14. Dumore, J.M. and Schols, R.S.: "Drainage Capillary - Pressure Functions and the Influence of Connate Water," *SPE Journal*, October 1974.
15. Dykstra,H.: "The Prediction of Oil Recovery by Gravity Drainage," *Journal of Petroleum Technology*, May 1978.
16. Hagoort, J.: "Oil Recovery by Gravity Drainage," *SPE Journal*, June 1980.
17. Haldorsen, H.H., Rego, C.A., Chang, D.M., Mayson, H.J., and Creveling, D.M. Jr.:

"An Evaluation of the Prudhoe Bay Gravity Drainage Mechanism by Complementary Techniques," paper SPE 13651, presented at the
18. SPE California Regional Meeting, held in Bakersfield, California, March 27-29, 1985.
19. Nectoux, A.: "Equilibrium Gas Oil Drainage: Velocity, Gravitational and Compositional Effects," paper presented at the 4th European Symposium on Enhanced Oil Recovery, held October 27-29, 1987 in Hamburg, 779.
20. Jacquin, Ch., Legait, B., Martin, J.M., Nectoux, A., Anterion, F., and Rioche, M.: "Gravity Drainage in a Fissured Reservoir with Fluids not in Equilibrium," *Journal of Petroleum Science and Engineering* (1989) **2**, 217.
21. Pavone, D., Bruzzi, P. and Verre, R.: "Gravity Drainage at Low Interfacial Tension," paper presented at the 5th European Symposium on Enhanced Oil Recovery, held October 27-29, 1989 in Budapest, 165.
22. Stensen, J.A., Skange, A. Monstad, P.,and Graue, A.: "The Effect of Interfacial Tension on Gas Gravity Drainage," paper presented at the 2nd North Sea Chalk Symposium, held June 11-12, 1990 in Copenhagen, Denmark.
23. Suffridge, E.E. and Renner, T.A.: "Diffusion and Gravity Drainage Tests to Support the Development of a Dual Porosity Simulator," paper presented at the 6th European IOR-Symposium, held May 21-23, 1991 in Stavanger, Norway.
24. da Vilva, F.V. and Meyer, B.: "Improved Formulation for Gravity Segregation in Naturally Fractured Reservoirs," paper presented at the 6th European IOR-Symposium, held May 21-23, 1991 in Stavanger, Norway.
25. Schechter, D.S., Zhou, D., and Orr, F.M. Jr.: "Low IFT Gravity Drainage and Imbibition," *Journal of Petroleum Science and Engineering* (November 1994), 283.
26. Luan, Z.: "Some Theoretical Aspects of Gravity Drainage in Naturally Fractured Reservoirs," aper SPE 28641, presented at the 69th Annual Technical Conference and Exhibition of SPE, held September 25-28, 1994 in New Orleans, Louisiana.
27. Espie, A.A., Brown, C.E., Narayanan, K.R. and Wilcox, T.C.: "A Laboratory Investigation of Gravity Drainage/Waterflood Interaction in Prudhoe Bay,"paper SPE 28614, presented at the 69th Annual Technical Conference and Exhibition of SPE, held September 25-28, 1994 in New Orleans, Louisiana.
28. Catalan, L.J.J., Dullien, F.A.L., and Chatzis, I.: "The Effects of Wettability and Heterogeneities on the Recovery of Waterflood Residual Oil with Low Pressure Inert Gas Injection Assisted by Gravity Drainage," *SPE Advanced Tech. Series*, **2**, No. 2, 1994.
29. Blunt, M., Zhou, D., and Fenwick, D.: "Three Phase Flow and Gravity Drainage in Porous Media," paper submitted to *Transport in Porous Media* for publication, May 1994.
30. Oyno, L., Uleberg, K., and Whitson, C. H.: "Dry Gas Injection Fractured Chalk Reservoirs -- An Experimental Approach," paper SCA 9527 presented at the 1995 SCA Conference, San Francisco, California, August 20-22, 1995.
31. Guo, B.: "Modeling of Gravity Drainage Under Constant and Varying Capillary Pressure," proceedings of Naturally Fractured Reservoir Forum, New Mexico Institute of Mining and Technology, March 2, 1995.
32. Schechter, D.S. and Guo, B.: "Mathematical Modeling of Gravity Drainage after Gas Injection into Fractured Reservoirs," paper SPE 35170 presented at the SPE Improved

Oil Recovery Symposium held in Tuls, Oklahoma April 22-24, 1996.
33. Crank, J.: *The Mathematics of Diffusion*, second edition, Oxford University Press, New York City (1975).
34. Carslaw, H.S. and Jaeger, J.C.: *Conduction of Heat in Solids*, second edition, Oxford University Press, New York City (1959).
35. Lopez de Ramos, A.L.: *Capillary-Enhanced Diffusion of CO_2 in Porous Media*, Ph.D. thesis, University of Tulsa, Tulsa, Oklahoma,1993.
36. Stalkup, F.I., Jr.: *Miscible Displacement*, SPE Textbook Series, Dallas, 1984.
37. Widom, B.: "Phase Equilibrium and Interfacial Structure," *Chemical Society Review* (1985), 121-139.

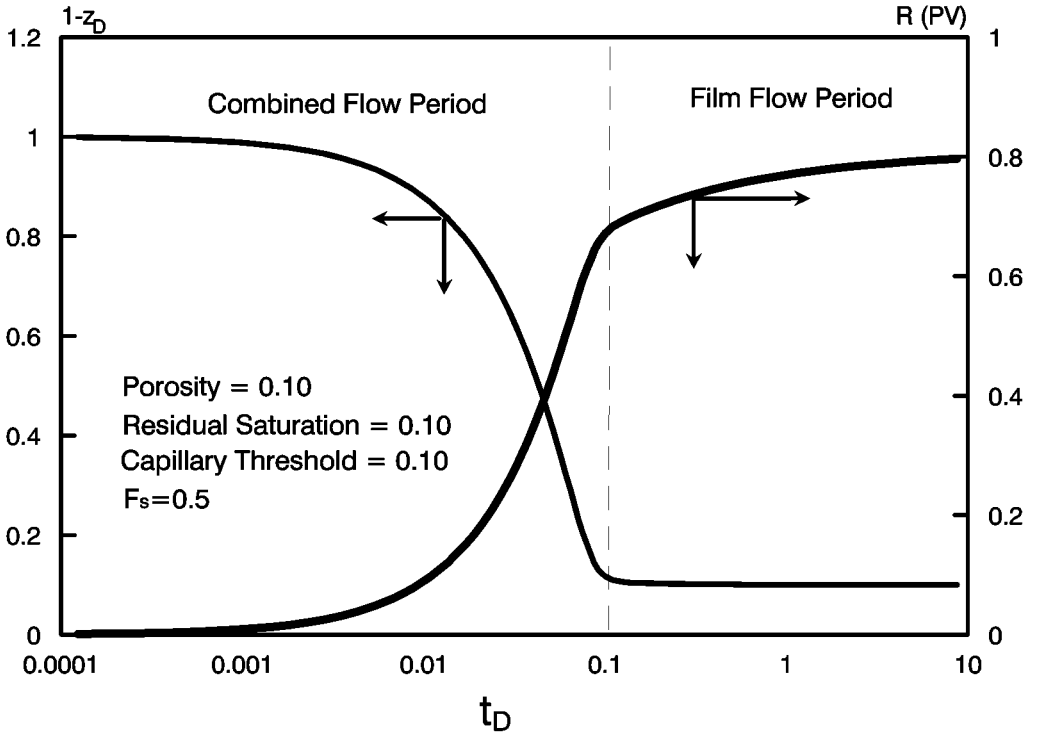

Fig. 4.5-1 —Solution to demarcator and (z_D) and recovery (R) for Fs =1

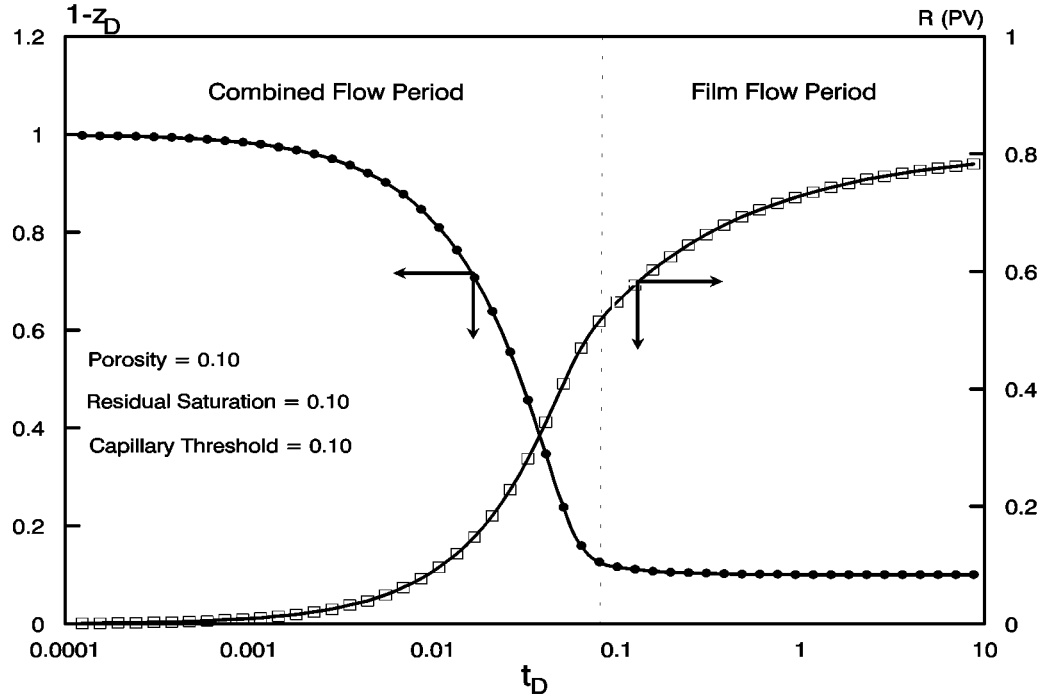

Fig. 4.5-2 —A typical solution for demarcator (z_D) movement and recovery (R)

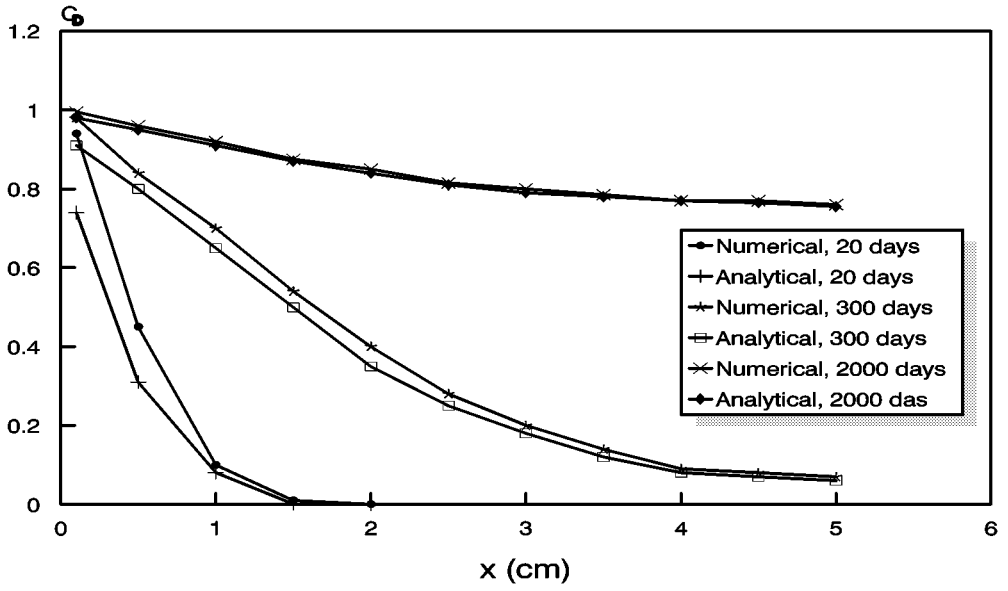

Fig. 4.5-3 —Model calculated dimensionless gas concentration diffusing into rock matrix from fracture faces

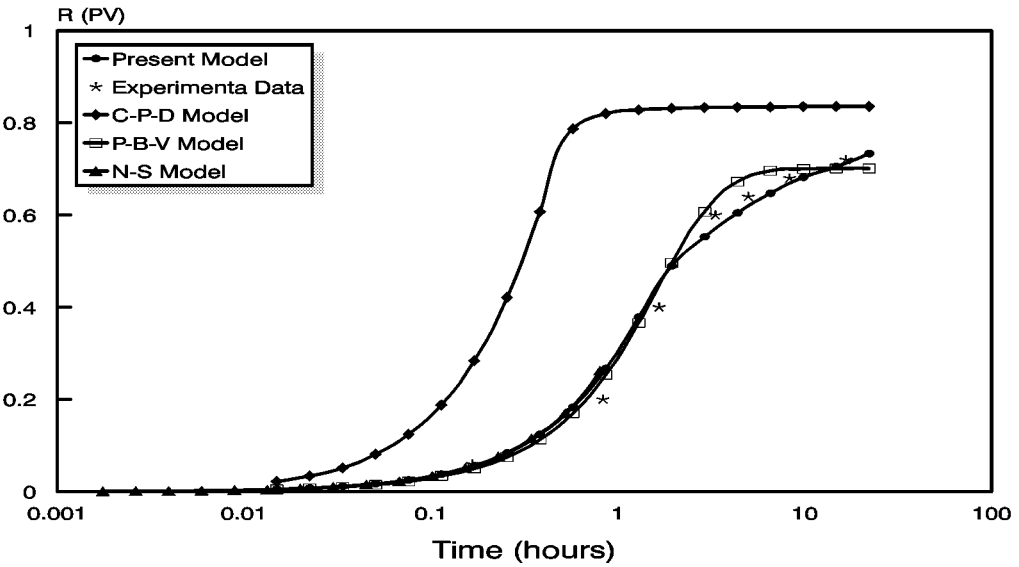

Fig. 4.5-4 —Comparison of calculated recoveries with experimental data

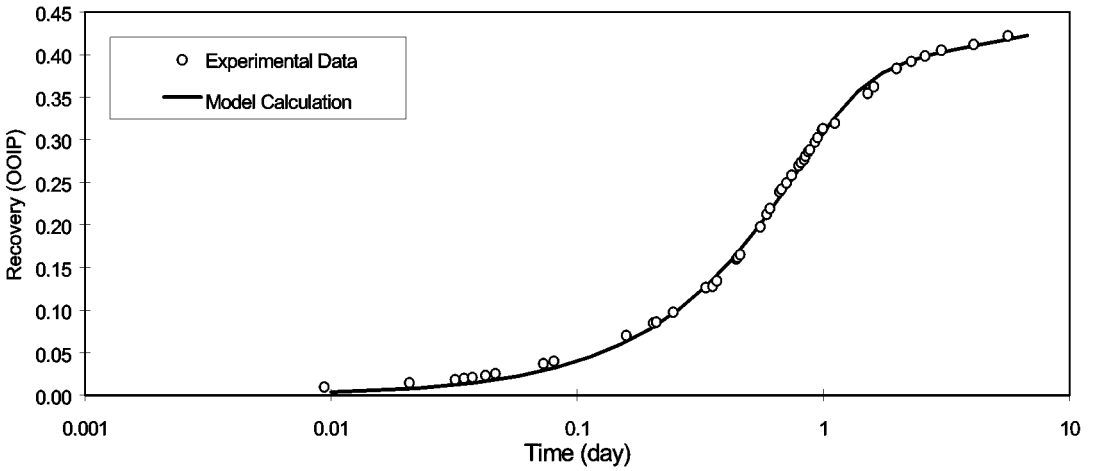

Fig. 4.5-5 —Comparison of calculated recovery with experimental data, CO_2/oil gravity drainage in a 500 md Berea core

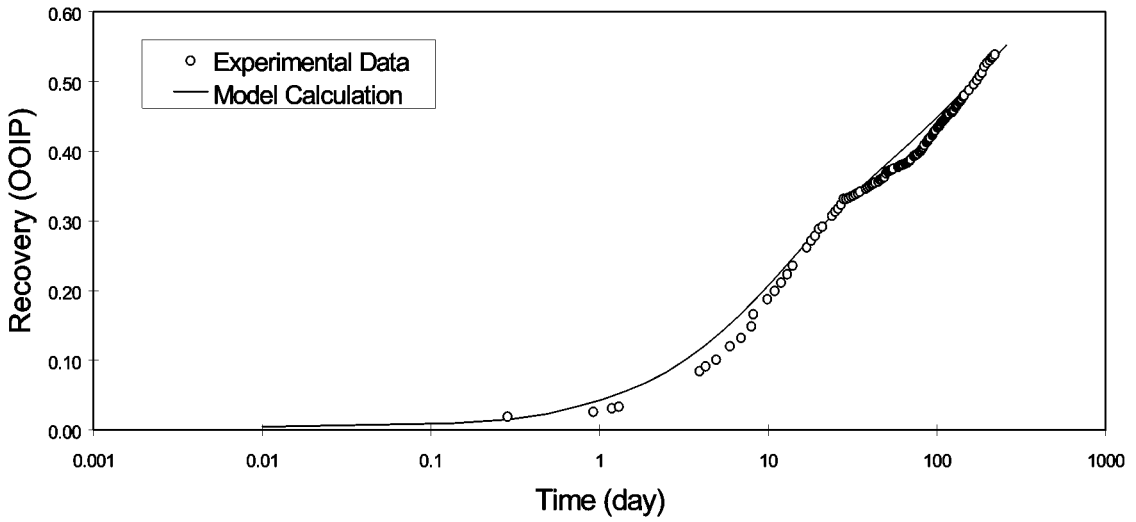

Fig. 4.5-6 —Comparison of calculated recovery with experimental data, CO_2/oil gravity drainage in a 50 md Berea core

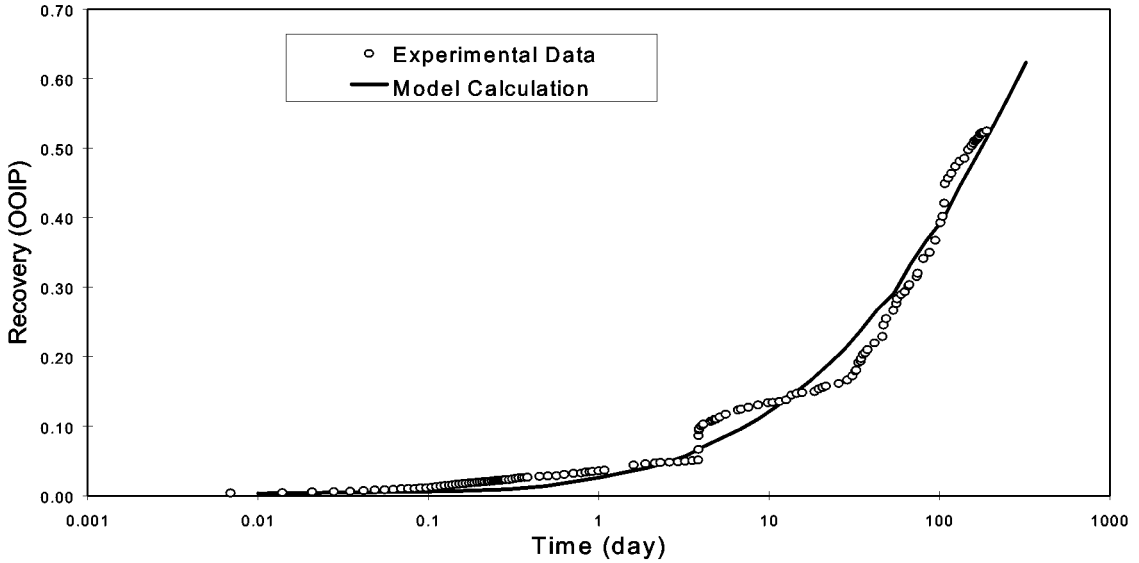

Fig. 4.5-7 —Comparison of calculated recovery with experimental data, CO_2/oil gravity drainage in a 0.01 md Spraberry core